Minho Lee Akira Hirose Zeng-Guang Hou
Rhee Man Kil (Eds.)

LNCS 8226

Neural Information Processing

20th International Conference, ICONIP 2013
Daegu, Korea, November 2013
Proceedings, Part I

Springer

Lecture Notes in Computer Science 8226

Commenced Publication in 1973
Founding and Former Series Editors:
Gerhard Goos, Juris Hartmanis, and Jan van Leeuwen

Editorial Board

David Hutchison
Lancaster University, UK

Takeo Kanade
Carnegie Mellon University, Pittsburgh, PA, USA

Josef Kittler
University of Surrey, Guildford, UK

Jon M. Kleinberg
Cornell University, Ithaca, NY, USA

Alfred Kobsa
University of California, Irvine, CA, USA

Friedemann Mattern
ETH Zurich, Switzerland

John C. Mitchell
Stanford University, CA, USA

Moni Naor
Weizmann Institute of Science, Rehovot, Israel

Oscar Nierstrasz
University of Bern, Switzerland

C. Pandu Rangan
Indian Institute of Technology, Madras, India

Bernhard Steffen
TU Dortmund University, Germany

Madhu Sudan
Microsoft Research, Cambridge, MA, USA

Demetri Terzopoulos
University of California, Los Angeles, CA, USA

Doug Tygar
University of California, Berkeley, CA, USA

Gerhard Weikum
Max Planck Institute for Informatics, Saarbruecken, Germany

Minho Lee Akira Hirose Zeng-Guang Hou
Rhee Man Kil (Eds.)

Neural Information Processing

20th International Conference, ICONIP 2013
Daegu, Korea, November 3-7, 2013
Proceedings, Part I

Springer

Volume Editors

Minho Lee
Kyungpook National University
1370 Sankyuk-Dong, Puk-Gu, Taegu 702-701, Korea
E-mail: mholee@knu.ac.kr

Akira Hirose
The University of Tokyo
7-3-1 Hongo, Bunkyo-ku, Tokyo 113-8656, Japan
E-mail: ahirose@ee.t.u-tokyo.ac.jp

Zeng-Guang Hou
Chinese Academy of Sciences, Institute of Automation
Key Laboratory of Complex Systems and Intelligence Science
Beijing 100190, China
E-mail: zengguang.hou@ia.ac.cn

Rhee Man Kil
Sungkyunkwan University
2066, Seobu-ro, Jangan-gu, Suwon 440-746, Korea
E-mail: rmkil@skku.edu

ISSN 0302-9743 e-ISSN 1611-3349
ISBN 978-3-642-42053-5 e-ISBN 978-3-642-42054-2
DOI 10.1007/978-3-642-42054-2
Springer Heidelberg New York Dordrecht London

Library of Congress Control Number: 2013951838

CR Subject Classification (1998): I.5, I.4, I.2, F.1, H.3, H.4, F.2, G.3, J.3, C.3

LNCS Sublibrary: SL 1 – Theoretical Computer Science and General Issues

© Springer-Verlag Berlin Heidelberg 2013

This work is subject to copyright. All rights are reserved by the Publisher, whether the whole or part of the material is concerned, specifically the rights of translation, reprinting, reuse of illustrations, recitation, broadcasting, reproduction on microfilms or in any other physical way, and transmission or information storage and retrieval, electronic adaptation, computer software, or by similar or dissimilar methodology now known or hereafter developed. Exempted from this legal reservation are brief excerpts in connection with reviews or scholarly analysis or material supplied specifically for the purpose of being entered and executed on a computer system, for exclusive use by the purchaser of the work. Duplication of this publication or parts thereof is permitted only under the provisions of the Copyright Law of the Publisher's location, in ist current version, and permission for use must always be obtained from Springer. Permissions for use may be obtained through RightsLink at the Copyright Clearance Center. Violations are liable to prosecution under the respective Copyright Law.
The use of general descriptive names, registered names, trademarks, service marks, etc. in this publication does not imply, even in the absence of a specific statement, that such names are exempt from the relevant protective laws and regulations and therefore free for general use.
While the advice and information in this book are believed to be true and accurate at the date of publication, neither the authors nor the editors nor the publisher can accept any legal responsibility for any errors or omissions that may be made. The publisher makes no warranty, express or implied, with respect to the material contained herein.

Typesetting: Camera-ready by author, data conversion by Scientific Publishing Services, Chennai, India

Printed on acid-free paper

Springer is part of Springer Science+Business Media (www.springer.com)

Preface

This volume is part of the three-volume proceedings of the 20th International Conference on Neural Information Processing (ICONIP 2013), which was held in Daegu, Korea, during November 3–7, 2013. ICONIP is the annual conference of the Asia Pacific Neural Network Assembly (APNNA). This series of conferences has been held annually since ICONIP 1994 in Seoul and has become one of the premier international conferences in the areas of neural networks.

Over the past few decades, the neural information processing community has witnessed tremendous efforts and developments from all aspects of neural information processing research. These include theoretical foundations, architectures and network organizations, modeling and simulation, empirical study, as well as a wide range of applications across different domains. Recent developments in science and technology, including neuroscience, computer science, cognitive science, nano-technologies, and engineering design, among others, have provided significant new understandings and technological solutions to move neural information processing research toward the development of complex, large-scale, and networked brain-like intelligent systems. This long-term goal can only be achieved with continuous efforts from the community to seriously investigate different issues of the neural information processing and related fields. To this end, ICONIP 2013 provided a powerful platform for the community to share their latest research results, to discuss critical future research directions, to stimulate innovative research ideas, as well as to facilitate multidisciplinary collaborations worldwide.

ICONIP 2013 received tremendous submissions authored by scholars coming from 30 countries and regions across six continents. Based on a rigorous peer review process, where each submission was evaluated by at least two qualified reviewers, about 270 high-quality papers were selected for publication in the prestigious series of *Lecture Notes in Computer Science*. These papers cover all major topics of theoretical research, empirical study, and applications of neural information processing research.

In addition to the contributed papers, the ICONIP 2013 technical program included a keynote speech by Shun-Ichi Amari (RIKEN Brain Science Institute, Japan), 5 plenary speeches by Yoshua Bengio (University of Montreal, Canada), Kunihiko Fukushima (Fuzzy Logic Systems Institute, Fukuoka, Japan), Soo-Young Lee (Brain Science Research Center, KAIST, Korea), Naftali Tishby (The Hebrew University, Jerusalem, Israel) and Zongben Xu (Xi'an Jiatong University, China). This conference also featured invited presentations, regular sessions with oral and poster presentations, and special sessions and tutorials on topics of current interest.

Our conference would not have been successful without the generous patronage of our sponsors. We are most grateful to our sponsors Korean Brain Research

Institute, Qualcomm Korea. We would also like to express our sincere thanks to the International Neural Network Society, European Neural Network Society, Japanese Neural Network Society, Brain Engineering Society of Korea, and The Korean Society for Cognitive Science for technical sponsorship.

We would also like to sincerely thank honorary chair Shun-ichi Amari, Soo-Young Lee, the members of the Advisory Committee, the APNNA Governing Board and past presidents for their guidance, the organizing chair Hyeyoung Park, the members of the Organizing Committee, special sessions chairs, Publication Committee and publicity chairs, for all their great efforts and time in organizing such an event. We would also like to take this opportunity to express our deepest gratitude to the members of the Program Committee and all reviewers for their professional review of the papers. Their expertise guaranteed the high quality of the technical program of the ICONIP 2013!

Furthermore, we would also like to thank Springer for publishing the proceedings in the prestigious series of *Lecture Notes in Computer Science*. We would, moreover, like to express our heartfelt appreciation to the keynote, plenary, panel, and invited speakers for their vision and discussions on the latest.

Finally, we would like to thank all the speakers, authors, and participants for their great contribution and support that made ICONIP 2013 a huge success.

This work was supported by the National Research Foundation of Korea Grant funded by the Korean Government.

November 2013

Minho Lee
Akira Hirose
Rhee Man Kil
Zeng-Guang Hou

Organization

Honorary Chair

Shun-ichi Amari	RIKEN, Japan
Soo-Young Lee	KAIST, Korea

General Chair

Minho Lee	Kyungpook National University, Korea

Program Chair

Akira Hirose	The University of Tokyo, Japan
Zeng-Guang Hou	The Chinese Academy of Sciences, China
Rhee Man Kil	Sungkyunkwan University, Korea

Organizing Chair

Hyeyoung Park	Kyungpook National University, Korea

Workshop Chair

Daijin Kim	POSTECH, Korea
Kyunghwan Kim	NT Research, Korea
Seong-Whan Lee	Korea University, Korea

Special Session Chair

Sung-Bae Cho	Yonsei University, Korea
Seiichi Ozawa	Kobe University, Japan
Liqing Zhang	Shanghai Jiao Tong University, China

Tutorial Chair

Seungjin Choi	POSTECH, Korea

Publication Chair

Yoonsuck Choe	Texas A&M University, USA
Hyung-Min Park	Sogang University, Korea
Seong-Bae Park	Kyungpook National University, Korea

Publicity Chair

Kazushi Ikeda	NAIST, Japan
Chi-Sing Leung	University of Hong Kong, Hong Kong
Shaoning Pang	Unitec Institute of Technology, New Zealand

Registration Chair

Min-Young Kim	Kyungpook National University, Korea

Financial Chair

Sang-Woo Ban	Dongguk University, Korea

Local Arrangement Chair

Doo-Hyun Choi	Kyungpook National University, Korea
Jong-Seok Lee	Yonsei University, Korea
Rammohan Mallipeddi	Kyungpook National University, Korea

Advisory Committee

Jonathan H. Chan, Thailand
Wlodzislaw Duch, Poland
Kunihiko Fukushima, Japan
Tom Gedeon, Australia
Aike Guo, China
Akira Iwata, Japan
Nik Kasabov, New Zealand
Irwin King, Hong Kong
Noboru Onishi, Japan
Ron Son, USA
Il Hong Suh, Korea
Shiro Usui, Japan
DeLiang Wang, USA
Lipo Wang, Singapore
Jun Wang, Hong Kong
Lei Xu, Hong Kong
Takeshi Yamakawa, Japan
Byoung-Tak Zhang, Korea
Li-Ming Zhang, China

Program Committee Members

Tani Jun
Soo-Young Lee
Sung-Bae Cho
Sungmoon jeong
Kyung-Joong Kim
C.K. Loo
Nung Kion Lee
Shan He
Dae-Shik Kim
Rubin Wang
Xin Yao
S. Ma
Honghai Liu
Joarder Kamruzzaman
Mallipeddi Rammohan
Zhirong Yang
Anto Satriyo Nugroho
Nikola Kasabov

Jonghwan Lee
Yaochu Jin
DaeEun Kim
Tingwen Huang
Fangxiang Wu
Dongbing Gu
Hongli Dong
Cesare Alippi
Kyung Hwan Kim
Lae-Jeong Park
Sang-Woong Lee
Sabri Arik
Chee-Peng Lim
Haibo He
Dat Tran
Kee-Eung Kim
Seungjin Choi
Robert (Bob) McKay
Xueyi (Frank) Wang
Jennie Si
Markus Koskela
Ivo Bukovský
Ryo Saegusa
El-Sayed El-Alfy
Hyeyoung Park
Bunthit Watanapa
Vinh Nguyen
Kalyana C. Veluvolu
Mufti Mahmud
Gil-Jin Jang
Hyung-Min Park
Jeounghoon Kim
Rhee Man Kil
Sang-Woo Ban
Masa Takatsuka
Chee Seng Chan
Pau-Choo Chung
Uvais Qidwai
Dong-Joo Kim
JongJin Lim
Sungoh Kwon
Long Cheng
Akitoshi Hanazawa
Andrzej Cichocki
Sheng Li
Oclay Kursun
Michel Verleysen
Peter Erdi
Qingsong Song
Bin Li
Huaguang Zhang
Derong Liu
Eric Matson
Mehdi Roopaei
Jacek Ma'ndziuk
Yang Shi
Zhiwu Lu
Xiaofeng Liao
Zhigang Zeng
Ding-Xuan Zhou
James Tin-Yau Kwok
Hsuan-Tien Lin
Osman Elgawi
Chao Zhang
Bo Shen
Nistor Grozavu
Younès Bennani
Jinde Cao
Li-Po Wang
Justin Dauwels
Andrew Leung
Bao-Liang Lu
Changyin Sun
Hong Yan
Abdesselam Bouzerdoum
Emili Balaguer Ballester
H. Tang
Roland Goecke
Jose Alfredo Ferreira Costa
Shri Rai
Kuntal Ghosh
TaeHyun Hwang
Alexander Rast
Yangming Li
Akira Hirose
Akira Iwata
Ko Sakai
Koichiro Yamauchi

Atsushi Shimada
Eiji Uchino
Hayao Shouno
Hayaru Shouno
Heizo Tokutaka
Hideki Asoh
Hiroaki Gomi
Hiroshi Dozono
Hiroshi Kage
Hiroshi Yamakawa
Hiroyuki Nakahara
Ikuko Nishikawa
Jinglu Hu
Jun Nishii
Katsumi Tateno
Katsunari Shibata
Kazuho Watanabe
Kazushi Ikeda
Kazuyuki Samejima
Keisuke Kameyama
Kenichi Tanaka
Kenichiro Miura
Kenji Doya
Kiyohisa Natsume
Masafumi Hagiwara
Michio Niwano
Mingcong Deng
Naoyuki Sato
Noboru Ohnishi
Seiichi Ozawa
Shin Ishii
Shinichiro Kano
Shunji Satoh
Shunshoku Kanae
Takashi Morie
Takashi Omori
Takeshi Aihara
Takio Kurita
Tao Ban
Tetsuya Yagi
Tohru Nitta
Tom Shibata
Toshiaki Omori
Toshihisa Tanaka
Yen-Wei Chen
Yoko Yamaguchi
Yoshikazu Washizawa

Table of Contents – Part I

Table of Contents – Part II

Table of Contents – Part III

Holistic Processing Is Not Always a Property of Right Hemisphere Processing- Evidence from Computational Modeling of Face Recognition

Bruno Galmar and Janet Hui-wen Hsiao

Department of Psychology, University of Hong Kong
Pokfulam Road, Hong Kong SAR
{brunogal,jhsiao}@hku.hk

Abstract. The hemispheric asymmetry literature traditionally posits that holistic processing (HP) is a property of right hemisphere (RH) processing. Nevertheless, a counterexample was recently found: for Chinese character recognition expertise, studies showed reduced HP (as measured in the composite task) and increased RH lateralization, revealing that these two effects may be separate processes. With a computational model of face recognition, in which we implement a theory of hemispheric asymmetry in perception that posits a low spatial frequency bias in the RH and a high spatial frequency bias in the left hemisphere (i.e., the Double Filtering by Frequency Theory of Ivry and Robertson), here we show that when the face recognition task relies purely on featural information, there is a negative correlation between HP and RH lateralization: HP increases whereas RH lateralization decreases with increasing stimulus dissimilarity. In contrast, when the face recognition task relies purely on configural information, there is a strong positive correlation between HP and RH lateralization: both HP and RH lateralization increase with increasing stimulus dissimilarity. These results suggest that HP and RH lateralization are separate processes that can be influenced differentially by task requirements.

Keywords: Holistic processing, hemispheric lateralization, face processing, connectionist modeling.

1 Introduction

Holistic processing (HP) of faces refers to the phenomenon of viewing faces as a whole instead of a set of parts. This HP effect is thought be a marker of human expertise in face processing [1]. In addition to the HP effect, face processing has been shown to involve right hemisphere (RH) lateralization, as indicated by the left side bias (LSB) effect: a chimeric face made from two left half faces from the viewer's perspective is usually judged more similar to the original face than one made from two right half faces [2,3]. In addition, fMRI studies show that an area inside the fusiform gyrus (*fusiform face area*) responds selectively to faces with larger activation in the RH than the left hemisphere (LH) [4]; ERP data also show that faces elicit larger N170 than other types of objects, especially in the RH [5].

M. Lee et al. (Eds.): ICONIP 2013, Part I, LNCS 8226, pp. 1–8, 2013.
© Springer-Verlag Berlin Heidelberg 2013

The HP effect has been shown to be linked to brain activation in face selective areas especially in the RH [6,7]. It has also been shown that the increase in HP after artificial object recognition training is correlated with right fusiform area activity [8]. These results are consistent with the hemispheric asymmetry literature that posits a holistic/analytic dichotomy between RH and LH processing [9], and suggest that HP and RH lateralization would go together. Nevertheless, a counterexample was recently found: Chinese character recognition experts have reduced HP and increased RH lateralization in processing Chinese characters compared with novices [10]. This effect suggests that holistic processing and RH lateralization may be separate processes that do not always go together.

Faces and Chinese characters differ in both featural and configural dimensions. In the featural dimension, faces consist of common features (i.e., the eyes, nose, and mouth) and the features of different faces usually look similar to each other; in contrast, Chinese character recognition involves discriminating different combinations of more than two hundred basic stroke patterns [11], which usually look dissimilar to each other. In the configural dimension, second-order spatial relations (i.e., distances) between face components have been shown to be more important in face recognition than in the recognition of other visual object classes [12], whereas this configural information is not important in Chinese character recognition, since changes in distance among character components do not change the character identity [13]. The difference between face and Chinese character recognition in their reliance on configural and featural information may explain the different relationships between HP and RH lateralization that were found between them. We hypothesize that HP and RH lateralization do not always go together, and it depends on the task requirements in either the featural or the configural dimension. We test this hypothesis by using faces that differ purely in configuration or purely in features in a face recognition task. We adopt a computational modeling approach. We introduce our model below.

2 Modeling

2.1 Hemispheric Processing Model

The model (Figure 1) is an instance of the intermediate convergence model of face recognition [14]. This model uses Gabor responses over the input images to simulate neural responses of cells in the early visual area, and Principal Component Analysis (PCA) to simulate possible information extraction processes beyond the early visual area. This PCA representation is then fed as the input to a two-layer feed-forward neural network. In addition, the model implements a theory of hemispheric asymmetry in perception, Double Filtering by Frequency theory (DFF) [15]. The theory posits that visual information coming into the brain goes through two frequency-filtering stages. The first stage involves attentional selection of a task-relevant frequency range. At the second stage, the LH amplifies high spatial frequency (HSF) information, while the RH amplifies low spatial frequency (LSF) information. For the second stage, we implemented two conditions. In the DFF condition (see Fig.1), the differential frequency bias in the two hemispheres is implemented by using two sigmoid functions assigning different weights to the Gabor responses in the two hemispheres. In the baseline condition, we set all weights to the Gabor responses to 1 so that there is no differential frequency bias between the two hemispheres.

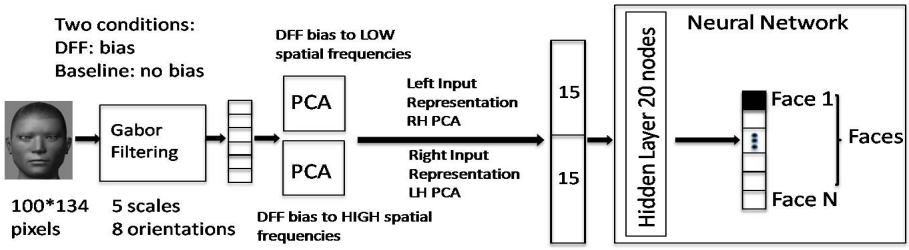

Fig. 1. Model of face recognition implementing a theory of hemispheric asymmetry in perception, the Double Filtering by Frequency (DFF) theory

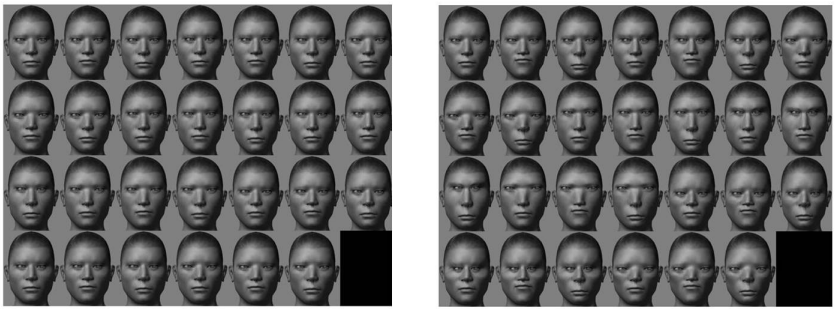

Fig. 2. Configural datasets. (a) baseline spacing of facial features, (b) increased spacing of facial features.

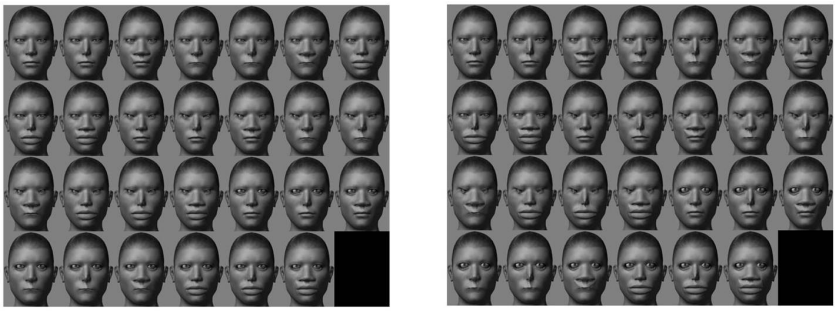

Fig. 3. Featural datasets. (a) baseline aspect of features, (b) aspect of features with increased magnitudes of changes compared to the baseline.

2.2 Configural vs. Featural Recognition Tasks

In a configural recognition task, all faces have the same eyes, nose, and mouth, but their configurations differ. In contrast, in a featural recognition task, all faces have the same configuration but the features differ in their aspects.

In order to investigate the relationship between HP and RH lateralization when the recognition tasks depend on either configural or featural information, we created both configural and featural face datasets in a controlled manner comparably to [16]. Face images of photorealistic human characters were created with the MakeHuman software [17]. We customized a default Asian face model to produce all the faces. While keeping all facial features (i.e., eyes, nose, and mouth) identical, we changed the size of the spacing between eyes and moved up or down eyes and mouth to create the 27 faces of the two configural sets (Figure 2). Figure 2a and 2b respectively shows the baseline configural set and the increased spacing (IS) dataset. Namely, faces in Figure 2b were made of bigger spacing between features than the faces in Figure 2a. Hence, faces in the IS dataset are more dissimilar to one another than faces in the baseline set. Having two datasets allowed us to examine the effect of stimulus similarity on HP and RH lateralization. In contrast, by changing the aspects of the mouth, the nose, and the eyes but without changing the locations of these features, we created the 27 faces of the featural sets (Figure 3). Figure 3a shows the baseline featural set. Faces in Figure 3b were obtained through bigger magnitudes in the changes of the aspects of the features. Consequently, faces in Figure 3b dataset are more dissimilar to one another than faces in the baseline set.

For each dataset in Figures 2 and 3, we created 10 new training datasets by randomly sampling without replacement 20 faces out of the total of 27 faces. The 10 corresponding testing datasets were derived by rendering each image slightly darker by multiplication by a scaling factor of 0.9. We used these datasets to examine how different recognition task requirements (configural vs. featural) modulate the relationship between the HP and RH lateralization effects. In both tasks, the model in Figure 1 was trained to recognize the stimuli in the corresponding dataset.

2.3 Modeling of the Composite Task and Measure of Holistic Processing

In human studies, HP is usually assessed through the composite paradigm [18]. We implemented the *complete* variant of the composite paradigm because of its robustness [18]. In this paradigm, two stimuli are presented briefly for example simultaneously. Participants attend to either the top or bottom halves of the stimuli and judge whether they are the same or different (see Figure 4). In congruent trials, the attended and irrelevant halves lead to the same response, whereas in incongruent trials, they lead to different responses. HP is indicated by interference from the irrelevant halves in matching the attended halves; it can be assessed by the performance difference between the congruent and the incongruent trials.

In face processing, the HP has been accounted for by computational models [19,20]. To assess HP in our model, we applied the method used by [21] which was inspired by [20]. Namely, after training we attenuated the Gabor responses of either the top or bottom half of the images in the test set by multiplying a factor of 0.125 to simulate directing the models' attention to the bottom or top half of the images respectively. We created 4 types of stimulus pairs corresponding to the 4 conditions in Figure 4 (see an example in Figure 5a). For each simulation, a different set of twenty pairs of images in each condition was randomly drawn to form the materials (80 pairs

in total). We calculated the correlation of the hidden layer representations in each pair as the similarity measure between them. A threshold was set to be the midpoint between the mean correlation of the "same" stimulus pairs and that of the "different" stimulus pairs. We assumed that the model responded "same" when the correlation of a pair was higher than the threshold, and responded "different" when the correlation was lower than the threshold. The HP effect was indicated by the discrimination performance difference between the congruent and incongruent trials measured by d'.

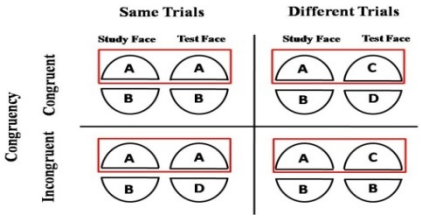

Fig. 4. Design of the composite task, with top halves attended

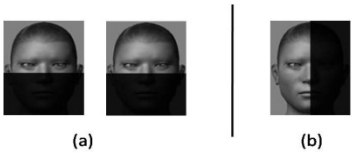

Fig. 5. (a) Illustrative example of a Congruent Same pair for the composite task where bottom half is attenuated. (b) Example of a left-lateralized stimulus for measuring lateralization effects.

2.4 Measuring Hemispheric Lateralization Effect

The left side (RH) bias was assessed by the accuracy difference between recognizing a left-lateralized stimulus (carrying RH/LSF information; see Figure 5b) as the original stimulus and recognizing a right-lateralized stimulus (carrying LH/HSF information) as the original one. We defined RH lateralization (RH/LSF preference, [14]) as the left side bias measured in the biased condition minus that measured in the baseline condition.

2.5 Modeling Details

In the present implementation, the face input (100 x 134 pixels) was first filtered with a grid (6 x 6) of overlapping 2D Gabor filters in quadrature pairs at five scales and eight orientations. The five scales corresponded to 2 to 32 cycles per face. The resulting Gabor vector representation of the face was split into left and right halves. The perceptual representation of each half was compressed into a 15-element representation using PCA. After PCA, each principal component was z-scored to equalize the contribution of each component in the model. The PCA representation was then fed to a feed-forward network with one hidden layer of 20 nodes. The number of nodes was determined empirically to allow efficient training of the network. The output layer of

the neural network had one output for each of the 20 faces of the testing set. The neural network was trained with gradient descent with adaptive learning rate backpropagation from the MATLAB® Neural Network Toolbox (Version 7.0.3). The network was trained for both 400 epochs and 150 epochs. 400 epochs was enough for all the models to reach almost perfect recognition rates on both training and testing sets (accuracy ~ 99%). However, we found a strong ceiling effect for the configural task on the baseline datasets: recognition rates for both left-lateralized stimuli and right-lateralized stimuli were very high (~ 98%) and so close that the size of RH lateralization effect was on average less than 1%. Training with only 150 epochs put an end to the ceiling effects while maintaining high recognition rates (accuracy ~ 90% for both training and testing sets). We thereafter reported results for simulations with a training of 150 epochs.

For each of the featural and configural task, we trained the model with the 20 different datasets. Hence, we collected for each task 20 data points of RH lateralization to plot against 20 data points of holistic Δd' (Congruent d' – Incongruent d'). We then tested for any correlation between RH lateralization and HP.

3 Results

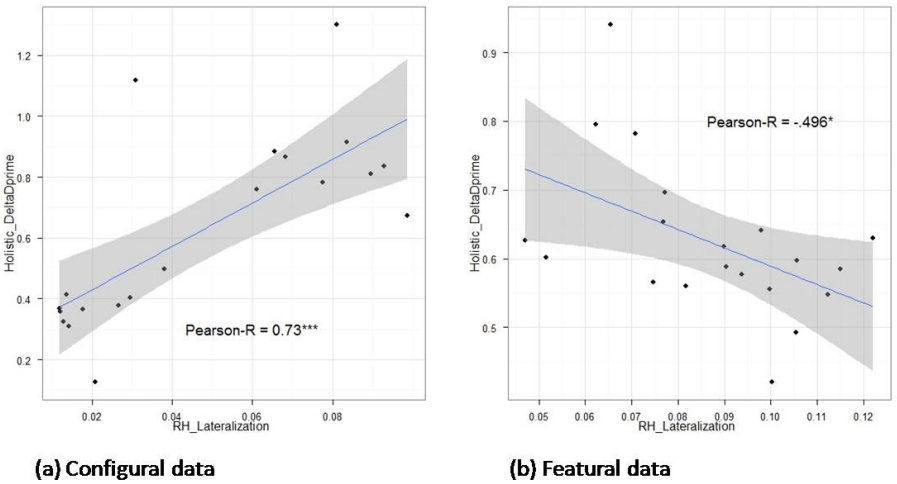

Fig. 6. Holistic Δd' plotted against RH lateralization for configural (a) and featural data (b)

3.1 Configural Processing

When the face recognition task relies purely on configural information, the main result is a strong and statistically significant positive correlation between HP and RH lateralization ($r = 0.73$, $p < 0.001$). In this case, HP and RH go together. HP and RH lateralization increase from baseline datasets to datasets with bigger spacing, i.e., with increasing stimulus dissimilarity ($t(9) = 7.32$, $p < 0.001$; $t(9) = 7.1$, $p < 0.001$).

3.2 Featural Processing

When face recognition task relies purely on featural information, the main result is a statistically significant negative correlation between HP and RH lateralization (r = -0.496, $p < 0.05$). In this case, HP and RH do not go together. HP increases whereas RH lateralization decreases from baseline datasets to datasets with bigger featural changes, i.e., with increasing stimulus dissimilarity ($t(9) = 2.93$, $p < 0.05$; $t(9) = -4.04$, $p < 0.05$).

4 Discussion and Conclusion

Here we investigated the relationship between HP and RH lateralization in configural and featural face recognition tasks through computational modeling. Our model implements a theory of hemispheric asymmetry in perception, the DFF theory, which posits a LSF bias in the RH and a HSF bias in the LH; this model and some variants have been shown to be able to account for both RH lateralization and HP in face recognition [14,19,20]. This study is the first computational work to show that for face stimuli, RH lateralization and holistic processing can be positively or negatively correlated depending upon the nature of the task: respectively configural or featural. A previous work [21] using letters arranged in a deformable triangular configuration as stimuli found also a negative correlation between HP and RH lateralization in a featural task and a weak positive correlation for a configural task.

Our finding of a positive correlation between HP and RH lateralization for the configural face recognition task is reminiscent of the fMRI findings [6,7] linking the HP effect to brain activation in face selective areas especially in the RH. Thus, our results suggest that face processing in real life may rely more on configural than featural information; this is consistent with the finding that configural/second-order spatial relation information is more important in face recognition than in the recognition of other visual object classes [12]. Besides, the finding of reduced HP and increased RH lateralization in expert Chinese character recognition [10] matches well with our finding of a negative correlation between HP and RH lateralization when the recognition task relies mainly on featural information, since expert Chinese character processing essentially involves featural processing and is invariant to configural changes [10].

To conclude, the present work using realistic face stimuli constituted new evidence to call in question the validity of the common assumption of holistic processing being a property of right hemisphere. Our results suggest that HP and RH lateralization are separate processes that can be influenced differentially by task requirements.

References

1. Bukach, C.M., Gauthier, I., Tarr, M.J.: Beyond faces and modularity: The power of an expertise framework. Trends Cogn. Sci. 10, 159–166 (2006)
2. Gilbert, C., Bakan, P.: Visual asymmetry in perception of faces. Neuropsychologia 11, 355–362 (1973)

3. Burt, D.M., Perrett, D.I.: Perceptual asymmetries in judgments of facial attractiveness, age, gender, speech and expression. Neuropsychologia 35, 685–693 (1997)
4. Kanwisher, N., McDermott, J., Chun, M.M.: The fusiform face area: a module in human extrastriate cortex specialized for face perception. J. Neurosci. 17, 4302–4311 (1997)
5. Rossion, B., Joyce, C.A., Cottrell, G.W., Tarr, M.J.: Early lateralization and orientation tuning for face, word, and object processing in the visual cortex. Neuroimage 20, 1609–1624 (2003)
6. Schiltz, C., Dricot, L., Goebel, R., Rossion, B.: Holistic perception of individual faces in the right middle fusiform gyrus as evidenced by the composite face illusion. J. Vision 10(2), 25, 1–16 (2010)
7. Harris, A., Aguirre, G.K.: The representation of parts and wholes in face-selective cortex. Journal of Cognitive Neuroscience 20(5), 863–878 (2008)
8. Gauthier, I., Tarr, M.J.: Unraveling mechanisms for expert object recognition: bridging brain activity and behavior. J. Exp. Psycho. Human 28, 431–446 (2002)
9. Bradshaw, J.L., Nettleton, N.C.: The nature of hemispheric specialization in man. Behav. Brain Sci. 4, 51–91 (1981)
10. Hsiao, J.H., Cottrell, G.W.: Not all expertise is holistic, but it be leftist: The case of Chinese character recognition. Psychol. Sci. 20(4), 455–463 (2009)
11. Hsiao, J.H., Shillcock, R.: Analysis of a Chinese phonetic compound database: Implications for orthographic processing. J. Psycholinguist Res. 35, 405–426 (2006)
12. Farah, M.J., Wilson, K.D., Drain, H.M., Tanaka, J.N.: What is "special" about face perception? Psychol. Rev. 105, 482–498 (1998)
13. Ge, L., Wang, Z., McCleery, J.P., Lee, K.: Activation of face expertise and the inversion effect. Psychol. Sci. 17, 12–16 (2006)
14. Hsiao, J.H., Shieh, D., Cottrell, G.W.: Convergence of the visual field split: hemispheric modeling of face and object recognition. J. Cognitive Neurosci. 20(12), 2298–2307 (2008)
15. Ivry, R., Robertson, L.C.: The Two Sides of Perception. MIT Press, Cambridge (1998)
16. Mondloch, C.J., Grand, R.L., Maurer, D.: Configural face processing develops more slowly than featural face processing. Perception 31, 553–566 (2002)
17. http://www.makehuman.org
18. Gauthier, I., Bukach, C.: Should we reject the expertise hypothesis? Cognition 103(2), 322–330 (2007)
19. Cottrell, G.W., Branson, K., Calder, A.J.: Do expression and identity need separate representations? In: Proc. of the 24th Annual Cognitive Science Conference (2002)
20. Richler, J.J., Mack, M.L., Gauthier, I., Palmeri, T.J.: Distinguishing Between Perceptual and Decisional Sources of Holism in Face Processing. In: Proc. of the 29th Annual Cognitive Science Conference (2007)
21. Hsiao, J.H., Cheung, K.C.F.: Computational exploration of the relationship between holistic processing and right hemisphere lateralization in featural and configural recognition tasks. In: Proc. of the 33th Annual Cognitive Science Conference (2011)

Dynamics of Scalp Potential and Autonomic Nerve Activity during Intelligence Test

Hafeez Ullah Amin[1], Aamir Saeed Malik[1,*], Ahmad Rauf Subhani[1], Nasreen Badruddin[1], and Weng-Tink Chooi[2]

[1] Centre for Intelligent Signal and Imaging Research (CISIR), Department of Electrical and Electronics Engineering, Universiti Teknologi PETRONAS, Perak, Malaysia
{aamir_saeed,nasreen.b}@petronas.com.my
[2] Advanced Medical and Dental Institute (AMDI), Universiti Sains Malaysia
wengtink@amdi.usm.edu.my

Abstract. The main objective of this study was to examine the changes in autonomic nervous system (ANS) and scalp potential during intelligence test (IQ). Electroencephalogram (EEG) and Electrocardiogram (ECG) signals were recorded simultaneously from eight healthy participants during IQ and resting states (eyes–closed and eyes-open). Heart rate (HR) and heart rate variability (HRV) were derived from ECG signal. EEG mean power was computed for five frequency bands (delta, theta, alpha, beta, and gamma) and analyzed in 12 regions across the scalp. The EEG frequency bands showed significant ($p<0.025$) changes between IQ test and rest states. Delta and theta at frontal (PF, AF, F) and temporal regions (FT, T, TP) and alpha activity at parietal (P), parieto-occipital (PO) and occipital (O) regions were significant. In beta and gamma bands, highly reduced mean power was found at P, PO, and O regions as compared to PF, AF, and F regions in IQ test. HR and low frequency in normalized unit (LFnu) were increased significantly ($p<0.05$ and $p<0.025$, respectively) in IQ test. Further, high frequency in normalized unit (HFnu) was decreased ($p<0.11$). Results showed parallel changes in scalp potential and automatic nervous activity during IQ test compared to rest conditions.

Keywords: EEG frequency bands, asymmetry, intelligence test, autonomic nervous system.

1 Introduction

In neurophysiological research, brain imaging techniques such as magnetic resonance imaging (MRI) [1] and electroencephalography (EEG) [2] allow researchers to view human brain activities non-invasively. EEG power analysis in different frequency bands indicates the number of neurons that activate or de-activate simultaneously during certain mental states [3]. EEG power is a measure that reflects the cortical

* Corresponding author.

M. Lee et al. (Eds.): ICONIP 2013, Part I, LNCS 8226, pp. 9–16, 2013.
© Springer-Verlag Berlin Heidelberg 2013

activity or cortical information processing. EEG power was positively correlated with performance in intelligence test [4]. Mostly, alpha and theta activities were associated with intelligence related tasks in previous studies. Positive connection was reported between intelligence and alpha power [5]. Alpha activity desynchronization and theta activity synchronization were explored in intelligence and complex cognitive tasks [6]. Increased sample entropy value was reported in intelligence test as compared to eye-closed condition [7].

Brain cortical activity is inversely related to alpha power, i.e., higher alpha power represents lower cortical activity and vice versa [8]. Inter-hemispheric EEG cortical activities during different mental and stress environment are investigated using alpha asymmetry index [4]. It is stable and widely accepted measure which inversely associates cortical hemispheric activity, i.e., positive alpha asymmetry value reflects greater relative left than right activity, and negative alpha asymmetry value indicates greater relative right than left activity [8].

Autonomic nervous system (ANS) consists of sympathetic nervous system (SNS) and parasympathetic nervous system (PSNS). These are responsible for heart-brain relationship [9, 10]. Heart behaves excitation and inhibition under SNS and PSNS influence, respectively. Heart rate variability (HRV) is a measure of heart SNS/PSNS innervation. The associated components of HRV power spectrum includes very low frequency (VLF: 0.04Hz), low frequency (LF: 0.04 to 0.15Hz), and high frequency (HF: 0.15 to 0.4Hz) [10]. HF component is influenced by parasympathetic activity, while LF follows both sympathetic and parasympathetic involvements. Further, the LF and HF can be expressed in normalized unit (nu), where nu is equal to LF or HF divided by total power minus VLF value. LF in normalized unit (LFnu) is attributed to sympathetic and the ratio of LF and HF is representation of sympathetic to parasympathetic distribution [9]. Recent ECG and EEG studies reported changes in ANS activity with mental arithmetic task [11].

Individuals who are strong in analytical and cognitive abilities are conventionally viewed as smart and intelligent [12]. Raven's Advance Progressive Matrices (APM) test is a psychological standardized cognitive ability test, which is used to measure an individual's higher order mental reasoning ability, logical thinking, and general intelligence. It is designed to discriminate among individuals of "superior intellectual ability". It is routinely used as a selection methodology for high stakes situations such as defense training, research, and medical education [13].

The purpose of this work is to study the behavior of EEG and ECG signal simultaneously in university students while performing intelligence test (IQ). Two research questions were investigated: 1) are there any changes in ANS during complex mental reasoning process? 2) Which brain regions show discrimination in EEG frequency bands between IQ test and rest states?

The paper is organized as follows: the material and method is described in section 2. Section 3 presents the EEG and ECG results and discussion, while conclusion and future work is given in Section 4.

2 Material and Method

2.1 Participants

This study was approved by the Research Committee of Universiti Teknologi PETRONAS (UTP) and Human Research Ethics Committee of Universiti Sains Malaysia (USM). Eight healthy university students participated in the experiment. All participants had normal/corrected to normal vision and were free from any hearing impairments. They were right handed males between the age of 24 to 32 years (mean=28.6 ±4.20). They signed an informed consent document prior to the start of experiment. Participants were free from any medication, neurological disorder, or other head injury that may affect the experiment results. They did not experience Raven's Advance Progressive Matric (Raven's APM) test before.

2.2 Intelligence Test (IQ)

For this study, Raven's APM test was used to measure IQ. The detail procedure of Raven's APM test was adopted from [7] with 46 minutes (10 minutes for set-I and 36 minutes for set-II) administration time to complete it.

2.3 Procedure

Participants were seated in a partially sound-attenuated EEG experiment room and were briefed about the test. EEG and ECG data were collected simultaneously using 128-channel HydroCel Geodesic Net (see Fig. 2) and Polygraph Input Box (PIB). The impedance of all EEG electrodes was below 50 kΩ. The EEG recordings were recorded at 250 samples per seconds with reference to Cz. Data conditions were: (a) baseline rest states of eye-closed (EC) and eye open (EO) for 5 minutes each, (b) performing intelligence test "Raven's APM".

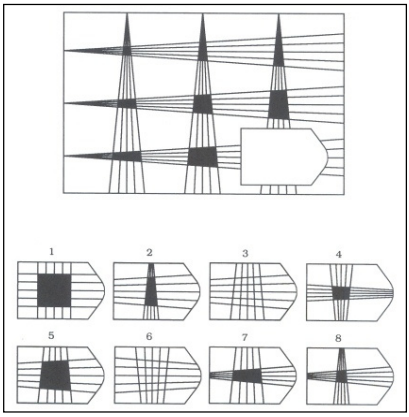

Fig. 1. Raven's Advance Progressive Matric

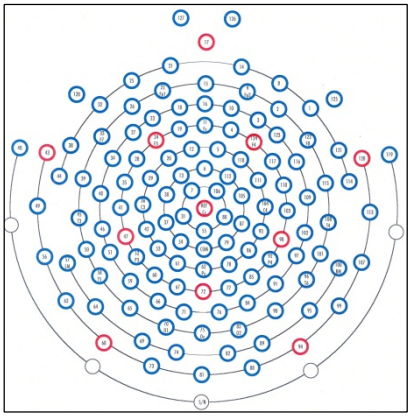

Fig. 2. Hydro Cel Geodesic 128-channel Net

2.4 Data Analysis

The EEG at each electrode site i was recorded as a time series $x_i^{(k)}$ per trial k. Thus, the whole data can be denoted as,

$$X^{(k)} = [x_1^{(k)}, x_2^{(k)}, x_3^{(k)} \ldots, x_{Ne}^{(k)}]^T \quad \in R^{Ne \times Ns} \tag{1}$$

Where, Ne=128 is the number of electrode sites, and Ns=250 represents sampling frequency.

Preprocessing. Raw EEG data were filtered by 1-48Hz band pass filter and artifacts were detected using waveform tools in net station software (EGI Inc.). Regression based model [14] was applied to remove the detected artifacts using EOG channels (EOG channel more than 140μV).

Mean Power. The time series data was transformed using Fast Fourier Transform (FFT) and spectral power density was computed using Welch method and Hanning window with NFFT=1024, 50% overlapping, and 2 seconds window segment (500 samples). Power was computed for each electrode of all the subjects and separated into frequency bands. The computed Power was averaged over regions for each subject and then grand mean was taken to find out frequency bands mean power over regions of all subjects.

The scalp regions were defined as: Prefrontal (PF): (9, 22, 5), Anterior Frontal (AF): (23, 3, 12, 26, 2 and 16), Frontal (F): (19, 4, 24, 124, 27, 123, 33, 122, and 11), Central (C): (30, 105, 36, 104, 41, 103), Parietal (P): (60, 85, 52, 92, 51, 97, 64, and 95), Temporal (T): (45, 108, 44, 114, 45, 108, 34, 116, 38, 121), Occipital (O): (70, 83, and 75), Fronto-Central (FC): (13, 112, 29, 111, 28, 117, 6), Centro-Parietal (CP): (37, 87, 42, 93, 47, 98, 55), Tempo-Parietal (TP): (58, 96, 46, 102), Fronto-Temporal (FT): (34, 116, 38, 121), and Parieto-Occipital (PO): (67, 77, 65, 90).

Alpha Asymmetry. Asymmetry indices were calculated for the eight pairs of electrodes by subtracting the natural logarithm of right site from the natural logarithm of left corresponding site [6]. A mean asymmetry index was calculated by averaging the corresponding pair of electrodes across subjects. EEG alpha asymmetry was computed for IQ data at prefrontal (FP1, FP2), mid-frontal (F3, F4), lateral frontal (F7, F8), central (C3, C4), anterior-temporal (T3, T4), posterior temporal (T5, T6), mid-Parietal (P3, P4) and occipital (O1, O2) pairs of electrodes. Where FP1=22, FP2=9, F3=24, F4=124, F7=33, F8=122, C3=36, C4=104, T3=45, T4=108, T5=58, T6=96, P3=52, P4=92, O1=70, O2=83.

ECG Analysis. For ECG measurements, EC, EO and IQ test data were analyzed for HR and HRV, low frequency in normalized unit (LFnu), high frequency in normalized unit (HFnu), and low and high frequency ratio (LF/HF) using bio-signal free matlab toolbox [15].

Statistical Analysis. Freidman non-parametric test was applied to determine the significant difference among the three conditions (Eyes closed, Eyes open, and IQ test). Further, most significant condition was determined by using Wilcoxon signed ranked test as post-hoc analysis.

3 Results and Discussion

3.1 HR and HRV

The HR and HRV were compared between rest states (EC, EO) and Intelligence test (IQ). There were statistically significant differences in HR (χ^2 (2) = 6.33, and p=0.04) and LFnu (χ^2 (2) = 9.0, and p=0.01) between rest condition and IQ test. Friedman test and post-hoc analysis has shown that in both HR and Lfnu, the IQ test has statistically significant difference from condition EC.

From Table 1, the HR (82.66 ± 13.45 beats per min) was significantly increased in IQ test compared with rest condition EC (74.97 ± 8.30 beats per min). LF/HF ratio was increased (χ^2 (2) = 5.33 and p=0.06) and Hfnu was decreased (χ^2 (2) = 4.33 and p=0.10). This result is consistent with the finding of [9] in mental arithmetic task and with [7] in playing video game.

The results showed that IQ test increased SNS and decreased PSNS activities, as reflected by significant rise in HR, LFnu and LF/HF and lower HFnu in IQ test as compared to rest conditions (see Table 1). Previously, LFnu, HFnu have been reported to relate with sympathetic and parasympathetic activities and LF/HF had been suggested as an index of sympathovagal balance [7, 9].

Table 1. HR and HRV in Rest states vs. Intelligence test (IQ)

Tasks	HR (beats/min)	HFnu	LFnu	LF/HF
EC	74.97 (08.30)	0.42 (0.07)	0.31 (0.06)	0.75 (0.23)
EO	78.79 (11.44)	0.35 (0.03)	0.35 (0.10)	1.07 (0.35)
IQ	82.66 (13.45)	0.34 (0.01)	0.38 (0.09)	1.15 (0.30)

Data arranged as: mean (standard deviation). EC (Eye Close), EO (Eye Open), IQ (Intelligent Quotient), HRV (heart rate variability), HR (heart rate), LF (low frequency), HF (High frequency), HFnu (high frequency in normalized unit), LFnu (low frequency in normalized unit).

3.2 EEG Dynamics

The values of region wise EEG mean power in delta, theta, alpha, beta, and gamma frequencies for three conditions (IQ, EC, and EO) are presented in Fig. 3 to Fig. 7. The results presented significant ($p<0.025$) positive mean difference in values of delta and theta at frontal and temporal regions (PF, AF, F; and FT, T, TP) and significant ($p<0.025$) negative mean power difference in values of alpha at parietal, parieto-occipital, and occipital regions between IQ and rest conditions. In beta and gamma, the mean power values reduced at PO and O regions in IQ test, while in rest conditions the values were slightly increased at the same regions.

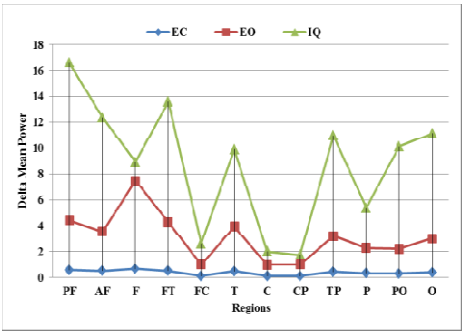

Fig. 3. EEG delta (1-3Hz) power for IQ, EO, and EC

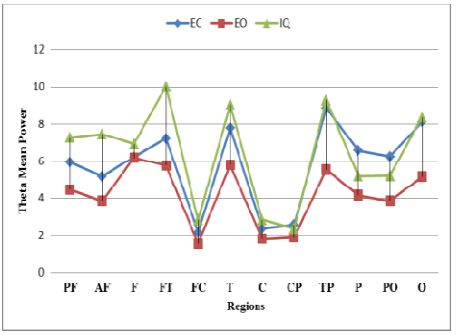

Fig. 4. EEG theta (4-7Hz) power for IQ, EO, and EC

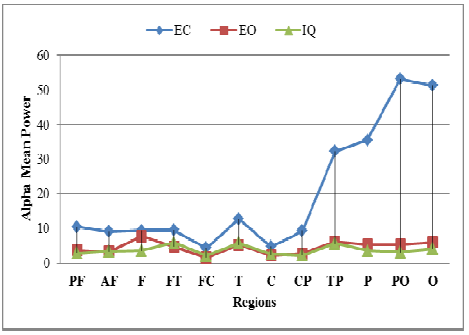

Fig. 5. EEG Alpha (8-13Hz) power for IQ, EO, and EC

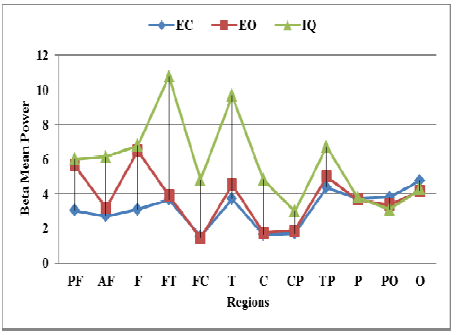

Fig. 6. EEG Beta (14-30Hz) power for IQ, EO, and EC

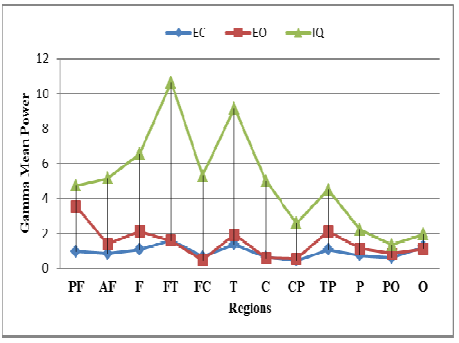

Fig. 7. EEG Gamma (31-48Hz) power for IQ, EO, and EC

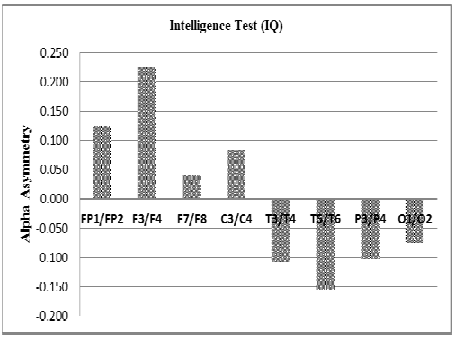

Fig. 8. Alpha Asymmetry for IQ test

All five-frequency bands discriminated mental IQ test from rest states activation. Mental reasoning and logical thinking related increases in EEG mean power were found in delta (1-3Hz; all regions) and were significant at (PF, AF, FT, T, TP, PO and O) compared to rest state. In theta (4-7Hz), the mean power was high at (PF, AF,

and FT), but reduced at (CP, P, and PO). In alpha (8-13Hz) the EEG mean power was reduced (see Fig. 5) at P, PO, and O regions in IQ test as compared to rest conditions. Further, in beta (14-30Hz), high EEG mean power was found at (FT, FC, T, C, and TP) regions in IQ, but reduced mean power value was observed at regions P, PO and O than rest conditions (see Fig. 6). In gamma (31-48Hz), mean power was high in all regions in IQ test as compared to rest conditions.

Overall, we found increase in mean power of delta, theta, beta and gamma in IQ test than rest states in frontal and temporal regions except P, PO and O where it decreased or similar to rest conditions.

The alpha asymmetry values (Fig. 8) presented high alpha activity at frontal and central regions and reduced alpha activity at temporal, parietal and occipital regions. These changes reflected high involvement of left hemispheric prefrontal, mid-frontal, lateral-frontal, and central regions while solving the problem in IQ test. Further, right anterior temporal (T3/T4), and all right posterior (C3/C4, P3/P4, and O1/O2) regions were found active in IQ test.

4 Conclusion

High delta and theta activity at frontal regions and reduced alpha and beta activity at parietal, parieto-occipital and occipital regions distinguished the IQ test from rest conditions. Simultaneously, increase in HR, LFnu, and LF/HF and decrease in HFnu values indicated sympathetic activation during IQ test. From asymmetry results, it can be concluded that during the IQ test the left frontal regions were active due to logical thinking and mental reasoning. In addition, the right temporal and parietal regions were active due to involvement of perception and working memory in the IQ test. Future work can be implemented with large number of subjects using other standard intelligence assessment test.

Acknowledgment. This study was funded by University Research Internal Funding (URIF: 10/2012), Universiti Teknologi PETRONAS, Malaysia.

References

1. Malik, A.S.: Simulation-based analysis of the resolution and SNR properties of partial k-space EPI. Concepts in Magnetic Resonance Part B: Magnetic Resonance Engineering 35, 232–237 (2009)
2. Amin, H.U., Malik, A.S., Badruddin, N., Chooi, W.-T.: Brain activation during cognitive tasks: An overview of EEG and fMRI studies. In: 2012 IEEE EMBS Conference on Biomedical Engineering and Sciences (IECBES), pp. 950–953 (2012)
3. Benedek, M., Bergner, S., Könen, T., Fink, A., Neubauer, A.C.: EEG alpha synchronization is related to top-down processing in convergent and divergent thinking. Neuropsychologia 49, 3505–3511 (2011)
4. Thatcher, R.W., North, D., Biver, C.: EEG and intelligence: Relations between EEG coherence, EEG phase delay and power. Clinical Neurophysiology 116, 2129–2141 (2005)

5. Doppelmayr, M., Klimesch, W., Stadler, W., Pöllhuber, D., Heine, C.: EEG alpha power and intelligence. Intelligence 30, 289–302 (2002)
6. Doppelmayr, M., Klimesch, W., Sauseng, P., Hödlmoser, K., Stadler, W., Hanslmayr, S.: Intelligence related differences in EEG-bandpower. Neuroscience Letters 381, 309–313 (2005)
7. Amin, H.U., Malik, A.S., Badruddin, N., Chooi, W.-T.: EEG mean power and complexity analysis during complex mental task. In: 2013 ICME International Conference on Complex Medical Engineering (CME), pp. 648–651 (2013)
8. Mikolajczak, M., Bodarwé, K., Laloyaux, O., Hansenne, M., Nelis, D.: Association between frontal EEG asymmetries and emotional intelligence among adults. Personality and Individual Differences 48, 177–181 (2010)
9. Subhani, A.R., Likun, X., Saeed Malik, A.: Association of Autonomic Nervous System and EEG Scalp Potential During Playing 2D Grand Turismo 5. In: Engineering in Medicine and Biology Society (EMBC), 2012 Annual International Conference of the IEEE, pp. 3420–3423 (2012)
10. Wu, G.-Q., Arzeno, N.M., Shen, L.-L., Tang, D.-K., Zheng, D.-A., Zhao, N.-Q., et al.: Chaotic Signatures of Heart Rate Variability and Its Power Spectrum in Health, Aging and Heart Failure. PLoS ONE 4, e4323 (2009)
11. Yu, X., Zhang, J., Xie, D., Wang, J., Zhang, C.: Relationship between scalp potential and autonomic nervous activity during a mental arithmetic task. Autonomic Neuroscience 146, 81–86 (2009)
12. Sternberg, R.J.: The theory of successful intelligence. Interamerican Journal of Psychology 39, 189–202 (2005)
13. Koczwara, A., Patterson, F., Zibarras, L., Kerrin, M., Irish, B., Wilkinson, M.: Evaluating cognitive ability, knowledge tests and situational judgement tests for postgraduate selection. Medical Education 46, 399–408 (2012)
14. Hoffmann, S., Falkenstein, M.: The correction of eye blink artefacts in the EEG: A comparison of two prominent methods. PLoS ONE 3 (2008)
15. Biosignal Tool Box, `http://biosig.sourceforge.net/help/index.html`

Planning as Inference in a Hierarchical Predictive Memory

Hansol Choi[1,*] and Dae-Shik Kim[2]

[1] Information & Electronics Research Institute, KAIST, Daejeon, South Korea
apine@kaist.ac.kr
[2] Department of Electrical Engineering, KAIST, Daejeon, South Korea
dskim@ee.kaist.ac.kr

Abstract. In the predictive brain hypotheses, the functional mechanism of the brain is suggested to infer the cause of current states within the predictions by brains. Recently, there have been several approaches to explain the action generation within the predictive brain hypotheses: the brain predicts the animal's own action, which the animal realizes to fulfill the prediction. In this study, we suggest a predictive brain models to produce the goal directed behaviors. We introduced the Planning as Inference (PAI) framework to a hierarchical predictive memory model. PAI is a computational framework for goal-directed behavior generation. PAI explains the decision of an action for a state in the probabilistic distribution. The distribution is inferred from the evidences of current state and the perspective evidence of goal achievement. We used a hierarchical predictive memory system to predict the agent's self-action states. Following to the PAI, the predictions were inferred from the evidence of the ongoing state and the evidence from assumption of the goal achievement. The agents realizes the predicted actions to minimize prediction errors. We implemented our method in embodied robotics system and our model could generate structured spontaneous behavior and goal directed behaviors. Our result opens understanding for the goal-directed behavior in predictive brain hypotheses.

Keywords: Planning as Inference, Hierarchical Predictive Memory, Hierarchical Temporal Memory, Predictive Coding.

1 Introduction

Brains are suggested to be probabilistic inference machines[1–3]. In the Bayesian brain hypotheses, the brain has a probabilistic model of the world which is optimized by the experiences. Brain generates predictions, against which the sensory inputs are tested to update the beliefs of the brains about their causes. Hierarchical predictive processing suggests the inference machinery in brains[4–7]. The system uses internal hierarchical generative models, which produces top-down prediction and the fed forward input signal is captured within the prediction. The predictive processing is in hierarchical manner that, higher region internal state is for more abstract

* Corresponding author.

M. Lee et al. (Eds.): ICONIP 2013, Part I, LNCS 8226, pp. 17–24, 2013.
© Springer-Verlag Berlin Heidelberg 2013

spatio-temporal patterns in the signal and lower level for more abstract and concrete. The belief for causes of an ongoing state is inferred in different temporal and spatial abstraction level in the multiple levels in hierarchical predictive processing frameworks.

The predictive brain hypotheses were originally introduced in the sensory perception domain but which was expanded for the action generations. For example, active inference [8–10] explains action generation as producing the predicted behavior from current states to minimize the prediction error. We wanted to explain the generation of goal directed behavior in the hierarchical predictive brain models. We adapted planning as inference (PAI) framework to a predictive brain model. The planning as inference framework (PAI)[11, 12] explains goal directed behavior as an inference problem. In the PAI, the decisions of each states follows a probabilistic distribution. The probabilistic distribution is inferred the evidence of current state and perspective evidence of the achievement of a goal state.

In this research, we demonstrated the generation of action sequences in an embodied system, using a hierarchical predictive memory within PAI framework. A hierarchical temporal memory (HTM)[13, 14] was used as a hierarchical memory model. The hierarchical memory system was trained to memorize the statistical structures of sensory-motor states from the primitive behavior of the robot system. The memory was used to generate the spontaneous behaviors by predict the probabilistic distribution of next behavior from current states. When perspective evidence of assuming the achievement of various goal states were given to the memory system, the robot could move its body to the goal state.

2 General Materials and Method

2.1 Robot and Training Task

We used a robotic hand with three digits (Fig.1A; homemade, Dynamixel Rx-28 motors, by Robotis ltd, Seoul, Korea). The positional state of each digit was a real number between 0.0 (fully folded) and 1.0 (fully open). Each digit could be in one of three action conditions: fold, hold and open, which had real number state of 0.0, 0.5 and 1.0 each. The state of the robot hand could be represented by a vector of six real values which is concatenation of the state of actions and positions. The robot action and positions were sampled every 0.2 second. The actions signal were delivered to robot control system in the middle of samplings. One state sample is action at the time and the position in the middle of the action step.

Basic action sequences were generated to train a hierarchical memory system. The basic action sequence represent the inherited and physical action constraint for the developmental systems. The memory for basic action sequence will be used as a seed for further action development. Random actions were selected for each digits used for actions. Each action was continued for the next step in probability of 1/3. By this method, we could produce action sequence with only limited structures.

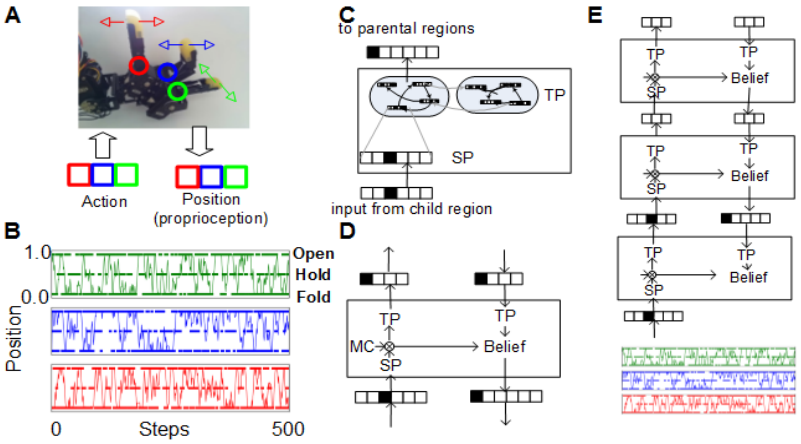

Fig. 1. A. The robot hand. Each color code represents one of three digits. B. The action and position states in the first 500 steps of training task. The state of each digits are shown. The bold line is action and the thin line is position. C. The structure of one region of hierarchical temporal memory. The spatial pooler (SP) detects spatial patterns and the temporal pooler (TP) detects temporal patterns of spatial patterns inside which, the spatial patterns have high temporal coincidences. D. Bayesian inference of the belief of cause for current robot state by trained HTM system. The likelihood of temporal patterns (TP) are computed from the markovian transition from previous belief (MC), the evidence for spatial patterns (SP) from bottom-up input. The current belief is computed with evidence from higher region. E. Overall architecture of our memory system used.

2.2 State Inference by Hierarchical Temporal Memory

Hierarchical temporal memory (HTM) was used for predictive hierarchical memory systems (Fig.2 CDE). A HTM is a hierarchical memory of spatio-temporal patterns. Higher regions store more abstract and longer sptaio-temporal patterns. Each region of HTM has two modules: a spatial pooler and temporal pooler. A spatial pooler stores unique 'spatial patterns' of the feed-forward states from children and a temporal pooler stores the 'temporal patterns' among the spatial patterns. The temporal patterns are set of spatial patterns, among which the transition probability are larger than some threshold. Each region of our model behaved in three phases: wait, learning and inference. One region is in wait phase until all its children nodes finish their learning phases. After learning phase of fixed number of steps, the inference phase follows.

The input to each region is vectors of probabilities of the temporal patterns of its children nodes. The spatial pooler memorizes unique spatial coincidences of the input patterns during learning. The temporal pattern finds temporal patterns between the coincidence patterns on its final step of learning. If a spatial pattern is followed by another spatial pattern more than some probability threshold, the two spatial patterns are grouped together in one temporal pattern. The learning propagates from the bottom region to the root region of HTM system.

After learning, HTMs infer the belief for cause of current input signals in Bayesian manner. The likelihood of states for each region is updated from feed forward signal, feed-back signal and internal markovian transition (Fig. 1D). The likelihood of current state is computed from the likelihood of previous states and markovian transition probabilities among the states determines. The likelihood is updated with the probability of feed forward input patterns (MC in Fig.1D). The feed forward probability of states are determined from the similarity between feed forward input pattern and spatial patterns (SP in Fig. 1D). The likelihood for temporal patterns are computed from the current likelihood and fed forward (left TP in Fig. 1D.). When the probabilities for temporal states are fed back (right TP in Fig 1D), the likelihood of spatial patterns updated with probability of spatial patterns from the top-down patterns (Belief in Fig 1D.). The belief for each spatial patterns are computed and fed down.

In experiments, we used three level HTM systems (Fig 1E). The spatial pooler of first level was composed of self-organizing map. The spatial pooler of other region behaved as George [13]. The temporal grouping threshold were 0.25, 0.2, 0.15 from bottom to top. HTM system was trained by the basic behavior to discover the spatio-temporal patterns in them.

3 Generation of Spontaneous Behavior by Inference in the Predictive Memory

3.1 Method

After the belief for the cause of current state is determined (grey part in Fig 2A), the hierarchical predictive memory was used to produce the prediction for next action. For each region, Markovian transition probability was used to determine the probability of next state from the belief of current states (MC in Fig 2A). The likelihoods were multiplied with the top-down prediction signal from the higher region, (TD prediction for next step in Fig2A). The prediction signal is feed down to its lower region. In the lowest region of HTM system, one of the spatial pattern is selected as a prediction signal by the probabilistic distribution. The motor realizes the predicted action.

3.2 Result and Discussion

The hierarchical predictive memory and non-hierarchical memory could produce some spontaneous behaviors. The behavior was more structured within the hierarchical memory model. It maintained same action state longer and showed staying in some positions more than non-hierarchical system (Fig 2BC). The spatio temporal pattern discovered by the hierarchical memory system might shape the motor behavior more regular structure. We believe that, the extraction of regular structure in the behavioral sequence might be able to build more regular structure for the behavior generated from the memory system. Our action generation reduces prediction error signal, which is suggested as the main function of brains in the predictive coding theories.

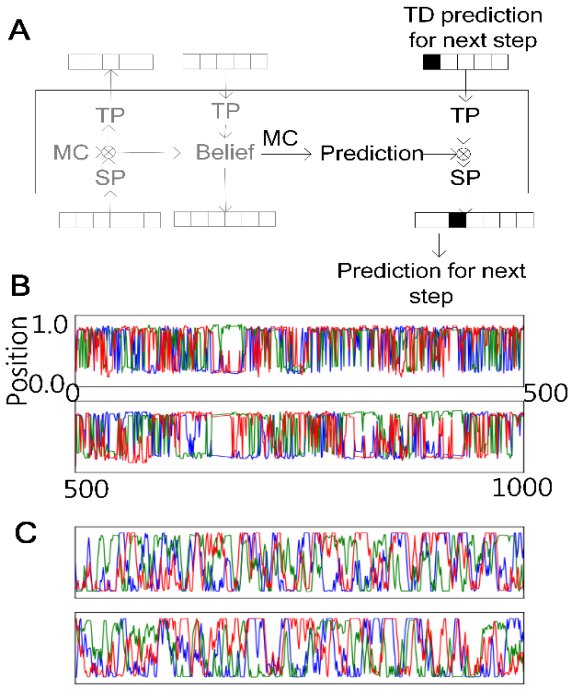

Fig. 2. Spontaneous behavior generation by prediction. A. The behavior generation by realizing prediction. The mechanism of one region is shown. The inference step for current belief of cause of input sequences are shown as grey (left side of box). Prediction of probabilisitic distribution of next step is built by markov transition probability (MC) from current Belief. The prediction is multiplied with the top-down prediction signal. The spontaneous behavior of hierarchical memory (B) and non-hierarchical system (C) is shown.

4 Generation of Goal Directed Behavior by Inference in Predictive Memory

4.1 Method

In the Planning as Inference framework, the motor actions are determined from probabilistic distribution of the next actions is inferred according to the evidence of assumed goal achievement and current state. As a result, the path to the goal state is inference within the memory system. We used PAI in our hierarchical predictive memory system. One of five goal states was selected in random order for 100 steps then replaced to other. When a goal state is selected, the goal state was assumed achieved and the belief for the cause of the goal state was inference in the HTM system (Fig. 3A, right side). The belief for the cause of the goal state is a likelihood which shares same domain to the belief for the current state. The two beliefs were merged together in the prediction condition (Fig 3A. center). As the chapter 3, the bottom level implemented predicted action.

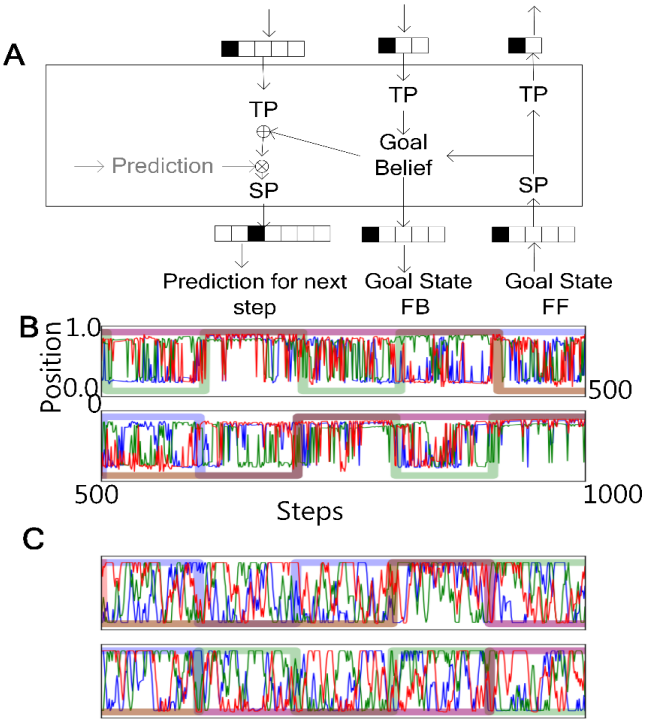

Fig. 3. The action of goal directed behavior. A. The behavior of a region. The left part of grey 'prediction' is same to the previous steps and omitted in this figure. The goal state is assumed achieved and the beliefs for the cause of the goal state is inference within the HTM (right part of the region.) The belief for goal biases the prediction for the next step to the goal. The behavior of the robot hand during goal directed behavior is shown. The bold transparent lines show the goals state and thin lines are the positions of digits. The robot hands achieved the goal states more in hierarchical predictive memory (B) than non hierarchical system(C).

4.2 Result and Discussion

The hierarchical predictive memory could achieve the goal state more than non-hierarchical memory system (Fig 3B,C Table 1, the probability of achieving target state is much higher when the goal is same to target in hierarchical memory system, but not in without hierarch). The prediction for next step was biased to the cause of goal state by reinforcing the common cause for the goal and current state was reinforced. In the neural systems, the common state will be the common representation that both state and goal state. Our result predicts that, the common cause state will be found in higher level of hierarchical memory system if the goal requires larger behavioral steps to achieve. More concrete and closer-to-achieve goals does not require procedure in higher memory system and it might be the sense of the problem hierarch and abstraction in human mind.

Table 1. Goal state achievement

Target	With hierarch		Without Hierarch	
	P(target|goal=target)	P(target|goal!=target)	P(target|goal=target)	P(target|goal!=target)
0	0.08 (700)	0.015 (2300)	0.035 (400)	0.02 (2437)
1	0.51(470)	0.07 (2530)	0.09 (600)	0.03 (2401)
2	0.38 (800)	0.13 (2200)	0.04 (436)	0.027 (2401)
3	0.014 (500)	8.0-e4 (2200)	0.017 (700)	0.014 (2137)
4	0.07 (500)	2.4e-4 (2500)	0.014 (701)	0.027(2136)

How the goal states are selected? One possibility is that inference system outside the motor hierarch might exist to activate the goal state. One region can have several different higher-level regions as parents. When some inference result of a sensory signal for a parental state outside the motor system is highly associated with the goal state in motor system, the sensory signal will produce the goal directed behavior. We expect some of autonomous stimulus-response type behavior can be produced in this kind of mechanisms. The other possibility is by the reward. A reward signal which is required in current condition might select the goal state that can achieve the request (if you are hungry, the goal states related to eating are inference). Those are required to be tested for further researches in computational and behavioral studies.

5 Overall Discussion

In this research, we suggested how the hierarchical predictive memory system can be used to embody the sensory-motor states of its own body and use the memory infer the belief for the cause of current state and predicting the state of next step. Our memory selects action based on the inferred probabilistic distribution of next actions to fulfill the prediction.

Acknowledgement. This research was supported by the Brain Research Program through the National Research Foundation of Korea funded by the Ministry of Science, ICT & Future Planning (NRF-2013-035057) and the Research Center Program of IBS(Institute for Basic Science) in Korea. (HQ1201).

References

1. Knill, D.C., Pouget, A.: The Bayesian brain: the role of uncertainty in neural coding and computation. Trends Neurosci. 27, 712–719 (2004)
2. Yuille, A., Kersten, D.: Vision as Bayesian inference: analysis by synthesis? Trends Cogn. Sci. 10, 301–308 (2006)
3. Doya, K.: Bayesian brain: Probabilistic approaches to neural coding. MIT Press (2007)
4. Clark, A.: Whatever next? Predictive brains, situated agents, and the future of cognitive science. Behav. Brain Sci. 36, 181–204 (2013)

5. Lee, T.S., Mumford, D.: Hierarchical Bayesian inference in the visual cortex. J. Opt. Soc. Am. 20, 1434–1448 (2003)
6. Friston, K.: Hierarchical Models in the Brain. Plos Comput. Biol. 4, e1000211 (2008)
7. Friston, K., Kilner, J., Harrison, L.: A free energy principle for the brain. J. Physiol.-Paris 100, 70–87 (2006)
8. Adams, R.A., Perrinet, L.U., Friston, K.: Smooth pursuit and visual occlusion: active inference and oculomotor control in schizophrenia. Plos One 7, e47502 (2012)
9. Friston, K., Mattout, J., Kilner, J.: Action understanding and active inference. Biol. Cybern. 104, 137–160 (2011)
10. Friston, K.J., Daunizeau, J., Kiebel, S.J.: Reinforcement Learning or Active Inference? Plos One 4, e6421 (2009)
11. Botvinick, M., Toussaint, M.: Planning as inference. Trends Cogn. Sci. 16, 485–488 (2012)
12. Solway, A., Botvinick, M.M.: Goal-directed decision making as probabilistic inference: A computational framework and potential neural correlates. Psychol. Rev. 119, 120–154 (2012)
13. George, D., Hawkins, J.: Towards a mathematical theory of cortical micro-circuits. Plos Comput. Biol. 5, e1000532 (2009)
14. Hawkins, J., George, D., Niemasik, J.: Sequence memory for prediction, inference and behaviour. Philos. Trans. R. Soc. Lond. B. Biol. Sci. 364, 1203–1209 (2009)

EEG-Based Cortical Localization of Neural Efficiency Related to Mathematical Giftedness

Li Zhang[1,*], Haixian Wang[1], and John Q. Gan[1,2]

[1] Research Center for Learning Science, Southeast University, Nanjing, Jiangsu 210096, China
{li_zhang,hxwang}@seu.edu.cn
[2] School of Computer Science and Electronic Engineering, University of Essex, Colchester, UK
jqgan@essex.ac.uk

Abstract. Using two inductive reasoning tasks with high and low levels of complexity, this electroencephalogram (EEG) study examined the relationship between gamma-band response (GBR) of human brain and neural efficiency in math-gifted and average-level adolescents. The event-related synchronization/desynchronization (ERS/ERD) maps of math-gifted subjects and average-level subjects were analyzed in the first place. Furthermore, by means of feature selection based on a sequential forward floating search (SFFS) algorithm, this study investigated the important EEG scalp locations for discriminating cortical areas between groups of subjects and between task conditions. The experimental results show that math-gifted adolescents can more efficiently recruit fronto-parietal cortices while performing both levels of inductive reasoning tasks. Right frontal and bilateral parietal cortices are suggested to be highly involved in neural efficiency related to mathematical giftedness.

Keywords: Neural efficiency, EEG analysis, gamma-band response, fronto-parietal cortices, mathematical giftedness.

1 Introduction

Neural efficiency hypothesis of intelligence suggests that individual difference in cognitive ability can be reflected by efficient recruitment of neural resource of the brain, which derives from the disuse of many brain areas irrelevant to good task performance and more extensive use of specific task-relevant areas [1]. Additionally, long-term training or skilled expertise resulting in reduced working memory load also affects individual's neural efficiency, which is manifested as a decrease of brain activation [2, 3]. Frontal lobe of the brain has typical working memory and cognitive control functions, the activation of which is correlated with monitoring requirement, memory load, or effort of tasks [4]. Therefore, improved working memory performance can result in reduced activation in frontal lobe. In addition, fronto-parietal network, some parts of parietal lobe, precuneus, thalamus, temporal and frontal gyrus have also been suggested to be involved in neural efficiency [1, 5].

* Corresponding author.

M. Lee et al. (Eds.): ICONIP 2013, Part I, LNCS 8226, pp. 25–32, 2013.
© Springer-Verlag Berlin Heidelberg 2013

Mathematically gifted adolescents have been found having enhanced functions in prefrontal, frontal, parietal and temporal cortices, and highly adaptive cognitive system for problem solving [5, 6]. However, the accurate brain regions are not explicitly located, where neural resource is "tuned" by individuals with mathematical intelligence or expertise [7]. It has been found that cognitive tasks induce widespread gamma-band response (GBR) in cortical EEG [8]. The increase of GBR (40 Hz) is closely related to attention, decision, high-order cognition, and shows close spatial correspondence with fMRI blood oxygenation level dependent (BOLD) variations in activated brain regions [9]. Meanwhile, the augmented gamma activity is discovered to be modulated by the complexity of cognitive tasks and correlated with working memory load of human brain [10, 11]. Based on the spatial distribution of EEG GBR features, this study aims to determine the cortical localization of neural efficiency on scalp electrodes through a feature (or channel) selection method and two mathematical reasoning tasks, which can maximally represent the discriminating cortical regions of efficient neural activation between math-gifted and average-level adolescents.

2 Materials and Methods

2.1 Subjects

In this study, the math-gifted group included 8 adolescents (5 males and 3 females with mean age 16.5) from the Science and Engineering Experimental Class at Southeast University (Nanjing, China), who had been awarded prizes in nationwide or provincial mathematical competitions. Therefore, they were viewed as proficient in mathematical and logical thinking. The control group was composed of 7 students (5 males and 2 females with mean age 16.3) from the Nanjing Fourth High School, who achieved average-level performance in mathematical tests of the school. Exclusion criteria included left handedness, neurological illness, and history of brain injury. All subjects were given informed consent and the study was approved by the Academic Committee of the Research Center for Learning Science, Southeast University, China.

2.2 Experimental Paradigm

The experiment in this study adopted two numerical inductive reasoning tasks with low to high complexity, similar to those used in [12]. The experimental protocol is shown in Figure 1. In Figure 1a, three numbers in the triangle were associated with a certain calculation rule, such as 'A+B=C' or 'A+C=B', and four numbers in the square were related to a calculation rule with increased complexity, such as 'A+B=C+D' or 'B=A+C+D'. Each trial of a task was constituted by three triangles/squares, which involved two basic processes, i.e., rule induction and rule application, as shown in Figure 1b. The rule induction process at the left of the arrow aimed to find the calculation rule from the first two triangles/squares, and the validity of this calculation rule was verified by the third triangle/square at the right of the arrow, i.e., rule application. The calculation rule only involved '+' and '-'.

Each task session was composed of a valid block and an invalid block. The valid block included 30 trials with congruent calculation rule between rule induction and rule application processes. The invalid block included 30 trials in which the rule in the application process was not congruent with that in the induction process.

The timeline of stimuli presentation is shown in Figure 1c and 1d. The trials in all the blocks of the two tasks were randomly presented. The onset of the stimulus started after presenting a fixation point for 1000ms and a blank screen for 500ms, and the triangles/squares were presented sequentially along the timeline with an interval of 2000ms, as shown in Figure 1c and 1d. Therefore, the rule induction process lasted for 4000ms and the rule application process had no time limit but was controlled by subjects. When the last triangle/square was presented, subjects were asked to judge whether the rules of the two processes were consistent or not as fast and as accurately as possible by pressing "K" for "valid" and "D" for "invalid" on the keyboard.

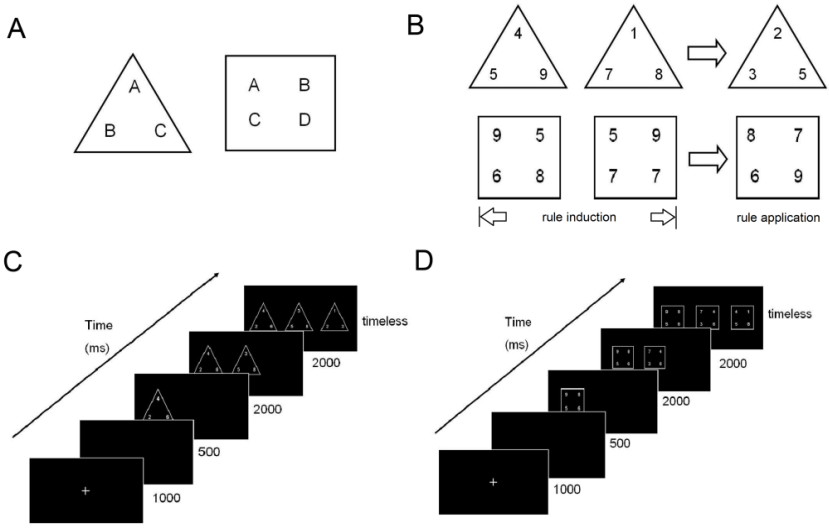

Fig. 1. Experiment protocol: (a) A triangle with three numbers and a square with four numbers; (b) Samples of numerical inductive reasoning tasks with two levels of complexity; (c) Timeline of stimuli presentation of low-complexity task; (d) Timeline of stimuli presentation of high-complexity task

2.3 EEG Recording and Preprocessing

The EEG data were recorded by a 60-channel Neuroscan international 10-20 system with sampling rate 1000 Hz. Reference electrodes were located at the bilateral mastoids of subjects, and electro-oculographic (EOG) signals were simultaneously recorded by four surface electrodes to monitor ocular movements and eye blinks.

The EEG signals were band-pass filtered between 1 Hz and 60 Hz. EEG trials were extracted using a time window of 4500ms, which covers 500ms pre-stimulus period and 4000ms post-stimulus period. After baseline-correction and artifacts rejection, 26 to 43 effective task trials were retained for each subject in each task session.

2.4 Extraction of Gamma Band Power Changes as Features

In the 4000ms period of the rule induction process, feature extraction was conducted from GBR (35-45Hz) in each EEG channel by calculating event-related synchronization/desynchronization (ERS/ERD), which was expressed as the percentage of power increase/decrease in relation to the baseline resting state:

$$ERS / ERD(f, \Delta t) = [A(f, \Delta t) - R(f)] / R(f)] \times 100\% \quad (1)$$

where Δt is a time window of 500 ms, $A(f, \Delta t)$ is power spectrum density at frequency f of an EEG signal in time range Δt, and $R(f)$ is power spectrum density at the same frequency in pre-stimulus interval of the signal. Positive value of Eq. (1) represents ERS and negative value is ERD.

By using a sliding window with a step of 25ms, gamma ERS/ERD was calculated for each time window (500ms) at a sample point within a trial. Therefore, each window overlapped the previous one by 475 sample points. The feature extraction of gamma ERS/ERD was conducted for all channels and 60 features in total were thus produced at each sample point within a trial.

2.5 Feature Selection by Sequential Forward Floating Search Algorithm

Inductive reasoning is mediated by the coordination of multiple brain areas, including prefrontal, frontal, parietal, and some subcortical regions, etc. [12, 13]. As an important moderating variable of neural efficiency, different brain areas show different activation dependency on learning, memory, effort, ability, etc. [1]. While confronting with tasks of (subjectively) low to high difficulty, individual cognitive level affects the investment of cortical resource, resulting in differential mental states. For localizing the common cortical regions of subjects that were maximally modulated by reasoning task complexity and logical thinking ability, a sequential forward floating search (SFFS) algorithm was used to conduct electrode-based cortical region detection. SFFS algorithm can obtain optimum combinations of "gamma ERS/ERD" features (and thus channels) by promoting classification accuracy through pairwise discrimination between mental states [14].

Let Y be the feature space composed of D features:

$$Y = \{y_j | j = 1,...,D\} \quad (2)$$

and X_k are the features selected from Y, which consists of k features with the best discrimination accuracy in the feature space

$$X_k = \{x_j | j = 1,...,k, x_j \in Y\}, k = 0,1,...,D \quad (3)$$

X_k is firstly initialized as an empty set with 0 feature selected, i.e., $X_0 = \phi$, $(k = 0)$. The feature selection procedure is conducted in "growing" and "pruning"

phases alternatively. During the growing phase, the best feature x^+ is added to the selected feature subset as follows,

$$X_{k+1} = X_k + x^+, \ k = k+1 \tag{4}$$

which makes the feature subset X_{k+1} have the highest discrimination, i.e.,

$$x^+ = \arg\max_{x \in Y - X_k} J(X_k + x) \tag{5}$$

Function J is mean classification accuracy achieved by linear discriminant analysis (LDA) with cross-validation. When $k > 2$, the selection procedure enters into pruning phase after growing in each iteration. During this phase, some features in X_k will be removed in turn. If the removal of x^- in X_k results in better discrimination, i.e.,

$$J(X_k - \{x^-\}) > J(X_k) \tag{6}$$

$$x^- = \arg\max_{x \in X_k} J(X_k - x) \tag{7}$$

then this feature will be deleted from X_k, i.e.,

$$X_{k-1} = X_k - x^-, \ k = k-1 \tag{8}$$

While k is up to the preset maximum number of selected features (channels), the selection procedure will end. In this study, the maximum number of accepted channels was set to 15. The feature selection based on binary-classification was conducted between subject groups in each task condition, and also conducted between tasks in each group respectively. In all the selected feature combinations, we could find the optimum scalp channel locations with the highest accuracy in discriminating mental operations and subject groups respectively.

3 Results and Discussions

3.1 Augmented Gamma Band Response in Fronto-Parietal Cortices

The increase of gamma power was found to be modulated by task complexity and task performer (math-gifted/average-level). As shown in Figure 2, the high-complexity task induces more gamma ERS in the two groups than the low-complexity task. Meanwhile, the math-gifted group shows different gamma ERS distribution compared with the control group in the two tasks, that is, the math-gifted adolescents recruited more resource in fronto-parietal cortices for complex task but less for simple

task. Fronto-parietal cortices are involved in event-related activation of logical reasoning, which are mainly manifested as gamma ERS distributed in frontal, sensorimotor, and parietal cortical regions. Other parts of the brain, such as prefrontal, temporal, occipital cortices also show increased gamma power.

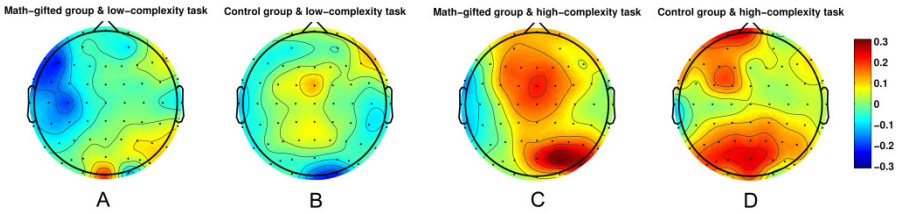

Fig. 2. EEG topological maps of group-averaged gamma ERS/ERD, with positive value representing ERS and negative value ERD: (a) Math-gifted group in low-complexity task; (b) Control group in low-complexity task; (c) Math-gifted group in high-complexity task; (d) Control group in high-complexity task.

3.2 Optimum Channel Combinations for Distinguishing Mental States

In Figure 3a, the math-gifted group shows the highest accuracy of 0.7302 in discriminating high-complexity and low-complexity tasks. Their brain regions that were maximally modulated by task complexity were located at frontal (F1 and F3), parietal-occipital (P2 and PO4) and sensorimotor (C1, C3, C4 and C6) cortices. Left-lateral frontal regions are responsive to implicit relation synthesis of numbers, right-lateral parietal regions are related to internal manipulation of numerical quantity, and occipital cortex reflects visual working memory and visual attention. It is notable that most selected electrodes are in sensorimotor regions, which could be attributed to efficient utilization of fronto-parietal network by math-gifted subjects. Gamma synchronized network plays the role of functional binding between posterior parietal cortex and frontal regions to complete numerical information processing. The increased gamma synchronization can be reflected by increased gamma power [8].

In the control group, only 5 electrodes were selected with the highest accuracy of 0.6707 in discriminating two tasks, which are FP1, POZ, PO6, PO8 and OZ, as shown in Figure 3b. These sites of scalp electrodes indicate that left-lateral prefrontal cortex and parieto-occipital cortices are the most significant brain regions affected by task complexity in average-level subjects. As prefrontal activity reflects attention and cognitive control and parieto-occipital cortices are related to visual response, task complexity change does not significantly affect gamma activity change within fronto-parietal cortical area in average-level subjects.

During the high-complexity task, except for electrodes PO7, OZ and O2 related to visual response, the channel combination with the highest accuracy of 0.6699 in discriminating the two groups focuses on right frontal-centroparietal regions (F2, FCZ, FC4, CZ and CP1), as shown in Figure 3c. Notably, math-gifted subjects show extensive gamma ERS in frontal cortex, especially enhanced right-lateral frontal cortex, as

shown in Figure 2. During numerical inductive reasoning, the right frontal regions conduct spatial information processing involved in arithmetic rules and are adequately utilized by math-gifted subjects.

By comparison, a higher accuracy of 0.7106 in discriminating the two groups was found in the low-complexity reasoning task. The topological map of channel combination sketches a characteristic of fronto-parietal distribution, as shown in Figure 3d, involving right frontal, right sensorimotor, and bilateral parietal regions (F6, FC2, C6, CP1, CP4, P3 and P4), which indicates that a coherent fronto-parietal cortical network might be involved in efficient operation by math-gifted subjects.

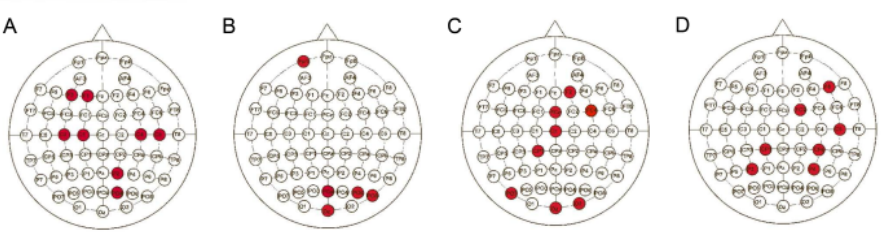

Fig. 3. Topological maps of optimal channel combinations based on SFFS: (a) Channel combination of math-gifted group between tasks; (b) Channel combination of control group between tasks; (c) Channel combination of high-complexity task between groups; (d) Channel combination of low-complexity task between groups.

4 Conclusions

This study shows that between math-gifted and control subjects, right-lateral frontal and bilateral parietal cortices represent the highly discriminating cortical areas where neural resource is effectively recruited by math-gifted adolescents to adapt to different internal requirement for cognitive processing. Specially, right frontal lobe was selected in both of the tasks through high utilization in the complex task and economical usage in the simple task by math-gifted subjects. The activation of right frontal lobe can be viewed as an optimum indicator of neural efficiency. The selected scalp locations coincide well with the important neural mechanism of math-gifted adolescents, i.e., highly developed right frontal lobe and bilateral fronto-parietal network [6, 15].

The results from this study are meaningful for mathematical learning of children and adolescents. Their neurodevelopment has adjustable characteristics based on neuroplasticity, especially for children and early adolescents whose frontal lobe still lies in a developing stage, e.g., laterality of frontal cortical activity can be modulated by on-line neurofeedback to improve individual's neural response.

Acknowledgements. This work was supported in part by the National Natural Science Foundation of China under Grant 61375118 and Grant 61075009, the Natural Science Foundation of Jiangsu Province under Grant BK2011595, and the Program for New Century Excellent Talents in University of China under Grant NCET-12-0115.

References

1. Neubauer, A.C., Fink, A.: Intelligence and Neural Efficiency. Neurosci. Biobehav. Rev. 33, 1004–1023 (2009)
2. Grabner, R.H., Neubauer, A.C., Stern, E.: Superior Performance and Neural efficiency: The Impact of Intelligence and Expertise. Brain Res. Bull. 69, 422–439 (2006)
3. Grabner, R.H., Stern, E., Neubauer, A.C.: When Intelligence Loses Its Impact: Neural Efficiency during Reasoning in a Familiar Area. Int. J. Psychophysiol. 49, 89–98 (2003)
4. Jaušovec, N., Jaušovec, K.: Differences in Induced Brain Activity during the Performance of Learning and Working-memory Tasks Related to Intelligence. Brain Cogn. 54, 65–74 (2004)
5. Wartenburger, I., Heekeren, H.R., Preusse, F.: Cerebral Correlates of Analogical Processing and Their Modulation by Training. Neuroimage 48, 291–302 (2009)
6. Prescott, J., Gavrilescu, M., Cunnington, R.: Enhanced Brain Connectivity in Math-gifted Adolescents: an fMRI Study Using Mental Rotation. Cogn. Neurosci. 1, 277–288 (2010)
7. Hoppe, C., Fliessbach, K., Stausberg, S.: A Key Role for Experimental Task Performance: Effects of Math Talent, Gender and Performance on the Neural Correlates of Mental Rotation. Brain Cogn. 78, 14–27 (2012)
8. Fitzgibbon, S.P., Pope, K.J., Mackenzie, L.: Cognitive Tasks Augment Gamma EEG Power. Clin. Neurophysiol. 115, 1802–1809 (2004)
9. Lachaux, J.P., Fonlupt, P., Kahane, P.: Relationship between Task-related Gamma Oscillations and BOLD Signal: New Insights from Combined fMRI and Intracranial EEG. Hum. Brain Mapp. 28, 1368–1375 (2007)
10. Lisman, J.: Working Memory: the Importance of Theta and Gamma Oscillations. Curr. Biol. 20, R490–R492 (2010)
11. Simos, P.G., Papanikolaou, E., Sakkalis, E.: Modulation of Gamma-band Spectral Power by Cognitive Task Complexity. Brain Topogr. 14, 191–196 (2002)
12. Lu, S.F., Liang, P.P., Yang, Y.H.: Recruitment of the Pre-motor Area in Human Inductive Reasoning: an fMRI Study. Cogn. Syst. Res. 11, 74–80 (2010)
13. Jia, X., Liang, P., Lu, J.: Common and Dissociable Neural Correlates Associated with Component Processes of Inductive Reasoning. Neuroimage 56, 2292–2299 (2011)
14. Dyson, M., Sepulveda, F., Gan, J.Q.: Localisation of Cognitive Tasks Used in EEG-based BCIs. Clin. Neurophysiol. 121, 1481–1493 (2010)
15. Desco, M., Navas-Sanchez, F.J., Sanchez-Gonzalez, J.: Mathematically Gifted Adolescents Use More Extensive and More Bilateral Areas of the Fronto-parietal Network than Controls during Executive Functioning and Fluid Reasoning Tasks. Neuroimage 57, 281–292 (2011)

An Object Recognition Model Using Biologically Integrative Coding with Adjustable Context

Jinwen Xiao and Hui Wei

School of Computer Science, Fudan University
Shanghai 200433, China
jinwen.fd@gmail.com, weihui@fudan.edu.cn

Abstract. Many existing models of object recognition have a hierarchical architecture. They are based on the theory of hierarchy in brain of primate and cognitive process of human. The feature is simple in low layer while complex in high layer. However, the simple feature are local without global clues in these computational models. In this paper, we propose a novel method to code orientation feature which is local feature derived from receptive field of simple cells. The integrative coding in each simple feature, utilizing the global context information such as angle between orientations, is different from other methods of coding batch-based. This coding is scale-invariance since we overlook the distance between orientations. In addition, it is a method of feature learning since the size of context can be adjusted automatically according to special recognition task. Experimental results on ETH-80 data set demonstrate the effectiveness of our model.

Keywords: hierarchical architecture, feature learning, sparse coding, receptive field(RF).

1 Introduction

Object recognition, which is to find given object from unseen image, plays an important role in computer vision. The investigative results in neurobiology indicate the hierarchical architecture exists in brain of primate. These results promote the development of deep architecture model in compute vision. Nowadays, many computational models with a deep hierarchical architecture simulate human vision to finish the task of object recognition[1,2,3,4].

Models inspired by biology are built mainly through simulating visual cortex. The Hubel-Wiesel model [5] is a classical model and becomes the basis of many modern models simulating visual cortex. Their work validates a hypothesis of orientation stimulation in Receptive Field(RF) of simple cells (RF is the region to which visual neurons response). The orientation feature, which resembles line segment with fixed length, can be combined to form higher semantic feature. Therefore, Many extensions of Hubel-Wiesel model are inspired by this type of orientation feature[4,6]. The prominent one is HMAX model[4]. It has a hierarchical architecture consists of four layer feature to represent object. Notice that the first layer is precisely orientation feature obtained by Gabor filter.

M. Lee et al. (Eds.): ICONIP 2013, Part I, LNCS 8226, pp. 33–41, 2013.
© Springer-Verlag Berlin Heidelberg 2013

Since the model aforementioned is biologically motivated, hierarchical architecture is the key characterization. The feature becomes more complex and abstract from low layer to high layer. Recently, deep learning become a hot tendency due to the intractable problem of deep training is efficiently solved by Hinton et al[1]. The key goal of deep learning is feature learning automatically beyond artificial feature according to special occasion. There have been some successful application of deep learning in computer vision[3] and natural language processing[7].

In this paper, we present a novel method using integrative coding to build a deep hierarchical architecture. The method adopts global information to code orientation feature since the context can be adjusted automatically in object recognition. So this is actually a method of feature learning, and it's suitable for generic object recognition. This type of coding overcome the limitation of traditional global coding which is susceptible to variety of object. In addition, it is different from some local coding, which only contain a descriptor in fixed range, i.e. shape context[8], SIFT[9], and HOG[10]. The local coding need some later concrete combination to represent object. We call this novel coding **I**ntegrative **C**oding with **A**djustable **C**ontext*(ICAC)*.

Note that *ICAC* is also a type of sparse coding. We overlook the distance between orientations and only keep the angle, so the feature vector of orientation is determined by angles relative to other orientations. The dictionary of basis is the lattices dividing the feature space to parts. Only few of the lattices is activated when coding each orientation.

The rest of this paper is organized as follows: Sec. 2 introduces the biological foundation and a novel orientation detection method. Our model is presented in Sec. 3, and Sec. 4 introduces the concrete algorithm of object recognition basing on our coding, Sec. 5 presents the experimental results. Finally, we conclude in Sec. 6.

2 Biological Foundation and Orientation Detection

2.1 Hierarchical Architecture in Biology

The object recognition of human vision is a hierarchical process. Fig. 1 shows the ventral stream of primate visual cortex. The hierarchical processing of the ventral stream is to achieve an optimal tradeoff between selectivity and invariance[11]. From eyes to visual cortex, the vision feature become more complex and abstraction. The layer is higher, the area of RF becomes larger. In Hubel-Wiesel model, as Fig. 2(a), every simple cell in V1 is sensitive to specified orientation stimulation by the response derived from RF of lateral geniculate nucleus(LGNs) or retinal ganglion cells(GCs). The simple cell is selective to produce orientation feature, then complex cell in V1 adopts pooling operation of orientation located in fixed area to achieve position- and scale-invariance. In HMAX model, this pooling operation is *max*. Therefore, through multiple feedforward feature transformation in hierarchical architecture, the abstract representation of object is produced for higher vision task such as object recognition.

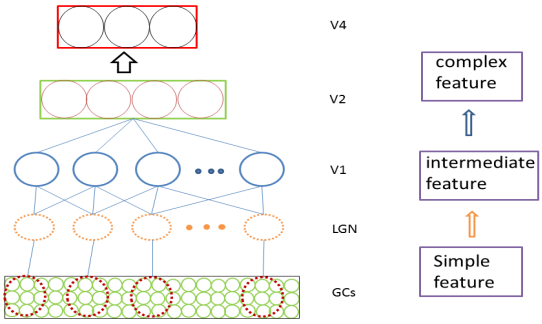

Fig. 1. ventral stream of primate visual cortex: a hierarchical architecture of human vision. The RF becomes larger and feature become more complex from low layer to high layer.

2.2 Orientation Detection

There are many approaches of orientation detection. In HMAX model, Gabor filter is used to acquire orientation feature map, but different coefficients are need to tuned to produce multiple feature maps. We adopt the newest work of orientation detection(OD)[6,12], which is a computational model inspired by Hubel-Wiesel model. Fig. 2 show the relation between them.

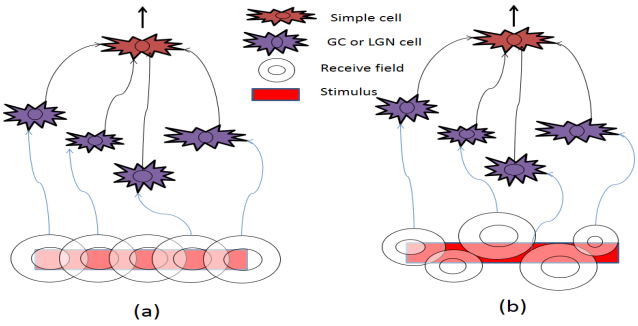

Fig. 2. Orientation detection model: (a) is the Hubel-Wiesel model, a biological model, (b) is the OD model, a computational model. In OD model, the center of RF isn't limited in line and the sizes are different. The red orientation stimulation located in the RF of LGNs or GCs activates the simple cell in V1.

In OD model, the center of RF of LGNs or GCs isn't limited one line and the size of each RF can be different. Only one orientation stimulation is located in the range of RF, the simple cell will be activated by the stimulation. After synthesizing the response of each simple cell, we get the orientation map of raw image.

3 Our Model

We push on the work of orientation detection by combine them to complex feature with context information. Instead of the simple *max* operation in HMAX model, we adopt integrative coding. For the sake of simplicity, we call simple cell as S and complex cell is C respectively, which is corresponding to HMAX model. The overall procedures of our model are showed as Fig. 3. Our main work is focus on the $ICAC$ in C to represent orientation derived from S, then take $ICAC$ as the input of classifier.

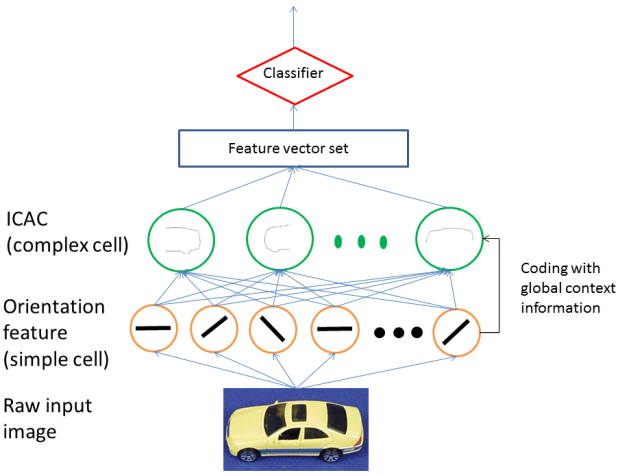

Fig. 3. Our model for object recognition. Firstly, utilize the result of OD model to produce the orientation map, then simulate the operation of complex cell to generate $ICAC$. Finally, we predict the object using classifier which takes $ICAC$ as input.

3.1 Integrative Coding in C Layer

We utilize the global context information of angle between orientations since the angle is insensitive to variety of position and scale. To develop the robustness of model, we add some extra angle information by link the the midpoint of each orientation, as Fig. 4 (a). So for each pair of orientation, there are two types of angles to delineate their context information, the angle θ_{oo} between **orientation and orientation**, the angle θ_{ol} between **orientation and link segment**. Like the shape context[8], SIFT[9], and HOG[10], we adopt histogram based representation, as Fig. 4(b). For a map $O = \{o_1, o_2, \ldots, o_n\}$ consists of n orientation features, we compute o_i's histogram feature using all global context information of angle related to other orientations. We divide the space of angle into parts, and count in every bins in which the orientation's angle located.

After coding each type of angle, we synthesize the two styles of histogram to one histogram to represent $ICAC$, as Fig. 4(c). Write formulation as follows,

$$H_i^{\theta_{oo}}(k) = \sharp\{o \neq o_i : A(o, o_i) \in bin(k)\} \tag{1}$$

$$H_i^{\theta_{ol}}(k) = \sharp\{l : A(l, o_i) \in bin(k)\} \tag{2}$$

$$H_i = H_i^{\theta_{oo}} \otimes H_i^{\theta_{ol}} \tag{3}$$

where "$\sharp$" indicates the amount of elements of set, $A(a, o_i), a \in \{o, l\}$ is the angle between a and o_i, and $bin(k)$ is the k-th bin containing fixed size of angle, i.e. $0 \sim 30°$, $\otimes$ is Cartesian product.

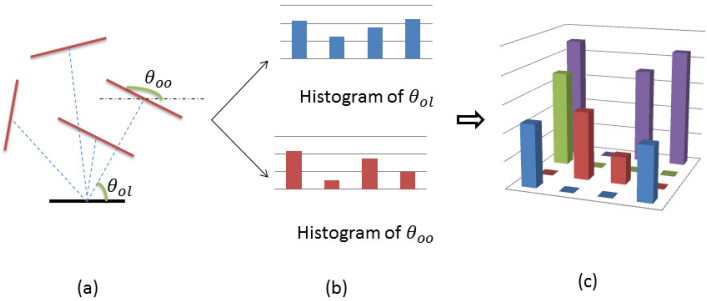

Fig. 4. Computing $ICAC$ of black orientation, (a) represents the orientation map and the angles, (b) shows two style of histogram θ_{oo}, θ_{ol} for orientation o_i, (c) is final $ICAC$ coding represented by histogram. Note that it is sparse.

3.2 Implementation of Object Recognition

To adjust context of $ICAC$ automatically and represent object in different occasion, we adopt histogram intersection as the measure of similarity of two $ACICs$, as follows,

$$Sim(H_i, H_j) = Inter(H_i, H_j) = \sum_{k=1}^{n\_bins} min\{H_i(k), H_j(k)\} \tag{4}$$

The matrix of intersection is the similarity matrix and can be regarded as kernel function in SVM classifier. This kernel is similar to Pyramid Match Kernel(PMK)[13]. When deformation happen to object, the value of intersection decreases and the non-zero parts is located in small range of context. Therefore, the context of $ICAC$ is adjusted by histogram intersection, and it is unsensitive to deformation. The method of object recognition is presented in Algorithm 1.

Algorithm 1. Object recognition using $ICAC$

Input : train objects set T and test object O.
Output: label of test object O.

Get M^T and M^O, the orientation map of T and O respectively using OD[]
$M \leftarrow M^T \bigcup M^O$
foreach $M_i \in M$ **do**
  compute histogram H_i, the $ICAC$ of M_i according to Equ. (3);
end
$H^T \leftarrow \{H_i : M_i \in M^T\}$
$H^O \leftarrow \{H_i : M_i \in M^O\}$
foreach $H_i^T \in H^T$ **do**
  foreach $H_j^O \in H^T$ **do**
    $Sim(H_i^T, H_j^O) \leftarrow (\sum_{k=1}^{n\_bins} min\{H_i^T(k), H_j^O(k)\})$
  end
end
$model$ = svm_train(H^T, Sim);
$label$ = svm_predict($H^O, model$);

Advantage. The angle between orientations remain unchanged under the variety of scale of object. To compute $ICAC$ of each orientation, we adopt relative angle between them, and take current orientation as reference. Therefore, like shape context or SIFT, it's inherently invariance to transform, rotation and scale. There are two points mainly different from other descriptors, 1) it utilize global information without ignoring any other orientation. Either shape context or SIFT is batch-based feature without global information. 2) the distance between orientations changes according to the scale of object, so $ICAC$ abandons the distance information between orientations greatly improving the scale-invariance, and still represents image completely.

4 Experimental Results

We experiment on the ETHZ-80 data set[14] using $ICAC$. The data set contain 8 categories with 80 different objects. There are 41 images with different views for each object. So there are total 3280 images in the set. Orientation map is got by OD model [6,12], Fig. 5 shows some orientation maps of ETH-80.

We use the LIBSVM package[15] as classifier for our model, and adopt *one-to-all* strategy to train classifier. To compute recognition rate, we take the $ICAC$ vectors to train SVM classifier. Each training set contains nearly 1000 $ICACs$. In test stage, we calculate the rate of correct predicting $ICACs$ in one test object. We run program in 10 times randomly, then calculate the average of right predicting rate. We set 144(12×12) bins for $ICAC$ space. Table. 1 shows our results with other 4 approaches basing on color, texture, global shape and local shape presented in[14]. Our model get highest recognition rate in apple, cow, dog and horse. Notice that $ICAC$ outperforms other 4 approaches in total recognition rate.

Fig. 5. Orientation feature: top row is the original images from ETH-80, containing 10 categories object, bottom row is the corresponding orientation feature map

Table 1. Recognition rate: we compare our results(*ICAC*) to 4 approaches, *Color* based, *Mag-Lap* basing on texture, *PCA Gray* basing on global shape and the *shape context*[14]

	Color	*Mag-Lap*	*PCA Gray*	*Cont. DynProg*	our model
apple	57.56%	80.24%	88.29%	76.34%	**90.33%**
car	62.93%	77.56%	97.07%	**100.0%**	93.89%
cow	86.59%	94.39%	62.44%	86.34%	**95.45%**
cup	79.36%	77.80%	96.10%	**99.02%**	82.54%
dog	34.63%	74.39%	66.34%	82.93%	**92.20%**
horse	32.68%	58.78%	77.32%	84.63%	**100%**
pear	66.10%	85.27%	**99.76%**	91.71%	90.07%
tomato	**98.54%**	97.07%	76.59%	70.24%	73.03%
total	64.85%	82.23%	82.99%	86.40%	**89.69%**

We describe the deviation of recognition rate in detail by 10 runs to show robustness of our model. As Fig. 6, most of the test objects, except for car and cup, are recognized stably with low deviation. Because the most boundaries of car and cup are line-like, the amount of orientation feature of them is relsatively less than other objects, and affects their recognition rate. The model, in which the recognition rate of most test objects are more than 80%, is robust to variety of object.

To measure the similarity between each pair of objects, we then adopt *one-to-one* method to train classifier. In this way, we get $64(8 \times 8)$ classifiers. Fig. 7 show the recognition rate with different pairs of training objects. The class of test object is same to training object. When objects are similar to each other, such as apple and tomato, the *ICACs* are similar and will produce weak classifier. So recognition rate is low when the positive object and negative object is similar. The results, as Fig. 7, demonstrate our hypothesis.

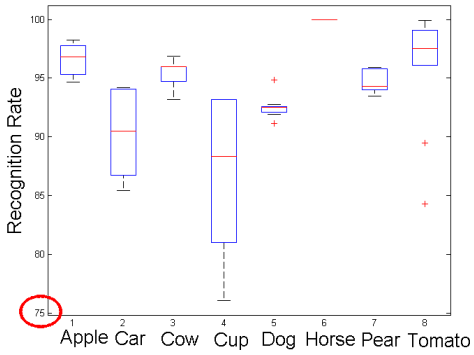

Fig. 6. Deviation of recognition in 10 runs. Most of objects are stable except for car and cup, in which the deviation of recognition is more than 5%. The lowest rate is 76%, and most objects are over 80%.

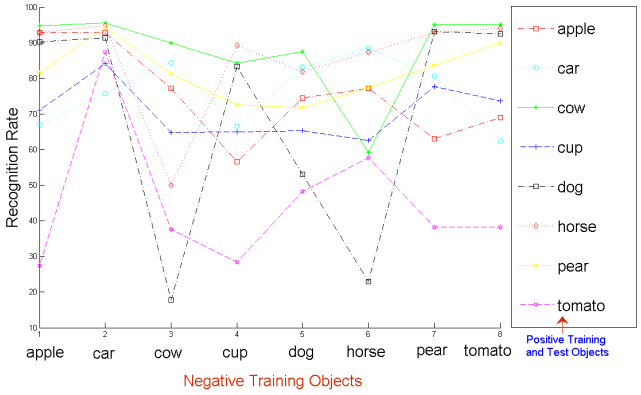

Fig. 7. Shape similarity measure using *one-to-one* classifier. The class of test is same to positive object. The horizontal ordinate is the negative objects in training. The positive and negative objects are more similar, the recognition rate is lower. Note that it's insignificant when positive and negative objects are the same class.

5 Conclusion

In all experiments aforementioned, we find that the non-zero coefficients set in *ICAC* feature vector is relatively small. This characteristic resembles sparse coding and could be used to simulate sparseness of activated neurons. Integrative Coding with Adjustable Context(*ICAC*) is novel global coding which surpass the limitation of fixed size. The context can be adjusted automatically to achieve feature learning in special recognition application. The model is biologically motivated and owns deep hierarchical architecture which is similar to human vision. Therefore, *ICAC* simulates the process of hierarchical vision effectively.

Acknowledgements. This work was supported by 973 Program (Project No.2010CB327900), the NSFC project (Project No. 30990260, 61375122, 81373556), and the National Twelfth 5-Year Plan for Science and Technology (Project No. 2012BAI37B06).

References

1. Hinton, G.E., Osindero, S., Teh, Y.W.: A fast learning algorithm for deep belief nets. Neural Computation 18(7), 1527–1554 (2006)
2. Jhuang, H., Serre, T., Wolf, L., Poggio, T.: A biologically inspired system for action recognition. In: IEEE 11th International Conference on Computer Vision, ICCV 2007, pp. 1–8. IEEE (2007)
3. Krizhevsky, A., Sutskever, I., Hinton, G.: Imagenet classification with deep convolutional neural networks. Advances in Neural Information Processing Systems 25, 1106–1114 (2012)
4. Serre, T., Wolf, L., Bileschi, S., Riesenhuber, M., Poggio, T.: Robust object recognition with cortex-like mechanisms. IEEE Transactions on Pattern Analysis and Machine Intelligence 29(3), 411–426 (2007)
5. Hubel, D.H., Wiesel, T.N.: Receptive fields, binocular interaction and functional architecture in the cat's visual cortex. The Journal of Physiology 160(1), 106 (1962)
6. Wei, H., Ren, Y., Li, B.M.: A collaborative decision-making model for orientation detection. Applied Soft Computing (2012)
7. Socher, R., Huang, E.H., Pennington, J., Ng, A.Y., Manning, C.D.: Dynamic pooling and unfolding recursive autoencoders for paraphrase detection. Advances in Neural Information Processing Systems 24, 801–809 (2011)
8. Belongie, S., Malik, J., Puzicha, J.: Shape matching and object recognition using shape contexts. IEEE Transactions on Pattern Analysis and Machine Intelligence 24(4), 509–522 (2002)
9. Lowe, D.G.: Distinctive image features from scale-invariant keypoints. International Journal of Computer Vision 60(2), 91–110 (2004)
10. Dalal, N., Triggs, B.: Histograms of oriented gradients for human detection. In: IEEE Computer Society Conference on Computer Vision and Pattern Recognition, CVPR 2005, vol. 1, pp. 886–893. IEEE (2005)
11. Tomaso, P., Thomas, S.: Models of visual cortex (2013), `http://www.scholarpedia.org/article/Models_of_visual_cortex`
12. Wei, H., Ren, Y.: An orientation detection model based on fitting from multiple local hypotheses. In: Huang, T., Zeng, Z., Li, C., Leung, C.S. (eds.) ICONIP 2012, Part II. LNCS, vol. 7664, pp. 383–391. Springer, Heidelberg (2012)
13. Grauman, K., Darrell, T.: The pyramid match kernel: Discriminative classification with sets of image features. In: Tenth IEEE International Conference on Computer Vision, ICCV 2005, vol. 2, pp. 1458–1465. IEEE (2005)
14. Leibe, B., Schiele, B.: Analyzing appearance and contour based methods for object categorization. In: Proceedings of the 2003 IEEE Computer Society Conference on Computer Vision and Pattern Recognition, vol. 2, II–409. IEEE (2003)
15. Chang, C.C., Lin, C.J.: LIBSVM: A library for support vector machines. ACM Transactions on Intelligent Systems and Technology 2, 27:1–27:27 (2011), Software available at `http://www.csie.ntu.edu.tw/~cjlin/libsvm`

Single-Trial Event-Related Potentials Classification via a Discriminative Dictionary Learning Scheme

Yue Huang[1,2], Jun Zhang[1,2], Xin Chen[1,2], Delu Zeng[1,2], Xinghao Ding[1,2,⋆], Dandan Zhang[3,⋆], and Qingfeng Cai[4]

[1] Key Lab of Underwater Acoustic Communication and Marine Information Technology, Ministry of Education, China
[2] Department of Communication Engineering, Xiamen University, China
[3] State Key Laboratory of Cognitive Neuroscience and Learning, Beijing Normal University, China
[4] The school of Economics, Xiamen University, China
dxh@xmu.edu.cn, zhangdd05@gmail.com

Abstract. Due to the better performances with large number of training samples, algorithms based on sparse representation have received more and more attentions in single-trial event-related potentials classification. Considered the burden from repeating psychological experiments, the classification with less training samples is still a challenge in both cognitive science and pattern recognition. In this paper, a discriminative dictionary learning based scheme is utilized to single-trial ERPs classification, in order to enhance the performance when the training sample size is small. After preprocessing, wavelet is employed to remove the strong background noise at first, and then a sparse representation recognition method based on discriminative dictionary learning, called D-KSVD, is applied to perform the classification on each testing trial. Experiments on ERPs epochs from risk decision test have demonstrated that proposed approach outperforms than existing sparse representation classifier when the training samples decrease dramatically.

Keywords: single-trial ERPs classification, sparse representation, less training samples, dictionary learning.

1 Introduction

Event-related potentials (ERPs), which is an important physical signals recorded from scalp, are electroencephalogram (EEG) in response to external stimuli in designed experiments [1]. ERPs analysis is mostly limited by its low signal-noise-ratio (SNR) due to strong ongoing EEG background and other noises [2]. Traditional ERPs denoising is averaging across several trials, in which trial-to-trial variability is missing. Single-trial ERPs classification is one of the important ways in neuroscience and cognitive science, since the brain dynamics on the

⋆ Corresponding authors.

M. Lee et al. (Eds.): ICONIP 2013, Part I, LNCS 8226, pp. 42–49, 2013.
© Springer-Verlag Berlin Heidelberg 2013

single-trial level reveals much richer information than conventionally averaged ERPs [3-4]. Most reports on single-trial classification select the features of the ERPs waveform at first, such as temporal features, spatial features, and spatio-temporal features; and then a classifier, e.g. support vector machine(SVM), k-nearest neighbor(KNN), logistic regression, linear discriminative analysis(LDA) are applied to perform the recognition[5-6]. Although fully studied, feature selection should still be carefully considered in this classification and may vary across different experiments paradigms. In additional, these methods are also sensitive to the training sample size.

Sparse representation (SR) has been widely used in signal and image processing, especially in addressing inverse problems, such as signal/image reconstruction, denoising, and pattern recognition. Sparse representation classifier (SRC) is one of the most popular classifiers, which is based on the assumption that each testing sample can only be linear represented by training samples in the same category, thus can be sparse linear represented by all the training samples. This significant model was first proposed for robust face recognition against occlusions and corruptions, and impressive results were reported [7-8]. More important, it is able to perform high classification accuracy without explicit feature extraction. This advantage makes it suitable for single-trial ERPs classification, where the appropriate feature extraction is still a challenge so far. Shin.et al proposed a SRC based scheme to classify the EEG signals in Brain-computer interfaces systems, in which common spatial pattern (CSP) is employed to filtered the original low SNR EEG signals to maximum the inter-class distances at first, and then SRC is applied to do the binary classification. After sparse decomposition and reconstruction with the coefficients, the testing sample is assigned to the category with smaller reconstruction error. The performances have demonstrated that this SRC based scheme is better than LDA classifier in EEG data classification [9].

Though satisfied performances were reported, SRC still has some limitations, one of that is it only has high classification accuracy with sufficient training samples. However, large training samples size requires repeating psychological experiments to acquire more ERPs epoches, which may make the subjects feel very tired at last and provide inaccurate responses. Dictionary design is one of the critical problems in sparse representation. In SRC model, the dictionary is simply formed with all the vectorized training samples, which only emphasize the representative power. The discriminative power of the dictionary can only be guaranteed when the training samples are sufficient. Therefore, its performances will decrease if the training samples size gets smaller. K-SVD is a widely used dictionary learning method in sparse representation and its application, e.g. compress sensing, reconstruction and denoising. The model seeks for the dictionary that yields sparse representations for the training signals. However, it is also emphasizing the representation rather than discrimination.

D-KSVD, another sparse representation classification method with discriminative dictionary, has been firstly reported for face recognition [10]. For D-KSVD, both training label prior and the idea of linear classifier are introduced to the K-SVD, in order to enforce its capability at having discriminative and

representative power simultaneously. D-KSVD has been proven to be robust in various training sample size [10].

In this paper, a discriminative dictionary learning based scheme is proposed for single-trial ERPs classification to enhance the classification accuracy, especially with less training samples. After preprocessing, popular wavelet is employed to remove the strong background noise, and then D-KSVD is applied to the testing trials recognition. The proposed scheme is validated with the real ERPs data from risk decision making test.

2 Experiments and Dataset

The ERPs data are generated from a risk decision-making experiment at Beijing Normal University. 20 students from Beijing Normal University are recruited as paid volunteers. The electroencephalogram (EEG) was recorded from 61 scalp sites using tin electrodes mounted in an elastic cap (NeuroScan Inc., Herndon, VA, USA), with an online reference to the right mastoid and off-line algebraic re-reference to the average of the left and right mastoids.

The experimental data could be interpreted as binary classifications of single-trial ERPs at a predefined psychological perspective: Label 9 and 99 are defined as low-risk option (small potential win or loss) and high-risk option (large potential win or loss) respectively. The binary classification demonstrated the predictive power of individuals risk-avoidant preference embedded in ERP trials. Detail descriptions are available in the original publications [11-12].

3 Methodology

Proposed discriminative dictionary learning scheme is summarized in Figure.1. Detail descriptions are presented step by step in the following.

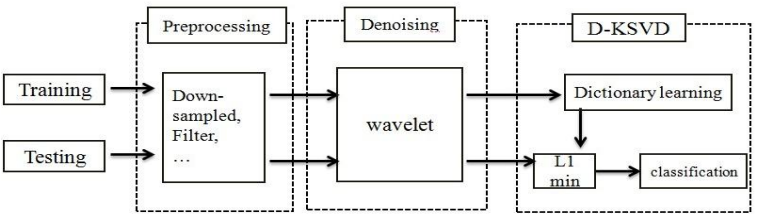

Fig. 1. summarization of the discriminative dictionary learning scheme

3.1 Preprocessing

EEG and electrooculogram (EOG) signals were amplified with a 0.05C100 Hz band-pass filter and continuously sampled at 1000 Hz. During the off-line

analysis, ocular artifacts were removed from the EEG signal using a regression procedure implemented in the Neuroscan software. Then, the EEG data were down-sampled to 250Hz and filtered with a 0.05-30 Hz finite impulse response filter with zero phase distortion. Filtered data were segmented beginning the onset of outcome and lasting for 1000 ms. All epochs are baseline-corrected with respect to the mean voltage over the 200ms preceding the onset of outcome.

3.2 Wavelet Denoising

Analysis of single-trial ERPs is most limited by the strong ongoing EEG background. Wavelet transform, a very popular approach in signal processing, has the capability of providing time-frequency decomposition. Compared with other algorithms for ERPs denoising, it has been proven to be more suitable for ERPs analysis, due to its optimal resolution both in time and in frequency domain. This denoising procedure contains wavelet decomposition, thresholding, and reconstruction, as detailed described in [13].

3.3 Classification

After denoising by wavelet, D-KSVD, which can be treated as an improved SRC model, is applied to classify each testing trial to predefined categories. The model formulate the problem of dictionary learning as [10]:

$$< \hat{D}, \hat{W}, \hat{\alpha} > = \underset{D,W,\alpha}{\arg\min} ||Y - D\alpha||_2 + \gamma||H - W\alpha||_2 + \beta||W||_2 s.t. ||\alpha||_0 < T \quad (1)$$

where Y is the testing sample, which contains all the testing trials; D is the dictionary learnt from all the training trials, α is the coefficient matrix, H is the label of training trials, W is the classifier parameters, γ and β is the scalars. Compared with the model of KSVD[14], it can be observed that (1) has two additional terms: $\|H - W\alpha\|_2$ and $\|W\|_2$. These are introduced from the linear classifier H=W+b, and b is set to 0 for simplicity.

Considered the convergence of the solution in the optimization problem, (1) can be rewritten into:

$$< D, W, \alpha > = \underset{D,W,\alpha}{\arg\min} || \begin{pmatrix} Y \\ \sqrt{\gamma} * H \end{pmatrix} - \begin{pmatrix} D \\ \sqrt{\gamma} * W \end{pmatrix} * \alpha||_2 \ \ s.t. \ \ ||\alpha||_0 < T \quad (2)$$

where the matrix $\begin{pmatrix} D \\ \sqrt{\gamma} * W \end{pmatrix}$ is column-wise normalized, as defined in the original K-SVD. So it is possible to drop the regularization term $\|W\|_2$.

Algorithm for single-trial denoised ERPs classification based on D-KSVD is summarized as:

1) dictionary orientation: All the trials, including training trials and testing trials are vectorized, for example, in our experiments, there are 61 channels, each

channel has 250 time points, a vector of 15,250 is employed to denote a trial. The dictionary orientation is defined as:

a) Training trials of each class are employed to learn a individual dictionary;

b) Dictionaries from different classes are combined to a new dictionary.

2) solve D and α in (2):

$$< \hat{d_k}, \hat{\alpha}_k >= \arg\min_{d_k, \alpha_k} ||E_k - d_k \alpha_k||_F \tag{3}$$

where $E_k = Y - \sum_{i \neq k} d_i \alpha_i$,and Y are the training trials, $\|\|_F$ is Frobenius norm. This problem can be addressed by singular value decomposition (SVD), exactly the same as in KSVD[14].

3) valid final dictionary D_1 and corresponding classifier parameters W_1 in (1):

$$\begin{aligned} D_1 &= \left\{ \frac{d_1}{||d_1||_2}, \frac{d_2}{||d_2||_2}, \frac{d_3}{||d_3||_2}, \cdots, \frac{d_k}{||d_k||_2} \right\} \\ W_1 &= \left\{ \frac{w_1}{||w_1||_2}, \frac{w_2}{||w_2||_2}, \frac{w_3}{||w_3||_2}, \cdots, \frac{w_k}{||w_k||_2} \right\} \end{aligned} \tag{4}$$

where d_i and w_i are the ith column of D and W in (2) respectively.

4) Calculate the sparse coefficient in (1):

$$< \hat{\alpha} >= \arg\min_{\alpha} ||y - D_1 \alpha||_2 + ||\alpha||_1 \tag{5}$$

This typical l1-norm optimization problem can be solved by orthogonal matching pursuit (OMP), which is effect and efficient.

5) Identify the label of testing sample:

$$label = W_1 \alpha \tag{6}$$

where is a vector, the label of the testing trial can be finally identified by the index of the largest value in vector.

4 Results and Analysis

All the experiments are implemented with Matlab 2010 with Intel Core CPU at 2.0G and 2G memory. As described before, proposed ERPs data are categorized into two classes, so our method is applied to binary classifications. Since each trial contained 250 points from 61 channels, a vector of 15,250 dimensions ($250 \times 61 = 15,250$) was used to denote a single trial in the classification. For each subject, training trials and testing trials are randomly selected to calculate the classification accuracy. To demonstrate the robustness of the proposed scheme, the experiments are implemented with four different training sample size: 100, 80, 60 and 40, which means the training data contains 100, 80, 60, and 40 trials. It should be mentioned that in each classification round, trials number for each category in training data is the same, as well as in the testing samples. For example, if training sample size is 100, 50 trials come from class 1 and 50 trials

are from class 2. For comparison, SRC is also employed to the same ERPs epochs after the same denoising procedure.

Average classification accuracy over all the subjects is presented with the four different training sizes from SRC and proposed method in Figure. 2(a). For more detail, two subject are randomly selected, and corresponding classification accuracy plots are also shown with different training sizes from two methods (Figure.2(b)(c)). It can be observed that the results from proposed discriminative dictionary learning scheme look similar as that of SRC based scheme if the training sample size is large, like 100 and 80. However, when the number of training trials decrease dramatically, like 60 and 40, proposed scheme is definitely

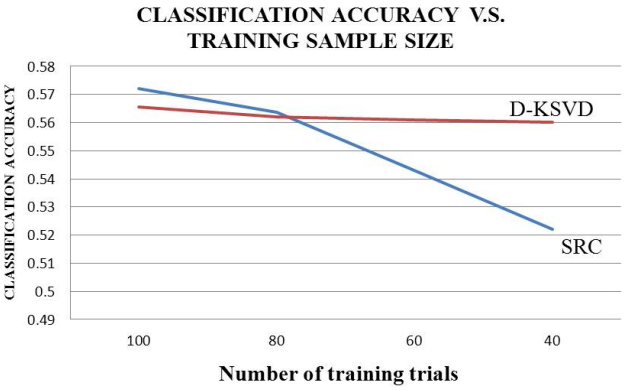

(a)

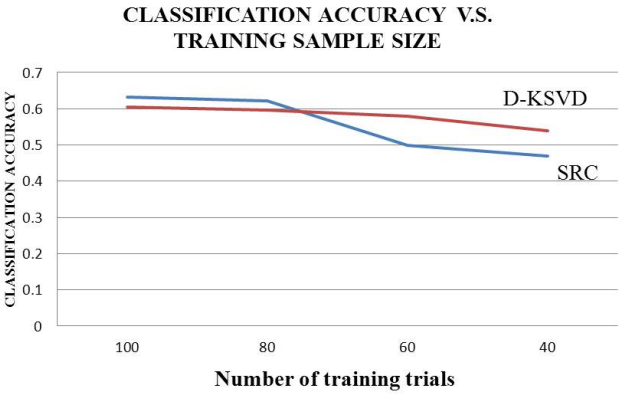

(b)

Fig. 2. (a)average classification accuracy over all the subjects between SRC-based scheme and proposed scheme at different training sizes; (b) classification accuracy over all the subjects between SRC-based scheme and proposed scheme at different training sizes for Subject 19;(c) classification accuracy over all the subjects between SRC-based scheme and proposed scheme at different training sizes for Subject 40

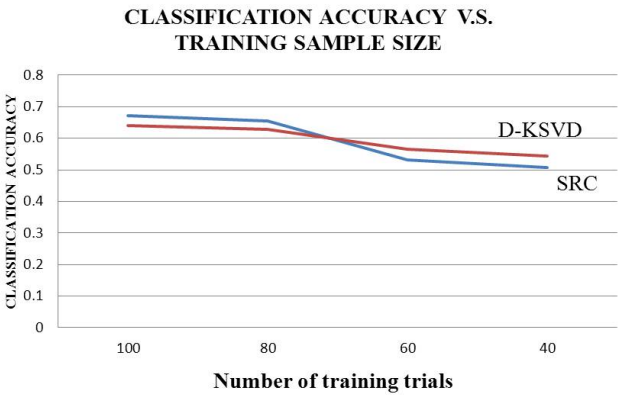

(c)

Fig. 2. (*Continued.*)

robust than SRC scheme, since the accuracy in both training sample size 60 and 40 from proposed scheme are higher than that of the SRC model.When the training sample size is less than 20, the accuracy of both SRC and D-KSVD dramatically decrease to less than 50%.

5 Conclusions

Due to the requirement from psychological experiments, a discriminative dictionary learning scheme is utilized for single-trial ERPs classification with less training samples. Each trial is denoised with wavelet transform at first, and then a sparse representation based classification with discriminative dictionary learning, D-KSVD, is applied for single-trial classification. Experiments on the psychological ERPs data have demonstrated the satisfied performances of the present approach.

Acknowledgments. The project is supported by the National Natural Science Foundation of China (No:30900328, 61172179, 61103121,71103150,81301278), the Natural Science Foundation of Fujian Province of China(NO:2012J05160), the National Key Technology R&D Program(2012BAI07B06),the Fundamental Research Funds for the Central Universities(No:2011121051,2013121023).

References

1. Blankertz, B., Curio, G., Muller, K.R.: Classifying Single Trial EEG: Towards Brain Computer Interfacing. NIPS 1, 157–164 (2002)
2. Parra, L., Alvino, C., Tang, A., Pearlmutter, B., Yeung, N., Osman, A., Sajda, P.: Linear spatial integration for single-trial detectionin encephalography. NeuroImage 17(1), 223–230 (2002)

3. Quian Quiroga, R., Garcia, H.: Single-trial event-related potentials with wavelet denoising. Clinical Neurophysiology 114(2), 376–390 (2003)
4. Stahla, D., Picklesa, A., Elsabbaghb, M., Johnsonc, M.H.: Novel Machine Learning Methods for ERP Analysis: A Validation From Research on Infants at Risk for Autism. Developmental Neuropsychology 37(3), 274–298 (2012)
5. Tomioka, R., Aihara, K., Muller, K.R.: Logistic regression for single trial EEG classification. NIPS 19, 1377–1384 (2007)
6. Stahla, D., Picklesa, A., Elsabbaghb, M., Johnsonc, M.H.: Novel Machine Learning Methods for ERP Analysis: A Validation From Research on Infants at Risk for Autism. Developmental Neuropsychology 37(3), 274–298 (2012)
7. Wright, J., Ma, Y., Mairal, J., Sapiro, G., Huang, T.S., Yan, S.: Sparse representation for computer vision and pattern recognition. Proceedings of the IEEE 98(6), 1031–1044 (2010)
8. Wright, J., Yang, A.Y., Ganesh, A., Sastry, S.S., Ma, Y.: Robust face recognition via sparse representation. IEEE Trans Pattern Anal. Mach. Intell. 31(2), 210–227 (2009)
9. Shin, Y., Lee, S., Lee, J., Lee, H.N.: Sparse representation-based classification scheme for motor imagery-based brain computer interface systems. Journal of Neural Engineering 9(5), 056002 (2012)
10. Zhang, Q., Li, B.: Discriminative k-svd for dictionary learning in face recognition. In: 2010 IEEE Conference on Computer Vision and Pattern Recognition (CVPR), pp. 2691–2698. IEEE Press (2010)
11. Zhang, D., Gu, R., Wu, T., Broster, L., Luo, Y., Jiang, Y., Luo, Y.: An An electrophysiological index of changes in risk decision-making strategies. Clinical Neuropsychologia 51(8), 1397–1407 (2013)
12. Gu, R., Ge, Y., Jiang, Y., Luo, Y.J.: Anxiety and outcome evaluation: the good, the bad and the ambiguous. Biol. Psychol. 85(2), 200–206 (2010)
13. Quiroga, R., Garcia, H.: Single-trial event-related potentials with wavelet denoising. Clinical Neurophysiology 114, 376–390 (2003)
14. Aharon, M., Elad, M., Bruckstein, A.: K-SVD: An Algorithm for Designing Overcomplete Dictionaries for Sparse Representation. IEEE Trans. Signal Processing 54(11), 4311–4322 (2006)

A Preliminary Study on Neural Basis of Collaboration as Mediated by the Level of Reasoning

Eun Kyung Jung[1], Jun Zhang[2], Soo-Young Lee[3], and Jong-Hwan Lee[1,*]

[1] Dept. of Brain and Cognitive Engineering, Korea University, Seoul, Korea
{labyrinth,jonghwan_lee}@korea.ac.kr
[2] Dept. of Psychology, University of Michigan, Ann Arbor, USA
junz@umich.edu
[3] Brain Science Research Center and Dept. of Electrical Engineering, KAIST, Daejeon, Korea
sy-lee@kaist.ac.kr

Abstract. In this study, we investigated the neural correlates of collaboration and the relationship between collaboration and the reasoning level (low; zeroth-order or high; first-order) of other person. Fourteen volunteers played a collaborative matrix game with a computerized agent and predicted the agent's behavior in the functional magnetic resonance imaging (fMRI) scan session. From the results, the collaboration game evoked neuronal activations within both the left and right insula. Also, in the collaboration game, insula activation was greater in the higher-order reasoning condition than the low-level reasoning condition of the agent. The insula area is known to be related with sense of agency, autonomic arousal, and motivation. The collaborative game may cause participants to be motivated and deeply involved in the emotional experience, such as achieving a common goal with other person. In this context, the increased activation within insula seemed to be associated with participants' motivational and emotional states while collaborating with other person.

Keywords: Functional magnetic resonance imaging, theory of mind, collaboration, reasoning order, insula, matrix game.

1 Introduction

Theory of mind (ToM) has been defined as the ability to understand desires, intentions, or beliefs of others [1] and its underlying neural mechanism have been studied for decades. Regions including medial prefrontal gyrus, posterior cingulate cortex, temporoparietal junction, and amygdala have been mainly reported as the ToM network [2, 3].

In particular, researchers have been focused on neural basis of cooperative behavior [4, 5, 6]. For example, Decety and colleagues (2004) investigated brain regions underlying collaboration and found medial frontal activation in collaboration condition. Also, brain regions related to reward processing were also found in collaborative

* Corresponding author.

M. Lee et al. (Eds.): ICONIP 2013, Part I, LNCS 8226, pp. 50–56, 2013.
© Springer-Verlag Berlin Heidelberg 2013

setting. For instance, Krill and Platek (2012) reported the activation in caudate and putamen, suggesting rewarding nature of collaboration.

On the other hand, some researchers have developed hierarchical model of ToM to explain depth of thoughts, or reasoning order [7, 8]. Reasoning order tells how a person can recursively predict the other person's behavior. Within this hierarchical model, a zeroth-order reasoner only considers his desires and beliefs to make a decision, without considering other person's desires or beliefs. A reasoner, who uses high level of reasoning, can infer other person's thoughts and make a decision based on the inference in a social context. Previous neuroimaging literatures have found that higher level of reasoning positively correlated with medial prefrontal or dorsal prefrontal cortex activation [9, 10], and these regions reflected successful mentalizing of other's behavior.

To our knowledge, however, there was no study investigating the relationship between collaboration and the reasoning order. This functional magnetic resonance imaging (fMRI) study aimed at investigation of the neural correlates of collaboration with a counterpart who had low or high level of reasoning.

2 Methods

2.1 Participants

Fourteen healthy right-handed students volunteered to participate in this study (8 males, age=23.6±3.7 year). They had no history of neurological and mental disorders such as depression, anxiety disorder, or borderline disorder. Once participants fully understood the experimental procedure, they gave written informed consent. Prior to fMRI experiment, all participants visited the laboratory and were trained to be familiar with the matrix game. The study procedure was approved by the Institutional Review Board of Korea University.

2.2 Experimental Paradigm

Each participant performed a 2 × 2 collaborative matrix game (modified from [7]) with either a myopic (zeroth-order) or a predictive (first-order) computer agent as an opponent. As shown in Fig. 1, the game matrix consisted of 4 cells labeled as A, B, C, and D, and each cell contained respective payoffs (between $1 and $4) for the participant (left) and the computer agent (right). The two players took turn and made a 'move' or a 'stay' decision by pressing buttons. The participant always started first at cell A. The game could be ended anywhere (A, B, C, or D) according to decisions made by the players. For example, if the participant decided to stay at cell A, the game ended at cell A and the computer agent was deprived of its chance to move at B. On the other hand, when the participant moved to cell B and the opponent moved to cell C, the game would be ended at cell C or cell D. The movement from C to D was determined based on the participant's advantage. The game was ended at cell D only when the participant's outcome was greater in cell D than cell C.

In a game, the participant was asked to win the payoffs as much as possible according to one of two instructions: 1) control condition: maximize own payoff regardless

of the opponent's payoff; 2) collaboration condition: maximize the summed payoff of the self and the opponent. The participants were required to predict the opponent's move, which was either of a 'move' or a 'stay' decision at cell B. The participants were told that they were going to play with a myopic (zeroth-order) or a predictive (first-order) opponent. A zeroth-order opponent makes a decision only based on his own payoffs at cell B and C. Meanwhile, a first-order opponent decides to move or stay with regards to his payoffs and the other player (the participant)'s payoffs at cell B, C, and D. The opponent's reasoning order was consistent during an fMRI scan, and the participants played games with zeroth-order opponent in one fMRI scan and first-order opponent in the other fMRI run. They were told that an order of opponent strategy would be randomly mixed across fMRI scans. To motivate participants to actively collaborate with the opponent, the participants were told that they would be playing with the human player which would be one of our study members. In fact, a computerized agent implemented with the zeroth- and first order reasoning was deployed during the game with pseudo-randomly generated response time.

In each of two fMRI scan runs, the participants performed 20 trials consisted of 10 pairs of matrix games. In each pair of matrix game, a single matrix game was used for both control condition and collaboration condition. During the fMRI experiment, participants went through a training run (about 4-6 min) and two task runs (about 12-15 min as shown in Fig. 1). Again, an opponent's reasoning order was counterbalanced across the participants to prevent a potential confounding effect.

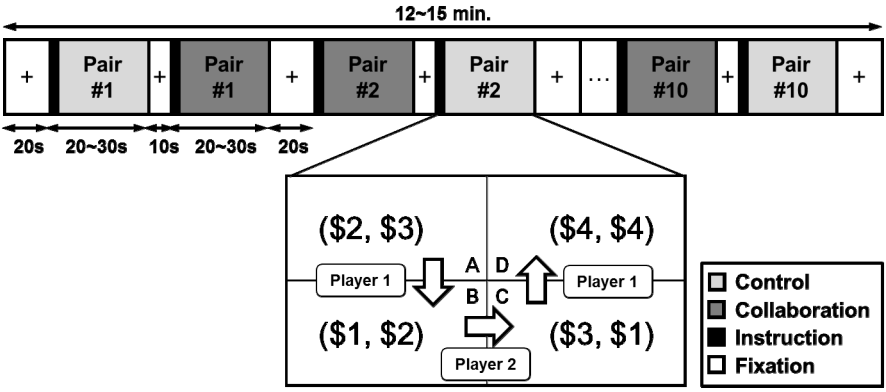

Fig. 1. Experimental protocol. Player 1: participant; Player 2: computerized opponent

2.3 fMRI Data Acquisition

The participant's response time (RT) and accuracy were recorded during fMRI scanning. After the fMRI scan runs, participants were asked how strong they believed that they were collaborating with a human opponent (perceived feeling of interaction; 1: least, 5: most), and how difficult the game was (1: easiest, 5: most difficult).

The fMRI experiment was conducted in a 3-T MR scanner with 12-channel head coil (Tim Trio, Siemens, Erlangen, Germany). The gradient-echo T_2* weighted echo planar imaging (EPI) was applied to measure neuronal activity based on blood-oxygenation

level-dependent (BOLD) mechanism (TR/TE=2000/30 ms, 35 slices parallel to the participant's bi-commissural plane, slice thickness=4 mm, in-plane voxel size=3×3 mm^2, matrix size=64×64, flip angle=90°, field of view=240 mm).

2.4 Data Analysis

Preprocessing. SPM8 (Wellcome Trust Centre for Neuroimaging, London, UK) was used for preprocessing of the obtained EPI data. In detail, a slice timing excluding the first 5 dummy volumes and head motions were corrected. The corrected EPI volumes were spatially normalized to the standard Montreal Neurological Institute (MNI) space and resampled with a 3 mm isotropic voxel size. Then, an 8 mm isotropic full-width at half-maximum Gaussian kernel was applied for spatial smoothing.

Statistical Analysis. The preprocessed data of each participant were analyzed using a general linear model in an individual level. Four different regressors were designed following the onset timing and durations for each of the prediction of the zeroth-/first-order opponent's move in control condition, prediction of the zeroth- /first-order opponent's move in collaboration condition. Then, a group-level analysis was conducted using the contrast of neuronal activations across individuals/participants via one sample *t*-test to compare game types (*i.e.,* collaboration vs. control), or opponent's reasoning orders (*i.e.,* first-order vs. zeroth-order).

3 Results

3.1 Behavioral Response

All participants performed the tasks successfully (accuracy=94.6±6.1%) and most of them reported that the task difficulty was moderate (overall difficulty=2.9±0.7). Also, participants reported that they felt active collaboration with the opponent (perceived feeling of interaction=3.9±1.0). In terms of response time, participants responded faster in zeroth-order condition (295.3±169.4 ms) than first-order condition (363.8±201.9 ms), and the effect was marginal (p=0.055).

3.2 Estimated Spatial Patterns Using fMRI Data

Fig. 2 shows the neural correlates of collaboration compared to control condition during the game. In zeroth-order condition, the left anterior insula was shown greater activations during the collaboration condition than the control condition. There was no brain region that showed greater neuronal activations from the control condition than the collaboration condition with the zeroth-order opponent. Table 1 shows the detailed information.

The left insula activation was also found while participants were collaborating with first-order opponent, whereas the middle temporal gyrus was shown greater activations in the control condition while playing with the first order opponent.

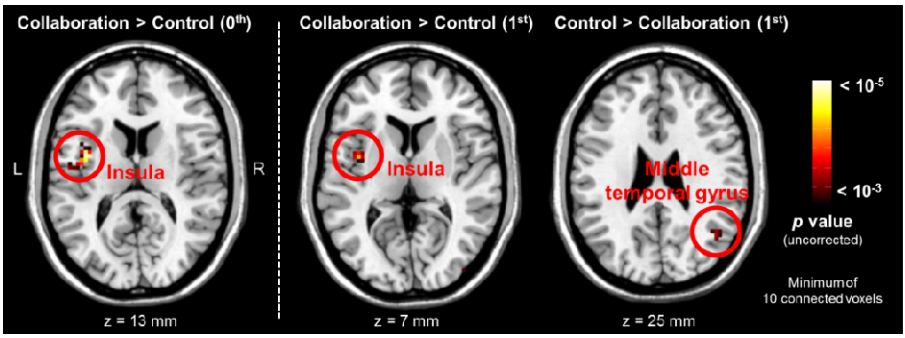

Fig. 2. Activated regions when collaborating with an opponent

Table 1. Activated regions in a collaboration (CB) and control (CN) condition

Condition	Region	L/R	MNI (mm)	t score	Cluster size
Zeroth-order					
CB > CN	Insula	L	-39, -1, 13	6.32	33
First-order					
CB > CN	Insula	L	-39, -1, 7	5.55	25
	Middle occipital gyrus	R	27, -94, 1	4.98	12
	Fusiform gyrus	R	45, -55, -26	4.37	11
CN > CB	Middle temporal gyrus	R	45, -61, 25	4.49	10

Fig. 3 shows the interaction between collaboration and opponent's reasoning order. A collaboration with first-order than zeroth-order opponent resulted in a greater activation in bilateral insula, and right precentral gyrus. However, the opposite contrast (*i.e.,* zeroth-order > first-order) did not reach a statistical significance. Table 2 shows the detailed information.

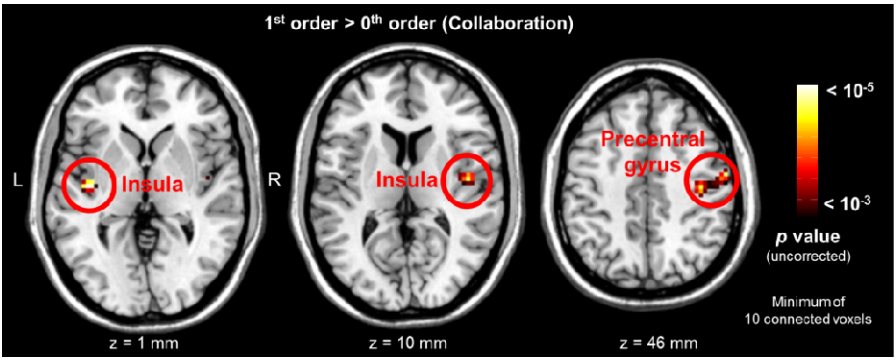

Fig. 3. Activated regions when collaborating with the opponent

Table 2. Activated brain regions depending on a reasoning order of opponent

Condition	Region	L/R	MNI (mm)	t score	Cluster size
Collaboration					
First > Zeroth	Insula	L	-42, -13, 1	4.41	30
	Precentral gyrus	R	57, -7, 46	4.13	138
	Insula	R	45, -10, 10	4.11	44
Control					
Zeroth > First	Lingual gyrus	R	30, -67, -8	4.66	19
First > Zeroth	Middle temporal gyrus	R	45, 14, -38	4.08	11

4 Discussion

In this study, we reported the neural basis of collaboration and its interaction with reasoning order. When participants were collaborating with a counterpart, the brain activations were found in the insula areas with much greater statistical significance in the high reasoning order (first-order) condition.

Prior studies have suggested that insula played an important role in social interactions [4, 11] and motivational process [12]. When an individual attributes the result of an action to the self, the activation within insula is increased and this activation may represent high level of sense of agency. This high-level of sense of agency strongly correlates with high motivational states and self-determined decision [12]. Thus, we may suppose that the activation within the insula reflects participant's engagement in the game that requires a social interaction. The positive effect of social interaction such as collaboration and competition on motivation has been widely known [13]. Based on the fact that participants reported increased level of engagement during the collaboration game than the control game, the collaborative game might require more motivational demand compared to the control game.

An anterior part of insula has known to be related to autonomic arousal, which is closely tied with emotional experience [14]. Indeed, the collaborative game with a counterpart was more likely to evoke participants' arousal, compared to control condition. This is because participants were asked to carefully consider the opponent's reasoning order in a collaboration condition. Furthermore, in order to collaborate with an opponent in a higher reasoning level (*i.e.,* first-order), participants had to be more attentive to the task to complete the task successfully. In this context, greater anterior insula activation may imply that participants were more attentive during the task to successfully reach the goal together.

In future study, we would try to remove non-neuronal artifacts including motion related as well as physiological artifacts to refine the neuronal components in the measured BOLD signals. We would also employ data-driven analytic methods such as principal component analysis and independent component analysis techniques followed by a connectivity analysis between brain regions. It would also be very interesting future study in the context of the ToM how the neuronal mechanism related to other types of social interaction such as competition are interpreted in relation to the collaboration.

5 Conclusion

In this study, we tried to figure out the neuronal mechanism underlying collaboration with other individual and found neuronal activations within bilateral insula areas. The level of insula activations was increased when deploying higher order reasoning collaborating with the opponent. This may suggest that collaborating with other people may recruit a great extent of motivational process in the insula area and future investigations to collect further evidences and utilities are warranted.

Acknowledgments. This research was supported by Air Force Office for Scientific Research (AFOSR) grant.

References

1. Fletcher, P.C., Happe, F., Frith, U., Baker, S.C., Dolan, R.J., Frackowiak, R.S.J., Frith, C.D.: Other minds in the brain: a functional imaging study of "theory of mind" in story comprehension. Cognition 57, 109–128 (1995)
2. Gallagher, H.L., Frith, C.D.: Functional imaging of 'theory of mind'. Trends. Cogn. Sci. 7, 77–81 (2003)
3. Frith, U., Frith, C.D.: Development and neurophysiology of mentalizing. Philos. Trans. R. Soc. Lond. B. Biol. Sci. 358, 459–473 (2003)
4. Decety, J., Jackson, P.L., Sommerville, J.A., Chaminade, T., Meltzoff, A.N.: The neural bases of cooperation and competition: an fMRI investigation. NeuroImage 23, 744–751 (2004)
5. Elliott, R., Völlm, B., Drury, A., McKie, S., Richardson, P., Deakin, J.F.W.: Co-operation with another player in a financially rewarded guessing game activates regions implicated in theory of mind. Soc. Neurosci. 1, 385–395 (2006)
6. Krill, A.L., Platek, S.M.: Working together be better: Activation of reward centers during a cooperative maze task. PLoS One 7, e30613 (2012)
7. Hedden, T., Zhang, J.: What do you think I think you think?: Strategic reasoning in matrix games. Cognition 85, 1–36 (2002)
8. Goodie, A.S., Doshi, P., Young, D.L.: Levels of theory-of-mind reasoning in competitive games. J. Behav. Dec. Making. 25, 95–108 (2012)
9. Coricelli, G., Nagel, R.: Neural correlates of depth of strategic reasoning in medial prefrontal cortex. Proc. Natl. Acad. Sci. U. S. A. 106, 9163–9168 (2009)
10. Yoshida, W., Seymour, B., Friston, K.J., Dolan, R.J.: Neural mechanisms of belief inference during cooperative games. J. Neurosci. 30, 10744–10751 (2010)
11. Farrer, C., Frith, C.D.: Experiencing oneself vs. another person as being the cause of an action: the neural correlates of the experience of agency. NeuroImage 15, 596–603 (2002)
12. Wager, T.D., Barrett, L.F.: From affect to control: Functional specialization of the insula in motivation and regulation. Psyc. Extra (2004)
13. Tauer, J.M., Harackiewicz, J.M.: The effects of cooperation and competition on intrinsic motivation and performance. J. Pers. Soc. Psychol. 86, 849–861 (2004)
14. Critchley, H.D., Elliott, R., Mathias, C.J., Dolan, R.J.: Neural activity related to generation and representation of galvanic skin conductance responses: an fMRI study. J. Neurosci. 20, 3033–3040 (2000)

Risk-Aware Recommender Systems

Djallel Bouneffouf, Amel Bouzeghoub, and Alda Lopes Gancarski*

Department of Computer Science, Télécom SudParis, UMR CNRS Samovar,
91011 Evry Cedex, France
{Djallel.Bouneffouf,Amel.Bouzeghoub,Alda.Gancarski}@it-sudparis.eu

Abstract. Context-Aware Recommender Systems can naturally be modelled as an exploration/exploitation trade-off (exr/exp) problem, where the system has to choose between maximizing its expected rewards dealing with its current knowledge (exploitation) and learning more about the unknown user's preferences to improve its knowledge (exploration). This problem has been addressed by the reinforcement learning community but they do not consider the risk level of the current user's situation, where it may be dangerous to recommend items the user may not desire in her current situation if the risk level is high. We introduce in this paper an algorithm named R-UCB that considers the risk level of the user's situation to adaptively balance between exr and exp. The detailed analysis of the experimental results reveals several important discoveries in the exr/exp behaviour.

1 Introduction

User feedback (e.g., ratings and clicks) and situation (e.g., location, time) have become a crucial source of data when optimizing a Context-Aware Recommender System (CARS). Knowledge about the environment must be accurately learned to avoid making undesired recommendations which may disturb the user in certain situations considered as critical or risky. For this reason, the CARS has to decide, for each new situation, whether so far learned knowledge should be exploited by selecting documents that appear more frequently in the corresponding user feedback, or if never seen documents should be selected in order to explore their impact on the user situation, increasing the knowledge about the environment. On one hand exploration prevents from maximizing the short-term reward since it may yield to negative reward. On the other hand, exploitation based on an uncertain environment prevents from maximizing the long-term reward because document rating values may not be accurate. This challenge is formulated as an exploration/exploitation (exr/exp) dilemma. One smart solution for exr/exp using the "multi-armed bandit problem" is the hybrid approach done by [7]. This approach combines the Upper Confident Bound (UCB) algorithm with the ϵ-greedy algorithm. By introducing randomness into UCB, authors reduce the trouble in estimating confidence intervals. This algorithm estimates both the mean reward of each document and the corresponding confidence interval. With

* Corresponding author.

M. Lee et al. (Eds.): ICONIP 2013, Part I, LNCS 8226, pp. 57–65, 2013.
© Springer-Verlag Berlin Heidelberg 2013

the probability 1-ϵ, this algorithm selects the document that achieves a highest upper confidence bound and, with the probability ϵ, it uniformly chooses any other document. The ϵ parameter essentially controls exr/exp. The problem is that it is difficult to decide in advance the optimal value of ϵ. We introduce in this paper an algorithm, named R-UCB, that computes the optimal value of ϵ by adaptively balancing exr/exp according to the risk of the user situation. We consider as risky or critical, a situation where it is dangerous to recommend uninteresting information for the user; this means that it is not desired, can yield to a trouble, or causes a waste of time for the user when reading a document which is not interesting for him in the current situation. In this case, the exploration-oriented learning should be avoided. R-UCB extends the UCB strategy with an update of exr/exp by selecting suitable user's situations for either exr or exp. We have tested R-UCB in an off-line evaluation with real data. The remaining of the paper is organized as follows. Section 2 reviews related works. Section 3 describes the algorithms involved in the proposed approach. The experimental evaluation is illustrated in Section 4. The last section concludes the paper and points out possible directions for future work.

2 Related Work

We refer, in the following, recent works that address the exr/exp trade-off (bandit algorithm) and the Risk-Aware Decision problem. Existing CARS systems are not considered in this paper, refer to [1] and [2] for further information.

Multi-armed Bandit Problem. Very frequently used in reinforcement learning to study exr/exp, the multi-documented bandit problem was originally described by [9]. Few research works are dedicated to study the contextual bandit problem in recommender systems, considering the user's behaviour as the context. In [7], authors extend UCB by dynamically updating outperforming both beginning and decreasing strategies. In [6], assuming the expected reward of a document is linear, they perform recommendation based on contextual information about the users' documents. To maximize the total number of user's clicks, this work proposes the LINUCB algorithm which is computationally efficient. [7, 6] describe a smart way to balance exr/exp, but do not consider the user's situation and its associated risk during the recommendation.

The Risk-Aware Decision. To the best of our knowledge, the risk-aware decision is not yet studied in recommender systems. However, it has been studied for a long time in reinforcement learning, where the risk is defined as the reward criteria that takes into account not only the expected reward, but also some additional statistics of the total reward, such as its variance or standard deviation [3]. The risk is measured with two types of uncertainties. The first, named parametric uncertainty, is related to the imperfect knowledge of the problem parameters. For instance, in the context of Markov decision processes, [5] proposes

to use the percentile performance criterion to control the risk sensitivity. The second type, termed inherent uncertainty, is related to the stochastic nature of the system, like [4], which consider models where some states are error states representing a catastrophic result. More recently, [10] developed a policy gradient algorithm for criteria that involves both the expected cost and the variance of the cost, and demonstrated the applicability of the algorithm in a portfolio planning problem. However, this work does not consider the risk of the situations in the exr/exp problem. A recent work, [11], treated the risk and proposed the VDBE algorithm to extend ϵ-greedy by introducing a state-dependent exploration probability, instead of hand-tuning. The system makes exploration in situations when the knowledge about the environment is uncertain, which is indicated by fluctuating action values during learning. In contrast, the amount of exploration is reduced as far as the system's knowledge becomes certain, which is indicated by very small or no value differences.

Our Contributions. As shown above, none of the mentioned works tackles the exr/exp problem considering the semantic risk level of the situation. This is precisely what we intend to do by exploiting the following new features: (1) Handling semantic concepts to express situations and their associated risk level. The risk level is associated to a whole situation and/or the concepts composing the situation; (2) Considering the risk level of the situation when managing exr/exp, which helps CARS to adapt them selves to environment dynamically. High exploration (resp. high exploitation) is achieved when the current user situation is "not risky" (resp. "risky"); (3) Assuming that exploring data in non-risky situations is useful for making a safety exploration in risky situations. Our algorithm performs exploration in risky situations by selecting the most interesting documents in non risky situations.

We improve the extension of UCB with ϵ-greedy (called here ϵ-UCB) because it gives the best results in an off-line evaluation done by [7]; however, our amelioration can be applied to any bandit algorithm.

3 The Proposed CARS Model

This section focuses on the proposed model, starting by introducing the key notions used in this paper.

***Situation*:** A situation is an external semantic interpretation of low-level context data, enabling a higher-level specification of human behaviour. More formally, a situation S is a n-dimensional vector, $S = (O_{\delta_1}.c_1, O_{\delta_2}.c_2, ..., O_{\delta_n}.c_n)$ where each c_i is a concept of an ontology O_{δ_i} representing a context data dimension. According to our need, we consider a situation as a 3-dimensional vector $S = (O_{Location}.c_i, O_{Time}.c_j, O_{Social}.c_k)$ where c_i, c_j, c_k are concepts of Location, Time and Social ontologies.

***User preferences*:** User preferences UP are deduced during the user navigation activities. $UP \subseteq D \times A \times V$ where D is a set of documents, A is a set of preference attributes and V a set of values. We focus on the following preference

attributes: *click*, *time* and *recom* which respectively correspond to the number of clicks for a document, the time spent reading it and the number of times it was recommended.

***The user model*:** The user model is structured as a case base composed of a set of situations with their corresponding UP, denoted $UM = \{(S^i; UP^i)\}$, where $S^i \in S$ is the user situation and $UP^i \in UP$ its corresponding user preferences.

We propose CARS to be modelled as a contextual bandit problem including user's situation information. Formally, a bandit algorithm proceeds in discrete trials $t = 1...T$. For each trial t, the algorithm performs the following tasks:

Task 1. Let S^t be the current user's situation, and PS the set of past situations. The system compares S^t with the situations in PS in order to choose the most similar one, S^p:

$$S^p = argmax_{S^i \in PS} sim(S^t, S^i) \tag{1}$$

The semantic similarity metric is computed by:

$$sim(S^t, S^i) = \frac{1}{|\Delta|} \sum_{\delta \in \Delta} sim_\delta(c^t_\delta, c^i_\delta) \tag{2}$$

In Eq. 2, sim_δ is the similarity metric related to dimension δ between two concepts c^t_δ and c^i_δ, and Δ is the set of dimensions (in our case Location, Time and Social). The similarity between two concepts of a dimension δ depends on how closely c^t_δ and c^i_δ are related in the corresponding ontology. To compute sim_δ, we use the same similarity measure as [8]:

$$sim_\delta(c^t_\delta, c^i_\delta) = 2 * \frac{deph(LCS)}{deph(c^t_\delta) + deph(c^i_\delta)} \tag{3}$$

In Eq. 3, LCS is the Least Common Subsumer of c^t_δ and c^i_δ, and $deph$ is the number of nodes in the path from the current node to the ontology root.

Task 2. Let D^p be the set of documents recommended in situation S^p. After retrieving S^p, the system observes rewards in previous trials for each document $d \in D^p$ in order to choose for recommendation the one with the greatest reward, which is the Click Through Rate (CTR) of a document. In Eq. 4, the reward of document d, $r(d)$, is the ratio between the number of clicks (v_i) on d and the number of times d is recommended (v_j).

$\forall d \in D^p, UP^i{=}(d, click, v_i) \in$ UP and $UP^j{=}(d, recom, v_j) \in$ UP we have:

$$r(d) = \frac{v_i}{v_j} \tag{4}$$

Task 3. The algorithm improves its document selection strategy with the new observation: in situation S^t, document d obtains a reward $r(d)$. Depending on the similarity between the current situation S^t and its most similar situation S^p, two scenarios are possible: (1) If sim(S^t, S^p) $\neq 1$: the current situation does not

exist in the case base; the system adds this new case composed of the current situation S^t and the current user preferences UP^t; (2) If $\text{sim}(S^t, S^p) = 1$: the situation exists in the case base; the system updates the case having premise the situation S^p with the current user preferences UP^t.

The ϵ-UCB Algorithm. For a given situation, the algorithm recommends a predefined number of documents, specified by parameter N using Eq. 5. Specifically, in trial t, this algorithm computes an index $b(d) = r(d) + c(d)$ for each document d, where: $r(d)$ (Eq. 4) is the mean reward obtained by d and $c(d)$ is the corresponding confidence interval, so that $c(d) = \sqrt{\frac{2 \times log(t)}{v_j}}$ and v_j is the number of times d was recommended. With the probability 1-ϵ, ϵ-UCB selects the document with the highest upper confidence bound $d_t = argmax_{d \in D^p} b(d)$; and with the probability ϵ, it uniformly chooses any other document.

$$d_t = \begin{cases} argmax_{d \in (D^p - RD)} b(d) & if\ q > \epsilon \\ Random(D^p - RD) & otherwise \end{cases} \tag{5}$$

In Eq. 5, D^p is the set of documents included in the user's preferences UP^p corresponding the most similar situation (S^p) to the current one (S^t); RD is the set of documents to recommend; $Random()$ is the function returning a random element from a given set; q is a random value uniformly distributed over [0, 1] which controls exr/exp; ϵ is the probability of recommending a random exploratory document.

Semantic Risk Level Computing. In real world, the exr/exp trade-off should be directly related to the risk level of the situation, this is why computing the risk level is indeed indispensable. To consider the semantic risk level of the situation in exr/exp, we add a risk level to each concept in a situation: $S = (O_{\delta_1}.c_1[cv_1], O_{\delta_2}.c_2[cv_2], ..., O_{\delta_n}.c_n[cv_n])$, where $CV = \{cv_1, cv_2, ..., cv_n\}$ is the set of risk levels assigned to concepts c_i ($i = 1..n$) and $cv_i \in [0, 1]$. $R(S)$ is the risk level of situation S. $R(S) \in [0, 1]$ and situations having $R(S) > th_R$ are considered as *risky* or *critical* situations (CS). The risk threshold th_R is described in Subsection 3. The risk of a concept varies from a domain to another and it is predefined by a domain expert. We conducted a study with professional mobile users, described in detail in Sec 4, where the domain expert is a commercial manager, and we considered, for example, the following set of critical situations: $CS = \{CS1, CS2, CS3\}$, $CS1 = (-, afternoon, manager)$, $CS2 = (company, morning, -)$, $CS3 = (-, -, client)$.

The risk level $R(S^t)$ of situation S^t is computed as follows:

$$R(S^t) = \begin{cases} R_c(S^t) \text{ if } CS = \emptyset, CV \neq \emptyset \\ R_m(S^t) \text{ if } CS \neq \emptyset, CV = \emptyset \\ \frac{1}{2} \times (\eta R_c(S^t) + \zeta R_m(S^t)) \text{ if } CS \neq \emptyset, CV \neq \emptyset \end{cases} \tag{6}$$

If only CV is known, Eq. 6 returns the risk $R_c(S^t)$ (Eq. 7) inferred from the situation concepts. If only CS is known, Eq. 6 returns the the risk $R_m(S^t)$ (Eq. 9)

extracted from the degree of similarity between the current situation S^t and the centroid critical situation S^m (Eq. 10). If CV and CS are both known, Eq. 6 returns the weighted mean between $R_c(S^t)$ and $R_m(S^t)$; η and ζ are respectively the weights associated to $R_c(S^t)$ and $R_m(S^t)$, where $\eta+\zeta = 2$. These weights are related to the application domain: if the domain is itself risky (e.g. healthcare and safety), the system considers that R_c is more important than R_m (during the experimental phase, η and ζ have both a value of 1). $R_c(S^t)$ gives a weighted mean of the risk level of the concepts:

$$R_c(S^t) = \frac{1}{|\Delta|}(\sum_{\delta \in \Delta} \mu_\delta cv_\delta^t) \tag{7}$$

In Eq. 7, cv_δ^t is the risk level of the dimension δ in S^t and μ_δ is the weight associated to dimension δ. μ_δ is set out by using an arithmetic mean as follows:

$$\mu_\delta = \frac{1}{|CS|}(\sum_{S^i \in CS} cv_\delta^i) \tag{8}$$

The idea in Eq. 8 is to get a measure of how risky are, in average, concepts of dimension δ in CS, computing the mean of all the risk levels associated to δ in CS. Being B the similarity threshold (this metric is fixed on the off-line evaluation) and S^m the critical situation centroid, $R_m(S^t)$ is computed as follows:

$$R_m(S^t) = \begin{cases} 1 - B + sim(S^t, S^m) \; if \; sim(S^t, S^m) < B \\ 1 \qquad otherwise \end{cases} \tag{9}$$

In Eq. 9, the situation risk level $R_m(S^t)$ increases when the similarity between S^t and S^m increases. The critical situation centroid is selected as follows:

$$S^m = argmax_{S^f \in CS} \frac{1}{|CS|} \sum_{S^e \in CS} sim(S^f, S^e) \tag{10}$$

The R-UCB Algorithm. To improve the adaptation of the ϵ-UCB algorithm to the risk level of the situations, the R-UCB algorithm (Alg. 1) computes the probability of exploration ϵ (line 2), by using the situation risk level $R(S^t)$ as indicated in Eq. 11. In Eq. 11. ϵ_{min} is the minimum exploration allowed in CS and ϵ_{max} is the maximum exploration allowed in non-CS (these two metrics are computed off-line using exponentiated gradient, which gives $\epsilon_{min} = 0.1$ and $\epsilon_{max} = 0.5$).

$$\epsilon = \epsilon_{max} - R(S^t) \times (1 - \epsilon_{min}) \tag{11}$$

Depending on the risk level of the current situation S^t, two scenarios are possible: (1) If $R(S^t) < th_R$, S^t is not critical(Alg. 1, line 3); the ϵ-UCB algorithm is used with $\epsilon > \epsilon_{min}$ (Eq. 11). (2) If $R(S^t) \geq th_R$, S^t is critical (Alg. 1, line 4); the ϵ-UCB algorithm is used with $\epsilon = \epsilon_{min}$, performing a high exploitation (Alg. 1, line 6, instruction 1). Based on our supposition that data in non critical situations

can be useful to infer optimal exploration in CS, the algorithm makes a safety exploration in CS by selecting the documents with the highest CTR in D^y (Alg. 1, line 6, instruction 2), where D^y is the set of documents recommended in the most similar situation S^y to S^t, $S^y \notin CS$ and computed using Eq. 1. We still consider random exploration (Alg. 1, line 6, instruction 3) which is indispensable to avoid documents selection in CS becoming less optimal. To summarize, the system makes a low and safety exploration when the current user's situation is critical (Alg. 1, line 6); otherwise (Alg. 1, line 3), the system performs high exploration. In this case, the degree of exploration decreases when the risk level of the situation increases (Eq. 11. To verify if S^t is critical, the risk threshold th_R is computed as indicated in Eq. 12. At the initialization phase, the domain expert may indicate risk levels for a set of concepts and/or situations. If risk levels on concepts are indicated, the expert defines the θ threshold; if risk levels on situations are indicated, the expert defines the B threshold.

$$th_R = \begin{cases} \theta \text{ if } CS = \emptyset, CV \neq \emptyset \\ B \text{ if } CS \neq \emptyset, CV = \emptyset \\ \frac{1}{2} \times (\eta\theta + \zeta B) \text{ if } CS \neq \emptyset, CV \neq \emptyset \end{cases} \quad (12)$$

Algorithm 1. The R-UCB algorithm

1: **Input:** $S^t, D^p, D^y, RD = \emptyset, B, N, \epsilon_{min,\epsilon_{max}}$ **Output:** RD
2: $\epsilon = \epsilon_{max} - R(S^t) \times (1 - \epsilon_{min})$ //$R(S^t)$ is computed as described in Eq.6
3: **if** $R(S^t) < th_R$ **then** $RD = \epsilon$-UCB(ϵ, D^p, RD, N) **else**
4: **for** $i = 1$ **to** N **do**
5: $q = Random(0, 1); k = Random(0, 1)$
6: $d_i = \begin{cases} argmax_{d \in (D^p - RD)} b(d) & \text{if} \quad q > \epsilon_{min} \\ argmax_{d \in (D^y - RD)} b(d) & \text{if} \quad q \leq k \leq \epsilon_{min} \\ Random(D^p) \; otherwise \end{cases}$
7: $RD = RD \cup d_i$
8: **end for**

4 Experimental Evaluation

We conducted a diary study with the collaboration of a software company. This company provides a history application, which records time, current location, social and navigation information of its users during their application use. The diary study took 2 months and generated 356 738 diary situation entries. From the diary study, we have obtained a total of 5 518 566 entries concerning the user's navigation (number of clicks and time spent), expressed with an average of 15.47 entries per situation.

Off-line Evaluation. To test the proposed R-UCB algorithm, in our experiments, we have firstly collected the 100 000 cases from the situations case base.

We then evaluate the existing algorithms by confronting them, at each iteration, to a case randomly selected and removed. We calculate the average CTR every 1000 iterations. The number N of documents returned by the CARS for each situation is 10 and we run the simulation during 10000 iterations, where all the tested algorithms have converged. In the first experiment, in addition to a pure exploitation baseline, we compare our algorithm to the ones described in the related work (Sec. 2): VDBE, EG-UCB, ϵ-UCB, beginning-UCB (ϵ-UCB with beginning strategy) and decreasing-UCB (ϵ-UCB with decreasing strategy). In Fig. 1, the horizontal axis represents the number of iterations and the vertical axis is the performance metric.

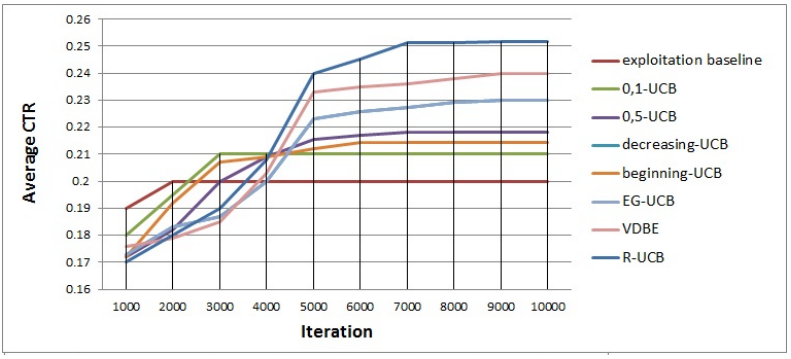

Fig. 1. Average CTR for exr/exp algorithms

R-UCB and VDBE effectively have the best convergence rates; VDBE increases the average CTR by a factor of 1.5 over the baseline and R-UCB, by a factor of 2. The improvement comes from a dynamic exr/exp, controlled by the risk level estimation. These algorithms take full advantage of exploration when the situations are not critic, giving opportunities to establish good results when the situations are critical. Finally, as expected, R-UCB outperforms VDBE, which is explained by the good estimation of the risk.

5 Conclusion

In this paper, we study the problem of exr/exp in CARS and propose a new approach that adaptively balances exr/exp regarding the risk level of the situation. We have validated our work with off-line studies which offered promising results. This study yields to the conclusion that considering the risk level of the situation on the exr/exp strategy significantly increases the performance of the recommender system. In considering these results, we plan to investigate public benchmarks.

References

1. Bouneffouf, D., Bouzeghoub, A., Gançarski, A.L.: A contextual-bandit algorithm for mobile context-aware recommender system. In: Huang, T., Zeng, Z., Li, C., Leung, C.S. (eds.) ICONIP 2012, Part III. LNCS, vol. 7665, pp. 324–331. Springer, Heidelberg (2012)
2. Bouneffouf, D., Bouzeghoub, A., Gançarski, A.L.: Hybrid-ϵ-greedy for mobile context-aware recommender system. In: Tan, P.-N., Chawla, S., Ho, C.K., Bailey, J. (eds.) PAKDD 2012, Part I. LNCS, vol. 7301, pp. 468–479. Springer, Heidelberg (2012)
3. Cherian, J.A.: Investment science: David g. luenberger. Journal of Economic Dynamics and Control 22(4), 645–646 (1998)
4. Geibel, P., Wysotzki, F.: Risk-sensitive reinforcement learning applied to control under constraints. J. Artif. Int. Res. 24(1), 81–108 (2005)
5. Howard, R.A., Matheson, J.E.: Risk-sensitive markov decision processes. Management Science 18(7), 356–369 (1972)
6. Li, L., Chu, W., Langford, J., Schapire, R.E.: A contextual-bandit approach to personalized news article recommendation. In: Proceedings of the 19th International Conference on World Wide Web, WWW 2010, pp. 661–670. ACM, USA (2010)
7. Li, W., Wang, X., Zhang, R., Cui, Y.: Exploitation and exploration in a performance based contextual advertising system. In: Proceedings of the 16th ACM SIGKDD International Conference on Knowledge Discovery and Data Mining, KDD 2010, pp. 27–36. ACM, USA (2010)
8. Mladenic, D.: Text-learning and related intelligent agents: A survey. IEEE Intelligent Systems 14(4), 44–54 (1999)
9. Robbins, H.: Some Aspects of the Sequential Design of Experiments. Bulletin of the American Mathematical Society 58, 527–535 (1952)
10. Sehnke, F., Osendorfer, C., Rückstieß, T., Graves, A., Peters, J., Schmidhuber, J.: Policy gradients with parameter-based exploration for control. In: Kůrková, V., Neruda, R., Koutník, J. (eds.) ICANN 2008, Part I. LNCS, vol. 5163, pp. 387–396. Springer, Heidelberg (2008)
11. Tokic, M., Ertle, P., Palm, U., Soffker, D., Voos, H.: Robust Exploration/Exploitation trade-offs in safety-critical applications. In: Proceedings of the 8th International Symposium on Fault Detection, Supervision and Safety of Technical Processes, pp. 660–665. IFAC, Mexico City (2012)

A Two Stage Approach for High School Timetabling

Moh'd Khaled Yousef Shambour[1], Ahamad Tajudin Khader[1], Ahmed Kheiri[2], and Ender Özcan[2]

[1] School of Computer Sciences, Universiti Sains Malaysia (USM), 11800, Pulau Pinang, Malaysia
[2] School of Computer Science, University of Nottingham, Jubilee Campus, Wollaton Road, Nottingham, NG8 1BB, UK

Abstract. There are different types of educational timetabling problems which are computationally difficult to solve. In this study, we deal with the High School Timetabling Problem which requires assignment of events, such as courses, and resources, such as classrooms, to time-slots under a set of different types of constraints. We describe an approach that hybridises an Evolutionary Algorithm variant and Simulated Annealing methods to solve this problem. This approach is tested over a set of real world instances obtained across different countries. The empirical results demonstrate the viability of the hybrid approach when compared to the previously proposed techniques.

1 Introduction

High school timetabling problem (HSTP) is a real-world hard combinatorial optimisation problem [7]. It seeks a search for the best event schedule and the best allocation of resources including the scheduling of classes, teachers, courses and students in a time slots in a high school institution subject to a set of constraints. These constraints are classified as *hard* and *soft* constraints. The hard constraints must be satisfied to ensure the feasibility of the solution whereas the soft constraints characterise preferences. The violation of the soft constraint does not destroy the feasibility but rather affecting the quality of the solution.

Due to the NP nature of high school timetabling problems, meta-heuristics are preferred in most of the previous studies. Approaches used in HSTP include simulated annealing [8], evolutionary algorithms [6], tabu search [15], adaptive large neighborhood search [20], hyper-heuristic [11], particle swarm optimisation [21], bee algorithms [14], integer programming [5], tiling algorithms [13], walk down jump up algorithm [24] and constraint programming approach [22]. [16] provided a recent survey on HSTP. In this study, we introduce a high school timetabling problem and combining Harmony Search Algorithm as an Evolution Strategy with Simulated Annealing approach (HSA-SA) as a solver to the problem. To the best knowledge of authors, this is the first work that employs HSA-SA for HSTP.

M. Lee et al. (Eds.): ICONIP 2013, Part I, LNCS 8226, pp. 66–73, 2013.
© Springer-Verlag Berlin Heidelberg 2013

Harmony search algorithm (HSA) is an Evolutionary Algorithm variant. It is a population-based metaheuristic named by Geem et al. (2001) [9]. Although it was introduced as new, soon after, HSA was classified as a special case of Evolution Strategies in [23]. In this study, we will adapt the terminology as used in [9] while discussing the algorithmic components. The terminology used in HSA is inspired from the process of musical improvisation where a group of musicians play the pitches of their musical instruments together seeking for a pleasing harmony as determined by aesthetic standards. Based on harmony memory size (HMS), harmony memory considering rate (HMCR), pitch adjusting rate (PAR) and the number of improvisations (NI), a new harmony vector X=x_1,x_2,.,x_n is generated. In optimisation process, musician (decision variable) plays (generates) a possible note (value of decision variable) for finding the best harmony (optimal solution). At each iteration, a candidate solution (harmony) is evaluated by objective function. The move acceptance criteria considers whether to keep or replace the new solution with the respect to the worst solution in the harmony memory. This cycle continues until the termination criteria (maximum NI or condition) is satisfied. HSA has been successfully applied to a range of real world optimisation problems, including job shop scheduling [25], task assignment problem [26], optimising energy consumption [10], nurse rostering problem [4] and university course timetabling [2]. More on HSA can be found in [3].

Simulated Annealing [1] is a probabilistic metaheuristic method in which at each iteration a new solution is generated. The new solution is accepted if it improved the previous solution. The non-improving solutions are accepted with a probability of $p_t = e^{-\frac{\Delta}{T}}$, where Δ is the quality change, and T is the method parameter, called temperature which regulates the probability to accept solutions with higher objective value (cost) [1].

Section 2 provides an overview of the high school timetabling problem dealt with in this work. Section 3 describes the proposed solver components that are tested for solving the high school timetabling problem. Section 4 provides the empirical results. Finally, Section 5 presents the conclusion.

2 International Timetabling Competition 2011 Datasets

Recently, the challenge has become increasingly highlighted when a group of researchers run the Third International Timetabling Competition (ITC2011) in 2011-2012 [17], with the goal of raising the profile of automated high school timetabling. The ITC2011 was run by the Centre for Telematics and Information Technology at the University of Twente in the Netherlands, aiming to drive a new era of research of automated high school timetabling. The participants of ITC2011 tackled 35 instances of the high school timetabling problem, taken from schools in 10 countries. The instances are defined by a standard data format based on XML schema called XHSTT (XML High School Timetabling) [18, 19]. Out of 17 registered participants to the competition, only 5 teams submitted solutions. The reason is unknown, but could be due to the large number of imposed constraints which makes the problem hard to handle in practice [19].

Briefly, the ITC2011 problem instances [19] contain four components including *times*, *resources*, *events/meetings* and *constrains*. Time represents indivisible interval of time during which event run. Resource represents the entity that attend event. For example: "T1" resource in "BrazilInstance3_XHSTT2013" instance refers to a teacher while resource "S1" in the same instance refers to a class. Event is a meeting between resources. Some events might be pre-assigned with time or resource; For example, the event "RE-3A" predefined the time to "Mon_1" in "ItalyInstance1_XHSTT2012A" instance. Also an event can be split into sub-events. Constraint represents the condition that a solution should satisfy, if possible. The ITC2011 problem instances contain 15 types of constraints. All constraints could be hard and soft according to a given instance. For more description, see [17–19].

2.1 Characteristics of the Problem Instances

In this work, twelve ITC2011 high school timetabling problem instances are used to study the effectiveness of the proposed HSA. The instances are small and medium in size taken from three countries: Brazil, Finland and Italy. Table 1 summarises the main characteristics of these instances. The datasets can be downloaded from the ITC2011 website [17].

Table 1. Datasets characteristics (*Times* total number of times. *Teachers*, *Rooms* and *Classes* are the total number of resources of resource type "Teacher", "Room" and "Class", respectively. *Events* total number of events.)

Country	Instance Name	Times	Teachers	Rooms	Classes	Events
Brazil	Instance1	25	8		3	21
Brazil	Instance2	25	14		6	63
Brazil	Instance3	25	16		8	69
Brazil	Instance4	25	23		12	127
Brazil	Instance5	25	31		13	119
Brazil	Instance6	25	30		14	140
Brazil	Instance7	25	33		20	205
Finland	ElementarySchool	35	22	21	60	291
Finland	SecondarySchool	35	25	25	14	280
Finland	SecondarySchool2	40	22	21	36	469
Italy	Instance1	36	13		3	42
Italy	Instance4	36	61		38	748

3 Harmony Search Algorithm and Simulated Annealing

HSA is a population-based meta-heuristic approach inspired by the musical improvisation process [9]. It iteratively improves the solutions stored in the harmony memory. It randomly perturbs a solution (vector of decision variables) via a number of improvisations and the harmony memory is updated during the

improvisations. At each improvisation, stored values of decision variables in the harmony memory are adapted according to Harmony Memory Consideration Rate (HMCR); and the variable values in the solution are adjusted according to a Pitch Adjustment Rate (PAR). This cycle continues until the stop criteria is met. The steps of the HSA are as follows [9].

Step 1. Initialise the Parameters: The HSTP variables are extracted from the HSTP instances. The variables vary from instance to instance such as existence of certain resource type(s), number of events (meetings) and number of hard and soft constraints. The parameters of HSA including: (i) Harmony Memory Consideration Rate (HMCR), the rate of selecting a value from Harmony Memory HM (memory consideration) or taking into account a random consideration; (ii) Harmony Memory Size (HMS), the number of solution vectors in the HM; (iii) Pitch Adjustment Rate (PAR), the rate of adjusting the values; and (iv) Number of Improvisations (NI), the number of iterations.

Step 2. Initialise the Harmony Memory: The HMS initial solutions are generated using the general solver of KHE implemented by Kingston [12]. The hard constraints of the initial solutions are, likely, violated and the following steps need to fix the violation of hard constraints. Each row in HM represents one solution of HSTP and $f(x)$ is the objective function value (Equation 1).

$$\mathsf{HM} = \begin{bmatrix} x_1^1 & x_2^1 & \ldots & x_N^1 \\ x_1^2 & x_2^2 & \ldots & x_N^2 \\ \vdots & \vdots & \ddots & \vdots \\ x_1^{HMS} & x_2^{HMS} & \ldots & x_N^{HMS} \end{bmatrix} = \begin{bmatrix} f(x^1) \\ f(x^2) \\ \vdots \\ f(x^{HMS}) \end{bmatrix} \tag{1}$$

Step 3. Improvise a New Harmony: The essential step in HSA is to improvise a new harmony vector $x'=(x'_1,x'_2,\ldots,x'_N)$ based on three operators: memory consideration, pitch adjustment and random consideration. In *memory consideration*, the values of the new harmony vector are randomly selected from the current values stored in HM $x_i^{'}$ with a probability of HMCR where HMCR $\in$ [0, 1]. In *random consideration*, decision variables are randomly assigned according to their possible range with a probability of (1-HMCR). Furthermore, if memory consideration failed to maintain the feasibility of the new solution, then the random consideration will be called. In *pitch adjustment*, the decision variable x_i of a new harmony vector is pitch adjusted with a probability of PAR, where PAR $\in$ [0,1]. In HSTP, pitch adjustment is a neighbourhood move. In this work, we have implemented three neighbourhood moves:

- Move Meeting (MM) moves the time slot t_1 of meeting m to time slot t_2.
- Swap Meeting (SM) swaps two meetings m_1 and m_2.
- Do Nothing (DN); each of which is selected with equal probability as shown in Equation 2.

$$\textbf{Adjust } x' = \begin{cases} MM & \text{if } 0 \leq \text{rand} < (PAR/3), \\ SM & \text{if } (PAR/3) \leq \text{rand} < (2.PAR/3), \\ DN & \text{if } (2.PAR/3) \leq \text{rand} < (PAR). \end{cases} \quad s.t\ rand \in [0,1] \tag{2}$$

Step 4. Update the Harmony Memory: If the new generated harmony solution vector $x'=(x'_1,x'_2,..,x'_N)$ has better quality than the worst harmony vector stored in HM in terms of the objective function (cost) value, then the worst harmony in HM will be replaced by the new harmony.
Step 5. Check the Stopping Criteria: Steps 3 and 4 are repeated until the maximum number of improvisations (NI) is reached.

After applying an iteration of the HSA, the Simulated Annealing method will be employed as a polishing procedure with the goal of improving the current best solution obtained. At each iteration one of 5 neighbourhoods is randomly selected and applied to the candidate solution. The neighbourhood moves are: Move Meeting; Swap Meeting; Swap Three Meetings (swaps meetings m_1 and m_2 then m_2 and m_3); Swap Block of Meetings (swaps time slot of meetings m_1 and m_2, but if the meetings have different duration, m_1 is moved to the following the last time slot occupied by m_2); and Task Split (split task into two). The first two moves are explained in step 3 of HSA. The temperature of the SA method is a function of the number of meetings.

4 Results

The parameter values of the HSA are chosen as HMS=5, HMCR=0.99, PAR=0.66 and NI=50. These values are decided after a set of exhaustive experiments using different combinations of values which is not reported in this paper due to space requirements. The proposed hybrid approach is implemented in C, under CenTos 6.4 operating system. The experiments are performed on an Intel(R) Xeon(R) CPU X7560 @2.27GHz with a memory of 4.00G.

The HSA-SA is tested on ITC2011 instances described in table 1. Solutions are evaluated in terms of *feasibility* (sum of weighted hard constraints violations) and *preferences* (sum of weighted soft constraints violations); and the goal is to minimise it. A solution with a cost value of 42.0013 indicates an infeasibility value of 42 and objective value of 13. Five competitors were submitted solutions to the ITC2011. HySST [11] applies a multi-stage hyper-heuristic on a set of mutational heuristics and hill climbers, GOAL [8] combines the iterated local search with simulated annealing, HFT [6] uses the evolutionary algorithms as a meta-heuristic to solve the problem, Lectio [20] applies an algorithm based on adaptive large neighbourhood search, and VAGOS [17].

Table 2 presents the performance comparison of the HSA-SA to the five competing approaches and the best publicly known (BPK) solutions before the five approaches found better solutions. The table shows the cost of the solutions obtained by the different approaches. The column KHE in the table shows the

average of five solutions produced by the general solver of KHE implemented by Kingston [12]. From the table, HSA-SA was able to produce feasible solutions to all the tested instances and enhance the initial solutions generated by the general solver of KHE. The proposed HSA-SA improved upon BPK in six out of seven instances. The HSA-SA performs the best on ElementarySchool and SecondarySchool2 instances. The HSA-SA produces a solution satisfying all the hard and soft constraints on SecondarySchool2 instance. The HSA-SA outperforms the HFT approach in all the instances. In BrazilInstance4, HSA-SA generates better solution than HySST. Note that in the table, "-" are shown to indicate that the solver did not submit solution for the instance. Most of the tested instances are taken from instances used during Round-1 of the ITC2011 competition, and the competitors were expected to submit solutions if it improved on the best solution previously known to the organisers of the competition. No restrictions were placed on the time limit or how the solutions could be obtained. For more details about the competition, see [19].

Table 2. The cost values obtained by KHE, HSA-SA, the best publicly known solution before the start of the ITC2011 (BPK), and the competitors solvers

Instance Name	KHE	HSA-SA	BPK	GOAL	HySST	Lectio	HFT	VAGOS
BrazilInstance1	0.0081	0.0020	0.0024	-	-	-	-	0.0011
Instance2	3.9999	0.0048	-	-	0.0044	0.0005	0.0082	0.0026
Instance3	3.9999	0.0154	-	-	0.0084	0.0048	0.0212	0.0047
BrazilInstance4	39.9999	0.0162	0.0112	-	0.0176	0.0090	0.0205	0.0078
Instance5	12.9999	0.0148	0.0225	-	-	-	-	0.0043
Instance6	11.9999	0.0186	0.0209	-	0.0150	0.0060	0.0347	0.0074
Instance7	22.9999	0.0234	0.0330	-	-	-	-	0.0122
ElementarySchool	10.0306	0.0003	-	0.0003	0.0003	0.0003	0.0003	-
SecondarySchool	43.9999	0.0090	0.0106	-	-	0.0088	-	-
SecondarySchool2	2.9999	0.0000	-	0.0000	0.0000	0.0000	0.0576	-
ItalyInstance1	0.3022	0.0020	0.0028	-	-	-	-	0.0012
ItalyInstance4	38.9999	0.0082	-	0.0061	0.0052	0.0078	0.8623	-

5 Conclusion and Future Directions

A unified high school timetabling problem which was a topic of a recent competition, referred to as ITC2011, is described in this study. ITC2011 provided a collection of high school timetabling problem instances collected from different countries across the world. The goal of the competition was to promote researchers and practitioners to deal with the real world complexities of the problem. We have combined an Evolution Algorithm variant and Simulated Annealing methods (HSA-SA) and tested on twelve ITC2011 benchmark instances as an initial study. The results show that the approach is sufficiently powerful producing high quality solutions. The proposed approach was able to generate solutions to the problem matching the quality of the best known solutions in two

occasions and near to the best known solutions for the other instances. As future work, we would like to analyse the influence of choice of parameter values of the approach and extend our experiments to all ITC2011 benchmark instances. Although the performance of the HSA-SA is evaluated on high school timetabling, it is also our intention to investigate its performance on the other educational timetabling problems, such as university course timetabling. Finally, we aim to improve the performance of the approach further by incorporating new move operators including particularly local search.

References

1. Abramson, D.A., Dang, H., Krisnamoorthy, M.: Simulated annealing cooling schedules for the school timetabling problem. Asia-Pacific Journal of Operational Research 16(1), 1–22 (1999)
2. Al-Betar, M.A., Khader, A.T.: A harmony search algorithm for university course timetabling. Annals of Operations Research 194(1), 3–31 (2012)
3. Alia, O.M., Mandava, R.: The variants of the harmony search algorithm: an overview. Artificial Intelligence Review 36(1), 49–68 (2011)
4. Awadallah, M.A., Khader, A.T., Al-Betar, M.A., Bolaji, A.: Nurse rostering using modified harmony search algorithm. In: Panigrahi, B.K., Suganthan, P.N., Das, S., Satapathy, S.C. (eds.) SEMCCO 2011, Part II. LNCS, vol. 7077, pp. 27–37. Springer, Heidelberg (2011)
5. Birbas, T., Daskalaki, S., Housos, E.: School timetabling for quality student and teacher schedules. Journal of Scheduling 12(2), 177–197 (2009)
6. Domrös, J., Homberger, J.: An evolutionary algorithm for high school timetabling. In: Proceedings of the Ninth International Conference on the Practice and Theory of Automated Timetabling (PATAT 2012), pp. 485–488 (2012)
7. Even, S., Itai, A., Shamir, A.: On the Complexity of Timetable and Multicommodity Flow Problems. SIAM Journal on Computing 5(4), 691–703 (1976)
8. Fonseca, G.H.G., Brito, S.S., Santos, H.G.: A simulated annealing based approach to the high school timetabling problem. In: Yin, H., Costa, J.A.F., Barreto, G. (eds.) IDEAL 2012. LNCS, vol. 7435, pp. 540–549. Springer, Heidelberg (2012)
9. Geem, Z.W., Kim, J.H., Loganathan, G.V.: A new heuristic optimization algorithm: Harmony search. Simulation 76(2), 60–68 (2001)
10. Hoang, D.C., Yadav, P., Kumar, R., Panda, S.: A robust harmony search algorithm based clustering protocol for wireless sensor networks. In: 2010 IEEE International Conference on Communications Workshops (ICC), pp. 1–5 (2010)
11. Kheiri, A., Özcan, E., Parkes, A.J.: Hysst: Hyper-heuristic search strategies and timetabling. In: Proceedings of the Ninth International Conference on the Practice and Theory of Automated Timetabling (PATAT 2012), pp. 497–499 (2012)
12. Kingston, J.H.: A software library for high school timetabling (2009), `http://sydney.edu.au/engineering/it/~jeff/khe/`
13. Kingston, J.H.: A tiling algorithm for high school timetabling. In: Burke, E.K., Trick, M.A. (eds.) PATAT 2004. LNCS, vol. 3616, pp. 208–225. Springer, Heidelberg (2005)
14. Lara, C., Flores, J.J., Calderón, F.: Solving a school timetabling problem using a bee algorithm. In: Gelbukh, A., Morales, E.F. (eds.) MICAI 2008. LNCS (LNAI), vol. 5317, pp. 664–674. Springer, Heidelberg (2008)

15. Minh, K.N.T.T., Thanh, N.D.T., Trang, K.T., Hue, N.T.T.: Using tabu search for solving a high school timetabling problem. In: Nguyen, N.T., Katarzyniak, R., Chen, S.-M. (eds.) Advances in Intelligent Information and Database Systems. SCI, vol. 283, pp. 305–313. Springer, Heidelberg (2010)
16. Pillay, N.: A survey of school timetabling research. Annals of Operations Research, 1–33 (2013)
17. Post, G.: Benchmarking project for high school timetabling (2011), http://www.utwente.nl/ctit/hstt/
18. Post, G., Ahmadi, S., Daskalaki, S., Kingston, J.H., Kyngas, J., Nurmi, C., Ranson, D.: An xml format for benchmarks in high school timetabling. Annals of Operations Research 194(1), 385–397 (2012)
19. Post, G., Gaspero, L., Kingston, J.H., McCollum, B., Schaerf, A.: The third international timetabling competition. Annals of Operations Research, 1–7 (2013)
20. Sørensen, M., Kristiansen, S., Stidsen, T.R.: International timetabling competition 2011: an adaptive large neighborhood search algorithm. In: Proceedings of the Ninth International Conference on the Practice and Theory of Automated Timetabling (PATAT 2012). pp. 489–492 (2012)
21. Tassopoulos, I.X., Beligiannis, G.N.: A hybrid particle swarm optimization based algorithm for high school timetabling problems. Applied Soft Computing 12(11), 3472–3489 (2012)
22. Valouxis, C., Housos, E.: Constraint programming approach for school timetabling. Computers and Operations Research 30(10), 1555–1572 (2003)
23. Weyland, D.: A rigorous analysis of the harmony search algorithm: How the research community can be misled by a "novel" methodology. International Journal of Applied Metaheuristic Computing 1(2), 50–60 (2010)
24. Wilke, P., Killer, H.: Walk down jump up algorithm a new hybrid algorithm for timetabling problems. In: Proceedings of the 8th International Conference on the Practice and Theory of Automated Timetabling (PATAT 2010), pp. 440–446 (2010)
25. Yuan, Y., Xu, H., Yang, J.: A hybrid harmony search algorithm for the flexible job shop scheduling problem. Applied Soft Computing 13(7), 3259–3272 (2013)
26. Zou, D., Gao, L., Li, S., Wu, J., Wang, X.: A novel global harmony search algorithm for task assignment problem. Journal of Systems and Software 83(10), 1678–1688 (2010)

Self-organized Neural Representation of Time

Michail Maniadakis and Panos Trahanias

Foundation for Research and Technology - Hellas, ICS, Greece
{mmaniada,trahania}@ics.forth.gr

Abstract. Time is crucially involved in most of the activities of humans and animals. However, the cognitive mechanisms that support experiencing and processing time remain largely unknown. In the present work we follow a self-organized connectionist modeling approach to study how time may be encoded in a neural network based cognitive system in order to provide suggestions for possible time processing mechanisms in the brain. A particularly interesting feature of our study regards the implementation of a single computational model to accomplish two different robotic behavioral tasks which assume diverse manipulation of time intervals. Examination of the implemented cognitive systems revealed that it is possible to integrate the main theoretical models of time representation existing today into a new and particularly effective theory that can sufficiently explain a series of neuroscientific observations.

1 Introduction

Over the last few decades, an increasing number of studies have demonstrated the accuracy with which animals and humans are able to estimate time. However, the exact cognitive mechanisms that enable the measurement of time remain largely unknown. Broadly speaking, there are two main theories explaining how our brain represents time [1,5]. The first is dedicated models (also known as extrinsic, or centralized) that assume clock-like mechanisms and thus yield an explicit metric of time. This is the oldest and most influential explanation on interval timing. The models included in this category employ mechanisms that are designed specifically to represent duration. Traditionally such models have followed an information processing perspective in which pulses that are emitted regularly by a pacemaker are temporally stored in an accumulator [4,3]. This has inspired the subsequent pacemaker approach that uses oscillations to represent clock ticks [13]. The Striatal Beat Frequency (SBF) model is the most famous example of this category, assuming that timing is based on the coincidental activation of basal ganglia neurons by cortical neural oscillators [12]. Other dedicated models assume monotonous increasing or decreasing processes to encode elapsed time [16,15]. The second category includes intrinsic models (also known as distributed) that describe time as a general and inherent property of neural dynamics [7,2]. According to this approach, time is intrinsically encoded in the activity of general purpose networks of neurons. Thus, rather than using a time-dedicated neural circuit, time coexists with the representation and processing of other external stimuli.

M. Lee et al. (Eds.): ICONIP 2013, Part I, LNCS 8226, pp. 74–81, 2013.
© Springer-Verlag Berlin Heidelberg 2013

Besides the human devised representations of time that have been discussed above, our brain may actually use a different approach to encode and process time. Self-organized computational modeling can serve as a complementary means to explore representational schemes [14], and thus facilitate convergence in the time representation debate. This is the aim of the present study which employs a robotic experimental setup to investigate alternative schemes of time representation. Interestingly, the perception and processing of time remains particularly unexplored in the field of robotic systems [9]. Given the essential role of time in nearly all our daily activities, research in the emerging branch of robotic time perception is expected to significantly contribute in the seamless integration of artificial agents into the heavily time-structured human societies.

In the present study, we consider two different time processing tasks namely Duration Comparison and Past Characterization, which are accomplished by the very same robotic cognitive system. This is in contrast to the time representation schemes mentioned above, which have been discussed in a theoretical basis without being associated to the accomplishment of specific tasks. More specifically, a Continuous Time Recurrent Neural Network (CTRNN) [10] is used to develop an "artificial brain" for the robotic agent. We use an evolutionary design procedure based on Genetic Algorithms to search possible configurations of the artificial brain that can accomplish the afore mentioned tasks. Subsequently, we study the mechanisms self-organized in the CTRNN to extract the characteristics of effective time perception mechanisms that may be also valid for interval processing in our brain. The obtained results showed that very effective neural schemes can be used for generating, representing, and processing time, by combining the key characteristics of the "dedicated and intrinsic theories of time".

In the following sections, we describe the experimental setup followed in the present study, the obtained CTRNN results, and how the latter compare to the time processing data of the brain.

2 Experimental Setup

The current study is an extension of our previous works [10,11,9], investigating time perception and processing mechanisms by artificial agents. While these works have focused on single tasks, the present study simultaneously addresses two different tasks with temporal characteristics in order to emphasize the generalization of the self-organized time processing mechanisms.

Due to space limitations, in the following we will mainly concentrate on the presentation of the tasks, describing very briefly the robotic agent and its connectivity to the Continuous Time Recurrent Neural Network that have been already presented in detail in [10,11].

The Robotic Agent. We simulate a two wheeled mobile robot equipped with 8 uniformly distributed distance, light and sound sensors. The distance sensors are mainly used during navigation to avoid robot bumping on the walls. The light sensor is used to receive a task-indicator informing the robot which one of the tasks is considered at a given experimental session. The sound sensor is

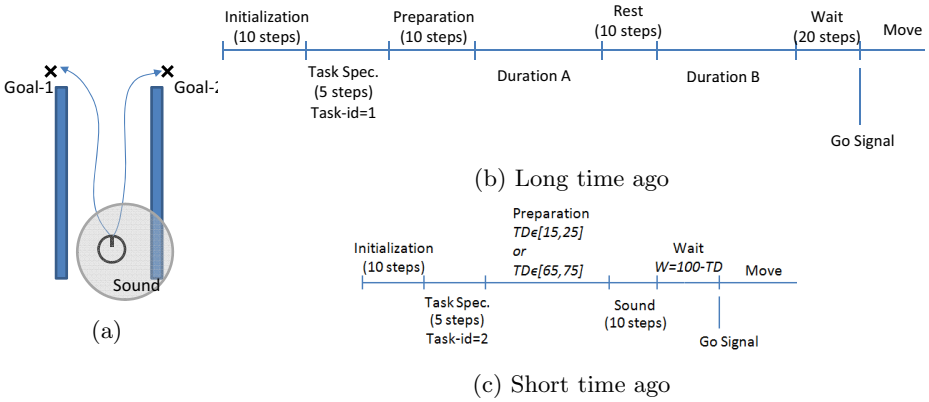

Fig. 1. Part (a) shows the experimental environment used in our study. Part (b) summarizes the experimental procedure followed in the Duration Comparison experiment. Part (c) summarizes the experimental procedure followed in the Past Characterization experiment.

used for the perception of temporal durations (i.e. the robot must perceive the duration of emitted sounds). The robotic cognitive system is implemented by a Continuous Time Recurrent Neural Network (CTRNN) similar to [10,11].

Duration Comparison. The scenario of this task assumes that the robot perceives two time intervals A and B, compares their duration and drives to the end of the corridor turning either to the left side in the case that A was shorter than B, or, to the right side in the case that A was longer than B (see Fig 1 (a)). The experiment starts with the simulated agent located at the bottom of the corridor environment. The robot remains at the initial position for a short initialization phase of 10 simulation steps, where it experiences a light cue indicating that the experimental procedure for the Duration Comparison task will follow (see Fig 1 (b)). Subsequently, after a short preparation phase, the agent experiences two sounds having temporal durations A and B, both of them randomly specified in the range $[10, 100]$. The two sounds are separated by a predefined rest period of 10 simulation steps. Just after sound B, the agent is provided 20 simulation steps to compare A and B, decide which one was longer and prepare its motion strategy. At the end of this period the robot is provided a "go" signal and it starts navigating across the corridor. In order to successfully complete the task, the agent has to navigate to the end of the corridor and turn right in the case that A interval was longer than B, or, turn left in the case that A interval was shorter than B.

Past Characterization. In this task, it is assumed that the robot experiences a sound and at a future time it judges whether this particular experience was at a short or long time ago. Similar to the previous task, the robot responds by driving along the corridor and turning either to the left side in the case that the sound event happened a long time ago, or, to the right side in the case that the event sound happened a short time ago (see Fig 1 (a)).

The experiment starts with the simulated mobile robot located at the beginning of the corridor. After a short initialization period, the agent experiences a

light cue indicating that the experimental procedure that will follow, concerns the Past Characterization task (see Fig 1 (b)). Subsequently, after a preparation interval with duration $TD \in [15, 25]$ for the case that the sound event was long time ago in the past, or $TD \in [65, 75]$ in the opposite case, the agent experiences a sound for a period of 10 steps. Then a wait period follows that is dynamically specified as $W = 100 - TD$ (i.e. the pair of TD and W, determines whether the sound experience of the agent has been in the short or long past). At the end of the wait period the agent is provided a "go" signal and it starts navigating towards the end of the corridor. If the sound experience was in the long past the agent must turn left, while if the sound experience was in the short past, the agent must turn right.

Performance Evaluation. To evaluate the response of the artificial agent in both the Duration Comparison and the Past Characterization task, we mark two different positions in the environment which are used as goal positions for the robot, as shown in Fig 1 (a). Depending on whether Goal1 or Goal2 is considered correct in a given experimental session, we measure the minimum distance D, between the agent's path and that goal position. Additionally, during navigation, we consider the number $Bumps$ of robot bumps on the walls. Thus, the success of the robotic agent to a given experimental session $i \in \{A > B, A < B, \}$ and $j \in \{LongPast, ShortPast\}$ is estimated by:

$$S_i = S_j = \frac{100}{D \cdot (Bumps + 1)} \tag{1}$$

By maximizing $S_{A>B}$, $S_{A<B}$ and $S_{LongPast}$, $S_{ShortPast}$ we aim at minimizing the distance from the goals therefore produce responses at the correct side of the corridor, as well as avoid bumping on the walls. The total capacity of the robot to accomplish the Duration Comparison and the Past Characterization task is estimated by considering robot's perfornace in all four possible cases as:

$$FIT = S_{A>B} \cdot S_{A<B} \cdot S_{LongPast} \cdot S_{ShortPast} \tag{2}$$

Evolutionary Procedure. We use a Genetic Algorithm (GA) to explore possible time perception and processing mechanisms in CTRNN-based cognitive systems. In short, we use a population of artificial chromosomes encoding possible CTRNN configurations (their synaptic weights and neural biases). Each candidate solution encoding a complete CTRNN is tested on both the Duration Comparison and the Past Characterization task, evaluated according to equation (2). The scores accomplished by the controllers are used to sort and evolve the population of chromosomes, therefore producing the next generation of candidate solutions. During reproduction, the best 30 individuals of a given generation mate with randomly selected individuals using single point crossover, to produce the next generation of CTRNNs. Mutation corresponds to the addition of up to 25% noise, in the parameters encoded to the chromosome, with each parameter having a probability of 4% to be mutated. This iterative evolutionary procedure is repeated for a predefined number of 500 generations.

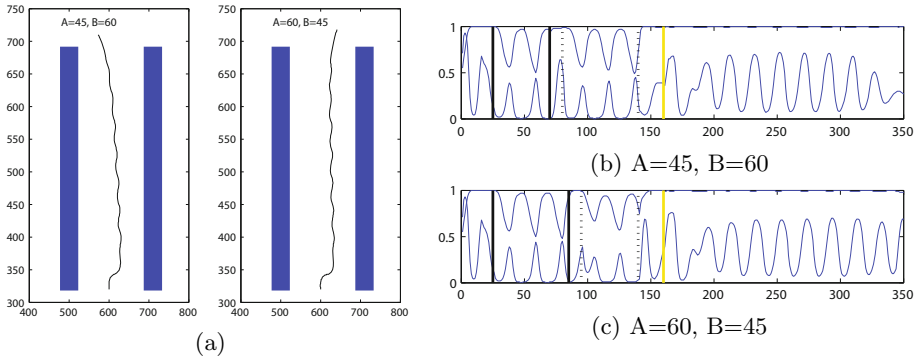

Fig. 2. Part (a) shows the performance of the agent when comparing two time intervals with lengths A=45, B=60 and A=60, B=45. Part (b) shows the activity of two CTRNN neurons that are actively participating in the measurement and comparison of A=45, B=60. Part (c) shows the activity of the same neurons for the case of A=60, B=45. In both plots the first two black vertical solid lines indicate the A period, and the next pair of black vertical dotted lines indicate the B period. The yellow line corresponds to the time that the "go" signal is given to the robot.

3 Results

We have evolved multiple CTRNNs running ten different GA processes. Five of the evolutionary procedures converged successfully configuring CTRNNs capable of processing time. Interestingly, the results obtained from the statistically independent evolutionary procedures exhibit common internal dynamics, which are discussed below using as a working example one representative solution.

Duration Comparison. The agent can successfully perceive and compare pairs of random temporal durations. The performance of the robot for two time intervals A and B with interchangeable durations 45 and 60 simulation steps is demonstrated in Fig 2(a).

We have examined the activity of CTRNN neurons to reveal the time processing mechanisms self-organized in the network. We observed that all CTRNN neurons are governed by oscillatory dynamics. This is in agreement to the dedicated-time models that assume oscillatory activity to implement a clock-like tick mechanism [3] that facilitates duration perception. However, besides the fact that the task is clearly separated into two distinct phases of (i) perception and (ii) action, some neurons remain active in the whole duration of the task which implies that time perception is mixed with the ordinary cognitive activity (i.e. neurons are not "dedicated" to time).

Additionally, neurons are not passively oscillating but seem to encompass crucial temporal information. In particular, Fig 2(b) show the activity of two neurons for the case of $A < B$ in Fig 2(a), and Fig 2(c) shows the activity of the same neurons for the case o $A > B$ in Fig 2(a). In both plots the amplitude of the oscillation increases as long as the agent experiences either interval A or B and thus, the difference between the two neurons is constantly decreasing in

relation to the length of the experienced duration. In other words, the amplitude of the oscillation can be actively used for counting the elapsed time. This observation extends the ideas behind the oscillatory models of time, suggesting that oscillations may not serve as passive ticks, but they might be actively involved in measuring time. Our results agree to both the oscillatory [12,13] and ramp [15] models, suggesting that the two mechanisms can be effectively integrated into the very same cognitive system and should not be considered as contradictory.

Another interesting observation regards duration resetting when turning from the A interval to the B interval. Typically, dedicated models assume a full reset of perceived duration, while intrinsic models assume no-reset [8]. According to our results, a reset-counting mechanism is activated by the end of A, because the amplitude of the oscillation of the two neurons at the end of A, is higher than the amplitude of the oscillation at the beginning of B. This is in agreement to the dedicated approach. However, in both Fig 2(b) and (c), time perception neurodynamics at the begging of A is different than that at the beginning of B. This suggests that the activity of neurons prior to the observation of a given duration affects the way that the network experiences the flow of time. In other words, the length of A affects the way that B is experienced, which is in agreement with the intrinsic representation of time [7]. This observation suggests a new type of duration resetting, which stands in the middle of the full reset and no reset. According to our results, it is possible for cognitive systems to use a dynamic resetting mechanism where the length of A determines the initial state during the perception of B. For example, when A is long the amplitude of the oscillation during perception of B starts from relatively low values (see Fig 2(b)), but when A is short the amplitude of the oscillation during perception of B starts from relatively high values (see Fig 2(c)).

The last observation additionally suggests that the amplitude of the oscillation is correlated with the likelihood that the currently observed duration will be judged as the longest in the experimental session. In other words, after experiencing a long A interval, in the early steps of B observation it is unlikely that B will be judged longer and the amplitude of the oscillation is low. As time progresses and the length of B increases, the probability that B will be considered longer is rising and thus the amplitude of the oscillation is also increasing. This mechanism explains how the robot decides whether A or B has been actually longer. It is noted that a similar observation with probabilistic information integrated into time-relevant neural activity has been also observed in macaque's brain [6] significantly enhancing the biological reliability of the mechanism revealed from our results.

Past Characterization. In this task, the robot characterizes the temporal distance of a given sound cue, as being either a short or long time ago. The behavior of the robot is shown in Fig 3 (a). In the first case, the robot experiences a sound 73 steps prior to the "go" signal while in the second case the robot experiences a sound 25 steps prior to the "go" signal. The agent successfully characterizes the two signals, driving to the end of the corridor and then turning left in the case of long time ago, but right in the case of short time ago.

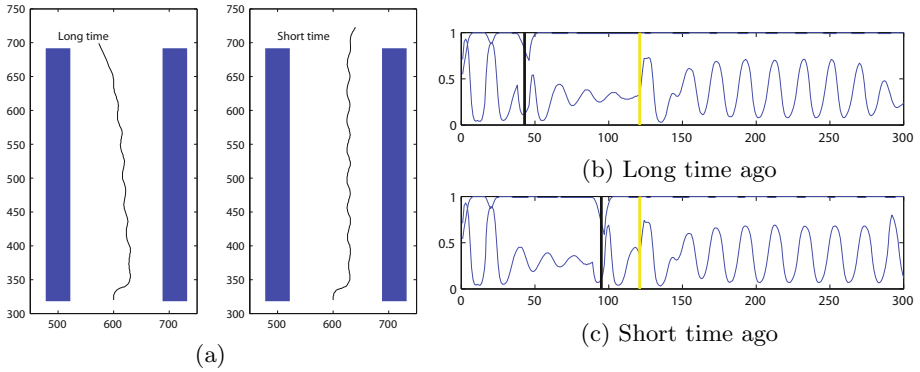

Fig. 3. Part (a) shows the performance of the robot when experiencing a sound cue "long time ago" and "short time ago". Parts (b) and (c) show the activity of the CTRNN neurons depicted also in Fig 2 for each one of the two cases in part (a). In both plots, the time of sound experiencing is indicated with a black vertical line. The yellow line corresponds to the time that the "go" signal is given to the robot.

Examining the internal activity of the CTRNN in Fig 3 (b) and (c), we observe that every time the sound is experienced, both neurons are temporally activated and subsequently, the one remains silent, but the other continues to oscillate with a constantly decreasing amplitude. Since amplitude effectively measures time duration, it is evident that a counting-down mechanism has been implemented in the CTRNN. While in the Duration Comparison task the amplitude of the oscillation was increasing as long as the sound cue was present, reverse counting does not require any sensory input and this mechanism is used for measuring the distance to a past sensory cue. In other words, when the amplitude is small then it has been a long time ago since the last experience of sound, but when the amplitude is large then it has been a short time since the last presentation of sound (i.e. there has been not enough time for the amplitude to decrease). Clearly, the observed neurodynamics suggest again that oscillatory activity may be not only used as a passive ticking mechanism but it is likely that they actively participate in the accomplishment of the task.

4 Discussion and Conclusions

To the best of our knowledge, none of the existing approaches for time representation can provide mechanisms that simultaneously explain the accomplishment of the two tasks discussed in the present study. The self-organized CTRNN dynamics considered in our work have revealed multiple points for bridging the currently contradictory theories into a new enhanced scheme with more explanatory power. More specifically, our results suggest that:

– Interval timing can be encoded in the activity of neurons supporting ordinary cognitive tasks.

– Oscillations can effectively facilitate the estimation of the elapsed time and the amplitude of the oscillatory activity may be used for accumulating duration (i.e. we may not need separate subsystems for ticking and counting).
– Active rather than passive oscillatory activity may underpin the implementation of time processing mechanisms in a range of different tasks.

In conclusion, the present work adopts a computational approach to investigate time representation in cognitive systems, suggesting the integration of time-representation approaches existing today. At the same time, the current work brings to the surface the issue of temporal cognition that remains largely unexplored in the field of autonomous artificial systems. In the future we intend to explore how time processing may facilitate robotic agents to accomplish tasks in the highly time-structured human environments.

References

1. Bueti, D.: The sensory representation of time. Frontiers in Integrative Neuroscience 5(34) (2011)
2. Dragoi, V., Staddon, J., Palmer, R., Buhusi, C.: Interval timing as an emergent learning property. Psychol. Review 110(1), 126–144 (2003)
3. Droit-Volet, S., Meck, W., Penney, T.: Sensory modality and time perception in children and adults. Behav. Process 74, 244–250 (2007)
4. Gibbon, J., Church, R., Meck, W.: Scalar timing in memory. In: Gibbon, J., Allan, L.G. (eds.) Timing and Time Perception, pp. 52–77. New York Academy of Sciences, New York (1984)
5. Ivry, R.B., Schlerf, J.E.: Dedicated and intrinsic models of time perception. Tr. in Cognitive Sciences 12(7), 273–280 (2008)
6. Janssen, P., Shadlen, M.N.: A representation of the hazard rate of elapsed time in macaque area lip. Nat. Neurosci. 8(2), 234–241 (2005)
7. Karmarkar, U.R., Buonomano, D.V.: Timing in the absence of clocks: Encoding time in neural network states. Neuron 53(3), 427–438 (2007)
8. Laje, R., Cheng, K., Buonomano, D.: Learning of temporal motor patterns: an analysis of continuous versus reset timing. Front. Integr. Neurosc. 5(61) (2011)
9. Maniadakis, M., Trahanias, P.: Temporal cognition: a key ingredient of intelligent systems. Frontiers in Neurorobotics 5 (2011)
10. Maniadakis, M., Trahanias, P., Tani, J.: Explorations on artificial time perception. Neural Networks 22, 509–517 (2009)
11. Maniadakis, M., Wittmann, M., Trahanias, P.: Time experiencing by robotic agents. In: Proc. 11th European Symposium on Artificial Neural Networks (2011)
12. Meck, W., Penney, T., Pouthas, V.: Cortico-striatal representation of time in animals and humans. Current Opinion in Neurobiology 18(2), 145–152 (2008)
13. Miall, C.: The storage of time intervals using oscillating neurons. Neural Computation 1, 359–371 (1989)
14. Ruppin, E.: Evolutionary autonomous agents: A neuroscience perspective. Nature Reviews Neuroscience 3(2), 132–141 (2002)
15. Simen, P., Balci, F., de Souza, L., Cohen, J., Holmes, P.: A model of interval timing by neural integration. J. Neuroscience 31, 9238–9253 (2011)
16. Staddon, J., Higa, J.: Time and memory: towards a pacemaker-free theory of interval timing. J. Exp. Anal. Behav. 71(2), 215–251 (1999)

An Enhanced Mental Model Elicitation Technique to Improve Mental Model Accuracy

Tasneem Memon, Jie Lu, and Farookh Khadeer Hussain

Decision Systems and e-Service Intelligence Laboratory (DeSI)
Centre for Quantum Computation and Intelligent Systems (QCIS)
University of Technology Sydney, Australia
{tasneem.memon,jie.lu,farookh.hussain}@uts.edu.au

Abstract. The causal mental model representation has been used extensively in decision support. Due to limited information requirements of this representation, that is *concepts* and *relationships*, the users are required to articulate only the mental models, without invoking the corresponding experiential knowledge stored in *associative memory*. The elicitation of mental models without being endorsed by experiential knowledge may lead to inaccurate, invalidated or biased mental models, and espoused theories, being stored for decision making. We introduce *SDA articulation/ elicitation cycle*, which invokes a user's *associative memory* during the articulation/elicitation process to validate mental models. It is argued in this paper that by engaging *associative memory* during the mental model articulation/elicitation process, the accuracy and validity of mental models can be improved, the biases can be reduced, and the theories-in-use can be elicited rather than the espoused theories. A case study is presented to demonstrate the working and contributions of the *SDA articulation/ elicitation cycle*.

Keywords: Mental model representation, mental model articulation/ elicitation, cognitive biases, cognitive decision support.

1 Introduction

The mental models have been used in decision system to understand, predict and solve problems in uncertain and vague situations [1, 2]. They are formed through experience, observation and ongoing learning processes in the human mind, and are the basis for the beliefs and subjective opinions of a person [3]. They provide the knowledge required to do the situation assessment, problem understanding and formulation, problem space identification and problem space segmentation [4,5]. Generally, the mental models used in decision making are represented as causal maps, containing *concepts* and *causal relationships* [2,6].There are inherent limitations, however, to this representation of mental models. In this paper, we will discuss two limitations of the current mental model representation; a) its limited capacity to facilitate elicitation of valid mental models from individuals with accuracy, and inability to store meaningful and contextual information about the mental models [7]; and b) its inability to filter cognitive

M. Lee et al. (Eds.): ICONIP 2013, Part I, LNCS 8226, pp. 82–89, 2013.
© Springer-Verlag Berlin Heidelberg 2013

biases during the mental model elicitation [8]. We will explore how these shortcomings can be mitigated to some extent by the *semantic de-biased associations (SDA) model*, which was proposed by Memon et al [9].

The paper is organised as follows. Section 2 gives the overview of the problems at hand and their background from the literature. In Section 3, the SDA model and its basic components are discussed briefly, followed introduction of *SDA-based articulation/elicitation cycle* for mental models, and mitigation of biases. Section 4 presents examples demonstrating the innovation of this cycle. Finally conclusion and future work are presented.

2 Literature Review

Mental models can be a powerful tool in solving complex and vague decision situations [10, 11]. However, there are various issues in the articulation, elicitation, and representation of mental models, which if not addressed, may lead to poor decisions. This paper addresses two issues; a) limited capability of current mental model representation used in DSS, to help articulate, elicit and store knowledge; and b) its limitation to facilitate de-biasing the mental models.

Due to the complex and intuitive nature of mental models, it is difficult to articulate them accurately [6,8]. The articulation of mental models, to some extent, depends upon the intended representation, such as *a causal map*. A person may describe their mental models through various techniques, such as a set of rules, a mind map, or statements [6]. Based on the intended representation, required entities (in the case of *causal maps*, *concepts* and *relationships*) are then elicited from these descriptions [12]. Several elicitation techniques have been proposed to get such as such as 3CM [13], *fuzzy cognitive mapping* [14] and diagrammatic interview method by Dray et al [15]. These techniques assume the mental models to be a network of *concepts* and *relationships*; thus, all that is extracted from the *descriptions* is the *concepts* and *relationships*. However, mental models are much complex structures than merely *causal maps* [16]. They work in conjunction with, and are supported by, our visuals and *associative memory* [8]. Every mental model is formed through an experience, having a historical background in the *associative memory*, which contains the reasons for its existence [17]. Thus its not sufficient to elicit and store the mental models in the form of *concepts* and *relationships*. It is essential to help an individual to remember the historical background (from *associative memory*) as well, and elicit it along with the mental model itself [18]. Engaging *associative memory* allows to avoid the phenomena where people articulate the "espoused theories", rather than the actual "theories-in-use", due to the poor insight into their own mental models [19]. Invoking *associative memory* will help to recall the situations in which the mental models were created, the reasons behind their creation, and their performance in terms of solving a problem. This in turn will give the person a clearer picture of what actually worked and why. Therefore, it is argued in this paper that by

incorporating *associative memory* into the current *causal map* representation for mental models, the following advantages can be achieved:

- Help individuals to articulate their mental models in a better and efficient way, by providing them with a template of what is required to be elicited,
- Improve the accuracy of the mental models by asking critical questions (see Section 3.1 for the details of the questions),
- Mitigate the biases during the elicitation process, as well as the at the time using these mental models, through the *contextual* and *objective information (performance measuring parameters)* extracted from the *associative memory*.

3 Basic Components of SDA Mental Model Representation

The mental model representation proposed in SDA model is comprised of *concepts*, *semantic relationships*, *cases* and performance measuring parameters *weight* and *success factor* [9]. Each link, consisting of two adjacent *concepts* with a *semantic relationship* between them, is named as *association*. Thus, the mental models in SDA are a network of *associations*, where each *association* has *contextual information* attached to it in the form of past *cases*, extracted from the *associative memory* during the *articuation/elicitation cycle* (see Section 3.1 for *SDA articulation/elicitation cycle*).

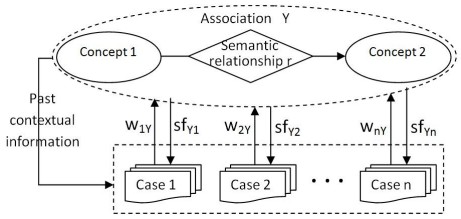

Fig. 1. Fundamental components of SDA-mental model representation

As can be seen from Fig. 1, *association Y* is formed through two concepts *concept 1* and *concept 2* connected with a *semantic relationship r*. The *association Y* has past *cases (1,2, ..., n)* attached to it. These *cases* contain the information about the past experiences, which led to the creation of the *mental model* represented by *association Y*. The information in each case includes:

1. What: The details of the problem/situation;
2. When: Date;
3. Where: Organization;
4. How:
   - The way this mental model (association) helped to solve the problem;
   - The extent to which this mental model (association) was effective in solving the problem *(weight)*;
5. Who: The decision maker (his credibility);
6. Which: (The kind of situations, in which this mental model (association) can be used successfully.

Fig. 2 shows the information contained in a *case* in SDA-based mental model representation [9]. The table contains *case_ID, Association_ID, Case_Details*

(the *what* question), *Case_Year (when), Case_Organisation (where), Future_Use (which) and Weight (how)*. Another important measuring parameter in SDA-based representation is the *success rate*. The success rate is used to measure the usefulness of an *association*). The *success rate* of an *association* is the average of all the *success factors* of that *association* for the corresponding cases (see [9]).

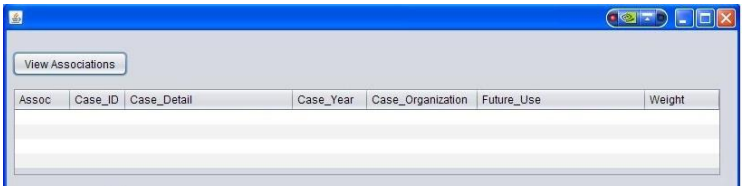

Fig. 2. Implementation of *Case* in SDA-based system

3.1 Articulation Elicitation Cycle in SDA

Mental models can be elicited through *direct* or *indirect* elicitation methods [12]. The direct elicitation allows users to describe main concepts of a domain in the form of words, symbols or pictures, and connect these together according to their understanding. While the indirect elicitation allows to derive mental models from text or the verbal communication with an individual.

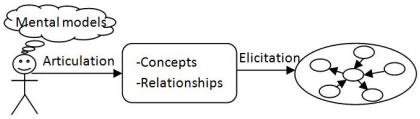

Fig. 3. Conventional articulation/elicitation process

Being direct elicitation approach, SDA model allows participants to view the illustration of their mental models immediately; thus verifying them instantly [12]. Most of the direct elicitation approaches focus on extracting *concepts* and *relationships*, and overlook the contents of *associative memory*, which contain the *experiential knowledge* behind these *concepts/relationships* [8]. As a result, the articulated mental models may be "espoused" or unproven theories, or inaccurate representations [19].

The SDA cycle improves the articulation/elicitation process by asking critical questions about a mental model, thus forcing the user to make a conscious effort to invoke and engage *associative memory*. The questions include:

- why does the user think what they think?
- which decision problem was this mental model used for?
- how helpful their mental model was in that situation?
- how did it solve the problem?
- what were the circumstances surrounding the decision problem?
- when and where did it occur?
- who was responsible for the decision making?
- what was the credibility of the decision maker(s)?
- where can this mental model be applied in the future?

During this process, the users may discover whether their mental models are an espoused theory, inaccurate, unproven or biased [20]; consequently, adjusting their mental models accordingly before the final elicitation. Asking appropriate question can help reduce the cognitive biases as well [8]. Fig 3 and 4 show the difference between the conventional mental model articulation/elicitation process and the SDA-based articulation/elicitation cycle, respectively.

3.2 Role of Associative Memory in Bias Reduction

The SDA model deals with four cognitive biases, *availability, contextual, framing* and *group biases*. However, here we will discuss only the ones affected by the contents of *associative memory*. These are, *contextual* and *framing*. Contextual bias is generated from the circumstances surrounding an experience. Same kind of problem, with different contextual information, may need different solutions [17]. In SDA, the contextual information extracted from the *associative memory* helps a decision maker distinguish between the current decision situation and the past decision cases stored, and determine the suitability of the corresponding mental model for the current decision situation.

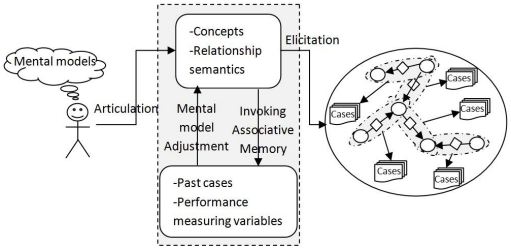

Fig. 4. The proposed technique: *SDA-based articulation/elicitation cycle*

Framing defines the inclinations, developed by the way a decision situation is presented [21]. In SDA, the *framing bias* is handled through various past *cases*, which are attached to certain mental model. These cases come from the *associative memories* of various users. Each case contains a *weight* showing the importance/effectiveness of the corresponding *association* for the case. The *weight*, being the factual data, can assist the user in avoiding framing bias, even if the presentation of decision situation is biased in the *case details (Case_Details in Fig. 2)*.

4 Demonstration of SDA Articulation/Elicitation Cycle

This section walks through the *SDA articulation/elicitation cycle*, demonstrating its effectiveness to facilitate mental model articulation and to improve their accuracy. The specific decision problem is: *How can we increase our sales/clientele?* The participants of this case study were required to articulate possible alternatives/solutions to this decision situation. Following are three selected decision alternatives, articulated by participants from various fields, which demonstrate how the *SDA articulation/elicitation cycle* deals with different scenarios.

Mental Model 1: Offer Incentives. The participant (from fashion industry) came up with the an alternative: "Sales/clientele can be increased by offering incentives". Since SDA model represents mental models in a human-centric manner

by incorporating *semantics*, the conversion of mental model described in natural language into SDA representation was effortless, which is:

Incentives *increase* Sales

Since the SDA model requires the contextual knowledge behind a mental model, the participant was required to recall the previous experience, to store as supporting *case*. The recalled experience (*case 123* Fig. 5) helped them to validate success of the mental model in the domain. This mental model was extracted from a *personal experience* and was validated by the positive outcome (*0.75 weight*) of the decision alternative (*association 012*).

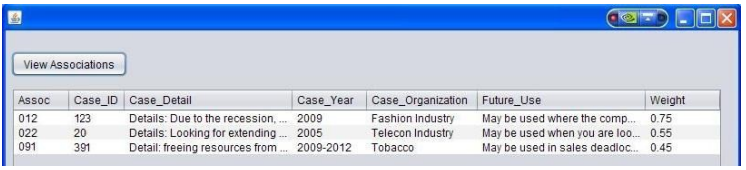

Fig. 5. The *Cases* elicited through the SDA articulation/elicitation cycle

Mental Model 2: Entering New Markets. The participant (from telecom industry) came up with the mental model "Sales/clientele can be increased by entering new markets", converted to SDA-based representation as:

Entering New Markets *increase* Sales

This mental model was based on the participant's observation. They observed a company entering the rural market rather than focusing on urban market, giving that company a big boost in sales. This mental model was validated by the positive results it brought for that company (*Case 022* in Fig 5).

Mental Model 3: Chasing Good Prospects Continuously. The participant (from tobacco industry) came up with the mental model "Sales/clientele can be increased by chasing good prospects (potential customers) continuously", converted into SDA-based representation as:

Pursuing good prospects continuously *increase* Sales

Initially, the participant was confident about pursuing good prospects continuously. But during the *questioning process* of *SDA articulation/elicitation cycle* to invoke *associative memory*, the participant was unable to recall a huge profit gained from long-chased prospects in the past few years. Rather, they realized that their company has gained more sales from pursuing new prospects, after freeing the resources from the long-held ones. As a result of this process, the participant corrected their mental model as: " Sales/clientele can be increased by freeing the resources from long-chased yet unfruitful Prospects". That is:

Sidelining long-chased prospects *increase* Sales

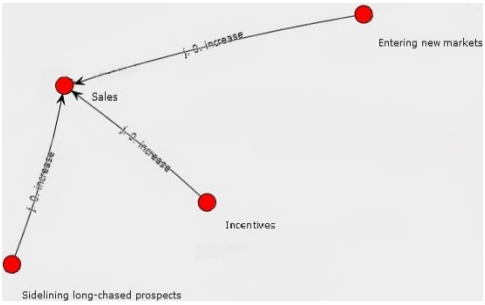

Fig. 6. The three mental models elicited for the domain *Increase in Sales*

Fig. 5 shows the final mental model in *case 091*. The initial mental model in this example was a deep-seated but inaccurate assumption, which was recognized by engaging *associative memory*, as the mental model could not be sufficiently validated by the past experiences of the participant. Rather, the participant developed a new and *validated* mental model by recalling past experiences. This example shows the effectiveness of *SDA articulation/elicitation cycle* in discarding inaccurate mental models. Fig. 6 shows the three mental models presented in this Section.

5 Conclusion and Future Work

This paper discussed the contributions of SDA-based mental model representation towards better articulation, elicitation and accuracy of mental models, in addition to the mitigation of biases. The *SDA articulation/elicitation cycle* for mental models was introduced in this paper. Compared to the conventional mental model elicitation techniques, the *SDA articulation/elicitation cycle* provides an improved way to elicit and validate mental models by engaging associative memory, and ensures their accuracy/validity by asking critical questions during the elicitation process. Furthermore, the SDA-based mental model representation allows the mitigation of *contextual* and *framing biases*.

References

1. Chermack, T.J.: Mental models in decision making and implications for human resource development. Advances in Developing Human Resources 5(4), 408–422 (2003)
2. Niu, L., Lu, J., Zhang, G.: Cognition-Driven Decision Support for Business Intelligence. Springer, Hiedelberg (2009)
3. Vosniadou, S.: Mental models in conceptual development. Model-Based Reasoning: Science, Technology, Values, 353–368 (2002)
4. Endsley, M.R.: Toward a theory of situation awareness in dynamic systems. Human Factors: The Journal of the Human Factors and Ergonomics Society 37(1), 32–64 (1995)
5. Schwenk, C.R.: The cognitive perspective on strategic decision making. Journal of Management Studies 25(1), 41–55 (1988)
6. Carley, K., Palmquist, M.: Extracting, representing, and analyzing mental models. Social Forces 70(3), 601–636 (1992)
7. Besnard, D., Greathead, D., Baxter, G.: When mental models go wrong: co-occurrences in dynamic, critical systems. International Journal of Human-Computer Studies 60(1), 117–128 (2004)

8. Kahneman, D., Lovallo, D., Sibony, O.: The big idea: Before you make that big decision. Harvard Business Review, 50–60 (June 2011)
9. Memon, T., Lu, J., Hussain, F.K.: Semantic de-biased associations (SDA) model to improve ill-structured decision support. In: Huang, T., Zeng, Z., Li, C., Leung, C.S. (eds.) ICONIP 2012, Part II. LNCS, vol. 7664, pp. 483–490. Springer, Heidelberg (2012)
10. Chen, J.Q., Lee, S.M.: An exploratory cognitive dss for strategic decision making. Decision Support Systems 36(2), 147–160 (2003)
11. Mintzberg, H.: The Nature of Managerial Work. Harpercollins College Div, New York (1973)
12. Jones, N.A., Ross, H., Lynam, T., Perez, P., Leitch, A.: Mental models: an interdisciplinary synthesis of theory and methods. Ecology and Society 16(1) (2011)
13. Kearney, A.R., Kaplan, S.: Toward a methodology for the measurement of knowledge structures of ordinary people: The conceptual content cognitive map (3cm). Environment and Behavior 29(5), 579–617 (1997)
14. Ozesmi, U., Ozesmi, S.L.: Ecological models based on peoples knowledge: a multi-step fuzzy cognitive mapping approach. Ecological Modelling 176(1-2), 43–64 (2004)
15. Dray, A., Perez, P., Jones, N., Page, C.L., D'Aquino, P., White, I., Auatabu, T.: The atollgame experience: from knowledge engineering to a computer-assisted role playing game. Journal of Artificial Societies and Social Simulation 9(1), 6 (2006)
16. Held, C.: Mental models as objectual representations. In: Carsten Held, M.K., Vosgerau, G. (eds.) Mental Models and the Mind Current Developments in Cognitive Psychology, Neuroscience, and Philosophy of Mind. Advances in Psychology, vol. 138, pp. 237–253. North-Holland (2006)
17. Ubel, P.A., Smith, D.M., Zikmund-Fisher, B.J., Derry, H.A., McClure, J., Stark, A., Wiese, C., Greene, S., Jankovic, A., Fagerlin, A.: Testing whether decision aids introduce cognitive biases: Results of a randomized trial. Patient Education and Counseling 80(2), 158–163 (2010)
18. Maqsood, T., Finegan, A.D., Walker, D.H.T.: Biases and heuristics in judgment and decision making: The dark side of tacit knowledge. Issues in Informing Science and Information Technology 1, 295–301 (2004)
19. Argyris, C., Schon, D.A.: Theory in practice: Increasing professional effectiveness. Jossey-Bass, Oxford (1974)
20. Gary, M.S., Wood, R.E.: Mental models, decision rules, and performance heterogeneity. Strategic Management Journal 32(6), 569–594 (2008)
21. Tversky, A., Kahneman, D.: The framing of decisions and the psychology of choice. Science 211(4481), 453–458 (1981)

Role of Gestalt Principles in Selecting Attention Areas for Object Recognition

Jixiang Shen, Amitash Ojha, and Minho Lee*

School of Electronics Engineering Kyungpook National University,
1370 Sankyuk-Dong, Puk-Gu, Taegu 702-701, South Korea
shenjixiang@naver.com, {amitashojha,mholee}@gmail.com

Abstract. Human attention plays an important role in human visual system. We assume that the Gestalt law is one of important factors to guide human selective attention. In this paper, we present a series of studies in which we hypothesized that regions of image that get more attention in an object recognition task, confirm to one or more gestalt principles and subconsciously attract human attention which eventually help in object recognition. In our study, we collected attention parts of images by analyzing eye movement of participants. Then we compared Gestalt scores of high attention parts with those of non-attended random parts. Our results suggest that continuity and symmetry of features attract human attention. We argue that an approach to analyze parts with high Gestalt scores can yield better than analyzing random parts of image in object recognition.

Keywords: Gestalt principle, selective attention, perception, symmetry, continuity, regularity.

1 Introduction

Attention plays an important role in human cognition. It allows selective processing of useful information while ignoring less important ones [1]. Attention can operate in multiple modalities but the most important among them is visual attention. Various theories and models have been proposed to describe the process of attention and its role in visual perception [2]. For example, James proposed, "spotlight model" [3]. The model suggests that attention works with "focus", "fringe", and "margin". The "focus" extracts high-resolution information from visual scene, "Fringe", surrounding focus, extracts crude information and the edge of this fringe is called the "margin". Eriksen proposed a model called the "zoom-lens model" which is similar to James' model [4]. This model postulates that deployment of attention can vary from a sharp focus to a broad window. While discussing attention, a distinction between bottom-up and top-down processes are also mentioned. According to James, bottom-up process is driven by the properties of the object [5] that can attract human attention subconsciously.

In AI, especially in computer vision, several attempts have been made to imitate human visual system using attention models. For example, Park et al. [6] used

* Corresponding author.

M. Lee et al. (Eds.): ICONIP 2013, Part I, LNCS 8226, pp. 90–97, 2013.
© Springer-Verlag Berlin Heidelberg 2013

independent component analysis (ICA) and entropy as a filter to select significant regions in an image. Similarly, Jeong et al. developed a model to generate saliency map based on the bottom-up and top-down processes [7].

In the bigger schema of our research, we are interested in developing an alternative cognitive model for object recognition using Gestalt principles. Gestalt theory [8] attempts to describe how people organize visual elements into group or unified wholes by applying various principles such as similarity, continuity, regularity, symmetry, etc. Moreover, we assume that principles of Gestalt guide human attention. In other words, features having properties for Gestalt grouping attract human attention and plays significant role in recognizing objects.

Rationale of our assumption is based on perception-action cycle [9]. According to perception-action cycle, top-down and bottom-up processes work in tandem and mutually contributes to the success of each other. Bottom-up information collects low-level perceptual features from environment and organizes it using various integration mechanisms (including gestalt principles) for partial perception (an estimate). In return, this partial perception, based on top-down process, guides attention for more specific features search to confirm and complete the perception process. Therefore it is reasonable to assume that features having similar patterns for possible grouping are attended in the case of perception. We try to confirm this assumption in our research.

In this paper, three studies are presented. We hypothesized that part of an image that gets maximum human attention in an object recognition task, confirms to some or at least one principle of Gestalt more significantly than non-attended random parts of the image. To test our hypothesis, we compared Gestalt scores (calculated using previously developed algorithms) of attention regions and non-attended random regions of an image. We call them "attention patches" and "random patches", respectively.

The rest of the paper is organized as follows: In section 2, we describe the Gestalt principle in general and principle of (1) continuity, (2) regularity and (3) symmetry in particular. In section 3, we present three studies In section 4, we discuss the implication and limitations of our study and at the end in section 5, we present our conclusions and possible future direction of this research.

2 Gestalt Principle

2.1 Principle of Regularity, Continuity and Symmetry

In general, Gestalt psychology attempts to describe how people organize visual elements into groups or unified wholes by applying various principles [10], such as similarity, proximity, continuity, regularity, symmetry, etc. We explored three of them namely principle of (1) continuity, (2) regularity and (3) symmetry in attended regions of an image. "Principle of continuity" suggests that humans tend to organize continuous parts of objects as a whole. For example in Fig. 1 (a), a cross is more prominently perceived than two right angle shapes. "Principle of regularity" postulates that elements of objects are perceptually grouped together if they form a pattern that is regular, simple, and in order. For example in Fig. 1 (b), two squares constructed using lines are arrayed so orderly and enhanced by irregular lines that these two squares can

be perceived easily in the complex background. “Principle of symmetry” suggests that humans perceive objects by considering parts that are symmetrical. For example, in Fig.1 (c), three pairs of symmetrical brackets are perceived rather than six individual brackets.

(a) (b) (c)

Fig. 1. (a) Cross, (b) Collinear pattern, (c) Law of symmetry

3 The Experiment

As mentioned above, we hypothesized that part of an image that gets maximum human attention in an object recognition task, confirms to some or at least one principle of Gestalt more significantly than non-attended random parts of the image. We conducted three related studies to test it. In first study, we collected regions of attention in an image by analyzing fixation count and fixation time (by analyzing eye-movement data) of participants while they did an object recognition task. In second study, we calculated Gestalt scores of regularity, continuity and symmetry in attention regions and non-attended random regions and then compared them. Gestalt scores were calculated using previously developed algorithms. High score for a particular principle in a particular patch meant that the patch is more likely to be grouped under that principle. In third study, we verified our assumption by only highlighting (1) attention areas with high Gestalt score (attention patches) and (2) non-attended random areas (random patches) and by presenting them to participants for an object recognition task

3.1 Study 1:Identifying Attention Regions Using Eye-Movement

In the first study, we collected images of 60 objects with complex background in three following categories: (1) Animals in natural scenes, (2) Objects of daily use in normal environment and (3) Vehicles in urban and rural environment. The objective of this study was to identify regions of an image that attracts attention of participants while they do object recognition task.

Participants and Procedure. 12 graduate students (3 females and 9 males) (mean age=21) from Kyungpook National University, Korea, participated in the study. Participants were shown 60 images, from three above-mentioned categories (20 each) randomly, on a 21 inch computer screen (1280x780). They were asked to look at the image and recognize the target object. There was no time limit and they were asked to press space bar once they had recognized the object. While participants performed the task, their eye-movement was recorded using Tobii eye tracker from a distance of

60-70 centimeters [11]. Although, the viewing was binocular, we only recorded the movement of left eye because of certain hardware constraints.

Output of the Study. Output of this study included eye movement samples of 12 participants for 60 images in complex background in three categories. We calculated mean (1) fixation count and (2) fixation time to acquire the most attended regions for each image. Fig. 2 shows an example of (b) gaze plot and (c) heat map of mean fixation. Based on this analysis, most attended regions were marked as areas of interest (AOI) and were collected as "attention patches". Same numbers of non-attended and random patches were also collected as "random patches" (having same size as attention patch) from all images. Both attention and random patches were used in the next study.

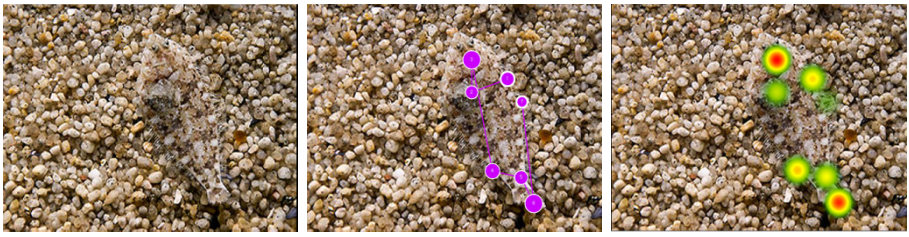

(a) (b) (c)

Fig. 2. Sample images with gaze plot; (a) original image, (b) gaze plot of one participant, (c) average heat map

3.2 Study 2: Analysis and Comparison of Gestalt Scores

In this study, we compared Gestalt scores of "attention patches" and "random patches" for all images. To acquire the score for three Gestalt principles namely: (1) Regularity, (2) Continuity and (3) Symmetry, we used previously developed algorithms. , Our method of calculating scores for these three principles of Gestalt is as follows:

Principle of Continuity. Principle of continuity is defined as the longest contour line in a patch. We followed Dou and Kong's [12] method for contour detection. Canny operator was used to get the edge information. We try to generate a smooth line as long as possible. To do this, we randomly take a start point A and set eight directions around it. If we find a neighbor edge point B, near by the start point, the direction of $\overrightarrow{AB}$ is seen as the initial direction of this line. In order to generate a smooth line, we search the edge point C nearby B where $\overrightarrow{BC} = \overrightarrow{AB}$. If there is no C, then we search the edge point C' nearby C where $\overrightarrow{BC'} = \overrightarrow{AB} \pm 45°$. The process of searching edge is repeated until no points are left.

Principle of Regularity. The regularity of point A is defined as the "surrounding edge pixels expanding acceleration". We use Canny operator to obtain edge information of the image. Then we check A's surrounding area (5x5 box, A is located in the

center of this box) and count number of edge pixels. We expand the box radius by 2 pixels (5x5, 7x7 …) each time and record number of added pixels. We believe that in the regular area the edge pixel increasing speed should approach a constant, which means the edge pixels expanding acceleration should be small and approach zero.

Suppose i is the current expanding time, P_i means count of edge pixels inside the current box. The acceleration of surrounding edge pixels are defined as:

$$R_A = |(P_{i+1} - P_i) - (P_i - P_{i-1})| \tag{1}$$

Smaller R_A means higher regularity. In order to measure the regularity of an image, we investigate the regularity of each edge point and calculate the average value.

$$R_{Image} = \sum_{i \in edgeonImage} \frac{R_i}{N} \tag{2}$$

Where N is the number of edge pixels in the image.

Principle of Symmetry. To test the symmetry of image, we consider the bottom-up saliency map (SM) with symmetry information method [7]. To generate a symmetry feature map, we take K-directional orientation features as input, and then compare the orientation features located on opposite sides. Take these information to generate Gaussian blurred pyramid orientation features with various scales, at finally symmetry axis S(f, n, k) at the$f$-th pyramid orientation feature is calculated using Eq. (3), where n is the location within an image, F is the total number of pyramids, M is the level of blurred images and k is the orientation direction, $GP_{o(m+f)}$ is (m+f) th orientation Gaussian pyramid, m represents a level of blurred image.$\gamma_k$and$\delta_k$are weight parameters and φ(x)=max(x,0). $\overline{k}$is the opposite of the k direction,$\overline{k}$= $K + \frac{K}{2}$,where K is the total number of directions being considered. For a location n=*(x,y)*, the locations n_r=(x_r, y_r) and n_l=(x_l, y_l) are obtained by Eq. (4):

$$\mathrm{S(f,n,k)} = \sum_{m=0}^{M-1} \sum_{k=0}^{K-1} \Big\{ \gamma_k \cdot \Big(GP_{o(m=f)}(n_r, k+r) + GP_{o(m+f)} \times \big(n_1, \overline{K-k}\big) \Big) - \delta_k \big| GP_{O(m+f)}(n_r, k+r) - GP_{o(m+f)} \times \big(n_1, \overline{K-k}\big) \big| \Big\},$$

$$\Big(f = 0,1 \cdots F - M, k = 0,1 \cdots \frac{K}{2} - 1 \Big) \tag{3}$$

$$x_r = x + A_{CM} \cos(\alpha_k), y_r = y + A_{CM} \sin(\alpha_k)$$

$$x_l = x - A_{CM} \cos(\alpha_k), y_l = y - A_{CM} \sin(\alpha_k)$$

$$\alpha_{\overline{k}} = \alpha_k + \pi, \alpha_k = \frac{2k\pi}{K}$$

$$A_{CM} = 2^m A_{c0,} \tag{4}$$

$A_{CM}$is the *m*-th distance between two opposite side locations. At finally using center surround difference and normalization (CSD&N) of symmetry axes in different scale to obtain feature map. We take average pixel of feature map to represent how symmetry the image is.

Results. By applying above-mentioned algorithms, we obtained the Gestalt scores for three Gestalt principles for all attention patches and random patches. We calculated the average score of all patches (attention and random) in all three categories namely (1) animals in natural scenes, (2) objects of daily life, and (3) vehicles in urban and rural backgrounds. As shown in Fig. 3, results suggest that scores of 'principle of regularity', 'principle of symmetry' and 'principle of continuity' were significantly high in attention patches than random patches. This difference was statistically significant, $F=(2,118)=5.32$, $p<0.01$.

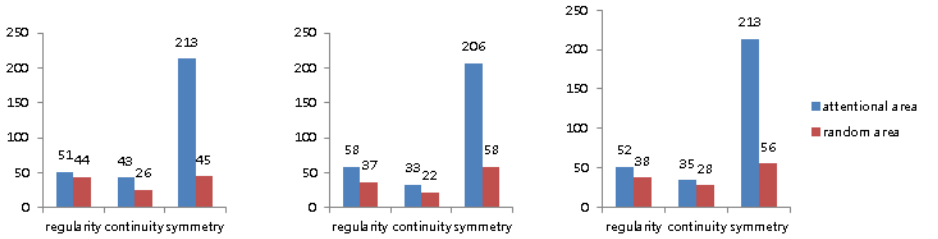

Fig. 3. Mean scores of principles of Gestalt in random and attention patches

3.3 Study 3: Recognition from Attention Areas

In this study, we wanted to test the ease and success of recognition of objects if they are presented with highlighted attention areas with high Gestalt score or randomly highlighted areas.

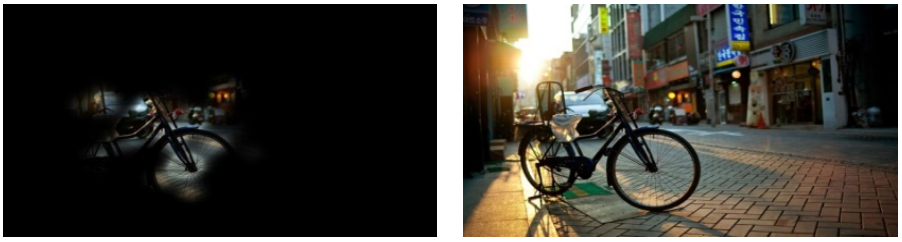

(a) (b)

Fig. 4. Sample image; (a) highlighted attention regions, (b) original image

Procedure. Seven graduate students (all males) (mean age=21) from Kyungpook National University, Korea, participated in this study. In this experiment 32 images were selected. In each of 16 images, high scoring attention areas (with high gestalt scores) were highlighted and rest of the image was darkened. Similarly, in each of

another 16 images, non-attended random areas were highlighted and rest of the image was darkened. Fig. 4 shows an example. Participants were asked to look at the image and identify the object. Once they had identified the object, they were asked to press the space bar. For analysis, we measured the response time and success.

Results. We found that it was easy for participants to recognize objects from those images that had attention areas (with high Gestalt score) highlighted. An average of 51.2% images was correctly identified with attention patches compared to 32.6% correctly identified images with random patches. Interestingly we also found that mean response time to recognize the object was significantly low in images that had attention areas highlighted (mean response time=2.8 seconds). Average response time to correctly recognize the object in those images that had random parts highlighted was 4.72 seconds. Difference between them was statistically significant. $t(1,30)=15.62$, $p<0.001$. Table 1 summarizes the results.

Table 1. Success and mean response time in object recognition task in study 3

No. of participants	Number of Pictures	Success	Mean response time
7	16 (attention patches)	51.2%	2.38 Seconds
7	16 (random patches)	32.6%	4.72 Seconds

4 Discussion and Conclusion

We had hypothesized that region of an image that gets maximum human attention in an object recognition task, confirms to some or at least one principle of Gestalt more significantly than non-attended random regions. Results of our study three support this hypothesis. We found that attention patches got high scores on principle of regularity, principle of continuity and principle of symmetry than random patches. This result indicates that regular, continuous and symmetrical features of objects are more likely to attract human attention. Moreover, the study also shows that participants could easily recognize objects from those images that had attention areas highlighted.

Overall, the results support the assumptions of perception-action cycle and also support the view that attention is partly guided by Gestalt principles. These results also suggest an approach for artificial object recognition. We argue that analyzing areas with high gestalt principles may yield better object recognition results than existing methods of randomly analyzing parts of image[13], [14].

In our future work, we would like to analyze more principles of Gestalt.

Acknowledgment. This research was supported the Converging Research Center Program through the Ministry of Science, ICT and Future Planning, Korea (2013K000333) (30%) and also the Industrial Strategic Technology Development. Program (10044009) funded by the Ministry of Knowledge Economy (MKE, Korea) (70%).

References

1. Anderson, J.R.: Cognitive psychology and its implications, 6th edn., p. 519 (2004)
2. Erich Rome, F.S., Christensen, H.I.: Computational visual attention systems and their cognitive foundations: A survey. ACM Transactions on Applied Perception (TAP) 7(1), 6 (2010)
3. Eriksen, C., Hoffman, J.: Temporal and spatial characteristics of selective encoding from visual displays. Perception & Psychophysics, 201–204 (1972)
4. Eriksen, C., St James, J.: Visual attention within and around the field of focal attention: A zoom lens model. Perception & Psychophysics, 225–240 (1986)
5. James, W.: The principles of psychology. Harvard UP, Cambridge (1890)
6. Park, S.-J., An, K.-H., Lee, M.: Saliency map model with adaptive masking based on independent component analysis. Neurocomputing 49, 417–422 (2002)
7. Jeong, S., Ban, S.-W., Lee, M.: Stereo saliency map considering affective factors and selective motion analysis in a dynamic environment. Neural Networks 21(10), 1420–1430 (2008)
8. Christianvon, E.: Übergestaltqualitäten. Vierteljahresschriftfür wissenschaftliche Philosophie, 249–292 (1890)
9. Vassilis, C.: Perception-Action Cycle: Models, Architectures, and Hardware, 1 (2011)
10. Todorovic, D.: Gestalt principles. Scholarpedia, 5345 (2008)
11. Beymer, D., Orton, P.Z., Russell, D.M.: An eye tracking study of how pictures influence online reading. In: Baranauskas, C., Abascal, J., Barbosa, S.D.J. (eds.) INTERACT 2007. LNCS, vol. 4663, pp. 456–460. Springer, Heidelberg (2007)
12. Dou Y, Kong L.: A novel approach based on saliency edges to contour detection. In: International Conference on Audio, Language and Image Processing, pp. 552–556. IEEE Press (2008)
13. Walther, D.: Selective visual attention enables learning and recognition of multiple objects in cluttered scenes. Computer Vision and Image Understanding, 41–63 (2005)
14. Rutishauser, U.: Is bottom-up attention useful for object recognition? In: 22th Conference of Computer of Society, vol. 2. IEEE Press, Washington (2004)

Detection of Error-Prone Cases for Word Sense Disambiguation

Yong-Jin Han, Sang-Jo Lee, Se Young Park, and Seong-Bae Park*

Kyungpook National University, Daegu, Korea
{yjhan,sjlee,sypark,sbpark}@sejong.knu.ac.kr

Abstract. Word sense disambiguation (WSD) is essential for natural language understanding applications such as machine translation, question & answering, and natural language interface, since the performance of such applications depends on the senses of lexicons. Thus, it is natural to consider lexicons as the most crucial features in WSD. However, due to the extensiveness of lexical space, WSD methods based on machine learning techniques with lexical features suffer from the sparse data problem. To tackle this problem, this paper proposes a hybrid approach which separately copes with an error-prone data due to sparsity. A data is regarded as error-prone if its nearest neighbors are relatively distant and their senses are uniformly distributed. Then, our hybrid approach focuses on such an error-prone data without tuning of a base method. In the experiments, the k-nearest neighbor method is used as a base method. If a data is determined as an error-prone case, it is processed by a prototype based method. The prototype based method takes an advantage from overall training examples rather than depends on only several neighbors. The experimental results on Senseval-3 nouns show that an error-prone data is effectively detected by the proposed method and our hybrid approach outperforms the ordinary k-nearest neighbor method and the prototype based method.

Keywords: Word Sense Disambiguation, Error-prone case, Data Sparseness.

1 Introduction

Word sense disambiguation (WSD) is an intermediate task, which is not an end in itself, but rather is necessary at one level or another to accomplish most natural language processing task. It is obviously essential for language understanding applications, such as machine translation, question & answering, and natural language interface, since the performance of such applications depends on the senses of lexicons.

Many current WSD studies rely on linguistic knowledge acquired from tagged text via machine learning methods. Statistical or alternative models are learned, and then applied to classify a word into a sense. The main problem faced by the

* Corresponding author.

M. Lee et al. (Eds.): ICONIP 2013, Part I, LNCS 8226, pp. 98–105, 2013.
© Springer-Verlag Berlin Heidelberg 2013

studies is the sparse data problem due to a representation of extensive feature space for the small amount of training examples. For example, the word arm occurs 266 times in a training dataset of Senseval-3 task, and its feature space easily exceeds the number of occurrences by representing the feature space with lexicons. In addition, most occurrences fall into a single sense and some of the senses are represented by only 3 or 6 occurrences.

There have been mainly two strategies to solve the sparse data problem in WSD. One is to use unlabeled data and appropriate learning techniques that can take advantage of them. The other one is to deal with sparsity by finding correlations among features. Dimension reduction technique such as SVD has been used for the latter strategy. The state-of-the-art method couples both of the strategies together.

As a solution of the sparse data problem, this paper proposes a novel, hybrid approach which separately copes with an error-prone data due to sparsity. Basically, the existing approaches deal with all examples equally. However, sparseness of data can be different due to the difference of amount of data according to senses. Note the previous example for the word arm which frequently occurs for one sense, but rarely occurs for some other senses.

In this paper, a data is regarded as error-prone if k-nearest neighbors are relatively distant and their senses are uniformly distributed. Then, our hybrid approach focuses on such an error-prone data without tuning of a base method.

In the experiments, the k-nearest neighbor method is used as a base method. If a data is determined as an error-prone case, it is processed by a prototype based method. The prototype base method takes an advantage from overall training examples rather than depends on only several neighbors. The experimental results on Senseval-3 nouns show that an error-prone data is effectively detected by the proposed method and the hybrid approach which separately copes with detected error-prone data outperforms the ordinary k-nearest neighbor method and the prototype based method.

2 Experimental Setting and Baseline Methods

We first describe the target wsd task and the evaluation methodology. Then, we will present the features used to represent the context and the ml algorithms applied.

2.1 Corpus and Evaluation

The experiments have been performed using nouns of the Senseval-3 English Lexical-Sample (S3LS) data [1]. We focus on the disambiguation of nouns for two reasons. Nouns constitute the largest portion of content words (48% of the content words in the Brown corpus [2] are nouns). For many tasks and applications nouns are the most frequently encountered and important part of speech.

The usual precision and recall were computed for each method. In all the cases reported here coverage was 100% and precision equaled recall, so we use recall in all tables.

2.2 Features

We refer features introduced in [3] which reports the state-of-the-art results. The feature types can be grouped in three main sets:
Local collocations: bigrams and trigrams formed with the words around the target. These features are constituted by stems or POS tags.
Syntactic dependencies: syntactic dependencies were extracted using heuristic patterns, and regular expressions defined with the POS tags around the target
Bag-of-words features: we extract the stems of the content words in the whole context.

Stems are extracted by using Porter stemmer and POS are analyzed by using LingPipe POS tagger (http://alias-i.com/ lingpipe) employing the Brown tagset. We don't use any external tool except them. Thus the last two feature sets are simple compared with [3].

2.3 ML Algorithms

For the experiments, two ml algorithms are used as baseline methods and applied to our hybrid approach. One algorithm is the k-nearest neighbor classification and the other one is the prototype based classification. Given an occurrence of a word, both of them return the most confident sense s_i, where $s_i \in S$, and S is a set of senses for the given word.

For both of the baseline methods, each occurrence context (instance) is represented as a vector, where each feature will have a 1 or 0 value to indicate the occurrence/absence of the feature.

The **k-nearest neighbor** (k-nn) is a memory based learning method, where the neighbors are the k most similar contexts, represented by feature vectors $\mathbf{n}_i$, of the test vector $\mathbf{x}$. The similarity among instances is measured as proximity of their vectors. In this paper, the proximity is defined as cosine similarity like the following:

$$proximity(\mathbf{x}, \mathbf{n}_i) = \frac{\langle \mathbf{x}, \mathbf{n}_i \rangle}{\|\mathbf{x}\| \|\mathbf{n}_i\|} \tag{1}$$

The test instance is labeled with the sense obtaining the maximum sum of proximities of the k most similar contexts. The k-nn is formally defined like the following:

$$s_i^* = \underset{s_i \in S}{\operatorname{argmax}} \sum_{j=1}^{k} \begin{cases} proximity(\mathbf{x}, \mathbf{n}_j) & \text{if } c_j = s_i \\ 0 & \text{otherwise} \end{cases} \tag{2}$$

, where $\mathbf{x}$ is a test instance vector, and $\mathbf{n}_j$ is a nearest neighbor ranked below or equal to k, and S is a set of senses for $\mathbf{x}$.

In the **prototype based classification**, one prototype is obtained from a set of training instances corresponding to one sense. The prototype for the sense is also represented as a vector of which features are appeared at least one time in the

set. A prototype for a sense s_i can be represented as a feature frequency vector $\mathbf{p}_{s_i} = \langle f_1, f_2, ..., f_n \rangle$, where f_j is the frequency of the i^{th} feature in the prototype vector. A widely used refinement to this prototype is to weight each feature based on inverse frequency in the training dataset. The motivation behind this weighting is that features appearing frequently in many instances have limited discrimination power, and for this reason they need to be de-emphasized. This is commonly done by multiplying the frequency of each feature by $log(N/sf_i)$, where N is the total number of instances in the training dataset, and sf_i is the number of instances that contain the i^{th} feature. Then, the prototype based classification is formally defined like the following:

$$s_i^* = \underset{s_i \in S}{\operatorname{argmax}} \, proximity(\mathbf{x}, \mathbf{p}_{s_i}), \tag{3}$$

where $\mathbf{x}$ is a test instance vector, and $\mathbf{p}_{s_i}$ is a prototype vector for sense s_i, and S is a set of senses for $\mathbf{x}$.

3 Detection of Error-Prone Cases

This section presents a heuristic method to detect error-prone cases due to data sparsity. A basic assumption underlying the heuristic method is that data sparsity is partially observed among all the training instances. Actually, there exists a major sense which frequently occurs rather than others and several senses are rarely occurred compared with the major sense. Intuitively, the rarely occurred senses can suffer from the sparse data problem than a major sense. In order to detect error-prone cases, the sparsity is investigated in vector space, since an occurrence of a sense is model in a form of a vector.

The proposed method is based on two heuristic measurements, *outlierness* of an instance and *uniformness* of senses corresponding neighbors of an instance. Outlierness is the degree to which an instance is outlier and it is related to sparseness of an instance. An outlier is an observation that is numerically distant from the rest of the data [4]. A few features of a sparse instance can be matched with features of its neighbors due to sparsity. This results in the sparse instance to be distance from its neighbors. Many studies on outlier detection are based on nearest neighbor method. In this paper, outlierness is measured by using an average proximity of k-nearest neighbors. Given an instance vector $\mathbf{x}$, outlierness is formally defined like the following:

$$outlierness(\mathbf{x}) = 1 - \frac{\sum_{j=1}^{k} proximity(\mathbf{x}, \mathbf{n}_j)}{k}, \tag{4}$$

where $\mathbf{n}_j$ is a nearest neighbor ranked below or equal to k.

Even though outlierness of an instance is high, the classification result by k-nn can be confident if all the neighbors fall into one sense. In this case, it is difficult to say that the instance is error-prone due to the high outlierness. In order to complement this case, uniformness of senses corresponding to neighbors

are measured for an test instance. Uniformness is the degree to which senses of neighbors scatters. If each neighbor of an instance fall into a different sense, ordinary k-nn can not decide a sense of the instance. This results in an error for the classification of the instance. In this paper, uniformness is measured by an entropy measurement. Uniformness is formally defined like the following:

$$uniformness(\mathbf{x}) = \sum_{s_i \in S} \frac{count(s_i) + 1}{k + 1} \log \frac{count(s_i) + 1}{k + 1}, \tag{5}$$

where S is a set of senses and $cout(s_i)$ return the number of the sense s_i observed in k nearest neighbors.

In order to avoid $log(0)$, 1 is added to the sense count and the denominator, respectively.

In this paper, a test instance is regarded as an an error-prone case if both of the outlierness and the uniformness are higher than certain thresholds. Let $T = \{t_o, t_u\}$ be a set of thresholds for outlierness and uniformness, respectively. Given test instance vector x, an error-prone case is formally determined like the following:

$$ep(\mathbf{x}, \mathbf{T}) = \begin{cases} 1 & \text{if } outlierness(x) > t_o \text{ and } uniformness(x) > t_u \\ 0 & \text{otherwise} \end{cases} \tag{6}$$

In this paper, the thresholds are determined by using a training dataset. Thus an error-prone case can be verified whether actually it is incorrectly classified by k-nn or not. For example, when both of the thresholds are set to 0, all training instances become error-prone cases. In this case, all the incorrectly classified instances are detected as error-prone cases. However, this is the worst case, since many error-prone cases are correctly classified.

In order to avoid correctly classified instances to be error-prone cases, the thresholds should be increased. However, it can cause to fail capturing error-prone cases which actually incorrectly classified. Thus there exist two risks: (1) a number of correctly classified instances become error-prone cases; (2) a number of incorrectly classified instances are not captured as error-prone cases. The first risk can be measured as the ratio of error-prone cases among correctly classified instances. Let D be a training dataset. Let $s_{\mathbf{x}}$ and $\hat{s_{\mathbf{x}}}$ be the true sense of instance $\mathbf{x}$ and the classified sense by k-nn, respectively. Then, the risk for correctly classified instances is formally defined like the following:

$$risk_{cor}(\mathbf{T}) = \frac{\sum_{\mathbf{x} \in D} ep(\mathbf{x}, \mathbf{T}) \mathbf{I}(s_{\mathbf{x}} = \hat{s_{\mathbf{x}}})}{\sum_{\mathbf{x} \in D} \mathbf{I}(s_{\mathbf{x}} = \hat{s_{\mathbf{x}}})}, \tag{7}$$

where $\mathbf{I}(\cdot)$ is an indicator function which returns 1 if a given condition is true, otherwise returns 0.

The second risk can be measured as the ratio of non-error-prone cases among incorrectly classified instances. It is formally defined like the following:

$$risk_{inc}(\mathbf{T}) = \frac{\sum_{\mathbf{x} \in D} (1 - ep(\mathbf{x}, \mathbf{T})) \mathbf{I}(s_{\mathbf{x}} \neq \hat{s_{\mathbf{x}}})}{\sum_{\mathbf{x} \in D} \mathbf{I}(s_{\mathbf{x}} \neq \hat{s_{\mathbf{x}}})} \tag{8}$$

Then, the pair of thresholds $\mathbf{T}$ is determined as the one which minimize both of the risks. That is,

$$\mathbf{T}^* = \underset{\substack{t_i \in \mathbf{T}, \\ 0<t_i<1}}{\operatorname{argmin}} \frac{risk_{cor}(\mathbf{T})\, risk_{inc}(\mathbf{T})}{risk_{cor}(\mathbf{T}) + risk_{inc}(\mathbf{T})}, \tag{9}$$

where $risk_{cor}(\mathbf{T}) \leq \delta$.

In equation 9, δ is a user parameter which prevents to decide majority correct results as error-prone cases. An appropriate $\mathbf{T}$ is found in a brute-force manner. That is, each threshold hold is increased step-by-step with a small increment and the risk is measured in each step. Finally, $\mathbf{T}$ is determined as the minimum risk case.

4 A Hybrid Approach for WSD

This section presents a hybrid approach to solve the sparse data problem for word sense disambiguation. A basic idea is to separately cope with error-prone cases due to data sparsity. In our hybrid approach, a base method is set to k-nn introduced in section 2.3. When a test instance determined as an error-prone case, it is classified by the prototype based method introduced in section 2.3.

A prototype vector can be regarded as as a summarization of training instance corresponding to one sense. It takes an advantage from this summarization. Even though a small number training instances are available for a sense, the prototype vector for the sense has more features matchable with a given test instance rather than its neighbors. Therefore the prototype based method can be robust for sparse test instances rather than the k-nn.

5 Results

In order to determine thresholds for outlerness and uniformness, δ is set to 0.2. After finding certain thresholds, risks by the thresholds show how they effectively separate error-prone cases from training datasets. Table 2 presents risks by using found thresholds. The risk $risk_{cor}$ for each noun is less than or equal to 0.2, since *delta* is set to 0.2. Most risks $risk_{inc}$ are shown less than 0.3 and half of the risks is shown less than or equal to 0.2. Thus it is possible to separate error-prone cases from a training dataset with sacrifice by slight risks.

The found thresholds were used to separately cope with error-prone cases in the proposed hybrid approach. Table 2 shows our baseline and hybrid methods, as well as the best method in the Senseval 3 competition [5] and the state-of-the-art method [3]. Though the-state-of-the-art method showed higher recall than S3Ls-best on overall words [3], S3LS-best shows the highest performance on nouns as shown in Table 2. The hybrid method outperforms the k-nn and shows comparable results with S3LS-best.

Table 1. Risks of detecting error-prone cases on training datasets ($\delta = 0.2$)

Nouns	$risk_{cor}$	$risk_{inc}$	Nouns	$risk_{cor}$	$risk_{inc}$	Nouns	$risk_{cor}$	$risk_{inc}$
Degree	0.19	0.29	Organization	0.16	**0.2**	Interest	0.19	0.25
Atmosphere	0.19	0.23	Image	0.19	0.34	Shelter	0.2	0.38
Bank	0.16	**0.07**	Party	0.2	**0.06**	Performance	0.2	0.23
Disc	0.19	0.39	Source	0.15	**0.08**	Paper	0.19	0.36
Arm	0.18	**0.10**	Audience	0.19	**0.16**	Plan	0.19	**0.17**
Difference	0.19	0.27	Judgment	0.19	**0.16**	Difficulty	0.16	**0.2**
Argument	0.10	0.41	Sort	0.05	**0.19**			

Table 2. Risks of detecting error-prone cases on training datasets ($\delta = 0.2$)

Methods	k-nn (Agirre 2005)	k-nn (Ours)	Prototype	Hybrid	S3LS-best
recall	70.6	67.0	70.7	71.2	72.9

6 Discussion and Related Work

The results show that the data sparsity becomes partially obstructed problems and can be detected as error-prone cases. The proposed hybrid method is very simple compared with the state-of-the-art methods [3,5]. However, the results by the proposed method are comparable with those by the existing methods. This is promising for the development of any other hybrid methods and applications based on the detection of error-prone cases.

Outlierness has been studied intensively in terms of the outlier detection problem [6,7]. The outlier detection has been used in a wide variety of application domains such as credit card, insurance, tax fraud detection, and so on. In these domains, an outlier is regarded as significant information by itself. In our context, an outlier is investigated as an error-prone case. To the best of our knowledge, this is the first approach to detect outliers as error-prone cases.

7 Conclusion

In this paper, we have explored error-prone case detection, trying to tackle sparse data partially observed in the training dataset. An error-prone case is investigated in a vector space and two measurements are proposed to detect error-prone cases. One measurement is outlierness which verifies average distance from a given instance to its neighbors. The other is uniformness which is measured as entropy of senses corresponding to neighbors. In the experiments, we show that error-prone cases are effectively separated from a training dataset with sacrifice by slight risks.

Also, we have proposed and evaluated a hybrid approach which separately copes with error-prone cases. The hybrid approach is based on two simple classifiers, the k-nn and the prototype based method. It improves the results for both of the classifiers and shows comparable results with the state-of-the-art results. These results are promising for applications based on the detection of error-prone cases and opens new hybrid methods possibilities.

Acknowledgement. This work was supported by the Industrial Strategic Technology Development Program (10035348, Development of a Cognitive Planning and Learning Model for Mobile Platforms) funded by the Ministry of Knowledge Economy(MKE, Korea).

References

1. Mihalcea, R., Chklovski, T., Kilgarriff, A.: The senseval-3 english lexical sample task. In: Senseval-3: Third International Workshop on the Evaluation of Systems for the Semantic Analysis of Text, Barcelona, Spain, pp. 25–28 (2004)
2. Francis, W.N., Kucera, H.: Computational analysis of present-day american english (1967)
3. Agirre, E., de Lacalle, O.L., Martınez, D.: Exploring feature spaces with svd and unlabeled data for word sense disambiguation. In: Proceedings of RANLP (2005)
4. Barnett, V., Lewis, T.: Outliers in statistical data, vol. 3. Wiley, New York (1994)
5. Gliozzo, A., Giuliano, C., Strapparava, C.: Domain kernels for word sense disambiguation. In: Proceedings of ACL, pp. 403–410. ACL (2005)
6. Aggarwal, C.C., Yu, P.S.: Outlier detection for high dimensional data. In: ACM Sigmod Record, vol. 30, pp. 37–46. ACM (2001)
7. Hodge, V.J., Austin, J.: A survey of outlier detection methodologies. Artificial Intelligence Review 22(2), 85–126 (2004)

Flexible Reasoning of Boolean Constraints in Recurrent Neural Networks with Dual Representation

Wonil Chang[1], Hyun Ah Song[2], and Soo-Young Lee[3]

[1] Electronics and Telecommunications Research Institute,
Daejeon 305-700, Republic of Korea
[2] Korea Institute of Science and Technology, Seoul, Republic of Korea
[3] Department of Electrical Engineering,
KAIST, Daejeon 305-701, Republic of Korea
{chang.wonil,hi.hyunah}@gmail.com, sylee@kaist.ac.kr

Abstract. In this paper, we propose a recurrent neural network that can flexibly make inferences to satisfy given Boolean constraints. In our proposed network, each Boolean variable is represented in dual representation by a pair of neurons, which can handle four states of true, false, unknown, and contradiction. We successfully import Blake's classical Boolean reasoning algorithm to recurrent neural network with hidden neurons of Boolean product terms. For symmetric Boolean functions, we designed an extended model of Boolean reasoning which can drastically reduce the hardware cost. Since our network has only excitatory connections, it does not suffer from oscillation and we can freely combine multiple Boolean constraints.

Keywords: Boolean constraint, Boolean reasoning, symmetric Boolean function, recurrent neural network.

1 Introduction

Everyday we do logical thinking; we interpret given conditions, reason based on them, and draw a conclusion. We are also able to fill in missing variables given the rest, which is called " problem solving . " These complex yet flexible human reasoning shows properties that are quite different from ordinary computation processes in machines. Then how can we mimic these flexible reasoning processes?

There are a number of studies on how humans actually conduct reasoning processes. In [1], the authors carefully observe how humans interpret given conditionals and understand causal relations when reasoning tasks are given. In [6], the authors designed several different types of thinking processes based on decision theory by neural networks with adequate weights according to given conditions.

Logical reasoning can take place on different level of cognitive task, from evaluation of Boolean functions to natural language processing. This paper focuses on biological computation model of Boolean reasoning. Majority of biological

M. Lee et al. (Eds.): ICONIP 2013, Part I, LNCS 8226, pp. 106–112, 2013.
© Springer-Verlag Berlin Heidelberg 2013

reasoning models are based on artificial neural networks (ANN). Initial reasoning models are restricted to compute logical functions in feed-forward network structure [8, 14, 15]. Advanced models use recurrent neural networks in Boolean reasoning so that it can cover both backward and forward boolean inference [11, 16]. For example, these networks not only compute AND operation of two binary input, but they also infer that given true output, all input must be true accordingly. The boolean reasoning systems tries to find a set of unknown binary variables that satisfy a number of given Boolean formula. This is a well-known satisfiability (SAT) problem [7] in computer science.

Many reasoning models adopt three-state logic to deal with unknown variables [4,11,13,16]. The three states are commonly encoded as positive (true), negative (false), and zero (unknown) activation of a single neuron. If we assign proper excitatory and inhibitory connectivity between neurons, it is possible to infer unknown values other neurons.

However, conventional recurrent neural networks are problematic in combining multiple boolean constraints into the unified system. The accumulation of synaptic weights from different constraints might cause wrong inference or oscillation of network. Therefore, most successful ANN-based inference models [11,16] are implemented to support only limited type of boolean operations such as AND, OR, and negation. And networks can not be fully parallelized due to undesirable interferences.

In this paper, we propose a flexible Boolean reasoning network that can include any kind of boolean constraints without restriction. Our network is able to handle four states(true, false, unknown, and contradiction) by dual representation of Boolean variables. The encoding of a boolean variable using a pair of neurons is not a new idea [12,14,15]. However, to our best knowledge, this paper presents the first boolean network model that can reason on all possible ways using dual representation. Since the network has only excitatory synapses, it is free from interference problem and oscillation.

The organization of paper is as follows. In Section 2, we explain our design of dual representation of variables. The structure of network for general Boolean constraints based on full extraction of prime implicants, or Blake Canonical Form (BCF) [3] is explained in Section 3. In Section 4, we introduce a simplified implementation of the network for symmetric Boolean constraints. We close our paper in Section 5.

2 Dual Representation

Our network adopts dual representation, where a Boolean variable is encoded by two neurons, each standing for 'true' and 'false,' respectively. A pair of neurons represent four possible states. If one of two neurons is active, it means that the variable is either true or false; If both of true and false neurons are active, it means given conditionals are in contradicting situation that we cannot satisfy the constraint; If both of the neurons are silent, it means not enough information is given and we cannot draw a conclusion from it. The description of four possible state representations are shown in Fig. 1.

Fig. 1. Dual representation of a Boolean variable in four possible states

In [11] and [16], boolean reasoning is performed on the basis of delicately-designed excitatory and inhibitory connections. When a neuron is involved in multiple constraints, the interference between neural interactions might lead to wrong conclusion. Dual representation has an important advantage over conventional single-neuron representation in that matter; we do not need to inhibit any neuron to inactivate. Instead, its counterpart is excited. Since our network has excitatory connections only, it does not suffer from interference problem. Also, it always converges fast without oscillation.

3 Reasoning Network for General Boolean Constraints

The neural connectivity is described as 'A conjunction of neurons $\rightarrow$ A neuron.' For example, consider a function $C = A$ AND B. Regardless of directions that distinguish inputs from outputs, we can derive multi-directional inference rules such as:

- If $C = 1$, $A = 1$ ($C \rightarrow A$)
- If $A = 1$ and $B = 1$, $C = 1$. ($AB \rightarrow C$) $\cdots$

Our goal is to make inferences based on the set of variables that satisfies a Boolean constraint

$$f(x_1, x_2, ..., x_N) = 0 \tag{1}$$

and then to make inferences based on the true configuration information.

In the example, its Boolean constraint is re-formulated as

$$f(A, B, C) = (A \text{ AND } B) \text{ XOR } C = 0. \tag{2}$$

Any kind of Boolean function can be transformed into Boolean constraint. We can make a table of configuration of variables and the constraint formula f:

A	B	C	f
0	0	0	0
0	0	1	1
0	1	0	0
0	1	1	1
1	0	0	0
1	0	1	1
1	1	0	1
1	1	1	0

The optimal structure of the the network is derived from Blake's canonical expressions [2], that uses prime implicants to represent the Boolean formula f in abstract form. An implicant of a Boolean formula f is a product term P_i such that $P_i \leq f$. A prime implicant of f is an implicant that cannot be included by a more general implicant. In (2), term $\bar{A}BC$ is an implicant of $f(A, B, C)$ but not a prime implicant since it is covered by another implicant $\bar{A}C$. Blake's canonical form (BCF), or complete sum of f is the sum of all prime implicants F_i in f.

$$BCF(f) = \sum_i F_i = 0 \tag{3}$$

Variable configuration set that satisfies f can be simply solved by checking BCF. If Boolean variables in the given conditions satisfy the Boolean formula $f = 0$, then $F_i = 0$ for all i. We can connect activation synapes to a varible x_i from other variables by

$$F_i/x_i \to \bar{x_i}, \tag{4}$$

where F_i/x_i is a quotient of F_i with respect to x_i. (For example, $\bar{A}B/B = \bar{A}$.) An example of the whole reasoning network for AND operation is shown in Fig. 2.

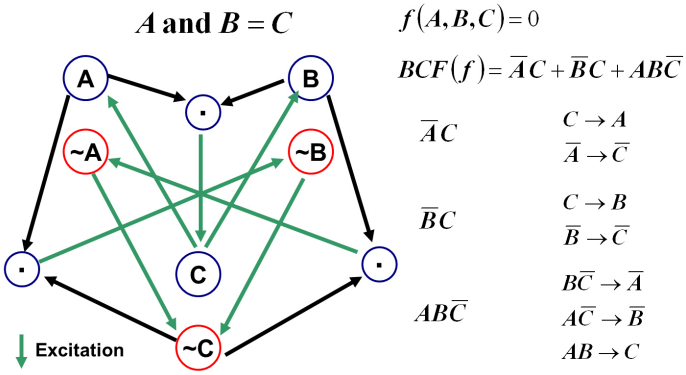

Fig. 2. Structure of network connection of AND operation

The product of boolean variables $(x_1, x_2, \ldots, x_N)$ is implemented by a single perceptron

$$h = \varphi\left(\sum_{i=1}^{N} w_i x_i - \theta\right) \tag{5}$$

with uniform pre-synaptic weight $w_i = 1$ for all i, threshold $\theta = N$, and the activation function

$$\varphi(\alpha) = \begin{cases} 1 & \text{if } \alpha \geq 0 \\ 0 & \text{otherwise.} \end{cases} \tag{6}$$

For Boolean equations with four variables or less, we can easily find prime implicants using Karnaugh-Map [5]. Extraction of prime implicants in general cases has been extensively studied for digital circuit optimization after the foundational work of Quinn and McCluskey [9]. However, it is known that the time complexity of full search for arbitrary boolean function is exponential with respect to the number of input variable [17]. And the number of prime implicants for a boolean function with N inputs is upper-bounded by $O(2^N)$ [10].

4 Optimized Reasoning Network for Symmetric Boolean Function

Symmetric Boolean function is a boolean function $f(x_1, x_2, \ldots, x_N)$ that satisfies

$$f(x_1, x_2, \ldots, x_N) = f\left(\pi(x_1, x_2, \ldots, x_N)\right) \tag{7}$$

for an arbitrary permutation π.

Symmetric boolean functions are expressed as functions in terms of total sum of input variables:

$$f(x_1, x_2, \ldots, x_N) = g\left(\sum_i x_i\right). \tag{8}$$

Note that $\sum_i x_i$ is the arithmetic sum (not Boolean sum) in this equation. And g is an arbitrary function.

By using summation of the variables as the unit to check truth table for a function, the time complexity of network design is reduced to polynomial order. We construct and search truth table of summation of variables, not value of variables themselves.

For example, take example of OR operation with three input $y_1 = \mathrm{OR}(x_1, x_2, x_3)$. The truth table based on the summation of variables can be constructed as shown below.

$\sum_i x_i$ \ $\sum_i y_i$	0	1
0	T	F
1	F	T
2	F	T
3	F	T

We can reformulate the original symmetric Boolean function in terms of alternative type of prime implicants $(a \le \sum_i x_i \le b) \cdot (c \le \sum_i y_i \le d)$, which we call "inequality prime implicants."

According to the truth table, $f(x_1, x_2, x_3, y_1) = g(\sum_i x_i, \sum_i y_i) = (0 \le \sum_i x_i \le 0) \cdot (1 \le \sum_i y_i \le 1) + (1 \le \sum_i x_i \le 3) \cdot (0 \le \sum_i y_i \le 0) = 0$.

Like (4), we can search for the connection between variables. Generalized rules is defined as follows:

If $(a \leq \sum_i x_i \leq b) \cdot (c \leq \sum_i y_i \leq d)$ is given,

$$\left.\begin{array}{l}(\sum_i y_i \geq c)\cdot\\(\sum_i y_i \leq d)\cdot\\(\sum_{j\neq i} x_j \geq a-1)\cdot\\(\sum_{j\neq i} \bar{x_j} \geq N-b)\end{array}\right\} \rightarrow \bar{x_i} \quad \left.\begin{array}{l}(\sum_i y_i \geq c)\cdot\\(\sum_i y_i \leq d)\cdot\\(\sum_{j\neq i} x_j \geq a)\cdot\\(\sum_{j\neq i} \bar{x_j} \geq N-b-1)\end{array}\right\} \rightarrow x_i$$

$$\left.\begin{array}{l}(\sum_i x_i \geq a)\cdot\\(\sum_i x_i \leq b)\cdot\\(\sum_{j\neq i} y_j \geq c-1)\cdot\\(\sum_{j\neq i} \bar{y_j} \geq N-d)\end{array}\right\} \rightarrow \bar{y_i} \quad \left.\begin{array}{l}(\sum_i x_i \geq a)\cdot\\(\sum_i x_i \leq b)\cdot\\(\sum_{j\neq i} y_j \geq c)\cdot\\(\sum_{j\neq i} \bar{y_j} \geq N-d-1)\end{array}\right\} \rightarrow y_i. \tag{9}$$

Inequality terms and their products in (9) are implemented in the same way as in (5). The number of inequality prime implicants for N-input symmetric Boolean functions is upper-bounded by $O(N)$. Compared to the previous model in section 3, the computational cost is significantly reduced.

5 Concluding Remarks

We proposed a flexible neural network that successfully handles Boolean constraint problems in multi-directions. Dual representation enables simple implementation of delicate reasoning rules. We described the learning process of the network using conventional Blake's reasoning algorithm. We also proposed an alternative type of prime implicant for abstract representation of symmetric Boolean constraints, which significantly reduced computational cost. Since the network use only excitatory synaptic connections, we guarantee stability of the process even for complex functions consisting of heavy constraints. We expect that our proposed network to be applied to solve complex and multi-directional Boolean constraint problems free of computational burden in more flexible manner.

Acknowledgments. This research was funded by the MSIP(Ministry of Science, ICT & Future Planning), Korea in the ICT R&D Program 2013 (Wonil Chang). Also, it was supported by Public Welfare & Safety Research Program through the National Research Foundation of Korea (NRF) funded by the Ministry of Education, Science and Technology (No. 2012-0006551, Hyun Ah Song).

References

1. Beller, S., Kuhnmünch, G.: What causal conditional reasoning tells us about people's understanding of causality. Thinking & Reasoning 13(4), 426–460 (2007)
2. Blake, A.: Canonical expressions in Boolean algebra. University of Chicago (1938)
3. Brown, F.M.: Boolean reasoning: the logic of Boolean equations. Courier Dover Publications (2003)

4. Dietz, E.-A., Hölldobler, S., Ragni, M.: A computational logic approach to the suppression task. In: Proceedings of the 34th Annual Conference of the Cognitive Science Society, pp. 1500–1505 (2012)
5. Karnaugh, M.: The map method for synthesis of combinational logic circuits. Transactions of the American Institute of Electrical Engineers, Part I: Communication and Electronics 72(5), 593–599 (1953)
6. Kowalski, R.A.: The logical way to be artificially intelligent. In: Toni, F., Torroni, P. (eds.) CLIMA 2005. LNCS (LNAI), vol. 3900, pp. 1–22. Springer, Heidelberg (2006)
7. Malik, S., Zhang, L.: Boolean satisfiability from theoretical hardness to practical success. Communications of the ACM 52(8), 76–82 (2009)
8. Mandziuk, J., Macukow, B.: A neural network performing boolean logic operations. Optical Memory and Neural Networks 2(1), 17–35 (1993)
9. Mccluskey, E.J.: Minimization of Boolean functions. The Bell System Technical Journal 35(5), 1417–1444 (1956)
10. McMullen, C., Shearer, J.: Prime implicants, minimum covers, and the complexity of logic simplification. IEEE Transactions on Computers 100(8), 761–762 (1986)
11. Spears, W.M.: A nn algorithm for boolean satisfiability problems. In: IEEE International Conference on Neural Networks, vol. 2, pp. 1121–1126. IEEE (1996)
12. Stenning, K., Lambalgen, M.: Semantic interpretation as computation in nonmonotonic logic: The real meaning of the suppression task. Cognitive Science 29(6), 919–960 (2005)
13. Stenning, K., Van Lambalgen, M.: Human reasoning and cognitive science. The MIT Press (2008)
14. Tan, C.L., Quah, T.S., Teh, H.H.: An artificial neural network that models human decision making. Computer 29(3), 64–70 (1996)
15. Teh, H.H.: Neural Logic Networks: A New Class of Neural Networks. World Scientific (1995)
16. Wang, G., Shi, H.: Tmlnn: triple-valued or multiple-valued logic neural network. IEEE Transactions on Neural Networks 9(6), 1099–1117 (1998)
17. Wegener, I.: The complexity of boolean functions (1987)

Multiple Kernel Learning Method Using MRMR Criterion and Kernel Alignment

Peng Wu[1,2], Fuqing Duan[1], and Ping Guo[1,⋆]

[1] Image Processing and Pattern Recognition Laboratory
Beijing Normal University
Beijing 100875, China
[2] Shandong Provincial Key Laboratory of Network Based Intelligent Computing
University of Jinan
Jinan 250022, China
pengwiseujn@gmail.com, fqduan@bnu.edu.cn, pguo@ieee.org

Abstract. Multiple kernel learning (MKL) is a widely used kernel learning method, but how to select kernel is lack of theoretical guidance. The performance of MKL is depend on the users' experience, which is difficult to choose the proper kernels in practical applications. In this paper, we propose a MKL method based on minimal redundant maximal relevance criterion and kernel alignment. The main feature of this method compared to others in the literature is that the selection of kernels is considered as a feature selection issue in the Hilbert space, and can obtain a set of base kernels with the highest relevance to the target task and the minimal redundancies among themselves. Experimental results on several benchmark classification data sets show that our proposed method can enhance the performance of MKL.

Keywords: minimal redundant maximal relevance, kernel alignment, kernel selection, multiple kernel learning.

1 Introduction

Multiple kernel learning (MKL) is an important kernel method, in which the most attractive character is so called 'kernel trick". MKL has been a hot research spot due to its success in lots of fields, such as bioinformatics [1], computer vision [2] and natural language processing [3]. MKL can be effortlessly derived from the canonical kernel method, i.e., support vector machine (SVM) [4]. Compared to SVM, MKL has a higher performance because of using a linear or nonlinear combination of several base kernels instead of only one specific kernel. Consequently, MKL aims at learning the combination coefficient of base kernels and some other parameters which are also learned by SVM. Lanckriet et al. [5] formulated it as a semi-definite programming problem. Bach et al. [6] reformulated it a quadratically constrained quadratic programming problem. Sonnenburg et al. [1] treated it as a second order cone programming problem that can be efficiently solved

⋆ Corresponding author.

M. Lee et al. (Eds.): ICONIP 2013, Part I, LNCS 8226, pp. 113–120, 2013.
© Springer-Verlag Berlin Heidelberg 2013

using interior point methods and Rakotomanon et al. [7] addressed it through a weighted 2-norm regularization formulation with an additional constraint on the weights that encourage sparse kernel combination. Recently, localized MKL proposed by Gonen et al. [8], and the two-stage techniques for learning kernels based on a notion of alignment for MKL reported in [9] are two representatives methods.

Almost exclusively, methods aforementioned leave the task of selecting base kernels to users. It would be difficult in practice to choose a set of appropriate base kernels without prior knowledge, which maybe degrade the performance of MKL. To alleviate the negative effects, one can produce as many as possible candidate kernels, e.g., a family of polynomial kernels of arbitrary degree or a family of Gaussian kernels with different variances restricted in a specific range, and use all of them directly as base kernels. However, base kernels selected like that contain much redundant information and will give rise to high computation cost. Alternatively, one can only choose partial kernels with the highest relevance to the target task. Actually, to select a set of base kernels from a prescribed set of candidate kernels can be treat as a feature selection problem within the Hilbert feature space. Feature selection methods allow obtaining shorter training time and enhanced generalization by reducing over-fitting when constructing predictive models [10]. One state-of-the-art feature selection method, i.e., minimal redundancy maximal relevance (MRMR) [11], can be used as a filter in order to obtain a minimal subset of candidate kernels by reducing the redundancies among the selected kernels to a minimum. In this paper, we propose a MKL method based on the combination of MRMR, which is used as a filter, and kernel alignment, which is used to measure the mutual dependence between candidate kernels and target kernel, to select base kernels to enhance the performance of MKL. Note that, kernel alignment has been used for leaning a combination kernel from a prescribed candidate kernels, see in [9] [12]. Contrast to the previous work, in this study we take kernel alignment to select a set of base kernels instead of a combination kernel, which leads us to be more flexible in choosing the final combination form (linear, nonlinear or data-dependent) of base kernels.

The remainder of this paper is organized as follows: Section 2 reviews MRMR and kernel alignment. In Section 3, we describe the proposed method in detail. Experimental results on several benchmark classification data sets are reported and analyzed in Section 4, and our conclusions and further work are presented in the last section.

2 Minimal Redundancy Maximal Relevance and Kernel Alignment

2.1 Minimal Redundancy Maximal Relevance

MRMR is a well-known feature selection method based on the maximal statistical dependence of the target class on the data distribution. The mutual

information is a quantity that measures the mutual dependence of two random variables. Given variables $\mathbf{x}$ and $\mathbf{y}$, the mutual information between them can be calculated as follows

$$I(\mathbf{x};\mathbf{y}) = \sum_{x\in\mathbf{X}}\sum_{y\in\mathbf{y}} \log\frac{p(x;y)}{p(x)p(y)}, \tag{1}$$

where $p(x;y)$, $p(x)$ and $p(y)$ denote the joint probability distribution function of $\mathbf{x}$ and $\mathbf{y}$, the marginal probability distribution function of $\mathbf{x}$ and the marginal probability distribution function of $\mathbf{y}$, respectively. The higher value of $I(\mathbf{x};\mathbf{y})$ indicates the more mutual information they share, i.e., $\mathbf{x}$ is more correlated to $\mathbf{y}$.

Let $\mathbf{X} = \{\mathbf{x}_1, \mathbf{x}_2, ..., \mathbf{x}_i\}$ be the whole feature set of a given data set, and $\mathbf{S}_m$, consisting of m features, be a selected subset of $\mathbf{X}$. Given $\mathbf{c}$, which represents the target class label, and $\mathbf{x}_i$, which represents a feature, we can obtain $\mathbf{S}_m$ by selecting the top m features in the descent order of $I(\mathbf{x}_i;\mathbf{c})$, but it is not a good scheme because of its failure in reducing the redundancy between the selected features. MRMR can select features that have the highest relevance to $\mathbf{c}$ and are also minimally redundant. In the algorithm of MRMR, first, all mutual information between candidate features and target class are calculated, and next, the mean mutual information between candidate features and the selected feature in subset $\mathbf{S}_{m-1}$, which has $m-1$ selected features, are calculated, and then to select the m_{th} feature from set $\{\mathbf{X}-\mathbf{S}_{m-1}\}$ according to the condition shown as follows:

$$\max_{\mathbf{x}_j\in\mathbf{X}-\mathbf{S}_{m-1}} [I(\mathbf{x}_j;\mathbf{c}) - \frac{1}{m-1}\sum_{\mathbf{x}_i\in\mathbf{S}_{m-1}} I(\mathbf{x}_j;\mathbf{x}_i)], \tag{2}$$

2.2 Kernel Alignment

In this paper, we use MRMR as a filter to select a set of base kernels from candidate kernels. The mutual information between two kernels can be calculated using kernel alignment which proposed by Cristianini et al. in [13]. Kernel alignment is a method to measure the similarity of two kernel matrices. Given a binary-class data set $\mathbf{S} = \{(\mathbf{x}_i, y_i)\}_{i=1}^{N}$, where y_i is the class label and $y_i \in \{-1, 1\}$, and $\mathbf{N}$ is the total number of samples, then the similarity between two kernel matrix on data set $\mathbf{S}$ is calculate by

$$A(\mathbf{S}, \mathbf{K}_1, \mathbf{K}_2) = \frac{\langle \mathbf{K}_1, \mathbf{K}_2\rangle_F}{\sqrt{\langle \mathbf{K}_1, \mathbf{K}_1\rangle_F \langle \mathbf{K}_2, \mathbf{K}_2\rangle_F}}, \tag{3}$$

where $\langle \mathbf{K}_1, \mathbf{K}_1\rangle_F$ is the inner product between kernel matrices, and the form is as follow

$$\langle \mathbf{K}_1, \mathbf{K}_2\rangle_F = \sum_{i,j=1}^{N} \mathbf{K}_1(x_i, x_j)\mathbf{K}_2(x_i, x_j). \tag{4}$$

If we consider $\mathbf{K}_2 = \mathbf{y}\mathbf{y}^T$, where $\mathbf{y}$ is the class vector of all samples, then we get

$$A(\mathbf{S}, \mathbf{K}_1, \mathbf{y}\mathbf{y}^T) = \frac{\left\langle \mathbf{K}_1, \mathbf{y}\mathbf{y}^T \right\rangle_F}{\sqrt{\langle \mathbf{K}_1, \mathbf{K}_1 \rangle_F \left\langle \mathbf{y}\mathbf{y}^T, \mathbf{y}\mathbf{y}^T \right\rangle_F}}. \tag{5}$$

In the next section, we will describe the proposed method in details.

3 The Proposed Method

The proposed method reported in this paper is based on a hybrid approach combining MRMR and alignment kernel (MRMRKA). The general algorithm of MRMRKA includes three steps: 1) some candidate kernels, or called candidate matrices, are generated based on the given data set, and 2) a set of base kernels is automatically selected by utilizing MRMRKA, and 3) the selected base kernels are fed into the process of MKL. The detailed steps are described as follows.

First, we obtain a set of candidate kernels. Kernel matrices are generated by the mapping of kernel functions. It is necessary to try to make use of several different kernel functions for getting some valid candidate kernels. Using linear kernel function, we generate the first kernel matrix, and the others can be generated by utilizing a family of polynomial kernel functions with different settings of the degree and a family of Gaussian kernel functions with variances in a prescribed interval.

Second, we select base kernels using MRMRKA. Given that the number of base kernels to be selected is m, the mutual information between candidate kernel matrices and target kernel matrix are calculated using (4), then select the candidate kernel with the maximal value of mutual information as the element of set $\mathbf{S}_1$. Then, use (2) or (3) to select the rest set $\mathbf{S}_i (2 \leq i \leq m)$. Note that, $I(\mathbf{x}_i; \mathbf{c})$ and $I(\mathbf{x}_i; \mathbf{x}_j)$ in (2) are substituted by (4) and (6), respectively.

Third, we execute MKL with the selected base kernels. Several MKL schemes can be chosen in this stage such as MKL based on semi-definite, MKL based on quadratically constrained quadratic programming, simpleMKL, localized MKL and so on.

4 Experiments

In this section, several experiments are done to test the proposed method on a number of classification data sets, and the experimental results of three different schemes to select base kernels in MKL are reported.

4.1 Data Sets and Preprocessing

Ten classification data sets which are available on the UCI machine learning archive [14] are adopted in the experiments, the detail informations about those data sets are shown in Table 1.

Table 1. Data sets information

Dataset	#Classes	#Attributes	#Instances
Blood	2	5	748
Breast	2	32	569
Control	6	60	600
Ecoil	5	8	336
Glass	7	10	214
Iris	3	5	150
Parkinsons	2	23	197
Seeds	3	7	210
Sonar	2	60	208
Wine	3	13	178

All raw data were preprocessed to have zero mean-value and unit variance. Each data set was divided randomly to three subsets with preserved class ratios. One of the three subsets was reserved as the testing set, and one of the remaining two was used as the training set and the other was used as the validation set. The validation sets of all data sets were used to optimize the parameter C, i.e., the trade-off parameter between model simplicity and classification error, by trying values $\{0.01, 0.1, 1, 10, 100\}$. The best C, i.e., leading to the highest classification accuracy on the validation set, was used to train the final classifier on the training set and its performance was measured over the testing set. The MKL scheme used in this study is LMKL due to its outstanding performance and we modified it to fit for multi-class classification tasks[1]. We repeated the experiment three times on each data set and reported the average classification accuracy as well as standard deviation.

4.2 Experimental Results and Comparison

For comparison, we adopt three schemes to select base kernels after producing candidate kernels: using all candidate kernels as base kernels (Method 1), selecting the top m kernels in the descent order of $A(\mathbf{S}, \mathbf{K}, \mathbf{y}\mathbf{y}^T)$ (Method 2), and selecting base kernels using MRMRKA. We produced forty candidate kernels on each data set, which consist of one linear kernel, four polynomial kernels with different degree values $\{2, 3, 4, 5\}$, and thirty-five Gaussian kernels with different variances whose values are limited in $[0.01, 1000]$.

We compared the performance of three schemes in terms of both computational time cost and classification accuracy, based on experiments on a quad-core 2.67G Xeon CPU running Windows 7 with the Matlab implementation. Table 2 shows the final results on all data sets. Note that, the number of selected base kernels, i.e., m, ranges from 2 to 16 in our experiments, so the results of Method 1 and Method 2 reported in Table 2 are the best classification accuracy. As we

[1] The original codes are available on `http://user.ics.aalto.fi/gonen/icml08.php`

Table 2. Classification results on all data sets

Dataset	Method 1		Method 2		MRMRKA	
	Accuracy	Time (s)	Accuracy	Time (s)	Accuracy	Time (s)
Blood	0.7590±0.0678	56±6.0	0.7711±0.0229	6±2.0	0.8005±0.0126	25±1.0
Breast	0.7964±0.2506	134±9.0	0.9613±0.0053	7±2.0	0.9754±0.0011	38±1.0
Control	0.9663±0.0816	1304±58	0.9680±0.0103	28±2.0	0.9731±0.0064	86±1.0
Ecoil	0.8142±0.0196	164±19	0.8443±0.0243	8±0.10	0.8682±0.0054	8±0.50
Glass	0.5728±0.0518	141±18	0.6122±0.0641	17±2.0	0.6352±0.0093	36±2.0
Iris	0.9804±0.0227	8±0.10	0.9804±0.0227	0.3±0.10	0.9804±0.0123	8±0.20
Parkinsons	0.8513±0.0335	21±8.0	0.8872±0.0506	6±2.0	0.9128±0.0196	7±2.0
Seeds	0.9275±0.0421	22±3.0	0.9372±0.0391	0.5±0.10	0.9420±0.0229	3±0.10
Sonar	0.5894±0.1034	108±29	0.5990±0.0549	0.6±0.10	0.6135±0.0474	6±0.50
Wine	0.9498±0.0269	48±3.0	0.9722±0.0170	2±0.40	0.9722±0.0092	13±0.20

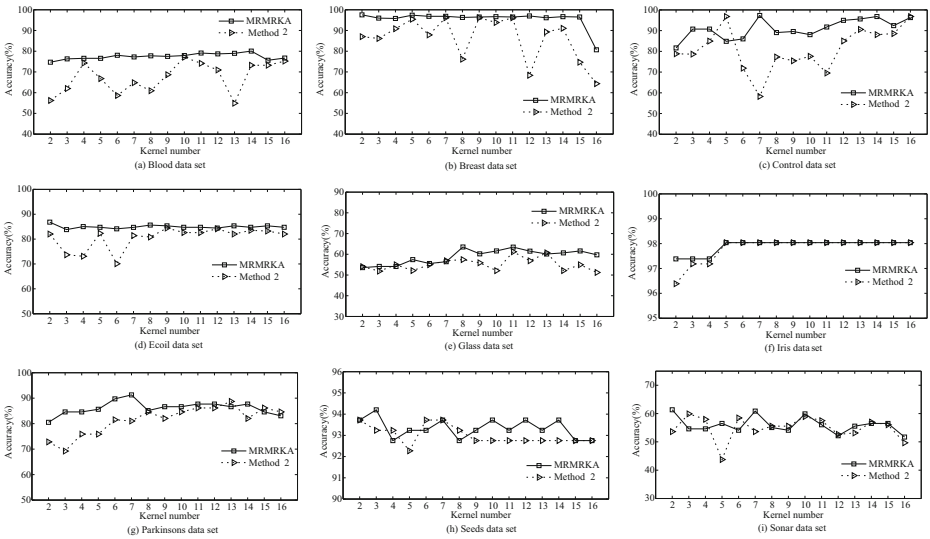

Fig. 1. Comparison of base kernels selected by MRMRKA and Method 2

can see from Table 2, MRMRKA obtains the best classification accuracy on all data sets. Both Method 2 and MRMRKA outperform Method 1 on all data sets. In addition, the time cost of Method 1 is higher than those of Method 2 and MRMRKA, because Method 1 does not take into count the redundancies among the selected base kernels and whether they are related to the target kernel, which undoubtedly has a negative effect on the efficiency and effectiveness of MKL. In the case of Method 2, the part of candidate kernels that are barely related to the target kernel is filtered in the selecting stage, but it does not take any measures to reduce the redundancies. Compared to Method 1 and Method 2, MRMRKA

selects the candidate kernels with the highest relevance to the target kernel and minimizes the redundancies among them, which makes it outperform the others. The time cost of MRMRKA is higher than that of Method 2 due to its a little bit more expensive, but the difference is acceptable. In general, Table 2 indicates MRMRKA gets a trade-off of the high accuracy and time cost.

We also examine that the number of selected kernels how to influence the performance of Method 2 and MRMRKA, and the results are shown in Fig. 1. The results demonstrate that the classification accuracy of MRMRKA fluctuates slightly with the change of m, in other words, when the number of selected base kernels is limited in a specific range, e.g., $[2, 16]$, the performance of MRMRKA are more stable than Method 2 in general. An important inspiration that can be drawn from the phenomenon is we can use cross-validation to select an optimal m by trying several finite values in practice. On the other hand, the fluctuation indicates that MRMRKA cannot entirely avoid the redundancies among the selected base kernels. To solve this kind problem, cross-validation can still be considered.

5 Conclusion and the Future Work

In this paper, in order to solve the problem of selecting base kernels in MKL, we propose a method which combine with MRMR and kernel alignment. The current results show that the proposed method can obtain a set of base kernels which can enhance the performance of MKL. There are two issues worth of further consideration. The first one is that only some medium-sized data sets are chosen in this study due to the computational time and space such kernels take when facing with large number of data samples, and the large scale data sets should be considered in the future work. The second one is that some other similarity measurements, such as Euclidean distance or Kullback-Leibler divergence can be utilized to measure the mutual dependence between kernels.

Acknowledgment. The research work in this paper was supported by the grants from the National Natural Science Foundation of China (Project No. 90820010, 61375045).

References

1. Sonnenburg, S., Rätsch, G., Schäfer, C., Schölkopf, B.: Large scale multiple kernel learning. The Journal of Machine Learning Research 7, 1531–1565 (2006)
2. Duan, L., Tsang, I.W., Xu, D., Maybank, S.J.: Domain transfer svm for video concept detection. In: IEEE Conference on Computer Vision and Pattern Recognition, pp. 1375–1381. IEEE (2009)
3. Qi, M., Tsang, I.W.: Efficient Multi-template Learning for Structured Prediction. IEEE Transactions on Neural Networks and Learning Systems 24(2), 248–261 (2013)
4. Vapnik, V.: The nature of statistical learning theory. Springer (1999)

5. Lanckriet, G.R., Cristianini, N., Bartlett, P., et al.: Learning the kernel matrix with semidefinite programming. The Journal of Machine Learning Research 5, 27–72 (2004)
6. Bach, F.R., Lanckriet, G.R., Jordan, M.I.: Multiple kernel learning, conic duality, and the smo algorithm. In: Proceedings of the Twenty-First International Conference on Machine Learning, pp. 41–48. ACM (2004)
7. Rakotomamonjy, A., Bach, F., Canu, S., et al.: Simplemkl. Journal of Machine Learning Research 9, 2491–2521 (2008)
8. Gönen, M., Alpaydin, E.: Loclized algorithms for multiple kernel learning. Pattern Recognition 46, 795–807 (2013)
9. Cortes, C., Mohri, M., Rostamizadeh, A.: Algorithms for learning kernels based on centered alignment. The Journal of Machine Learning Research 13, 795–828 (2012)
10. Guyon, I., Elisseeff, A.: An introduction to variable and feature selection. The Journal of Machine Learning Research 3, 1157–1182 (2003)
11. Peng, H., Long, F., Ding, C.: Feature selection based on mutual information criteria of max-dependency, max-relevance, and min-redundancy. IEEE Transactions on Pattern Analysis and Machine Intelligence 27(8), 1226–1238 (2005)
12. Afkanpour, A., Szepesvari, C., Bowling, M.: Alignment based kernel learning with a continuous set of base kernels. arXiv preprint arXiv:1112.4607 (2011)
13. Cristianini, N., Shawe-Taylor, J., Elisseeff, A., et al.: On kernel-target alignment. In: NIPS, pp. 367–373 (2001)
14. Bache, K., Lichman, M.: UCI machine learning repository (2013)

Bimodal Incremental Self-Organizing Network (BiSON) with Application to Learning Chinese Characters

Andrew P. Papliński[1] and William M. Mount[2]

[1] Monash University, Australia
Andrew.Paplinski@monash.edu
[2] University of New South Wales, Australia
w.mount@adfa.edu.au

Abstract. We present a recurrent learning system that can incrementally integrate stimuli in two modalities, visual and auditory. The system consists of five self-organizing modules, each mapping input stimuli into respective latent spaces. Two sensory modules convert the input stimuli into an internal 3-D "neuronal code". The central module integrates the bimodal information, and through modulatory top-down feedback influences the organization of data in two unimodal association units. Two feedback gains control the strength of the feedback connection. As an example we selected a set of Chinese characters and related spoken words. It is shown that the learning system can build a stable neuronal structure for incrementally applied visual and auditory stimuli.

Keywords: Multimodal Learning, Visual and Auditory stimuli, Recurrent networks, Self-organization, Chinese characters.

1 Introduction

It is well acknowledged that human languages are inherently cross-modal, requiring both written and spoken components to realize their full potential. Interesting accounts of the origins of human written and spoken language can be found in [7] and many others.

Due to the redundancy between the visual-signing (gestural, drawing or writing) and auditory-speech systems, spoken cross-modal references to symbolic names, as well as written representations of spoken signals, allowed for an increasingly rich repertoire of utterances, words and characters. These could be combined to describe the physical and mental world in more abstract terms and the argument goes that as languages became more sophisticated, they became increasingly embedded in the complex culture within which they co-evolved [3].

Some important differences in the way the human brain processes pictographic languages in general and Chinese in particular is described in [2]. As processing of the radicals and oriented brush strokes comprising the 50,000 or so known Chinese characters is very different from that of phonetically based languages such

M. Lee et al. (Eds.): ICONIP 2013, Part I, LNCS 8226, pp. 121–128, 2013.
© Springer-Verlag Berlin Heidelberg 2013

as English, a different set of phonological and orthographic skills are required in Chinese language acquisition [16].

Language processing is fundamental to human cognitive ability and involves multiple cortical networks and pathways across visual, auditory and other modalities. Large brain networks used in reading are discussed in [5]. See also [14] and [15] for some of our own efforts to develop simplified models of such networks.

While language comprehension and production requires the function of multiple cortical areas acting in concert, a region on the left hemisphere, the left superior temporal sulcus (STS) has been advanced as the main site for integration of visual and auditory speech information [3]. Recent fMRI studies support the key role of this region in the fusion of letters and speech sounds in the human brain[1].

Previous results of applying our models to the problem of integration of phonemes and letters in Chinese and Swedish are reported in [4] and [8] respectively. A related modelling framework is used in this case, however later enhancements for sequential feed-forward and recurrent learning [15] and incremental learning [11] provides an opportunity to revisit the problem of learning Chinese characters and associated sounds.

By incrementally building up sensory, unimodal associative and fused bimodal representations within our simplified five module network, a consistent way in which a human child or a computational agent may learn essential features of Chinese or any other spoken and written language is suggested.

2 The Structure of the Learning System

The structure of our bimodal incremental learning system is presented in Fig. 1. The function of the system is to receive sensory information across two modalities, visual and auditory, and integrate these representations. As an example, we use Chinese characters and their utterances as inputs to our system. We have experimented previously with Chinese characters in [4] and more recently [13].

The main part of the learning systems consists of five interconnected self-organizing modules. Two **sensory** level modules, **Vis** and **Aud**, process visual and auditory stimuli, respectively, converting coded sensory information, $\mathbf{x}_V$ and $\mathbf{x}_A$ into the standard internal representation of signals $\mathbf{y}_V$ and $\mathbf{y}_A$. In the next hierarchical level, two **unimodal association** modules, **UV** and **UA**, combine the signals from the sensory level, $\mathbf{y}_V$ and $\mathbf{y}_A$, with the modulating top-down feedback signals, $\mathbf{y}_{VA}$, produced by the top level **bimodal association** module, **V+A**. The strength of the top-down modulatory feedback is controlled by two gain parameters, g_{UV} and g_{UA}, at the input to the respective unimodal association modules.

The bimodal association module is presented here as a central part of the learning system. We can hypothesize that this module may also be activated by endogenous thoughts and can be used to drive modal effector systems, one for writing and one for articulation.

Following our previous works [14,15,8], the building block of our system is a self-organizing module (map) with the following characteristics (see Fig. 2):

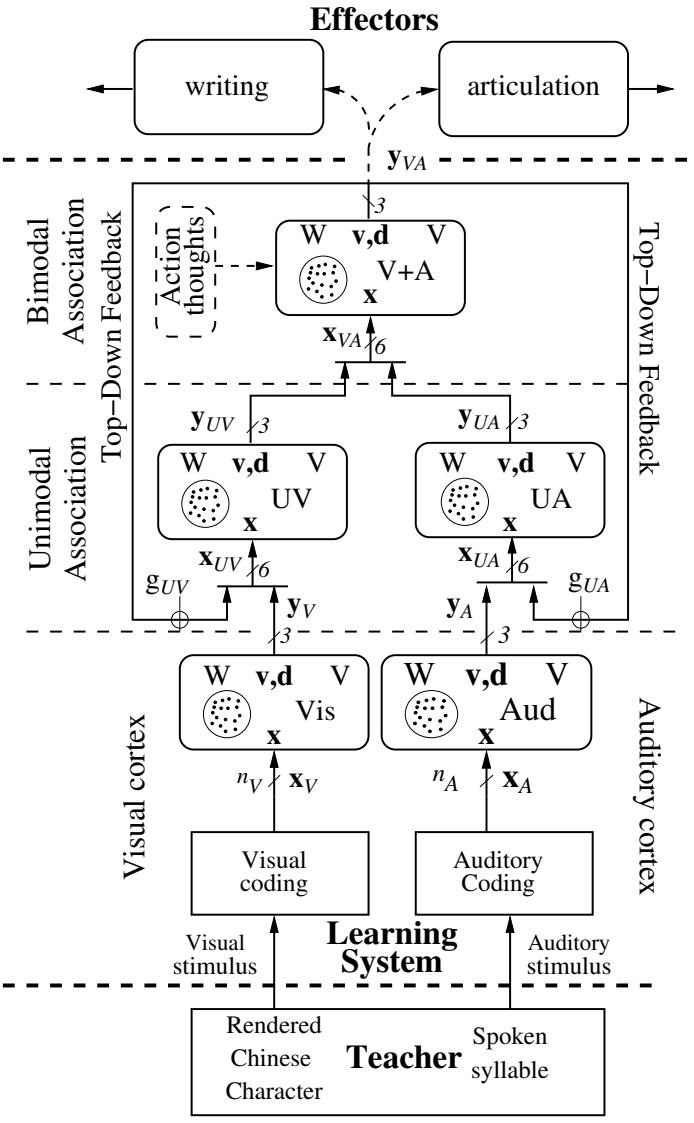

Fig. 1. The structure of the incremental learning system. The main part of the system consists of five self-organizing modules: Vis, UV, Aud, UA and V+A.

- The neuronal units (shown as yellow dots in Figures 2 and 4) are randomly distributed inside a unit circle, rather than on a uniformed rectangular grid.
- A constant number (stochastically) of neuronal units per stimulus, ϵ, is maintained to simulate the redundancy observed in biological systems.
- All stimuli vectors are projected on a unity hypersphere. Therefore, a simplified "dot-product" version of the Kohonen learning law [9] may be used.

Central to our processing architecture are the outputs from self-organizing modules, for example, $\mathbf{y}_V$ in Fig. 1. Note that dimensionality of all output vectors is 3. Such an output vector is a concatenation of the 2-D position vector of the winning neuron and its postsynaptic activity, namely,

$$\mathbf{y} = [\mathbf{v}_w \; d_w] = \mathcal{K}(\mathbf{d}), \quad \mathbf{d} = W \cdot \mathbf{x} \tag{1}$$

where W is an $M \times D$ matrix of parameters, the weight matrix, M being the number of nodes (neurons), and $\mathcal{K}$ is the Winner-Takes-All function identifying the position of the neuronal node $\mathbf{v}_w$ for which the post-synaptic activity $\mathbf{d} = W \cdot \mathbf{x}$ attains the maximum.

These output signals implement a ubiquitous "neuronal code", providing a unified way for information labels to be exchanged between modules of the network. It should be emphasized that the positions of neurons are considered in a latent space, not the physical one. This implies that during incremental learning the physical position of participating neurons is not affected.

3 The Incremental Learning Process

Our incremental learning process for a single iSOM has been introduced in [11]. We refer to this paper for detailed comparisons with other structures that may appear similar, in particular, a variety of growing SOMs. One fundamental difference is that during the learning process, we maintain a stochastically constant ratio between the number of neuronal units and the number of current stimuli.

In our case this expected ratio is always greater than one, implying that more than one neuron is used to represent a percept. This can be contrasted with other applications of SOMs where the number of of neurons is typically less than the number of data points. A study into the increased persistence and stability of percepts provided by such neural representations is presented in [6].

The incremental learning process starts with a small number, say $n = 3$, of initial stimuli and consists of two main steps:

Feedforward learning: We start with setting two feedback gains g_{UV} and g_{UA} to zero, thus opening the feedback loops and

- generate the number of neuronal units proportional to the number of stimuli, $m = n\epsilon$, say $3 \times 16 = 48$
- generate initial weights to be located around the north pole of the unity hypersphere
- perform the "dot-product" learning law for all maps, for all initial stimuli, for a set number of epochs, say 100.

Recurrent learning: We set the feedback gains to required values, e.g., $g_{UV} = g_{UA} = 0.5$ and repeat the learning process with one basic modification: after completing learning **for each stimulus**, we re-evaluate outputs from all 3 interconnected modules, namely, $\mathbf{y}_{UV}$, $\mathbf{y}_{UA}$ and $\mathbf{y}_{VA}$, until the values of the outputs settle. This typically happens after just two steps (see [14,15] for more details)

Adding more stimuli: Now we add new stimuli, one at a time, and repeat the two learning steps above with the following modification:

- generate the additional number of neuronal units proportional to the increment in the number of stimuli, $m_i = n_i\epsilon$, say $1 \times 16 = 16$
- initialize weights of the new m_i units to be equal to the weights of the closest neighbours.
- continue learning in the open and closed loop as above.

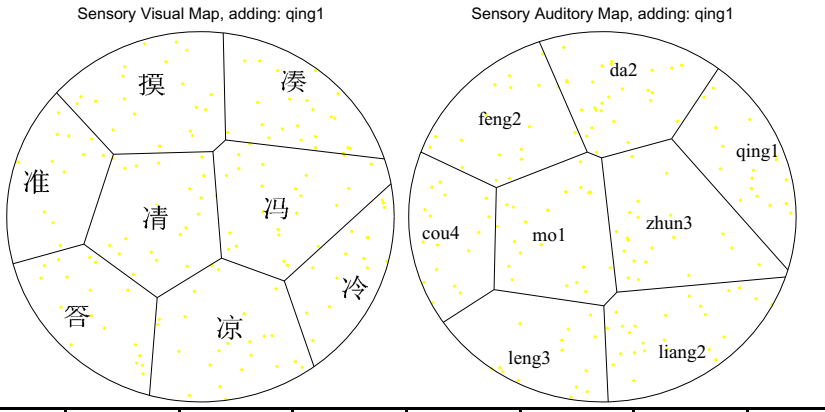

巴	ba1	模	mo2	打	da3	悌	ti4	冲	chong1	冯	feng2	决	jue2	泯	min3
拔	ba2	抹	mo3	大	da4	苛	ke1	凑	cou4	淦	gan4	冷	leng3	凝	ning3
把	ba3	漠	mo4	梯	ti1	咳	ke2	淮	cui1	涸	gu4	凉	liang2	凄	qi1
爸	ba4	搭	da1	綈	ti2	可	ke3	凋	diao1	减	jian3	冽	lie4	清	qing1
摸	mo1	答	da2	體	ti3	客	ke4	凍	dong4	凈	jing4	凌	ling2	淮	zhun3

Fig. 2. The sensory maps after 8 stimuli. The set of characters and their pinyin names are included.

This incremental process elegantly solves the problem of initialization of weights. Less effective random initialization is performed only for a small number of initial neurons. The result of learning after application of 8 stimuli is shown in Fig. 2.

Topological ordering of the stimuli needs to be considered in the context of the feature vectors used. For the visual channel we used an angular integral of Radon Transform (aniRT) discussed in [13] for the 20,000 Chinese characters and in [12,10] for other types of visual objects.

In the table of Fig. 2, the first 20 characters are grouped according to similarities in pronunciation, while the second set of 20 have a similar structure in terms of the aniRT coefficients. Each rendered character, is converted into a 91 component vector (91 being the size of the diagonal of the image). As described in [13] very few components are required to differentiate between characters, although some more are needed to capture details of the visual object.

For the auditory channel, we follow our previous work [14,8,4] where melcepstral coefficients are used to represent frequency of the speech sounds. We use

12 coefficients per frame, with 3 frames overlapping by 50%. We also add the duration of the utterance, so that we have 38-D feature vectors after projecting up on the unity hypersphere. An example of such coding is given in Fig. 3.

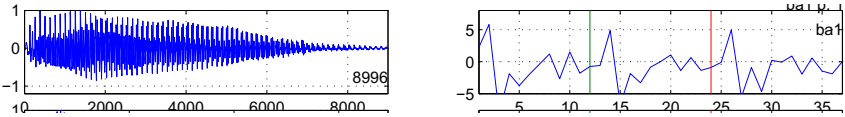

Fig. 3. Representing the 'ba1' sound in the melcepstral domain: 8996 speech samples are coded by 36 melcepstral coefficients. Normalized number of samples is also included as the first coefficient in the right-hand side plot.

If we continue the process of learning adding incrementally more and more stimuli, after 40 stimuli we obtain five maps as presented in Fig. 4. Again, at the sensory level it is easy to spot the topological ordering in both modalities. At the unimodal association level the topological arrangement of the stimuli is influenced by the top down feedback. Finally, the bimodal map presents the fusion of information from two modalities. In this paper we concentrate on the issue of the incremental learning which is performed for the congruent stimuli presented on the visual and auditory channels. The reader is referred to our previous works for considerations related to noisy and incongruent stimuli.

4 Discussion

While the sensory maps develop independently in a feedforward learning mode, the influence of top-down feedback during the recurrent learning phase ensures that cross-modal relationships are encoded in the unimodal and bimodal maps. Significantly, even though crossmodal information is not explicitly contained in either the visual or auditory information presented alone, the BiSON model ensures that the inherently bimodal structure of the words or characters comprising the natural language (in this case Chinese) is effectively encoded and learned.

A further enhancement would be to explore interactive learning and communication through the addition of character articulation and writing effector modules. This could introduce a third sensori-motor modality to our multimodal language framework. Finally, by extending this architecture to include simplified modules for central perceptual, evaluative and task-orientation functions, we hope to develop a sophisticated multilayered learning model where the symbolic elements or tokens of a spoken and written language represent meaningful mental objects and concepts within an interactive setting.

5 Conclusion

We present a recurrent learning system vaguely mimicking some basic cortical areas related to integration of visual and auditory information. In the example,

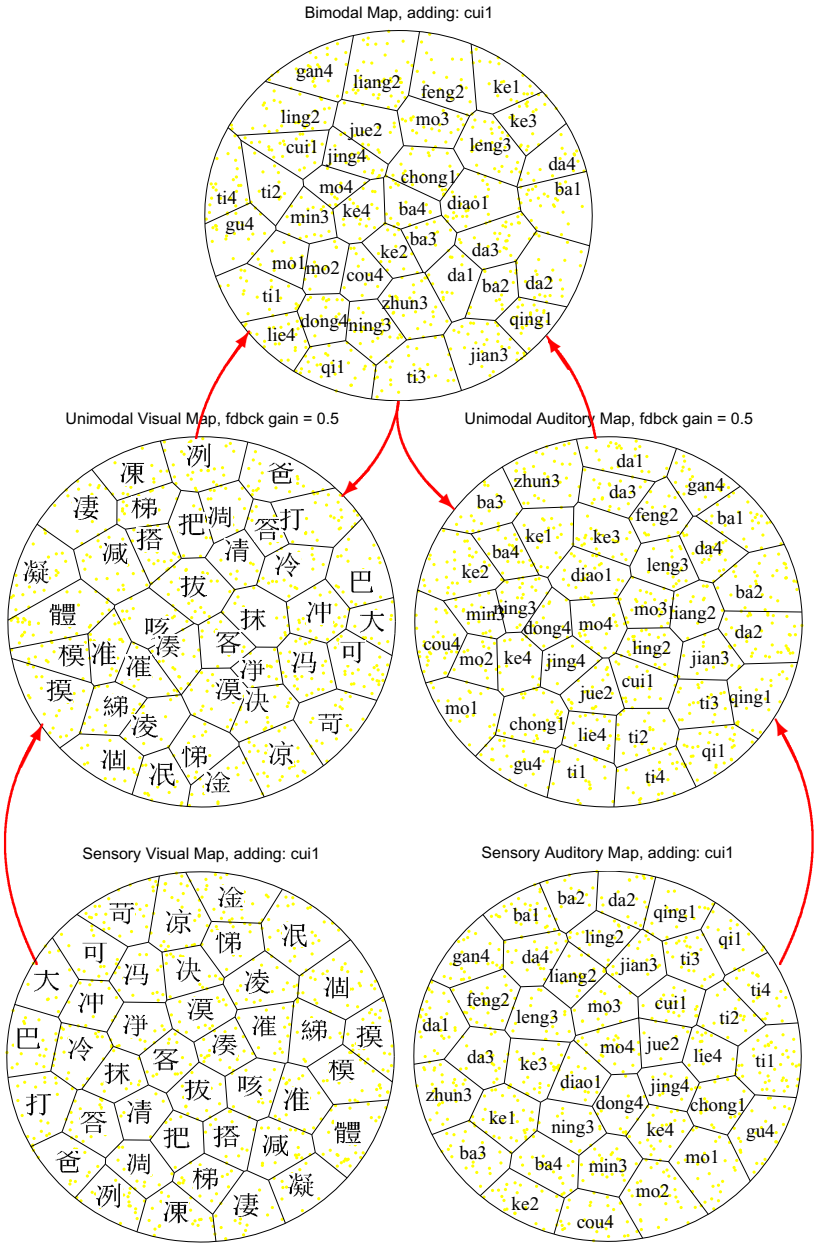

Fig. 4. The five interconnected maps developed after incremental application of 40 stimuli

the system 'reads' Chinese characters and simultaneously 'listens' to their pronunciation. At each stage, we add one more visual-auditory stimulus and the learning system incorporates it into its 5-map structure. Despite the recurrent

nature of the system, it converges to a fixed point after a only small number of recurrent iterations. The bimodal module plays the central part of the system for fusion of the bimodal percepts and from which effectors for writing and speaking can be driven.

The software used in this paper is written in MATLAB and is available upon request.

References

1. Atteveldt, N.M.: Speech Meets Script: FMRI Studies on the Integration of Letters and Speech Sounds. University of Maastricht (2006)
2. Bookheimer, S.: How the brain reads Chinese characters. Neuroreport 12(1) (January 2001)
3. Calvert, G.A., Brammer, M.J., Iversen, S.D.: Crossmodal identification. Current Biology 2, 247–253 (1998)
4. Chou, S., Papliński, A.P., Gustafsson, L.: Speaker-dependent bimodal integration of Chinese phonemes and letters using multimodal self-organizing networks. In: Proc. Int. Joint Conf. Neural Networks, Orlando, Florida, pp. 248–253 (August 2007)
5. Dehaene, S.: Reading in the Brain. Viking (2009), `http://pagesperso-orange.fr/readinginthebrain/figures.htm`
6. Druckmann, S., Chklovskii, D.B.: Over-complete representations on recurrent neural networks can support persistent percepts. Advances in Neural Information Processing Systems (2010)
7. Fitch, W.T.: The Evolution of Language. Cambridge University Press (2010)
8. Jantvik, T., Gustafsson, L., Papliński, A.P.: A self-organized artificial neural network architecture for sensory integration with applications to letter–phoneme integration. Neural Computation 23, 2101–2139 (2011)
9. Kohonen, T.: Self-Organising Maps, 3rd edn. Springer, Berlin (2001)
10. Papliński, A.P.: Rotation invariant categorization of visual objects using Radon transform and self-organizing modules. In: Wong, K.W., Mendis, B.S.U., Bouzerdoum, A. (eds.) ICONIP 2010, Part II. LNCS, vol. 6444, pp. 360–366. Springer, Heidelberg (2010)
11. Papliński, A.P.: Incremental self-organizing map (iSOM) in categorization of visual objects. In: Huang, T., Zeng, Z., Li, C., Leung, C.S. (eds.) ICONIP 2012, Part II. LNCS, vol. 7664, pp. 125–132. Springer, Heidelberg (2012)
12. Papliński, A.P.: Rotation invariant categorization of colour images using Radon transform. In: Proc. WCCI–IJCNN, pp. 1408–1413. IEEE (2012)
13. Papliński, A.P.: The angular integral of the radon transform (aniRT) as a feature vector in categorization of visual objects. In: Guo, C., Hou, Z.-G., Zeng, Z. (eds.) ISNN 2013, Part I. LNCS, vol. 7951, pp. 523–531. Springer, Heidelberg (2013)
14. Papliński, A.P., Gustafsson, L., Mount, W.M.: A model of binding concepts to spoken names. Aust. Journal of Intelligent Information Processing Systems 11(2), 1–5 (2010)
15. Papliński, A.P., Gustafsson, L., Mount, W.M.: A recurrent multimodal network for binding written words and sensory-based semantics into concepts. In: Lu, B.-L., Zhang, L., Kwok, J. (eds.) ICONIP 2011, Part I. LNCS, vol. 7062, pp. 413–422. Springer, Heidelberg (2011)
16. Siok, W., Fletcher, P.: The role of phonological awareness and visual orthographic skills in Chinese reading acquisition. Developmental Psychology 37(6), 886–889 (2001)

Keyword Extraction from Dialogue Sentences Using Semantic and Topical Relatedness

Yunseok Noh, Jeong-Woo Son, and Seong-Bae Park

School of Computer Science and Engineering, Kyungpook National University, Korea
{ysnoh,jwson,sbpark}@sejong.knu.ac.kr

Abstract. Dialogue reflects interests of the participants at that moment. Thus, it is desirable to extract keywords from each dialogue sentence as soon as they are spoken, because the keywords from dialogue can be used for various fields importantly such as personal assistant services, advertisement, and so on. This paper proposes a novel method of keyword extraction from dialogue sentences. The proposed method determines a word as a keyword by using semantic information of words in a dialogue sentence. That is, the proposed method extracts the keywords that are more semantically important within their sentences and more topically related to the dialogue. In the experiments on the ICSI meeting corpus, the proposed method achieves the state-of-the-art performance.

Keywords: Keyword extraction, Dialogue sentences, Semantic relatedness.

1 Introduction

Variety of sensory data can be used to help humans in many situations using its plentiful information. Smart phones which now are regarded as micro-computers have already shown many such cases like iPhone's Siri or some augmented reality services using their camera. Because language includes semantics on its own and dialogue among humans reflects their interest at that moment, the information extracted from such audio sensory data can be used for various fields importantly. For instance, a dialogue sentence can be used as features to inference the intention and the situation of the dialogue participants.

In order to exploit dialogue sentences as informative data, keywords should be extracted first, because, in a dialogue, there are many redundant words that provide no information such as habitual words like *'sort of'* or *'um'*. A dialogue has a number of topics and each dialogue sentence may deal with some topics in the dialogue. Thus, informative sentences are much related with those of the topics, while non-informative ones may consist of habitual words. Therefore, extracting keywords from dialogue sentences should consider whether the sentence is semantically related to the entire dialogue topics and how much related to the topics. With this semantic information, the words that are more important semantically should be chosen as keywords.

M. Lee et al. (Eds.): ICONIP 2013, Part I, LNCS 8226, pp. 129–136, 2013.
© Springer-Verlag Berlin Heidelberg 2013

There have been some studies that focus on the spoken genres. Liu et al. proposed a number of keyword extraction methods [5] for the meeting transcripts. They conducted the keyword extraction through TFIDF-based and TextRank-based methods with some NLP techniques. However, these methods use whole meeting scripts not for each sentence to extract keywords, because they focus on only the characteristics of texts from spoken language such as unstructured and ill-formed sentences. Song et al. [7] proposed a method which extracts keywords from each utterance in a meeting. They constructed a history graph which contains all of keywords from all of previous meetings. Then, they expand the graph of current utterance using the history graph to make up for the deficient information of the current utterance. Since the history graph is accumulated without distinction of topics, the graph includes some irrelevant keywords. Therefore, even though the theme of the expanded graph is similar with that of current utterance, it can contain different topics from the topics of current utterance.

This paper proposes an unsupervised keyword extraction from dialogue sentences. The proposed method uses semantic information derived from a global knowledge base, specifically Wikipedia, to represent the topics of dialogue and compute semantic relatedness between words and sentences. The proposed method deals with semantic importance of words with two aspects. First, the *local* word importance finds semantic importance of words in a sentence. To do this, a semantic graph of the sentence is generated, where the nodes are words in the sentence and the edges are weighted by semantic relatedness between nodes. Then, TextRank algorithm [6] is applied to reveal words which are semantically centered. Second, the proposed method uses global word importance. The *global* importance of a word is defined as how strongly a word corresponds to the topics of the dialogue. The global importance is determined by semantic relatedness between the word and dialogue. These local and global word importances are linearly summed. After the importance of a word is measured with both aspects, a weight of the sentence is applied to them. The weight of the sentence denotes the similarity between topics in the sentence and those in the dialogue. Thus, this weight can prevent to extract keywords from sentences without any information for the dialogue.

The evaluation of the proposed method is done with the ICSI meeting corpus [3]. In the experiments, the proposed method outperforms all existing methods including both methods of Liu et al. [4,5] and the history graph-based model [7]. This result proves the effectiveness of the proposed method in keyword extraction from dialogue sentences.

2 Keyword Extraction for Dialogue Sentences

Let D_t be a set of dialogue sentences at time t. Thus, D_t is defined as $D_t = \{d_1, d_2, , d_t\}$, where d_i denotes the sentence generated at time i. Then, the task of keyword extraction is to extract keywords from d_t by using D_t. That is, the proposed method extracts keywords from d_t immediately based on D_{t-1} and d_t itself. To extract keywords, a score function $f(w_i^t)$ is first defined as

$$f(w_i^t) = Li(w_i^t) + Gi(w_i^t), \tag{1}$$

where w_i^t is the i-th word in d_t and both $Li(w_i^t)$ and $Gi(w_i^t)$ are function to measure the local and global word importance respectively. The local word importance denotes the topical importance of w_i^t in d_t, while the global word importance means the topical importance of w_i^t in D_t. When it is assumed that both importance measures are prepared, the task can be easily achieved just by choosing words whose scores are over a threshold θ.

2.1 Local Word Importance

Local word importance $Li(w_i^t)$ is determined by using the semantic graph of the dialogue sentence in this paper. To make a semantic graph G_t for the sentence d_t, the proposed method employs Explicit Semantic Analysis (ESA) [2] which is a typical semantic relatedness measure using Wikipedia. When a sentence d_t is spoken, ESA maps each word onto a vector space which is explicitly defined by Wikipedia concepts. Let T be a set of Wikipedia concepts, then a word w_i^t in a sentence is expressed as a concept vector c_i^t

$$c_i^t = \langle \Phi_1(w_i^t), \Phi_2(w_i^t), , \Phi_{(|T|)}(w_i^t) \rangle.$$

Here $\Phi_k(w_i^t)$ is the weight of the k-th concept for w_i^t and is given as

$$\Phi_k(w_i^t) = tf(w_i^t, a_j) \cdot idf(w_i^t, T),$$

where a_j is an article of the j-th Wikipedia concept in T.

To build G_t, we first generate concept vectors c_i^t for all words $w_i^t \in W_t$, where W_t is a set of words in d_t. Then, it is excluded words whose concept vectors contain only zeros. After the filtering out, the remained m unique words in d_t are used as the vertices of the semantic graph G_t, since these words can represent some topics. That is, the semantic graph G_t is defined as an undirected graph $(V_t \times E_t)$, where V_t is the set of remained words, and E_t is a set of edges and each edge represents how much two vertices are semantically tied by its weight score. This semantic relatedness for each $e_{ij}^t \in E_t$ that links between vertices v_i^t and v_j^t is defined as

$$ew_{ij}^t = sim(c_i^t, c_j^t) = \frac{c_i^t \cdot c_j^t}{\| c_i^t \| \| c_j^t \|}, \tag{2}$$

In the case of $ew_{ij}^t = 0$, which means no semantic relatedness between v_i^t and v_j^t, the edge e_{ij}^t is discarded.

After the semantic graph G_t is built, the local semantic importance of words can be obtained by graph-based ranking algorithms. In the proposed method TextRank algorithm [6] is adopted. TextRank was introduced to extract keyword and sentence from natural language texts and it is designed based on PageRank. The local semantic importance of each $v_i^t \in V_t$ is finally computed by following TextRank algorithm:

$$WS(v_i^t) = (1-d) + d * \sum_{v_j^t \in adj(v_i^t)} \frac{ew_{ji}^t}{\sum_{v_k^t \in adj(v_j^t)} ew_{jk}^t} WS(v_j^t), \tag{3}$$

where $0 \leq d \leq 1$ is a damping factor and $adj(v_i^t)$ denotes the vertex v_i^t's neighbors.

2.2 Global Word Importance

The global word importance $Gi(w_i^t)$ of a word w_i^t treats a semantic relationship between the word and the dialogue D_{t-1}. Since the local word importance considers the semantic relationships only within a sentence d_t, the global word importance can reflect a different aspect of word in the score.

ESA can be also used for the global word importance. However, unlike the local word importance, a modification of ESA is needed to handle the dialogue sentences. Each dialogue sentence usually has short length and it can be mixed some semantically important words and less important one together. When a sentence d_t is given, its concept vector is obtained with sum of concept vectors for words in the sentence. Thus, the vector can be easily misled by some valueless words.

To solve this problem, ESA is modified as TextRank-ESA that uses weighted sum of words to generate an concept vector of a sentence. The weights for words are obtained by TextRank algorithm on the semantic graph of the sentence. That is, in TextRank-ESA, each word is weighted by its local word importance in Equation (3). As a result, the concept vector of the sentence d_t is defined as

$$trC^t = \sum_{i=1}^{n} WS(v_i^t) \cdot c_i^t \tag{4}$$

where n is the number of words in a sentence.

Table 1 shows a difference between the ordinary ESA and TextRank-ESA. The left part of Table 1 shows an ESA concept vector representation of a dialogue sentence *'you can speak into it and ask for movie information'*. In this sentence *'movie'* and *'information'* should be regarded as important words. However, the concepts in the ESA vector are confused by the concepts from *'speak'*. On the other hand, the right part of Table 1 shows the concept vector from the same sentence by TextRank-ESA. Comparing with ordinary concept vector, concept vector of TextRank-ESA represents the sentence semantically well about *'movie'* and *'information'*.

The global word importance is measured with semantic relatedness between a word w_i^t in the sentence d_t and the dialogue D_{t-1}. Thus, the concept vector for D_{t-1} is required. Similar with Equation (4), the concept vector for D_{t-1} is also determined by the sum of weighted concept vectors of all words in D_{t-1}. That is,

$$trC^{D_{t-1}} = \sum_{d_k \in D_{t-1}} \sum_{w_i^k \in d_k} WS(v_i^{D_{t-1}}) \cdot c_i^k,$$

where $WS(v_i^{D_{t-1}})$ is from the semantic graph $G_{D_{t-1}}$ of D_{t-1}. This graph is constructed by simply combining semantic graphs of all sentences in D_{t-1}. Then, for the global word importance for w_i^t, Equation (2) is used to compare c_i^t (the concept vector of w_i^t) and $trC^{D_{t-1}}$ (the concept vector of D_{t-1}).

Table 1. Semantic representations of ESA and TextRank-ESA for a dialogue sentence

#	Input text: "you can speak into it and ask for movie information"	
	ESA	TextRank-ESA
1	Internet Movie Database	Internet Movie Database
2	Yahoo! Movies	Yahoo! Movies
3	Relatively Speaking (play)	Geographic Names Information System
4	Universally Speaking	Hong Kong Movie DataBase
5	Motivational speaking	Jane's Information Group

2.3 Keyword Extraction from Dialogue Sentence

The proposed method is performed with two semantic factors of words mentioned above. The word occupies semantically important status in a sentence should be much considered as a keyword. At the same time, the word which is more related to the topics of the dialogue is also taken into account more importantly.

Considering these two semantic factors as same weight, the word importance of each word in a sentence d_t is computed as follows.

$$WI(w_i^t) = \frac{1}{Z} WS(v_i^t) + sim(c_i^t, trC^{D_{t-1}}), \tag{5}$$

where z denotes the normalization factor to bound the value of $WS(v_i^t)$ from 0 to 1. When Equation (5) is used as a score function in Equation (1), keywords are always extracted even for the sentences only with noise. Thus, in the proposed method, a sentence importance is applied to penalize sentences without information. This importance reflects how the topics of a sentence are consistent in the topics of the dialogue. If a sentence has small score in this factor, it results in extracting no keywords from the sentence. The sentence importance is also simply measured by computing semantic relatedness between two concept vectors of the sentence and the dialogue. Thus, it is defined as $SI(d_t) = sim(trC^t, trC^{D_{t-1}})$.

When the sentence level semantic factor is applied to Equation (5), it gives rise to a problem that keywords are not extracted in the early stage of a dialogue. This is because the first sentence always has 0 value of $SI(d_t)$. Thus, this is a critical obstacle to extract keywords from sentences at the beginning of dialogue. To prevent them, we rescale $SI(d_t)$ between 0.5 and 1. Consequently, the score function in Equation (1) is conducted as $KS(w_i^t) = \frac{1+SI(d_t)}{2} WI(w_i^t)$.

3 Experiments

3.1 Data Set

The proposed method is evaluated with the ICSI meeting corpus [3]. Table 2 shows simple statistics of the ICSI meeting corpus data. There exist total 201 of topic segments in the 26 meetings. That means that each meeting has about

Table 2. Simple statistics of the ICSI meeting corpus

Information	Value
The number of meetings	26
The number of segments	201
The number of topic segments used actually	140

8 topics on average. Among 201 topic segments, 61 segments have no keywords. In experiments, such segments are discarded, and remaining 140 segments are actually used. We performed experiments by regarding these 140 topic segment as dialogues.

There are two parameters for the proposed method. A damping factor is adjusted as 0.85 and a threshold performing a border line for keywords is set to 0.2. Unfortunately, the keywords of the ICSI meeting corpus are not provided for each sentence in a dialogue. The corpus only provides keywords just on topic segment level. To measure the proposed method with the data set, we borrow the idea of [7]. First, keywords are extracted from each dialogue sentence by the proposed method and then all of them are accumulated with their score. Unlike [7] who conducted post-computation to fit their method to the data, keywords are selected by just the accumulated scores which are normalized. Keywords that have the score higher than threshold 0.03 and ranked within top-10 are chosen for each topic segment.

To generate concept vectors, a Wikipedia snapshot as of May 2, 2012 is used. We followed all settings to refine Wikipedia articles for constructing an inverted index by [2].

3.2 Experimental Result

The evaluation is carried out with F-measure and the weighted relative score (WRS). WRS is defined by that a higher score is given to an extracted keyword when more annotators agree the extracted one as a keyword. The proposed method uses total three semantic factors for a dialogue sentence, so the effect of each factor was explored. Table 3 shows the performances of the partial methods with each semantic factor of the proposed method. As shown in this table, all factors have its own room. In every time adding a factor, both F-measure and WRS had been improved. This experimental result shows that each semantic factor provide a different point of view to reveal semantically more significant keywords.

The proposed method is also compared with four previous studies. The first and second methods are proposed by Liu et al. [5] which are TFIDF- and TextRank-based methods with some NLP techniques. The third method is the maximum entropy model which is a supervised learning model [4]. The forth method is a graph-based method which uses the history graph and it reported the state-of-the art performance in unsupervised keyword extraction [7]. History

Table 3. The performance of partial factor of the proposed method

Method	f-measure	WRS
Local word importance	0.318	0.473
Local + global word importance	0.336	0.488
Proposed method	0.380	0.612

Table 4. The performances of various methods on the ICSI corpus

Method	f-measure	WRS
TFIDF-Liu	0.290	0.404
TextRank-Liu	0.277	0.380
ME model	0.312	0.401
History graph-based	0.334	0.533
Proposed method	**0.380**	**0.612**

graph-based method is also designed to extract keywords from each dialogue sentence, so it is compared to our method directly.

Table 4 shows the result. As shown in this table, the proposed method outperforms all others with respect to both measures, F-measure and WRS. The proposed method achieves the best performance with 0.380 in F-measure. Even in the history graph based method [7], it shows 4.6% and 7.9% worse F-measure and WRS than those of the proposed method. These experimental results prove that the proposed method efficiently reflects the characteristics of dialogue sentences by using semantic information. Therefore, it can be concluded that the consideration of semantic relations among words within a sentence and the topics of the whole dialogue are crucial in keyword extraction from dialogue sentences.

4 Conclusion

In this paper, we proposed a novel method for extracting keywords from dialogue sentences. As soon as a sentence is spoken, the proposed method generates keywords from the sentence that best describe the sentence. By considering the semantic information in the sentence itself and the dialogue, the proposed method extracts keywords that reflect the topics organizing the main stems of the dialogue. Local and global word importance reflects the semantic importance of a word for both a sentence and a dialogue respectively. On the other hand, the topics on the sentence itself are also considered by using the sentence importance. The proposed method was evaluated with the ICSI meeting corpus. According to the results of our experiments on the corpus, the proposed method showed the best performance of extracting keywords from dialogue sentences.

Acknowledgements. This research was supported by the Converging Research Center Program through the Ministry of Science, ICT and Future Planning, Korea (2013K000333).

References

1. Frank, E., Paynter, G.W., Witten, I.H., Gutwin, C., Nevill-Manning, C.G.: Domain-specific Keyphrase extraction. In: Proceedings of the 18th IJCAI, pp. 265–270 (1999)
2. Gabrilovich, E., Markovitch, S.: Computing Semantic Relatedness using Wikipedia-based Explicit Semantic Analysis. In: Proceedings of the 20th IJCAI, pp. 1606–1611 (2007)
3. Janin, A., Baron, D., Edwards, J., Ellis, D., Gelbart, D., Morgan, N., Peskin, B., Pfau, B., Shriberg, E., Stolcke, A., Wooters, C.: The ICSI meeting corpus. In: Proceedings of ICASSP, pp. 364–367 (2003)
4. Liu, F., Liu, F., Liu, Y.: Automatic Keyword Extraction for the Meeting Corpus using Supervised Approach and Bigram Expansion. In: Proceedings of IEEE SLT, pp. 180–184 (2008)
5. Liu, F., Pennell, D., Liu, F., Liu, Y.: Unsupervised Approaches for Automatic Keyword Extraction using Meeting Trascripts. In: Proceedings of NAACL, pp. 620–628 (2009)
6. Mihalcea, R., Tarau, P.: Textrank: Bringing Order into Texts. In: Proceedings of EMNLP, pp. 404–411 (2004)
7. Song, H.-J., Go, J., Park, S.-B., Park, S.-Y.: A Just-In-Time Keyword Extraction from Meeting Transcripts. In: Proceedings of NAACL, pp. 888–896 (2013)
8. Turney, P.D.: Learning Algorithms for Keyphrase Extraction. Information Retrieval 2, 303–336 (2000)

Exogenous and Endogenous Based Spatial Attention Analysis for Human Implicit Intention Understanding

Young-Min Jang, Rammohan Mallipeddi, and Minho Lee*

School of Electronics Engineering, Kyungpook National University
1370 Sankyuk-Dong, Puk-Gu, Taegu 702-701, South Korea
ymjang@ee.knu.ac.kr, {mallipeddi.ram,mholee}@gmail.com

Abstract. In this paper, we develop a novel human implicit intention understanding model by mimicking the human-like visual attention and brain information processing mechanisms. In other words, the proposed model considers a hybrid cognitive neural system, which comprises of spatial attention model obtained based on exogenous and endogenous attention models. Generally, information can be selected via top-down or endogenous mechanisms depending on the goals of the observers while salient objects or events attract spatial attention via bottom-up or exogenous mechanisms allowing a rapid and efficient reaction to unexpected but important events. Given a visual stimulus, the spatial analysis module identifies the objects of interest by correlating the salient areas obtained from the exogenous module and the eye gaze information obtained from the endogenous module. Then, corresponding to an intent, each of the identified objects are classified in to one of the two classes – intent object or non-intent object, by analyzing the features such as fixation length (FL), fixation count (FC) and pupil size (PS) corresponding to each object. In the proposed model, support vector machine (SVM) is trained for classifying the different objects. Experimental results show that the proposed model generates plausible performance based on hybrid cognitive neural system.

Keywords: human implicit intent, spatial attention, endogenous, exogenous, human computer interface & interaction, eye tracking.

1 Introduction

The process of concentrating on a particular aspect of the environment selectively, while ignoring other things is referred to as 'attention'. Attention is a central feature of human cognition, which can be driven by internal goals or by external stimulation. The time course of attention also varies depending on the cognitive task at hand. In general, goal-driven attention is referred to as top-down or endogenous attention, whereas stimulus-driven attention or attention driven by the external events in an environment is referred to as bottom-up or exogenous attention [1]. In the present work, we develop a hybrid system comprising of both endogenous and exogenous

* Corresponding author.

M. Lee et al. (Eds.): ICONIP 2013, Part I, LNCS 8226, pp. 137–144, 2013.
© Springer-Verlag Berlin Heidelberg 2013

attention models to understand human implicit intention. The proposed model classifies human implicit intention in real-world indoor environment based on spatial attention. The spatial attention can be obtained by analyzing a correlation between the endogenous attention and the exogenous attention. The endogenous attention can be obtained by using human eye gaze information and the exogenous attention can be obtained by using the selective attention model. The classification of human implicit intention based on eye movement analysis has been studied in [2]. In [3], the authors introduced a brain-like model to generate a selective attention model based on bottom-up saliency map (SM) to determine reason of interest (ROI) in a visual stimulus image. In this paper, we propose a model considering both psychological and cognitive aspects to classify various identified objects into intent and non-intent objects while visualizing a natural scene. An intent object refers to an object, which is related to a particular intention while a non-intent object refers to an object that does not possess any relationship corresponding to an intention. For example, objects such as 'knife' and 'bread' are related with the intention "Eat Bread" and are referred to as intent objects. In contrast, objects such as 'noodle', which do not bear any relationship to the given intent are referred to as non-intent objects.

The paper is organized as follows: Section 2 presents an outline of the proposed human implicit intention understanding model based on hybrid cognitive neural system such as endogenous and exogenous spatial attention. Section 3 presents experimental results of the proposed model in natural scenes. Section 4 concludes the paper with some suggestions towards future research.

2 Proposed System

As shown in Figure 1, the architecture of the proposed human implicit intention understanding system consists of 1) human eye-movement analyzer in the endogenous attention module, 2) bottom-up saliency map to understand natural-scenes in the exogenous attention module, 3) spatial attention module to correlate the outputs of endogenous and exogenous modules and 4) a SVM classifier to classify the objects into intent and non-intent objects using FL, FC and PS.

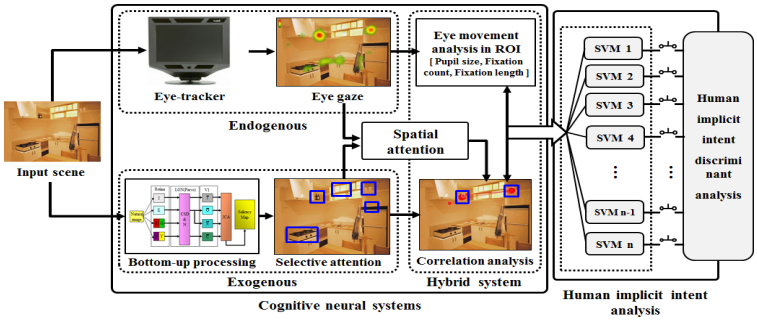

Fig. 1. Human implicit intent understanding system based on cognitive neural system

Given a visual stimulus image, the exogenous module, comprising of biological selective attention model, identifies objects as per human subject's preference. At the same time, the exogenous module containing the eye-tracker analyses the human eye gaze corresponding to different objects of interest in the visual stimulus. To analyze human eye movements, the endogenous module contains the Tobii 1750 eye tracking system software development kit (SDK) [4]. Based on the correlation between endogenous and exogenous modules the spatial attention module identifies objects of interest. The objects corresponding to a particular intent, among various other objects, can be identified based on some features such as FL, FC and PS. In other words, , objects can be classified as an intent object or a non-intent object by analyzing the eye movement features of each object.

2.1 Endogenous and Exogenous Mechanisms for Human Implicit Intent Understanding

Researchers in psychology have described two different aspects related to how human minds attend interesting objects present in an environment. The first aspect is called bottom-up processing, also known as stimulus-driven attention or exogenous attention. In other words, exogenous attention is driven by the properties of objects. For instance, some processes, such as motion or a sudden loud noise, can attract human attention subconsciously. [5]. The second aspect is called top-down processing. It is also known as goal-driven, endogenous attention or executive attention. Endogenous attention is under the control of a human subject attending to a particular scene or task [5]. In this work, we develop a novel approach for a human implicit intention understanding system based on selective attention model and human eye-movement in natural scenes.

2.2 Human Eye Movement Analysis in Endogenous Attention Model

In human cognitive processes, eye movements are known to be correlated with endogenous attention. [1, 2]. Therefore, is assumed that humans may generate specific eye movement patterns according to different implicit intentions during visual search. Accordingly, eye movement patterns can be considered as possible factor for recognizing the human implicit intention. In this paper, we analyze the characteristics of eye movement patterns, measured using the Tobii 1750 eye track system SDK, to verify it's correlation with implicit intent. We found that the FL, FC and PS variation are most significant features to distinguish between intent and non-intent objects. Also, we employ the baseline model proposed in [6] to minimize the effect of pupillary light reflex, which is a result of the illumination variation in a visual stimuli.

2.3 Natural Scene Understanding Based on Exogenous Attention Analysis

Figure 2 shows the exogenous attention based on bottom-up SM model [3]. The bottom-up SM is employed for scene understanding based on salient area detection in natural scene[3]. To implement a human-like efficient exogenous attention system,

we consider the bottom-up SM model, which reflects the functions of the retina cells, the lateral geniculate nucleus (LGN) and the visual cortex. We use edge, intensity, and color information based on brain information processing mechanism during an input stimulus. In the selective attention model, the on-center and off-surround operation is implemented by using the Gaussian pyramid images with different scales from 0 to n, where each level is further sub-sampled into 2^n. Then, the center-surround mechanism is implemented as the difference operation between the fine and coarse scales of the Gaussian pyramid images. The four feature maps (, $\overline{O}$, $\overline{S}$, and $\overline{C}$) are obtained by the center-surround difference and normalization (CSD&N) algorithm [3]. The constructed feature maps ($\overline{I}$, $\overline{O}$, $\overline{S}$, and $\overline{C}$) are then integrated by an independent component analysis (ICA) algorithm, which is based on entropy maximization [3, 7]. The states that human visual cortical feature detectors might be the end result of a redundancy reduction process. The authors in [7] argued that ICA is the best way to reduce redundancy. After the convolution between the channel of the feature maps and the filters obtained by ICA learning, SM is computed by integrating all feature maps for each location.

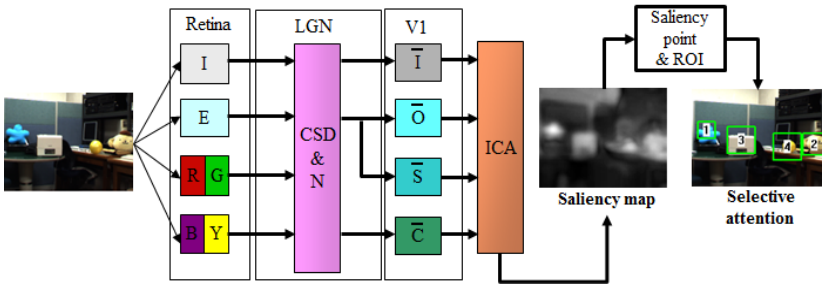

Fig. 2. Exogenous attention for object detection based on bottom-up saliency map

2.4 Hybrid Spatial Attention Area Based on Endogenous and Exogenous Attention Models

Figure 3 shows the hybrid spatial attention. Given a visual stimulus, the bottom-up saliency map, present in the exogenous attention module, identifies the attention areas corresponding to the objects of interest.

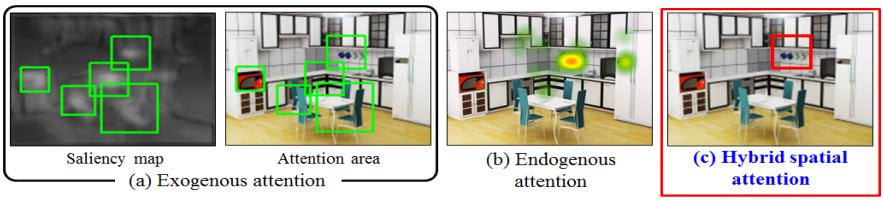

Fig. 3. Hybrid spatial attention

Fig. 3 (a) shows a result of the exogenous attention module based on saliency map. For the same given visual stimulus, the eye tracking system in the exogenous attention module analyses the human gaze information corresponding to the different objects present. Fig. 3(b) shows a result of the eye gaze analyzer present in the endogenous attention module. Finally, the spatial attention module identifies the objects of interest based on the correlation between exogenous and endogenous modules. Fig. 3(c) shows the results of hybrid spatial attention module.

3 Experimental Results

3.1 Human Eye Movement Pattern Analysis

To verify that the features such as FL, FC and PS variation are significant to classify the objects into intent and non-intent objects, we instructed participants to search for a particular interesting object in the visual stimuli. Figure 4 shows the experimental image and distribution of the parameters corresponding to the different objects. Fig.4 (a) shows the stimulus image, Fig. 4(b) shows the result of raw data analysis using FC, Fig. 4 (c) shows the result using FL, and Fig. 4 (d) shows the result of PS variation.

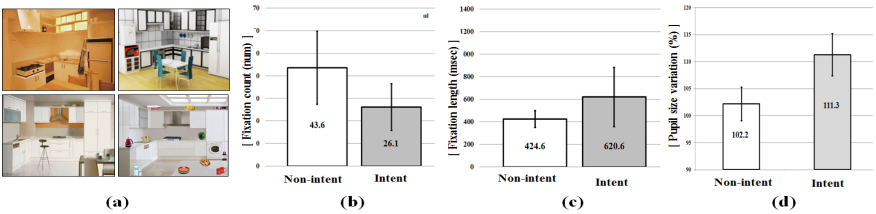

Fig. 4. Human eye movement

Notice that the results in fig. 4 clearly indicate that the FL, FC and PS variation are significant features to classify various objects into intent and non-intent objects in a given visual scene.

3.2 Salient Object Determination by Selective Attention Model

In the proposed system, the exogenous model is based on the bottom-up selective attention model. Recently, the authors in [3] proposed a SM model ($\bar{I}+\bar{C}+\bar{O}+\bar{S}+ICA$) including a symmetry feature map and an ICA filter to integrate the feature information[3]. Figure 5 shows the bottom-up SM processing. Results suggest that $\bar{I}+\bar{C}+\bar{O}+\bar{S}+ICA$ SM model generates more robust object preferable attention.

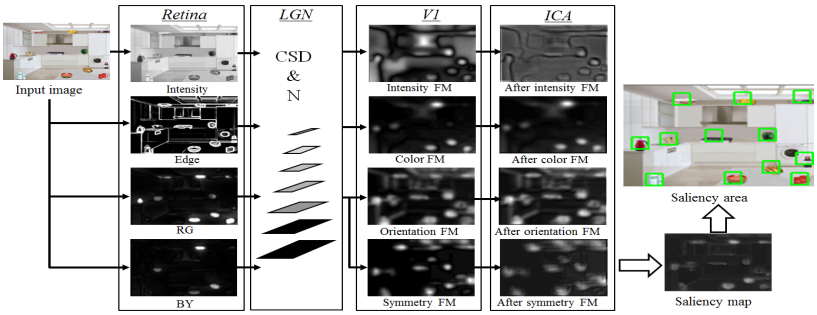

Fig. 5. Bottom-up SM processing

3.3 Human Implicit Intent Understanding Based on Hybrid Spatial Attention

In this paper, we proposed human implicit intent understanding based on hybrid spatial attention mechanism in brain processing. The hybrid spatial attention model based on endogenous and exogenous attention is used to identify the objects of interest which are further classified as intent and non-intent objects based on the eye movement analysis. Figure 6 shows the results of hybrid spatial attention for identifying the objects of interest. Then, the eye movement features such as FL, FC and PS variation corresponding to each of the selected object are measured. Based on the measured features, the trained SVM can classify objects into intent and non-intent objects. Fig. 6 shows the process of identifying the objects of interest using spatial attention model. Fig. 6 (a) shows the result of the exogenous model while Fig. 6 (b) shows the result of the eye gaze analysis. Fig. 6 (c) shows the result of the hybrid spatial attention model based on intersection area of exogenous attention area endogenous attention areas.

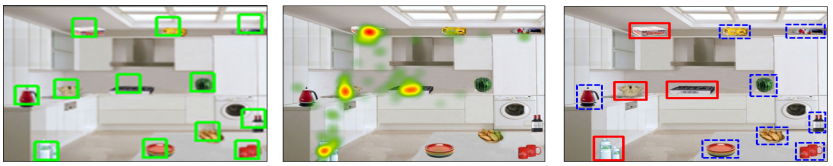

(a) Exogenous attention Based on SM model

(b) Endogenous attention based on eye gaze area

(c) Hybrid spatial attention based on exogenous and endogenous

Fig. 6. Hybrid spatial attention to determine objects of interest

For the experiment, data from 29 participants were collected. 10 randomly selected samples were used for training the SVM, while the remaining 19 samples were used for testing. The experimental visual stimulus included 12 different objects. During the data collection, participants were given the visual stimulus and they were asked to search for objects related to each of the following 4 intent conditions: 1) I_1: Cook Noodle, 2) I_2: Make Coffee, 3) I_3: Have Bread and Wine and 4) I_4: Eat Watermelon. Table 1 shows the features (FL, FC and PS) corresponding to all 12 objects during 4 different intent conditions. Notice that for I_1 objects such as 'noodle', 'pot', 'gas

range' and 'water' have significant difference in feature values (highlighted) compared to other objects in the visual stimulus. Similar kind of observations were made in the case of I_2, I_3 and I_4. Therefore, based on the features the trained SVM can easily classify the objects into intent and non-intent objects according to different intent conditions. The training and testing performance of the SVM is presented in Table 1. Based on the results, it can be observed that the proposed system is robust in identifying the transition in different human implicit intents during a visual stimulus search.

Table 1. Variation in the features corresponding to different intent conditions and classification

		Noodle	Coffee	Knife	Kettle	Pot	Gas range
I_1	FC(num)	**47.7±4.9**	4.6±1.4	2.2±1.2	5.8±2.1	**75.9±4.8**	**76.5±6.8**
	FL(msec)	**600±67.9**	97.0±27.7	50.2±25.9	96.4±31.4	**613±55.3**	**607±51.7**
	PS(%)	**98.8±5.8**	36.7±9.7	15.0±7.2	34.2±10.6	**107.8±3.0**	**108.5±3.1**
I_2	FC(num)	2.1±1.0	**63.3±6.4**	2.9±1.2	**67.0±6.2**	12.7±3.3	5.9±1.8
	FL(msec)	35.4±17.8	**703±64.2**	50.5±21.2	**646.3±72**	154.1±31.7	92.6±22.5
	PS(%)	14.6±6.9	**97.5±5.6**	17.6±7.3	**96.1±6.8**	58.4±11.0	49.1±11.3
I_3	FC(num)	0.5±0.5	0.6±0.6	0.8±0.5	0.3±0.3	1.9±0.9	1.7±0.9
	FL(msec)	9.6±9.6	11.7±11.7	17.2±11.9	6.2±6.2	31.0±15.3	36.8±21.1
	PS (%)	3.6±3.6	3.5±3.5	7.1±4.9	3.4±3.4	14.8±7.0	14.5±6.9
I_4	FC(num)	0.4±0.4	1.2±0.6	**86.9±9.6**	0.4±0.4	3.1±1.1	3.7±1.6
	FL(msec)	9.6±9.6	24.1±11.7	**730±94.2**	8.2±8.2	56.6±18.3	64.3±23.1
	PS (%)	3.2±3.2	13.8±6.5	**91.9±6.3**	3.4±3.4	28.9±8.9	25.3±8.6
SVM	Training (%)	95.5±0.7	93.8±0.9	92.0±0.8	89.8±0.9	96.0±0.7	94.0±0.7
	Test(%)	90.9±0.7	89.7±0.9	88.4±0.7	87.4±0.8	88.4±0.7	90.4±0.9

		Watermelon	Water	Dish	Bread	Cup	Wine
I_1	FC(num)	1.8±0.8	**46.2±4.8**	3.0±1.1	1.7±0.6	1.0±0.7	0.8±0.8
	FL(msec)	36.4±15.4	**543.0±51.8**	60.7±21.9	43.2±16.8	19.9±13.8	9.2±9.2
	PS(%)	20.5±8.6	**110.4±3.0**	29.7±10.2	25.9±9.8	7.0±4.9	4.6±4.6
I_2	FC(num)	2.1±0.9	**40.6±5.2**	2.8±1.1	8.8±1.9	**54.9±6.4**	3.1±1.4
	FL(msec)	46.0±20.0	**438.2±42.4**	51.3±20.0	126.6±22	**773±10.1**	56.8±22.2
	PS(%)	20.3±8.6	**106.9±4.8**	25.4±9.6	63.7±11.3	**103.9±6.2**	23.8±9.0
I_3	FC(num)	3.7±1.4	1.6±0.8	2.9±1.5	**93.5±6.5**	**71.8±6.8**	**71.4±7.1**
	FL(msec)	74.9±27.2	28.2±13.8	39.7±16.7	**681.5±47**	**626±95.4**	**571±40.6**
	PS(%)	26.7±9.2	17.0±8.2	21.0±8.9	**110.0±3.3**	**111.3±3.4**	**110.4±3.5**
I_4	FC(num)	**75.3±5.4**	0.9±0.5	**77.7±6.6**	4.5±1.7	0.3±0.3	0.9±0.7
	FL(msec)	**695.0±70.6**	22.7±12.9	**710±68.8**	71.9±23.2	8.9±8.9	12.3±8.8
	PS(%)	**106.1±2.8**	11.6±6.6	**108.8±2.9**	30.8±9.6	3.5±3.5	8.1±5.7
SVM	Training (%)	98.8±0.4	95.8±0.7	97.5±0.6	98.8±0.4	97.0±0.6	98.3±0.5
	Test(%)	94.4±0.7	93.8±0.8	94.1±0.7	97.5±0.6	96.3±0.2	96.6±0.5

4 Conclusion and Future Works

In this paper, we presented a novel approach for understanding human implicit intent based on hybrid cognitive neural system. The model included endogenous and exogenous attention modules. In a given visual stimulus, the spatial attention model identifies the objects of interest based on the correlation between the salient objects provided by the exogenous model and the gaze information provided by the endogenous model. Each of the identified objects obtained from the spatial attention

model are then classified into intent and non-intent objects based on features such as FL, FC and PS, SVM classifier was used to classify the objects. Experimental results confirmed plausible performance by the proposed system. To verify and enhance the performance of the proposed system, a more thorough investigation based on the experiments using complex natural scenes reflecting various situations are needed. In addition, as a future work, we would like to implement a prototype for human intention monitoring system.

Acknowledgement. This research was supported by the OTRP for Brain Science through the NRF Korea funded by the MEST (2013034988) (50%) and also the CRCP through the Ministry of Science, ICT and Future Planning, Korea (2013K000333) (50%).

References

1. Posner, M.I., Cohen, Y.: Components of visual orienting. In: Boumaand, H., Bouwhuis, D.G. (eds.) Attention and Performance X, pp. 531–556. Erlbaum, Hillsdale (1984)
2. Jansen, B.J., Booth, D.L., Spink, A.: Determining the informational, navigational, and transactional intent of Web queries. Information Processing and Management 44, 1251–1266 (2008)
3. Sungmoon, J., Sang-Woo, B., Minho, L.: Stereo saliency map considering affective factors and selective motion analysis in a dynamic environment. Neural Networks 21(10), 1420–1430 (2008)
4. Eye tracking system of Tobii Technology, `http://www.tobii.com/`
5. Theeuwes, J.: Exogenous and endogenous control of attention - the effect of visual onsets and offsets. Perception & Psychophysics 49(1), 83–90 (1991)
6. Young-Min, J., Mallipeddi, R., Sangil, L., Ho-Wan, K., Minho, L.: Human implicit intent transition detection based on pupillary analysis. In: IEEE International Conference on Neural Networks (IJCNN), Brisbane, Australia, pp. 1–7 (2012)
7. Sang-Jae, P., Kwang-Hwan, A., Minho, L.: Saliency map model with adaptive masking based on independent component analysis. Neurocomputing 49, 417–422 (2002)

Electroencephalogram Dynamics during Social Communication among Multiple Persons

Naoyuki Sato, Taiki Sato, Takeya Okazaki, and Mitsuru Takami

Department of Complex and Intelligent Systems, School of Systems Information Science, Future University Hakodate, 116-2 Kamedanakano-cho, Hakodate-shi, Hokkaido 041-8655, Japan
{satonao,b1009092,b1009088,b1009155}@fun.ac.jp
http://www.fun.ac.jp/~satonao/

Abstract. The brain dynamics of social behavior are important for understanding the group intelligence that occurs in humans. Coordinated behavior between two subjects has been used as an experimental model of social behavior, but the creativity occurring in a group of multiple persons has not yet been discussed. In this study, a rhythmic communication task was proposed as a model of social communication, and simultaneous electroencephalogram (EEG) of three subjects were evaluated. Results showed that the decrease of theta-band power in the EEG was correlated with the rhythm delay in the ensemble pattern, and the decreases of upper and lower alpha-band power were associated with the rhythm tempo and the rareness of ensemble pattern. This suggests that the theta- and alpha-band powers in the EEG associate with social communication and cross-frequency EEG dynamics is essential for understanding the creativity in the social behavior.

Keywords: brain oscillations, electroencephalogram, creativity, social coordination, music, synchronization.

1 Introduction

The brain dynamics of social behavior are important for understanding the group intelligence that emerges between multiple persons; as the saying goes, "two (or more) heads are better than one". Social behavior is thought to include various sub-processes, such as perception, action, emotion etc. [1]; thus, its experimental model is important for the investigation. One model is a coordinated behavior between two subjects. Tognoli et al. (2007) [2] evaluated electroencephalogram (EEG) during an alternative tapping task of two subjects and showed the association between sub-components of EEG alpha power and the social behavior. Moreover, inter-brain synchronization was also shown to increase during coordinated behavior [3]. These studies produced the important clues for understanding the intelligence in social behavior; however, the creativity that can occur in groups of multiple persons has not yet been discussed. Since the neural mechanisms of creativity have been discussed in terms of divergent thinking,

M. Lee et al. (Eds.): ICONIP 2013, Part I, LNCS 8226, pp. 145–152, 2013.
© Springer-Verlag Berlin Heidelberg 2013

artistic performance, and insight [4], some experimental model of creativity in social communication is thought to be important for the understanding of social behavior.

In this study, a rhythmic communication task among multiple persons was proposed and simultaneous EEG signals of three subjects were evaluated. During the task, the subjects used a tapping button to sound a note and they were asked to tap voluntary with listening rhythms of others. Although they were not explicitly asked to produce synchronous or asynchronous tapping, the tap timings of subjects is expected to be intermittently entrained to the group ensemble (see, a review by Repp [5]).Then, the rareness of the ensemble pattern was used to measure the creativity in the rhythmic communication. Moreover, music emotion was shown to be correlated with EEG signals [6,7] and other physiological indices [8]. Multiple regression analysis of EEG signals with these indices was expected to be able to decompose sub-process of creativity in the social behavior.

2 Methods

Twelve subjects with mean age of 21.0 years (ranging from 20 to 22 years; 8 males, 10 right-handed) to part in the experiment after giving informed consent. All of them had no specific experience for musical instruments. The Ethics Committee in Future University approved the experiment.

A rhythmic communication task was performed by a set of three subjects with their eyes closed. Each subject used a keyboard with a single button to sound a note of different tone (528 Hz (C), 660 Hz (E) and 792 Hz (G) with a 100 ms duration). The subjects were asked to tap the button with their right finger voluntary while listening to the rhythms produced by others. Every subject participated in a session of 20 min.

During the task, EEG signals were acquired using two Neuroscan amplifiers (SymAmpI, Neuroscan, Texas, USA) with Ag/AgCl electrodes and a TEAC amplifier (Polymate AP-216, TEAC, Japan) with active electrodes. Electrodes provided 9 EEG channels (F3, Fz, F4, C3, Cz, C4, P3, Pz and P4), an electrooculography (EOG) channel and an electrocardiography (ECG) channel on left wrist. EEG data (0.3-100Hz band pass, 500Hz sampling rate) were referenced to a Fz electrode during measurement and re-referenced to linked-earlobes for analysis.

The following five regressors were considered in the multiple regression analysis of EEG signals. First was the tap interval (TI) of each subject. Second was the smallest shift of tap with others (TS). Preceding and following taps were given by positive and negative values, respectively. Third was the tap pattern information (PI) that was calculated by probability map of tap shifts with two others. This value was thought to associate with creativity in the rhythmic communication. Fourth was the heart beat interval (R-R interval, RRI) that was shown to correlate with the music perception [8]. Last was an index of parasympathetic nervous activity given by heart rate variability (HRV), log(LF/HF) where LF

and HF denotes 0.04-0.15 Hz and 0.15-0.3 Hz component of R-R interval, respectively. This value was shown to correlate with emotion during performance and perception of music [9].

Tapping-related instantaneous frequency-energy characteristics for EEG were calculated with the Morlet wavelet transformation (width=6) from 4 to 20 Hz in 0.5 Hz step. Multiple regression analysis of the logarithmic EEG power at frequency f and time t from the k-th tap timing was performed by using the following equation [10]:

$$E(f,t,k) = \beta_0 + \beta_i(f,t) \sum_{i=1}^{5} R_i(t,k) \quad (1)$$

where R_i denotes value of the low-pass filtered(<1Hz) i-th regressor at time t with the k-th tap timing and β_i is regression slope for the i-th regressor that will be statistically evaluated. Taps with an interval less than 0.5 sec were discarded from the analysis. The comparison was made separately for each electrode, each frequency, and then averaged across all participants. Statistical value was given by $p < 0.001$ with spatial extent of 300 pixels in the frequency-energy map (time bin: 2 ms, spectral bin: 0.5 Hz) without any correction for multiple comparison.

3 Results

Fig.1a shows tap timing of three subjects. Distribution of the tap interval is shown in Fig.1b where average tap interval across all subjects was 0.64 ± 0.20 sec (ranged 0.27-0.91 sec). Tap intervals of three subjects in the same session appeared similarly distributed. Fig.1c shows a cross-correlation of tap sequences between two subjects in the same session, where the tap sequences in two sessions were found significantly synchronous at zero shift but those in the remaining two session were not ($p<0.05$). Fig. 1d-f show three repressors, the tap interval, the tap shift and the tap information. Tap intervals between subjects in the same session was found to be significantly correlated (with 0.5 Hz-sampling, r=0.08 (ranging from -0.04 to 0.16), t-value: 6.42, $p<0.001$).

Fig. 2 shows ECG signals of three subjects in the same session and their R-R interval and heart rate variability. Both of R-R interval and the heart rate variability were found to show significant inter-subject correlation (with 0.5 Hz-sampling, RRI: r=0.11 (ranging from -0.08 to 0.34), t-value:9.32, $p<0.001$; HRV: r=-0.07 (ranging from -0.18 to 0.23), t-value: 5.58, $p<0.001$).

Before applying these regressors to EEG regression analysis, collinearity of these regressors should be evaluated. Variance inflation factor among five regressors were found less than 1.3 indicating that the collinearly was not a problem in the regression analysis. However, correlation between R-R interval and the heart rate variability was found to be ranged widely in comparison to others (Fig. 3). Thus, four regressors except for the heart rate variability were applied to the following regression analysis.

Fig.4 shows EEG signals at a Cz electrode of three subjects in the same session. Fig. 4b shows a time-frequency plot of EEG wavelet power of a subject,

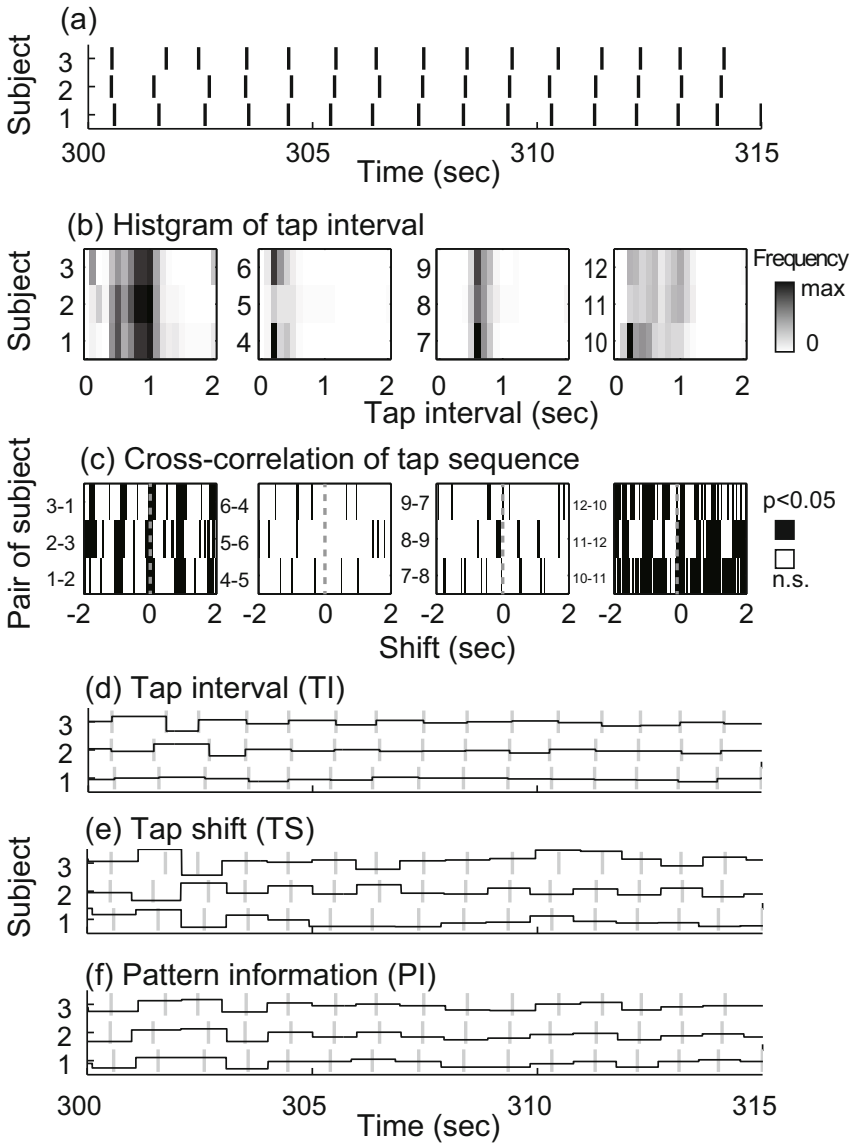

Fig. 1. Result of tap sequences. (a) Tap sequences of three subjects in a session. (b) Distributions of tap interval of each subject. Different map indicates different session. Tap frequency is shown by gray scale. (c) Cross-correlation of tap sequences between two subjects in the same session. Black represents significant correlation defined by the permutation test ($p<0.05$). (d, e, f) Temporal evolution of three kinds of repressors, tap interval (d), tap shift (e), and tap pattern information (f). Vertical lines indicate tap timing of each subject.

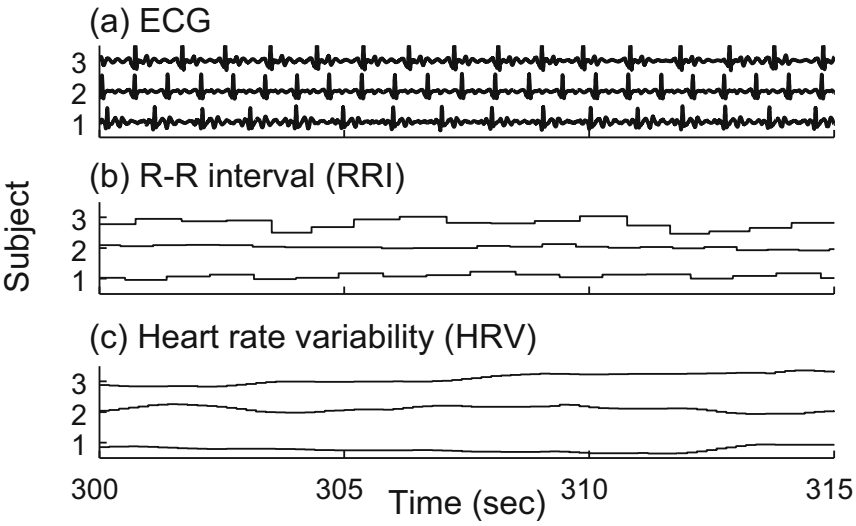

Fig. 2. Result of ECG signals. (a) Temporal evolution of ECG signals of three subjects. (b, c) Temporal evolution of two regressors, R-R interval (b) and heart rate variability (c).

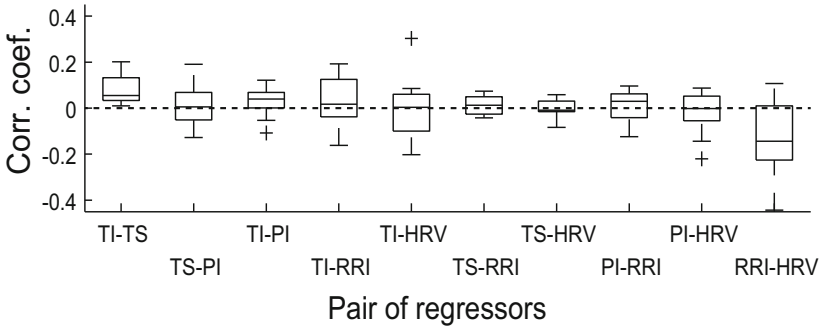

Fig. 3. Correlation coefficient between regressors

where the continuously increase of alpha-band power in EEG and no obvious tap-related change were shown. When the induced EEG power with a baseline of the averaged power from -300 to -200 ms before tapping was calculated, a significant increase of beta-band power was found at the tap timing dominantly in the left hemisphere. Since all tapping were performed with the right index finger, this effect is thought to be a motion-related activity.

Fig. 5 shows result of multiple regression analysis. Tap interval was found to correlate with EEG 12 Hz power where topographic pattern of the statistical value was shown dominantly in the frontal region. Tap shift showed a significant correlation to the EEG 6 Hz power after 250 ms of tap timing. Tap pattern information was found to correlate with EEG 10 Hz power before the tapping. R-

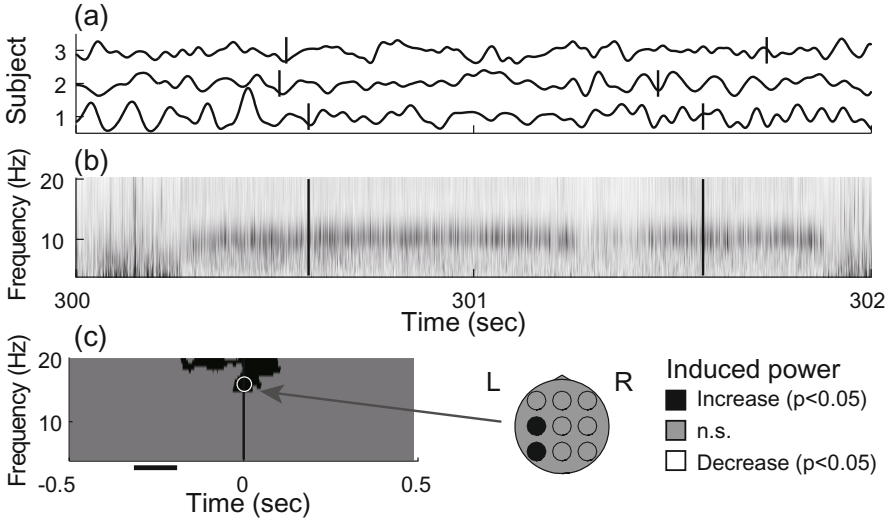

Fig. 4. Result of EEG measurement. (a) Temporal evolution of EEG at a Cz electrode. (b) Time-frequency plot of EEG wavelet power of Subject 1. (c) Induced EEG power of tapping where baseline was given by averaged EEG power from -300 to -200 ms of the tap timing. Black and white indicate significant increase and decrease of EEG power, respectively. Figure in right column shows a topographical map of the statistical value for the induced EEG power.

R interval was shown to significantly correlate with EEG 10 Hz power dominantly in the occipital region. These results indicated that the different aspect of the rhythmic interaction can be associated with different components in the EEG ranging over spectral band and locations in the topographical map.

4 Discussion

Three spectral band powers in the EEG were found to be significantly correlated to regressors that were expected to associate with rhythmic communication (Fig. 6). First, the decreases of lower alpha-band power in the occipital region were shown to associate with the rareness of ensemble pattern. This effect may be thought to associate with creativity during rhythmic communication. However, the desynchronization of occipital alpha is also known to associate with the attention during oddball tasks (see a review by Klimesch (1999) [11]) and social coordination [2]. Second, the decrease of upper alpha-band power in the frontal region was found to associate with the slower tempo of the tapping. Although the desynchronization of upper alpha is thought to be associated with semantic memory [11], the interpretation of the current result is unclear. Third, the decrease of theta-band EEG power in the frontal region was found to correlate with the preceding tap in the ensemble. In the previous reports, the decrease of frontal midline theta was shown to associate

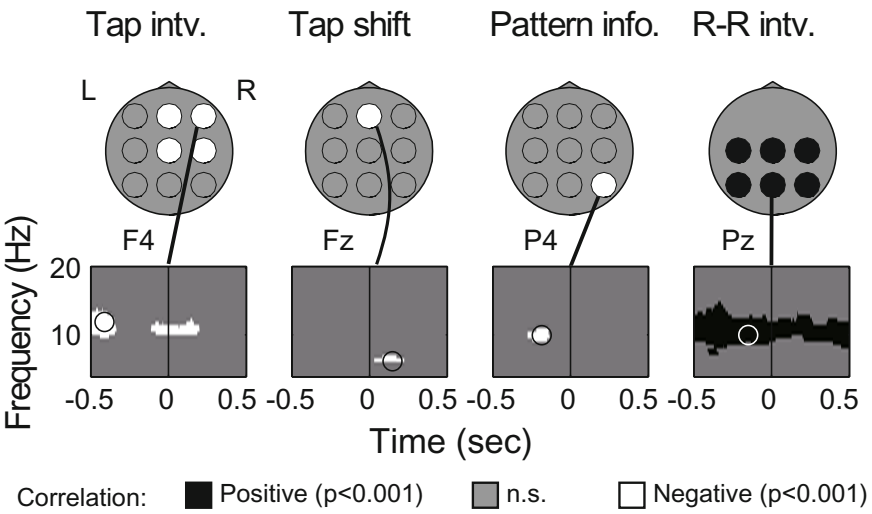

Fig. 5. Result of multiple regression analysis. Upper topographic map shows the statistical values for regression slopes of each regressor, of which time and frequency were chosen by a point in the time-frequency plots of the statistical values showing the largest statistical value over all electrodes. Circle indicates location of each electrode. Black and white indicate positive and negative correlations, respectively. Lower plot shows time-frequency map of the statistical value at an electrode having the largest statistical value.

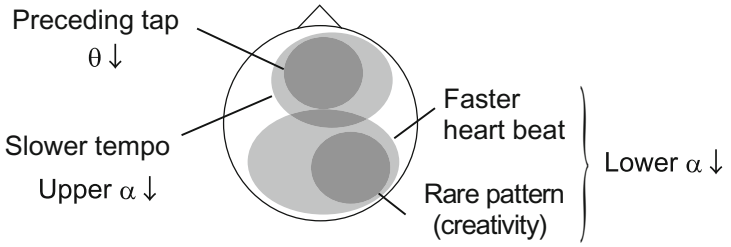

Fig. 6. Summary of the results. Decrease in the upper and lower alpha-band powers and the theta-band power in the EEG over distributed region were found to associate with the rhythmic communication.

with unpleasant music [6], episodic memory encoding [11] and smaller mental effort. The current result may be interpreted as that the preceding tap needed a lower mental effort in comparison to the following tapping.

The current task of rhythmic communication was shown to be useful as a tool for decomposing multiple brain dynamics during the communication. However, there are some concerns that should be improved. First, it may be a problem that the ensemble appeared monotonic and noteless and its tempo was mostly constant (see, Fig. 2b). To induce a more rich and musical ensemble, some explicit

instructions on the individual role in the ensemble may be necessary. Second, the set of regressors was not unique and the regressor associated with creativity should be further explored. In the current study, the tap pattern information was used to measure the rareness of the ensemble pattern, but in the future it should be improved to detect 'creative' ensemble pattern.

In summary, the current results suggest that the multiple aspects of social communication associated with different spectral components in the EEG and the cross-frequency dynamics of the EEG over cortical areas are essential for understanding the creativity during social behavior. As a future study, inter-subject EEG dynamics may be also important for understanding their more detailed roles in social communication.

Acknowledgments. This work was supported by a Grant-in-Aid for Scientific Research on Innovative Areas "Neural creativity for communication (No.4103)" (24120714) of MEXT, Japan.

References

1. Adolphs, R.: Cognitive neuroscience of human social behaviour. Nat. Rev. Neurosci. 4, 165–178 (2003)
2. Tognoli, E., Lagarde, J., DeGuzman, G.C., Kelso, J.A.: The phi complex as a neuromarker of human social coordination. Proc. Natl. Acad. Sci. USA 104, 8190–8195 (2007)
3. Hasson, U., Ghazanfar, A.A., Galantucci, B., Garrod, S., Keysers, C.: Brain-to-brain coupling: a mechanism for creating and sharing a social world. Trends Cogn. Sci. 16, 114–121 (2012)
4. Dietrich, A., Kanso, R.: A review of EEG, ERP, and neuroimaging studies of creativity and insight. Psychol. Bull. 136, 822–848 (2010)
5. Repp, B.H.: Sensorimotor synchronization: a review of the tapping literature. Psychon. Bull. Rev. 12, 969–992 (2005)
6. Sammler, D., Grigutsch, M., Fritz, T., Koelsch, S.: Music and emotion: electrophysiological correlates of the processing of pleasant and unpleasant music. Psychophysiology 44, 293–304 (2007)
7. Schmidt, L.A., Trainor, L.J.: Frontal brain electrical activity (EEG) distinguishes valence and intensity of musical emotions. Cognition and Emotion 15, 487–500 (2001)
8. Krumhansl, C.L.: An exploratory study of musical emotions and psychophysiology. Can. J. Exp. Psychol. 51, 336–353 (1997)
9. Nakahara, H., Furuya, S., Obata, S., Masuko, T., Kinoshita, H.: Emotion-related changes in heart rate and its variability during performance and perception of music. Ann. New York Acad. Sci. 1169, 359–362 (2009)
10. Jacobs, J., Hwang, G., Curran, T., Kahana, M.J.: EEG oscillations and recognition memory: theta correlates of memory retrieval and decision making. NeuroImage 32, 978–987 (2006)
11. Klimesch, W.: EEG alpha and theta oscillations reflect cognitive and memory performance: a review and analysis. Brain Res. Brain Res. Rev. 29, 169–195 (1999)

Amygdala Activation Is Associated with Sense of Presence during Viewing 3D-surround Cinematography

Akitoshi Ogawa, Cecile Bordier, and Emiliano Macaluso

Santa Lucia Foundation, Neuroimaging Laboratory, via Ardeatina 306
00179 Rome, Italy
{a.ogawa,c.bordier,e.macaluso}@hsantalucia.it
http://www.slneuroimaginglab.com/

Abstract. Cinematographic stimuli have been previously used to probe functional mapping of naturalistic stimuli, leaving whether such stimuli are also associated with a subjective increase of the sense of presence (SoP). In this functional magnetic resonance imaging, we investigated whether the SoP evaluation of 3D-surround cinematographic stimuli was associated with any change of activity within emotion-related areas, in particular the amygdala. The subjects evaluated several scenes of a commercial 3D movie presented in four different conditions: 3D vision with surround sounds (3D-Surround), 2D-Surround, 3D-Mono, and 2D-Mono. The behavioral results showed that the stereoscopic viewing, but not surround sound, increased SoP scores. The whole-brain imaging results showed that the middle occipital gyrus was involved in evaluating the SoP. The planned anatomical ROI analysis showed that also activity in the right amygdala increased with increasing SoP scores. The results suggest that 3D vision enhances the SoP and this is associated with activation of both visual cortex and emotion-related brain region.

Keywords: stereoscopy, surround sounds, sense of presence, functional MRI.

1 Introduction

Previous human brain imaging studies used cinematography to track dynamic changes of specific visual and auditory features (e.g. motion, loudness) [1-3]. Functional imaging using such naturalistic stimuli can help us to corroborate the findings of traditional laboratory paradigms that employ well-controlled but simple and stereotyped stimuli. Studies with naturalistic stimuli can help extending the results of standardized paradigms to ecologically-valid situations more similar to real life [4].

Stereoscopic vision contributes to representing the spatial layout of elements in complex visual scenes. Related to this, surround sounds can provide us with rich, multi-sources auditory scenes and enhance spatial perception. The spatial coherence between visual and auditory signals can further enhance the awareness of three-dimensional space and of being in a scene (e.g. sense of presence (SoP) [5]). In addition, previous studies showed that higher-level signals (e.g. emotional content) can also influence the SoP [6, 7], suggesting a possible association between SoP and brain activity within emotion-related regions (e.g. amygdala, see [8, 9]).

M. Lee et al. (Eds.): ICONIP 2013, Part I, LNCS 8226, pp. 153–160, 2013.
© Springer-Verlag Berlin Heidelberg 2013

In this functional magnetic resonance imaging (fMRI) study, we investigated the neural correlates of the SoP appraisal associated with audio-visual 3D-surround stimuli. Participants viewed short clips extracted from a commercial 3D movie. In different trials, the stimuli were shown with stereoscopic 3D or standard 2D vision, and with surround or monaural audition. After each clip, participants were asked to give score about their subjective SoP on that trial (Fig. 1A). We asked whether complex (3D- and/or surround-) stimuli would affect the SoP appraisal, and whether this would correlate with activity of emotion-related areas; e.g. the amygdala [8, 9] that previous studies associated with SoP [6, 7]. We performed a planned anatomical ROI analysis on the amygdale, as well as the whole-brain analysis.

2 Materials and Methods

2.1 Subjects

Sixteen Italian subjects (aged 21 – 39, mean = 27.3 years, 12 females and 4 males) with no history of neurological or psychiatric illness participated in this study. They had normal or corrected-to-normal visual acuity and reported no difficulty of hearing. They gave written informed consents prior to the experiment. The ethical committee of Santa Lucia Foundation has approved this study.

2.2 Stimuli and Task

The participants were presented with short movie segments, extracted from the 3D Italian version of The Three Musketeers (Constantin Film, Frankfurt, Germany). The clips were presented in qHD resolution with the frame rate of 24 Hz. We used three different movie segments / clips, each with a duration of 10.4 s. Each of the segments was presented in four different conditions, including: 3D-Surround, 3D-Mono, 2D-Surround, and 2D-Mono. The order of conditions was counterbalanced across the subjects using a balanced Latin square. On each trial, subjects were asked to watch/listen to the clip and to score the SoP on a 5-points Likert scale, within 8.32 s after the end of the clip (Fig. 1A).

Stimulus presentation was controlled using the psychophysics toolbox [10] running on Matlab (Mathworks, Inc.). The video-clips were presented using an LCD projector (NEC Corp., NP216G) operating at 120 Hz and synchronized with a linear polarizer (DepthQ®, Lightspeed Design Inc.). The subjects wore a MR-compatible passive 3D eyewear that allowed them to perceive stereoscopic vision in the 3D conditions. The sounds were delivered using a multi-speakers system constructed ad-hoc for surround presentation in the MR scanner, together with the mono sound delivered via standard MR-compatible headphones.

2.3 Image Acquisition

A Siemens Allegra (Siemens Medical Systems, Erlangen, Germany) 3T scanner equipped for echo-planar imaging (EPI) was used to acquire functional magnetic resonance images. A head-sized quadrature volume coil was used for radio frequency

transmission and reception. Mild cushioning minimized head movement. Thirty-two slices of functional images were acquired using blood oxygenation level dependent imaging (192 mm × 192 mm × 120 mm, in-plane resolution = 64 × 64, pixel size = 3 mm × 3 mm, thickness = 2.5 mm, 50% distance factor, TR = 2.08 s, TE = 30 ms), covering the entire cerebrum. We acquired 116 scans in this task. The first four scans were discarded to ensure magnetization equilibrium.

2.4 fMRI Analyses

We used SPM8 (Wellcome Department of Cognitive Neurology, University College London) on Matlab to process the acquired images. In preprocessing, we performed slice-timing collection, realignment, normalization to the EPI template of SPM8 and spatial smoothing (FWHM = 8 mm). High-pass filters of 128 s were used to remove low frequency noise.

First, we performed a 2×2 within-subject ANOVA with 4 conditions given by the crossing of "vision" (3D/2D) and "audition" (Surround/Mono). Non-sphericity correction was used to account for any unequal variance between conditions and correlated repeated-measures [11]. Within this model we assessed the main effects of 3D vision and surround audition, plus any interaction between the two. The whole-brain threshold was set to p-FWE-corr. = 0.05 at the cluster-level, after applying a voxel-level threshold of p-unc. = 0.001 to find activated clusters.

In a separate analysis, we used a regression approach to further investigate brain activity that correlated with the SoP evaluation scores. For this, the subject-specific "1-st level analyses" included a single condition-regressor, which was modulated according to the individual SoP evaluation scores measured on each and every trial. At the group level, we assessed the modulatory effect using a one-sample t-test. We performed a whole-brain analysis, as well as a more targeted analysis that considered specifically the amygdale (cf. [5, 12-13]). For this, the parameter estimates associated with the SoP scores were extracted and averaged over voxels, using the MarsBaR toolbox [14]. P-values were corrected for the number of ROIs (i.e. 2, left and right amygdale) using with Bonferroni correction.

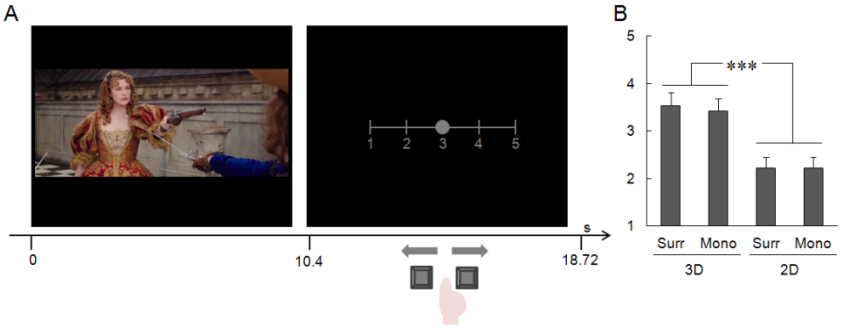

Fig. 1. A. Schematic illustration of one trial. The subject watched a 10.4 s movie-clip and evaluated the SoP on the 5-point Likert scale. For the evaluation, the subject pushed two buttons to left/right move the visual indicator. B. The behavioral data of the SoP evaluation. The graph shows the average SoP scores (± s.e.m.). The subjects scored higher for 3D than for 2D. Error bars are standard error. ***$p < 0.001$.

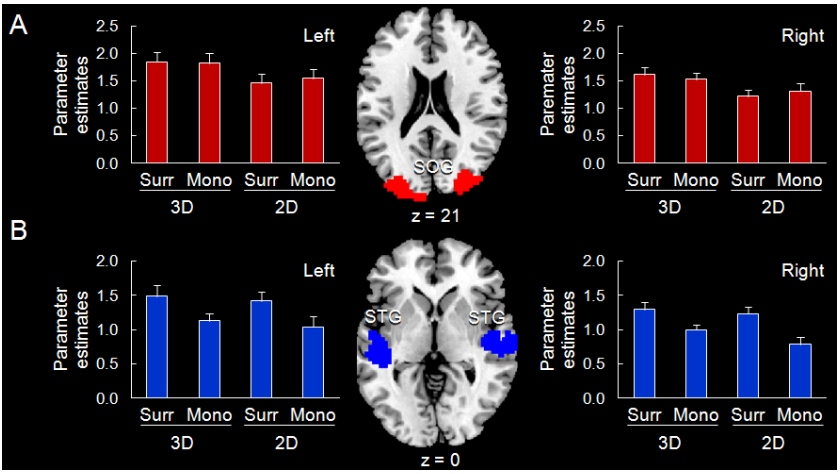

Fig. 2. A. The activation of SOG in the contrast of "3D > 2D" is shown on coronal and axial sections. Parameter estimates for the SOG cluster are shown on each side, with activity plotted separately in the four conditions. Error bars are standard errors. B. The activation of STG for the contrast "Surround > Mono" sounds is shown on an axial section. The signal plots show the parameter estimates in the four conditions. Error bars are standard errors.

3 Results

3.1 Behavioral Result

The subjects were asked to evaluate the SoP of short video-clips using a 5-points Likert scale (Fig. 1A). Each of the clip was presented four times, with different viewing/listening conditions. The results of the repeated-measures ANOVA with the factors of "vision" (3D/2D) × "audition" (Surround/Mono) showed that the 3D viewing, but not surround sound, significantly augmented the SoP ($F(1, 15) = 30.2$, $p < 0.001$, Fig. 1B), without any interaction between the two modalities.

Table 1. Summary of brain activation in the whole brain analysis

Contrast/Regions		MNI coordinates of peak			*z*-score (peak)	*p*-value (cluster)	Number of voxels
		X	*y*	*z*			
3D > 2D							
Left	SOG	–24	–96	20	4.22	0.007	158
Right	SOG	33	–87	23	5.25	< 0.001	394
Left	PCG	–42	–33	68	4.93	< 0.001	371
Right	Cerebellum	24	–54	–28	4.05	0.023	117
Surr > Mono							
Left	STG	–48	–24	2	4.22	0.001	209
Right	STG	48	–15	–1	4.67	0.002	231

3.2 Imaging Results

The contrast comparing "3D > 2D" stimuli showed activation of the superior occipital gyrus (SOG, Fig. 2A), consistent with previous studies of stereoscopy [15-17]. In addition, we observed the activation in the post-central gyrus (PCG) and the cerebellum (Table 1). The surround sounds activated the superior temporal gyrus (STG) including the Heschl's gyri and planum temporale (PT, see Fig. 2B). The anatomical classification of the surround-effect confirmed that the functional activation comprised TE sub-regions on the posterior part of auditory cortex (Table 2).

We used trial-by-trial parametric analyses to further assess the relationship between stimulus processing and SoP. At the whole-brain level, this showed that activity in the middle occipital gyrus increased linearly with increasing SoP scores (see Fig. 3), consistent with the results of the ANOVA showing an effect of 3D in dorso-lateral occipital cortex, cf. Table 1 and Fig. 2A.

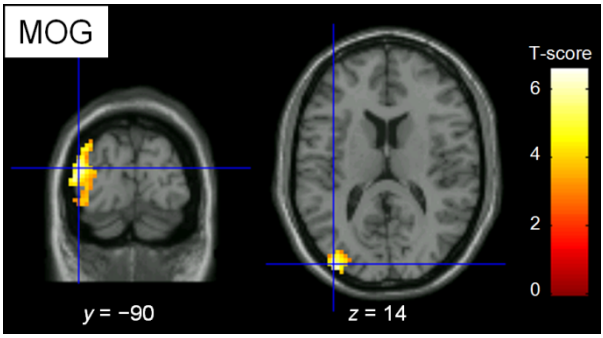

Fig. 3. The activation of the left MOG observed in the parametric analysis using SoP scores. The peak in MNI coordinates was (x = −39, y = −90, z = 14) with z-score = 4.37. The cluster size was 140. The cluster level p-FWE-corr. = 0.007.

Table 2. The classification of auditory activation using SPM anatomy toolbox [18]

	Left			Right		
Surr > Mono	TE1.0	TE1.1	TE1.2	TE1.0	TE1.1	TE1.2
	26.0%	60.2%	3.9%	39.9%	24.1%	3.7%

Next we performed the ROI analysis considering specifically the BOLD responses in the amygdalae. The results showed that the activity of the right amygdala was significantly associated with the SoP score ($t(15) = 2.31$, p-corr. < 0.05, Fig. 4), while no such effect was detected in the left amygdala ($t(15) = 1.16$, p-corr. > 0.1).

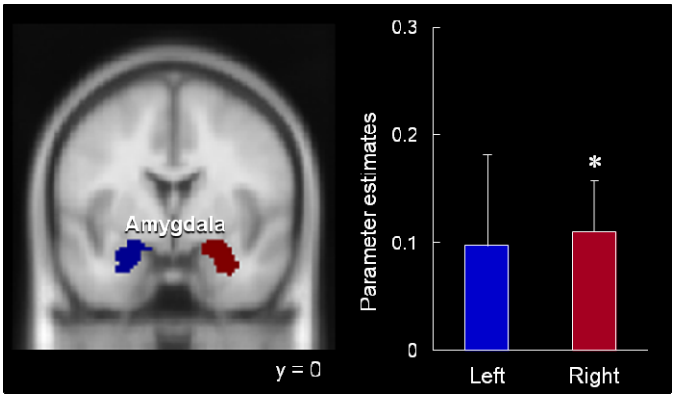

Fig. 4. The effect of SoP scores in the right amygdala. The panel on the left shows the anatomical-defined ROIs on the coronal section (y = 0). The right panel shows the parameter estimates associated with the SoP, extracted and averaged separately for the two ROIs. A significant effect (*) was observed in the right amygdala, but not in the left amygdala. Error bars are standard errors.

4 Discussion

We investigated the neural correlates of subjective SoP using complex audiovisual stimuli. Behavioral data showed that stereoscopic 3D based on binocular disparity was psychologically effective in increasing the SoP of the scene. Consistent with the previous studies, we confirmed that stereoscopic images activated dorso-lateral occipital visual areas, probably including area V3A [17, 19]. A regression analysis using trial-specific SoP scores revealed that activity in the middle occipital gyrus co-varied with subjective SoP. In addition, a more targeted analysis of activity in the amygdale revealed an effect of SoP in the right hemisphere only (Fig. 4). By contrast, surround sounds did not affect the SoP judgment. At the neutral level, the processing of surround sounds was associated with activation of the superior temporal gyrus, including the primary auditory cortex and the planum temporale.

Although we did not measure any autonomic response (e.g. skin conductance), the effect of SoP in right amygdala suggests an impact of stereoscopic viewing on the emotional response to the complex visual stimuli. Previous studies showed that movies evoking the emotion of fear (e.g. cliff, roller coaster) enhanced the SoP [6]. Here, the behavioral data measured during scanning highlighted that stereoscopic 3D viewing enhanced the SoP. Taken together behavioral and imaging data suggest that 3D viewing enhances the SoP through the evoking of emotional experience in right amygdala.

The presentation of 3D images lead to an increase of the SoP scores in this study, while previous studies reported controversial results [13, 20]. This may be due to the many factors that contribute to spatial perception in complex visual scenes. For example, together with binocular disparity, the in-depth spatial layout of objects can be obtained because of motion parallax. Further, 3D structure-from-motion also

constitutes a possible source of complex visuo-spatial signals, also traditionally associated with activation of the occipital-parietal cortex [21-23]. Indeed, the simultaneous presentation with both binocular disparity and visual motion evokes the stronger and more accurate 3D perception than either depth cues presented alone [24]. All these static and dynamic factors are likely to contribute to the elevated SoP scores and the increased activation in dorso-lateral occipital cortex that we found here in the 3D viewing conditions.

The surround sounds provided our subjects with spatially rich (multi-sources) auditory input. The imaging data showed that this was associated with activation of the posterior auditory cortex and the planum temporale, consistent with the role of these regions in auditory spatial processing [25]. Unexpectedly, this auditory manipulation did not influence the SoP evaluation scores. Thus, the auditory spatial information presented in this study was psychologically less influential to the SoP evaluation than 3D vision. This may indicate some segregation of visual and auditory spatial processing in the current context, as also evidenced by the lack of any significant interaction between the two modalities. Nonetheless, future studies we seek using audio-visual stimuli entailing a more explicit spatial correspondence / relationship between the two modalities, which may reveal stronger interactions between the two senses and/or some influence of sounds-spatiality on SoP.

In conclusion, our findings showed that the occipital cortex - putatively including V3A/B - was involved in the SoP evaluation, in parallel with the behavioral results that the stereoscopic viewing lead to an augmented SoP. Moreover, the right amygdala was also associated with SoP. We suggest that stereoscopic viewing increased the subjective SoP, via enhanced scene processing in emotion-related brain areas.

References

1. Bartels, A., Zeki, S.: Functional brain mapping during free viewing of natural scenes. Hum. Brain Mapp. 21, 75–85 (2004)
2. Bartels, A., Zeki, S., Logothetis, N.K.: Natural vision reveals regional specialization to local motion and to contrast-invariant, global flow in the human brain. Cereb. Cortex 18, 705–717 (2008)
3. Bordier, C., Puja, F., Macaluso, E.: Sensory processing during viewing of cinematographic material: Computational modeling and functional neuroimaging. Neuroimage 67, 213–226 (2013)
4. Rust, N.C., Movshon, J.A.: In praise of artifice. Nat. Neurosci. 8, 1647–1650 (2005)
5. Sanchez-Vives, M.V., Slater, M.: From presence to consciousness through virtual reality. Nat. Rev. Neurosci. 6, 332–339 (2005)
6. Regenbrecht, H., Schubert, T., Friedmann, F.: Measuring the sense of presence and its relations to fear of heights is virtual environments. Int J. Hum.-Comput. Int. 10, 233–249 (1998)
7. Baumgartner, T., Speck, D., Wettstein, D., Masnari, O., Beeli, G., Jäncke, L.: Feeling present in arousing virtual reality worlds: prefrontal brain regions differentially orchestrate presence experience in adults and children. Front Hum. Neurosci. 2, 8 (2008)
8. Adolphs, R., Tranel, D., Damasio, H., Damasio, A.R.: Fear and the human amygdala. J. Neurosci. 15, 5879–5891 (1995)

9. Lanteaume, L., Khalfa, S., Régis, J., Marquis, P., Chauvel, P., Bartolomei, F.: Emotion induction after direct intracerebral stimulations of human amygdala. Cereb. Cortex 17, 1307–1313 (2007)
10. Brainard, D.H.: The Psychophysics Toolbox. Spat. Vis. 10, 433–436 (1997)
11. Friston, K.J., Glaser, D.E., Henson, R.N., Kiebel, S., Phillips, C., Ashburner, J.: Classical and Bayesian inference in neuroimaging: applications. Neuroimage 16, 484–512 (2002)
12. Chiao, J.Y., Iidaka, T., Gordon, H.L., Nogawa, J., Bar, M., Aminoff, E., Sadato, N., Ambady, N.: Cultural specificity in amygdala response to fear faces. J. Cogn. Neurosci. 20, 2167–2174 (2008)
13. Ijsselsteijn, W., de Ridder, H., Freeman, J., Avons, S.E., Bouwhuis, D.: Effects of Stereoscopic Presentation, Image Motion, and Screen Size on Subjective and Objective Corroborative Measures of Presence. Presence 10, 298–311 (2001)
14. Brett, M., Anton, J.-L., Valabregue, R., Poline, J.-B.: Region of interest analysis using an SPM toolbox. Annual Meeting of Organization for Human Brain Mapping. Sendai Japan (2002)
15. Tootell, R.B., Mendola, J.D., Hadjikhani, N.K., Ledden, P.J., Liu, A.K., Reppas, J.B., Sereno, M.I., Dale, A.M.: Functional analysis of V3A and related areas in human visual cortex. J. Neurosci. 17, 7060–7078 (1997)
16. Tsao, D.Y., Vanduffel, W., Sasaki, Y., Fize, D., Knutsen, T.A., Mandeville, J.B., Wald, L.L., Dale, A.M., Rosen, B.R., Van Essen, D.C., Livingstone, M.S., Orban, G.A., Tootell, R.B.: Stereopsis activates V3A and caudal intraparietal areas in macaques and humans. Neuron 39, 555–568 (2003)
17. Neri, P., Bridge, H., Heeger, D.J.: Stereoscopic processing of absolute and relative disparity in human visual cortex. J. Neurophysiol. 92, 1880–1891 (2004)
18. Eickhoff, S.B., Stephan, K.E., Mohlberg, H., Grefkes, C., Fink, G.R., Amunts, K., Zilles, K.: A new SPM toolbox for combining probabilistic cytoarchitectonic maps and functional imaging data. Neuroimage 25, 1325–1335 (2005)
19. Anzai, A., DeAngelis, G.C.: Neural computations underlying depth perception. Curr. Opin. Neurobiol. 20, 367–375 (2010)
20. Baños, R.M., Botella, C., Rubió, I., Quero, S., García-Palacios, A., Alcañiz, M.: Presence and emotions in virtual environments: the influence of stereoscopy. Cyberpsychol. Behav. 11, 1–8 (2008)
21. Paradis, A.L., Cornilleau-Pérès, V., Droulez, J., Van De Moortele, P.F., Lobel, E., Berthoz, A., Le Bihan, D., Poline, J.B.: Visual perception of motion and 3-D structure from motion: an fMRI study. Cereb. Cortex 10, 772–783 (2000)
22. Paradis, A.L., Droulez, J., Cornilleau-Pérès, V., Poline, J.B.: Processing 3D form and 3D motion: respective contributions of attention-based and stimulus-driven activity. Neuroimage 43, 736–747 (2008)
23. Vanduffel, W., Fize, D., Peuskens, H., Denys, K., Sunaert, S., Todd, J.T., Orban, G.A.: Extracting 3D from motion: differences in human and monkey intraparietal cortex. Science 298, 413–415 (2002)
24. Ban, H., Preston, T.J., Meeson, A., Welchman, A.E.: The integration of motion and disparity cues to depth in dorsal visual cortex. Nat. Neurosci. 15, 636–643 (2012)
25. Alink, A., Euler, F., Kriegeskorte, N., Singer, W., Kohler, A.: Auditory motion direction encoding in auditory cortex and high-level visual cortex. Hum. Brain Mapp. 33, 969–978 (2012)

Correlated Inhibitory Firing and Spike-Timing-Dependent Plasticity

Ichiro Sakurai[1,*], Shigeru Kubota[2], and Michio Niwano[1]

[1] Research Institute of Electrical Communication, Tohoku University, Laboratory for Nanoelectronics and Spintronics, Japan
{i_sakurai,niwano}@riec.tohoku.ac.jp
[2] Graduate School of Science and Engineering, Yamagata University, Japan
kubota@yz.yamagata-u.ac.jp

Abstract. Cortical inhibition by γ-aminobutyric acid (GABA) has been widely suggested to be required to trigger ocular dominance (OD) plasticity in the visual cortex. However, there is also evidence that only the circuits mediated by specific $GABA_A$ receptors can induce OD plasticity, which implies the importance of localized GABA circuits in this process. In this study, to investigate the role of local inhibition in visual plasticity, we simulated the synaptic dynamics regulated by lateral and backward inhibition. The lateral inhibition facilitated competitive interactions between different groups of excitatory correlated inputs, which were required to elicit experience-dependent synaptic modifications. Conversely, the backward inhibition suppressed such competitive interactions, which prevented synapses from reflecting past sensory experience. Our results suggest that the interactions between lateral and backward inhibition may regulate the timing and level of cortical plasticity by modulating the activity-dependent competitive function.

Keywords: STDP, GABA inhibition, Firing correlation, Synaptic competition, Visual cortex.

1 Introduction

The closure of one eye during a postnatal critical period shifts the response properties of visual cortical cells to favor the inputs from the open eye [1]. Experimental evidence has suggested that this ocular dominance (OD) plasticity may be induced by cortical inhibition mediated by GABA [2-7]. When the development of GABA function is suppressed by the selective deletion of an isoform of the GABA synthetic enzyme, the onset of OD plasticity is delayed until inhibition is pharmacologically restored [2]. Similarly, OD plasticity can be prematurely triggered by the pharmacological enhancement of GABAergic function [3]. These observations suggest that there is a threshold inhibition level required for the induction of OD plasticity.

* Corresponding author.

M. Lee et al. (Eds.): ICONIP 2013, Part I, LNCS 8226, pp. 161–167, 2013.
© Springer-Verlag Berlin Heidelberg 2013

However, there is also evidence that not all GABA functions are involved in controlling OD plasticity [7]. By employing a knockin mutation to α subunits that render $GABA_A$ receptors (GABAARs) insensitive to benzodiazepines, it has been demonstrated that GABA circuits mediated by only α1-containing receptors can elicit visual plasticity [6]. Considering that GABAARs containing the α1 subunits are mainly located at somatic synapses that receive inputs from parvalbumin (PV)-positive cells [7, 8], the local inhibitory pathways mediated by PV cells might be highly involved in plasticity.

To study the role of localized inhibition in cortical plasticity, we simulated a neuron receiving two groups of correlated inputs, as in a visual cortical cell receiving inputs from both eyes, and compared the effects of lateral vs. backward inhibition on the synaptic dynamics with spike-timing-dependent plasticity (STDP) [9, 10].

2 Methods

We construct a simplified model of a visual cortical cell to compare the effects of local inhibition on synaptic dynamics, as shown in Fig. 1. A postsynaptic cell is described by using an integrate-and-fire neuron. The neuron receives random inputs from 1000 excitatory and 200 inhibitory synapses. To simulate sensory inputs from two eyes to a visual cortical cell, the excitatory synapses are assumed to consist of two equally sized groups [11].

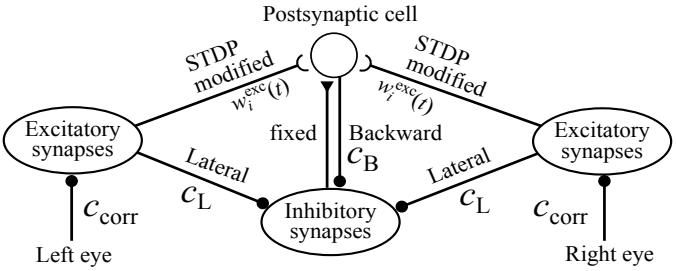

Fig. 1. Simulation model network

2.1 Neural Model

Excitatory and inhibitory synaptic currents are described as a conductance-based model [12]. The conductances of the excitatory and inhibitory synapses obey $g_{exc}(t) = g^{max}_{exc}\, w_{exc}{}^{i}(t)\, \exp(-t/\tau_{exc})$, $g^{inh}(t) = g^{max}_{inh}\, (e/\tau_{inh})\, t\, \exp(-t/\tau_{inh})$, respectively. g^{max}_{exc} and g^{max}_{inh} are maximum conductance. τ_{exc} and τ_{inh} are time constant of synaptic current. $w_{exc}{}^{i}(t)$ is the weight of each excitatory synapse and temporally modified by STDP (see below).

2.2 Poisson Input Model

We assume that each group of excitatory synapses receives correlated inputs resulting from the activities of the retinal ganglion cells in each eye. Furthermore, we introduce the lateral and backward connections to activate the inhibitory synapses, as shown in Fig. 1. There is evidence that, under sufficiently strong noisy conditions, as in the *in vivo* state, the postsynaptic firing probability is approximately proportional to the summation of the postsynaptic potentials (PSPs) [13]. Therefore, we assume that the activation times of all of the presynaptic inputs are described by simple non-stationary Poisson processes, the rate of which depends on the PSPs [14].

With this assumption, the instantaneous firing rate of the two groups of excitatory synapses ($r^{exc}{}_1(t)$ and $r^{exc}{}_2(t)$) and that of inhibitory synapses ($r^{inh}(t)$) are described as

$$r_i^{exc}(t) = c_{corr} \sum_f \varepsilon(t - t_I^f) + r_{uncorr}^{exc} \quad (i = 1, 2), \tag{1}$$

$$r^{inh}(t) = \frac{c_L}{n_{exc}} \sum_i \sum_f \varepsilon(t - t_{exc,i}^f) + c_B \sum_f \varepsilon(t - t_{post}^f) + r_{uncorr}^{inh} \tag{2}$$

Here, $\varepsilon(t)$ is a function that describes the time course of PSPs, and $\varepsilon(t) = (t/\tau_e{}^2)e^{-t/\tau e}$ for $t > 0$ and $\varepsilon(t) = 0$ otherwise. In Eq. (1), $t^f{}_I$ denotes the arrival time of the fth spike to the ith group of excitatory synapses from retinal ganglion cells, and $t^f{}_I$ is determined with a homogeneous Poisson process with a frequency of r_{inp} (= 5 Hz). The spike arrival times for the two groups are independent, and therefore, the activities of the different groups are uncorrelated to each other. The parameter c_{corr} is to decide the strength of the input correlation for each group, and $r^{exc}{}_{uncorr}$ is a component of the activation rate corresponding to the uncorrelated firing. In Eq. (2), $t^f{}_{exc,\ i}$ and $t^f{}_{post}$ represent the fth firing time of the ith excitatory synapse and the postsynaptic cell, respectively. Thus, c_L and c_B determine the strength of the lateral and backward inhibition, respectively (Fig. 1). n_{exc} is the number of excitatory synapses, and $r^{inh}{}_{uncorr}$ represents the activation rate of the uncorrelated firing of the inhibitory synapses.

2.3 Synaptic Inputs and Modification

STDP is assumed to act on all the excitatory synapses that converge on a postsynaptic cell (Fig. 1). With the time lag Δt between the pre- and postsynaptic spikes, the change in the synaptic efficacy Δw by STDP is described as

$$\text{if a pre or postsynaptic cell fires, } w_i^{exc}(t) \to w_i^{exc}(t) + \Delta w,$$
$$\Delta w = \begin{cases} A_+ e^{-\Delta t/\tau_+}, & \text{for } \Delta t > 0, \\ -A\_e^{\Delta t/\tau_-}, & \text{for } \Delta t < 0, \\ 0, & \text{for } \Delta t = 0. \end{cases} \tag{3}$$

Here, A_+ and A_- denote the size of long-term potentiation (LTP) and long-term depression (LTD), respectively. τ_+ and τ_+ determines the temporal width of the STDP curve. We simply assume that the amounts of STDP by all of the spike pairs are linearly summed and that the upper bounds $w_{\max}$ and lower bounds $w_{\min}$ limit the magnitude of the synaptic weights [11, 12].

2.4 Estimation of Competition

To estimate synaptic competition intensities, we obtained averaged excitatory synaptic weights of all 1000 synapses and each excitatory synapse group,

$$< w_1 >= \sum_{i=1}^{500} w_i^{exc}(t), \quad < w_2 >= \sum_{i=501}^{1000} w_i^{exc}(t), \quad < w >= \sum_{i=1}^{1000} w_i^{exc}(t). \tag{4}$$

Then we redefined $<w_1>$ and $<w_2>$ as their magnitude,

$$\begin{aligned} (< w_1 >, < w_2 >) &= (< w_L >, < w_S >), \text{ if } < w_1 > \; > \; < w_2 >, \\ (< w_2 >, < w_1 >) &= (< w_L >, < w_S >), \text{ if } < w_2 > \; > \; < w_1 >. \end{aligned} \tag{5}$$

In the present work we particularly focused on the ratio between $<w_L>$ and $<w_S>$. When the ratio $<w_L>/<w_S>$ is larger than 2, we regard that competition is strong.

3 Results

In order to explore the role of local inhibitory pathways, we first simulated synaptic modification dynamics during an experiment with monocular deprivation (MD), which was followed by reverse suture of the other eye (Fig. 2) [15]. The OD shift caused by MD has been shown to rely on the difference in the temporal correlations of retinal afferent activities rather than on the difference in the input activity levels between the two eyes [16, 17]. Therefore, we incorporated the effects of MD by decreasing the strength of the correlation (c_{corr}) for the input group that corresponded to the deprived eye.

Figure 2A (left column) shows the time course of the average weights of the two groups $<w_1>$ and $<w_2>$ with neither lateral nor backward inhibition. Here, the excitatory synapses of both groups were initially activated by the same input correlation ($c_{\text{corr}} = 0.6$). For the first period of MD (200 ks < t < 400 ks; black arrow), the input correlation of $<w_L>$ group at 200 ks was removed by decreasing c_{corr} to 0. The input correlation of this group was recovered after the termination of the first MD at 400 ks. In contrast, the correlation of the other group was eliminated for 600 ks < t < 800 ks (black arrow), which corresponded to the reverse suture (second MD). Both groups maintained input correlation after t > 800 ks. The figure shows that, during MD, the group whose input correlation had been removed was strongly weakened so that the non-deprived group became dominant, as has been shown in many experiments (e.g., [1]). However, following the termination of MD, both of the groups rapidly converged to a state where the average weights fluctuated irregularly with

nearly the same levels as each other. Furthermore, the temporal average of the weight distributions of the two groups did not significantly differ after each period of MD, which means that the synaptic pattern cannot reflect which group has received MD.

However, when lateral inhibition was incorporated (Fig. 2B), either group became dominant, even in the absence of MD, suggesting the involvement of competitive interactions between the different groups [18]. Following the first period of MD, the group that had received deprivation was maintained weak, while the group that had not received deprivation was maintained strong. Furthermore, the switching between the dominant and recessive groups occurred by the second MD, and the result of switching was maintained even after the termination of this period of MD. Thus, the weight distributions after each period of MD (Fig. 2B, right two figures) clearly reflected which input group had received deprivation during a recent period of MD. The comparison between Figs. 2A and 2B shows that past sensory experience can be embedded into synaptic patterns only in the presence of the competitive interactions by the lateral inhibition. Importantly, such experience-dependent synaptic modifications disappeared again when a weak level of backward inhibition was additionally introduced (Fig. 2C). In Fig. 2C, as in the case of neither lateral nor backward inhibition (Fig. 2A), the weight distributions of the two groups converged to be nearly the same after the end of MD (Fig. 2C, right two figures), and, therefore, the synaptic weights could not retain the information about the past input experience.

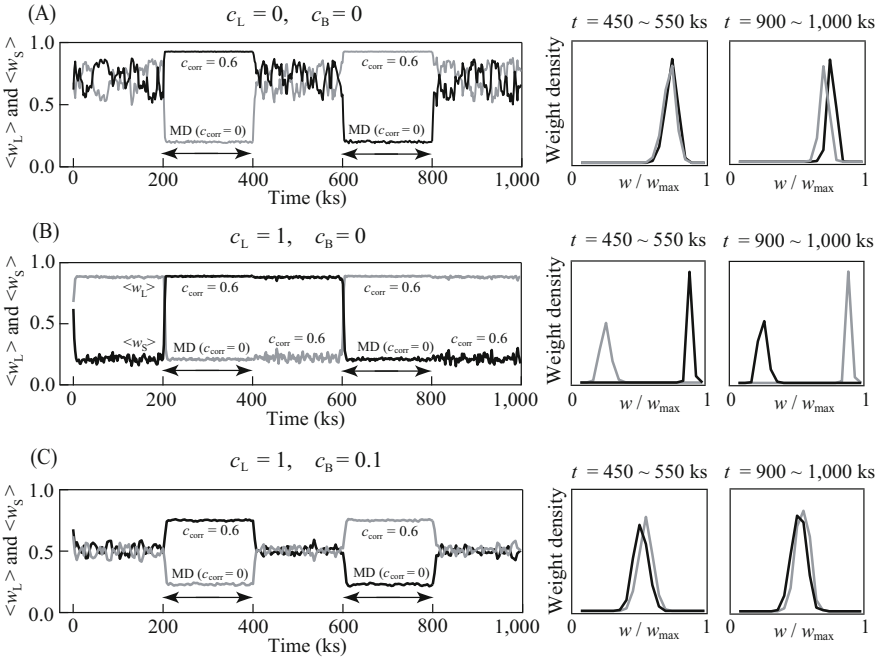

Fig. 2. Synaptic modification dynamics in response to MD and reverse suture

The results in Fig. 2 suggested the importance of activity-dependent competition, through which information about past sensory experience is stabilized in synaptic pattern [18]. In order to elucidate how the competitive function is regulated by local inhibition, we plotted the average weights of the two groups at the equilibrium state of STDP by changing the level of input correlation (c_{corr}) for three different values of c_L and c_B (Fig. 3). With neither lateral nor backward inhibition (Fig. 3A), the induction of competition was restricted in a small range of c_{corr} ($0.3 < c_{corr} < 0.6$). However, by introducing lateral inhibition (Fig. 3B), the competitive range of c_{corr} was widely prolonged ($0.2 < c_{corr} < 0.8$), showing that lateral inhibition promoted the emergence of competition. In contrast, a low level of backward inhibition was sufficient to prevent the induction of competition for all values of c_{corr} (Fig. 3C). These results indicate that lateral inhibition can promote the competitive interaction, whereas backward inhibition strongly suppresses it.

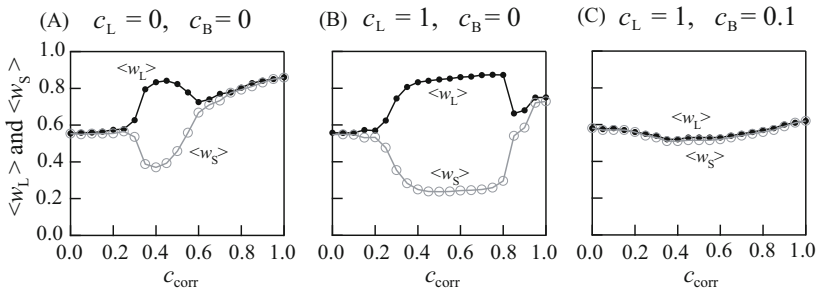

Fig. 3. The average weights of the two groups at the equilibrium of STDP

4 Discussion

We showed that a high level of lateral inhibition facilitated the ability of STDP to introduce the between-group competition (Fig. 3B). In contrast, backward inhibition prevents the induction of competition and counterbalances the effects of lateral inhibition (Fig. 3C). The effect of lateral inhibition in facilitating competition can be partly explained by the fact that this type of inhibition can promote precise postsynaptic spikes in response to inputs and therefore strengthens the input-output correlation that is required for inducing competition by STDP [8, 18]. The suppressive effect of backward inhibition on competition could be attributed to the fact that such rapid feedback can weaken the input-output correlation in cases where multiple postsynaptic spikes occur following inputs [19].

Furthermore, we demonstrated that, in the presence of competitive interaction provided by the lateral inhibition, which group becomes dominant depends on past sensory experience, thus providing a basis of experience-dependent plasticity (Fig. 2B). This synaptic function that reflects the past experience of inputs disappeared when backward inhibition prevented competitive interaction (Fig. 2C). When two groups of synapses are segregated by competition, there exist two stable synaptic patterns, such that one group and the other group is dominant. However, in the absence of competition, the weight distributions of both the groups are identical so that the system is monostable (as in Figs. 2A and 2C).

Our results suggest that the local inhibitory transmission by the lateral and backward inhibition may strengthen and weaken the ability of neurons to induce experience-dependent OD plasticity, respectively. This may explain an involvement of localized inhibitory circuits, as suggested by physiological experiments [3, 4].

References

1. Wiesel, T.N.: Postnatal development of the visual cortex and the influence of environment. Nature 299, 583–591 (1982)
2. Hensch, T.K., Fagiolini, M., Mataga, N., Stryker, M.P., Baekkeskov, S., Kash, S.F.: Local GABA circuit control of experience-dependent plasticity in developing visual cortex. Science 282, 1504–1508 (1998)
3. Fagiolini, M., Hensch, T.K.: Inhibitory threshold for critical-period activation in primary visual cortex. Nature 404, 183–186 (2000)
4. Fagiolini, M., Fritschy, J.M., Low, K., Mohler, H., Rudolph, U., Hensch, T.K.: Specific GABAA circuits for visual cortical plasticity. Science 303, 1681–1683 (2004)
5. Hensch, T.K.: Critical period plasticity in local cortical circuits. Nature Rev. Neurosci. 6, 877–888 (2005)
6. Lazarus, M.S., Huang, Z.J.: Distinct maturation profiles of perisomatic and dendritic targeting GABAergic interneurons in the mouse primary visual cortex during the critical period of ocular dominance plasticity. J. Neurophysiol. 106, 775–787 (2011)
7. Burkhalter, A.: Many specialists for suppressing cortical excitation. Front. Neurosci. 2, 155–167 (2008)
8. Pouille, F., Scanziani, M.: Enforcement of temporal fidelity in pyramidal cells by somatic feed-forward inhibition. Science 293, 1159–1163 (2001)
9. Bi, G.Q., Poo, M.M.: Synaptic modifications in cultured hippocampal neurons: Dependence on spike timing, synaptic strength, and postsynaptic cell type. J. Neurosci. 18, 10464–10472 (1998)
10. Sakurai, I., Kubota, S., Niwano, M.: A model for ocular dominance plasticity controlled by feedforward and feedback inhibition (submitted)
11. Song, S., Abbott, L.F.: Cortical development and remapping through spike timing-dependent plasticity. Neuron 32, 339–350 (2001)
12. Song, S., Miller, K.D., Abbott, L.F.: Competitive Hebbian learning through spike-timing-dependent synaptic plasticity. Nat. Neurosci. 3, 919–926 (2000)
13. Gerstner, W., Kistler, W.M.: Spiking neuron models. Cambridge University Press, Cambridge (2002)
14. Kempter, R., Gerstner, W., van Hemmen, J.L.: Hebbian learning and spiking neurons. Phys. Rev. E 59, 4498–4514 (1999)
15. Antonini, A., Gillespie, D.C., Crair, M.C., Stryker, M.P.: Morphology of single geniculocortical afferents and functional recovery of the visual cortex after reverse monocular deprivation in the kitten. J. Neurosci. 18, 9896–9909 (1998)
16. Rittenhouse, C.D., Siegler, B.A., Voelker, C.A., Shouval, H.Z., Paradiso, M.A., Bear, M.F.: Stimulus for rapid ocular dominance plasticity in visual cortex. J. Neurophysiol. 95, 2947–2950 (2006)
17. Kuhlman, S.J., Lu, J., Lazarus, M.S., Huang, Z.J.: Maturation of GABAergic inhibition promotes strengthening of temporally coherent inputs among convergent pathways. PLoS Comput. Biol. 6, e1000797 (2010)
18. Kubota, S., Kitajima, T.: Possible role of cooperative action of NMDA receptor and GABA function in developmental plasticity. J. Comput. Neurosci. 28, 347–359 (2010)
19. Ramoa, A.S., Paradiso, M.A., Freeman, R.D.: Blockade of intracortical inhibition in kitten striate cortex: Effects on receptive field properties and associated loss of ocular dominance plasticity. Exp. Brain Res. 73, 285–296 (1988)

Spectral Power Estimation for Unevenly Spaced Motor Imagery Data

Junhua Li[1,2], Zbigniew Struzik[2], Liqing Zhang[1], and Andrzej Cichocki[2]

[1] MOE-Microsoft Key Laboratory for Intelligent Information and Intelligent Systems, Shanghai Jiao Tong University, Shanghai, 200240, China
junhua.li@riken.jp, zhang-lq@cs.sjtu.edu.cn
[2] Laboratory for Advanced Brain Signal Processing, Brain Science Institute, RIKEN, Saitama, 351-0198, Japan
{zbigniew.struzik,a.cichocki}@riken.jp

Abstract. The human brain can send a command to external devices or communicate with the outside environment by the means of a brain computer interface (BCI) system. The effectiveness depends on how precisely specific brain activities can be identified from EEG. Noise is usually mixed into the EEG signal, and cannot be separated or filtered out in some cases. In a practical BCI system, the whole segment of EEG is discarded when a portion of that segment is contaminated by extreme noise or artifacts. This leads to the weakness that the BCI system cannot output decoding results during the period of that discarded segment. In order to solve this problem, we employed a Lomb-Scargle periodogram to estimate the spectral power based on an unevenly spaced segment, a portion of which has been removed due to noise contamination. According to the classification results of motor imagery data, the accuracy is not dramatically decreased along with increased proportion of data removal.

Keywords: Spectral Power Estimation, Brain Computer Interface, Motor Imagery, Unevenly Spaced Data, Classification.

1 Introduction

Brain computer interface (BCI) has attracted increasing attention of researchers coming from diverse research fields, and is one of interdisciplinary research hotspots. With a BCI system, healthy people can obtain fantastic manipulation experience contrary to their familiar perception [1], and disabled people can restore their abilities of communication [2] and degenerated motor function [3-4]. In the practical application of a BCI system, the intention of the user needs to be translated into a control command continuously in order to give the user an experience of smooth manipulation. This requires all EEG segments to be included for decoding. If some of EEG segments are discarded due to noise contamination, there is no output of commands during the periods of those discarded segments. Hence, it would be good to utilize the remaining portion of EEG segment after removing the portion of noise contamination. The power features are commonly used to distinguish different motor

M. Lee et al. (Eds.): ICONIP 2013, Part I, LNCS 8226, pp. 168–175, 2013.
© Springer-Verlag Berlin Heidelberg 2013

imageries (e.g., left-hand and right-hand motor imageries) [5-7], because power features are robust in represent of information underlying motor imagery. For the complete EEG segment, Fourier transform can be used to transform temporal data points into spectral domain, but it is impossible to process unevenly spaced data like the EEG segment after removing a portion of noise contamination. In order to utilize the segments with unevenly spaced data points to let user feel smooth manipulation, we employed Lomb-Scargle periodogram to estimate the spectral power [8-9] and support vector machine (SVM) [10-11] to predict the class of motor imagery. Two categories of data are used to prove the feasibility of the method. One is the simulated data and the other is two-class motor imagery data. We used simulated data to illustrate that spectral power can be correctly estimated when data come to be unevenly spaced after removing some data points of them. And, we used real motor imagery data to demonstrate that classification accuracy does not dramatically decreased when different proportional portions of segments have been removed. Hence, the method of combination of Lomb-Scargle periodogram and SVM is suitable for using in the BCI system when a portion of segment has be removed.

2 Data Acquisition

The simulated data were generated by mixing two sinusoidal signals, which are 3Hz and 6Hz, respectively. The maximal amplitude of 3Hz sinusoid signal was 1.5 times of that of the 6Hz sinusoid signal. The motor imagery data came from three subjects. Fourteen electrodes were used to record the EEG signal on the sensorimotor cortex while the subject was conducting motor imagery at sampling rate of 250 Hz. Those electrodes were referenced at the mastoids behind ears and grounded at AFz. Each subject participated in four sessions. Each session consists of 15 trials, each of which was four-second length. Subject conducted either left hand motor imagery or right hand motor imagery according to the cue shown on the computer monitor.

3 Method

We first divided a four-second trial into 25 segments of one-second length with an overlap of 87.5%. A segment is denoted by X, which is N by T matrix. Where N is the number of channels, and T is the number of sampling points. Spectral power of each channel time series $y(t_i)$ is estimated by the Lomb-Scargle periodogram [8-9]. The estimated spectral power at frequency Ω_f can be obtained through minimizing the following sum of difference squares:

$$\min_{\substack{a>0 \\ \phi\in[0,2\pi]}} \sum_{i=1}^{T} (y(t_i) - \alpha\cos(\Omega_f t_i + \phi))^2 . \quad (1)$$

Let

$$a = \alpha \cos \phi \tag{2}$$

and

$$b = -\alpha \sin \phi , \tag{3}$$

we can rewrite equation (1) as:

$$\min_{a,b} \sum_{i=1}^{T} (y(t_i) - a\cos(\Omega_f t_i) - b\sin(\Omega_f t_i))^2. \tag{4}$$

The optimal parameters $\hat{a}, \hat{b}$ can be obtained through minimizing equation (4)

$$\begin{bmatrix} \hat{a} \\ \hat{b} \end{bmatrix} = R^{-1} r \tag{5}$$

where

$$R = \sum_{i=1}^{T} \begin{bmatrix} \cos(\Omega_f t_i) \\ \sin(\Omega_f t_i) \end{bmatrix} \begin{bmatrix} \cos(\Omega_f t_i) & \sin(\Omega_f t_i) \end{bmatrix} \tag{6}$$

and

$$r = \sum_{i=1}^{T} \begin{bmatrix} \cos(\Omega_f t_i) \\ \sin(\Omega_f t_i) \end{bmatrix} y(t_i) . \tag{7}$$

The power of specific frequency Ω_f is then estimated with respect to optimal parameters $\hat{a}, \hat{b}$ as follows:

$$\begin{aligned} &\frac{1}{T} \sum_{i=1}^{T} \left(\begin{bmatrix} \hat{a} & \hat{b} \end{bmatrix} \begin{bmatrix} \cos(\Omega_f t_i) \\ \sin(\Omega_f t_i) \end{bmatrix} \right)^2 \\ &= \frac{1}{T} \begin{bmatrix} \hat{a} & \hat{b} \end{bmatrix} R \begin{bmatrix} \hat{a} \\ \hat{b} \end{bmatrix} \\ &= \frac{1}{T} r^{\mathrm{T}}(\Omega_f) R^{-1}(\Omega_f) r(\Omega_f) . \end{aligned} \tag{8}$$

Similarly, the minimization of squares mentioned above is used to estimate spectral powers at all frequencies. After that, spectral estimation for one channel is finished. Those steps are repeated for all channels and all segments to get the spectral powers. Because the frequency range of 8-30 Hz is mostly related to motor imagery task [7],

we divided that band into four subbands with a bandwidth of 5 Hz (i.e., 8-12 Hz, 13-17 Hz, 18-22 Hz, and 23-27 Hz). Subband powers were obtained by averaging spectral powers within the corresponding frequency band range for each channel. Then, subband powers (four features for each channel) for all channels are concatenated into a feature vector:

$$F = [f_{11}, f_{12}, f_{13}, f_{14}, f_{21}, f_{22}, f_{23}, f_{24}, \cdots, f_{N1}, f_{N2}, f_{N3}, f_{N4}]^{\mathrm{T}}, \quad (9)$$

where N is the number of channels. Subsequently, features are normalized as:

$$f_{qp} = \log\left(\frac{f_{qp}}{\sum_{i=1}^{N}\sum_{j=1}^{4} f_{ij}}\right). \quad (10)$$

The normalized features were fed into a linear SVM classifier to distinguish which class it belongs to.

4 Results

4.1 Simulated Data

Figure 1 shows the spectral power estimation from a mixed signal, which mingles two sinusoidal signals with 3 Hz and 6 Hz respectively. From top left to bottom right, spectral power estimations for the complete signal, proportional data point removals from 10% to 80% are shown, respectively. The data points removed are chosen randomly. The powers shown in figure 1 were normalized by dividing by a proportional factor (1-p, p is the removed percentage) in order to keep the same scale between cases of different proportional data removal. For example, the estimated power is divided by the proportional factor of 0.7 when 30% of data points are removed from the signal. From figure 1, we can see the components at 3 Hz and 6 Hz can be better estimated even up to 80% of data point removal.

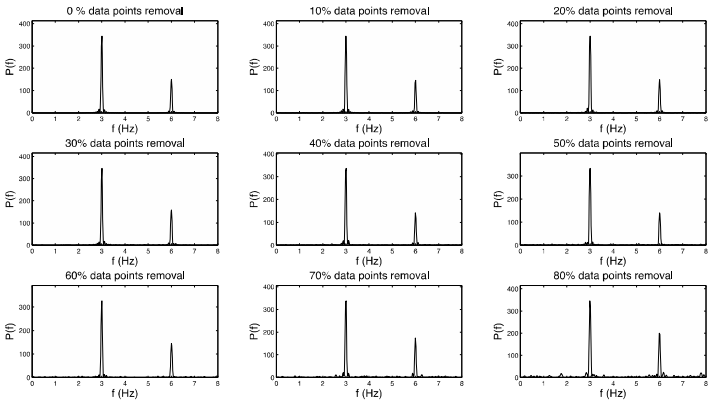

Fig. 1. Spectral power estimations for the complete signal and signals after data point removal

4.2 Real Motor Imagery Data

In this section, we showed results tested on real motor imagery data. The proposed method can solve the problem that the whole segment has to be discarded due to partial noise contamination on that segment, if the classification accuracy for segments with data removal can remain the same or slightly decrease. Here, we used two ways to randomly remove data points. One is that data points are randomly removed (see figure 2 for an example). The other is data blocks are randomly removed (see figure 3 for an example). The width of removed blocks is generated according to a normal distribution with a mean of 20 and standard deviation of 10.

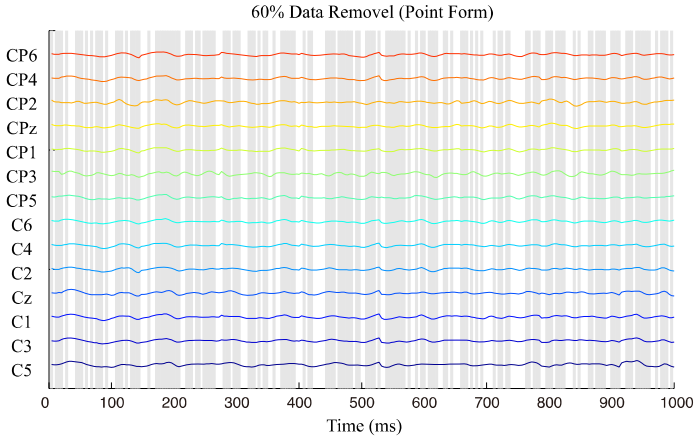

Fig. 2. An example of data point removal. The data points shown with gray background are removed while data points shown with white background are retained.

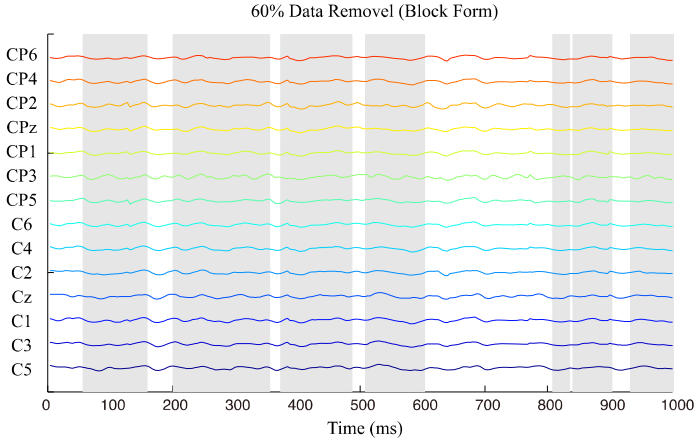

Fig. 3. An example of block point removal. The data points shown with gray background are removed while data points shown with white background are retained.

The data from the preceding session were used for training and the data from the following session were used for testing. Sliding time window accuracies were calculated through the number of correct classification segments divided by the number of all segments. A trial was classified to the class that most of sliding time windows within that trial belonged to. Then, trial accuracies were obtained by the ratio of correct classification trials. Figure 4 and figure 5 show testing accuracies for the conditions of data point removal and data block removal, respectively. In general, the accuracies for all sessions of all subjects are not dramatically decreased. Trial accuracies varied more than that of sliding time window across different proportional portions of data removal. The reason is that trial was counted as correct classification trial even if the number of correct classification sliding time windows is one more than that of wrong classification sliding time windows, and vice versa. Therefore, in some cases, trial accuracy changed greatly while sliding time widow accuracy did not change too much. A comparable classification accuracy can be achieved even when 80% of data were removed. The high accuracies can be kept no matter how many data points were removed from 10% to 80% for subject 1, especially for session 2 and session 3. The accuracies for 80% data removal are largely worse than that for 70% data removal for subject 1 in the condition of block data removal. It seems that our method is relatively sensitive to the form of block data removal.

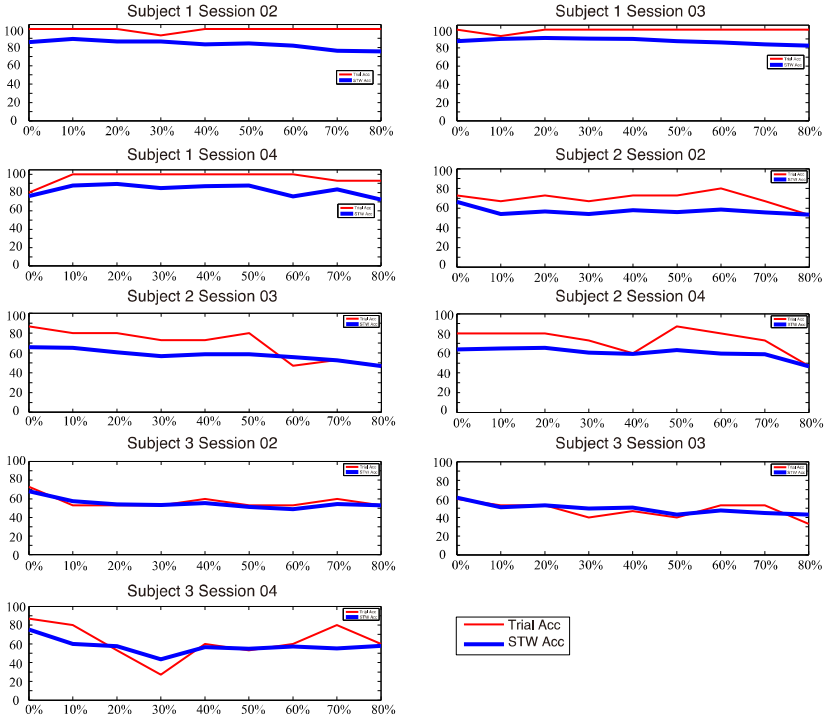

Fig. 4. Classification accuracies for the form of data point removal. The thin red lines represent trial accuracies, and the bold blue lines represent sliding time window accuracies.

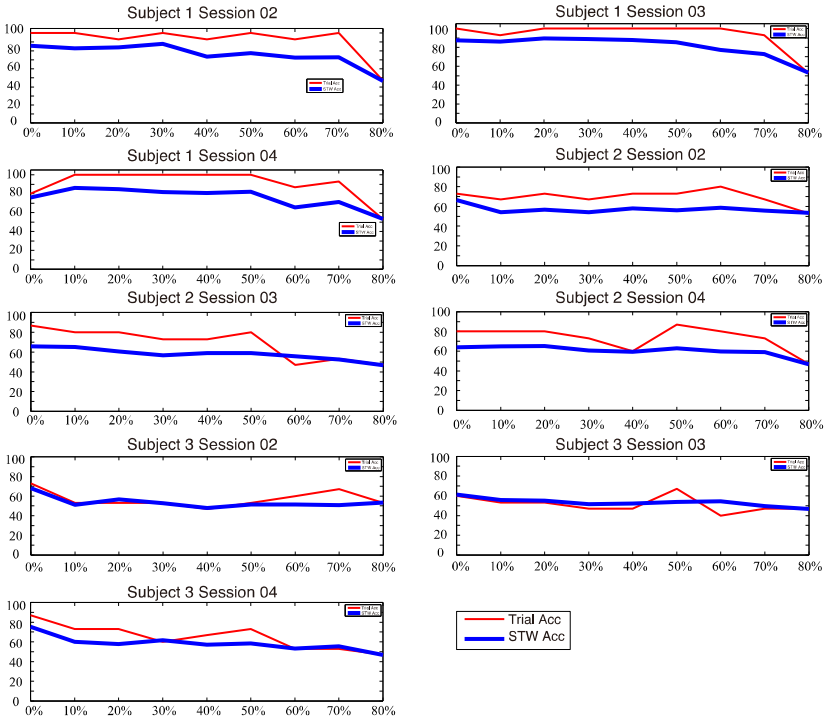

Fig. 5. Classification accuracies for the form of block point removal. The thin red lines represent trial accuracies, and the bold blue lines represent sliding time window accuracies.

5 Conclusion

We proposed the combination of Lomb-Scargle periodogram and SVM classifier to distinguish the EEG segment with a portion of data removal due to noise contamination. The results indicated that classification accuracy was not dramatically decreased when different percentages of data were removed. Therefore, the classification performance using the proposed method for segments with data removal is acceptable for a BCI application system. This means that the segment with noise contamination can still be utilized to output commands after only removing the noisy portion, rather than discarding the whole segment, which is conventionally taken by the BCI system. In brief, the proposed method can achieve comparable classification performance even when most of data points of a segment have been removed. It avoids the problem that there is no output of commands when a segment is discarded, because Fourier transform cannot be used to estimate spectral power after a portion of data has been removed due to noise contamination.

Acknowledgments. The work was in part supported by the National Natural Science Foundation of China (Grant No. 61272251, 91120305), and in part supported by the NSFC-JSPS International Cooperation Program (Grant No. 61111140019).

References

1. Li, J., Liu, Y., Lu, Z., Zhang, L.: A Competitive Brain Computer Interface: Multi-person CarRacing System. In: 35th Annual International Conference of the IEEE EMBS, Osaka, Japan, July 3-7, pp. 2200–2203 (2013)
2. Muller, K.R., Tangermann, M., Dornhege, G., Krauledat, M., Curio, G., Blankertz, B.: Machine Learning for Real-time Single Trial EEG Analysis: from Brain-computer Interfacing to Mental State Monitoring. J. Neurosci. Methods. 167(1), 82–90 (2008)
3. Li, J., Liang, J., Zhao, Q., Li, J., Hong, K., Zhang, L.: Design of Assistive Wheelchair System Directly Steered by Human Thoughts. Int. J. Neural Syst. 23(3), 1350013 (2013)
4. Pfurtscheller, G., Muller, G.R., Pfurtscheller, J., Gerner, H.J., Rupp, R.: 'Thought'-Control of Functional Electrical Stimulation to Restore Hand Grasp in A Patient withTetraplegia. Neurosci. Lett. 351(1), 33–36 (2003)
5. Pfurtscheller, G., Guger, C., Muller, G., Krausz, G., Neuper, C.: Brain Oscillations Control Hand Orthosis in A Tetraplegic. Neurosci. Lett. 292(3), 211–214 (2000)
6. Palaniappan, R.: Utilizing Gamma Band to Improve Mental Task Based Brain-computer Interface Design. IEEE Trans. Neural Syst. Rehabil. Eng. 14(3), 299–303 (2006)
7. Li, J., Zhang, L.: Active Training Paradigm for Motor Imagery BCI. Exp. Brain Res. 219(2), 245–254 (2012)
8. Lomb, N.R.: Least-squares Frequency Analysis of Unequally Spaced Data. Astrophys. Space Sci. 39(2), 447–462 (1976)
9. Stoica, P., Li, J., He, H.: Spectral Analysis of NonuniformlySampled Data: ANew Approach Versus the Periodogram. IEEE Trans. Signal Process. 57(3), 843–858 (2009)
10. Vapnik, V.: The Nature of Statistical Learning Theory. Springer, New York (1995)
11. Hearst, M.A., Dumais, S.T., Osman, E., Platt, J., Scholkopf, B.: Support Vector Machines. IEEE Intell. Syst. 13(4), 18–28 (1998)

Fuzzy Logic-Based Automatic Alertness State Classification Using Multi-channel EEG Data

Ahmed Al-Ani[1], Mostefa Mesbah[2], Bram Van Dun[3], and Harvey Dillon[3]

[1] Faculty of Engineering and Information Technology, University of Technology, Sydney, Ultimo NSW 2007 Australia
[2] School of Computer Science and Software Engineering, The University of Western Australia, Crawley WA 6009 Australia
[3] National Acoustic Laboratories, Australian Hearing Hub, Level 4, Macquarie University, NSW 2190 Australia
ahmed@eng.uts.edu.au, mmesbah@ieee.org, {Bram.VanDun,Harvey.Dillon}@nal.gov.au

Abstract. This paper represents an attempt to automatically classify alertness state using information extracted from multi-channel EEG. To reduce the amount of data and improve the performance, a channel selection method based on support vector machine (SVM) classifier has been performed. The features used for the EEG channel selection process and subsequently for alertness classification represent the energy values of the five EEG rhythms; namely δ, θ, α, β and γ. In order to identify the feature/channel combination that leads to the best alertness state classification performance, we used a fuzzy rule-based classification system (FRBCS) that utilizes differential evolution in constructing the rules. The results obtained using the FRBCS were found to be comparable to those of SVM but with the added advantage of revealing the rhythm/channel combination associated with each alertness state.

Keywords: Alertness classification, EEG, fuzzy rule-based system.

1 Introduction

The detection of alertness state has recently attracted much attention due to its link to the human ability to process information. The traditional approach to identification of alertness state through monitoring the subject's face was found to be unreliable due to a number subject-dependent factors such as age and shape of eyes. This situation is further compounded by the the inter-rater disagreement. In addition to this, visual identification is tedious task that requires full attention from the assessor. The existing automatic alertness state detection methods can be broadly divided into signal-based and video-based. Methods that fall into the first category use physiological signals such as the electroencephalogram (EEG), electromyogram (EMG), electrooculogram (EOG), and electrocardiogram (ECG) for alertness identification. Among these signals, EEG and more specifically the five EEG rhythms; namely δ (up to 4 Hz), θ (4 - 8 Hz), α (8

M. Lee et al. (Eds.): ICONIP 2013, Part I, LNCS 8226, pp. 176–183, 2013.
© Springer-Verlag Berlin Heidelberg 2013

- 13 Hz), β (13 - 30 Hz), and γ (30 - 100 Hz) has been the most widely used. Some authors attempted to identify patterns characteristic of different alertness states. For example, the authors in [1] associated reduction in vigilance with a decrease in the amplitude, quantity and frequency of the posterior α rhythm and increase in slow wave components. Nakamura et. al. [2] characterized the reduction in vigilance level by (i) decrease in the amplitude, quantity and frequency of the posterior dominant rhythm (or the waves with an approximately constant period usually in the α band) and with the maximum amplitude at the occipital or parieto-occipital region of the head and (ii) increase in slow wave components. Most of the authors, however, adopted the discrete vector feature approach to classification. Features were extracted from one or more of the main four physiological signals, namely EEG, EOG, EMG, and ECG [3,4], using different time-domain, frequency-domain and time-frequency domain based techniques. These features were then fed to different classifiers, such as ANN [3] and SVM [4] to be assigned to either two states (alert/drowsy) [4] or three states of alertness (alert/drowsy/asleep) [3]. A number of video-based methods have been proposed in the literature, such as [5]. However, one needs to deal with a number of issues when using video-based methods, such as occlusions, target displacement and the large variability in eye shapes and facial expressions. In this work we opted for the first option. More specifically we used electrical potentials recorded from the brain following an audio stimulus. These signals are known as cortical auditory evoked potential (CAEP) responses.

In our initial work [6], we showed that high frequency rhythms perform, in general, better than the low frequency ones and that a single channel would not be sufficient for achieving good discrimination between the different alertness states. This paper presents an extension of our initial work, where we propose a two-stage process to 1) identify the cortical regions more suitable for discriminating between alertness states and 2) construct a set of "if-then" rules involving combination of EEG rhythm and channel spatial location instead of the widely used black box classifier. A fuzzy rule-based classification system (FRBCS) is used to assign the classifier input information to one of the four predefined alertness states. A differential evolution (DE) optimization based searching technique is introduced to construct the fuzzy-based rules used by the classifier.

The paper is organized as follows: the fuzzy rule-based classification system is described in section 2. Section 3 presents the the DE-based method for constructing the fuzzy rules. Experimental results and conclusions are given in sections 4 and 5 respectively.

2 Fuzzy Rule Based Classification System for Alertness Detection

The fuzzy rule-based classification system (FRBCS) has been used in many classification problems [7,8,9] due to its transparent model built on linguistic variables. This property makes it more attractive for problems that require transparent mapping from the input variables to the output categories, such

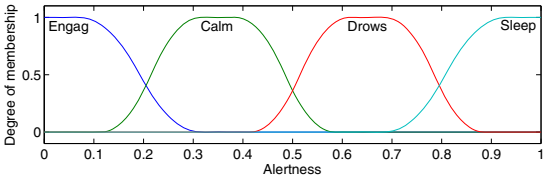

Fig. 1. Alertness membership functions

as medical diagnosis; a property not available in many of the widely used classification algorithms. For the particular problem of alertness state detection, there is another advantage for using FRBCS, namely the reduction of the effect of inconsistency in labeling data by the participating subjects or the human experts. This is achieved by allowing a certain degree of overlap between adjacent states, as shown in Fig. 1.

FRBCS computes the values of an output vector for a given input vector using fuzzy memberships and a pre-defined set of "if-then" rules. The FRBCS design involves 1) defining the membership functions, 2) estimating their parameters and 3) construction of the fuzzy rules. This paper focuses on the construction of rules, as our aim is to identify a limited number of rules that each has a small number of antecedent variables. Some of the widely used methods for constructing the rules are based on artificial neural networks [10] and genetic algorithms [11]. Although these methods have achieved good results in certain applications, we decided to build our own FRBCS for the following reasons. Firstly, we want to control the construction of the rules by starting with a number of rules equal to NC (number of alertness classes), then keep adding another set of NC rules until there is no improvement. The reason behind this approach is to identify the important rule for each of the NC classes, then the second best set of rules that complement the existing ones and so on. Secondly, we want to control the rule complexity, where we aim at constructing "simple" rules that are easy to interpret. Hence, we want no more than K variables in the antecedent part of the rule, where K is a user defined variable. This will help to reveal the relationships between the EEG rhythm/channel combinations and each of the alertness states. Thirdly, differential evolution was shown to possess good exploration capability of the search space [12,13], and hence, we decided to use it here to search for the best variable combination for each rule.

Each feature support is partitioned into three regions, namely "low", "medium" and "high". The Features are first normalized between 0 and 1 before being fuzzified using a pi-shaped membership function. This membership function requires four parameters, which represents the transition points from 0 to 1 and then from 1 to 0. The fuzzification process is performed according to the following steps:

- sort the data samples of each feature and identify the 6%, 47%, 53%, and 94% smaller data samples and assign those values to pp, which is a vector that has four elements
- the parameters of the "low" are: $[-pp(2), -pp(1), pp(1), pp(2)]$

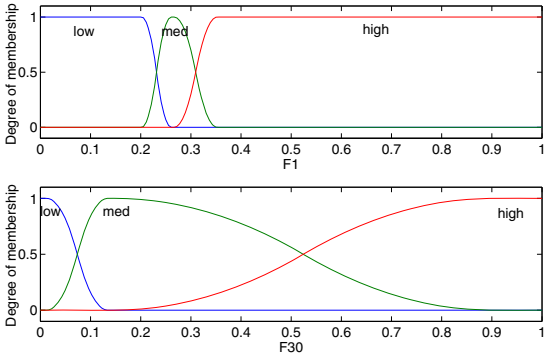

Fig. 2. Membership functions of two different features

– the parameters of the "medium" are: $[pp(1), pp(2), pp(3), pp(4)]$
– the parameters of the "high" are: $[pp(3), pp(4), 2 - pp(4), 2 - pp(3)]$

Although based on this procedure, the generated shape of the membership functions associated with different features may not be similar, each of the three membership regions of a given feature will approximately have the same number of samples with their counterparts of another feature. The reason behind this is that we don't want the "low" region to represent a small portion of samples for feature F_i and large portion of samples for feature F_j. The same is true for the "medium" and "large" regions. Fig. 2 shows the membership functions of two different features.

Rules will have the following format:

Rule n : If F_{n1} is MF_{n1} and . . . and F_{nk} is MF_{nk} then Class is C_n

where MF_{n1} is the membership function associated with feature F_{n1} in rule n, and C_n is one of the alertness state.

We decided not to assign weights to the rules, as we wanted to find the best rule for each class. Rules would then be added to the ones that have already been identified. The next section describes the rule construction process.

3 Construction of Fuzzy Rules Using Differential Evolution

The construction of rules with limited number of antecedent variables (no more than k) is implemented using differential evolution (DE). We modified the code[1] of our previously developed DE-based feature selection algorithm (DEFS) [13] to suit this particular problem. In the DEFS algorithm, the original NF features are distributed among M wheels and one feature is selected from each wheel, i.e, M represents the desired number of features to be selected. The selection of

[1] Available online at: `http://services.eng.uts.edu.au/~ahmed/`

features is optimized using the differential combination and uniform crossover operators of the DE algorithm.

For rule construction, each feature in the antecedent part is represented by one of the four possibilities {low, medium, high, none}, while the consequent part is represented by one of the four possibilities {engaged, calm, drowsy, sleeping}. The number of wheels is set to $NF \times NC$, where NF and NC are the number of features and classes respectively. Each wheel represents one of the features for a given class, and one rule is constructed for each class. The objective is to search for the best membership for each features in the antecedent part of each of the four rules. For each member of the population, the algorithm starts by allowing only k features per rule that are randomly chosen to be assigned a membership function other than "none". Based on the population size, it is unlikely that all members of the population to start with "none" for any of the features. During the optimization process, the DE operators may produce more than k features with a value other than "none". In such case, some of those (randomly chosen) will be reset to "none". The population size is set to 100, all other parameters are kept unchanged.

The output values are obtained for each member of the population by evaluating the fuzzy system (defuzzification). The output values are then used to calculate the class-wise classification accuracy of the training set, which in turn used as the "fitness function". It is important to mention that this approach is computationally expensive, and hence, it is not recommended to substitute existing classification methods. However, as mentioned earlier, the main aim of this work is to search for the "best" rhythm/channel combination for each of the alertness states.

4 Experiments and Analysis of Results

Ten normal hearing adult subjects, with an age range of 24 to 53 years, participated in the experiment. A 21 ms /g/ speech sound stimulus was presented every 1175 ms at 55 dB sound pressure level as part of a cortical auditory evoked potential study. Data was recorded using a Neuroscan system that has 64 EEG channels, with the reference channel close to Cz (vertex). Subjects were asked to press one of three buttons every 30 seconds to indicate their level of alertness, i.e, engaged, calm but not drowsy, and drowsy. Each recording session lasted one hour, divided into 6 divisions of 10 minutes each. If the subject did not provide an input in any of the divisions, he/she was considered to have fallen asleep.

The recorded signal was divided into windows of 5 seconds with overlap of 3 seconds. For each window five features corresponding to the energy in the five EEG frequency bands were extracted. Each 10 consecutive windows were grouped to form a segment, and for each subject 75% of the segments were used for training and the remaining 25% for testing. Training windows from all 10 subjects were used to train a multi-class linear support vector machine (SVM) classifier.

For the sake of channel selection, we started by evaluating the performance of each of the 64 channels and its neighbours, where each channel is represented

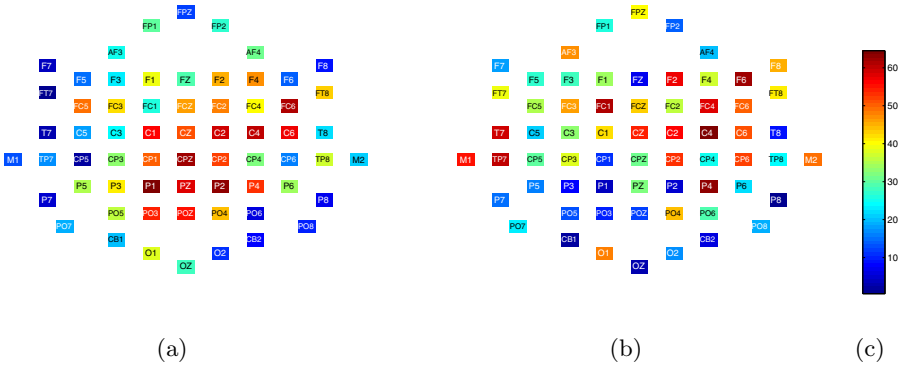

(a) (b) (c)

Fig. 3. Ranked channel performance based on (a) a single channel and its surroundings, and (b) a single channel and its surroundings with {P1, CP1, P3, PZ, PO3}

using the five EEG rhythms, where based on our initial study we found that a single channel would not be sufficient to discriminate between the four alertness states. The ranked results of the 64 channels shown in Fig. 3(a) indicate that channel P1 and its surroundings {CP1, P3, PZ, PO3} achieved best performance with an average class-wise accuracy of 60.39%. We have then fixed those five channels and added each of the remaining channels, one at a time, along with its neighbours. We found that channel C4 and its surroundings {FC4, C2, C6, CP4} is the best set that complements the existing five channels with an average combined class-wise accuracy of 69.83%, as shown in Fig 3(b).

The obtained performance using 10 channels is lower than that obtained in our initial study [13] because in that study the classifier was trained on the data of each subject individually, while here data from all 10 subjects was used to train the classifier. Note that inconsistency in labeling between the different subjects make the classification task harder.

In order to reveal relationships between the rhythm/channel combination and each alertness state, the construction of fuzzy rules process described in the previous section has been applied to the 10 "best" channels selected by the SVM classifier. The number of elements to be optimized for each rule is 50 (5 rhythms $\times$ 10 channels). We have run the algorithm 5 times, where in each run 4 rules are added to the already identified ones. The sixth run has hardly made any improvement, and hence we decided not to consider it. The obtained rules are:

1. If (γ_{C6} is low) and (θ_{CP1} is high) and (γ_{P3} is med) and (θ_{PO3} is high) then sleeping
2. If (β_{C4} is high) and (β_{P1} is med) and (θ_{PO3} is med) and (β_{PO3} is med) then drowsy
3. If (γ_{FC4} is low) and (α_{CP1} is high) and (α_{PZ} is high) and (γ_{PZ} is med) then calm
4. If (α_{C4} is med) and (δ_{FC4} is high) and (β_{P1} is med) and (δ_{PZ} is med) then engaged
5. If (γ_{FC4} is high) and (θ_{PZ} is high) and (β_{PZ} is high) and (δ_{PO3} is med) then sleeping
6. If (δ_{FC4} is low) and (γ_{C2} is high) and (γ_{P1} is med) and (γ_{PZ} is high) then drowsy
7. If (γ_{C4} is low) and (γ_{C2} is high) and (γ_{P3} is low) and (β_{PZ} is low) then calm
8. If (β_{C4} is low) and (θ_{P3} is low) and (γ_{PO3} is med) then engaged
9. If (γ_{P1} is low) and (γ_{CP1} is high) and (γ_{CP4} is high) then sleeping
10. If (θ_{P3} is low) and (θ_{P1} is high) and (α_{P1} is high) and (γ_{PZ} is high) then drowsy
11. If (δ_{FC4} is low) and (α_{P1} is high) and (θ_{PZ} is low) then calm

12. If (γ_{P3} is high) and (β_{PO3} is low) then engaged
13. If (β_{C2} is low) and (θ_{CP1} is high) and (β_{PZ} is high) and (θ_{PO3} is low) then sleeping
14. If (θ_{C4} is low) and (γ_{FC4} is low) and (β_{P3} is low) and (γ_{PO3} is low) then drowsy
15. If (γ_{C6} is high) and (δ_{CP4} is high) and (β_{PZ} is high) and (δ_{PO3} is med) then calm
16. If (α_{C4} is med) and (α_{C6} is high) and (α_{P1} is med) and (α_{CP1} is low) then engaged
17. If (θ_{C4} is low) and (θ_{C2} is high) and (β_{PZ} is high) and (α_{PO3} is high) then sleeping
18. If (β_{P1} is high) and (γ_{P1} is high) and (δ_{P3} is low) and (γ_{PZ} is high) then drowsy
19. If (γ_{C6} is low) and (θ_{PZ} is high) and (γ_{PZ} is low) and (θ_{PO3} is high) then calm
20. If (θ_{P3} is low) and (γ_{PO3} is high) then engaged

The first four rules produced an accuracy of 58.27%, while using all 20 rules enhanced the accuracy to 67.16%, which is not too different from the results obtained using the SVM classifier. These rules indicate that all five rhythms influence the alertness state classification, especially the higher frequency ones. Note that although the proposed rule construction mechanism does not prevent conflicts between rules, the obtained rules perform well when considered together. These rules indicate that the four alertness states are mainly associated with:

- Sleeping: high β and θ rhythms in the P1 region
- Drowsy: med/high γ, med/high β, med/low θ and low δ
- Calm: med/low γ, high α and med/high θ
- Engaged: med/high γ and low θ in the P1 region. Med/low β and med α

As mentioned in the introduction, existing methods associate drowsiness with a reduction in the α rhythm and increase in slow wave components. The constructed FRBCS rules on the other hand utilized all five EEG rhythms. Hence, in order to verify the importance of the middle three rhythms (θ, α and β), we conducted another experiment using the same set of 10 channels, where we trained the SVM classifier using (i) θ only, (ii) α only, (iii) β only, (iv) θ and β, and (v) θ, α and β. We got the following respective average class-wise accuracies: 45.97%, 36.88%, 39.73%, 56.38%, and 57.80%. These results indicate that utilizing all five rhythms can lead to noticeably better performance than the middle three ones only, which support the constructed antecedent terms of the FRBCS rules.

The confusion matrix obtained using the FRBCS, shown in 1, indicates that the classifier tends to achieve lower misclassification rates with the increase of distance from the true class. For example, when the true class is engaged (column 5), misclassification with sleeping is close to zero, a slightly higher misclassification with the drowsy class, while the highest misclassification was achieved with calm, which is the closest class to engaged. Further improvements are expected to be achieved when optimizing the membership function parameters for each features.

Table 1. Confusion matrix of the FRBCS (T: True, P: Predicted)

P \ T	Sleeping	Drowsy	Calm	Engaged
Sleeping	0.93	0.04	0.07	0.02
Drowsy	0.06	0.65	0.24	0.19
Calm	0.01	0.25	0.55	0.24
Engaged	0.00	0.06	0.14	0.55

5 Conclusion

We presented in this paper a fuzzy rule-based classification system (FRBCS) that utilized differential evolution in constructing the rules. We have shown that the FRBCS is capable of achieving comparable results to that of the well-established SVM classifier. The main advantage of FRBCS is that it transparently maps the input features to the target categories. The obtained rules reveal that importance of combined frequency rhythms of the considered channels in differentiating between the different alertness states.

References

1. Varri, A., Hirvonen, K., Hasan, J., Loula, P., Haikkinen, V.: A computerized analysis system for vigilance studies. Computer Methods and Programs in Biomedicine 39, 113–124 (1992)
2. Nakamura, M., Sugi, T., Ikeda, A., Kakigi, R., Shibasaki, H.: Clinical application of automatic integrative interpretation of awake background. EEG: quantitative interpretation, report making, and detection of artifacts and reduced vigilance level. Electroencephalography and Clinical Neurophysiology 98, 103–112 (1996)
3. Kiymik, M.K., Akin, M., Subasi, A.: Automatic recognition of alertness level by using wavelet transform and artificial neural network. Journal of Neuroscience Methods 139, 231–240 (2004)
4. Yeo, M.V.M., Li, X., Shen, K., Wilder-Smith, E.P.V.: Can SVM be used for automatic EEG detection of drowsiness during car driving? Safety Science 47, 115–124 (2009)
5. Ji, Q., Zhu, Z., Lan, P.: Real-time nonintrusive monitoring and prediction of driver fatigue. IEEE Transactions on Vehicular Technology 53(4), 1052–1068 (2004)
6. Al-Ani, A., Van Dun, B., Dillon, H., Rabie, A.: Analysis of Alertness Status of Subjects Undergoing the Cortical Auditory Evoked Potential Hearing Test. In: Huang, T., Zeng, Z., Li, C., Leung, C.S. (eds.) ICONIP 2012, Part I. LNCS, vol. 7663, pp. 92–99. Springer, Heidelberg (2012)
7. Avci, E., Avci, D.: The speaker identification by using genetic wavelet adaptive network based fuzzy inference system. Expert Systems with Applications 36(6), 9928–9940 (2009)
8. Chi, Z., Yan, H., Pham, T.: Fuzzy algorithms with applications to image processing and pattern recognition. World Scientific, Singapore (1996)
9. Yan, H., Zou, Z., Wang, H.: Adaptive neuro fuzzy inference system for classification of water quality status. Journal of Environmental Sciences 22(12), 1891–1896 (2010)
10. Iyatomi, H., Hagiwara, M.: Adaptive fuzzy inference neural network. Pattern Recognition 37, 2049–2057 (2004)
11. Ishibuchi, H., Yamamoto, T., Nakashima, T.: IEEE Transactions on Systems, Man, and Cybernetics-Part B: Cybernetics 35(2), 359–365 (2005)
12. Price, K.V., Storn, R.M., Lampinen, J.A.: Differential Evolution: A Practical Approach to Global Optimization. Springer (2005)
13. Al-Ani, A., Alsukker, A., Khushaba, R.N.: Feature subset selection using differential evolution and a wheel based search strategy. Swarm and Evolutionary Computation 9, 15–26 (2013)

Neuronal Mechanism of Speech Hearing: An fMRI Study

Hojung Kang and Jong-Hwan Lee*

Department of Brain and Cognitive Engineering, Korea University
Seoul 136-713, Korea
{writeyours,jonghwan_lee}@korea.ac.kr

Abstract. It is well known that bilateral superior temporal gyrus (STG) specialize in speech perception. However, there is no study to explicitly represent the interaction between the bilateral STG depending on hearing condition (*i.e*. binaural or monaural hearing) based on neuroimaging findings. To this end, speech sentences containing numerical sound(s) were provided in binaural, monaural left and monaural right hearing condition. Participants were asked to correctly identify the presented numerical sound and speech hearing performance was calculated based on the number of correctly identified sounds. From the results, neuronal activations of the right STG were shown significantly different levels of neuronal activations across the three hearing conditions. In addition, the neuronal networks that are functionally connected with this right STG and associated with the speech hearing were iteratively identified in the bilateral STG. The reported findings support the importance of the right STG toward the enhancement of the speech hearing performance.

Keywords: Speech perception, superior temporal gyrus, hearing performance, binaural hearing, monaural hearing, functional magnetic resonance imaging, functional connectivity.

1 Introduction

Recent functional magnetic resonance imaging (fMRI) studies have reported that the neuronal activations in the right superior temporal gyrus (STG) as well as the left STG are crucial in speech perception including speech hearing [1, 2, 3, 4]. It has also been found that functional (correlated activations between brain regions) and effective (causal activations between distinct brain regions) connectivity patterns between bilateral STG associated with speech perception [5, 6, 7]. However, there have been limited studies that explicitly examined the neuronal responses in the STG and interactions between the bilateral STG, which are associated with speech perception performance depending on each type of hearing conditions (i.e. binaural or monaural hearing). We hypothesized that there would be distinct (1) neuronal activations in the STG depending on hearing conditions in association with speech hearing and (2) functional connectivity (FC) patterns between bilateral STG that are tightly associated with speech hearing performance.

M. Lee et al. (Eds.): ICONIP 2013, Part I, LNCS 8226, pp. 184–190, 2013.
© Springer-Verlag Berlin Heidelberg 2013

2 Methods

2.1 Study Participants and Experimental Design

Healthy right-handed male native Korean volunteers (n=12; age=25.3±1.7; Edinburg's handedness score=89.8±10.7 [8]) participated in this study. The English ability of the participants to perform task paradigm was evaluated using Wide Range Achievement Test (Blue version; score=60.4±5.2; [9]). In the experiment, the participants performed a task run which lasted 486 seconds. As shown in Fig. 1, the task run was consisted of 18 trials. Each trial was divided into speech hearing block and response block. In speech hearing block, auditory stimuli were pseudo-randomly presented either in binaural hearing (BH), monaural hearing in the left ear (MH_L), or right ear (MH_R) condition for 6 times in each condition via a MR-compatible auditory headset (NordicNeuroLab; www.nordicneurolab.com). The auditory stimuli consisted of eighteen English sentences containing numerical words (*i.e.*, "Two dollars and fifty cents."). In the response block, the participants were instructed to select a target numerical word accurately (*i.e.*, '15' vs. '50'), which was presented in the speech hearing block, using by a button response box (Current Design; www.curdes.com). A speech hearing (SH) score was defined as the correctly identified number of trials. Thus, the maximum SH score in each hearing condition is 6.

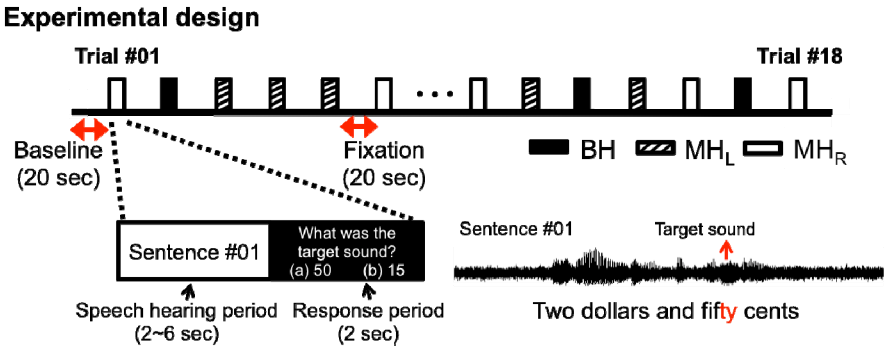

Fig. 1. Experimental design of speech hearing of numerical target sound

2.2 fMRI Data Acquisition and Preprocessing

The blood-oxygen-level-dependent (BOLD) fMRI data were acquired via a 3-T scanner (Tim Trio, Siemens, Erlangen, Germany). A gradient-echo echo-planar-imaging (EPI) pulse sequence was used to measure the neuronal activations based on BOLD mechanism (248 volumes; TE/TR=30/2000 ms; FA=90°; FOV=24×24 cm^2; in-plane voxel=64×64; number of slices=36 without a gap between slices). Five volumes at the beginning were excluded and the remaining EPI volumes were preprocessed using SPM8 software toolbox (www.fil.ion.ucl.ac.uk/spm) using default parameters with an order of slice timing correction, head motion correction,

normalization to the Montreal Neurological Institute (MNI) coordinates with a 3 mm isotropic voxel size, and spatial smoothing using an 8 mm isotropic full-width at half-maximum Gaussian kernel.

2.3 Definition of Regions-of-Interest (ROIs)

A general linear model (GLM) method was applied to estimate the degree of neuronal activation using the preprocessed BOLD signal [12]. Each of the three hearing conditions with 6 hearing blocks was modeled as separate regressor in a design matrix using onset timings and durations of the each of the blocks. The coefficients (β-values) of the three regressors for each of the three hearing conditions were estimated from the GLM approach based on least-squares algorithm [12]. The neuronal activation was estimated using averaged β-values within 19 voxels around foci with maximum β-value from spatial patterns for each hearing condition. To define the regions of interest (ROIs) that showed a main effect of hearing condition on neuronal activation, one-way repeated measures analysis of variance (ANOVA: uncorrected $p<0.001$ with minimum of 20 connected voxels) was administered. Then, the ROIs that are tightly linked with the speech hearing were identified using a regression analysis with neuronal activation of ROIs and average speech hearing scores in each of the three hearing conditions.

2.4 Identification of Neuronal Networks Associated with Speech Hearing

To estimate the FC patterns associated with each hearing condition (*i.e.,* BH, MH_L and MH_R), the preprocessed BOLD time-series (TS) was voxel-wisely separated into each trial. Subsequently, the separated BOLD TS were temporally concatenated as a single BOLD TS for each of the three hearing conditions. The partial FC analysis was applied to remove potential confounding artifacts included in the BOLD signals due to non-neuronal origins such as head movements and physiological artifacts. In detail, three principal components (PCs) of the BOLD signals in each of the white matter and cerebrospinal fluid were extracted via principal component analysis. Then, the 6 PCs, global mean BOLD signal, and 6 head motion parameters were regressed out from the BOLD signal in voxel wise across a whole brain area. The ROIs tightly linked with the speech hearing score were used as seed regions of the FC analysis. More specifically, the average BOLD signal in proximity of the ROI (i.e. 19 neighboring voxels) was obtained and subsequently used as a reference BOLD signal for the FC analysis. The FC level in each voxel was calculated from Pearson's correlation coefficient (CC) between averaged BOLD signal of the seed ROI and the BOLD signal of the corresponding voxel. The resulting CC values were converted into normally distributed z-scores using Fisher's r-to-z transform to normalize the FC levels across a whole brain for each participant and to proceed group-level analysis.

In the group-level, One-way ANOVA test was conducted using the FC patterns with z-scores and the speech hearing scores across subjects as covariate. This procedure was carried out to identify the brain regions whose the FC level from the seed ROI was tightly linked with speech hearing score (uncorrected $p<0.005$ with

minimum of 20 connected voxels). If identified brain regions were not in proximity with seed regions of the FC analysis (i.e. > 8mm in distance), these regions were considered as a new seed ROI. Then, the newly identified seed ROI was used for the subsequent FC analysis. This repeated FC analysis with speech hearing scores as covariate in the one-way ANOVA framework was continued until there is no seed region was identified.

3 Results

3.1 Behavioral Results

In the statistical analysis of speech hearing score across three conditions (*i.e.*, BH, MH_L, or MH_R), the main effect of hearing condition was estimated from one-way repeated measures ANOVA (p=1.6×10^{-3}). In addition, a paired t-test was conducted to compare hearing scores between binaural and monaural hearing condition. In detail, speech hearing score in BH condition (5.75±0.13) was significantly greater compared to MH_L (4.75±0.18) and MH_R (4.3±0.40) conditions with statistical significance values of p=1.29×10^{-4} and p=7.60×10^{-3}, respectively.

3.2 Language-Related Regions

Fig. 2 shows the main effect across the speech hearing conditions. The neuronal activations were found in right STG (peak t-score=13.75; 40 voxels; [45, -22, 1] mm), right superior frontal gyrus (SFG; peak t-score=17.75; 114 voxels; [24, 20, 49] mm), right angular gyrus (peak t-score=13.07; 25 voxels; [42, -73, 46] mm), left SFG (peak t-score=34.54; 87 voxels; [-24, 11, 64] mm), and left middle frontal gyrus (peak t-score=19.57; 26 voxels; [-36, 41, 37] mm). As shown in Fig. 3, the levels of neuronal activations in each of these brain regions were significantly greater from the BH condition compared to MH_L and MH_R conditions. From the regression analysis, the neuronal activations in the right STG showed significant correlation with speech hearing score (R^2=0.21, p=0.003), whereas the neuronal activations of the remaining regions were not significantly correlated with speech hearing score (Fig. 3).

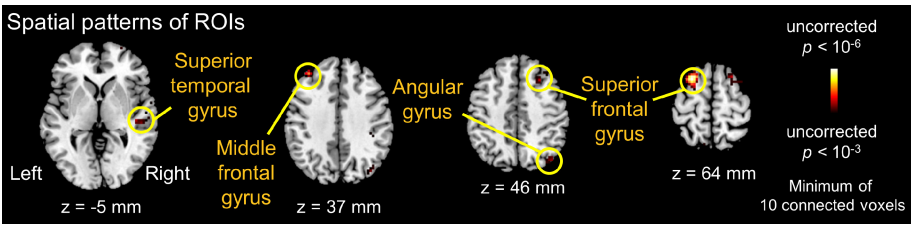

Fig. 2. Identified regions of interest (ROIs) that showed main effect of hearing conditions on neuronal activation

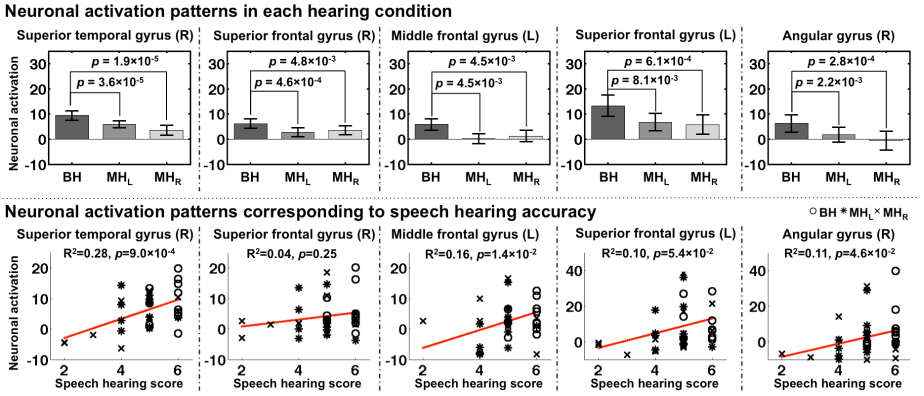

Fig. 3. Neuronal activation levels of ROIs and association with speech hearing accuracy

3.3 Language-Related Network

From the repeated FC analysis, language-related network was identified in the areas including left middle temporal gyrus (MTG; [-54, -40, -2] mm) which is in Wernicke's area. As shown in Fig. 4, the left MTG was functionally connected with right STG ([45, -22, 1] mm), right MTG ([63, -10, -17] mm), left MTG ([-66, -16, -2] mm), left STG ([-45, -19, 7] mm) and left STG ([-66, -40, 13] mm). The FC level between the brain regions of language-related network was significantly correlated with the speech hearing score (R^2>0.2, p<0.005). From a paired t-test between a pair of the hearing conditions, it was identified that the FC level was shown a marginal level of significance (p<0.05) from the BH condition than the MH_R condition except the FC level between left MTG ([-54, -40, -2] mm) and left STG ([-45, -19, 7] mm). The corresponding FC levels across all three hearing conditions were tightly correlated with the speech hearing scores (p<0.005).

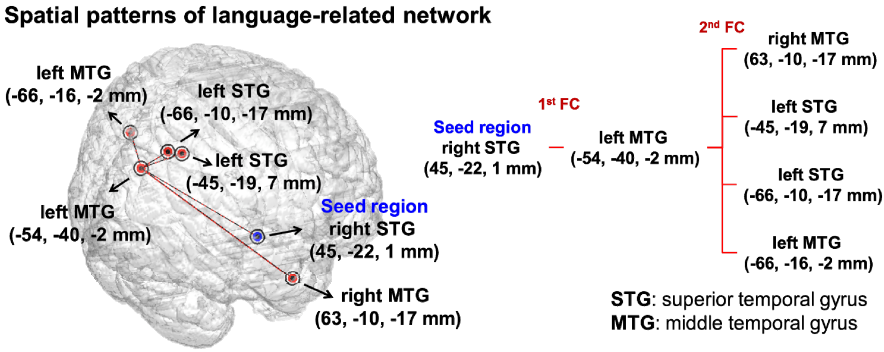

Fig. 4. Neuronal networks whose FC levels were significantly correlated with speech hearing score (uncorrected p<0.005 with minimum of 20 connected voxels)

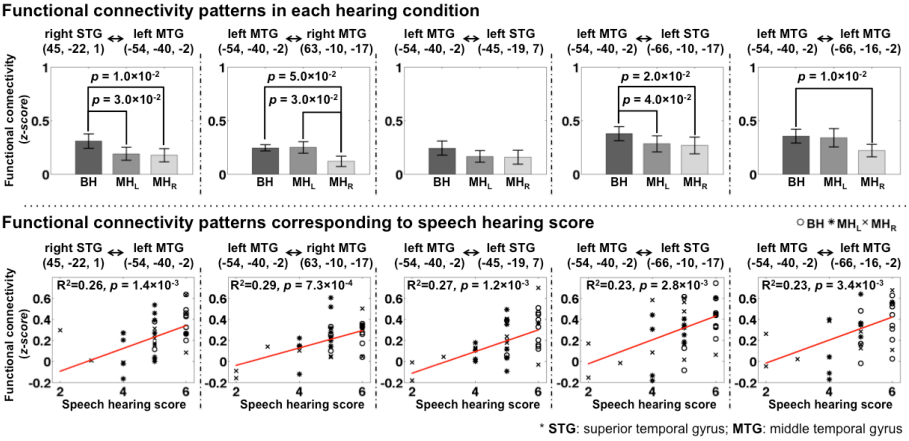

Fig. 5. Functional connectivity (FC) levels of the speech hearing related ROIs and a link between the FC levels across the ROIs and speech hearing scores

4 Discussion

In this study, we reported that there are distinct neuronal networks tightly linked with the speech hearing performance. More specifically, the neuronal activation level in the right STG was significantly correlated with the speech hearing score with greater level of from the BH and MH_L conditions than the MH_R condition. The language performance is known to be dominant in the left STG for the right-handed. Thus, this result may suggest that the right STG is crucial in speech hearing, whereas previous studies reported that contralateral STG was activated according to sound direction [10, 11].

From FC analysis, it was identified that FC level between right STG and left MTG was significantly correlated with speech hearing score. This result may indicate that the interaction between left STG and right MTG, reportedly the Wernicke's area, enhanced the speech hearing performance.

5 Conclusion

In this study, we present that the right STG is crucial in enhancement of the speech hearing performance. Moreover, it appears that the FC patterns from the right STG are tightly correlated with the speech hearing performance with much greater statistical significance compared to the correlation between the neuronal activity levels and speech hearing performance. Further investigation would be warranted to justify the reported findings via test-retest evaluation (1) applying supplementing analytical methods including various preprocessing algorithms to further reduce artifactual noises and (2) employing systematic experimental settings.

Acknowledgments. This research was supported in part by Basic Science Research Program through the National Research Foundation of Korea (NRF) grant funded by the Ministry of Education, Science and Technology (MEST) (2012-0002342) and in part by Samsung Electronics, Inc.

References

1. Hugdahl, K.: Lateralization of cognitive processes in the brain. Acta Psychol. 105, 211–235 (2000)
2. Matsumoto, R., Imamura, H., Inouchi, M., Nakagawa, T., Yokoyama, Y., Matsuhashi, M., Mikuni, N., Miyamoto, S., Fukuyama, H., Takahashi, R., Ikeda, A.: Left anterior temporal cortex actively engages in speech perception: A direct cortical stimulation study. Neuropsychologia 49, 1350–1354 (2011)
3. Van Ettinger-Veenstra, H.M., Ragnehed, M., Hällgren, M., Karlsson, T., Landtblom, A.-M., Lundberg, P., Engström, M.: Right-hemispheric brain activation correlates to language performance. NeuroImage 49, 3481–3488 (2010)
4. Van Ettinger-Veenstra, H.M., Ragnehed, M., McAllister, A., Lundberg, P., Engström, M.: Right-hemispheric cortical contributions to language ability in healthy adults. Brain and Lang. 120, 395–400 (2012)
5. Faust, M., Ben-Artzi, E., Vardi, N.: Semantic processing in native and second language: Evidence from hemispheric differences in fine and coarse semantic coding. Brain and Lang. 123, 228–233 (2012)
6. Van den Noort, M., Specht, K., Rimol, L.M., Ersland, L., Hugdahl, K.: A new verbal reports fMRI dichotic listening paradigm for studies of hemispheric asymmetry. NeuroImage 40, 902–911 (2008)
7. Bitan, T., Lifshitz, A., Breznitz, Z., Booth, J.R.: Bidirectional connectivity between hemispheres occurs at multiple levels in language processing but depends on sex. J. Neurosci. 30, 11576–11585 (2010)
8. Oldfield, R.C.: The assessment and analysis of handedness: The Edinburgh inventory. Neuropsychologia 9, 97–113 (1971)
9. Robertson, G.J., Wilkinson, G.S.: Wide Range Achievement Test 4. Psychological Assessment Resources, Lutz (2006)
10. Jäncke, L., Wüstenberg, T., Schulze, K., Heinze, H.J.: Asymmetric hemodynamic responses of the human auditory cortex to monaural and binaural stimulation. Hear. Res. 170, 166–178 (2002)
11. Stefanatos, G.A., Joe, W.Q., Aguirre, G.K., Detre, J.A., Wetmore, G.: Activation of human auditory cortex during speech perception: Effects of monaural, binaural, and dichotic presentation. Neuropsychologia 15, 301–315 (2008)
12. Huettel, S.A., Song, A.W., McCarthy, G.: Functional magnetic resonance imaging, 2nd edn. Sinauer Associates, Inc., Sunderland (2009)

Neuronal Synfire Chain via Moment Neuronal Network Approach

Xiangnan He[1], Wenlian Lu[1], and Jianfeng Feng[2]

[1] Center for Computational Systems Biology, Fudan University, Shanghai, P.R. China
[2] Center for Scientific Computing, Warwick University, Coventry CV4 7AL, UK

Abstract. In this letter, we use a novel method to analyse the stability synchronisation propagation in neuronal networks via the moment neuronal network approach developed recently. Here, the stability of synfire chain is twofold, including the stability of both the synchronisation in the cluster and the asynchronisation out of the cluster. Under the framework of the moment neuronal network, we model the dynamics of the Pearson correlation coefficients via evolution field equations. Thus, we study the stability of synfire chain via looking into the attractors of the model. Based on analytic and numerical approaches, In particular, we point out that the variance of the neuronal spike rate should be updated with the synfire propagation. Also, we find out that the balance between the excitation and inhibition PSPs and a suitable size of the cluster can enhance the stability of synfire chain.

1 Introduction

Synchronisation phenomenon in neuronal networks has been widely studied in both experiment [1–3] and theoretical model [4, 5]. It is well-known that in a spiking neuronal network, spikes of different neurons could easily synchronize and propagate their activity through layers. Refs. [6, 7] established a model called *synfire chain* to depict the synchronisation propagation by the *complete transmission line* architecture first proposed in [8]. A feed-forward network is used to model the synchronisation propagation in volleys through sparsely cortical neuronal network, which forms a chain-like dynamics. In this scenario, the computational methods can be utilised to realize and analyse the stability of a synfire chain by setting circuit model on node, for example, the leaky integrate-and-fire (LIF) model and Hodgkin-Huxley model model [9–13].

Refs. [9] proposed an approach of pulse-packets to study the stability synfire chains. With two variables, the width of the neuron cluster and the variance of the timing of evoking spikes in the cluster, the synfire chain can be regarded as behaviours of the attractors of dynamical systems with respect to the two variables. By this manner, a lot of characteristics of synfire chain have been found. The size of the neuron cluster is essential for a stable synfire chain, which should be larger than a threshold value [9, 10] but has a risk to explode if the size is too large [11]. The balance between the size of the IPSP and EPSP is suggested as a good choice to be embed synfire chains a sparsely locally connected random network [10, 12, 13]. Also, as shown in [14], increasing firing rates can enhance synchronisation.

M. Lee et al. (Eds.): ICONIP 2013, Part I, LNCS 8226, pp. 191–198, 2013.
© Springer-Verlag Berlin Heidelberg 2013

In comparison to most of the literature where synfire chain is discussed via the timing variance of the pulse-packets, in this letter, we use Pearson correlation coefficients (CCs) of the firing rates of an assemble of neurons to define synchronisation [14]. For a pair of neurons (a, b), the shift-correlation between them in a sliding window with length T is defined as $\rho_T = \lim_{L\to\infty} cov(n_a, n_b)/\sqrt{Var(n_a)Var(n_b)}$, where $n_i(t)$ is the number of spikes in a time interval $[t, t+T]$ subtracting the mean firing rate in a T-length time interval, $i = a, b$. Thus, the correlation coefficient of spike strains are defined as its limit $\rho = \lim_{T\to\infty} \rho_T$, which equals to the cross-correlation [14]. One can see that $\rho = 1$ implies complete synchronisation between two processes.

2 Preliminary

2.1 A Multilayered Architecture

We consider a feed-forward multilayered network as shown in Fig. 1 with random couplings structure. At each layer, there are exactly N nodes (an even integer), which is denoted as the set $\mathcal{N}^t$, where t is the index of the layer. Among them, $N_E = 4N/5$ nodes are E-neurons (the set $\mathcal{E}^t$) and the other $N_I = N/5$ are I-neurons (the set $\mathcal{I}^t$). At the t-th layer, each node has $K_E = \lambda N_E$ exciting synaptic input couplings from the E-neurons at the $t-1$-th layer and $K_I = \lambda N_I$ inhibiting synaptic input couplings from the I-neurons at the $t-1$-th layer. Here $\lambda \in (0, 1)$ is the density of the random network. Let $\mathcal{W}^t \subset \mathcal{E}^t$ be the cluster of neurons at each layer, where synfire chain occurs possibly with the size $\#\mathcal{W}^t = W$. We couple the neurons at the neighbour layers by the following way: each neuron in $\mathcal{W}^t$ receives couplings from all neurons in $\mathcal{W}^{t-1}$; except that, all couplings are randomly picked with equal probability to fit the in-degrees as mentioned above. We assume the relative strength of inhibitory synapses $g = 4$ and denote the size proportion between IPSP and EPSP as r: Let $w_{ij} = w_0$ if $j \in \mathcal{E}$ and there is a synaptic coupling from j to i and $w_{ij} = -rgw_0$ if $j \in \mathcal{I}$ and there is a synaptic coupling from j to i; otherwise $w_{ij} = 0$, where $w_0 > 0$ is a constant.

2.2 Moment Map

The framework of the moment neuronal network (MNN) approach developed recently [15, 16] enables us to describe the dynamics of CCs by evolution field equations. Thus, the stability of synnfire chain can be regarded as dynamics of the CC evolution equations. To minimally brief this approach, we start with a LIF neuronal network with N neurons which depicts the potential activity of the i-th neuron as follows:

$$\tau_m dV_i(t) = -V_i(t)dt + I_{ext,i} + I_{syn,i},\ i = 1, \cdots, N, \tag{1}$$

where τ_m is the capacitance constant, $I_{ext,i}$ is the external current stimulus, and $I_{syn,i}$ is the synaptic stimulus from the neighbourhood to the neuron i:

$$I_{syn,i} = \sum_j w_{ij}^E dN_j^{i,E}(t) + \sum_k w_{ik}^I dN_k^{i,I}(t),$$

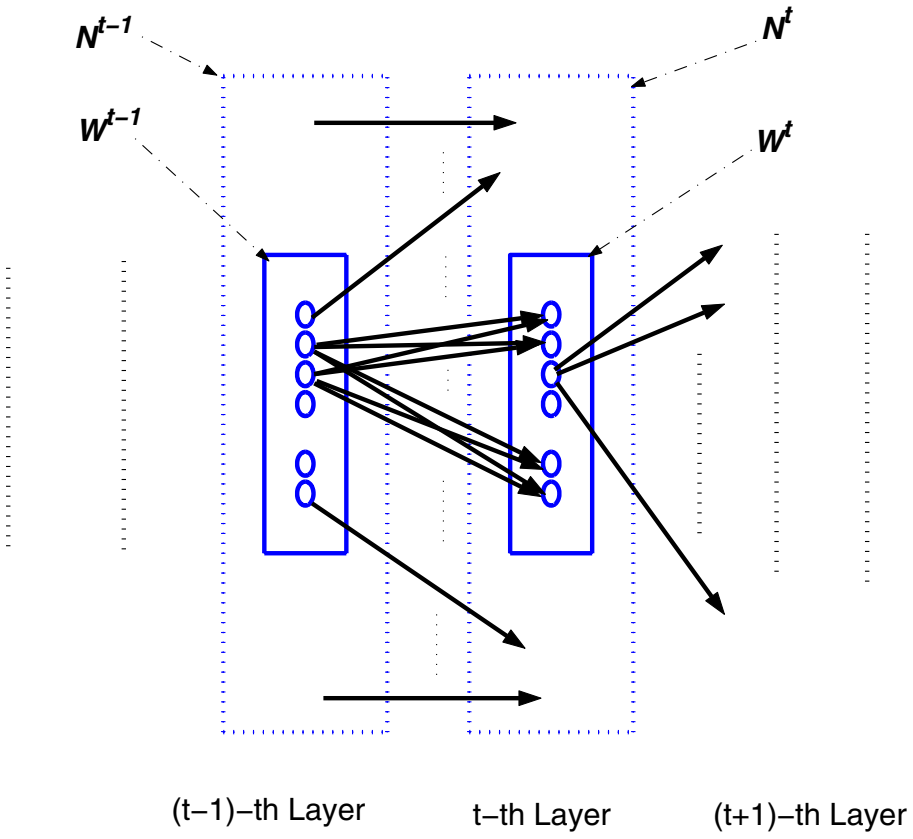

Fig. 1. Feed-forward network architecture. Neurons are represented as circles and couplings as arrows. The solid blue box represents the cluster at each layer where synchrony propagates and the dash black box represents the whole network at each layer.

where w_{ij}^E and w_{ik}^I are the EPSP and IPSP sizes from the j-th and l-th pre-synaptic neuron respectively and $N_j^{i,E}(t)$ and $N_l^{i,I}(t)$ are spike pulses from the exciting j-th and inhibiting l-th pre-synaptic neurons respectively, which are described as random point processes. The main idea of the moment neuronal network is to represent (approximate) the spike activity of a neuron (a point process) as Gaussian processes: $dN_j^{i,v}(t) \sim \mu_j^{i,v}dt + \sqrt{\tau_m}\sigma_j^{i,v}dB_j^{i,v}$, where $B_j^{i,v}, j = 1, \cdots, N$ are correlated Brownian motions. Thus, we use correlated Ornstein-Uhlenbeck (OU) processes to approximate the dynamics of the membrane potentials:

$$\tau_m dV_i(t) = -V_i(t)dt + \hat{\mu}_i dt + \sqrt{\tau_m}\hat{\sigma}_i dB_i(t),\ i = 1, \cdots, N, \tag{2}$$

where $\hat{\mu}_i = \sum_{j,v}\sum_{v=I,E} w_{ij}^v \mu_j^i$, $\hat{\sigma}_i = \sqrt{\sum_{j,k}\sum_{v,u=I,E} w_{ij}^v \sigma_j^{i,v} \rho_{jk}^{i,v,u} w_{ik}\sigma_k^{i,u}}$. Here, $\rho_{jk}^{i,v,u}$ is the correlation coefficient between the j-th and k-th synaptic inputs j and k to the neuron i, $u, v = I, E$, respectively. We still approximate the output spike trains as Gaussian processes, which enables us to establish a map from the first and second-order moments of the input spiking trains to those of spiking trains in the term of Siegert's expression [**?**]

$$\begin{aligned} \Gamma : (\mu_{in}, \sigma_{in}, \Sigma_{in}) &\to (\mu_{out}, \sigma_{out}, \Sigma_{out}) \\ \mu_{out} &= \mathcal{S}_1(\hat{\mu}, \hat{\sigma}) && (3) \\ \sigma_{out} &= \mathcal{S}_2(\hat{\mu}, \hat{\sigma})\sqrt{\mathcal{S}_1(\hat{\mu}, \hat{\sigma})} && (4) \\ \rho_{out,i,j} &= \Phi(\rho_{in,i,j}),\ i, j = 1, \cdots, N. && (5) \end{aligned}$$

By this way, we can describe the spike trains (rates) of neurons in the network as a Gaussian random field. The moment neuronal network approach aims to describe the spike activities of neuronal network by a the Gaussian random field via the evolution equations of these moments. For the details, we refer readers to [16].

With the moment map above, we derive evolution equations over CCs if we consider feed-forward or recurrent networks. In a multi-layered feed-forward LIF neuronal network as illustrated in Fig. 1, we rewrite Eq. (5) to yield the following maps from the CCs of the neuronal network's t-th layer to those of the $t+1$-th layer:

$$\rho_{ij}^{t+1} = \Phi_{ij}^t\left(\frac{\sum_{k,l} W_{ik}^t W_{jl}^t \rho_{kl}^t}{\sqrt{\sum_{k,l} W_{ik}^t W_{il}^t \rho_{kl}^t}\sqrt{\sum_{k,l} W_{jk}^t W_{jl}^t \rho_{kl}^t}}\right),\ i, j = 1, \cdots, N. \tag{6}$$

Here, $W_{ik}^t = w_{ik}\sigma_k(t)$, where $\sigma_k(t)$ is the variance of the spike rate of neuron k at the t-th layer, ρ_{kl}^t is the CC between the spike trains of the neuron pair (k, l) at t-th layer, and $\Phi_{ij}^t(\cdot)$ is the CC map. Therefore, a synfire chain is described as an attractor of the system (6) satisfying that the CC of intra-group is near 1 but the other CCs are near zero. In mathematical terms, for certain small $\epsilon > 0$ and $\delta > 0$, the system (6) has an attractor

$$\Lambda_{\epsilon,\delta} = \left\{[\rho_{i,j}]_{i\neq j} :\ \rho_{ij} > 1-\epsilon,\ \text{for } (i,j) \in \mathcal{W}\times\mathcal{W};\ |\rho_{ij}| < \delta,\ \text{otherwise}\right\}.$$

So, the stability of a synfire chain is twofold. On the one hand, the CC between the neuron in the cluster of synchrony are large and near 1; on the other hand, the other CC,

between the pairs of neurons, which are not both in the cluster, are low, near 0. Thus, under the framework of the moment neuronal network, the stability of synfire chain can be measured as the locations of the attractors of (6). To the best of our knowledge, all the related references up to now focused on the case with constant variance, i.e., $\sigma_k(t)$ does not change with layer t. However, in this letter, we consider constant w_{ij}, identical map $\Phi_{ij}^{(\cdot)}$ but adaptive variance $\sigma_k(t)$, which means the variance is updated by the moment map [16] in synchronization propagation.

We have proved in [16] under the assumption that all neurons are excited or inhibited and $\Phi = id$, if the network has spanning trees, then the network can synchronize quickly. However, in fact, in a real-world neuronal network, the CCs of the whole network with the spontaneous activities are kept at a low values from 0.1 to 0.2 but nonzero. Also, by considering the composite of the numerator of (6), one can see that all excited or inhibited network is not good to keep CCs in low values [13]. Therefore, we has reason to believe that to realize a stable synfire chain, an optimal environment is that in the group, the neurons are all with the same types of cells, intra-group graph topology is compact, and the others have proportional EPSPs and IPSPs.

Following the MNN framework, we study the stability of synfire chain by investigating the distribution of the attractors of the CCs in the feed-forward multi-layered network. We consider two classes of CCs. One is composed of the CCs between pairs of neurons both belonging to the cluster $\mathcal{W}^t$: $\{\rho_{i,j}^t\}_{(i,j)\in\mathcal{W}^t\times\mathcal{W}^t, i\neq j}$; the other is composed of the other CCs, i.e, between the pairs of neurons of which at least one do not belong to $\mathcal{W}^t$: $\{\rho_{i,j}^t\}_{(i,j)\notin W^t\times\mathcal{W}^t, i\neq j}$. We exclude the self-correlation in both classes.

3 Methods

The mean field method allows us to analytically study the the dynamics of moment map (3)-(5), especially the map for CCs (5)(or equivalently (6)). We use $\mu_{\pm}^t$ to represent the mean firing rates of the neuronal spike rate in$(+)$ or out of$(-)$ the cluster $(i,j) \in \mathcal{W}^t \times \mathcal{W}^t$ at the layer t. Also, $\sigma_{\pm}$ and $\rho_{\pm}^t$ denote the corresponding mean variances and mean CCs respectively. Let $\Phi_{\pm}$ be the mean-field CC map corresponding to $\rho_{\pm}^t$. Here, we focus on the CCs among $\mathcal{W}^t \times \mathcal{W}^t$ and those among $\mathcal{N}^t \times \mathcal{N}^t - \mathcal{W}^t \times \mathcal{W}^t$.

By the mean field method, we can transform (6) as follows:

$$\rho_{\pm}^{t+1} \approx \Phi_{\pm}(\rho_{\pm}^t) = \Phi_{\pm}\left(\frac{A_{\pm}^t}{B_{\pm}^t}\right), \tag{7}$$

where $A_{\pm}^t$ represent the correlation between the synaptic inputs of two neurons in $\mathcal{W}^t$ and at least one of them in $\mathcal{N}^t - \mathcal{W}^t$ respectively and $B_{\pm}^t$ represent their variance accordingly, in the mean field sense.

Via directly algebra, it can be seen that the highest terms with respect to K in dominator and numerator are both $(r-1)^2 K_E^2 (\sigma_-^t)^2 \rho_-^t$ as the network size $N \to \infty$, which leads that ρ_-^t will go near 1. So, in a network of a large size, to guarantee that the CCs except among the group are small, the balanced network $(r = 1)$ is optimal. This could also be verified by numerical simulation.

In a balanced network, $\{A_{\pm}^t, B_{\pm}^t\}$ can be simplified as

$$
\begin{aligned}
A_+^t &= W\Big\{2K_E\sigma_-^t(\sigma_+^t-\sigma_-^t)\rho_-^t+(\sigma_+^t)^2(1-\rho_+^t)-\lambda(\sigma_-^t)^2(1-\rho_-^t)\Big\}+5\lambda K_E(\sigma_-^t)^2(1-\rho_-^t)\\
&\quad + W^2\Big\{(\sigma_+^t)^2(\rho_+^t-\rho_-^t)+(\sigma_+^t-\sigma_-^t)^2\rho_-^t\Big\},\\
B_+^t &= W\Big\{2K_E\sigma_-^t(\sigma_+^t-\sigma_-^t)\rho_-^t+(\sigma_+^t)^2(1-\rho_+^t)-(\sigma_-^t)^2(1-\rho_-^t)\Big\}+5K_E(\sigma_-^t)^2(1-\rho_-^t)\\
&\quad + W^2\Big\{(\sigma_+^t)^2(\rho_+^t-\rho_-^t)+(\sigma_+^t-\sigma_-^t)^2\rho_-^t\Big\},\\
A_-^t &= W\Big\{2\lambda K_E\sigma_-^t(\sigma_+^t-\sigma_-^t)\rho_-^t+\lambda^2(\sigma_+^t)^2(1-\rho_+^t)-\lambda^2(\sigma_-^t)^2(1-\rho_-^t)\Big\}+5\lambda K_E(\sigma_-^t)^2(1-\rho_-^t)\\
&\quad + W^2\Big\{\lambda^2(\sigma_+^t)^2(\rho_+^t-\rho_-^t)+\lambda^2(\sigma_+^t-\sigma_-^t)^2\rho_-^t\Big\},\\
B_-^t &= W\Big\{2\lambda K_E\sigma_-^t(\sigma_+^t-\sigma_-^t)\rho_-^t+\lambda(\sigma_+^t)^2(1-\rho_+^t)-\lambda(\sigma_-^t)^2(1-\rho_-^t)\Big\}+5K_E(\sigma_-^t)^2(1-\rho_-^t)\\
&\quad + W^2\Big\{\lambda^2(\sigma_+^t)^2(\rho_+^t-\rho_-^t)+\lambda^2(\sigma_+^t-\sigma_-^t)^2\rho_-^t\Big\}. \qquad (8)
\end{aligned}
$$

Eq.(8) implies that the evolution of CCs (or equivalently $\rho_{\pm}^t$) in a balanced network is triggered by both cluster size W and the variances $\sigma_{\pm}^t$. To better mimic the dynamics of synfire chain, we update the variance of the neuronal spike rate with the propagation. Also, we consider the limit state. That is to say, $\rho_{\pm}^t$ and $\sigma_{\pm}^t$ have already reached the invariant state and thus were denoted by $\rho_{\pm}$ and $\sigma_{\pm}$ respectively. In fact, under the MNN framework, the firing rates, variances and CCs will all arrive the invariant state soon. By regarding $A_{\pm}/B_{\pm}$ as a function of W, it is obvious that both A_+/B_+ and A_-/B_- are monotonous and bounded, thus there exists a W_0 such that $A_+/B_+ - A_-/B_-$ reaches maximum. In this way, we could define $W = W_0$ as the optimal size of cluster to maintain the synfire propagation.

Although it is hard to obtain a precise expression of the optimal cluster size W_0, the derivation below gives a easy way to find a suboptimal cluster size W_1 which is enable to maintain the synfire chain.

Theorem 1. *In a balanced network, there exist at least one suitable cluster size W_1 to realize the synfire, i.e., $\rho_+ \geq 1-\epsilon$ and $\rho_- \leq \delta$, if we choose ϵ and δ satisfying $\epsilon \geq \lambda\frac{1-\delta}{\delta}$.*

Proof. Let $P = 5K_E\sigma_-^2(1-\rho_1)$, $Q = [\sigma_+^2(\rho_+-\rho_-)+(\sigma_+-\sigma_-)^2\rho_-]$ and $R = 2K_E\sigma_-(\sigma_+-\sigma_-)\rho_- + (\sigma_+)^2(1-\rho_+) - (\sigma_-)^2(1-\rho_-)$ in (8), we derive

$$
\begin{cases}
\rho_+ = A_+/B_+ \geq \frac{\lambda P+QW^2+RW}{P+QW^2+RW} \geq \frac{\lambda P+\lambda QW^2+RW}{P+\lambda QW^2+RW}\\
\rho_- = A_-/B_- \leq \frac{\lambda P+\lambda^2 QW^2+\lambda RW}{P+\lambda^2 QW^2+\lambda RW}
\end{cases}
$$

from Eq. (8) via simple algebra. By choosing W_1 such that $a\lambda P = \lambda^2 QW_1^2 + \lambda RW_1$, the synfire condition $\rho_+ \geq 1-\epsilon$ and $\rho_- \leq \delta$ could be transformed to

$$
\begin{cases}
\frac{\lambda+a}{1+a} \geq 1-\epsilon \Longleftrightarrow a \geq \frac{1-\lambda}{\epsilon} - 1\\
\frac{(1+a)\lambda}{1+a\lambda} \leq \delta \Longleftrightarrow a \leq \frac{\delta-\lambda}{\lambda(1-\delta)}
\end{cases}.
$$

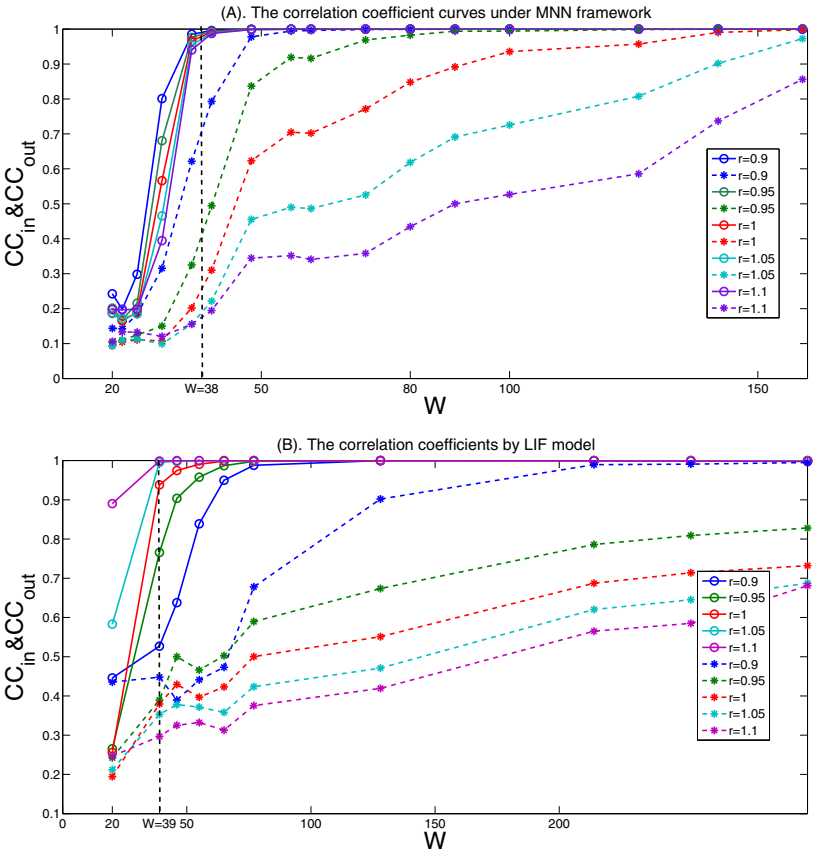

Fig. 2. The correlation coefficient curves under MNN framework (LIF model). The solid line represents ρ_+ and the dash line records ρ_- in both figures. CC curves with different inhibitory and excitatory strength ratio r are denoted by different colors. The vertical black dash line $W = 38$ ($W = 39$) is the critical point at which synfire chain maintains in each case. When the cluster size $W < 20$, the firing rate is almost vanished via neuronal propagation, therefore both (A) and (B) has a blank area ($W < 20$) in the figure.

To guarantee the existence of a, we combine the above two inequality to get $\frac{1-\lambda}{\epsilon} - 1 \leq a \leq \frac{\delta-\lambda}{\lambda(1-\delta)}$, which leads to our requirement $\epsilon \geq \lambda\frac{1-\delta}{\delta}$. Also, for any positive number a, by solving the quadratic equation $a\lambda P = \lambda^2 Q W_1^2 + \lambda R W_1$, we obtain an estimation for suboptimal cluster size $W_1 = \frac{-\lambda R + \sqrt{\lambda^2 R^2 + 4a\lambda^3 QP}}{2\lambda^2 Q} = 2a(\sqrt{(R/P)^2 + 4a\lambda Q/P} + R/P)^{-1}$, which depends on the variance $\sigma_\pm$ but not the size of the neuron network N.

4 General Results

Fig. 2**A** shows the iteration results of system (6) in terms of CCs as a function of cluster size W for different r. Meanwhile, Fig. 2**B** simulates a LIF network (1) on the multi-layered feed-forward network to verify the results obtained by the system (6). Both figures show that the CCs curves shifts up with the decrease of the strength between inhibitory and excitatory input r. Also for fixed r, the whole CCs (both in and out) increased as the increase of the size of the cluster W. In addition, for a balanced network, we could divide the whole horizontal axis into three segments according to the behavior of the neuronal network:

- $W = 20$ or less: the synchronized phenomenon will disappear both in and out because the firing rate μ is decreasing via propagation;
- $W = 40$ or so: the synchronized phenomenon only maintained in the strongly connected group, that is, the synfire chain appears;
- $W = 100$ or bigger: the whole network get synchronized.

References

1. Reyes, A.D.: Nat. Neurosci. 6, 593 (2003)
2. Ikegaya, Y., et al.: Science 304, 559 (2004)
3. Diesmann, M., Gewaltig, M.-O., Aertsen, A.: Nature 402, 529 (1999)
4. Campbell, S.R., Wang, D.L., Jayaprakash, C.: Neural Computation 11, 1595 (1999)
5. Masuda, N., Aihara, K.: Phys. Rev. E 64, 051906 (2001)
6. Abeles, M.: Isr. J. Med. Sci. 18, 83 (1982)
7. Abeles, M.: Corticonics, neural circuits of the cerebral cortex (CUP, 1991)
8. Griffith, J.S.: Biophys. J. 3, 299 (1963)
9. Aertsen, A., Diesmann, M., Gewaltig, M.O.: Physiol, J. (Paris) 90, 243 (1996)
10. Aviel, Y., Mehring, C., Abeles, M., Horn, D.: Neural Comput. 15, 1321 (2003)
11. Mehring, C., Hehl, U., Kubo, M., Diesmann, M., Aertsen, A.: Biol. Cybern. 88, 395 (2003)
12. van Vreeswijk, C., Sompolinsky, H.: Neural Comput. 10(6), 1321 (1998)
13. Lewis, T.J., Rinzel, J.: J. Comput. Neurosci. 14, 283 (2003)
14. De La Rocha, J., et al.: Nature 448, 802 (2007)
15. Feng, J.F., Deng, Y., Rossoni, E.: Phys. Rev. E 73, 041906 (2007)
16. Lu, W., Enrico, R., Feng, J.F.: NeuroImage 52, 913 (2010)
17. Feng, J.F.: J. Theor. Biol. 222, 151 (2003)

Biomarker Development on Alcohol Addiction Using EEG

Pham Lam Vuong[1], Likun Xia[1], Aamir Saeed Malik[1], and Rusdi Bin Abd Rashid[2]

[1] Center for Intelligent Signal and Imaging Research (CISIR)
Department of Electrical and Electronic Engineering,
Universiti Teknologi PETRONAS, Malaysia
[2] Department of Psychological Medicine, Faculty of Medicine, University of Malaya

Abstract. Alcohol addiction is harmful to society, economy and personal health. Alcohol addiction treatments intend to help addicted individuals reduce and stop compulsive alcohol use. Using biomarker, the clinicians could determine if drugs are having a desirable effect much earlier and given in correct dose for treatment. This paper will provide an up-to-date review of the state of the art in biomarker development for alcohol addiction treatment using electroencephalography (EEG) including EEG methodologies and their applications.

Keywords: Biomarker, alcohol addiction, EEG, predict.

1 Introduction

Alcohol addiction is characterized by an increased tolerance and physical dependence on alcohol that affect individual's ability to control alcohol consumption safely and cause withdraw symptoms once stop drinking. The harmful use of alcohol results in approximately 2.5 million deaths each year [1]. Alcohol damages almost every organ in the body, including the brain.

The harmful effects of alcohol addiction may be reduced through treatment policies. Biomarkers could help increase treatment efficiency by 1) combining with other screening tools (CAGE, MINI, …) to identify individuals with alcohol-related problems or who are at risk, 2) identifying the subset of abstainers at highest risk for relapse [2-3] and 3) evaluating new medications or behavioral interventions by giving outcome measures in earlier stage. Electroencephalography (EEG) is a non-invasive technique that detects electrical impulses in the brain due to neuronal activity using electrodes placed on the patient's scalp. EEG and related methodologies offer the promise of new biomarker for alcohol addiction treatment.

2 EEG Methodology and Alcoholism

Over the last decade, there has been a rapid development of EEG study on the harmful effect of alcohol addiction to brain. EEG may be recorded with the

M. Lee et al. (Eds.): ICONIP 2013, Part I, LNCS 8226, pp. 199–206, 2013.
© Springer-Verlag Berlin Heidelberg 2013

continuous electroencephalogram (EEG) or with the event-related brain potential (ERP) during cognitive and sensory tasks. The study of ERPs with new method of time frequency domain analysis, have revealed the phenomenon of event-related oscillation (ERO) which provide greater utility in understanding brain function than the traditional ERP.

2.1 Electroencephalogram (EEG)

Resting EEG is frequency-dependent, spontaneous and continuous neural activity during a restful or specific mental state. EEG signal can be decomposed into bands with different frequencies reflecting various types of brain activities, most commonly: delta (0-3.5 Hz), theta (4-7.5 Hz), alpha (8-12.5 Hz), beta (13-28.5 Hz) and gamma (> 29 Hz). In several studies, fast bands like alpha, beta, and gamma could be divided into sub-bands [2-4].

Many studies have shown higher tonic theta power in alcoholics than respective matched controls, and also in heavy drinkers compared to light drinkers and non-alcohol subjects. The elevated theta reflects a deficiency in the information-processing capacity of the central nervous system (CNS). By comparing 307 alcohol-dependent (AD) subjects with 307 alcohol control (AC) subjects in eyes closed state, Rangaswamy [5] found the result of an increase theta at all scalp loci, prominent at the central and parietal in male, and at the parietal in female. Moreover by using mental rehearsal tasks for testing frontal activities, Bruin et al [6] stated that heavy drinkers had more synchronization in the theta band than light drinkers during an eyes-closed condition. On the contrary, there are other studies reporting decreased slow bands activity (delta, theta) in their alcoholic patients [2], [4], [7]. Evaluating EEG relative power, Bauer [3] showed a slight increase in theta power in relapse-prone and no different found in abstinent-prone compared with non-alcohol control subjects after 6 months monitoring. Some other studies also showed a significant decrease in theta power over frontal regions associated with cortical atrophy when compared detoxified patients with controls [4], [7] . These results and conclusions were not consistent with each other's about the changes in theta power. However, the methodology and participant recruited criteria (alcoholics vs. detoxified patients) used by these studies are different. So it may be an indicator of the recovery of alcoholics. The relationship between theta power and the developing of alcoholism and, state-related condition need more investigation. Anyway, changing in resting theta did not seem to be present in the offspring of alcoholics, which may indicate a state-dependent condition.

Alpha rhythm was also found different between abstainers (the ones who keep stopping alcohol consumption after receiving treatment) and relapsers (abstainers who fall into addicted in alcohol again). The alpha rhythm is the predominant EEG rhythm in the relaxed alert state. Decrease in alpha activity in alcoholics is indicative of a deficiency in retrieving information from memory, and in attention. It is obtained both with eyes-open and eyes-closed, especially in the eyes-closed condition over the occipital regions. Ehlers and Phillips [8-9] suggested that alcohol dependence was associated with lower spectral power in the alpha frequency range. However, in their

studies, low voltage alpha was recorded to be exited in both alcoholics and controls, and there was no significant different between controls and alcoholics. Winterer [2] and Bauer [3] also showed especially less frontocentral alpha activity in relapsers compared with abstainers.

One of the robust and consistent resting EEG findings in alcoholism is the increased beta band activity in alcoholics and their high-risk offspring. Increased beta power in the EEG of alcoholics, particularly the increased fast beta (>20Hz) in the relapsers, has been well documented [2-4], [7], [10]. The increased beta power in the resting EEG may be an electrophysiological index of the imbalance in the excitation–inhibition homeostasis in the cortex. The quantitative EEG (QEEG) and relapse classification studies of detoxified alcohol-dependent patients as compared with normal controls [2] showed good predict ability of beta band power with correct classification rates of 83-85% using multilayer perception neuronal network (NN) with one layer 2-20 neurons [2] and 74,3% using logistic regression [3]. However, Winterer's study showed poor specificity with just 60-73% correct abstainers' classification. In contrast, Bauer's study showed improved specificity (85%) but poor sensitivity and (61%). Beta band predictive needs more studies and replications with different methods to improve its predictive rate, especially in medication treatment. The resting EEG beta power [11] also proved that it was more heritable and closer to gene action than clinical diagnosis (e.g. alcohol dependence).

These findings indicate that resting EEG is very promising state biomarker for future studies that can help in alcohol addiction treatment by predicting relapse patients.

2.2 Event-Related Potential (ERP)

ERPs are time-locked voltage fluctuations in the brain in response to a sensory, motor, or cognitive event. They are extracted from a set of EEG trial epochs by means of filtering and signal averaging. Early components with latency less than 100ms reflect sensory processes and contain small amplitude, while later components with larger amplitude reflect higher cognitive computations.

Most ERP studies in investigating the electrophysiological deficits in alcoholics and individuals at risk focused on the large positive P300 or P3 component that occurs between 300ms and 700ms after a 'significant' stimulus and is not related to its physical features. The lower amplitude of P3 components are related with the inefficient allocation of resources during neural processing and underlying CNS hyper excitability in alcoholics and individuals at risk. Many studies [12-16] showed that waveform of P3 to task-relevant target stimuli (P3b) are of significantly lower voltage and more delayed latency in abstinent alcoholics than in non-alcoholics, particularly over parietal regions. P3 deficit occurs in both visual and auditory tasks, but more consistent for visual tasks. Suresh [16] indicated that lower P3 amplitude presented under effect of alcohol in both genders for auditory oddball task, but more significant in male patients. Kamarajan [15] showed that alcoholics manifested low amplitude P3b components to not only target (Go) stimuli, but also to rare non-target (NoGo) stimuli, and there is less different between these two conditions in alcoholics.

Porjesz's studies suggested that low P3 voltages might not be reversible, but precede alcoholism, or recover more slowly after long abstinent periods [17]. Porjesz and colleagues also noted that alcoholics who were members of Alcoholics Anonymous still manifest low P3 amplitudes after extremely prolonged abstinent (3-10 years). However, 63.9% of the participants were correctly classified by Li Wan et al. [18] using P3 as the first predictor in the discrimination function. The result indicated that there was different in P3b between relapsers and abstainers. Thus, the P3 amplitude can be taken as a marker of risk and provides excellent endophenotype for genetic studies.

The P300 response can be divided into two subcomponents based on differing in task and subject-state correlates, latency, topography on the scalp and generating structure: P3a and P3b. P3a is recorded in response to novel non-target stimuli and has more frontal-central distribution with latency from 220-280ms. It is thought to reflect the initial signal evaluation. Posteriorly distributed P3b has a longer latency 300-700ms and is evoked by the rare target stimuli. Marinkovic et al. [13] reported about the decrease of P3a following a low dose of alcohol. The study also indicated that alcohol had a greater reducing effect on P3a amplitude to unattended rare stimuli than to P3b with attended rare stimuli. The result suggested P3a as a potential screening tool for alcohol dependent. Anderson [19] examined P3a amplitude as a direct predictor of treatment success for substance dependence. By using discriminant function analysis, he confirmed that P3a amplitude was a robust predictor of treatment completion, and more sensitive than other measures including substance abuse severity.

Stimulus processing is not a simple cognitive process of P300 but is composed of different stages with electrophysiological correlates; for example, perception level with P100 and N170, attention level with N200, and decision level with P300. The P300 is functionally linked to decisional processes and cognitive processing before activating the motor response, which is deficient in alcoholics. There are other ERP measures that can differentiate alcohol addictions from controls such as Mismatch negativity (MMN) and Brain-stem auditory-evoked potential (BAEP). Marco [20] reported about the deficit in P50 auditory sensory gating in abstinent chronic alcoholics. Curtin [21] indicated the relationship between alcohol and cognitive function from the reduced N450 and a more tonic, negative slow wave (NSW) associate with behavioral impairment resulted from failure in cognitive control function in alcohol consumption. More investigating about the early impairments in ERP signal may help to reveal the reason of deficit observed in cognitive processing of alcoholic patients.

2.3 Event-Related Oscillation (ERO)

For the classical approach to the study of ERP, ongoing EEG is treated as 'noise', in which the ERP signal is embedded. The ongoing oscillation is canceled out when extracting ERP by performing average, which results in the loss of critical information about variability upon single trials in neural activity.

New studies in time-frequency domain suggested that ERP represent the composition of electrical neural activities that evoked from multiple sources in the brain, and consist of superimposed event-related oscillation (ERO) of different spectral EEG bands that are related to sensory and cognitive processing. ERO can be divided into the same bands as spontaneous resting EEG, but with different reflection of brain function. Fast frequencies correspond to synchronization of groups of neurons in local areas, whereas slow frequencies are involved in larger distances synchronization.

Several studies have demonstrated that P3 responses are primarily the outcome of theta and delta oscillations elicited during cognitive processing of stimuli [22-27]. Jones et al. [27] indicated that frontally focused theta band activity (4–5 Hz) and a posterior distributed delta band activity constitute the P300 ERP waveform. The theta component formed the N200 and the early part of the P300 wave, and the delta component formed the main part of the P300 wave. These delta and theta EROs were derived from several cognitive paradigms, including the oddball task, Go/NoGo task, and a gambling task, to study alcoholism and related clinical conditions. Evoked delta and theta power were found to be significantly decreased among alcoholics compared with control subjects when processing the target stimuli in a visual oddball [26], [28] and Go/NoGo paradigm [23-24]. Fein et al. [25] found that the long-term abstinent alcoholics (LTAAs) showed a significantly larger theta ERS to the target stimulus compared with the non-alcoholic controls (NACs). Fein et al. [28] continued showing that theta ERS was larger in both short-term abstinent alcoholics (STAA) and LTAA compared to controls. The magnitude of the enhancement in STAA was greater than in LTAA. The significant different between long term and short term abstinence may be the indicator of brain function recovery from alcohol consumption. Significantly lower evoked delta ERO power, total delta and theta ERO power in LTAA provide an alternative and comparable representation of the reduced P3b amplitude for assessing recovery progress or relapse prediction. About the inherited risk of abusing alcohol, Rangaswamy [29] founded the decrease of total theta power and total evoked delta power for visual targets in high risk alcoholism's offspring.

Rangaswamy [29] and Ajayan [30] highlighted the evoked gamma. The responding suppression of gamma band activity to target stimuli observed in the frontal region of alcoholics may be associated with cognitive processes [30]. Based on the early phase-locked gamma oscillation during visual perception and the difference in gamma band energies, Ramaswamy [31-32] proposed evoked gamma as a screening tool and confirmed with accuracy of 91.12% using multilayer perceptron NN.

3 Discussion

In clinical practice using EEG, there are few reports about early relapse detecting method for alcoholic addiction treatment. Resting EEGs and ERPs components have been studied for predicting patients with high risk of relapse but the accuracy is still not accurate enough for clinical practice. The new EEG phenomenon (evoked theta, evoked delta, induced theta ERS, gamma oscillation) of EROs may be candidate for assessing treatment progress.

Following the review, there is still no study about the association between a deficit in gamma band and the duration of abstinent and its ability for discriminating between relapsers and abstainers.

Regarding the induce theta ERS, its differences between alcoholic and control groups have not been well defined [28]. Induced theta activity tends to increase with increased memory load and/or allocation of attention to task demands [33][30].

From these problems we can hypothesize:

1. The new sensitive and specific EEG biomarker will help increase treatment efficiency and to determine if drugs have a desirable effect much earlier.
2. Induce theta promises a "state marker" by showing different between abstain-prone and relapse-prone.
3. Delineating induced theta ERS effects in alcoholics appears to be the nature and modality of the discrimination task.

Acknowledgment. This work is supported by the Fundamental Research Grant Scheme, Ministry of High Education (MOHE), Malaysia.

References

1. World Health Organization, Global status report on alcohol and health. World Health Organization, Geneva, Switzerland (2011)
2. Winterer, G., Klöppel, B., Heinz, A., Ziller, M., Dufeu, P., Schmidt, L.G., Herrmann, W.M.: Quantitative EEG (QEEG) predicts relapse in patients with chronic alcoholism and points to a frontally pronounced cerebral disturbance. Psychiatry Research 78(1-2), 101–113 (1998)
3. Bauer, L.O.: Predicting relapse to alcohol and drug abuse via quantitative electro encephalography. Neuropsychopharmacology 25(3), 332–340 (2001)
4. Saletu-Zyhlarz, G.M., Arnold, O., Anderer, P., Oberndorfer, S., Walter, H., Lesch, O.M., Böning, J., Saletu, B.: Differences in Brain Function Between Relapsing and Abstaining Alcohol-Dependent Patients, Evaluated by Eeg Mapping. Alcohol and Alcoholism 39(3), 233–240 (2004)
5. Rangaswamy, M., Porjesz, B., Chorlian, D.B., Choi, K., Jones, K.A., Wang, K., Rohrbaugh, J., O'Connor, S., Kuperman, S., Reich, T., Begleiter, H.: Theta Power in the EEG of Alcoholics. Alcoholism: Clinical and Experimental Research 27(4), 607–615 (2003)
6. de Bruin, E.A., Bijl, S., Stam, C.J., Böcker, K.B., Leon Kenemans, J., Verbaten, M.N.: Abnormal EEG synchronisation in heavily drinking students. Clinical Neurophysiology 115(9), 2048–2055 (2004)
7. Coutin-Churchman, P., Moreno, R., Añez, Y., Vergara, F.: Clinical correlates of quantitative EEG alterations in alcoholic patients. Clinical Neurophysiology 117(4), 740–751 (2006)
8. Ehlers, C.L., Phillips, E., Schuckit, M.A.: EEG alpha variants and alpha power in Hispanic American and white non-Hispanic American young adults with a family history of alcohol dependence. Alcohol 33(2), 99–106 (2004)
9. Ehlers, C.L., Phillips, E.: Association of EEG alpha variants and alpha power with alcohol dependence in Mexican American young adults. Alcohol 41(1), 13–20 (2007)

10. Rangaswamy, M., Porjesz, B., Chorlian, D.B., Wang, K., Jones, K.A., Bauer, L.O., Rohrbaugh, J., O'Connor, S.J., Kuperman, S., Reich, T., Begleiter, H.: Beta power in the EEG of alcoholics. Biological Psychiatry 52(8), 831–842 (2002)
11. Rangaswamy, M., Porjesz, B., Chorlian, D.B., Wang, K., Jones, K.A., Kuperman, S., Rohrbaugh, J., O'Connor, S.J., Bauer, L.O., Reich, T., Begleiter, H.: Resting EEG in offspring of male alcoholics: beta frequencies. International Journal of Psychophysiology 51(3), 239–251 (2004)
12. Costa, L., Bauer, L., Kuperman, S., Porjesz, B., O'Connor, S., Hesselbrock, V., Rohrbaugh, J., Begleiter, H.: Frontal P300 decrements, alcohol dependence, and antisocial personality disorder. Biological Psychiatry 47(12), 1064–1071 (2000)
13. Marinkovic, K., Halgren, E., Maltzman, I.: Arousal-related P3a to novel auditory stimuli is abolished by a moderately low alcohol dose. Alcohol and Alcoholism 36(6), 529–539 (2001)
14. Maurage, P., Campanella, S., Philippot, P., de Timary, P., Constant, E., Gauthier, S., Miccichè, M.-L., Kornreich, C., Hanak, C., Noel, X., Verbanck, P.: Alcoholism leads to early perceptive alterations, independently of comorbid depressed state: An ERP study. Neurophysiologie Clinique/Clinical Neurophysiology 38(2), 83–97 (2008)
15. Kamarajan, C., Porjesz, B., Jones, K.A., Choi, K., Chorlian, D.B., Padmanabhapillai, A., Rangaswamy, M., Stimus, A.T., Begleiter, H.: Alcoholism is a disinhibitory disorder: neurophysiological evidence from a Go/No-Go task. Biological Psychology 69(3), 353–373 (2005)
16. Suresh, S., Porjesz, B., Chorlian, D.B., Choi, K., Jones, K.A., Wang, K., Stimus, A., Begleiter, H.: Auditory P3 in Female Alcoholics. Alcoholism: Clinical and Experimental Research 27(7), 1064–1074 (2003)
17. Porjesz, B., Begleiter, H.: Human brain electrophysiology and alcoholism, pp. 139–182. Plenum Press (1985)
18. Wan, L., Baldridge, R.M., Colby, A.M., Stanford, M.S.: Association of P3 amplitude to treatment completion in substance dependent individuals. Psychiatry Research 177(1-2), 223–227 (2010)
19. Anderson, N.E., Baldridge, R.M., Stanford, M.S.: P3a amplitude predicts successful treatment program completion in substance-dependent individuals. Subst Use Misuse 46(5), 669–677 (2011)
20. Marco, J., Fuentemilla, L., Grau, C.: Auditory sensory gating deficit in abstinent chronic alcoholics. Neuroscience Letters 375(3), 174–177 (2005)
21. Curtin, J.J., Fairchild, B.A.: Alcohol and cognitive control: Implications for regulation of behavior during response conflict. Journal of Abnormal Psychology 112(3), 424–436 (2003)
22. Krause, C.M., Aromäki, A., Sillanmäki, L., Åström, T., Alanko, K., Salonen, E., Peltola, O.: Alcohol-induced alterations in ERD/ERS during an auditory memory task. Alcohol 26(3), 145–153 (2002)
23. Kamarajan, C., Porjesz, B., Jones, K.A., Choi, K., Chorlian, D.B., Padmanabhapillai, A., Rangaswamy, M., Stimus, A.T., Begleiter, H.: The role of brain oscillations as functional correlates of cognitive systems: a study of frontal inhibitory control in alcoholism. International Journal of Psychophysiology 51(2), 155–180 (2004)
24. Kamarajan, C., Porjesz, B., Jones, K., Chorlian, D., Padmanabhapillai, A., Rangaswamy, M., Stimus, A., Begleiter, H.: Event-Related Oscillations in Offspring of Alcoholics: Neurocognitive Disinhibition as a Risk for Alcoholism. Biological Psychiatry 59(7), 625–634 (2006)

25. Andrew, C., Fein, G.: Induced theta oscillations as biomarkers for alcoholism. Clinical Neurophysiology 121(3), 350–358 (2010)
26. Rangaswamy, M., Porjesz, B.: From event-related potential to oscillations: genetic diathesis in brain (dys) function and alcohol dependence. Alcohol Research & Health (September 2008)
27. Jones, K.A., Porjesz, B., Chorlian, D., Rangaswamy, M., Kamarajan, C., Padmanabhapillai, A., Stimus, A., Begleiter, H.: S-transform time-frequency analysis of P300 reveals deficits in individuals diagnosed with alcoholism. Clinical Neurophysiology 117(10), 2128–2143 (2006)
28. Gilmore, C.S., Fein, G.: Theta event-related synchronization is a biomarker for a morbid effect of alcoholism on the brain that partially resolve with extended abstinence. Brain and Behavior 2(6), 796–805 (2012)
29. Rangaswamy, M., Jones, K.A., Porjesz, B., Chorlian, D.B., Padmanabhapillai, A., Kamarajan, C., Kuperman, S., Rohrbaugh, J., O'Connor, S.J., Bauer, L.O., Schuckit, M.A., Begleiter, H.: Delta and theta oscillations as risk markers in adolescent offspring of alcoholics. International Journal of Psychophysiology 63(1), 3–15 (2007)
30. Padmanabhapillai, A., Porjesz, B., Ranganathan, M., Jones, K.A., Chorlian, D.B., Tang, Y., Kamarajan, C., Rangaswamy, M., Stimus, A., Begleiter, H.: Suppression of early evoked gamma band response in male alcoholics during a visual oddball task. International Journal of Psychophysiology 60(1), 15–26 (2006)
31. Sharmilakanna, Ramaswamy, P.: Neural Network Classification of Alcohol Abusers Using Power in Gamma Band Frequency of VEP Signals. Multimedia Cyberscape Journal 1 (2003)
32. Ramaswamy, P.: Screening for Chronic Alcoholic Subjects Using Multiple Gamma Band EEG: A Pilot Study. JCS&T 7(2), 182–185 (2007)
33. Krause, C.M., Sillanmäki, L., Koivisto, M., Saarela, C., Häggqvist, A., Laine, M., Hämäläinen, H.: The effects of memory load on event-related EEG desynchronization and synchronization. Clinical Neurophysiology 111(11), 2071–2078 (2000)

Constructing Brain Connectivity Graph by Modified Sparse Representation

Jing Ren and Haixian Wang*

Key Laboratory of Child Development and Learning Science of Ministry of Education, Research Center for Learning Science, Southeast University, Nanjing, Jiangsu, 210096, P.R. China
{220112990,hxwang}@seu.edu.cn

Abstract. In the field of neuroimaging, fMRI is an important tool for brain connectivity analysis. However, the architecture of functional connectivity within the human brain connectome cannot be exactly interpreted at the voxel level by using the traditional correlation analysis. To address this problem, we propose a modified sparse representation (MSR) method to construct the connectivity graph in an automatical and efficient way. The MSR approach uses the sparse representation instead of the correlation coefficient to relate brain regions or voxels. Degree centrality (DC), closeness centrality (CC), betweenness centrality (BC), and eigenvector centrality (EC) are employed to extract the features of fMRI connective patterns. With the extracted features, we then experimentally compare affirmative and negative sentences processing on the Star/Plus database, which shows significant difference via MSR method. Compared with the traditional correlation method, MSR shows higher significance between the two cognitive processing tasks.

Keywords: modified sparse representation, degree centrality, closeness centrality, betweenness centrality, eigenvector centrality.

1 Introduction

Functional magnetic resonance imaging (fMRI) is one of the fundamental tools for us to investage brain activity[1]. Through fMRI neuroimaging, numerous neuroscientific studies were carried out on the connectivity analysis[2]. Among the methods of identifying the functional networks of cognitive states from fMRI data, an informative graph makes sense for us to understand brain patterns. The nodes in a graph are set as the brain regions and voxels while the edges are represented by correlations. Functional connectivity between brain regions or voxels is classically represented by a "connectivity matrix" [3-5]. The elements of the matrix are generally obtained by computing correlations between different brain regions or voxels at different time courses. Then we need to set a correlation threshold to yield a weighted matrix which enabling the computation of properties. Since the purpose of the constructed connectivity matrix is to find patterns of different cognitive states, the following characters are desired[6].

* Corresponding author.

M. Lee et al. (Eds.): ICONIP 2013, Part I, LNCS 8226, pp. 207–214, 2013.
© Springer-Verlag Berlin Heidelberg 2013

Robustness to data noise. The traditional connectivity matrix is founded on pair-wise correlation, which is very sensitive to data noise. Graph structure is easy to change when unfavorable noise comes in.

Sparsity. Traditional method means around 10% of possible connections between nodes to construct a sparse network. Because of utility of average measure, it misses the specificity of individuals. Modified sparse representation (MSR) can automatically construct a sparse matrix by solving l1 norm problem[7, 8].

Best preserved data structure. The structure of fMRI data may vary greatly at different regions of brain. Traditional connectivity matrix, however, uses a fixed value to determine the threshold of whole data. Unfortunately, not all regions make the same contribution to every cognitive task.

In this paper, we propose an optimized method to evaluate the functional connectivity. We firstly constructed a "connectivity matrix" of the data set based on MSR framework which computes a directed graph with weighted edge. Secondly, several centrality parameters - in particular "degree centrality", "betweenness centrality", "closeness centrality" and "eigenvector centrality" are computed to best preserve brain map[9].

The outline of this paper is as follows. Section 2 defines sparse connectivity matrix in detail and shows the definition of four centrality measures. We introduce the method from a brief introduction of sparse representation and then show its advantages. In section 3, we apply this measure on Star/Plus database which is a cognitive task fMRI database. For complementary, a comparison is made between correlation method and sparse connectivity matrix. At last, we give a conclusion and discussion in section 4.

2 Methods

2.1 Motivation

The sparse connectivity matrix is motivated by the limitations of classical graph construction methods[10]. Because fMRI data contains far more noise than useful signal, most of voxels may have tiny correlations with others. In that case, some voxels should be ignored. Note that a graph construction process includes both graph edge weight setting and threshold of neighborhood selection, which significantly influence the performance of connectivity matrix. Some researchers have shown that most of the existing correlations between voxels can be constructed from the linear representation view [11] and unified under a graph framework. Sparse represent is an important way to design the connectivity matrix which reflects the linear correlation between voxels. Here we present a modified method to design weight matrix straightforwardly based on sparse representation theory [12], through which the sparsity can be optimally and naturally derived.

2.2 Sparse Adjacency Matrix

MSR framework constructs a weight matrix which can explicitly characterize connectivity. Given a set of samples $\{y_i\}_{i=1}^{n}$, where $y_i \in R^m$, denotes each voxel's

time sequence, let $A=[y_1, y_2,..., y_n]\in R^{m\times n}$ be the data matrix, each column of which is a time course. We first seek a sparse reconstructive weight vector w_i for each y_i through the following modified ℓ_1 minimization problem:

$$\min ||A\omega_i - y_i||^2 + \lambda \sum_{i=1}^{n} \omega_i \quad \text{s.t.} \quad \omega_i \geq 0, i = 1, \ldots, n \tag{1}$$

where $\omega_i = [\omega_{i1},...,\omega_{i,i-1},0,\omega_{i,i+1},...,\omega_{in}]^T$ is an n-dimensional nonnegative vector in which the i-th element is equal to zero because y_i has removed from A, and the elements $\omega_{ij}, j\neq i$ denote the contribution of each y_j to reconstruct y_i.

After computing the weight vector $\tilde{\omega}_{ij}$ for each $y_i, i=1,2,...,n$, we can define the sparse connectivity matrix $W=(\tilde{\omega}_{ij})_{n\times n}$ as follows:

$$\mathrm{W} = [\widetilde{\omega_1}, \widetilde{\omega_2}, \ldots, \widetilde{\omega_n}]^T \tag{2}$$

where $\tilde{\omega}_i$ denotes the optimal solution of equation. The element $\tilde{\omega}_{ij}$ in W is not only coefficient measure between samples y_i and y_j, but also a consideration of whole y. In this sense W is essentially different from the adjacency weigh matrix in connectivity.

2.3 Four Centrality Parameters

Within the scope of graph theory and network analysis, there are various measures of the centrality that determine the relative importance of a node. Here we introduce four measures of centrality that are widely used in network analysis.

Degree Centrality. For a weighted graph, degree centrality (DC) is defined as the sum of weights from edges connecting to a node which can be computed as in equation:

$$\mathrm{DC(i)} = \sum_{j=1}^{N} a_{ij} \tag{3}$$

Eigenvector Centrality. Eigenvector centrality (EC)[13], is simply the first eigenvector of the adjacency matrix, which corresponds to the largest eigenvalue λ_1:

$$\mathrm{Ax} = \lambda \mathrm{x} \quad \text{or equivalently } \mathrm{x} = \frac{1}{\lambda} Ax, x_i = \mu \sum_{j=1}^{n} a_{ij} x_j \tag{4}$$

with proportionality factor $\mu = 1/\lambda$ so that x_i is proportional to the sum of similarity scores of all nodes connected to it.

Betweenness Centrality. Node betweenness centrality (BC) measures how many of the shortest paths between all other node pairs in the network pass through the node,

which can assess the communication role of a node within the functional network and is defined as follows[14]:

$$x_i = \sum_{i \neq j, i \neq k, j \neq k} \frac{\sigma_{jk}(i)}{\sigma_{jk}} \tag{5}$$

where σ_{jk} is the number of shortest geodesic paths from j to k, and $\sigma_{jk}(i)$ is the number of shortest geodesic paths from j to k that pass through node i.

Closeness Centrality. Closeness centrality (CC) emphasizes the distance of a node to all others in the network by focusing on the average of the shortest distance of a node to others. The closeness centrality x_i of some node i is defined as:

$$c_i = \sum_j d_{ij} \tag{6}$$

where d_{ij} is the number of links in the shortest path from node i to node j.

3 Experiment Data

We obtained data Star/Plus fMRI from Carnegie Mello database, which has already been preprocessed and selected some Regions of Interest (ROI). The experiment data was schemed to generate three distinctive states of the brain, which could respectively be called "being rest", "during affirmative sentences" and "during negative sentences". Each subject have 54 trials, 4 nonsense trials, 20 affirmative trials, 20 negative trials and 10 rest-state trials. Each trial contains 55 time points. We explored two questions in this paper. First, whether there is any difference when subject make an affirmative or a negative judgment[15]. The experiment also find whether these strategies have dissimilar brain patterns.

4 Results

In order to reduce the calculation, a t-test should be set to find most active voxels among affirmative data, negative data and rest-state data first. Then we depict the sparse connectivity matrix for two cognitive states via MSR.

To fully understand the change in neuro-circuitry, we compared negative sentences and affirmative sentences via centrality characteristics. As shown in Fig. 1, voxels in Right-pars triangularis (RTRIA) exhibited high centrality and high similarity across centrality measures during negative state. Retrosplenial cortex (RSPL) shows high similarity in affirmative state. Besides, RSPL, Left temporal (LT) demonstrate high centrality in both states when computing EC. In BC, negative states have more voxels with high value than affirmative, i.e., it needs more hubs to connect active regions. However, affirmative state has high EC than negative state. For completion, we do the same processing with the traditional connectivity matrix and compare two algorithms.

Fig. 2 compares the Eigenvector centrality and Betweenness centrality using both two algorithms. We set the threshold of the correlation connectivity as top 15 percent [16]. Using MSR to reconstruct the connectivity matrix can select the voxels which make most contribution and play the most important role in information transfer. We carry on a t test between affirmative and negative states in both two algorithms. CC shows significant differences in both MSR and correlation algorithms. However, only by calculating via MSR, DC, BC and EC shows significant differences. In addition, even though both algorithms perform difference on affirmative and negative states, the significant level of MSR is higher than correlation method. In order to avoid type I errors, false positive rate has been made to the result calculated by MSR. In this dataset, the value of false positive rate is less than 5 % ($\alpha = 0.01$).

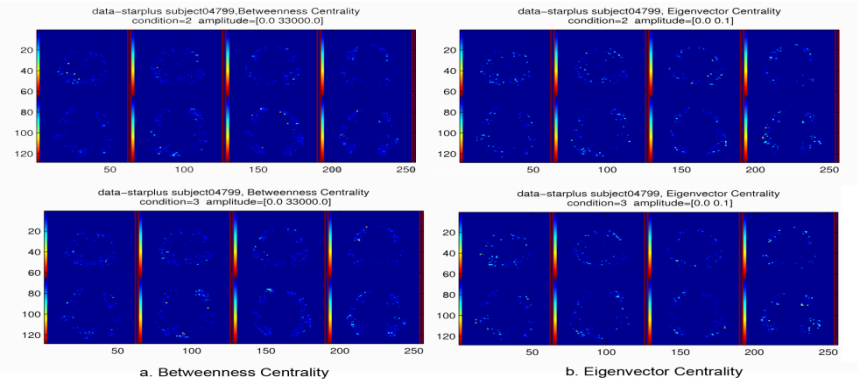

Fig. 1. Betweenness centrality and eigenvector centrality in affirmative and negative states

MacLeod, Hunt, and Mathews (1978) have shown that some subjects use spatial or pictorial image representations to compare the meaning of sentences and pictures. Most subjects show the pattern of Time of Affirmative (TA) < Time of Negative (TN) while a few subjects looks like TA=TN instead. In other words, which kind the sentence is will not is a factor affecting their verification times.

Table 1. T-test of affirmative and negative states. (* H=0 indicates that the null hypothesis ("means are equal") cannot be rejected at the 5% significance level. H=1 indicates that the null hypothesis can be rejected at the 5% level. * P value is the probability of observing the given result. Small values of P cast doubt on the validity of the null hypothesis.)

	MSR		**correlation**	
	H	P	H	P
DC	1	1.20e-17	0	1
EC	1	7.71e-68	0	0.9269
CC	1	7.55e-60	1	1.19e-05
BC	1	4.33e-07	0	0.9167

By comparing different subject's EC in different trials, we find that there exist two patterns obviously. In one situation, affirmative sentences and negative sentences have different direction eigenvectors. Even though, the amplitude in some voxels of both side stay large. Besides that, there indeed has difference in other voxels, i.e. not all voxels in affirmative sentences act the same in negative condition. Second figure have much less differences than above one (Fig. 3). Only a few voxels show difference on the amplitude.

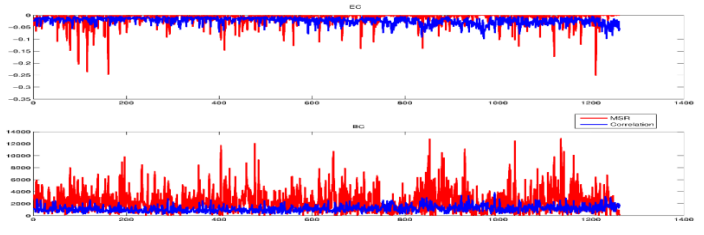

Fig. 2. Result of two algorithms

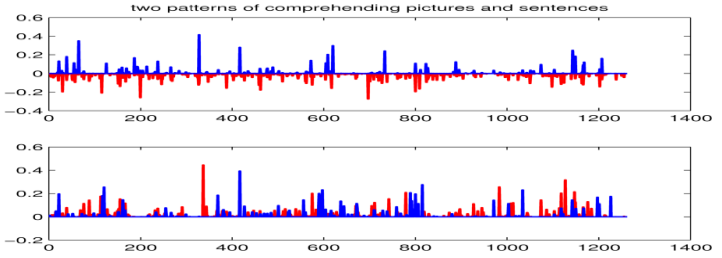

Fig. 3. Two patterns of comprehending pictures and sentences

5 Conclusion

According to this paper, we find a new solution which can automatically calculate correlation matrix, called MSR. Then we use some centrality parameters to evaluate characteristics of the connectivity graph and compare centrality and similarity among three states and four centrality parameters. In sum, we developed a quicker, more effective method and verify the suspicions of MacLeod, Hunt, and Mathews (1978).

6 Discussion

Since fMRI data is generally high-dimension data but with lots of noise, MSR can filter some noise and leave the effective signal via a linear representation, i.e., it keeps the sparse characters of matrix and saves the storage space. Also, MSR extremely accelerate the computing velocity and decrease the complex of computation.

In traditional method, we need to set a threshold in order to avoid the interference of small correlation values. Recently however, [17]point out that a threshold makes it sensitive to the construction of connectivity matrix. On contrast to this, our algorithm is optimized, since it does not involve any hyper-parameters. In addition, coefficient connectivity focuses on pairwise comparison while l1 norm can be regarded as the correlation among whole data. In this way, sparse connectivity is a generalized expression of correlation method.

However, the solution of MSR is an iteration process that different voxel sequence may need different iteration times. So the time complexity need to be further improved.

Acknowledgements. This work was supported in part by the National Natural Science Foundation of China under Grant 61375118 and Grant 61075009, the Natural Science Foundation of Jiangsu Province under Grant BK2011595, and the Program for New Century Excellent Talents in University of China under Grant NCET-12-0115.

References

1. Shirer, W.R., Ryail, S., Rykhlevskaia, E.: Decoding Subject-driven Cognitive States with Whole-brain Connectivity Patterns. Cerebral Cortex 22, 158–165 (2012)
2. Horwitz, B., Horovitz, S.G.: Introduction to Research Topic–Brain Connectivity Analysis: Investigating Brain Disorders. Part 1: The Review Articles. Frontiers in Systems Neuroscience 6, 1–2 (2012)
3. Ryali, S., Chen, T.W., Kaustubh, S.: Estimation of Functional Connectivity in fMRI Data Using Stability Selection-based Sparse Partial Correlation with Elastic Net Penalty. Neuroimage 59, 3852–3861 (2011)
4. Norman, K.A., Polyn, S.M., Detre, G.J.: Beyond Mind-reading: Multi-voxel Pattern Analysis of fMRI Data. Trends in Cognitive Sciences 10, 424–430 (2006)
5. Zhang, J., Cheng, W., Wang, Z.G.: Pattern Classification of Large-scale Functional Brain Networks: Identification of Informative Neuroimaging Markers for Epilepsy. PLoS One 7, e36733 (2012)
6. Bullmore, E., Sporns, O.: Complex Brain Networks: Graph Theoretical Analysis of Structural and Functional Systems. Nature Reviews Neuroscience 10, 186–198 (2009)
7. Qiao, L., Chen, S., Tan, X.: Sparsity Preserving Projections with Applications to Face Recognition. Pattern Recognition 43, 331–341 (2010)
8. Donoho, D.L., Tsaig, Y.: Fast Solution of l1-norm Minimization Problems When the Solution May Be Sparse. Department of Statistics, Stanford University (2006)
9. Lohmann, G., Margulies, D.S., Horstmann, A.: Eigenvector Centrality Mapping for Analyzing Connectivity Patterns in fMRI Data of the Human Brain. PLoS One 5, e10232 (2010)
10. Druckmann, S., Chklovskii, D.B.: Over-complete Representations on Recurrent Neural Networks Can Support Persistent Percepts. Advances in Neural Information Processing Systems 23, 541–549 (2010)
11. Richiardi, J., Van De Ville, D., Eryilmaz, H.: Low-dimensional Embedding of Functional Connectivity Graphs for Brain State Decoding. In: 2010 First Workshop on. 2010 Brain Decoding: Pattern Recognition Challenges in Neuroimaging (WBD). IEEE (2010)

12. Donoho, D.L.: Compressed Sensing. IEEE Transactions on Information Theory 52, 1289–1306 (2006)
13. Bonacich, P., Lloyd, P.: Calculating Status with Negative Relations. Social Networks 26, 331–338 (2004)
14. Buckner, R.L., Sepulcre, J., Talukdar, T.: Cortical Hubs Revealed by Intrinsic Functional Connectivity: Mapping, Assessment of Stability, and Relation to Alzheimer's Disease. The Journal of Neuroscience 29, 1860–1873 (2009)
15. MacLeod, C.M., Hunt, E.B., Mathews, N.N.: Individual Differences in the Verification of Sentence-Picture Relationships. Journal of Verbal Learning and Verbal Behavior 17, 493–507 (1978)
16. Napoletani, D., Sauer, T.D.: Reconstructing the Topology of Sparsely Connected Dynamical Networks. Physical Review-Section E-Statistical Nonlinear and Soft Matter Physics 77, 26103 (2008)
17. Salvador, R., Suckling, J., Schwarzbauer, C.: Undirected Graphs of Frequency-dependent Functional Connectivity in Whole Brain Networks. Philosophical Transactions of the Royal Society B: Biological Sciences 360, 937–946 (2005)

Computational Intelligence Methods Based Design of Closed-Loop System

Juri Belikov[1], Eduard Petlenkov[2], Kristina Vassiljeva[2], and Sven Nõmm[1]

[1] Institute of Cybernetics, Tallinn University of Technology,
Akadeemia tee 21, 12618, Tallinn, Estonia
{jbelikov,sven}@cc.ioc.ee
[2] Department of Computer Control, Tallinn University of Technology,
Ehitajate tee 5, 19986, Tallinn, Estonia
{eduard.petlenkov,kristina.vassiljeva}@ttu.ee

Abstract. The paper describes a unified algorithm for both parametric and structural identification. The approach combines three typical techniques such as neural networks, statistics and genetic algorithm. A specific structure of the neural network is used that allows to design a controller directly from parameters of the identified model. The control strategy based on reference model is discussed. Finally, the proposed solution is illustrated by numerical example.

Keywords: Computational intelligence, nonlinear systems.

1 Introduction

Mathematical model usually becomes the basis for describing behavior of the real-life processes. It can be derived in several ways either by understanding the nature of the process and using physical laws to describe it, or by identification procedure based on constructing approximate equations from the measured data. The second approach is inherently more simple. Identification can be used as a starting point for the further analysis of the system and design of a control algorithm. Based on the requirements, restrictions and nature of the model, it can be represented via nonlinear differential or difference equations.

In most practical applications, when employing identification techniques one relies on *a priori* structural assumptions made for the process model. This assumption implies that the structure of the overall system is known before the identification procedure. Thus, it remains to find suitable parameters of the model. A lot of efficient techniques for parameter estimation are available once the model structure has been chosen. However, this choice is not trivial [9]. Usually, there is no any knowledge about what system dynamics can be significant and how accurate identified model has to be. Therefore, structural identification represents a more challenging problem, especially when one deals with complex system involving large number of parameters.

Structural identification methods can be formally divided into two groups, i.e. classical and non-classical methods. Classical methods have rigorous mathematical principles, see [4], [14]. The typical examples include the least square

M. Lee et al. (Eds.): ICONIP 2013, Part I, LNCS 8226, pp. 215–224, 2013.
© Springer-Verlag Berlin Heidelberg 2013

estimation [2], [6] and H_∞ filtering [5]. On the contrary, non-classical methods rely on heuristic mathematical methods. The most popular are artificial neural networks and genetic algorithms. Compared to classical methods, one of the main strengths of non-classical methods in structural identification is generally better robustness in achieving global optimum, see [14]. The structural identification is associated with many problems, especially if the model is derived not only for analysis, but also for control purposes. The typical problems are natural requirements such as simplicity of the identified model, including order and functions to be used, relevant dependencies between different variables, accuracy of the obtained model, etc [9]. Based on the mentioned requirements the main task is to maintain a balance between simplicity and accuracy.

Usually, non-classical methods are used separately. However, the authors of this paper do believe that using benefits of various techniques from different areas can lead to synergy and as a result to development of a new and more reliable algorithm. Therefore, in this paper we mainly employ the mathematical tools based on neural networks, genetic algorithm and statistics to develop a novel approach to both parametric and structural identification of the system with a primary focus on control application. This paper has to be understood as an intermediate step towards creating the complete procedure which allows to design the appropriate compensator, including various requirements to be met by the control system, for the plant starting from the available input-output (i/o) data. Note that the proposed solution is implemented in MATLAB environment. The choice of the software is motivated by the fact that it allows to create a complete solution involving all the necessary steps such as collecting i/o data from the process, identification, simulation, designing controller and creating interface for communication with plants via special toolboxes like Real-Time Windows Target.

The preliminary results of this paper were partly presented in [16]. Unlike [16], this paper presents a more detailed analysis and differs in several ways. First, in order to obtain practical results, we performed a significant code refactoring and implemented additional parts of code that made the computational process faster and more robust. Application of genetic algorithm has allowed to reduce number of connections in corresponding neural network which resulted in lower number of weights to be identified and in turn reduced computational complexity of the entire process. Second, the reference model is incorporated into the control loop. It expands the class of problems that can be solved via the proposed approach. Reference control can be used in various situations. For example, one can predefine the desired dynamics of behavior for the transient process via selecting the appropriate zeros and poles for the closed-loop system. Third, the designed controller is based on the i/o feedback linearization technique, whereas previously the state feedback linearization approach was utilized. Finally, the mathematical model of the process is excluded from the analysis and the i/o data is assumed to be available from measurements.

2 Preliminaries

Hereinafter, we use the notation ξ for a variable $\xi(t)$, $\xi^{[k]}$ for the kth-step forward time shift $\xi(t+k)$ and $\xi^{[-l]}$ for the lth-step backward time shift $\xi(t-l)$ with $k, l \in \mathbb{Z}^+$. Moreover, to simplify the exposition of the material, in this paper we restrict our attention to the case of single-input single-output systems (SISO).

The nonlinear control systems are typically represented either by the higher order input-output difference equation

$$y^{[n]} = \varphi(y, y^{[1]}, \ldots, y^{[n-1]}, u, u^{[1]}, \ldots, u^{[s]}), \tag{1}$$

or by the state equations

$$\begin{aligned} x^{[1]} &= f(x, u) \\ y &= h(x) \end{aligned} \tag{2}$$

where $x(t) : \mathbb{Z} \to \mathcal{X} \subset \mathbb{R}^n$ is the state variable, $u(t) : \mathbb{Z} \to \mathcal{U} \subset \mathbb{R}$ is the input, $y(t) : \mathbb{Z} \to \mathcal{Y} \subset \mathbb{R}$ is the output, $\varphi : \mathcal{Y}^n \times \mathcal{U}^{s+1} \to \mathbb{R}$, $f : \mathcal{X} \times \mathcal{U} \to \mathcal{X}$ and $h : \mathcal{X} \to \mathcal{Y}$ are the real analytic functions. Moreover, we assume that $s < n$ are non-negative integers.

The system represented by equation (1) is called a discrete-time Nonlinear AutoRegressive eXogenous (NARX) model. On the one hand, such structure is capable to identify a wide class of complex processes with a high degree of accuracy, see [8]. On the other hand, from the control point of view, it has several drawbacks. The most important for our studies is linearizability by output feedback. Namely, this property is not always possible to guarantee [13]. Thus, to overcome available obstacles, the so-called Additive NARX (ANARX) structure was proposed, which is a modification of the NARX model with separated time instances [7]

$$y^{[n]} = \sum_{i=1}^{n} f_i(y^{[n-i]}, u^{[n-i]}). \tag{3}$$

Note that (3) can always be linearized by the dynamic output feedback, see [13]. The main idea of feedback linearization technique consists in modifying the system structure by appropriate feedback, so that the i/o equation of the closed-loop system becomes linear. After that it is possible to apply all the standard control methods for linear systems to meet the required goals.

3 Modeling and Validation

In this section we explain the basic steps and mathematical tools, used in the developed algorithm, to identify the model from the i/o data, verify it and design the controller. Roughly speaking, procedure consists of three main parts: (a) modeling using neural networks (NN); (b) validation procedure based on cross correlation test; (c) modification of the obtained NN-based model.

Step A: Neural Networks

In order to perform analysis and design of the appropriate controller for the process, one is usually interested in mathematical equations. Note that to maintain a sufficient level of accuracy it is necessary to use nonlinear equations. In fact, one can derive the model from the first principles, e.g. modeling a physical process relying on the Newton equations. However, most likely in many cases such approach will result in a quite complex model. Therefore, it is more common to start from the measured i/o data of a system and try to determine a mathematical relation between variables without going into the details of what is actually happening inside the process. The most popular candidates are so-called NARX type structures. The model from this class can be easily identified using approach based on neural networks. Note that (3) is a subclass of (1), and can be identified by NNs as

$$y^{[n]} = \sum_{i=1}^{n} C_i \cdot \phi_i(W_i \cdot [y^{[n-i]}, u^{[n-i]}]^{\mathrm{T}}), \tag{4}$$

where for each ith sublayer there are separate set of activation function and corresponding matrices of synaptic weights.

Remark 1. In this paper, we use NARX structure to identify the model, because in most cases it can more accurately describe the unknown process. However, due to the limitations listed above we use ANARX model for control purposes to identify the model and derive the corresponding controller.

Remark 2. Moreover, we assume that both NN-NARX and ANARX models perfectly describe the process meaning that $\hat{y} = y$ (where $\hat{y}$ is the output of the neural network), in order to avoid additional notation.

Example 1. Consider the discrete-time model of the controlled van der Pol oscillator, derived in [1]

$$y^{[2]} = \theta_1 y^{[1]} - \theta_2 y + \theta_3 y^2 y^{[1]} + \theta_4 y^3 + \theta_5 u, \tag{5}$$

where $\theta_i \in \mathbb{R}$ for $i = 1, \ldots, 5$. In order to identify this system by ANARX model, a neural network of the following structure should be chosen

$$y = C_1 \cdot \phi_1(W_1[y^{[-1]}, u^{[-1]}]^{\mathrm{T}}) + C_2 \cdot \phi_2(W_2 \cdot [y^{[-2]}, u^{[-2]}]^{\mathrm{T}}), \tag{6}$$

and parameters of matrices C_1, W_1, C_2, W_2 have to be estimated.

Step B: Correlation-test-based Validation Procedure

Next, we briefly summarize the basic facts about model validation procedure and refer the interested reader to [10] and the references therein. Model validation constitute an important step in answering the question whether the derived model is adequate enough to represent the underlying process or not. While

there is large variety of model validation techniques, in many practical cases model quality is described by mean square error (MSE) or some similar criteria, whereas question of model validity is ignored. Lower levels of MSE do not necessary imply model validity. Failure to pass validity test may lead to inadequate performance of the model which in turn would affect the quality of any controller built on the basis of such model. Unlike the case of linear systems, validation of nonlinear models is more complicated [3]. In [19] development of the so-called Omni-Directional Cross-Correlation Functions (ODCCF) based procedure for nonlinear model validation was proposed. Later in [18] it was adopted for neural networks based nonlinear models. While validation test gives an answer if model is valid or not it does not provide any quantitative measure of validity. In [10] ODCCF based procedure was adopted to compare quality of identified neural networks based models, quantitative parameter q summarizing the values of ODCCFs was derived. This parameter may be seen as an average of all the values of cross correlations functions. Therefore, lower values of the parameter indicate better model model quality with respect to validity. The advantage of the recalled approach can be seen in application to the analysis of the quality of both NN-NARX and NN-ANARX type models, see [10].

Step C: Genetic Algorithm

Compared to NN-NARX the structure of (4) is simpler, due to the reduced number of interconnections. However, even this model can be further modified without loss of related advantages. The latter means that it is possible to modify the structure of resulting neural network to make it more similar to that one of the original model. Such a flexibility allows in some sense to make a step towards the structural and parametric identification. Thus, to deal with parametric identification we decided to employ the tools of neural networks described in Step A. However, to perform structural identification we use approach based on the canonical genetic algorithm (GA), see [17].

Any genetic algorithm consists of two typical components: (i) encode the neural network model and (ii) construct evaluation function. Further, we briefly describe the basic moments of each component and the overall algorithm.

Encoding can be understood as a conversion of the mathematical description of a neural network into terms of genetic algorithm. First, we need to determine the length of the gene as $l = 2N$, where N is the possible[1] maximal order of identified system. Note that we deal with destructive algorithm. It is initialized with the neural network of the form (4) and starts to eliminate unnecessary sublayers, nodes and connections. Next, in order to describe the structure, we use binary notation $g := \{g_j\}_{j=1}^{l}$ with $g_j \in \{0, 1\}$, where the presence and absence of connections between input is indicated by 1 and 0, respectively. The

[1] In this paper we assume the grey box model case meaning that at least some knowledge of the identified process is available, and it is possible to estimate a good (that is slightly higher than the real order) upper bound. This can be done, for example, by preliminary regression analysis.

basic idea of filling the gene can be illustrated as follows: for each pair of the output and input $y^{[n-i]}$ and $u^{[n-i]}$ the corresponding connection with sublayer has to be checked. In case of affirmative answer 1 is placed into the sequence, otherwise 0 is appended. This procedure stops after n steps.

Example 2. Consider the model from Example 1. Since the term $u^{[1]}$ is not presented in equation (5), we can drop it from the NN-based version (6) to make the structure more similar to the one of the original model as $y = C_1 \cdot \phi_1(W_1 y^{[-1]}) + C_2 \cdot \phi_2(W_2 \cdot [y^{[-2]}, u^{[-2]}]^{\mathrm{T}})$. Thus, it can be encoded via 4-element gene as $g = \{1, 0, 1, 1\}$.

The next problem is to choose certain criteria to evaluate the validity of the identified model. The choice is not unique. One of the possibilities is to use the statistical approach described in Step B. However, alone it does not cover the complete picture of what requirements can be made to the model. Nevertheless, the quality indicators, proposed in [16], are reasonable candidates. In that case a problem of multi-objective function optimization should be solved. We rely on the following three criteria:

1. $e = \mathrm{e}^{-k \cdot MSE} - 1$ is the error of the closed-loop control, where k is a proportional coefficient;
2. $\hat{o}$ is the normalized order of the identified model;
3. q is the statistics based quality parameter described on Step B.

Summarizing the above information, evaluation function can be defined by using weighted sum method as

$$f := k_1 e + k_2 \hat{o} + k_3 q, \tag{7}$$

where k_1, k_2, k_3 are weighted coefficients showing the effect of each criterion on the final quality of the model. Note that the restriction $k_1 + k_2 + k_3 = 1$ has to be imposed, because $e, \hat{o}, q$ are normalized in the range $[0, \ldots, 1]$.

Next, the population consisting of N_m different candidate models is constructed. After that, for each individual of the population the fitness function is calculated on the basis of evaluation function. In case of proportionate-based selection individuals are picked out to create offspring based on the ranking of the individual within a given population, i.e. according to $f_i/\bar{f}$, where f_i, for $i = 1, \ldots, N_m$, is the evaluation associated with particular gene and $\bar{f}$ is the average evaluation of all genes in the population. Thus, the fitness function is always defined with respect to other individuals of the current population. Roulette selection technique and single point crossover are used to perform the reproduction process. In order to avoid premature convergence of the algorithm, mutation is applied. Elitism (selection of the first best parents) is used to improve the performance of GA, see [15], [17].

4 Control Strategy

The procedure, described in Section 3, allows to obtain an accurate model of the process. Since the specific structure of the controller is used, control technique

based on the reference model can be easily applied. The latter can be useful in various applications like trajectory tracking and path planning to avoid significant overshootings or high control signals. Next, we briefly recall the approach from [12]. The closed-loop system can be represented as follows

$$y^{[n]} + a_1 y^{[n-1]} + \cdots + a_n y = b_1 v^{[n-1]} + \cdots + b_n v, \tag{8}$$

where $a_i, b_i \in \mathbb{R}$ for $i = 1, \ldots, n$ are parameters of the reference model defining the dynamics of the closed-loop control system. Thus, the desired zeros and poles can be predefined at the stage of designing the control system. Moreover, the parameters can be chosen thereby to guarantee the input-output stability of the closed-loop system. Equation (8) can be incorporated into the control loop as follows

$$\begin{aligned}
\eta_1 &= a_1 y - b_1 v + C_1 \cdot \phi_1(W_1 \cdot [y, u]^{\mathrm{T}}) \\
\eta_1^{[1]} &= \eta_2 + b_2 v - a_2 y - C_2 \cdot \phi_2(W_2 \cdot [y, u]^{\mathrm{T}}) \\
&\vdots \\
\eta_{n-2}^{[1]} &= \eta_{n-1} + b_{n-1} v - a_{n-1} y - C_{n-1} \cdot \phi_{n-1}(W_{n-1} \cdot [y, u]^{\mathrm{T}}) \\
\eta_{n-1}^{[1]} &= b_n v - a_n y - C_n \cdot \phi_n(W_n \cdot [y, u]^{\mathrm{T}})
\end{aligned} \tag{9}$$

Here $v(t) : \mathbb{Z} \to \mathcal{V} \subset \mathbb{R}$ is a reference signal. Next, in order to simplify the calculation of the control signal, we assume $\phi_1(\cdot)$ to be linear activation function [11] $u = T_2^{-1}(\eta_1 - (a_1 + T_1)y + b_1 v)$, where $T = C_1 \cdot W_1$ and $T = \begin{bmatrix} T_1 & T_2 \end{bmatrix}$ and T_2 is a nonsingular square matrix. The overall structure of the corresponding control system is represented in Fig. 1.

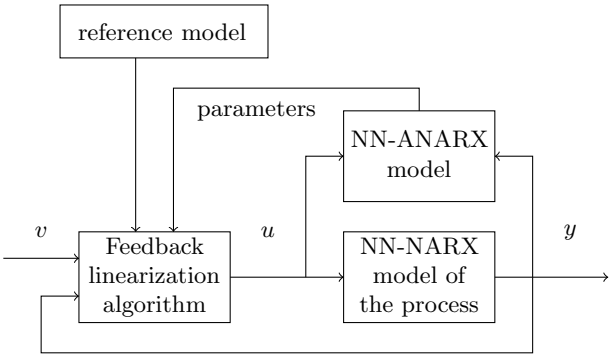

Fig. 1. Control system design procedure

Once the algorithm from Section 3 was terminated and the corresponding controller (9) was designed, NN-NARX model has to be replaced by the process.

5 Illustrative Example

The model of a liquid level system of interconnected tanks [3] is represented by the input-output equation

$$\begin{aligned} y^{[3]} &= 0.43y^{[2]} + 0.681y^{[1]} - 0.149y + 0.396u^{[2]} + 0.014u^{[1]} - 0.071u \\ &\quad - 0.351y^{[2]}u^{[2]} - 0.03(y^{[1]})^2 - 0.135y^{[1]}u^{[1]} - 0.027(y^{[1]})^3 \\ &\quad - 0.108(y^{[1]})^2u^{[1]} - 0.099(u^{[1]})^3. \end{aligned} \tag{10}$$

Though model (10) belongs to ANARX model class (3), it can still be treated as unknown plant. In fact, this can be seen as advantage, since it allows to see whether the algorithm is capable to find a model with correct structure or not. To obtain the i/o data, system (10) was simulated. Initial population of 50 randomly created models was generated. Levenberg-Marquardt (LM) algorithm was used to perform the training for neural networks in the population. The maximum order for some of models was found to be 6. Next, the algorithm described in Section 3 was performed. Orders of the models in the last generation were either 3 or 4 and mean square errors were within acceptable limits. The fact that the final models were of the third and fourth order indicates that that the proposed technique converges to the original system order. After that the control algorithm from Section 4 was used to test capabilities of the obtained model. The following linear discrete-time reference models of the third-order was chosen $G(z) = k\frac{z^2}{z^3+0.15z^2-0.59z-0.221}$ with poles $p_1 = 0.85$, $p_2 = -0.5 + 0.1j$, $p_3 = -0.5 - 0.1j$, zeros $n_1 = 0$, $n_2 = 0$, and $k = 0.0678$ being the scalar gain, calculated to obtain the steady-state. This model was chisen to guarantee smooth transient process. According to (9), equations of controller can be derived as

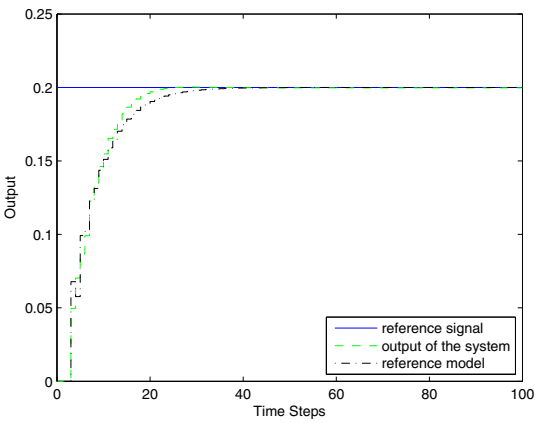

Fig. 2. Closed-loop simulation

$$u = T_2^{-1}(\eta_1 - (a_1 + T_1)y + b_1 v)$$
$$\eta_1^{[1]} = \eta_2 + b_2 v - a_2 y - C_2 \cdot \phi_2(W_2 \cdot [y, u]^{\mathrm{T}})$$
$$\eta_2^{[1]} = b_3 v - a_3 y - C_3 \cdot \phi_3(W_3 \cdot [y, u]^{\mathrm{T}})$$

where $T = C_1 \cdot W_1$, $T = \begin{bmatrix} T_1 \, T_2 \end{bmatrix}$ and ϕ_2, ϕ_3 being hyperbolic tangent sigmoid transfer function. The closed-loop system was simulated with the step function v, and the quality of tracking algorithm is depicted in Fig. 2.

The small deviation between the reference model and output of the system can be explained by the fact that the model used to design the controller is only approximation of the original process and contains a certain error. To conclude, one can see that the proposed technique provides acceptable tracking results.

6 Discussion and Conclusions

The paper describes a unified algorithm for both parametric and structural identification. The approach combines three common techniques: (*i*) neural network with specific structure is used to perform the parametric identification; (*ii*) correlation-test-based procedure is used to validate the obtained model in addition to the common measuring tools; (*iii*) genetic algorithm is used to provide the structural identification within a predefined class of models. Such approach allows to combine the mentioned methods to design the closed-loop control system from the unified point of view. Moreover, the control strategy relies on the reference model that can be important in a number of various applications.

Several intermediate subproblems are solved that assist to create the full-fledged application. The further steps will include automatic code and driver generation to design control for an arbitrary (stable) process, starting from the measured i/o data. There are a number of additional subtasks to be solved like implementation of alternative optimization techniques that can possibly result in a more robust models and reduce the computational time. Another problem which still far from complete solution is a calculation of the control signal in case of MIMO systems. Finally, the approximated model of the process results in the presence of the steady state error. The latter has to be incorporated to the control algorithm to increase its performance. The mentioned items will make the primary subjects for the future research.

Acknowledgments. The work was supported by the European Union through the European Regional Development Fund, the target funding projects SF0140113As08 and SF0140018s08 of Estonian Ministry of Education and Research. S. Nõmm was additionally supported by the ESF grant N8365. J. Belikov and E. Petlenkov were additionally supported by the ESF grant N8738.

References

1. Anderson, S.R., Kadirkamanathan, V.: Modelling and identification of nonlinear deterministic systems in delta-domain. Automatica 43, 1859–1868 (2007)
2. Berana, J., Ghoshb, S., Schella, D.: On least squares estimation for long-memory lattice processes. Journal of Multivariate Analysis 100(10), 2178–2194 (2009)
3. Billings, S.A., Fadzil, M.B.: The practical identification of systems with nonlinearities. In: The 7th IFAC/IFORS Symposium on Identification and System Parameter Estimation, York, UK, pp. 155–160 (July 1985)
4. Caravani, P., Watson, M.L.: Recursive least-square time domain identification of structural parameters. Journal of Applied Mechanics 44(1), 135–140 (1977)
5. Gao, H., Meng, X., Chen, T.: A parameter-dependent approach to robust H_∞ filtering for time-delay systems. IEEE Transactions on automatic control 53(10), 2420–2425 (2008)
6. Hu, X.J., Lagakos, S.W., Lockhart, R.A.: Generalized least squares estimation of the mean function of a counting process based on panel counts. Statistica Sinica 19, 561–580 (2009)
7. Kotta, Ü., Zinober, A.S.I., Liu, P.: Transfer equivalence and realization of nonlinear higher order input-output difference equations. Automatica 37(11), 1771–1778 (2001)
8. Leontaritis, I.J., Billings, S.A.: Input-output parametric models for non-linear systems Part I: deterministic non-linear systems. International Journal of Control 41(2), 303–328 (1985)
9. Leva, A., Piroddi, L.: A neural network-based technique for structural identification of SISO systems 1, 135–138 (1994)
10. Nõmm, S., Kotta, Ü.: Comparison of neural networks-based ANARX and NARX models by application of correlation tests. In: International Joint Conference on Neural Networks, San Jose, CA, USA, pp. 2113–2118 (July-August 2011)
11. Petlenkov, E.: NN-ANARX structure based dynamic output feedback linearization for control of nonlinear MIMO systems. In: The 15th Mediterranean Conference on Control and Automation, Athena, Greece, pp. 1–6 (June 2007)
12. Petlenkov, E.: Model reference control of nonlinear systems by dynamic output feedback linearization of neural network based ANARX models. In: The 10th International Conference on Control Automation Robotics and Vision, Hanoi, Vietnam, pp. 1119–1123 (December 2008)
13. Pothin, R., Kotta, Ü., Moog, C.H.: Output feedback linearization of nonlinear discrete time systems. In: The IFAC Conference on Control Systems Design, Bratislava, Slovak Republic, pp. 181–186 (2000)
14. Shinozuka, M., Yun, C.B., Imai, H.: Identification of linear structural dynamic systems. Journal of the Engineering Mechanics Division 108(6), 1371–1390 (1982)
15. Sivanandam, S.N., Deepa, S.: Introduction to Genetic Algorithms. Springer, Berlin (2008)
16. Vassiljeva, K., Petlenkov, E., Nomm, S.: Evolutionary design of the closed loop control on the basis of NN-ANARX model using genetic algorithm. In: Huang, T., Zeng, Z., Li, C., Leung, C.S. (eds.) ICONIP 2012, Part I. LNCS, vol. 7663, pp. 592–599. Springer, Heidelberg (2012)
17. Whitley, D.: Genetic algorithms and neural networks. In: Genetic Algorithms in Engineering and Computer Science, pp. 191–201. John Wiley & Sons Ltd. (1995)
18. Zhang, L.F., Zhu, Q.M., Longden, A.: A correlation-test-based validation procedure for identified neural networks. IEEE Transactions on Neural Networks 20(1), 1–13 (2009)
19. Zhu, Q.M., Zhang, L.F., Longden, A.: Development of omni-directional correlation functions for nonlinear model validation. Automatica 43, 1519–1531 (2007)

Integral Policy Iteration for Zero-Sum Games with Completely Unknown Nonlinear Dynamics

Hongliang Li, Derong Liu*, and Ding Wang

The State Key Laboratory of Management and Control for Complex Systems
Institute of Automation, Chinese Academy of Sciences, Beijing 100190, China
{hongliang.li,derong.liu,ding.wang}@ia.ac.cn

Abstract. In this paper, we develop a model-free integral policy iteration algorithm to learn online the Nash equilibrium solution of two-player zero-sum differential games with completely unknown nonlinear continuous-time dynamics. The developed algorithm updates value function, control and disturbance policies simultaneously. To implement this algorithm, three neural networks are used to approximate the game value function, the control policy and the disturbance policy. The least squares method is used to estimate the unknown parameters of the neural networks. The effectiveness of the developed scheme is demonstrated by a simulation example.

Keywords: Adaptive dynamic programming, Policy iteration, Neural networks, Zero-sum games.

1 Introduction

Adaptive dynamic programming [1] method has received significantly increased attention owing to its learning and optimal capacities. A synchronous policy iteration (PI) algorithm [2] was derived to learn online the continuous-time optimal control with known dynamics, and it was extended to the optimal control problem for unknown nonlinear systems [3][4]. An integral reinforcement learning (RL) algorithm [5][6] was derived to obtain direct adaptive optimal control for partially unknown linear and nonlinear systems. In [7], a continuous-time Q-learning method was proposed for completely unknown systems. An integral Q-learning [8][9] was presented for continuous-time systems without the exact knowledge of the system dynamics. A computational adaptive optimal control algorithm [10] was presented for continuous-time linear systems with completely unknown system dynamics.

Game theory [11] provides an ideal environment to study multi-player optimal decision and control problems. The Nash equilibrium solution is usually obtained by means of offline iterative computation, and the exact knowledge of the system dynamics is required. An offline PI algorithm [12] was derived for zero-sum games with constrained input nonlinear continuous-time systems. In

* Corresponding author. Tel.: +86-10-82544761; Fax: +86-10-62650912.

M. Lee et al. (Eds.): ICONIP 2013, Part I, LNCS 8226, pp. 225–232, 2013.
© Springer-Verlag Berlin Heidelberg 2013

[13], four action networks and two critic networks were used to obtain the saddle point solution of nonlinear zero-sum games. An online synchronous PI [14] was presented to solve the continuous-time zero-sum game for nonlinear systems with known dynamics. In [15], an actor-critic-identifier structure was used to develop an approximate online solution for zero-sum games subject to continuous-time nonlinear uncertain dynamics. An online integral RL [16] was proposed for zero-sum differential games without any knowledge on the internal system dynamics. In [17], an online simultaneous policy update algorithm was proposed for zero-sum games with partial unknown systems while updating policies of both control player and disturbance player simultaneously.

However, it is difficult for us to obtain the exact system dynamics for many practical systems. In this paper, an online model-free integral PI algorithm is developed to learn the Nash equilibrium solution of a two-player zero-sum differential game with completely unknown nonlinear systems. The developed algorithm updates value function, control and disturbance policies simultaneously. To implement this algorithm, one critic neural network (NN) and two action NNs are used to approximate the game value function, the control policy and the disturbance policy respectively, and the least squares method is used to estimate the unknown parameters.

2 Problem Formulation

Consider a class of nonlinear continuous-time dynamical systems described by

$$\dot{x} = f(x) + g(x)u + k(x)d \tag{1}$$

where $x \in \mathbb{R}^n$ is the system state with initial state x_0, $u \in \mathbb{R}^m$ is the control input, and $d \in \mathbb{R}^q$ is the external disturbance input. Assume that $f(x) \in \mathbb{R}^n$, $g(x) \in \mathbb{R}^{n\times m}$ and $k(x) \in \mathbb{R}^{n\times q}$ are unknown, and that $x = 0$ is an equilibrium point of the system (1).

Define the infinite horizon performance index

$$\begin{aligned} J(x_0, u, d) &= \int_0^\infty (x^\mathsf{T} Q x + u^\mathsf{T} R u - \gamma^2 d^\mathsf{T} d)\mathrm{d}\tau \\ &\triangleq \int_0^\infty r(x, u, d)\mathrm{d}\tau \end{aligned} \tag{2}$$

with $Q = Q^\mathsf{T} \geq 0$, $R = R^\mathsf{T} > 0$, a prescribed constant $\gamma \geq \gamma^* \geq 0$, where γ^* denotes the smallest γ for which the system (1) is stabilized. For the feedback policy $u(x)$ and the disturbance policy $d(x)$, we define the game value function as

$$V(x_t, u, d) = \int_t^\infty (x^\mathsf{T} Q x + u^\mathsf{T} R u - \gamma^2 d^\mathsf{T} d)\mathrm{d}\tau. \tag{3}$$

Then, we define the two-player zero-sum differential game as

$$\begin{aligned} V^*(x_0) &= \min_u \max_d V(x_0, u, d) \\ &= \min_u \max_d \int_0^\infty (x^\mathsf{T} Q x + u^\mathsf{T} R u - \gamma^2 d^\mathsf{T} d)\mathrm{d}\tau \end{aligned} \tag{4}$$

where the control policy player $u(x)$ seeks to minimize the game value function while the disturbance policy player $d(x)$ desires to maximize it. The goal is to find the saddle point (u^*, d^*) which satisfies the following inequalities

$$J(x_0, u, d^*) \geq J(x_0, u^*, d^*) \geq J(x_0, u^*, d) \tag{5}$$

for any state feedback control policy u and disturbance policy d. The saddle point can be obtained by solving the following continuous-time Hamilton-Jacobi-Isaacs (HJI) equation [11]

$$\begin{aligned} 0 =& x^\mathsf{T} Q x + \nabla V^\mathsf{T}(x) f(x) + \frac{1}{4\gamma^2} \nabla V^\mathsf{T}(x) k(x) k^\mathsf{T}(x) \nabla V(x) \\ & - \frac{1}{4} \nabla V^\mathsf{T}(x) g(x) R^{-1} g^\mathsf{T}(x) \nabla V(x) \end{aligned} \tag{6}$$

where $\nabla V^\mathsf{T}(x) = (\partial V(x)/\partial x)^\mathsf{T}$. $V^*(x)$ is the positive definite solution of (6), and the Nash equilibrium solution of the zero-sum game is

$$u^* = -\frac{1}{2} R^{-1} g^\mathsf{T}(x) \nabla V^*(x) \tag{7}$$

$$d^* = \frac{1}{2\gamma^2} k^\mathsf{T}(x) \nabla V^*(x). \tag{8}$$

3 Model-Free Integral PI for Zero-Sum Games

First, we present a PI algorithm for zero-sum games with known dynamics.

Algorithm 1. (PI for Zero-sum Games)
Step 1: Give an initial stabilizing control policy u_1 and disturbance d_1. Set $i = 1$.
Step 2 (Policy Evaluation): For the system (1) with policies u_i and d_i, solve the following Lyapunov equation for V_i

$$0 = r(x, u_i, d_i) + \nabla V_i^\mathsf{T}(x) \big(f(x) + g(x) u_i(x) + k(x) d_i(x) \big). \tag{9}$$

Step 3 (Policy Improvement): Update the control and disturbance policies by

$$u_{i+1}(x) = -\frac{1}{2} R^{-1} g^\mathsf{T}(x) \nabla V_i(x) \tag{10}$$

$$d_{i+1}(x) = \frac{1}{2\gamma^2} k^\mathsf{T}(x) \nabla V_i(x). \tag{11}$$

Step 4: If $\|V_i - V_{i-1}\| \leq \zeta$ (ζ is a prescribed small positive real number), stop and output V_i; else, set $i = i + 1$ and go to *Step* 2.

It can be shown that Algorithm 1 is equivalent to Newton's method [17]. The sequences of V_i, u_i, and d_i obtained in Algorithm 1 converge to the optimal value function of HJI, the saddle point u^* and d^* respectively, as $i \to \infty$.

Next, we will develop an online model-free integral PI algorithm for zero-sum games with completely unknown systems. To relax the assumptions of exact

knowledge on $f(x)$, $g(x)$ and $k(x)$, we denote e_1 and e_2 to be the exploration signals added to the control policy u_i and disturbance policy d_i respectively. The exploration signals are assumed to be any non-zero measurable signal which is exactly known a priori and bounded by $e_M > 0$, i.e., $\|e_1\| \leq e_M$, $\|e_2\| \leq e_M$. Then, the original system (1) becomes

$$\dot{x} = f(x) + g(x)(u_i + e_1) + k(x)(d_i + e_2). \tag{12}$$

The derivative of the value function with respect to time is calculated as

$$\dot{V}_i(x) = \nabla V^{\mathsf{T}}(x)\big(f(x) + g(x)(u_i + e_1) + k(x)(d_i + e_2)\big). \tag{13}$$

Integrating (13) from t and $t+T$ with any time interval $T > 0$ and considering (9)–(11), we have

$$\begin{aligned} V_i(x_{t+T}) - V_i(x_t) = &- \int_t^{t+T} r(x, u_i, d_i)\mathrm{d}\tau - 2\int_t^{t+T} u_{i+1}^{\mathsf{T}} R e_1 \mathrm{d}\tau \\ &+ 2\gamma^2 \int_t^{t+T} d_{i+1}^{\mathsf{T}} e_2 \mathrm{d}\tau \end{aligned} \tag{14}$$

where the values of the state at time t and $t+T$ are denoted with x_t and x_{t+T}.

Equation (14) plays an important role in relaxing the assumption of the knowledge of system dynamics, since $f(x)$, $g(x)$ and $k(x)$ do not appear in (14). Thus we obtain the online model-free integral PI algorithm for zero-sum games.

Algorithm 2. (Online Model-free Integral PI for Zero-sum Games)
Step 1: Give an initial stabilizing control policy u_1 and disturbance d_1. Set $i = 1$.
Step 2 (Policy Evaluation and Improvement):
For the system (12) with policies u_i and d_i, and exploration signals e_1 and e_2, solve the following equation for V_i, u_{i+1} and d_{i+1}

$$\begin{aligned} V_i(x_t) = &V_i(x_{t+T}) + \int_t^{t+T} r(x, u_i, d_i)\mathrm{d}\tau \\ &+ 2\int_t^{t+T} u_{i+1}^{\mathsf{T}} R e_1 \mathrm{d}\tau - 2\gamma^2 \int_t^{t+T} d_{i+1}^{\mathsf{T}} e_2 \mathrm{d}\tau. \end{aligned} \tag{15}$$

Step 3: If $\|V_i - V_{i-1}\| \leq \xi$ (ξ is a prescribed small positive real number), stop and output V_i; else, set $i = i + 1$ and go to *Step* 2.

Remark 1. This algorithm updates the value function, control policy and disturbance policy at the same time. Furthermore, it will not be affected by the errors between the identification model and the real system, and it can respond fast to the change of the system dynamics. To guarantee the persistence of excitation condition, the state may need to be reset during the iterative process [17], but it results in technical problems for stability analysis of the closed-loop system. An alternative way is to add exploration noises [14] which may make the solution different from the exact one determined by the HJI. Compared with these methods, the solution obtained by our method is exactly the same as the one determined by solving HJI by considering the effects of exploration noises.

4 Online Implementation Using Neural Networks

To implement Algorithm 2, one critic NN and two action NNs are used to approximate the value function, control and disturbance policies respectively. For simplicity, we let $m = q = 1$. Note that the algorithm presented above can be applied to multi-input systems. For (15), $V_i(x)$, $u_{i+1}(x)$, and $d_{i+1}(x)$ can be represented on a compact set Ω by single-layer NNs as

$$V_i(x) = (W_i^1)^{\mathsf{T}}\phi_1(x) + \varepsilon_i^1(x) \tag{16}$$

$$u_{i+1}(x) = (W_{i+1}^2)^{\mathsf{T}}\phi_2(x) + \varepsilon_{i+1}^2(x) \tag{17}$$

$$d_{i+1}(x) = (W_{i+1}^3)^{\mathsf{T}}\phi_3(x) + \varepsilon_{i+1}^3(x) \tag{18}$$

where $W_i^1 \in \mathbb{R}^{N_1}$, $W_i^2 \in \mathbb{R}^{N_2}$ and $W_i^3 \in \mathbb{R}^{N_3}$ are the unknown bounded ideal weights, $\phi_1(x) \in \mathbb{R}^{N_1}$, $\phi_2(x) \in \mathbb{R}^{N_2}$ and $\phi_3(x) \in \mathbb{R}^{N_3}$ are the activation functions, and $\varepsilon_i^1(x) \in \mathbb{R}$, $\varepsilon_{i+1}^2(x) \in \mathbb{R}$ and $\varepsilon_{i+1}^3(x) \in \mathbb{R}$ are the bounded NN approximation errors. As the number of neurons in the hidden layer goes to infinity, the approximation errors go to zero uniformly. Since the ideal weights are unknown, the outputs of critic NN and action NNs are

$$\hat{V}_i(x) = (\hat{W}_i^1)^{\mathsf{T}}\phi_1(x) \tag{19}$$

$$\hat{u}_{i+1}(x) = (\hat{W}_{i+1}^2)^{\mathsf{T}}\phi_2(x) \tag{20}$$

$$\hat{d}_{i+1}(x) = (\hat{W}_{i+1}^3)^{\mathsf{T}}\phi_3(x) \tag{21}$$

where $\hat{W}_i^1$, $\hat{W}_{i+1}^2$ and $\hat{W}_{i+1}^3$ are the current estimated weights.

Using above expressions (19)–(21), (15) can be rewritten to be a general compact form

$$\psi_k^{\mathsf{T}} \begin{bmatrix} \hat{W}_i^1 \\ \hat{W}_{i+1}^2 \\ \hat{W}_{i+1}^3 \end{bmatrix} = \theta_k \tag{22}$$

with

$$\theta_k = \int_{t+(k-1)T}^{t+kT} r(x, u_i, d_i)\mathrm{d}\tau \tag{23}$$

$$\psi_k = \Big[\big(\phi_1(x_{t+(k-1)T}) - \phi_1(x_{t+kT})\big)^{\mathsf{T}}, -2\int_{t+(k-1)T}^{t+kT} Re_1\phi_2^{\mathsf{T}}(x)\mathrm{d}\tau, \\ 2\gamma^2 \int_{t+(k-1)T}^{t+kT} e_2\phi_3^{\mathsf{T}}(x)\mathrm{d}\tau \Big]^{\mathsf{T}} \tag{24}$$

where the measurement time is from $t + (k-1)T$ to $t + kT$. Since (22) is only a 1-dimensional equation, we cannot guarantee the uniqueness of the solution. Similar to [8], we use the least squares sense method to solve the parameter vector

over a compact set Ω. For any positive integer K, we denote $\Phi_i = [\psi_1, \ \ldots, \ \psi_K]$ and $\Theta_i = [\theta_1, \ \ldots, \ \theta_K]^\mathsf{T}$. Then, we have the following K-dimensional equation

$$\Phi_i^\mathsf{T} \begin{bmatrix} \hat{W}_i^1 \\ \hat{W}_{i+1}^2 \\ \hat{W}_{i+1}^3 \end{bmatrix} = \Theta_i. \tag{25}$$

If Φ_i^T has full column rank, the parameters can solved by

$$\begin{bmatrix} \hat{W}_i^1 \\ \hat{W}_{i+1}^2 \\ \hat{W}_{i+1}^3 \end{bmatrix} = (\Phi_i \Phi_i^\mathsf{T})^{-1} \Phi_i \Theta_i. \tag{26}$$

Therefore, we need to have the number of collected points K at least $K_{\min} = rank(\Phi_i) = N_1 + N_2 + N_3$, which will make $(\Phi_i \Phi_i^\mathsf{T})^{-1}$ exist. The least squares problem in (26) can be solved in real time by collecting enough data points generated from the system (9).

5 Simulation Study

To demonstrate the effectiveness of the online model-free integral PI algorithm, we consider the following nonlinear system

$$\dot{x} = \begin{bmatrix} -0.25x_1 \\ 0.5x_2^3 - 0.5\gamma^{-2}x_1^2 x_2 - 0.5x_2 \end{bmatrix} + \begin{bmatrix} 0 \\ x_2 \end{bmatrix} u + \begin{bmatrix} 0 \\ x_1 \end{bmatrix} d. \tag{27}$$

We assume that the exact knowledge of the dynamics (27) is fully unknown. In the value function, the matrices Q and R are identity matrices of appropriate dimensions, and $\gamma = 2$. The optimal value function of the zero-sum game is $V^*(x) = 2x_1^2 + x_2^2$.

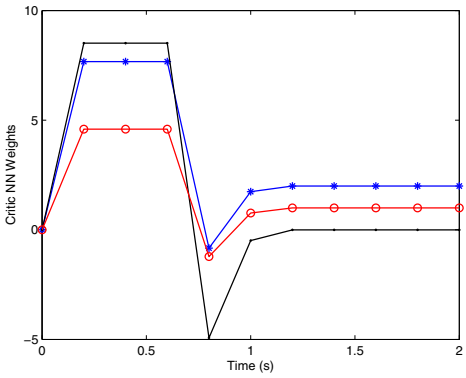

Fig. 1. Convergence of the game value function V_i

Set the initial state $x_0 = [-0.4\ 0.4]^\mathsf{T}$ and the stop criterion $\xi = 10^{-5}$. The NN activation functions are chosen as $\phi_1(x) = \phi_2(x) = \phi_3(x) = [x_1^2\ \ x_1x_2\ \ x_2^2]^\mathsf{T}$. The parameters of the critic NN and action NNs are all initialized to zero. The simulation is conducted using data obtained along the system trajectory at every $T = 0.01s$. The least squares problem is solved after 20 data samples are acquired, and thus the parameters of the NNs are updated every $0.2s$. Using the developed algorithm, Fig. 1 presents the evolution of the weights $\hat{W}_1^i$ during the learning process. It is clear that the critic NN weights approximately converge to the true weights $[2\ \ 0\ \ 1]^\mathsf{T}$. Thus the approximate value function can be obtained at $t = 2s$, i.e., $V_{10} = [1.9972\ \ -0.0053\ \ 0.9973]\phi_1(x)$.

6 Conclusion

In this paper, we develop an integral PI algorithm to solve online the Nash equilibrium solution for two-player zero-sum differential games with completely unknown nonlinear continuous-time dynamics. This ends up to a fully model-free method solving the HJI forward in time for the first time. We demonstrate the effectiveness of the developed scheme by a simulation example.

Acknowledgment. This work was supported in part by the National Natural Science Foundation of China under Grants 61034002, 61233001, and 61273140.

References

1. Lewis, F.L., Liu, D.: Reinforcement Learning and Approximate Dynamic Programming for Feedback Control. Wiley, Hoboken (2012)
2. Vamvoudakis, K.G., Lewis, F.L.: Online Actor-critic Algorithm to Solve the Continuous-time Infinite Horizon Optimal Control Problem. Automatica 46, 878–888 (2010)
3. Zhang, H., Cui, L., Zhang, X., Luo, Y.: Data-driven Robust Approximate Optimal Tracking Control for Unknown General Nonlinear Systems Using Adaptive Dynamic Programming Method. IEEE Trans. Neural Netw. 22, 2226–2236 (2011)
4. Bhasin, S., Kamalapurkar, R., Johnson, M., Vamvoudakis, K.G., Lewis, F.L., Dixon, W.E.: A Novel Actor-critic-identifier Architecture for Approximate Optimal Control of Uncertain Nonlinear Systems. Automatica 49, 82–92 (2013)
5. Vrabie, D., Pastravanu, O., Abu-Khalaf, M., Lewis, F.L.: Adaptive Optimal Control for Continuous-time Linear Systems Based on Policy Iteration. Automatica 45, 477–484 (2009)
6. Vrabie, D., Lewis, F.L.: Neural Network Approach to Continuous-time Direct Adaptive Optimal Control for Partially Unknown Nonlinear Systems. Neural Netw. 22, 237–246 (2009)
7. Mehta, P., Meyn, S.: Q-learning and Pontryagins Minimum Principle. In: Proceedings of the 48th IEEE Conference on Decision and Control, pp. 3598–3605 (2009)
8. Lee, J.Y., Park, J.B., Choi, Y.H.: Integral Q-learning and Explorized Policy Iteration for Adaptive Optimal Control of Continuous-time Linear Systems. Automatica 48, 2850–2859 (2012)

9. Lee, J.Y., Park, J.B., Choi, Y.H.: Integral Reinforcement Learning with Explorations for Continuous-time Nonlinear Systems. In: Proceedings of the 2012 IEEE World Congress on Computational Intelligence, pp. 1042–1047 (2012)
10. Jiang, Y., Jiang, Z.P.: Computational Adaptive Optimal Control for Continuous-time Linear Systems with Completely Unknown Dynamics. Automatica 48, 2699–2704 (2012)
11. Basar, T., Olsder, G.J.: Dynamic Noncooperative Game, 2nd edn. SIAM, Philadelphia (1997)
12. Abu-Khalaf, M., Lewis, F.L., Huang, J.: Neurodynamic Progarmming and Zero-sum Games for Constrained Control Systems. IEEE Trans. Neural Netw. 19, 1243–1252 (2008)
13. Zhang, H., Wei, Q., Liu, D.: An Iterative Adaptive Dynamic Programming Method for Solving a Class of Nonlinear Zero-sum Differential Games. Automatica 47, 207–214 (2011)
14. Vamvoudakis, K.G., Lewis, F.L.: Online Solution of Nonlinear Two-player Zero-sum Games using Synchronous Policy Iteration. Int. J. Robust. Nonlinear Control 22, 1460–1483 (2012)
15. Johnson, M., Bhasin, S., Dixon, W.E.: Nonlinear Two-player Zero-sum Game Approximate Solution Using a Policy Iteration Algorithm. In: Proceedings of Conference on Decision and Control and European Control Conference, pp. 142–147 (2011)
16. Varbie, D., Lewis, F.L.: Adaptive Dynamic Programming for Online Solution of a Zero-sum Differential Game. J. Control Theory Appl. 9, 353–360 (2011)
17. Wu, H.N., Luo, B.: Neural Network Based Online Simultaneous Policy Update Algorithm for Solving the HJI Equation in Nonlinear H_∞ Control. IEEE Trans. Neural Netw. and Learn. Syst. 23, 1884–1895 (2012)

A Novel Muscle Coordination Method for Musculoskeletal Humanoid Systems and Its Application in Bionic Arm Control

Haiwei Dong[1] and Setareh Yazdkhasti[2]

[1] Devision of Engineering, New York University AD, Electra Street, Abu Dhabi, UAE
haiwei.dong@nyu.edu
[2] College of Engineering, Al Ghurair University, Academic City, Dubai, UAE
s.yazdkhasti@ieee.org

Abstract. The muscle force control of musculoskeletal humanoid system has been considered for years in motor control, biomechanics and robotics disciplines. In this paper, we consider the muscle force control as a problem of muscle coordination. We give a general muscle coordination method for mechanical systems driven by agonist and antagonist muscles. Specifically, the muscle force is computed by two steps. First, the initial muscle force is computed by pseudo-inverse. Here, the pseudo-inverse solution naturally satisfies the minimum total muscle force in the least squares sense. Second, the initial optimized muscle force is optimized by taking the optimization criteria of distributing muscle force in the middle of its output force range. The two steps provide an even-distributed muscle force. The proposed method is validated by a movement tracking of a bionic arm which has 5 degrees of freedom and 22 muscles. The force distribution property, tracking accuracy and efficiency are also tested.

Keywords: Muscle Force Computation, Arm Movement Control, Redundancy Solution.

1 Introduction

Several research works in different disciplines have been distributed in order to understand the muscle control of the musculoskeletal humanoid systems. The initial scientific works in human motor control consider the muscle control as coordination of sensor input and motor output. The sensor-motor coordination is explained by modeled central nervous system [1]. Later, the muscle control is dealt with in biomechanics. Here, the basic idea is building an accurate muscle model, setting all the constraints in muscle space and joint space (such as force limit, motion boundary, time delay etc.) and using global optimization to solve the problem as a whole [2][3]. As the global optimization is computationally very exhaustive task, parallel computation is introduced to reduce the computational time [4]. There have been two successful commercial software packages to simulate human movement: AnyBody Modeling System by AnyBody Technology and SIMM by MusculoGraphics. Recently, with the development of artificial muscle

M. Lee et al. (Eds.): ICONIP 2013, Part I, LNCS 8226, pp. 233–240, 2013.
© Springer-Verlag Berlin Heidelberg 2013

technology, many muscle-like actuators are available, such as cable-driven actuator, pneumatic actuator, and so on. By using these new actuators, robotic researchers built a number of musculoskeletal humanoid robots, such as ECCE from University of Zurich, Kenshiro from University of Tokyo, Lucy from Vrije Universiteit Brussel, etc. These robots provide physical platforms to emulate muscle force control of musculoskeletal systems. However, the control of these musculoskeletal humanoid system is still under development. Regarding the coincidence with electromyogram (EMG) measurement, there has been one paper written by Anderson and Pandy, stating that the muscle force curve computed by the global optimization looks similar with the real EMG measurement when doing extreme movement of high jumping [4].

Actually, the muscle force control can be considered as muscle coordination. As there exists redundancy in joint space, muscle space and impedance space, the solution of the muscle coordination is not unique [5]. Based on different criteria, the muscle coordination solutions are different. For example, Pandy considered the criterion of the minimum of the overall energy-consuming of muscles[3]. Dong et al. chose the criterion to be "anti-fatigue", i.e., the load was distributed evenly among muscles [6]. If we only focus on the control performance without considering energy-consuming or force distribution, the problem is easier. In Tahara et al.'s research, the muscle force is distributed from computed joint torque. PD control is then used for each muscle's control [7]. Actually, from the neuroscience research, the muscle force control is also influenced by the body movement patterns. The dynamics of the musculoskeletal system has order parameter which can determine the phase transition of movements. These scenarios are found in finger movement and limb movement patterns [8].

In this paper, we give a general muscle coordination method for mechanical systems driven by agonist and antagonist muscles. Specifically, the muscle force is computed by two steps. First, the initial muscle force is computed by pseudo-inverse. Here, the pseudo-inverse solution naturally satisfies the minimum total muscle force in the least squares sense. Second, the initial optimized muscle force is optimized by taking the optimization criteria of distributing muscle force in the middle of its output force range. The two steps provide an even-distributed muscle force. The proposed method is validated by a movement tracking of a bionic arm which has 5 degrees of freedom and 22 muscles. The force distribution property, tracking accuracy and efficiency are also tested.

2 Muscle Coordination

2.1 Pseudo-inverse in Initial Muscle Force Computation

In this subsection, we use pseudo-inverse to compute the initial muscle force. The input is the desired joint trajectory and muscle force boundary. The output is the minimum muscle force under the sense of least-squares. The basic idea is firstly creating a linear equation based on the description of the acceleration contribution in joint space and muscle space, respectively. Then the muscle activation level is calculated by solving the above linear equation. Finally, the muscle

force is computed by scaling the muscle activation level with its corresponding maximum muscle force.

The general dynamic equation of the musculoskeletal systems can be written in the general form

$$H(q,t)\,\ddot{q} + C(q,t)\,\dot{q} + G(t) = f(F_m) \tag{1}$$

where $f(F_m)$ maps muscle force F_m to joint torque. Here, we transform it into the following form

$$\ddot{q} = \underbrace{H(q,t)^{-1} f(F_m)}_{\ddot{q}_\Gamma} + \underbrace{\left(-H(q,t)^{-1}(C(q,t)+G(t))\right)}_{\ddot{q}_{\Lambda\Xi}} \tag{2}$$

The above equations indicate that in the joint space, the acceleration contribution comes from 1): joint torque Γ, 2): centripetal, coriolis and gravity torque $\Lambda + \Xi$. Hence, we can compute the acceleration contribution from joint torque $\ddot{q}_\Gamma$ by Eq.2. Whereas, from another viewpoint, in the muscle space, each muscle has its acceleration contribution. Here, we assume the total muscle number is n_{muscle}. For the j-th ($1 \le j \le n_{muscle}$) muscle, its maximum acceleration contribution can be written as

$$\ddot{q}_{m,j,max} = H(q,t)^{-1}\,\Gamma_{j,max} \quad (1 \le j \le n_{muscle}) \tag{3}$$

where

$$\begin{aligned}
&\Gamma_{1,max} = J_m^T \left[\, F_{m,1,max}\ 0\ 0 \cdots 0\ 0 \,\right]^T \\
&\Gamma_{2,max} = J_m^T \left[\, 0\ F_{m,2,max}\ 0 \cdots 0\ 0 \,\right]^T \\
&\cdots \\
&\Gamma_{n_{muscle},max} = J_m^T \left[\, 0\ 0\ 0 \cdots 0\ F_{m,n_{muscle},max} \,\right]^T
\end{aligned}$$

By combining the above two computational ways of acceleration contribution in joint space and muscle space, we can build a linear equation

$$\left[\, \ddot{q}_{m,1,max}\ \ddot{q}_{m,2,max} \cdots \ddot{q}_{m,n_{muscle},max} \,\right] \left[\, \sigma_1\ \sigma_2 \cdots \sigma_{n_{muscle}} \,\right]^T = \ddot{q_\Gamma} \tag{4}$$

where $\left[\, \sigma_1\ \sigma_2 \cdots \sigma_{n_{muscle}} \,\right]^T$ is a vector of muscle activation levels. The muscle activation level is a scalar in the interval $[0,1]$, representing the percentage of maximum contraction force of muscle. It is noted that $\ddot{q}_{m,j,max}$ ($1 \le j \le n_{muscle}$) and $\ddot{q_\Gamma}$ are vectors. The dimensions of $\ddot{q}_{m,j,max}$ and $\ddot{q_\Gamma}$ are the same equaling to the joint number. Supposing the total joint number is n_{joint}, $\ddot{q}_{m,j,max}$ and $\ddot{q_\Gamma}$ can be written in the form

$$\ddot{q}_{m,j,max} = \begin{bmatrix} \ddot{q}_{m,j,1} \\ \ddot{q}_{m,j,2} \\ \vdots \\ \ddot{q}_{m,j,n_{joint}} \end{bmatrix}_{n_{joint}\times 1}, \quad \ddot{q}_\Gamma = \begin{bmatrix} \ddot{q}_{\Gamma,1} \\ \ddot{q}_{\Gamma,2} \\ \vdots \\ \ddot{q}_{\Gamma,n_{joint}} \end{bmatrix}_{n_{joint}\times 1} \tag{5}$$

Considering Eq.4, we can use pseudo-inverse to compute muscle activation level

$$\left[\sigma_1\ \sigma_2 \cdots\ \sigma_{n_{muscle}}\right]^T = \left(\left[\ddot{q}_{m,1,max}\ \ddot{q}_{m,2,max} \cdots\ \ddot{q}_{m,n_{muscle},max}\right]\right)^+ \ddot{q_\Gamma} \tag{6}$$

where $(\cdot)^+$ is the pseudo-inverse of $(\cdot)$. Therefore, the muscle force can be calculated as a product of maximum contraction force and activation level

$$F_{m,ini} = \left[F_{m,1,max} \cdot \sigma_1 \cdots\ F_{m,n_{muscle},max} \cdot \sigma_{n_{muscle}}\right]^T \tag{7}$$

2.2 Gradient Descent in Muscle Force Optimization

The computed initial muscle force $F_{m,ini}$ dose not consider the physical constraints of muscles, which are: 1) the maximum output force of muscle is limited; 2) muscle can only contract. Here, we use gradient descent to make muscle force satisfy the above constraints. The basic idea is to find a gradient direction in the null space of the pseudo-inverse solution obtained in Step 1 to relocate the initial muscle force $F_{m,ini}$ to an optimized state, which satisfies muscle constraints 1) and 2).

We assume each muscle force is limited in the interval from $F_{m,j,min}$ to $F_{m,j,max}$ for $1 \leq j \leq n_{muscle}$. Our objective is to find a gradient direction to make each muscle force $F_{m,j}$ equal or greater than $F_{m,j,min}$, and equal or less than $F_{m,j,max}$. Considering the muscle force boundary constraints, one possible way is to make the output force of each muscle be closest to the middle point between $F_{m,j,min}$ and $F_{m,j,max}$. The physical meaning of this method is to distribute overall load to all the muscles evenly where each muscle works around its proper working load. Based on this load distribution principle, the muscles can continually work for a long time. According to the above muscle force distribution principle, we choose a function h as

$$h\left(F_m\right) = \sum_{j=1}^{n_{muscle}} \left(\frac{F_{m,j} - F_{m,j,mid}}{F_{m,j,mid} - F_{m,j,max}}\right)^2 \tag{8}$$

where

$$0 \leq F_{m,j,min} \leq F_{m,j} \leq F_{m,j,max},\ F_{m,j,mid} = \frac{F_{m,j,min} + F_{m,j,max}}{2}$$
$$j = 1, 2, \cdots, n_{muscle}$$

We define F_{in} as a vector representing the internal force of muscles generated by redundant muscles which has the same dimension with F_m. We calculate F_{in} as the gradient of the function h, i.e.,

$$F_{in} = K_{in}\ \nabla h|_{F_{m,ini}} = K_{in} \begin{bmatrix} 2\frac{F_{m,ini,1} - F_{m,1,mid}}{F_{m,1,mid} - F_{m,1,max}} \\ 2\frac{F_{m,ini,2} - F_{m,2,mid}}{F_{m,2,mid} - F_{m,2,max}} \\ \vdots \\ 2\frac{F_{m,ini,n_{muscle}} - F_{m,n_{muscle},mid}}{F_{m,n_{muscle},mid} - F_{m,n_{muscle},max}} \end{bmatrix} \tag{9}$$

where K_{in} is a scalar matrix controlling the optimization speed. It is easy to prove that the direction of F_{in} points to $F_{m,i,mid}$. We map the internal force F_{in} into F_m space (i.e., pseudo-inverse solution's null space) as

$$g\left(F_{in}\right) = \left(I - \left(J_m^T\right)^+ J_m^T\right) F_{in} \tag{10}$$

where I is an identity matrix having the same dimension with muscle space. According to Moore-Penrose pseudo-inverse, $g\left(F_{in}\right)$ is orthogonal with the space of $F_{m,ini}$. Finally, the optimized muscle force is calculated as

$$F_m = F_{m,ini} + g\left(F_{in}\right) \tag{11}$$

3 Evaluation

3.1 Bionic Arm Modeling

First of all, we define symbols for the convenience of derivation. $Rot(\theta, x)$, $Rot(\theta, y)$ and $Rot(\theta, z)$ are rotation matrices between different frames x, y, and z axis where θ is the rotation angle. $Trans(d_x, d_y, d_z)$ is transition matrix within a frame where d_x, d_y, and d_z are the transition distances in x, y, and z directions, respectively. T_i^j is the transfer matrix from frame i to frame j. In this simulation, we defined the frame 1 to 5 as shown in Fig.1 (a). Joint angles $[\theta_1, \theta_2, \theta_3, \theta_4, \theta_5]^T$ are the rotational angles corresponding to Frame 1 to Frame 5, respectively. The range of shoulder angle is set as from -20 to 100 degrees, and the range of the elbow is set as from 0 to 170 degrees. Here, we use Muscular Skeletal Modeling Software (MSMS) [9] to create the virtual bionic arm, based on which, we make animation to evaluate the movement computed by the proposed method (Fig.1 (b)).

In the simulation, the bionic arm is composed of two parts: shoulder and elbow. In total, the model is composed of five rotational degrees of freedom (DOF) where three of them are in the shoulder joint (shoulder abduction-adduction, shoulder flexion-extension and shoulder external-internal rotation), and two are in the elbow joint (elbow flexion-extension and forearm pronation-supination). The parameters setting of the bionic arm is based on the real data of a human upper limb. The setting of length, mass, mass center position and inertia coefficients are from [10]. There are 22 muscles configured in the model. The specific configuration of the muscles, i.e., coordinate setting of the origins and insertions in the Gleno-Humeral joint coordinate system (X_{GH}, Y_{GH}, Z_{GH}), are from [11].

3.2 Performance

We used the above bionic arm model to test the proposed method. Without loss of generality, the desired trajectory of the five rotational joints is sine signal: amplitude: -1/3π; frequency: 1; phase: 0; bias: 1/3π. The maximum muscle force $F_{m,i,max}$ $(1 \leq i \leq 22)$ is set as 100N. The total simulation time is set as 10s.

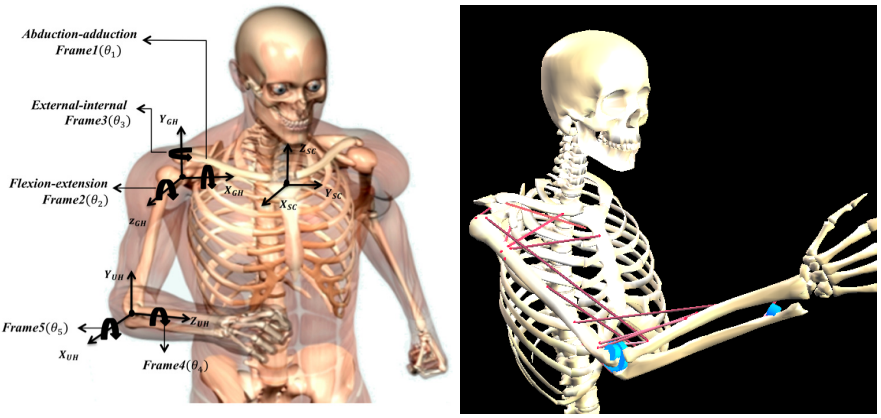

(a) (b)

Fig. 1. Bionic arm. (a) Frame setting of the bionic arm. (b) Snapshot of the arm movement in Muscular Skeletal Modeling Software (MSMS).

"Anti-fatigue" Force Distribution. As there are 22 muscles configured in this model, the result can provide an insight on the muscle force distribution. Fig.2 (a-b) show the computed muscle force in the initial pseudo-inverse step (Subsection 2.1) and in the optimized gradient descent step (Subsection 2.2), respectively. In each subfigure, the upper part is the muscle force distribution statistics. The horizontal axis is the muscle index and the vertical axis is the average percentage ratio of the specific muscle force amplitude to its corresponding maximum muscle force $F_{m,max}$. The lower part is the muscle force curves where the horizontal axis is, similarly, the muscle index and vertical axis is the simulation time. By comparing (a) and (b), we can see that the initial muscle force optimization provides large variance ($\sigma \doteq 0.04$) in muscle force. In contrast, the optimized muscle force gives smaller variance ($\sigma \doteq 0.02$) in muscle force.

Tracking Accuracy. We recorded the tracking error of the five joint angles. The tracking performance is shown in Fig.2 (c). The horizontal axis is the simulation time, from 0 to 10s. The vertical axis is the joint index, from q_1 to q_5 in rad. It shows that the tracking error for the five joints is within the range of 10^{-3} rad, indicating that the proposed method has a good tracking property.

Efficiency. The simulation environment is MacBook Air laptop. The basic configuration of the computer is listed below: processor: 1.7GHz Intel Core i5; memory: 4GB 1333 MHz DDR3; startup disk: Macintosh HD 200GB; operation system: Mac OS X Lion 10.7.4 (11E53). The computational time is shown in Fig.2 (d) where the horizontal axis is the time index representing simulation time (from 0 to 10s). Vertical axis is the accumulative computational time in s. It shows that the computational time is nearly linear which means the proposed method approximately consumes equal time to compute muscle force for different arm postures.

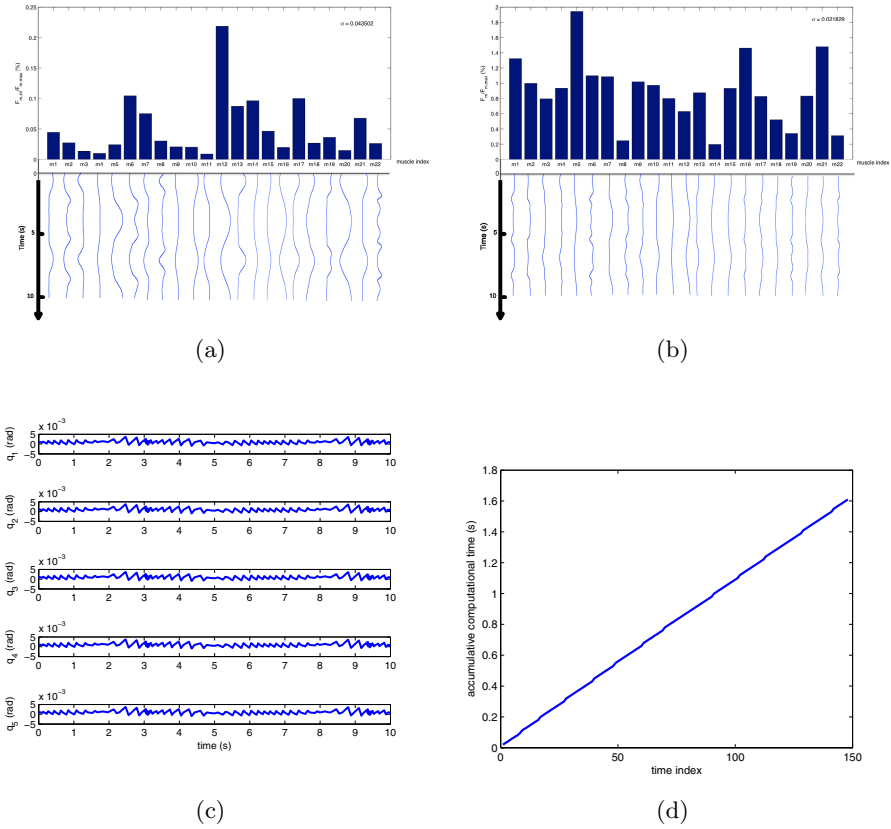

Fig. 2. Performance evaluation in force distribution, tracking accuracy and efficiency. (a)Initial muscle force distribution. (b) Optimized muscle force distribution. (c) Tracking error of the joints. (d) Accumulative computational time.

4 Conclusion

This paper gives a general solution for muscle force control of the musculoskeletal humanoid systems. The two steps of muscle force coordination compute the muscle force satisfying the muscle force constraints. The proposed method is tested by a bionic arm with 5 degrees of freedom and 22 muscles. The results show that the proposed method provides an evenly-distributed muscle forces efficiently.

References

1. Wise, S., Shadmehr, R.: Motor Control. In: Encyclopedia of the Human Brain, pp. 137–157 (2002)
2. Garner, B.A., Pandy, M.G.: A kenematic model of the upper limb based on the visible human project (vhp) image dataset. Computer Methods in Biomechanics and Biomedical Engineering 2, 107–124 (1999)
3. Pandy, M.: Computer modeling and simulation of human movement. Annual Review of Biomedical Engineering 3, 245–273 (2001)
4. Anderson, F., Pandy, M.: A dynamic optimization solution for vertical jumping in three dimensions. Computer Methods in Biomechanics and Biomedical Engineering 2, 201–231 (1999)
5. Yamaguchi, G.: Dynamic Modeling of Musculoskeletal Motion: A Vectorized Appoach for Biomechanical Analysis in Three Dimensions. Springer (2005)
6. Dong, H., Mavridis, N.: Muscle force distribution for adaptive control of a humanoid robot arm with redundant bi-articular and mono-articular muscle mechanism. Artificial Life and Robotics (2013)
7. Tahara, K., Luo, Z., Arimoto, S., Kino, H.: Sensory-motor control mechanism for reaching movements of a redundant musculo-skeletal arm. Journal of Robotic Systems 22, 639–651 (2005)
8. Kelso, J.A.: Dynamic Patterns. MIT Press (1995)
9. Khachani, M., Davoodi, R., Loeb, G.: Musculo-skeletal modeling software (msms) for biomechanics and virtual rehabilitation. In: Proceeding of American Society of Biomechanics Conference (2007)
10. Nagano, A., Yoshioka, S., Komura, T., Himeno, R., Fukashiro, S.: A three-dimensional linked segment model of the whole human body. International Journal of Sport and Health Science 3, 311–325 (2005)
11. Maurel, W., Thalmann, D., Hoffmeyer, P., Beylot, P., Gingins, P., Kalra, P., Magnenat, N., Hoffmeyer, P.: A biomechanical musculoskeletal model of human upper limb for dynamic simulation. In: Proceedings of the Eurographics Computer Animation and Simulation Workshop (1996)

Effects of Cost Structure in Optimal Control on Biological Arm Movement: A Simulation Study

Yuki Ueyama

Department of Rehabilitation Engineering
Research Institute of National Rehabilitation Center for Persons with Disabilities
4-1 Namiki, Tokorozawa, Saitama 359-8555, Japan
ueyama-yuki@rehab.go.jp

Abstract. We have to choose muscle activation pairs of agonist and antagonist muscles from a variety of combinations to achieve a movement. Even though there is a redundancy problem, we could immediately solve the problem and generate movements with a characteristic muscle activation pattern that the muscle pairs burst alternatively as the biphasic or triphasic shape. In this paper, in order to investigate requirements that derive the muscle activation pattern, we carried out numerical simulations of arm movement using a musculoskeletal arm model and an approximately optimal feedback control law with changing the cost structure. As a result, the muscle activation pattern could be reproduced by the simulation with a cost form composed by four terms, i.e., position, velocity, force and energy consumption. Thus, the muscle activations may correspond to cost terms. Furthermore, we suggest that the brain also regulate the force as well as the spatial accuracy and efficiency in the absence of any force interaction.

Keywords: Motor control, Reaching, Cost function, Muscle, Monkey.

1 Introduction

A biological motor system consists of many joints and muscles, forming a redundant system with multiple dimensions of freedom. The central nervous system (CNS) has to solve some redundancy problems, e.g., determining a movement trajectory and a pattern of muscle activity consisting of pairs of agonist and antagonist muscles. Besides, it was reported that the muscle activation pattern is equivalent to other movements loaded by an external force when the movements are kinematically same and the dynamics is well learned even if the amount of muscle activations is increased [1]. The typical pattern has been found that the agonist and antagonist muscles burst alternatively as the biphasic or triphasic pattern of muscle activation in single-joint reaching movements [2]. In addition, we also observed the muscle activation pattern in multi-joint movements in a monkey [3]. However, it has been suggested that most of motor control and planning models (i.e., the minimum jerk model and other criterions) could not predict a specific muscle action, e.g., a muscle co-contraction depending on tasks [4-6].

M. Lee et al. (Eds.): ICONIP 2013, Part I, LNCS 8226, pp. 241–248, 2013.
© Springer-Verlag Berlin Heidelberg 2013

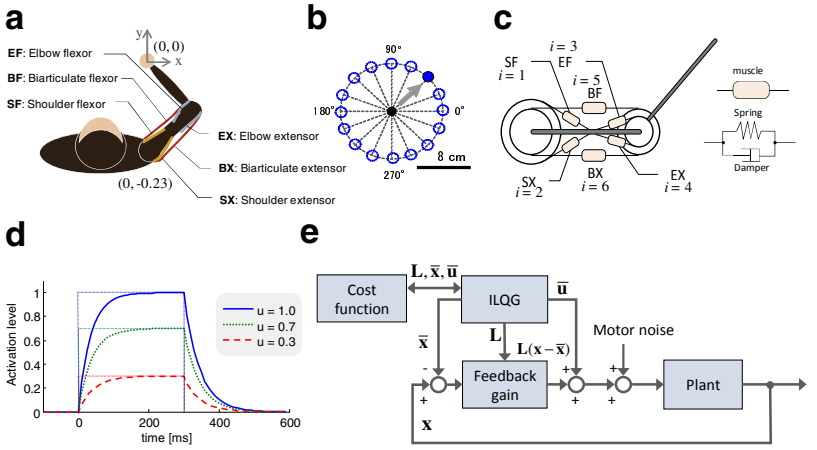

Fig. 1. Simulation model. (a) Setup of the center-out reaching task. The start position is 23-cm forward away from the round axis of the shoulder. (b) Reaching targets of the task. The targets are aligned as an 8-cm radial circle around the start position. (c) 2-link 6-muscle arm model. (d) Muscle activation dynamics. (e) Block diagram of the ILQG optimal control law.

Recently, optimal feedback control (OFC) theory has been proposed [7], and it is a plausible control model that could solve the redundancy problem. In addition, the theory could predict variability of movement phenomena [4, 5, 8]. In neural studies, it also has been suggested that primary motor cortex provides a neural substrate for integrating shoulder and elbow motion information into joint torque for fast feedback control [9].

In this study, we applied the iterative linear-quadratic-Gaussian (ILQG) method [10], which is an approximately OFC, to the biological arm dynamics and examined a role of cost structure formed by kinetic terms in order to investigate a source of the muscle activation pattern. As a result, the OFC could selectively coordinate muscles according to the movement direction, and an interlaced cost of the terminal position, velocity, force, and the entire energy consumption could induce similar activation patterns reported in previous studies [2, 3]. Consequently, we suggest that the brain may control the body according to an OFC mechanism adapting a cost function composed at least the four terms.

2 Methods

We simulated arm movements for a center-out reaching task using the iterative linear-quadratic-Gaussian (ILQG) method [10] and a 2-joint 6-muscle arm model (Fig.1a-c). The ILQG method constructs an affine feedback control law by minimizing a quadratic approximation to optimize a cost function, and could predict dynamic stiffness during arm movement [8].

2.1 The Two-Joint Six-Muscle Arm Model

We considered the monkey's arm to be a two-joint arm that was composed of the shoulder and elbow joints (Fig.1a). The joint variables were calculated in accordance with the kinematics of the monkey, and the joint angles were defined as a vector, $\boldsymbol{\theta} = [\theta_{sh}, \theta_{el}]^T$. The subscripts '*sh*' and '*el*' represent the shoulder and elbow variables, respectively. Thus, the dynamics of the monkey's arm in horizontal space is denoted by

$$\mathbf{M}(\boldsymbol{\theta})\ddot{\boldsymbol{\theta}} + \mathbf{C}(\boldsymbol{\theta}, \dot{\boldsymbol{\theta}}) = \boldsymbol{\tau}, \tag{1}$$

where $\boldsymbol{\tau} \in R^2$ corresponds to the joint torque vector. $\mathbf{M}(\boldsymbol{\theta}) \in R^{2\times 2}$, $\mathbf{C}(\boldsymbol{\theta}, \dot{\boldsymbol{\theta}}) \in R^2$ are the inertia matrix, the coriolis vector, respectively, and are represented by the link parameters, i.e., mass m_i, length l_i, distance from the joint center of the mass l_{gi}, and moment of inertia I_i (i = 1: upper arm, i = 2: forearm).

Although there are a large number of muscles that act on the arm in the horizontal plane, we have modeled only two degrees of freedom actuated by six muscle groups: elbow flexors (EF), elbow extensors (EX), shoulder flexors (SF), shoulder extensors (SX), biarticulate flexors (BF), and biarticulate extensors (BX) (Fig.1c). The joint torque is a function of its moment arms $\mathbf{A} \in R^{2\times 6}$ and the muscle tension $\mathbf{T} \in R^6$, and it is given by $\boldsymbol{\tau} = \mathbf{A} \cdot \mathbf{T}$. The moment arm is defined as the perpendicular distance from the muscle's line of action to the joint's center of rotation, given by

$$\mathbf{A} = \begin{bmatrix} \alpha_{11} & -\alpha_{12} & 0 & 0 & \alpha_{15} & -\alpha_{16} \\ 0 & 0 & \alpha_{23} & -\alpha_{24} & \alpha_{25} & -\alpha_{26} \end{bmatrix}.$$

Here, we used the Kelvin-Voigt model, consisting of an elastic element for static isometric contraction. The jth muscle tension T_j (j = 1, 2, …, 6) is determined from the muscle activation a_j and muscle length $L_j(\boldsymbol{\theta})$, and muscle-contraction velocity $V_j(\dot{\boldsymbol{\theta}}) = -dL_j(\boldsymbol{\theta})/dt$, according to the formula;

$$\begin{cases} T_j^{cmd} = K_j(a_j) \cdot \left[L_j(\boldsymbol{\theta}) - L_j^{rest}(a_j) \right]_+, & [\cdot]_+ := \max\{\cdot, 0\}, \\ T_j = T_j^{cmd} - B_j(a_j) \cdot V_j(\dot{\boldsymbol{\theta}}) \end{cases} \tag{2}$$

where $K_j(a_j)$, $B_j(a_j)$, and $L_j^{rest}(a_j)$ are the muscle elasticity, viscosity, and resting length, respectively. T_j^{cmd} is the active contraction force that must be generated as a positive value, similar to actual muscles, to generate the commanded torque with the moment arms. The values of muscle parameter in equation (2) are determined from the muscle activation as

$$K_j(a_j) = k^0 + k^1 a_j, \quad B_j(a_j) = b^0 + b^1 a_j, \quad L_j^{rest}(a_j) = L_j^{rest0} - L^{rest1} a_j, \tag{3}$$

where k^0, b^0 and L_j^{rest0} are the intrinsic elasticity, viscosity, and resting length of the *j*th muscle, respectively, and k^1, b^1 and L^{rest1} represent the variation in elasticity, viscosity, and resting length depending on the muscle activation, respectively. L_j^{rest0} was set to the muscle length at an optimal joint angle that allowed the muscle to generate maximal force. Note that, since constant components of the muscle length do not affect the arm dynamics, the muscle length vector $\mathbf{L}(\boldsymbol{\theta}) \in R^6$ could be denoted in a simplistic form by $\mathbf{L}(\boldsymbol{\theta}) \approx -\mathbf{A}^T\boldsymbol{\theta}$.

The muscle activation a_j is not equal to the instantaneous neural input u_j, but is generated by passing u_j thorough a filter that describes the calcium dynamics modeled with a first-order non-linear filter (Fig.1d) as

$$\dot{a}_j = \frac{(1+\sigma_u\varepsilon)u_j - a_j}{t(u_j, a_j)}, \text{ with } t(u_j, a_j) = \begin{cases} t_{deact} + u_j(t_{act} - t_{deact}) & u_j > a_j \\ t_{deact} & otherwise \end{cases}.$$

The input-dependent activation dynamics are faster than the constant deactivation dynamics. Thus, they were set as t_{act} = 40 [ms], t_{deacct} = 50 [ms].

The parameters required for the model are provided in Table 1-3.

2.2 Approximately Optimal Feedback Control

We transformed the 2-joint 6-muscle model into a state-space model. The control object was denoted by the state variable $\mathbf{x} = \begin{bmatrix} \boldsymbol{\theta}^T & \dot{\boldsymbol{\theta}}^T & \boldsymbol{\tau}_{cmd}^T & \mathbf{a}^T \end{bmatrix}^T$, where $\mathbf{a} \in R^6$ is the muscle activations, and $\boldsymbol{\tau}_{cmd} \in R^2$ is commanded torques which are removed the muscle viscosity component from the actual torques [11]. Using non-linear functions $F(\mathbf{x})$ and $G(\mathbf{x})$, the dynamics of the 2-joint 6-muscle arm model at time step t could be written into a state-space equation described as $\mathbf{x}_{t+1} = F(\mathbf{x}_t) + G(\mathbf{x}_t)\cdot(\mathbf{I} + \boldsymbol{\sigma}_\mathbf{u}\boldsymbol{\varepsilon}_t)\mathbf{u}_t$. Note that the non-linear functions $F(\mathbf{x})$ and $G(\mathbf{x})$ are defined just for a descriptive purpose to represent the dynamics in an affine form. In practice, they were given as locally linearized forms around each state at time t to obtain an approximately OFC law. Neural input $\mathbf{u}_t$ is disturbed by a signal-dependent, multiplicative noise that exists in the neural system [12]. The signal-dependent noise is given by $\boldsymbol{\varepsilon}_t$, a zero-mean Gaussian white noise with unity covariance ($\boldsymbol{\varepsilon}_t \in R^2$ is a vector). The magnitude of the signal-dependent noise was set by the scaling parameter $\boldsymbol{\sigma}_\mathbf{u}$ ($\boldsymbol{\sigma}_\mathbf{u}$ = 0.2 in this study).

Table 1. Link parameters

		l_i [m]	l_{gi} [m]	m_i [kg]	I_i [kg m^2]
Upper arm	(i = 1)	0.15	0.075	0.5	3.8×10^{-3}
Forearm	(i = 2)	0.21	0.12	0.5	9.1×10^{-3}

Table 2. Moment arms and optimal joint angles

Muscle	Moment arm α_{ij} [cm]		Optimal joint angle [deg]	
	$i = 1$	$i = 2$	$i = 1$	$i = 2$
$j = 1$	2.6	-	45	-
$j = 2$	1.3	-	15	-
$j = 3$	-	1.2	-	90
$j = 4$	-	1.7	-	110
$j = 5$	0.7	1.6	45	100
$j = 6$	2.5	1.1	15	100

Table 3. Muscle parameters

L^{rest1} [m]	k^0 [N m^{-1}]	k^1 [N m^{-1}]	b^0 [(N·s) m^{-1}]	b^1 [(N·s) m^{-1}]
0.02	50	30,000	2.5	300

The approximately OFC law for ILQG is given by $\mathbf{u}_t = \bar{\mathbf{u}}_t + \mathbf{L}_t(\mathbf{x}_t - \bar{\mathbf{x}}_t)$, where $\bar{\mathbf{u}}_t$ is an open-loop control component, $\mathbf{L}_t$ is the feedback control gain, and $\bar{\mathbf{x}}_t$ is a nominal trajectory (Fig.1e). The parameters $\bar{\mathbf{u}}_t$, $\mathbf{L}_t$, and $\bar{\mathbf{x}}_t$ were computed iteratively using the Levenberg-Marquardt algorithm to optimize the following cost function;

$$J = \min_{\mathbf{u}(\cdot)} \Big[w_p \left\| \mathbf{p}(\boldsymbol{\theta}(T_f)) - \mathbf{p}^* \right\|^2 + w_v \left\| \dot{\mathbf{p}}(\boldsymbol{\theta}(T_f), \dot{\boldsymbol{\theta}}(T_f)) \right\|^2 + w_f \left\| \mathbf{F}_{cmd}(\boldsymbol{\theta}(T_f), \boldsymbol{\tau}_{cmd}(T_f)) \right\|^2 + \frac{1}{T_f} \int_0^{T_f} \left\| \mathbf{u} \right\|^2 dt \Big], \tag{4}$$

where $\mathbf{p}(\boldsymbol{\theta}(T_f))$, $\mathbf{F}_{cmd}(\boldsymbol{\theta}(T_f), \boldsymbol{\tau}_{cmd}(T_f))$ are the end-point position and commanded force which corresponds to the commanded torque, in Cartesian space at a terminal time T_f = 400 [ms]. They are given by the forward kinematics. Additionally, $\mathbf{p}^*$ is a target position in Cartesian space, and w_p, w_v, w_f are cost weights of the position, velocity, and force accuracies at the terminal state, respectively. On the right-hand side of equation (4), the first, second and third terms evaluate the end-point accuracy; the fourth term, which is the sum of the squares of the neural inputs during the movement, evaluates the effort cost.

2.3 Center-Out Reaching Movement

We examined a center-out reaching movement task in this study. The position of the movement start was set to a position 23 cm in front of the shoulder (Fig.1a), and 16 targets were aligned as an 8-cm radial circle around the start position (Fig.1b).

The simulations were carried out to make three cases of requirement of the movement manipulating the terminal cost weights (Table 4). In Case 1, the terminal cost weights were zero except the positional cost. This task corresponded a shooting

Table 4. Cost weight values

Cost weight		Case 1	Case 2	Case 3	Case 4
w_p	(Position)	1.0×10^3	1.0×10^3	1.0×10^3	1.0×10^4
w_v	(Velocity)	0	1.0×10^2	0	5.0×10^2
w_f	(Force)	0	0	5.0	1.0×10

task has the end-point passed the target. In Case 2, the terminal cost weight of the end-point force was zero. It required movements under kinematic constraints. In Case 3 required achieving a movement under kinetic constraints. The task ordered to regulate the end-point force to zero at the movement end. In other words, it was required to maintain the final position after the task.

An initial state of muscle activation levels was set to maintain the initial posture, (i.e., [x, y] = [0, 0]), as the joint torque was equal to zero. The simulations used simple Euler integration with 10 ms time step.

3 Results

The hand trajectories were varied slightly curved or nearly straight lines in accordance with the direction excepting Case 3 in which there were some trajectories changed the movement directions suddenly (Fig. 2c). In Case 1, the tangential velocities did not converge to zero at the movement end, and the joint torques were weakly generated at the movement onset. In Case 2, the velocities were to be zero. However, they were sometimes shaped trapezoidal form, and the torques were generated the opposite direction of the movements in order to break the speed. In Case 3, the velocities sometimes burst at the movement end, and the torques were drastically increased and converged to zero at the movement end. In Case 4, the velocities were closed to zero in gradual curves, and showed clear bell-shaped profiles. In addition, the negative and positive torques were changed alternatively, and converged to zero at the movement end.

Moreover, the muscle activities were also varied according to the cases. In Case 1, agonist muscles were activated once just after the movement start. In Case 2, agonist and antagonist muscles were activated alternatively at just after the movement start and the movement end, respectively. In Case 3, the muscles were activated once, however, the timing was divided into two patterns, i.e., after the movement onset or before the movement end. In Case 4, the muscles were activated once or twice. Especially to the SF and BX muscles, when they took a role as an agonist muscle, they were activated twice at the movement start and end. On the other hand, there were single activations at the middle time of the movement when they would be an antagonist muscle.

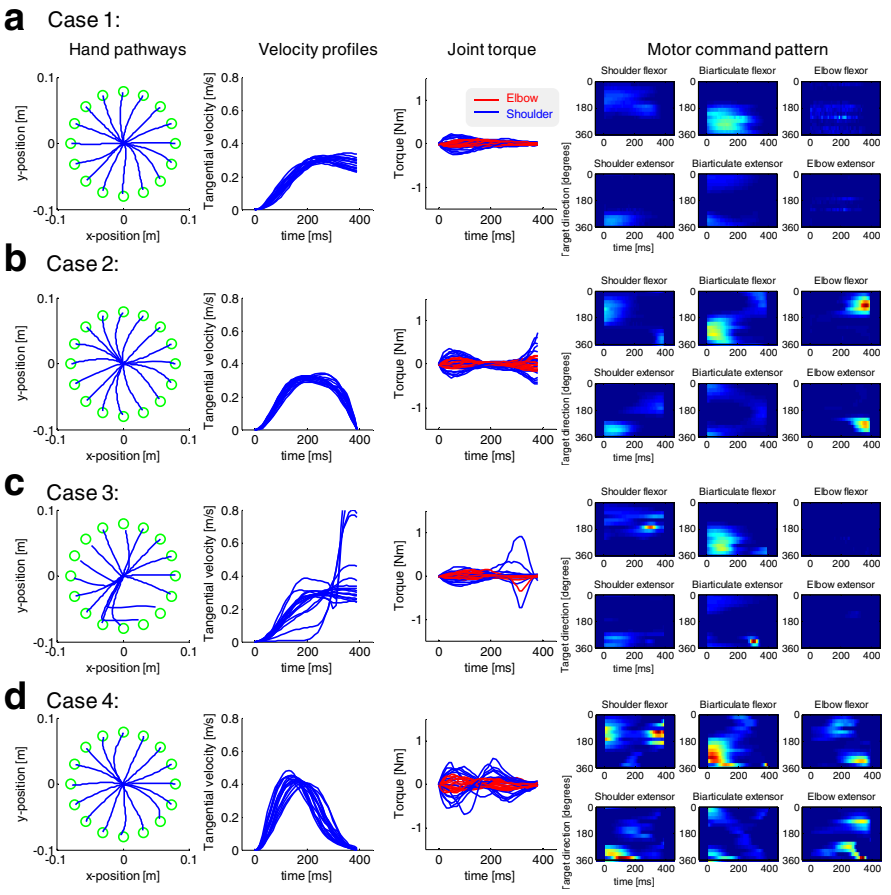

Fig. 2. Simulation results. Each row respectively shows hand pathways, velocity profiles, joint torque profiles, and motor command patterns from the left to right. In the rightmost row, the motor command patterns plotted as a function of time and target direction. Light color indicates high value and dark color indicates low value. The values are normalized by the highest activation level in each muscle across all cases. (a)-(d) respectively represent the Case 1–4.

4 Conclusion

We carried out numerical simulations of biological arm movement using an approximately OFC approach. Additionally, we adapted four types of cost structures in order to examine influences to motor behavior, i.e., kinematic trajectory and muscle activity. As a result, the positional cost made first agonist muscle activation to induce the movement. The velocity cost corresponded to the antagonist muscle activation to stop the movement. There were single-peaked pattern of motor command in the case of the cost function without the force term, and joint torques at terminal time was not converged to zero (Fig. 2). In contrast, a cost function with the

position and force terms was not sufficient to make a bell-shaped velocity curve. However, a cost structure including the position, velocity and force terms could generate diphasic motor command patterns, and the velocity and torque converged to zero at the terminal state similar to experimental measurements [2]. In this cost form, the force term induced the second agonist muscle activation to suppress an opposite torque generated by the antagonist muscle which was activated to reduce the movement speed. Furthermore, the muscles were activated selectively in accordance with the movement directions similar to previous studies. This result indicates that the OFC could coordinate muscles adequately according to the movement direction.

In conclusion, we suggest that the CNS may control the body according to an optimal control mechanism adapting a cost function regulating the force as well as the spatial accuracy and efficiency in the absence of any force interaction.

References

1. Darainy, M., Ostry, D.J.: Muscle cocontraction following dynamics learning. Exp. Brain Res. 190, 153–163 (2008)
2. Hallett, M., Shahani, B.T., Young, R.R.: EMG analysis of stereotyped voluntary movements in man. J. Neurol. Neurosurg. Psychiatry. 38, 1154–1162 (1975)
3. Ueyama, Y., Miyashita, E.: Devising a Robotic Arm Manipulandum for Normal and Altered Reaching Movements to Investigate Brain Mechanisms of Motor Control. Instrum. Sci. Technol. 41, 251–273 (2013)
4. Ueyama, Y., Miyashita, E.: Signal-Dependent Noise Induces Muscle Co-Contraction to Achieve Required Movement Accuracy: A Simulation Study with an Optimal Control. Curr. Bioinform. 8, 16–24 (2013)
5. Mitrovic, D., Klanke, S., Osu, R., Kawato, M., Vijayakumar, S.: A Computational Model of Limb Impedance Control Based on Principles of Internal Model Uncertainty. PLoS One 5, e13601 (2010)
6. Osu, R., Kamimura, N., Iwasaki, H., Nakano, E., Harris, C.M., Wada, Y., Kawato, M.: Optimal impedance control for task achievement in the presence of signal-dependent noise. J. Neurophysiol. 92, 1199–1215 (2004)
7. Todorov, E., Jordan, M.I.: Optimal feedback control as a theory of motor coordination. Nat. Neurosci. 5, 1226–1235 (2002)
8. Ueyama, Y., Miyashita, E.: Optimal Feedback Control for Predicting Dynamic Stiffness during Arm Movement. IEEE Trans. Ind. Electron. 61 (in press, 2014)
9. Pruszynski, J.A., Kurtzer, I., Nashed, J.Y., Omrani, M., Brouwer, B., Scott, S.H.: Primary motor cortex underlies multi-joint integration for fast feedback control. Nature 478, 387–390 (2011)
10. Li, W., Todorov, E.: Iterative linearization methods for approximately optimal control and estimation of non-linear stochastic system. Int. J. Contr. 80, 1439–1453 (2007)
11. Nakano, E., Imamizu, H., Osu, R., Uno, Y., Gomi, H., Yoshioka, T., Kawato, M.: Quantitative examinations of internal representations for arm trajectory planning: minimum commanded torque change model. J. Neurophysiol. 81, 2140–2155 (1999)
12. Harris, C.M., Wolpert, D.M.: Signal-dependent noise determines motor planning. Nature 394, 780–784 (1998)

Outdoor Self-Localization of a Mobile Robot Using Slow Feature Analysis

Benjamin Metka[1], Mathias Franzius[2], and Ute Bauer-Wersing[1]

[1] University of Applied Sciences Frankfurt,
Nibelungenplatz 1, 60318 Frankfurt am Main, Germany
{bmetka,ubauer}@fb2.fh-frankfurt.de
[2] Honda Research Institute Europe GmbH,
Carl-Legien-Straße 30, 63073 Offenbach, Germany
Mathias.Franzius@honda-ri.de

Abstract. We apply *slow feature analysis* (SFA) to the problem of self-localization with a mobile robot. A similar unsupervised hierarchical model has earlier been shown to extract a virtual rat's position as slowly varying features by directly processing the raw, high dimensional views captured during a training run. The learned representations encode the robot's position, are orientation invariant and similar to cells in a rodent's hippocampus.

Here, we apply the model to virtual reality data and, for the first time, to data captured by a mobile outdoor robot. We extend the model by using an omnidirectional mirror, which allows to change the perceived image statistics for improved orientation invariance. The resulting representations are used for the notoriously difficult task of outdoor localization with mean absolute localization errors below 6%.

Keywords: Self-Localization, SFA, Mobile Robot, Biomorphic System, Omnidirectional Vision, Outdoor Environment.

1 Introduction

Self-localization is a crucial ability for animals. In rats, hippocampal place cells fire when the animal is in a certain location and these cells are strongly driven by visual input [13]. How does the brain extract position information from the raw visual data it receives from the retina? While the sensory signals of single receptors may change very rapidly, e.g., even by slight eye movement, the brain's high level representations of the environment (where am I, what objects do I see?) typically change on a much lower timescale. This observation has lead to the concept of slowness learning ([1–4]).

It has been shown earlier that slowly varying features extracted from the visual input of a virtual rat can model place cells and head-direction cells [5, 10]. Recordings from rats' place cells in open field experiments typically show that cells encode the animal's own position, invariant to head direction. Theoretical analysis of the biomorphic model in [10] has shown that in slowness learning,

M. Lee et al. (Eds.): ICONIP 2013, Part I, LNCS 8226, pp. 249–256, 2013.
© Springer-Verlag Berlin Heidelberg 2013

the resulting representation strongly depends on the movement statistics of the animal. To achieve position encoding with invariance to head direction, for example, a relatively large amount of head rotation around the yaw axis compared to translational movement is required during mapping of the environment.

In this pilot study, we extend the results from [10] by applying the model to a mobile robot in an outdoor environment for the first time. Furthermore, we extend the system by using an uncalibrated omnidirectional mirror[1], which allows to easily add simulated rotation of the camera system. Thus the system finds orientation-invariant representations of its own position without having to rotate the camera or the robot much[2]. In the next section, we briefly describe the model as introduced in [10], and explain our extensions to the model.

2 Model for Learning Self-Localization

Slow Feature Analysis. SFA solves the following objective [3]: given a multi-dimensional input signal $\boldsymbol{x}(t)$, find instantaneous scalar input-output functions $g_j(\boldsymbol{x})$ such that the output signals $y_j(t) := g_j(\boldsymbol{x}(t))$ minimize $\Delta(y_j) := \langle \dot{y}_j^2 \rangle_t$ under the constraints $\langle y_j \rangle_t = 0$ (zero mean), $\langle y_j^2 \rangle_t = 1$ (unit variance), $\forall i < j : \langle y_i y_j \rangle_t = 0$ (decorrelation and order) with $\langle \cdot \rangle_t$ and $\dot{y}$ indicating temporal averaging and the derivative of y, respectively.

The Δ-value is a measure of the temporal slowness of the signal $y_j(t)$. It is given by the mean square of the signal's temporal derivative, so small Δ-values indicate slowly varying signals. The constraints avoid the trivial constant solution and ensure that different functions g code for different aspects of the input. We use the MDP [8] implementation of SFA, which is based on solving a generalized eigenvalue problem.

Orientation Invariance. The goal for our self-localizing robot is to extract the robot's position on the x- and z-axis as slowly varying features and become invariant to orientation. As stated above, learned slow features strongly depend on the movement pattern of the mobile robot during training. In order to achieve orientation invariance, the orientation of the robot has to change on a faster timescale than its position during training. A constantly rotating robot with a fixed camera is inconvenient to drive, and a robot with a rotating camera is undesirable for mechanical stability and simplicity. As an alternative, we simulate additional robot rotation, which is illustrated in Fig. 1.

Network Architecture and Training. As input image dimensionality is too high to learn slow features in a single step, we employ a hierarchical converging network. The network consists of several convergent layers, each consisting of multiple identical nodes arranged on a regular grid. The numbers of nodes and layers are depicted in Fig. 2. Each node performs a sequence of steps: linear SFA for dimensionality reduction, quadratic expansion of the reduced signals, and another SFA step for slow feature extraction. The nodes in the lowest layer

[1] The omnidirectional mirror we used is actually a chrome-colored plastic egg warmer.
[2] Note that also for 360° field of view, orientation invariance is nontrivial.

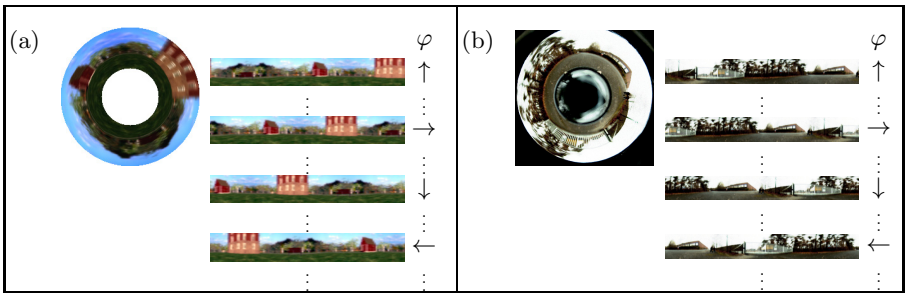

Fig. 1. Simulated rotation for (a) simulator and (b) real world experiments. The circular image of the surrounding is transformed to a panoramic view with periodic boundaries. Rotation is simulated for every view from one location by sliding a window over the panoramic image with increments of 5 pixels. Thus the variable φ denotes the relative orientation w.r.t. the robot's global orientation. Arrows indicate a relative orientation of 0°, 90°, 180° and 270°.

process patches of 10x10 RGB image pixels and are positioned every five pixels. In the lower layers the number of nodes and their dimensionality depends on the concrete setting, but dimensionality is chosen to be a maximum of 300 for numerical stability. The highest layer contains a single node, whose first (i.e., slowest) 8 outputs $y_j(t)$ we use for all experiments and which we call SFA-output units. The layers are trained subsequently with all training images. Instead of training each node individually, a single node per layer is trained with stimuli from all node locations in its layer and replicated throughout the layer after training. This technique is similar to weight sharing in Neural Networks[3].

Analysis of Learned Representations. How well does a learned output encode position, how much orientation dependency does it have? According to [10], the sensitivity of a SFA-output function $f_j, j = 1...8$ to the spatial position $\boldsymbol{r} = (x, z)$ is characterized by its mean positional variance $\eta_{\boldsymbol{r}}$ over all orientations φ: $\eta_{\boldsymbol{r}} = \langle \mathrm{var}_{\boldsymbol{r}}(f(\boldsymbol{r}, \varphi)) \rangle_{\varphi}$. Similarly, the sensitivity to the orientation φ is characterized by its mean orientation variance η_{φ} over all positions $\boldsymbol{r}$: $\eta_{\varphi} = \langle \mathrm{var}_{\varphi}(f(\boldsymbol{r}, \varphi)) \rangle_{\boldsymbol{r}}$. In the ideal case $\eta_{\boldsymbol{r}} = 1$ and $\eta_{\varphi} = 0$, if a function only codes for the robot's position on the x- and z-axis and is completely orientation invariant. The spatial information encoded by an output will be visualized by two dimensional *spatial firing maps* (see Fig. 2c, 3a, 5a). They illustrate the unit's output value color-coded for every position $\boldsymbol{r} = (x, z)$ for a fixed orientation, which is indicated by an arrow. A unit which codes for the position on a certain axis produces a map that shows a color gradient along this axis. If the SFA-units are perfectly orientation invariant these maps should look the same regardless of the specific orientation.

[3] Note that this design is chosen only for its computational efficiency and that network performance *increases* for individually learned nodes.

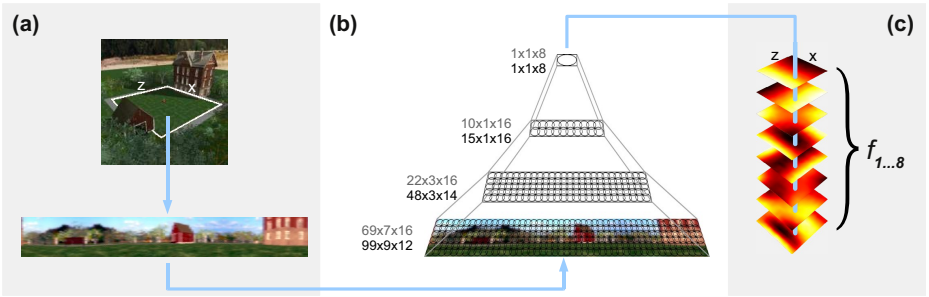

Fig. 2. Model architecture. (a) The robot's view associated with a certain position $r = (x, z)$ is steadily captured and transformed to a panoramic view. (b) The view is processed by the four layer network. Numbers of nodes in each layer are given for the simulator (gray) and real world (black) experiments, respectively. Each node performs linear SFA for dimensionality reduction followed by SFA on the expanded outputs for slow feature extraction. (c) Eight slowest SFA-outputs $f_{1...8}$ over all positions r. The color coded outputs, so-called *spatial firing maps*, ideally show characteristic gradients along the coordinate axes and look the same independent of the specific orientation. Thus SFA outputs $f_{1...8}$ at position r are the orientation invariant encoding of location.

3 Experiments

The procedure is to record the views and corresponding metric coordinates of the robot from every position during training- and test-runs. After the training step, we need to quantify and visualize the encoded spatial information of the SFA-outputs in a metric way. Therefore we compute a regression function from the SFA-outputs to the metric ground truth positions and subsequently apply it to SFA-outputs.

3.1 Simulated Environment

The model was first applied in a virtual reality simulator to validate the extended model under fully controllable settings. The virtual robot was placed on discrete positions forming a regular 30x30 grid. We recorded 624 omnidirectional RGB images for the training set and 196 for test set and transformed them to panoramic views with a resolution of 350x40 pixel (Fig. 1a).

Results. All resulting SFA-units have a high spatial structure and are almost completely orientation invariant as their outputs for the training views have a mean positional variance $\eta_r \approx 1$ and the mean orientation variance η_φ ranges from 0.00 (f_1) to 0.17 (f_8). This is also reflected by the *spatial firing maps* in Fig. 3a which show an obvious encoding for the position on the coordinate axes and look nearly identical under different orientations.

Since the views of the training- and test-run are identical for the same location we only use the test data for the regression analysis. Random 50/50 splits are used to train the regression and evaluate the coordinate prediction. Repeating

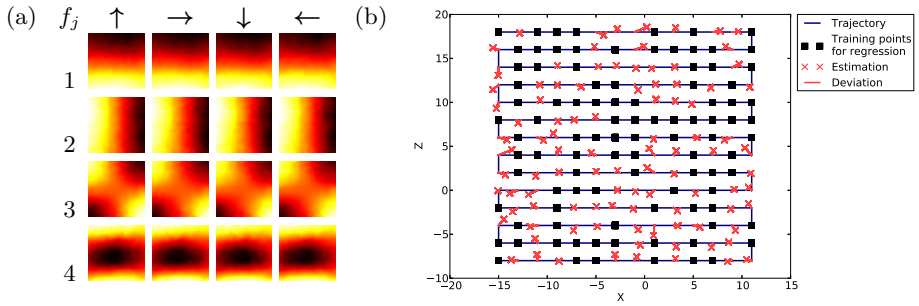

Fig. 3. Simulated Environment. (a) *Spatial firing maps* of the four slowest SFA-outputs $f_{1\ldots4}$ for relative orientations $0°, 90°, 180°$ and $270°$. Obviously the first and second outputs are spatially orthogonal, coding for z- and x-position, respectively. Output values are monotonically increasing from north to south and east to west. The third unit is a mixture of the first two units and unit four is a higher oscillating representation of the first unit. (b) Ground truth and estimated coordinates computed by the regression. Estimations are averaged over the windows of the simulated rotation for one location.

it 100 times results in an overall mean absolute error (MAE) for the x- and z-coordinate estimation of 1.83% and 1.68%, relative to the coordinate range of the test run (Fig. 3b). Thus the experiment has shown the capability of our extended model to replicate results from [10].

3.2 Real World Environment

The experiment was transferred to an outdoor scenario to examine how the model copes with real-world conditions like a non-static environment, changing light conditions and noisy sensor readings. We used a suitable mobile robot (*Pioneer 3AT*) equipped on top with an omnidirectional vision system (Fig. 4a). Outdoor experiments were done within an area of approximately 5x7 meters on asphalted ground. Test data was recorded directly after the training data. The training and test sets consist of 5900 and 2800 RGB panoramic images with a resolution of 600x60 pixel. During training and test phase the robot was moved with a wireless joystick at a maximum velocity of 40 cm/s in a grid like trajectory so that the translations along the x- and z-axis were fairly equal distributed with respect to the traveled distance (Fig. 4b).

Unlike in the simulator framework the true position of the robot has to be acquired independently through an external monitoring system. For indoor applications several approaches based on sensors mounted on the room ceiling have been proposed (e.g. [12]), but said approaches turned out to be unfeasible for outdoor applications. To keep ground truth acquisition flexible and robust we mounted a 30cm cube on the robot with optical, binary markers attached to its facets (Fig. 4a). A stationary camera was installed to capture images of the whole area throughout the training- and test-runs. 3d-pose was computed, based on

(a) 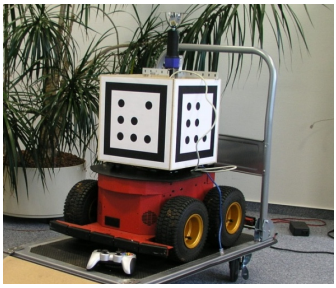

(b) 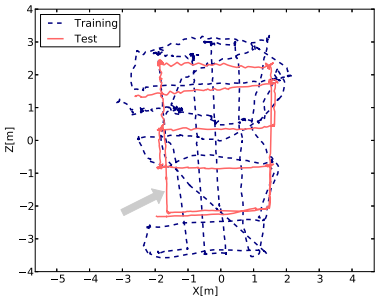

Fig. 4. (a) Pioneer 3AT equipped with omnidirectional vision system and marker-box. (b) Captured trajectories of the training- and test-run on an area of approximatly 5x7 meters. The arrow indicates a region in the south-west which has been passed during the test-run but was not part of the training trajectory.

the features of the detected markers, by solving the *Perspective-n-Point problem*. Implementation is based on the *OpenCV*-library [11]. In an experimental setup with a HD-webcam the method provided a detection up to a distance of nine meters with a MAE of about 3cm (0.3%), as verified by laser distance meter.

Results. All SFA-units of the network have a mean positional variance $\eta_r \approx 1$ and their mean orientation variance η_φ ranges from 0.00 (f_1) to 0.05 (f_8) and thus are almost only coding for spatial position while being orientation invariant. Note that the lower magnitude of η_φ, compared to the simulation results, is caused by the faster changing orientation due to the robot's additional real rotation.

As expected the *spatial firing maps* in Fig. 5a do not encode position as clearly as in the simulation due to the non-static environment and the inhomogeneous distribution of position and velocity. *Spatial firing maps* of the first unit encode the position on the z-axis, while x-position is less obvious encoded in the maps of units three and four.

In contrast to the simulation we compute the regression from the SFA-outputs to the metric ground truth positions for the training data and apply it to SFA outputs on the test set. The resulting MAE is 0.23m (5.3%) for the x-coordinate and 0.175m (3.7%) for the z-coordinate and the standard deviation amounts to 0.20 and 0.13. Higher errors can be noticed in a small area in the west that was not passed in the training-run (see Fig. 4b) and an area in the south west, which could also be noticed in the *spatial firing map* with the highest SFA-outputs. Another prominent area with higher errors is located in the north west, where the maps of units two and three show discontinuities. Minor deviations can be observed at turning points in the trajectory, where vibrations of the vision system caused distortions in the unwarped panoramic images. Even though the coding for the x-position is less obvious compared to the simulation, it is apparently sufficient for self-localization.

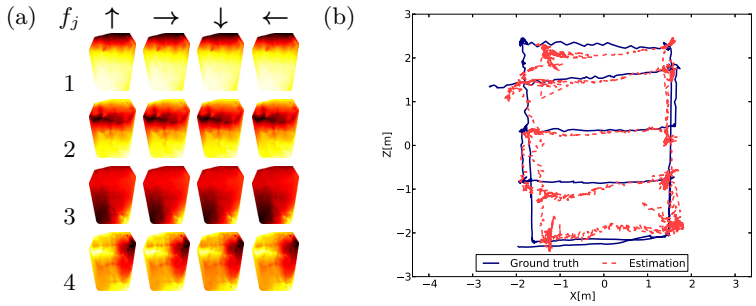

Fig. 5. Real world environment. (a) *Spatial firing maps* of the four slowest SFA-outputs $f_{1...4}$ for relative orientations $0°, 90°, 180°$ and $270°$. First SFA-output encodes the position on the z-axis with low values in the north and high values in the south. Notice the area in the south-west with highest values. This region has been passed multiple times, so that environmental changes led to variations. Second unit is a higher oscillating representation of the first one, which indicates that other varying components of the configuration space changed at least twice as fast as the z-position. Units three and four suggest weak encoding of the x- and z-position. (b) Ground truth and estimated position for the test run. Estimations are averaged over the simulated rotation for one location.

4 Summary and Conclusion

We systematically transferred the biologically motivated concept of SFA step by step into a self-localization task of a mobile robot and successfully showed its application in an outdoor environment. Despite its simplicity the system demonstrates reasonable performance. Explorations in the simulated environment have shown that SFA combined with simulated rotation of an omnidirectional view allows self-localization with errors of under 2% relative to the coordinate range. Experiments in the outdoor environment showed an average self-localization accuracy of 0.23m (5.3%) for the x-coordinate and 0.175m (3.7%) for the z-coordinate, which is significantly smaller than the robot's own size (approx. 50x50cm).

The problem of visual self-localization in unknown environments has been investigated in great detail as an inherent part of the Simultaneous Localization and Mapping (SLAM) algorithms (e.g., [9]). Visual SLAM approaches typically require highly calibrated optics and extract local image descriptors, like SIFT or SURF, at regular time intervals to characterize a scene. Typical errors given in the SLAM literature are about 1% to 5% with respect to travelled route. Although localization accuracies are hard to compare in this context, relative errors of our approach are within the same order of magnitude. Our core system, as described in Section 2, however, focuses on simplicity and biological plausibility as it is derived from a model of rat navigation. It repeats the same unsupervised learning in a converging hierarchy which yields location-specific and orientation-invariant slow feature

representations by itself and is based on cheap uncalibrated hardware (but note [7]). It is important to emphasize that unlike in SLAM approaches our aim is not to simultaneously map and locate. Instead the approach, presented here, learns a map of orientation invariant slow feature representations. These are projected to metric space using a supervised regression step. Please note that an autonomous robot does not necessarily need metric coordinates to navigate, but instead it can follow gradients directly in slow feature space.

We have proven the concept of SFA self-localization in real world environments, but nevertheless the experimental results suggest issues that need further investigation: (i) Achieving the orientation invariant representation based on smaller window sizes of the simulated rotation is desirable since it speeds up computation and extends the capabilities of the model to identify objects that were not present during the training phase. (ii) The apparently weak representation of the x-position in the outdoor environment may be due to global changes in the environment, which vary on an equal time-scale as the robot's translation or are not decorrelated (orthonormal) to it. In this respect, choosing another feature representations than the raw pixel values could help to exclude known, changing variables from the configuration space and furthermore improve model performance, if applied to data sets captured at different daytimes or even seasons for the same training area.

References

1. Földiak, P.: Learning invariance from transformation sequences. Neural Comput. 3, 194–200 (1991)
2. Stone, J.V., Bray, A.: A learning rule for extracting spatio-temporal invariances. Network-Comp. Neural 6, 429–436 (1995)
3. Wiskott, L., Sejnowski, T.: Slow feature analysis: Unsupervised learning of invariances. Neural Comput. 14(4), 715–770 (2002)
4. Körding, K., Kayser, C., Einhäuser, W., König, P.: How are complex cell properties adapted to the statistics of natural scenes? J. Neurophysiol. 91(1), 206–212 (2004)
5. Wyss, R., König, P., Verschure, P.: A model of the ventral visual system based on temporal stability and local memory. PLoS Biol. 4, 1–8 (2006)
6. Berkes, P., Wiskott, L.: Slow feature analysis yields a rich repertoire of complex cell properties. J. Vision 5(6) (2005)
7. Milford, M., Schulz, R., Prasser, D., Wyeth, G., Wiles, J.: Learning spatial concepts from RatSLAM representations. Robot Auton Syst. 55(5), 403–410 (2007)
8. Zito, T., Wilbert, N., Wiskott, L., Berkes, P.: Modular toolkit for data processing (mdp): a python data processing framework. Front Neuroinform 2(8) (2009)
9. Davison, A., Reid, I., Molton, N., Stasse, D.: MonoSLAM: Real-time single camera SLAM. IEEE Trans Pattern Anal. Mach. Int. 29(6), 1052–1067 (2007)
10. Franzius, M., Sprekeler, H., Wiskott, L.: Slowness and sparseness lead to place, head-direction, and spatial-view cells. PLoS Comp. Biol. 3(8) (2007)
11. Bradski, G.: The OpenCV Library. Dr. Dobb's Journal of Software Tools (2000)
12. Smith, A., Balakrishnan, H., Goraczko, M., Priyantha, N.: Tracking Moving Devices with the Cricket Location System. MobiSys (2004)
13. Jeffery, K., O'Keefe, J.: Learned interaction of visual and idiothetic cues in the control of place field orientation. Exp. Brain Res. 127(2), 151–161 (1999)

RBF-Based Neuro-Adaptive Controller for a Knee Joint Rehabilitation Orthosis

Said Talbi, Boubaker Daachi, and Karim Djouani

Laboratoire Images, Signaux et Systèmes Intelligents (LISSI, E. A.3956)
University of Paris-Est Créteil
61 avenue du Général de Gaulle, 94010 Créteil, France
said.talbi.0503@gmail.com

Abstract. In this paper, we address a knee joint orthosis control for rehabilitation purposes. Only the structure of the system's dynamic model is supposed to be known. Inertia of the knee-shank-orthosis system is identified on-line using an adaptive term. In order to approximate all of the other dynamics (viscous and solid frictions, gravity related torque, etc.), we use an RBF Neural Network (RBFNN) with no off-line prior training. Adaptation laws of the neural parameters and the inertia adaptive term are derived from the closed loop system's overall stability study using Lyapunov's theory. The study considers three cases: wearer being completely inactive or applying either a resistive or an assistive torque. Simulation results and conducted analysis show the effectiveness of the proposed approach.

Keywords: RBFNN, neuro-adaptive control, rehabilitation, knee joint orthosis, Lyapunov theory.

1 Introduction

Exoskeletons can be used to assist, restore or enhance the wearer's motor skills. For the exoskeleton to completely meet the wearer's needs, it has to be correctly controlled. When it comes to lower limb exoskeleton control, several works can be found and summarized as follows. In [9], a powered leg orthosis for gait rehabilitation is described. The authors propose controllers which can apply suitable forces on the leg so that it moves on a desired trajectory. In [10], the application of EMG signals for motion control is addressed. In [11], an active ankle-foot orthosis is presented where the impedance of the orthotic joint is modulated throughout the walking cycle to treat drop-foot gait. In [7], a portable active knee rehabilitation orthotic device is designed to train stroke patients to correct knee hyperextension during stance and stiff-legged gait. In [8], the Hybrid Assistive Limb-5 is a bipedal locomotion system that has been developed to be worn by the elderly and the disabled, in order to assist them in their daily tasks.

Generally, it is not possible to establish an accurate dynamic model that takes account of dynamic changes related to the wearer's desired movements. Indeed, the wearer can be completely inactive or apply either an assistive or

M. Lee et al. (Eds.): ICONIP 2013, Part I, LNCS 8226, pp. 257–266, 2013.
© Springer-Verlag Berlin Heidelberg 2013

a resistive torque. In order to take account of these different situations, it is advisable to design adaptive control schemes [4]. Training techniques are widely used to construct adaptive control laws and neural networks are some of the tools that belong to those techniques [1,5,13]. They can have fixed or adaptive parameters. As to fixed parameters neural networks [14], a robustness term is often considered in order to take account of dynamic changes [12]. Whereas in adaptive parameters neural networks, we use adaptation laws that can, for instance, be derived from the system's overall stability study. The advantage of neural networks is the possibility of incorporating some prior knowledge about the system to be controlled. Indeed, the dynamic model structure of robotic systems is generally known [15], which allows us to associate to neural networks, adaptive control approaches that have proven efficient.

RBFNN are universal approximators for unknown dynamics and they have already been used to control non linear systems. Compared to MLPNN that learn globally, RBFNN can have a very faster convergence because they learn locally. Moreover, they are better suited for approximating systems with relatively fewer inputs [2]. Every RBF neuron contains an activation function centered around a point from the input space. For a given input, the hidden neuron output is the height of the activation function at that point. The activation function allows the neuron to react only to a narrow region of the input space: the region around which it is centered. RBFNN can be either static with fixed parameters or dynamic with time varying adaptive parameters [6].

The paper is organized as follows: Section 2 presents the knee-shank-orthosis system modeling, its structure and the dynamics to be approximated by the RBFNN. Section 3 explains the neural approximation principle, the activation functions and the method we have used to determine the centers of the gaussian activation functions. In Sect. 4, we detail the proposed RBFNN controller and the closed loop system's overall stability study. Simulation results with case study are presented in Sect. 5. Finally we conclude with some perspectives.

2 System Modeling

We consider the knee-shank-orthosis system having one degree of freedom (DoF) given in [1]. The dynamic model of the considered system is given by the following differential equation [15]:

$$\tau + \tau_k = J\ddot{q} + \tau_g \cos(q) - A\ sign(\dot{q}) - B\dot{q} \tag{1}$$

This equation (1) can be re-written as follows:

$$\begin{aligned} \tau &= J\ddot{q} + \gamma(q, \dot{q}) - \tau_k \\ \gamma(q, \dot{q}) &= \tau_g \cos(q) + A\ sign(\dot{q}) + B\dot{q} \end{aligned} \tag{2}$$

Where:

- τ : control input (orthosis torque);
- τ_k : knee torque (bounded);
- $J = J_{or} + J_k$: inertia of the system (orthosis (or) + knee (k));
- $\tau_g \cos(q) = (\tau_{g_{or}} + \tau_{g_k}) \cos(q)$: gravitational force;
- $A\ sign(\dot{q}) = (A_{or} + A_k)\ sign(\dot{q})$: solid friction torque;
- $B\dot{q} = (B_{or} + B_k)\dot{q}$: viscous friction torque;
- q : actual position of the knee
- q_d : desired position of the knee;
- $\dot{q}$: actual velocity of the knee;
- $\dot{q}_d$: desired velocity of the knee;
- $\ddot{q}$: actual acceleration of the knee;
- $\ddot{q}_d$: desired acceleration of the knee;

Synthesis of the proposed neuro-adaptive control law considers that only the structure of the dynamic model is known. This means that J and γ are assumed to be unknown. With this formulation, it is possible to take account of other unmodeled dynamics.

3 Neural Approximation

We suppose there exists an optimal neural representation of the function $\gamma(q, \dot{q})$ based on RBFNN having a linear output. There exists then an optimal vector θ containing the weights between the hidden layer and the neural network's output [3]. Therefore, we can write:

$$\gamma(q, \dot{q}) = \theta^T \phi(q, \dot{q}) + \epsilon(q, \dot{q}) \tag{3}$$

$\epsilon(q, \dot{q})$ representing the bounded neural approximation error [3]. As there is no method allowing us to exactly determine the vector θ, we use its approximation that we note $\hat{\theta}$. With this, we obtain:

$$\hat{\gamma}(q, \dot{q}) = \hat{\theta}^T \phi(q, \dot{q}) \tag{4}$$

As we are using gaussian functions in the hidden layer, the function $\phi(q, \dot{q})$ can be written as:

$$\phi(q, \dot{q}) = \begin{pmatrix} e^{-\pi\left(\left(\frac{q-c_1^q}{\sigma_q}\right)^2 + \left(\frac{\dot{q}-c_1^{\dot{q}}}{\sigma_{\dot{q}}}\right)^2\right)} \\ e^{-\pi\left(\left(\frac{q-c_2^q}{\sigma_q}\right)^2 + \left(\frac{\dot{q}-c_2^{\dot{q}}}{\sigma_{\dot{q}}}\right)^2\right)} \\ \vdots \\ e^{-\pi\left(\left(\frac{q-c_n^q}{\sigma_q}\right)^2 + \left(\frac{\dot{q}-c_n^{\dot{q}}}{\sigma_{\dot{q}}}\right)^2\right)} \end{pmatrix} \tag{5}$$

Where n is the number of neurons in the hidden layer. In order to obtain a linear parametrization, parameters σ_q, $\sigma_{\dot{q}}$, ${c_i}^q$ and ${c_i}^{\dot{q}}$ $(i = 1, ..., n)$ have to be set to given values. In our case, the centers are arranged in a grid covering the input space.

Each two successive centers related to the position q are separated by a distance Δ_q, and each two successive centers related to the velocity $\dot{q}$ are separated by a distance $\Delta_{\dot{q}}$. Standard deviations σ are determined by the following equations [16]:

$$\sigma_q = \frac{2}{\Delta_q}\sqrt{\frac{log(2)}{\pi}} \qquad \sigma_{\dot{q}} = \frac{2}{\Delta_{\dot{q}}}\sqrt{\frac{log(2)}{\pi}}$$

4 RBFNN Adaptive Controller and Stability Study

The proposed control law is given as follows :

$$\tau = \hat{J}v + \hat{\gamma}(q, \dot{q}) - Ks \tag{6}$$

Consider the following variables:

$$v = \ddot{q}_d - \lambda\dot{e} \qquad e = q - q_d \qquad \dot{e} = \dot{q} - \dot{q_d} \qquad (K > 0 \qquad \lambda > 0)$$

$$\begin{aligned} s &= \dot{e} + \lambda e \\ \tilde{J} &= \hat{J} - J \\ \tilde{\gamma}(q, \dot{q}) &= \hat{\gamma}(q, \dot{q}) - \gamma(q, \dot{q}) \\ &= \hat{\theta}^T\phi(q, \dot{q}) - \theta^T\phi(q, \dot{q}) - \epsilon(q, \dot{q}) \\ &= \tilde{\theta}^T\phi(q, \dot{q}) - \epsilon(q, \dot{q}) \end{aligned}$$

Using equations (2) and (6), we obtain the following closed loop dynamics:

$$\begin{aligned} \hat{J}v + \gamma(q, \dot{q}) - Ks &= J\ddot{q} + \gamma(q, \dot{q}) - \tau_k \\ \hat{J}v - J\ddot{q} + \hat{\gamma}(q, \dot{q}) - \gamma(q, \dot{q}) + \tau_k - Ks &= 0 \\ Jv - J\ddot{q} + \tilde{J}v + \tilde{\gamma}(q, \dot{q}) + \tau_h - Ks &= 0 \\ -J\dot{s} + \tilde{J}v + \tilde{\gamma}(q, \dot{q}) + \tau_k - Ks &= 0 \\ J\dot{s} &= \tilde{J}v + \tilde{\gamma}(q, \dot{q}) + \tau_k - Ks \\ &= \tilde{J}v + \tilde{\theta}^T\phi(q, \dot{q}) - \epsilon(q, \dot{q}) + \tau_k - Ks \end{aligned}$$

Let's consider the Lyapunov positive definite function:

$$V = \frac{1}{2}Js^2 + \frac{1}{2}\frac{1}{\alpha}\tilde{J}^2 + \frac{1}{2\mu}\tilde{\theta}^T\tilde{\theta} \tag{7}$$

Taking its time derivative yields:

$$\begin{aligned}
\dot{V} &= sJ\dot{s} + \frac{1}{\alpha}\tilde{J}\dot{\tilde{J}} + \frac{1}{\mu}\tilde{\theta}^T\dot{\tilde{\theta}} \\
\dot{V} &= s(\tilde{J}v + \tilde{\theta}^T\phi(q,\dot{q}) - \epsilon(q,\dot{q}) + \tau_k - Ks) + \frac{1}{\alpha}\tilde{J}\dot{\tilde{J}} + \frac{1}{\mu}\tilde{\theta}^T\dot{\tilde{\theta}} \\
&= V_1 + V_2 + V_2 \\
V_1 &= -Ks^2 - s\epsilon(q,\dot{q}) + s\tau_k \\
V_2 &= s\tilde{J}v + \frac{1}{\alpha}\tilde{J}\dot{\tilde{J}} \\
V_3 &= s\tilde{\theta}^T\phi(q,\dot{q}) + \frac{1}{\mu}\tilde{\theta}^T\dot{\tilde{\theta}}
\end{aligned}$$

We choose the following adaptation laws:

$$\dot{\tilde{J}} = \dot{\hat{J}} = -\alpha\ s\ v \tag{8}$$

$$\dot{\tilde{\theta}} = -\mu\ s\ \phi(q,\dot{q}) \tag{9}$$

We obtain:

$$\begin{aligned}
V_2 &= V_3 = 0 \\
\dot{V} &= V_1 = -Ks^2 - s\epsilon(q,\dot{q}) + s\tau_k
\end{aligned}$$

In order to carry on stability analysis, we consider the following two cases:

Case 1. Neural approximation errors and muscular effort are equal to zero

$$\dot{V} = V_1 = -Ks^2 \leq 0$$

Invoking Barbalat's Lemma [19], we can say that s goes to zero because $\dot{V}$ is checked definite negative. Hence considering (8) and (9), $\tilde{\theta}$ and $\tilde{J}$ are bounded. The controller (6) ensures the free moving orthosis is asymptotically stable ($q \to q_d$ and $q \to \dot{q}_d$).

Case 2. Neural approximation errors and muscular effort are different from zero

$$\dot{V} = V_1 = -Ks^2 - s\epsilon(q,\dot{q}) + s\tau_k$$

Using Young's inequalities, we can write:

$$\begin{aligned}
\dot{V} &\leq -Ks^2 + |s|\,(|\epsilon(q,\dot{q})| + |\tau_k|) \\
&\leq -Ks^2 + \frac{(|\epsilon(q,\dot{q})| + |\tau_k|)^2}{2K} + \frac{Ks^2}{2} \\
&\leq -\frac{K}{2}s^2 + \frac{(|\epsilon(q,\dot{q})| + |\tau_k|)^2}{2K}
\end{aligned}$$

For $\dot{V}$ to be negative or zero:

$$\frac{K}{2}s^2 \geq \frac{(|\epsilon(q,\dot{q})| + |\tau_k|)^2}{2K}$$
$$|s| \geq \frac{|\epsilon(q,\dot{q})| + |\tau_k|}{K}$$

In this case, overall stability and convergence is ensured towards a bounded region of radius $\frac{|\epsilon(q,\dot{q})|+|\tau_k|}{K}$ because $\epsilon(q,\dot{q})$ and τ_k are bounded. Every time s tries to get out of this region, $\dot{V}$ becomes negative and the controller draws it immediately back in. Consequently and under the hypothesis that $q, \dot{q}, q_d, \dot{q}_d$ are bounded, the errors e and $\dot{e}$ are bounded and converge to zero when K is large enough.

5 Simulation Results

Our simulations are realized using data identified experimentally in a previous work [1]. The orthosis is worn by a healthy subject of $90kg$ weight and $1.87m$ height. The parameters of both the orthosis and the subject have been identified using the weighted least square method [17], the regression equations of Zatsiorsky [20] and the passive pendulum test [18]. The knee-orthosis system's identified parameters are given in Table 1. The RBFNN contains seven hidden neurons and doesn't need to be trained off-line. Moreover, the output weights don't need to be initialized.

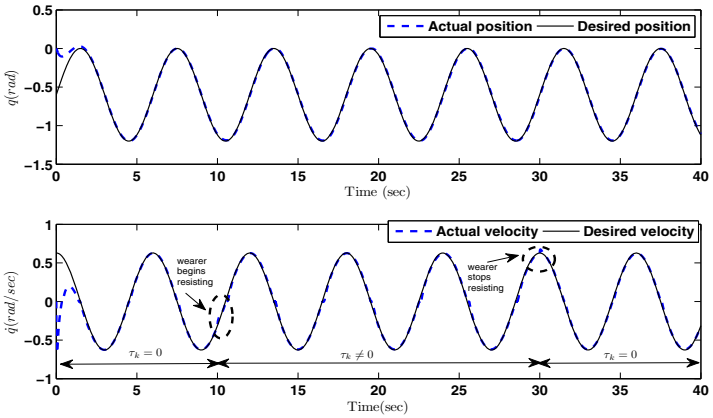

Fig. 1. Trajectory tracking when the wearer applies a resistive effort

The chosen control parameters $\lambda = 2,\ K = 20$ and the adaptation laws parameters $\alpha = 10,\ \mu = 10$ ensure good perfomance as it will be shown in the following tests. Desired position and velocity trajectories should be determined by a rehabilitation expert. The tests are realized using sinusoidal trajectories. For position

Table 1. Knee-shank-orthosis system parameters

Parameter	Symbol	Value
Inertia	J	$0.4Kg \cdot m^2$
Solid friction coefficient	A	$0.6N \cdot m$
Viscous friction coefficient	B	$1N \cdot ms \cdot rad^{-1}$
Gravity torque	τ_g	$5N \cdot m$

and velocity space inputs of respectively $[-1.2,\ 0]\ rad$ and $[-0.6,\ 0.6]\ rad/s$, we put $\Delta_q = 0.2\ rad$ and $\Delta_{\dot{q}} = 0.2\ rad/s$ in order to have seven gaussian centers for both desired inputs (q_d) and $(\dot{q}_d)$.

In a first test, the wearer applies a resistive torque between instants $10sec$ and $30sec$ as it's depicted in Fig. 2. We can see on the same figure that the torque calculated by the proposed controller reacts consequently, becoming larger to compensate the resistive human torque. The global applied torque remains unchanged after two insignificant transient phases at instants $10sec$ and $30sec$.

Trajectory tracking purposes are achieved as it can be seen on Fig. 1. Any neural network needs an adaptation time in order to learn the overall dynamics of the system. In our case, using RBFNN allows for a relatively small training time (less than $2sec$). We can see at instants $10sec$ and $30sec$, slight perturbations due to the resistive human torque. They are soon corrected thanks to the calculated torque.

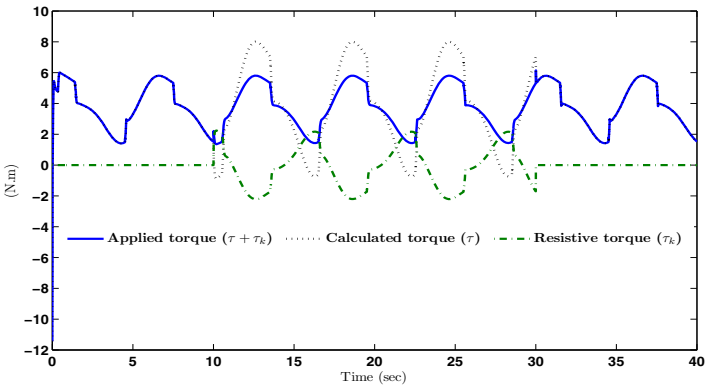

Fig. 2. Applied, calculated and human resistive torques

The second test is similar, the only difference is that this time the wearer applies an assistive torque: a torque that goes along with the calculated one. Figure 4 shows that the moment the human assistive torque is applied, the RBFNN calculated torque becomes smaller for the global applied torque to remain unchanged. This means that we will have the same performances as if there were no human torque applied but with less energy consumption.

Figure 3 shows good trajectory tracking performance with no obvious perturbations. This means that changes of the human torque are well and quickly taken care of, with always a small training period.

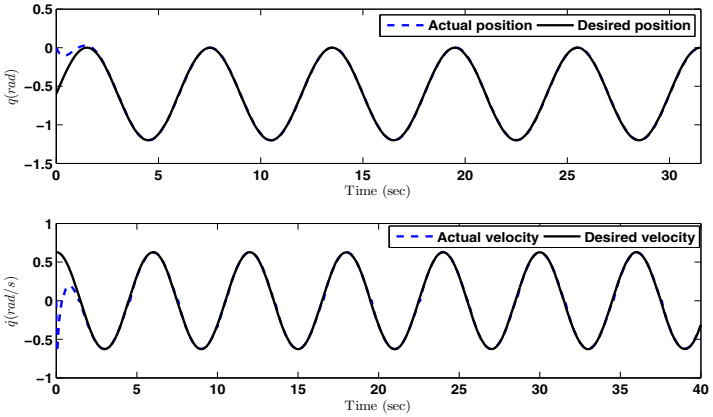

Fig. 3. Trajectory tracking when the wearer applies an assistive effort

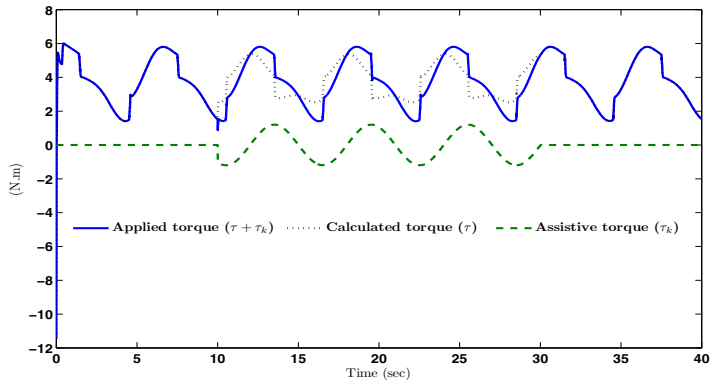

Fig. 4. Applied, calculated and human assistive torques

6 Conclusion

In this paper, we have proposed a control law based on adaptive RBFNN for a knee joint rehabilitation orthosis. No particular prior knowledge has been required except some of what is valid for any robotic system. Lyapunov's approach has been used to analyze the closed loop system's overall stability, and to establish the adaptation laws of the RBFNN weights and the inertia adaptive term. The objective of such an approximation scheme is to guarantee a good trajectory tracking with minimum prior knowledge of the system. Indeed, it is not about

identifying every unknown parameter, but it is about identifying the overall dynamics, which allows achieving trajectory tracking. Different situations have been studied (passive wearer, active wearer). For further works, we are studying an experimental validation protocol on a disabled subject.

References

1. Rifai, H., Mohammed, S., Daachi, B., Amirat, Y.: Adaptive control of a human-driven knee joint orthosis. In: IEEE International Conference on Robotics and Automation, pp. 2486–2491. St. Paul, USA (2012)
2. Memarian, H., Balasundram, S.K.: Comparison between Multi-Layer Perceptron and Radial Basis Function Networks for Sediment Load Estimation in a Tropical Watershed. Journal of Water Resource and Protection 4, 870–876 (2012)
3. Yumei, M., Lijun, L., Dong, N.: A Note on Approximation Problems of Neural Network. International Mathematical Forum 5(41), 2037–2041 (2010)
4. Achili, B., Daachi, B., Amirat, Y., Ali-Cherif, A.: A robust adaptive control of a parallel robot. International Journal of Control 83(10), 2107–2119 (2010)
5. Achili, B., Daachi, B., Ali-Cherif, A., Amirat, Y.: Robust neural adaptive force controller for a C5 parallel robot. In: IEEE International Conference on Advanced Robotics, Munich, Germany, pp. 1–6 (June 2009)
6. Martins, N.A., Bertol, D.W., Lombardi, W.C., De Pieri, E.R., de, E., Neto, B.C.: Neurocontrollers for Trajectory Tracking Problem of a Nonholonomic Mobile Robot. In: Proceedings of the 17th World Congress. The International Federation of Automatic Control, July 6-11. Seoul, Korea (2008)
7. Weinberg, B., Nikitczuk, J., Patel, S., Patritti, B., Mavroidis, C., Bonato, P.: Design, Control and Human Testing of an Active Knee Rehabilitation Orthotic Device. In: IEEE International Conference on Robotics and Automation, Roma, Italy, April 10-14 (2007)
8. Suzuki, K., Mito, G., Kawamoto, H., Hasegawa, Y., Sankai, Y.: Intention-based walking support for paraplegia patients with robot suit HAL. Advanced Robotics 21(12), 1441–1469 (2007)
9. Banala, S.K., Kulpe, A., Agrawal, S.K.: A Powered Leg Orthosis for Gait Rehabilitation of Motor-Impaired Patients. In: IEEE International Conference on Robotics and Automation, Roma, Italy, April 10-14 (2007)
10. Fleischer, C., Wege, A., Kondak, K., Hommel, G.: Application of EMG signals for controlling exoskeleton robots. Biomed Tech (Berl) 51(5-6), 314–319 (2006)
11. Blaya, J.A., Herr, H.: Adaptive Control of a Variable-Impedance Ankle-Foot Orthosis to Assist Drop-Foot Gait. IEEE Transactions on Neural Systems and Rehabilitation Engineering 12(1), 24–31 (2004)
12. Gong, J.Q., Yao, B.: Neural network adaptive robust control of nonlinear systems in semi-strict feedback form. Automatica 37, 1149–1160 (2001)
13. Gong, J.Q., Yao, B.: Neural Network-based Adaptive Robust Control of a Class of Nonlinear Systems in Normal Form. In: Proceedings of the American Control Conference Chicago, Illinois (June 2000)
14. Benallegue, A., Meddah, D.Y., Daachi, B.: Neural network identification and control of a class of non linear systems. In: Proceedings of the 16th IMACS World Congress, Lausanne, Switzerland (2000)
15. Khalil, W., Dombre, E.: Modélisation, identification et commande des robots. Hermes Science Publication, Paris (1999)

16. Meddah, D.Y., Benallegue, A.: A Stable Neuro-Adaptive Controller for Rigid Robot Manipulators. Journal of Intelligent and Robotic Systems 20, 181–193 (1997)
17. Swevers, J., Ganseman, C., Bilgin, D., De-Schutter, J., Van Brussel, H.: Optimal Robot Excitation and Identification. IEEE Transactions on Robotics and Automation 13(5), 730–740 (1997)
18. Stein, R.B., Zehr, E.P., Lebiedowska, M.K., Popovic, D.B., Scheiner, A., Chizeck, H.J.: Estimating mechanical parameters of leg segments in individuals with and without physical disabilities. IEEE Transactions on Rehabilitation Engineering 4(3), 201–211 (1996)
19. Haddock, J., Kristzen, T., Terjki, J.: Comparison theorems and convergence properties for functional differential equations with infinite delay. Acta Sci. Math. 52, 399–414 (1988)
20. Zatsiorsky, V., Seluyanov, V.: The mass and inertia characteristics of the main segments of the human body. Biomechanics VIII-B, 1152–1159 (1983)

On the AER Stereo-Vision Processing: A Spike Approach to Epipolar Matching

Manuel Jesus Domínguez-Morales[1], Elena Cerezuela-Escudero[1], Fernando Perez-Peña[2], Angel Jimenez-Fernandez[1], Alejandro Linares-Barranco[1], and Gabriel Jimenez-Moreno[1]

[1] Robotic and Technology of Computers Lab, University of Seville, Spain
{mdominguez,ecerezuela,ajimenez,alinares,gaji}@atc.us.es
[2]Applied Robotics Research Lab, University of Cadiz, Spain
fernandoperez.pena@uca.es

Abstract. Image processing in digital computer systems usually considers visual information as a sequence of frames. These frames are from cameras that capture reality for a short period of time. They are renewed and transmitted at a rate of 25-30 fps (typical real-time scenario). Digital video processing has to process each frame in order to detect a feature on the input. In stereo vision, existing algorithms use frames from two digital cameras and process them pixel by pixel until it finds a pattern match in a section of both stereo frames. To process stereo vision information, an image matching process is essential, but it needs very high computational cost. Moreover, as more information is processed, the more time spent by the matching algorithm, the more inefficient it is. Spike-based processing is a relatively new approach that implements processing by manipulating spikes one by one at the time they are transmitted, like a human brain. The mammal nervous system is able to solve much more complex problems, such as visual recognition by manipulating neuron's spikes. The spike-based philosophy for visual information processing based on the neuro-inspired Address-Event- Representation (AER) is achieving nowadays very high performances. The aim of this work is to study the viability of a matching mechanism in a stereo-vision system, using AER codification. This kind of mechanism has not been done before to an AER system. To do that, epipolar geometry basis applied to AER system are studied, and several tests are run, using recorded data and a computer. The results and an average error are shown (error less than 2 pixels per point); and the viability is proved.

Keywords: Address-Event-Representation, spike, neuromorphic engineering, stereo, epipolar geometry, vision, dynamic vision sensors, retina.

1 Introduction

In recent years there have been numerous advances in the field of vision and image processing, because these matters can be applied for scientific and commercial purposes to numerous fields such as medicine, industry or entertainment. As it can be deduced, the images are two dimensional while the daily scene is three dimensional.

M. Lee et al. (Eds.): ICONIP 2013, Part I, LNCS 8226, pp. 267–275, 2013.
© Springer-Verlag Berlin Heidelberg 2013

This means that, between the passage from the scene (reality) and the image, there is a loss of what we call the third dimension. Nowadays, society has experienced a great advance in these aspects: 2D vision has given way to 3D viewing. Industry and research teams have started to study this field in depth, obtaining some mechanisms for 3D representation using more than one camera. Trying to resemble the vision of human beings, researchers have experimented with two-camera-based systems inspired by human vision. Following this, a new branch of research has been developed, focused on stereoscopic vision [1]. In this branch, researchers try to obtain three-dimensional scenes using two digital cameras. Thus, we try to get some information that could not be obtained with a single camera, i.e. distance estimation.

By using digital cameras, researchers have made a breakthrough in this field, going up to create systems able to achieve the above. However, digital systems have some problems that, even today, have not been solved completely. In any process of stereoscopic vision, image matching is the main problem that has consumed a large percentage of research resources in this field, and it is still completely open to research. Matching is the process performed in every stereo system to find the pixel within a camera matrix which corresponds to a particular one of the opposite camera. This process is critical, because it allows obtaining high-level results like distance calculation [2-3] or shape description. The main problem related to image matching is the computational cost needed to obtain appropriate results. There are lots of high-level algorithms used in digital stereo vision that can solve this problem, but they involve a high computational cost. Nowadays, mathematicians are trying to use several techniques in order to reduce the number of possible matches in the second camera. Calibration mechanisms and Epipolar Geometry are applied to pre-configure these systems and to obtain better and more optimal results.

In parallel to all these computational vision evolution, Neuromorphic Engineering arises, whose operation principles are based on the biological models themselves. Brains perform powerful and fast vision processing using millions of small and slow cells working in parallel in a totally different way. Primate brains are structured in layers of neurons, where the neurons of a layer connect to a very large number (~104) of neurons in the following one [4]. Connectivity mostly includes paths between non-consecutive layers, and even feedback connections are present.

Vision sensing and object recognition in brains are not processed frame by frame; they are processed in a continuous way, spike by spike, in the brain-cortex. The visual cortex is composed of a set of layers [4], starting from the retina. The processing starts when the retina captures the information. In recent years significant progress has been made in the study of the processing by the visual cortex. Many artificial systems that implement bio-inspired software models use biological-like processing that outperform more conventionally engineered machines [5-7]. However, these systems generally run at extremely low speeds because the models are implemented as software programs. For real-time solutions direct hardware implementations are required. A growing number of research groups around the world are implementing these principles onto real-time spiking hardware through the development and exploitation of the so-called AER (Address Event Representation) technology.

AER was proposed by the Mead lab in 1991 [8] for communicating between neuromorphic chips with spikes. Every time a cell on a sender device generates a spike, it transmits a digital word representing a code or address for that pixel, using an external inter-chip digital bus (the AER bus, as shown in Fig. 1). In the receiver the spikes are directed to the pixels whose code or address was on the bus. Thus, cells with the same address in the emitter and receiver chips are virtually connected by streams of spikes. Arbitration circuits ensure that cells do not access the bus simultaneously. Usually, AER circuits are built with self-timed asynchronous logic.

Several works are already present in the literature regarding spike-based visual processing filters. Serrano et al. presented a chip-processor able to implement image convolution filters based on spikes that work at very high performance parameters (~3GOPS for 32x32 kernel size) compared to traditional digital frame-based convolution processors [9-10]. There is a community of AER protocol users for bio-inspired applications in vision and audition systems. One of the goals of this community is to build large multi-chip and multi-layer hierarchically structured systems capable of performing complicated array data processing in real time. The power of these systems can be used in computer based systems under co-processing.

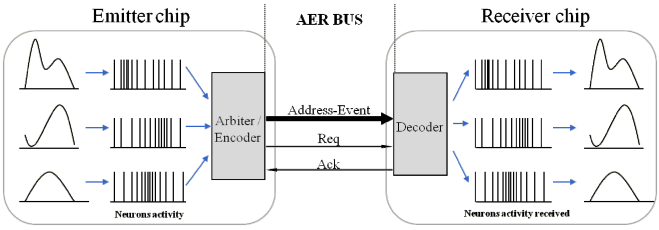

Fig. 1. Rate-coded AER inter-chip communication scheme

The optical sensor used by these research groups is the DVS128 AER retina [11]. This sensor works in such a way that each pixel only detects the derivate in time of the luminosity. That means that this retina only perceives luminosity variations or, as it is very common, objects in movement. This fact simplifies the amount of information transmitted, and it helps the researcher to focus on the important information of the scene. First, the epipolar geometry principles used in stereo vision image matching algorithms will be described. After that, these principles will be applied to a stereo vision AER system with the information obtained by the DVS-retina. Finally, the results and error measurements will be shown.

2 Epipolar Geometry

Epipolar geometry [12] is the intrinsic projective geometry between two views. It is independent of scene structure, and it only depends on the cameras' internal parameters and relative pose. The epipolar geometry between two views is essentially the geometry of the intersection of the image planes with the pencil of planes having

the baseline as axis (the baseline is the line joining the camera centers). This geometry is motivated by considering the search for corresponding points in stereo matching.

Suppose a point *X* in space is imaged in two views (one from each camera), at *x* in the first, and *x'* in the second. In this case, the relation between the corresponding image points *x* and *x'*, the spatial point *X* and the camera centers is that all of them are coplanar (located in the same plane, π). Clearly, the rays back-projected from *x* and *x'* intersect at *X*, and the rays are coplanar, lying in π. This latter property is the most significant in searching for a correspondence (see Fig. 2).

Supposing now that we know only *x*, we may ask how the corresponding point *x'* is constrained. The plane π is determined by the baseline and the ray defined by *x*. From above we know that the ray corresponding to the point *x'* lies in π, hence the point *x'* lies on the line of intersection *l'* of π with the second image plane. This line *l'* is the image in the second view of the ray back-projected from *x*. In terms of a stereo correspondence algorithm the benefit is that the search for the point corresponding to *x* does not need to cover the entire image plane but it can be restricted to the line *l'*. The importance of this fact is that, if a transformation mechanism between *x* and line *l'* can be obtained using a pre-calibration step, a simple AER spiking system implemented on programmable hardware (FPGA, etc.) will be able to discriminate the possible matches calculating the opposite epipolar line. To do that, the spikes building blocks can be used to operate with simple elements between spikes [13]. This mechanism needs the Fundamental Matrix to do that transformation.

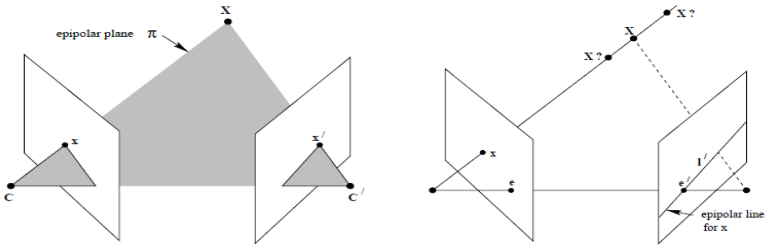

Fig. 2. Epipolar geometry explanation

Next, a quick introduction to the calibration mechanism will be shown, as well as the projection matrixes calculation.

3 Pre-calibration Summary

Camera calibration is, mainly, finding the internal quantities of the camera that affect the imaging process, like the position of the image center, the focal length, the lens distortion, etc. These parameters are joined to obtain the 'camera matrix'. This is an important process for rebuilding a world model. Several calibration mechanisms exist in classical computer vision. Some of them use a two-step process to obtain the

camera matrix: first approach and optimization. Pin-Hole is the most used camera model (the way in which the camera system interacts with the world). This fact, determines the mechanism used to calibrate the system.

In this work, a Pin-Hole model [14] and a Tsai calibration mechanism [15] have been used to calibrate the system. Also, as Tsai used in his experiments, a calibration grid was built to allow the retina to see the calibration points. In this case, the way in which the retina works (section 1) obstructs the calibration process because, in order to obtain good calibration results, the objects used in the calibration process cannot be in movement (remember that the retina only perceives the variation of the luminosity). Hence, the calibration grid built is different from the one used before. It is composed of a matrix of *8 by 8* LED lights and has been connected to a microcontroller that switches on and off each one of the LEDs. The calibration system is shown in Fig.3.

By capturing the information from the LED grid and processing it in a computer, the *64* projection points are obtained on each retina (after the application of some image filters). Using the Tsai mechanism [15], both camera matrixes (one for each retina) are calculated (first step). These matrixes are used to determine the 2D points in each retina, related to the 3D points in the space. Also, they have the internal information about each retina (internal parameters), so they describe the physical and the environmental properties of the cameras. Next step is testing and error measurement: using several space points and testing the conversion from 3D to 2D points, the final result is an average error of less than 1%. Also, these matrixes are optimized (second step) using the Faugeras mechanism [16]. After testing, new matrixes work with an error even smaller than the one obtained before (around 0.8%).

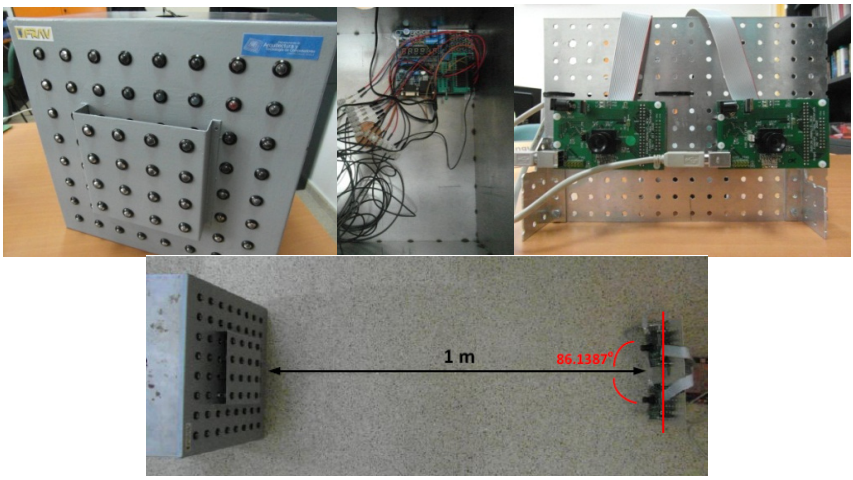

Fig. 3. Calibration system description

The main question is: having the 2D point of one retina, how can it be determined which point in the other retina corresponds to the same 3D point? This is necessary in order to obtain the coordinates of the 3D point and this process is known as the 'matching' step. To do that, in this work, epipolar geometry is applied to obtain the epipolar lines related to these points. Next, the mechanism used to calculate the epipolar lines from both projection matrixes will be shown.

4 Epipolar Lines Applied to a Calibrated AER Stereo-Vision System

The aim of this work, given a 2D point coordinates from one retina, is to discriminate the possible matches on the second retina. To do this, the epipolar line within the matching point will be calculated. Summarizing the classical machine vision principles, given a camera matrix *P* and a 3D point coordinates (X, Y, Z); the 2D point represented on the retina (U, V) is obtained using equation 1.

$$\begin{pmatrix} U \\ V \\ t \end{pmatrix} = P \begin{pmatrix} X \\ Y \\ Z \\ 1 \end{pmatrix}, \qquad P = \begin{pmatrix} q_{11} & q_{12} & q_{13} & q_{14} \\ q_{21} & q_{22} & q_{23} & q_{24} \\ q_{31} & q_{32} & q_{33} & q_{34} \end{pmatrix}, \qquad t = scale\ factor \tag{1}$$

To obtain the epipolar line, the inverse process will be done: given a 2D point from one of the retinae, the corresponding 3D point should be determined and, with its information and using the camera matrix of the second retina, the 2D coordinates of the second one will be obtained. However, a transformation from 3D to 2D entails a loss of information, so the distance information (coordinate *Z*) is impossible to obtain given only one 2D point (inverse process). So, how can the matching point (2D point in the other retina) be obtained? As said before, the final result will give the line within which the matching point is, not the exact point itself. The triangulation process is necessary to find the intersection of the rays projected from both retinae. Using the Pin-Hole model and both camera matrixes, the equation system can be modified to obtain the fundamental matrix (combining both retinae cameras), resulting on equation 2.

$$F \cdot M = 0, \qquad where\ M = \begin{pmatrix} X_i & Y_i & Z_i & \lambda \end{pmatrix}^t$$

$$F = \begin{pmatrix} P_{L1,1} - u_i \cdot P_{L3,1} & P_{L1,2} - u_i \cdot P_{L3,2} & P_{L1,3} - u_i \cdot P_{L3,3} & P_{L1,4} - u_i \cdot P_{L3,4} \\ P_{L2,1} - v_i \cdot P_{L3,1} & P_{L2,2} - v_i \cdot P_{L3,2} & P_{L2,3} - v_i \cdot P_{L3,3} & P_{L2,4} - v_i \cdot P_{L3,4} \\ P_{R1,1} - u'_i \cdot P_{R3,1} & P_{R1,2} - u'_i \cdot P_{R3,2} & P_{R1,3} - u'_i \cdot P_{R3,3} & P_{R1,4} - u'_i \cdot P_{R3,4} \\ P_{R2,1} - v'_i \cdot P_{R3,1} & P_{R2,2} - v'_i \cdot P_{R3,2} & P_{R2,3} - v'_i \cdot P_{R3,3} & P_{R2,4} - v'_i \cdot P_{R3,4} \end{pmatrix}, \tag{2}$$

where *M* is the spatial point, (u_i, v_i) are the coordinates of the 2D points projected on the left retina, (u'_i, v'_i) are the coordinates of the 2D point projected on the right retina, P_L is the left camera matrix, P_R is the right camera matrix and *F* is the fundamental matrix (to obtain a 3D point given both 2D points). This system is solved using Singular-Value Decomposition (SVD), obtaining the resulting points in the last

column of the V matrix: $(V_{1,4} \;\; V_{2,4} \;\; V_{3,4} \;\; V_{4,4})^t$. Finally, dividing by the scale factor: $(V_{1,4}/V_{4,4} \;\; V_{2,4}/V_{4,4} \;\; V_{3,4}/V_{4,4} \;\; V_{4,4}/V_{4,4})^t$;which is: $(X_i \;\; Y_i \;\; Z_i \;\; 1)^t$. The system *F*, can be obtained step by step, starting on the projection matrixes. Demonstration:

$$q_{11}X + q_{12}Y + q_{13}Z + q_{14} = u = Ut, \qquad q_{21}X + q_{22}Y + q_{23}Z + q_{24} = v = Vt$$
$$q_{31}X + q_{32}Y + q_{33}Z + q_{34} = t \tag{3}$$

Using *t*:
$$\begin{aligned} q_{11}X + q_{12}Y + q_{13}Z + q_{14} &= U(q_{31}X + q_{32}Y + q_{33}Z + q_{34}) \\ q_{21}X + q_{22}Y + q_{23}Z + q_{24} &= V(q_{31}X + q_{32}Y + q_{33}Z + q_{34}) \end{aligned} \tag{4}$$

Grouping the coefficients of the 3D coordinates:

$$\begin{aligned} (q_{11} - Uq_{31})X + (q_{12} - Uq_{32})Y + (q_{13} - Uq_{33})Z + (q_{14} - Uq_{34}) = 0 \\ (q_{21} - Vq_{31})X + (q_{22} - Vq_{32})Y + (q_{23} - Vq_{33})Z + (q_{24} - Vq_{34}) = 0 \end{aligned} \tag{5}$$

Changing the name of the previous expressions for a_1, b_1, c_1, d_1, a_2, b_2, c_2 and d_2:

$$a_1X + b_1Y + c_1Z + d_1 = 0, \qquad a_2X + b_2Y + c_2Z + d_2 = 0$$
$$X = \frac{Z(b_1c_2 - b_2c_1) + (b_1d_2 - b_2d_1)}{(a_1b_2 - a_2b_1)}, \qquad Y = \frac{Z(a_2c_1 - a_1c_2) + (a_2d_1 - a_1d_2)}{(a_1b_2 - a_2b_1)} \tag{6}$$

With the given values of one vision sensor, two equations with three unknown terms can be obtained. Summarizing, given the 2D point of one retina, the line in space, where the 3D point is, can be calculated (line *l*). Using two 3D random points situated on *l* and calculating its projections on the second retina, two 2D points are obtained. The line obtained by linking these 2D points is known as the 'epipolar line' (placed on the second retina): the matching point has to be situated over it. Using two random *Z* coordinates (i.e. *-10* and *10*), two 3D points are calculated. With these points, their projections over the second retina are calculated using its camera matrix. After that, the projected line on the second retina can be shown using the inclination calculated between both 2D points. If there is no error, the matching point must be situated on this line. Next, results and error measurements will be shown.

5 Matching Results and Error Measurement

With the results, epipolar lines between both retinas have been calculated. To see all the data, Fig.4 shows the epipolar lines obtained from the opposite retina and the 'target' points of this retina. In one case, it shows the epipolar lines calculated from the right retina with the points projected on the left retina. The other case is the opposite. To appreciate them better, examples have been run with *64* and *8* points.

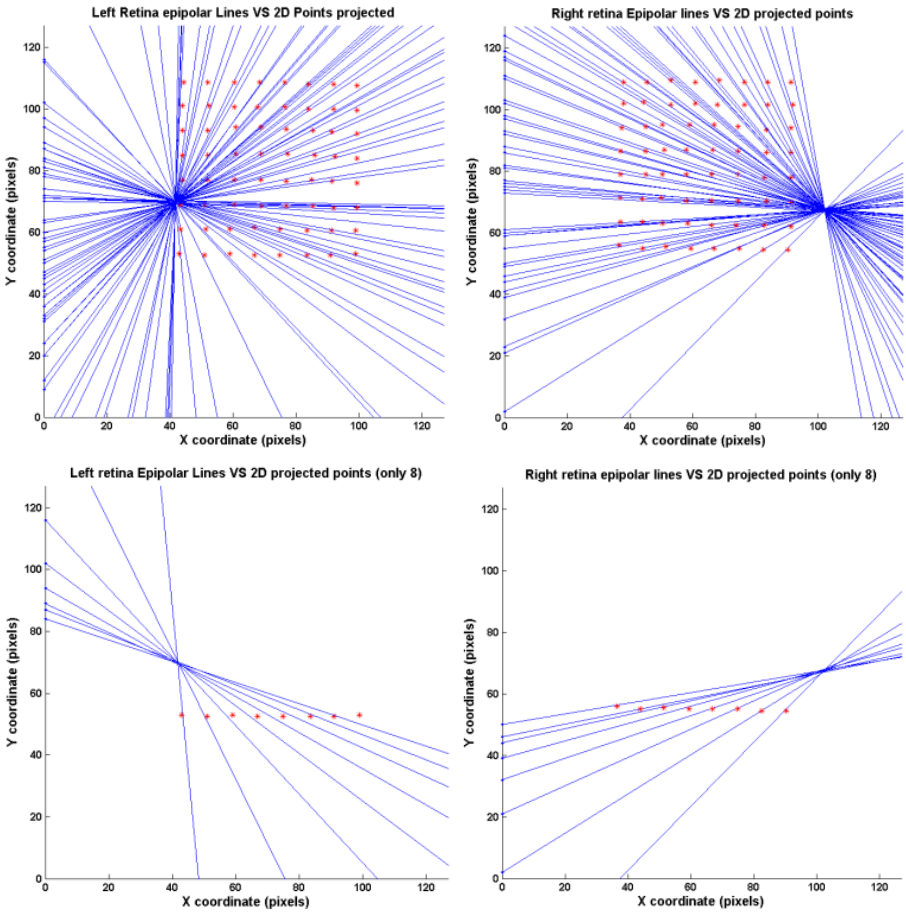

Fig. 4. Epipolar lines VS 2D projected points

It is easier to understand the results by watching the 8-point tests. For example: in the bottom-left image (left retina), the first point is the one in the left. A red asterisk can be seen, which is the point captured by the left retina, and a blue line passing next to the point, which is the epipolar line obtained by the right retina and projected on the left retina. As it can be seen, the point is situated over the line (almost no error).

To calculate the error, the distance between each epipolar line to the point itself has been calculated. Average error for the 64-point test is *2.2299* pixels per point for the left retina and *1.3957* for the right one. For the 8–point test the average error is *1.4240* for the left retina and *1.2239* for the right one. The obtained error is tolerable.

6 Conclusions

In this work, a matching algorithm based on epipolar geometry and a calibrating step has been tested under a neuromorphic AER-DVS stereo vision system. Mathematical

principles have been shown and demonstrated. The implemented system has been detailed, tested using sixty-four 3D points coordinates and its error has been measured. All the results, errors, graphs and formulas have been presented.

The proposed system obtains a tolerable error (less than 2 pixels per point) to work under a spiking system with two DVS128 retinae [11]. It has been proved that this mechanism works with spiking data and under the restrictions of an AER system.

As further research, the next step is to implement the full mechanism into programmable hardware, like FPGAs, in order to obtain an autonomous system without the computer intervention.

References

1. Barnard, S.T., Fischler, M.A.: Computational Stereo. Journal ACM CSUR 14(4) (1982)
2. Dominguez-Morales, M., et al.: An approach to distance estimation with stereo vision using Address-Event-Representation. In: International Conference on Neural Information Processing, ICONIP (2011)
3. Dominguez-Morales, M., et al.: Live Demonstration: on the Distance Estimation of Moving Targets with a Stereo-Vision Aer System. In: ISCASS (2012)
4. Shepherd, G.M.: The Synaptic Organization of the Brain, 3rd edn. Oxford University Press (1990)
5. Lee, J.: A Simple Speckle Smoothing Algorithm for Synthetic Aperture Radar Images. Man and Cybernetics SMC-13 (1981)
6. Crimmins, T.: Geometric Filter for Speckle Reduction. Applied Optics 24, 1438–1443 (1985)
7. Linares-Barranco, A., et al.: AER Convolution Processors for FPGA. In: ISCASS (2010)
8. Sivilotti, M.: Wiring Considerations in analog VLSI Systems with Application to Field-Programmable Networks. Ph.D. Thesis, Caltech (1991)
9. Cope, B.: Implementation of 2D Convolution on FPGA, GPU and CPU. I.C. Report (2006)
10. Cope, B., et al.: Have GPUs made FPGAs redundant in the field of video processing? FPT (2005)
11. Lichtsteiner, P., Posh, C., Delbruck, T.: A 128×128 120dB 15 us Asynchronous Temporal Contrast Vision Sensor. IEEE Journal on Solid-State Circuits 43(2), 566–576 (2008)
12. Hartley, R., Zisserman, A.: Multiple View Geometry in Computer Vision, 2nd edn. Cambridge University Press (2004)
13. Jimenez-Fernandez, A., et al.: Building Blocks for Spike-based Signal Processing. In: IEEE International Joint Conference on Neural Networks, IJCNN (2010)
14. Rosenfeld, A.: First Textbook in Computer Vision: Picture Processing by Computer. Academic Press, New York (1969)
15. Tsai, R.Y.: A versatile camera calibration technique for high-accuracy 3D machine vision metrology using off-the-shelf TV cameras and lenses. IEEE Int. Journal Robotics and Automation. 3(4), 323–344 (1987)
16. Faugeras, O.: Three-dimensional computer vision: a geometric viewpoint. MIT Press (1993)

SVITE: A Spike-Based VITE Neuro-Inspired Robot Controller

Fernando Perez-Peña[1,*], Arturo Morgado-Estevez[1], Alejandro Linares-Barranco[2], Manuel Jesus Dominguez-Morales[2], and Angel Jimenez-Fernandez[2]

[1] Applied Robotics Research Lab, University of Cadiz, Spain
{fernandoperez.pena,arturo.morgado}@uca.es
[2] Robotic and Technology of Computers Lab, University of Seville, Spain
{alinares,mdominguez,ajimenez}@atc.us.es

Abstract. This paper presents an implementation of a neuro-inspired algorithm called VITE (Vector Integration To End Point) in FPGA in the spikes domain. VITE aims to generate a non-planned trajectory for reaching tasks in robots. The algorithm has been adapted to work completely in the spike domain under Simulink simulations. The FPGA implementation consists in 4 VITE in parallel for controlling a 4-degree-of-freedom stereo-vision robot. This work represents the main layer of a complex spike-based architecture for robot neuro-inspired reaching tasks in FPGAs. It has been implemented in two Xilinx FPGA families: Virtex-5 and Spartan-6. Resources consumption comparative between both devices is presented. Results obtained for Spartan device could allow controlling complex robotic structures with up to 96 degrees of freedom per FPGA, providing, in parallel, high speed connectivity with other neuromorphic systems sending movement references. An exponential and gamma distribution test over the inter spike interval has been performed to proof the approach to the neural code proposed.

Keywords: Spike systems, Motor control, VITE, Address Event Representation, Neuro-inspired, Poisson, Neuromorphic engineering, Anthropomorphic robots.

1 Introduction

The implementation presented belongs to the Neuromorphic engineer field. The main goal of this discipline is to develop artificial systems which emulate the biological systems. The biological systems, such as: vision and audio systems, speech recognition and control of complex movements, carry out with their tasks with a large efficiency still unknown in the artificial systems. The neuromorphic engineer community use as many features as possible of the human nerve system to reach their goal. Inside this group, engineers try to build up a complete net of neurons in any device.

* This work was supported by the Spanish grant (with support from the European Regional Development Fund) BIOSENSE (TEC2012-37868-C04-02).

M. Lee et al. (Eds.): ICONIP 2013, Part I, LNCS 8226, pp. 276–283, 2013.
© Springer-Verlag Berlin Heidelberg 2013

One problem to face with is the way of designing and implementing those neuromorphic systems. If we look through the literature, we can find sensors like retinas and cochleas based on VLSI chips [1] and [2] and spike-based control architectures based on FPGA [3], [4] and [5] and also on chips [6]. These neural controllers are based on the third generation of artificial neural networks (ANN): the spiking neural networks (SNN). The main advantages of the FPGA implementations are the reconfigurability and the low cost. In this work we use a FPGA for our purpose and architecture based on blocks which mimic the neural behavior by using spikes to carry out the spatial-temporal information.

Other important issue is about the neural code [7]. From past experiments it is known that neurons do not have the same response to identical stimulus at any time [7]. Thus, they follow a distribution and the most popular one is the Poisson [8], although there are others, like Rate-coded [9], more typical in VLSI or renewal process [8]. The system presented has a deterministic spike source (Rate-coded) which is in front of the neuronal principles. But, due to the way of the translation performed it is achievable a gamma distribution for the inter spike interval at the output of the system. This point has been checked by a comparative with theoretical expected.

Nevertheless, since neurons communicate in a point-to-point manner and it is possible to integrate several thousands of artificial neurons into the same electronic device (VLSI chip or FPGA), new communication strategies has been taken, as the Address-Event-Representation (AER) protocol [10]. AER map each neuron with a fixed address which is transmitted through the interconnected neuron system. By using AER protocol, all neurons are continuously sending information about their excitation level to the central system and it could be processed in real time by a higher layer.

AER is based on the concept which mimics the structure and information coding of the brain. Thus AER let us process the information in real time. That's one of the reasons of using it: the provided speed. Other one is the scalability that allows it by parallel connections.

The entire architecture consists of an AER retina [1], two layers: processing and actuation one (FPGA implemented) and finally a robotic platform. This paper is focused on the processing layer where is implemented the VITE (Vector Integration To Endpoint) algorithm [11]. The translation into spikes paradigm takes a step forward a complete spike-based processing architecture: from the retina to the robot.

In the next section, the algorithm and its translation are described. Also, details of the blocks are presented. Then in section three we describe both families from Xilinx used; the advantages and disadvantages are enumerated. In section four the results are presented: a comparative between both FPGA models in terms of hardware resources consumption with a brief description of the robotic platform and the test to check the neural code. Finally, to sum up, a discussion about the results achieved is presented.

2 VITE Algorithm

This neuro-inspired algorithm [11] is used for calculating a non-planned trajectory. It computes the difference between the target and the present position. It models

planned human arm movements. In contrast to approaches which require the stipulation of the desired individual joint positions, this trajectory generator operates with desired coordinates of the end vector and generates the individual joint driving functions in real-time employing geometric constraints which characterize the manipulator.

In Fig. 1 the block diagram of the algorithm and the translation into spikes domain are shown.

The target position will be supplied by the AER retina [1] to the processing layer (the first one of the architecture). With a mapping function, this layer will generate the spikes according to the reaching target. As was previously noted, this source is deterministic at its firing rate.

Then, the difference between present position and the received from the retina at each time is calculated. The output of the algorithm will be supplied to the second layer of the architecture: the actuation layer. Thus, the FPGA design should include an input and output port in order to carry out with the communication protocol.

Taking a closer look at the translated blocks:

- The Spike Hold & Fire block performed the subtraction between the present position and the target position; both signals are spike streams. The block has two decreasing counters to storage the number of spikes at the input and a combinational circuit to manage these counters and the output.
- The Spikes Integrate & Generate block allows us to integrate the DV (Difference Vector) signal (again a spike stream). This block is composed by a spike counter and a spike generator. The latter uses a parameter called IG_FD (Integrate & Generate_FrequencyDivider) to divide the clock signal and generate the output stream according to this division.
- The Low Pass Filter consists of a Hold & Fire block and an Integrate & Generate block. The output of this second block feed the second input of the hold & fire. The other input comes from previous block in the diagram.

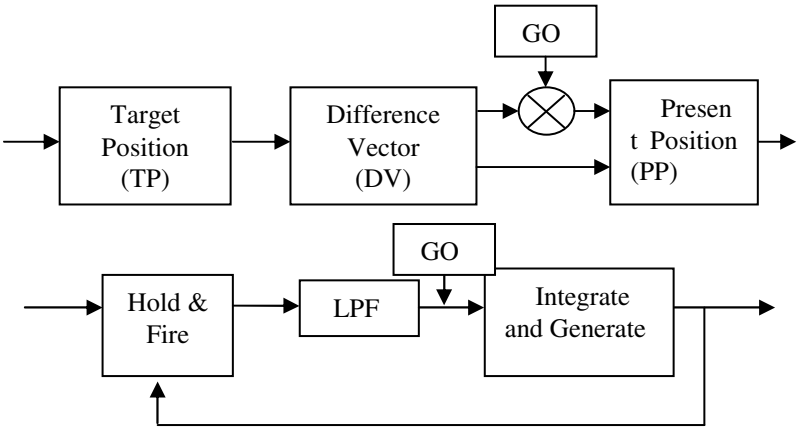

Fig. 1. Top: block diagram of the VITE algorithm. Bottom: block diagram generated from existing spikes processing blocks in [12][13].

- The GO block will be present at the Integrate & Generate block input to put on speed the DV signal. This block copies the task of the multiplier present in the classic algorithm. But if we look through the neuromorphic's engineer point of view, a multiplication is not present in the human nerve system. So, it accomplishes the task injecting spikes according with the desired speed at each time. To do so, it has a counter to generate the number of spikes that should be injected. This block is the key to achieve a Poisson distribution.

These blocks are described in depth in [12] and [13].

At the final design, for each algorithm synthetized in the FPGA a FIFO memory is included to prevent spike loosing problems. The memory receives the spikes produced by the algorithm and delivers to the output interface. So it is very important the total capacity in the device selection.

3 Implementation

Two different FPGA has been used to implement the system using a commercial Xilinx PCB (Virtex5 platform) and the AER-node board (Spartan-6), that has been developed by authors' lab under the Spainsh Research Project VULCANO.

The Virtex-5 device used is the XC5VFX30T which was designed to hold high performance embedded systems. It has two slices per CLB, reaching a total of 5,120 slices and 20,480 flip-flops available. The RAM capacity for this device is up to 2,448 Kb within blocks of 18 Kb. The prototyping board used is AES-V5FXT-EVL30-G from Avnet and it is based on the device described. To achieve the requirements of input/output ports a daughter card was used.

The Spartan-6 device used is the XC6SLX150T which was designed to hold high volume applications at a low cost device. Also it provides high speed serial connectivity. It has two slices per CLB too, reaching a total of 23,038 slices and 184,304 flip-flops available. The RAM capacity for this device is up to 4,824 Kb within blocks of 18 Kb.

The AER Node platform used can be connected in a mesh (using high-speed serial LVDS links) allowing any 2D neuromorphic architecture.

The board has four 2.5Gbps serial ports (SATA connectors) in order to communicate with other neuromorphic chips. These ports take advantage of the eight GTP transceiver ports available in the device.

Furthermore, the board includes two parallel ports of 30-bit to use the standard parallel spike-based AER protocol, both directly and through specialized daughter boards that increase the functionality.

In order to deliver to the FPGA the data necessary for the algorithm execution, a daughter board (plug-in) is connected. It consists of a microcontroller connected to the FPGA through SPI (Serial Peripheral Interface) protocol. The data delivered are configuration parameters for each block. Also the target used as input is delivered.

Figure 2 shows both hardware platforms.

4 Results

We have made two comparisons. On the one hand hardware resources consumption comparative and on the other hand a power consumption comparative between both devices.

4.1 Hardware Resources Consumption

In general, to measure the hardware consumption in a FPGA, two points should be considered: the dedicated resources included to build up complex devices such as multipliers and the configurable logic blocks (CLBs) for general purpose.

The algorithm does not use any complex structure. It just needs counters and hardware to carry out simple arithmetic operations. Therefore the measurements are focused into the available slices at the FPGA.

We have synthesized the algorithm, including the spikes generator and other options like the spikes monitor and the interface with other neuromorphic chips. Table one and two present the data for both devices with the reports obtained.

In these tables, the first column describes implemented elements for each case. The next column shows the amount of slices needed to synthetized the units for each FPGA. The following column represents the maximum number of units that could be allocated for each FPGA. The final column shows device total capacity for all the synthesis performed.

Results evidenced that with additional elements to the algorithm, the amount of slices needed to synthetize is higher. It is remarkable that the interface with other neuromorphic chips does not provoke an increment in the hardware resources consumption. Consequently the final implementation for a complete architecture will consist of the algorithm and the interface. However, the design and test phases need a monitor in order to check the right behavior of the algorithm.

All the results presented in this section, avoid using the FIFO memory because it uses special architecture presents in both devices.

Table 1. Hardware resources consumption details by Virtex5 and Spartan 6 devices

	Number of Slices		Max. blocks in the device		Use by one block (%)	
	Virtex	Spartan	Virtex	Spartan	Virtex	Spartan
Algorithm	208	238	24	96	4.062	1.033
Algorithm plus monitor	478	533	10	43	9.33	2.31
Algorithm plus interface	215	242	23	95	4.2	1.05
Algorithm plus monitor and interface	478	533	10	43	9.33	2.31

4.2 Robotic Platform

The algorithm presented has been applied to a fixed robotic platform to check it. Fig.2 shows the hardware implementation and the result of the position reached when the target is fixed at (123,110) in the frame of reference of the retina.

The robotic platform is a stereo-vision robot with four degrees of freedom powered by DC motors. The power supply requirement of the motors is 24 Vdc. The manufacturer of the motors is Harmonic Drive and the model is RH-8D6006. The structure of the robotic platform is made so that the motors of the y axis are crossed to their axis and have a transmission belt to move the arm.

We propose to use PFM (Pulse Frequency Modulation) to run the motors to take advantage of the spikes produced by the algorithm. Also, PFM is the closest one to the neural system within motor-neurons.

Four units of VITE were replicated in order to control each motor with an independent way. It allows developing synchronized movements by adjusting GO signal in each algorithm.

The main limitation was due to the motor driver and the opto-coupler present in the power stage. These units have a low switching frequency, just 40 Khz and our algorithm generates higher spike rates. Thus, we have modified the spikes generator in the algorithm to generate 40 Kevents per second as it maximum firing rate.

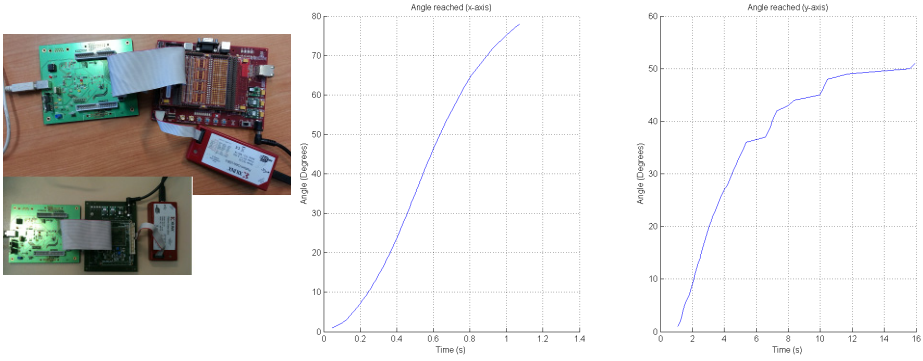

Fig. 2. Left: Virtex 5 at the top and Spartan 6 at the bottom. In both pics appear the programming tool and a special board to monitor the spikes (input and output) [14]. Right: Angle Vs. time reached for both axis with (123,110) input. The retina has 128x128 pixels.

4.3 Inter-Spikes-Intervals Distribution Analysis

In this section, we analyze the InterSpike-Interval(ISI) achieved at the output of the system. As was previously noted, the spike source is deterministic, i.e. it has a one to one mapping between stimulus and response. We are going to compare the inter spike interval with the expected one from a Poisson-like source [15]. The expected ISI of a Poisson process follows an exponential distribution. Also a gamma approach is included in the comparative; it means a renewal process (where the firing probability

depends on both: the instantaneous firing rate and the time since the most recent previous spike) [8].

To measure how well the observed distribution of ISIs follows the theoretical exponential or gamma distribution, a comparative between the histogram of ISI read for the speed profile at the input of the integrator superimposed with the theoretical ISI density has been done. As long as the firing rate has dependence with time in our GO block (spikes are injected increasingly within time) and with previous spike in the Hold and Fire block, the ISI follows a gamma distribution.

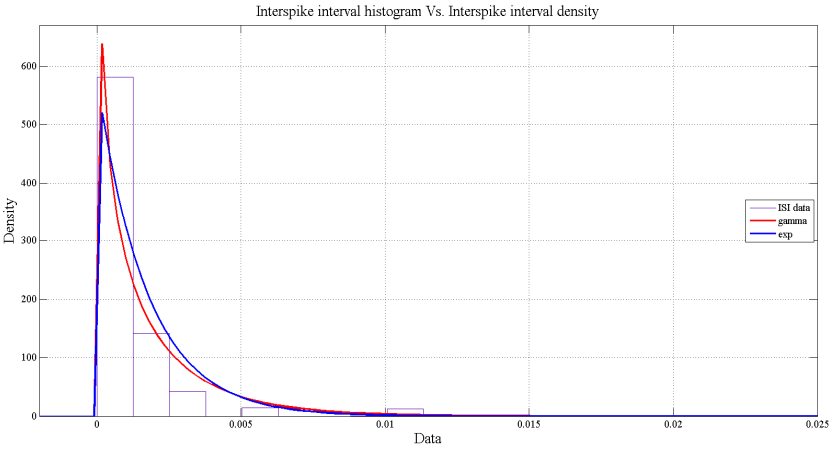

Fig. 3. Comparative between the empiric histogram for ISI and the theoretical defined by exponential and gamma distribution

5 Discussion and Conclusions

We have presented an implementation and a proof of a neuroinspired algorithm in two different devices. The results exhibit a huge advantage using the Spartan 6 device and a well adjust to a Poisson distribution. A total of 96 algorithms can be fitted at the board. The memory requirements are achieved for both devices because we need to storage at maximum 2,048 bytes and both of them have higher capacity. Otherwise, the power consumption is 789 mW for the Virtex-5 device and is 112 mW for the Spartan6 (estimated values with the XPE tool by Xilinx). These values show a big difference between both devices due to the resources used for each one as it has been presented in previous section.

Moreover, the achieved results take into account the slices used by the component in charge of the (Serial Peripheral Interface bus) SPI communication. So, it is possible to avoid that communication and improve the hardware resources consumption.

However, the Virtex device used for the comparison was not the top of the family in contrast with the Spartan 6. With the top Virtex, more algorithms can be fitted but it not allows high speed communication in front of Spartan 6 device.

Also, the proof included to check the neuroinspired features of the algorithm implemented within a digital system shows a good approach to a stochastic gamma distribution for ISI. It reveals a renewal process for the spike train signal even using a deterministic spikes source.

To sum up, the Spartan 6 device can provide a large number of replicated systems in order to control a high number of muscles (mimic by motors) carrying out intended movements in a neuroinspired way. It also allows serial and parallel communication with other neuromorphic chips.

References

1. Lichtsteiner, P., Posch, C., Delbruck, T.: A 128 × 128 120 dB 15 μs latency asynchronous temporal contrast vision sensor. IEEE J. Solid-State Circuits 43, 566–576 (2008)
2. Hafliger, P.: Adaptive WTA with an analog VLSI neuromorphic learning chip. IEEE Trans. Neural Netw. 18, 551–572 (2007)
3. Linares-Barranco, A., Paz-Vicente, et al.: AER neuro-inspired interface to anthropomorphic robotic hand. In: Proceedings of IJCNN, Vancouver, pp. 1497–1504 (2006)
4. Linares-Barranco, A., Gomez-Rodriguez, F., Jimenez-Fernandez, A., Delbruck, T., Lichtensteiner, P.: Using FPGA for visuo-motor control with a silicon retina and a humanoid robot. In: Proceedings of ISCAS 2007, pp. 1192–1195. IEEE Press, New Orleans (2007)
5. Pearson, M.J., Pipe, A.G., Mitchinson, B., Gurney, K., et al.: Implementing Spiking Neural Networks for Real-Time Signal-Processing and Control Applications: A Model-Validated FPGA Approach. IEEE Trans. Neural Networks 18, 1472–1487 (2007)
6. Xiuqing, W., Zeng-Guang, H., Anmin, Z., Min, T., Long, C.: A behavior controller based on spiking neural networks for mobile robots. Neurocomputing 71, 655–666 (2008)
7. Rieke, F., Warland, D., Steveninck, R., Bialek, W.: Spikes Exploring the neural code. MIT Press, Cambridge (1999)
8. Dayan, P., Abbot, L.: Theoretical Neuroscience. MIT Press, Cambridge (2001)
9. Linares-Barranco, A., Jimenez-Moreno, G., Linares-Barranco, B., Civit-Ballcels, A.: On algorithmic rate-coded AER generation. IEEE Transactions on Neural Networks 17(3), 771–788 (2006)
10. Sivilotti, M.: Wiring Considerations in Analog VLSI Systems with Application to Field-Programmable Networks, Ph.D. Thesis, California Institute of Technology, Pasadena CA (1991)
11. Bullock, D., Grossberg, S.: The VITE model: A neural command circuit for generating arm and articulator trajectories. In: Kelso, J.A.S., Mandell, A.J., Shlesinger, M.F. (eds.) Dynamic Patterns in Complex Systems, pp. 305–326. World Scientific Publishers, Singapore (1988)
12. Jimenez-Fernandez, A., Jimenez-Moreno, G., et al.: A Neuro-Inspired Spike-Based PID Motor Controller for Multi-Motor Robots with Low Cost FPGAs. Sensors 12(4), 3831–3856 (2012)
13. Perez-Peña, F., Morgado-Estevez, A., Linares-Barranco, A., et al.: Towards AER VITE: building spike gate signal. In: 19th ICECS, Seville, pp. 881–884 (2012)
14. Berner, R., Delbruck, T., Civit-Balcells, A., et al.: A 5 Meps $100 USB2.0 Address-Event Monitor-Sequencer Interface. In: ISCAS, New Orleans, LA, pp. 2451–2454 (2007)
15. Linares-Barranco, A., Osterb, M., Cascado, D., Jiménez, G., et al.: Inter-spike-intervals analysis of AER Poisson-like generator hardware. Neurocomputing 70, 2692–2700 (2007)

A Neurodynamic Optimization Approach to Robust Pole Assignment for Synthesizing Linear Control Systems Based on a Convex Feasibility Problem Reformulation

Xinyi Le and Jun Wang

Department of Mechanical and Automation Engineering, The Chinese University of Hong Kong, Shatin, New Territories, Hong Kong
xyle,jwang@mae.cuhk.edu.hk

Abstract. A neurodynamic optimization approach to robust pole assignment for synthesizing linear control systems is presented in this paper. The problem is reformulated from a quasi-convex optimization problem into a convex feasibility problem with the spectral condition number as the robustness measure. Two coupled globally convergent recurrent neural networks are applied for solving the reformulated problem in real time. Robust parametric configuration and exact pole assignment of feedback control systems can be achieved. Simulation results of the proposed neurodynamic approach are reported to demonstrate its effectiveness.

Keywords: Robust pole assignment, recurrent neural networks, state feedback control, global convergence.

1 Introduction

As it is known that the performance of a control system is mainly determined by its poles, pole assignment is a basic approach for linear control system design. Various specifications for control systems can be achieved via proper pole assignment. Since practical control systems can hardly be precisely modeled or they are often subject to parameter uncertainties, the robustness properties should to be optimized to improve the control system performance. The robust pole assignment problem is then first formulated by Kautsky et al. [9] through minimizing the spectral condition number of the eigenvector matrix. Frobenius norm was considered to replace spectral norm in the condition number and its additive substitutes by [1] and [11]. Some other robustness measures and various optimization approaches to robust pole assignment problem were widely investigated in [2, 3, 5, 8, 12, 13, 17, 18, 20]. However, because of the nonconvexity of the condition numbers and their variants as robust measures, the existing methods cannot guaranteed to achieve the global optimality.

Neurodynamic optimization has been widely developed for more than three decades. Different from feedforward neural networks, recurrent neural networks are dynamic systems *per se* and suitable for modeling and optimizing dynamical systems. Optimization based on recurrent neural networks have several advantages such as guaranteed optimality, expended applicability, improved convergence properties, and reduced model complexity; e.g., [4, 6, 7, 10, 14, 15, 21–24]. In this paper, a novel optimization approach

M. Lee et al. (Eds.): ICONIP 2013, Part I, LNCS 8226, pp. 284–291, 2013.
© Springer-Verlag Berlin Heidelberg 2013

based on recurrent neural networks to robust pole assignment is proposed via convex reformulation. As spectral condition number is quasi-convex, this problem is reformulated into a convex feasibility problem with some adjustable parameter. The method is capable of optimizing the spectral condition number of the eigensystem while making exact pole assignment. Simulation results substantiate the effectiveness and illustrate the characteristics of the proposed neural network.

2 Preliminaries and Problem Formulation

Consider a linear time-invariant control system as follows:

$$\dot{x}(t) = Ax(t) + Bu(t),\ x(0) = x_0, \tag{1}$$

where $x \in \Re^n$ is the state vector, $u \in \Re^m$ is the control vector, $A \in \Re^{n\times n}$, and $B \in \Re^{n\times m}$ are known coefficient matrices associated with $x(t)$ and $u(t)$, respectively. Assuming the control system (1) is completely controllable and observable, the state feedback control law:

$$u(t) = r(t) + Kx(t) \tag{2}$$

can be applied to control the state of the system. Closed-loop control system is as follows:

$$\dot{x}(t) = (A + BK)x(t) + Br(t), x(0) = x_0, \tag{3}$$

where $r \in \Re^m$ is a reference input vector, and $K \in \Re^{m\times n}$ is a feedback gain matrix. Based on the controllability assumption of pair (A, B), there exists at least one feedback matrix K. Feedback gain matrix K may be chosen by using different design strategies, such as optimal control or pole assignment methods, depending on the design requirements. In this paper, the robustness performance of a system is considered as a main issue.

For a particular choice of almost any set of real and self-conjugate complex desired poles $\lambda_1, \lambda_2, ..., \lambda_n$ of the closed loop system, robust pole assignment for state feedback is to find such a K to improve the robustness performance. The existence and construction of such a feedback gain may be characterized as follows.

A matrix is said to be real pseudo-diagonal if it is a real block-diagonal matrix containing diagonal elements for real eigenvalues and (2×2)-blocks of the form:

$$\begin{bmatrix} \sigma_i & \omega_i \\ -\omega_i & \sigma_i \end{bmatrix}$$

for complex conjugate eigenvalue pairs $\sigma_i \pm \omega_i j$, where $j = \sqrt{-1}$. Denote spec(M) as the set of eigenvalues of the matrix M. Given a real pseudo-diagonal matrix $\Lambda \in \Re^{n\times n}$ with spec$(\Lambda) = (\lambda_1, \lambda_2, ..., \lambda_n)$, find real matrix K and nonsingular matrix Z satisfying

$$(A + BK)Z = Z\Lambda. \tag{4}$$

It is shown in [9] that, given Λ and Z nonsingular, then there exists K as a solution to eqn. (4) if and only if

$$Q_2^T(AZ - Z\Lambda) = 0, \text{ where } \mathrm{B} = [\mathrm{Q}_1\ \mathrm{Q}_2]\begin{bmatrix} R \\ 0 \end{bmatrix} \tag{5}$$

The factorization of matrix B can be obtained via QR factorization of B with $Q = [Q_1\ Q_2]$ being orthogonal and R being nonsingular [9], where $Q_1 \in \Re^{n\times m}, Q_2 \in \Re^{n\times(n-m)}$, and $R \in \Re^{m\times m}$. Furthermore, K then is given by

$$K = R^{-1}Q_1^T(Z\Lambda Z^{-1} - A). \tag{6}$$

By using Kronecker product and vectorization techniques, constraints equation (5) can be written as

$$Mz = 0, \tag{7}$$

where $z = vec(Z)$, $M \in \Re^{mn\times n^2}$, and

$$M = [I_n \otimes Q_2^T A - \Lambda^T \otimes Q_2^T]. \tag{8}$$

As the existence of multiple solutions on K based on eqns. (5) and (6), additional robustness property can be to optimized to improve the systems' performance. If the system matrix A is offset by a perturbation or uncertainty term Δ, it can be rewritten as

$$AZ + \Delta Z + BKZ = Z(\Lambda + Z^{-1}\Delta Z). \tag{9}$$

The perturbed system is stable if $(\Lambda + Z^{-1}\Delta Z)$ is stable. It is known in [9] that the robust stability can be guaranteed if

$$\|\Delta\|_2 < \frac{\min_{1\le j\le n}|\mathrm{Re}(\lambda_\mathrm{j})|}{\kappa_2(Z)}, \tag{10}$$

where λ_j $(j = 1, 2, ...n)$ are the eigenvalues of Λ, $\mathrm{Re}(\cdot)$ is its real part, and $\kappa_2(Z) = \sqrt{\lambda_{\max}(Z^TZ)/\lambda_{\min}(Z^TZ)}$ is the spectral condition number of the eigensystem. $\lambda_{\max}$ and $\lambda_{\min}$ are the largest and smallest eigenvalues. From eqn. (10) we can see that a smaller $\kappa_2(Z)$ will lead to a bigger bound of Δ. Hence, minimizing the conditioning κ_2 becomes a focal point.

As the optimal solutions of κ_2 and κ_2^2 is the same, κ_2^2 may be minimized instead of κ_2. $\kappa_2^2 = \lambda_{\max}(Z^TZ)/\lambda_{\min}(Z^TZ)$ is quasiconvex with $\lambda_{\max}(Z^TZ)$ convex, $\lambda_{\min}(Z^TZ)$ concave, and $\lambda_{\max}(Z^TZ) \ge 0$, $\lambda_{\min}(Z^TZ) \ge 0$. Take

$$\phi_\mu(z) = \lambda_{\max}(Z^TZ) - \mu\lambda_{\min}(Z^TZ). \tag{11}$$

For fixed μ, ϕ_μ is convex in Z. In addition, $\phi_\mu \le 0$ is equivalent to $\lambda_{\max}(Z^TZ)$ $/\lambda_{\min}(Z^TZ) \le \mu$. Consider the convex feasibility problems as follows:

$$\phi_\mu(z) \le 0, Mz = 0. \tag{12}$$

The optimal solution of κ_2^2 can be found according to the following steps. First, given $\mu_0 = 1$, then solve the convex feasibility problem (12). Second, if (12) is feasible, then increase μ. Otherwise, decrease μ. Finally μ will be convergent to the optimal κ_2^2.

3 Neurodynamic Approaches

Neurodynamic optimization approaches are suitable for convex problems; e.g., [7, 14, 15, 21–24]. In particular, [15] proposed a one-layer recurrent neural network, which is capable for convex optimization with both linear equity constraints and inequity constraints. The neurodynamic equation is presented as follows:

$$\epsilon_1 \frac{dz}{dt} = -M^T g_{[-1,1]}(Mz) - \sigma(t)(I - M^T(MM^T)^{-1}M)\nabla\phi_\mu(z) g_{[0,1]}(\phi_\mu(z)), \quad (13)$$

where ϵ_1 is a positive scaling constant, $\sigma(t)$ is a positive gain function of time t, $\nabla\phi_\mu(z)$ is the gradient of the inequity constraint function $\phi_\mu(z)$, $g_{[l,h]}(y)$ is a vector valued discontinuous activation function with its components are defined as

$$g_{[l,h]}(y) = \begin{cases} h, & y > 0 \\ [l,\ h], & y = 0 \\ l, & y < 0 \end{cases} \quad (14)$$

Let $t_S = \epsilon_1 \|Mz_0\|_1 / \lambda_{\min}(MM^T)$, where $\lambda_{\min}$ is the minimum eigenvalue of the matrix, and z_0 is the initial state of neural network. Function $\sigma(t)$ is a monotone non-decreasing function:

$$\sigma(t) = \begin{cases} 0, & \text{if t} < \text{t}_\text{S} \\ 1, & \text{if t} \geq \text{t}_\text{S} \end{cases} \quad (15)$$

It is proved in [15] that the state vector z of the recurrent neural network in eqn. (13) is globally convergent to the feasible region $S = \{z | Mz = 0\}$ in finite time and stays there thereafter. Globally convergence for convex problem can be guaranteed. $\nabla\phi_\mu(Z)$ can be derived as follows:

$$\nabla\phi_\mu(Z) = 2Z(v_{\max} v_{\max}^T - \mu v_{\min} v_{\min}^T), \quad (16)$$

where $\lambda_{\max}$ and $\lambda_{\min}$ are the largest and smallest eigenvalues of $Z^T Z$, $v_{\max}$ and $v_{\min}$ are corresponding nominal eigenvectors.The parameter μ can be adjusted according to the following rules:

$$\epsilon_2 \frac{d\mu}{dt} = \begin{cases} 1, & \phi_\mu(z) > 0 \\ 0, & \phi_\mu(z) = 0 \\ -1, & \phi_\mu(z) < 0 \end{cases} \quad (17)$$

Based on eqns. (13), (16), and (17), robustness performance can be optimized.

In (16), $\nabla\phi_\mu(Z)$ contains the eigenvalues and eigenvectors of $Z^T Z$, which cannot be calculated directly. [19] offers a simple and concise model for computing the largest eigenvalue $\lambda_{\max}$ and corresponding eigenvector $v_{\max}$, and the smallest eigenvalue $\lambda_{\min}$ and corresponding eigenvector $v_{\min}$ on symmetric and positive semi-definite matrices $Z^T Z$. Similar results can also be seen in [16, 19]. The dynamic equations are presented as follows:

$$\epsilon_3 \frac{du_{\max}}{dt} = Z^T Z u_{\max} - u_{\max}^T Z^T Z u_{\max} u_{\max}, \tag{18}$$

$$\epsilon_3 \frac{du_{\min}}{dt} = (-Z^T Z + \lambda_{\max} I) u_{\min} - u_{\min}^T (-Z^T Z + \lambda_{\max} I) u_{\min} u_{\min}, \tag{19}$$

$$\lambda_{\max} = \bar{u}_{\max}^T Z^T Z \bar{u}_{\max}, v_{\max} = \bar{u}_{\max}, \tag{20}$$

$$\lambda_{\min} = \bar{u}_{\min}^T Z^T Z \bar{u}_{\min}, v_{\min} = \bar{u}_{\min}, \tag{21}$$

where ϵ_3 is a positive scaling constant and $u_{\max}, u_{\min} \in \Re^n$. Denote equilibrium vector of $u_{\max}$ as $\bar{u}_{\max}$ and $u_{\min}$ as $\bar{u}_{\min}$. Then the largest eigenvalue $\lambda_{\max}$, smallest eigenvalue $\lambda_{\min}$ and the corresponding eigenvectors $v_{\max}$ and $v_{\min}$ can be computed. According to [19], the convergence of the recurrent neural network can be guaranteed with nonzero $u_{\max}(0)$ and $u_{\min}(0)$.

The robust pole assignment processes for synthesizing state feedback control systems is delineated in Fig. 1, where one recurrent neural network (RNN_1) described in eqns. (13), (16), and (17) is responsible for conditioning optimization and another recurrent neural network (RNN_2) described in eqns. (18) and (19) is used for computing the largest and smallest eigenvalues and corresponding eigenvectors.

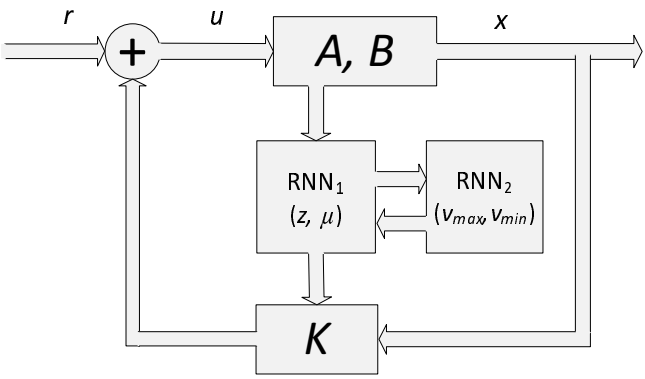

Fig. 1. Block diagram of the neurodynamic-based state feedback control system via robust pole assignment

4 Simulation Results

Example as follows will be discussed in detail to demonstrate the effectiveness and characteristics of the proposed method. Consider a chemical reactor model in [1] :

$$A = \begin{bmatrix} 1.3800 & -0.2077 & 6.7150 & -5.6760 \\ -0.5814 & -4.2900 & 0.0000 & 0.6750 \\ 1.0670 & 4.2730 & -6.6540 & 5.8930 \\ 0.0480 & 4.2730 & 1.3430 & -2.1040 \end{bmatrix}, B = \begin{bmatrix} 0 & 0 \\ 5.679 & 0 \\ 1.1360 & -3.1460 \\ 1.1360 & 0 \end{bmatrix}.$$

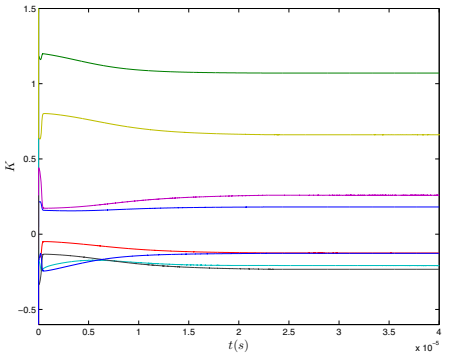

Fig. 2. Transient behaviors of feedback gain matrix K of RNN_2

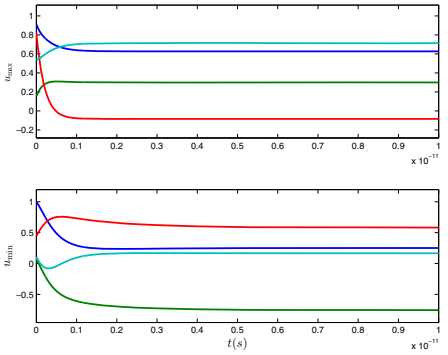

Fig. 3. Transient behaviors of state variables $u_{\max}$ and $u_{\min}$ in RNN_2

Let close-loop poles $\lambda = [-0.2, -0.5, -5.0566, -8.6659]$. Take $\epsilon_1 = \epsilon_2 = 10^{-6}$, and $\epsilon_3 = 10^{-12}$, exact pole assignment and global convergence of the condition number can be achieved. Fig. 2 depicts the transient behaviors of feedback gain matrix K of RNN_1. Fig. 3 demonstrate the transient behaviors of state variables $u_{\max}$ and $u_{\min}$ in RNN_2. The steady values of K are computed as follows:

$$K = \begin{bmatrix} 0.181 & -0.125 & 0.257 & -0.232 \\ 1.069 & -0.216 & 0.659 & -0.129 \end{bmatrix},$$

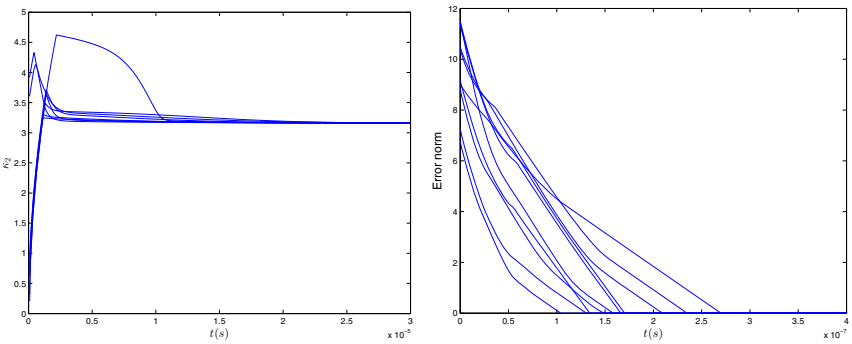

(a) (b)

Fig. 4. Transient behaviors of the condition numbers and error norm $\|Q_2^T(AZ - Z\Lambda)\|_2$ of the state feedback control system within first three microseconds in Example 2.

Fig. 4 depicts the transient behaviors of the spectral condition number κ_2 and the norm of constraints $\|Q_2^T(AZ - Z\Lambda)\|_2$ from different initial states, which substantiated the exact pole assignment and the global convergence properties of the neurodynamic approach. To test the robustness further, let a perturbation be $\Delta_1 = 0.0048A$ and

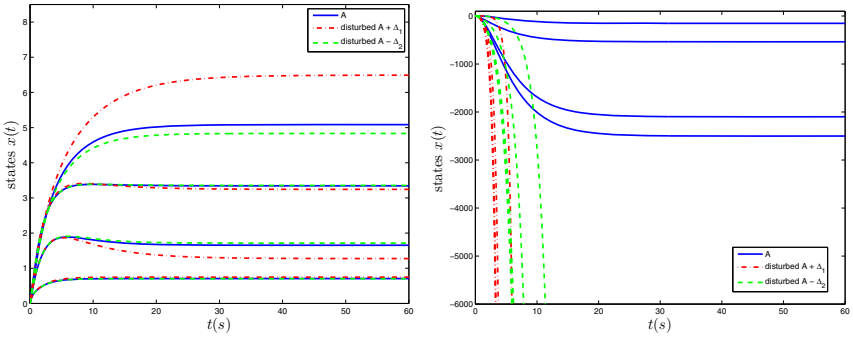

Fig. 5. Transient behaviors of the unperturbed and perturbed eigensystems with optimal K and feasible K' in Example 2

$\Delta_2 = 0.0048A^T$, which both satisfied with eqn. (12). In Fig. 5, the solid lines illustrate the state variables corresponding to A without any perturbation, the dashed lines to $A-\Delta_1$, and the dotted lines to $A+\Delta_2$ with the perturbation, controlled with optimal K, where the initial value of x_0 is zero and the reference input is a step vector. From Fig. 5. a, we can see that the state variables are stable within $60s$. In contrast, for state feedback control with exactly the same closed-loop poles and same perturbations Δ_1 or Δ_2 using the following feedback gain matrix without optimal conditioning K', the state variables of the perturbed eigensystem with $A-\Delta_1$ or $A+\Delta_2$ are no longer stable as shown in Fig. 5. b.

$$K' = \begin{bmatrix} -49.0855 & -4.2600 & -37.8612 & 35.7530 \\ -9.2461 & -1.0275 & -7.5757 & 7.5744 \end{bmatrix},$$

5 Conclusions

In this paper, a novel neurodynamic approach is proposed for the synthesis of linear state feedback control systems via robust pole assignment. By the reformulation from a quasi-convex measure; i.e., the spectral condition number, into a convex feasibility problem, the proposed approach is capable of robustness optimization. The performance and characteristics of the neurodynamic approach are substantiated by using a benchmark problem. Neurodynamics-based robust pole assignment also shows great potential to extend into linear descriptor systems and linear parameter-varying systems.

References

1. Byers, R., Nash, S.G.: Approaches to robust pole assignment. International J. Control 49(1), 97–117 (1989)
2. Chu, E.K.: Pole assignment via the schur form. Systems & Control Letters 56(4), 303–314 (2007)

3. Ho, D.W., Lam, J., Xu, J., Tam, H.K.: Neural computation for robust approximate pole assignment. Neurocomputing 25(1), 191–211 (1999)
4. Hopfield, J.J., Tank, D.W.: Neural computation of decisions in optimization problems. Biological Cybernetics 52(3), 141–152 (1985)
5. Hu, S., Wang, J.: A gradient flow approach to on-line robust pole assignment for synthesizing output feedback control systems. Automatica 38(11), 1959–1968 (2002)
6. Hu, X., Wang, J.: Solving pseudomonotone variational inequalities and pseudoconvex optimization problems using the projection neural network. IEEE Trans. Neural Networks 17(6), 1487–1499 (2006)
7. Hu, X., Wang, J.: Design of general projection neural networks for solving monotone linear variational inequalities and linear and quadratic optimization problems. IEEE Trans. Systems, Man, and Cybernetics, Part B 37(5), 1414–1421 (2007)
8. Jiang, D., Wang, J.: Augmented gradient flows for on-line robust pole assignment via state and output feedback. Automatica 38(2), 279–286 (2002)
9. Kautsky, J., Nichols, N.K., Van Dooren, P.: Robust pole assignment in linear state feedback. International J. Control 41(5), 1129–1155 (1985)
10. Kennedy, M.P., Chua, L.O.: Neural networks for nonlinear programming. IEEE Trans. Circuits and Systems 35(5), 554–562 (1988)
11. Lam, J., Van, W.Y.: A gradient flow approach to the robust pole-placement problem. International J. Robust and Nonlinear Control 5(3), 175–185 (1995)
12. Le, X., Wang, J.: Neurodynamic optimization approaches to robust pole assignment based on alternative robustness measures. In: Proc. Interntional Joint Conference on Neural Networks (2013)
13. Le, X., Wang, J.: Robust pole assignment for synthesizing feedback control systems using recurrent neural networks. IEEE Trans. Neural Networks and Learning Systems (in press, 2013)
14. Liu, Q., Wang, J.: A one-layer recurrent neural network with a discontinuous hard-limiting activation function for quadratic programming. IEEE Trans. Neural Networks 19(4), 558–570 (2008)
15. Liu, Q., Wang, J.: A one-layer recurrent neural network for constrained nonsmooth optimization. IEEE Transactions on Systems, Man, and Cybernetics, Part B: Cybernetics 41(5), 1323–1333 (2011)
16. Oja, E.: Neural networks, principal components, and subspaces. Int. J. Neural Systems 1(1), 61–68 (1989)
17. Rami, A.M., El Faiz, S., Benzaouia, A., Tadeo, F.: Robust exact pole placement via an lmi-based algorithm. IEEE Trans. Automatic Control 54(2), 394–398 (2009)
18. Soh, Y.C., Evans, R.J., Petersen, I.R., Betz, R.E.: Robust pole assignment. Automatica 23(5), 601–610 (1987)
19. Tang, Y., Li, J.: Notes on recurrent neural network model for computing largest and smallest generalized eigenvalue. Neurocomputing 73(4), 1006–1012 (2010)
20. Tits, A.L., Yang, Y.: Globally convergent algorithms for robust pole assignment by state feedback. IEEE Trans. Automatic Control 41(10), 1432–1452 (1996)
21. Xia, Y., Wang, J.: A general methodology for designing globally convergent optimization neural networks. IEEE Trans. Neural Networks 9(6), 1331–1343 (1998)
22. Xia, Y., Wang, J.: A general projection neural network for solving monotone variational inequalities and related optimization problems. IEEE Trans. Neural Networks 15(2), 318–328 (2004)
23. Xia, Y., Wang, J.: A recurrent neural network for nonlinear convex optimization subject to nonlinear inequality constraints. IEEE Trans. Circuits and Systems I 51(7), 1385–1394 (2004)
24. Xia, Y., Wang, J.: A recurrent neural network for solving nonlinear convex programs subject to linear constraints. IEEE Trans. Neural Networks 16(2), 379–386 (2005)

sEMG Based Joint Angle Estimation of Lower Limbs Using LS-SVM

Qingling Li[1,*], Yu Song [2], Zengguang Hou[3], and Bin Zhu[1]

[1] Department of Mechanical Engineering,
China University of Mining & Technology, Beijing, China
doudouhit@163.com, xcumtzhubin@126.com
[2] School of Electronic & Information Engineering,
Beijing Jiaotong University, Beijing, China
songyu@bjtu.edu.cn
[3] State Key Laboratory of Management and Control for Complex Systems
Institute of Automation, Chinese Academy of Science,Beijing, China
hou@compsys.ia.ac.cn

Abstract. In this paper, a new estimation model based on least squares support vector machine (LS-SVM) is proposed to build up the relationship between Surface electromyogram (sEMG) signal and joint angle of the lower limb. The input of the model is 2 channels of preprocessed sEMG signal. The outputs of the model are joint angles of the hip and the knee. sEMG signal is acquired from 7 motion muscles in treadmill exercise. And two channels of them are selected for dynamic angle estimation for their strong correlation with angle data. Angle estimation model is constructed by 2 independent LS-SVM based regression model with radial basis function (RBF). It is trained using part of the sample sets acquired in 10s exercise duration and test by all data. Experimental result shows proposed method has good performance on joint angles estimation based sEMG. Root mean square error (RMSE) of prediction knee and hip joint angles is 3.02° and 2.09° respectively. It provide new human-machine interface for active rehabilitation training of SCI, stroke or neurological injury patients.

Keywords: sEMG, LS-SVM, Angle estimation, Rehabilitation.

1 Introduction

SEMG is the weak electrical potential recorded by electrodes from the skin. It reflects muscle activity and function accurately and objectively. sEMG has been widely used in clinical rehabilitation and sport science fields for neuromuscular disorders diagnosis and fatigue analysis. Especially in clinical rehabilitation fields, for its strong relationship with human autonomous motions, sEMG is taken as a non-invasive control means for human-machine interface devices such as prosthesis, rehabilitation robot, power assist exoskeleton. Its application greatly enhances the convenience and efficiency of these rehabilitation systems and helps reconstruct neuromuscular function for people affected by stroke and spinal cord injury (SCI).

M. Lee et al. (Eds.): ICONIP 2013, Part I, LNCS 8226, pp. 292–300, 2013.
© Springer-Verlag Berlin Heidelberg 2013

Clinical rehabilitation system is divided into three types: mechanical assistant devices, power feedback system and biofeedback system. Traditional mechanical rehabilitation assistance devices provide passive exercises for patients without feedback such as continuous passive motion machine. In some newly developed systems, human motion and force information are introduced as control signal. They are called power feedback system such as Lokomat [1], MIT-manus [2], MIME [3]. The last one take bio-information especially sEMG as control signal in order to excite patients' autonomous motions and promote nerve repair and regeneration. For the better effects of reconstruct motion function for patients, it arouses many researchers' interests.

In the biofeedback system, the key issue that researchers focus on is how to capture human active motion intention from sEMG signals. At present, human motion researches based on sEMG signal are divided into qualitative and quantitative analysis. The typical application of the former is motion recognition [4] [5]. Many researchers have been engaged in higher accuracy and fewer channels for qualitative motion recognition based on sEMG signal and gained remarkable achievements.

With further application research of human-machine interface (HMI) based on sEMG signal, quantitative sEMG analysis is expected to supply continuous real-time control. Javad Hashemi et al. proposed a calibration method for the amplitude of the sEMG signals collected from biceps brachii at different joint angles [6]. In Jimson's study, the parameters of muscle activation model considered electromechanical delay was taken as the input of neural network to predict finger joint angles. Results showed correlation as high as 0.92 between the actual and predicted metacarpophalangeal joint angles for periodic finger flexion movements and 0.85 for non-periodic movements [7]. In order to suppress pathological tremor effectively by exoskeleton system, Shengxin Wang et al. extracted the linear profile-curve of sEMG, and explored the relationship between sEMG signals and angle with the radial basis function neural network [8]. In many other researches, various feature extraction and classification methods are applied to quantitative analysis for sEMG signal. The essence of these researches is to capture human active motion intention from sEMG signal, and then supply continuous and real-time motion control information for assist devices.

With successful application of quantitative analysis for sEMG, there are still some disadvantages. Estimation accuracy of continuous variable is the key problem for motion control of assistant devices, and it is very important for natural motion of subjects. In this research, sEMG signals acquired from normal lower limb are used to estimate continuously hip and knee joint angle, which will be taken as control instruction for rehabilitation robot for the affected lower limb. Because in clinic, almost all persons affected by stroke or SCI have clinical manifestation of hemiplegia in varying degrees. That means unilateral limb injury for the patient. Therefore, rehabilitation training of the affected limb controlled by the normal limb is feasible and effective. It has been verified by many related researches. Continuous estimation of lower limb joint angle with high accuracy is the core of this rehabilitation strategy and also what we interested in. It contains two main key technologies, that is feature extraction meof sEMG signals for data compression and estimation algorithm for joint angles. In the following content, sEMG data acquisition and preprocess, estimation model design and experimental results will be explained in detail.

2 Methods

2.1 Data Acquisition

Treadmill exercise is a common training movement for SCI and stroke patients in clinical rehabilitation. Considering the character of unilateral injury, data were acquired from a normal volunteer in a gymnasium. As shown in Fig 1, during the treadmill exercise, sEMG signals of 7 lower limb muscles including vastus rectus muscle (VR), vastus lateralis muscle (VL), semitendinosus muscle (SM), biceps muscle of thigh (BM), tibialis anterior muscle (TA), extensor pollicis longus (EP), and gastrocnemius muscle (GM) were sampled with frequency of 2000Hz by Flexcomp, which is the production of Thought Technology Ltd., Canada. 7 pairs of Ag/Agcl electrode with glue solution were sticked on muscle belly with a distance of 2cm, where the signal amplitude is up to the maximum. sEMG is easily disturbed by environmental noise, some preparations including shaving and cleaning the skin surface should be done before experiment. The raw sEMG signal contains noise and a large amount of data. Before applying for angle estimation it must be preprocessed with the following procedure.

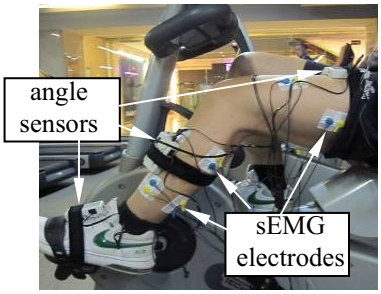

Fig. 1. sEMG and joint angle signal acquirement in treadmill exercise

2.2 Signal Processing

sEMG signal is very weak, non-stationary and random. It is easy to be disturbed by industrial frequency and the other environmental noise. It must de-noise and preprocess for further application. The power spectrum of electromyography mainly concentrates between 20Hz to 500Hz. Conseuquently, a notch filter with 50Hz (industrial frequency of 50Hz in China), a band-pass filter with low cut-off frequency of 20Hz and the high of 500Hz and DC component elimination are applied to the raw sEMG. sEMG after primary de-noising is sent to following two process steps:

(1) Integral absolute value (IAV) sEMG is taken as zero mean Gaussian distribution in time domain. Its amplitude is random and vibrates frequently across zero. IAV method describes the envelop characters of sEMG as

$$sEMG_I(n) = \frac{1}{W} \cdot \sum_{i=n\cdot(W-1)+1}^{n\cdot W} \left| sEMG(i) \right| \tag{1}$$

where $sEMG_I(n)$ is IAV of de-noised sEMG on the interval $i \in [W \cdot (n-1)+1, W \cdot n]$. As mentioned above, the sampling frequency of 2000Hz is higher than that of joint angle 100Hz. The integral window width is set to 20 in experiment to synchronize the frequency of sEMG and joint angle.

(2) The envelop of the sEMG signals get from last step still vibrates very much. Actually amplitude of sEMG reflects the contract level of corresponding muscle. And joint angle variation is the result of muscle contraction. So a two order low-pass Butterworth filter with cut-off frequency of 5Hz is used for data smoothing. Fig.2 shows comparison figure of raw and preprocessed sEMG signal of each muscle. The output data is applied directly for subsequent multi-joint angles estimation of lower limb.

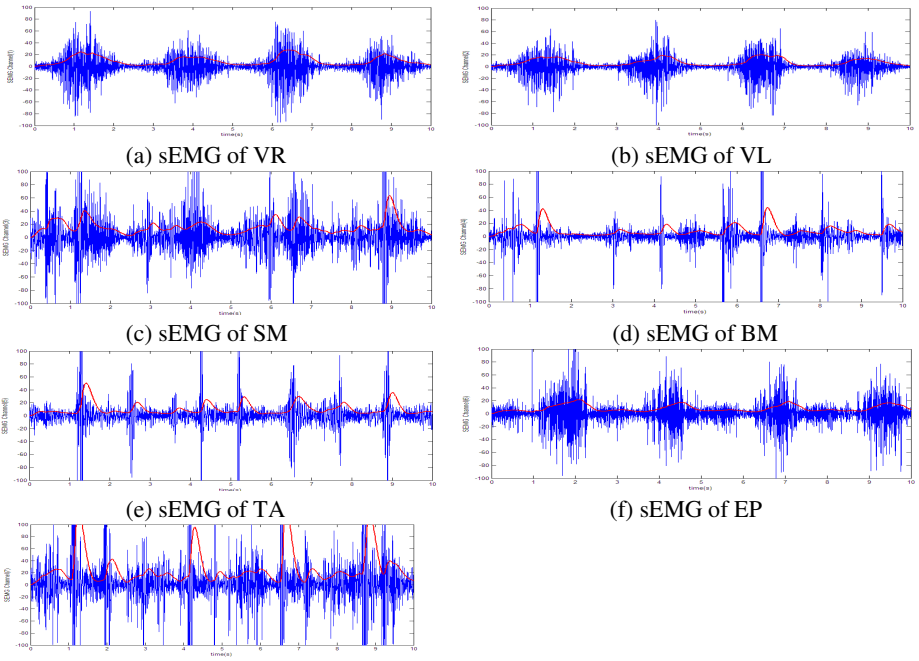

(a) sEMG of VR (b) sEMG of VL

(c) sEMG of SM (d) sEMG of BM

(e) sEMG of TA (f) sEMG of EP

(g) sEMG of GM

Fig. 2. Raw and envelop sEMG signal of 7 channels muscles in treadmill exercises

2.3 Joint Angles Estimation

2.3.1 Least Squares Support Vector Machines (LS-SVM)

Support vector machine (SVM), the most young and practical machine learning algorithm was proposed by Vapnik and his co-workers. It has been paid wide attention in recent years for merits of small classification and approximation error, simple mathematical forms and excellent generalization performance. So it is widely

used for pattern recognition and function regression.LS-SVM is an improvement model of SVM. In the model, the inequality constraint conditions are replaced by equality constraints. Consequently, quadratic programming problem was simplified as the problem of solving linear equation groups. It simplifies the complexity of calculation and accelerates solving process.

In this research, joint angle estimation based on sEMG can be regarded as a function regression problem or function fitting. That means obtaining an optimal function as follow for mapping relationship between x and y for given training set $(x_1, y_1)\ldots(x_l, y_l)$:

$$f(x) = w^{\mathrm{T}}\varphi(x) + b \tag{2}$$

where $\varphi(x)$: $R^n \to R^m$ is the nonlinear mapping from input space to high-dimension feature space. It can translate nonlinear regression to the linear. LS-SVM regression algorithm can be described solving following constraint optimization problem:

$$\text{Minimize}\quad J(w,e) = \frac{1}{2}w^{\mathrm{T}}w + \frac{1}{2}\gamma\sum_{i=1}^{L} e_i^2 \tag{3}$$

with constraint condition $y_i = w^{\mathrm{T}}\varphi(x) + b + e_i$, $i = 1,\cdots,L$, where w is the weight variable, e is the error variable, b is the offset and γ is penalty factor. Lagrange function is defined as

$$L(w,b,e,\alpha) = J(w,e) - \sum_{i=1}^{L}\alpha_i\left\{w^{\mathrm{T}}\phi(x) + b + e_i - y_i\right\} \tag{4}$$

where α_i is the Lagrange multiplier. According to KKT conditions, Derivatives of $L(w,b,e,\alpha)$ with respect to w,b,e,α respectively is set to be 0 to get

$$\begin{cases} \dfrac{\partial L}{\partial w} = 0 \to w = \sum_{i=1}^{L}\alpha_i\varphi(x_i) \\ \dfrac{\partial L}{\partial b} = 0 \to \sum_{i=1}^{N}\alpha_i = 0 \\ \dfrac{\partial L}{\partial e} = 0 \to \alpha_i = \gamma e_i, \\ \dfrac{\partial L}{\partial \alpha} = 0 \to w^{\mathrm{T}}\varphi(x_i) + b + e_i - y_i = 0 \end{cases} \quad ,i = 1,\cdots,L \tag{5}$$

Let kernel function $K(x_i,x_j) = \varphi(x_i)\varphi(x_j)$, the optimal problem mentioned above is replaced by solving linear equations

$$\begin{bmatrix} 0 & 1 & \cdots & 1 \\ 1 & K(x_i,x_j) + 1/\gamma & \cdots & K(x_i,x_j) \\ \vdots & \vdots & \ddots & \vdots \\ 1 & K(x_i,x_j) & \cdots & K(x_i,x_j) + 1/\gamma \end{bmatrix}\begin{bmatrix} b \\ \alpha_1 \\ \vdots \\ \alpha_l \end{bmatrix} = \begin{bmatrix} 0 \\ y_1 \\ \vdots \\ y_l \end{bmatrix} \quad ,i,j = 1,\cdots,L \tag{6}$$

Lagrange multiplier α_i and the offset b is solved from equation (6) and taken into $w = \sum_{i=1}^{L}\alpha_i\varphi(x_i)$ to get fitting function of training set as

$$f(x)=\sum_{i=1}^{L}\alpha_k K(x_i,x_j)+b \tag{7}$$

2.3.2 Design of Regression Model

Processing result of 7 channels sEMG signal by IAV and Butterworth smoothing is shown in Fig. 2. Angle data of the hip and knee joint in Fig. 3 has a periodic change for treadmill motion. By comparing the waveform changes, it is obvious that sEMG signal of each muscle has different performance of correlation with joint angle data for treadmill motion. sEMG of VR and VL is strong correlation with angle data. sEMG of EP has some correlation with angle variation and sEMG of SM, BM, TA and GM has low correlation with angle. Accordingly, sEMG of VR and VL is utilized as the input of SVM and joint angle of the hip and knee as the output y.

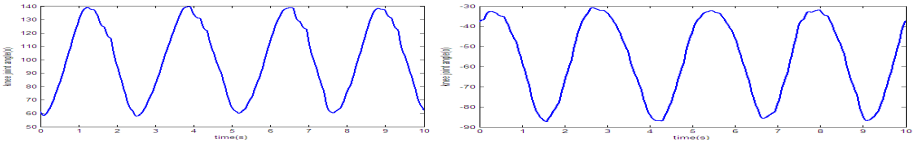

(a) Angle of the knee joint (b) Angle of the hip joint

Fig. 3. Measured joint angle of the lower limb in treadmill exercises

In order to make full use of dynamic information of sEMG amplitude, a m-order model is proposed to describe the relationship of sEMG and joint angles of lower limb. That means joint angle y_k in a moment is thought be determined by sEMG signal from the present to the next follow m-k moment $\{x_k, x_{k-1},...,x_{k-m}\}$. The nonlinear relationship between sEMG and joint angles is described as

$$y_k = f(x_k, x_{k-1},...,x_{k-m}) \tag{8}$$

In experiments, two channels sEMG data strong correlated with joint angle are used to construct the input of SVM and *m* is set to 10. As a result, the input dimension of regression is 20, which is expressed as

$$x_k=\left[sEMG_k^{VR},sEMG_{k-1}^{VR},\ldots sEMG_{k-10}^{VR},sEMG_k^{VL},sEMG_{k-1}^{VL},\ldots sEMG_{k-10}^{VL}\right]^{\mathrm{T}}\in R^{20\times 1} \tag{9}$$

The output of LS-SVM is two channels joint angle, which is

$$y_k=\left[\theta_k^{Knee},\theta_k^{Hip}\right]^{\mathrm{T}}\in R^{2\times 1} \tag{10}$$

LS-SVM based regression model consists of two independent LS-SVMs. As Fig. 4, where LSSVM(1) maps nonlinear relationship between sEMG and the knee joint angle, and LSSVM(2) maps the relationship between sEMG and the hip joint angle.

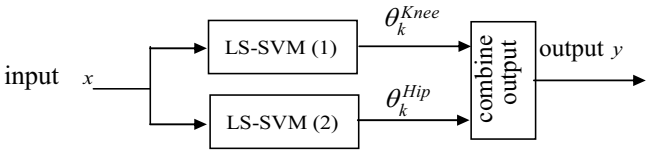

Fig. 4. The structure of LS-SVM based regression model

2.3.3 Joint Angle Estimation

Sampling frequency of sEMG after IAV preprocessing mentioned in section 2.2 is changed to 100Hz. As a result, preprocessed sEMG has the same frequency as joint angle. The sampling process lasts 10 seconds. Acquired 1000 sets of sEMG-joint angle data are sent to 10-order model (eq.9) for final 991 couples data, from which 198 couples are extracted every 5 data as training sample. All 991 sets are used to test performance of proposed LS-SVM regression model.

In this paper, Coarse-fine search with cross validation is used to determine two unknown parameters in LS-SVM, σ and γ. Search range of the kernel parameter σ^2 and penalty factor γ is set to [0.08， 12] and [0.05， 200] respectively. The logarithmic scale is employed for the parameter space (Fig.5). Each is linearly divided into 10 parts. 100 intersections of corresponding grid lines are set to the test point of parameters. On each point, cross validation method is applied to test the performance of LS-SVM. The specific steps are: All samples are randomly divided into 10 parts. 9 of them are for training and the rest is for regression performance testing. After 10 times of training and testing sets transforming for each couple kernel parameters, regression performance is evaluated by mean squared error of 10 times of test result called cross validate rate. As shown in Fig.5, grid points of coarse search for kernel parameters are highlighted with black " • ". Error contour of cross validation rate describes different parameter performance and determines the scope of optimum parameters. Based on the result, the search range is reset for fine search. Grid point is highlighted with "×" in Fig. 5. Its number is still 100 and the search process is the same as cross validation method. The result of optimum parameters are listed in table 1. Then, all 198 samples are used to calculate their Lagrange multiplier α and unknown parameter b.

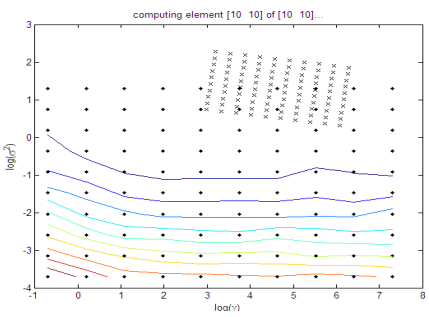

(a)Parameter optimization of LS-SVM(1),

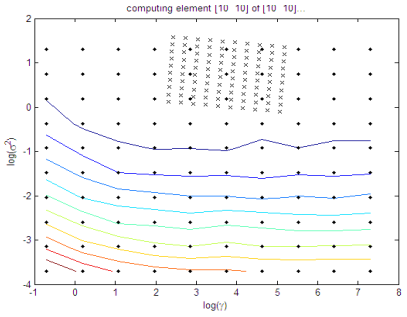

(b)Parameter optimization of LS-SVM(2)

Fig. 5. Parameter optimization process of two independent LS-SVM

Table 1. Parameters of LS-SVM based regression model

Parameter	LS-SVM(1)	LS-SVM(2)
kernel parameter σ^2	6.197982	1.45296
penalty factor γ	187.2391	25.8838

In order to test performance of the trained LS-SVM regression model, two channels of sEMG data are sent into the model to estimate joint angle of the hip and the knee. Fig.6 shows good contact ratio between prediction and measured angle data. Root mean square error (RMSE) is calculated to quantitatively analyze performance:

$$RMSE = \sqrt{\frac{1}{N-1}\sum_{k=1}^{N}\left(\bar{\theta}_k - \theta_k\right)^2} \tag{11}$$

where $\bar{\theta}_k$ and θ_k is estimated and measured joint angle, N is test samples number .

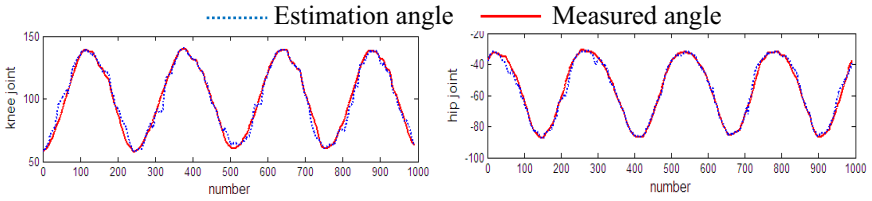

(a)The knee joint angle estimation (b)The hip joint angle estimation

Fig. 6. sEMG based continuous joint angle estimation in treadmill exercise using LS-SVM

The outputs of estimation model based on LS-SVM are the hip joint angle and the knee joint angle. In experiment, the RMSE of prediction knee joint angle with the proposed model is 3.02° , and that of estimation hip joint angle is 2.09° .

3 Conclusions and Discussions

sEMG signal directly reflects human active motion intention, it is the best human-machine interface for active rehabilitation training of SCI, stroke or neurological injury patients. In this paper, we use LS-SVM to predict dynamic joint angle of the lower limb from sEMG signals. The input of the model derives from 7 Channels sEMG of lower limb muscles in treadmill exercise. Considering the data dimension of the input and correlation between sEMG and joint angle, sEMG of VR and VL after preprocess of de-noising, envelop calculation and filtering is selected for joint angle estimation. Finalized input of estimation model is a 20 dimensions processed sEMG and the output is two joint angles of the hip and the knee. Estimation model is constructed by 2 independent LS-SVM based regression model. Parameters of the established LS-SVM model are determined after the coarse and fine search. Statistics result of angle estimation using proposed method is represented with RMSE of prediction angle. That of the knee and the hip joint angle is 3.02° and 2.09°

respectively. This model based LS-SVM can successfully judge human motion intention and accurately estimate joint angle of the limb by using sEMG. It can provide new control strategy for rehabilitation robot or other motion assist devices.

Acknowledgments. This research is supported in part by the National Natural Science Foundation of China (Grants #61005070 and #61175076) and the Fundamental Research Funds for the Central Universities (Grant #2012QJ01)

References

1. Mayr, A., Kofler, M., Quirbach, E., et al.: Prospective, blinded, randomized crossover study of gait rehabilitation in stroke patients using the Lokomat gait orthosis. Neurorehabilitation and Neural Repair 21(4), 307–314 (2007)
2. Krebs, H.I., Volpe, B.T., Aisen, M.L., et al.: Increasing productivity and quality of care: Robot-aided neuro-rehabilitation. Journal of Rehabilitation Research and Development 37(6), 639–652 (2000)
3. Lum, P.S., Burgar, C.G., Van der Loos, H.F.M., et al.: The MIME robotic system for upper-limb neuro-rehabilitation: results from a clinical trial in subacute stroke. In: Proceeding of the 9th IEEE International Conference on Rehabilitation Robotics, pp. 511–514 (2005)
4. Ando, T., Okamoto, J., Fujie, M.G.: Optimal Design of a Micro Macro Neural Network to Recognize Rollover Movement. In: IEEE/RSJ International Conference on Intelligent Robots and Systems (2009 IEEE IROS), pp. 1615–1620 (2009)
5. Kim, J., Mastnik, S., André, E.: EMG-based hand gesture recognition for real-time biosignal interfacing. In: The 13th International Conference on IUI, pp. 30–39 (2008)
6. Hashemi, J., Morin, E., Mousavi, P., Hashtrudi-Zaad, K.: Joint Angle-based EMG Amplitude Calibration. In: The 33rd Annual International Conference of the IEEE EMBS, pp. 4439–4442 (2011)
7. Ngeo, J., Tamei, T., Shibata, T.: Continuous Estimation of Finger Joint Angles using Muscle Activation Inputs from Surface EMG Signals. In: The 34th Annual International Conference of the IEEE EMBS, pp. 2756–2759 (2012)
8. Wang, S., Gao, Y., Zhao, J., Yang, T., Zhu, Y.: Prediction of sEMG-Based Tremor Joint Angle Using the RBF Neural Network. In: Proceeding of 2012 IEEE International Conference on Mechatronics and Automation, pp. 2103–2108 (2012)

Optimal Proposal Distribution FastSLAM with Suitable Gaussian Weighted Integral Solutions

Qingling Li[1,*], Yu Song[2], ZengGuang Hou[3], and Bin Zhu[1]

[1] Department of Mechanical Engineering,
China University of Mining & Technology, Beijing, China
doudouhit@163.com, xcumtzhubin@126.com
[2] School of Electronic & Information Engineering, Beijing Jiaotong University, Beijing, China
songyu@bjtu.edu.cn
[3] Institute of Automation, Chinese Academy of Science, Beijing, China
hou@compsys.ia.ac.cn

Abstract. One of the key issues in Gaussian SLAM is to calculate nonlinear transition density of Gaussian prior, i.e. to calculate Gaussian Weight Integral (GWI) whose integrand is with the form *nonlinear function*×*Gaussian prior density*. Up to now, some GWI solutions have been applied in SLAM (e.g. linearization, unscented transform and cubature rule), and different SLAM algorithms were derived based on theirs GWI solutions. While, how to select suitable GWI solution for SLAM is still lack of theoretical analysis. In this paper, we proposed an optimal proposal FastSLAM algorithm with suitable GWI solutions. The main contributions of this work lies that: (1) an unified FastSLAM framework with optimal proposal distribution is summarized; (2) a SLAM dimensionality based GWI solution selection criterion is designed; (3) we propose a new SLAM algorithm. The performance of the proposed SLAM is investigated and compared with the FastSLAM2.0 and UFastSLAM using simulations and our opinion is confirmed by the results.

Keywords: Mobile Robot, SLAM, Unscented Transform, Cubature Rule.

1 Introduction

The Rao-Blackwellized particle filter (RBPF) [1] based SLAM algorithm was introduced by Montemerlo in 2003. Now it has became popular in SLAM due to its low computational cost and robustness for incorrect data association. The algorithm has two editions: FastSLAM1.0 [2] and FastSLAM2.0 [3]. The former utilizes common particle filter to track robot path, and each particle independently keeps a feature landmark map based on a set of EKFs. To overcome particle set degeneracy in FastSLAM1.0, the FastSLAM2.0 utilizes EKF to design better proposal distribution. Based on the similar idea, Gristti proposed an adaptive grid map FastSLAM [4]. The technique combines laser scan-matching with mobile robot odometry to optimize the proposal distribution

* Corresponding author.

M. Lee et al. (Eds.): ICONIP 2013, Part I, LNCS 8226, pp. 301–309, 2013.
© Springer-Verlag Berlin Heidelberg 2013

of particle filter. Sim proposed a stereo vision FastSLAM, and the particle proposal distribution was designed by using visual odometery prior [5]. Kim proposed Unscented FastSLAM [6], which utilizes scaled unscented transformation [7][8] to estimate the nonlinear transition density of Gaussian prior. In [9], a non-static environment FastSLAM was proposed by sampling new generation particles from multiple ancestor priors. Moreno designed a new approach to fuse the grid-map and feature-map for FastSLAM [10]. In our previous work, a Cubature FastSLAM [11] was derived by utilizing cubature rule [12] as the Gaussian weighted integral solutions.

One of the key issues in Gaussian SLAM is to calculate nonlinear transition density of Gaussian prior, i.e., to calculate Gaussian Weight Integral (GWI). Up to now, some GWI solutions have been applied in SLAM filter. While, how to choose a suitable GWI solution for SLAM is still lack of theoretical analysis. In this paper, the GWI solution selection problem is discussed and a new SLAM with better GWI solution is derived. The rest paper is organized as follows: Section 2 gives a brief review of FastSLAM and a unified optimal proposal FastSLAM is summarized. A GWI solution selection criterion is discussed in Section 3. In Section 4 we proposed a SLAM algorithm with suitable GWI solutions. Section 5 presents simulations, followed by the conclusions.

2 Unified FastSLAM with Optimal Proposal

2.1 Brief Review of FastSLAM

The key idea of FastSLAM is to estimate the joint posterior $p(\boldsymbol{s}^k, \boldsymbol{\Theta} | \boldsymbol{z}^k, \boldsymbol{u}^{k-1})$ about the map $\boldsymbol{\Theta} = \boldsymbol{\theta}_1 \cdots \boldsymbol{\theta}_M$ and the mobile robot path $\boldsymbol{s}^k = \boldsymbol{s}_1 \cdots \boldsymbol{s}_k$ based on a set of observations $\boldsymbol{z}^k = \boldsymbol{z}_1 \cdots \boldsymbol{z}_k$ and control inputs $\boldsymbol{u}^{k-1} = \boldsymbol{u}_0 \cdots \boldsymbol{u}_{k-1}$. Based on conditional independence property of the full SLAM problem, the joint posterior $p(\boldsymbol{s}^k, \boldsymbol{\Theta} | \boldsymbol{z}^k, \boldsymbol{u}^{k-1})$ is factored as

$$p(\boldsymbol{s}^k, \boldsymbol{\Theta} | \boldsymbol{z}^k, \boldsymbol{u}^{k-1}) = p(\boldsymbol{s}^k | \boldsymbol{z}^k, \boldsymbol{u}^{k-1}) \cdot \prod_{m=1}^{M} p(\boldsymbol{\theta}_m | \boldsymbol{s}^k, \boldsymbol{z}^k, \boldsymbol{u}^{k-1}) \tag{1}$$

In FastSLAM, the path posterior $p(\boldsymbol{s}^k | \boldsymbol{z}^k, \boldsymbol{u}^{k-1})$ is estimated with a particle filter and the map $p(\boldsymbol{\Theta} | \boldsymbol{s}^k, \boldsymbol{z}^k, \boldsymbol{u}^{k-1})$ is analytically estimated utilizing M separate Kalman filters. Each particle for the FastSLAM is assembled by the robot path and the landmarks:

$$\boldsymbol{S}_k^{[i]} = < \boldsymbol{s}^{k,[i]}, \left(\boldsymbol{\mu}_k^{[i][1]}, \boldsymbol{\Sigma}_k^{[i][1]}\right) \cdots \left(\boldsymbol{\mu}_k^{[i][M]}, \boldsymbol{\Sigma}_k^{[i][M]}\right) > \tag{2}$$

where, $[i]$ and $[m]$ are indicate index of the particle and the landmark; $\boldsymbol{s}^{k[i]}$ is robot path hypothesis; $(\boldsymbol{\mu}_k^{[i][m]}, \boldsymbol{\Sigma}_k^{[i][m]})$ is the Gaussian representation of the mth feature landmark.

2.2 Unified FastSLAM Framework with Optimal Proposal

The noisy robot motion model and environment observation motion model are

$$\begin{cases} \boldsymbol{s}_k = f\left(\boldsymbol{s}_{k-1}, \boldsymbol{u}_{k-1} + \boldsymbol{\delta u}_{k-1}\right) \\ \boldsymbol{z}_k = h\left(\boldsymbol{s}_k, \boldsymbol{\mu}_{k-1}^{[m]}\right) + \boldsymbol{\delta z}_k \end{cases} \tag{3}$$

where, $\boldsymbol{s}_k \in \mathbb{R}^{n_s}$ is the robot pose; $\boldsymbol{z}_k \in \mathbb{R}^{n_z}$ is the observation; f and h are the nonlinear robot motion and observation model, respectively; $\boldsymbol{u}_{k-1} \in \mathbb{R}^{n_u}$ is the control input in the

time interval $[k-1,k)$, $\boldsymbol{\delta u}_{k-1} \in \mathbb{R}^{n_u}$ is control noise with covariance $\boldsymbol{Q}$; $\boldsymbol{\delta z}_{k-1} \in \mathbb{R}^{n_z}$ is observation noise with covariance $\boldsymbol{R}$; $\boldsymbol{\mu}_{k-1}^{[m]} \in \mathbb{R}^{n_\mu}$ is the $[m]$-th landmark state.

To predict new robot state $\boldsymbol{s}_k^{[i]}$, the previous robot state $\boldsymbol{s}_{k-1}^{[i]}$ requires to be augmented with the control input, given by

$$\bar{\boldsymbol{a}} = \begin{pmatrix} \boldsymbol{s}_{k-1}^{[i]} \\ \boldsymbol{u}_{k-1} \end{pmatrix}, \boldsymbol{P}_a = \begin{pmatrix} \boldsymbol{P}_{k-1}^{[i]} & \boldsymbol{0} \\ \boldsymbol{0} & \boldsymbol{Q} \end{pmatrix} \tag{4}$$

Where, $\bar{\boldsymbol{a}} \in \mathbb{R}^{n_s+n_u}$ and $\boldsymbol{P}_a \in \mathbb{R}^{(n_s+n_u)\times(n_s+n_u)}$ are the augmented robot state and its covariance, respectively. $\boldsymbol{s}_{k-1}^{[i]} \in \mathbb{R}^{n_s}$ and $\boldsymbol{P}_{k-1}^{[i]} \in \mathbb{R}^{n_s \times n_s}$ are the previous mean and covariance of the robot state. The augmented state $\boldsymbol{a}$ satisfies Gaussian $\boldsymbol{a} \sim \mathcal{N}(\bar{\boldsymbol{a}}, \boldsymbol{P}_a)$.

Consequently, the predicted robot state and its covariance are calculated by

$$\begin{aligned} \boldsymbol{s}_{k,k-1}^{[i]} &= \int f^*(\boldsymbol{a})\, \mathcal{N}(\bar{\boldsymbol{a}}, \boldsymbol{P}_a)\, d\boldsymbol{a} \\ \boldsymbol{P}_{k,k-1}^{[i]} &= \int \left[f^*(\boldsymbol{a}) - \boldsymbol{s}_{k,k-1}^{[i]} \right] \left[f^*(\boldsymbol{a}) - \boldsymbol{s}_{k,k-1}^{[i]} \right]^{\mathrm{T}} \mathcal{N}(\bar{\boldsymbol{a}}, \boldsymbol{P}_a)\, d\boldsymbol{a} \end{aligned} \tag{5}$$

When a landmark with index $[m]$ is revisited by the robot, the robot state and its covariance can be updated. To do this, $\boldsymbol{s}_{k|k-1}^{[i]}$ and $\boldsymbol{P}_{k|k-1}^{[i]}$ are augmented by integrating the robot state and the revisited landmark state into one Gaussian, that is

$$\bar{\boldsymbol{b}} = \begin{pmatrix} \boldsymbol{s}_{k,k-1}^{[i]} \\ \boldsymbol{\mu}_{k-1}^{[i][m]} \end{pmatrix}, \boldsymbol{P}_b = \begin{pmatrix} \boldsymbol{P}_{k,k-1}^{[i]} & \boldsymbol{0} \\ \boldsymbol{0} & \boldsymbol{\Sigma}_{k-1}^{[i][m]} \end{pmatrix} \tag{6}$$

where, $\bar{\boldsymbol{b}} \in \mathbb{R}^{n_s+n_\mu}$ and $\boldsymbol{P}_b \in \mathbb{R}^{(n_s+n_\mu)\times(n_s+n_\mu)}$ are the augmented prediction state and its covariance, respectively. The density of $\boldsymbol{b}$ is Gaussian distribution $\mathcal{N}(\bar{\boldsymbol{b}}, \boldsymbol{P}_b)$.

Based on $\mathcal{N}(\bar{\boldsymbol{b}}, \boldsymbol{P}_b)$, the predicted measurement $\boldsymbol{z}_{k,k-1}^{[i][m]}$, the measurement innovation covariance $\boldsymbol{P}_{zz}^{[i][m]}$ and the cross covariance $\boldsymbol{P}_{sz}^{[i][m]}$ are calculated as

$$\begin{aligned} \boldsymbol{z}_{k,k-1}^{[i][m]} &= \int h^*(\boldsymbol{b})\, \mathcal{N}(\bar{\boldsymbol{b}}, \boldsymbol{P}_b)\, d\boldsymbol{b} \\ \boldsymbol{P}_{zz}^{[i][m]} &= \int \left[h^*(\boldsymbol{b}) - \boldsymbol{z}_{k,k-1}^{[i][m]} \right] \left[h^*(\boldsymbol{b}) - \boldsymbol{z}_{k,k-1}^{[i][m]} \right]^{\mathrm{T}} \mathcal{N}(\bar{\boldsymbol{b}}, \boldsymbol{P}_b)\, d\boldsymbol{b} + \boldsymbol{R} \\ \boldsymbol{P}_{sz}^{[i][m]} &= \int \left[[\boldsymbol{I}_{n_s \times n_s} \quad \boldsymbol{0}_{n_s \times n_\mu}] \boldsymbol{b} - \boldsymbol{s}_{k,k-1}^{[i]} \right] \left[h^*(\boldsymbol{b}) - \boldsymbol{z}_{k,k-1}^{[i][m]} \right]^{\mathrm{T}} \mathcal{N}(\bar{\boldsymbol{b}}, \boldsymbol{P}_b)\, d\boldsymbol{b} \end{aligned} \tag{7}$$

The state update is performed based on standard Kalman filtering algorithm

$$\boldsymbol{K}_s = \boldsymbol{P}_{sz}^{[i][m]} \left(\boldsymbol{P}_{zz}^{[i][m]} \right)^{-1} \qquad \begin{cases} \bar{\boldsymbol{s}}_k^{[i]} = \boldsymbol{s}_{k,k-1}^{[i]} + \boldsymbol{K}_s \left(\boldsymbol{z}_k^{[m]} - \boldsymbol{z}_{k,k-1}^{[i][m]} \right) \\ \boldsymbol{P}_k^{[i]} = \boldsymbol{P}_{k,k-1}^{[i]} - \boldsymbol{K}_s \boldsymbol{P}_{zz}^{[i][m]} \left(\boldsymbol{K}_s \right)^{\mathrm{T}} \end{cases} \tag{8}$$

where, $\boldsymbol{z}_k^{[m]}$ is the true sensor measurement for $[m]$-th revisited landmark.

For the multiple observations case, Eq.6- Eq.8 are repeated for each landmark, and $\bar{\boldsymbol{s}}_k^{[i]}$ and $\boldsymbol{P}_k^{[i]}$ are updated based on their previously updated one. When the update

routine is accomplished, the new robot state $\boldsymbol{s}_k^{[i]}$ is sampled from the Gaussian $\mathcal{N}\left(\bar{\boldsymbol{s}}_k^{[i]}, \boldsymbol{P}_k^{[i]}\right)$, and its importance factor $\omega_k^{[i]}$ is calculated as

$$\omega_k^{[i]} = \prod_m \left\{ \frac{1}{\sqrt{\left|2\pi \boldsymbol{P}_{zz}^{[i][m]}\right|}} \exp\left[-\frac{\left(\boldsymbol{z}_{k,k-1}^{[i][m]} - \boldsymbol{z}_k^{[m]}\right)^{\mathrm{T}} \left(\boldsymbol{z}_{k,k-1}^{[i][m]} - \boldsymbol{z}_k^{[m]}\right)}{2\boldsymbol{P}_{zz}^{[i][m]}} \right] \right\} \tag{9}$$

where, $\boldsymbol{z}_{k|k-1}^{[i][m]} - \boldsymbol{z}_k^{[m]}$ and $\boldsymbol{P}_{zz}^{[i][m]}$ are the measurement innovation and the innovation covariance matrix for the $[m]$-th landmark.

For each revisited landmark with index $[m]$, the landmark state equation and observation equation are modeled as

$$\begin{cases} \mathcal{N}(\boldsymbol{\mu}, \boldsymbol{\Sigma}) = \mathcal{N}\left(\boldsymbol{\mu}_{k-1}^{[i][m]}, \boldsymbol{\Sigma}_{k-1}^{[i][m]}\right) \\ \boldsymbol{z}_k^{[i][m]} = h(\boldsymbol{s}_k^{[i]}, \boldsymbol{\mu}_{k-1}^{[i][m]}) + \delta z_k \end{cases} \tag{10}$$

where, $\boldsymbol{s}_k^{[i]}$ is the "known" robot state; $\boldsymbol{\mu}_{k-1}^{[i][m]}$ and $\boldsymbol{\Sigma}_{k-1}^{[i][m]}$ are the mean and the covariance of the $[m]$-th revisited landmark, respectively.

The predicted measurement and its covariance with the known robot state are

$$\begin{aligned} \boldsymbol{z}_{k,k-1}^{*[i][m]} &= \int h\left(\boldsymbol{\mu}, \boldsymbol{s}_k^{[i]}\right) \mathcal{N}(\boldsymbol{\mu}, \boldsymbol{\Sigma}) d\boldsymbol{\mu} \\ \boldsymbol{P}_{zz}^{[m]} &= \int \left[h\left(\boldsymbol{\mu}, \boldsymbol{s}_k^{[i]}\right) - \boldsymbol{z}_{k,k-1}^{*[i][m]} \right] \left[h\left(\boldsymbol{\mu}, \boldsymbol{s}_k^{[i]}\right) - \boldsymbol{z}_{k,k-1}^{*[i][m]} \right]^{\mathrm{T}} \mathcal{N}(\boldsymbol{\mu}, \boldsymbol{\Sigma}) d\boldsymbol{\mu} + \boldsymbol{R} \\ \boldsymbol{P}_{\boldsymbol{\mu}\boldsymbol{z}}^{[m]} &= \int \left[\boldsymbol{\mu} - \boldsymbol{\mu}_{k-1}^{[i][m]} \right] \left[h\left(\boldsymbol{\mu}, \boldsymbol{s}_k^{[i]}\right) - \boldsymbol{z}_{k,k-1}^{*[i][m]} \right]^{\mathrm{T}} \mathcal{N}(\boldsymbol{\mu}, \boldsymbol{\Sigma}) d\boldsymbol{\mu} \end{aligned} \tag{11}$$

The state update of the $[m]$-th revisited landmark is accomplished by a Kalman filter

$$\boldsymbol{K}_{\mu} = \boldsymbol{P}_{\mu z}^{[m]} \left(\boldsymbol{P}_{zz}^{[m]}\right)^{-1} \qquad \begin{cases} \boldsymbol{\mu}_k^{[i][m]} = \boldsymbol{\mu}_{k-1}^{[i][m]} + \boldsymbol{K}_{\mu} \left(\boldsymbol{z}_k^{[m]} - \boldsymbol{z}_{k,k-1}^{*[i][m]} \right) \\ \boldsymbol{\Sigma}_k^{[i][m]} = \boldsymbol{\Sigma}_{k-1}^{[i][m]} - \boldsymbol{K}_{\mu} \boldsymbol{P}_{zz}^{[m]} (\boldsymbol{K}_{\mu})^{\mathrm{T}} \end{cases} \tag{12}$$

For the $[n]$-th new visited landmark, the measurement $\boldsymbol{z}_k^{[n]}$ and its covariance $\boldsymbol{R}$ are used to initialize the landmark's Gaussian representation, given by

$$\begin{aligned} \boldsymbol{\mu}_k^{[i][n]} &= \int h^{-1}\left(z, \boldsymbol{s}_k^{[i]}\right) \mathcal{N}\left(\boldsymbol{z}_k^{[n]}, \boldsymbol{R}\right) dz \\ \boldsymbol{\Sigma}_k^{[i][n]} &= \int \left[h^{-1}\left(z, \boldsymbol{s}_k^{[i]}\right) - \boldsymbol{\mu}_k^{[i][n]} \right] \left[h^{-1}\left(z, \boldsymbol{s}_k^{[i]}\right) - \boldsymbol{\mu}_k^{[i][n]} \right]^{\mathrm{T}} \mathcal{N}\left(\boldsymbol{z}_k^{[n]}, \boldsymbol{R}\right) dz \end{aligned} \tag{13}$$

3 Solutions for Gaussian Weighted Integral

Without loss generality, an unify form of the nonlinear functions in SLAM can be defined as $\boldsymbol{y} = g(\boldsymbol{x})$ with $\boldsymbol{x} \in \mathbb{R}^{n_x}$ satisfies Gaussian $\mathcal{N}(\bar{\boldsymbol{x}}, \boldsymbol{P}_x)$, then the following two GWIs are used to calculate the nonlinear transition density $\mathcal{N}\left(\bar{\boldsymbol{y}}, \boldsymbol{P}_y\right)$

$$\begin{aligned} \bar{\boldsymbol{y}} &= \int g(\boldsymbol{x}) \mathcal{N}(\bar{\boldsymbol{x}}, \boldsymbol{P}_x) d\boldsymbol{x} = \int g\left(\sqrt{\boldsymbol{P}_x}\boldsymbol{t} + \bar{\boldsymbol{x}}\right) \mathcal{N}(\boldsymbol{0}, \mathbf{I}) d\boldsymbol{t} \\ \boldsymbol{P}_y &= \int g\left(\sqrt{\boldsymbol{P}_x}\boldsymbol{t} + \bar{\boldsymbol{x}}\right) g^{\mathrm{T}}\left(\sqrt{\boldsymbol{P}_x}\boldsymbol{t} + \bar{\boldsymbol{x}}\right) \mathcal{N}(\boldsymbol{0}, \mathbf{I}) d\boldsymbol{t} - \bar{\boldsymbol{y}}(\bar{\boldsymbol{y}})^{\mathrm{T}} \end{aligned} \tag{14}$$

3.1 GWI Solutions Utilized in SLAM

1) **Linearization.** The linearization solution are utilized in FastSLAM1.0 and FastSLAM2.0, in which the GWI is calculated based on the first-order linearization of the nonlinear function g, denote as $g(\boldsymbol{x}) \approx g(\bar{\boldsymbol{x}}) + g'(\bar{\boldsymbol{x}})(\boldsymbol{x} - \bar{\boldsymbol{x}})$. And the transition density $\mathcal{N}(\bar{\boldsymbol{y}}, \boldsymbol{P}_y)$ is easily obtained by $\bar{\boldsymbol{y}} \approx g(\bar{\boldsymbol{x}})$ and $\boldsymbol{P}_y \approx g'(\boldsymbol{x})\boldsymbol{P}_x g'(\boldsymbol{x})^{\mathrm{T}}$.
2) **Unscented Transform.** In UT, $2n_x + 1$ sigma-points $\{\mathcal{X}_i\} = \{\bar{\boldsymbol{x}} \pm (\sqrt{(n_x + \kappa)\boldsymbol{P}_x})_i\}$ are utilized to capture some low-order moments of the prior Gaussian $\mathcal{N}(\bar{\boldsymbol{x}}, \boldsymbol{P}_x)$. And the transformed sigma-point set $\{\mathcal{Y}_i\}$ is computed by passing the $\{\mathcal{X}_i\}$ through the nonlinear function g, as $\{\mathcal{Y}_i = g(\mathcal{X}_i)\}$. So, $\mathcal{N}(\bar{\boldsymbol{y}}, \boldsymbol{P}_y)$ are obtained by weighted linear regression of $\{\mathcal{Y}_i\}$, given by $\bar{\boldsymbol{y}} \approx \sum \omega_c \mathcal{Y}_i$ and $\boldsymbol{P}_y \approx \sum \omega_g [\mathcal{Y}_i - \bar{\boldsymbol{y}}][\mathcal{Y}_i - \bar{\boldsymbol{y}}]^{\mathrm{T}}$.
3) **Cubature Rule.** The GWI are calculated by using $2n_x$ cubature-points, given by $\bar{\boldsymbol{y}} \approx \sum_{j=1}^{2n_x} g(\sqrt{\boldsymbol{P}_x}\boldsymbol{\xi}_j + \bar{\boldsymbol{x}}) / 2n_x$ and $\boldsymbol{P}_y \approx \sum_{j=1}^{2n_x} g(\sqrt{\boldsymbol{P}_x}\boldsymbol{\xi}_j + \bar{\boldsymbol{x}}) g^{\mathrm{T}}(\sqrt{\boldsymbol{P}_x}\boldsymbol{\xi}_j + \bar{\boldsymbol{x}}) / 2n_x - \bar{\boldsymbol{y}}\bar{\boldsymbol{y}}^{\mathrm{T}}$ .where, the cubature-point set is calculated as $\{\boldsymbol{\xi}_j\} = \sqrt{n_x}\{[1]_j\}$, and $\{[1]_j\} \in \mathbb{R}^{n_x}$ are the $2n_x$ intersection points of the n_x dimension coordinate axes with the unit hypersphere.

Table 1 and Table 2 show the moment characteristics and numerical characteristics for the three GWI solutions, respectively.

Table 1. Moment Characteristics for Different GWI Solutions

GWI Solutions	One-dimensional Gaussian case (n=1)	Multiple-dimensional Gaussian case (n>1)
Linearization	up to the 1-th order	up to the 1-th order
Unscented Transform	up to the 5-th order	up to the 3-th order
Cubature Rule	up to the 3-th order	up to the 3-th order

Table 2. Numerical Calculation Characteristics

	Numerical stbility factor		Is the $\boldsymbol{P}_y$ non-negative definite?	
	$n \le 3$	$n > 3$	$n \le 3$	$n > 3$
Unscented Transform	1	$2n/3 - 1$	yes	unsure
Cubature Rule	1	1	yes	yes

3.2 Criterion for Select Suitable GWI Solution

The UT is a dimensionality sensitive GWI solution. For the low dimensional cases ($n \le 3$), the moments of sigma-point set can hit some the 4-th order moments, and the transformed covariance is nonnegative definiteness, also the stability factor is as good as cubature rule. While, for high dimensional Gaussian cases (n>3), the transformed covariance may be negative definiteness, and the stability factor $\mathrm{S}_{\mathrm{UT}} = (2n/3) - 1$ is increased with n. Compared with UT, the cubature rule is a dimensionality insensitive

GWI solution both from moment characteristic and numerical characteristic. For any Gaussian dimensionality n, the cubature rule based GWI solution is correctly calculated up to the 3-order nonlinearity, and the non-negative definiteness of the transformed covariance can be guaranteed, also the stability factor always equal to 1. Based on above analysis, we design a dimensionality based GWI solution selection criterion: (i) for the case of dimensionality $n<3$, the UT is better than cubature rule because of partial of the fourth order moments of piror Gaussian are preserved by sigma-point set; (ii) for $n=3$, the cubature rule is equivalent to the UT; (iii) for $n>3$, cubature rule is a good choice because the transformed covariance by UT may be negative definiteness and as well the numerical stability factor is increased linearly with n for UT.

3.3 Proposed FastSLAM with Suitable GWI Solutions

From Section 2, four main parts are included in SLAM: (1) particle state prediction, (2) particle state updating, (3) revisited landmarks updating and (4) new landmarks initialization. Because each part of the algorithm has its own Gaussian dimensionality n, hence the suitable GWI solution for each part can be selected for SLAM implementation.

1) For the particle state prediction, the dimensionality of augmented robot state $\boldsymbol{a}$ is beyond three (i.e. $n_s + n_u > 3$, see Eq.4). Therefore, the cubature rule is a better GWI solution. For example, in 3D.O.F SLAM, the vehicle state is $\boldsymbol{s} = (x, y, \theta)^{\mathrm{T}}$ and the control input is comprised by velocity and steering angle. So, the dimensionality of the augmented state $\boldsymbol{a}$ is 5. For the case, the predict covariance $\boldsymbol{P}_{k,k\text{-}1}^{[i]}$ (in Eq.5) may be negative definite with UT because the weight of center sigma-point is negative $\omega_0 = -2/3 < 0$. Also, the numerical stability factor of the UT is bad due to $\mathrm{S_{UT}} = 2.33 > 1$;

2) For the particle state update part, the dimensionality of augmented robot state $\boldsymbol{b}$ is also larger than 3 (i.e. $n_s + n_\mu > 3$, see Eq.6). So, the cubature rule is selected as GWI solution with the same reasons for the first part.

3) For the revisited landmarks updating step and the new landmarks initialization step, the dimensionalities of Gaussians are determined by the landmark state $\boldsymbol{\mu}$ and the measurement $\boldsymbol{z}$, respectively. For the two steps, the UT is selected as GWI solution. There are two reasons for the utilization of UT: on one hand, the SLAM covariance matrixes are all nonnegative definiteness with UT, and the numerical stability factor is as good as cubature rule. On the other hand, the errors for the fourth order moments of the sigma-point set are smaller than that of cubature point set.

4 Simulation Results

The performance of the proposed SLAM is compared with FastSLAM2.0 and UFastSLAM. The simulation scenario is a $100\mathrm{m} \times 100\mathrm{m}$ size rectangular shaped map with 41 landmarks. For each simulation run, the robot starts with its initial state $s_0 = [0,0,0]^{\mathrm{T}}$, and then travels along six global planning points until closes the loop. Fig.1 is the result of the proposed SLAM (The measurement noise is set to be 0.1 m in range, 6° in bearing, and the control noise is set to be 0.5 m/s in velocity, 2^{o} in steering

angle). As can be seen, the robot path tracking is converged and landmarks are accurately positioned.

Two noise levels are used in simulations. With each noise level, ten independence SLAM simulation runs were carried out for each SLAM. For the first noise level, the measurement noise is set to be 0.1 m in range, 1° in bearing, and the robot control noise is set to be 0.3 m/s in velocity, 1^{o} in steering angle. As it can be seen from Fig.2, the vehicle path error of the proposed SLAM is lower than that of other two algorithms, and the landmarks are more accurately mapped by proposed SLAM. For the second noise level, the noise parameters are increased: the measurement noise is set to be 0.1 m in range, 6° in bearing, and the control noise is set to be 0.5 m/s in velocity, 2^{o} in steering angle. We can see from Fig.3, the SLAM errors for the three algorithms are increased with the noise level. And among the three algorithms, the proposed SLAM has the lowest SLAM errors both for vehicle localization and for environmental mapping.

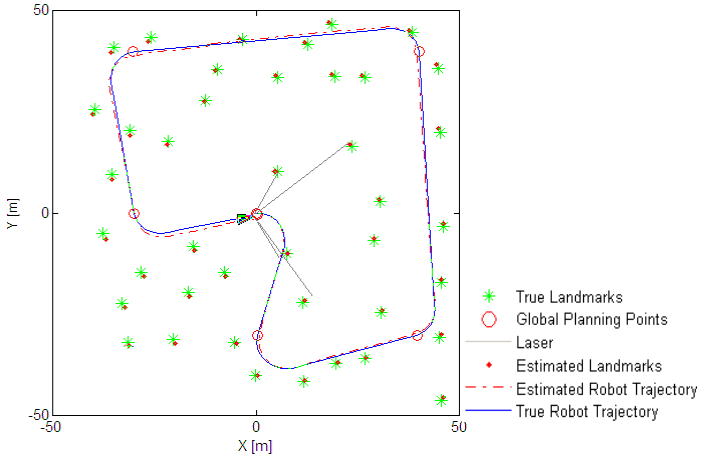

Fig. 1. Performance of the proposed SLAM

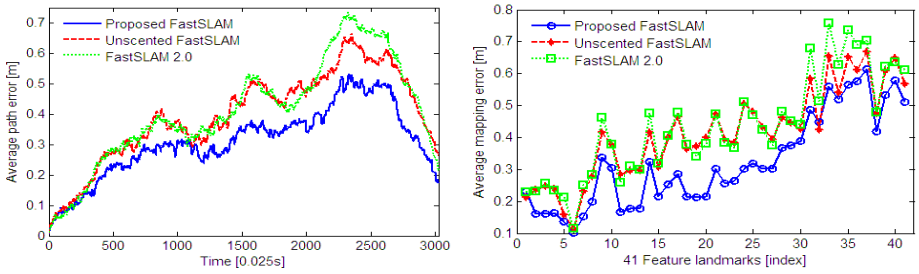

(a) Average error norm for vehicle path (b) Average error norm for 41 feature landmarks

Fig. 2. Performance evaluation for SLAM algorithms with the measurement noise is 0.1 m in range, 1° in bearing, and the control noise is 0.3 m/s in velocity, 1° in steering angle

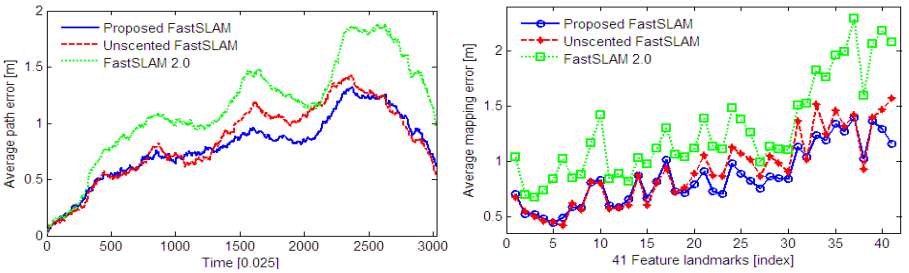

(a) Average error norm for vehicle path (b) Average error norm for 41 feature landmarks

Fig. 3. Performance evaluation for SLAM algorithms with the measurement noise is 0.1 m in range, 6° in bearing, and the control noise is 0.5 m/s in velocity, 2° in steering angle

5 Conclusion

In this paper, we proposed a new FastSLAM by choosing the suitable GWI solutions for different parts of the SLAM implementations. In proposed SLAM, the cubature rule is utilized to construct the particle filter proposal distribution and the unscented transform is used to initialize the Gaussian representations of the environment feature landmarks and to estimate the posteriors of revisited feature landmarks. The effectiveness of the proposed SLAM is verified by SLAM simulations. Results show that the proposed SLAM outperforms FastSLAM2.0 and UFastSLAM.

Acknowledgments. This research is supported by the National Nature Science Foundation of China (Grants #61005070 and #61175076).

References

1. Doucet, A., Freitas, N.D.: Rao-Blackwellised particle filtering for dynamic Bayesian networks. In: Sixteenth Conference on Uncertainty in Artificial Intelligence, pp. 176–183 (2000)
2. Montemerlo, M., Thrun, S.: Simultaneous localization and mapping with unknown data association using FastSLAM. In: IEEE International Conference on Robotics and Automation, ICRA, pp. 1985–1991 (2003)
3. Montemerlo, M., Thrun, S., Koller, D., et al.: FastSLAM2.0: an improved particle filtering algorithm for simultaneous localization and mapping that provably converges. In: Eighteenth International Joint Conference on Artificial Intelligence (IJCAI), pp. 1151–1156 (2003)
4. Grisetti, G., Stachniss, C., Burgard, W.: Improved techniques for grid mapping with Rao-Blackwellized particle filters. IEEE Transactions on Robotics (TRO) 23(1), 34–46 (2007)
5. Sim, R., Elinas, P., Little, J.: A study of the Rao–Blackwellised particle filter for efficient and accurate vision-based SLAM. International Journal on Computer Vision (IJCV) 74(3), 303–318 (2007)

6. Kim, C., Sakthivel, R., Chung, W.K.: Unscented FastSLAM: a robust and efficient solution to SLAM problem. IEEE Transactions on Robotics (TRO) 24(4), 808–820 (2008)
7. Julier, S.J., Uhlmann, J.K.: Unscented filtering and nonlinear estimation. Proceedings of the IEEE 92(3), 401–422 (2004)
8. Julier, S.J.: A new method for the nonlinear transformation of means and covariances in filters and estimators. IEEE Transactions on Automatic Control 45(3), 477–482 (2000)
9. Lee, J.S., Kim, C.: Robust RBPF-SLAM using sonar sensors in non-static environments. In: IEEE International Conference on Robotics and Automation (ICRA), pp. 250–256 (2010)
10. Moreno, L., Garrido, S., Blanco, D.: Bridging the gap between feature-and grid-based SLAM. Robotics and Autonomous Systems (RAS) 58, 140–148 (2010)
11. Song, Y., Li, Q.L., Kang, Y.F., Song, Y.D.: CFastSLAM: a new Jacobian free solution to SLAM problem. In: IEEE International Conference on Robotics and Automation (2012)
12. Arasaratnam, I., Haykin, S.: Cubature kalman filters. IEEE Transaction on Automatic Control (TAC) 54(6), 1254–1269 (2009)

BCI Control of Whole-Body Simulated Humanoid by Combining Motor Imagery Detection and Autonomous Motion Planning

Karim Bouyarmane[1,⋆], Joris Vaillant[2,3], Norikazu Sugimoto[4], François Keith[2,3], Jun-ichiro Furukawa[1,5], and Jun Morimoto[1]

[1] ATR Computational Neuroscience Laboratories, Kyoto 619-0288, Japan
[2] CNRS-Montpellier 2 University LIRMM, 34000 Montpellier, France
[3] CNRS-AIST JRL, UMI3218/CRT, Tsukuba, Ibaraki 305-8568, Japan
[4] National Institute of Information and Communications Technology, Osaka 565-0871, Japan
[5] Osaka University, Osaka 565-0871, Japan
karim.bouyarmane@atr.jp

Abstract. In this paper we demonstrate the coupling of an autonomous planning and control framework for whole-body humanoid motion, with a brain-computer interface (BCI) system in order to achieve online real-time biasing and correction of the offline planned motion. Using the contact-before-motion planning paradigm, the humanoid autonomously plans, in a first stage, its motion to reach a desired goal configuration or contact location. In the second stage of the approach, the humanoid executes the planned motion and the user can exert online some control on the motion being executed through an EEG decoding interface. The method is applied and demonstrated in a dynamics simulator with full collision-detection on a model of the humanoid robot HRP2.

Keywords: Humanoid Whole-Body Control, Motor Imagery BMI, Motion Planning.

1 Introduction

Within humanoid robotics research, one natural question that immediately pops up in mind is the possibility of using the human brain motor functions to control the motion of a humanoid robot, the same way the human does to control the movements of their own body. This is basically the brain-machine interfacing (BMI) problem, with the "machine" here being instantiated as a humanoid robot, an intuitively natural hardware for implementing human brain motor control.

On the applicative side, brain-computer interface (BCI) systems provide promising perspectives for assistive applications directed towards motion-impaired users, enabling control of robotic prostheses or robotic assistants in daily-life tasks, among which humanoid-designed ones are of particular interest, since the non-expert user can easily be familiar with what to expect from

⋆ Corresponding author.

M. Lee et al. (Eds.): ICONIP 2013, Part I, LNCS 8226, pp. 310–318, 2013.
© Springer-Verlag Berlin Heidelberg 2013

a humanoid robot in terms of motion capabilities and general dexterity. Moreover, using legged humanoids allows to integrate them directly in a daily-life environment that is designed for human activities and that accounts for human motion capabilities, without requiring to adapt the existing environment to the particular kinematics of the robot assistant.

These perspectives motivate our study. We propose to couple two components that appear necessary to reach these goals, namely a motion planning and control (MPC) framework for humanoid, with a non-invasive brain-signal measuring and decoding system. We base our study on state-of-the-art works that had been independently done on both ends, adapting them to allow their assembly as the two building blocks of the proposed integrated framework (Fig. 1).

This coupling of humanoid controller with BCI system has been achieved in previous works [1][2][3]. These works consider the problem from the following angle: the humanoid with its black-box walking controller (walking pattern generator) is seen as a mobile robot that can be commanded to walk forward, backward, or to turn right and left in a 2D plan (it can even be an actual mobile robot, ie. equipped with wheels rather than legs, in some of these works [4]), and the BCI command is generally generated through visual stimulation techniques (SSVEP [4][3][2] or P300 [1]).

We however chose to investigate alternative approaches from both ends. From the humanoid MPC end, we do not target cyclic walking motion, but general acyclic whole-body behaviours of which walking would be a particular instance. By doing so, we are able to take full profit of the dexterous capabilities of the humanoid design that initially motivate its use, for instance in climbing arbitrary-height stairs or using obstacles as contact support to reach the goal. We achieve this by exploiting our previously proposed multi-contact MPC paradigm for humanoids [5]. From the BCI end, we generate the command signal with motor imagery (MI) techniques rather than visual stimulation, which constitute the state of the art in non-invasive BCI. In the present work, the MI decoding technique that we adapted from previous application on the control of one-DOF robot and of standing-up/sitting-down motion of exoskeleton [6] allows to generate a three-valued discrete command for a one-dimensional feature of the whole-body motion, in this case the motion along a generalized notion of "vertical axis" of the moving end-limb, such as the foot of the swing leg in a biped motion for instance. However we believe, from recent and ongoing studies, that the MI approach can in the near future enable the control of a two-dimensional continuous feature of the motion [7][8].

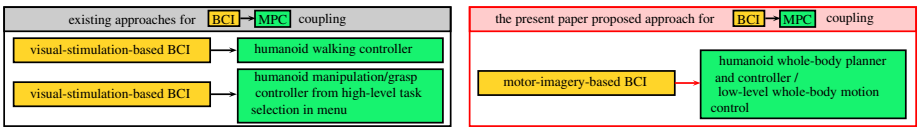

Fig. 1. Overview of the two-component coupling framework

The rest of this paper is organized as follows. The two components of the framework, the MPC scheme for the humanoid, and the MI BCI decoding scheme, are respectively recalled in sections 2 and 3, section 4 presents the strategy we retained for coupled exploitation of these components in our applicative perspective, and section 5 comments an illustrative experiment. Finally section 6 concludes the paper.

2 Humanoid Whole-Body Motion Planning and Control

We recall our work on humanoid MPC [5]. The aim here is to autonomously generate a whole-body motion of the humanoid that realises a desired task, thus sparing the user the tedious task of designing the high-DOF motion and allowing high-level (task-level) control, in line with state-of-the-art BCI capabilities.

Note that we do not make a priori assumption on the nature of the motion, e.g. cyclic walking, and thus the planning does not occur at path planning level for a walking robot, nor at footstep planning level for an a priori biped motion [9][10][11] but rather at the high-dimensional configuration space level of whole-body humanoid motion, including the free-floating component. Classic approaches operating at this level for humanoids adapted randomized planning techniques considering the humanoid with fixed foot locations as the fixed root of its kinematic tree [12][13][14][15]. Our approach merges these two planning levels (footstep planning for cyclic walking, whole-body motion on fixed foot locations) and is classified within the contact-before-motion planning category [16]. The motion generation is done in two stages.

First, planning offline the sequence of changes in *contact state* with the environment, each of which is associated with an inverse-kinematics realizing configuration [17]. By running a greedy best-first search algorithm on all possible pairings (contacts) between a robot link surface and an environment surface to be added or removed to the contact state being explored, we obtain our sequence. See details in [18][5].

In the second stage, an online controller tracks successively each of these intermediate postures (called a *step*), removing or adding a contact at each step. It is formulated as a Quadratic Program (QP) optimization problem with weighted tasks that are defined according to a finite-state machine (FSM) consisting of two states: "Move CoM" state when removing a contact from the current stance, and"Move Contact Link" state when adding a contact to the current stance. See [19] for the detailed formulation of the QP and FSM states.

3 BCI Decoding

As non-invasive brain signal acquisition device we used an EEG system (64 channels and sampling rate of 2048 Hz). The brain signals are decoded and classified using the method applied and presented in the previous work [6], based on the spectral regularization matrix classifier [20][21], that we recall here.

The EEG signals, of covariance matrices $\mathbf{C}$ considered as input, are classified into two classes, labelled with the variable k, with respective output probabilities (at sampled time t): $P(k_t = +1|\mathbf{C}_t) = \frac{1}{1+\exp(-a_t)}$, and $P(k_t = -1|\mathbf{C}_t) = \frac{\exp(-a_t)}{1+\exp(-a_t)}$, with $a_t = \mathrm{tr}[\mathbf{W}^\top \mathbf{C}_t] + b$, and where $\mathbf{W}$ is the parameter matrix to be learned (b is a constant-valued bias).

To learn $\mathbf{W}$ the minimization problem $\min \sum_{t=1}^{n} \ln(1+\exp(-k_t a_t)) + \lambda \|\mathbf{W}\|_1$, is solved, λ being the regularization variable ($\lambda = 14$ in the application below) and $\|\mathbf{W}\|_1 = \sum_{i=1}^{r} \sigma_i[\mathbf{W}]$ being the spectral l_1-norm of $\mathbf{W}$ (r is the rank of $\mathbf{W}$ and $\sigma_i[\mathbf{W}]$ its i-th singular value).

Once the classifier learned, the 7-30 Hz band-pass-filtered measured EEG signals are decoded online, by down-sampling them from 2048 Hz to 128 Hz, and applying Lapace filtering and common average substraction to remove voltage bias. Their covariance matrix, initialized at $\mathbf{C}_t = \mathbf{x}_t^\top \mathbf{x}_t$ for the first time step $t = 1$, where $\mathbf{x}_t \in \mathbb{R}^{1\times 64}$ denotes the filtered EEG signals, are updated at every time step following $\mathbf{C}_t = \frac{1}{N}\mathbf{x}_t^\top \mathbf{x}_t + \frac{N-1}{N}\mathbf{C}_{t-1}$, and used to compute the classification probabilities above.

Finally, the three-valued discrete command c_t that is sent to the robot is selected from these probabilities through the following hysteresis ($P_{\mathrm{thresh}} = 0.6$)

$$c_t = \begin{cases} +1 & \text{if } P(k_t = +1|\mathbf{C}_t) > P_{\mathrm{thresh}} \text{ and } c_{t-1} \neq +1\,, \\ -1 & \text{if } P(k_t = -1|\mathbf{C}_t) > P_{\mathrm{thresh}} \text{ and } c_{t-1} \neq -1\,, \\ 0 & \text{otherwise}\,. \end{cases} \tag{1}$$

4 Coupling the Two Components

The command c_t devised in Eq. (1) is sent to the online humanoid whole-body controller via UDP protocol at 128 Hz frequency and used to modify the planned and autonomously executed motion of the humanoid robot as described below.

When the robot is executing a step that requires moving a link to a planned contact location (state"Move Contact Link" of the FSM), then instead of tracking directly the goal contact location, we decompose the motion of the the contact link into two phases: a lift-off phase in which the link first tracks an intermediate position located at a designated way-point, followed by a touch-down phase in which the link tracks its final goal location in the contact sequence. This two-phase decomposition allows the link to avoid unnecessary friction with the environment contact surface and to avoid colliding with environment features such as stairs. Each of these two phases correspond to a sub-state of the meta-state "Move Contact Link" of the FSM, namely "Go to Way-point" and "Go to Goal" states. Finally, in order to avoid stopping the motion of the contact link at the way-point and to ensure a smooth motion throughout the step, the transition between the two sub-states is triggered when the contact link crosses a threshold plan before reaching the tracked way-point. For clarity of the presentation we will not go into this detail.

A default position of the intermediate way-point is automatically pre-set by the autonomous framework using the following heuristic: Let P_s and P_g denote

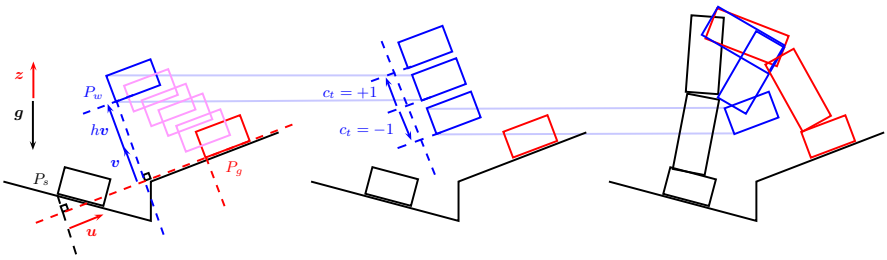

Fig. 2. Way-point moving strategy. Only the swing foot is represented. In black its initial position at the beginning of the step, in red its target final position as planned at the end of the step, in blue its way-point position at mid-step. Left: a default position is set for the way-point based on its final position. Middle: by sending the command c_t the user can bring up or down the position of the way point (in this case down). Right: the resulting executed motion of the swing leg.

respectively the step start and goal positions of the contact link, $\boldsymbol{g}$ the gravity vector, $\boldsymbol{z} = -\boldsymbol{g}/\|\boldsymbol{g}\|$ the unit vector opposite to $\boldsymbol{g}$, and $\boldsymbol{u} = \overrightarrow{P_s P_g}/\|\overrightarrow{P_s P_g}\|$ the unit vector from P_s to P_g. Finally let $\boldsymbol{v} = \boldsymbol{u} \times (\boldsymbol{z} \times \boldsymbol{u})$ be the unit vector normal to $\boldsymbol{u}$ and in the plan defined by $\boldsymbol{u}$ and $\boldsymbol{z}$. The way-point P_w is defined as (see Fig. 2) $P_w = P_g - \frac{1}{2}\overrightarrow{P_s P_g} + h\,\boldsymbol{v}$, where h is the hand-tuned user-defined parameter that specifies the height of the steps. The command c_t that comes from BCI decoding system is finally used to modify in real-time this way-point position P_w by modifying its height h. Let δh denote a desired height control resolution, then the modified position of the way-point through the brain command c_t becomes

$$P_w(c_t) = \begin{cases} P_g - \frac{1}{2}\overrightarrow{P_s P_g} + (h + c_t\,\delta h)\,\boldsymbol{v} & \text{if } t = 1\,, \\ P_w(c_{t-1}) + c_t\,\delta h\,\boldsymbol{v} & \text{if } t > 1\,. \end{cases} \tag{2}$$

The command c_t could have been used in other ways, however two principles should stand in any BCI low-level control of humanoid motion 1) the full detailed motion, that cannot be designed joint-wise by the BCI user, should be autonomously planned and executed from high-level (task-level) command, and 2) the brain command can then be used to locally correct or bias the autonomously planned and executed motion. The way-point is a key-feature to be controlled according to these two principles as it helps overcome the shortcomings of the autonomous collision-avoidance constraint in the QP controller. This collision-avoidance constraint acts as a repulsive field when the way-point of the link acts as an attracting field of the contact link. The resultant field can display local extrema corresponding to equilibrium situations in which the link stops moving though without completing its tracking task. Manual user intervention, here through the brain command, is then necessary to un-block the motion of the link by moving the way-point. The brain command is thus used for low-level correction of the inherent limitations of autonomous planning endeavours.

5 Illustrative Experiment

We describe now the experiment we designed (Fig. 3, left) (and illustrative video which can be downloaded at `www.cns.atr.jp/~karim/iconip2013.wmv`).

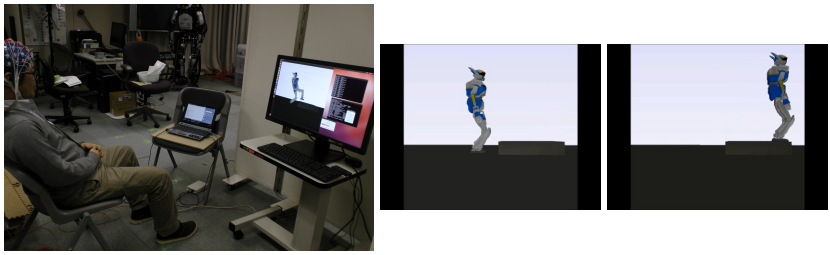

Fig. 3. Left: Experiment setup. Right: Initial and goal configurations.

An initial and goal configurations are pre-specified manually by the user among a finite number of locations in the environment (Fig. 3, right). In this case the initial configuration is standing in front of a stair and the goal task is to go up on the stair. This selection is for now done manually, but it can later be selected also through a brain command by embedding the strategy described in this work within a hierarchical framework such as in [3][4], that will switch between the behaviour of selecting the high-level goal task and the low-level motion control. Offline, the framework autonomously plans the transition sequence (Fig. 4), then the online controller is executed (Fig. 5).

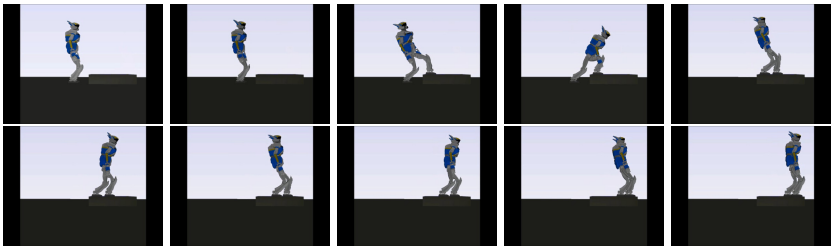

Fig. 4. The autonomously offline planned sequence of intermediate static configurations. The second posture removes the left foot contact from the stance by shifting all the weight on the right foot support. The third posture moves the now support-free left foot and adds it to the stance, etc.

The user wears an EEG cap and is trained with 3 training sessions of approximately 5 min each to learn the parameter of the classifier, through a MI task consisting of imagining respectively left arm and right arm movements for going up and down. The user has visual feed-back from the simulator on the desktop computer screen. The decoding of the BCI command is done in real-time and

Fig. 5. Tracking the BCI-controlled way-point, ie. the user controlled motion: in the extreme left figure the small black sphere in front of the swing foot indicates the way-point position that the user can control. When the swing foot reaches the black sphere (second figure) it keeps following it according to the user commands (go up or down) in the subsequent figures (up then down then up).

implemented in Matlab, and the brain command is then sent via UDP protocol to the dynamics simulator process implemented in C++.

We tested the way-point control strategy in the second step of the motion (the first contact-adding step along the sequence). The user controlled the position of a black sphere that represents the way-point tracked by the foot of the robot in real-time, while autonomously keeping balance and avoiding self-collisions, joint limits, and collision with the environment. We then externally (manually) triggered the FSM transition to the following step and left the autonomous controller complete the motion without brain control. See the video.

Fig. 6 illustrates the control performances of the BCI decoder. Table 1 gives computation time figures executed on a Dell Precision T7600 Workstation equipped with a Xeon processor E5-2687W (3.1GHz, 20M).

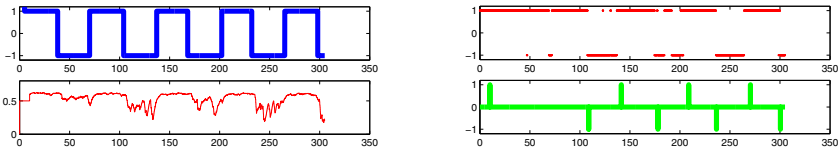

Fig. 6. BCI decoding performances. On the horizontal axis is step number t. From top to bottom and left to right: the command cue in thick blue, the decoded brain activities ($P(k_t = +1|\mathbf{C}_t)$) in thin red, the probability 0.5 thresholded estimated classified label (ie. $P(k_t = +1|\mathbf{C}_t) \geq 0.5$ or < 0.5) in thick red point marker, the command c_t sent to the robot (based on the threshold $P_{\text{thres}} = 0.6$) in thick green.

From this experiment, we confirmed that the MPC framework can be coupled with the BCI decoding system in real-time and that the robot can safely realize the task while receiving and executing the brain command.

Table 1. Execution time figures (not including OpenGL rendering time)

Offline planning	2.7sec
Average online control command (QP) (@ 200Hz)	2.661ms
Average online simulation step (@ 1kHz)	0.389ms
BCI classifier training and learning session	$\sim$ 30min
Average online BCI signal buffering (@ 2048Hz)	0.137ms
Avg online BCI classification (@ 128Hz) no control signal sent ($c_t = 0$)	0.204ms
Avg BCI classification (@ 128Hz) control signal sent ($c_t = +1$ or -1)	6.20ms

6 Discussion and Future Work

This work demonstrated the technical possibility of real-time online low-level control of whole-body humanoid motion using motor-imagery-based BCI.

We achieved it by coupling an existing EEG decoder and whole-body multi-contact acyclic planning and control framework. This coupling allowed us to control a one-dimensional feature of the high-DOF whole-body motion, designed as the generalized height of moving link way-point, in a discrete way.

We aim now at continuous control of two-dimensional feature of this whole-body motion, allowing not only the control of the tracked way point but also of a corresponding threshold plan that decides when to trigger the transition between the lift-off and touch-down phases. We believe this can be achieved based on the previous work done for example on two-dimensional cursor control [7].

Finally, we aim at porting this framework from the simulation environment to the real robot control.

Acknowledgments. This work is supported with a JSPS Postodoctoral Fellowship for Foreign Researchers, ID No. P12707. A part of this study is the result of Brain Machine Interface Development carried out under the Strategic Research Program for Brain Sciences by the Ministry of Education, Culture, Sports, Science and Technology (MEXT) of Japan. J.M. was partially supported by MEXT KAKENHI Grant Number 23120004 and by Strategic International Cooperative Program, JST. J.V. and F.K. were partially suported by grants from the RoboHow.Cog FP7 `www.robohow.eu`, Contract N288533. The authors would like to thank Abderrahmane Kheddar for valuable use of the AMELIF dynamics simulation framework.

References

1. Bell, C.J., Shenoy, P., Chalodhorn, R., Rao, R.P.N.: Control of a humanoid robot by a noninvasive brain-computer interface in humans. Journal of Neural Engineering 5, 214–220 (2008)
2. Gergondet, P., Druon, S., Kheddar, A., Hintermuller, C., Guger, C., Slater, M.: Using Brain-Computer Interface to Steer a Humanoid Robot. In: IEEE International Conference on Robotics and Biomimetics, Phuket, Thailand, pp. 192–197 (2011)
3. Chung, M., Cheung, W., Scherer, R., Rao, R.P.N.: A Hierarchical Architecture for Adaptive Brain-Computer Interfacing. In: Proceedings of the Twenty-Second International Joint Conference on Artificial Intelligence, vol. 2, pp. 1647–1652 (2011)
4. Bryan, M., Green, J., Chung, M., Chang, L., Scherery, R., Smith, J., Rao, R.P.N.: An Adaptive Brain-Computer Interface for Humanoid Robot Control. In: 11th IEEE-RAS International Conference on Humanoid Robots, Bled, Slovenia, pp. 199–204 (2011)
5. Bouyarmane, K., Kheddar, A.: Humanoid robot locomotion and manipulation step planning. Advanced Robotics 26(10), 1099–1126 (2012)
6. Noda, T., Sugimoto, N., Furukawa, J., Sato, M., Hyon, S., Morimoto, J.: Brain-controlled exoskeleton robot for bmi rehabilitation. In: 12th IEEE-RAS International Conference on Humanoid Robots, Osaka, Japan, pp. 21–27 (2012)

7. Wolpaw, J.R., McFarland, D.J.: Control of a two-dimensional movement signal by a noninvasive brain-computer interface in humans. Proceedings of the National Academy of Sciences 101(51), 17849–17854 (2004)
8. Miller, K.J., Schalk, G., Fetza, E.E., den Nijs, M., Ojemanne, J.G., Rao, R.P.N.: Cortical activity during motor execution, motor imagery, and imagery-based online feedback. Proceedings of the National Academy of Sciences (2010)
9. Kuffner, J.J., Nishiwaki, K., Kagami, S., Inaba, M., Inoue, H.: Footstep Planning Among Obstacles for Biped Robots. In: IEEE/RSJ International Conference on Intelligent Robots and Systems, Maui, HI, vol. 1, pp. 500–505 (2001)
10. Chestnutt, J., Kuffner, J., Nishiwaki, K., Kagami, S.: Planning Biped Navigation Strategies in Complex Environments. In: IEEE-RAS International Conference on Humanoid Robots, Munich, Germany (2003)
11. Chestnutt, J., Lau, M., Kuffner, J.J., Cheung, G., Hodgins, J., Kanade, T.: Footstep Planning for the ASIMO Humanoid Robot. In: IEEE International Conference on Robotics and Automation, Barcelona, Spain, pp. 629–634 (2005)
12. Kuffner, J.J., Kagami, S., Nishiwaki, K., Inaba, M., Inoue, H.: Dynamically-Stable Motion Planning for Humanoid Robots. Autonomous Robots 12, 105–118 (2002)
13. Yamane, K., Kuffner, J., Hodgins, J.K.: Synthesizing Animations of Human Manipulation Tasks. ACM Transactions on Graphics (Proc. SIGGRAPH 2004) 23(3) (August 2004)
14. Yoshida, E., Kanoun, O., Esteves, C., Laumond, J.P.: Task-driven Support Polygon Reshaping for Humanoids. In: 6th IEEE-RAS International Conference on Humanoid Robots, Genova, Italy, pp. 208–213 (2006)
15. Yoshida, E., Laumond, J.-P., Esteves, C., Kanoun, O., Sakaguchi, T., Yokoi, K.: Whole-body locomotion, manipulation and reaching for humanoids. In: Egges, A., Kamphuis, A., Overmars, M. (eds.) MIG 2008. LNCS, vol. 5277, pp. 210–221. Springer, Heidelberg (2008)
16. Hauser, K., Bretl, T., Latombe, J.-C., Harada, K., Wilcox, B.: Motion Planning for legged Robots on Varied Terrain. International Journal of Robotics Research 27(11-12), 1325–1349 (2008)
17. Bouyarmane, K., Kheddar, A.: Static multi-contact inverse problem for multiple humanoid robots and manipulated objects. In: 10th IEEE-RAS International Conference on Humanoid Robots, Nashville, TN, pp. 8–13 (2010)
18. Bouyarmane, K., Kheddar, A.: Multi-contact stances planning for multiple agents. In: IEEE International Conference on Robotics and Automation, Shanghai, China, pp. 5546–5353 (2011)
19. Bouyarmane, K., Kheddar, A.: Using a multi-objective controller to synthesize simulated humanoid robot motion with changing contact configurations. In: IEEE/RSJ International Conference on Intelligent Robots and Systems, San Fransisco, pp. 4414–4419 (2011)
20. Tomioka, R., Aihara, K.: Classifying matrices with a spectral regularization. In: 24th International Conference on Machine Learning, New York, pp. 895–902 (2007)
21. Tomioka, R., Muller, K.R.: A regularized discriminative framework for EEG analysis with application to brain-computer interface. NeuroImage 49, 415–432 (2010)

Performance Improvement via Bagging Competitive Associative Nets for Multiobjective Robust Controller Using Difference Signals

Weicheng Huang, Shuichi Kurogi, and Takeshi Nishida

Kyushu Institute of Technology, Tobata, Kitakyushu, Fukuoka 804-8550, Japan
ko@kurolab2.cntl.kyutech.ac.jp,
{kuro,nishida}@cntl.kyutech.ac.jp
http://kurolab2.cntl.kyutech.ac.jp

Abstract. So far, we have shown that, using difference signals of a plant to be controlled, a single CAN2 (competitive associative net) is capable of leaning piecewise Jacobian matrices of nonlinear dynamics of the plant. Here, the CAN2 is an artificial neural net for learning efficient piecewise linear approximation of nonlinear function. Furthermore, a multiobjective robust controller is obtained by means of combining the GPC (generalized predictive controller) and a switching scheme of multiple CAN2s to cope with plant parameter change and control objective change. This paper focuses on an improvement of control performance by means of replacing single CAN2 by bagging CAN2. We analyze to show the effectiveness of the present method via numerical experiments of a crane system.

Keywords: Multiobjective robust control, Switching of multiple bagging CAN2s, Difference signals, Generalized predictive control, Jacobian matrix of Nonlinear plant.

1 Introduction

So far, we have constructed a robust controller which uses multiple CAN2s (competitive associative nets) and difference signals of the plant to be controlled [1, 2]. Here, the CAN2 is an artificial neural net introduced for learning efficient piecewise linear approximation of nonlinear function by means of competitive and associative schemes [4–6]. Thus, a CAN2 is capable of leaning piecewise Jacobian matrices of nonlinear dynamics of a plant by means of using difference signals of the plant for the input to the CAN2, In [1], we have constructed a robust controller using multiple CAN2s which have learned the differential dynamics of the plant for several parameter values. In [2], we have focused on a multiobjective robust control, where we consider two conflicting control specifications for a crane system: one is to reduce settling time with allowable overshoot and the other is to reduce overshoot with allowable settling time. Our method provides a controller to flexibly cope with those specifications by means of switching two sets of CAN2s obtained through several control and learning iterations. From the point of view of multiobjective control, there are a number of research studies [8]. However, the control of the crane itself is neither so easy nor clarified so much for such methods to be applied.

M. Lee et al. (Eds.): ICONIP 2013, Part I, LNCS 8226, pp. 319–327, 2013.
© Springer-Verlag Berlin Heidelberg 2013

In this paper, we try to improve the control performance by means of using bagging CAN2s. Here, the bagging (bootstrap aggregation) scheme is expected to reduce the variance and the overfitting of the prediction by a single learning machine [9]. Thus, we expect that bagging CAN2s provide more stable control performance than single CAN2s in the present application. In the next section, we show a formulation of the present method. In Sect. 3, we examine the effectiveness of the method through numerical experiments applied to a nonlinear crane system involving changeable parameter values, such as rope length and load weight.

2 Multiobjective Robust Controller Using Difference Signals and Bagging CAN2s

We formulate the controller using difference signals and multiple bagging CAN2s to cope with parameter change.

2.1 Plant Model Using Difference Signals

Suppose a plant to be controlled at a discrete time $j = 1, 2, \cdots$ has the input $u_j^{[\mathrm{p}]}$ and the output $y_j^{[\mathrm{p}]}$. Here, the superscript "[p]" indicates the variable related to the plant for distinguishing the position of the load, (x, y), shown below. Furthermore, we suppose the dynamics of the plant is given by

$$y_j^{[\mathrm{p}]} = f(\boldsymbol{x}_j^{[\mathrm{p}]}) + d_j^{[\mathrm{p}]} \ , \tag{1}$$

where $f(\cdot)$ is a nonlinear function which may change slowly in time and $d_j^{[\mathrm{p}]}$ represents zero-mean noise with the variance σ_d^2. The input vector $\boldsymbol{x}_j^{[\mathrm{p}]}$ consists of the input and output sequences of the plant as $\boldsymbol{x}_j^{[\mathrm{p}]} \triangleq \left(y_{j-1}^{[\mathrm{p}]}, \cdots, y_{j-k_y}^{[\mathrm{p}]}, u_{j-1}^{[\mathrm{p}]}, \cdots, u_{j-k_u}^{[\mathrm{p}]}\right)^T$, where k_y and k_u are the numbers of the elements, and the dimension of $\boldsymbol{x}_j^{[\mathrm{p}]}$ is given by $k = k_y + k_u$. Then, for the difference signals $\Delta y_j^{[\mathrm{p}]} \triangleq y_j^{[\mathrm{p}]} - y_{j-1}^{[\mathrm{p}]}$, $\Delta u_j^{[\mathrm{p}]} \triangleq u_j^{[\mathrm{p}]} - u_{j-1}^{[\mathrm{p}]}$, and $\Delta \boldsymbol{x}_j^{[\mathrm{p}]} \triangleq \boldsymbol{x}_j^{[\mathrm{p}]} - \boldsymbol{x}_{j-1}^{[\mathrm{p}]}$, we have the relationship $\Delta y_j^{[\mathrm{p}]} \simeq f_{\boldsymbol{x}} \Delta \boldsymbol{x}_j^{[\mathrm{p}]}$ for small $\|\Delta \boldsymbol{x}_j^{[\mathrm{p}]}\|$, where $f_{\boldsymbol{x}} = \partial f(\boldsymbol{x})/\partial \boldsymbol{x} \,\big|_{\boldsymbol{x}=\boldsymbol{x}_{j-1}^{[\mathrm{p}]}}$ indicates the Jacobian matrix (row vector). If $f_{\boldsymbol{x}}$ does not change for a while after the time j, then we can predict $\Delta y_{j+l}^{[\mathrm{p}]}$ by

$$\widehat{\Delta y}_{j+l}^{[\mathrm{p}]} = f_{\boldsymbol{x}} \widetilde{\Delta \boldsymbol{x}}_{j+l}^{[\mathrm{p}]} \tag{2}$$

for $l = 1, 2, \cdots$, recursively. Here, $\widetilde{\Delta \boldsymbol{x}}_{j+l}^{[\mathrm{p}]} = (\widetilde{\Delta y}_{j+l-1}^{[\mathrm{p}]}, \cdots, \widetilde{\Delta y}_{j+l-k_y}^{[\mathrm{p}]}, \widetilde{\Delta u}_{j+l-1}^{[\mathrm{p}]}, \cdots, \widetilde{\Delta u}_{j+l-k_u}^{[\mathrm{p}]})^T$, and the elements are given by

$$\widetilde{\Delta y}_{j+m}^{[\mathrm{p}]} = \begin{cases} \Delta y_{j+m}^{[\mathrm{p}]} \text{ for } m < 1 \\ \widehat{\Delta y}_{j+m}^{[\mathrm{p}]} \text{ for } m \geq 1 \end{cases} \quad \text{and} \quad \widetilde{\Delta u}_{j+m}^{[\mathrm{p}]} = \begin{cases} \Delta u_{j+m}^{[\mathrm{p}]} \text{ for } m < 0 \\ \widehat{\Delta u}_{j+m}^{[\mathrm{p}]} \text{ for } m \geq 0. \end{cases} \tag{3}$$

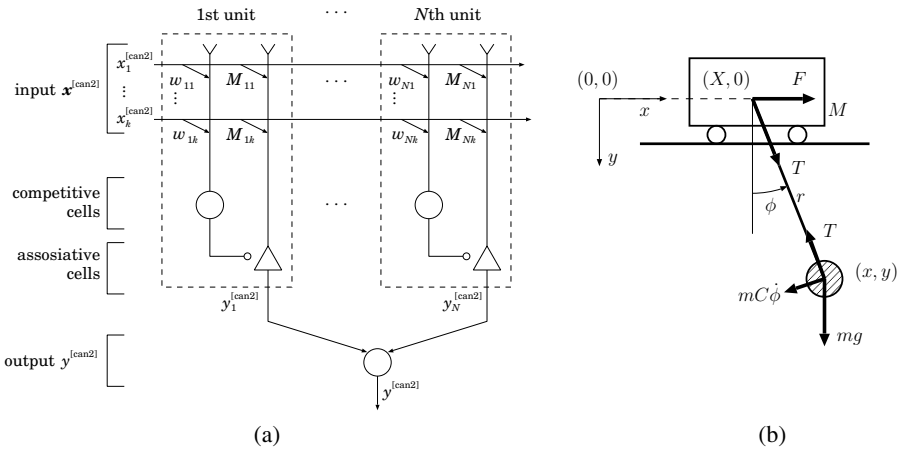

Fig. 1. Schematic diagram of (a) CAN2 and (b) overhead traveling crane system

Here, $\widehat{\Delta u}^{[p]}_{j+m}$ $(m \geq 0)$ is the predictive input (see Sect. 2.3). Then, we have the prediction of the plant output from the predictive difference signals as

$$\widehat{y}^{[p]}_{j+l} = y^{[p]}_j + \sum_{m=1}^{l} \widehat{\Delta y}^{[p]}_{j+m}. \tag{4}$$

2.2 Single and Bagging CAN2 for Learning and Identifying Nonlinear Plants

A single CAN2 has N units. The ith unit has a weight vector $\boldsymbol{w}_i \triangleq (w_{i1}, \cdots, w_{ik})^T \in \mathbb{R}^{k\times 1}$ and an associative matrix (row vector) $\boldsymbol{M}_i \triangleq (M_{i1}, \cdots, M_{ik}) \in \mathbb{R}^{1\times k}$ for $i \in I = \{1, 2, \cdots, N\}$ (see Fig. 1(a)). For a given dataset $D^{[n]} = \{(\Delta \boldsymbol{x}^{[p]}_j, \Delta y^{[p]}_j) \mid j = 1, 2, \cdots, n\}$ obtained from the plant to be controlled, we train a CAN2 by feeding the input and output of the CAN2 as $(\boldsymbol{x}^{[can2]}, y^{[can2]}) = (\Delta \boldsymbol{x}^{[p]}_j, \Delta y^{[p]}_j)$. We employ an efficient batch learning method shown in [7]. Then, for an input vector $\Delta \boldsymbol{x}^{[p]}$, the CAN2 after the learning predicts the output $\Delta y^{[p]} = f_{\boldsymbol{x}} \Delta \boldsymbol{x}^{[p]}$ by

$$\widehat{\Delta y}^{[p]} = \boldsymbol{M}_c \Delta \boldsymbol{x}^{[p]}, \tag{5}$$

where c denotes the index of the unit selected by

$$c = \underset{i\in I}{\operatorname{argmin}} \|\Delta \boldsymbol{x}^{[p]}_j - \boldsymbol{w}_i\|^2. \tag{6}$$

For a bagging CAN2, we generate a number of bags $D^{[n\alpha^\sharp, l]}$ for $l = 1, 2, \cdots, b$ by means of resampling with replacement from $D^{[n]}$, where b is the number of bags, $n\alpha$ denotes the number of elements in each bag and α is a constant which we call

bagsize ratio. Let $\mathrm{CAN2}^{[l]}$ be a single CAN2 for learning the lth bag $D^{[n\alpha^{\sharp},l]}$. After the learning for all bags, we execute the bagging prediction of $\Delta y^{[\mathrm{p}]} = f_{\boldsymbol{x}}\Delta \boldsymbol{x}^{[\mathrm{p}]}$ by

$$\widehat{\Delta y}^{[\mathrm{p}]} = \frac{1}{b}\sum_{l=1}^{b} \widehat{\Delta y}^{[\mathrm{p}][l]} = \boldsymbol{M}^{[\mathrm{bag}]}\Delta \boldsymbol{x}^{[\mathrm{p}]}. \tag{7}$$

Here, $\widehat{\Delta y}^{[\mathrm{p}][l]} = \boldsymbol{M}_c^{[l]}\Delta \boldsymbol{x}^{[\mathrm{p}]}$ and $\boldsymbol{M}_c^{[\mathrm{bag}]} = (1/b)\sum_{l=1}^{b}\boldsymbol{M}_c^{[l]}$, where $\boldsymbol{M}_c^{[l]}$ denotes $\boldsymbol{M}_c$ in (5) selected by (6) for $\mathrm{CAN2}^{[l]}$.

As we have explained in [2], the Jacobian matrix $f_{\boldsymbol{x}}$ is not the function of $\Delta\boldsymbol{x}$, but a Jacobian matrix $f_{\boldsymbol{z}} = \partial f/\partial \boldsymbol{z}$ for an enlarged differential vector $\Delta \boldsymbol{z}_j^{[\mathrm{p}]} = (\Delta y_{j-1}^{[\mathrm{p}]}, \cdots, \Delta y_{j-k_y'}^{[\mathrm{p}]}, \Delta u_{j-1}^{[\mathrm{p}]}, \cdots, \Delta u_{j-k'}^{[\mathrm{p}]})$ for $k_y' = k + k_y$ and $k_u' = k + k_u$ is considered to be a function of $\Delta\boldsymbol{z}$ when the plant parameter does not change for a while. This indicates that we can estimate Jacobian matrix if we observe the input and output for a certain duration of time of the plant. This conjecture is supposed to be applicable to many nonlinear plants. Thus, with $\Delta\boldsymbol{x}_j^{[\mathrm{p}]}$ in (6) replaced by an enlarged $\Delta\boldsymbol{z}_j^{[\mathrm{p}]}$, we can select an appropriate unit corresponding to the Jacobian matrix.

2.3 GPC Using Difference Signals

The GPC (Generalized Predictive Control) is an efficient method for obtaining the predictive input $\widehat{u}_j^{[\mathrm{p}]}$ which minimizes the following control performance index [10]:

$$J = \sum_{l=1}^{N_y}\left(r_{j+l}^{[\mathrm{p}]} - \widehat{y}_{j+l}^{[\mathrm{p}]}\right)^2 + \lambda_u \sum_{l=1}^{N_u}\left(\widehat{\Delta u}_{j+l-1}^{[\mathrm{p}]}\right)^2, \tag{8}$$

where $r_{j+l}^{[\mathrm{p}]}$ and $\widehat{y}_{j+l}^{[\mathrm{p}]}$ are desired and predictive output, respectively. The parameters N_y, N_u and λ_u are constants to be designed for the control performance. We obtain $\widehat{u}_j^{[\mathrm{p}]}$ by means of the GPC method as follows; the CAN2 at a discrete time j can predict $\Delta y_{j+l}^{[\mathrm{p}]}$ by (2) and then $\widehat{y}_{j+l}^{[\mathrm{p}]}$ by (4). Then, owing to the linearity of these equations, the above performance index is written as

$$J = \|\boldsymbol{r}^{[\mathrm{p}]} - \boldsymbol{G}\Delta\boldsymbol{u}^{[\mathrm{p}]} - \overline{\boldsymbol{y}}^{[\mathrm{p}]}\|^2 + \lambda_u\|\widehat{\Delta\boldsymbol{u}}\|^2 \tag{9}$$

where $\boldsymbol{r}^{[\mathrm{p}]} = \left(r_{j+1}^{[\mathrm{p}]}, \cdots, r_{j+N_y}^{[\mathrm{p}]}\right)^T$ and $\widehat{\Delta\boldsymbol{u}}^{[\mathrm{p}]} = \left(\widehat{\Delta u}_j^{[\mathrm{p}]}, \cdots, \widehat{\Delta u}_{j+N_u-1}^{[\mathrm{p}]}\right)^T$. Furthermore, $\overline{\boldsymbol{y}}^{[\mathrm{p}]} = \left(\overline{y}_{j+1}^{[\mathrm{p}]}, \cdots, \overline{y}_{j+N_y}^{[\mathrm{p}]}\right)^T$ and $\overline{y}_{j+l}^{[\mathrm{p}]}$ is the natural response $\widehat{y}_{j+l}^{[\mathrm{p}]}$ of the system (1) for the null incremental input $\widehat{\Delta u}_{j+l}^{[\mathrm{p}]} = 0$ for $l \geq 0$. Here, we actually have $\overline{y}_{j+l}^{[\mathrm{p}]} = y_j^{[\mathrm{p}]} + \sum_{m=1}^{l}\overline{\Delta y}_{j+m}^{[\mathrm{p}]}$ from (4), where $\overline{\Delta y}_{j+l}^{[\mathrm{p}]}$ denotes the natural response of the difference system of (2) with $\boldsymbol{J}_f$ replaced by $\boldsymbol{M}_c$. The ith column and the jth row of the matrix $\boldsymbol{G}$ is given by $G_{ij} = g_{i-j+N_1}$, where g_l for $l = \cdots, -2, -1, 0, 1, 2, \cdots$ is the unit step response $y_{j+l}^{[\mathrm{p}]}$ of (4) for $\widehat{y}_{j+l}^{[\mathrm{p}]} = \widehat{u}_{j+l}^{[\mathrm{p}]} = 0$ $(l < 0)$ and $\widehat{u}_{j+l}^{[\mathrm{p}]} = 1 (l \geq 0)$. It is easy to derive that the unit response g_l of (4) is obtained as the impulse response of (2). Then, we have $\widehat{\Delta\boldsymbol{u}}^{[\mathrm{p}]}$ which minimizes J by $\widehat{\Delta\boldsymbol{u}}^{[\mathrm{p}]} = (\boldsymbol{G}^T\boldsymbol{G} + \lambda_u\boldsymbol{I})^{-1}\boldsymbol{G}^T(\boldsymbol{r}^{[\mathrm{p}]} - \overline{\boldsymbol{y}}^{[\mathrm{p}]})$, and then we have $\widehat{u}_j^{[\mathrm{p}]} = u_{j-1}^{[\mathrm{p}]} + \widehat{\Delta u}_j^{[\mathrm{p}]}$.

2.4 Control and Training Iterations

To improve the control performance, we execute iterations of the following phases.

(i) **control phase:** Control the plant by a default control schedule at the first iteration, and by the GPC using the bagging CAN2s obtained by the training phase otherwise.
(ii) **training phase:** Train the bagging CAN2s with the dataset $D^{[n]} = \{(\Delta \boldsymbol{x}_j^{[\mathrm{p}]}, \Delta y_j^{[\mathrm{p}]} | j = 1, 2, \cdots, n)\}$ obtained in the control phase.

The control performance at an iteration depends on the bagging CAN2 obtained at the previous iterations. So, for the actual control of the plant, we use the best bagging CAN2 obtained through a number of iterations. We store and selectively use multiple best bagging CAN2s for multiple objectives in multiobjective control.

2.5 Switching Multiple Bagging CAN2s for Robustness to Parameter Change

To cope with parameter change of the plant, we employ the following method to switch bagging CAN2s. Let $\mathrm{CAN2}^{[\mathrm{bag}][\theta_s]}$ denote the best bagging CAN2 obtained for the plant with parameter θ_s ($s \in S = \{1, 2, \cdots, |S|\}$) through the control and training iterations as described above.

Step 1: At each discrete time j in the control phase, obtain $\boldsymbol{M}^{[\mathrm{bag}][\theta_s]}$ for all $s \in S$. where $\boldsymbol{M}^{[\mathrm{bag}][\theta_s]}$ denotes $\boldsymbol{M}^{[\mathrm{bag}]}$ given in (7) of $\mathrm{CAN2}^{[\mathrm{bag}][\theta_s]}$.

Step 2: Select the s^*th bagging CAN2, or $\mathrm{CAN2}^{[\mathrm{bag}][\theta_{s^*}]}$, which provides the minimum MSE (mean square prediction error) for the recent N_e outputs,

$$s^* = \underset{s \in S}{\operatorname{argmin}} \frac{1}{N_e} \sum_{l=0}^{N_e - 1} \| \Delta y_{j-l}^{[\mathrm{p}]} - \widehat{\Delta y}_{j-l}^{[\mathrm{p}][s]}) \|^2 \ , \tag{10}$$

where $\widehat{\Delta y}_{j-l}^{[\mathrm{p}][s]}$ is the predictive output of $\mathrm{CAN2}^{[\mathrm{bag}][\theta_s]}$ at time $j - l$.

3 Numerical Experiments of Crane System

In order to examine the effectiveness of the present method, we execute numerical experiments on the following crane system shown in [2].

3.1 Overhead Traveling Crane System

We consider the overhead traveling crane system shown in Fig. 1(b). From the figure, we have the position and motion equations as

$$(x, y) = (X + r \sin \phi, r \cos \phi) \tag{11}$$

$$m(\ddot{x}, \ddot{y}) = (-T \sin \phi - mC\dot{\phi} \cos \phi, mg - T \cos \phi - mC\dot{\phi} \sin \phi) \tag{12}$$

$$M\ddot{X} = F + T \sin \phi \tag{13}$$

where (x, y) and m are the position and the weight of the suspended load, $(X, 0)$, M and F are the position, weight and driving force of the trolley, r and ϕ are the length and the angle of the rope, T is the tension of the rope, and C is the viscous damping coefficient. From (11) and (12), we have the nonlinear second order differential equation of ϕ given by $r\ddot{\phi} + (C + 2\dot{r})\dot{\phi} + g\sin\phi + \ddot{X}\cos\phi = 0$. Thus, with (13), the transition of the state $\boldsymbol{x} = \left(\phi, \dot{\phi}, X, \dot{X}\right)^T$ is given by

$$\dot{\boldsymbol{x}} = h(\boldsymbol{x}) = \begin{bmatrix} \dot{\phi} \\ -\dfrac{C + 2\dot{r}}{r}\dot{\phi} - \dfrac{g}{r}\sin\phi - \dfrac{F + T\sin\phi}{rM}\cos\phi \\ \dot{X} \\ \dfrac{F + T\sin\phi}{M} \end{bmatrix}, \tag{14}$$

where $T = m\sqrt{(\ddot{x} + C\dot{\phi}\cos\phi)^2 + (\ddot{y} - g + C\dot{\phi}\sin\phi)^2}$ is also a function of $\boldsymbol{x}$. The control objective is to move the horizontal position of the load, $x = X + r\sin\phi$, to a destination position x_d by means of operating F.

3.2 Parameter Settings

The control objective is to move the load position of the crane from $x = 0$ to the destination position $x_d = 5$m within the overshoot $x_{\rm OS}$ less than 100mm. We obtain discrete signals by $u_j^{[\rm p]} = F(jT_v)$ and $y_j^{[\rm p]} = x(jT_v)$ with (virtual) sampling period $T_v = 0.5$s. Here, we use virtual sampling method shown in [3], where the discrete model is obtained with T_v (virtual sampling period) while the observation and operation are executed with shorter actual sampling period $T_a = 0.01$s. We use $k'_y = k'_u = 4$ for enlarged input vector $\Delta\boldsymbol{x}_j^{[\rm p]}$, and $N_y = 20$, $N_u = 1$ and $\lambda_u = 0.01$ for the GPC. We used $N_e = 8$ samples for (10).

We use a model crane with trolley weight $M = 100$kg, damping coefficient $C = 0.5$m/s, maximum driving force $F_{\max} = 10$N. We denote the crane with the rope length r and load weight m by $\mathrm{CRANE}^{[r,m]}$ or $\mathrm{CRANE}^{[\theta]}$ for $\theta = (r, m)$. We examine the robustness to 90 combinations of $r = 2, 3, \cdots, 10$ [m] and $m = 10, 20, \cdots, 100$ [kg]. Before this examination, we train CAN2s with $\mathrm{CRANE}^{[\theta_s]}$ for $\theta_s = (2, 10)$, (2,100), (10,10), (10,100) for $s = 1$, 2, 3, 4, respectively. Let $\mathrm{CAN2}_{\rm OS}^{[\theta_s]}$ and $\mathrm{CAN2}_{\rm ST}^{[\theta_s]}$ denote the best CAN2 which have achieved smallest overshoot and settling time, respectively, for $\mathrm{CRANE}^{[\theta_s]}$ through 20 control and training iterations. Here, at each iteration, we use the data of the current and previous iteration for the dataset to train the CAN2 because the number of obtained data becomes huge and time consuming as the number of iterations increases and the control performance does not seem improved even if we use all data. In order to uniquely select the CAN2, the overshoot $x_{\rm OS}$ and the settling time $t_{\rm ST}$ are ordered by $x_{\rm OS} + \epsilon t_{\rm S}$ and $t_{\rm ST} + \epsilon x_{\rm OS}$, respectively, with small $\epsilon = 10^{-5}$. We have used the set of CAN2s, or $\mathrm{CAN2}_{\rm OS}^{[\theta_S]} = \{\mathrm{CAN2}_{\rm OS}^{[\theta_s]} | s \in S\}$ and $\mathrm{CAN2}_{\rm ST}^{[\theta_S]} = \{\mathrm{CAN2}_{\rm ST}^{[\theta_s]} | s \in S\}$, for the present switching controller. We similarly obtain the sets of bagging CAN2s, i.e. $\mathrm{CAN2}_{\rm OS}^{[\rm bag][\theta_S]}$ and $\mathrm{CAN2}_{\rm ST}^{[\rm bag][\theta_S]}$. We use the number of bags to

Table 1. Statistical summary of overshoot and settling time obtained in the control of the crane for 90 combinations of rope lengths and load weights. The boldface figures indicate the best (smallest) result in each block.

CAN2 employed	tuned N for $(\theta_1,\theta_2,\theta_3,\theta_4)$	settling time $t_{\rm ST}$ [s]				overshoot $x_{\rm OS}$[mm]			
		mean	min	max	std	mean	min	max	std
$\mathrm{CAN2}_{\rm ST}^{[\theta_S]}$	(20,30,20,8)	**21.4**	19.6	**24.1**	**0.8**	22.4	**0**	67	13.9
$\mathrm{CAN2}_{\rm ST}^{[\mathrm{bag}][\theta_S]}$	(30,20,6,8)	22.0	**19.1**	26.0	1.2	**11.4**	**0**	**57**	**12.3**
$\mathrm{CAN2}_{\rm OS}^{[\theta_S]}$	(30,20,10,6)	27.1	22.4	36.4	2.6	3.3	**0**	**38**	5.6
$\mathrm{CAN2}_{\rm OS}^{[\mathrm{bag}][\theta_S]}$	(20,30,20,8)	**26.1**	**19.6**	**29.7**	**2.4**	**0.7**	**0**	**38**	**4.1**
$\mathrm{CAN2}_{\rm OS}^{[\mathrm{bag}][\theta_S^+]}$	(20,30,20,8)	**25.2**	21.3	30.7	**1.9**	**0.2**	**0**	**5**	**0.8**

be $b = 10$ and the bag size ratio $\alpha = 0.7$. We have optimized the number of units for each single and bagging CAN2 from $N = 40$, 30, 20, 10, 8, 6, 4, which indicates the number of piecewise regions of piecewise linear approximation by the CAN2.

3.3 Results and Analysis

A statistical summary of achieved overshoot $x_{\rm OS}$ and settling time $t_{\rm ST}$ is shown in Table 1, and four examples of time course of the input F and the output X and x for the best and the worst control using bagging CAN2s is shown in Fig. 2. From Fig. 2, we can see the performance in time by the best (top) and the worst (bottom) controllers for reducing settling time (left) and overshoot (right), respectively.

From Table 1, we can see that all controller has achieved overshoot less than the allowable 100mm. The top two rows indicate the results by the controllers for reducing settling time, and we can see that the mean, maximum (max) and standard deviation (std) of the settling time are not improved by the bagging $\mathrm{CAN2}_{\rm ST}^{[\mathrm{bag}][\theta_S]}$, while other performance is improved. The third and fourth rows indicate the results by the controllers for reducing overshoot, and we can see that all values are improved (reduced) by bagging $\mathrm{CAN2}_{\rm OS}^{[\mathrm{bag}][\theta_S]}$ from single $\mathrm{CAN2}_{\rm OS}^{[\theta_S]}$.

In order to examine these results precisely, we show the settling time and overshoot for each of 90 parameter values in Fig. 3. From the figure on the left, we can see that single $\mathrm{CAN2}_{\rm ST}^{[\theta_S]}$ has achieved better performance than bagging $\mathrm{CAN2}_{\rm ST}^{[\mathrm{bag}][\theta_S]}$ on average and it does not seem reasonable to improve the performance from the result of the bagging $\mathrm{CAN2}_{\rm ST}^{[\mathrm{bag}][\theta_S]}$. On the other hand, the result of overshoot on the right of Fig. 3 shows that bagging $\mathrm{CAN2}_{\rm OS}^{[\mathrm{bag}][\theta_S]}$ has achieved no overshoot ($x_{\rm OS} = 0$) except 8 cases, and the biggest overshoot $x_{\rm OS} = 38$mm occurs at $(r, m) = (2, 80)$. Thus, we train to make a new bagging $\mathrm{CAN2}_{\rm OS}^{[\mathrm{bag}][2,80]}$ and add it to $\mathrm{CAN2}_{\rm OS}^{[\mathrm{bag}][\theta_S]}$ as $\mathrm{CAN2}_{\rm OS}^{[\mathrm{bag}][\theta_S^+]} = \mathrm{CAN2}_{\rm OS}^{[\mathrm{bag}][\theta_S]} \cup \mathrm{CAN2}_{\rm OS}^{[\mathrm{bag}][2,80]}$. The performance achieved by $\mathrm{CAN2}_{\rm OS}^{[\mathrm{bag}][\theta_S^+]}$ is shown in the bottom row of Fig. 1 and in the right of Fig. 3. As we can see that the mean, maximum (max) and standard deviation (std) are improved from $\mathrm{CAN2}_{\rm OS}^{[\mathrm{bag}][\theta_S]}$, and the number of cases accompanied with positive overshoot are reduced to 5 from 8.

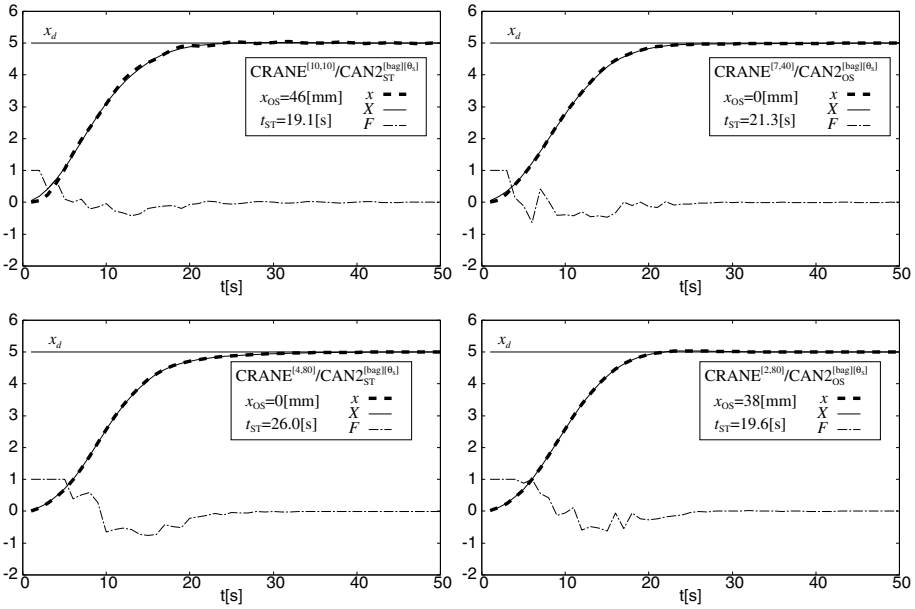

Fig. 2. Examples of time course of x[m], X[m] and F[10N]. Among the control for 90 parameter values, the results of the smallest (best) and biggest (worst) settling time by $\mathrm{CAN2}^{[\mathrm{bag}][\theta_S]}_{\mathrm{ST}}$ are shown in top left and bottom left, respectively, and those of the smallest and biggest overshoot by $\mathrm{CAN2}^{[\mathrm{bag}][\theta_S]}_{\mathrm{OS}}$ are shown in top right and bottom right, respectively.

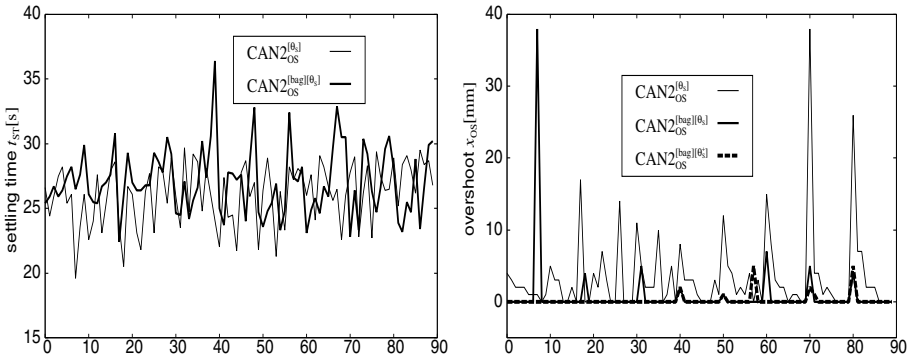

Fig. 3. Experimental result of settling time t_{ST} [s] (left) and overshoot x_{OS} [mm] (right) in the control of the crane for 90 combinations of rope lengths r[m] and load weights m[kg]. The horizontal axis indicates the parameter values ordered as $(r, m) = (2, 10), (2, 20), \cdots, (10, 100)$.

Here, note that we have a different result in our previous study [2], where the mean and the maximum overshoot are 0.02 and 2, respectively, but the mean settling time are 32.0s by $\mathrm{CAN2}_{\mathrm{OS}}^{[\theta_S]}$. The difference is owing that a constant number of units $N = 20$ for all $\mathrm{CAN2}_{\mathrm{OS}}^{[\theta_s]}$ $(s = 1, 2, 3, 4)$ is used in [2] which derives smaller overshoot but larger settling time on average. By means of tuning N for each θ_s in the present experiments, we have achieved smaller settling time while the overshoot is reduced by augmenting the set of bagging CAN2s as shown above.

4 Conclusion

We have focused on an improvement of control performance by means of replacing single CAN2s by bagging CAN2s of the robust controller using difference signals which we are developing. Via numerical experiments of a crane system, we have shown the effectiveness of the present method. From the point of view of multiobjective control, two objectives to reduce settling time and overshoot have different properties. Namely, in the present method, the settling time is reduced by tuning the number of units, N, of the CAN2s, while the overshoot is reduced by using bagging CAN2s replacing single CAN2s and the augmentation of bagging CAN2(s) for reducing plant-parameter-specific overshoot(s). We would like to analyze the present method much more in our future research, especially the effect and the role of the enlargement of the dimensionality of the input vector to the CAN2.

Acknowledgments. This work was supported by JSPS KAKENHI Grant Number 24500276.

References

1. Kurogi, S., Yuno, H., Nishida, T., Huang, W.: Robust control of nonlinear system using difference signals and multiple competitive associative nets. In: Lu, B.-L., Zhang, L., Kwok, J. (eds.) ICONIP 2011, Part III. LNCS, vol. 7064, pp. 9–17. Springer, Heidelberg (2011)
2. Huang, W., Kurogi, S., Nishida, T.: Robust controller for flexible specifications using difference signals and competitive associative nets. In: Huang, T., Zeng, Z., Li, C., Leung, C.S. (eds.) ICONIP 2012, Part V. LNCS, vol. 7667, pp. 50–58. Springer, Heidelberg (2012)
3. Kurogi, S., Nishida, T., Sakamoto, T., Itoh, K., Mimata, M.: A simplified competitive associative net and a model-switching predictive controller for temperature control of chemical solutions. In: Proc. of ICONIP 2000, pp. 791–796 (2000)
4. Kurogi, S., Ren, S.: Competitive associative network for function approximation and control of plants. In: Proc. NOLTA 1997, pp. 775–778 (1997)
5. Kohonen, T.: Associative Memory. Springer (1977)
6. Ahalt, A.C., Krishnamurthy, A.K., Chen, P., Melton, D.E.: Competitive learning algorithms for vector quantization. Neural Networks 3, 277–290 (1990)
7. Kurogi, S., Sawa, M., Ueno, T., Fuchikawa, Y.: A batch learning method for competitive associative net and its application to function approximation. In: Proc. of SCI 2004, vol. 5, pp. 24–28 (2004)
8. Deb, K.: Multi-Objective Optimization Using Evolutionary Algorithms. John Wiley & Sons (2009)
9. Optiz, D., Maclin, R.: Popular ensemble methods: an empirical study. Journal of Artificial Intelligence Research 11, 169–198 (1999)
10. Clarki, D.W., Mohtadi, C.: Properties of generalized predictive control. Automatica 25(6), 859–875 (1989)

Semi Supervised Autoencoders: Better Focusing Model Capacity during Feature Extraction

Hani Almousli and Pascal Vincent

Université de Montréal
Dept. IRO, CP 6128, Succ. Centre-Ville, Montréal, Québec, H3C 3J7, Canada
{almouslh,vincentp}@iro.umontreal.ca

Abstract. Previous work showed that unsupervised layer-wise pre-training can be used to overcome the difficulty of training a deep architecture. In this paper, we address one of the limitations when using unsupervised models like regularized autoencoders to learn features that we hope to be useful for a subsequent supervised task, namely their blindness to that specific task. We propose to change the cost function to focus on accurate reconstruction of input features that seem more useful for the supervised task. This is achieved by using A-norm in the minimized reconstruction error instead of Euclidean-norm. Through the choice of an appropriate A-matrix, the capacity of the model can be steered towards modeling relevant information for the classification task. Comparative experiments with the proposed denoising autoencoder variant show that this way of proceeding yields extracted features that achieve better classification performance on several datasets.

Keywords: Neural Network, Deep Learning, Semi-Supervised Learning, Pre-training, Learning Representation, Autoencoder, Denoising Autoencoder, Convolutional Net.

1 Introduction

Both theoretical studies [1, 23] and many practical successes [19–21] demonstrate the advantage of using deep architectures to model complex data distributions and to achieve good classification performance on chal-lenging recognition tasks. It is believed that deep multi-layered models can learn more complex functions producing more meaningful representations [2, 3]. Similarly [4] showed empirically that deeper layers are able to learn more complex features than shallow ones. Training deep network is a difficult optimization problem [5]. But much progress has been made with the seminal work on Deep Belief Networks [25] that uses layer-by-layer pre-training of Restricted Boltzmann Machine to initialize each layer of the deep network. It has since been shown that various forms of regularized autoencoders can be used instead of RBMs [6, 18]. Unlike PCA or ICA, RBMs and autoencoders are able to produce non-linear features and can thus be stacked to build a deep architecture [7, 18]. Finally, a deep network is initialized with the parameters obtained during pre-training and fine-tuned

M. Lee et al. (Eds.): ICONIP 2013, Part I, LNCS 8226, pp. 328–335, 2013.
© Springer-Verlag Berlin Heidelberg 2013

using the labeled data. This makes optimization faster by starting from a good initialization and has also been shown to have a beneficial regularization effect [8]. In this paper, we concentrate on improving the features extracted by autoencoders. Our main motivation for the present work is the observation that the current way of pre-training, being purely unsupervised, is blind to the supervised task we ultimately want the deep network to solve (such as classification). It does not exploit valuable knowledge of the label, and could thus learn features that remove or deemphasize input information that would be useful for predicting the labels. In the present work we instead investigate using a form of semi-supervised learning during the pre-training phase. Our hypothesis here is that we can exploit the large amount of unlabeled data, using an unsupervised model, but without completely ignoring the information contained in the few labeled data. At the end of the day, we care about the features that are relevant for the desired supervised task. Yet training (unsupervised) in a blind way may not give us the best explanatory features for classification. Luckily, this can be fixed with a very simple change to the reconstruction cost function, specifically by choosing a more appropriate metric for the reconstruction error, as we will describe in section 3. We validated our hypothesis by applying the new cost function on different da-tasets and we showed that choosing the right metric gives a good boost to the classifi-cation accuracy. The paper is organized as follows; section 2 reviews briefly different types of autoencoders. Section 3 describes our semi-supervised autoencoder approach and we provide experimental validation of the idea in Section 4.

2 Autoencoder Variants

Basic Autoencoder (AE). Introduced back in the eighties [9], it is a special kind of neural network which has its input as the target. At that time it was used for dimensionality reduction. We start by *encoding* the input x to get a lower dimensional representation$f(x)$ and from that representation we try to *reconstruct* the input again as $g(f(x))$. Training will minimize the total discrepancy between reconstruction and original input using squared error L. Formally, the encoding, decoding and the cost function can be expressed as:

$$f(x) = h = sigmoid(Wx + b) \; . \tag{1}$$

$$g(h) = o = sigmoid(W^T h + c) \; . \tag{2}$$

$$L(x) = \sum\nolimits_{x \in D} ||g(f(x)) - x||^2 \; . \tag{3}$$

Denoising Autoencoder (DAE). The idea of the DAE [10] is to corrupt input ($\breve{x}$) and try to reconstruct back the uncorrupted one (x) so that we learn more robust and useful features than with the basic AE. More formally, we will have:

$$f(\breve{x}) = h = sigmoid(W\breve{x} + b) \; . \tag{4}$$

$$L(x) = \sum\nolimits_{x \in D} ||g(f(\breve{x})) - x||^2 \; . \tag{5}$$

Other Regularized Autoencoders. There are several other types of autoencoders which can be considered as regularized versions of the basic AE. Contractive Autoencoder [11] was inspired from the DAE but uses an analytical approach to induce robustness instead of using random corruptions of the input. Alternatively, sparse autoencoders [6, 12, 13] impose a sparsity constraint on the hidden representation. Predictive Sparse Decomposition [14] which can be seen as a kind of AE is used as a practically successful blend of sparse coding [24] and autoencoders.

3 Semi-Supervised Autoencoder (SSAE)

All unsupervised pre-training methods are based on the hypothesis that the marginal probability distribution of the input $p(x)$ contains some relevant information about the conditional probability of the label given the input $p(y|x)$ [15]. However, depending on the task it is unclear how helpful modeling the marginal input distribution will be for the goal supervised task. Especially since the unsupervised models are typically capacity limited (which is necessary for good generalization), what aspects of the distribution will they devote their capacity to modeling? Imagine that we train an autoencoder on face images, how much information do the resulting features learned in this purely unsupervised way retain about the faces emotions? Are these features also helpful if we want to know whether the person is male or female? We thus propose to steer the autoencoder variant towards focusing its capacity for modeling aspects of the input that are more likely relevant for the supervised task. For this purpose, we will use simple knowledge easily extracted from $p(y|x)$ using the few labeled data. Let x_1, x_2 and x_3 be visible variables and y be the target variable (e.g. class) we want to predict later. If the information of y given x_1 is significantly larger than the information of y given x_2 then the model should concentrate more on explaining (or retaining information about) x_1 rather than x_2 because the classifier may benefit from it more. On the other hand, if knowing x_3 gives us nothing about y, then there is no need to waste model capacity in modeling x_3. Since our models are capacity limited, it is worth to figure out the important factors to concentrate on during the unsupervised phase. The pre-training phase can thus disregard input features that are deemed mostly irrelevant to the supervised task from an early stage. We expect that pre-training each layer in this way, since it already acknowledges the target, will learn parameters and features likely be closer to an optimal solution for the supervised task. We believe that this can also help in the later supervised fine-tune phase in deep networks, leading to fewer vanishing gradient problems during back propagation. To steer the capacity of an autoencoder we propose a simple change to the reconstruction error that can be applied to any autoencoder type. We will use DAE, as an example, to study the effect of the new learning criterion. We call the resulting approach semi supervised denoising autoencoder (SSDAE). If we denote $g(f(\breve{x}))$ in equation (5) as $r(\breve{x})$, then the usual cost function with squared reconstruction error for one sample can be expressed as:

$$L(x) = (r(\breve{x}) - x)^2 = (r(\breve{x}) - x)^T I(r(\breve{x}) - x) \ . \tag{6}$$

where I is the identity matrix.

We propose to replace I by a new matrix A and thus minimize the A norm of the reconstruction error:

$$L(x) = (r(\breve{x}) - x)^T A(r(\breve{x}) - x) \ . \tag{7}$$

where A is a matrix that was chosen to reflect the dependency between the visible vector $x$and the label y. The only constraint that A must satisfy is to be positive semi-definite in order to have a nonnegative cost. Note that if A is not full rank, then there will be a subspace that has zero cost or zero A norm (the null-space of A). If reconstruction is imperfect along directions from this null-space, the cost wont penalize it. Thus model capacity can be employed towards better modeling input information more likely to be useful for later predicting y. The tricky question is how to choose A. We may define it based on prior knowledge or belief regarding what the most relevant in the input for the supervised task is. Alternatively, we can define a diagonal A based on a measure the mutual information $I[x_i, y]$ between each input variable x_i and the label:

$$I[x_i, y] = H[y] - H[y|x_i] \ . \tag{8}$$

$$H[y] = -\sum p(y) \ln p(y) \ . \tag{9}$$

$$H[y|x_i] = -\sum p(y, x_i) \ln p(y|x_i) \ . \tag{10}$$

Or we can define a diagonal A using a heuristic based on the importance given to each input feature in the solution learned by a standard supervised learning algorithm such as linear SVM, logistic regression, random forest, etc...

4 Experiments and Results

All experiments were conducted using python and theano [17]. SSDAE was tested on several datasets: Toronto Faces Dataset (TFD) [26], MNIST and CIFAR100. Both DAE and SSDAE with one hidden layer, rectifier activation function, and tied weights were launched and the learned hidden representation was finally fed to a linear SVM. For simplicity, all experiments used a diagonal matrix A (although a more general matrix form could conceivably be used). Two different heuristics were used to build it:

1. Hand-crafted A using a nave heuristic based on prior knowledge of the task:
   (a) For MNIST we assigned each pixel a weight proportional to its probability of being active as measured on average in the training set. This means that back-ground pixels which are always zeros on all digits will have no effect on the cost function.

(b) For TFD, whose examples are frontal aligned faces, we reasoned that mouth and eyebrow regions were more important than others (like cheeks) for figuring out the emotion. So we attributed pixels in these regions a weight of 1, while all others were given a weight of 0.5.

2. A is chosen based on the importance given to each input feature in the solution learned by a random forest classifier [16]. Specifically, bagging is used to build different decision trees using m different attributes from n where $m < n$. e.g. $n = 48 * 48$ for TFD. The more often the attribute is used in higher layers, the more im-portant it is deemed. The figure below shows the resulting pixel importance ob-tained for MNIST and TFD.

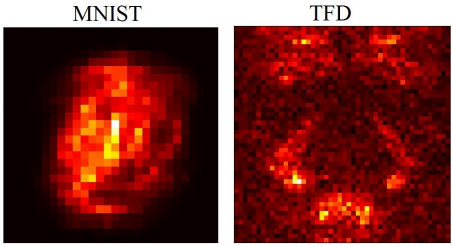

Fig. 1. Pixels Importance for TFD and MNIST using Random Forests

Table 1 shows that SSDAE with an A matrix built based on the second criterion gives the best classification result on all tested datasets. Note that SSDAE achieves a better performance than regular DAE on both TFD and MNIST. On the other hand, no tangible benefit is achieved on CIFAR100. This result was expected since for TFD and MNIST information most relevant for classification is clearly con-centrated on some pixels more than others (TFD and MNIST are relatively well aligned) while it is not the case in CIFAR100.

Table 1. Comparision between SSDAE and DAE on different datasets.

TFD (*accuracy* %)						
	Fold 0	**Fold 1**	**Fold 2**	**Fold 3**	**Fold 4**	**Final**
SSDAE (hand-crafted)	77.30	75.97	75.81	76.89	73.11	75.82
SSDAE(random forest)	79.57	78.80	76.89	78.08	73.11	**77.29**
DAE	77.30	76.56	75.93	76.17	72.38	75.67
MNIST (*error rate*)						
SSDAE(random forest)	**1.17**					
SSDAE (hand-crafted)	1.24					
DAE	1.28					
CIFAR 100 (*error rate*)						
SSDAE(random forest)	**29.98**					
DAE	29.52					

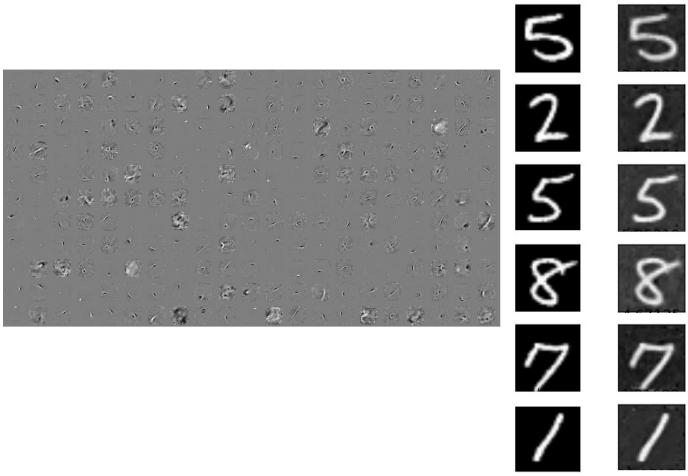

Fig. 2. Some MNIST filters trained using SSDAE and the reconstruction of some images

Figure 2 shows some of the learned filters for MNIST and the reconstruction for some images that have never been seen during training. It can be seen that the recon-struction is noisy for the background, as could be expected.

Finally, we wanted to check if SSDAE helps when we assign its parameters to a neural network and fine-tune it. To check this hypothesis, we trained an SSDAE on 9*9 TFD patches centered on pixels whose position was sampled according to pixels importance distribution (diagonal of A). We then used these parameters to initialize a convolutional net with one convolutional layer, max-pooling, and one fully-connected hidden-layer. The motivation for this experiment was to compare with [22] where a different variation of CAE that disentangles the factors of the hidden units was trained on TFD random patches, and resulting parameters were similarly used as initialization for a convolutional net. The approach of [22] yielded around 1% accuracy boost on the classification compared to CAE only. In our experiment, we did not use anything to disentangle the factors of variation. All we did was using the proposed SSDAE for pre-training. Results are shown in table 2.

Although SSDAE pre-training did not reach 85%, the performance boost obtained with the much simpler principle underlying the modification we propose in the SSDAE is nevertheless remarkable. As we mentioned earlier, the new criteria can be tested with any autoencoder type.

Table 2. Comparision between SSDAE and DAE on different datasets

	TFD					
	Fold 0	**Fold 1**	**Fold 2**	**Fold 3**	**Fold 4**	**Final**
SSDAE	85.42	84.33	85.03	85.03	82.48	84.48
(Rifai et al,2012)	-	-	-	-	-	85.00

5 Conclusion and Future Work

We have proposed a very simple way to use semi-supervised learning in the pre-training phase of deep networks, to steer model capacity towards modeling infor-mation more relevant for the supervised task of interest. We have seen that simple heuristics can effectively be used to build a better suited reconstruction metric for autoencoders, producing more useful features for classification. Resulting features were empirically shown to significantly improve classification performance of SVMs. They were also shown to provide a good initialization point for deep network fine-tuning, allowing SSDAE to reach performance gains not far from those obtained by more sophisticated approaches. Future research directions include: training deeper models with this approach in-vestigating further heuristics for matrix A, including non-diagonal versions as well as the possibility to simultaneously learn metric A together with the network parameters.

References

1. Bengio, Y., Le Cun, Y.: Scaling learning algorithms towards AI (2007)
2. Hinton, G.: Connectionist learning procedures. Artificial Intelligence 40, 185–234 (1989)
3. Utgo, P., Stracuzzi, D.: Many-layered learning. Neural Computation 14, 2497–2539 (2002)
4. Lee, H., Grosse, R., Ranganath, R., Ng, A.: Convolutional deep belief networks for scalable unsupervised learning of hierarchical representations. In: International Conference on Machine Learning (2009)
5. Bengio, Y., Lamblin, P., Popovici, D., Larochelle, H.: Greedy layer-wise training of deep networks. In: Advances in Neural Information Processing Systems, vol. 19, pp. 153–160 (2007)
6. Lee, H., Ekanadham, C., Ng, A.: Sparse deep belief net model for visual area V2. In: Platt, J., Koller, D., Singer, Y., Roweis, S. (eds.) Advances in Neural Information Processing Systems, Cambridge, MA (2008)
7. Bengio, Y., Courville, A., Vincent, P.: Perspectives, Unsupervised Feature Learning and Deep Learning: A Review and New., Montreal (2012)
8. Erhan, D., Bengio, Y., Courville, A., Bengio, S.: Why Does Unsupervised Pretraining Help Deep Learning. Journal of Machine Learning Research 11, 625–660 (2010)
9. Rumelhart, D., Hinton, G.: Williams: Learning representations by backpropagation (1986)
10. Vincent, P., Larochelle, H., Bengio, Y., Manzagol, P.-A.: Extracting and Composing Robust Features with Denoising Autoencoders (2008)
11. Rifai Salah, P.: Contractive Autoencoders: Explicit Invariance During Feature Extraction (2011)
12. Ranzato, M., Poultney, C., Chopra, S., LeCun, Y.: Efficient learning of sparse representations with an energy based model (2007)
13. Goodfellow, I., Le, Q., Saxe, A., Ng, A.: Measuring invariances in deep networks. In: NIPS, pp. 646–654 (2009)
14. Kavukcuoglu, K., Ranzato, M., LeCun, Y.: Fast inference in sparse coding algorithms with applications to object recognition (2008)

15. Bengio, Y.: Learning deep architectures for AI. Foundations and Trends in Machine Learning (2009)
16. scikit-learn, `http://scikit-learn.org/stable/modules/ensemble.html#feature-importance-evaluation` (accessed 2013)
17. Bergstra, J., Breuleux, O., Bastien, F., Lamblin, P., Pascanu, R., Desjardins, G., Turian, J., Warde-Farley, D., Bengio, Y.: Theano: a CPU and GPU math expression compiler. In: Proceedings of the Python for Scientific Computing Conference, SciPy (2010)
18. Vincent, P., Larochelle, H., Lajoie, I., Bengio, Y., Manzagol, P.: Stacked Denoising Autoencoders: Learning Useful Representations in a Deep Network with a Local Denoising Criterion (2010)
19. Krizhevsky, A., Sutskever, I., Hinton, G.: ImageNet classification with deep convolutional neural networks. In: Advances in Neural Information Processing Systems (2012)
20. Seide, F., Li, G., Yu, D.: Conversational speech transcription using context-dependent deep neural networks. In: Interspeech (2011)
21. Schwenk, H., Rousseau, A., Attik, M.: Large pruned or continuous space language models on a gpu for statistical machine translation. In: Workshop on the Future of Language Modeling for HLT (2011)
22. Rifai, S., Bengio, Y., Courville, A., Vincent, P., Mirza, M.: Disentangling factors of variation for facial expression recognition (2012)
23. Bengio, Y.: Learning Deep Architecture for AI, Montreal, Canada (2007)
24. Olshausen, B., Field, D.: Sparse coding with an overcomplete basis set: a strategy employed by V1. Vision Research 37, 3311–3325 (1997)
25. Hinton, G., Osindero, S., Teh, Y.: A fast learning algorithm for deep belief nets 18, 1527–1554 (2006)
26. Susskind, J., Anderson, A., Hinton, G.: The Toronto Face Database, Toronto (2010)

Maximum-Margin Framework for Training Data Synchronization in Large-Scale Hierarchical Classification

Rohit Babbar, Ioannis Partalas, Eric Gaussier, and Massih-Reza Amini

Laboratoire d'Informatique de Grenoble
Université Joseph Fourier, Grenoble, France
firstname.lastname@imag.fr

Abstract. In the context of supervised learning, the training data for large-scale hierarchical classification consist of (i) a set of input-output pairs, and (ii) a hierarchy structure defining parent-child relation among class labels. It is often the case that the hierarchy structure given a-priori is not optimal for achieving high classification accuracy. This is especially true for web-taxonomies such as Yahoo! directory which consist of tens of thousand of classes. Furthermore, an important goal of hierarchy design is to render better navigability and browsing. In this work, we propose a maximum-margin framework for automatically adapting the given hierarchy by using the set of input-output pairs to yield a new hierarchy. The proposed method is not only theoretically justified but also provides a more principled approach for hierarchy flattening techniques proposed earlier, which are ad-hoc and empirical in nature. The empirical results on publicly available large-scale datasets demonstrate that classification with new hierarchy leads to better or comparable generalization performance than the hierarchy flattening techniques.

1 Introduction

Large-scale web taxonomies, e.g. the Open Directory Project (ODP), consist of millions of websites, distributed among hundreds of thousand classes which are arranged in a tree hierarchy. For example, ODP has around 5 million websites and the hierarchy contains over 1 million classes. Due to the ever-increasing scale of data from various sources on the web, there is a definite requirement to partially or fully eliminate the manual effort involved in managing such taxonomies. In this context, large-scale hierarchical classification systems aim to automatically classify documents to target classes using also the hierarchical information. The main challenge in large-scale hierarchical classification is to exploit the hierarchical structure to design a scalable classification system which has acceptable prediction accuracy as well as training and prediction speed. In order to evaluate the current state of art in this domain, open challenges such as the Pascal Large Scale Hierarchical Text Classification (LSHTC)[1] have been organized.

[1] http://lshtc.iit.demokritos.gr/

M. Lee et al. (Eds.): ICONIP 2013, Part I, LNCS 8226, pp. 336–343, 2013.
© Springer-Verlag Berlin Heidelberg 2013

Most approaches exploit the hierarchy structure to design appropriate loss functions for classification and use it to apply the divide-and-conquer paradigm to keep the scale of the classification problem manageable. However, the taxonomy structure given a-priori as part of the training data may not be best suited to yield high classification accuracy due to the following reasons:

1. Large-scale web taxonomies are designed with an intent of better user-experience and navigability, and not for the goal of classification.
2. Taxonomy design is subject to certain degree of arbitrariness based on personal choices and preferences of the editors.
3. The large-scale nature of such taxonomies poses difficulties in manually designing good taxonomies for classification.

In the recent work by [3] on relatively smaller taxonomies, the impact of arbitrariness on loss-function design is minimized by appropriately calibrating the edge distance between the true and predicted class. In similar spirit of taxonomy adaptation, approaches based on flattening the hierarchy such as [7,9], have been proposed in LSHTC for large-scale settings which lead to improvement in classification accuracy as compared to using the original hierarchy. The motivation for these hierarchy flattening approaches is to minimize the error propagation due to a longer cascade from the root to leaves. Hierarchy flattening approaches remove entire levels in the hierarchy by replacing all the parents in that level by its children. This is illustrated in Figure 1 where the first and the third levels of the hierarchy are removed. Such approaches based on flattening entire levels suffer from the following drawbacks:

– These are based on ad-hoc heuristics and a-priori it is not clear which levels in the hierarchy should be flattened. This is crucial for hierarchies such as Yahoo! Directory which have more than 10 levels.
– Excessive flattening leads to increase in training and prediction speed, both of these factors adversely impact applicability of the resulting hierarchical classifiers in many scenarios of practical importance.

In order to tackle the incompatibility of the given hierarchy structure among target classes and the set of input-output pairs in large-scale hierarchical classification, we propose a principled strategy for adapting the hierarchy to better suit the classification problem at hand.

1.1 Our Contributions

In this work, we present a margin-based framework for choosing the most appropriate candidate nodes for replacement by their children nodes rather than all the nodes in a level. The proposed approach for taxonomy adaptation is based on well-founded theoretical results for generalization error analysis of margin-based classifiers deployed in a tree-based top down cascade [5]. The replacement is performed only for those classes which are more likely to be confused with other classes at the same level in the hierarchy. We exploit the margin information obtained at optimality while training the one-vs-rest classifiers to determine

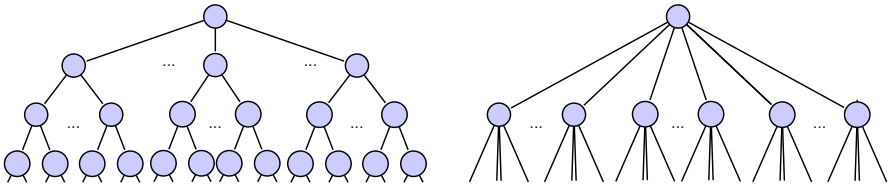

Fig. 1. Flattening the first and the third levels (right) of the original hierarchy (left)

the extent of confusion for each candidate class. This approach can be seen as synchronization of the two components of training data, taxonomy information on one hand and the set of input-output pairs on the other hand.

The proposed method is based on a more principled approach for node replacement as compared to ad-hoc methods based on flattening entire layers. As a result, our method is easily applicable to taxonomy structures in which the cascade length is arbitrarily long. Another advantage of our approach is that by choosing the most relevant candidates for replacement, it limits the extent of flattening and maintains the over-all hierarchical structure.

1.2 Other Related Work

Some of the earlier studies on exploiting hierarchy among target classes for the purpose of text classification, such as [2,4], in which the number of target classes were limited to a few hundreds. However, the work by [6] is among the pioneering in hierarchical classification towards addressing Web-scale directories such as Yahoo! directory consisting of over 100,000 target classes. The authors analyze the performance with respect to accuracy and training time complexity for flat and hierarchical classification. More recently, prevention of error propagation by applying *Refined Experts* trained on a validation set was proposed in [1]. In this approach, bottom-up information propagation is performed by utilizing the output of the lower level classifiers in order to improve classification at top level. Deep Classification [10] proposes to first identify a much smaller subset of target classes. Prediction of a test instance is then performed by re-training Naive Bayes classifier on the subset of target classes identified from the first step.

2 Problem Setup

In single-label multi-class hierarchical classification, the training data can be represented by a set of input-output pairs $S = \{(\mathbf{x}^{(i)}, y^{(i)})\}_{i=1}^{N}$ and hierarchical structure among target classes $\mathcal{G}$. In the context of text classification, $\mathbf{x}^{(i)} \in \mathcal{X}$ denotes the vector representation of document i in the input space $\mathcal{X} \subseteq \mathbb{R}^d$. Assuming that there are K classes denoted by the set $\mathcal{Y} = \{1 \dots K\}$, the label $y^{(i)} \in \mathcal{Y}$ represents the class associated with the instance $\mathbf{x}^{(i)}$. The hierarchy in the form of rooted tree is given by $\mathcal{G} = (\mathcal{V}, \mathcal{E})$ where $\mathcal{V} \supseteq \mathcal{Y}$ denotes the set

of nodes of $\mathcal{G}$, and $\mathcal{E}$ denotes the set of edges with parent-to-child orientation. Let $v_0 \in \mathcal{V}$ denote the root node of the hierarchy tree. In this setup, the leaves of the tree which form the set of target classes, which is given by $\mathcal{Y} = \{u \in \mathcal{V} : \nexists v \in \mathcal{V}, (u,v) \in \mathcal{E}\}$. Since the class hierarchy represents a transition from general to specialization of a concept as one traverses from root towards leaves, the documents which belong a particular leaf node also belong to all the nodes on the path from the root to that lead node.

In the above setup, given a new test instance $\mathbf{x}$, the goal is to predict the class $\widehat{y}$. This is done by making a sequence of predictions iteratively in a top-down fashion starting from the root until a leaf node is reached. At each non-leaf node $v \in \mathcal{V}$, a score $f_c(\mathbf{x}) \in \mathbb{R}$ is computed for each child c and the child $\widehat{c}$ with the maximum score is predicted i.e. $\widehat{c} = \underset{c:(v,c)\in\mathcal{E}}{\operatorname{argmax}} f_c(\mathbf{x})$.

In addition to being *highly accurate* for prediction, we also focus on *prediction speed*, which are two seemingly contradicting design requirements for a machine learning algorithm.

The motivation of approaches based on layer flattening such as [7,9] illustrated in Figure 1 is that by reducing the length of the cascade, the extent of propagation error can be reduced. However, these approaches lead to multiple folds increase in training time as shown in [9]. Prediction speed also suffers by employing excessive flattening as studied in the work by [6] showing that the space complexity of a flat classifier is much higher than a hierarchical model. Moreover, for predicting an unseen test instance in a K class problem, one needs to evaluate $O(K)$ classifiers in flat classification as against $O(\log K)$ classifiers in a top-down manner. In order to achieve a better trade-off among various metrics of interest in large-scale hierarchical classification, we next propose a technique for hierarchy adaptation which not only provides comparable or better performance to level flattening techniques but also maintains the overall hierarchical structure to enjoy faster training and prediction speed.

3 Taxonomy Adaptation in Large-Scale Hierarchical Classification

In this section, we propose a principled approach to adapt the taxonomy given a-priori as part of the training data by using the input-output pairs to output a taxonomy which leads to better accuracy. For our analysis, we focus on $L2$-regularized $L2$-loss linear Support Vector Machine (SVM), wherein the decision function $f_c(\mathbf{x})$ is modeled as a linear classifier such that $f_c(\mathbf{x}) = \mathbf{w}_c^T\mathbf{x}$. To learn an SVM-based discriminative classifier for node v, we solve the following optimization problem for each child c of v

$$f_c^* = \min_{\mathbf{w}_c} \left[\frac{1}{2}{\mathbf{w}_c}^T\mathbf{w}_c + C \sum_{\{i:y^{(i)}\in L_v\}} (\max(0, 1 - \operatorname{sgn}(y^{(i)} \circ L_c){\mathbf{w}_c}^T\mathbf{x}^{(i)}))^2 \right] \quad (1)$$

where L_v denotes the set of leaves in the subtree rooted at node v and C denotes the parameter for mis-classification penalty. We focus on one-vs-rest

technique to tackle the multi-class nature of the classification problem of identifying the most relevant child c of parent node v and hence y_i and L_c are related such that

$$\text{sgn}(y^{(i)} \circ L_c) = \begin{cases} +1 & \text{if } y^{(i)} \in L_c \\ -1 & \text{otherwise} \end{cases}$$

3.1 Margin-Based Approach to Taxonomy Adaptation

We derive our intuition from the recently proposed result[2] on the generalization error of maximum-margin classifiers deployed in the tree structure which can be stated as follows:

Theorem 1. *[5] Let m random input-output pairs are correctly classified using $\mathcal{G}$ containing $|\mathcal{V}|$ decision nodes with margins $\{\gamma_j, \forall j \in \mathcal{G}\}$, then the generalization error, with probability greater than $1-\delta$, is less than*

$$\frac{130R^2}{m}(D' log(4em) log(4m) + |\mathcal{V}| log(2m) - log(\frac{2}{\delta}))$$

where $D' = \sum_j^{|\mathcal{V}|} \frac{1}{\gamma_j^2}$ and R is the radius of the ball containing the distribution's support.

Though the above result is stated for the separable case, it indicates that in order to achieve better generalizability, one needs to decrease the quantity D'. Clearly, this quantity can be reduced if one removes those nodes from the tree which correspond to lower margin. The decision nodes with lower margin correspond to those classification problems which are relatively harder as compared to those nodes at which higher margin can be achieved. This is illustrated in Figure 2, in which not all nodes at a layer are replaced by their children but only those for which the margin is among the lowest. This strategy essentially lead to reducing the effective VC dimension or the Rademacher complexity of the overall hierarchical classifier and leading to a reduction in the generalization error in accordance with the Theorem 1.

Since we deal with the non-separable case, we need to remove those nodes for which the inverse of the margin and empirical error are jointly maximum. This quantity is captured for each decision node $c \in \{\mathcal{V}/v_0\}$ by the optimal value obtained from the objective function value f_c^* as given in Equation 1. For each parent node $v \in \mathcal{V}$, we consider the respective value of f_c^* $\forall c \in \mathcal{V}, (v,c) \in \mathcal{E}$ for each child c of v. The values f_c^* are sorted in decreasing order, which represents the preferential ordering of the nodes to be considered for flattening. Top r-ranked nodes are flattened for which f_c^* is among the highest, where r is chosen based on the distribution of these values. Typically, the value f_c^* is larger for a node which has more documents assigned to the leaves of the sub-tree rooted at that node, node sizes are taken into account in choosing the top r candidate nodes for replacement. Once the difference between the f_c^* values of the current

[2] The theorem can be found in the supplementary material of [5].

and next candidate child node is more than the previous difference, the flattening procedure for the current parent node is stopped. This process is repeated for all the parent nodes in the hierarchy irrespective of the length of the cascade. The algorithmic depiction of the procedure is shown in Algorithm 1. Note that the value of parameter C does not significantly affect the ordering of the nodes pruned by the proposed algorithm.

Since the algorithm maintains the overall hierarchy structure, it benefits from the properties of low space complexity and faster prediction, as we demonstrate in the next section. It was also observed that the resulting hierarchy after applying the transformation as given by the algorithm leads to more balanced classification problems at various levels.

Algorithm 1. The proposed comparative evaluation procedure.

Require: a hierarchy $\mathcal{G}$, input-output set S
  Train $L2$-regularized,$L2$-loss SVM in a top-down manner
  $gap \leftarrow 0$
  for $v \in \mathcal{V}$ **do**
    Sort the child nodes in decreasing order of f_c^* taking into account the class sizes
    Flatten 1st and 2nd ranked child nodes, say c_1 and c_2
    $gap = f_{c_1}^* - f_{c_2}^*$
    $c_{prev} \leftarrow c_2$ ▷ Set the previous flattened node to c_2
    for $c \in \mathcal{V} - \{c_1, c_2\}, (v, c) \in \mathcal{E}$ **do**
      if $f_{c_{prev}}^* - f_c^* < gap$ **then**
        Flatten c
        $gap \leftarrow f_{c_{prev}}^* - f_c^*$
        $c_{prev} \leftarrow c$ ▷ Set the previous flattened node to c
      else
        break
      end if
    end for
  end for
  return $\mathcal{G}$

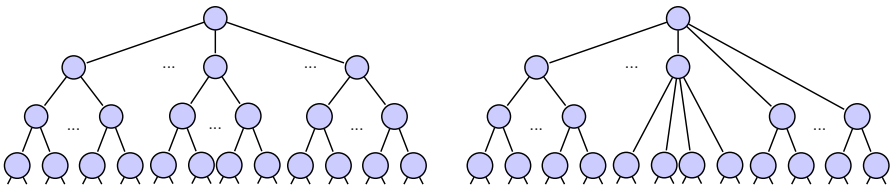

Fig. 2. Partial flattening (right) of the original hierarchy (left) for the proposed method

4 Experiments and Results

We use the publicly available DMOZ data set(excluding the validation set) from the LSHTC 2010 (**DMOZ-1**) and a subset of DMOZ from the LSHTC 2011 (**DMOZ-2**). The datasets, after having been pre-processed by stemming and stopword removal, appear in the LibSVM format. Table 1 presents the numeric values corresponding to the important properties of the dataset.

Table 1. Dataset Properties

Properties	DMOZ-1	DMOZ-2
Tr. Set Size	93,805	36,834
Feature Set Size	347,255	155,641
Target Classes	12,294	3,672
Test Set Size	34,880	36,834

We compare four strategies to evaluate their impact on classification accuracy : (i) Fully Hierarchical (FH) technique which uses the original hierarchy, (ii) Top Level Flattening (TLF) by removing the first layer, (iii) Multiple Level Flattening by removing first and third levels (MLF) as proposed in [7,9] and (iv) the proposed Margin-based strategy for Taxonomy Adaptation (MTA). We do not compare with our previous work on adaptive classifier selection in large-scale hierarchical classification [8], since the accuracy results using that approach were marginally better than FH method. We use Liblinear to train the models for L2-regularized L2-loss support vector classification. In order to maintain consistency, the value of the penalty parameter C was fixed to 1, for all the four methods.

As shown in Figure 3, the proposed method MTA achieves comparable or better accuracy as compared to the entire layer flattening techniques, MLF and TLF. The s-test [11] ($p < 0.001$) showed statistical differences of MTA over FH and TLF. Table 2 presents the comparison on **DMOZ-1** dataset for training time (including re-training), model sizes and prediction speed. Clearly, since the proposed MTA method preserves the overall hierarchical structure of the taxonomy it achieves better values for these metrics of practical significance.

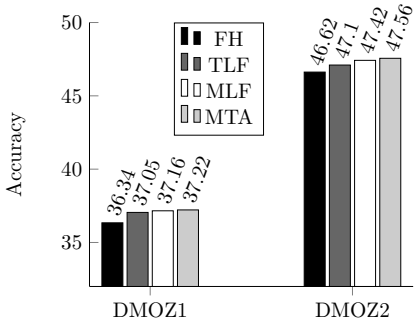

Fig. 3. Accuracy Comparison

Table 2. Comparison of MLF and MTA Training Time, Model size on hard-disk and Prediction Time for the DMOZ-1 dataset

Properties	MLF	MTA
Tr. Time (in hours)	6.3	3.2
Tr. Model Size (in GB)	7.8	4.2
Pred. Time (in mins)	55	17

5 Conclusion

We presented a principled method for automatically adapting the given hierarchy of classes, in large scale hierarchical classification, to output a new hierarchy which leads to better generalization. The proposed approach is backed by well-founded theoretical insights and exploits the margin information to identify those decision nodes in the hierarchy which correspond to relatively harder classification problems and removing those nodes to minimize the impact of propagation of error. Not only does it lead to comparable or better accuracy, but enjoys favourable training and prediction speed. This approach can be viewed as an instance of a more general paradigm of making the two parts of the input in a supervised learning problem more compatible.

Acknowledgments. This work was partly supported by the French National Research Agency (ANR), Class-Y project (ANR-10-BLAN-0211), and by the European Commission (EC), BioASQ project (FP7/2007-2013, ICT-2011.4.4(d)). The views expressed by the authors in this paper represent their own.

References

1. Bennett, P.N., Nguyen, N.: Refined experts: improving classification in large taxonomies. In: Proc. 32nd Int'l ACM SIGIR, pp. 11–18. ACM (2009)
2. Cai, L., Hofmann, T.: Hierarchical document categorization with support vector machines. In: CIKM, pp. 78–87. ACM (2004)
3. Dekel, O.: Distribution-calibrated hierarchical classification. In: Advances in Neural Information Processing Systems, pp. 450–458 (2009)
4. Dekel, O., Keshet, J., Singer, Y.: Large margin hierarchical classification. In: Proceedings of the 21st International Conference on Machine Learning, ICML 2004, pp. 27–34 (2004)
5. Gao, T., Koller, D.: Discriminative learning of relaxed hierarchy for large-scale visual recognition. In: IEEE International Conference on Computer Vision (ICCV), pp. 2072–2079 (2011)
6. Liu, T.-Y., Yang, Y., Wan, H., Zeng, H.-J., Chen, Z., Ma, W.-Y.: Support vector machines classification with a very large-scale taxonomy. SIGKDD Explor. Newsl., 36–43 (2005)
7. Malik, H.: Improving hierarchical svms by hierarchy flattening and lazy classification. In: 1st Pascal Workshop on Large Scale Hierarchical Classification (2009)
8. Partalas, I., Babbar, R., Gaussier, E., Amblard, C.: Adaptive classifier selection in large-scale hierarchical classification. In: Huang, T., Zeng, Z., Li, C., Leung, C.S. (eds.) ICONIP 2012, Part III. LNCS, vol. 7665, pp. 612–619. Springer, Heidelberg (2012)
9. Wang, X., Lu, B.-L.: Flatten hierarchies for large-scale hierarchical text categorization. In: Fifth IEEE International Conference on Digital Information Management, pp. 139–144 (2010)
10. Xue, G.-R., Xing, D., Yang, Q., Yu, Y.: Deep classification in large-scale text hierarchies. In: Proc. 31st Int'l ACM SIGIR, pp. 619–626. ACM
11. Yang, Y., Liu, X.: A re-examination of text categorization methods. In: Proceedings of the 22nd International ACM SIGIR, pp. 42–49. ACM (1999)

Selected Random Subspace Novelty Detection Filter

Fatma Hamdi

CGI BC
Paris la Défense 92097, France
firstname.secondname@cgi.com

Abstract. In this paper we propose a solution to deal with the problem of novelty detection. Given a set of training examples believed to come from the same class, the aim is to learn a model that will be able to distinguich examples in the future that do not belong to the same class. The proposed approach called Selected Random Subspace Novelty Detection Filter ($SRS - NDF$) is based on the bootstrap technique, the ensemble idea and model selection principle. The $SRS - NDF$ method is compared to novelty detection methods on publicly available datasets. The results show that for most datasets, this approach significantly improves performance over current techniques used for novelty detection.

1 Introduction

The task of novelty detection consists of identifing a new data that differs from those used in the training phase of a machine learning system. Several important works in the machine learning literature have addressed the issue of novelty detection and broad reviews of the subjet can be found in [1] and [2]. Novelty detection is an important learning problem, the basic idea is to build a decision rule that distinguishes *normal* from *novel* pattern. Since we can never train a machine learning system on all possible data that the system may deal with, it becomes important that it is able to detect *new* data. In order to overcome the limitations of individual learning algorithms and face the necesstiy of high classification performance specially in some critical domains, many researchers have been interested in ensemble methods. The aim of these techniques is to produce and combine multiple classifiers. Bagging [4], Boosting [5], random forest [8] and their variants are the most popular examples of this methodology. Bagging, a name derived from bootstrap aggregation, was the first effective method of ensemble learning and is one of the simplest methods of arching.

Generally the ensemble methods [16] work on two steps. The first one is the production of homogeneous or heterogeneous models. Models built from the same learning algorithm are called homogeneous and others that derive from running different learning algorithms on the same data set are called heterogeneous. The second step is the agregation of the models. Several techniques here include voting, weighted voting, selection and stacking. The ensemble selection algorithms was proposed to determine the good sub ensemble of classifiers. In supervised

M. Lee et al. (Eds.): ICONIP 2013, Part I, LNCS 8226, pp. 344–351, 2013.
© Springer-Verlag Berlin Heidelberg 2013

classification, it is known that selective classifier ensembles can always achieve better results compared to traditional ensemble methods [16]. The ensemble selection also called in the litterature ensemble prunning, ensemble overproduce or choose paradigm, consists in choosing a subset of l classifiers from the initial ensemble of size L ($l \leq L$). The selection of classifiers is based on predefined criteria. Generally the proposed approaches rearrange the initial ensemble and select a subset of ensemble members from the sorted list.

In this paper we present a learning model called Selected Random Subspace Novelty Detection Filter ($SRS - NDF$). It is a new approach to novelty detection, wich involves learning from only one class of traning example. We have a sample from one distribution *normal samples*, and our purpose is to differentiate between these normal examples and those that do not appear to come from the same distribution (*novelty*). The $SRS-NDF$ is an extension of our novelty detection model ($RS - NDF$) proposed in [17]. $SRS - NDF$ is based on the bootstrap technique, the ensemble idea [16] and model selection principle [18]. The methodologies for the production and combination of multiple predective models is a very active research area and it is commonly referred to ensemble method. The advantages of these methods are the improvement of the models estimation and the potential improvement of the scalability of their learning algorithms. The main idea of our approach is to perform classifier selection from an initial pool of filters [3] obtained with the ($RS - NDF$) algorithm. The proposed method works by evaluating the qualities of all obtained filters in terms of pertinence. Next we use the scree test [19] to choose the part of pertinent filters to build our final system.

The rest of the paper is organized as follow: Section 2 introduces the basic concepts of the Selected Random Subspace Novelty Detection Filter. Section 3 describes the databases and the experimental protocol. In section 4 we show validation results and their evaluation. Conclusion is given in section 5.

2 Selected Random Subspace Novelty Detection Filters

2.1 Principle of the Kohonen and Oja's Novelty Filter

In 1976, Kohonen and Oja [3] introduced an orthogonalising filter which extracts the parts of an input vector that are, new, with respect to previously learned patterns. This is the desired functionality of a novelty filter. The novelty filter shows the novelties in an input pattern with respect to previously learned patterns. Furthermore, the novelty filter can distinguish the missing parts from the added parts in the input pattern with respect to the previously learned patterns. The construction of the filter is based on Greville's theorem [15]. This theorem gives a recursive expression to estimate the transfer function of the network as follows:

$$\Phi_k = \Phi_{k-1} - \frac{\tilde{\mathbf{x}}_k \tilde{\mathbf{x}}_k^T}{\| \tilde{\mathbf{x}}_k \|^2} \tag{1}$$

where $\mathbf{x}_k = [x_1, x_2, ..., x_d]^T$ is a d-dimensional vector from the reference data matrix; $\tilde{\mathbf{x}} = \Phi_{k-1}\mathbf{x}_k$ represents the orthogonal projection of the vector $\mathbf{x}_k$ in the

subspace of novelty (Φ_{k-1}). This subspace is orthogonal to the space defined by the first $k-1$ reference data and $\Phi_0 = I$.

An interesting alternative approach was given by Kassab and al. [6], [7], that introduces the identity matrix in the learning formula for considering separately all training examples, and consequently all their features. During the learning phase, features which frequently appear in the training examples become more and more habituated as compared to the less frequent ones. This helps to more discriminate the relevant and irrelevant examples.The new learning rule is then defined as:

$$\Phi_k = \mathbf{I} + \Phi_{k-1} - \frac{\tilde{\mathbf{x}}_k \tilde{\mathbf{x}}_k^T}{\parallel \tilde{\mathbf{x}}_k \parallel^2} \tag{2}$$

where $\tilde{\mathbf{x}}_k = (\mathbf{I} + \Phi_{k-1})\mathbf{x}_k$ and Φ_0 is zero, or null matrix. The work described in this paper uses this new learning rule.

For the novelty detection problem, two proportions can be computed:

- *Novelty proportion*: this measure quantifies the novelty of an input data with respect to data that has been previously seen during the training.

$$N_{\mathbf{x}_i} = \frac{\parallel \tilde{\mathbf{x}}_i \parallel}{L \times \parallel \mathbf{x}_i \parallel} \tag{3}$$

  where L is the number of examples used for the training.
- *The habituation proportion*: this measure calculates the similarity of an example with the previously learned one: $H_{\mathbf{x}_i} = 1 - N_{\mathbf{x}_i}$.
  This proportion could be considered as the classification score of an example x_i. It indicates the probability that x_i belongs to the novel class.

To determine a detection threshold for each filter, the following principle was used:

- Scores (output's filter) attributed to the learning data can be used as a good indicator of the scores of data which can be positive and which are easy to detect because they are strongly similar to the data used for the learning. Consequently, the average of these scores can be admitted as a higher limit for the detection threshold.
- The scores attributed to available data for learning before their use, can be used as a good indicator of the scores of data which are positive but which are less easy to detect. Consequently, the average of these scores can be admitted as a lower limit for the detection threshold.

2.2 SRS-NDF Algorithm

In this section, we present an extention for the novelty detection algorithm $RS-NDF$. The $RS-NDF$ [17] approach uses multiple versions of a training set by using a double bootstrap, i.e. sampling with replacement on examples and sampling without replacement on features. Each of these data sets is used to train

a different NDF model. The $RS-NDF$ is then an ensemble of NDF, induced from bootstrap samples of the training data, using random features and examples selection in the model induction process. Prediction is made by aggregating (majority vote) the predictions of the ensemble to create a single output. Our method, called $SRS-NDF$, consists in selecting the ensemble members from a set of individuals filters wich gives better results, in terms of pertinence, than the original ensemble. $SRS-NDF$ belongs to the model selection approaches that reorder the original ensemble members based on pertinence criteria and select a subset of ensemble members from the sorted list using the scree test. $SRS-NDF$ works by evaluating the "index of balanced accuracy" and "diversity" of the filters in the $RS-NDF$ and selecting the promising filters. The final solution is achieved by combining all the selected filters from the original ensemble. To study the pertinence of each filter fl we used the following function:

$$Pertinence_{\alpha}(fl_1) = \alpha \times IBA_{\alpha}(fl_i) + (1-\alpha) \times mean(Div_{\alpha}(fl_i); fl_i); i \in [1, NF] \tag{4}$$

Where $IBA_{\alpha}(fl_i)$ and $Div_{\alpha}(fl_i)$ stands respectively for the index of balanced accuracy [20] and the diversity of the filter fl_i. The index of balanced accuracy is defined by the product of two terms Dominance and Gmean [20]. The first term is a simple measure evaluating the correct predictions of each filter, the second term is the geometric mean of accuracies measured separately on each class. The asset of IBA measure is the ability to distinguish the contribution of each class for overall performance. This means that different combinations of the true positive rate and the true negative rate don't provide the same IBA value and gives the pertinence to the positive class. This measure computes the area of a rectangular region in a two-dimensional space called "Balanced Accuracy Graph". The diversity of two classifiers consist on assigning differents labels to the same examples. Many measures have been proposed to quantify the diversity between two classifiers. In our work, we propose to use the mean Frobenius distance between the transfer matrix of fl_i and the other filters in $RS-NDF$. The coefficient α, $0 \leq \alpha \leq 1$, is a control parameter that balances the accuracy and diversity. The pertinence is then defined as a weighted combination of the diversity and accuracy. Once the pertinence have been calculated for a given α, we then used an established statistical method, scree test, to select the most important filters. This statistical test was initially developed to provide a visual technique to select eigenvalues for principal components analysis.

The basic idea is to generate a curve associated with eigenvalues, allowing random behavior to be identified. The number of components retained is equal to the number of values preceding this "scree". Often the "scree" appears where the slope of the graph changes radically. We therefore needed to identify the point of maximum deceleration in the curve.

Assuming that we have pertinence vector $\mathbf{Per}_k = (Per_{1k}, Per_{2k}..., Per_{jk}, ..., w_{nk})$. Thus we have to process the steps: **Scree Test Acceleration Factor**

1. Sort the pertinence in descending order $\mathbf{Per}_k$. The we obtain a new order $\mathbf{Per}_k = (Per^1_{..}, Per^2_{..}..., Per^i_{..}, ..., Per^n_{..})$; where Per^i indicates the index order.
2. Compute the first difference $df_i = Per^i_{..} - Per^{i+1}_{..}$;
3. Compute the second difference (acceleration) $acc_i = df_i - df_{i+1}$
4. Find the scree: $\max_i (abs(acc_i) + abs(acc_{i+1}))$
5. Cut and consider all the filters until the scree; (use initial indices of filter before sorting)

The SRS-NDF learning algorithm is shown below:

Algorithme 1. Selected Random Subspace Novelty Detection Filter

Repeate for all $\alpha \in [0, 1]$

1. Construct the $RS - NDF$ with NF filters.
2. Calculate the IBA of filters $= IBA_\alpha(1), ..., IBA_\alpha(NF)$.
3. Calculate the diversity of filters $= Div_\alpha(1), ..., Div_\alpha(NF)$.
4. Calculate the pertinence of filters $= Pertinence_\alpha(1), ..., Pertinence_\alpha(NF)$. $Pertinence_\alpha(fl_1) = \alpha \times IBA_\alpha(fl_1) + (1 - \alpha) \times meanDiv_\alpha(fl_1)$; $fl_i; i \in [1, NF]$
5. Select the subset of models using the ScreeTest $= SelectedFilters_\alpha$
6. Calculate the IBA of the selected filters $= IBA_{SelectedFilters_\alpha}$
7. $\alpha = \alpha + 0, 1$

Until $\alpha = 1$

- Select the subset with the best value of IBA
- Aggregate the predictions of the selected ensemble and save the novelty detection results in D.

3 Experiments

3.1 Databases Description

We performed several experiments on many relevant data sets: $Spectf$, $Waveform$, $Wine$ and $Yeast$ from the UCI repository [9] , and Oil [11]. These data sets are summarized in table 1. Since all of the datasets are for binary or multi-class classification problems, they were transformed into novelty detection context. We chose randomly, from each data set, a class as the novelty class and collapsed the rest of the classes into one, and use the modified datasets to evaluate the performance of our approach.

Table 1. Data Set summary

Dataset	Dimension	Size	Size of Novelty class
Oil	48	937	41
Spectf	44	187	15
Waveform	21	5000	1647
Wine	13	178	59
Yeast	8	1484	244

3.2 Performance Measurement and Experimental Protocol

To evaluate the performance of our approach we used several metrics such as true negative rate (Acc-), true positive rate (Acc+)(recall), precision, F-measure and G-mean. These metrics have been widely used for comparaison.

For each dataset, the performance of the classifier ensemble obtained by $SRS-NDF$ was compared to the unpruned filter ensemble obtained from $SR-NDF$, the basic model NDF and the traditional novelty detection methods : The one class Support Vector Machines (SVM) [14], The Principal Components Analysis (PCA) [13], The auto-associative Multi Layers Perceptron (MLP) [12].

We also used the Area under the ROC Curve (AUC) [10]. There are several methods to estimate the area under the ROC curve. In the case of binary classification, the balanced AUC_b is defined as:

$$AUC_b = \frac{Acc- + Acc+}{2} \tag{5}$$

4 Results

For each database, the six approaches have been used and their results have been evaluated in terms of the six performances metrics. The table 2 below shows the performance of the different algorithms on all data sets.

Based on the table above, some conclusions can be drawn.

The results of *wine* data set shows that $SRS-NDF$ is the superior approach to novelty detection. Our approach outperforms the results obatained by all others methods on all metrics. For $Waveform$ dataset, $SRS-NDF$ shows a great improvement over all algorithms on $Acc-$, $Acc+$, AUC_b and $G-mean$ metrics. Except on *precision* and $F-measure$, $RS-NDF$ gives the better results. For $Spectf$ dataset, our algorithm outperforms the other methods on $Acc+$ and $F-measure$ but gives a slightly inferior results on AUC_b and $G-mean$. Genarally our proposed approach $SRS-NDF$ gives better results compared to $RS-NDF$ on $Acc+$ and $F-measure$ metrics. The $Acc+$ measure represents the models capacity to detect the novelty class. We chose this metric in purpose to show the good capacity of $SRS-NDF$ to detect the novelty class. As we can see, $SRS-NDF$ shows excelent results comparing to $RS-NDF$ on all datasets. Considering the $F-measure$, our algorithm gives favorable improvement over $RS-NDF$ on Oil, $Wine$ and $Spectf$ datasets. For $Waveform$ data, $RS-NDF$ outperforms our proposed approach. This metric, that combines

Table 2. Performance comparison on all data sets

Wine	$Acc-$ $(Recall)$	$Acc+$	$Prec$	$F-$ $measure$	AUC_b	$G-$ $mean$
MLP	0,78	0,68	0,83	0,81	0,73	0,73
ACP	0,60	0,69	0,80	0,68	0,65	0,64
SVM-1C	0,68	0,76	0,81	0,73	0,72	0,71
NDF	0,84	0,78	0,88	0,86	0,81	0,81
RS-NDF	0,87	0,85	0,92	0,89	0,86	0,86
SRS-NDF	**0,90**	**0,93**	**0,93**	**0,91**	**0,92**	**0,92**
Waveform						
MLP	0,67	0,35	0,51	0,58	0,51	0,48
ACP	0,68	0,35	0,68	0,68	0,51	0,49
SVM-1C	0,88	0,22	0,70	0,78	0,55	0,44
NDF	0,68	0,57	0,77	0,72	0,63	0,62
RS-NDF	0,85	0,53	**0,79**	**0,82**	0,69	0,67
SRS-NDF	**0,90**	**0,60**	0,70	0,78	**0,75**	**0,70**
Spectf						
MLP	0,60	0,78	0,42	0,49	0,69	0,68
ACP	0,51	0,82	0,43	0,47	0,67	0,65
1-SVM	0,73	0,74	0,43	0,54	0,74	0,74
NDF	**0,76**	0,75	0,45	0,56	**0,76**	**0,76**
RS-NDF	0,69	0,79	**0,47**	0,56	0,74	0,74
SRS-NDF	0,64	**0,84**	0,44	**0,58**	0,74	0,74
Yeast						
MLP	0,77	0,23	0,84	0,80	0,50	0,39
ACP	0,68	0,66	0,91	0,78	0,67	0,67
SVM-1C	0,90	0,13	0,84	0,87	0,51	0,34
NDF	0,88	0,19	0,85	0,86	0,54	0,41
RS-NDF	**0,94**	0,29	0,87	**0,90**	0,62	0,52
SRS-NDF	0,93	**0,53**	**0,93**	**0,90**	**0,72**	**0,70**
Oil						
MLP	0,96	0,15	0,96	0,96	0,55	0,38
ACP	0,94	0,24	0,96	0,95	0,59	0,48
SVM-1C	0,90	0,35	**0,97**	0,93	0,62	0,56
NDF	0,91	0,37	**0,97**	0,94	0,64	0,58
RS-NDF	0,94	0,22	0,96	0,95	0,58	0,46
SRS-NDF	**0,98**	**0,46**	0,95	**0,97**	**0,72**	**0,69**

precision and recall measures, is commonly used in the information retrieval area as performance measure.

The $G-mean$ results on all datasets confirmed the good performances of our approach $SRS-NDF$. As we can see, our method gives better results comparing to $RS-NDF$. The Gmean of accuracies, measured separatly on each class, is associated to a point in theROC curve and the idea is to maximize the accuracies of both classes while keeping them blanced.

5 Conclusion

This paper introduced a filter ensemble selection method to improve the Random Subspace Novelty Detection Filter ($RS-NDF$) by adaptively trading off diversity and accuracy according to the data. The proposed approach $SRS-NDF$ is based on the orthogonal projection operators, the bootstrap method and the ensemble selection paradigm. Several metrics are computed on publicly available datasets and significant improvements were obtained by $SRS-NDF$ comparing to existing methods.

References

1. Markou, M., Singh, S.: Novelty detection: a review - part 1: statistical approaches. Signal Processing 83, 2481–2497 (2003)
2. Markou, M., Singh, S.: Novelty detection: a review - part 2: neural network based approaches. Signal Processing 83, 2499–2521 (2003)
3. Kohonen, T., Oja, E.: Fast Adaptive Formation of Orthogonalizing Filters and Associative Memory in Recurrent Networks of Neuron-Like Elements. Biological Cybernetics 21, 85–95 (1976)
4. Breiman, L.: Bagging Predictors. Machine Learning 24(2), 123–140 (1996)
5. Freund, Y., Saphire, R.E.: Experiments with a new boosting algorithm. In: The 13th International Conference on Machine Learning, pp. 276–280 (1996)
6. Kassab, R., Lamirel, J.-C., Nauer, E.: Novelty Detection for Modeling Users Profile. In: The 18th International FLAIRS Conference, pp. 830–831 (2005)
7. Kassab, R., Alexandre, F.: Incremental Data-driven Learning of a Novelty Detection Model for One-Class Classification Problem with Application to High-Dimensional Noisy Data. Machine Learning 74(2), 191–234 (2009)
8. Breiman, L.: Random forest. Machine Learning (2001)
9. Asuncion, A., Newman, D.J.: UCI Machine Learning Repository. University of California, Irvine (2007)
10. Bradeley, P.W.: The use of area under the ROC curve in the evaluation of machine learning algorithms. Pattern Recognition 30, 1145–1159 (1997)
11. Kubat, M., Holte, R.C., Matwin, S.: Machine Learning for the Detection of Oil Spills in Satellite Radar Images. Machine Learning 30, 195–215 (1998)
12. Rumelhart, D.E., Hinton, G.E., Williams, R.J.: Learning internal representation by error propagation. In: Parallel Distributed Processing: Explorations in the Microstructures of Cognition, pp. 318–362. MIT Press (1986)
13. Jolliffe, I.T.: Principal Component Analysis. Springer Series in Statistics. Springer, Berlin (1986)
14. Scholkopf, B., Platt, J., Shawe-Taylor, J., Smola, A.J., Williamson, R.C.: Estimating the support of a high-dimensional distribution. Neural Computation (1999)
15. Greville, T.N.E.: Some applications of the pseudoinverse of a matrix. SIAM Rev. (1960)
16. Zhang, Y., Burer, S., Street, W.N.: Ensemble prunning via semi-denite programming. Journal of Machin Learning Reasearch 7, 1315–1338 (2006)
17. Hamdi, F., Bennani, Y.: Learning Random Subspace Detection Filter. In: International Joint Conference in Neural Networks, IJCNN (2011)
18. Caruna, R., Niculescu Mizil, A., Grew, G., Ksikes, A.: Ensemble selection from librairiesof models. In: The 21st International Conference on Machin Learning (2004)
19. Catell, R.: The scree test for the number of factor. Multivariate Behaviorial Research, 245–276 (1966)
20. García, V., Mollineda, R.A., Sánchez, J.S.: Index of balanced accuracy: A performance measure for skewed class distributions. In: Araujo, H., Mendonça, A.M., Pinho, A.J., Torres, M.I. (eds.) IbPRIA 2009. LNCS, vol. 5524, pp. 441–448. Springer, Heidelberg (2009)

Peripheral Nerve Localization by Frequency-Based Electrical Stimulation

Dilok Puanhvuan[1], Sorayouth Chumnanvej[1,2], Sarawin Khemmachotikun[1], and Yodchanan Wongsawat[1]

[1] Department of Biomedical Engineering, Faculty of Engineering, Mahidol University, {dilok.ee52,khemmachotikun.s}@gmail.com, yodchanan.won@mahidol.ac.th

[2] Department of Surgery, Faculty of Medicine, Ramathibodi Hospital, Mahidol University, Thailand sorayouth@gmail.com

Abstract. During surgery, the nervous system is at risk if surgeon could not localize nerve's location. In case of tumor blocked, the surgeon can completely not visualize the nerve due to the tumor. Hence, nerve localization is very important during to operation. Generally, the neurophysiologic intra-operative monitoring (NIOM) has alarming feature, when the surgeon irritated the nerve, they could pre-localize the nerve. However, this alarming is quite sensitive since it sometime alarms even when the surgeon hints other area expected the nerve. This would makes the surgeon qualitative evaluates location of the nerve. This study proposed the new modality of nerve localization. The nature of compound muscle action potential (CMAP) was used in this study. Given a frequency-based electrical stimulation to a targeted area, the CMAP would response if and only if the stimulating electrode was placed directly to the nerve. The results from preliminary study in animal revealed that applying the stimulation at 30Hz and 0.3Volt with 1.5 millimeters width of a bipolar electrode gave highest CMAP detection accuracy (97.5%).

Keywords: Electrical Nerve Stimulation, Nerve Localization, EMG, CMAP.

1 Introduction

Nerve localization during surgery is very important. For example, in the case of vestibular schwannoma, cranial nerve 7th (facial nerve) possibly be damaged by the surgeon due to a blocked tumor. If the facial nerve is permanently damaged, the patient would be facial palsy. Presently, there is a commercialized product available called neurophysiologic intra-operative monitoring (NIOM). The NIOM has a feature that can alarm the surgeon when they are closing to the nerve. When a surgical tool irritates directly to the nerve, there will be a spike and burst of nerve discharge appear on a free running electromyography (EMG). This nerve discharge is then converted to sound which the sound level indicates a level of irritation [1-3]. Therefore, the surgeon can aware of damaging and pre-localize the facial nerve. However, this warning is

M. Lee et al. (Eds.): ICONIP 2013, Part I, LNCS 8226, pp. 352–359, 2013.
© Springer-Verlag Berlin Heidelberg 2013

quite sensitive. Without directly irritating to the nerve i.e. during tumor removal or dissection, there still is a warning sound the surgeons and makes them qualitative evaluated location of the nerve. The surgeon sometime obsoletes this warning. There is another kind of nerve response called compound muscle action potential (CMAP), it normally uses for facial nerve function preservation [4, 5]. Given an electrical stimulus to the nerve, there will be a pulse response appears at some latency after stimulus. Amplitude of the CMAP response indicates a remaining nerve function. 50% decreasing in amplitude is considered as a safety criteria [4].

This study proposes a new technique of nerve localization that could help the surgeon quantitative localizes the nerve. We employed the nature of the CMAP response that it surely elicits when the stimulating electrode place exactly to the nerve. Instead of using the alarming sound from nerve irritation, this study used stimulating electrodes that contained electrical stimuli. We hypothesized that if we apply an electrical stimulation at some frequency, the CMAP would and would not response at the same frequency after applying the stimulus train to the nerve and other area (i.e. around the nerve and the tumor), respectively. Hence, we could identify whether a current position of a stimulating electrode is the nerve or not.

This work is a preliminary investigation that was studied in animal trials. The sciatic nerve of a rat is used for representing the facial nerve in a human. Agarose gel is use for mimicking a tumor tissue. There are many parameters that need to be figured out for being an optimally frequency-based electrical stimulation i.e. frequency, voltage, pulse duration and the width between anode and cathode.

2 Materials and Methods

2.1 Signal Acquisition and Electrical Nerve Stimulation

The experiment was conducted under animal ethic approval. This study included 4 sciatic nerves of 2 male Sprague-Dawley rats (age, 8 weeks; weight, 300 grams). Fig. 1(a) shows an overview of the signal acquisition and the electrical nerve stimulation systems. Bipolar needle electrodes that placed on the Tibialis anterior, Gastrocnemius, Vastuslateralis and Semimembranosus muscles of the rat's leg are used for EMG signals recording. These EMG signals were sampled at 1 kHz sampling frequency and amplified by 200 gains in the biomedical instrument named "BIOPAC MP35" (BIOPAC systems, Inc., USA). This study used a constant voltage stimulator called "BSLSTMB Stimulator" (BIOPAC systems, Inc., USA) for applying electrical nerve stimulation. The BSLSTMB stimulator generates a defined voltage level and frequency to the sciatic nerve via bipolar needle electrodes as shown (See Fig. 1(b)) and also sent the pulses feedback to the acquisition system.

The "BIOPAC BSL 4.0 MP35"software was used for electrical nerve stimulation and signal recording setups, monitoring and recording all of the acquiring data (EMG, pulses feedback). During the experiment, sound and video were recorded via a webcam synchronously with the signal acquisition time.

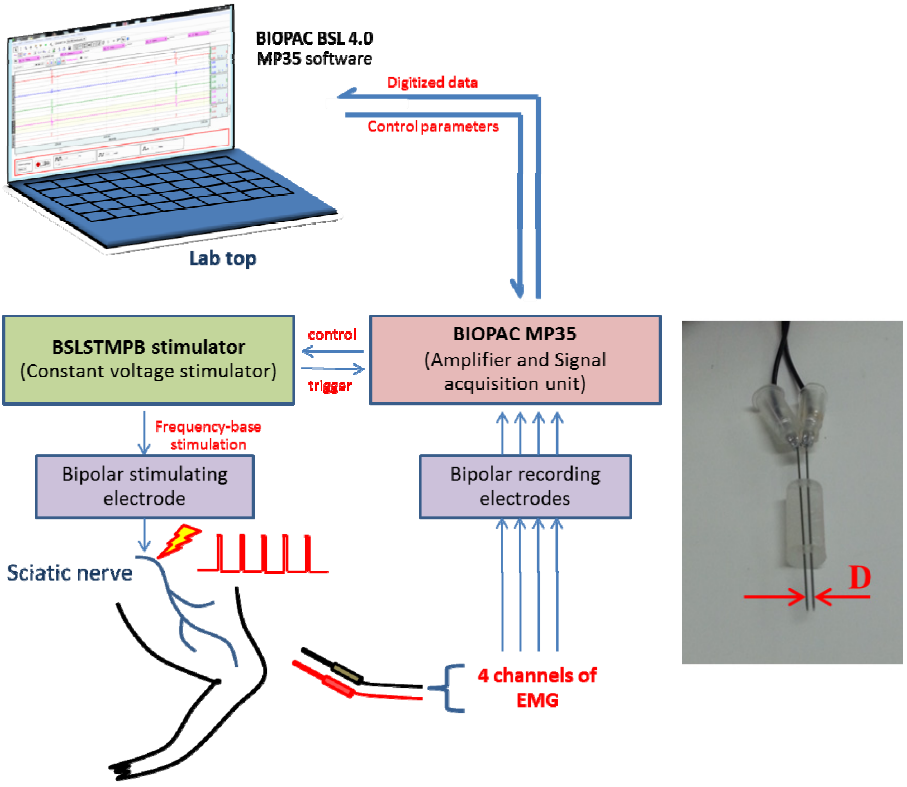

Fig. 1. (a) Block diagram of signal acquisition and frequency based electrical nerve stimulation. (b) The bipolar stimulating electrode was fixed at the width D.

2.2 Experimental Procedure

When all equipment mentioned in the Fig. 1(a) was completely setup, the experiment was first started on the left sciatic nerve by the sequent as follows;

1. Anesthetize the rat by 80 mg/kg ketamine and 10 mg/kg xylazine and wait until the rat was anesthesia [6].
2. Place a needle electrode subdermally to the defined locations on the operating leg. The ground electrode was placed at the anterior part of the higher hind limb.
3. Start surgery to find the sciatic nerve. Fig. 2(a) shows a picture of the sciatic nerve.
4. Perform mind irritation by a pure needle electrode and the forceps direct to nerve and around the nerve.
5. Fix the bipolar stimulating electrodes at 1 mm width by the handmade needle holder as shown in Fig. 1(b). This width would not greater than the targeted nerve (approximately 1.8 mm diameter of facial nerve [7]).

6. Apply the frequency based electrical stimulation directly to the nerve and around the nerve by varying frequency[1] and voltage[2]. Fig. 2(b) was capture during the experiment when applying electrical stimulation directly to the nerve.
7. Repeat the 5th and 6th sequences with 1.5 mm width of the bipolar needle electrode.
8. Place a mimic tumor tissue to the nerve as shown in Fig. 2(c). This tumor phantom is agarose gel that was prepared by mixing agarose powder with PBS (Phosphate Buffer Saline, pH 7.4). 0.65% agarose gel was considered as a realistic brain phantom [8]. However, the density of a tumor mass is higher than brain matter. Hence, this study used 1% agarose gel for mimicking a tumor tissue.
9. Push directly to the mimic tumor tissue by a pure needle electrode and the forceps.
10. Fix the bipolar needle electrodes at 1 mm width.
11. Apply the frequency based electrical stimulation directly to mimic tumor tissue by varying frequency and voltage at 15, 30, 45 Hz and 0.15, 0.20, 0.25 and 0.30 volt, respectively.
12. Repeat the sequent number 2-11 to the right side of the rat's sciatic nerve.

After both sciatic nerves were operated, the rat was terminated by over dosing at three the anesthetic dose [6].

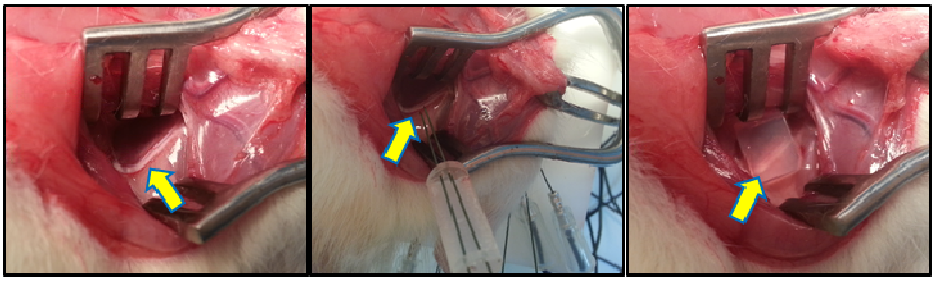

(a) (b) (c)

Fig. 2. Rat's sciatic nerve; (a) the location of the sciatic nerve, (b) the sciatic nerve during stimulation and (c) the mimic tumor (Agarose gel) on the sciatic nerve

2.3 CMAP Responses Detection

The recorded 4 EMG channels were filtered by digital highpass filter at 300 Hz cut off frequency. Given electrical pulse stimulation directly to the nerve, the CMAP response was elicited as shown Fig. 3 (red/thick line). Conversely, applying a stimulus to other area, there was no CMAP response appeared after stimulation (See Fig. 3

[1] The varied frequencies (15, 30, 45 Hz) were assumed which based on refractory period of the neuron (10 ms) [7]. Therefore, maximum frequency should not exceed a half of 100Hz.

[2] The varied voltages (0.15, 0.2, 0.25, 0.3 volt) were assumed according to the voltage different of action potential (depolarization (30mV) – membrane potential (-70mV) = 100 mV) [7]. Therefore, the stimulating voltage should higher than 0.1 volt.

(blue/thin line)). Regarding to the characteristic of the CMAP, it has high variation compared with none CMAP signal. Hence, we could simply detect the CMAP by calculating the variance of the CMAP response comparing with the baseline.

Samples between 1-8 milliseconds after stimulus were segmented according to the feedback stimulation pulse. An array of this sample was used for calculating the variance. If the variance of a target array is greater than **threshold × base line variance**, this response would be considered as CMAP. This base line variance was calculated from a normal condition.

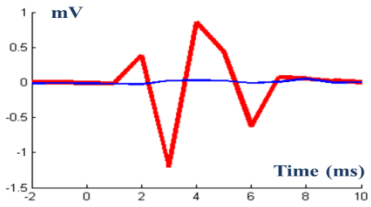

Fig. 3. CMAP (red/thick line) and none CMAP responses (blue/thin line) after given electrical stimulus (at time zero)

3 Results

There was no significant change of EMG signals when irritating direct and indirect to nerve by pure needle electrode. When the nerve was irritated by the forceps (surgical equipment), there was burst and spike of nerve discharge appeared on EMG data as shown in Fig. 4. In addition, irritating around the nerve and onto the mimic tumor also had those nerve discharge appeared on EMG signals.

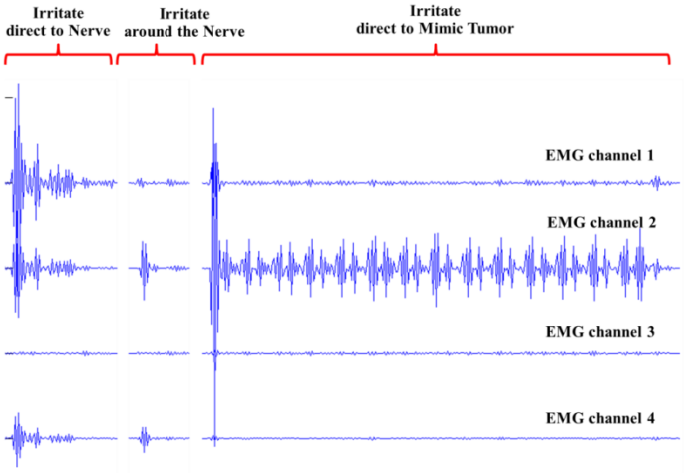

Fig. 4. Burst (a) and spike (b) of nerve discharge on EMG signals after irritated the nerve, around the nerve and onto the mimic tumor by the forceps

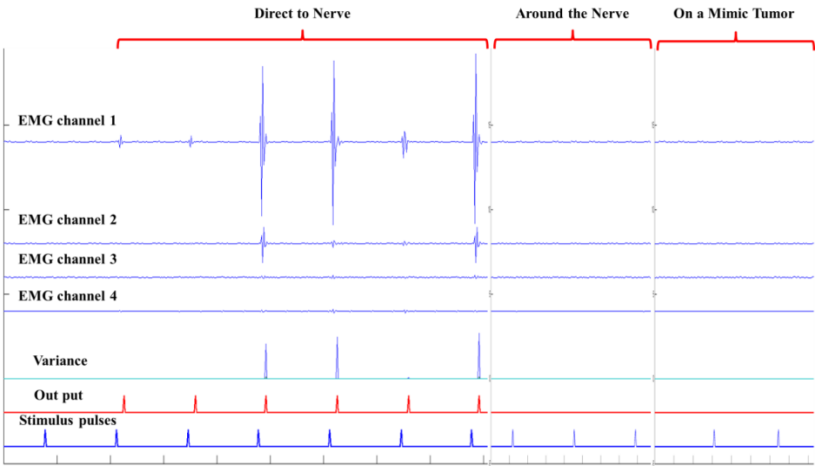

Fig. 5. EMG signal during applying frequency-based electrical stimulation onto the nerve, around the nerve and mimic tumor tissue

Fig. 5 shows the EMG signal during applying frequency-based electrical stimulation onto the nerve, around the nerve and mimic tumor tissue. The results revealed that there was the CMAP response elecited according to the stimulus pulse when the stimulating electrode was place right to the nerve. Conversely, placing the stimulating eletrode to other area could not activate any CMAP response. This information support our hypothesis and it could be used for nerve nerve localization. The EMG channels 1 to 4 were segmented according to the stimulus pulses (see Fig. 5 (bottom line)). The segmented EMG data was calculated variance compared with the base line variance. For offline analysis, this experiment was set the threshold at 100. The classification result was shown in Fig. 5 (red line)) that was able to detect the CMAP response.

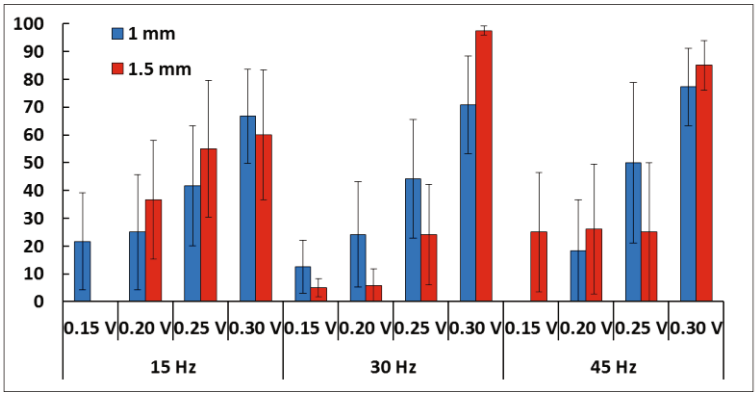

Fig. 6. The averaged CMAP detection accuracy of 4 sciatic nerves (2 rats). Red and blue bars are averaged accuracies of CMAP detection by 1 and 1.5 millimeters width of electrode.

Fig. 6 shows offline CMAP detection accuracy. This accuracy was averaged by 4 sciatic nerves. Red and blue bars are averaged accuracies of CMAP detection by 1 and 1.5 millimeters width of bipolar needle electrode, respectively. The stimulation was applied in 3 frequencies (15, 30 and 45 Hz) and 4 voltage levels (0.15, 0.20, 0.25 and 0.30 volt). The results showed that increasing in voltage level, the accuracy also increased in both 1 and 1.5 millimeters width electrode. 0% detection accuracy could be found at lowest voltage (0.15 volt). If the voltage was high enough (0.3 volt), the CMAP could response to entire stimulus pulse and make CMAP detection accuracy closed to 100%. The stimulation parameters of 30Hz and 0.30 volts showed greatest performance of CMAP detection accuracy.

4 Discussion

Burst and spike EMGs of nerve discharge were occurred when the nerve was irritated. However, this nerve discharge could be seen even when the surgical tool irritated other area for example; around the nerve and onto the tumor (See Fig. 4). This Burst and spike EMGs might be caused by tumor and nerve compression [1-3]. There was no nerve discharge after irritate the nerve by the needle. It might be caused from the small size of the needle electrode compared with the surgical tool.

There was no CMAP response after applied an electrical stimulation pulse to other area excepted for the nerve. This would be the new modality of nerve localization that could make the surgeon precisely and accurately localizing the nerve. The simple CMAP detection algorithm by calculating variance of a small sampling window would make the system rapidly detect the CMAP response in on-line experiment.

Given electrical stimulus at low voltage sometime could not activate the CMAP response and made the CMAP detection algorithm failed to detect. This might be caused by the different impedance in each position of a stimulation point. This problem could be solved by increasing the voltage level. However, applying at high stimulating voltage might damage the nerve. Nevertheless, there is another type of electrical stimulation called constant current stimulator which can regulate a current at the same level even when there is difference in impedance [9]. The problem of varying impedance might be solved by this stimulator. Stimulating frequency at 30 Hz showed a highest CMAP detection accuracy. The wider length between anode and cathode (1.5 mm) of bipolar needle electrode show a better CMAP detection accuracy. However, the width of the bipolar needle electrode should not be wider than the nerve bundle diameter. Otherwise, the nerve could not be stimulated due to the gap.

5 Conclusion

Irritating the nerve by pure needle electrode could not elicit burst or spike EMG. Hence, it was unable to use for nerve localization. The traditional technique of using the burst and spike EMG in NIOM could be used for nerve localization. However, the surgeon needs to have high experience due to the burst and spike EMG were sometime happened when the surgical equipment irritated around the nerve and onto the mimic tumor. This nerve localization method is qualitatively evaluated by the surgeon.

Applying the frequency-based electrical stimulation directly to the nerve could elicit the CMAP response while it could not occur in other areas (around the nerve and onto the mimic tumor tissue). By using this principle, we could then localize the nerve by detecting the CMAP response. The proposed CMAP detection algorithm could be detected CMAP response. The highest CMAP detection accuracy (97.5%) could be found when applying the frequency-based electrical nerve stimulation at 30Hz, 0.3Volt, 1 millisecond of pulse width and 1.5 millimeter width between cathode and anode. The study proposed the new modality of nerve localization. The present study successfully identified and localized position of the sciatic nerve in a rat model. We believe that the proposed method could also be used for nerve localization in the human model. The surgeon could more quantitative localize the nerve by using our proposed technique.

Acknowledgement. This projected is supported in part by Thailand Center of Excellence for Life Sciences (TCELS) and the Government funding of Mahidol University, Thailand.

References

1. Kombos, T., Suess, O., Kern, B.C., Funk, T., Pietilä, T., Brock, M.: Can continuous intraoperative facial electromyography predict facial nerve function following cerebellopontine angle surgery? Neurol Med. Chir (Tokyo) 40, 501–507 (2000)
2. Romstöck, J., Strauss, C., Fahlbusch, R.: Continuous electro-myography monitoring of motor cranial nerves during cerebellopontine angle surgery. J. Neurosurg. 93, 586–593 (2000)
3. Prass, R.L., Lüders, H.: Acoustic (loudspeaker) facial electromyographic monitoring: Part 1. Evoked electromyographic activity during acoustic neuroma resection. Neurosurgery 19, 392–400 (1986)
4. Amano, M., Kohno, M., Nagata, O., Tahiguchi, M., Sora, S., Sato, H.: Intraoperative continuous monitoring of evoked facial nerve electromyograms in acoustic neuroma surgery. Acta Neurochir. 153, 1059–1069 (2011)
5. Silverstein, H., Willcox, T.O., Rosenberg, S.I., Seidman, M.D.: Prediction of facial nerve function following acoustic neurona resection using intraoperative facial nerve stimulation. Laryngoscope 104, 539–544 (1994)
6. Meredith, A., Redrobe, S.: The BSAVA Manual of Exotic Pets, 4th edn. John Wiley & Sons (2002)
7. Chen, Z.J., Gillies, G.T., Broaddus, W.C., Prabhu, S.S., Fillmore, H., Mitchell, R.M., Corwin, F.D., Fatouros, P.: A realistic brain tissue phantom for intraparenchymal infusion studies. J. Neurosurg. 101(2), 314–322 (2004)
8. Marieb, E.N., Hoehn, K.: Human Anatomy & Physiology, 8th edn. Pearson (2010)

A Novel Complex-Valued Fuzzy ARTMAP for Sparse Dictionary Learning

Chu Kiong Loo, Ali Memariani, and Wei Shiung Liew

Faculty of Computer Science and Information Technology
University of Malaya
Kuala Lumpur, Malaysia
ckloo.um@um.edu.my, ali_memariani@siswa.um.edu.my,
liew.wei.shiung@gmail.com

Abstract. This work extends the simplified fuzzy ARTMAP (SFAM) to a complex-valued (CV-SFAM) version which is able to work with spatio-temporal data produced in receptive fields of visual cortex. The CV-SFAM's ability for incremental learning distinguishes CV-SFAM from other complex-valued neural networks, which provides the ability to preserve learned data while learning new samples. We considered different scales and orientations of Gabor wavelets to form a dictionary. This work takes advantage of a locally competitive algorithm (LCA) which calculates more regular sparse coefficients by combining the interactions of artificial neurons. Finally, we provide an experimental real application for biological implementation of sparse dictionary learning to recognize objects in both aligned and non-aligned images.

Keywords: complex-valued simplified fuzzy ARTMAP, sparse coding, dictionary learning, genetic optimization, body expression.

1 Introduction

Complex-valued neural networks (CVNN) are a type of neural nets dealing with complex-valued information using complex-valued variables and parameters [3]. They are variety of fields in which the CVNNs provide proper information representations. So far most of the applicable fields are related to wave phenomena, e.g., measurements and communications using waves such as radar image processing, quantum computation, learning electron-wave devices, ultrasonic imaging and so on. The wavelength-dependent dynamics of optical circuit leads to adaptive optical routers in optical wavelength-division-multiplexed communications, variable optical connections, frequency-domain parallel information processing, etc. The carrier-frequency-dependent neural behavior realizes both the adaptability and controllability in neural networks [3].

CVNNs were first introduced by Aizenberg as phasor where amplitude was fixed [5]. Multiple-valued associative memory is developed with memory capacity [6]. Many works attempted to derived complex form of linear models using complex linear systems, e.g. complex steepest descent [7] [8] and backpropagation

M. Lee et al. (Eds.): ICONIP 2013, Part I, LNCS 8226, pp. 360–368, 2013.
© Springer-Verlag Berlin Heidelberg 2013

learning [9]. Complex-valued activation functions are discussed in both separate and integrated real-imaginary forms [10] [11].

However, the previous work of CVNNs are poor in preserving learned data after new learning arrivals which causes the stability-plasticity dilemma [12]. One approach to face with this is using incremental learning as in fuzzy ARTMAP [18] and fuzzy min-max [14] neural networks.

Simplified fuzzy ARTMAP (SFAM) is a modification of fuzzy ARTMAP [13] as a two-layer neural network which has been successfully used for pattern recognition [15] [16] [17]. Adjustable learning rate and incremental learning capability makes it suitable for real-time applications. With fast learning rates its computational complexity could be compared to a multi-layered perceptron [18]. Furthermore, neural structure of SFAM combined with fuzzy operators, models a human-like behavior [2] [15]. However, using real-valued input features, SFAM is not able to be used in most of the vision applications in which data is intrinsically complex. Complex fuzzy set theory has been proposed in by Ramot et al. [19] [20]. This work applies complex fuzzy operators in order to develop a novel complex-valued SFAM (CV-SFAM).

We applied the proposed model on patterns of different objects in images. Patterns are extracted using a sparse dictionary learning algorithm which is inspired by experimental findings of functional magnetic resonance imaging (fMRI) of mammalian brain. Learning method is tested in presence of noise; since SFAM networks are sensitive to noise [17] learned images are also filtered during the sparse coding. Classification results are compared to the state of the art algorithms. Furthermore, we applied the algorithm to recognize emotions based on body expression data which is inspired by the action based behavior in psychology. Classification results are compared to those of human recognitions.

1.1 Complex Fuzzy Sets

Classical fuzzy logic applies real-valued functions to represent the membership; in order to show the phase term another dimension is added to the membership function [16] [19] [20] [21]. Though the fuzziness remains a real value in range [0,1]. It should be noted that the concept of using complex input numbers into a fuzzy inference system is different from applying fuzzy number into a system of inference. The latter introduced as a fuzzy set with real-valued features as input and complex-valued in the output. However, in most of the computer vision problems input images are preprocessed with complex transforms (Fourier and windowed Fourier families) which provides the complex data as features for machine learning algorithms.

A complex fuzzy set allows membership functions in a set to be specified by a complex number. Membership function μ of any element x, in a complex fuzzy set S, is replaced by complex-valued grade of membership of the general form:

$$\mu(x) = r_s(x).e^{iw\mu(x)} \tag{1}$$

where $r_s(x) \in [0, 1]$. The amplitude term retains the traditional notion of "fuzziness", by the representation of membership of variable x of set S, same as original

fuzzy set theory amplitude term ranges between 0 to 1 and with a phase term zero μ will go back to its original fuzzy definition. The phase term denotes the assertion of multiple-valued complex fuzzy set theory and represent the lag of time in a time frequency domain.

Given two complex fuzzy sets A and B on U with complex valued membership function $\mu_A(x)$, $\mu_B(x)$ respectively, complex fuzzy union could be defined as [19] [20] [21]:

$$\mu_{A\vee B}(x) = [r_{A(x)\oplus r_{B(x)}}].e^{iW_{A\vee B}(x)} \tag{2}$$

where $\oplus$ represents the t-conrom and $W_{A\vee B}$ is defined as:

$$\text{Sum} : W_{A\vee B} = W_A + W_B \tag{3}$$

$$\text{Max} : W = max(W_A, W_B) \tag{4}$$

$$\text{Winner Take All} : W_{A\vee B} \begin{cases} W_A, rA > rB \\ W_B, rB > rA \end{cases} \tag{5}$$

1.2 Dictionary Learning by Gabor Wavelets

Decomposition methods extract key information from images and videos in order to create a highly-compressed and simplified representation of the original using only a handful of elementary functions. A set of functions is called a dictionary. Representation is thus achieved by linear combination of elements in the dictionary. To improve the quality of representation, a common approach is to use an orthogonal subset of a large dictionary containing all possible elements.

Textons are developed as a mathematical representation of basic image objects [22]. Images are coded by a dictionary of Gabor and Laplacian of Gaussian elements; Responses to the dictionary elements is combined by transformed component analysis. Furthermore, sparse approximation helps to find a more general object models in terms of scale and posture [23]. Active basis model [1] provides a deformable template using Gabor wavelets as dictionary elements. They also proposed a shared sketch algorithm (SSA) inspired by AdaBoost.

1.3 Sparse Coding Using Artificial Neurons

Response to a dictionary of Gabor wavelets is an overcomplete representation. Sparse coding is the method of selecting a proper subset of responses to represent the image (signal). In addition to biological motivations, sparse coding is necessary to avoid redundant information. Having a fixed number of features, redundancy may cause loss of essential information which is going to be encoded in the lower levels (Figure 1).

Optimum sparse coding minimizes the number of nonzero coefficients, which is an NP-hard optimization problem. We applied a locally competitive algorithm

Fig. 1. Edge detection using Gabor wavelets, A. Original image [1], B. edge detected image with a large number of features without sparsity, C. edge detected image with a small number of features where sparsity is enforced.

(LCA) [4] to enforce local sparsity. Unlike classical sparse coding algorithms, LCA uses a parallel neural structure inspired by biological model. In previous works, there is no real application that has been applied using LCA, although some simulation results are shown. Here an empirical experiment based real application of body expression recognition, is proposed to provide an evidence for the practical utility of Holonomic Brain Model as dictionary learning method by LCA.

Atkinson et al. developed a dataset for both static and dynamic body expressions. The dataset contains 10 subjects (5 female) and covers five emotions (anger, disgust, fear, happiness and sadness)[24]. The bodily expressive action stimulus test (BEAST) [25] provides a dataset for recognizing four types of emotions (anger, fear, happiness, sadness) which is constructed using non-professional actors (15 male, 31 female). Body expressions are validated with a human recognition test.

1.4 Complex-Valued Simplified Fuzzy ARTMAP (CV-SFAM)

CV-SFAM is a two-layer network in which the magnitudes of raw data are scaled to the range of 0 and 1 and further passed through a complement coder. The complement coder normalizes the input vector and stretched to double the size by adding its complement. For an input vector a with length d, the complement coded vector I is [2]:

$$I = (\mu_\nu, \mu_{\bar{\nu}}) = (\mu_{\nu_1}, ..., \mu_{\nu_d}, \mu_{\bar{\nu_1}}, ..., \mu_{\bar{\nu_d}}) \tag{6}$$

$$|I| = |\mu_\nu, \mu_{\bar{\nu}}| = d \tag{7}$$

where the norm $|.|$ is defined as:

$$|a| = \sum_{i=1}^{d} a_i \tag{8}$$

Activation of output nodes are based on their complex fuzzy t-norm (see appendix). Activation function of output node j in response to input node i is:

$$T_{ij} = \frac{u_{I_i \wedge W_{ij}}(v)}{\alpha + |\mu_{w_{ij}}|} \tag{9}$$

where α is a small value greater than zero, and w_{ij} is the weight between nodes i and j. Output nodes form a category according to their complex fuzzy t-conorm:

$$C = \underset{j}{max}(T_j) \tag{10}$$

Match tracking category C is based on the vigilance parameter ρ. The network is in state of resonance if:

$$\text{Match} = \frac{|\mu_{I \wedge W}(v)|}{|\mu_I(v)|} \geq \rho \tag{11}$$

where W is the weight factor for all the output nodes. Otherwise, a mismatch reset happens and the magnitude of T_j is set to zero, and C will be updated using the complex fuzzy t-conorm. The vigilance parameter ρ determines the minimum match for an input to be assigned to the category node C.

Since the norm of the complete coded vector I is constant and equal to the number of features, matching the function could be rewritten as:

$$\text{Match} = \frac{|\mu_{I \wedge W}(v)|}{d} \tag{12}$$

In the state of resonance, updated weights are calculated based on a linear combination of their match and old weights, given the learning rate β:

$$W_{ij}^{new} = \beta(I_i \wedge W_{ij}) + (1 - \beta)W_{ij} \tag{13}$$

We applied a supervised approach to recognize two types of objects in images; First a pixel-wise approach for aligned objects which combines the learned samples of objects in each class to form a prototype and second a feature based approach for non-aligned objects in which Gabor wavelets are localized to represent a potential match between specific scale and orientation and edges of objects. Both approaches are fed into a synergetic neural network to perform a classification task.

2 Proposed Method

2.1 Pixel-Wised Approach

Images are scaled to have the exact same size. Each image is convolved with all the elements in the dictionary. Then sparse coding is enforced to minimize the representing elements for each pixel. Finally, remaining parts are reconstructed to generate the sparse superposition of the image. For pixel values in the local area LCA has the following steps:

1. Compute the response (convolution) of I_i with all the elements in the dictionary.

$$C_j = \langle GW_j, I_j \rangle \tag{14}$$

(Set $t = 0$ and $u_j(0) = 0$, for $j = 1, ..., n$).

2. Determine the active nodes by activity thresholding.
3. For each pixel, calculate the internal state of element j, $u_j(t)$.

$$u_j = \frac{1}{\tau}[C_j(t) - u_j(t) - \sum_{j \neq k} \Phi_{j,k}.a_j(t)] \tag{15}$$

$$\Phi_{j,k} = \langle GW_j.GW_k \rangle \tag{16}$$

4. Compute sparse coefficients $a_j(t)$ for $u_j(t)$.

$$a_j(t+1) = T_\lambda(u_j(t)) \tag{17}$$

$$T_{(\alpha,\gamma,\lambda)}(u_j) = \frac{u_j - \alpha\lambda}{1 + e^{-\gamma(u_j - \lambda)}} \tag{18}$$

5. If $a_j(t-1) - a_j(t) > \delta$, then $t \leftarrow t+1$ and go to step 2, otherwise finish.

2.2 Detecting Objects with Shape Changes

Original SFAM used pixel-wised features to represent an object which is not robust in case objects are in a variable shapes (e.g. different body emotions of human). In this case, we construct a template model as a collection of Gabor wavelet features included in the dictionary which represents the general characteristics of all body posture classes.

Test images are convolved with the components of the template model. Sparsity is then enforced to catch the best fit over the specific posture. LCA thresholding strategy enables us to remove redundancies effectively (producing sparse coefficients with exactly zero values). Number of output Gabor wavelets are fixed in order to make the comparison with trained prototype of each class. Features are selected based on their highest response to the training images; furthermore, each feature is allowed to perturb slightly in terms of location and orientation. In this aspect our template construction is a modification of shared sketch algorithm [1]. For each image i feature value v_{ij} corresponded to the selected Gabor wavelet j, is determined as the following:

$$v_{ij} = \gamma_i C_{ij} - \log(Z(\gamma_i)) \tag{19}$$

where γ_i is derived by maximum likelihood estimation and Z is the partition function. Therefore, boundaries of object are segmented out with before the result is given to CV-SFAM.

3 Experimental Result

Performance of ARTMAP-based classifiers are sensitive to a number of parameters. To achieve optimum recognition rates, a genetic algorithm was employed to optimize parameters such as training sequence and feature subset selection [26] [27].

3.1 Aligned Images

The proposed algorithm is used to classify four classes of animals . Each image used in classification contains an animal object. Image objects are obtained from different animals in variety of postures, and shapes. Gabor wavelets are generated in a (20, 20) matrix and images are resized to (50, 50).

Result of classification is a tag for each image representing the corresponding class. For each class 10 images are selected randomly to form the test set. Remaining images are used for training. Using cross validation classification is performed over all the images. This result is compared to Active Basis Model (ABM). Learning method can effectively detect the edge patterns and represent the main components of objects. This leads to have more distinguishable object definitions (specifically between classes of Bear and Wolf) rather than shared sketching used in ABM.

Table 1. Classification result of aligned images

	Bear	Cat	Cow	Wolf
CV-SFAM	62%	87%	78%	58%
ABM	87%	100%	76%	60%
# of images	60	70	60	50

3.2 Classification of Emotions Using Body Expressions (Non-aligned Images)

We applied the BEAST data set to classify four classes of basic emotions. Gabor wavelets are generated in a (20, 20) matrix and images are resized to have 500 pixels in row and relatively scaled pixels in column. Images are divided into train and test sets for each class 10 images are selected randomly to form the train data and the rest are included for test. Different scenarios are considered to train the model. Classification accuracies of different trained SFAMs are compared with results of human recognition.

Table 2. Classification result of non-aligned images

	Anger	Fear	Happiness	Sadness
Min	93.33	88.00	88.00	100.00
BEAST(human)	93.60	93.90	85.40	97.80

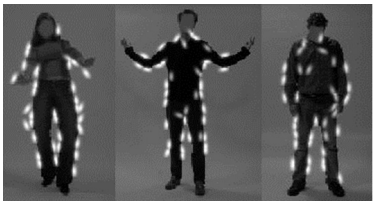

Fig. 2. Features extracted for emotion classes of fear, happiness, and sadness

4 Conclusion

We proposed a biologically-plausible approach for recognition of aligned and non-aligned objects. Our learning algorithm is inspired by the holonomic brain theory. LCA is applied to enforce sparsity on a dictionary of Gabor wavelets. Regarding the parallel structure of the learning method, implementation could be optimized via parallel processing which is essential for real-time applications.

Furthermore, a SFAM neural network is combined with Gabor wavelet features which make it applicable for recognition of non-aligned objects. Gabor features also enhance the model to use images with different size. Effect of background is also removed because of recognition is based on the pattern of edges; Though sparse coding is robust in presence of classical noise since dot noise does not follow any meaningful shape pattern intrinsically.

Experimental results supported the real application of locally competitive sparse coding as a learning method using a biological implementation.

Acknowledgement. This study was funded by UM IPPP research grant FL006-2011 ("Productive Aging Through ICT"), and HIR-MOHE grant H-22001-00-B000010.

References

1. Wu, Y.N., Si, Z., Gong, H., Zhu, S.C.: Learning active basis model for object detection and recognition. International Journal of Computer Vision 90(2), 198–235 (2010)
2. Kasuba, T.: Simplified Fuzzy ARTMAP. AI Experts 8, 18–25 (1993)
3. Hirose, A.: Complex-Valued Neural Networks Fertilize Electronics. In: Hirose, A. (ed.) Complex-Valued Neural Networks, 2nd edn. SCI, vol. 400, pp. 3–8. Springer, Heidelberg (2012)
4. Rozell, C.J., Johnson, D.H., Baraniuk, R.G., Olshausen, B.A.: Sparse coding via thresholding and local competition in neural circuits. Neural Computation 20(10), 2526–2563 (2008)
5. Aizenberg, I., Aizenberg, N.N., Vandewalle, J.P.: Multi-Valued and Universal Binary Neurons: Theory, Learning and Applications. Springer (2000)
6. Noest, A.J.: Discrete-state phasor neural networks. Rapid Communications 38(4), 2196–2199 (1988)
7. Widrow, B., McCool, J., Ball, M.: The complex LMS algorithm. Proceedings of the IEEE 63(4), 719–720 (1975)
8. Hanna, A.I., Mandic, D.P.: A fully adaptive normalized nonlinear gradient descent algorithm for complex-valued nonlinear adaptive filters. IEEE Transactions on Signal Processing 51(10), 2540–2549 (2003)
9. Leung, H., Haykin, S.: The complex backpropagation algorithm. IEEE Transactions on Signal Processing 39(9), 2101–2104 (1991)
10. Kim, M.S., Guest, C.C.: Modification of backpropagation networks for complex-valued signal processing in frequency domain. In: IEEE/INNS International Joint Conference on Neural Networks, pp. 27–31 (1990)
11. Nitta, T.: An extension of the back-propagation algorithm to complex numbers. Neural Networks 10(8), 1391–1415 (1997)

12. Su, M.C., Lee, J., Hsieh, K.L.: A new ARTMAP-based neural network for incremental learning. Neurocomputing 69(16), 2284–2300 (2006)
13. Carpenter, G.A., Grossberg, S., Markuzon, N., Reynolds, J.H., Rosen, D.B.: Fuzzy ARTMAP: A neural network architecture for incremental supervised learning of analog multidimensional maps. IEEE Transactions on Neural Networks 3(5), 698–713 (1992)
14. Simpson, P.K.: Fuzzy min-max neural networks. IEEE Transactions on Neural Networks 3(5), 776–786 (1992)
15. Vakil-Baghmisheh, M.T., Pavesic, N.: A fast simplified fuzzy ARTMAP network. Neural Processing Letters 17(3), 273–316 (2003)
16. Loo, C.K., Rao, M.V.C.: Accurate and reliable diagnosis and classification using probabilistic ensemble simplified fuzzy ARTMAP. IEEE Transactions on Knowledge and Data Engineering 17(11), 1589–1593 (2005)
17. Rajasekaran, S., Pai, G.A.V.: Image recognition using Simplified Fuzzy ARTMAP augmented with a moment based feature extractor. International Journal of Pattern Recognition and Artificial Intelligence 14(8), 1081–1095 (2000)
18. Palaniappan, R., Eswaran, C.: Using genetic algorithm to select the presentation order of training patterns that improves simplified fuzzy ARTMAP classification performance. Applied Soft Computing 9(1), 100–106 (2009)
19. Ramot, D., Milo, R., Friedman, M., Kandel, A.: Complex fuzzy sets. IEEE Transactions on Fuzzy Systems 10(2), 171–186 (2002)
20. Ramot, D., Friedman, M., Langholz, G., Kandel, A.: Complex fuzzy logic. IEEE Transactions on Fuzzy Systems 11(4), 450–461 (2003)
21. Dick, S.: Toward complex fuzzy logic. IEEE Transactions on Fuzzy Systems 13(3), 405–414 (2005)
22. Zhu, S.C., Guo, C.E., Wang, Y., Xu, Z.: What are textons? International Journal of Computer Vision 62(1-2), 121–143 (2005)
23. Figueiredo, M.A.T.: Adaptive sparseness for supervised learning. IEEE Transactions on Pattern Analysis and Machine Intelligence 25(9), 1150–1159 (2003)
24. Atkinson, A.P., Dittrich, W.H., Gemmell, A.J., Young, A.W.: Emotion perception from dynamic and static body expressions in point-light and full-light displays. Perception 33(6), 717–746 (2004)
25. de Gelder, B.V.D., Stock, J.: The Bodily Expressive Action Stimulus Test (BEAST). Construction and Validation of a Stimulus Basis for Measuring Perception of Whole Body Expression of Emotions. Frontiers in Psychology 2(181) (2011), doi:10.3389/fpsyg.2011.00181 (accessed May 7th 2013)
26. Loo, C.K., Liew, W.S., Sayeed, M.S.: Genetic Ensemble Biased ARTMAP Method of ECG-Based Emotion Classification. In: Watanabe, T., Watada, J., Takahashi, N., Howlett, R.J., Jain, L.C. (eds.) Intelligent Interactive Multimedia: Systems & Services. SIST, vol. 14, pp. 299–306. Springer, Heidelberg (2012)
27. Loo, C.K., Cheong, S.F., Seldon, M.A., Mand, A.A., Muthu, K.S., Liew, W.S., Lim, E.: Genetic-Optimized Classifier Ensemble for Cortisol Salivary Measurement Mapping to Electrocardiogram Features for Stress Evaluation. In: Anthony, P., Ishizuka, M., Lukose, D. (eds.) PRICAI 2012. LNCS, vol. 7458, pp. 274–284. Springer, Heidelberg (2012)

A Neural Network Model for Large-Scale Stream Data Learning Using Locally Sensitive Hashing

Aminah Ali Siti Hajar, Kiminori Fukase, and Seiichi Ozawa

Graduate School of Engineering, Kobe University,
1-1 Rokko-dai, Nada-ku, Kobe 657-8501, Japan
{aminah,111t256t}@stu.kobe-u.ac.jp, ozawasei@kobe-u.ac.jp

Abstract. Recently, mining knowledge from stream data such as access logs of computer, commodity distribution data, sales data, and human lifelog have been attracting many attentions. As one of the techniques suitable for such an environment, active learning has been studied for a long time. In this work, we propose a fast learning technique for neural networks by introducing Locality Sensitive Hashing (LSH) and a local learning algorithm with LSH in RBF networks.

Keywords: neural networks, incremental learning, stream data learning, locally sensitive hashing.

1 Introduction

The rapid growth of storage technology and computer networks has brought the opportunity for researchers to get involved in the processing of large-scale stream data which consists of collecting data in real time, storing, mining and analyzing the knowledge from data. To process large-scale stream data, it is important to choose a suitable learning algorithm that is capable to learn in real time. Incremental learning has an ability to process large data [1] in chunk and update the parameters after learning each chunk. Such type of learning keep and update only the minimum information on a classifier model. Therefore, it requires relatively small memory and short learning time. On the other hand, batch learning is not suitable because it needs to store all training data, which consume a large memory capacity. Due to the limited memory, it is certainly impossible to process large-scale stream data online using the batch learning. Therefore, the learning of large-scale stream data should be conducted incrementally.

Another criteria to be considered for learning large-scale data is to select essential data to be learned. The selection of essential data is often conducted based on the margin of classifier outputs. Even if a large number of data are given as a stream, there is no guarantee that all the data are useful for learning and can efficiently improved the accuracy of test data. Besides, in supervised learning, a large training data correspond to a larger number of data to be labeled by a supervisor. Hence, selecting the most useful training data can reduce not only the amount of supervision required for effective learning [2], but also the processing time due to the decreasing number of training data.

M. Lee et al. (Eds.): ICONIP 2013, Part I, LNCS 8226, pp. 369–376, 2013.
© Springer-Verlag Berlin Heidelberg 2013

Although Nearest Neighbors (NNs) search plays an important role in various machine learning areas, it has a limitation when a high dimensional data is given. To overcome this problem, Locality Sensitive Hashing (LSH) provides an alternative to process high-dimensional data by approximating similarity search problem [3][4][5]. In a general hashing, every input is assigned to a different bucket to avoid collision, while inputs of LSH are assigned to the same bucket when the input data are close to each other. Consequently, LSH is able to search similar data faster because LSH can find the nearest neighbors in linear time as opposed to the quadratic pair-wise approach of the conventional nearest neighbor, which give advantage to high dimensional data and large-scale data. However, a major limitation of LSH is originated from its large memory consumption; that is, to keep both high recall and high precision, a large hash table is needed.

The paper is organized as follows. In Section 2, we describe the proposed learning model which employs an active learning algorithm of Resource Allocating Network with Long-Term Memory (RAN-LTM) where LSH is adopted to select only useful training data from a large chunk. The performance evaluation of the proposed method is carried out in Section 3, and Section 4 states the conclusions of this work.

2 Proposed Method

2.1 Basic Idea

The data selection based on output margins is one of the most frequently used approaches in active learning. The conventional RAN-LTM method requires the calculation of output margins for every training data candidates. Hence, such a margin-based method results in increasing the number of Radial Basis Function (RBF) units and consequently increasing the computational time. Therefore, as more data are given at a time, real-time learning becomes more difficult.

In the proposed method, to avoid the repetition of the output margin calculation, we divide the data into buckets where adjacent data are grouped in the same bucket. To do this, we propose a data selection method using LSH by combining with the margin-based method, where only unknown data in a new bucket are learned by RAN-LTM, whereas data in a not-empty bucket are ignored during the learning phase. However, by only implementing this idea, the learning time is not drastically reduced because the learning time strongly depends on the number of RBF bases [6]. Therefore, instead of learning all RBF bases, we propose a local learning algorithm in which only RBF bases with high activations for a training data are selectively learned (see Fig. 1). The algorithm of the proposed method is summarized in Algorithm 1.

2.2 LSH-Based Data Selection

How to Determine Hash Functions. The first step to build the LSH-based data selection is to define hash functions such that similar data are fallen into

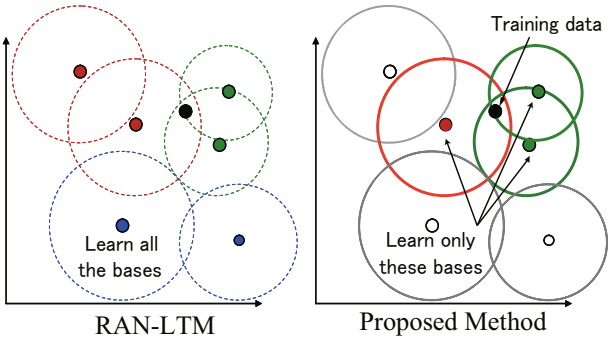

Fig. 1. RBF bases learned in RAN-LTM and in the proposed method

the same bucket. In general, the more hash functions we define, the higher approximation accuracy for an input space we obtain. Nevertheless, it leads to the construction of a bigger hash table that requires not only larger memory capacity but also longer processing time. Therefore, it is important to choose a proper number of hash functions.

Here, we adopt Principle Component Analysis (PCA) to generate a proper number of hash functions by controlling the threshold of the accumulation ratio. Since data are often distributed within a low-dimensional subspace spanned by eigenvectors with some major components, we can approximate an input space with several regions within such a subspace. Let k be the subspace dimensions obtained by PCA. Then, the following linear transformation is considered to define buckets in LSH:

$$\boldsymbol{v} = \boldsymbol{U}_k^T \boldsymbol{x} \tag{1}$$

where $\boldsymbol{x} = \{x_1, \cdots, x_n\}^T$, $\boldsymbol{U}_k = \{\boldsymbol{u}_1, \cdots, \boldsymbol{u}_k\}$, and $\boldsymbol{v} = \{v_1, \cdots, v_k\}^T$ are an n-dimensional input vector, the matrix of k eigenvectors, and the k-dimensional projection vector, respectively. In the proposed method, the buckets in LSH are defined by the regions, which are partitioned based on the k projection values v_i $(i = 1, \cdots, k)$.

The next step is to define the values of a hash function. Here, let us define a set of hash functions $H(\boldsymbol{x})$ as follow:

$$\boldsymbol{H}(\boldsymbol{x}) = \{h_1(\boldsymbol{x}), h_2(\boldsymbol{x}), \cdots, h_{2k-1}(\boldsymbol{x}), h_{2k}(\boldsymbol{x})\} \tag{2}$$

where

$$h_{2i-1}(\boldsymbol{x}) = \begin{cases} 0 & (v_i \leq -\theta_x) \\ 1 & (-\theta_x < v_i \leq 0) \\ 0 & (0 < v_i \leq \theta_x) \\ 1 & (v_i > \theta_x) \end{cases} \tag{3}$$

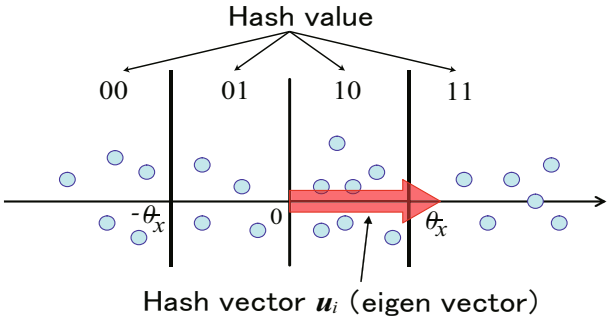

Fig. 2. Calculation of hash values using an eigenvector

$$h_{2i}(\boldsymbol{x}) = \begin{cases} 0 & (v_i \leq -\theta_x) \\ 0 & (-\theta_x < v_i \leq 0) \\ 1 & (0 < v_i \leq \theta_x) \\ 1 & (v_i > \theta_x) \end{cases}. \tag{4}$$

As seen in Eqs. (3) and (4), the projection value v_i is divided into four regions (see Fig. 2); that is, v_i is encoded into a 2-bits hash value: "00", "01", "10" or "11".

Creating Hash Table. A hash table is composed of the three items: hash value, prototype and margin flag. Initial training data are recorded as prototypes in a hash table. The calculation of an output margin Δz is conducted by subtracting the second largest output z_{c_2} from the largest output z_{c_1} as follows:

$$\Delta z = z_{c_1} - z_{c_2}. \tag{5}$$

The margin flag is set to 1 if the output margin Δz exceeds the threshold θ_m and 0 otherwise:

$$\text{margin flag} = \begin{cases} 0 & (\Delta z \leq \theta_m) \\ 1 & (\Delta z > \theta_m). \end{cases} \tag{6}$$

Selection of RBF Bases. Each training data is encoded in a binary hash value whose length is two times the number of hash functions. Then, this sequence is converted into a decimal as an index. The index is used to check if an incoming data is similar to a prototype that has already been registered in a hash table.

The next step is to check margin flags. If the flag of the matched prototype is '1', it means the classifier is well trained around the prototype; therefore, there is no need to train a given data. On the contrary, if the flag is '0', it means a given data should be trained.

The following three models are compared in our study: the conventional margin-based data selection plus the global learning of RAN-LTM, the LSH-based data

Algorithm 1. Learning Algorithm

Input: A set of p initial training data $\boldsymbol{X}_0 = \{(\boldsymbol{x}_i, d_i)\}_{i=1}^{p} \in R^{n \times p}$, thresholds of accumulation ratio, output margin, and partition θ, θ_m, θ_x.

Perform PCA for $\boldsymbol{X}_0$ and obtain k eigenvectors $\boldsymbol{U}_k$ such that the accumulation ratio of a subspace spanned by $\boldsymbol{U}_k$ is larger than θ.
for all $(\boldsymbol{x}_i, d_i)$ **do**
  Calculate a projection vector $\boldsymbol{v}_i$ by Eq. (1).
  Calculate hash value $\boldsymbol{H}(\boldsymbol{x}_i)$ by Eqs. (2)-(4).
  Calculate *margin flag* by Eqs. (5)-(6).
  Register $\boldsymbol{H}(\boldsymbol{x}_i)$, $(\boldsymbol{x}_i, d_i)$, *margin flag* in hash table.
end for
loop
  Input: A new training data $(\boldsymbol{x}_i, d_i)$.
  Calculate $\boldsymbol{v}_i$ for $\boldsymbol{x}_i$ by Eq. (1).
  Calculate hash value $\boldsymbol{H}(\boldsymbol{x}_i)$ by Eqs. (2)-(4).
  if $\boldsymbol{H}(\boldsymbol{x}_i)$ does not exist in hash table **then**
    Learn RAN-LTM with $(\boldsymbol{x}_i, d_i)$.
    Calculate *margin flag* by Eqs. (5)-(6).
    Register $\boldsymbol{H}(\boldsymbol{x}_i)$, $(\boldsymbol{x}_i, d_i)$, *margin flag* in hash table.
  else if *margin flag* $= 0$ **then**
    Learn RAN-LTM with $(\boldsymbol{x}_i, d_i)$.
    Calculate *margin flag* by Eqs. (5)-(6).
    Update hash table with *margin flag*.
  end if
end loop

selection plus the global learning of RAN-LTM, and the LSH-based data selection plus the local learning of RAN-LTM. For the notational convenience, let us denote them *Margin-Global*, *LSH-Local*, *LSH-Global* in the following.

3 Experiments

3.1 Parameters Selection and Preparation of Data for Experiment

To evaluate the performance of the propose method, we use the 3 benchmarks datasets (Adult, Bank and Shuttle data) from the University of California at Irvine Machine Learning Repository [7] in Table 1. The information of these datasets are shown in Table 1. The data are divided into two groups; training data and test data. The performance evaluation is carried out through the 2-fold cross-validation, where each fold is repeated 15 times with different training sequences.

We carry out the two experiments and display the result of the mean and standard deviation of the recognition rate and the learning time. The experiments are as follow:

1. To find out the proper setting for subregions which gives the definition of hash functions using LSH.

Table 1. Evaluated dataset

Dataset	#Attribute	#Class	#Data
Adult	14	2	45222
Bank	16	2	45211
Shuttle	9	5	58000

2. To compare the performance of data selection and learning strategy between the three models: Margin-Global, LSH-Global and LSH-Local.

There are two important parameters that should be chosen properly: the threshold of output margins θ_m and the threshold of the accumulation ratio in PCA θ. In this experiment, we empirically determine as $\theta_m = 0.05$ and $\theta = 0.9$. In addition, we assume that the number of initial data is 500 and the size of data chunk in the incremental phase is 1000. The data are normalized between -1 and +1 in order to determine easily another parameter θ_x in Eqs. (3), (4) in the next section.

3.2 A Study on the Effect of Region Partitions in LSH

It is also important to determine the parameter θ_x in Eqs. (3), (4) which determines the partitions (buckets) of LSH in every subspace spanned by an eigenvector. Therefore, we examine the effects of θ_x on the recognition accuracy and learning time.

Tables 2 (a) and (b) show the recognition accuracy and the learning time in LSH-Local when θ_x are changed from 0.1 to 0.7. As seen in Table 2 (a), the highest recognition accuracy is obtained for Adult and Bank at $\theta_x = 0.3$ and the same recognition accuracy is obtained for Shuttle at any θ_x. The shortest learning time for Adult and Shuttle is again obtained at $\theta_x = 0.3$, and for Bank at $\theta_x = 0.7$ as shown in Table 2 (b). In addition, the recognition accuracy is significantly decreased as θ_x increases except for Adult, while the learning time is significantly increased when θ_x is increased except for Bank.

¿From the above results, θ_x should be chosen between 0.2 and 0.4 to have high recognition accuracy in proper learning time. Hence, let us choose the threshold $\theta_x = 0.3$ and fixed at this value in the following experiments.

3.3 Performance Evaluation

Table 3 shows the recognition accuracy and the learning time for the 3 different methods: Margin-Global, LSH-Global and LSH-Local. We can see that Margin-Global gives the highest recognition accuracy for all datasets, but it requires longer learning time. On the other hand, LSH-Local can learn quite faster compared to LSH-Global and Margin-Global for all datasets. Especially, the learning time is significantly reduced for Adult dataset, although LSH-Local has a little lower recognition accuracy compared to the other two models. The main reason

Table 2. Influence of the range parameter θ_x on (a) recognition accuracy [%] and (b) learning time [sec.]

(a) Recognition rate [%]

	0.1	0.2	0.3	0.4	0.5	0.6	0.7
Adult	76.9 ± 1.0	77.0 ± 0.8	77.0 ± 0.9	76.9 ± 1.0	76.6 ± 0.9	76.1 ± 1.1	75.3 ± 1.5
Bank	83.0 ± 1.5	82.8 ± 1.8	83.0 ± 1.6	82.9 ± 1.8	82.9 ± 1.3	81.2 ± 1.9	81.1 ± 2.2
Shuttle	99.6 ± 0.1	99.6 ± 0.1	99.6 ± 0.2	99.6 ± 0.1	99.6 ± 0.2	99.6 ± 0.1	99.6 ± 0.1

(b) Learning time [sec.]

	0.1	0.2	0.3	0.4	0.5	0.6	0.7
Adult	96.4 ± 13.3	99.6 ± 9.0	93.6 ± 12.1	95.5 ± 12.6	98.0 ± 14.9	101.7 ± 17.5	100.7 ± 19.1
Bank	45.9 ± 6.0	49.2 ± 5.4	47.3 ± 5.0	46.4 ± 5.2	43.5 ± 4.7	45.0 ± 5.8	39.1 ± 4.8
Shuttle	39.6 ± 26.1	33.9 ± 39.3	19.3 ± 17.1	28.4 ± 33.3	27.1 ± 33.3	27.9 ± 13.2	42.8 ± 24.6

Table 3. Performance comparison among Margin-Global, LSH-Global, and LSH-Local with regards to (a) recognition accuracy [%] and (b) learning time [sec.]

(a) Recognition rate [%]

	Margin-Global	LSH-Global	LSH-Local
Adult	78.3 ± 1.3	77.4 ± 1.0	77.0 ± 0.9
Bank	84.1 ± 1.8	83.4 ± 1.3	83.0 ± 1.6
Shuttle	99.8 ± 0.1	99.6 ± 0.2	99.6 ± 0.2

(b) Learning time [sec.]

	Margin-Global	LSH-Global	LSH-Local
Adult	2269.2 ± 234.0	123.9 ± 19.7	93.6 ± 12.1
Bank	123.4 ± 17.9	48.0 ± 7.2	47.3 ± 5.0
Shuttle	42.1 ± 9.1	32.5 ± 28.2	19.3 ± 17.1

for the shorter learning time relies on the decrease in the number of learned RBF bases, because the computational complexity of the weight learning in the least squares method is $O(J^3)$, where J is the number of RBF bases.

The recognition accuracies are different between the margin-based method and the two LSH-based methods. One of the reasons is that Margin-Global can adapt to the temporal change in data distributions during the incremental learning. However, in the LSH-based methods, the hash functions are generated in the initial learning phase, and they are fixed during the incremental phase.

4 Conclusions and Future Work

In this paper, we propose an active learning model for RAN-LTM called LSH-Local where a proper number of training data are selected based on LSH and output margins from a large chunk of data. The experimental results for the three UCI datasets demonstrate that although the recognition accuracy is relatively lower than that in Margin-Global, the number of RBF bases is decreased and the learning time is significantly shortened. The reduction in the learning time is

shown obviously especially for the large dataset (Adult). Therefore, we conclude that the proposed LSH-Local can achieve fast learning without scarifying the recognition accuracy significantly and is suitable for the large-scale stream data.

There still remain several open problems in the proposed LSH-Local. Although the learning time is reduced, the accuracy is also a little bit lower than the conventional margin-based model. One of the reasons is that the hash functions of LSH are only generated in the initial learning and are not adapted incrementally. One way to solve this problem is that the proposed LSH-Local can be extended not only by updating hash functions incrementally but also by increasing the number of hash functions. This can be attained by introducing Incremental PCA (IPCA) [8] into the proposed LSH-Local. However, there is one problem for this. After updating/increasing hash functions, the hash table should also be updated properly without unexpected forgetting of the previous knowledge. If this problem is solved, it is expected that the idea of fast processing for large-scale stream data using LSH would work well. As another problem, the parameter θ_x should also be set properly in the LSH-based data selection. As mentioned in 3.3, θ_x is determined only from the initial training data and it is fixed during the incremental learning. Since the data distributions are always changed over time, θ_x should be adapted to the change in the data distributions.

The above issues are left as our future work.

References

1. Sun, N., Guo, Y.: A modified incremental learning approach for data stream classification. In: Sixth International Conference on Internet Computing for Science and Engineering, Henan, pp. 122–125 (2012)
2. Melville, P., Mooney, R.J.: Diverse ensembles for active learning. In: Proc. 21th International Conf. on Machine Learning, Banff, CA, pp. 584–591 (2004)
3. Gu, X., Zhang, Y., Zhang, L., Zhang, D., Li, J.: An improved method of locality sensitive hashing for indexing large-scale and high-dimensional features. Signal Processing 93(8), 2244–2255 (2013)
4. Lee, K.M., Lee, K.M.: Similar pair identification using locality-sensitive hashing technique. In: Joint 6th International Conference on Soft Computing and Intelligent Systems (SCIS) and 13th International Symposium on Advanced Intelligent Systems (ISIS), Kobe, pp. 2117–2119 (2012)
5. Shen, H., Li, T., Li, Z., Ching, F.: Locality sensitive hashing based searching scheme for a massive database. In: IEEE SoutheastCon 2008, Huntsville, AL, USA, pp. 123–128 (2008)
6. Ozawa, S., Toh, S.-L., Abe, S., Pang, S., Kasabov, N.: Incremental learning of feature space and classifier for face recognition. Neural Networks 18(5-6), 575–584 (2005)
7. `http://archive.ics.uci.edu/ml/`
8. Ozawa, S., Pang, S., Kasabov, N.: Incremental learning of chunk data for on-line pattern classification systems. IEEE Trans. on Neural Networks 19(6), 1061–1074 (2008)

Robots That Can Play with Children: What Makes a Robot Be a Friend

Muhammad Attamimi[1], Kasumi Abe[1], Akiko Iwasaki[2], Takayuki Nagai[1], Takayuki Shimotomai[2], and Takashi Omori[2]

[1] Department of Mechanical Engineering and Intelligent Systems, The University of Electro-Communications, 1-5-1 Chofugaoka, Chofu-shi, Tokyo 182-8585, Japan
[2] Department of Electrical Engineering, Tamagawa University, 6-1-1 Tamagawa-gakuen, Machida-shi, Tokyo 194-8610, Japan
{m_att,k_ishii}@apple.ee.uec.ac.jp, tnagai@ee.uec.ac.jp
iwska2re@engs.tamagawa.ac.jp, {shimotomai,omori}@lab.tamagawa.ac.jp

Abstract. In this paper, a playmate robot system, which can play with a child, is proposed. Unlike many therapeutic service robots, our proposed system is implemented as a functionality of the domestic service robot with a high degree of freedom. This implies that the robot can use its body and toys for playing high-level games with children, i.e., beyond therapeutic play, using its physical features. The proposed system currently consists of ten play modules, including a chatbot, card playing, and drawing. To sustain the player's interest in the system, we also propose an action-selection strategy based on a transition model of the child's mental state. The robot can estimate the child's state and select an appropriate action in the course of play. A portion of the proposed algorithms was implemented on a real robot platform, and experiments were carried out to design and evaluate the proposed system.

Keywords: Playmate robots, child's mental modeling, and Markov decision process.

1 Introduction

Several problems, such as, child neglect by caregiver and deterioration in the quality of play for a child, exist in the circumstances surrounding children. We believe that "robotic playmates" would greatly help to solve these problems. In this study, we propose a playmate system for humanoid robot that can play with a child using its body and toys. The robot is designed to have ten play modules covering important play areas for development, and can play with a child by switching among these modules.

Playmates are required to play with children for as long as possible. To ensure that their play with a child lasts for a long duration, human playmates observe a child well. For sustaining a child's interest, the playmate estimates the child's mental state to select appropriate actions from a finite set of actions in a timely fashion. Therefore, playmates should sustain a child's interest in play and forge a

M. Lee et al. (Eds.): ICONIP 2013, Part I, LNCS 8226, pp. 377–386, 2013.
© Springer-Verlag Berlin Heidelberg 2013

good relationship with the child. We think that two factors, which we call "degree of interest" (DOI) and "degree of familiarity" (DOF), are very important and are improved by selecting actions according to the child's estimated mental state.

We propose an action-selection strategy based on a transition model of the child's mental state, which enable the robot to sustain a child's interest and forge good relationship with the child. The regularity of the gaze, smile intensities, and the motion are measured for this estimation, and the play modules are switched with the strategy of sustaining the child's interest in the play. Moreover, the robot selects appropriate actions according to the child's estimated mental state, which is based on the Markov decision process (MDP).

Several robotic playmates have been proposed [1]–[4]. Works in [1] and [3], were aimed at achieving robots that could engage in therapeutic play with autistic children. Attempts to extract play primitives have also been made [2] and [4]. In contrast to these works, our contributions are (1) the implementation of actual play modules, (2) the development of the action selection model based on the child's estimated inner state, (3) integration of the play modules with the action selection model, and (4) evaluation of the proposed playmate robot.

2 Overview of the Proposed Playmate Robot

The playmate system is implemented as a functionality of a domestic service robot. The robot is designed to play with a child using the implemented play modules, which cover several types of play to promote child development. The robot plays interactively with the child, switching play modules according to the child's mental state. Moreover, the most important purpose of the proposed system is to ensure its ability to play with a child for as long as possible. To this end, the system switches among play modules and selects strategies such as praise and competition according to the player's mental state. The player's mental state (e.g., bored) is estimated from the player's gaze, smile, and motion.

2.1 Robot Platform

In this work, the robot platform "DiGORO" was used. This robot has two arms with six degrees of freedom (DOF) each, a two-DOF neck, and a one-DOF waist. Thus, the robot can play with toys and its body. The underbody is based on omnidirectional wheels and has the capability to move around in an indoor environment using laser-based online simultaneous localization and mapping (SLAM). A real-time 3D sensor, which consists of calibrated CCD and time-of-flight (TOF) cameras [5], is mounted on its head. This sensor enables the robot to record the appearance of persons and objects online and recognize them with high accuracy [6]. Five onboard PCs work in parallel by coordination through TCP/IP connections. All computations are carried out inside the robot, and hence, it works properly even when no wireless network is available.

2.2 Modules of Play

The robot is designed to play using the implemented ten play modules, which cover all types of play to promote child development. The ten play modules that we are currently working on are (a) chatbot, (b) card playing, (c) drawing, (d) rock–paper–scissors, (e) picture-book reading, (f) hide and seek, (g) rhythmic movement, (h) blocks, (i) make-believe play, and (j) learning of novel play.

3 Action Selection and Mental State Estimation

To ensure continuous play with a child for a long duration, the robot predicts the mental state of the child and selects its next action accordingly. It is natural for us to select an action based on the observed child's behavior, and when the child gets bored with the current play, we usually engage the child in another play. Obviously, if the robot continues the same play in such a situation, the play will soon end. To this end, we first conducted an observation to analyze the play between a kindergarten teacher and a child. The results were used for designing the interaction between the robot and a child based on MDP. Next, experiments on the play between the robot and a child were conducted to test the mental state estimation method and to estimate the parameters for the model of action selection.

3.1 Observation of Play

We videotaped the play between a professional kindergarten teacher and a child. Two children (one boy and one girl) participated in this experiment. The children individually played with the teacher for thirty minutes each. The teacher selected which games to play. After each play period, we interviewed the teacher while watching the recorded video. The purpose of this interview was to discover the behavioral strategy of the teacher for engaging the child in play.

3.2 Modeling a Child's Play

We generated a child's play model including the child's mental state transition and the kindergarten teacher's action strategy from the observation (Fig. 1 (a)). It is a state transition model of the children's mental states, the action strategy of the teacher, and the process of becoming bored, which is a full complex model. "Nervous," "Familiar," "Enjoying," "Bored," and "Change of interest" represent the child's mental state transitions. The output from the child's mental state is the child's behavior, and the input is the kindergarten teacher's action strategy which is taken according to child's DOI in the play.

The model in Fig. 1 (a) is simplified to make it implementable on the robot, and we generated an action selection model. The child's mental state transition model, which corresponds to the action selection model for the robot, is illustrated in Fig. 1 (b). The playmate robot uses this model to select an action for sustaining the child's interest in the current play. It can predict the next state of the child by taking a specific action using the mental state transition model. Therefore, it is possible for the system to select an action that can keep the child engaged in play, i.e., by trying to confine the child's state to S_1 or S_2.

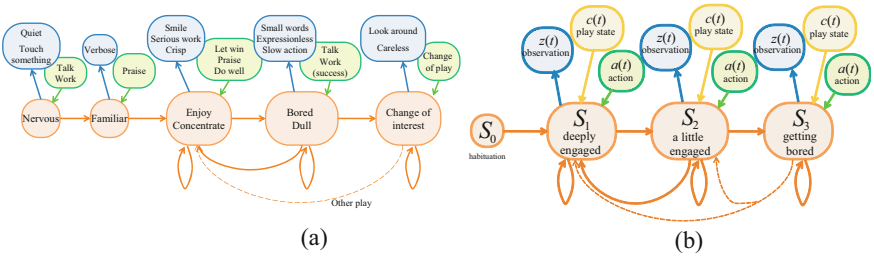

Fig. 1. Child's mental modeling: (a) Model of child's play including the child's mental state transition and the kindergarten teacher's action strategy and (b) Child's mental state transition model in play

Child's Inner State. In the figure, S_0, S_1, S_2, and S_3 represent the child's inner states of "habituation," "deeply engaged," "a little engaged," and "getting bored," respectively. The "habituation" state occurs once when the child first meets the robot. Therefore, during the play between the robot and the child, the states shift among S_1, S_2, and S_3.

Observation. $z(t)$ in Fig. 1 represents observable features for estimating the child's mental state. The output probability of $z(t)$ prescribes the child's current mental state. Details pertaining to the state estimation are described later.

Play State. In the model, $c(t)$ represents the state of play, such as types of play, a turn, and success or failure of the action. The play state is important since the available actions depend on the current state. Therefore, $c(t)$ is always referred to by the robot to select its action. The total number of play states is $(kind) \times (turn = 3) \times (success = 3)$. *kind* represents types of play, which include a card game, rock–paper–scissors game, and so on. *turn* has three values: child's turn, robot's turn, and the other turn. *success* takes the values success, failure, or nothing.

Actions. The variable $a(t)$ indicates a set of robot actions, which is designed with reference to the strategy of the kindergarden teacher. There are eight actions in total at the abstract level: (1) make a willful mistake, (2) react to the child's action, (3) react to its own action, (4) tantalize, (5) change the tempo of the play, (6) do nothing special (simply continue to play), (7) recommend changing to a different type of play, and (8) recommend continuing the same type of play.

The possible actions of the robot are constrained by the play state $c(t)$; e.g., the robot cannot flip over the card when it is the child's turn. Thus, each play state has a set of available actions $a\{c(t)\}$. The robot selects an action from the current list of available actions accordingly. The child's mental state transition model in Fig. 1 (b) has transition probability $p(S_k|S_n, a_n, c)$ as a parameter. The number of values this parameter can take is 8 $(number\ of\ state\ transitions) \times (number\ of\ play\ states) \times 8$ $(number\ of\ actions)$. This parameter is calculated based on the experiment of observing the play between two children and a kindergarten teacher.

Action Selection of the Robot. The robot acts based on the strategy of the kindergarten teacher. One important strategy is selecting an action according to the child's mental state. The process of the robot performing an action selection entails the following: (1) observing the child, (2) estimating the child's current mental state, (3) deciding the play state and set of actions available, and (4) selection of the action. The robot first estimates the child's mental state S_n from the observation $z(t)$. The set of available actions is automatically determined from the current play state $c(t)$. The robot then selects an action that has a high probability of transition to S_1 or S_2:

$$a(t) = \underset{a}{\operatorname{argmax}}\, p(S_n(t+1)|S_n(t), a\{c(t)\}). \tag{1}$$

The robot performs this action selection with each change in the play state.

3.3 Mental State Estimation

In the proposed system, the regularity of the gaze, smile intensities, and the motion are used for estimating the child's mental state. These three features appeared to be useful in our foregoing observational analysis. In [7], the authors found that similar cues are valid for detecting child engagement with a robot.

The regularity of the gaze $d(t)$ is defined as the frequency of the player's gaze on the robot or the area related to the play. Let $h(t) \in \{0, 1\}$ represent a state of the face direction at time t. $h(t)$ takes the value one when the player's face is in the direction of the play-related region and takes zero otherwise. Then, $d(t)$ can be calculated as $d(t) = \sum_{k=t}^{t+\ell-1} h(k)/\ell$, where ℓ denotes the length of a frame. The direction of the child's gaze is estimated via head tracking based on the 3D head-pose estimation [8]. The method in [9] is used for estimating smile intensities $s(t)$. $s(t)$ is averaged over a frame, and it ranges from 0 to 1. The motion cue is also useful since the motion of children becomes large as they lose interest. The motion $m(t)$ is measured by the distance between the current and previous positions of the face. $m(t)$ is normalized by the distance between the eyes to eliminate individual variation. $m(t)$ is also averaged over a frame, and it takes a value between 0 to 1. The length of a frame is chosen to be 5 s.

The output probability $p(z(t)|S_n)$ of each feature $z(t) = d(t), s(t), m(t)$ at the state S_n is modeled by a normal distribution using the foregoing experimental data. The likelihood $L_n(t)$ of the state S_n when the observation $z(t) = d(t), s(t), m(t)$ was observed is

$$L_n(t) = p(d(t)|S_n) \times p(s(t)|S_n) \times p(m(t)|S_n). \tag{2}$$

The state that has the highest likelihood is determined as the estimated mental state,

$$S_n(t) = \underset{S_n}{\operatorname{argmax}}\, L_n(t). \tag{3}$$

(a) (b)

Fig. 2. (a) Scenes of the experiment: the playmate robot, top view of the experiment, and children playing with the robot, are respectively depicted from left to right. (b) Action selection model based solely on play states.

4 Experiments

4.1 Experimental Setup

The model discussed in the previous section was implemented on DiGORO. To compare with our proposed method, we defined the state model (Fig. 2 (b)). In the state model, the robot selects an action randomly from the available actions at the play state $c(t)$. This means that the robot selects an action depending only on the current play state, and it does not care about the child's mental state.

We conducted a verification experiment using the robot in the decorated room as shown in Fig. 2 (a). Six children (three boys and three girls, with an average age of 5.5 years) participated in this experiment. Each participant was asked to sit in front of the robot and play card playing (concentration) and the game of rock–paper–scissors with it. This was because these two kinds of play work stably and are suited to the experiment from a safety viewpoint. The experiment started with five minutes of icebreaking conversation soon after the child entered the room. Then, the child played with the robot for about thirty minutes before leaving the room.

4.2 Estimation of the Child's Mental State

The child's mental states were estimated by using images from a camera that was set in front of the robot at 5-s intervals during the experiment. The proposed model used this estimated result for selecting the robot's next action. To compare with the teacher's evaluation, which will be explained later, 2 is assigned to S_1, 1 is assigned to S_2, and 0 is assigned to S_3. We call this the estimated degree of interest (DOI).

4.3 Evaluation and Questionnaires

We requested three professional kindergarten teachers to annotate each child's mental state in the range from 0 to 4, which we call annotated DOI, at 5-s intervals, by watching a video capturing the frontal view of the child. The average of the three teacher's ratings was used as the baseline. All the teachers were also asked to complete a questionnaire about the target child, which consisted of 13 items (that are listed below) concerning robots and the experiment, and 10 items about the personality of the child.

Table 1. Correlation coefficient between estimated DOI and annotated DOI

Child's ID	C1	C2	C3	C4	C5	C6
Correlation coefficient	0.22	0.21	0.12	0.01	0.52	0.53
Minimum value of ref.	0.59	0.91	2.00	2.00	1.41	0.67

Q1: Is the child interested in generic robots? (no / yes)
Q2: Does the child like generic robots? (yes / no)
Q3: Through this experiment, did the child get more interested in generic robots? (lost / developed interest)
Q4: Through this experiment, did the child come to like generic robots? (come to dislike / like)
Q5: Does the child like the robot used in this experiment? (no / yes)
Q6: How does the child find the robot used in this experiment? (scary / friendly)
Q7: How does the child feel about the robot used in this experiment? (uncool / cool)
Q8: How does the child feel about the size of the robot used in this experiment? (small / large)
Q9: How does the child feel about this experiment? (boring / enjoyable)
Q10: Was the child in a good mood before playing with the robot? (in a bad / good mood)
Q11: Did the child get into a good mood after playing with the robot? (get in a bad / good mood)
Q12: Does the child want to play with the robot again? (no / yes)
Q13: Does the child think of the robot as a human? (as a machine /as a human)

4.4 Results

Four children (two with the proposed model and two with the state model) out of the six played with the robot until the prescribed end of the experiment period. Because the remaining two children (one with the proposed model and one with the state model) refused to continue the play, the experiment was aborted after about fifteen minutes. One of these two children was scared of the robot and the height of the seat. These things were directly responsible for the child's refusal to continue the play. The other child tested the robot to see if she could trust it. She frequently took actions irrelevant to the play, such as shaking the table and showing an injury to the robot, among other actions. Since the robot could not respond to these actions, the play between the child and the robot was disrupted.

4.5 State Estimation

We smoothed estimated DOI values for 5 points and calculated the correlation coefficient between smoothed estimated DOI and each child's annotated DOI values. Table 1 shows the correlation coefficients. The estimated DOI is positively correlated with the annotated DOI in all six children($p < 0.05$, two-sided, sign test). This result is acceptable from the viewpoint of action selection using the model.

For the case where the minimum value of the annotated DOI is larger than 2, the correlation coefficients are low. This implies that the estimation accuracy of the state "the child is interested in the play" is not high. To discover the cause of this bad performance, we examined the data, finding that S_1 and S_2 share similar feature vectors in this experimental setting. This means that discriminating S_1 from S_2 by the feature vector used in this experiment is difficult. However, both S_1 and S_2 can be said to be the interested states of children, and actions

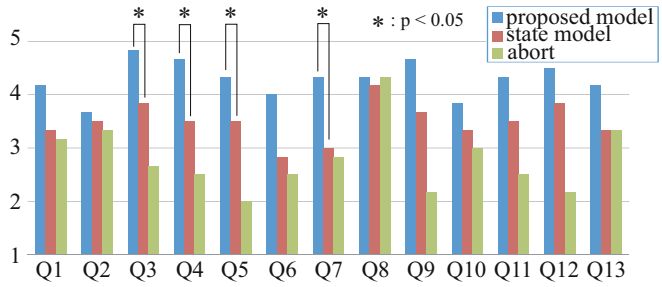

Fig. 3. Average scores for each questionnaire. See the text for details on Q1–Q13.

selected in both states are behaviors that encourage the children in the states of engagement. Therefore, the inability of the system to discriminate between S_1 and S_2 can be disregarded. Estimating S_3, the state in which the child gets bored, is more important during the play.

We thus measured the accuracy of estimating the child's state with two levels, i.e., $S_1 + S_2 = S_1^{'}$ and S_3. In this case, the recognition accuracy increased from ∼40% to ∼70%.

4.6 Comparison between Proposed Model and State Model

The subjects can be divided into three groups. The first group consists of subjects playing with the robot that selects its action using the proposed model (model group). The second group contains subjects playing with the robot that selects its actions using the state model (state group). The last group consists of subjects who aborted the play in the experiment (abort group). Figure 3 shows the average questionnaire scores for each group. The responses to Q3, Q4, Q5, and Q7 exhibit significant differences between the model and state group according to a t-test ($p < 0.05$). Q3 to Q5 are questions pertaining to whether the experiment affects the result, such as "Does the child like the robot used in this experiment?" In contrast, responses to other questions that pertain to the robot in general, such as Q2 "Does the child like generic robots?," show no significant differences. This implies that the proposed model leads to a better impression of the robot and the experiment than the state model. Given that the average scores of Q9 "How does the child feel about this experiment? (boring / enjoyable)" and Q12 "Does the child want to play with the robot again?" for the model group are higher than those for the state group, the selecting actions by the proposed model may affect the relationship between the robot and the child, and the relationship influences whether the robot can play with the child over a long duration.

To validate this questionnaire's result, we try to evaluate a relationship between the robot and the child in quantitative form. Figures 4(a) and (b) show the DOIs (annotated) of two participants, one from the model group (Fig. 4(a)) and one from the state group (Fig. 4 (b)). Figures 4(c) and (d) illustrate the frequency of gazing at the robot and the table by the children. This plot is the 5-minute

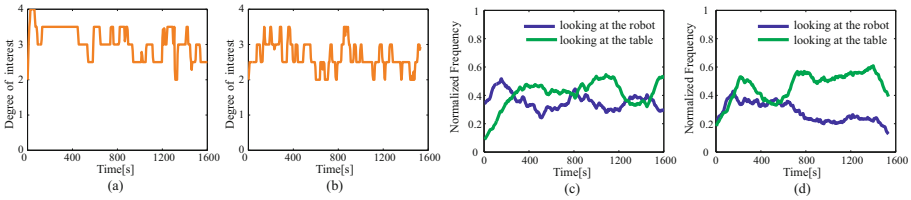

Fig. 4. The results of two participants: (a) plot of the baseline DOI for the model group, (b) plot of the baseline DOI for the state group, (c) plot of the normalized frequency of gazing at the robot and the table for the model group, and (d) plot of the normalized frequency of gazing at the robot and the table for the state group‘.

moving average. The figures indicate that both DOIs have no tendency of causing children to get bored. This suggests that every child enjoyed playing. However, the frequency of the child gazing at the robot and the table greatly differed between the two groups. Both groups often gazed at the robot at first, and the model group gazed at the robot and the table at about the same rate over time (average: table 54%, robot 46%). In the state group, the frequency of gazing at the table gradually reduced (average: table 62%, robot 38%). A particularly noteworthy point is that at the end of a card game, which is at about 700 to 1300 s in Fig. 4(c) and 500 to 1050 s in Fig. 4(d), the frequency of gazing at the robot increases and exceeds the frequency of looking at the table at 700 and 1300 s in Fig. 4(c) and at 500 s in Fig. 4(d). This implies that the child gazed at the robot to observe the robot's reaction at the end of the card game. This is similar to the situation in which the child looks at the kindergarten teacher after finishing something because the child wants to observe the teacher's reaction. In contrast, despite the card game also ending at 1050 s in Fig. 4(d), the frequency of gazing at the robot did not increase. In the state model, the child provides less attention to the robot during the play. The same thing can be said for the remaining two children who played until the prescribed end of the experiment period.

This result shows that selecting actions by using the mental state transition model for the play between the child and the robot is as effective as indicated by the questionnaire's result. Appropriate behavior of the robot based on the model helps to maintain a good relationship with the child.

The DOIs exhibit no difference between the model and state groups; however, the frequencies of the child's gaze differ. These results indicate that there are two important factors involved for the robot to be able to play with the child for as long as possible. One is the engagement in play, represented by the DOI. The other factor is the relationship between the robot and the child, represented by the regularity of the gaze. The relationship affects the child's urge to play with the robot again, which is indicated, for example, by the response to Q9 "How does the child feel about this experiment? (boring / enjoyable)" and Q12 "Does the child want to play with the robot again?" Therefore, this factor is certainly important to sustain play for a long duration. In addition, these results indicate that the relationship can be measured directly from the regularity of the gaze.

5 Conclusion and Future Work

To continuously play with a child for a long duration, a robot has to sustain the child's interest and forge a good relationship with it. This study proposes a playmate robot system consisting of multiple, switchable play modules that help to sustain a player's interest for as long as possible. We also propose a model of the inner state of the player, which is used by the robot for action selection. We implemented basic functions of the play modules in our service robot and verified that they work reasonably well through experiments involving child–robot interactive play. The result shows that the robot's action selection using the proposed model created a good relationship between the robot and the child. However, many challenges remain to be addressed in a future work, for example, the implementation of the modules and, in particular, the testing of the playmate robot with a larger number of children.

References

1. Dautenhahn, K., Werry, I., Rae, J., Dickerson, P., Stribling, P., Ogden, B.: Robotic Playmates: Analysing Interactive Competencies of Children with Autism Playing with a Mobile Robot. In: Dautenhahn, K., Bond, A., Canamero, L., Edmonds, B. (eds.) Socially Intelligent Agents—Creating Relationships with Computers and Robots, pp. 117–124. Kluwer Academic Publishers (2002)
2. Howard, A.M., Park, H.W., Kemp, C.C.: Extracting Play Primitives for a Robot Playmate by Sequencing Low-Level Motion Behaviors. In: Proc. of IEEE Int. Symp. on Robot and Human Interactive Communication, pp. 360–365 (August 2008)
3. Trevor, A.J.B., Park, H.W., Howard, A.M., Kemp, C.C.: Playing with Toys: Towards Autonomous Robot Manipulation for Therapeutic Play. In: Proc. of ICRA, pp. 2139–2145 (May 2009)
4. Park, H.W., Howard, A.M.: Understanding a Child's Play for Robot Interaction by Sequencing Play Primitives Using Hidden Markov Models. In: Proc. of ICRA, pp. 170–177 (May 2010)
5. Attamimi, M., Mizutani, A., Nakamura, T., Nagai, T., Funakoshi, K., Nakano, M.: Real-Time 3D Visual Sensor for Robust Object Recognition. In: Proc. of IROS, pp. 4560–4565 (October 2010)
6. Attamimi, M., Mizutani, A., Nakamura, T., Sugiura, K., Nagai, T., Iwahashi, N., Okada, H., Omori, T.: Learning Novel Objects Using Out-of-Vocabulary Word Segmentation and Object Extraction for Home Assistant Robots. In: Proc. of ICRA, pp. 745–750 (May 2010)
7. Castellano, G., Pereira, A., Leite, I., Paiva, A., McOwan, P.W.: Detecting User Engagement with a Robot Companion Using Task and Social Interaction-based Features. In: Proc. of the 2009 International Conference on Multimodal Interfaces, pp. 119–126 (November 2009)
8. Kinoshita, K., Konishi, Y., Lao, S., Kawade, M.: Facial Feature Extraction and Head Pose Estimation Using Fast 3D Model Fitting. In: MIRU 2008, pp. 1325–1329 (2008) (in Japanese)
9. Konishi, Y., Kinoshita, K., Lao, S., Kawade, M.: Real-Time Estimation of Smile Intensities. In: Proc. of Interaction 2008., vol. 4(2008), pp. 47–48 (2008) (in Japanese)

Concurrent Acquisition of the Meaning of Sentence-Final Particles and Nouns Through Human-Robot Interaction

Natsuki Oka, Xia Wu, Chie Fukada, and Motoyuki Ozeki

Graduate School of Science and Technology, Kyoto Institute of Technology

Abstract. Sentence-final particles serve an important role in spoken Japanese, because they express the speaker's mental attitudes toward a proposition and/or an interlocutor. They are acquired at early ages and occur very frequently in everyday conversation. However, there has been little proposal for a computational model of the acquisition of sentence-final particles. In this paper, we report on a study in which a robot learns how to react to utterances that have a sentence-final particle and gives appropriate responses based on rewards given by an interlocutor, and at the same time, learns the meaning of nouns. Preliminary experimental result shows that the robot learns to react correctly in response to *yo*, which expresses the speaker's intention to communicate new information, and to *ne*, which denotes the speaker's desire to confirm that some information is shared, and also learns the correct referents of nouns.

Keywords: language acquisition, function words, reinforcement learning.

1 Introduction

Sentence-final particles serve the important role of expressing the speaker's mental attitudes. They are acquired at early ages and occur very frequently in everyday conversation. Ohshima et al. proposed a robot that uses sentence-final particles in order to draw the hearer's attention [4]. Research on the computational model of language acquisition is rapidly increasing [1]. However, to the best of our knowledge, there has been no proposal for a computational model of the acquisition of sentence-final particles except for our earlier reports [3,5].

In the preceding reports, we dealt with the following two usages of sentence-final particles *yo* and *ne*, (although there are several other usages of *yo* and *ne*):

- The informing usage of *yo*: informing the listener of information that seems new to the listener [2].
- The agreement requesting usage of *ne*: requesting an agreement on information that seems to be shared between the speaker and the listener [2].

The purpose of the study was to get a robot to learn a series of appropriate physical reactions to a speaker's mental attitude expressed with a sentence-final particle. We used a robot, instead of a virtual agent, because the reactions to be learned included

M. Lee et al. (Eds.): ICONIP 2013, Part I, LNCS 8226, pp. 387–394, 2013.
© Springer-Verlag Berlin Heidelberg 2013

the gaze direction, which is difficult for a virtual agent to express accurately. The robot learned appropriate reactions based on rewards given by its interlocutor.

In general, responses from a robot include the following:

1. physical reactions such as a nod, turning of its face in the direction of the referent of the utterance, etc.
2. utterances
3. inner information processing such as memorizing new information received, etc.

Among the three items listed, 1 and 2 are observable by an interlocutor; however, item 3 cannot be directly observed, which makes it difficult for him/her to give appropriate rewards in accordance with the robot's response, and inappropriate rewards make it difficult for the robot to learn appropriate responses. Our earlier study [3,5] only dealt with item 1. The robot thus only acquired outward behaviors, and did not learn inner information processing such as remembering the name of an object. While, this study deals with item 3 as well as item 1. Although it does not cover item 2, we believe that utterances can be learned as well as physical reactions because both are observable.

The remainder of this paper is organized as follows. We describe our preceding computational model for the acquisition of physical reactions to sentence-final particles in Section 2. We explain our new model for learning the invisible inner processing and demonstrate the leaning capability of the model in Section 3. Finally, we outline future work and conclude this paper in Section 4.

2 Acquisition of Appropriate Physical Reactions

2.1 Computational Model

In this study, the robot learned appropriate physical responses to the two usages of sentence-final particles *yo* and *ne* based on the rewards given by an interlocutor. We formulated the problem as a reinforcement learning (RL) process. State in RL consisted of the utterance of the interlocutor, the referents of the utterance, objects within the eyesight of the robot, and others. For simplicity, we assumed that the rewards are given every time without fail, and excluded delayed rewards, which simplified the action value update as follows:

$$Q(s,a) \leftarrow Q(s,a) + \alpha\big(r - Q(s,a)\big),$$

where $Q(s,a)$ is an action-value function, that is, the value of taking action a in state s, α is the learning rate, and r is the reward.

2.2 Experiments

We conducted three experiments: The robot learned (1) the informing usage of *yo*, specifically, the usage that relates the name of an object (Exp. 1), (2) the agreement requesting usage of *ne* (Exp. 2), and (3) the informing usage of *yo*, specifically, the usage that relates the existence of an object (Exp. 3).

Fig. 1 shows the experimental environment utilized. The general procedure used was as follows: The participant talks to the robot using a sentence-final particle, and he/she indicates the associated object with his/her hand by touching the object or pointing to it. The robot recognizes the word uttered using registered-word voice recognition, and identifies the object being referred to with Kinect by detecting the interlocutor's hand. It then reacts by randomly combining at most three of the following four elemental actions: nodding, turning its face toward the interlocutor's face, turning its face toward the object in question, or turning its face toward a different object. The participant gives a reward of 1 or -1 to the robot using a mouse, and the robot learns which action sequences result in the most reward using Q-learning.

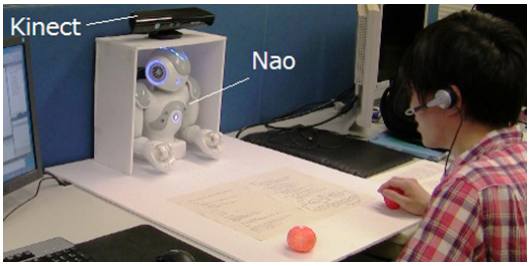

Fig. 1. Experimental environment for the earlier study. The participant talked to the robot using a sentence-final particle, and the robot learned physical reactions to it.

Fig. 2 gives examples of the sentence uttered in each experiment. While the participants were informed that the robot does not know the names of the objects on the table in Experiment 1, they were informed that the robot knows the names in Experiments 2 & 3. Please note that the participants talked about the object at which the robot looked in Experiments 1 & 2, but they talked about the object at which the robot did not look in Experiment 3.

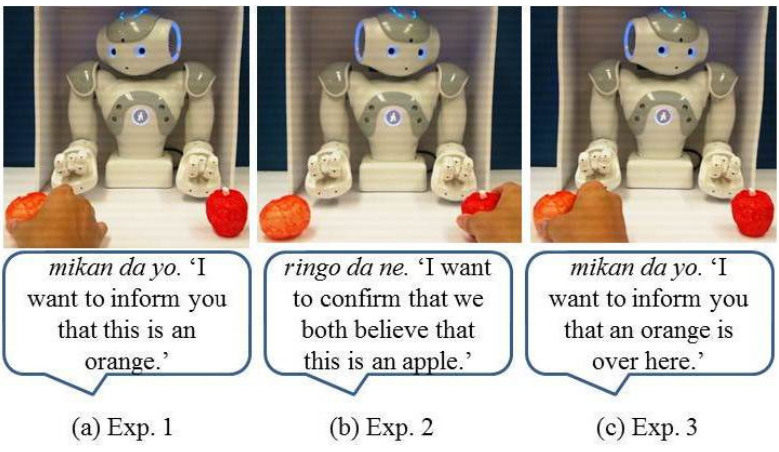

Fig. 2. Examples of the sentence uttered in each experiment

2.3 Results and Discussion

The main learning results are shown in Table 1 (see [3,5] for more details). The results indicate that the robot learned to react more or less correctly in response to sentence-final particles *yo* and *ne*. Several action sequences resulted in the opposite action values to those that were expected by us; these are indicated by colored cells in the table.

We found that there were individual differences in the evaluation of the robot's actions, and the aforementioned reversed evaluations were mostly observed for specific participants. This means that adaptation to an individual user is worthwhile.

Table 1. Main results of action-value learning. For each experiment, action sequences that have the top five action values are shown in descending order. Action sequences consisted of at most three elemental actions. "Face" represents the elemental action of turning the robot's face toward the interlocutor's face; "object" represents the action of turning toward the relevant object; and "other" signifies the action of turning toward another object.

Exp. 1: Instructing names			Exp. 2: Requesting agreement			Exp. 3: Informing existence		
1st	2nd	3rd	1st	2nd	3rd	1st	2nd	3rd
nod	object	object	nod	face	-	face	nod	object
object	nod	object	nod	other	object	object	nod	other
nod	other	object	nod	nod	nod	other	object	nod
other	nod	object	face	face	nod	face	other	-
nod	other	other	face	nod	nod	face	other	nod

3 Learning Invisible Inner Processing

The robot described in the previous sections learned appropriate reactions such as turning toward an apple and nodding on hearing a sentence containing a sentence-final particle. However, it only acquires outward behaviors, and does not learn inward processing such as remembering the name of an object.

In this section, we explain our idea for learning inward processing as well as outward behaviors. Learning inner processing from rewards is much more difficult than learning visible behaviors. This is because accurate rewards are not always given for invisible inner processing. For example, it is probable that even though a reward was given when the robot nodded, it subsequently turns out that the robot does not actually remember the name.

3.1 Computational Model

In order to resolve the aforementioned issue, we employed the following policies: (1) the robot should learn from delayed rewards; and (2) the state space of learning, i.e., the number of states and actions, should be as small as possible. We employed the

latter policy because it is difficult to obtain sufficient data for complicated learning when the data comes only from interaction with humans.

We thus set out a simple state space, shown in Fig. 3, in the first place. An important difference from the standard reinforcement learning (RL) is the alternate actions between a human and a robot. Human actions are represented by dashed arrows and robot's actions are expressed with solid arrows in Fig. 3, and both actions cause state transitions. While the robot acts according to the learned action values as in the standard RL, human actions are decided independently of the action values in the state space.

One of the robot's actions in Fig. 3, "memorize and nod," is the act of memorizing a pair of a word, such as apple, which is a segment of speech, and an image of an object in front of its eyes, and nodding. "Compare and move neck according to the result" is the act of nodding if the currently presented word-image pair is the same as the pair in memory, shaking its head if the current pair disagrees with the stored pair, or no neck motion otherwise.

We use the learning algorithm shown in Fig. 4, which is a modified version of Sarsa(λ) [6]. The modification includes the following: (1) alternate actions between the human and the robot; and (2) use of a replacing trace [6] instead of an eligibility trace.

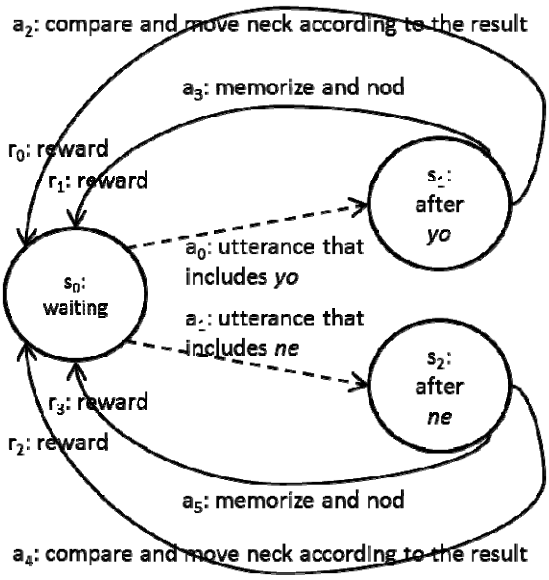

Fig. 3. State transition diagram. Dashed arrows represent human actions, and solid arrows depict robot's actions that include inner processing.

Initialize $Q(s,a) = 0;\ e(s,a) = 0$, for all s, a
Initialize $s = s_0$
Repeat
  Human's turn:
    The human takes action a
    Observe $r,\ s';\quad r = 0$ for human actions
    $s \leftarrow s'$
  Robot's turn:
    Choose a from s using policy derived from Q (ε-greedy)
    Take action a
    Observe $r,\ s'$
    $\delta \leftarrow r + \gamma Q(s', a') - Q(s,a);\ Q(s', a') = 0$ for human actions
    $e(s,a) \leftarrow 1$
    For all $s,\ a$:
      $Q(s,a) \leftarrow Q(s,a) + \alpha\delta e(s,a)$
      $e(s,a) \leftarrow \gamma\lambda e(s,a)$
    $s \leftarrow s'$
until the end of episode

Fig. 4. Learning algorithm for inward processing: a modified version of Sarsa(λ) [6]

3.2 Preliminary Experiment

A preliminary experiment with five participants was conducted. The setting of the experiment was similar to that described in Section 2.2 except for the number of objects on the table; not two but one. In this experiment, three kinds of objects, an orange, an apple, and a banana, were provided. A participant selected one of the three objects, put it in front of the robot, and talked about it.

At first, the robot did not know the meaning of sentence-final particles *yo* and *ne*, nor the names of the three objects. The participant tried to teach the two sentence-final particles and the three nouns to the robot. Learning rate α was set to 0.1, and probability for random action selection ε was set to 0.1. In order to simplify the analysis of the experimental results as a first step, discount rate γ was set to 0, that is, the robot learned only from immediate rewards, in this preliminary experiment.

Table 2 shows a typical example of the progress of learning. In this case, the robot concurrently and successfully learned the two sentence-final particles, which are shown in the action value columns, and the three nouns, which are indicated in the contingency table column. The action value columns demonstrate that appropriate inner processings have positive values, and an inappropriate processing has a negative value. Another inappropriate processing has not been tried. An incorrect pair 'object: apple'-'name: orange' is stored in the contingency table, but it is not serious because the correct pair 'object: apple'-'name: apple' has more counts.

We, however, found that not every participant succeeded in teaching. There was a participant who gave punishment every time when the robot nodded after hearing sentence-final particle yo, and the robot failed to learn the meaning of yo. In order to deal with this kind of unusual but consistent rewards, we plan to revise the fixed relation between inward processing and outward behavior to flexible one.

Table 2. Typical example of the progress of learning in the preliminary experiment. "A","O", and "B" respectively stand for apple, orange, and banana. "M" and "C" represent the inward processing of memorizing and comparison, respectively. The first data row indicates that the participant put an apple in front of the robot and said "*ringo da yo*" (which means, "I want to inform you that this is an apple"), then the robot memorized the name of the object and nodded, and then the participant gave a reward and the robot updated the action value. The names of the objects in the robot's memory are represented as a 3×3 contingency table.

object	noun used	particle used	inner process	action	reward	action value				contingency table
						yo		*ne*		
						M	C	M	C	
A	A	*yo*	M	nodding	+1	0.10				obj\n: A O B; A: 1 0 0; O: 0 0 0; B: 0 0 0
A	O	*ne*	M	nodding	−1			−0.10		obj\n: A O B; A: 1 0 0; O: 1 0 0; B: 0 0 0
A	A	*yo*	M	nodding	+1	0.19				obj\n: A O B; A: 2 0 0; O: 1 0 0; B: 0 0 0
A	O	*ne*	C	shaking	+1				0.10	
B	B	*ne*	M	nodding	−1			−0.19		obj\n: A O B; A: 2 0 0; O: 1 0 0; B: 0 0 1

4 Conclusions and Future Work

In this paper, we outlined a computational model for learning appropriate physical reactions to utterances that have a sentence-final particle. Our experimental results indicated that the robot learned to react more or less correctly in response to yo and ne.

We then proposed a learning algorithm for inward information processing as well as outward physical behaviors. The result of the preliminary experiment seems promising, and we plan to conduct thorough experiments to test whether the meaning of both the sentence-final particles and nouns can be learned at the same time. We also plan to investigate the relation between the complexity of the state space and the amount of interaction necessary for learning.

Acknowledgement. This work was supported by JSPS KAKENHI 21500137 and 25330260.

References

1. Alishahi, A.: Computational Modeling of Human Language Acquisition, Morgan & Claypool (2010)
2. Kinsui, S.: Latest information on Linguistics: Japanese language study: Sentence-final particles *yo* and *ne*. Gengo 22(4), 118–121 (1993) (in Japanese)
3. Ogami, R., Matsuoka, H., Araki, O., Shibata, R., Takaoka, Y., Tsuchisaka, Y., Wu, X., Fukada, C., Ozeki, M., Oka, N.: Meaning acquisition of function words through human-robot interaction: Viewing the meaning of sentence-final particles as appropriate actions for utterances. Paper Presented at Human-Agent Interaction Symposium 2012, 2D-7 (2012) (in Japanese)
4. Ohshima, N., Ohyama, Y., Odahara, Y., De Silva, P.R.S., Okada, M.: Talking-ally: Intended persuasiveness by the utilizing hearership and addressivity. In: Proceedings of the Fourth International Conference on Social Robotics, pp. 317–326 (2012)
5. Oka, N., Ogami, R., Wu, X., Fukada, C., Ozeki, M.: Acquiring the meaning of sentence-final particles *yo* and *ne* through human-robot interaction. Paper Presented at the First International Conference on Human-Agent Interaction, Sapporo, Japan (2013)
6. Sutton, R.S., Barto, A.G.: Reinforcement learning: An introduction. MIT Press, Cambridge (1998)

Intention Estimation and Recommendation System Based on Attention Sharing

Sangwook Kim[1], Jehan Jung[2], Swathi Kavuri[1], and Minho Lee[1,*]

[1] School of Electronics Engineering,
[2] Department of Sensor and Display Engineering,
Kyungpook National University
1370, Sankyuk-Dong, Puk-Gu, Taegu 702-701, South Korea
{sangwook,crossjjh}@ee.knu.ac.kr,
{swati.kavuri,mholee}@gmail.com

Abstract. In human-agent interactions, attention sharing plays a key role in understanding other's intention without explicit verbal explanation. Deep learning algorithms are recently used to model these interactions in a complex real world environment. In this paper we propose a deep learning based intention estimation and recommendation system by understanding humans attention based on their gestures. Action-object affordances are modeled using stacked auto-encoder, which represents the relationships between actions and objects. Intention estimation and object recommendation system according to human intention is implemented based on an affordance model. Experimental result demonstrates meaningful intention estimation and recommendation performance in the real-world scenarios.

Keywords: intention estimation, recommendation system, attention sharing, deep learning, action-object affordance.

1 Introduction

One of the main roles of artificial cognitive agents such as robots is to help people to achieve their intended goals. In order to recognize human intention, it is important for a robot to understand the cognitive status of humans as well as the given environment. Humans pay attention to the interesting parts of information related to their intention. Cognitive psychologists call this phenomenon as 'selective attention' [1-3]. So, to predict others' intention, it is essential to understand their attention. This cognitive ability to understand other's attention is called attention sharing or joint attention [4, 5]. Attention sharing is the shared focus of two individuals on an object. It is achieved when an individual pays his/her attention on an object by means of eye-gazing, pointing or other verbal and non-verbal indications. If a robot could share attention then it can predict human intention and provide adequate services.

Selective attention reduces cognitive load. However, environmental distractions generally disturb user's attention. In this case, cognitive robots can aim to assist the

* Corresponding author.

M. Lee et al. (Eds.): ICONIP 2013, Part I, LNCS 8226, pp. 395–402, 2013.
© Springer-Verlag Berlin Heidelberg 2013

intrinsically limited cognitive ability of humans. Since human intentions are usually related with objects in an environment, robot agents should know the affordance. Affordance is the concept, defined by Gibson [6], which represents the relationships or possibilities between actions and objects. The robot can exploit this type of knowledge to understand the world in terms of actions and objects to infer the user's intention based on objects of attention in a given environment. In [7], authors proposed an object categorization method based on affordances between visual objects and actions obtained from human behavior. In [8], object affordances were modeled with Bayesian networks. These networks are the probabilistic representation of dependencies which can be used to understand human actions. This understanding can be used to build robots, which can imitate human behavior. Several stochastic models have been adopted for an intention recognition system. Hidden Markov model (HMM) was used as a recognition model [9] to model the causality or dependency between successive measurements. Dynamic Bayesian networks (DBN) were also used to model user's intention [10]. It modeled connections between intentions, observed user actions and sensory modalities. This model obtained actions like explicit gestures but didn't consider user's attention and objects related to actions. In [11], authors tried to recognize human intention by analyzing the change in distance between the observed human's hand and the objects in the scene over several frames. In their model, stacked denoising auto-encoder (SDA) was used which learns distance between object and humans and predicts an object for which the person is currently reaching. However, a limitation of this system system is that it tries to understand user's current behavior and fails to recommend the objects needed for a user. In [12], authors classified intentions given objects using naïve Bayes classifier [13] and used eye-tracking data from virtual environment. But this model only performed intention classification and couldn't explain affordances between intentions and objects. In this model recommendation of objects was just assumed to be obtained indirectly by sending a query containing the intention to virtual database.

In this paper, we propose a system that can recognize human intention and recommend corresponding objects based on user's attention sharing and affordances. In order to model, acquire and use affordances, we obtain the selective attention areas by attention sharing based on human gesture understanding.

The rest of this paper is organized as follows: In Section 2, we describe the structure and the algorithm of the proposed model. In Section 3 we present the experimental results to evaluate the performance of the proposed model. Finally, we draw our conclusions in Section 4.

2 Proposed Model

2.1 Overall Structure

Main tasks of the proposed model are intention estimation and recommendation for the user. To do this, it is required to have functionalities such as attention sharing, affordance learning, intention estimation, and recommendation based on affordance model. The structure of intention estimation and recommendation system is shown in Fig. 1.

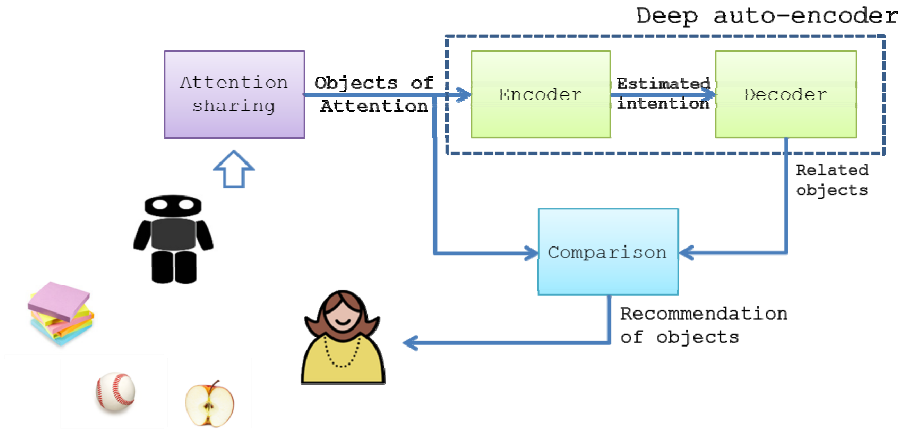

Fig. 1. The structure of the proposed system

In this model, gestures are used to obtain objects of user's attention. Once the user points out an intended or interesting object to a the robot calculates the pointing vector from angles of user's body gesture and estimate the joint area of pointing vector and objects in the sight. Based on objects of attention, user intention is estimated by using affordance model. If there is an object which is missed by user's attention but needs to be recommended strongly based on affordance information, the system recommends the missed object to the user. Procedure of the proposed model is explained in following subsections in detail.

2.2 Attention Sharing

In the proposed model, one of our aims is to implement attention sharing for external artificial agent. It is necessary for a robot to understand human behavior and communicate with them. But, at present, there are no robot platforms which can perceive stereo vision and human skeleton in the 3D space easily. Therefore, we used the Kinect for attention sharing [14]. Kinect is a popular device in motion sensing field because of its ability to detect human body and capture its motion in real time. For an interactive communication a robot can be used to recommend some objects to the user. The procedure is like this: The user stand in front of Kinect device and robot is placed to the side of the user. Kinect recognizes the gestures made by the humans and provides this information to the robot for joint sharing of attention. The user points out an object with his/her right arm. The robot understands human motion and looks at the same object. The user tries again to point another object and the robot follows. Actually, when the user points out an object, pointing position is not stable. It has lots of vibration and it makes some error. So, we used 5 seconds to obtain stability while selecting an object. After objects of attention are perceived, they are used to estimate the user's intention.

Fig. 2. An example scene of attention sharing

2.3 Intention Estimation and Object Recommendation

Intention estimation and recommendations are based on affordance. In the proposed model, affordance is modeled using stacked auto-encoder which is the one of the deep learning structure [15]. Deep network structure is known for its ability to capture high-order relationships or features that are unobservable directly. Although they are considered as powerful high-level feature extracting machines, deep machines were impractical because of absence of efficient learning algorithm. At last G. Hinton and his colleagues proposed Restricted Boltzmann Machine (RBM) network with contrastive divergence [16] and deep networks became popular in many machine-learning fields. Stacked auto-encoder consists of restricted Boltzmann machine (RBM) layers [17]. Boltzmann machine is a stochastic machine, which has a binary state with the probability and has the constraint that nodes are not connected with nodes in the same layer. By restricting those connections, more efficient learning algorithms can be used to train the network.

Stacked auto-encoder involves two complementary parts, (1) the encoder part and (2) the decoder part. The encoder extracts high-order features of data and transforms

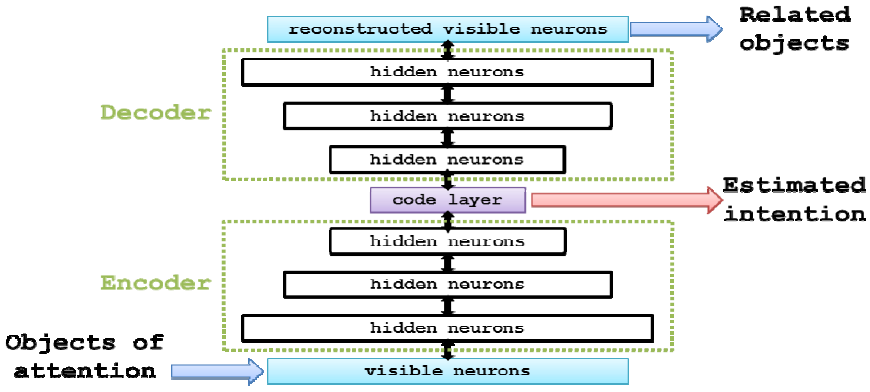

Fig. 3. The structure of deep auto-encoder

data to a relatively low-dimensional space. The decoder, the counterpart of the encoder, tries to recover the data with original dimension from the encoded vector.

These two parts are used to model the bidirectional affordance between intention and objects. The encoder estimates intentions and the decoder reconstructs corresponding objects. Each node of RBM has a probability of the activation as a result of the training. At the code layer, these probabilities are evaluated and compared to decide most adequate intention for a given object of attention. Then, in the decoder part, objects related to the intention are reconstructed and objects that are reconstructed but not presented in user's attention are recommended. The learning of the auto-encoder consists of two phases. At first, the network is pre-trained and subsequently performs the fine-tuning training.

Input vectors for RBM represent the combination of objects of attention. For example, among 5 objects, if objects 1, 2 and 3 get user's attention, the input vector are set to [1 1 1 0 0]. And target code is encoded in a same way. If there are 3 different intentions, target vectors of intentions 1, 2 and 3 become [1 0 0], [0 1 0] and [0 0 1], respectively. This vector is used as the teaching signal.

For the test, if test input is given to visible neurons of the stacked auto-encoder, user's intention is estimated and represented as the vector in code layer such as [0.1 0.8 0.2]. Then the index of the maximum element of the code vector is decided as the label of the estimated intention. After that, the vector is sent to the decoder part and finally at uppermost layer, the combination of related objects corresponding to the intention vector is reconstructed. With reconstructed related objects, the objects to recommend are decided as

$$\{obj_{recommended}\} = \{obj_{reconstructed}\} \backslash \{obj_{attention}\}, \quad (1)$$

where $obj_{reconstructed}$ is obtained by uppermost layer, $obj_{attention}$ is the input objects which is the result of attention sharing, and set operator \ is the relative complement. Then $obj_{recommend}$ is relative complement of $obj_{reconstructed}$ in $obj_{attention}$.

3 Experimental Results

3.1 Experimental Environment

To show the performance of the proposed intention recognition and object recommendation, an experimental environment was set up. For obtaining the user's attention, we used Microsoft Kinect. The 12 objects related to intentions are used for the experiment. Users were asked to point out intended objects. Fig. 4 shows the picture of an experimental environment. Objects are a ramen, a coffee bottle, tea bags of green tea, rice cakes, an electric kettle, a pot, a dish, bottles of water, a mug and forks.

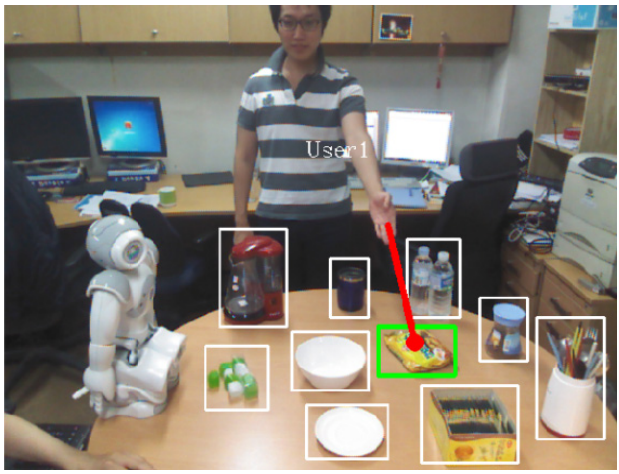

Fig. 4. Environmental scene during experiments

The four different intentions used for the experiment were 'eat ramen', 'eat rice cake', 'drink coffee', and 'drink green tea'. Participants were required to indicate objects that were needed to achieve specific intention. Then objects of attention were obtained by attention sharing. The sample data are expressed as

$$\mathbf{x} = [x_1, \ldots, x_n], \tag{2}$$

where n is the number of objects used in the experiment. x_i, i-th elements of data $\mathbf{x}$, is set to 1 if the user pointed i-th object out and x_i is 0 otherwise. n is ten in this experiment.

3.2 Experimental Results

The deep auto-encoder consists of 7 hidden layers which have dimensionalities 200, 100, 50, 15, 50, 100, 200, respectively. The number of epochs for training is set to 50. Table 1 shows the intention estimation accuracy. Intentions from 1 to 4 are 'eat ramen', 'eat rice cake', 'drink coffee' and 'drink green tea', sequentially. Among five persons who participated in experiments, data of four person randomly selected are used to train and remaining one person's data are used to test.

Table 1. The accuracy of intention estimation

	Intention 1	Intention 2	Intention 3	Intention 4
Training data	100 %	100 %	100 %	100 %
Test data	100 %	100 %	100 %	100 %

As shown in the table, the model demonstrates the perfect intention estimation performance despite the fact that each participant had different selections or preferences

of objects corresponding to their intentions. Due to several environmental distractions, it is common that subjects' attention tend to miss some objects required for specific intention. For those cases, we tested the intention estimation with randomly selected missing objects. Table 2 shows the performance in the case that one object is missing. For this experiment, all five participants' data were used to train and test was performed with randomly selected missing objects.

Table 2. The accuracy of intention estimation with a missing object

	Intention 1	Intention 2	Intention 3	Intention 4
Test data with a missing object	83.3 %	79.7 %	45.7 %	91 %

Intention 3 and 4 are 'drink coffee' and 'drink green tea', respectively. These intentions share some same objects such as bottles of water and a mug cup . Thus intention 3 is easily confused with intention 4 when there is a missing object. Conclusion

In this paper, we proposed an intention estimation and recommendation system based on attention sharing using gesture understanding and affordance model. Intention estimation and recommendation are modeled in a stacked auto-encoder consisting of an encoder part and a decoder part.. Experimental result shows that the model has perfect intention estimation accuracy when there is no missing object and shows meaningful generalization performance even though there is a missing object. Recommendation of object was also successful.

In our future work, we shall attach a stereo system on the robot itself to make the robot track the user to recognize his/her attention. We also plan to implement systems that can recognize multiple behaviors of users such as head position, eye-gaze and so on. We assume that multi-modal attention sharing will increase the performance of intention recognition.

Acknowledgement. This research was supported by the Industrial Strategic Technology Development Program (10044009) (50%) and the R&D program (10041826) (50%) funded by the Korea Ministry of Knowledge Economy (MKE) and the Korea Evaluation Institute of Industrial Technology (KEIT).

References

1. Duncan, J.: Selective attention and the organization of visual information. Journal of Experimental Psychology. General 113, 501–517 (1984)
2. Treisman, A.M.: Strategies and models of selective attention. Psychological Review 76 (1969)
3. Ban, S.-W., Jang, Y.-M., Lee, M.: Affective saliency map considering psychological distance. Neurocomputing 74, 1916–1925 (2011)
4. Kozima, H.: Attention-sharing and behavior-sharing in human-robot communication. In: IEEE International Workshop on Robot and Human Communication (1998)

5. Moore, C.E., Dunham. P.J.: Joint attention: Its origins and role in development. Lawrence Erlbaum Associates, Inc. (1995)
6. Gibson, J.J.: The ecological approach to visual perception. Psychology Press (1986)
7. Kjellström, H., Romero, J., Kragić, D.: Visual object-action recognition: Inferring object affordances from human demonstration. Computer Vision and Image Understanding 115, 81–90 (2011)
8. Montesano, L., et al.: Learning Object Affordances: From Sensory-Motor Coordination to Imitation. IEEE Transactions on Robotics 24, 15–26 (2008)
9. Zhu, C., Cheng, Q., Sheng, W.: Human intention recognition in smart assisted living systems using a hierarchical hidden Markov model. In: IEEE International Conference on Automation Science and Engineering, pp. 253–258 (2008)
10. Schrempf, O.C., Hanebeck, U.D.: A generic model for estimating user-intentions in human-robot cooperation. In: Proceedings of the 2nd International Conference on Informatics in Control, Automation and Robotics, vol. 5 (2005)
11. Kelley, R., Wigand, L., Hamilton, B., Browne, K., Nicolescu, M., Nicolescu, M.: Deep networks for predicting human intent with respect to objects. In: Proceedings of the Seventh Annual ACM/IEEE International Conference on Human-Robot Interaction, pp. 171–172 (2012)
12. Hwang, B., Jang, Y.-M., Mallipeddi, R., Lee, M.: Probabilistic human intention modeling for cognitive augmentation. In: IEEE International Conference on Systems, Man, and Cybernetics (SMC), pp. 2580–2584 (2012)
13. Rish, I.: An empirical study of the naive Bayes classifier. In: IJCAI 2001 Workshop on Empirical Methods in Artificial Intelligence, pp. 41–46 (2001)
14. Shotton, J., Sharp, T., Kipman, A., Fitzgibbon, A., Finocchio, M., Blake, A., Cook, M., Moore, R.: Real-time human pose recognition in parts from single depth images. Communications of the ACM 56, 116–124 (2013)
15. Vincent, P., Larochelle, H., Lajoie, I., Bengio, Y., Manzagol, P.A.: Stacked denoising autoencoders: Learning useful representations in a deep network with a local denoising criterion. The Journal of Machine Learning Research 9999, 3371–3408 (2010)
16. Hinton, G.E., Osindero, S., Teh, Y.-W.: A fast learning algorithm for deep belief nets. Neural Computation 18, 1527–1554 (2006)
17. Hinton, G.E., Salakhutdinov, R.R.: Reducing the dimensionality of data with neural networks. Science 313(5786), 504–507 (2006)

A Cursor Control Based Chinese-English BCI Speller*

Conghui Chen[1], Jing Yang[1], Yanbing Huang[1], Jie Li[2], and Bin Xia[1]

[1] Electrical Engineering Department, Shanghai Maritime University, Shanghai, China
binxia@shmtu.edu.cn
[2] Department of Computer Science, Tongji University, Shanghai, China

Abstract. In this work, a motor imagery based 2-D cursor control strategy was applied to spell English character in a three-layer interface. Pinyin input method was integrated with English speller to input Chinese characters. A chatting system based on the BCI speller and instant messenger was designed and tested. The online experimental results demonstrated that three subjects all achieved good performance.

Keywords: Motor Imagery, Chinese-English Speller, Pinyin input method.

1 Introduction

Brain-computer interface (BCI) system is a new kind of human-machine interaction, which creates a direct channel, different from the normal peripheral nervous system and muscle tissue, between human brain and external word [1]. Electroencephalogram (EEG) signals are often used in BCI system to record electric action of neuronal groups, which provide important information for the processing of brain information.

Many people with serious neuromuscular disorders have lost their ability to speak or write. In order to help them to communicate with others, researchers started to build a novel speller system based on EEG signals. One kind of such speller system was based on P300, its oddball paradigm (OP) of visual matrix was first described by Farwell and Dochin in 1988 [2], and later researchers had developed this paradigm. A four-choice and three presentation modes based on the OP was implemented in a system with limited number of choices [3]. The time-frequency instead of time domain EEG features were used to improve the performance of the P300 speller [4]. Another widely accepted BCI speller was based on steady-state visual evoked potentials (SSVEP). In literature [5], a high rate online SSVEP speller was presented with 16 targets, and its frequencies ranged from 8Hz to 15.5Hz with an interval of 0.5Hz.

* The work was supported by Innovation Program of Shanghai Municipal Education Commission (Grant No.12ZZ150) and the National Natural Science Foundation of China (Grant No. 61105122) and the Ministry of Transport of the Peoples Republic of China (Grant No. 2012319810190) and the Fundamental Research Funds for the Central Universities (Grant No. 0800219202).

M. Lee et al. (Eds.): ICONIP 2013, Part I, LNCS 8226, pp. 403–410, 2013.
© Springer-Verlag Berlin Heidelberg 2013

Compared with P300 and SSVEP, Motor Imagery (MI) was rarely used in BCI speller for its limited distinguishable EEG states. In a MI speller experiment [6], subjects were asked to imagine the moving of his/her left hand, right hand, feet and tongue, and the corresponding EEG signals were translated into 4 different select commands for a spelling application. To overcome the limitation of command, Hex-o-Spell speller paradigm was put forward by Berlin BCI research group [7]. In this speller paradigm, only two states classified by the BCI system were used, one to rotate the arrow in the center of the hexagon interface, the other was used to stop the arrow and choose the target block.

Most of BCI spellers are designed for English, which are not suitable to input Chinese because Chinese characters are not alphabetic writing. An input method based on strokes, which was widely used in mobile phone in China, was combined with a P300 speller to input Chinese characters, and the accuracy of it was up to 90% [8]. A group in University of Hong Kong presented a shape-based method called the First-Last to input Chinese characters. They also combined the input method with a P300 speller and realized the input of Chinese characters, with the accuracy of 59.4% and the SPL of 77s [9]. Pinyin input method, which uses English characters to represent the pronunciation of Chinese characters, is often used to input Chinese characters. To combine Chinese and English input in the same interface, we developed a Chinese-English BCI speller based on 2-D cursor control, which inputted English characters in Oct-o-spell paradigm and spelled Chinese characters using Pinyin input method.

In this paper, we focused on a MI based speller, and use the asynchronous 2D cursor control strategy with Oct-o-Spell paradigm. Pinyin input method was used to input Chinese characters. Online chatting system based on the Chinese-English BCI speller was tested and achieved good performance.

2 Materials and Methods

2.1 Asynchronous 2D Control Paradigm

In previous study [10], we presented a three-class (left hand, right hand and feet) motor imagery based BCI for asynchronous 2D cursor control. For EEG signals got from the subjects, we used Common Spatial Pattern to extract the features [11-12] and Support Vector Machine (SVM) to discriminate the three-class MI patterns. The results from the SVM classifier were three decimals ranged from 0-1 and the sum of them equaled to 1. They represented the probabilities for doing the three MI tasks. An ONSwitch was used to get control for the 2D cursor [13]. To switch it on, subjects can do any of the three MI tasks so that the corresponding possibilities can exceed the threshold in a certain period of time. After turn on the switch, subjects can control the movement of the cursor by doing MI tasks. During the process, the probabilities, marked as P1, P2, P3, were projected to three vectors, as shown in Fig.1. The angle between each two vectors was 120 degree and the length of the vector was equal to the value of the probability. To hit the target located in the area between two vectors, the user

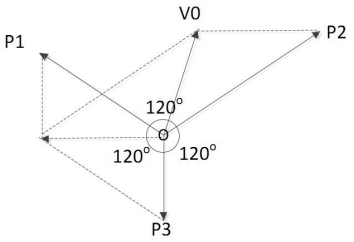

Fig. 1. The mapping of three predict probabilities

performed two corresponding motor imagery tasks simultaneously to generate a speed vector, by which the cursor was drove directly to the target.

2.2 Spell Paradigm

GUI Design. In this paper, we presented a three-layer of Oct-o-spell paradigm shown in Fig.2.

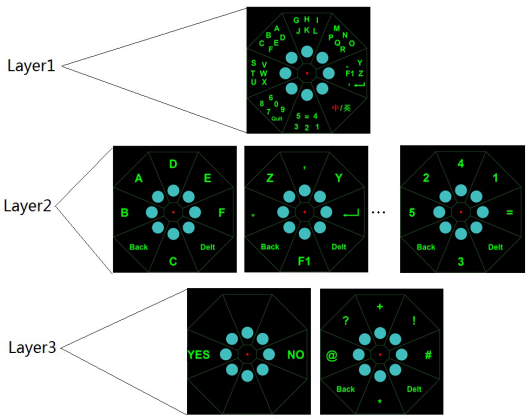

Fig. 2. The mapping of three predict probabilities

In the first layer, 26 letters, 10 figures and 5 symbols (‘Quit, ‘=’, ‘↵’, ‘,, ‘., ‘F1) were divided into eight blocks. In the second layer, 7 different interfaces were designed to unfold the blocks in the first layer. Only two symbols in the second layer connected to the third layers. One was ‘F1, connected to a third layer with 6 punctuations: ‘*, ‘@, ‘?, ‘+, ‘!, ‘#. The other one was ‘Quit, connected to a third layer with ‘YES and ‘NO blocks, which was used to quit the speller system.

Spell Paradigm. To spell a character or to output a command, the subject should move the cursor to choose the target block in two or three steps. A block, which contains the target character in first layer, was chosen at step 1. Then the interface would extend to the corresponding second layer. The target character can be chosen in the second layer at step 2. If 'Quit or 'F1 in the second layer was chosen, the interface extended to third layer. Then, the target character can be chosen in the third layer. To choose a target block, the user should perform the three MI tasks to move cursor to hit the circle of the target block.

To choose a target block, the user should perform the three MI tasks to move cursor to hit the circle of the target block. If a wrong block was selected, the 'Back' command in every unfolded layer can be chose to back to previous layer. If a wrong character was output, subjects can control the cursor to enter any of the second layers to choose the 'Delt' command to delete it.

Intelligent Input Method. Instead of developing a new input method, we adopted a Pinyin input method called Sougou Pinyin input method. It can work in Chinese input mode and English input mode, and has an intelligent function of predictive text enter.

For the speller system, the default status was English input state. Subjects can switch it to Chinese input state by choosing switch block in the first layer of the interface. To input a Chinese word '你好 '(How are you?), the subject can input 5 letters 'nihao' , the Pinyin of the Chinese word, and the input method software translated the Pinyin to the corresponding Chinese words.

3 Experiments

3.1 Subject

Three healthy subjects (sub1,sub2,sub3, all males) aged from 19 to 26 (average 21±3.4) paid to participate in this study. Sub1 had previous experience of MI and sub2, sub3 were naive. All of the subjects were in good health, and they submitted their consent to be involved in the study.

3.2 EEG Recording and Signal Processing

Subjects sat in front of a computer and wore the electrode cap. Thirteen channels (FC3 FCZ FC4 C5 C3 C1 CZ C2 C4 C6 CP3 CPZ CP4) in motor cortex area were selected and placed according to the international 10-20 system. The EEG signals were collected by a 16 channel g.USBamp system with 256Hz sampling rate and were preprocessed by a band-pass filtered between 5-30 Hz. The ground and reference electrodes were separately placed on Fz and the right earlobe respectively.

3.3 Online Experiments

Three-Class MI Training. All subjects were required to attend a three class MI training program. During the training, subjects imagined the movement of

their left hand, right hand and feed according to the prompts in system interface. The training program would not stop until the accuracy for every MI tasks was higher than 85%. Then the data would be saved as a classifier model for the following experiment.

Online English and Chinese Copy Spelling Experiment. We chose 15 English words, "women, desk, water, hand, memory, zone, baby, face, taxi, june, quick, video, golf, hour, pencil", and 10 Chinese words (show in Fig.3). A complete trail contained all the 25 words. Before spelling each word, 3 seconds were left for subjects to prepare. Each word should be spelled within 60 seconds, and the system would automatically turn to next word after the word was correct spelled or the trial running out of time.

你好	渴了	吃了吗	早上好	对不起	晚安	没关系	谢谢	记住了	听不见
How are you	Thirst	Do you have a meal	Good morning	Sorry	Good night	Never mind	Thank you	Remember	Cannot hear

Fig. 3. Chinese words and their means for online copy spelling

Online Chatting Experiment. By connecting MI speller with instant messenger (QQ, Tencent.), subjects can chat online. The GUI is showed in Fig.4. The left part of the interface is the Chinese-English speller, and the right part is the instant messenger. Subjects used MI speller to spell Chinese or English words, and these words would be caught and displayed in send windows of the instant messenger. After entering the whole message, subjects can send it by choosing the '↵' in block 5.

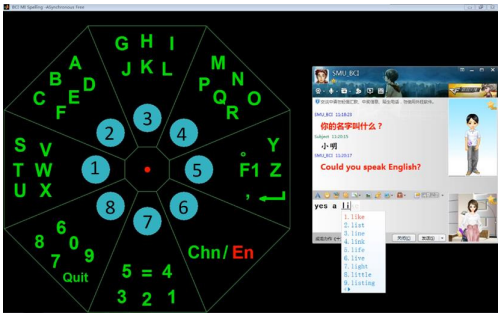

Fig. 4. Interface of the online chatting system

4 Result

The accuracy, letter per minute (LPM) and information transfer rate (ITR), were calculated to evaluate the performance of the MI speller. ITR is calculated as formula (1):

$$ITR = [\log_2 N + P\log_2 P\log_2 \frac{1-P}{N-1}]\frac{60}{trial\_length}. \quad (1)$$

Where N is the number of classes (N=8), P is the accuracy, trial_length is the average time of spelling a character.

As shown in Table 1, all three subjects achieve good performance in English copy spelling experiment. The accuracies of three subjects are all above 95% and Sub3's is 99.17%. On average of all subjects, the performance reaches 96.63% of accuracy, 10.15 LPM, 62.39bits/min ITR. In Chinese copy spelling experiment, Sub3 performs the best with the accuracy of 98.65%, the LPM of 70.1, the ITR of 66.41bits/min.

Table 1. Average Accuracy , LPM and ITR in English and Chinese copy spelling experiment

	English copy			Chinese copy		
	Accuracy	LPM	ITR	Accuracy	LPM	ITR
Sub1	95.18	15.62	56.86	82.82	5.41	34.76
Sub2	95.54	6.77	59.13	94.94	5.22	48.02
Sub3	99.17	8.07	72.19	98.65	7.40	66.41
Mean	96.63	10.15	62.39	92.13	6.01	49.73
SD	2.21	4.78	8.27	8.28	1.21	15.89

In online chatting experiment, we prepared 6 questions, alternating in English and Chinese. All the questions and answers (from Sub1) are showed in Fig.5.

Question	Answer	Question	Answer
Could you speak English?	yes a little	你的名字叫什么？（What's your name?）	小明 (xiao ming)
Where are you from?	i come from shanghai	你来自哪里？(Where are you from?)	上海 (Shanghai)
What are you doing now?	the experiment of bci	你有什么爱好? (what's your hobby?)	我喜欢游泳 (swimming)

Fig. 5. One of the question and answer from Sub1

When answering the questions, subjects were sometime out of mind and thus lost the control for the cursor, so the cursor would enter the wrong block. To

correct the mistake, subjects used 'Back' to return to the previous layer or 'Delt' to delete the wrong output. As showed in Table 2, Sub1 has the highest accuracy of 96.60% and Sub2 the lowest accuracy of 96.10%. On average of all subjects, the performance reaches 5.53 LPM and 30.86bits/min ITR.

Table 2. Average Accuracy, LPM and ITR in online chatting experiment

	Accuracy	LPM	ITR
Sub1	96.60	5.76	32.25
Sub2	96.10	5.14	28.83
Sub3	96.29	5.69	31.49
Mean	96.33	5.53	30.86
SD	0.25	0.34	1.80

5 Discussion and Conclusion

In this study, we developed a Chinese-English speller system with the Oct-o-Spell paradigm based on 2D cursor control. Compared to the interface of Hex-o-Spell, the Oct-o-Spell can display more symbols for its structure of octagon, which is necessary for the input of Chinese characters using Pinyin input method. To improve the speed of letter selection, instead of directly using the three-class commands, we adopted a novel method in [10] to compose the three vectors, which represented the probabilities of three-class motor imagery, to decide the movement of cursor in any direction.

Based on the Chinese-English speller and instant messenger, we developed an online chatting system. All the subjects achieved good performance in the online experiment. Compared to the speller based on P300 [3-4] and SSVEP [14-15], our results are satisfactory.

References

1. Wolpaw, J.R., Birbaumer, N., McFarland, D.J., Pfurtscheller, G., Vaughan, T.M.: Brain Computer interfaces for communication and control. Clinical Neurophysiology 113(6), 767–791 (2002)
2. Farwell, L.A., Donchin, E.: Talking off the top of your head: toward a mental prosthesis utilizing event-related brain potentials. Electroencephalography and Clinical Neurophysiology 70(6), 510–523 (1988)
3. Sellers, E.W., Kubler, A., Donchin, E.: Brain-computer interface research at the University of South Florida Cognitive Psychophysiology Laboratory: the P300 speller. IEEE Transactions on Neural Systems and Rehabilitation Engineering 14(2), 221–224 (2006)
4. Ming, D., An, X., Wan, B., Qi, H., Zhang, Z., Hu, Y.: A P300-speller based on event-related spectral perturbation (ERSP). In: 2012 IEEE International Conference on Signal Processing, Communication and Computing (ICSPCC), pp. 63–66. IEEE (2012)

5. Cao, T., Wang, X., Wang, B., Wong, C.M., Wan, F., Mak, P.U., Vai, M.I.: A high rate online SSVEP based brain-computer interface speller. In: 2011 5th International IEEE/EMBS Conference on Neural Engineering (NER), pp. 465–468. IEEE (April 2011)
6. Volosyak, I., Cecotti, H., Valbuena, D., Graser, A.: Evaluation of the Bremen SSVEP based BCI in real world conditions. In: IEEE International Conference on Rehabilitation Robotics, ICORR 2009, pp. 322–331. IEEE (June 2009)
7. Blankertz, B., Dornhege, G., Krauledat, M., Schröder, M., Williamson, J., Murray-Smith, R., Mller, K.R.: The Berlin Brain-Computer Interface presents the novel mental typewriter Hex-o-Spell (2006)
8. Sun, K.T., Huang, T.W., Chen, M.C.: Design of Chinese spelling system based on ERP. In: 2011 IEEE 11th International Conference on Bioinformatics and Bioengineering (BIBE), pp. 310–313. IEEE (October 2011)
9. Minett, J.W., Zheng, H.Y., Fong, M.C., Zhou, L., Peng, G., Wang, W.S.: A Chinese Text Input Brain Computer Interface Based on the P300 Speller. International Journal of Human-Computer Interaction 28(7), 472–483 (2012)
10. Xia, B., Yang, H., Zhang, Q., Xie, H., Yang, W., Li, J., An, D.: Control 2-dimensional movement using a three-class motor imagery based Brain-Computer Interface. In: 2012 Annual International Conference of the IEEE Engineering in Medicine and Biology Society (EMBC), pp. 1823–1826. IEEE (August 2012)
11. Pfurtscheller, G., Neuper, C., Guger, C., Harkam, W.A.H.W., Ramoser, H., Schlogl, A., Pregenzer, M.A.P.M.: Current trends in Graz brain-computer interface (BCI) research. IEEE Transactions on Rehabilitation Engineering 8(2), 216–219 (2000)
12. Ramoser, H., Muller-Gerking, J., Pfurtscheller, G.: Optimal spatial filtering of single trial EEG during imagined hand movement. IEEE Transactions on Rehabilitation Engineering 8(4), 441–446 (2000)
13. Xia, B., An, D., Chen, C., et al.: A mental switch-based asynchronous brain-computer interface for 2D cursor control. Accepted by EMBS (2013)
14. Lopez-Gordo, M.A., Pelayo, F., Prieto, A.: A high performance SSVEP-BCI without gazing. In: The 2010 International Joint Conference on Neural Networks (IJCNN), pp. 1–5. IEEE (July 2010)
15. Yamaguchi, T., Omori, K., Irie, J., Inoue, K.: Feature extraction from EEG signals in SSVEP spelling system. In: Proceedings of SICE Annual Conference 2010, pp. 58–62. IEEE (August 2010)

Performance Comparison of Spatial Filter with Multiple BMFLCs for BCI Applications

Yubo Wang, Venkateswarlu Gonuguntla, Ghufran Shafiq, and Kalyana C. Veluvolu

School of Electronics Engineering, Kyungpook National University
702-701 Daegu, South Korea
veluvolu@ee.knu.ac.kr

Abstract. The subjects can learn to modulate their EEG pattern to achieve multiple targets in brain-computer interface systems. The modulation can occur in both α and β bands of the EEG signal. To successfully identify these modulated EEG patterns, multiple band-limited multiple Fourier linear combiner (BMFLCs) are employed to estimate the amplitude variations in EEG. To achieve better signal to noise ratio, spatial filter is paired with BMFLC for classification with linear discriminant analysis. Various existing spatial filters are paired with BMFLC and the performance is compared to identify the best spatial filters for classification of four targets in BCI Competition 2003 data set II(a). Results show that the Tikhonov regularized common spatial filter (TRCSP) paired with BMFLC provides better accuracy in comparison with other spatial filters.

Keywords: Brain-computer interface, BMFLC, Spatial filter, LDA.

1 Introduction

Brain-computer interface (BCI) is an alternative communication pathway that can translate various brain signals to computer command. Among current existing brain signal collection techniques, the Electroencephalography(EEG) has been widely applied to BCI system due to its easy of implementation, cost efficiency and non-invasiveness. Event-related (de)synchronization(ERD/ERS) is the amplitude decreasing of α band amplitude over sensorimotor cortex as the subject performs a motor imagery or actual limb movement whereas ERS is the amplitude increasing related to motor activity [2]. Thanks to the neuron plasticity, the subjects are able to learn to modulate their EEG signal to achieve a multi-tasks BCI system [3]. In BCI competition 2003 data set IIa, the subject was asked to modulate their EEG signal in motor cortex for a 4-classes BCI experiment [4].

For a BCI system, pre-processing and feature extraction form the core part of classification. The amplitude of EEG signal is weak as compared to the noise source and the volume conduction of the human skull, the measured surface EEG may not be an accurate measure of the electrical activity of underlying cortex [5]. Moreover, such patterns ERD/ERS that can be decoded from EEG are also

M. Lee et al. (Eds.): ICONIP 2013, Part I, LNCS 8226, pp. 411–418, 2013.
© Springer-Verlag Berlin Heidelberg 2013

localized [2]. The various spatial filters such as common average reference (CAR), Laplacian based spatial filter and common spatial filter (CSP) are designed to improve the signal-to-noise ratio (SNR) of the EEG signal [5].

The feature extraction is significantly affect the performance of the BCI systems. The feature extraction algorithm should be able to track both the time-varying amplitude and frequency characteristics of the EEG signal. For the 4-classes BCI system, the band-power in α and β bands are generally employed as features [4]. For computation of the band-power from EEG, bandpass filter and autoregressive (AR) model based methods are popular [4]. However, the bandpass filter based method offers poor frequency resolution and the AR model rely on interpolation. A method that can directly track the amplitude and frequency changes in EEG signal is desired. The band-limited multiple Fourier linear combiner (BMFLC) employs a truncated Fourier series as the signal model and estimates the Fourier coefficients with an adaptive algorithm. The suitability of BMFLC for BCI systems was earlier demonstrated for two-class problems [6, 7].

In this paper, we extended the existing BMFLC method to estimate the amplitude variation in α and β bands simultaneously. Before sending the signal to BMFLC, we employed various of spatial filter to improve the SNR of the EEG signal. Various existing spatial filters are paired with BMFLC and the performance are compared to identify the best spatial filter that can be paired with BMFLC for four class classification in this paper.

2 Methods

2.1 Band-Limited Multiple Fourier Linear Combiner (BMFLC)

The existing BMFLC divides a pre-defined frequency band $[\omega_1, \cdots, \omega_n]$ into n equally distributed divisions and estimates the amplitude of each frequency component by using least-mean-square algorithm (LMS) [6, 7]. Although the estimation accuracy is high, the LMS algorithm cannot guarantee an accurate estimation of amplitude variation. To improve the tracking ability of the existing BMFLC, BMFLC with Kalman filter (BMFLC-KF) was later developed [8]. The state-space model of BMFLC-KF can be given by

$$y_k = \mathbf{x}_k^T \mathbf{w}_k + v_k; \quad \mathbf{w}_{k+1} = \mathbf{w}_k + \eta_k \tag{1}$$

where $\mathbf{x}_k$ and $\mathbf{w}_k$ are defined as

$$\mathbf{x}_k = \left\{ \begin{bmatrix} \sin(\omega_1 k) & \sin(\omega_2 k) & \cdots & \sin(\omega_n k) \end{bmatrix}^T \atop \begin{bmatrix} \cos(\omega_1 k) & \cos(\omega_2 k) & \cdots & \cos(\omega_n k) \end{bmatrix}^T \right\}; \mathbf{w}_k = \left\{ \begin{bmatrix} a_{1k} & a_{2k} & \cdots & a_{nk} \end{bmatrix}^T \atop \begin{bmatrix} b_{1k} & b_{2k} & \cdots & b_{nk} \end{bmatrix}^T \right\} \tag{2}$$

Assume that v_k and η_k are independent Gaussian process with zero mean and covariance of R and $\mathbf{Q}$ respectively. The Kalman filter iteration can be given as

$$\mathbf{K}_k = \mathbf{P}_k \mathbf{x}_k^T [\mathbf{x}_k^T \mathbf{P}_k \mathbf{x}_k + R]^{-1} \tag{3}$$

$$\hat{\mathbf{w}}_{k+1} = \hat{\mathbf{w}}_k + \mathbf{K}_k (y_k - \mathbf{x}_k^T \hat{\mathbf{w}}_k) \tag{4}$$

$$\mathbf{P}_{k+1} = [\mathbf{I} - \mathbf{K}_k \mathbf{x}_k] \mathbf{P}_k + \mathbf{Q} \tag{5}$$

where $\hat{\mathbf{w}}_k = \mathbf{E}[\mathbf{w}_k|\mathbf{y}_{k-1}]$ denotes the mathematical expectation of $\mathbf{w}$ at time instant k with respect to previous observation $\mathbf{y}$ at $k-1$, $\mathbf{P}_k$ is the estimated state error covariance and $\mathbf{K}_k$ is the Kalman gain. The Kalman filter starts with the initial condition $\hat{\mathbf{w}}_0 = \mathbf{0}$ and $\mathbf{P}_0 = \mathbf{I}$. The estimated weights $\hat{\mathbf{w}}_k$ forms the time-frequency mapping of a given signal.

2.2 Optimal Band Selection

As stated in our early study [6], the motor function induced ERD/ERS occurs in a subject-specific reactive band. By incorporating this optimal band, the classification accuracy is improved compared to usage of the whole α band [7]. The optimal band can be visualized in the time-frequency map that is obtained by BMFLC. By averaging the weights of BMFLC over time, the optimal band is characterized as the peak in the resultant spectrum. For details, see [6].

2.3 Spatial Filters

The irrelevant information in EEG signal mainly comes from two sources: the non-EEG source and the EEG source. The former one is the noise that comes from electricity activity outside the brain and the latter one is the EEG components that does not give information to the desired EEG pattern [5]. The spatial filter is designed to eliminate the noise effect of both sources. In this paper, we employed common average reference (CAR) and Laplacian spatial filter to preprocess the EEG signal [5].

In the CAR, the EEG signal is re-referenced to the average value of the potentials that recorded from the whole EEG montage. If the electrodes are equally spaced and the potential is generated by point sources, the CAR gives a spatial potential distribution with mean value of zero. Moreover, the CAR removes the wide spread noise such as EMG [5].

The Laplacian spatial filter on the other hand is mainly focused on local information. By using the second order derivative of the instantaneous spatial potential distribution, the Laplacian spatial filter is targeted at recovering the electrical activity of the radial sources underneath the electrodes. The Laplacian spatial filter can be written in the following form [5]:

$$V_i^{LAP} = V_i^{ER} - \sum_{j=1}^{n} g_{ij} V_j^{ER} \tag{6}$$

where $g_{ij} = 1/d_{ij} \frac{1}{\sum_{j=1}^{n} 1/d_{ij}}$, n is the total number of electrodes, d_{ij} is the distance between electrodes i and j, V_i^{ER} is the referenced potential of electrode i. Two variant Laplacian spatial filters, namely large Laplacian (LLap) and small Laplacian (SLap) are used in this paper. The d_{ij} is 3cm and 6cm for LLap and SLap respectively [5].

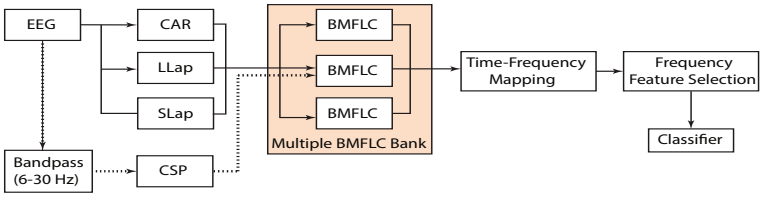

Fig. 1. System Structure

Common Spatial Filters. As the variance of EEG signal is directly related to the band-power, the common spatial filter (CSP) which tries to maximize the variance of band-pass filtered EEG in one condition while minimizing the variance in the other condition [9] can be directly beneficial for improving the performance of the band-power based BCIs.

The original CSP is an optimal process that tries to find the coefficients of w that maximize the following cost function.

$$J(w) = \frac{w^T \mathbf{X}_1^T \mathbf{X}_1 w}{w^T \mathbf{X}_2^T \mathbf{X}_2 w} = \frac{w^T C_1 w}{w^T C_2 w} \tag{7}$$

where $\mathbf{X}_i$ is the cascaded EEG signal from ith condition and C_i is the corresponding variance estimation. The original CSP has the tendency of overfitting and sensitive to noise, a regularization term is used to overcome those effects. Due to the superior performance, the Tikhonov regularized CSP (TRCSP) that was proposed in [9] is used in this paper. The cost function of TRCSP is given as

$$J(w) = \frac{w^T C_1 w}{w^T C_2 w + \alpha w^T \mathbf{I} w} = \frac{w^T C_1 w}{w^T (C_2 + \alpha \mathbf{I}) w} \tag{8}$$

where the penalty term in TRCSP is $\alpha w^T \mathbf{I} w$ that penalizes each channel equally. α is selected such that the performance of a LDA classifier is maximized with a 10-fold cross validation. The optimization of equation (8) is done by solving the following Lagrange equation

$$L(\lambda, w) = w^T C_1 w - \lambda (w^T (C_2 + \alpha \mathbf{I}) w - 1) \tag{9}$$

The solution of equation (9) is equivalent to the eigenvalue problem given by $(C_2 + \alpha \mathbf{I})^{-1} C_1 w = \lambda w$. The spatial filter w that maximizes the equation (9) are obtained with eigenvectors $M = (C_2 + \alpha \mathbf{I})^{-1} C_1$.

The signal processing flowchart is shown in Fig.1. The solid line indicates the signal path for CAR, LLap and SLap whereas the dash line indicates the path for TRCSP. Before applying TRCSP, the EEG signal is bandpass filtered between $6 - 30$Hz which covers the α and β band. Three BMFLCs are used simultaneously to estimated the amplitude from $6 - 30$Hz. The cut-off frequency for three BMFLCs are $[f_l = 6Hz, f_h = 14Hz]$, $[f_l = 14.5Hz, f_h = 22Hz]$ and $[f_l = 22.5Hz, f_h = 30Hz]$ respectively. The frequency spacing is set to $\Delta f = 0.5Hz$ based on earlier studies [6, 7].

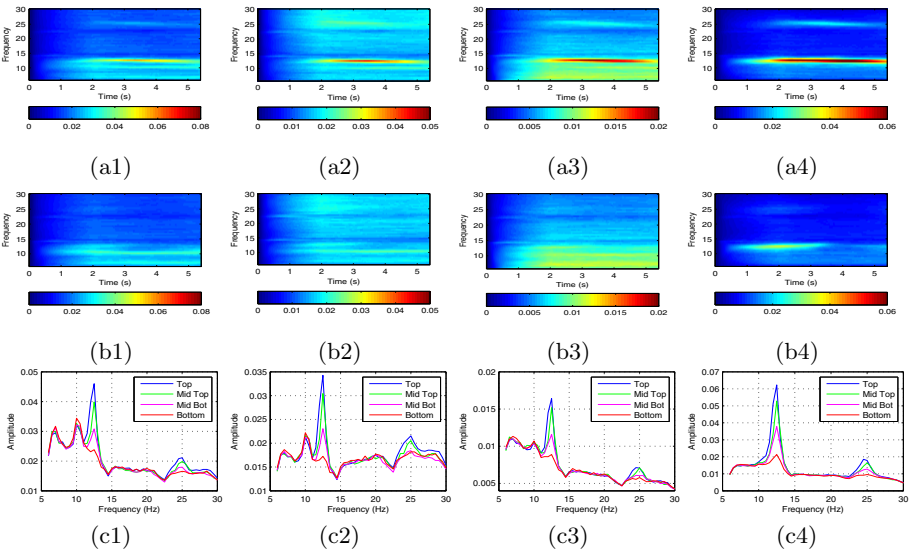

Fig. 2. The time-frequency mapping of top target and bottom target are shown in first and second row respectively. The results of CAR, LLap, SLap and TRCSP are shown from first column to the last column. The reactive band selection is shown in the last row. The results are obtained from subject AA.

3 Results

3.1 Data Set

The data set used in this paper is Data set IIa in BCI competition 2003. Total three subjects EEG data are given in this data set. The EEG signal is recorded from 64 electrodes according to the international 10/20 system. The sampling frequency of the signal is 160Hz. During the experiment, the subject sat on a reclining chair in front of a computer screen. The experiment starts with 1s blank screen. The target is given at the right edge of the screen in one of four possible locations (*e.g.* Top, Middle Top, Middle Bottom and Bottom). At 2s, a cursor appears at the center of left edge of the screen and start to travel to the right edge at constant speed. The location of the cursor is controlled by the α and β rhythm amplitude which were collected from 1-3 EEG channels of the subjects. The amplitude of EEG is estimated by an AR algorithm and then feed to a linear function to calculate the location of the cursor. Trial stops when the cursor arrived at the right edge. For more details, please see [4].

3.2 Time-Frequency Mapping and Optimal Band Selection

As the experiment is designed to train the subject to modulate their motor cortex activity and according to the experiment protocol, the EEG signal from electrode

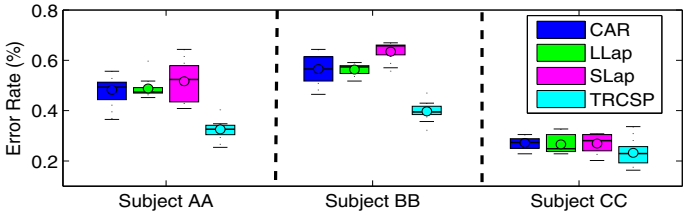

Fig. 3. Classification error for different spatial filters

C3 in international 10/20 system is used as the base signal for CAR, LLap and SLap. For TRCSP, the most significant spatial filter which shows clearly motor cortex localization is used.

The time-frequency mappings are obtained by averaging the estimated weights from BMFLC of all trials of a given task. For subject AA and subject CC, the amplitude decrease as the target move from top to the bottom whereas the inverse pattern is observed for subject BB. For all subjects, the amplitude achieves its maximum or minimum level at top and bottom target. The results of top and bottom target of subject AA are shown in Fig.2(a1)-(a4) and Fig.2(b1)-(b4) respectively. It is shown that for CAR, SLap and TRCSP, the α and β band amplitude modulation can be identified between top and bottom target from the time-frequency mapping. For LLap, the time-frequency mapping in β band becomes blurry, only the α band modulation can be observed. Among all the methods, the TRCSP shows the clearest modulation pattern in both the bands. The contrast of the modulation pattern also outperforms the rest of the spatial filters.

As we observed from time-frequency mapping, the frequency modulation happens in a localized frequency range. To obtain the optimal frequency band of the subject, four frequency spectrums corresponding to top target, middle-top (Mid-Top), middle-bottom (Mid-Bot) and bottom target are extracted from the time-frequency mapping by averaging the time-frequency weights over time. The extracted frequency spectrums are calculated and shown in Fig.2(c1)-(c4). For all spatial filters, two peaks which lay in α and β band respectively can be identified. And the amplitude intensity change is clearly shown as the height difference of the peak regarding to each target. Although, all spatial filters provide a similar frequency range in both bands, only the spectrum obtained from TRCSP shows a smoothed spectrum estimation.

3.3 Classification

After identifying the optimal band for all the subjects, the corresponding weights that are estimated by BMFLC are used as features for LDA. In this paper, a trial-wise classification scheme is adopted. For training a classifier on a complete experiment trial, the weights of BMFLC in the optimal band for 1s window are extracted and averaged from 2s to 4s with 500ms overlapping. The resultant

weights are cascaded to form one feature vector for that trial. The LDA classifier is trained and tested with a 10-fold cross-validation scheme. The error rate of the classifier is shown in boxplot (Fig.3).

The classification error averaged over subject for CAR LLap, and SLap are 43%, 45% and 47% respectively. For TRCSP, the average error rate over subject is 31%. Despite the successful identification of optimal band and clear pattern in time-frequency mapping, the CAR, LLap and SLap with multiple BMFLCs for subject AA and subject BB shows around 20% worse in classification error compared to the TRCSP. For subject CC, although the performance of CAR, LLap and SLap is worse, the difference in error rate is only 4% compared to TRCSP. The average classification error of TRCSP with multiple BMFLCs are 32%, 39% and 23% for subject AA, subject BB and subject CC respectively. In the average level, the TRCSP based classifier shows the lowest classification error among all spatial filter based classifier. The results obtained with TRCSP based classifier results are comparable to the winning results of BCI competition [4]. The future work will focus on improving the performance of the identified BMFLC-TRCSP combination.

4 Discussion

As the amplitude tracking ability of BMFLC depends on the number of frequency components that need to be estimated, the single BMFLC cannot be used to estimate a wide frequency range of EEG signal. To tackle this problem, the wide frequency range is divided into small bands of interest and multiple BMFLCs were operated.

The time-frequency mapping obtained by using the weights from the multiple BMFLCs shows clear amplitude modulation in both α and β bands. The optimal band identified from the time-frequent mapping is consistent with the results obtained in [4].

Although the amplitude modulation can be observed from the signal that is preprocessed by CAR, LLap, SLap and TRCSP, the classification error obtained from LDA is low for CAR, LLap and SLap for two subjects out of three. We hypothesize two reasons for this failure. First, as the electrodes that are used during the feedback of the experiment are prefixed, the activity may not occur at the selected electrode locations. Second, as the time-frequency mapping is calculated by averaging all trails of a target, it can be easily affected by some trials with large amplitude.

On the other hand, the TRCSP based classifier provides good accuracy in classification. For three subjects, it shows low error rate that is comparable with the wining entry of this BCI Competition data set. As the TRCSP tries to maximize the variance with respect to two classes, it employs information from all electrodes. Therefore, it does not require an accurate electrode localization as compared to CAR, LLap and SLap.

5 Conclusion

In this paper, multiple BMFLCs with different types of spatial filters are used to generate features for a LDA classifier. The results indicate that multiple BMFLCs can be used to estimate a wide range of frequency for BCI system as the amplitude estimation in both α and β bands are required. The amplitude modulation of a 4-classes BCI experiment can be identified from the time-frequency mapping that is produced by multiple BMFLCs. The optimal band is also identified for all the subjects. The classification error result indicates that the TRCSP is a better choice to pair with BMFLC for feature extraction.

Acknowledgments. This research was supported by the Basic Science Research Program through the National Research Foundation of Korea (NRF) funded by the Ministry of Education, Science and Technology (Grant No. 2011-0023999).

References

1. Pfurtscheller, G., Muller-Putz, G.R., Scherer, R., Neuper, C.: Rehabilitation with Brain-Computer Interface Systems. Computer 41, 1–8 (2008)
2. Pfurtscheller, G., da Silva, F.H.: Event-related EEG/MEG synchronization and desynchronization: basic principles. Clinical Neurophysiology 110, 1842–1857 (1999)
3. Shih, J.J., Krusienski, D.J., Wolpaw, J.R.: Brain-Computer Interfaces in Medicine. Mayo Clinic Proceedings 87, 268–279 (2012)
4. Blanchard, G., Blankertz, B.: BCI Competition 2003–Data set IIa: spatial patterns of self-controlled brain rhythm modulations. IEEE Transactions on Biomedical Engineering 51(6), 1062–1066 (2004)
5. McFarland, D.J., McCane, L.M., David, S.V., Wolpaw, D.J.: Spatial Filter Selection for EEG-based Communication. Electroencephalography and Clinical Neurophysiolog 103, 386–394 (1997)
6. Veluvolu, K.C., Wang, Y., Kavuri, S.S.: Adaptive estimation of EEG-rhythms for optimal band identification in BCI. Journal of Neuroscience Methods 203 (2012)
7. Wang, Y., Veluvolu, K.C., Cho, J.H., Defoort, M.: Adaptive estimation of EEG for subject-specific reactive band identification and improved ERD detection. Neuroscience Letters 528(2), 137–142
8. Wang, Y., Veluvolu, K.C., Lee, M.: Time-frequency analysis of band-limited eeg with bmflc and kalman filter for bci applications. Journal of Neuro Engineering and Rehabilitation (2013) (under revision)
9. Lotte, F., Guan, C.: Regularizing common spatial patterns to improve BCI designs: unified theory and new algorithms. IEEE Transactions on Biomedical Engineering 58(2), 355–362

Causal Neurofeedback Based BCI-FES Rehabilitation for Post-stroke Patients

Hang Wang,Ye Liu, Hao Zhang, Junhua Li, and Liqing Zhang

MOE-Microsoft Key Laboratory for Intelligent Computing and Intelligent Systems,
Department of Computer Science and Engineering, Shanghai Jiao Tong University,
Shanghai 200240, China
{extented,lyyx000,zh_chaos,juhalee,lqzhang}@sjtu.edu.cn

Abstract. BCI-FES therapy has been proved to be an effective way to help post-stroke patients restore motor function of paralyzed limbs. In the existing BCI-FES system, patients can only asynchronously receive feedback in the form of FES or robot-assisted arm movements, and such a system does not provide a positive feedback corresponding to patient's motor imagery. In this work, we propose a causal related BCI-FES rehabilitation training platform, consisting top-down and bottom-up causal chains to achieve a better rehabilitation performance. We compare our system with a popular BCI-FES system on EEG data recorded from ten patients divided in two groups. The results show that almost all patients have achieved improvements in the motor function recovery after our training.

1 Introduction

Brain Computer Interface (BCI) is a direct communication pathway between the brain and external devices [1]. Through some advanced signal processing techniques, BCI system is able to catch the brain signals diffused from brain cortex and transforms some regular signals into control commands, making it come true that only by internal imagination can we human control external objects.

Electroencephalography (EEG), as the most commonly used member of various bio-signals, is the recording of electrical activity along the scalp [2]. EEG signals can be easily recorded by non-invasive approaches. Therefore, its easy acquisition has attracted many researcher' attention [3,4]. Motor imagery, as a kind of EEG, is a mental process by which an individual rehearses or simulates a given motor action by minds. Due to the discriminative property of human's motor imagery, recognition and classification problem about motor imagery EEG have been generally conducted recently [5,6].

BCI and EEG researches have been widely directed at fields related with rehabilitation training, that is, assisting, augmenting or repairing human cognitive and sensory-motor functions. A typical application is to utilize BCI techniques and motor imagery to construct a rehabilitation training system for stroke patients. Several significant related works have been conducted: Cuntai Guan and its team firstly proposed a motor imagery-based Brain Computer Interface robotic rehabilitation for stroke in BCI-Award 2010 [7]. Soekadar proposed a more complex paradigm for improving the efficacy of ipsilesional Brain Computer Interface training in neurorehabilitation of chronic stroke

M. Lee et al. (Eds.): ICONIP 2013, Part I, LNCS 8226, pp. 419–426, 2013.
© Springer-Verlag Berlin Heidelberg 2013

[8]. Meng and Gao brought the Function Electrical Stimulation (FES) into BCI rehabilitation system [9].

However, these studies focus on how to set up a rehabilitation system without considering the neurophysiological mechanism for rehabilitation, i.e. whether the system take effects is determined not only by system constructions but also by the inner causality relationship between BCI techniques and traditional therapies. In our study, a multimodal BCI-FES rehabilitation training system integrated with active learning mechanism is proposed for clinical treatments for post-stroke patients [5][10][11][12]. In this system, we build up a closed rehabilitation loop consisted of two complementary causalities: (1) Top-down chain: with an instructed hint, stroke subjects begin the internal motor imagery. Then followed FES stimulations are inserted on the corresponded limbs(muscles), causing factual movements of paralyzed part of bodies. (2) Bottom-up chain: after the imagery-movement process, other external stimulations, such as acoustic and visual prompts are provided by the system to help subjects finish the whole imagery task and prepare for following ones. The two causality chains complement each other and cooperate as a closed BCI-FES stimulation loop, which, to some extent, attempts to simulates normal subjects' natural motor imagery-action process and reconstruct the neuroncircuit between paralysis limbs and corresponding pathological brain areas [13]. Two months experiments have been conducted in clinical environment. Motor imagery EEG and clinical parameters have been recorded, analyzed and compared to verify the effectiveness of our system and proposed paradigm.

The rest part of this paper is organized as follows: section 2 gives a detailed introduction about our system, data collection and experiment setup. Section 3 demonstrates the experiment results about the rehabilitation performance and comparisons with other traditional paradigms are also given. Section 4 gives a brief conclusion about this study.

2 Method

2.1 System Overview

In order to obtain EEG data and use the data to do the experiment, our BCI-FES rehabilitation training system is consisted of 5 modules: real-time data acquisition module, data storage and analysis module, visualization module, multi-modal feedback module and human effect training module. Fig. 1 provides a brief illustration of the whole system.

Our system aims at recovering the motor ability on patients after a unilateral cerebral infarction. Patients try to use motor imagery to finish some tasks based on daily behavior in Virtual Reality(VR) scenario, and get the chances to retrain the neuron function of their impaired cortex by active motor imagery directed by active training tasks. In our system, data acquisition module collects raw EEG data while subjects imagining movement of their limbs. For each segment of data, we use feature extraction and classification algorithm in the data storage and analyze module to assign a two-class label to it. Using the output (classification) result as a command signal, multi-modal feedback module gives a related feedback in different modal including visual, auditory and tactile responses. Patients can actively adjust their mental states when receiving the feedback responses or choose to finish their imagery tasks with the help of feedback

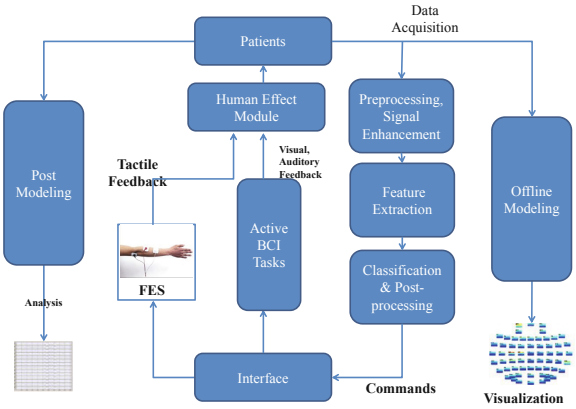

Fig. 1. A brief view of BCI-FES rehabilitation training system

signals when get stuck. It's worth mentioned that the raw EEG data will be sent to visualization module concurrently for real-time observations and further usages when the system is running.

2.2 Data Acquisition and Processing

We select 19 electrodes that can cover primary areas of motor imagery for left and right hands to collect raw EEG data in the data acquisition module. After removing artifacts, we filter the EEG into the band 8-30Hz. Sliding window method is introduced to cut raw EEG data into small time sequences for online classification. We record every one-second time interval to cut EEG data into small pieces using a 0.125 second step length. Sliding window method can increase the diversity of data without loss of continuity.

2.3 Feature Extraction and Classification Method

Raw EEG data collected from post-stroke patients is weak and noisy. if we use the traditional method of feature extraction and classification, motor imagery patten will be flooded among the noisy pattern. Independent Component Analysis(ICA), which is widely used to separate effective data and noisy one, is involved in our system. Different from processing processing normal subjects' EEG, we first apply ICA on the post-stroke EEG data and project the raw data into most independent sources. In this way, ICA explores both high order statistics and temporal structures of source signals, and separates true motor imagery signals and noise. We choose sources that reflect brain activity most, and Common Spatial Pattern(CSP) [14]. as the most widely used feature extraction method , is applied on the effective sources. After feature extraction, Support Vector Machine (SVM) algorithm is used as classification method [15,16]. We trained a 2-class classifier of left and right-handed motor imagery, and use classification results to guide multi-modal feedback module.

2.4 Multi-modal Feedback

Existing BCI-FES stroke rehabilitation therapy, with loss of timeliness, cannot construct a causal routine between damaged cortex and nerve system.

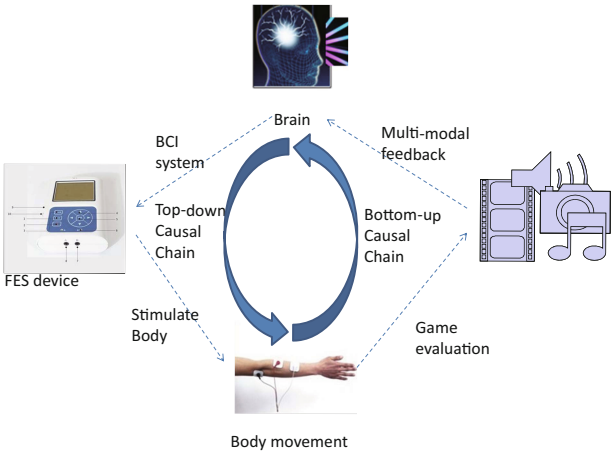

Fig. 2. Causal circuit in our system, including top-down and bottom-up causal chain

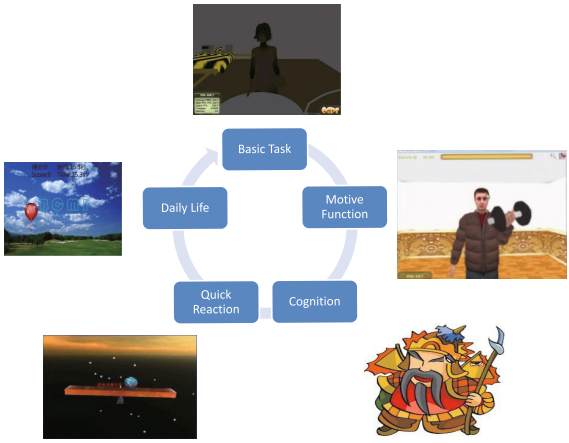

Fig. 3. Illustration for five different BCI motor imagery related tasks, covering 5 categories of daily behaviors

In our system, we first ask patients to finish some imaginary tasks. While patients are trying to finish their tasks, FES stimulation, are evolved to stimulate the disabled limbs. Patients try to control their limbs in an alternative way: starting from motor imagery, and

resulting in real body movement, forming a top-down causal chain of motor function. On the same time, multi-modal feedback, including visual, auditory and tactile signal, returns a evaluation of the motor imagery to patients' brain, which can be treated as a bottom-up causal chain of motor cognition. Combining the two chains, our system constructs a causal circuit, and helps patients to train on basic motor function recovery.

In the experiment, patients are asked to finish 5 tasks that cover 5 different categories of daily missions, as shown in Fig. 3, including training for basic physiological requirements, motor function recovering, quick reaction, daily behavior and compound task cognition. Patients can relearn the life skills from the tasks, and achieve the ability that return to normal life.

3 Result

Five stroke patients participated in our causal related rehabilitation system's experiment. For comparison, another five patients also participate in our traditional rehabilitation system. Both the two groups received regular therapies such as physical therapy, exercise therapy and acupuncture therapy in hospital. We evaluate the performance of our system in two aspects of online recognition performance and motor function recovery.

3.1 Online Recognition Performance

All the patients took part in several sessions, between each session there are 2 minutes for rest. Each session consist of 18 trials and each trial lasted for 4 seconds. For the sake of real-time response of online systems, the sliding window strategy is applied to

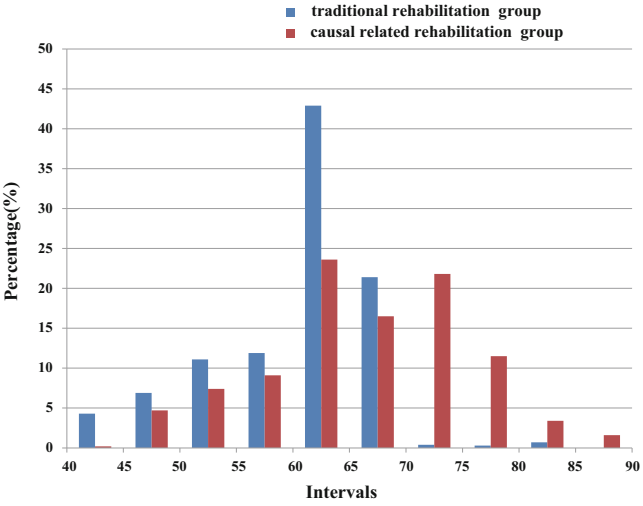

Fig. 4. A comparison in online accuracies of causal related rehabilitation group and previous rehabilitation group. x axis stands for the accuracy intervals (with step: 5%). y axis represents the statistics count of a specific accuracy interval.

produce recognition result every 0.125s [17] with the window size 1000 ms. CSP is employed to extract features for each trial constructed by the sliding window strategy. Afterwards, these features are fed to a SVM classifier for parameter adjustment. Finally, online accuracy of the next session is calculated using these parameters. Online accuracies of all the sessions for all the patients in the two groups are calculated and counted in small scattered intervals. Fig. 4 gives a comparison in online accuracies of causal related rehabilitation group and previous rehabilitation group at the end of the rehabilitation training. It is obvious that online accuracies of previous rehabilitation group mainly concentrate in 60%-70% (totally 64.3%) while 60%-80% hold the largest proportion for the causal related rehabilitation group (totally 73.4%). Moreover, patients in the causal related rehabilitation group became more familiar with the mental task, and finally the online accuracy can even reach 90%.

3.2 Motor Function Recovery

Clinical indices recorded in the whole training period show that there are significant improvement in motor function of upper limbs for all the patients. In order to observe the brain's activity in affected hemisphere after training, event-related desynchornization (ERD) phenomenon [14] is also observed of the patient recovered best in the previous rehabilitation group and the causal related rehabilitation group. All trials are extracted from all the sessions and reconstructed in spatial-spectral-temporal domain. Afterwards, we average all the trials to remove noise. Fig. 5 shows the time-frequency graphs to illustrate the ERD phenomenon of the affected cortex (C4) in the two groups. Active frequency band mainly concentrates in 8-12Hz (α). It is easy to find that the the duration of

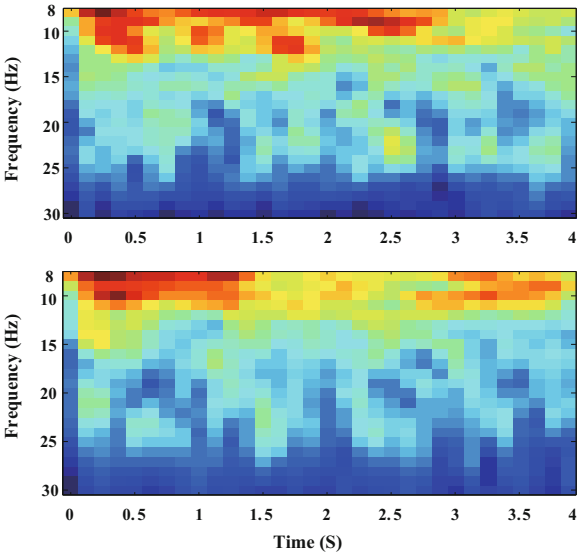

Fig. 5. Time-frequency graphs of the affected cortex (C4) of patients trained with previous rehabilitation system and causal related rehabilitation system

ERD phenomenon becomes longer and the desynchornization becomes more obviously after training for the patient trained with causal related rehabilitation system, indicating that our system promotes the motor function recovery of stroke patients. Based on the multi-modal feedback, our system attempts to establish a closed loop between the brain cortex and the upper limbs and help patients restore neural pathway.

4 Conclusion

In this study, we introduce a novel causal feedback based BCI-FES system. As a new paradigm of rehabilitation training, our system can achieve a better training performance for almost all subjects. After our training, one can observe ERD appears longer and become desynchornization more. Moreover, clinical rehabilitation parameters of patients in our experiment is higher than patients using old BCI-FES system, indicating a better rehabilitation therapy.

Acknowledgement. The work was supported by the National Natural Science Foundation of China (Grant No. 61272251, 91120305) and the NSFC-JSPS International Cooperation Program (Grant No. 61111140019).We would like to acknowledge Prof. Yi Wu's group at Huashan Hospital for both supporting and conducting clinical rehabilitation experiments.

References

1. Wolpaw, J.R., Birbaumer, N., McFarland, D.J., Pfurtscheller, G., Vaughan, T.M.: Brain–computer interfaces for communication and control. Clinical Neurophysiology 113(6), 767–791 (2002)
2. Buch, E., Weber, C., Cohen, L.G., Braun, C., Dimyan, M.A., Ard, T., Mellinger, J., Caria, A., Soekadar, S., Fourkas, A., et al.: Think to move: a neuromagnetic brain-computer interface (bci) system for chronic stroke. Stroke 39(3), 910–917 (2008)
3. Zhao, Q., Zhang, L., Cichocki, A.: EEG-based asynchronous BCI control of a car in 3D virtual reality environments. Chinese Science Bulletin 54(1), 78–87 (2009)
4. Li, J., Zhang, L., Tao, D., Sun, H., Zhao, Q.: A prior neurophysiologic knowledge free tensor-based scheme for single trial EEG classification. IEEE Transactions on Neural Systems and Rehabilitation Engineering 17(2), 107–115 (2009)
5. Zhang, H., Liang, J., Liu, Y., Zhang, L.: Gaussian mixture modeling in stroke patients' rehabilitation EEG data analysis. In: EMBC 2013. IEEE (accepted 2013)
6. Zhao, Q., Caiafa, C., Mandic, D., Chao, Z., Nagasaka, Y., Fujii, N., Zhang, L., Cichocki, A.: Higher-order partial least squares (hopls): A generalized multi-linear regression method (2012)
7. Guger, C., Allison, B., Edlinger, G.: State of the art in bci research: Bci award 2011. In: Brain-Computer Interface Research, pp. 1–5. Springer (2013)
8. Soekadar, S.R., Birbaumer, N., Cohen, L.G.: Brain–computer interfaces in the rehabilitation of stroke and neurotrauma. In: Systems Neuroscience and Rehabilitation, pp. 3–18. Springer (2011)
9. Meng, F., Tong, K.-Y., Chan, S.-T., Wong, W.-W., Lui, K.-H., Tang, K.-W., Gao, X., Gao, S.: Bci-fes training system design and implementation for rehabilitation of stroke patients. In: IEEE International Joint Conference on Neural Networks, IJCNN 2008 (IEEE World Congress on Computational Intelligence), pp. 4103–4106. IEEE (2008)

10. Liu, Y., Zhang, H., Wang, H., Li, J., Zhang, L.: BCI-FES rehabilitation training platform integrated with active training mechanism. In: IJCAI 2013 Workshop on Intelligence Science 2013 (WIS 2013) (accepted 2013)
11. Li, J., Zhang, L.: Active training paradigm for motor imagery BCI. Experimental Brain Research 219(2), 245–254 (2012)
12. Liu, Y., Li, M., Zhang, H., Li, J., Jia, J., Wu, Y., Cao, J., Zhang, L.: Single-trial discrimination of EEG signals for stroke patients: A general multi-way analysis. In: EMBC 2013. IEEE (accepted 2013)
13. Mulder, T.: Motor imagery and action observation: cognitive tools for rehabilitation. Journal of Neural Transmission 114(10), 1265–1278 (2007)
14. Ramoser, H., Muller-Gerking, J., Pfurtscheller, G.: Optimal spatial filtering of single trial EEG during imagined hand movement. IEEE Transactions on Rehabilitation Engineering 8(4), 441–446 (2000)
15. Bishop, C.M., Nasrabadi, N.M.: Pattern recognition and machine learning, vol. 1. Springer, New York (2006)
16. Chang, C.-C., Lin, C.-J.: LIBSVM: a library for support vector machines. ACM Transactions on Intelligent Systems and Technology (TIST) 2(3), 27 (2011)
17. Li, J., Zhang, L.: Bilateral adaptation and neurofeedback for brain computer interface system. Journal of Neuroscience Methods 193(2), 373–379 (2010)

Phase Synchrony for Human Implicit Intent Differentiation

Ukeob Park, Kalyana C. Veluvolu, and Minho Lee*

School of Electronics Engineering, Kyungpook National University
1370 Sankyuk-Dong, Puk-Gu, Taegu 702-701, South Korea
uepark@ee.knu.ac.kr, {veluvoluk,mholee}@gmail.com

Abstract. This paper focuses on discriminating user's intent to real images based on phase synchrony in EEG. The goal is to differentiate user's navigational intention and informational intention with real world scenario's. In this paper, we first calculate Phase locking Value (PLV) between all electrode pairs in EEG collection montage. We identified several most significant pairs (MSP) to construct brain functional connectivity patterns in different bands, theta band (4~7Hz), alpha (8~13Hz), beta-1 (14~22Hz), beta-2 (23~30Hz). Based on the PLV variation in the selected MSP's, the user intent can be classified. This paper demonstrates the potential of these identified brain electrode pairs in cognitive detection and task classification for future BCI applications.

Keywords: brain-computer interface (BCI), electroencephalographic (EEG), phase synchrony, brain connectivity, intent recognition.

1 Introduction

Brain cognitive fusion technology is an emerging and most promising fusion technology floating in modern society / future of the 21st century. Especially, according to FET2012 January [1], it was written that cognitive science is one of the most important future technology. Information & Communication Technology (ICT) systems should serve as empathic cognitive extensions of their users, being active and instrumental in driving interactions with computers as well as with other humans, hereby learning and adapting with the user. Brain plasticity and behavior is needed in order to interact between human and computer for understanding the impact on Human development [1]. According to the theory of mind [2], human beings have a natural way to represent, predict and interpret the intention expressed explicitly or implicitly by the others. For an efficient human computer interaction system it is necessary for a system to understand the intention of a human. Intention recognition is a relatively new field that is being widely used in web applications [3] and internet security [4]. Many researchers have investigated the decision discrimination in a variety of ways. In particular, upon analyzing the brain science, EEG method is a non-invasive measurement of brain's electrical activity which has a good temporal resolution. Also, to understand

* Corresponding author.

M. Lee et al. (Eds.): ICONIP 2013, Part I, LNCS 8226, pp. 427–433, 2013.
© Springer-Verlag Berlin Heidelberg 2013

brain cognition, connectivity plays an important role. Phase synchronization (PS) analysis has been well demonstrated to be a very useful method to infer functional connectivity with multichannel neural signals, e.g., electroencephalography (EEG)[5].

In this paper, we propose the classification of user Navigational / informational intention with phase estimation based on the EEG data. In particular, the paper's goal is to identify the brain connectivity related to user's navigation/information intent thru visual-experiments based on static images that is closest to the practical scenarios. We provide a reference, difference of PLV, for determining the intent of the user (Navigational / Informational intent).

This paper is organized as follows: Methods for PLV and Most significant pair's selection are discussed in Section 2. Section 3 details on the results obtained and Section 4 concludes the paper.

2 Methods

PLV synchronization measures the synchronization level of EEG at every time instant between any two electrode pairs in the range of (0 - 1) [5, 6]. Therefore, the aim of this study is to represent user's change in intent over time as a quantitative representation of PLV.

2.1 Phase Locked Value (PLV)

EEG phase differences are often used to compute "directed coherence" which is a measure of the directional flow of information between two EEG electrode sites [7]. EEG phase difference is also used to estimate conduction velocity and synaptic integration time [8, 9]. Phase locking value (PLV) is a measure for studying the synchronization phenomena in EEG signals. It is similar to cross spectrum but independent of amplitude of the two signals [5]. Making use of PLV, we can measure synchronization between all electrode pairs in EEG collection montage. Synchronization measure PLV formula is as follows [5]:

$$\mathrm{PLV} = \frac{1}{N} \left| \sum_{n=1}^{N} \exp(j\{\Delta\Phi(t,n)\}) \right| \tag{1}$$

Where N is of the total number of trials, $\theta(t,n)$is the phase difference $\Phi_1(t,n) - \Phi_2(t,n)$ between pair of brain nodes, and t is the time of each period. The range of PLV values varies between 0 and 1.PLV = 1, means perfect coupling of electrode pairs and PLV = 0, means not coupled at all.

2.2 Intention Basis for Discrimination

PLV Difference. To identify the network map, we need to identify the PLV difference between the two events (Information intent and Navigation intent). The PLV difference for all electrode pairs in two events provide the measure of how each electrode PLV varies between the two events [11].

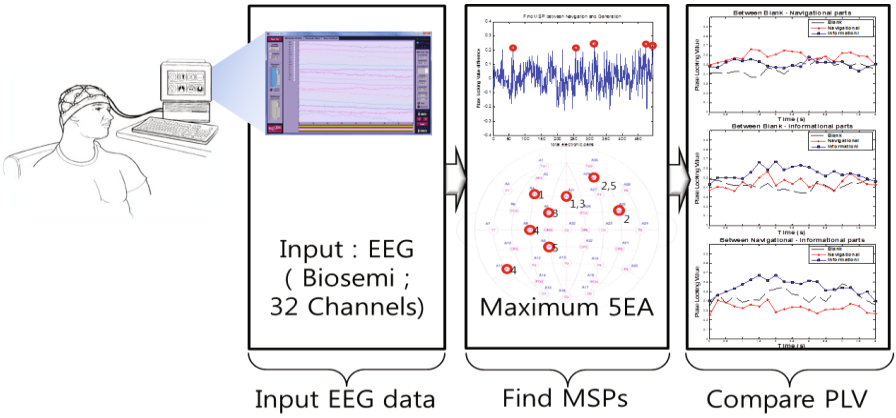

Fig. 1. Totally analysis process

In Fig. 2, the experiment timing scheme is shown. Thee PLV determined during informational and navigational intent periods is used to obtain the PLV difference for all electrode pairs. The difference PLV between navigational and informational periods is the key for classification in this paper.

The Most Significant Pairs (MSP). The MSP represents the most reactive electrode pairs (electrode pairs/locations) of brain compared between the two events (information intent /navigation intent and rest). This is shown in Fig.1. After determining the PLV of total electrode pair of each informational part and navigational part, we define the most significant pair (MSP), the electrode pair that has the most PLV difference between these two events. The formula for the MSP can be as follows.

$$\text{MSP} - \text{I} = \underset{e}{argmax}\{PLV_{information} - PLV_{rest}\} \tag{2}$$

$$\text{MSP} - \text{N} = \underset{e}{argmax}\{PLV_{navigation} - PLV_{rest}\} \tag{3}$$

Where MSP-I and MSP-N corresponds to MSP's identified for information intent and navigation intent. In Eq. (2) and (3), e represents electrode pairs. It is possible to identify both the brain connectivity and the most reactive electrode pairs based on PLV from Eq.(2) and (3). Recently, the work in [11] identified 5 most significant pairs for classification of motor imagery tasks. In this work, we follow similar procedure for identification of 5 MSP's. One may also choose more number of MSP's (say 10 MSP's or 20 MSP's).

2.3 Experimental Setup and Data Collection

Ten healthy subjects participated in the study. EEG data from 32 channels were recorded with biosemi (www.biosemi.com) amplifier. The timing scheme of the experiment is shown in Fig. 2. Subjects had to perform the following tasks during each trial.

Navigational intent.: To focus on the image present on the screen.

Informational intent.: To search for the specific object in the displayed image.

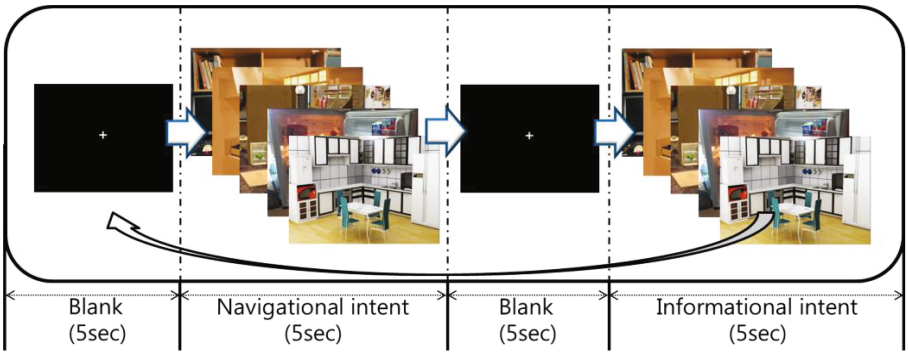

Fig. 2. Procedure of the block diagram for the synchronization of Phase estimation

One session consisted of 5 trials and in each trial, different navigation/informational intent images that were close to a real-life scenario were shown to the subject as shown in Fig. 2 [10]. 5 sessions were conducted and hence a total of 25 trials/subject. Blank images shown between the intent was to prevent the mixing of intents. Random images in each sequence were presented to avoid the induction of intent in subjects due to the iterative nature of the experiment.

3 Results

We selected 5 $\mathrm{MSP}-\mathrm{N}$ and $5\mathrm{MSP}-\mathrm{I}$ identified in theta band to classify navigational and informational intents, $MSP-N$ and $MSP-I$ are identified using (2) and these pairs are subject-intent specific. Fig. 3 shows the results obtained with three subjects. Identified reactive pairs 5 $MSP-N$ and 5 $MSP-I$ are shown in the Fig. 3. The average PLV of 5 $MSP-N$ and 5 $MSP-I$ during both the events for three subjects are also illustrated.

One can easily observe the $MSP-N$ having higher PLV level compared to $MSP-I$ during navigational intent duration and vice versa during informational intent duration. The difference in PLV level of navigational intent and informational intent is crucial for the intent classification. The difference in PLV level of identified MSP's can be calculated using the following equation set:

$$DPLVN = \langle PLV_N^{MSP-N} \rangle - \langle PLV_N^{MSP-I} \rangle \tag{4}$$

$$DPLVI = \langle PLV_I^{MSP-N} \rangle - \langle PLV_I^{MSP-I} \rangle \tag{5}$$

Where $DPLVN$ is the difference in PLV level of 5 electrode pairs $MSP-N$ to $MSP-I$ during navigational period and $DPLVI$ is the difference in PLV level of $MSP-N$ to $MSP-I$ during informational intent duration, $\langle\ \rangle$ being the mean operator.

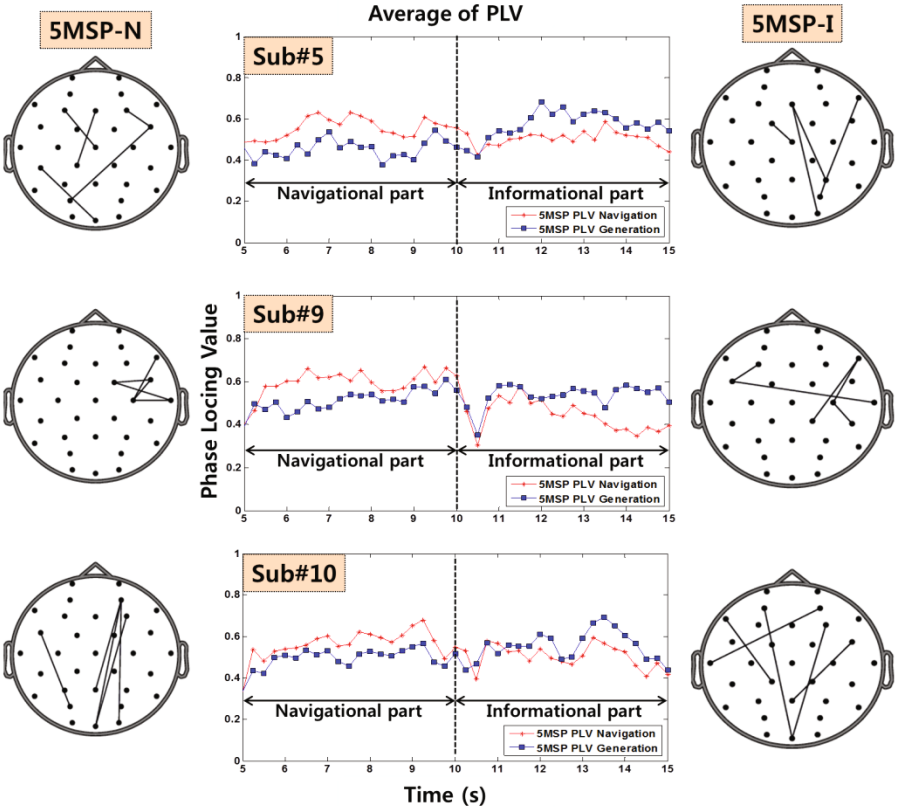

Fig. 3. Comparison of $MSP-N$ and $MSP-I$ in θ band during navigational intent and informational intent

$DPLVN$ is positive during navigational intent, it shows that the PLV level of $MSP-N$ is high compared to $MSP-I$ and vice-versa during the informational intent. This relative difference change can be identified in all the subjects. The average PLV of 5 $MSP-I$ and 5 $MSP-N$ for all subjects in all the selected bands during navigational intent and informational intent are shown in bar plots (Fig. 4). Table 1 is filled by values of Fig. 4.and difference means the difference of PLV level in Eq. (4) and (5). The relative change can be clearly identified in all the frequency bands. Thus, it is clear that the proposed method can clearly differentiate between both the events.

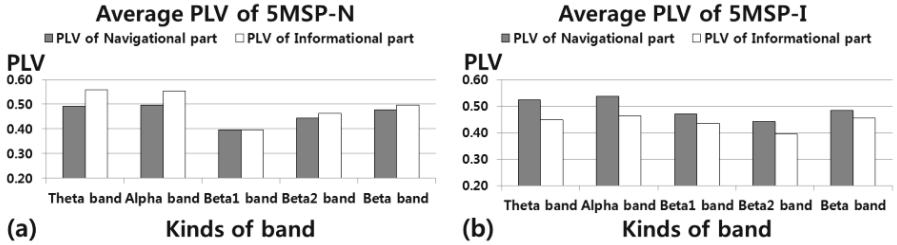

Fig. 4. Average PLV of 5 $MSP-I$ and 5 $MSP-N$ during a) navigational intent b) informational intent

Table 1. Average PLV-N/I of 5MSP and difference of PLV-N/I at each band

Kinds of band	Navigation period			Information period		
	PLV-N	PLV-I	Difference	PLV-N	PLV-I	Difference
θ band	0.52	0.45	0.0749	0.49	0.56	0.0667
α band	0.54	0.46	0.0719	0.50	0.55	0.0570
β1 band	0.47	0.44	0.0346	0.40	0.40	-0.0001
β2 band	0.44	0.40	0.0463	0.44	0.46	0.0195
β band	0.48	0.45	0.0284	0.48	0.50	0.0185

4 Conclusions

In this paper, we proposed a method to differentiate the user's intent given a real picture based on the phase synchrony of EEG. We identified most significant PLV varying pairs between user's navigational and information generating period. These significant pairs demonstrate the variation in functional connectivity and the applicability of this method for BCI applications.

Our future research will focus on determining the user's intent based on multimodal biometric data using the same proposed method. We finally plan to apply these methods for human-robot interaction systems.

Acknowledgement. This research was supported by the Original Technology Research Program for Brain Science through the National Research Foundation of Korea(NRF) funded by the Ministry of Education, Science and Technology (2013034988) (50%) and also the Converging Research Center Program funded by the Ministry of Education, Science and Technology (2013K000333) (50%).

References

1. European Communities: Future and Emerging Technologies, In: Information Society and Media (2012) ISBN 978-92-79-12971-1
2. Premack, D., Woodruff, G.: Does the chimpanzee have a theory of mind? Behav. Brain Sci. 1, 515–526 (1978)
3. Chen, Z., Lin, F., Liu, H., Ma, W.Y., Wenyin, L.: User Intention Modelling in Web Applications Using Data Mining. World Wide Web-Internet and Web Information Systems Journal 5, 181–192 (2002)
4. Spyrou, T., Darzentas, J.: Intention Modelling: Approximating Computer User Intentions for Detection and Prediction of Intrusions. Computers & Security 15, 395 (1996)
5. Sun, J., Hong, X., Tong, S.: Phase synchronization analysis of EEG signals: an evaluation based on surrogate tests. IEEE Trans. Biomed. Eng. 59, 2254–2263 (2012)
6. Lachaux, J.-P., Rodriguez, E., Martinerie, J., Varela, F.J.: Measuring Phase Synchrony in Brain Signals. Hum. Brain Mapp. 8, 194–208 (1999)
7. Kamiński, M., Blinowska, K.J.: A new method of the description of the information flow in the brain structures. Biol. Cybern. 65, 203–210 (1991)
8. Suzuki, H.: Phase relationships of alpha rhythm in man. Jpn. J. Physiol. 24, 569–586 (1974)
9. Nunez, P.: Electrical Fields of the Brain. Oxford University Press, Mass (1981)
10. Jang, Y.-M., Mallipeddi, R., Lee, M.: Human Implicit Intent Transition Detection Based on Pupillary Analysis. In: IEEE World Congress on Computational Intelligence WCCI 2012, Brisbane, Australia, pp. 10–15 (2012)
11. Gonuguntla, V., Wang, Y., Veluvolu, K.C.: Phase Synchrony in Subject-Specific Reactive Band of EEG for Classification of Motor Imagery Tasks. In: 35th Annual International IEEE EMBS Conference, Osaka, Japan (accepted 2013)

Wheelchair Control Based on Multimodal Brain-Computer Interfaces

Jie Li[1], Hongfei Ji[1], Lei Cao[1], Rong Gu[2], Bin Xia[3], and Yanbing Huang[3]

[1] Department of Computer Science and Technology, Tong Ji University, Cao an Highway No. 4800, Shanghai, China
[2] Department of Electronic Science and Technology, Tong Ji University, Cao an Highway No. 4800, Shanghai, China
[3] Institute of Information Engineering, Shanghai Maritime University, Haigang Ave No. 1550, Shanghai, China

Abstract. Electroencephalogram (EEG) based brain-computer interfaces (BCIs) for wheelchair control have great value for those with devastating neuromuscular disorders. Although there have been many attempts to implement EEG-based wheelchair control systems by P300, steady state visual evoked potential (SSVEP), and motor imagery (MI) related event-related desynchronization/synchronization (ERD/ERS), the number of simultaneous control commands in those BCI systems is strictly limited, and those BCI control do not work for a non-negligible portion of users due to the problem of BCI Illiteracy. In this paper, we develop a multimodal BCI based wheelchair control system, the user could employ subject-optimized mental strategies to produce multiple commands to control the wheelchair, which include ERD/ERS, SSVEP, and simultaneous ERD/ERS and SSVEP. It could not only help address "BCI illiteracy", but also provide simultaneous control commands for complex control. Experiment results demonstrate the proposed system is effective and flexible in practical application.

Keywords: BCI, wheelchair control, multimodal, BCI Illiteracy.

1 Introduction

Electroencephalogram (EEG) based brain-computer interfaces (BCIs) provide a potentially powerful new communication channel for people to mentally control machines through translating brain electrical activities into machine codes or commands[1]. EEG based BCIs for wheelchair control have great value for those with devastating neuromuscular disorders, such as the amyotrophic lateral sclerosis (ALS), brainstem stroke, cerebral palsy, and spinal cord injury.

There have been many attempts to implement EEG-based wheelchair control systems relying on one of following typical EEG activity for control: steady state visual evoked potential (SSVEP), event-related desynchronization /synchronization (ERD/ERS) and P300 evoked potential. For examples, an asynchronous BCI based on MI task helped the subject to control a wheelchair to go or stop by

M. Lee et al. (Eds.): ICONIP 2013, Part I, LNCS 8226, pp. 434–441, 2013.
© Springer-Verlag Berlin Heidelberg 2013

imagination of feet movements in virtual reality (VR)[2]. A 2-class MI based BCI for robotic wheelchair control was shown by Tsui et al.[3], and a real wheelchair was steered by three different kinds of MI tasks, i.e. left, right and feet motor imageries corresponded to turn left, turn right, and go forward respectively[4]. Wheelchair was designed to run on predefined paths to the target location by detecting P300 potentials[5,6], and also demonstrated in SSVEP-based BCI system equipped with a safety layer and navigation software[7]. However, in generally, it is still challenging to design an effective and flexible BCI system for real wheelchair control in practical application since the number of control commands, especially for simultaneous commands, in those BCI systems is strictly limited. Furthermore, recently, many BCI groups reported the forementioned BCI control could not work for a non-negligible portion of users (estimated 15% to 30%) due to the problem of "BCI illiteracy"[8,9]. This problem exists across different BCI approaches, although some possible solution, such as improved signal processing, training, have been explored, it is still not solved since some of the users can not produce detectable patterns of brain activity necessary to a particular BCI approach[10,11].

Therefore, we develop a multimodal BCI based wheelchair control system, the user could employ subject-optimized mental strategies to produce multiple commands to control wheelchair, which could be ERD/ERS, SSVEP, or simultaneous ERD and SSVEP. It can not only help address "BCI illiteracy", but also provide more and simultaneous control commands for complex control. Experiment results demonstrate the proposed system is effective and flexible in practical application.

The remainder of this paper is organized as follows. The Methods, including experiment Setup, system paradigm, subject-optimized control algorithm are described in Section 2. Section 3 presents experiments and results, and section 4 finally concludes the paper.

2 Methods

2.1 Experiment Setup

In order to evaluate the proposed multimodal BCI, three healthy male subjects, aged from 21 to 30, took part in the experiment. Multi-channel EEG data were acquired by Gtec Amplifier (g.tec, Graz, Austria), sampled at 256Hz and then band-pass filtered within 5-30 Hz. Channels located at standard positions of the 10-20 international system as FC3, FC4, C5, C3, C1, CZ, C2, C4, C6, CP3, CP4, POZ, O1, OZ, and O2, totally 15 channels, were used in this study. The ground and reference electrodes were respectively fixed on medial frontal cortex and the right earlobe.

In the data collection stage, each subject was seated in front of a notebook computer, keeping arms on the chair arms with hands relaxing. SSVEPs were generated by the stimuli box equipped on the desktop of the wheelchair (see left panel in Fig. 1), in which four light-emitting diodes (LEDs), separately flicking

at the frequency of 7Hz, 8Hz, 9Hz, 11Hz, were used as the visual stimuli. EEG signals are acquired continuously, and then transferred to the notebook computer through an USB port. The translated control commands would be sent to the wheelchair by a wireless communication module.

2.2 System Paradigm

Fig. 1 presents the multimodal BCI system paradigm. First, multichannel EEG signals are collected by electrodes located in the occipital and parietal lobes; Second, MI based ERD/ERS and SSVEP features are analysed. In details, For the MI task, we used common spatial patterns (CSP)[12] algorithm to detect the spectral discriminations by calculating discriminative spatial patterns that maximized the variance of one class and at the same time minimized the variance of the other. Here, four generalized eigenvectors from both ends of the spectrum were selected as spatial patterns, and only channels in motor related parietal lobe, i.e., FC3, FC4, C5, C3, C1, CZ, C2, C4, C6, CP3, CP4 were considered. The MI features were calculated by projecting the EEG data to the CSP patterns. The features of SSVEP were obtained by canonical correlation analysis (CCA) algorithm simultaneously. CCA is a multivariable statistical method used when there are two sets of data, which may have some underlying correlation[13]. Here, multiple correlation coefficients between the the sinusoidal reference signals at stimulating frequency, and EEG signals from multiple channels located in the occipital lobes, i.e. POZ, O1, OZ, and O2, were calculated as SSVEP related features. Then in order to evaluate the performance of different mental strategies, support vector machine (SVM) classifiers with linear radial basis function (LRB) is applied to calculate the cross accuracies for each task, considering its good generalization ability in minimizing the vapnik-chervonenkis (VC) dimension and achieving a minimal structural risk[14].

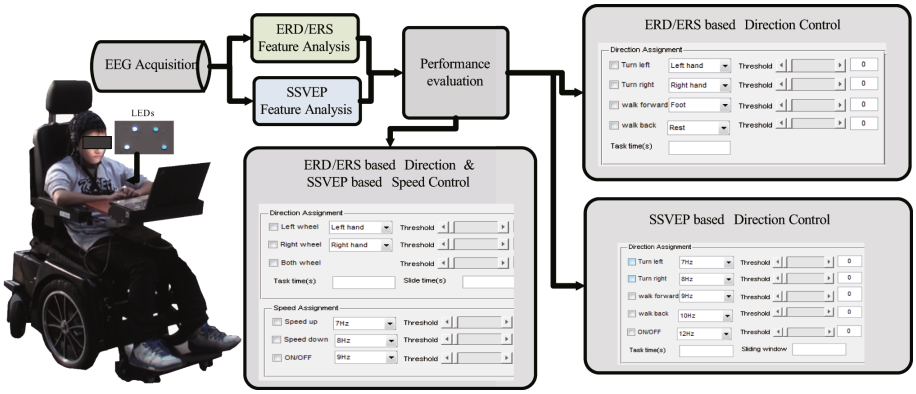

Fig. 1. The proposed multimodal BCI system paradigm for real wheelchair control

Finally, base on the SVM classification results, the wheelchair can be controlled by subject-optimized mental strategies to produce multiple commands, which include ERD/ERS, SSVEP, and simultaneous ERD and SSVEP. For the subject who is only good at the SSVEP task, then the aforementioned SSVEP features are translated into direction control commands automatically. Similarly, the ERS/ERS features are used to set the direction if the subject has a poor performance at the MI task. Note that, the system translates the MI and SSVEP classification results into simultaneous commands to control the speed and direction at the same time if the subject could achieve good performances at both of the two mental tasks.

2.3 Subject-Optimized Control Algorithm

Most of BCI systems for wheelchair control are based on only one typical EEG activity pattern, while the proposed multimodal BCI firstly evaluates the subject's performance in different activities, and then provides subject-optimized mental strategies to produce multiple commands to control a wheelchair. The control model is given in the following:

```
multimodal control algorithm (Output R_{l,t+1},R_{r,t+1} )
    { Assuming R_{l,t} and R_{r,t} represent the left and right
     wheels' rotation rate at the tth update respectively.
      f_{MI}, denoting the classification result for MI,is +1 for
     left hand movement and -1 for the right hand.
      f_{SSVEP} is given by the classification result for SSVEP.
     In the SSVEP mode, +1 for the LED representing "turn left"
     and -1 for "turn right".
     In the MI&SSVEP mode, +1 for the LED representing "speed up"
     and -1 for "speed down".
       TurningFactor, SpeedFactor are predefined tuning and speed
     parameters.
      }
 Switch controlmode
  Case  SSVEP mode
   R_{l,t+1}=R_{l,t} - f_{SSVEP} * TurningFactor + Given_speed;
   R_{r,t+1}=R_{r,t} + f_{SSVEP} * TurningFactor + Given_speed;
  Case  MI mode
   R_{l,t+1}=R_{l,t} - f_{MI} * TurningFactor + Given_speed;
   R_{r,t+1}=R_{r,t} + f_{MI} * TurningFactor + Given_speed;
  Case  MI&SSVEP mode
   R_{l,t+1}=R_{l,t} - f_{MI}*TurningFactor + f_{SSVEP}*SpeedFactor;
   R_{r,t+1}=R_{r,t} + f_{MI}*TurningFactor + f_{SSVEP}*SpeedFactor;
 end.
```

(A motorized wheelchair with differential drive has been retrofitted to receive the control commands by a bluetooth interface. By assigning different rotation rate for two motor wheels respectively, it can be steered in specific speed and direction.)

3 Experiments and Results

To evaluate the effectiveness of the proposed multimodal BCI system, and assess the capabilities of subjects' multimodal manipulation, a realtime control experiment was carried out in the real-word scenarios. Subjects were required to accomplish a complex navigation circuit in a public open space as soon as possible. Fig. 2 shows the circuit map, the subject should leave the start point and reach the stop point by passing the breakpoint and avoiding obstacles, and a possible path in an ideal situation is marked with red dotted line.

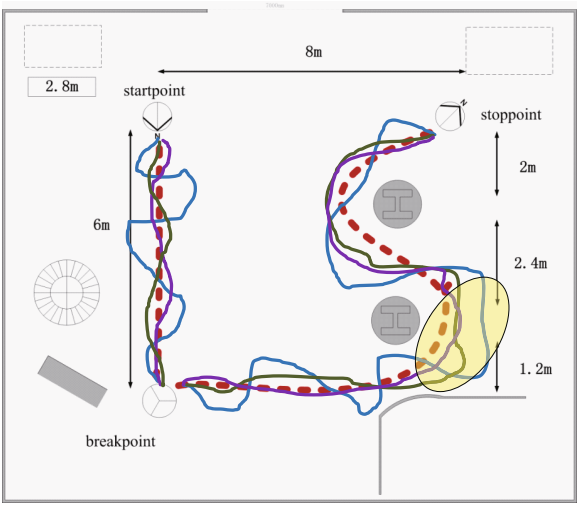

Fig. 2. The circuit map in the wheelchair control experiment. The subject was required to accomplish complex navigation circuit as soon as possible, the red dotted line stands for a possible path in an ideal situation. The green, purple, and blue lines denote the actual paths for Sub.1, Sub.2, Sub.3 respectively.

Before to control the real wheelchair, three subjects have been evaluated according to the proposed paradigm. They were all required to carry out the MI tasks and SSVEP tasks. The MI task consisted of three runs, each run had 10 trials for each class. In each trial, the subject was required to imagine the movements of the left or right hand for about 2s indicated by an arrow appeared on the computer screen. While in the SSVEP tasks, the subject was instructed to keep his eyes focusing on one of the LEDs according to an auditory digit cue, i.e., one of the 1, 2, 3, 4, corresponding to the serial number of LEDs, The goal of this session was to help select the mental strategy and calculate classification model in the following control experiment.

According to the aforementioned MI and SSVEP feature extraction and classification methods, the classification accuracies were calculated as the performance evaluation for each mental task, and then the proposed system would selected

Table 1. The performance in the wheelchair control experiment for each subject

	SSVEP accuracy	MI accuracy	selected strategy	time consuming
Sub.1	98.3%	99.4%	SSVEP and MI	274 (s)
Sub.2	57.9%	100%	MI	298 (s)
Sub.3	96.7%	58.3%	SSVEP	376 (s)

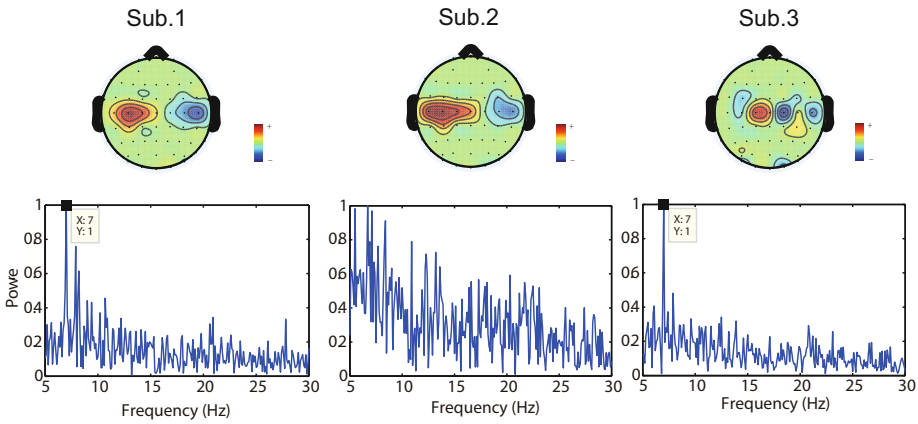

Fig. 3. The top line shows the power changes within 5-30Hz in the scalp map, and the bottom row shows power spectral density (PSD) of the EEG signal recorded at channel OZ for each subject when he navigated in the continuous turn-left area (marked with a yellow oval in Fig. 2). (In this experiment, for sub.2, left hand and right hand imagery were used to control wheelchair to turn left and right respectively; for sub.3, focusing on the LEDs flicking at the frequency of 7 and 9 Hz corresponded to left turn and right turn respectively. For Sub.1, left hand and right hand imagery were used to control the wheelchair to turn left and right, and at the same time, focusing on the LEDs flicking at the frequency of 7 and 9 Hz were used to control the wheelchair to speed up and speed down.)

subject-optimized mental strategy to produce multiple commands. Table 1 gives the performance and the selected strategies.

In the following wheelchair control experiment, all subjects reached the stop-point without collision, and their actual paths were showed in Fig. 2 , which are generally consistent with the predefined circuit. The time to accomplish the circuit is also listed in table 1 for each subject. It can been seen, by subject-optimized control mode, all subjects could complete the required task successfully even though Sub.2 and Sub.3 are almost illiterate in SSVEP or MI tasks. Sub.1 achieved the least time consuming since he could control the speed and direction of the wheelchair simultaneously, which would improves the control efficiency greatly. Among all subjects, Sub.3 spent the most time. Experiment path records show that he spent a lot of time to adjust the drive direction due to excessive turnings (see Fig. 2), which was probably caused by the reflection delay of SSVEP.

Fig. 3 illustrates the power changes within 5-30Hz in the scalp map, and the power spectral density (PSD) for each subject when he navigated in a continuous turn-left area (marked with a yellow oval in Fig. 2). It is obvious that the subjects applied the optimized mental activities in this multimodal BCI. Note that Sub.1 did the left hand imagery and focusing on the LEDs at 7Hz tasks to control wheelchair to accelerate and turn left at the same time. The simultaneously generated commands help this subject to reduce the consuming time effectively.

4 Conclusion

In this paper, a multimodal BCI based wheelchair control system is developed, and the user could employ subject-optimized mental strategies to produce multiple commands, to control wheelchair, which include ERD/ERS, SSVEP, and simultaneously ERD and SSVEP. It could not only help address "BCI illiteracy", but also provide more even simultaneous control commands for complex control. Experiment results demonstrate the proposed system is effective and flexible in practical application.

Acknowledgments. The work was supported by the the Fundamental Research Funds for the Central Universities (Grant No. 0800219202) the National Natural Science Foundation of China (Grant No. 61105122,61103071,61272271), and Natural Science Foundation Program of Shanghai (Grant No. 12ZR1434000).

References

1. Blankertz, B., Curio, G., Muller, K.R.: Classifying single trial EEG: Towards brain computer interfacing. Advances in Neural Information Processing Systems 1, 157–164 (2002)
2. Leeb, R., Friedman, D., Mller-Putz, G.R., Scherer, R., Slater, M., Pfurtscheller, G.: Self-paced (asynchronous) BCI control of a wheelchair in virtual environments: a case study with a tetraplegic. Computational Intelligence and Neuroscience (2007)
3. Tsui, C.S.L., Gan, J.Q., Hu, H.: A self-paced motor imagery based brain-computer interface for robotic wheelchair control. Clinical EEG and Neuroscience 42(4), 225–229 (2011)
4. Li, J., Liang, J., Zhao, Q., Li, J., Hong, K., Zhang, L.: Design of assistive wheelchair system directly steered by human thoughts. International Journal of Neural Systems 23(3) (2013)
5. Iturrate, I., Antelis, J.M., Kubler, A., Minguez, J.: A noninvasive brain-actuated wheelchair based on a P300 neurophysiological protocol and automated navigation. IEEE Transactions on Robotics 25(3), 614–627 (2009)
6. Rebsamen, B., Guan, C., Zhang, H., Wang, C., Teo, C., Ang, M.H., Burdet, E.: A brain controlled wheelchair to navigate in familiar environments. IEEE Transactions on Neural Systems and Rehabilitation Engineering 18(6), 590–598 (2010)
7. Mandel, C., Luth, T., Laue, T., Rofer, T., Graser, A., Krieg-Bruckner, B.: Navigating a smart wheelchair with a brain-computer interface interpreting steady-state visual evoked potentials. In: IEEE/RSJ International Conference on Intelligent Robots and Systems, IROS 2009, pp. 1118–1125. IEEE (October 2009)

8. Blankertz, B., Vidaurre, C.: Towards a cure for BCI illiteracy: machine learning based co-adaptive learning. BMC Neuroscience 10(suppl. 1), 85 (2009)
9. Vidaurre, C., Blankertz, B.: Towards a cure for BCI illiteracy. Brain Topography 23(2), 194–198 (2010)
10. Tan, D.S., Nijholt, A.: Brain-Computer Interfaces: applying our minds to human-computer interaction. Springer (2010)
11. Blankertz, B., Sanelli, C., Halder, S., Hammer, E.M., Kübler, A., Müller, K.R., Dickhaus, T.: Predicting BCI performance to study BCI illiteracy (2009)
12. Ramoser, H., Muller-Gerking, J., Pfurtscheller, G.: Optimal spatial filtering of single trial EEG during imagined hand movement. IEEE Transactions on Rehabilitation Engineering 8(4), 441–446 (2000)
13. Lin, Z., Zhang, C., Wu, W., Gao, X.: Frequency recognition based on canonical correlation analysis for SSVEP-based BCIs. IEEE Transactions on Biomedical Engineering 53(12), 2610–2614 (2006)
14. Chang, C.C., Lin, C.J.: LIBSVM: a library for support vector machines. ACM Transactions on Intelligent Systems and Technology (TIST) 2(3), 27 (2011)

Pushing Stochastic Gradient towards Second-Order Methods – Backpropagation Learning with Transformations in Nonlinearities

Tommi Vatanen[1], Tapani Raiko[1], Harri Valpola[1], and Yann LeCun[2]

[1] Department of Information and Computer Science
Aalto University School of Science
P.O. Box 15400, FI-00076, Aalto, Espoo, Finland
first.last@aalto.fi
[2] New York University
715 Broadway, New York, NY 10003, USA
firstname@cs.nyu.edu

Abstract. Recently, we proposed to transform the outputs of each hidden neuron in a multi-layer perceptron network to have zero output and zero slope on average, and use separate shortcut connections to model the linear dependencies instead. We continue the work by firstly introducing a third transformation to normalize the scale of the outputs of each hidden neuron, and secondly by analyzing the connections to second order optimization methods. We show that the transformations make a simple stochastic gradient behave closer to second-order optimization methods and thus speed up learning. This is shown both in theory and with experiments. The experiments on the third transformation show that while it further increases the speed of learning, it can also hurt performance by converging to a worse local optimum, where both the inputs and outputs of many hidden neurons are close to zero.

Keywords: Multi-layer perceptron network, deep learning, stochastic gradient.

1 Introduction

Learning deep neural networks has become a popular topic since the invention of unsupervised pretraining [3]. Some later works have returned to traditional back-propagation learning in deep models and noticed that it can also provide impressive results [5] given either a sophisticated learning algorithm [8] or simply enough computational power [2]. In this work we study back-propagation learning in deep networks with up to five hidden layers, continuing on our earlier results in [9].

In learning multi-layer perceptron (MLP) networks by back-propagation, there are known transformations that speed up learning [7, 10, 11]. For instance, inputs are recommended to be centered to zero mean (or even whitened), and nonlinear functions are proposed to have a range from -1 to 1 rather than 0 to 1 [7]. Schraudolph [11, 10] proposed centering all factors in the gradient to have zero mean, and further adding linear shortcut connections that bypass the nonlinear layer. Gradient factor centering changes the gradient as if the nonlinear activation functions had zero mean and zero slope on

M. Lee et al. (Eds.): ICONIP 2013, Part I, LNCS 8226, pp. 442–449, 2013.
© Springer-Verlag Berlin Heidelberg 2013

average. As such, it does not change the model itself. It is assumed that the discrepancy between the model and the gradient is not an issue, since the errors will be easily compensated by the linear shortcut connections in the proceeding updates. Gradient factor centering leads to a significant speed-up in learning.

In this paper, we transform the nonlinear activation functions in the hidden neurons such that they have on average 1) zero mean, 2) zero slope, and 3) unit variance. Our earlier results in [9] included the first two transformations and here we introduce the third one. We explain the usefulness of these transformations by studying the Fisher information matrix and the Hessian, e.g. by measuring the angle between the traditional gradient and a second order update direction with and without the transformations.

It is well known that second-order optimization methods such as the natural gradient [1] or Newton's method decrease the number of required iterations compared to the basic gradient descent, but they cannot be easily used with high-dimensional models due to heavy computations with large matrices. In practice, it is possible to use a diagonal or block-diagonal approximation [6] of the Fisher information matrix or the Hessian. Gradient descent can be seen as an approximation of the second-order methods, where the matrix is approximated by a scalar constant times a unit matrix. Our transformations aim at making the Fisher information matrix as close to such matrix as possible, thus diminishing the difference between first and second order methods. Extended version of this paper with the experimental details can be found in arXiv [12] and Matlab code for replicating the experiments is available at

`https://github.com/tvatanen/ltmlp-neuralnet`

2 Proposed Transformations

Let us study a MLP-network with a single hidden layer and shortcut mapping, that is, the output column vectors $\mathbf{y}_t$ for each sample t are modeled as a function of the input column vectors $\mathbf{x}_t$ with

$$\mathbf{y}_t = \mathbf{A}\mathbf{f}\left(\mathbf{B}\mathbf{x}_t\right) + \mathbf{C}\mathbf{x}_t + \boldsymbol{\epsilon}_t, \tag{1}$$

where $\mathbf{f}$ is a nonlinearity (such as $\tanh$) applied to each component of the argument vector separately, $\mathbf{A}$, $\mathbf{B}$, and $\mathbf{C}$ are the weight matrices, and $\boldsymbol{\epsilon}_t$ is the noise which is assumed to be zero mean and Gaussian, that is, $p(\epsilon_{it}) = \mathcal{N}\left(\epsilon_{it}; 0, \sigma_i^2\right)$. In order to avoid separate bias vectors that complicate formulas, the input vectors are assumed to have been supplemented with an additional component that is always one.

Let us supplement the $\tanh$ nonlinearity with auxiliary scalar variables α_i, β_i, and γ_i for each nonlinearity f_i. They are updated before each gradient evaluation in order to help learning of the other parameters $\mathbf{A}$, $\mathbf{B}$, and $\mathbf{C}$. We define

$$f_i(\mathbf{b}_i\mathbf{x}_t) = \gamma_i\left[\tanh(\mathbf{b}_i\mathbf{x}_t) + \alpha_i\mathbf{b}_i\mathbf{x}_t + \beta_i\right], \tag{2}$$

where $\mathbf{b}_i$ is the ith row vector of matrix $\mathbf{B}$. We will ensure that

$$\sum_{t=1}^{T} f_i(\mathbf{b}_i\mathbf{x}_t) = 0, \ \sum_{t=1}^{T} f_i'(\mathbf{b}_i\mathbf{x}_t) = 0, \ \text{and} \tag{3}$$

$$\left[\sum_{t=1}^{T} \frac{f_i(\mathbf{b}_i\mathbf{x}_t)^2}{T}\right]\left[\sum_{t=1}^{T} \frac{f_i'(\mathbf{b}_i\mathbf{x}_t)^2}{T}\right] = 1 \tag{4}$$

by setting α_i, β_i, and γ_i to

$$\alpha_i = -\frac{1}{T}\sum_{t=1}^{T} \tanh'(\mathbf{b}_i\mathbf{x}_t) \tag{5}$$

$$\beta_i = -\frac{1}{T}\sum_{t=1}^{T} [\tanh(\mathbf{b}_i\mathbf{x}_t) + \alpha_i\mathbf{b}_i\mathbf{x}_t] \tag{6}$$

$$\gamma_i = \left\{\frac{1}{T}\sum_{t=1}^{T} [\tanh(\mathbf{b}_i\mathbf{x}_t) + \alpha_i\mathbf{b}_i\mathbf{x}_t + \beta_i]^2\right\}^{1/4}\left\{\frac{1}{T}\sum_{t=1}^{T} \left[\tanh'(\mathbf{b}_i\mathbf{x}_t) + \alpha_i\right]^2\right\}^{1/4}. \tag{7}$$

One way to motivate the first two transformations in Equations (3a) and (3b), is to study the expected output $\mathbf{y}_t$ and its dependency of the input $\mathbf{x}_t$:

$$\frac{1}{T}\sum_t \mathbf{y}_t = \mathbf{A}\frac{1}{T}\sum_t \mathbf{f}(\mathbf{B}\mathbf{x}_t) + \mathbf{C}\frac{1}{T}\sum_t \mathbf{x}_t \tag{8}$$

$$\frac{1}{T}\sum_t \frac{\partial \mathbf{y}_t}{\partial \mathbf{x}_t} = \mathbf{A}\left[\frac{1}{T}\sum_t \mathbf{f}'(\mathbf{B}\mathbf{x}_t)\right]\mathbf{B}^T + \mathbf{C}. \tag{9}$$

We note that by making nonlinear activations $\mathbf{f}(\cdot)$ zero mean in Eq. (3a), we disallow the nonlinear mapping $\mathbf{A}\mathbf{f}(\mathbf{B}\cdot)$ to affect the expected output $\mathbf{y}_t$, that is, to compete with the bias term. Similarly, by making the nonlinear activations $\mathbf{f}(\cdot)$ zero slope in Eq. (3b), we disallow the nonlinear mapping $\mathbf{A}\mathbf{f}(\mathbf{B}\cdot)$ to affect the expected dependency of the input, that is, to compete with the linear mapping $\mathbf{C}$. In traditional neural networks, the linear dependencies (expected $\partial\mathbf{y}_t/\partial\mathbf{x}_t$) are modeled by many competing paths from an input to an output (e.g. via each hidden unit), whereas our architecture gathers the linear dependencies to be modeled only by $\mathbf{C}$. We argue that less competition between parts of the model will speed up learning.

Transformations can also be motivated by observing that they make the non-diagonal parts of the Fisher information matrix closer to zero [9] and keep the diagonal of the Fisher information matrix similar in scale [12].

The goal of Equation (4) is to normalize both the output signals (similarly as data is often normalized as a preprocessing step – see,e.g., [7]) and the slopes of the output signals of each hidden unit at the same time. This is motivated by observing that the diagonal of the Fisher information matrix contains elements with both the signals and their slopes. By these normalizations, we aim pushing these diagonal elements more

similar to each other. As we cannot normalize both the signals and the slopes to unity at the same time, we normalize their geometric mean to unity.

The effect of the first two transformations can be compensated exactly by updating the shortcut mapping $\mathbf{C}$ by

$$\begin{aligned}\mathbf{C}_{\text{new}} = \mathbf{C}_{\text{old}} &- \mathbf{A}(\boldsymbol{\alpha}_{\text{new}} - \boldsymbol{\alpha}_{\text{old}})\mathbf{B} \\ &- \mathbf{A}(\boldsymbol{\beta}_{\text{new}} - \boldsymbol{\beta}_{\text{old}})\,[0 \;\; 0 \ldots 1]\,,\end{aligned} \tag{10}$$

where $\boldsymbol{\alpha}$ is a matrix with elements α_i on the diagonal and one empty row below for the bias term, and $\boldsymbol{\beta}$ is a column vector with components β_i and one zero below for the bias term. The third transformation can be compensated by

$$\mathbf{A}_{\text{new}} = \mathbf{A}_{\text{old}}\boldsymbol{\gamma}_{\text{old}}\boldsymbol{\gamma}_{\text{new}}^{-1}, \tag{11}$$

where $\boldsymbol{\gamma}$ is a diagonal matrix with γ_i as the diagonal elements.

Schraudolph [11, 10] proposed centering the factors of the gradient to zero mean. It was argued that deviations from the gradient fall into the linear subspace that the shortcut connections operate in, so they do not harm the overall performance. Transforming the nonlinearities as proposed in this paper has a similar effect on the gradient. Equation (3a) corresponds to Schraudolph's *activity centering* and Equation (3b) corresponds to *slope centering*.

3 Empirical Comparison to a Second-Order Method

Here we investigate how linear transformations affect the gradient by comparing it to a second-order method, namely Newton's algorithm with a simple regularization to make the Hessian invertible.

We compute an approximation of the Hessian matrix using finite difference method, in which case k-th row vector $\mathbf{h}_k$ of the Hessian matrix $\mathbf{H}$ is given by

$$\mathbf{h}_k = \frac{\partial(\nabla E(\boldsymbol{\theta}))}{\partial\theta_k} \approx \frac{\nabla E(\boldsymbol{\theta} + \delta\boldsymbol{\phi}_k) - \nabla E(\boldsymbol{\theta} - \delta\boldsymbol{\phi}_k)}{2\delta}, \tag{12}$$

where $\boldsymbol{\phi}_k = (0, 0, \ldots, 1, \ldots, 0)$ is a vector of zeros and 1 at the k-th position, and the error function $E(\boldsymbol{\theta}) = -\sum_t \log p(\mathbf{y}_t \mid \mathbf{x}_t, \boldsymbol{\theta})$. The resulting Hessian might still contain some very small or even negative eigenvalues which cause its inversion to blow up. Therefore we do not use the Hessian directly, but include a regularization term similarly as in the Levenberg-Marquardt algorithm, resulting in a second-order update direction

$$\Delta\boldsymbol{\theta} = (\mathbf{H} + \mu\mathbf{I})^{-1}\nabla E(\boldsymbol{\theta}), \tag{13}$$

where $\mathbf{I}$ denotes the unit matrix. Basically, Equation (13) combines the steepest descent and the second-order update rule in such a way, that when μ gets small, the update direction approaches the Newton's method and vice versa.

Computing the Hessian is computationally demanding and therefore we have to limit the size of the network used in the experiment. We study the MNIST handwritten digit classification problem where the dimensionality of the input data has been reduced to

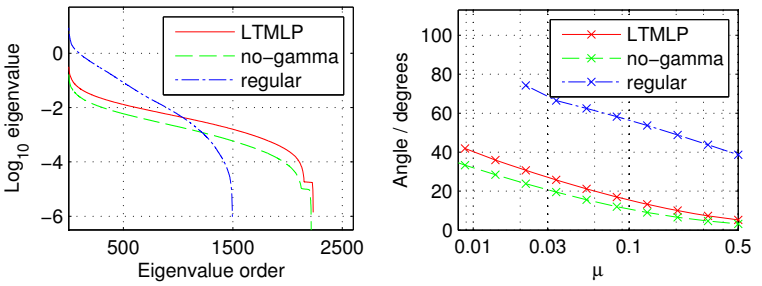

(a) Eigenvalues (b) Angles

Fig. 1. Comparison of (a) distributions of the eigenvalues of Hessians (2600×2600 matrix) and (b) angles compared to the second-order update directions using LTMLP and regular MLP. In (a), the eigenvalues are distributed most evenly when using LTMLP. (b) shows that gradients of the transformed networks point to the directions closer to the second-order update.

30 using PCA with a random rotation [9]. We use a network with two hidden layers with architecture 30–25–20–10. The network was trained using the standard gradient descent with weight decay regularization. Details of the training are given in [12].

In what follows, networks with all three transformations (*LTMLP*, linearly transformed multi-layer perceptron network), with two transformations (*no-gamma* where all γ_i are fixed to unity) and a network with no transformations (*regular*, where we fix $\alpha_i = 0$, $\beta_i = 0$, and $\gamma_i = 1$) were compared. The Hessian matrix was approximated according to Equation (12) 10 times in regular intervals during the training of networks. All figures are shown using the approximation after 4000 epochs of training, which roughly corresponds to the midpoint of learning. However, the results were parallel to the reported ones all along the training.

We studied the eigenvalues of the Hessian matrix (2600×2600) and the angles between the methods compared and second-order update direction. in the same training phase, after epoch number 4000. The distribution of eigenvalues in Figure 1a for the networks with transformations are more even compared to the regular MLP. Furthermore, there are fewer negative eigenvalues, which are not shown in the plot, in the transformed networks. In Figure 1b, the angles between the gradient and the second-order update direction are compared as a function of μ in Equation (13). The plots are cut when $\mathbf{H} + \mu\mathbf{I}$ ceases to be positive definite as μ decreases. Curiously, the update directions are closer to the second-order method, when γ is left out, suggesting that γs are not necessarily useful in this respect.

Figure 2 shows histograms of the diagonal elements of the Hessian after 4000 epochs of training. All the distributions are bimodal, but the distributions are closer to unimodal when transformations are used (subfigures (a) and (b))[1]. Furthermore, the variance of the diagonal elements in log-scale is smaller when using LTMLP, $\sigma_{\mathrm{a}}^2 = 0.90$, compared to the other two, $\sigma_{\mathrm{b}}^2 = 1.71$ and $\sigma_{\mathrm{c}}^2 = 1.43$. This suggests that when transformations are used, the second-order update rule in Equation (13) corrects different elements of the

[1] It can be also argued whether (a) is more unimodal compared to (b).

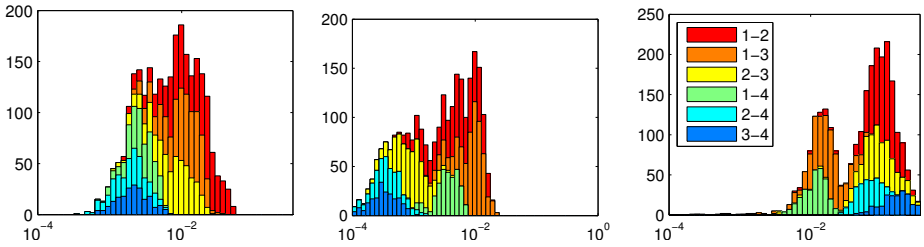

(a) LTMLP (b) no-gamma (c) regular

Fig. 2. Comparison of distributions of the diagonal elements of Hessians. Coloring according to legend in (c) shows which layers to corresponding weights connect (1 = input, 4 = output). Diagonal elements are most concentrated in LTMLP and more spread in the networks without γ (no-gamma, regular). Notice the logarithmic x-axis.

gradient vector more evenly compared to a regular back-propagation learning, implying that the gradient vector is closer to the second-order update direction when using all the transformations.

To conclude this section, there is no clear evidence in way or another whether the addition of γ benefits the back-propagation learning with only α and β. However, there are some differences between these two approaches. In any case, it seems clear that transforming the nonlinearities benefits the learning compared to the standard back-propagation learning.

4 Experiments: MNIST Classification

We use the proposed transformations for training MLP networks for MNIST classification task. Experiments are conducted without pretraining, weight-sharing, enhancements of the training set or any other known tricks to boost the performance. No weight decay is used and as only regularization we add Gaussian noise with $\sigma = 0.3$ to the training data. Networks with two and three hidden layers with architechtures 784–800–800–10 (solid lines) and 784–400–400–400–10 (dashed lines) are used. Details are given in [12].

Figure 3 shows the results as number of errors in classifying the test set of 10 000 samples. The results of the regular back-propagation without transformations, shown in blue, are well in line with previously published result for this task. When networks with same architecture are trained using the proposed transformations, the results are improved significantly. However, adding γ in addition to previously proposed α and β does not seem to affect results on this data set. The best results, 112 errors, is obtained by the smaller architecture without γ and for the three-layer architecture with γ the result is 114 errors. The learning seems to converge faster, especially in the three-layer case, with γ. The results are in line what was obtained in [9] where the networks were regularized more thoroughly. These results show that it is possible to obtain results comparable to dropout networks (see [4]) using only minimal regularization.

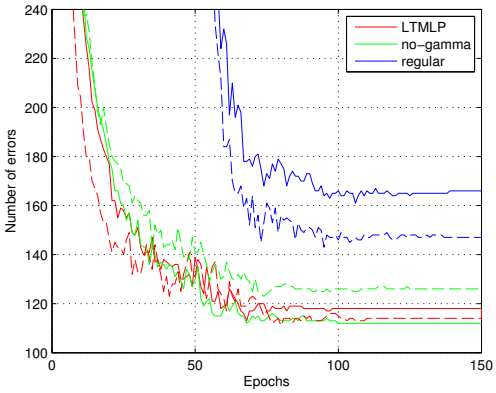

Fig. 3. The error rate on the MNIST test set for LTMLP training, LTMLP without γ and regular back-propagation. The solid lines show results for networks with two hidden layers of 800 neurons and the dashed lines for networks with three hidden layers of 400 neurons.

5 Discussion and Conclusions

We have shown that introducing linear transformation in nonlinearities significantly improves the back-propagation learning in (deep) MLP networks. In addition to two transformation proposed earlier in [9], we propose adding a third transformation in order to push the Fisher information matrix closer to unit matrix (apart from its scale). The hypothesis proposed in [9], that the transformations actually mimic a second-order update rule, was confirmed by experiments comparing the networks with transformations and regular MLP network to a second-order update method. However, in order to find out whether the third transformation, γ, we proposed in this paper, is really useful, more experiments ought to be conducted. It might be useful to design experiments where convergence is usually very slow, thus revealing possible differences between the methods. As hyperparameter selection and regularization are usually nuisance in practical use of neural networks, it would be interesting to see whether combining dropouts [4] and our transformations can provide a robust framework enabling training of robust neural networks in reasonable time.

The effect of the first two transformations is very similar to gradient factor centering [11, 10], but transforming the model instead of the gradient makes it easier to generalize to other contexts: When learning by by Markov chain Monte Carlo, variational Bayes, or by genetic algorithms, one would not compute the basic gradient at all. For instance, consider using the Metropolis algorithm on the weight matrices, and expecially matrices $\mathbf{A}$ and $\mathbf{B}$. Without transformations, the proposed jumps would affect the expected output $\mathbf{y}_t$ and the expected linear dependency $\partial \mathbf{y}_t / \partial \mathbf{x}_t$ in Eqs. (8)–(9), thus often leading to low acceptance probability and poor mixing. With the proposed transformations included, longer proposed jumps in $\mathbf{A}$ and $\mathbf{B}$ could be accepted, thus mixing the nonlinear part of the mapping faster. For further discussion, see [9], Section 6. The implications of the proposed transformations in these other contexts are left as future work.

References

[1] Amari, S.: Natural gradient works efficiently in learning. Neural Computation 10(2), 251–276 (1998)

[2] Ciresan, D.C., Meier, U., Gambardella, L.M., Schmidhuber, J.: Deep big simple neural nets excel on handwritten digit recognition. CoRR, abs/1003.0358 (2010)

[3] Hinton, G.E., Salakhutdinov, R.R.: Reducing the dimensionality of data with neural networks. Science 313(5786), 504–507 (2006)

[4] Hinton, G.E., Srivastava, N., Krizhevsky, A., Sutskever, I., Salakhutdinov, R.: Improving neural networks by preventing co-adaptation of feature detectors. CoRR, abs/1207.0580 (2012)

[5] Krizhevsky, A., Sutskever, I., Hinton, G.E.: Imagenet classification with deep convolutional neural networks (2012)

[6] Le Roux, N., Manzagol, P.A., Bengio, Y.: Topmoumoute online natural gradient algorithm. In: Advances in Neural Information Processing Systems 20, NIPS 2007 (2008)

[7] LeCun, Y.A., Bottou, L., Orr, G.B., Müller, K.-R.: Efficient backProp. In: Orr, G.B., Müller, K.-R. (eds.) NIPS-WS 1996. LNCS, vol. 1524, pp. 9–48. Springer, Heidelberg (1998)

[8] Martens, J.: Deep learning via Hessian-free optimization. In: Proceedings of the 27th International Conference on Machine Learning, ICML (2010)

[9] Raiko, T., Valpola, H., LeCun, Y.: Deep learning made easier by linear transformations in perceptrons. Journal of Machine Learning Research - Proceedings Track 22, 924–932 (2012)

[10] Schraudolph, N.N.: Accelerated gradient descent by factor-centering decomposition. Technical Report IDSIA-33-98, Istituto Dalle Molle di Studi sull'Intelligenza Artificiale (1998)

[11] Schraudolph, N.N.: Centering neural network gradient factors. In: Orr, G.B., Müller, K.-R. (eds.) NIPS-WS 1996. LNCS, vol. 1524, pp. 207–548. Springer, Heidelberg (1998)

[12] Vatanen, T., Raiko, T., Valpola, H., LeCun, Y.: Pushing stochastic gradient towards second-order methods – backpropagation learning with transformations in nonlinearities (pre-print, 2013), `http://arxiv.org/abs/1301.3476`

Two-Layer Contractive Encodings with Shortcuts for Semi-supervised Learning

Hannes Schulz[1], Kyunghyun Cho[2], Tapani Raiko[2], and Sven Behnke[1]

[1] Autonomous Intelligent Systems, Computer Science Institute VI
University of Bonn, Germany
{schulz,behnke}@ais.uni-bonn.de
[2] Department of Information and Computer Science
Aalto University School of Science, Finland
{kyunghyun.cho,tapani.raiko}@aalto.fi

Abstract. Supervised training of multi-layer perceptrons (MLP) with only few labeled examples is prone to overfitting. Pretraining an MLP with unlabeled samples of the input distribution may achieve better generalization. Usually, pretraining is done in a layer-wise, greedy fashion which limits the complexity of the learnable features. To overcome this limitation, two-layer contractive encodings have been proposed recently—which pose a more difficult optimization problem, however. On the other hand, linear transformations of perceptrons have been proposed to make optimization of deep networks easier. In this paper, we propose to combine these two approaches. Experiments on handwritten digit recognition show the benefits of our combined approach to semi-supervised learning.

Keywords: Multi-Layer Perceptron, Two-Layer Contractive Encoding, Linear Transformation, Semi-Supervised Learning.

1 Introduction

Multi-layer perceptrons (MLP) are provably powerful enough to learn any nonlinear classification or regression task [8]. While networks with a single—possibly very wide—hidden layer suffice in principle, deep networks—having multiple hidden layers—can be much more efficient. Without proper initialization or regularization it is, however, difficult to achieve good generalization with deep MLPs (see, e.g., [1]).

Layer-wise pretraining, which initializes the parameters of an MLP in an unsupervised manner, was proposed to overcome this problem [7,12,3]. This is motivated by the cost of data acquisition. Frequently, only a few manually annotated training examples are available together with a vast amount of easily obtainable *unlabeled* samples from the input distribution. Semi-supervised learning [5] aims to utilize not only the labeled examples but also the unlabeled samples to improve generalization performance of a classifier. Unsupervised pretraining of MLPs naturally fits to this setting, as the layer-wise learning of representations does not require any labels.

In short, deep MLPs can be initialized with pretraining using vast amounts of unlabeled input samples and subsequently finetuned with (few) labeled examples.

M. Lee et al. (Eds.): ICONIP 2013, Part I, LNCS 8226, pp. 450–457, 2013.
© Springer-Verlag Berlin Heidelberg 2013

Layer-wise pretraining has the problem that the complexity of the learnable features is limited to a linear mapping of the inputs followed by a non-linear output transformation, such as rectification or sigmoidal squashing. To overcome this limitation, Schulz and Behnke recently proposed two-layer contractive encodings for unsupervised learning the next layer of representation [15]. This approach requires training a regularized autoencoder with three hidden layers—a complex non-linear optimization problem.

Here, we propose to add shortcuts to the autoencoder, which allows for learning a combination of simple and complex features. Our training procedure utilizes the method of linearly transforming perceptrons, recently proposed by Raiko et al. [10].

We evaluate the proposed two-layer encoding with shortcuts method on the task of semi-supervised classification of handwritten digits and show that it achieves better generalization than greedy pretraining methods when only a few labeled examples are available.

2 Motivation

2.1 Unsupervised Pretraining and Supervised Finetuning of Deep MLPs

Unsupervised pretraining is a natural way to incorporate vast amounts of unlabeled input samples into the training of MLPs (see, e.g., [7]). As the MLP parameters are initialized in an *unsupervised* manner, all available samples including both labeled and unlabeled ones may be exploited during pretraining. Training continues with supervised finetuning of the whole model which uses only the labeled examples. One example for such an approach is [11] which showed that pretraining helps improving generalization performance when only a few labeled samples together with a large amount of unlabeled samples were available.

The most prominent method for pretraining MLPs is layer-wise learning of the next level of representation [7,3,12]. This greedy method sequentially trains—on the basis of the so far learned representations—local autoencoders or local generative models between consecutive layers in an unsupervised manner.

One hypothesis by Bengio et al. [1,2] on why the greedy layer-wise pretraining helps in semi-supervised learning is that stacking of unsupervised neural networks disentangles factors of variations and that the untangled representations make discriminative learning easier. With only a linear mapping, followed by a non-linear transfer function, the complexity of the local recodings is limited, however. Hence, greedy layer-wise pretraining may fail to disentangle non-linear manifolds introduced by common input variations, such as translation, rotation, or scaling of input images. One way to overcome the limitations of greedy layer-wise pretraining is to make the local encoding models more powerful.

2.2 Limitations of Simple Local Models

One example where simple local models, i.e. models with a single hidden layer, fail to discover features that are inherently nonlinear has been described by Schulz and Behnke [15]. In certain cases, it was shown that greedy layer-wise pretraining could actually hurt the overall performance of an MLP.

To overcome this limitation, Schulz and Behnke [15] proposed a two-layer contractive encoding as a way to pretrain an MLP with more powerful local models. The experiments in [15] revealed that a better classification performance can be achieved by using the two-layer contractive encoding as a building block than by using a neural network with a single hidden layer.

In the two layer encoding, the autoencoder is a deep neural network itself, having three hidden layers. Hence, it might be difficult to train with stochastic gradient methods (SGD). To deal with this problem, Raiko et al. [10] proposed to linearly transform each hidden neuron, while also introducing connections that skip the hidden layer. They showed that in this way, it is possible to train a deep neural network directly with good generalization performance. This approach effectively makes SGD similar to second-order optimization methods [16] without sacrificing its computational advantages.

In this paper, we propose to combine the two techniques, allowing for complex local models, but also having shortcuts that realize the simple parts of the encodings. We provide empirical evidence that it is beneficial to use both the two-layer contractive encoding and the linear transformation for pretraining. In other words, we claim that a less greedy pretraining approach requires both well-founded regularization and a powerful learning algorithm.

3 Background

In this section, we discuss each one of those two methods combined on our approach—the linear transformations and the two-layer contractive encoding—in more detail.

3.1 Linear Transformations in Perceptrons

Let us focus on a single hidden layer within a possibly deep MLP network. The inputs to this layer are denoted $\mathbf{x}_t$ and its outputs are $\mathbf{y}_t$, where t is the sample index. We allow short-cut connections that by-pass one or more hidden layers, i.e. the inputs may be distributed over several previous layers of the network. The mapping from $\mathbf{x}_t$ to $\mathbf{y}_t$ is modeled as

$$\mathbf{y}_t = \mathbf{A}\mathbf{f}\left(\mathbf{B}\mathbf{x}_t\right) + \mathbf{C}\mathbf{x}_t, \tag{1}$$

where $\mathbf{f}$ is a nonlinearity (such as $\tanh$) applied to each component of the argument vector separately and $\mathbf{A}$, $\mathbf{B}$, and $\mathbf{C}$ are weight matrices. In order to avoid separate bias vectors that complicate formulas, the input vectors $\mathbf{x}_t$ are assumed to have been supplemented with an additional component that is always one.

Let us supplement the $\tanh$ nonlinearity with auxiliary scalar variables α_i and β_i for each nonlinearity f_i. They are updated during training in order to help learning of the other parameters $\mathbf{A}$, $\mathbf{B}$, and $\mathbf{C}$. We define

$$f_i(\mathbf{b}_i\mathbf{x}_t) = \tanh(\mathbf{b}_i\mathbf{x}_t) + \alpha_i\mathbf{b}_i\mathbf{x}_t + \beta_i, \tag{2}$$

where $\mathbf{b}_i$ is the ith row vector of matrix $\mathbf{B}$. We will ensure that

$$0 = \sum_{t=1}^{T} f_i(\mathbf{b}_i\mathbf{x}_t), \qquad 0 = \sum_{t=1}^{T} f_i'(\mathbf{b}_i\mathbf{x}_t) \tag{3}$$

by setting α_i and β_i to

$$\alpha_i = -\frac{1}{T}\sum_{t=1}^{T} \tanh'(\mathbf{b}_i\mathbf{x}_t), \qquad \beta_i = -\frac{1}{T}\sum_{t=1}^{T} \left[\tanh(\mathbf{b}_i\mathbf{x}_t) + \alpha_i \mathbf{b}_i\mathbf{x}_t\right].$$

These seemingly arbitrary update rules are motivated below.

The effect of changing the transformation parameters α_i and β_i are compensated exactly by updating the shortcut mapping $\mathbf{C}$ by

$$\mathbf{C}_{\text{new}} = \mathbf{C}_{\text{old}} - \mathbf{A}(\boldsymbol{\alpha}_{\text{new}} - \boldsymbol{\alpha}_{\text{old}})\mathbf{B} - \mathbf{A}(\boldsymbol{\beta}_{\text{new}} - \boldsymbol{\beta}_{\text{old}})\,[0 \;\; 0 \ldots 1]\,, \tag{4}$$

where $\boldsymbol{\alpha}$ is a matrix with elements α_i on the diagonal and one empty row below for the bias term, and $\boldsymbol{\beta}$ is a column vector with components β_i and one zero below for the bias term. Thus, any change in α_i and β_i does not change the overall mapping from $\mathbf{x}_t$ to $\mathbf{y}_t$ at all, but they do change the optimization problem instead.

One way to motivate the transformations in Equations (3), is to study the expected output $\mathbf{y}_t$ and its dependency on the input $\mathbf{x}_t$:

$$\frac{1}{T}\sum_t \mathbf{y}_t = \mathbf{A}\left[\frac{1}{T}\sum_t \mathbf{f}(\mathbf{B}\mathbf{x}_t)\right] + \mathbf{C}\left[\frac{1}{T}\sum_t \mathbf{x}_t\right] \tag{5}$$

$$\frac{1}{T}\sum_t \frac{\partial \mathbf{y}_t}{\partial \mathbf{x}_t} = \mathbf{A}\left[\frac{1}{T}\sum_t \mathbf{f}'(\mathbf{B}\mathbf{x}_t)\right]\mathbf{B}^T + \mathbf{C} \tag{6}$$

We note that by making nonlinear activations $\mathbf{f}(\cdot)$ zero mean in Eq. (3) (left), we disallow the nonlinear mapping $\mathbf{A}\mathbf{f}\,(\mathbf{B}\cdot)$ to affect the expected output $\mathbf{y}_t$, that is, to compete with the bias term. Similarly, by making the nonlinear activations $\mathbf{f}(\cdot)$ zero slope in Eq. (3) (right), we disallow the nonlinear mapping $\mathbf{A}\mathbf{f}\,(\mathbf{B}\cdot)$ from affecting the expected dependency on the input, that is, to compete with the linear short-cut mapping $\mathbf{C}$. In traditional neural networks, the linear dependencies (expected $\partial\mathbf{y}_t/\partial\mathbf{x}_t$) are modeled by many competing paths from an input to an output (e.g. via each hidden unit), whereas this architecture gathers the linear dependencies to be modeled only by $\mathbf{C}$.

In [10] it was shown experimentally that less competition between parts of the model will speed up learning. In [16], more careful connections to second-order optimization methods were drawn.

3.2 Two-Layer Contractive Encoding

A common regularizer for MLPs is the L_2 penalty on the weight matrices. This regularizer is well-motivated for linear methods (e.g. ridge regression or logistic regression), where it penalizes strong dependence of $\mathbf{y}$ on few variables in $\mathbf{x}$, and thus ensures invariance of $\mathbf{y}$ to small changes in $\mathbf{x}$. For MLPs, which contain saturating non-linearities, this desirable property can be achieved with strongly positive or negative weights as well. Rifai et al. [14] show that the generalization of the L_2-norm penalty to the case where non-linearities are involved in the computation of $\mathbf{y}$ is a penalty on the Frobenius norm of the Jacobian $\|J_{\mathbf{y}}(\mathbf{x})\|_F$ ("contractive" regularization). [14,13] demonstrate that

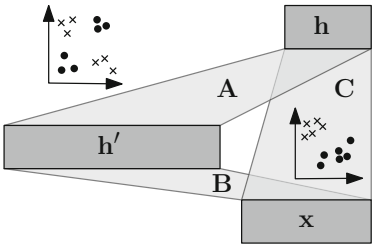

Fig. 1. Schematic visualization of our encoder. Features $\mathbf{h}$ of input $\mathbf{x}$ are determined both by a one-layer encoder via $\mathbf{C}$, and by a two-layer encoder via $\mathbf{B}$ and $\mathbf{A}$. Contractive regularization [14] and two-layer contractive regularization [15] are used to learn stable linear/non-linear representations in $\mathbf{h}$, respectively. Linear transformations in the two-layer part are moved to $\mathbf{C}$ using compensations [10] (not shown).

pretraining simple auto-encoders with the contractive penalty produces features which identify the data manifold and can aid finetuning. However, Schulz and Behnke [15] demonstrate that auto-encoders with one hidden layer can fail to identify stable features in the input when their variables in $\mathbf{x}$ are XOR-related. They generalize the contractive regularizer to the two-layer case,

$$\|J_{\mathbf{h}}(\mathbf{x})\|_F^2 = \sum_n^N \sum_m^M \left(1 - \mathbf{h}_n^2\right)^2 \left(\sum_k^K \mathbf{A}_{nk}\mathbf{B}_{km}(1 - \mathbf{h'}_k^2)\right)^2 , \tag{7}$$

where $\mathbf{x} \in \mathbb{R}^M, \mathbf{B} \in \mathbb{R}^{K\times M}, \mathbf{A} \in \mathbb{R}^{N\times K}$, and $\mathbf{h} = \tanh(\mathbf{A}\tanh(\mathbf{Bx})) = \tanh(\mathbf{Ah'})$.

In this paper, we argue that while two-layer encodings are harder to learn, we can combine their ability to detect highly non-linear features with the easy-to-learn one-layer encodings by introducing shortcuts. Shortcut weights $\mathbf{C}$ from the input to the second hidden layer can be regularized as in [14], while the two-layer encoder is regularized as in [15]. We employ linear transformations and compensations (Sec. 3.1) to ensure that simple features continue to be learned by the shortcut weights, while the two-layer part of the encoder can focus on the difficult features. For this purpose, we extend the two-layer contractive regularizer to account for the linear transformations in (1) and (2),

$$\|J_{\mathbf{h}}(\mathbf{x})\|_F^2 = \sum \left(1 - \mathbf{h}^2\right)^{2^T} \left(\mathbf{C} + \mathbf{A}(\mathbf{B}^\alpha + \mathbf{B'})\right)^2 , \tag{8}$$

where $\mathbf{B}^\alpha_{km} = \alpha_k \mathbf{B}_{km}$, $\mathbf{B'}_{km} = \mathbf{B}_{km}(1 - \tanh^2(\mathbf{B}_{k\cdot}\mathbf{x}))$. Fig. 1 illustrates the proposed encoder structure.

4 Experiments

We evaluate the proposed approach in a semi-supervised setting using a handwritten digit dataset (MNIST, [9]). We assume that only 1200 training samples have their labels available, while all the other training samples are unlabeled. The task is to use an MLP trained on the training samples to classify 10,000 test samples.

4.1 Model and Learning

Our base model is a multi-layer perceptron (MLP) with two hidden layers having $\tanh$ hidden neurons. The output of the MLP is

$$\mathbf{y} = \mathbf{W}\left(\tanh\left(\mathbf{A}\tanh\left(\mathbf{Bx}\right)\right)\right), \tag{9}$$

Table 1. Classification accuracies depending on training strategy on MNIST using 1200 labeled examples, and the size of the second hidden layer fixed to 100. Standard deviations are over 10 trials with different draws of the training set.

Strategy	Test Error	Std. Dev.
S	13.27	1.47
U+S	8.835	0.33
C+U+S	8.989	0.25
T+U+S	9.132	0.19
2C	8.77	0.43
C+T+U+S	**8.695**	0.41

where $\mathbf{W}$, $\mathbf{A}$ and $\mathbf{B}$ are weight matrices. We have omitted biases for simplicity of notation. As baseline we trained this MLP both with and without pretraining. For the pretrained MLP we consider the bottom two layers as an autoencoder with two hidden layers and trained them using both labeled and unlabeled samples.

When the hidden neurons, or perceptrons, in the MLP were linearly transformed, we added shortcut connections from the input to the second hidden layer to maintain the equivalence after the transformation. In that case, the output of the MLP is

$$\mathbf{y} = \mathbf{W}\mathbf{h} = \mathbf{W}\tanh(\mathbf{A}\mathbf{h}' + \mathbf{C}\mathbf{x}), \tag{10}$$

where $\mathbf{h}' = \tanh(\mathbf{B}\mathbf{x}) + \mathbf{B}^{\alpha}\mathbf{x} + \boldsymbol{\beta}$, and $\mathbf{C}$ is the weight matrix of the shortcuts.[1].

As a comparison, we tried both using either one of the two-layer contractive encoding and the linear transformation and using both of them together. In this way, we can easily see the effectiveness of the proposed way of using both approaches together.

Specifically, we used six different training strategies:

1. **S**: MLP trained with labeled samples only
2. **U+S**: MLP pretrained with unlabeled samples and finetuned
3. **2C**: MLP pretrained with stacked contractive auto-encoders
4. **C+U+S**: MLP pretrained and finetuned with two-layer contractive encoding
5. **T+U+S**: MLP with shortcuts pretrained and finetuned with linear transformation
6. **C+T+U+S**: MLP with shortcuts pretrained and finetuned using both the two-layer contractive encoding and linear transformation

We estimated hyperparameters such as learning rates, weight decay constant, regularization strength and the size of the first hidden layer using hyperopt [4]. The number of training epochs is determined with early stopping. For pre-training, we minimized reconstruction error on a 10 000 sample validation set for every training strategy. We then determined 1200 labeled training samples randomly and employed five-fold cross validation and hyperopt to determine learning rates for finetuning on the cross-entropy loss function. To reduce overfitting induced by the small size of labeled samples, we fixed the number of hidden neurons in the second hidden layer to 100 (see, e.g., [3]). The weight matrices $\mathbf{A}$ and $\mathbf{B}$ were initialized randomly according to the normalized scale [6], while $\mathbf{C}$ was initialized with zeroes.

[1] When we pretrained the MLP as a two-layer contractive encoding, we tied the weights $\mathbf{A}$ and $\mathbf{B}$ between the encoder and decoder. However, we did not share $\mathbf{C}$, α_l's and β_l's.

Once the hyperparameters were found, we evaluated each strategy by training 10 MLPs with different sets of randomly sampled 1200 labeled training samples and classifying the held-out test samples.

4.2 Result and Analysis

In Table 1, the resulting classification accuracies for all six strategies are presented. As expected, any approach with pretraining significantly outperforms the case where only labeled samples were used for supervised training (**S**). The best performing strategy was the one which pretrained the MLP as the two-layer contractive encoding using the linear transformation (**C+T+U+S**). This strategy was able to outperform the strategies **U+S**, **C+U+S** as well as **T+U+S**. Our proposed method also has a slight advantage over the stacked contractive auto-encoder (**2C**).

Interestingly, using either the two-layer contractive encoding or the linear transformation only turned out to be just as good as the naïve pretraining strategy (**U+S**). This suggests that it is not easy to train the two-layer contractive encoding well without a good training algorithm. Only when training became easier by linearly transforming perceptrons to have zero-mean and zero-slope on average, we were able to see the improvement (**C+T+U+S**), which confirms our claim.

5 Conclusions

In this paper, we claimed that pretraining a multi-layer perceptron (MLP) with two-layer local models can be improved by having both good regularization based on minimizing the Jacobian of hidden activations with respect to the input [15,14] and powerful learning algorithm based on linearly transforming hidden neurons [10,16]. We focused on validating this claim in a semi-supervised setting where only few labeled samples and vast amount of unlabeled samples are available.

We empirically demonstrated the validity of our claim by considering a task of classifying handwritten digits using an MLP when only 1200 training samples out of 60,000 were assumed to have annotated labels. It was clear from the experiment that pretraining indeed helps significantly when there are only few labeled training examples. Furthermore, we were able to see that generalization performance could be improved by pretraining an MLP with a two-layer contractive encoding using the linear transformation, confirming the validity of our claim.

The experiments reported in the paper are, however, limited in two dimensions. Firstly, the structure of the MLP was limited to have only two hidden layers, and a small fixed-size second hidden layer, which makes it important for future research to evaluate the proposed method with larger and deeper models. Secondly, it will be desirable to evaluate the proposed method with other datasets.

Acknowledgements. This work was supported by the Academy of Finland (Finnish Centre of Excellence in Computational Inference Research COIN, 251170).

References

1. Bengio, Y.: Learning deep architectures for AI. Foundations and Trends in Machine Learning 2(1), 1–127 (2009)
2. Bengio, Y., Courville, A., Vincent, P.: Representation learning: A review and new perspectives. IEEE Transactions on Pattern Analysis and Machine Intelligence Special Issue on Learning Deep Architectures (2013); early Access
3. Bengio, Y., Lamblin, P., Popovici, D., Larochelle, H.: Greedy layer-wise training of deep networks. In: Schölkopf, B., Platt, J., Hoffman, T. (eds.) Advances in Neural Information Processing Systems, vol. 19, pp. 153–160. MIT Press, Cambridge (2007)
4. Bergstra, J., Bardenet, R., Bengio, Y., Kgl, B.: Algorithms for hyper-parameter optimization. In: Shawe-Taylor, J., Zemel, R., Bartlett, P., Pereira, F., Weinberger, K. (eds.) Advances in Neural Information Processing Systems, vol. 24, pp. 2546–2554 (2011)
5. Chapelle, O., Schölkopf, B., Zien, A. (eds.): Semi-Supervised Learning. MIT Press, Cambridge (2006)
6. Glorot, X., Bengio, Y.: Understanding the difficulty of training deep feedforward neural networks. In: Proceedings of the Thirteenth International Conference on Artificial Intelligence and Statistics (AISTATS), JMLR Workshop and Conference Proceedings, vol. 9, pp. 249–256. JMLR W&CP (2010)
7. Hinton, G., Salakhutdinov, R.: Reducing the dimensionality of data with neural networks. Science 313(5786), 504–507 (2006)
8. Hornik, K., Stinchcombe, M., White, H.: Multilayer feedforward networks are universal approximators. Neural Networks 2(5), 359–366 (1989)
9. LeCun, Y., Bottou, L., Bengio, Y., Haffner, P.: Gradient-based learning applied to document recognition. Proceedings of the IEEE 86(11), 2278–2324 (1998)
10. Raiko, T., Valpola, H., LeCun, Y.: Deep learning made easier by linear transformations in perceptrons. In: Proceedings of the Fifteenth Internation Conference on Artificial Intelligence and Statistics (AISTATS), JMLR Workshop and Conference Proceedings, vol. 22, pp. 924–932. JMLR W&CP (April 2012)
11. Ranzato, M., Huang, F.J., Boureau, Y.L., LeCun, Y.: Unsupervised learning of invariant feature hierarchies with applications to object recognition. In: IEEE Conference on Computer Vision and Pattern Recognition (CVPR), pp. 1–8 (2007)
12. Ranzato, M., Poultney, C., Chopra, S., LeCun, Y.: Efficient learning of sparse representations with an energy-based model. In: Schölkopf, B., Platt, J., Hoffman, T. (eds.) Advances in Neural Information Processing Systems 19, pp. 1137–1144. MIT Press, Cambridge (2007)
13. Rifai, S., Mesnil, G., Vincent, P., Muller, X., Bengio, Y., Dauphin, Y., Glorot, X.: Higher order contractive auto-encoder. In: Gunopulos, D., Hofmann, T., Malerba, D., Vazirgiannis, M. (eds.) ECML PKDD 2011, Part II. LNCS, vol. 6912, pp. 645–660. Springer, Heidelberg (2011)
14. Rifai, S., Vincent, P., Muller, X., Glorot, X., Bengio, Y.: Contractive auto-encoders: Explicit invariance during feature extraction. In: Getoor, L., Scheffer, T. (eds.) Proceedings of the 28th International Conference on Machine Learning (ICML), pp. 833–840. ACM, New York (2011)
15. Schulz, H., Behnke, S.: Learning two-layer contractive encodings. In: Villa, A.E.P., Duch, W., Érdi, P., Masulli, F., Palm, G. (eds.) ICANN 2012, Part I. LNCS, vol. 7552, pp. 620–628. Springer, Heidelberg (2012)
16. Vatanen, T., Raiko, T., Valpola, H., LeCun, Y.: Pushing stochastic gradient towards second-order methods – backpropagation learning with transformations in nonlinearities. arXiv:1301.3476 [cs.LG] (May 2013)

Deep Network with Support Vector Machines

Sangwook Kim, Swathi Kavuri, and Minho Lee*

School of Electronics Engineering, Kyungpook National University,
1370 Sankyuk-Dong, Puk-Gu, Taegu 702-701, South Korea
sangwook@ee.knu.ac.kr,{swati.kavuri,mholee}@gmail.com

Abstract. Deep learning methods aims at learning features automatically at multiple levels that allow the system to learn complex functions mapping the input to the output directly from data. This ability to automatically learn powerful features will become increasingly important as the amount of data and range of applications to machine learning methods continues to grow. In this context we propose a deep architecture model using Support Vector Machine (SVM) which has inherent ability to select data points important for classification with good generalization capabilities. Since SVM can effectively discriminate features, we used support vectors with kernel as non-linear discriminant features for classification. By stacking SVMs in to multiple layers, we can obtain deep features without extra feature engineering steps and get robust recognition accuracy. Experimental results show that the proposed method improves generalization performance on Wisconsin Breast Cancer dataset.

Keywords: pattern recognition, deep learning, support vector machine.

1 Introduction

Classification results of learning algorithms are inherently limited in performance by the features extracted [1]. Deep learning is required to learn complicated function that can represent higher level extractions. Deep learning architectures consist of multiple intermediate layers rather than a single hidden layer, and adequate learning algorithm to train those layers. For the deep learning, multiple layers are expected to replace manual domain-specific feature engineering [2]. Also, recent neuroscience researches have provided backgrounds to deep feature extraction [1]. Besides the early attentions to the importance of deep architecture [3,4], deep learning was not prevalent since there was no effective learning method applicable for existing learning machines except few models [5,6]. Restricted Boltzmann Machine (RBM) is a generative stochastic neural network that can learn a probability distribution over its set of inputs and initially, was invented by Smolensky in 1986 [7]. But as G. Hinton et al. proposed the RBM network with contrastive divergence [8], deep architectures using RBM network become popular for many pattern recognition and machine learning application and start to win prizes at several pattern recognition competitions without complex manual feature engineering. Although well-trained RBM networks show

* Corresponding author.

M. Lee et al. (Eds.): ICONIP 2013, Part I, LNCS 8226, pp. 458–465, 2013.
© Springer-Verlag Berlin Heidelberg 2013

good performance, the learning algorithm requires setting user determined meta-parameters such as the learning rate, the momentum, the weight-cost, the sparsity target, the initial values of the weights, the number of hidden units and the size of each mini-batch [9]. Without careful considerations or optimal engineering of these parameters the training would not be performed well or easily fall into the over-fitting problem. This gives an unsuccessful generalization performance.

Support Vector Machine is the supervised machine learning algorithm and is proposed by Vladimir N. Vapnik [10]. SVM is widely adopted for classification and regression especially with kernel trick which makes predictions for new inputs depend only on the kernel function evaluated at a sparse subset of the training data points [11]. SVM constructs maximal-margin hyper-plane which discriminates different patterns efficiently and maximal-margin enables the high generalization performance since the generalization errors can be bounded in terms of margins.

In this paper, we propose deep learning algorithm with support vector machines which allow the training of layer by layer learning. By stacking SVM, we can extract high-order discriminative features with support vectors which maximize the margin and guarantees generalization performance. The proposed method for deep learning requires setting a few user determined parameters such as the number of layers which improves its applicability to various domains of engineering.

The rest of this paper is organized as follows. In Section 2, we describe the structure and the algorithm of the proposed model. In Section 3 we present the experimental results to evaluate the performance of the proposed. Finally, we draw our conclusions in Section 4.

2 Proposed Model

2.1 Support Vector Machine

Support vector machine is the supervised learning method and widely used in classification and regression tasks. For the linearly separable problem, SVM obtains maximal-margin hyper-plane and the distance from the hyper-plane to the nearest data points on each side is maximized.

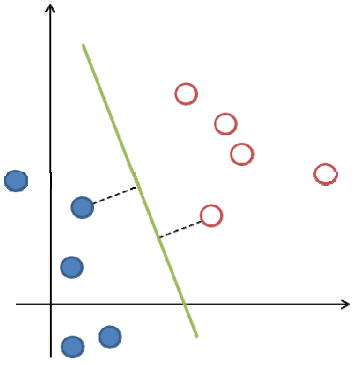

Fig. 1. Example of maximal-margin hyper-plane

Support vectors of SVM indicate the closest training data points to the hyper-plane. Binary classification problem using linear models can be represented as:

$$y(\mathbf{x}) = \mathbf{w}^T\mathbf{x} + b, \tag{1}$$

where $\mathbf{w}$ denotes the weight vector, $\mathbf{x}$ is input vector and b is a bias parameter of the linear decision function. SVM weights represent the importance of the corresponding input or feature for the classification.

The training data set which consists of N input patterns is represented as $\mathbf{x}_1, \ldots, \mathbf{x}_N$, and corresponding target can be expressed as $t_1, \ldots, t_N$ where $t_i \in \{-1, 1\}$, $i=1, \ldots, N$. The target label of new data point $\mathbf{x}$ is predicted with the sign of $y(\mathbf{x})$. Then if the training data set is linearly separable and the model is trained to classify training data correctly, $t_i y(\mathbf{x}_i)>0$ for all training data. The training of the parameters of SVM is constrained optimization problem which minimizes:

$$L(\mathbf{w}, b, \mathbf{a}) = \frac{1}{2}\|\mathbf{w}\|^2 - \sum_{i=1}^{N} a_i\{t_i(\mathbf{w}^{\mathrm{T}}\mathbf{x_i} + b) - 1\}, \tag{2}$$

where $\mathbf{a}=(a_1,\ldots,a_N)^{\mathrm{T}}$ and a_i are Lagrange multiplier [10]. To get the optimum of above problem, we can set the derivatives with respect to $\mathbf{w}$ and b equal to zero. Then we get

$$\mathbf{w} = \sum_{i=1}^{N} a_i t_i \mathbf{x}_i, \tag{3}$$

$$0 = \sum_{i=1}^{N} a_i t_i. \tag{4}$$

And the dual representation of the above problem in Eq. (2) can be derived as the maximization problem:

$$L(\mathbf{a}) = \sum_{i=1}^{N} a_i - \frac{1}{2}\sum_{i=1}^{N}\sum_{j=1}^{N} a_i a_j t_i t_j K(\mathbf{x}_i, \mathbf{x}_j), \tag{5}$$

with respect to a subject to the constraints

$$a_i \geq 0, i = 1, \ldots, N, \tag{6}$$

$$\sum_{i=1}^{N} a_i t_i = 0. \tag{7}$$

where a_i are obtained by training the SVM and $K(\mathbf{x}, \mathbf{x}')$ is the linear inner product of $\mathbf{x}$ and $\mathbf{x}$'. Support vectors are the training samples whose corresponding a_i values are nonzero. In this representation, weights disappear and the problem only depends on the set of a_i, t_i and $\mathbf{x}_i$. Since this is convex optimization problem, any local optimum is global optimum. Once we get a set of a_i, $\mathbf{w}$ and b are calculated using (3) and (4), respectively. With these parameters, a new data can be tested using equation (1). By substituting $\mathbf{w}$ in Eq. (1) using Eq. (3), the equation for classification of new data $\mathbf{x}$ become

$$y(\mathbf{x}) = \sum_{i=1}^{N} a_i t_i K(\mathbf{x_i}, \mathbf{x}) + b. \tag{8}$$

Because the optimization of Eq. (5) satisfies the Karush-Kuhn-Tucker (KKT) conditions, $a_i=0$ or $t_i y(\mathbf{x}_i)=1$ for every data point. Then only points which have $a_i>0$ affects

the classification and these data points are support vector. Since those points satisfies $t_i y(\mathbf{x}_i)=1$, so they are laid on maximum margin hyper-plane. SVM formulation therefore depends on the support vectors to define boundaries, which are the sample points at the discriminatory boundary and within the separating margins of the two classes.

2.2 Deep Network with Support Vector Machine

SVM obtains maximal margin hyper-plane to achieve high generalization performance. In this subsection, deep architecture with support vectors is explained. As described in the introduction section, multiple layers of deep architecture have a role to extract high-order features for recognition. Deep architecture with SVM is also used to capture features which are helpful to discriminative patterns.

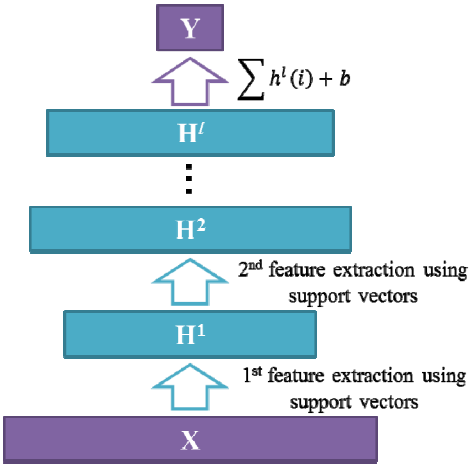

Fig. 2. The structure of the proposed model

Fig. 2 shows the structure of the proposed model. There are multiple hidden layers and each hidden layer extract discriminative features using support vectors of previous layer and corresponding multipliers. In previous subsection, linearly separable problem is solved with linear inner product of support vector and input vector. When we use the non-linear kernel instead of the inner product operation, SVM can discriminate linearly non-separable patterns also. Gaussian RBF (Radius Basis Function) kernel is most popular and represented as:

$$K(\mathbf{x}, \mathbf{x}') = \exp\left(-\frac{\|\mathbf{x}-\mathbf{x}'\|^2}{2\acute{o}^2}\right). \tag{9}$$

Feature extraction is represented in detail in Fig. 3.

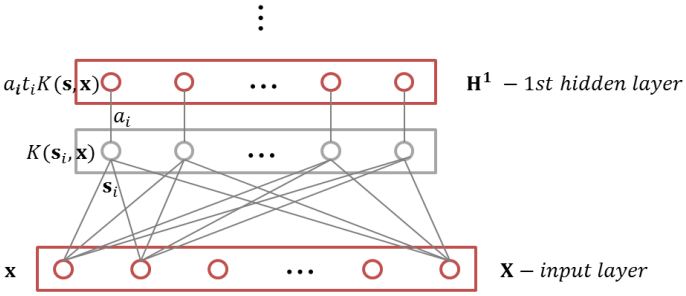

Fig. 3. Feature extraction between layers

The training of the first weight set is extracted from original training data. Let *m*-dimensional *N* input patterns of training data are $\mathbf{x}_1, \ldots, \mathbf{x}_N$. From the training data we get *m*-dimensional *p* support vectors $\mathbf{s}_1, \ldots, \mathbf{s}_p$ and corresponding Lagrange multipliers $a_1, \ldots, a_p$ and target labels $t_1, \ldots, t_p$as described in previous subsection 2.1. The activation values of the next layer are calculated as:

$$\mathbf{h}^1(i) = a_i t_i K(\mathbf{s}_i, \mathbf{x}), \tag{10}$$

where $\mathbf{h}^1(i)$ is the *i*-th element of the first hidden layer. Here *b* is not used except at the final layer since *b* is a just bias for the classification and it does not affect the intrinsic distribution of the data. The dimensionality of $\mathbf{h}^1$ is *p*, the number of support vectors of the input layer. The training of the weight connecting the input layer with the first hidden layer is completed, and weights of the next layers are trained layer by layer in the same manner. However, the training data for the next layers is the feature data transformed by previous layers rather the original data points. By feature extraction between the first layer and the next layer, original data $\mathbf{x} \in \mathbf{R}^m$ is transformed to $\mathbf{h}^1 \in \mathbf{R}^p$. For example, to train the second hidden layer, we can obtain the *p*-dimensional *N* training data $\mathbf{h}^1{}_1, \ldots, \mathbf{h}^1{}_N$ by projecting original data $\mathbf{x}_1, \ldots, \mathbf{x}_N$ on the transformed feature space whereas target values $t_1, \ldots, t_N$ are not changed. With these $\mathbf{h}^1{}_1, \ldots, \mathbf{h}^1{}_N$ and $t_1, \ldots, t_N$, the next layer also could be trained. Training procedures can be represented in algorithm 1.

Algorithm 1. Training of the Deep SVM
INPUT:
$\mathbf{X}^1$:={$\mathbf{x}_1$, …, $\mathbf{x}_N$} is training data
t :={t_1, …, t_N} is the set of corresponding target labels
K() := the RBF kernel function
n_layers := the number of layers

PROCEDURE:
FOR i=1:n_layers
{$\mathbf{S}^i$, $\mathbf{a}^i$, b^i} <= SVM($\mathbf{X}^i$,**t**)

```
  t_s^i := target labels corresponding S^i
  p := the number of support vectors S^i

  FOR j=1:N
    X^(i+1)_j <= {t_s^i_1*a^i_1*K(S^i_1,X^i_j),…, t_s_p*a^i_p*K(S^i_p,X^i_j)}
  END
END
```

OUTPUT:
S, a, t_s, b

To test the new data point, the input vector is given to the first layer and which is mapped to the next layer using Eq. (10). At the highest layer, final classification is decided by using the sign of function

$$y(\mathbf{x}) = \sum_{i=1}^{l} a_i t_i K(\mathbf{s}_i, \ddot{o}(\mathbf{x})) + b, \tag{11}$$

where $\mathbf{s}_i$ is i-th support vector, l is the number of support vectors of the final layer, and $\ddot{o}(\mathbf{x})$ represents transformed feature of test data $\mathbf{x}$ by hidden layers.

3 Experimental Results

The recognition performance of the proposed model is tested on Wisconsin Breast Cancer Database [12]. This breast cancer databases was obtained from the University of Wisconsin Hospitals, Madison from Dr. William H. Wolberg. The data samples contain 9 attributes of Clump Thickness, Uniformity of Cell Size, Uniformity of Cell Shape, Marginal Adhesion, Single Epithelial Cell Size, Bare Nuclei, Bland Chromatin, Normal Nucleoli and Mitoses. Each attribute has the integer value from 1 to 10. Each sample has the class of benign or malignant. The dimensionality of data patterns is 9 and the number of data samples is 367. Among 367 data samples, 200 samples are benign and 157 are malignant. In our experiment, the training set consists of randomly selected 100 and 84 samples and the test set is remaining 100 and 83 samples for benign and malignant cancer respectively. Sigma of the RBF kernel parameter of SVM is set to 5 and the number of layers is 3. Table 1 shows the number of support vectors and classification accuracies.

Table 1. Recognition performance

	1st layer	2nd layer	3rd layer
Dimensionality	34	25	31
Training accuracy	100 %	100 %	100 %
Test accuracy	91.2 %	92.3 %	95.6 %

Table 1 shows the perfect accuracy on training data. There are some errors on the test set. But, test accuracy is increased as layers are stacked. This demonstrates the superior generalization performance of the proposed model to shallow network.

Table 2. Performance comparison with other models

	SVM	Deep SVM	Denoising auto-encoder
Training accuracy	100 %	100 %	100 %
Test accuracy	91.2 %	95.6 %	91.9 %

Table 2 shows the comparison of classification accuracies with several models. To test the accuracy of denoising auto-encoder [13], 3 hidden layers are used and each layer from bottom to top hidden layer has 34, 25 and 31 nodes respectively. For the training of denoising auto-encoder, mini-batch algorithm is used to make the learning efficient and 200 epochs are done to train the network. The result shows the superior generalization performance of the proposed model.

4 Conclusion

In this paper, we proposed the deep network to achieve discriminative power of high-order feature space by stacking SVMs as layers. Hidden layers use support vector and its corresponding multiplier to extract features of the input vector. Experimental results tested on Wisconsin Breast Cancer Database demonstrate that although the test performance on training set is perfect on every layer, higher layer's SVMs show better generalization performance, i.e., they have better classification accuracies on test data than lower layers. In future works, we would test the system on high-dimensional data and try to implement the incremental learning of the architecture. Error-based fine-tuning of weights also can be considered.

Acknowledgement. This research was supported by the Industrial Strategic Technology Development Program (10044009) (50%) and the R&D program (10041826) (50%) funded by the Korea Ministry of Knowledge Economy (MKE) and the Korea Evaluation Institute of Industrial Technology (KEIT).

References

1. Arel, I., Rose, D.C., Karnowski, T.P.: Deep machine learning-A new frontier in artificial intelligence research. IEEE Computational Intelligence Magazine 5, 13–18 (2010)
2. Bengio, Y.: Learning deep architectures for AI. Foundations and Trends in Machine Learning 2 (2009)
3. Utgoff, P.E., David, J.S.: Many-layered learning. Neural Computation 14, 2497–2529 (2002)

4. Tesauro, G.: Practical issues in temporal difference learning. Reinforcement Learning, pp. 33–53. Springer US (1992)
5. LeCun, Y., et al.: Backpropagation applied to handwritten zip code recognition. Neural computation 1, 541–551 (1989)
6. Fukushima, K.: Neocognitron: A self-organizing neural network model for a mechanism of pattern recognition unaffected by shift in position. Biological cybernetics 36, 193–202 (1980)
7. Smolensky, P.: Information processing in dynamical systems: Foundations of harmony theory (1986)
8. Hinton, G.E., Osindero, S., Teh, Y.-W.: A fast learning algorithm for deep belief nets. Neural Computation 18, 1527–1554 (2006)
9. Hinton, G.E.: A practical guide to training restricted Boltzmann machines. Momentum 9 (2010)
10. Cortes, C., Vapnik, V.: Support-vector networks. Machine Learning 20, 273–297 (1995)
11. Bishop, C.M.: Pattern recognition and machine learning. Springer, New York (2006)
12. Bennett, K.P., Mangasarian, O.L.: Robust linear programming discrimination of two linearly inseparable sets. Optimization Methods and Software 1, 23–34 (1992)
13. Vincent, P., et al.: Stacked denoising autoencoders: Learning useful representations in a deep network with a local denoising criterion. The Journal of Machine Learning Research 9999, 3371–3408 (2010)

Hierarchical Representation Using NMF

Hyun Ah Song[1,⋆] and Soo-Young Lee[1,2]

[1] Department of Electrical Engineering,
KAIST, Daejeon 305-701, Republic of Korea
[2] Department of Bio and Brain Engineering,
KAIST, Daejeon 305-701, Republic of Korea
hi.hyunah@gmail.com,
sylee@kaist.ac.kr

Abstract. In this paper, we propose a representation model that demonstrates hierarchical feature learning using nsNMF. We stack simple unit algorithm into several layers to take step-by-step approach in learning. By utilizing NMF as unit algorithm, our proposed network provides intuitive understanding of the feature development process. It is able to represent the underlying structure of feature hierarchies present in complex data in intuitively understandable manner. Experiments with document data successfully discovered feature hierarchies of concepts in data. We also observed that proposed method results in much better classification and reconstruction performance, especially for small number of features.

Keywords: Hierarchical representation, NMF, unsupervised feature learning, multi-layer, deep learning.

1 Introduction

Humans are efficient learning machines. We can easily extract features from complex data, and understand them. How do we do this? We take hierarchical feature extraction strategy. By breaking a complex problem into several simple problems, we solve one by one throughout multiple stages [2]. By integrating simple solutions throughout the layers, algorithm is able to solve complex problem even without involving complex mathematical functions. Visual cortex supports this hierarchical information processing mechanism well [6].

With these biological evidences, researchers have been paying attention to hierarchical feature extracting approaches. One best known algorithm is Deep Belief Network (DBN) introduced in 2006 [5] where Hinton showed first success in training deep architectures of Restricted Boltzmann Machines (RBMs) in greedy layer-wise manner. With the success of training deep architectures, several variants of deep learning have been introduced; auto-encoders stacked into several layers [3, 8], stacking NMF into several layers [1, 4, 10].

Although these multi-layered algorithms take hierarchical approaches in feature extraction and provide efficient solution to complex problems, they do not

⋆ Hyun Ah Song is now at KIST (Korea Institute of Science and Technology).

M. Lee et al. (Eds.): ICONIP 2013, Part I, LNCS 8226, pp. 466–473, 2013.
© Springer-Verlag Berlin Heidelberg 2013

provide us intuitive relationships of features in form of hierarchies that are learned throughout the hierarchical structure; Most of deep learning networks allow both addition and subtraction of features in the hierarchical learning process, and this results in intricate representation of feature development process that is quite hard to follow intuitively.

In this paper, we propose a hierarchical data representation model, hierarchical multi-layer non-negative matrix factorization. (This is extended version of [11].) We extend a variant of NMF algorithm [7], nsNMF [9] into several layers for hierarchical learning. By stacking algorithm that restricts non-negativity, we allow only additional operation of features in process of developing feature hierarchies. We demonstrate intuitive feature development process along the layers, and display hierarchies present in the data set by learning relationships between features across the layers. We also prove that instead of one step learning, hierarchical approach learns more meaningful and helpful features, which leads to better distributed representations, and results in better performance in classification and reconstruction for small number of features.

The organization of the paper is as follows. In Section 2, we introduce unit algorithm of our hierarchical network, nsNMF. Then we look into the structure of our proposed network in Section 3. We explain the intuitive understanding of our hierarchical feature extraction process in Section 4. We demonstrate the experimental result of our proposed network using Reuters document data set in Section 5, and close our paper in Section 6.

2 Non-smooth Non-negative Matrix Factorization (nsNMF)

Proposed network is constructed by stacking nsNMF [9] into several layers. Non-smooth non-negative matrix factorization (nsNMF) is a variant of NMF that restricts sparsity constraint. Basic NMF decomposes non-negative input data $\mathbf{X}$ into non-negative $\mathbf{W}$ and $\mathbf{H}$, which are features and corresponding coefficients or data representation respectively. It aims to reduce error between original data $\mathbf{X}$ and its reconstruction $\mathbf{WH}$: $C = \frac{1}{2}\|\mathbf{X} - \mathbf{WH}\|^2 = \frac{1}{2}\sum_{i=1}^{m}\sum_{j=1}^{n}(X_{ij} - \sum_{k=1}^{f} W_{ik}H_{kj})^2$.

To apply sparsity constraint to standard NMF, a sparsity matrix $\mathbf{S}$ is introduced in [9]: $\mathbf{S} = (1-\theta)\mathbf{I}(k) + \frac{\theta}{k}\mathbf{ones}(k)$. k is number of features, and θ is parameter for smoothing effect, in range of 0 to 1. $\mathbf{I}$(k) is identity matrix of size k x k, and $\mathbf{ones}$(k) is a matrix of size k x k with all components of 1s. We smooth a matrix by multiplying it with $\mathbf{S}$. The closer θ is to 1, more smoothing effect is applied. During alternative update, we smooth $\mathbf{H}$ matrix by multiplying $\mathbf{S}$ and $\mathbf{H}$ during iterations as $\mathbf{H}$=$\mathbf{SH}$. To compensate the loss of sparsity by smoothing, $\mathbf{W}$ becomes sparse.

3 Multi-layer Architecture

The proposed hierarchical multi-layer NMF structure comprise of several layers of unit algorithm. The structure is described in Fig. 1.

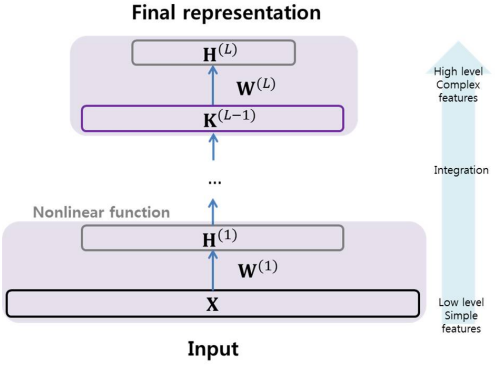

Fig. 1. Overall architecture of hierarchical multi-layer NMF network

We first train each layer separately. We process outcome of each layer $\mathbf{H}^{(l)}$ to get $\mathbf{K}^{(l)}$ as $K_{kj}^{(l)} = f\left(\frac{H_{kj}^{(l)}}{M_{kj}^{(l)}}\right)$, where $M_{kj}^{(l)} = \frac{\sum_{k'=1}^{f} H_{k'j}^{(l)}}{f}$. $f(\cdot)$ is nonlinear function, and the superscript of each term denotes layer index, where l denotes index of layer, $l = 1, 2, ...L$. Processed data representation of $\mathbf{K}^{(l)}$ is used as input to next layer: Using nsNMF, $\mathbf{K}^{(l)}$ is decomposed into $\mathbf{W}^{(l+1)}$ and $\mathbf{H}^{(l+1)}$: $\mathbf{K}^{(l)} \approx \mathbf{W}^{(l+1)}\mathbf{H}^{(l+1)}$. We repeat this process by extending layers for $l = 1, 2, ...L$. After training of layers 1 to L separately, we use outcome of separate training as initialization, and train the whole network jointly. The cost function for joint training is $C = \frac{1}{2}\sum_{i=1}^{m}\sum_{j=1}^{n}(X_{ij} - \sum_{k=1}^{f} W_{ik}^{(1)}\widetilde{H_{kj}^{(1)}})^2$, where $\widetilde{H_{kj}^{(l)}}$ is the reconstruction of $H_{kj}^{(l)}$, which can be computed via back propagation of errors from the last layer to the l^{th} layer. Computation can be described in simpler form as similar to [1] in equation (1).

$$W_{ik}^{(l)} \leftarrow W_{ik}^{(l)} \frac{\left(\mathbf{Nu}^{(l)}\widetilde{\mathbf{H}^{(l)^T}}\right)_{ik}}{\left(\mathbf{De}^{(l)}\widetilde{\mathbf{H}^{(l)^T}}\right)_{ik}}, \text{ and } H_{kj}^{(l)} \leftarrow H_{kj}^{(l)} \frac{\left(\mathbf{W}^{(l)^T}\mathbf{Nu}^{(l)}\right)_{kj}}{\left(\mathbf{W}^{(l)^T}\mathbf{De}^{(l)}\right)_{kj}}, \text{ where} \quad \text{(1a)}$$

$$\mathbf{Nu}^{(l)} = \begin{cases} \mathbf{X} & \text{if } l = 1 \\ \left(\mathbf{W}^{(l-1)^T}\mathbf{Nu}^{(l-1)}\right) \odot \left(\mathbf{M}^{(l-1)} f^{-1'}\left(\mathbf{W}^{(l)}\mathbf{H}^{(l)}\right)\right) & \text{otherwise} \end{cases} \quad \text{(1b)}$$

$$\mathbf{De}^{(l)} = \begin{cases} \widetilde{\mathbf{X}} & \text{if } l = 1 \\ \left(\mathbf{W}^{(l-1)^T}\mathbf{De}^{(l-1)}\right) \odot \left(\mathbf{M}^{(l-1)} f^{-1'}\left(\mathbf{W}^{(l)}\mathbf{H}^{(l)}\right)\right) & \text{otherwise} \end{cases} \quad \text{(1c)}$$

Here, $\widetilde{\mathbf{X}} = \mathbf{W}^{(1)}\widetilde{\mathbf{H}^{(1)}}$, and can be computed as shown in (2).

$$\widetilde{\mathbf{H}^{(l)}} = \begin{cases} \mathbf{H}^{(l)} & \text{if } l = L \\ \mathbf{M}^{(l)} \odot f^{-1}\left(\mathbf{W}^{(l+1)}\widetilde{\mathbf{H}^{(l+1)}}\right) & \text{if } l = L-1, ..., 1 \end{cases} \quad (2)$$

$\mathbf{M}^{(l)}$ is a matrix of column-wise mean of $\mathbf{H}^{(l)}$, and $f^{-1}(\cdot)$ is inverse nonlinear function.

After training until the last layer, final data representation $\mathbf{H}^{(L)}$ is acquired. This is the activation information of complex features, which is the integration of features throughout the layers, $\mathbf{W}^{(1)}\mathbf{W}^{(2)}...\mathbf{W}^{(L)}$.

4 Intuition of Hierarchical NMF Feature Learning in Image

In this section, we provide intuitive understanding of hierarchical feature learning of our proposed network. The hierarchical feature learning displays what kind of features develop at each layer, and how features from the lower layer are combined together to form higher layer features. Other deep learning algorithms also learn hierarchical features that are combination of lower layer features. However, since they do not restrict the sign of the values to be positive, combination of features involves subtraction of features as well, and this yields feature development process hard to follow, and representation of features are not intuitively understood. In contrast, hierarchical NMF provides intuitive understanding of feature hierarchies by allowing only weighted summations among the features during the hierarchical learning process. This can be interpreted as simply adding lego blocks to construct a complete structure.

In order to help better understanding, we demonstrate the feature learning process using image data, MNIST digit data[1].

In Fig. 2, the construction process of data using learned features is described in feature hierarchy structure. First layer learns very simple spot-like features $\mathbf{W}^{(1)}$ which can be seen as the basic building blocks. In the second layer $\mathbf{W}^{(2)}$, combinations of these first layer features are learned in distributed pattern. Integration through two layers produces complex blocks by combining $\mathbf{W}^{(1)}$ according to $\mathbf{W}^{(2)}$. We can intuitively follow the process by building up features in weighted summation manner due to non-negativity constraint which allows simple add-ons. The combination of complex feature is again combined to represent an original data.

As explained in above demonstration, our proposed hierarchical network learns features as the building blocks of data, and provides intuitive hierarchical process, discovering feature hierarchies present in the complex data.

5 Experiment with Document Data

We applied our proposed network to document database. We used "Reuters-21578 collection, distribution 1.0"[2] as input data. We sorted top 10 categories from ModApte split, and reduced dimension to 1000 by removing stop-words.

[1] Available at: `http://yann.lecun.com/exdb/mnist/`

[2] The Reuters-21578, Distribution 1.0 test collection is available from David D. Lewis professional home page, currently: `http://www.research.att.com/~lewis`

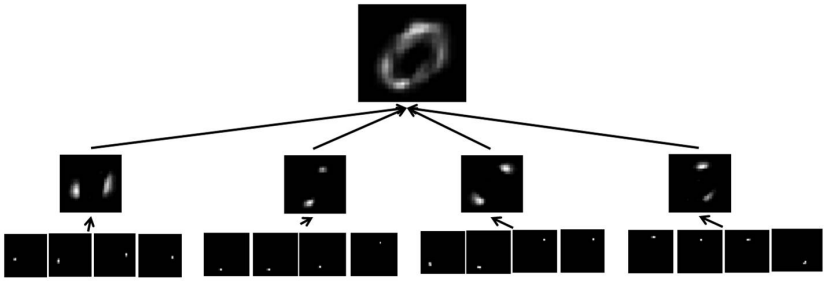

Fig. 2. Feature hierarchy of MNIST database. Images in order of $\mathbf{W}^{(1)} \rightarrow \mathbf{W}^{(1)} * \mathbf{W}^{(2)} \rightarrow \widetilde{\mathbf{X}}$, from bottom to top.

There are 5786 training samples and 2587 test samples. We constructed two-layered network with number of hidden neurons as 160 (1000-160-a, where 'a' denotes dimension of final data representation).

5.1 Feature Hierarchies

In Fig. 3, an example of top 10 words in learned high level features via integration of two layers, $\mathbf{W}^{(1)} * \mathbf{W}^{(2)}$, is displayed. Simple observation reveals which topic each feature represents: grain, money, crude, interest, coffe, trade, earn, acq, grain, and ship.

tonnes	dollar	oil	bank	coffee	trade	cts	inc	tonnes	two
u.s.	exchange	gas	pct	international	u.s.	div	corp	u.s.	last
wheat	yen	petroleum	rate	market	japan	vs	company	wheat	port
grain	six	energy	prime	meeting	two	record	unit	grain	spokesman
corn	current	production	savings	tonnes	international	qtly	co	corn	union
export	japan	crude	first	new	general	april	sale	export	one
sales	market	barrels	interest	prices	japanese	prior	acquisition	sales	no
april	currency	pct	market	sugar	products	pay	sell	april	week
tender	rates	prices	national	year	yen	march	terms	tender	pay
department	rate	price	stg	export	agreement	sets	industries	department	today

Fig. 3. An example of $\mathbf{W}^{(1)} * \mathbf{W}^{(2)}$

As in Fig. 2, features shown in Fig. 3 are part of hierarchy of concepts in Reuters. An example of how concepts form hierarchies in Reuters is shown in Fig. 4. In Fig. 4 (a), three first layer features $\mathbf{W}^{(1)}$s are weighted summed to form second layer feature $\mathbf{W}^{(2)}$. By observing words in each feature, we see that lower layer features cover small scope of the topic, containing various words. However, when they proceed to higher layer, they converge to represent one big common concept of 'oil,' with their top four words being synonyms of 'oil.'

Based on Fig. 4 (a), we can construct a concept hierarchy in Reuters as shown in Fig. 4 (b). By hierarchical concept diagram, we can observe that big broad topic 'oil' (words indicated in red color) contains various other oil related words that are colored in blue in the low level. Also, we can observe how some words

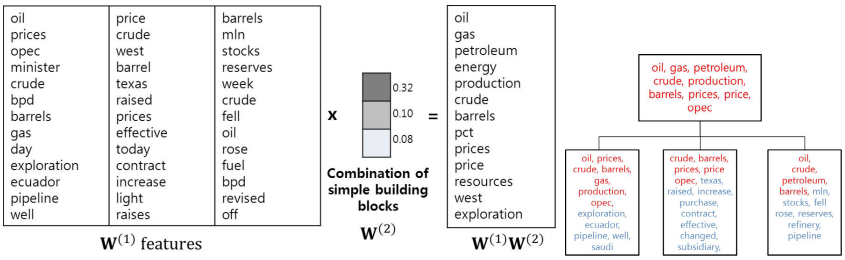

Fig. 4. Concept hierarchy in Reuters. (a) Experimental results, and (b) diagram of result in (a).

are extracted together to comprise a feature to show their relations with each other in first layer: words 'exploration, ecuador, pipeline, well, saudi' form a distinct group, same for 'texas, increase, purchase, contract, effective', and 'mln, stocks, fell, rose, reserves, refinery'; this grouping information can be interpreted as sub-topics under the topic 'oil'. If we used single layered network, all we could have observed would be those red words that indicate topic 'oil'. However, by hierarchical representation, we can observe deeper into the data structure more in detail by showing contents of blue words, and their groupings in low level.

5.2 Classification and Reconstruction Property

The classification and reconstruction property for various 'a' (dimension for $\mathbf{H}^{(L)}$) is shown in Fig. 5 (a) and (b), respectively. For classifier, we used SVM. We calculated reconstruction error as: Mean reconstruction error $= \frac{\sum_{i=1}^{m}\sum_{j=1}^{n}|X_{ij}-\widetilde{X_{ij}}|}{mn}$. The proposed hierarchical feature extraction method results in much better classification and reconstruction, especially for small number of features, compared to standard network that consists of only one layer. Even at dimension of 20, our proposed network displays the maximum performance it can reach after convergence. This supports that taking step-by-step approach by learning features in hierarchical manner provides better chance of learning meaningful features out of complex data; first layer pre-processes complex data by breaking it down into small units, lessening the burden for the second layer so that second layer just needs to learn how to combine these units.

In Fig. 6, we show two examples of reconstruction, the same word with the same color. In the first example, the reconstruction via our proposed network (c) returns most of significant words present in the original data (a). Also, it successfully learned the importance of words, by displaying word sequence similar to the original. In contrast, the standard network (b) misses key words and fails to capture the importance of the words, showing words in mixed order compared to the original. The second example shows similar result with the first example. In (e), single layer feature confuses the subject of the topic by containing words

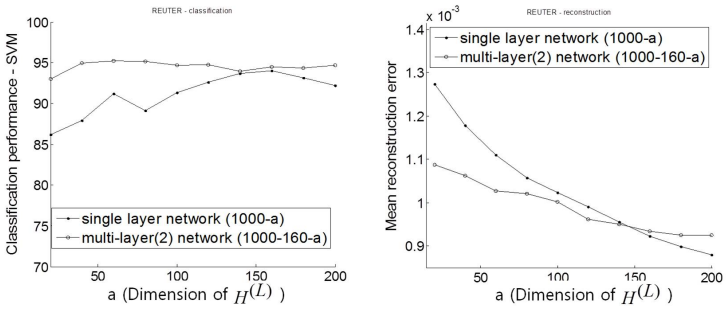

(a) (b)

Fig. 5. (a) Reuters data classification, and (b) Reuters data reconstruction

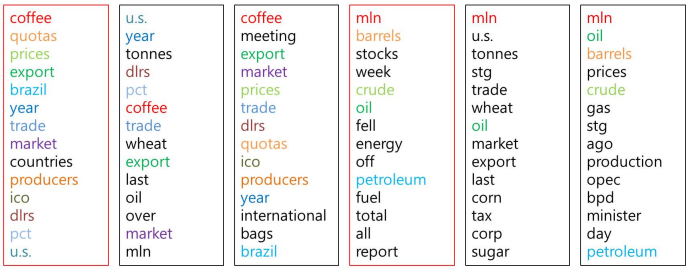

(a) (b) (c) (d) (e) (f)

Fig. 6. Two examples of original data, and reconstruction by standard (single-layerd) and proposed network in (a), (b), (c), and (d), (e), (f), respectively

'wheat', 'oil', 'corn', and 'sugar' altogether. However, our proposed network (f) correctly extracted key words related to subject 'oil'.

6 Conclusion

In this paper, we proposed a hierarchical representation model of nsNMF, by taking step-by-step approach in learning of the features in complex data. Our proposed network discovers feature hierarchies present in complex data and demonstrate them in intuitively understandable manner by learning feature relationships among the layers in non-negative approach. By simple addition and accumulation of features, we are able to understand the data structure and construct a hierarchy based on the information learned by the network. We also show that our proposed network provides better performance in classification and reconstruction compared to the single-layered network for small number of dimensions provided for final data representation. As a further work, we would like to apply our proposed network to various types of data for discovering underlying feature hierarchies in complex data.

Acknowledgments. This research was supported by Basic Science Research Program through the National Research Foundation of Korea (NRF) funded by the Ministry of Science, ICT and Future Planning (2011-0029816 and 2012-0008681).

References

1. Ahn, J.-H., Choi, S., Oh, J.-H.: A multiplicative up-propagation algorithm. In: Proceedings of the Twenty-First International Conference on Machine Learning, p. 3. ACM (2004)
2. Bengio, Y.: Learning deep architectures for ai. Foundations and Trends in Machine Learning 2(1), 1–127 (2009)
3. Bengio, Y., Lamblin, P., Popovici, D., Larochelle, H.: Greedy layer-wise training of deep networks. Advances in Neural Information Processing Systems 19, 153 (2007)
4. Cichocki, A., Zdunek, R.: Multilayer nonnegative matrix factorisation. Electronics Letters 42(16), 947–948 (2006)
5. Hinton, G.E., Osindero, S., Teh, Y.W.: A fast learning algorithm for deep belief nets. Neural Computation 18(7), 1527–1554 (2006)
6. Hubel, D.H., Wiesel, T.N.: Receptive fields, binocular interaction and functional architecture in the cat's visual cortex. The Journal of Physiology 160(1), 106 (1962)
7. Lee, D.D., Seung, H.S.: Learning the parts of objects by non-negative matrix factorization. Nature 401(6755), 788–791 (1999)
8. Marcrquote Aurelio Ranzato, C.P., Chopra, S., LeCun, Y.: Efficient learning of sparse representations with an energy-based model. Advances in neural information processing systems 19, 1137–1144 (2007)
9. Pascual-Montano, A., Carazo, J.M., Kochi, K., Lehmann, D., Pascual-Marqui, R.D.: Nonsmooth nonnegative matrix factorization (nsnmf). IEEE Transactions on Pattern Analysis and Machine Intelligence 28(3), 403–415 (2006)
10. Rebhan, S., Eggert, J.P., Gross, H.-M., Körner, E.: Sparse and transformation-invariant hierarchical NMF. In: de Sá, J.M., Alexandre, L.A., Duch, W., Mandic, D.P. (eds.) ICANN 2007. LNCS, vol. 4668, pp. 894–903. Springer, Heidelberg (2007)
11. Song, H.A., Lee, S.Y.: Hierarchical data representation model-multi-layer nmf. arXiv preprint arXiv:1301.6316 (2013)

Understanding Dropout: Training Multi-Layer Perceptrons with Auxiliary Independent Stochastic Neurons

KyungHyun Cho

Department of Information and Computer Science
Aalto University School of Science, Finland
kyunghyun.cho@aalto.fi

Abstract. In this paper, a simple, general method of adding auxiliary stochastic neurons to a multi-layer perceptron is proposed. It is shown that the proposed method is a generalization of recently successful methods of dropout [5], explicit noise injection [12,3] and semantic hashing [10]. Under the proposed framework, an extension of dropout which allows using separate dropping probabilities for different hidden neurons, or layers, is found to be available. The use of different dropping probabilities for hidden layers separately is empirically investigated.

Keywords: Multi-layer Perceptron, Stochastic Neuron, Dropout, Deep Learning.

1 Introduction

In this paper, we describe a simple extension to a multi-layer perceptron (MLP) that unifies some of the recently proposed training tricks for training an MLP. For example, the proposed extension is a generalization of using dropout for training an MLP [5].

The proposed method extends a conventional, deterministic MLP by augmenting each hidden neuron with an auxiliary stochastic neuron of which activation needs to be sampled. The activation of the added stochastic neurons is independent of all other variables in the MLP, and the weight of the edge connecting from the auxiliary neuron to the existing hidden neuron is fixed and not learned. Consequently, learning the parameters of the extended MLP does not require any special learning algorithm but can use a standard backpropagation [9].

This paper starts by briefly describing the proposed method of adding auxiliary stochastic neurons to an MLP. Then, it is described how dropout [5] and explicit noise injection [12,3] as well as semantic hashing [10] are all special cases of the proposed framework. Understanding the method of dropout under the proposed framework reveals that it is possible to use separate dropping probabilities for hidden neurons in a single MLP, and empirical investigation is provided on using different dropping probabilities for separate hidden layers.

2 Perceptron with Auxiliary Stochastic Neuron

For each hidden neuron $h_j^{[l]}$ in the l-th hidden layer, we introduce an independent stochastic neuron $r_j^{[l]}$ connected to $h_j^{[l]}$ with the edge weight $u_j^{[l]}$. The edge weight

M. Lee et al. (Eds.): ICONIP 2013, Part I, LNCS 8226, pp. 474–481, 2013.
© Springer-Verlag Berlin Heidelberg 2013

$u_j^{[l]}$ is *not* learned but fixed to a certain constant either indefinitely or for each forward computation[1].

The auxiliary stochastic neuron $r_j^{[l]}$ follows a predefined probability distribution, and its value is sampled at each evaluation of $h_j^{[l]}$. Since there is no incoming edge to the auxiliary neuron, the neuron is independent of any other variable in the MLP. In this case, the activation of the j-th hidden neuron in the l-th layer is

$$h_j^{[l]} = \phi\left(\sum_i h_i^{[l-1]} w_{ij}^{[l-1]} + r_j^{[l]} u_j^{[l]}\right),$$

where ϕ is a nonlinear function. $h_i^{[l-1]}$ and $w_{ij}^{[l-1]}$ are the i-th hidden neuron in the $(l-1)$-th hidden layer and the edge weight between $h_i^{[l-1]}$ and $h_j^{[l]}$, respectively. A hyperbolic tangent function $\tanh(\alpha)$ or a rectified linear function $\max(0, \alpha)$ is a common choice. See Fig. 1 for the illustration.

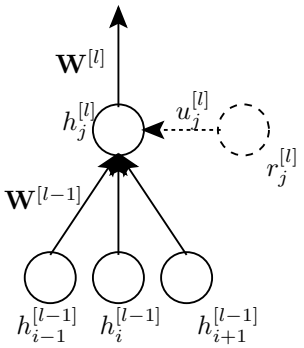

Fig. 1. Illustration of adding an auxiliary stochastic hidden neuron (marked by a dashed circle)

2.1 Learning and Prediction

It is straightforward to learn the parameters of this MLP. Since we do not attempt to learn $u_j^{[l]}$, a usual backpropagation [9] can be used. Only difference from the ordinary MLP which does not have auxiliary stochastic neurons is that the activations of the auxiliary neurons need to be sampled during the forward computation.

However, with a fixed set of parameters, either learned or predetermined by a user, it is not trivial to make a prediction given a new sample. Due to the stochastic activation of the auxiliary neurons, each forward computation of the output neurons will differ. A most obvious approach is to compute the output activation several times, and take the average or pick the most frequent one. This is however not preferred due to the increased computational cost as well as potentially high variance.

Another, more preferred way is to compute the expected activation of the output neurons over the distribution defined by the auxiliary stochastic neurons. This is often difficult as well due to the use of nonlinear activation functions. However, it is possible to linearize the computational path by approximating each nonlinear function linearly and push down the expectation operator to each auxiliary neuron. One can, then, compute and use the approximate expected activation of the output neurons as the final prediction.

[1] The author acknowledges that a similar method of a hidden neuron having an independent noise source, called a *semi-hard stochastic neuron*, has been recently proposed in [1] independently of this work.

3 Understanding Dropout with Auxiliary Stochastic Neurons

A dropout is a regularization technique which forces the activations of a randomly selected half of hidden neurons in each layer to zero when training an MLP. Just like the proposed method of adding auxiliary stochastic neurons training an MLP with dropout changes the forward computation only and leaves the error backpropagation as it is.

3.1 Training

Let us consider an MLP using rectified linear hidden neurons. Then, learning with dropout is equivalent to training an MLP with auxiliary stochastic neurons of which each follows Bernoulli distribution with mean $p = 0.5$. We fix the weight $u_j^{[l]}$ of the edge connecting from the auxiliary stochastic neuron to a hidden neuron to negative infinity. Then, the activation of $h_j^{[l]}$ is

$$h_j^{[l]} = \begin{cases} \max(0, \alpha_j^{[l]}) & \text{, if } r_j^{[l]} = 0 \\ 0 & \text{, if } r_j^{[l]} = 1 \end{cases} \tag{1}$$

This is equivalent to using dropout in training an MLP.

This exact procedure applies to any hidden neuron which has an activation function that converges to zero in the limit of negative infinity. A logistic sigmoid activation function is one such example. In cases of other types of activation functions, other ways of fixing the connection strengths between a hidden neuron and its corresponding auxiliary neuron are needed.

3.2 Testing

When an MLP was trained using a procedure of dropout, it was proposed in [5] that outgoing weights be halved to compensate for the loss of approximately half of hidden neurons during training phase. With a mild approximation, here we show that this procedure of halving the outgoing weights corresponds to computing the expected activation of output neurons over the auxiliary stochastic neurons.

If we linearly approximate the expectation of the output neurons, we may push the expectation operator all the way down to the evaluation of the activation of each hidden neuron $h_j^{[l]}$. Because the activation is dropped to zero with probability 0.5, the expected activation of $h_j^{[l]}$ becomes, for instance in the case of a rectified linear hidden neuron in Eq. (1),

$$\mathbb{E}\left[h_j^{[l]}\right] = \frac{1}{2}\max\left(0, \sum_i h_i^{[l-1]} w_{ij}^{[l-1]}\right).$$

It is clear to see that this is effectively equivalent to halving the outgoing weights.

Linear approximation is unnecessary, and computing the expectation becomes exact, if the output neurons are linear and there is only a single layer of hidden neurons. This agrees well with the original formulation of dropout in [5] which formulated the

procedure of halving the outgoing weights as taking a geometric average of exponentially many neural networks that share parameters. However, this procedure, in both perspectives, becomes approximate as the number of nonlinear hidden layers increases.

From the proposed framework, we can see that, albeit informally, this procedure of halving the outgoing weights is well approximated if the activation function of each hidden neuron can be approximated well linearly. There are two potential consequences from this. Applying dropout to hidden neurons below an activation function which may not be well approximated linearly, such as max-pooling, will not work well, which has been noticed already by previous work (see, e.g., [14,6]). Secondly, a piece-wise linear activation function such as the rectified linear function is well-suited for using dropout. This agree well with recent finding that another piece-wise linear activation function called maxout works well with dropout [4].

By this formulation, we can extend the original dropout by dropping each hidden neuron with probability p instead of 0.5. In that case, in testing time, the outgoing weight will be multiplied by $1-p$. Furthermore, this allows us to use different dropping probabilities for hidden neurons. If we denote the dropping probability of each hidden neuron by $p_j^{[l]}$, this will correspond to multiplying all outgoing weights $w_{jk}^{[l]}$ of the j-th hidden neuron in the l-th hidden layer with $1 - p_j^{[l]}$.

4 Other Special Cases

In this section, we describe two other training schemes and how they are realized as special cases of the proposed procedure of adding auxiliary stochastic neurons. The two training schemes we discuss here are denoising [12,3] and semantic hashing [10].

4.1 Explicit Noise Injection: Denoising Autoencoder

A denoising autoencoder (DAE) [12] is an MLP that aims to reconstruct a clean sample given an explicitly corrupted input. The DAE is an obvious special case of the proposed general framework. In this section, we consider adding additive white Gaussian noise to each input component.

A DAE can be constructed from an ordinary autoencoder by adding an additional hidden layer between the input and the first hidden layer. The additional layer has as many hidden neurons as the number of input variables. Each hidden neuron ν_i is connected to the i-th input component x_i *only* with weight 1 and has an auxiliary stochastic neuron r_i which follows a standard Normal distribution.

The activation of ν_i is linear and defined to be

$$\nu_i = x_i + r_i u_i,$$

where u_i is the connection strength between ν_i and r_i. Each time ν_i is computed, the activation of r_i is sampled from a standard Normal distribution. This is equivalent to explicitly adding additive white Gaussian noise with variance r_i^2.

Once training is over, we can compute the hidden activation of the original DAE by first computing the expected activation of ν_i. Since $\mathbb{E}[r_i] = 0$, the activation of ν_i

is simply a copy of the input x_i. In other words, we can use the learned parameters as if they were the parameters of an ordinary autoencoder trained without explicitly adding noise.

By further adding more intermediate hidden layers with auxiliary stochastic neurons, we can emulate adding multiple types of noise sequentially to input. For instance, a common practice of adding white Gaussian noise and dropping a small portion of input components can be achieved by adding another intermediate hidden layer that drops some components randomly, just like dropout described in Section 3.

This method of explicitly injecting noise to input is obviously applicable to a standard MLP that performs classification [3,8]. Furthermore, under the proposed framework this method naturally allows us to add noise even to hidden neurons, which may work as a regularization similarly to using dropout. This idea of adding noise to hidden neurons as well as input variables has recently been applied to a deep generative stochastic network in [2].

4.2 Semantic Hashing

Semantic hashing was proposed in [10] to extract a binary code of a document using a deep autoencoder with a small sigmoid bottleneck layer. One of the important details of the training procedure in [10] was to add white Gaussian noise to the input signal to the bottleneck layer to encourage the activations of the hidden neurons in the bottleneck layer to be as close to 0 or 1 as possible.

This procedure is exactly equivalent to adding an auxiliary stochastic neuron to each bottleneck hidden neuron. The activation of each auxiliary stochastic neuron is sampled from a standard Normal distribution and is multiplied with the connection strength which corresponds to the variance of the added noise. Since the connection strength is fixed and the auxiliary stochastic neuron is independent from the input or any other neuron, an ordinary backpropagation can be used without any complication resulting from the stochastic auxiliary neurons.

Again, once the parameters were learned, one may safely ignore the added auxiliary stochastic neurons as their means are zero.

5 Experiments

Although this paper focuses on interpreting various recently proposed training schemes under the proposed framework of adding auxiliary stochastic neurons. We were able to find some potentially useful extensions of those existing schemes by understanding them from this new perspective. One of them is to extend the usage of dropout by using different dropping probabilities for hidden neurons, and another is to inject white Gaussian noise to hidden neurons.

In this section, we present preliminary experiment result showing the effect of (1) using a separate dropping probability for each hidden layer and (2) injecting white Gaussian noise to the *input* of each hidden neuron.

Settings. We trained MLPs with two hidden layers having 2000 rectified linear neurons each on handwritten digit dataset (MNIST, [7]) using either dropout with separate dropping probabilities for the two hidden layers or injecting white Gaussian noise.

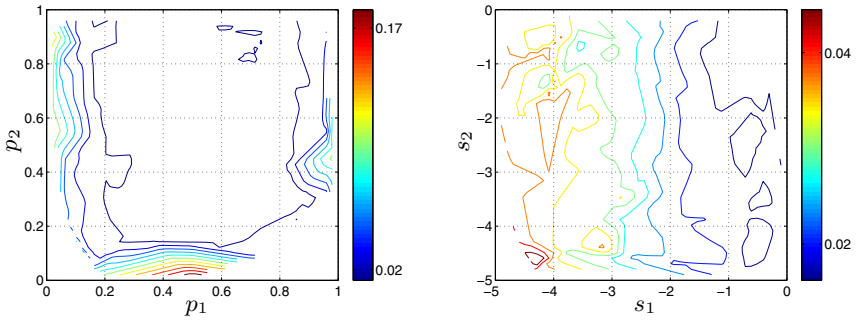

(a) (b)

Fig. 2. Contour plots of interpolated classification errors. (a) Figure obtained by the MLPs trained using separate dropping probabilities p_1 and p_2 for two hidden layers. (b) Figure obtained by the MLPs trained by injecting white Gaussian noise to the inputs to hidden neurons using separate standard deviations s_1 and s_2 for two hidden layers. These figures are best viewed in color.

To see the effect of choosing separate dropping probabilities for hidden layers, we trained 100 MLPs with a dropping probability p_l with the l-th hidden layer randomly selected from the interval $[0, 1]$. Similarly, 100 MLPs were trained with separate noise variances for hidden layers, where the exponent s_l of a noise variance for the l-th hidden layer was randomly chosen from $[-5, 0]$.

Before training each MLP, $60,000$ training samples were randomly split into training and validation sets with ratio $3 : 1$. Learning was early stopped by checking the prediction error on the validation set, while the maximum number of epochs was limited to 100[2]. We used a recently proposed method, called ADADELTA [13], to adapt learning rates automatically. Since we fixed the size of an MLP, this effectively means that there were no other hyperparameters to tune.

Result and Analysis. The result for the first experiment tested using separate dropping probabilities for hidden layers is shown in Fig. 2 (a). Interestingly, it can be observed that any dropping probability near 0.5 resulted in relative good accuracy. However, when any extreme dropping probability close to either 0 or 1 was used for the first hidden layer (p_1), the performance dropped significantly regardless of the dropping probability of the second hidden layer (p_2). Using too small dropping probability in the second hidden layer also turned out to hurt the generalization performance significantly. This suggests that the original proposal of simply dropping approximately half of hidden neurons in each hidden layer from [5] is already a good choice.

In Fig. 2 (b), the result of the second experiment is shown. In general, it shows that the generalization performance of an MLP is highly affected by the level of noise injected at the first hidden layer, which is in accordance with the previous research showing that adding noise to the input improves the classification accuracy on test samples [8]. However, a closer look at the figure shows that adding noise to the upper hidden layer helps achieving better generalization performance (see the upper right corner of the figure).

[2] Almost all runs were early-stopped before 100 epochs.

One important lesson from these preliminary experiments is that it is possible to achieve better generalization performance by carefully tuning auxiliary stochastic neurons. This amounts to, for instance, choosing different dropping probabilities in the case of dropout and injecting different levels of Gaussian noise. Further and deeper investigation using various architectures and datasets is, however, required.

6 Discussion

In this paper, we have described a general method of adding auxiliary stochastic neurons in a multi-layer perceptron (MLP). This procedure effectively makes hidden neurons in an MLP stochastic, but does not require any change to the standard backpropagation algorithm which is commonly used to train an MLP.

This proposed method turned out to be a generalization of a few recently introduced training schemes. For instance, dropout [5] was found to be a special case having binary auxiliary neurons with connection strengths dependent on the input signal. A method of explicitly injecting noise to input neurons [3,8] used by, for instance, a denoising autoencoder [12] was found to be an obvious application of the proposed use of auxiliary stochastic neurons following standard Normal distribution. Furthermore, we found that a trick of making the activations of hidden neurons in the bottleneck layer of an autoencoder used for semantic hashing [10] is equivalent to simply adding a white Gaussian auxiliary stochastic neuron to each hidden neuron in a bottleneck layer.

This paper, however, did not attempt to explain why, for instance, dropout helps achieving better generalization performance. Training an MLP with dropout under the proposed framework does not differ greatly from the ordinary way of training. The only difference is that some randomness is explicitly defined and injected via auxiliary stochastic neurons. It is left for future to investigate whether this simple injection of randomness causes a favorable performance of an MLP trained with dropout, or there exist more behind-the-scene explanations.

One important thing to note is that the proposed method is *not* equivalent to building an MLP with stochastic activation functions. It may be possible to find an equivalent model with auxiliary stochastic neurons, but it is not guaranteed nor expected that every stochastic MLP can be emulated by an ordinary MLP augmented with auxiliary stochastic neurons. However, one advantage of using the proposed method of adding auxiliary neurons compared to a true stochastic MLP is that there is no need for modifying the standard backpropagation or designing a new learning algorithm (see, e.g., [1,11]).

By understanding the method of dropout under the proposed framework, another extension was found, which allows using a separate dropping probability for each hidden layer. Similarly, we observed that it is also possible, under the proposed framework, to inject white Gaussian noise at each hidden layer instead of injecting only at the input. In the experiments, we provided empirical evidence showing that better generalization performance may be achieved by using separate dropping probabilities for different hidden layers in the case of dropout as well as injecting white Gaussian noise to hidden layers. As the experiments were quite limited, however, further extensive evaluation is required in future.

References

1. Bengio, Y.: Estimating or propagating gradients through stochastic neurons. arXiv:1305.2982 [cs.LG] (May 2013)
2. Bengio, Y., Thibodeau-Laufer, É.: Deep generative stochastic networks trainable by backprop. arXiv:1306.1091 [cs.LG] (June 2013)
3. Bishop, C.M.: Training with noise is equivalent to Tikhonov regularization. Neural Computation 7(1), 108–116 (1995)
4. Goodfellow, I., Warde-Farley, D., Mirza, M., Courville, A., Bengio, Y.: Maxout Networks. In: Proceedings of the 30th International Conference on Machine Learning (ICML 2013), JMLR Workshop and Conference Proceedings, vol. 28, pp. 1319–1327. JMLR W&CP (June 2013)
5. Hinton, G., Srivastava, N., Krizhevsky, A., Sutskever, I., Salakhutdinov, R.: Improving neural networks by preventing co-adaptation of feature detectors. arXiv:1207.0580 [cs.NE] (July 2012)
6. Krizhevsky, A., Sutskever, I., Hinton, G.: ImageNet classification with deep convolutional neural networks. In: Bartlett, P., Pereira, F., Burges, C., Bottou, L., Weinberger, K. (eds.) Advances in Neural Information Processing Systems, vol. 25, pp. 1106–1114 (2012)
7. LeCun, Y., Bottou, L., Bengio, Y., Haffner, P.: Gradient-based learning applied to document recognition. Proceedings of the IEEE 86, 2278–2324 (1998)
8. Raiko, T., Valpola, H., LeCun, Y.: Deep learning made easier by linear transformations in perceptrons. In: Proceedings of the Fifteenth Internation Conference on Artificial Intelligence and Statistics (AISTATS 2012), JMLR Workshop and Conference Proceedings, vol. 22, pp. 924–932. JMLR W&CP (April 2012)
9. Rumelhart, D.E., Hinton, G., Williams, R.J.: Learning representations by back-propagating errors. Nature 323, 533–536 (1986)
10. Salakhutdinov, R., Hinton, G.: Semantic hashing. International Journal of Approximate Reasoning 50(7), 969–978 (2009)
11. Tang, Y., Salakhutdinov, R.: A new learning algorithm for stochastic feedforward neural networks. In: ICML 2013 Workshop on Challenges in Representation Learning, Atlanta, Georgia (2013)
12. Vincent, P., Larochelle, H., Lajoie, I., Bengio, Y., Manzagol, P.A.: Stacked denoising autoencoders: Learning useful representations in a deep network with a local denoising criterion. Journal of Machine Learning Research 11, 3371–3408 (2010)
13. Zeiler, M.D.: ADADELTA: An adaptive learning rate method. arXiv:1212.5701 [cs.LG] (December 2012)
14. Zeiler, M., Fergus, R.: Stochastic pooling for regularization of deep convolutional neural networks. In: Proceedings of the First International Conference on Learning Representations, ICLR 2013 (2013)

Measuring the Usefulness of Hidden Units in Boltzmann Machines with Mutual Information

Mathias Berglund, Tapani Raiko, and KyungHyun Cho

Department of Information and Computer Science
Aalto University School of Science, Finland
firstname.lastname@aalto.fi

Abstract. Restricted Boltzmann machines (RBMs) and deep Boltzmann machines (DBMs) are important models in deep learning, but it is often difficult to measure their performance in general, or measure the importance of individual hidden units in specific. We propose to use mutual information to measure the usefulness of individual hidden units in Boltzmann machines. The measure serves as an upper bound for the information the neuron can pass on, enabling detection of a particular kind of poor training results. We confirm experimentally, that the proposed measure is telling how much the performance of the model drops when some of the units of an RBM are pruned away. Our experiments on DBMs highlight differences among different pretraining options.

Keywords: Deep learning, restricted Boltzmann machine, deep Boltzmann machine, pruning, structural learning, mutual information.

1 Introduction

Restricted Boltzmann machines (RBMs) and deep Boltzmann machines (DBMs) are important models in *deep learning*, helping to achieve state-of-the-art performance in many tasks. However, both models are also known to be difficult to train [1, 2].

If training of an RBM or DBM is not successful, it is often assumed that the hidden neurons do not learn to detect features that are useful for the task the Boltzmann machine (BM) is expected to perform. Whether training is successful is often measured by directly testing the performance of the trained model in this task at hand. The model is therefore often treated as a "black box" only evaluated based on final performance.

When training RBMs or DBMs, it would be beneficial to gain deeper insights into the details of a learned model beyond a mere final performance measure. One way to shed light on the underlying functionality of a particular model is to collect statistics of the individual neurons. E.g. in tasks where the visible neurons of the BM represent pixels in pictures, it is standard practice to visualize the learned weights.

Structural learning is an additional field where measuring the importance of individual neurons is crucial. One approach in structural learning is to add or prune neurons while training the model (see e.g. [3–5]). In general, the benefit of such an approach includes decreasing the number of hyperparameters that need to be defined a priori [4], better expected generalization, and faster performance [6]. However, it is unclear how training a BM is affected by adding or pruning neurons while training.

M. Lee et al. (Eds.): ICONIP 2013, Part I, LNCS 8226, pp. 482–489, 2013.
© Springer-Verlag Berlin Heidelberg 2013

In this paper, we propose to use mutual information between the observation vector and a single hidden unit for evaluating its importance.

After reviewing RBMs and DBMs in Sect. 2, we propose the mutual information (MI) measure for studying the importance of individual hidden units of a BM in Sect. 3. Experimenting with RBMs in Sect. 4, we demonstrate the usefulness of the measure in pruning and adding neurons as well as visualizing the progress of learning. In Sect. 5, we compare pretraining choices of a DBM using the proposed measure.

2 Boltzmann Machines: Background

2.1 Restricted Boltzmann Machines

A restricted Boltzmann machine (RBM) [7] is a variant of a Boltzmann machine that has a bipartite structure such that each visible neuron is connected to all hidden neurons and each hidden neuron to all visible neurons, but there are no edges between the same type of neurons. An RBM defines an energy of each state $(\mathbf{x}, \mathbf{h})$ by

$$-E(\mathbf{x}, \mathbf{h} \mid \boldsymbol{\theta}) = \mathbf{b}^\top \mathbf{x} + \mathbf{c}^\top \mathbf{h} + \mathbf{x}^\top \mathbf{W} \mathbf{h}, \tag{1}$$

and assigns the following probability to the state via Boltzmann distribution: $p(\mathbf{x}, \mathbf{h} \mid \boldsymbol{\theta}) = \frac{1}{Z(\boldsymbol{\theta})} \exp\{-E(\mathbf{x}, \mathbf{h} \mid \boldsymbol{\theta})\}$, where $\boldsymbol{\theta} = \{\mathbf{b}, \mathbf{c}, \mathbf{W}\}$ is a set of parameters consisting of visible and hidden biases as well as weights between visible and hidden neurons. $Z(\boldsymbol{\theta})$ is a normalization constant that makes the probabilities sum up to one.

2.2 Deep Boltzmann Machines

A deep Boltzmann machine (DBM) was proposed in [8] as a relaxed version of an RBM. A DBM simply stacks multiple additional layers of hidden units on the layer of hidden units of an RBM. As was the case with an RBM, consecutive layers are fully connected, while there is no edge among the units in one layer.

The energy function is defined as

$$-E(\mathbf{x}, \mathbf{h} \mid \boldsymbol{\theta}) = \mathbf{b}^\top \mathbf{x} + \mathbf{c}_{[1]}^\top \mathbf{h}_{[1]} + \mathbf{x}^\top \mathbf{W} \mathbf{h}_{[1]} + \sum_{l=2}^{L} \left(\mathbf{c}_{[l]}^\top \mathbf{h}_{[l]} + \mathbf{h}_{[l-1]}^\top \mathbf{U}_{[l-1]} \mathbf{h}_{[l]} \right), \tag{2}$$

where L is the number of hidden layers. The state and biases of the hidden units at the l-th hidden layer and the weight matrix between the l-th and $(l+1)$-th layers are respectively defined by $\mathbf{h}_{[l]} = \left[h_1^{[l]}, \ldots, h_{q_l}^{[l]} \right]^\top$, $\mathbf{c}_{[l]} = \left[c_1^{[l]}, \ldots, c_{q_l}^{[l]} \right]^\top$, $\mathbf{U}_{[l]} = \left[u_{ij}^{[l]} \right]$, where q_l is the number of the units in the l-th layer and $\mathbf{U}_{[l]} \in \mathbb{R}^{q_l \times q_{l+1}}$.

2.3 Why Interested in Boltzmann Machines?

RBM is an important basic building block of deep neural networks. In [9] it was shown that an MLP with many hidden layers can be trained well by greedily pretraining each pair of consecutive layers as an RBM. Furthermore, deep generative models such as

deep belief networks and DBMs were found to be easily trainable if the parameters were initialized by greedy layer-wise pretraining using an RBM [10, 8]. DBM was found to be effective at initializing the parameters of an MLP as well [8].

Furthermore, both RBM and DBM have been found to be useful on their own, as well. RBM and DBM were used to achieve high predictive performance on collaborative filtering [11], multimodal learning [12] and hierarchical feature extraction [13].

However, all these achievements by RBM and DBM require that these neural networks were trained *well*. Several recent research showed that training RBM and DBM is difficult, and that inappropriately trained ones may neither perform well on their own nor as a part of another model [1, 2]. Although computing log-likelihood by estimating the normalizing constant [14] has been oft-used to evaluate RBMs and DBMs, it is computationally expensive and does not tell much about how much contribution each hidden neuron makes. Hence, in this paper we try to explore one potential measure that can be used to evaluate the contribution of each hidden neuron in RBM and DBM.

3 Mutual Information Measure for Hidden Units

Neural networks such as multi-layer perceptron (MLP) networks are often criticized for being *black boxes*, that is, it is difficult to understand what the individual neurons are doing. One measure that can easily be studied is the variance of the neuron activation across samples (see e.g. [15]). The underlying rationale is that neurons with constant activation across the samples cannot convey any discriminative information about the samples. However, as Boltzmann machines are stochastic, measuring activation variance is clearly not appropriate, as even a neuron with constant activation probability could have a high activation variance.

We therefore propose to measure the *relevant* activity (or importance) of a single hidden neuron h_j in Boltzmann machines by measuring the mutual information (MI) $I(\mathbf{x}, h_j)$ between the observation vector (or the set of visible neurons) $\mathbf{x}$ and the hidden neuron h_j. Specifically, the MI-measure of the hidden unit MI_j is

$$\begin{aligned}
\mathrm{MI}_j = I(\mathbf{x}, h_j) &= \sum_{h_j=0}^{1} \sum_{\mathbf{x}} P(\mathbf{x}, h_j) \log_2 \left(\frac{P(h_j \mid \mathbf{x})}{P(h_j)} \right) \\
&= \sum_{h_j=0}^{1} \left[-P(h_j) \log_2 \left(P(h_j) \right) + \sum_{\mathbf{x}} P(\mathbf{x}) P(h_j \mid \mathbf{x}) \log_2 \left(P(h_j \mid \mathbf{x}) \right) \right] \\
&\approx \sum_{h_j=0}^{1} \left[-P(h_j) \log_2 \left(P(h_j) \right) + \sum_{t=1}^{T} \frac{1}{T} P(h_j \mid \mathbf{x}_t) \log_2 \left(P(h_j \mid \mathbf{x}_t) \right) \right].
\end{aligned}$$

We use the logarithm with base 2 in order to get the amount of information as bits. It is easy to show that the mutual information between the binary hidden neuron h_j and the visible neurons $\mathbf{x}$ ranges from 0 to 1 bit, and defines the upper bound of the average information the hidden neuron can convey about the state of the visible neurons $\mathbf{x}$. The measure is also independent of the particular task that the model learned by the Boltzmann machine is supposed to perform.

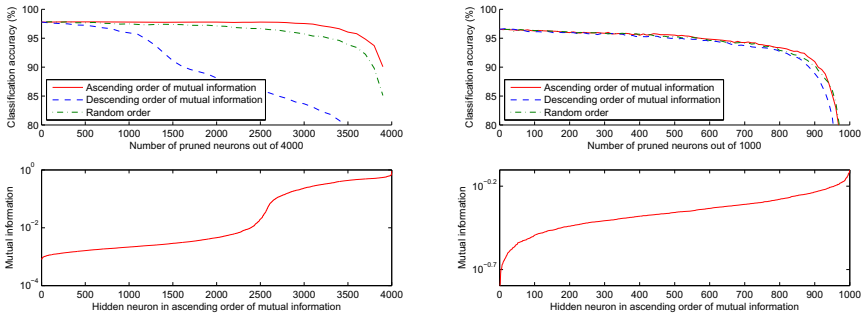

Fig. 1. Classification accuracy development when pruning neurons. *Left:* Original RBM was trained with 4000 hidden neurons for 1000 epochs using standard gradient. *Right:* Original network was trained with 1000 hidden neurons using enhanced gradient for 100 epochs.

Note that the MI-measure cannot measure how well the hidden unit works together with other hidden units. For instance, maximizing the MI-measure could not be used as the objective of training Boltzmann machines since training using such a criterion could lead to each hidden unit representing the same feature. However, the MI-measure serves as a useful measure of the upper bound for how useful the hidden neuron can be for any task the Boltzmann machine is trained for. Therefore, the hidden neurons with almost zero MI-measure will also be almost useless in any task. This is a particularly useful measure when training Boltzmann machines, as certain common training situations yield neurons with a very low MI-measure.

4 Experiments on Restricted Boltzmann Machines

This section studies the use of MI-measure as a measure of the usefulness of hidden neurons in the case of RBMs by (1) pruning, (2) adding new hidden neurons during training, and (3) visualizing the progress of training.

4.1 Pruning Neurons after Training

We tested the contribution of neurons with varying mutual information to a simple classification task. We trained an RBM with 4000 hidden neurons on the MNIST data set [16], and used the hidden neuron activations as inputs to a logistic classifier. We then pruned 100 hidden neurons at a time in order of the MI-measure. We did this both in ascending and descending order, in addition to randomly pruning 100 neurons at a time. The remaining neuron activations were then used as features in the classifier.

The results of the tests are shown in Fig. 1 (left). As predicted, the classification performance does not drop markedly when pruning neurons with very low MI-measure.

We also did a similar exercise for a 1000 hidden neuron RBM, where we used the enhanced gradient [1] in training. The results clearly differ from the previous model, in that the MI-measure is not clearly related to importance in the classification task. As can be seen from Fig. 1 (right), this model differs from the previous in that all hidden

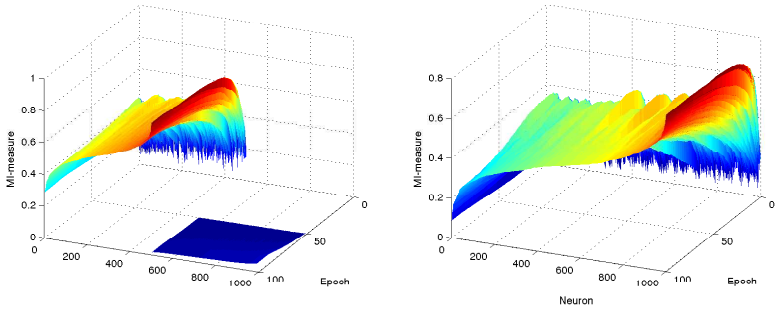

Fig. 2. MI-measure of RBM where 500 hidden neurons are added in the middle of the training (left) vs. a normal RBM with 1000 hidden neurons from the start of the training (right). Both models were trained for 100 epochs.

neurons have a fairly high MI-measure. Therefore, no neurons have a low enough MI-measure as to not be able to convey enough information about the observations $\mathbf{x}$. This clearly reveals that high MI-measure is not always an accurate indicator of high significance for the classification task – only a sufficiently low MI-measure can confidentially predict that a neuron is not useful.

4.2 Adding Neurons during Training

One potential way to learn an optimal structure of an RBM would be to add neurons to the hidden layer. This has bee studied e.g. in [4, 3]. However, it is possible that adding neurons to a layer of hidden units where the previous hidden units have been trained for some time would not be beneficial, as the added neurons might not learn relevant structures in addition to the already co-adapted hidden neurons. In order to test that hypothesis, we trained an RBM of 500 hidden neurons for 50 epochs, after which we added another 500 hidden neurons to the model and trained it for another 50 epochs. The development of the MI-measure can be seen in Fig. 2.

We again used the hidden neuron activations as features for a logistic classifier and compared the performance of the two models. The table lists the median accuracy from three runs. The performance of the model with added features is clearly inferior to the model trained with 1000 hidden neurons for 100 epochs.

	500 hidden units	500 + 500 hidden units	1000 hidden units
Class. accuracy	95.22 %	95.45 %	96.49 %

When examining the MI-measure of the 500 neurons added after 50 epochs, it is clear that the measure stays considerably lower than for the 500 neurons added in the beginning. It is also worth noting that even during the 50 epochs, the mutual information stays much lower than the level the original 500 neurons reached already after only a few epochs of training. This would support the hypothesis that the neurons added later are not able to find very relevant features easily. We therefore recommend caution when considering naively adding neurons parallel to already trained neurons in an RBM.

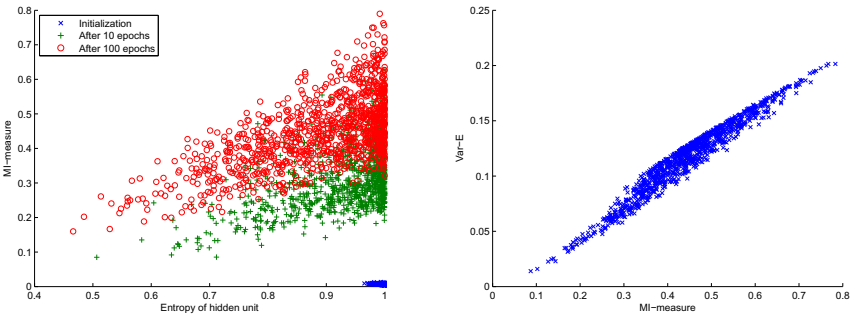

Fig. 3. *Left:* Mutual information of a hidden unit with the observation vector (MI-measure) plotted against the entropy of the hidden unit at different stages of learning. *Right:* Variance of the expected activation (Var-E) of each hidden neuron plotted against the MI-measure after 100 epochs of training for an RBM with 1000 hidden neurons.

4.3 Relations to Entropy and Variance

One use for the proposed measure is simply to visualize the progress of learning.

In Fig. 3 (left), we plot the entropy $H(h_j) = -\sum_{h_j=0}^{1} P(h_j) \log_2 (P(h_j))$ of the hidden units against their MI-measure in the initialization phase, after 10 epochs, and after 100 epochs. We see that training increases their mutual information on average, but also decreases the entropy on some hidden neurons.

It can be seen in Fig. 3 (right) that the MI-measure has a close resemblance to the variance over samples of the expected activation $\text{Var-E}_j = \text{Var}_t \left(E_{P(h_j|\mathbf{x}_t)} [h_j] \right)$. Var-E highlights that the stochastic variation in $P(h_j \mid \mathbf{x}_t)$ does not count as relevant activity, whereas variation over the data index t does. Note that we used Var-E for studying neurons in Fig. 9 of [1].

5 Experiments on Deep Boltzmann Machines

Although Deep Boltzmann Machines [8] have been used with great success in several applications, they are generally considered difficult to train. One method that has been essential in alleviating that difficulty is greedy layer-wise pretraining.

In order to illustrate this difficulty, we trained two DBMs with two layers of 1000 hidden neurons for 100 epochs: the first without any pretraining, and the second one with two-stage pretraining [2]. The hidden neuron activations of both of the models were used as features for a logistic classifier. As can be seen from Fig. 4 the mutual information of especially the second layer was extremely low without pretraining. The mutual information is in fact so low, that the entire second layer only conveys on average a maximum of 1.5×10^{-10} bits of information about the observations. This illustration strengthens the hypothesis that the difficulty in training DBMs relates to the model not learning useful features of the data.

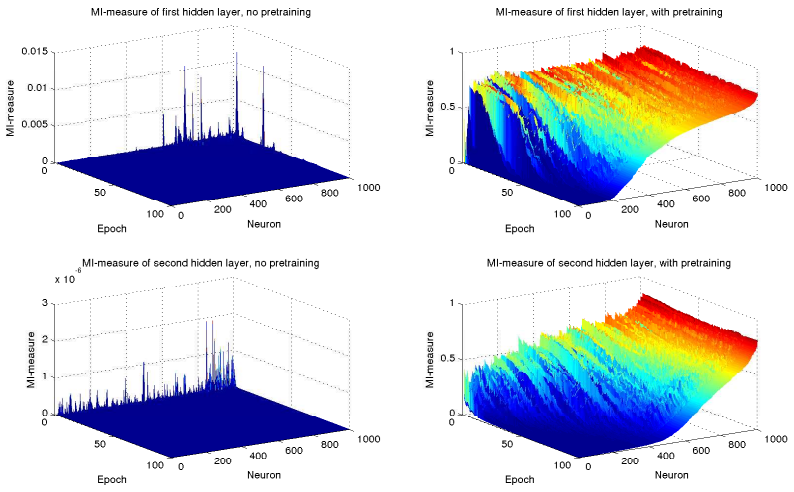

Fig. 4. MI-measure of a DBM with two layers of hidden units without pretraining (left) and with pretraining (right)

6 Discussion

We propose using mutual information between the observation vector and a single hidden unit (MI-measure) for evaluating the importance of individual hidden units of a Boltzmann machine. Following the progress of this measure during training would be useful at least for noticing situations where some of the units are not useful at all. We demonstrated several cases where it could happen. Firstly, training a large RBM with traditional gradient can include a lot of inactive units. Secondly, when an RBM has already learned a representation of the data, and new units are introduced in it, it is rather difficult to make them useful. Thirdly, when training deep Boltzmann machines without layer-wise pretraining, all the neurons in especially the upper layers might be useless.

We found that the MI-measure should only very cautiously be used as such to rank neuron importance among the active neurons, since it rather serves as an upper bound of importance. This might be due to at least two phenomena: Firstly, the MI-measure ignores the interaction among hidden units, and Boltzmann machines produce very distributed representations of data since each unit can only retain at most one bit of information. Secondly, it is well known that sparse representations perform well especially for classification tasks [17]. Sparse features have a lower entropy, and Fig. 3 shows that units with lower entropy tend to have a lower MI-measure, too. This would suggest that perhaps some combination of entropy and MI-measure could be used as a more accurate measure of usefulness in the future. Another direction in which to continue the work is to study the mutual information of the latent representation and class labels, assuming they are available. This has been proposed as a learning criterion by Peltonen and Kaski [18].

References

1. Cho, K., Raiko, T., Ilin, A.: Enhanced gradient for training restricted Boltzmann machines. Neural Computation 25(3), 805–831 (2013)
2. Cho, K., Raiko, T., Ilin, A., Karhunen, J.: A two-stage pretraining algorithm for deep Boltzmann machines. In: Proceedings of the 23rd International Conference on Artificial Neural Networks (to appear, September 2013)
3. Zhou, G., Sohn, K., Lee, H.: Online incremental feature learning with denoising autoencoders. In: Proceedings of the Fifteenth International Conference on Artificial Intelligence and Statistics (AISTATS 2012), pp. 1453–1461 (2012)
4. Adams, R.P., Wallach, H.M., Ghahramani, Z.: Learning the structure of deep sparse graphical models. In: Proceedings of the Thirteenth International Conference on Artificial Intelligence and Statistics (AISTATS 2010), pp. 1–8 (2010)
5. Engelbrecht, A.P.: A new pruning heuristic based on variance analysis of sensitivity information. Transactions on Neural Networks 12(6), 1386–1399 (2001)
6. Reed, R.: Pruning algorithms-a survey. Transactions on Neural Networks 4(5), 740–747 (1993)
7. Smolensky, P.: Information processing in dynamical systems: foundations of harmony theory. In: Parallel Distributed Processing: Explorations in the Microstructure of Cognition. Foundations, vol. 1, pp. 194–281. MIT Press, Cambridge (1986)
8. Salakhutdinov, R., Hinton, G.: Deep Boltzmann machines. In: Proceedings of the Twelfth Internation Conference on Artificial Intelligence and Statistics (AISTATS 2009), pp. 448–455 (2009)
9. Hinton, G., Salakhutdinov, R.: Reducing the dimensionality of data with neural networks. Science 313(5786), 504–507 (2006)
10. Hinton, G., Osindero, S., Teh, Y.W.: A fast learning algorithm for deep belief nets. Neural Computation 18(7), 1527–1554 (2006)
11. Salakhutdinov, R., Mnih, A., Hinton, G.: Restricted Boltzmann machines for collaborative filtering. In: Proceedings of the 24th International Conference on Machine Learning (ICML 2007), pp. 791–798. ACM, New York (2007)
12. Srivastava, N., Salakhutdinov, R.: Multimodal learning with deep boltzmann machines. In: Bartlett, P., Pereira, F.C.N., Burges, C.J.C., Bottou, L., Weinberger, K.Q. (eds.) Advances in Neural Information Processing Systems 25, pp. 2231–2239 (2012)
13. Lee, H., Grosse, R., Ranganath, R., Ng, A.: Convolutional deep belief networks for scalable unsupervised learning of hierarchical representations. In: Proceedings of the 26th Annual International Conference on Machine Learning (ICML 2009), pp. 609–616. ACM (2009)
14. Salakhutdinov, R.: Learning and evaluating Boltzmann machines. Technical Report UTML TR 2008-002, Department of Computer Science, University of Toronto (June 2008)
15. Glorot, X., Bengio, Y.: Understanding the difficulty of training deep feedforward neural networks. In: Proceedings of the Thirteenth International Conference on Artificial Intelligence and Statistics (AISTATS 2010), pp. 249–256 (May 2010)
16. LeCun, Y., Bottou, L., Bengio, Y., Haffner, P.: Gradient-based learning applied to document recognition. Proceedings of the IEEE 86, 2278–2324 (1998)
17. Ranzato, M., Boureau, Y.L., LeCun, Y.: Sparse feature learning for deep belief networks. In: Platt, J., Koller, D., Singer, Y., Roweis, S. (eds.) Advances in Neural Information Processing Systems 20, pp. 1185–1192. MIT Press, Cambridge (2008)
18. Peltonen, J., Kaski, S.: Discriminative components of data. IEEE Transactions on Neural Networks 16(1), 68–83 (2005)

Prediction of Ionospheric Perturbations Using Artificial Neural Network. Application to ISL Instrument Data- DEMETER Mission

Sid-Ali Ouadfeul, Victor Tourtchine, and Leila Aliouane

LIMOSE, Faculté des Sciences,
Université M'hamad Bougara de Boumerdes,
Avenue de l'indépendance, Boumerdes, Algeria
LABOPHYT, Faculté des Hydrocarbures et de la Chimie,
Université M'hamad Bougara de Boumerdes,
Avenue de l'indépendance, Boumerdes, Algeria
SOuadfeul@ymail.com

Abstract. In this paper, a tentative of prediction of Instrument Langmuir (ISL) installed in the DEMETER satellite is implanted. Prediction is based on the Multilayer Perceptron (MLP) neural network model. The MLP machine is composed of three layers, an input layer with four neurons, a hidden layer with ten neurons and an output layer with the same number of units like the input layer. Parameters to be predicted are electrons and ions density, electrons temperatures and plasma potential. Application to the data of orbit 27447-1 recorded two days before the Laquila earthquake of 06 April 2009 clearly shows the power of the artificial neural network in the prediction of ionospheric perturbations and Plasma analysis.

Keywords: ISL Demter, MLP, Prediction.

1 Introduction

The artificial neural networks (ANNs) have been widely used in physics (Peterson, 1992, Lynch et al, 2001, Ouadfeul and Aliouane, 2013). In plasma physics the ANNs are used by many authors to characterize it. Teng et al (2010) have used a multilayer perceptron algorithm and radial based function algorithm in order to predict the plasma density in a plasma system, the effectiveness of two artificial neural network models is demonstrated. Wei el al (2009) have established an artificial neural network (ANN) model using a back-propagation training algorithm in order to predict the plasma spatial distribution in an electron cyclotron resonance (ECR) — plasma-enhanced chemical vapor deposition (PECVD) plasma system. In this paper we test the efficiency of the Multilayer Perecptron (MLP) for prediction of ionosphere parameters recorded by DEMETER Satellite Langmuir instruments. We start by describing the instrument and the data, after that we describe the neural network MLP machine with detailing its training parameters, the technique is applied to real data

M. Lee et al. (Eds.): ICONIP 2013, Part I, LNCS 8226, pp. 490–497, 2013.
© Springer-Verlag Berlin Heidelberg 2013

recorded two days before the main shock of L'Aquila earthquake. We finalize the paper by results interpretation and a conclusion.

2 Langmuir Instrument and DEMETER Satellite

DEMETER satellite is designed to study ionospheric disturbances related to earthquake, volcano and human activity, and to detect the electromagnetic environment in global scale (Lebreton , 2012). The satellite has quasisolar-synchronous circular orbit with declination 98.23°, weight 130 kg and height 710 km (which decreased to 660 km in the middle of December, 2005). Its life was supposed to be two years. However, it is still operating now. The Langmuir probe is in principle a simple and very versatile space plasma diagnostic instrument for in situ measurements. A classical Langmuir probe uses a single sensor, which may be of different geometry (cylindrical or spherical). The DEMETER Langmuir Probe (ISL: Instrument Sonde de Langmuir) comprises two Langmuir Probe sensors. It includes a classical cylindrical sensor (5 cm long, dia 6 mm) and a 4-cm diameter spherical Segmented Langmuir Probe (SLP) whose surface is divided in six 1-cm disk sections (Lebreton, 2012, Zhang et al, 2009). A set of instruments were deployed on the satellite, including ICE to detect electric field from DC to 3.5 MHz; IMSC to measure the magnetic field from a few Hz to 20 kHz; IAP to detect ion density and temperature and so on; ISL, Langmuir probe to measure the electron density and temperature. Two kinds of data with different operating modes are provided: survey mode with low sampling rate and burst mode with high sampling rate as the satellite flies over the seismic zones. The mission center of DEMETER provides the data that can be downloaded and Quicklook images (Zhang et al, 2009). Detailed data guide can be referred to the website of DEMETER, http://demeter .cnrs-orleans.fr.

The Langmuir probe is in principle a simple and very versatile space plasma diagnostic instrument for in situ measurements. A classical Langmuir probe uses a single sensor, which may be of different geometry (cylindrical or spherical). The DEMETER Langmuir Probe (ISL: Instrument Sonde de Langmuir) comprises two Langmuir Probe sensors. It includes a classical cylindrical sensor (5 cm long, dia 6 mm) and a 4-cm diameter spherical Segmented Langmuir Probe (SLP) whose surface is divided in six 1-cm disk sections (Lebreton , 2012).

3 The Multilayer Perceptron

Multilayer feed-forward networks form an important class of neural networks. Typically the network consists of a set of sensory units or input nodes, that constitute the input layer, one or more hidden layers of neurons or computation nodes, and an output layer. Multi-layer Perceptron (MLP) neural networks with sufficiently many nonlinear units in a single hidden unit layer have been established as universal function approximators. The advantages of the MLP are: Hidden unit outputs (basis functions)

change adaptively during training, making it unnecessary for the user to choose them beforehand. The number of free parameters in the MLP can be unambiguously increased in small increments by simply increasing the number of hidden units.

The basic functions are bounded making overflow errors and round-off errors unlikely. The MLP is a feed-forward network consisting of units arranged in layers with only forward connections to units in subsequent layers. The connections have weights associated with them. Each signal traveling along a link is multiplied by its weight.

The input layer, being the first layer, has input units that distribute the inputs to units in subsequent layers. In the following (hidden) layer, each unit sums its inputs and adds a threshold to it and nonlinearly transforms the sum (called the net function) to produce the unit output (called the activation). The output layer units often have linear activations, so that output activations equal net function values.

The layers sandwiched between the input and the output layers are called hidden layers, and the units in the hidden layers are called hidden units (Ouadfeul and Aliouane, 2012, 2013).

4 Application to Real Data

To check the efficiency of the Multilayer perecptron neural network model in the prediction of ionospehric perturbations, data of the 04 April 2009 recorded by the ISL instrument two days before of Italian earthquake of L'Aquila are analyzed. Let us start by giving more details about this huge seismic disaster.

4.1 L' Aquila Earthquake

The 2009 L'Aquila earthquake occurred in the region of Abruzzo, in central Italy (see Fig. 01). The main shock occurred at 03:32 CEST (01:32 UTC) on 6 April 2009, and was rated 5.8 or 5.9 on the Richter scale and 6.3 on the moment magnitude scale; its epicenter was near L'Aquila, the capital of Abruzzo, which together with surrounding villages suffered most damage. There have been several thousand foreshocks and aftershocks since December 2008, more than thirty of which had a Richter magnitude greater than 3.5.

The earthquake was felt throughout central Italy; 297 people are known to have died, making this the deadliest earthquake to hit Italy since the 1980 Irpinia earthquake. In a subsequent inquiry of the handling of the disaster, seven members of the Italian National Commission for the Forecast and Prevention of Major Risks were accused of giving "inexact, incomplete and contradictory" information about the danger of the tremors prior to the main quake. On 22 October 2012, six scientists and one ex-government official were convicted of multiple manslaughter for downplaying the likelihood of a major earthquake six days before it took place. They were each sentenced to six years' imprisonment.

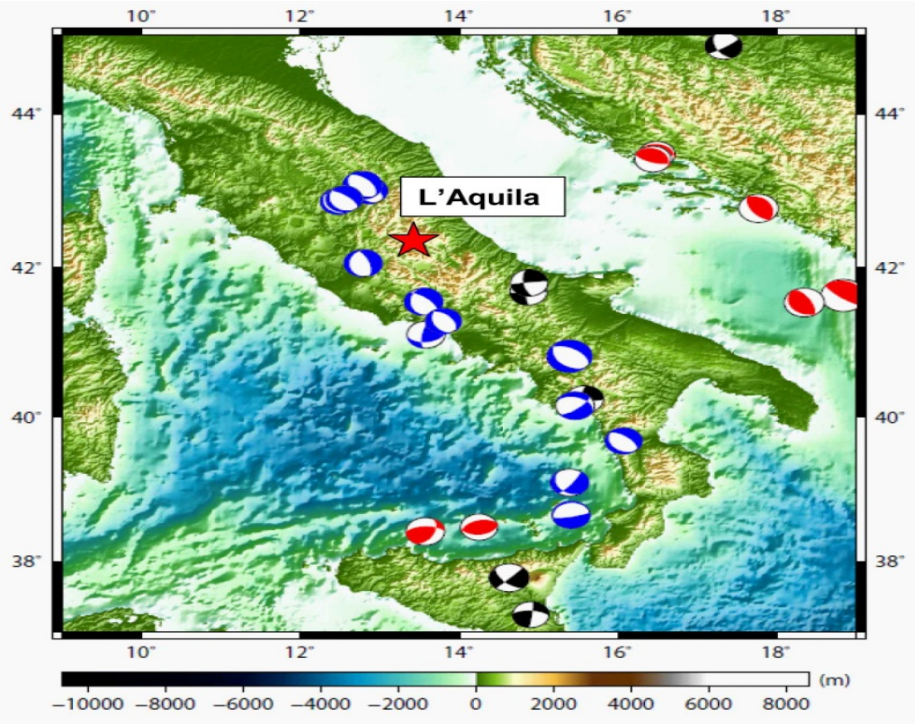

Fig. 1. Map of Italy centered around the L'Aquila region

4.2 Data Analysis

Data of ISL Langmuir DEMETER satellite recorded two days before then main shock of L'Aquila earthquake are analyzed by the multilayer perceptron, the goal is check the efficiency of the MLP neural network to predict future time series. Parameters to be predicted are: Electron Density, Ion Density, Electron temperature and Plasma potential. A neural network machine of three layers is implanted, the input layer is constituted of four neurons, and the hidden layer is composed of 10 neurons and an output layer of four neurons. The first 640 samples recorded by the ISL instrument are used as input (see Fig. 2); the second 640 samples are used as a desired output of the MLP machine (see Fig. 3).

In the training stage weights of connection are optimized to minimize the root mean square error between the desired output and the calculated output by the MLP machine. To check the power of the MLP machine for prediction of these parameters, a generalization of this implanted machine is done. At this step the second 640 samples are now used as an input of the MLP machine, the goal is to predict a future time series of 300 samples.

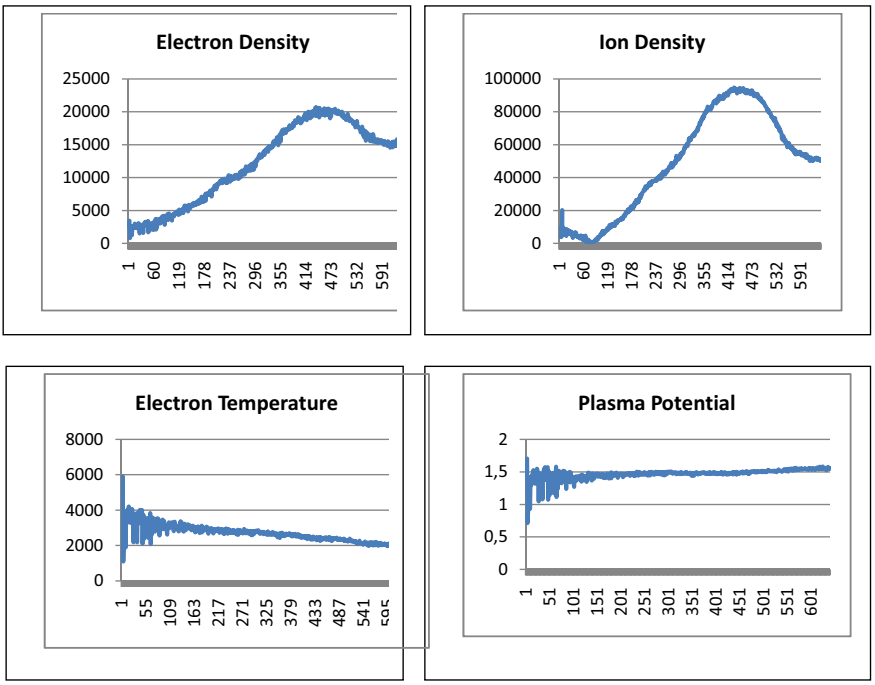

Fig. 2. Input of the Multilayer Perceptron neural network machine

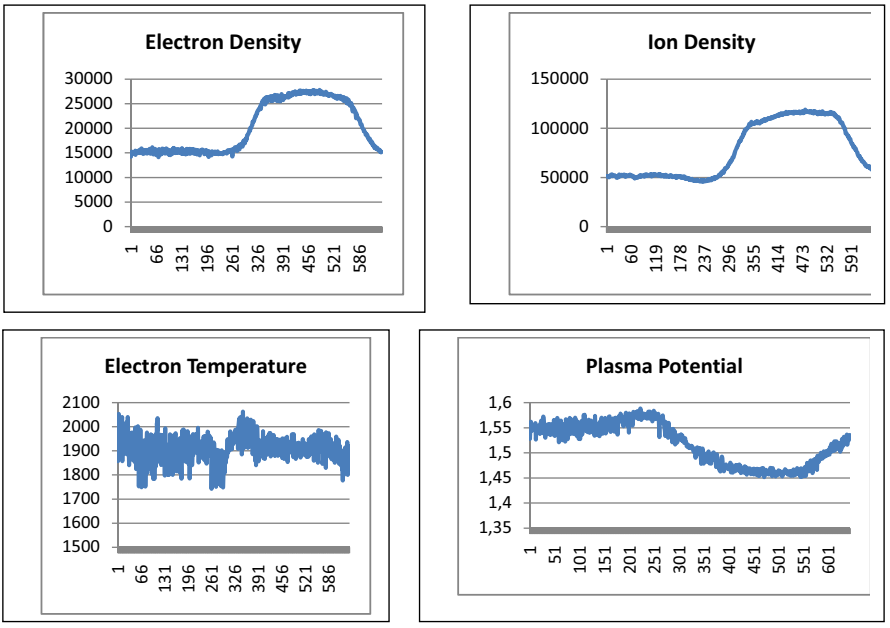

Fig.3. Desired output of the MLP machine

5 Results, Interpretation and Conclusion

Graphs of predicted plasma parameters are presented in black color in Fig. 4, Red graphs are the recorded parameters by the ISL Demeter satellite. Comparison between the two graphs clearly shows that the implanted neural network machine has the capacity and the memory to provide future ionosphere parameters. We can see that the ANN machine has a good memory for the most of each time series, however the machine start to lose slightly the memory at the end of each series.

The implanted machine can greatly be used for prediction of ionosphereic perturbations, which have a big relation with seismic activity; the artificial neural network method plays an important role in the seismic hazard prevention. We suggest testing other neural network models like the Radial Basis Function (RBF) to decide about which kind of neural network can be used for prediction of ISL Langmuir satellite data.

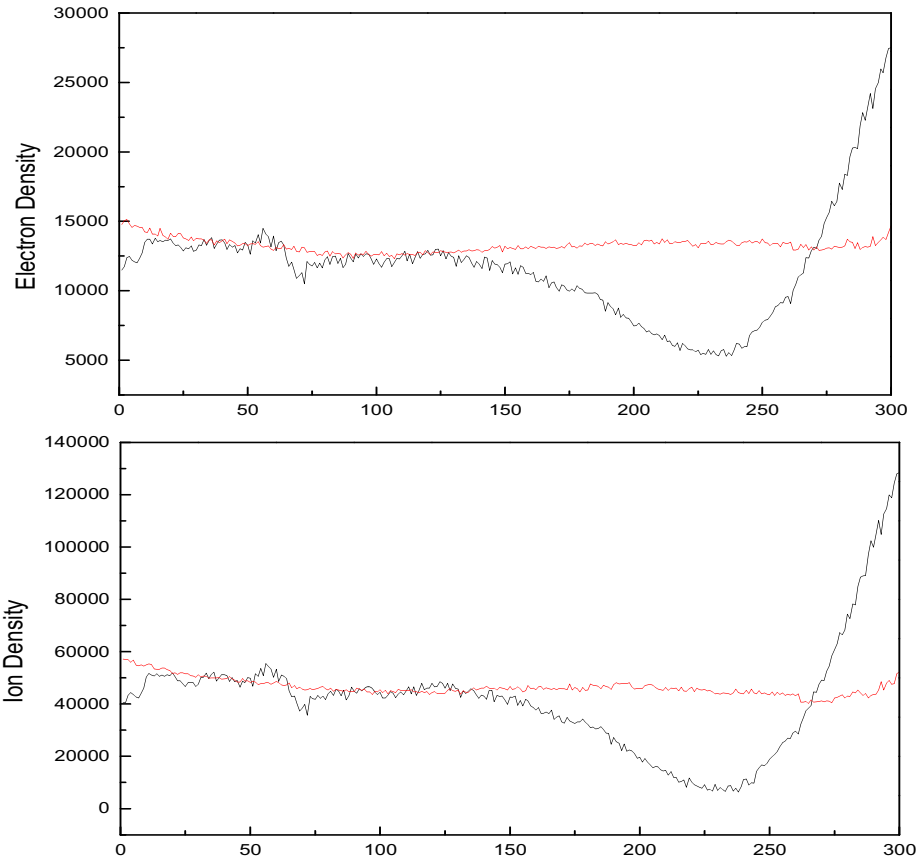

Fig. 4. Predicted plasma ionospheric parameters (black color) compared to recorded parameters by DEMETER satellite (red color)

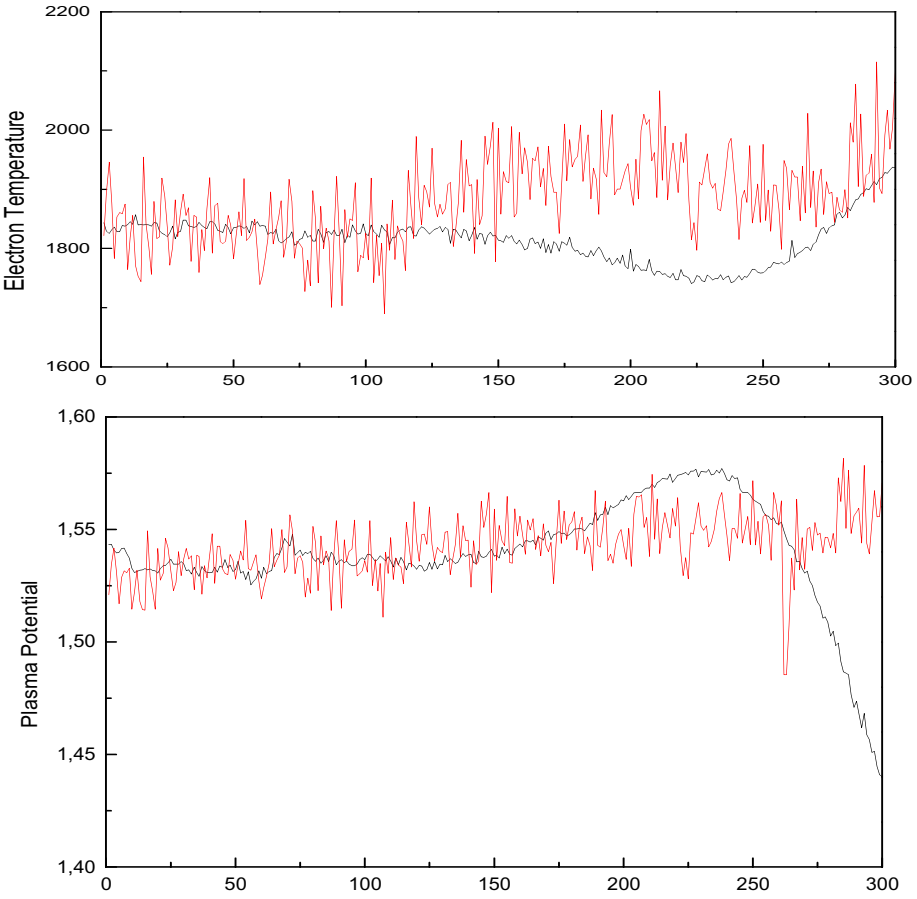

Fig. 4. (*Continued*.)

References

1. Peterson, C.: Neural Networks in High Energy Physics. In: Plenary talk presented at the "Computing in High Energy Physics", Annecy, France, September 21-25, 1991 (1992)
2. Lynch, M., Patel, H., Abrahamse, A., Rupa Rajendran, A., Medsker, L.: Neural network applications in physics. In: Proceedings of the International Joint Conference on Neural Networks, IJCNN 2001, vol. 3, pp. 2054–2058 (2001), doi:10.1109/IJCNN.2001.938482
3. Leberton, J.-P.: On the issue of surface contamination of a Langmuir Probe sesor: Demter IS results. Geophysical Research Abstrcats 14, EGU2012-13806
4. Ouadfeul, S.-A., Aliouane, L.: Lithofacies prediction from well log data using a multilayer perceptron (MLP) and Kohonen's self-organizing map (SOM) – a case study from the Algerian Sahara. Pattern Recogn. Phys. 1, 59–62 (2013), doi:10.5194/prp-1-59-2013
5. Ouadfeul, S.-A., Aliouane, L.: Lithofacies Classification Using the Multilayer Perceptron and the Self-organizing Neural Networks. In: Huang, T., Zeng, Z., Li, C., Leung, C.S. (eds.) ICONIP 2012, Part V. LNCS, vol. 7667, pp. 737–744. Springer, Heidelberg (2012)

6. Teng, W., Xiang-Dong, G., Wei, L.: Characterisation of the plasma density with two artificial neural network models. Chinese Phys. B 19, 070505 (2010), doi:10.1088/1674-1056/19/7/070505
7. Wei, L., Jun-Fang, C., Teng, W.: Prediction of the plasma distribution using an artificial neural network. Chinese Phys. B 18 2441 (2009), doi:10.1088/1674-1056/18/6/053
8. Zhang, X., Qian, J., Ouyang, X., Shen, X., Cai, J., Zhao, S.: Ionospheric electromagnetic perturbations observed on DEMETER satellite before Chile M7.9 earthquake. Earthquake Science 22(3), 251–255 (2009)

A Modified Hidden Weight Optimization Algorithm Based Neural Network Model for Permeability Prediction from Well-Logs Data

Leila Aliouane, Sid-Ali Ouadfeul, and Amar Boudella

LABOPHYT, Faculté des Hydrocarbures et de la Chimie,
Université M'hamad Bougara de Boumerdes,
Avenue de l'indépendance, Boumerdes, Algeria
lil_aldz@yahoo.fr
Algerian Petroleum Isntitute, IAP
Avenue 1er Novembre, Boumerdes, Algeria
SOuadfeul@ymail.com
Geophysics Department, FSTGAT, USTHB, Algiers, Algeria

Abstract. The mail goal of the current paper is to establish a Multilayer perceptron (MLP) neural network machine for rock permeability prediction from well-logs data. The MLP machine is composed of three layers, an input layer with 05 neurons a hidden layer with five neurons, the output layer is composed with one neuron. Well-logs data to be used as an input are: the natural gamma ray, the bulk density of the rock, the Macro-resistivity, the velocity of the compression wave and the neutron porosity. The output of the machine is the predicted permeability. Well-logs data of a pilot borehole located in the Algerian Sahara are used for the training, where the modified hidden weight optimization (MHWO) algorithm is used. Generalization to a second borehole located in the neighbourhood of the pilot borehole clearly shows that the implanted MLP machine using the MHWO can greatly improve reservoir characterization.

Keywords: MLP, MHWO, prediction, permeability.

1 Introduction

The permeability is one of principal task in reservoir characterization where the main goal is to establish numerical model of formation rock physical properties (porosity, water saturation and permeability) in order to provide input data for oil and gas reservoir numerical simulation. Generally speaking, permeability K is a function of the properties of the pore space, such as porosity Φ and several structural parameters.

The traditional method obtaining permeabiliy is mainly through prediction based on well logging using either an empirical relationships (Balan et al, 1995; Ellis and Singer, 2007) or some forms of statistical regression. The empirical models may not be applicable in regions with different depositional environments without making adjustments to constants or exponents in the model. Also, significant uncertainty

M. Lee et al. (Eds.): ICONIP 2013, Part I, LNCS 8226, pp. 498–502, 2013.
© Springer-Verlag Berlin Heidelberg 2013

exists in the determination of irreducible water saturation and cementation factor in these models (Elis and Singer, 2007). In fact, the problem of well-logging interpretation is a highly non-linear mapping problem. So, the artificial neural network is an effective way to solve complex non-linear mapping problem (Aliouane et al, 2012; Tian et al, 2012, Aliouane et al 2013b).

Artificial Neural Networks (ANN) is relatively popular numerical tool in geosciences, mainly, in petrophysics, this last decade. ANN provide very useful in applications where conventional computation methods are inadequate. They have been used in lithofacies classification and petrophysical parameters estimation (Aminian et al, 2005; Aminzadeh et al, 2000; Ouadfeul and Aliouane, 2013; Aliouane et al, 2013a).

Most methods used in permeability prediction by ANN is Backpropagation Neural Network (BPNN). It seems to be the most promising one in the literature (Mohaghegh et al, 1995; Mohaghegh et al, 1996). BPNN is the most popular among all ANN techniques in permeability prediction mainly because it is quite similar to Multiple Regression. In the present work, the goal is to use other learning algorithm for the Feed-Forward such as the Modified Hidden Weight Optimization algorithm (Yu et Manry, 2002).

2 Modified Hidden Weight Optimization Algorithm

The output weight optimization-hidden weight optimization (OWO-HWO) feed forward network training algorithm alternately solves linear equations for output weights and reduces a separate hidden layer error function with respect to hidden layer weights. Here, a new hidden layer error function is proposed which de-emphasizes net function errors that correspond to saturated activation function values. In addition, an adaptive learning rate based on the local shape of the error surface is used in hidden layer training. For more details about the HWO algorithm, we invite authors to the paper of Yu and Manry (2002).

3 Application to Real Data

Triassic reservoirs are generally shaley, clay in the pore space of a reservoir may affect the performance of a reservoir very adversely. The amount and kind of clay, as well as distribution throughout the reservoir rock, has an important bearing on liquid permeability, whereas a small amount has little effect on porosity.

Recordings of petrophysical parameters of two wells situated in Algerian Sahara (Well-A and Well-B) have been exploited. These are: Gamma ray (GR), Bulk Density (RHOB), Neutron Porosity (NPHI), Sonic Travel Time (DT) and Macro-Resistivity (LLD). In addition, measured permeability of core rocks in the same reservoir interval is used. Fig.1 and Fig.2 present the composite log of the studied wells.

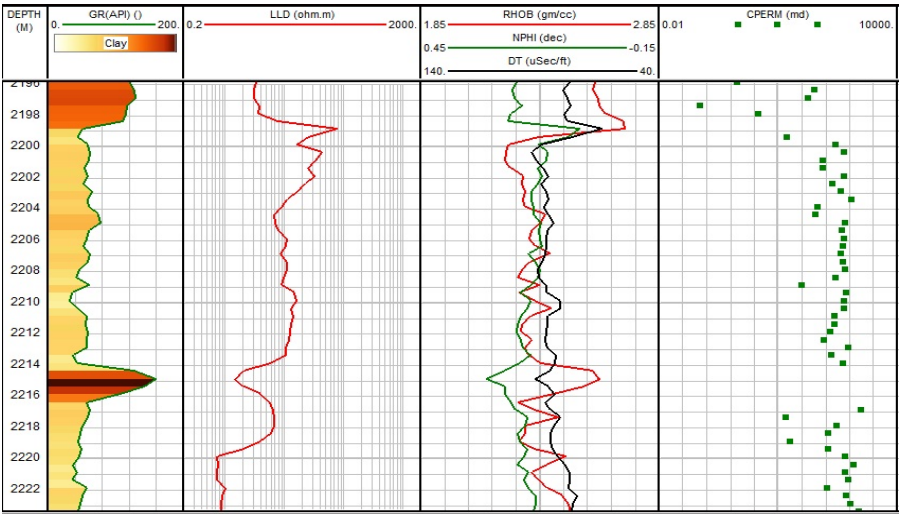

Fig. 1. Petrophysiscal parameters of well-A

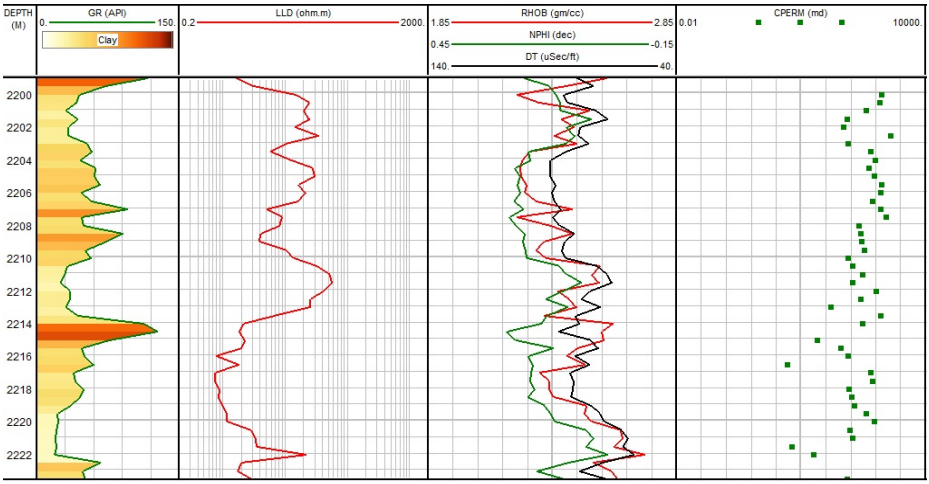

Fig. 2. Petrophysiscal parameters of well-B

3.1 Permeability Prediction by HWO

A neural network MLP machine to predict permeability in the borehole Well-B is implanted. The machine is composed with three layers, an input layer with five neurons, a hidden layer with seven neurons and an output layer with one neuron that corresponds to the predicted permeability. The borehole Well-B is used as a pilot

borehole for the training of the MLP machine, at this stage the measured core rock permeability is used as a desired output. The machine is trained in a supervised mode using the HWO-OWO algorithm. Fig. 3.a shows the calculated output of the MLP machine for the pilot borehole by propagating the set of well-logs data used as an input compared with the desired output.

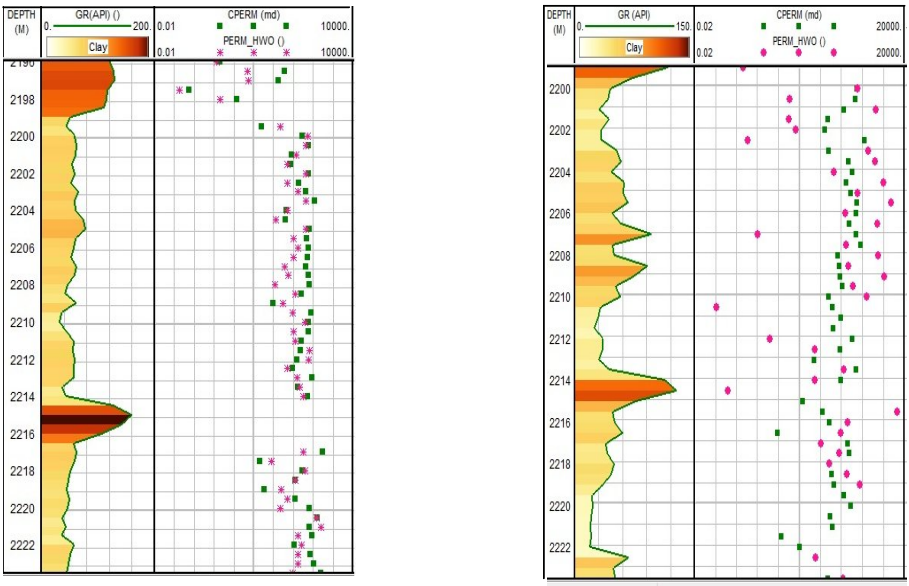

Fig. 3. Predicted and core Permeability: (a) Well-A; (b) Well-B.

4 Results Interpretation and Conclusions

Comparison between the calculated and the desired outputs of the Pilot borehole (Well-A) shows that the calculated permeability using the MLP machine (PERM_HWO) is very close to the measured core rocks permeability (CPERM). This proves the good training of the MLP machine in the pilot borehole Well-A.

The measured well-logs data for the borehole Well-B are propagated through the implanted MLP machine and an output is calculated using the optimized weights of connection. At this step no desired output is needed. Fig.3.b shows the predicted permeability (PERM_HWO) compared to the measured core rocks permeability (CPERM), obtained results show that the MLP machine has given generally acceptable results, expect some depth points (example 2212.5m and 2214.5m) where the PERM_HWO has given results not close to core rock results. This is explained by the no sufficiency of training data, so the neural network needs more training data to generalize better.

We suggest application of the whole process to large data to extract a final decision about the training algorithm.

References

1. Aliouane, L., Ouadfeul, S., Djarfour, N., Boudella, A.: Lithofacies prediction from well logs data using different neural network models. In: Proceeding INSTICC, International Conference on Pattern Recognition. Applications and Methods (2013a)
2. Aliouane, L., Ouadfeul, S., Djarfour, N., Boudella, A.: Permeability Prediction Using Artificial Neural Networks. A comparative study between Back Propagation and Levenberg-Marquardt learning algorithms. In: LNESS. Springer (in press, 2013b)
3. Aliouane, L., Ouadfeul, S.-A., Djarfour, N., Boudella, A.: Petrophysical parameters estimation from well-logs data using Multilayer Perceptron and Radial Basis Function neural networks. In: Huang, T., Zeng, Z., Li, C., Leung, C.S. (eds.) ICONIP 2012, Part V. LNCS, vol. 7667, pp. 730–736. Springer, Heidelberg (2012)
4. Aminian, K., Ameri, S.: Application of artificial neural networks for reservoir characterization with limited data. Journal of Petroleum Science and Engineering 49, 212–222 (2005)
5. Aminzadeh, F., Barhen, J., Glover, C.W., Toomarian, N.B.: Reservoir parameter estimation using hybrid neural network. Computers & Geosciences 26, 869–875 (2000)
6. Balan, B., Mohaghegh, S., Ameri, S.: State-Of-The-Art in Permeability Determination from Well Log Data: Part 1- A Comparative Study, Model Development. In: Eastern Regional Conference & Exhibition, West Virginia, U.S.A. SPE, vol. 30978 (1995)
7. Mohaghegh, S., Balan, B., Amri, S.: Permeability Determination from Well Log Data. Presented at SPE Eastern Regional Conference and Exhibition, held in Morgantown, West Virginia. SPE, vol. 30978 (1995)
8. Mohaghegh, S., Ameri, S., Arefi, R.: Virtual Measurement of Heterogeneous Formation Permeability Using Geophysical Well Log Responses. The Log. Analyst, 32–39 (March/April 1996)
9. Ellis, D.V., Singer, J.M.: Well logging for earth scientists, 2nd edn. Springer (2007)
10. Tian, Y., Zhang, Q., Cheng, G., Liu, X.: An Application of BF Neural Networks for Petroleum Reservoir Characterization. In: IEEE Third Global Congress on Intelligent Systems (2012), doi:10.1109/GCIS.2012.75
11. Ouadfeul, S.-A., Aliouane, L.: Lithofacies prediction from well log data using a multilayer perceptron (MLP) and Kohonen's self-organizing map (SOM) – a case study from the Algerian Sahara. Pattern Recogn. Phys. 1, 59–62 (2013), doi:10.5194/prp-1-59-2013
12. Yu, C., Manry, M.T.: A modified hidden optimization algorithm for feedforward neural networks. In: Conference Record of the Thirty-Sixth Asilomar Conference on Signals, Systems and Computers, vol. 01(2), pp. 1034–1038 (2002)

WebVRGIS: A P2P Network Engine for VR Data and GIS Analysis

Zhihan Lv[1,2], Shafiq Ur Réhman[1,2], and Ge Chen[3]

[1] Shenzhen Institutes of Advanced Technology, Chinese Academy of Science, P.R.C
[2] Tillmpad fysik och elektronik, Umeå University, Umeå, 90187, Sweden
[3] Ocean University of China, Qingdao, 266100, P.R.C
zh.lv@siat.ac.cn, shafiq.urrehman@umu.se, webvr@vip.qq.com

Abstract. A Peer-to-peer(P2P) network engine for geographic VR data and GIS analysis on 3D Globe is proposed, which synthesizes several latest information technologies including web virtual reality(VR), 3D geographical information system(GIS), 3D visualization and P2P network. The engine is used to organize and present massive spatial data such as remote sensing data, meanwhile to share and online publish by P2P based on hash. The P2P network makes a mapping of the users in real geographic space and the user avatar in the virtual scene, as well as the nodes in the virtual network. It also supports the integrated VRGIS functions including 3D spatial analysis functions, 3D visualization for spatial process and serves as a web engine for 3D globe and digital city.

Keywords: P2P network, WebVR, VRGIS, Big data, 3D Globe.

1 Introduction

With the development of VR (Virtual Reality) technology and widely applications in various areas, the requirements to VR are also increasing rapidly. Users do not only need to obtain the landscape geospatial data dynamically but also need to perform some analyses, calculations, managements and transfers based on data. Virtual Reality Geographical Information System (VRGIS), a combination of geographic information system and virtual reality technology [8] has become a hot topic. With the popularity of network, the VRGIS platform based on the network environment also becomes a trend. The application of VRML, X3D and other online VR technologies have achieved networking of VR systems, because of the mass data, the network bandwidth constraints of transmission, a large number of request and multi-user collaboration controls, the online virtual reality technology still face numerous challenges. To improve the accuracy of modeling, the city planning has an increasingly high demand for the realistic display of VR system, however this will inevitably lead to the growth of the volume of data transmission. Virtual scene from a single building to the city scale is also resulting in the increased amount of data. The increasing number of user increase the server load and in more severe cases the server has to deny the services. These challenges and problems directly lead the on-line VR

M. Lee et al. (Eds.): ICONIP 2013, Part I, LNCS 8226, pp. 503–510, 2013.
© Springer-Verlag Berlin Heidelberg 2013

technology failure to provide high-quality service to public base on the current network frame. Currently, few companies are investing mass of money to set up a large amount of data server nodes in order to break through the bottleneck of the network transmission speed. Therefore it is necessary to seek new, more efficient and more economical mechanism to create a WebVRGIS system on Internet. Using advanced computer technology to construct digital city has attracted the attentions from many walks of life. By integrating the friendly interactive interface of Virtual Reality System and spatial analysis specialty of Geographical Information System, WebVRGIS is preferred in practical applications, especially by the geography and urban planning. Urban simulation is becoming widely noticed nowadays, and some simulation systems have been developed in this area;e.g., ArcView3D Analyst, Imagine Virtual GIS, GeoMedia, etc. The above mature platforms are limited to a single computer running, while the publish methods based on network environment are proposed. WebVRGIS engine supports steadily real time navigation in virtual scenes which are constructed with massive, multi-dimensional data from various sources. VR and GIS modules are integrated seamlessly. All kinds of requirements for large-scale landscape simulation and a data management can be satisfied. 3D urban landscape database with various data sources can be produced to implement spatial analysis and 3D visualization and published in the Internet environment.

2 Background

In the early 1990s, Koller and others had an integration research about VR and GIS, and put forward the concept of VRGIS [9]. VRGIS is based on VR technology as a front-end interaction with users and supports GIS spatial data storage, processing, query and analysis functions of the system from bottom. With the development of VR technology and computer hardware technology, massive data management and 3D visualization technologies have been greatly improved. In VR field, massive data management and accelerated rendering technology include the following areas of study such as architecture design based on out-of-core, accelerate the 3D rendering, network optimization. However, most of current commercial platforms lack a timely application of these research results, which makes the combination of VR and GIS not in place and reduces the speed of city digitization. WebVRGIS integrates various up-to-date VR technologies, which can solve the problems in 3D visualization of massive data, P2P based massive 3D data share, realize the seamless integration of VR and GIS and provide a strong support for the city digitization. The stand-alone environment VRGIS [7] was developed. Based on VRGIS platform, WebVRGIS updates the overall framework as well as part sorts of key technologies, in which can support data publish on the network, and to support the mass data transmission and large numbers of users online simultaneously based on P2P technology.

3 Engine Overview

WebVRGIS engine designation uses object-oriented project database, whose data storage and management are based on object-oriented nodes, which is divided as core, middle and extended level. The core level is responsible for the organization and management of data and P2P virtual network management and also integrating rendering engine. The middle level supports the interface by encapsulating the core level and exporting the accessing interface for the extended level. The extended level implements extended function to fulfill the demand on application layer. With design patterns such as factory, visitor and singleton, the engine has good flexibility and extensibility.

4 Key Technology

Both VR and GIS systems need massive data, which can be provided from various sources. In the engine, DEM and DOM are used to construct the virtual terrain, and a 3DS MAX plug-in is developed to implement the combination of WebVRGIS and 3DS MAX. Because the virtual city needs massive data and computes too much, WebVRGIS engine introduces several optimization and acceleration technologies. Build up a P2P virtual network for multi-users and accelerate the 3D data transmission speed. VR and GIS modules are integrated seamlessly in the engine.

4.1 Support of Massive Geospatial Data

Virtual city simulation encounters the problem about massive data, which means that the data is dozens of GB or even more, and too large to load in the memory at one time. The WebVRGIS engine is designed to support massive data. Data transfer methods used in WebVRGIS engine make the ability of present large-scale scenes perform well online.

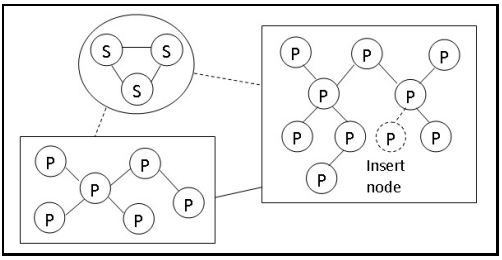

Fig. 1. Network Topology Structure of WebVRGIS

P2P Based VR and GIS Data Sharing. WebVRGIS exploits hybrid P2P structure. Cavagna et al has proposed a P2P model based on theory of space division of Voronoi diagram [5], to the transfer of cites 3D (three-dimensional) scene for online games, it supports streaming 3D scene index structure PBTree [11] for the 2.5D data compression out of the 3D model. Varvello et al combined the KAD network model with the mathematical model of the virtual environment [13], and tested in Second life as a framework [12]. Hu et al. have developed a set of P2P model Flod [14] based on the Voronoi diagram theory of the space partition. The model has solved the problem of user neighbors distributed storage by dynamic classification method. However, the global scope of the real geo-spatial environment is relatively stationary; there is no need of dynamic division. WebVRGIS exploit hash value to index VR and GIS data. In order to avoid the information silos, there are one and/or more servers to keep the hash value of all the users logged, the level of health, distances list, etc. Each client will connect with the server at first, request information of users which have higher health level in the list. After receiving the user list, the client disconnects with the server, the list received is integrated with the existing list to form a new one, and then it tries to update and make connections with other clients. Hash value is utilized as index of data block and user nodes, the XOR algorithm is used to calculate the logical distance. Obtained logical distance determines the distance between the nodes in the network and the user avatar in the 3D scene. Further more, the relative position can be obtained. This approach makes a mapping of the user in real geographical space and the user avatar in the virtual scene, as well as the nodes in the virtual network. Figure 1 is the virtual P2P network topology structure in WebVRGIS. WebVRGIS has following major components:

SERVER. The server is not necessary, but a sufficient condition for each node to be linked in the virtual network. Server uses I/O completion port ($IOCP$), which provide an efficient threading model for processing multiple asynchronous I/O requests on a multiprocessor system. After the server is initialized, the system created several threads, each thread do the I/O operation with Internet through IOCP. The server is not only used to preserve the user list, but also can be used as the Internet server providing the transit services for the whole P2P network, and make the connection request penetrate the firewalls and NAT smoothly, and improved the rate of nodes connection.

P2P Virtual Network. The client is adopted the P2P scheduling algorithm which is belong to the Kademlia algorithm [10]. Figure 2 is the P2P Engine hierarchy of P2P virtual network.

General P2P Service Layer. Kademlia regards each client as a node in P2P virtual network. That store and query the object information use $(key, value)$ methods. The key is a $128-bit$ identifier. When it is used in node identifier, $value$ is calculation by IP address and port. When used for data identifier, $value$ is the content of the data block. The result of two hash value XOR operation is the logical distance. Each $(key, value)$ stored in the node which has the shortest logic distance from the value. The routing table is constructed by the table called $K-B$ (K bucket). For each $i(0 \leq i \leq 128)$, each node

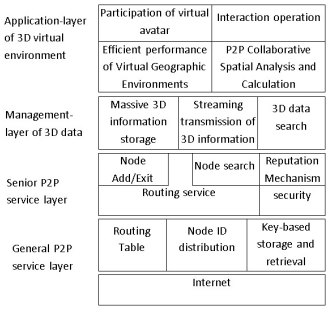

Fig. 2. P2P Engine hierarchy

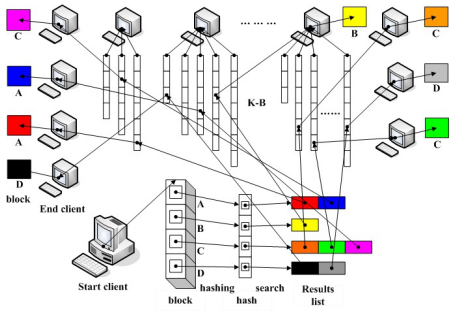

Fig. 3. File Block Search Process

have kept some node information that in the range of $m(2i < m < 2i+1)$,the table structure of which is the same as that of server-side. Each $K-B$ has the data item that has the same ID prefix no more than k. The location of the $K-B$ is arranged according to the time order. In each node, using binary tree structure organizes the $K-B$ and neighboring node hash, and storing them in the leaf nodes. As shown in Figure 3.

Senior P2P Service Layer. The responsibilities of this layer is to monitor the nodes adding and withdraw behavior in real-time, and the node searching traverse in the data structure. The data changing and traverse of the data structure based on Hash value are referenced since Kademlia. During the node query process, the configuration will be automatic transmitted, the node sends and receives the massage meanwhile update their routing table. Because each query gets information from the $K-B$ that closer to the target node, this mechanism ensures the effect that every recursive operation can reduce at least $1bit$, as well as half of the distance. Because of using the index mode divide the interval, for a network containing N nodes, at most inquiry $logN$ step, the target node can be accurately located.

Management-Layer of Remote Sensing Data. The data searching process which is the most important function of P2P is realized in this layer. Node makes the published file information store in certain position of Kademlia, If each message has a $128-bit$ ID, information will be stored in the corresponding nodes. Each piece of information contains three parameters: $< File\ Hash\ Value,\ Publisher\ IP\ Address,\ Publisher\ Port >$ at least. The publisher will store the information in the node whose ID equals file hash value. For any node, it stored the information of the publishers who publish the same file. The object in large-scale scene is stored as a number of model files according to different LOD level. Model file contains the hash values of textures, not only the file names. After downloading and parsing the model file, a texture hash list will be got, and then searching the hash list in the virtual network. While finding the file list, dividing this file as blocks and then searching the hash value of every block, the result is stored in the transmission list.

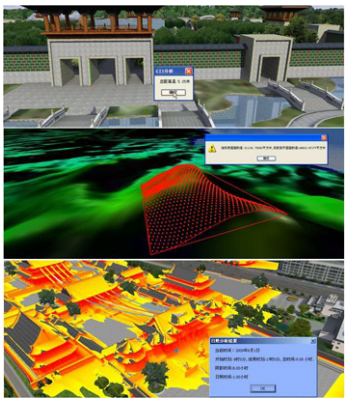

Fig. 4. VR-GIS function on web

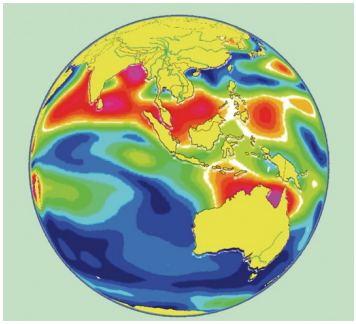

Fig. 5. The Sea Surface Temperature in WebVR-GIS

4.2 Seamless Integration of VR and GIS

Data sharing and function unification are the main goals of the integration of VR and GIS. By abstracting VR data and GIS data uniformly and inheriting their traits, the engine provides uniform external access interface and makes nodes have their own render and access mode, so that unification and sharing of VR and GIS data are achieved. As to the function unification, 3DGIS analysis functions are developed based on the uniform geospatial data. Combining the data's 3D traits, GIS analysis algorithm is applied in the 3D virtual scene, includes: measurement of the point, lines, faces and volumes, flooding analysis, muter-invisibility analysis, contour analysis, shadow analysis, path analysis, etc. The top one in Figure 4 shows the result of measure an arch door distance. The others in Figure 4 show 3D area measuring and sunshine analysis.

4.3 Multi-dimensional Data Support

The geometry data model is designed complied with the simple feature rules of *OGCOpenGIS*. Map establish optional indexing mechanism either $R-tree$ or $quad-tree$. Each geometry regarding a data record is stored into the feature dataset with unique index. It is released for com, as a server-side real-time vector data rendering engine, meanwhile provide web service interface for the browser-side. The engine supports almost every format of vector and raster data by integrating the FDO [1] of OSGEO and GDAL/OGR [2]. The fused data can be published on the surface of 3D digital earth divided following the digital earth data blocking mechanism. We use WebVRGIS to do verification. The Figure 5 shows the outcome of the fusion of spatial patterns of identified principal precipitation modes with the global land vector data [6].

Fig. 6. 2008 Qingdao Olympic Sailing

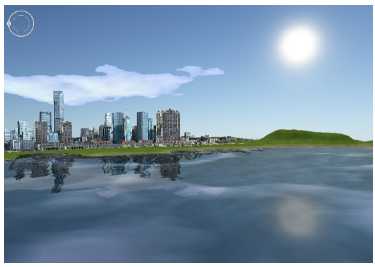

Fig. 7. Shenzhen Coastal

5 Implementation and Application

The oriented city region simulation WebVRGIS engine is developed based on OpenGL and C++, which integrates VR and GIS seamlessly and supports massive data. It was released in the forms: application and Com components. Based on WebVRGIS engine, we have developed some applications. We have tested the engine on a PC with a i3 M330 2.13GHz CPU, 8 GB, and an GeForce GT 330M GPU (1GB) by using data of Shenzhen city which about 8G including 62sq.km. DEM, DOM and model files exported from 3DS Max. The experiment can run 24fps averagely. Figure 6 and Figure 7 proves the applications, and the virtual scene of 2008 Olympic regatta in Qingdao rendered in WebVRGIS is shown in Figure 6, and the virtual Shenzhen seashore is shown in Figure 7.

6 Conclusion and Perspectives

WebVRGIS engine is developed, in which the integration of VR and GIS is researched. In the engine, massive data shared by the two systems (VR&GIS) is supported by the P2P virtual network. It can meet the requirements for virtual city construction, GIS analysis. GIS data has several characteristics, ie. large scale, diverse predictable and real-time, which falls in the range of definition of Big Data defined by Intel Fellow Faye Briggs [4]. In 2008, Nature published a special issue concerned with the subject of Big Data [3], which makes people focus on the use of existed massive data (ie. analysis, visualization). The future work will focus on the augmented reality extended application of WebVRGIS engine and more intelligent process with considerable urban image search algorithm. At the same time, we have plans to play full potential of P2P, combined with the advantage of the cloud computing, provide the cooperating VR/AR roaming function and GIS analysis for multi-users.

Acknowledgments. The authors are thankful to the National Natural Science Fund of China(61070147), National Natural Science Fund for the Youth of China(41301439) and Shenzhen Scientific & Research Development Fund(JC201105190951A).

References

1. Feature data object (fdo), http://fdo.osgeo.org/
2. Geospatial data abstraction library, http://www.remotesensing.org/gdal/
3. Big data specials. Nature, 455(7209) (September 2008)
4. Briggs, F.: Large data - great opportunities. Presented at IDF 2012, Beijing (2012)
5. Cavagna, R., et al.: P2p network for very large virtual environment. In: Proc. ACM Symp. V. R. Soft. and Tech. (2006)
6. Chen, G.: A novel scheme for identifying principal modes in geophysical variability with application to global precipitation. J. Geophys. Res. 111, 11103 (2006)
7. Chen, G.: etc. An integrated vrgis navigation platform for city region simulation. Comput. Animat. Virtual Worlds 21(5), 499–507 (2010)
8. Huang, B., Jiang, B., Li, H.: An integration of gis, virtual reality and the internet for visualization, analysis and exploration of spatial data (2001)
9. Koller, D., et al.: Virtual gis: A real-time 3d geographic information system. In: Proc. 6th Conf. on Vis. (1995)
10. Maymounkov, P., Mazières, E.: Kademlia: A peer-to-peer information system based on the xor metric. In: 1st Int. Workshop on Peer-to-Peer Sys. (2002)
11. Royan, J., Bouville, C., Gioia, P.: Pbtree: A new progressive and hierarchical representation for network-based navigation in densely built urban environments. Annales Des Telecommunications 60(11-12), 1394–1421 (2005)
12. Varvello, M., Diot, C., et al.: P2p second life: experimental validation using kad. In: Infocom, Rio De Janeiro (2009)
13. Varvello, M., et al.: A networked virtual environment over kad. In: Proceedings of the 2007 ACM CoNEXT Conference (2007)
14. Yun Hu, S., et al.: Flod: A framework for peer-to-peer 3d streaming. In: Proc. 27th Conf. Computer Communication, INFOCOM 2008 (2008)

Ionospheric Data Analysis of Demeter Sattelite Using Neural Network: Application to IAP Instrument

Sid-Ali Ouadfeul, Leila Aliouane, and Victor Tourtchine

LIMOSE, Faculté des Sciences,
Université M'hamad Bougara de Boumerdes,
Avenue de l'indépendance, Boumerdes, Algeria
LABOPHYT, Faculté des Hydrocarbures et de la Chimie,
Université M'hamad Bougara de Boumerdes,
Avenue de l'indépendance, Boumerdes, Algeria
SOuadfeul@ymail.com

Abstract. In this paper, we use the artificial neural network for prediction of ionospheric perturbations by the analysis of the Instrument Plasma Analyzer (IAP) data using the Multilayer Perceptron (MLP) neural network. Data that are used as an input and output for the training of the MLP machine are: the Helium, Electron and Ions densities, Ions temperature, Ions speed and direction. The MLP machine is composed with an input layer, an output layer and a hidden layer. Application to the Demeter satellite data of orbit 27447-1 shows that the MLP neural network machine can give good results for plasma disturbances and can be used for prediction of seismo-ionospheric perturbations.

Keywords: IAP, Demeter, MLP, disturbances, prediction.

1 Introduction

The artificial intelligence has becoming a very useful tool in plasma physics (Rozhansky et al, 2013; Svensson et al, 1999). In earth plasma the artificial intelligence is used for analysis of data recorded by satellite missions (Taylor et al, 2007). French DEMETER (Detection of Electro-Magnetic Emissions Transmitted from Earthquake Regions) micro-satellite mission had been especially designed to provide global scale observations in the topside ionosphere over seismically active regions (Bankov et al, 2010). In this paper, we used the Multilayer perceptron neural network for prediction of ionosphere plasma parameters recorded by the Instrument Plasma Analyze (IAP) installed on board of DEMETR mission; the goal is to predict future plasma parameters which are: Number of Hydrogen particles in the plasma (NH+), number of Helium (NHe+) and Oxygen particles (NO+), ions temperature (NI+), ions speed (VS and VZ), angles of ions arrival (VOX and VOZ).

2 Instrument Plasma Analyzer (IAP)

The IAP (Instrument Analyseur de Plasma) experiment installed on consists of two analyzers: APR (Analyseur à Potentiel Retardateur, Retarding Potential Analyzer)

M. Lee et al. (Eds.): ICONIP 2013, Part I, LNCS 8226, pp. 511–519, 2013.
© Springer-Verlag Berlin Heidelberg 2013

performs the energy analysis of ram direction ions and ADV (Analyseur pour Direction de Vitesse, Velocity Direction Analyzer) determines the average angles of arrival of the ions. APR measurements allow determining the density, temperature and bulk energy of the ionospheric ions. IAP has 2 Survey modes of operation a medium energy resolution mode for APR providing a complete set of plasma parameters every ~ 360 ms and a high energy resolution mode with a lower temporal resolution providing a complete set of measurements every 720 ms. Density fluctuations from ADV measurements are available with a time resolution of 12.8 ms. There is also one Burst mode of operation featuring high energy and high temporal resolution with a complete set of plasma parameters every ~ 360 ms. Density fluctuations are available with a time resolution of 6.4 ms. The objective of the IAP experiment is to characterize the state of the ionospheric plasma, in order to detect perturbations that may be associated with seismic activity and to provide the plasma parameters that are needed to analyze the data from the plasma wave instruments, ICE and IMSC. As a secondary objective, near real time ionospheric data can be provided for space weather purposes.

3 The Multilayer Perceptron Neural Network

Multilayer feed-forward networks form an important class of neural networks. Typically the network consists of a set of sensory units or input nodes, that constitute the input layer, one or more hidden layers of neurons or computation nodes, and an output layer. Multi-layer Perceptron (MLP) neural networks with sufficiently many nonlinear units in a single hidden unit layer have been established as universal function approximators. For more details about the MLP, we invite readers to the papers of Ouadfeul and Aliouane (2012, 2013).

4 Data Analysis, Results and Conclusion

A multilayer neural network machine with three layers is implanted; the input layer is composed with eight neurons that correspond to the eight IAP plasma parameters, a hidden layer of seven neurons (obtained by test) and an output layer of eight neurons that correspond also to the IAP plasma parameters. Data of orbit 27447-1 that sweep L'Aquila area two days before the main chock of 09 April 2009 are used for the training of the neural network machine. The first time series of 151 (see Fig. 01) samples is used as an input, however the second 151 samples are used as an output (see Fig. 02). The implanted MLP machine is trained in a supervised learning and weights of connection are optimized. To check the efficiency of this neural machine the second time series is used as an input and an output is calculated by propagating the input via this machine, at this stage no training is needed since the weights of

connection are calculated in the first stage. Obtained results are compared with the actual recorded plasma parameters (see Fig. 3), one can observe that the MLP machine is able to provide an acceptable model of parameters, however at the end of each time series the artificial neural network machine start to lose the memory, by consequence the MLP neural network has not long term memory, so we need always to update the weights of connection to give exact results. We suggest application of the whole process to data of other orbit to generalize its efficiency and generalize a rule.

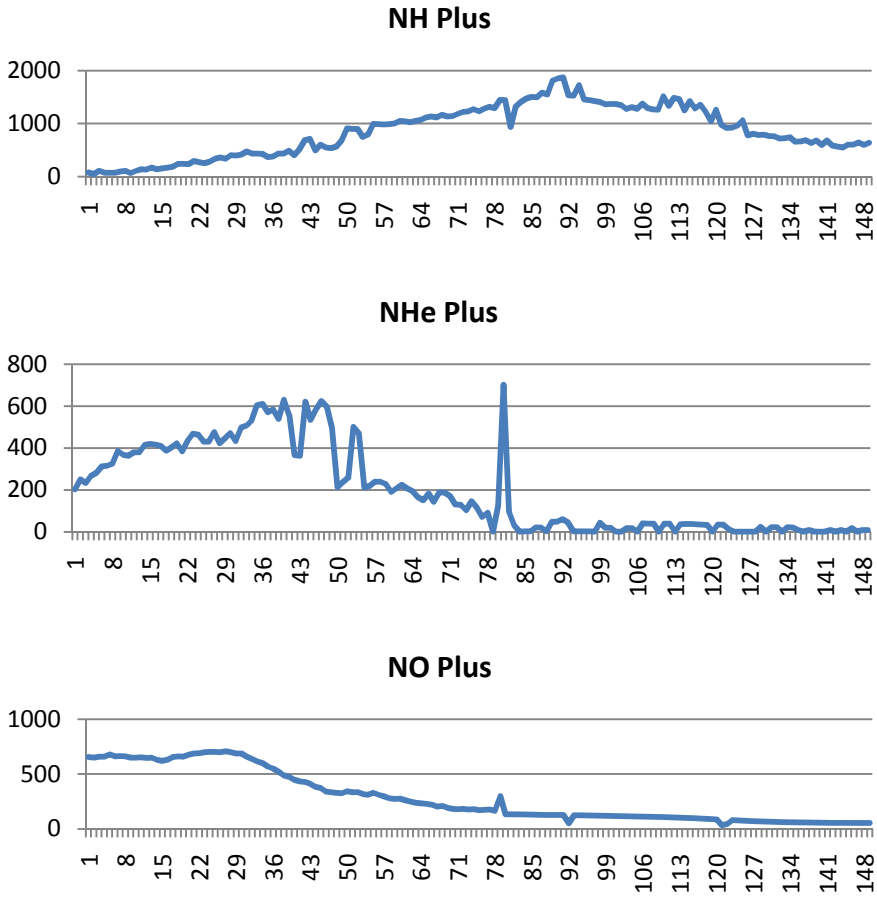

Fig. 1. First 151 samples of IAP instrument parameters of DEMETER satellite used for the MLP training

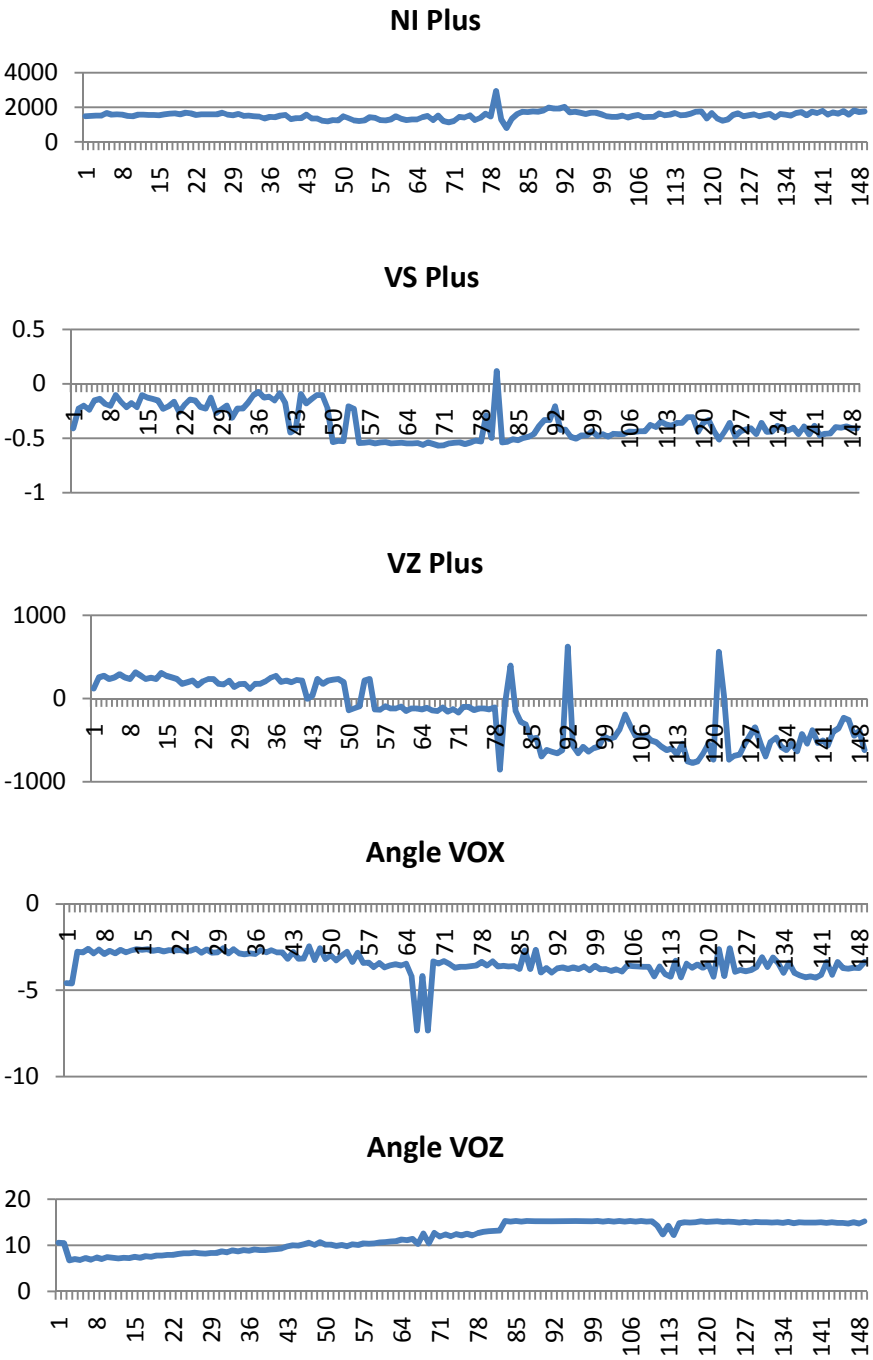

Fig. 1. (*Continued.*)

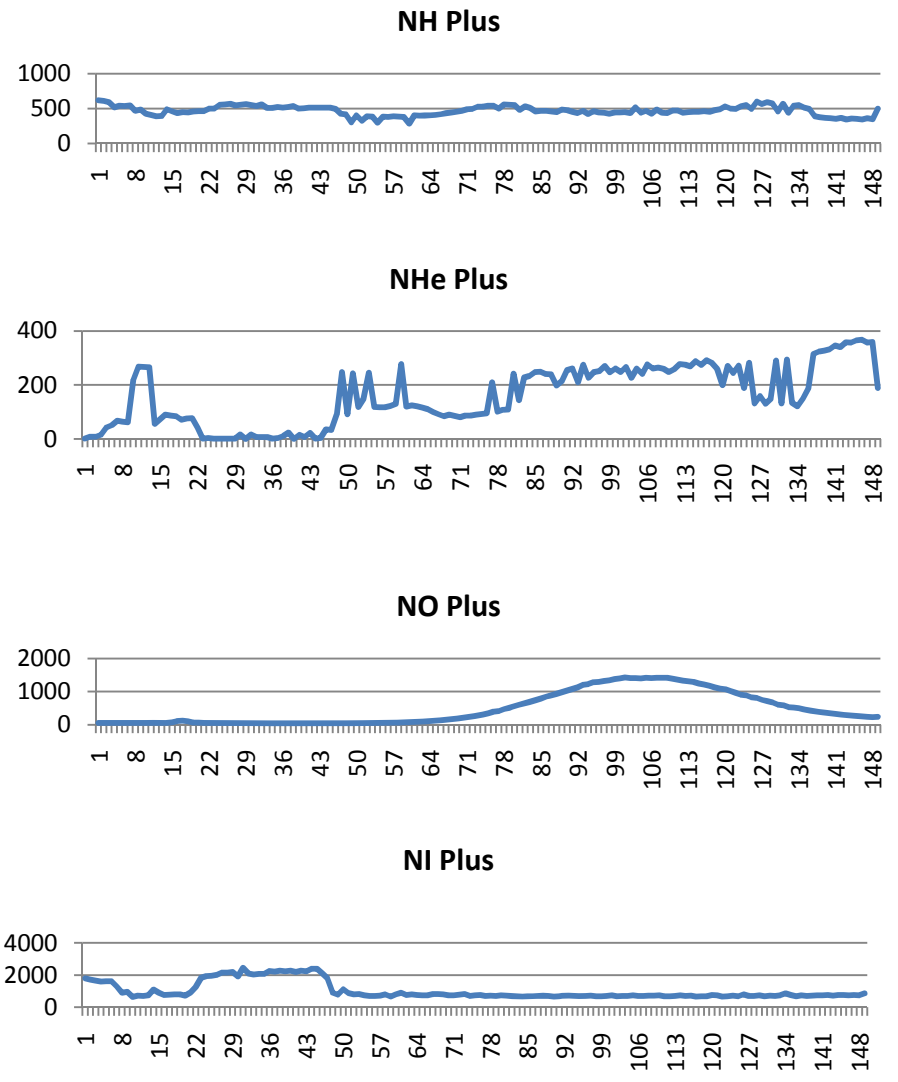

Fig. 2. Second 151 samples of IAP instrument used as an output for the MLP training

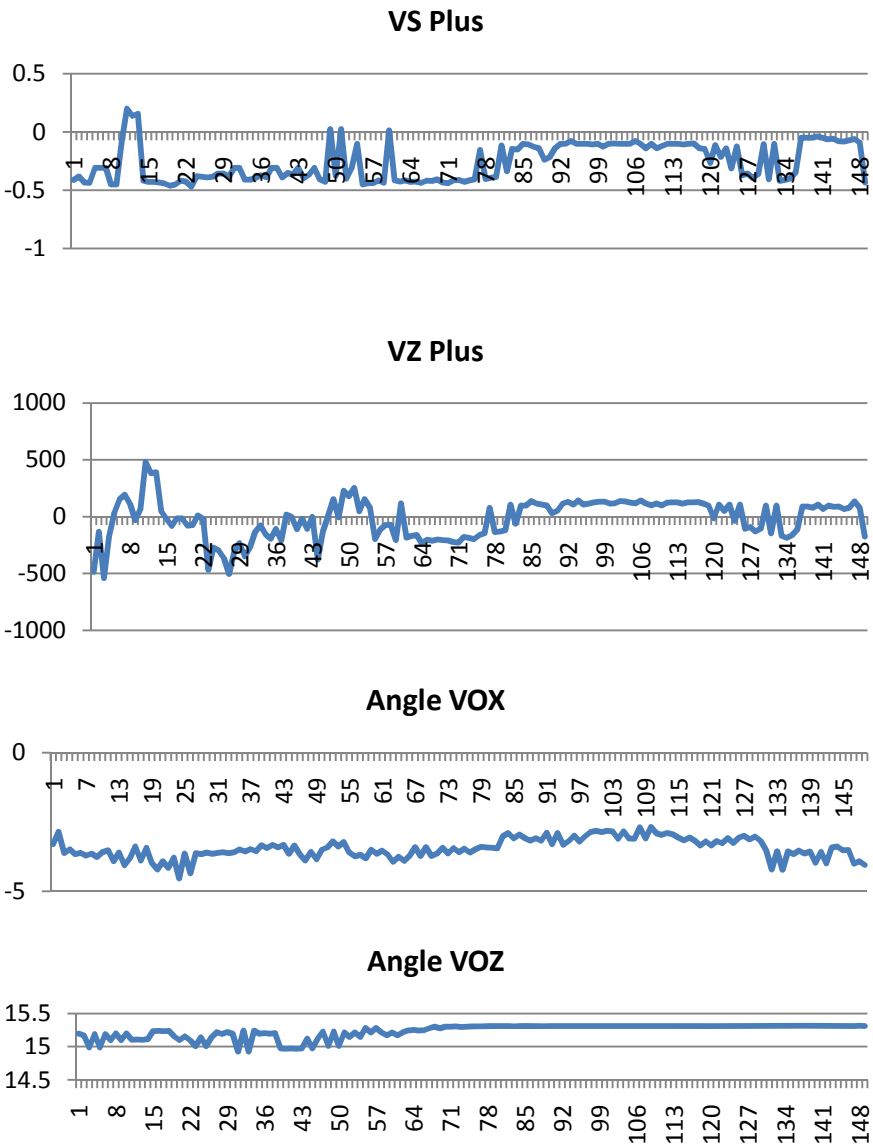

Fig. 2. (*Continued.*)

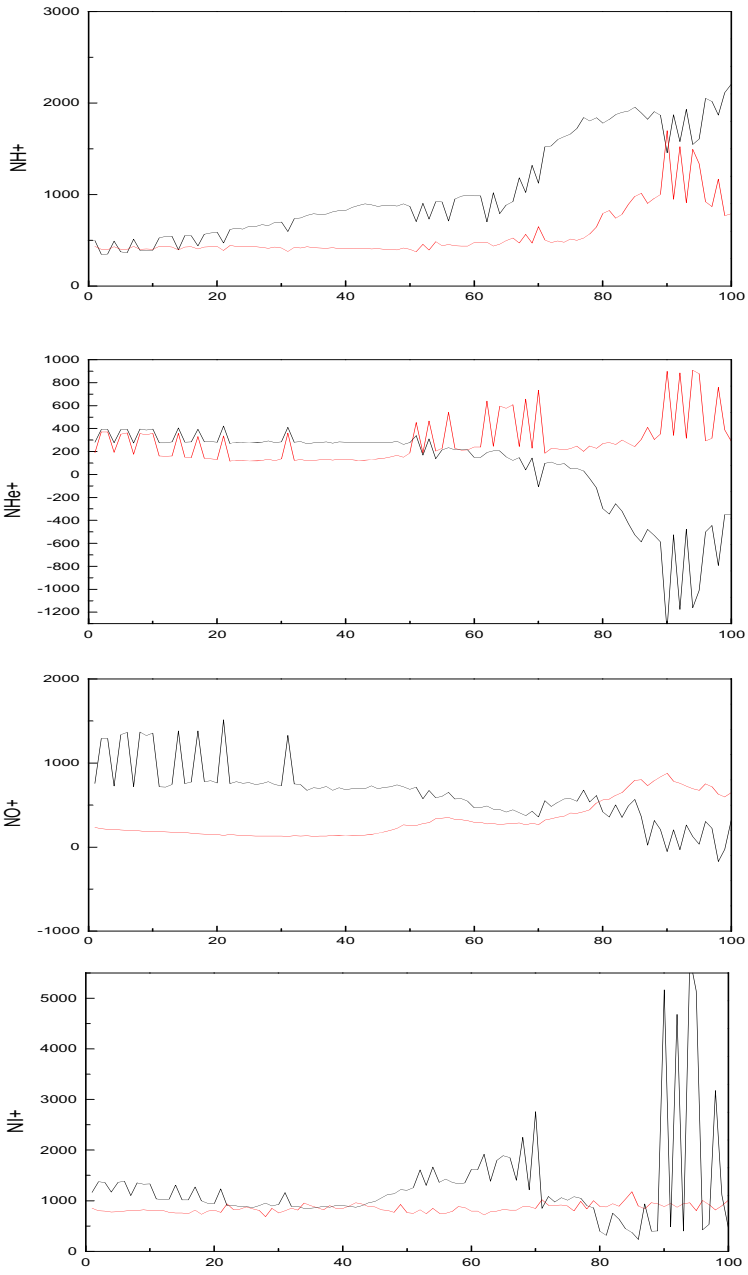

Fig. 3. Predicted IAP plasma parameters using the implanted MLP machine

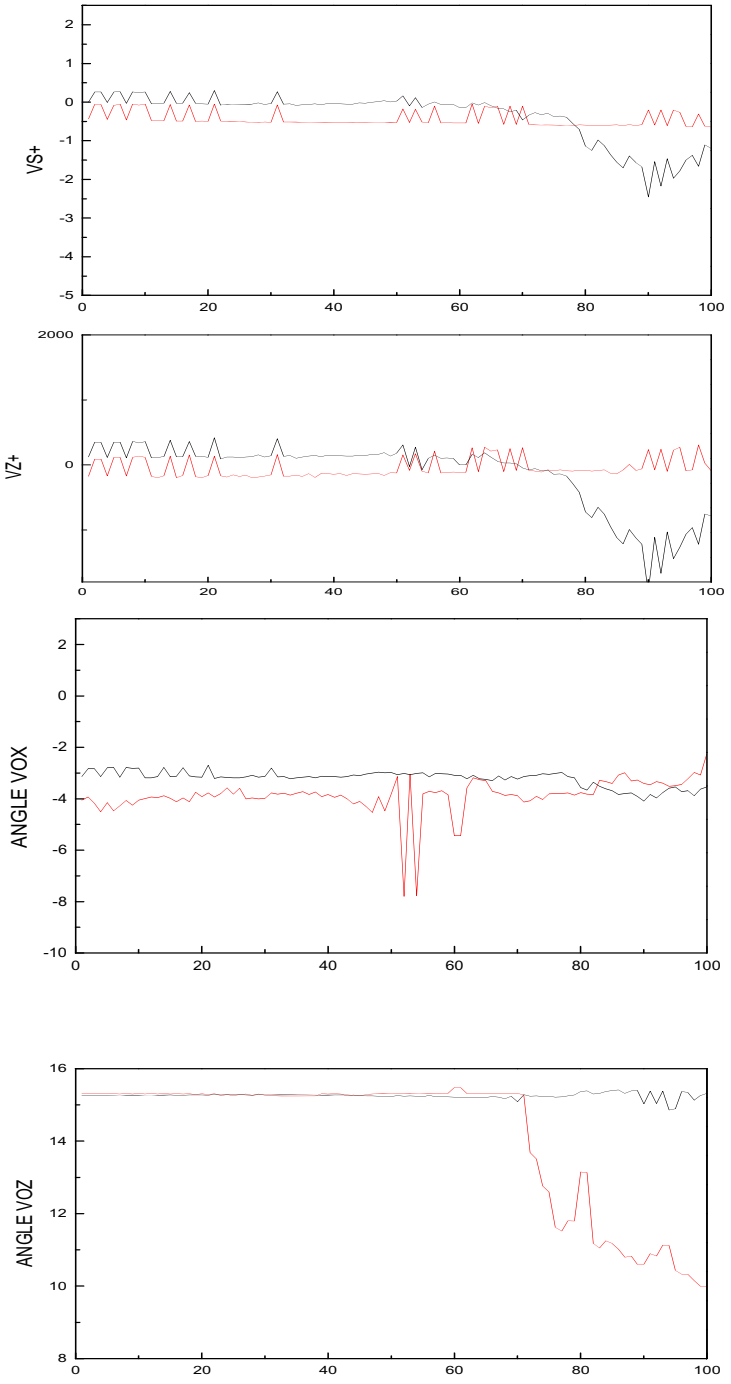

Fig.3. (*Continued.*)

References

1. Bankov, L.G., Parrot, M., Heelis, R.A., Berthelier, -J., Marinov, P.G., Vassileva, A.K.: DEMETER and DMSP satellite observations of the disturbed H+/O+ ratio caused by Earth's seismic activity in the Sumatra area during December 2004. Advances in Space Research 46(4), 419–430 (2010)
2. Ouadfeul, S.-A., Aliouane, L.: Lithofacies prediction from well log data using a multi-layer perceptron (MLP) and Kohonen's self-organizing map (SOM) – a case study from the Algerian Sahara. Pattern Recogn. Phys. 1, 59–62 (2013), doi:10.5194/prp-1-59-2013
3. Ouadfeul, S.-A., Aliouane, L.: Lithofacies Classification Using the Multilayer Perceptron and the Self-organizing Neural Networks. In: Huang, T., Zeng, Z., Li, C., Leung, C.S. (eds.) ICONIP 2012, Part V. LNCS, vol. 7667, pp. 737–744. Springer, Heidelberg (2012)
4. Rozhansky, V., Molchanov, P., Veselova, I., Voskoboynikov, Kirk, A., Fishpool, G., Boerner, P., Reiter, D., Coster, D.: Modeling of the edge plasma of MAST Upgrade with a Super-X divertor including drifts and an edge transport barrier. Plasma Phys. Control. Fusion (2013), doi:10.1088/0741-3335/55/3/035005
5. Svensson, J., von Hellermann, M., König, R.: Analysis of JET charge exchange spectra using neural networks. Plasma Phys. Control. Fusion 41, 315 (1999), doi:10.1088/0741-3335/41/2/016
6. Taylor, M., Diaz, A.I.: On the deduction of galaxy abundances with evolutionary neural networks. Publications of the Astronomical Society of the Pacific (2007)

A Simplified Cerebellum-Based Model for Motor Control in Brain Based Devices

Vui Ann Shim, Chris Stephen Naveen Ranjit, Bo Tian, and Huajin Tang

Institute for Infocomm Research, 1 Fusionopolis Way,
#21-01 Connexis, 138632, Singapore
{shimva,btian,htang}@i2r.a-star.edu.sg, ranjitcsn@gmail.com

Abstract. The cerebellar system is implicated in motor learning for movement coordination. In this paper, we suggest a simplified cerebellar model with priority-based delayed eligibility trace learning rule (S-CDE) that enables a mobile agent to randomly navigate in an environment. The depth information from a simulated laser sensor is encoded as neuronal region activity for velocity and turn rate control. A priority-based delayed eligibility trace learning rule is proposed to maximize the usage of input signals for learning in synapses on Purkinje cell and cells in the deep cerebellar nuclei. Asymmetric weighted sum and velocity signal conversion algorithms are designed to facilitate training in an environment containing turns of varying curvatures. S-CDE is developed as a brain-based device and tested on a simulated mobile agent which had to randomly navigate maps of Singapore and Hong Kong expressways.

Keywords: Brain-based devices, cerebellum, priority-based delayed eligibility trace learning rule, error signals, motor control.

1 Introduction

The study of the cerebellum in neuroscience, physiology, and neuroimaging has resulted in several consistent findings that implicates the cerebellar system in motor learning [1,2,3]. Error signal, the difference between reference and actual movement coordinations, has been proposed to regulate learning in the cerebellar system through synaptic eligibility traces [4]. The error signals are transmitted from the inferior olive (IO) to cerebellar regions via climbing fibers [5,6].

Inspired by the above findings, McKinstry *et al.* [7] proposed a cerebellar-based computational model with delayed eligibility trace learning rule (CDE) that learns to predict corrective motor control actions based on the experiences of reflex responses. CDE is developed as a brain-based device (BBD) [8], which is a famous platform to construct a computational model of neuroscience by incorporating features of neuroanatomy and neurophysiology of vertebrates. Visual input from a color camera is preprocessed in the middle temporal visual area (MT). Important visual features are extracted and used to trigger associations between visual cues and proper motor controls. They also suggested a delayed eligibility trace rule to govern the plasticity of synapses onto Purkinje cell (PC)

M. Lee et al. (Eds.): ICONIP 2013, Part I, LNCS 8226, pp. 520–527, 2013.
© Springer-Verlag Berlin Heidelberg 2013

and deep cerebellar nuclei (DCN). This training rule is used to learn proper motor responses, given certain visual cues, such that error signals are avoided. The error signals are generated using input from infrared sensors, to govern the learning in PC and DCN. A laser range finder is used to detect collisions and initiate collision avoidance behavior. The results demonstrated a smooth traversal of curved paths, with each path comprised of nearly identical turn curvatures.

However, CDE suffers from several limitations. First, the complexity of CDE, which consists of 28 neural areas, 27,688 neurons, about 1.6 million synaptic connections, and three input modalities may limit its practicality in real machines. Second, CDE is inept at effective motor learning in environments with varied turn curvatures due to its limited utilization of synaptic inputs for learning. Consequently, this leads to a predicted third limitation, that is the dependence on error signals to support learned predictive motor control signals even after training for decent traversal of environments with varied turn curvatures. Lastly, there is a limit to the volatility of input stimuli, beyond which learning becomes impaired. This limitation is caused by an insufficient eligibility trace decay rate in the learning rule implemented in CDE.

With regard to the aforementioned limitations, we propose a simplified cerebellar model with priority-based delayed eligibility trace learning rule (S-CDE). First, we utilize a simulated laser sensor to generate environmental depth information. This is the only input modality, which dramatically reduces complexity of the model since visual processing in CDE imposes extravagant complexity on the system compared to its cerebellar portion. Second, a priority-based delayed eligibility trace learning rule is suggested to maximize the usage of input signals for synaptic learning on plastic connections to PC and DCN areas. This is done by introducing a mechanism to prematurely re-trigger eligibility traces upon encountering more salient synaptic inputs. Third, an increased eligibility trace decay rate is used to allow for increased input volatility. The proposed model is developed as a brain-based device and tested in a simulated mobile agent which had to randomly and smoothly navigate maps of the Singapore(SG Map) and Hong Kong(HK Map) expressways.

2 A Simplified Cerebellar Model for Motor Control

A simplified cerebellar model with priority-based delayed eligibility trace rule (S-CDE) is proposed. Compared to CDE, three major modifications, including a simplified system architecture, introduction of an eligibility trace re-triggering mechanism, and an increased eligibility trace decay rate, have been made.

2.1 System Architecture

The system architecture of S-CDE is presented in Fig. 1. A single vector of input from a laser sensor is the only sensory perception the S-CDE has of its environment. The laser streams are preprocessed, such that the sensory input is split into four different streams, each in an appropriate semantic format for the subregion it is being fed into. This modification eliminates the need for extensive

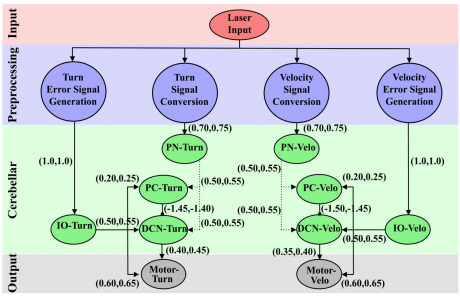

Fig. 1. System architecture of S-CDE which comprises of a sensory input layer, a pre-processing layer, a cerebellar layer, and a motor output layer. Closed arrowheads denote excitatory connections and circular endpoints denote inhibitory connections. Solid lines denote non-plastic connections while dotted lines denote plastic connections. The initial synaptic weights (c) are uniformly generated in between the maximum and minimum values as indicated near to the projections. Other settings, including learning rate (h), persistence (ω), and firing threshold (σ), are identical to the settings used in CDE [7].

processing of visual cues from a camera, thus, reducing the computational complexity. In total, the S-CDE has eight neuronal regions, 800 neuronal units, and 40,600 synaptic connections. The derivation of error signals from the laser input also eliminates the need for other input modalities. S-CDE can be divided into a sensory input layer, a pre-processing layer, a cerebellar layer, and an output motor layer. The cerebellar layer can be further divided into symmetrical *Turn* and *Velo* regions for handling turn rate and velocity computations respectively.

Sensory input is preprocessed and fed to the *PN-Turn* and *PN-Velo* areas. Error signals are derived from a subset of the sensory input and are subject to similar pre-processing before being fed to IO (*IO-Turn* and *IO-Velo*). In the cerebellar layer, PN areas(*PN-Turn* and *PN-Velo*) are linked to PC (*PC-Turn* and *PC-Velo*) and DCN (*DCN-Turn* and *DCN-Velo*) areas via plastic connections. PC controls DCN via disinhibition through its inhibitory connections, which in turn provide predictive control signals for turn rate and velocity to motor areas (*Motor-Turn* and *Motor-Velo*). Error signals from IO govern motor learning in the cerebellar regions (IO→PC and IO→DCN) and initially drive motor output in early stages of training (IO→*Motor-Turn* and IO→*Motor-Velo*).

2.2 Neuronal Responses

Standard neuronal dynamics that are implemented in BBDs are employed in S-CDE [8]. Synaptic connections can be either plastic or non-plastic and voltage-dependent or voltage-independent. In S-CDE, only voltage independent connections are used as suggested in CDE [7]. Defining j as a parent node and i as a child node, the voltage-independent connection from j to i is formulated as:

$$VI_{ij}(t) = w_{ij}s_j(t) \tag{1}$$

where w_{ij} is the synaptic weight between unit i and j, and s_j is the activation state of unit j. The activity of the neuronal areas are updated as:

$$s_i(t+1) = \phi\left(tanh\left(\sum_{j=1}^{N}(VI_{ij}(t)) + \omega s_i(t)\right)\right), \phi(x) = \begin{cases} 0; \text{ if } x < \sigma_i \\ x; \text{ otherwise} \end{cases} \quad (2)$$

where N is the number of synapses onto unit i, ω is the persistence of unit activity, and σ_i is the firing threshold of unit i.

2.3 Priority-Based Delayed Eligibility Trace Learning Rule

The synaptic strengths of the plastic connections are subject to change as follows:

$$\Delta w_{ij}(t+1) = \alpha s_i(t) \times P_j(t) \times s_i(t) \times (IO(t) - 0.02) \quad (3)$$

where α is a fixed learning rate, $P_j(t)$ is the priority eligibility trace, $s_i(t)$ is the activity of unit i and $IO(t)$ is the IO unit activity. The formulation of $P_j(t)$ is

$$P_j(t+1) = \begin{cases} 0 & \text{if } t < delay \\ s_j(t - delay) & \text{if } s_j(t - delay) \geq \epsilon \\ 0.6 \times P_j(t) & \text{otherwise} \end{cases} \quad (4)$$

where s_j is the activity of unit j, ϵ is an activity threshold and *delay* is the number of cycles offset from the current simulation cycle.

The delayed eligibility trace learning rule is used to determine the eligibility of a synapse for plasticity and if so, the amount of synaptic weight change required. The original delayed eligibility trace learning rule employed by the CDE suffers from three limitations. First, it is inept at effective motor learning in environments with varied turn curvatures. This is because once an eligibility trace over a synapse is triggered, subsequent input over that synapse is ignored for some time. Any important inputs arriving during this window is neglected, thus impairing the learning process. Second, due to the impaired learning process, the effectiveness of learned predictive motor control is limited. This would predictably create a dependence on error signals to supplement predictive motor control signals for decent traversal of such environments. Third, there is a limit to the volatility of input stimuli, beyond which learning becomes impaired. This volatility is inversely proportional to the distance between turns in a path. The input volatility limit is determined by the onset of consecutive eligibility traces during traversal of a rapid series of turns.

To overcome these limitations, a prioritized-learning concept is integrated into the learning rule. Instead of ignoring all inputs, an eligibility trace can be re-triggered if subsequent synaptic input is greater than that which triggered the initial eligibility trace. By doing so, salient inputs always have the priority for learning. Additionally, the eligibility trace decay rate has been increased from 0.9 to 0.6 to allow for a higher input volatility limit. The combined effect of the re-triggering mechanism and a higher eligibility trace decay rate is more effective predictive motor control and a higher input volatility limit, which increases learning accuracy and effectiveness when traversing relatively difficult paths.

2.4 Motor Output

Turn Rate Computation. Turn rate(°/cycle) is updated every cycle as a function of activity in the *Motor-Turn* area. Activity in the area is interpreted using population vector decoding. Each neuronal unit in *Motor-Turn* has a preferred turn-rate magnitude and direction. For explanatory purposes, neuronal units in *Motor-Turn* are indexed as t_1 to t_{100}. Units t_1 to t_{50} have a rightward preference of direction, and the preferred turn-rate magnitude of each unit grows linearly with its index. Units t_{51} to t_{100} have a leftward preference of direction, and the preferred turn-rate magnitude of each unit shrinks linearly as its index increases. To convert the activity in *Motor-Turn* to a specific turn rate, a combination of symmetric difference and population vector decoding techniques are used, expressed in equation 5(left). The resulting vector is the nett asymmetric activity in *Motor-Turn*, indexed as a_1 to a_{50}, where preferred turn-rate magnitude grows with the index, negative values indicate a leftward contribution, and positive values indicate a rightward contribution. The turn rate is calculated as shown in equation 5(right), where n is the size of $\tilde{\mathbf{a}}$ and γ is a constant defining the maximum turn rate.

$$\tilde{\mathbf{a}} = \begin{bmatrix} a_1 \\ \vdots \\ a_{50} \end{bmatrix} = \begin{bmatrix} t_1 \\ \vdots \\ t_{50} \end{bmatrix} - \begin{bmatrix} t_{100} \\ \vdots \\ t_{51} \end{bmatrix} \;;\; TurnRate = \sum_{i=1}^{n} \left\{ i \times \frac{\gamma}{100}(a_i) \right\} \tag{5}$$

Velocity Computation. Velocity(pixels/cycle) is updated every cycle as a function of activity in the *Motor-Velo* area. Activity in the area is interpreted using population vector decoding. For explanatory purposes, neuronal units in *Motor-Velo* are indexed as v_1 to v_{100}, and each has a preferred amount of braking, the magnitude of which grows linearly with its index. The conversion of activity in *Motor-Velo* to a specific velocity value is expressed in the equations below.

$$Velocity = \begin{cases} V_{max} & \text{if } \sum_{i=1}^{n} v_i = 0 \\ \| V_{max} - \beta(V_{max} - 1) \| & \text{otherwise} \end{cases} \;;\; \beta = \frac{\sum_{i=1}^{n}(i \times v_i)}{100 \sum_{j=1}^{n} v_j} \tag{6}$$

where β is a braking coefficient, a parameter that controls the amount of braking used by the agent ranging from 0 to 1, n is the size of *Motor-Velo*, v_i is the i^{th} unit of *Motor-Velo*, and V_{max} is a constant defining the maximum velocity. Through this formulation, a minimum velocity of 1 pixel/cycle is imposed.

Agent Behavior. The simulated mobile agent is given an innate behavior to move forward at a maximum speed of 6 pixels/cycle. If a collision occurs, the agent rotates in place until it is able to continue moving from its collision coordinate.

3 Results

S-CDE is developed as a brain-based model and tested in a simulated mobile agent which has to randomly and smoothly navigate SG Map and HK Map shown in Fig. 2 (a-b). Note that this simulation does not take into account physical laws such as inertia. The simulated agent is equipped with a single laser sensor and its motor capabilities are defined in terms of turn rate (°/cycle) and velocity (pixels/cycle). The simulation was executed in MATLAB on a MacBook Pro computer with a 2.66 GHz processor. One simulation cycle takes ∼25 ms.

First, experiments were conducted using SG Map to calibrate the length of the delay used in the S-CDE agent. The delays tested were 0, 3, 5 and 8 cycles. The delay resulting in the lowest motor error after 7000 simulation cycles of traversing SG Map is the calibrated delay value. Motor error for each cycle is quantified by taking the ratio of the strength of the error signal generated in the preprocessing layer to the maximum possible strength of the error signal. As a control for the experiments, a simulated agent using a reflexive motor controller was also included, which was purely driven by error signals from IO and had no predictive capabilities. This was achieved by lesioning its $DCN \rightarrow Motor$ connections. The experiments were repeated to calibrate the delay for the CDE agent, using delay values of 2, 3 and 5. The calibration of S-CDE and CDE also served as the training phase. Fig. 2 (c-d) shows a sample of S-CDE region activity during training. Following that, training effectiveness was ascertained by lesioning all connections originating from IO ($IO \rightarrow PC, IO \rightarrow DCN, IO \rightarrow Motor$) in both agents. Again, a reflexive agent was used as a control. Both SG Map and HK Map were used to evaluate training effectiveness in familiar and unfamiliar environments respectively.

Motor error output during delay calibration for both S-CDE and CDE are shown in Fig. 3 (a-b). Calibrated delays for S-CDE and CDE were determined to be 5 and 2 cycles respectively. S-CDE achieved a lower motor error rate than CDE. CDE ignores subsequent input for some time once input surpasses a threshold. If a long delay is used, CDE would only learn based on the initiation of a turn and block input arising from traversing the rest of the turn. A short

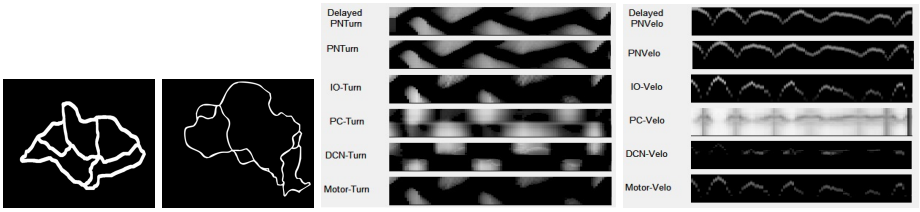

Fig. 2. (a) SG Map has a narrow average path width of 40 pixels. (b) HK map is about three times larger, and has wide average path width of 60 pixels. (c) Activity in turn-related regions during training. (d) Activity in velocity-related regions during training.

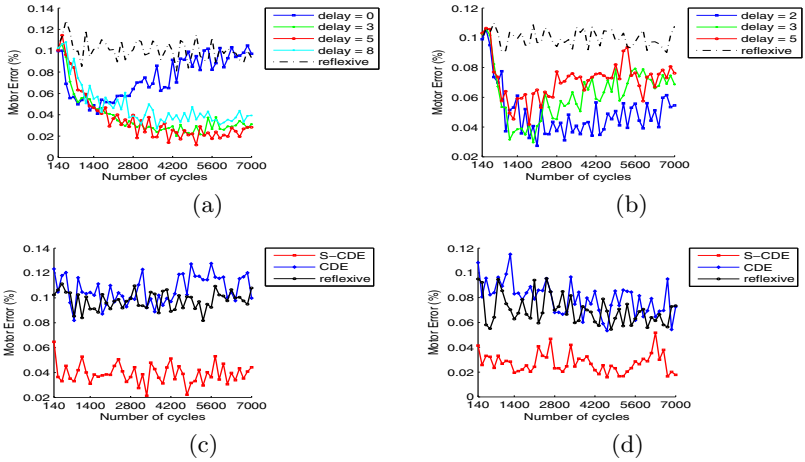

Fig. 3. Motor error during delay calibration of (a) S-CDE and (b) CDE. Motor error during training effectiveness assessment of S-CDE and CDE in (c) familiar (SG Map) and (d) unfamiliar (HK Map) environments.

enough delay would enable CDE to learn based on input from several points during the turn. However, using such a short delay severely limits the predictive capability of CDE, making it prone to higher motor error rates. S-CDE is able to base its learning on input received throughout a turn due to its re-triggering mechanism, thus resulting in lower motor error rates.

As shown in Fig. 3 (c-d), during training effectiveness evaluation, S-CDE successfully demonstrated effective predictive motor control while traversing both SG Map and HK Map despite only having prior exposure to one. CDE fails to traverse either environment satisfactorily. Due to the limited predictive capability previously mentioned, predictive motor control signals for sharp turns were generated too late to avoid impending collisions. The change in motor error rates for CDE between delay calibration and training effectiveness evaluation corroborate with the initial prediction of CDE's dependence on error signals after training for traversal of environments with varied turn curvatures. The performance of S-CDE in both maps during training effectiveness evaluation was comparable to that achieved at the end of delay calibration, which strongly suggests effective retention of learned predictive responses, and demonstrates its robustness in an unfamiliar environment.

4 Conclusion

In this paper, a simplified cerebellar model for predictive motor control has been presented. It has a simplified neural architecture due to the reduction of input modalities. It has demonstrated effective motor learning in environments with varied turn curvatures because of the introduction of the priority-based delayed eligibility trace learning rule. It is also robust while traversing new environments.

Acknowledgments. This work was supported by the Agency for Science, Technology, and Research, Singapore under SERC Grant 0921570130.

References

1. Houk, J.C., Buckingham, J.T., Barto, A.G.: Learning in and from brain-based devices. Behavioral and Brain Sciences 19(3), 368–383 (1996)
2. Llinás, R.R.: Cerebellar motor learning vs. cerebellar motor timing: The climbing fiber story. The Journal of Physiology 589(14), 3423–3432 (2011)
3. Schlerf, J., Ivry, R.B., Diedrichsen, J.: Encoding of sensory prediction errors in the human cerebellum. The Journal of Neuroscience 32(14), 4913–4922 (2012)
4. Medina, J.F., Carey, M.R., Lisberger, S.G.: The representation of time for motor learning. Neuron 45(1), 157–167 (2005)
5. Ito, M.: Error detection and representation in the olivo-cerebellar system. Frontiers in Neural Circuits 7(1), 1–8 (2013)
6. Wolpert, D.M., Miall, R.C., Kawato, M.: Internal models in the cerebellum. Trends in Cognitive Sciences 2(9), 338–347 (1998)
7. McKinstry, J.L., Edelman, G.M., Krichmar, J.L.: A cerebellar model for predictive motor control tested in a brain-based device. Proceedings of the National Academy of Sciences 103(9), 3387–3392 (2006)
8. Edelman, G.M.: Learning in and from brain-based devices.. Science 318(5853), 1103–1105 (2007)

How Difficult Is It for Robots to Maintain Home Safety? – A Brain-Inspired Robotics Point of View

Gyanendra Nath Tripathi[1], David Chik[1], and Hiroaki Wagatsuma[1,2]

[1] Department of Brain Science and Engineering, Kyushu Institute of Technology, 2-4 Hibikino, Wakamatsu-Ku, Kitakyushu 808-0196, Japan
[2] RIKEN BSI
tripathi-gyanendra-nath@edu.brain.kyutech.ac.jp,
{chik-david,waga}@brain.kyutech.ac.jp

Abstract. The cognition-based human intelligence, that is driven by emotion and feeling will definitely change the robot learning, memory, attention and decision making mechanism. The aim of paper is to give in depth investigation on how the robot learning based on emotion and feeling will give a new dimension to its performance. It means that self-learning is not just dependent upon a logical brain and proper embodiment; rather a feedback in terms of emotion and feeling based on experience is required for self-learning. It is the feedback in the form of feeling and emotion that plays a vital role in a complete self-learning process and this makes the robot more human.

Keywords: emotion, intelligence, service robot, dynamical system, feeling of pain, mobile-robot.

1 Introduction

"Learning" is a beautiful word, but it's hard to implement into robots. Contextual decision-making is required in a dynamical environment when we are asked to take care of everything around the house. At home, everything is drastically changing including rules which family members had just shared it yesterday. The change of rules is sometime non-logical and may occur depending on emotional fluctuations in mum's policy, or dad's whims. Classifications of assumptions, parameters and variables are necessary to form a learning paradigm and provide its implementation method into engineering systems. In cognitive science and psychology, child's cognitive development has been studied from observations of child's behavior and acquisitions of various skills. Jean Piaget [1] focused on the transitions of learning schemes during the developmental process and noticed an organized pattern of thought and behavior, called "schema." On the other hand, what factors exist in child's mind subjectively, as well-established knowledge or ill-defined borders, remains unsolved. This is the gap between objective and subjective representations. Science basically needs repeatability, objectivity and quantitative assessment. Repeatability is the base to confirm whether it is true or not by reproduction of the

M. Lee et al. (Eds.): ICONIP 2013, Part I, LNCS 8226, pp. 528–536, 2013.
© Springer-Verlag Berlin Heidelberg 2013

same phenomenon under equivalent conditions. Objectivity is a need to be observed by anyone. Finally we have to take into account various factors based on quantitative comparisons. Everyday events are not countable, but we treat it in a form of countable factors for implementation into robot's intelligence. Ontology, epistemology and axiology are the philosophical trinity. From the ontological argument, the perfect circle does not exist in the real world but it exists in our minds. Similarly any object is never be indentified by a combination of countable attributes happens in an epistemological sense. For example, once you define cup as a container with handle, and then the cup with a broken handle is never be recognized as a cup. Interestingly the dictionary describes that the definition of the cup is "a small open container usually used for drinking," which highlights the purpose of its use for drinking. It is closely related to axiology, and it is asking why the cup exists, for what the cup is made of and for whom the cup exists for. This sense slightly exceeds the range of objective and logical thinking. The robot, an external observer without any desire, is unable to understand what it is for. It is difficult for the robot to determine its own behavior if it is not arisen from its significance of existence. The cup is meaningless if robots never use it for themselves. Thus, recognition of cups is the same as seeing wayside stones. This paper discusses epistemological aspects of our everyday events for robots. Especially to focus on what is the ideal and abstract internal representation that happens in the real environment (ontology), how to effectively recognize objects (epistemology), plus the values and risks of what has occurred and will occur (axiology).

2 Definition of Intelligence

Intelligence can be defined as "the capacity to acquire and apply knowledge by means of thought and reason," which leaves many aspects we must be considered [2]. Hubert Dreyfus [3] noticed a limited capacity for understanding the meaning of sentences to represent a situation and conversation among kids by introducing the following sentence from a story of Eugene Charniak, who was a student of Marvin Minsky:

Today was Jack's birthday. Penny and Janet went to the store. They were going to get presents. Janet decided to get a kite. "Don't do that," said Penny. "Jack has a kite. He will make you take it back."

Dreyfus noted that "the goal is to construct a theory that explains how the reader understands that "it" refers to the new kite, not the one Jack already owns." *i.e.* Jack will make Janet take back the kite if Jack already owns a similar kite. Here we get into details about what its difficulty for algorithmic procedures, or robot, to understand the exact meaning, and consider it as propositions: 1) relationship between sentences for capturing the whole meaning contextually (sentences that are not in linear combinations), 2) emotional feeling and reactions of people who play their roles in the story (biological sense), 3) recursive procedure that is necessary to predict what will happen next (prospective information). On the first proposition, we can take a look at the performance in the current technology from a popular online translation

website, and an example of the translation result to Japanese and the reversal translation back to English (English → Japanese → English) can be obtained as

It was a birthday of Jack today. I went to the store and Janet penny. They were going to get the gift. Janet has decided to get the kite. "Please do not do it," Penny said. "Jack, you have a kite. He will make you get it back."

How do we evaluate the above result? As shown in Table 1, the translated sentences were reproduced in a similar manner. If you calculate a ratio between numbers of correct (C) and semi-correct (C') sentences and wrong sentences (W) and the correctness can be evaluated as a quantitative value such as approximately 86% (=6/7 sentences). However we humans feel a sense of confusion to read the second sentence "I went to the store." Who am "I"? Is it a reader as an external observer? Or, is it someone in the story except Penny, Janet and Jack? This false step of the translation may mislead the reader to understand the whole meaning of the sentences because of a confusion of the word "it" indicates. This result indicates that the machine translation does not bridge between sentences appropriately in a sense of contextual implication. This is the point of proposition 1, which suggests that a one-by-one independent translation tends to ignore contextual interpretations. Probabilistic language models and Bayesian probability models based on conditional probabilities known as $P(A \mid B)$ become increasingly precise if the condition B includes all the past events and $P(A \mid B)$ is obtained from large data sets. The difficulty comes from the trade-off between two factors, because the more consideration of a long past history the more the event becomes "rare." Therefore, some other common principle is necessary to be considered for concatenating fragments of sentences into continuous meanings.

Table 1. Comparison between original sentences and machine translations

#	Original	Machine Translation by E→J→E	c/w
1	Today was Jack's birthday.	It was a birthday of Jack today.	C
2	Penny and Janet went to the store.	I went to the store and Janet penny.	W
3	They were going to get presents.	They were going to get the gift.	C
4	Janet decided to get a kite.	Janet has decided to get the kite.	C
5	"Don't do that," said Penny.	"Please do not do it," Penny said.	C
6	Jack has a kite.	Jack, you have a kite.	C'
7	He will make you take it back.	He will make you get it back.	C'

On the second proposition, emotional sense is the most difficult part for robots to implement because it is impossible to substitute for logical reasoning. Emotion is one aspect of intelligence, which is an expression of accumulated internal senses and feedbacks influenced in a particular environment attention, past memory, leaning of common sense and then it affects decision making in some cases (R. J. Dolan, et al. Science 298, 1191 (2002)). Cognition of emotion is a type of meta-cognition that includes the subjective knowledge of emotional state and emotional processes

(Markku S. Hannula, University of Turku). Going back to the Charniak's story, the point is observed in the reason why "Jack will make you take it back," and we can estimate the reason naturally as Jack already owns a similar kite. Why? If the kite was cookies and cakes, the story would be different and Jack may want them even though he already has. If Jack's hobby is a collection of baseball cards, he desires cards even more. In this case, we can imagine that Jack will be disappointed when he sees the kite, he will be more happy to have a gift of another toy. Penny and Janet are excited to plan a birthday surprise gift for him. Disappointment, happiness and exciting are emotional reactions, which are never felt by robots with reality. If there is a possible way to interpret people's emotional feelings and reactions, robots become more intelligent to extend the solvable range of various tasks [4]. However, the emotion involves personal and subjective experiences, social behaviors and cognitive senses shared against human [4]. The emotion involves motive, desire, intention, belief, perception and sensations [5]. How do we can implement those things into robots? Some approaches of emotional evaluation to implement agent-based systems have been explored in a hierarchical functional structure [6][7].

Third proposition focuses on time, or prospective events. The last sentence "He will make you take it back" represents an estimation of future events as

$event(t)$: Janet gives Jack a present she brought in the store,

$event(t+1)$: Jack recognizes the present as a kite and remembers his owns a kite,

$event(t+2)$: Jack asks Janet to go back to the shop for returning the kite.

According to the dictionary, "take something back" means to return it to the place where it came from. The sentence may be interpreted with the meaning of Jack will return the kite back by himself if the description is "Jack will take it back," but the sentence uses a causative verb, make, producing an effect, especially to indicate that Jack will force Janet to do something. Thus, with the above three propositions, future events are represented in a compressed form from this short sentence. Interestingly, this sentence gave additional information regarding the expectation from Jack,

$event(t+3)$: Janet returns the kite to the shop and gets another present instead of the kite.

It offers a glimpse of Jack's personality through a part of the sentence as "He will make you …" The reader guesses that Jack is a self-assured person, does not hesitate to express his own desire, and asks Janet to get another present.

Indeed, automated approaches to reproduce the human ability on situation recognition is the hard problem because it need to deal appropriately and effectively with the following points. 1) by concatenating contextually fragments into a consistent form to provide the whole meaning (beyond linear combinations), 2) speculation or cognitive rehearsal of emotional feeling and reactions of persons participating in the story (a simulated biological sense), 3) recursive procedure to reconstruct future events as a prediction by focusing on a key person (prospective information and direction of the story), as discussed the above. The next section is getting into deeper into the emotional aspect of the brain and exploring a potential of brain-inspired design for its implementation.

3 Emotion, Feeling of Pain and Self-awareness

Evaluation of an event or object with respect to "value" is substantially influenced by emotional judgment in a subconscious level [8][9][10]. Joseph Ledoux [11] takes into account an existence of animal's emotion as well as what the human possess, which is in some cases exposed as conscious emotions by exceeding a threshold level of accumulated subconscious feelings [12]. In a review of the brain mechanism to maintain emotional judgment by focusing on the amygdala function, Ledoux [11] admits a plausibility of psychodynamics perspective by Sigmund Freud, a neurologist and psychoanalysist, who augured that the conscious level of our mind is similar to the tip of the iceberg which could be seen, while the unconscious level is hidden, or unaware and yet governs the conscious level. Similarly, there is a viewpoint that conscious emotions are close to immediate awareness and easily accessible, like a meta-cognition, and it continuously binds with subconscious feelings of body and sensations in a form of strap or winding staircase for making of consciousness [13].

This implies that unless an artificial reproduction of chemosensory systems and integumentary sense organs we have, it is impossible to reconstruct the same consciousness into a robot. Once we focus on a functional part such as a meta-level cognition, a solution can be found in a flexible decision making like switching rules depending on the situational change [14]. Attentional control is also the key to consider in the engineering viewpoint.

Assuming a practical situation for keeping safe from inattention at home environment, we start to consider "feeling of pain" to avoid a critical situation. According to a textbook for health and safety trainers [15] risk of injury gradually shifts with respect to characteristics of infant and child (Table 2). A possible way to obtain the same ability as humans is 1) to form the body as it is (organized biochemically like stem cells) or to acquire through 2) imitation (effective in motor skills), 3) observation and imagination (guess what happens based on physical laws) and by 4) instructions of emotional feelings via verbal communications (literature based; extension of imagination). It is difficult for robots to trace the child's cognitive development completely (Asada) because the robot is not organized by the same ingredients as the child and to take time for training like twenty years.

The above example of risks is depending on situations that the child is in now and the level of knowledge that the child has now. Fear and curiosity vary a great deal in the age. The feeling of pain and emotional reactions has a significant relationship with a process of prediction and decision to act (Fig.1). The person keeps on training his mind how to stand and walk in every attempt. It implies that a robot also needs to have feeling of pain neither an emotion, which can drive to memorize what happened and to predict what will happen. We simply consider that feelings and emotions is a core of the self-awareness as an alertness, which differs from reward and punishment. Implicit and procedural learning without conscious attentions can be done by reward and punishment, called reinforcement learning. Feelings are fundamentals for the existence of representation of 'self' [13] such as basis of self-protection, self-motivation, self-confidence, self-abhorrence, self-accusation, self-actualization, and so on. Another clue to consider the self-awareness as alertness is time property (Fig.2).

Table 2. Physical risks of injury at home according to established knowledge [14]

Age	Characteristics	Risk of Injury	Prevention Tips
Birth to 3 months	• Eat, sleeps, cries • Begins grasping and Rolling over unexpectedly • Needs support of head and neck	• Falls from couches, tables, changing tables and bed • Burns from hot liquids	• Never leave infants alone on beds, chairs or other high surfaces • Check water temperature in the bath • Keep small object and toys away
4 to 6 months	• Sits with support • Plays with open hands • Put things in mouth • Curious about surroundings • Wants to test, touch and shake objects	• Falls • Burns from hot liquids • Choking and suffocation	(the same as above 3 tips)
7 to 12 months	• Sits alone • Very curious about everything • Crawls • Starts to walk • Explores surroundings • Pulls things • Likes to go outside • Imitates movements of adults and others	(the above 3 tips) + • Drowning	(the above 3 tips) + • Keep hot foods and liquids out of the reach of children • Put guards around radiators, hot pipes and other hot surfaces • Always carefully supervise; never leave alone near any water (tubs, toilets, buckets, and pool)

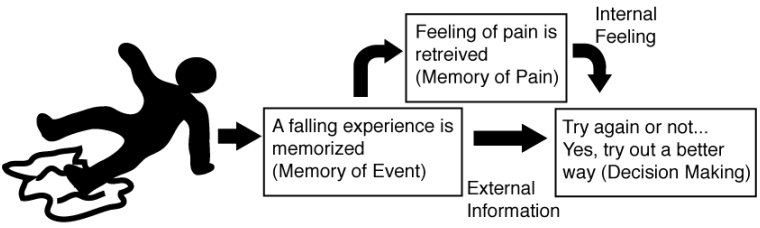

Fig. 1. A situation to perceive an event to be dangerous. Firstly the person experienced something wrong and felt a pain. Secondly, the one concerns its repeatability because of the pain and think a causal relation on the event. If the one is aware that the act of walking is a cause of slipping, a future decision is in the naïve balance whether the one should walk or not, as a conflict. The one walks if the intension exceeds the level of the fear, knowledge specifies causes in more detail, recognition of a situational change by preparing for prevention of the event, and so on.

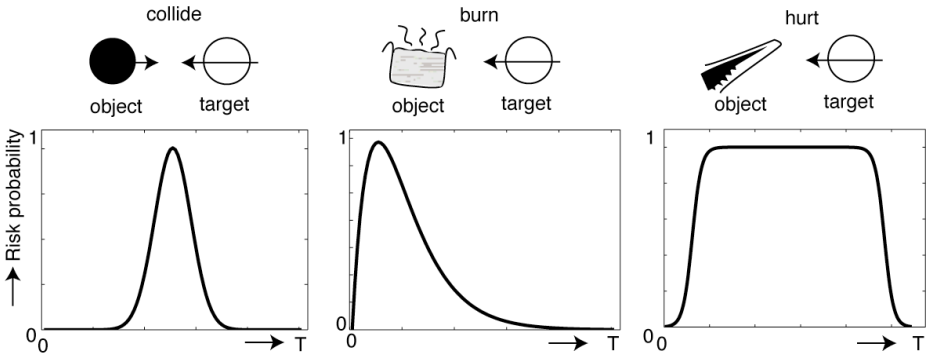

Fig. 2. Example of time courses of happening dangerous events. A sudden event (left), event with a risky time envelope (middle), event with alternative options whether it is risky or not (right). Those events have different temporal characters.

4 Meta Level Cognition or Primordial Sense

How do we can implement realistic feelings into robots? It should be beyond learning theories and paradigms, which are defined in a sense of acquisition of specific skills increasingly, because we were not born as a 'tabula rasa' [16]. Sympathy without action cannot be treated by behaviorism and input-output mapping systems. The 'emotional judgment' is considered as unimportant rather than logical judgment in human cases but it is necessary to generate the sympathy and difficult to reduce a set of logical processes. Focusing on being biological systems, having fate of death and living in the unstable environment and unstable body, the concept of emotions can be extended into primitive self-consistent systems of information representation. We hypothesize that following three are included in the primitives and consider the possibility to describe them by a mathematical model of dynamical systems:

Feeling of Pain. A sense of lose. Knowing about something that will be gone, or having an anticipation of lose. The simplest dynamics of internal value H_p is described as

$$\frac{dH_p}{dt} = -f\left(H_p, \theta\right) \tag{1}$$

where f denotes a non-linear function to control the decrease rate with a limit of time, which is defined as the threshold θ including external forces.

Lack of Satisfaction. Filling actions. Filling something or someone in a hole or empty space. The simplest dynamics of internal value H_s is described as

$$\frac{dH_s}{dt} = g\left(H_s, \theta'\right) - \omega \tag{2}$$

where g denotes a control function with a threshold θ' and ω is a constant of abrasion.

Awe and Wonder. Decisions biased fear and curiosity. To inhibit the current motion when it detects something strange, or else, to enhance and trigger a motion when it finds something new and different. Those two factors are considered as exclusive each other. The simplest dynamics of decisions D according to a mapping of internal value A is described as

$$\begin{aligned} D(A) &= Mapping(A), \\ \frac{dA}{dt} &= F(A,\theta_F) \oplus C(A,\theta_C) \end{aligned} \tag{3}$$

where F and C respectively denote functions on fear and curiosity with control parameters θ_F and θ_C.

5 Concluding Remarks

In the present paper, we discussed how difficult a robot maintains home safety by monitoring and external observations even if verbal instructions are given, and then we noticed that the seriousness is staying on learning paradigms especially in input-output mapping and statistical learning theories ignoring temporal changes. We suggested that a possible and effective implementation is found in modeling of internal and spontaneous processes according to time and values. Values are still difficult to treat because we go back to the same unsolved question if the designer embeds the values into the robot according to external observations. However the key is, once a value is defined according to the purpose of the robot, the temporal change of the value should be described as dynamical system with a limit of time, instability and ambivalent. Such a process is like filling water into a cup with a small hole in the bottom. Learning in robot is not isolated from a property of having a body, which is restricted kinetically and physically. In other words, the robot follows the physical law of time and space. Therefore, the embedded intelligence has a fate to conquer the dimension of space and time. This is a case study for assessments of service robots at home, sharing space and time with humans, particularly undeveloped children. If we build a robot with emotion in a form of dynamical systems [11] will perform more like human in terms of learning, memory, attention and decision making mechanism. A development of artificial mind will change the way of robots performance at places like home and office environment.

Acknowledgments. The authors also gratefully acknowledge helpful supports in the Brain-IS project in Dept. of Brain Science and Engineering, Kyushu Institute of Technology. This work is partially supported by JSPS KAKENHI (22300081) and JSPS KAKENHI (24650107).

References

1. Piaget, J.: The Origins of Intelligence in Children (Cook, M., Trans.). International Universities Press, New York (1952)
2. Legg, S., Hutter, M.: A Collection of Definitions of Intelligence. In: Goerizel, B., Wang, P. (eds.) Advances in Artificial General Intelligence: Concepts, Architectures and Algorithms, pp. 17–24. IOS Press (2007)
3. Dreyfus, H.L.: What Computers Still Can't Do: A Critique of Artificial Reason. The MIT Press (1992)
4. Ortony, A., Clore, G.L., Collins, A.: The Cognitive Structure of Emotions. Cambridge University Press (1990)
5. Sloman, A., Croucher, M.: Why robots will have emotions. In: Proceedings of 7th IJCAI, pp. 197–202 (1981)
6. Minsky, M.: The Society of Mind. Simon & Schuster (1988)
7. Singh, P.: Examining the society of mind. Computing and Informatics 22, 521–543 (2003)
8. Johnsrude, I.S., Owen, A.M., White, N.M., Zhao, W.V., Bohbot, V.: Impaired Preference Conditioning after Anterior Temporal Lobe Resection in Humans. J. Neurosci. 20(7), 2649–2656 (2000)
9. Dolan, R.J.: Emotion, cognition, and behavior. Science 298, 1191–1194 (2002)
10. Friston, K.J., Tononi, G., Reeke Jr., G.N., Sporns, O., Edelman, G.M.: Value-dependent selection in the brain: simulation in a synthetic neural model. Neuroscience 59(2), 229–243 (1994)
11. Ledoux, J.: The Emotional Brain: The Mysterious Underpinnings of Emotional Life. Simon & Schuster (1998)
12. Wagatsuma, H., Saito, M.: A Phenomenological Model of Emotional Intelligence-Emotion Prevents a Dispute. In: Proc. Ann. Conf. Japanese Neural Network Society, JNNS 2012, No. P3-23 (2012)
13. Damasio, A.: Descartes' error: Emotion, Reason and the Human Brain. Vintage Book (2006)
14. Maniadakis, M., Tani, J.: Dynamical systems account for meta-level cognition. In: Asada, M., Hallam, J.C.T., Meyer, J.-A., Tani, J. (eds.) SAB 2008. LNCS (LNAI), vol. 5040, pp. 311–320. Springer, Heidelberg (2008)
15. Zamani, A.R., Anderson, B., Evinger, S.: Health and Safety in the Child Care Setting: Prevention of Injuries, A Curriculum for the Training of Child Care Providers. In: Module 2, 2nd edn., The California Child Care Health Program (1998)
16. Pinker, S.: The Blank Slate: The Modern Denial of Human Nature. Penguin Books (2003)

Development of Proactive and Reactive Behavior via Meta-learning of Prediction Error Variance

Shingo Murata[1], Jun Namikawa[2], Hiroaki Arie[1], Jun Tani[3], and Shigeki Sugano[1]

[1] Waseda University, Tokyo, Japan
[2] Brain Science Institute, RIKEN, Saitama, Japan
[3] Korea Advanced Institute of Science and Technology, Daejeon, Republic of Korea

Abstract. This paper investigates a possible neurodynamic mechanism that enables autonomous switching between two basic behavioral modes, namely a "proactive mode" and a "reactive mode." In the proactive mode, actions are generated as intended, whereas in the reactive mode actions are generated in response to the sensory state. We conducted neurorobotics experiments to investigate how these two modes can develop and how a robot can learn to switch autonomously between the two modes as necessary by utilizing our recently developed dynamic neural network model. Tasks designed for the robot included switching between proactive imitation of other's predictable movements using acquired memories and reactive following of other's unpredictable movements through iterative learning of alternating predictable and unpredictable movement patterns. The experimental results revealed that this "meta-learning" capability can lead to self-organization of adequate contextual dynamical structures that can perform autonomous switching between the different behavioral modes.

Keywords: Recurrent neural network, humanoid robot, neurorobotics.

1 Introduction

Humans can behave either proactively or reactively depending on the situation by autonomously switching between these two behavioral modes. Proactive behavior is generated with top-down intentions to achieve intended goals robustly in predictable situations. Reactive behavior on the other hand is generated by flexibly responding to sensory inputs in unpredictable situations. Although competence for generating both types of behavior and for developing the ability to switch autonomously between the two modes as necessary is believed to be essential for both artificial agents and humans, the relevant mechanisms involved in doing so have not been studied in depth [1].

Let us consider a case where a subject imitates new movements demonstrated by a trainer in a synchronized manner. If the trainer tends to demonstrate completely unpredictable movement patterns, all the subject can do is simply follow

M. Lee et al. (Eds.): ICONIP 2013, Part I, LNCS 8226, pp. 537–544, 2013.
© Springer-Verlag Berlin Heidelberg 2013

the demonstrated patterns reactively. In such a situation, the subject cannot perform prediction and there would be a delay between the movements demonstrated by the trainer and those performed by the subject. However, if the trainer demonstrates specific repeatable patterns mixed with unpredictable ones in a continuously generated sequence, the subject might become able to imitate the repeating parts proactively by acquiring the internal model of the trainer's predictable movements and the prediction error might then be minimized during this proactive part of imitating behavior. In fact, this observation has been confirmed in psychological experiments involving tracking tasks [2, 3].

In the context of proactive behavior learning for robots, Tani and colleagues have shown that recurrent neural network (RNN)-based models can learn to predict perceptual consequences of actions in navigation problems [4] as well as predict perceptual sequences for sets of intended actions in object manipulation tasks [5,6]. RNN-based models, however, can face a problem associated with the deterministic nature of the prediction. RNNs as deterministic dynamical systems cannot learn to extract stochastic properties hidden in non-deterministic or noisy temporal sequences, and even if RNNs are forced to learn such sequences, the learning processes tends to become corrupted with the accumulation of errors.

To address this problem, Namikawa and colleagues recently proposed a novel continuous-time RNN (CTRNN) model referred to as stochastic CTRNN (S-CTRNN) model that can learn to predict not only the mean of the next perceptual state, but also the predictability of the state itself in terms of prediction error variance [7, 8].

In the present study, the authors speculate that the S-CTRNN model can solve the aforementioned essential problem concerning autonomous switching between intention-based proactive behavior and perception-guided reactive behavior. We conducted neurorobotics experiments to examine whether the model could be applied to this problem. Based on an analysis of the experimental results, this paper proposes a possible mechanism of learning both proactive and reactive behavior as well as switching between these two different behavioral modes.

2 Neural Network Model

2.1 Forward Dynamics

The internal state of the i-th neuron at time step $1 \leq t$ ($u_{t,i}$) is updated in accordance with

$$u_{t,i} = \begin{cases} \left(1 - \dfrac{1}{\tau_i}\right) u_{t-1,i} + \dfrac{1}{\tau_i} \left(\displaystyle\sum_{j \in I_I} w_{ij} x_{t,j} + \sum_{j \in I_C} w_{ij} c_{t-1,j} + b_i \right) & (i \in I_C), \\ \displaystyle\sum_{j \in I_C} w_{ij} c_{t,j} + b_i \quad (i \in I_O \cup I_V), \end{cases} \tag{1}$$

where I_I, I_C, I_O, and I_V are the neuron index sets, τ_i is the time constant of the i-th neuron, $w_{i,j}$ is the weight of the connection from the j-th to the i-th

neuron, $c_{t,j}$ is the activation value of the j-th context neuron at time step t, $x_{t,j}$ is the j-th external input at time step t, and b_i is the bias of the i-th neuron.

The respective activation values of context unit $c_{t,i}$, output unit $y_{t,i}$, and variance unit $v_{t,i}$ are calculated as follows:

$$c_{t,i} = \tanh(u_{t,i}) \qquad (i \in I_C), \tag{2}$$

$$y_{t,i} = \tanh(u_{t,i}) \qquad (i \in I_O), \tag{3}$$

$$v_{t,i} = \exp(u_{t,i}) \qquad (i \in I_V). \tag{4}$$

2.2 Training Method

The network is trained through maximum likelihood estimation by utilizing the gradient descent method [9].

Here, the learnable parameters of the network, including the weight of the connection, the bias, and the initial internal state are denoted by $\boldsymbol{\theta}$. Let $X = (\boldsymbol{x}_t)_{t=1}^{T}$ be an input sequence, where T is the length of the sequence. In this case, the probability density function of training data $\hat{y}_{t,i}$ is defined as

$$p(\hat{y}_{t,i} \mid X, \boldsymbol{\theta}) = \frac{1}{\sqrt{2\pi v_{t,i}}} \exp\left(-\frac{(y_{t,i} - \hat{y}_{t,i})^2}{2v_{t,i}}\right), \tag{5}$$

where $y_{t,i}$ and $v_{t,i}$ are the outputs generated by the network and $\hat{y}_{t,i}$ is the training data. This equation is derived with the assumption that the observable data sequence is embedded into additive Gaussian noise.

The likelihood function L_{out} parameterized by $\boldsymbol{\theta}$, is denoted by

$$L_{\text{out}} = \prod_{t=1}^{T} \prod_{i \in I_O} p(\hat{y}_{t,i} \mid X, \boldsymbol{\theta}). \tag{6}$$

The network generates a prediction of the prediction error in the form of a variance $v_{t,i}$. The network can avoid unstable learning sequences since the variance functions as an inverse weighting factor for the mean square error $(y_{t,i} - \hat{y}_{t,i})^2$. More specifically, the effect of the prediction error is reduced when the variance is large (as the error is divided by the variance), whereas the effect is increased when the variance is small. Therefore, the amount of error back-propagation can be autonomously reduced in the case of learning unpredictable parts of temporal sequences. This relaxes the predictive learning of sequences consisting of predictable and unpredictable parts.

The training method involves choosing the most appropriate value for the parameter $\boldsymbol{\theta}$ by maximizing the likelihood L_{out}. More precisely, we used the gradient descent method with a momentum term as the training procedure.

3 Robot Experiments

3.1 Experiment Environment

A small humanoid robot "NAO" was used in robot experiments. The robot was seated on the floor and a display was placed in front of it. The task for the robot

was to imitate the movement of a colored target circle shown on the display by moving its right arm. In the experiments, the target circle was assumed to correspond to the tip of the trainer's hand. The display presented a continuous spatiotemporal sequence of the moving target consisting of alternating "predictable" and "unpredictable" parts, which are presented as a state transition graph as in Fig. 1(a).

The test in this case was designed to examine whether the robot could adapt to both phases and to switch autonomously between proactive imitation (based on top-down prediction for predictable patterns) and reactive following (by simply tracking unpredictable patterns) as a result of iterative learning. We compared two types of situations depending on whether an explicit cue indicating the current mode of demonstrated patterns was present or absent. Since in the absence of the cue the network was expected to develop self-organized functions for detecting the current mode, the task necessarily became more difficult. In the experiments, the explicit cue indicating a transition between predictable and unpredictable movements was a change in the color of the target circle. Specifically, the circle was red when the movements were predictable and blue otherwise.

The joint angles of the robot's head were controlled to fixate automatically on the center of the target circle. Therefore, the direction of the head was treated as "vision" in these experiments. For this reason, only the joint angles of the head and the right arm were used during the imitation process, and the remaining angels were fixed.

Figure 1(b) shows an overview of the constructed system. The S-CTRNN model was used as a forward model in controlling the robot. Input to the network was provided as actual vision $\hat{s}_t$, and the outputs were in the form of predicted visuo-proprioception s_{t+1} and p_{t+1} and the corresponding variances $v^{(s)}_{t+1}$ and $v^{(p)}_{t+1}$. The predicted proprioception p_{t+1} was sent to the robot in the form of target joint angles, which acted as motor commands for the robot in generating movements. In performing the imitation task with a cue presented, the hue $\hat{h}_t$ was used as the explicit cue.

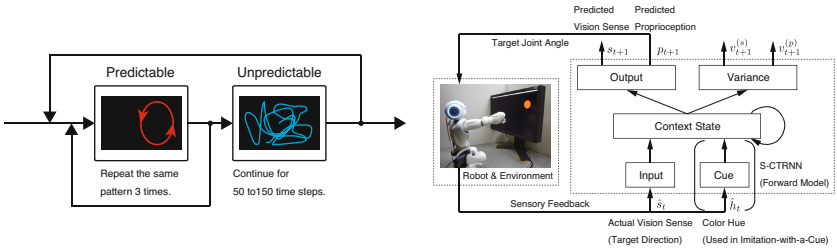

Fig. 1. (a) Task for the robot experiments. The color of the moving target circle was changed from red (predictable) to blue (unpredictable) in the case where the imitation task was performed with a cue. (b) System overview.

3.2 Obtaining Training Sequences

In order to obtain training sequences, the robot was manually controlled before the training phase. In the same environment as that used in the action generation test, a colored target circle shown on a display was moved in a pattern that the robot was expected to imitate.

The angles defining the orientation of the robot's head (yaw and pitch) were controlled to fixate automatically on the target circle. Furthermore, the angles of the right arm (shoulder pitch, shoulder roll, and elbow roll) were controlled to imitate the target circle by means of inverse kinematics by utilizing the changes in the head angles. While the robot was moving, the joint angles of its head and right arm were recorded as vision and proprioception, respectively.

For the imitation task performed with a cue, the horizontal and vertical elements of the hue, which represent the hue angle, were used. On the other hand, for the imitation task without a cue, we eliminated the hue elements from the training data used in the imitation task with a cue.

4 Results

We trained the S-CTRNN for each task, where the number of context neurons was $M = 30$ and the time constant was $\tau = 10$. We trained each network for 1,000,000 training steps. We used 20 training sequences, each of which consisted of two parts – one predictable pattern and two unpredictable parts – which alternated with each other.

Here, we define "appropriate actions" for the imitation task as actions associated with a small prediction error. In the case of predictable patterns, by behaving proactively (i.e, by using its internal model for predictable environments), the robot successfully minimized the prediction error to almost zero. On the other hand, in the case of unpredictable patterns, the prediction error was not minimized to zero since an internal model had not been acquired for it. Nevertheless, the prediction error was reduced to some extent by reactively following the target's movements.

4.1 Imitation with a Cue

The robot was able to imitate or generate appropriate actions and to switch between the proactive and reactive behavior. Figure 2(a) presents the actual vision, predicted visuo-proprioception, variance sequences, and neural states generated by the trained network. In Fig. 2(a), we can see the correlations between the regions of increase and decrease in the values of the hue and those of the predicted variances.

4.2 Imitation without a Cue

Figure 2(b) illustrates the time series generated by the trained network. In this experiment, training was carried out under the same conditions except that the

hue was not included. For this reason, the robot was forced to focus its attention on the movement pattern of the target circle.

In Fig. 2(b), we can see the increase and decrease in the variances corresponding to the transitions between predictable and unpredictable parts. We can also see that there is a time delay when the variance decreases during the transition from an unpredictable to a predictable part. In contrast, when the transition is from a predictable to an unpredictable part, there is no time delay.

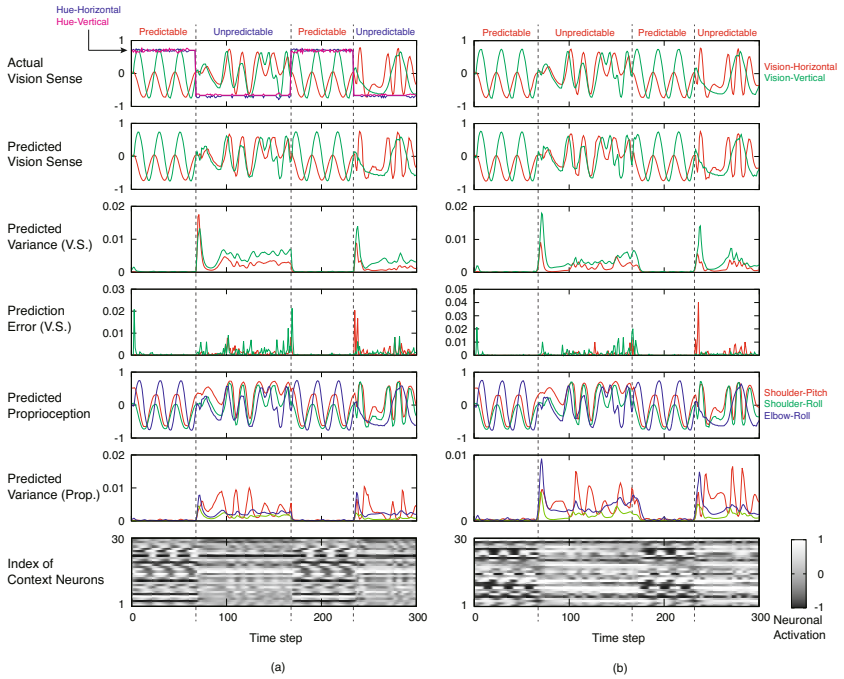

Fig. 2. Time series generated by the trained S-CTRNN and prediction error associated with vision. These are examples of imitation with a cue (a) and imitation without a cue (b).

5 Analysis

We constructed a phase plot based on a principal component analysis (PCA) encompassing all context neurons. Figure 3(a) illustrates the changes in context activation for the experiment with a cue, where the dimensionality was reduced from 30 to 3. In this figure, the predictable part is represented by a red line and the unpredictable part is represented by a blue line in accordance with the target color. Shifts in the context activation trajectories between the two modes can be seen in the plot. The trajectory on the left side in the phase plot converges toward a limit-cycle attractor in the proactive mode, whereas the trajectory is perturbed on the right side in the reactive mode as a result of receiving fluctuating visual sequence patterns.

Figure 3(b) illustrates the changes in context activation for the experiment without a cue. Although there is not an explicit cue, which indicates current mode of the demonstrated patterns, the context activation similar to the case with a cue can be seen in the plot.

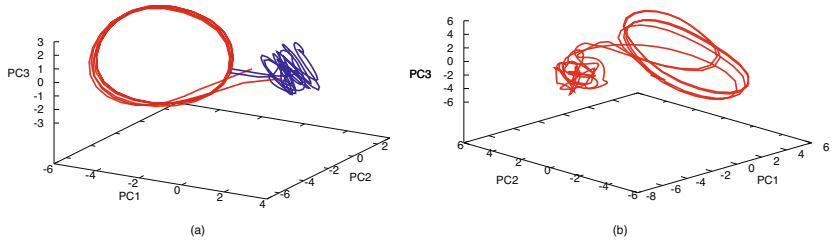

Fig. 3. (a) Changes in context activation in the experiment with a cue. The dimensionality in this case was reduced from 30 to 3 by PCA. The predictable part is represented by a red line and the unpredictable part is represented by a blue line. (b) Changes in context activation in the experiment without a cue.

Both with and without an explicit cue indicating a transition between predictable and unpredictable parts, we confirmed that context dynamics plays a role in switching between the proactive and reactive modes.

6 Summary and Conclusions

This paper presented neurorobotics experiments designed to investigate how proactive and reactive behavioral modes can be developed and how they can be switched autonomously as the situation demands.

The experimental tasks were designed to train a humanoid robot to switch between two behavior, namely proactively imitating other's movements by utilizing acquired memories and reactively following other's unpredictable movements through iterative learning of such alternating behavioral patterns. We conducted two experiments (with/without a cue case), and the S-CTRNN model was utilized in the experiments. In both experiments, the robot was able to generate both a proactive behavior for the predictable part and a reactive behavior for the unpredictable part, as well as to switch autonomously between the two. Phase space analysis of the context state confirmed that the switching mechanism emerged from self-organization in the context dynamics through "meta-learning" of prediction of the predictability itself.

Acknowledgement. This study was supported by grants from the Institute for Infocomm Research, Agency for Science, Technology and Research (A*STAR), Singapore (AH/OCL/1082/0111/I2R) and the Industrial Strategic Technology Development Program, MKE, Korea (10044009).

References

1. Braver, T.S.: The variable nature of cognitive control: a dual mechanisms framework. Trends Cogn. Sci. 16(2), 106–113 (2012)
2. Pew, R.W.: Levels of analysis in motor control. Brain Res. 71(2-3), 393–400 (1974)
3. Grafton, S.T., Salidis, J., Willingham, D.B.: Motor learning of compatible and incompatible visuomotor maps. Journal of Cognitive Neuroscience 12(2), 217–231 (2001)
4. Tani, J.: Model-based learning for mobile robot navigation from the dynamical systems perspective. IEEE Transactions on Systems, Man, and Cybernetics Part B: Cybernetics 26(3), 421–436 (1996)
5. Ito, M., Noda, K., Hoshino, Y., Tani, J.: Dynamic and interactive generation of object handling behaviors by a small humanoid robot using a dynamic neural network model. Neural Networks 19, 323–337 (2006)
6. Yamashita, Y., Tani, J.: Emergence of functional hierarchy in a multiple timescale neural network model: a humanoid robot experiment. PLoS Comput. Biol. 4(11), e1000220 (2008)
7. Namikawa, J., Nishimoto, R., Arie, H., Tani, J.: Synthetic approach to understanding meta-level cognition of predictability in generating cooperative behavior. In: Yamaguchi, Y. (ed.) Advances in Cognitive Neurodynamics (III), pp. 615–621. Springer (2013)
8. Murata, S., Namikawa, J., Arie, H., Sugano, S., Tani, J.: Learning to reproduce fluctuating time series by inferring their time-dependent stochastic properties: Application in robot learning via tutoring. IEEE Transactions on Autonomous Mental Development (2013)
9. Namikawa, J., Tani, J.: A model for learning to segment temporal sequences, utilizing a mixture of rnn experts together with adaptive variance. Neural Netw. 21(10), 1466–1475 (2008)

A Comparison between the Use of ESNN on Long Stereo-EEG Recordings and Their Largest Lyapunov Exponent Profiles for Epileptic Brain Analysis

Maurizio Fiasché[1], Lino Nobili[2], and Bruno Apolloni[1]

[1] Department of Computer Science, University of Milan, Italy
maurizio.fiasche@ieee.org
[2]Centre of Sleep Medicine, Centre for Epilepsy Surgery "C. Munari"
Department of Neuroscience, Niguarda Hospital, Milan, Italy

Abstract. In the last 25 years many works in literature about the capability to detect or predict the occurrence of epileptic seizures, starting from the electroencephalogram (EEG) signal analysis, have often hypothesized that the epileptogenic activity is the result of an abnormal electrical activity hyper-synchronization of different points in an epileptic brain. We already proposed our method to integrate Neural Networks (NN) and the largest Lyapunov exponent (Lmax) for capturing brain dynamics through long stereo-EEG (sEEG) data recorded. In this paper we want to compare the use of a classical Evolving Spiking NN (ESNN) on long sEEG recordings with the integrated method previously proposed. Results are interesting and encourage us to develop, in the next future, a framework for EEG signal analysis.

Keywords: Largest Lyapunov Exponent, Rosenstein Algorithm, Spiking Neural Networks, ESNN, Epileptic Seizure, Epilepsy, integrated approach.

1 Introduction

Epilepsy is thought as a combination of processes generated by a an abnormal electroencephalographic hyper-synchronization of different brain areas. It is well known nowdays, following this literature, that -ictal is the phase during seizure, post-ictal refers to the state after the event, inter-ictal is the state between a post-ictal state and the next pre-ictal one [1]. Observing EEG, brain activity in the ictal state (during a seizure) is very different from the normal activity with respect to pattern of neuronal firing, thus, detection of seizures can be challenging even from a visual inspection of the EEG by a valued trained neurologist for a variety of reasons. Prediction of seizures is even more challenging because there is very little confirmed knowledge of the exact mechanism responsible for the seizure, nevertheless a lot of works has been published about in the last 25 years. Effective computational techniques for automatic seizure detection and prediction could be very useful as decision support systems and have a great impact on diagnosis and treatment of epilepsy, also with outstanding economic fallout. With this view a lot of literature has been published on seizure detection and predictability, and seizure prediction times from minutes to hours have

M. Lee et al. (Eds.): ICONIP 2013, Part I, LNCS 8226, pp. 545–552, 2013.
© Springer-Verlag Berlin Heidelberg 2013

been reported with certain measures derived from the theory of dynamical systems, capable of extracting information from the EEG, allowing the detection of a preictal state. Starting from these studies, and considering the brain as a complex dynamical system, we can consider EEG recordings as its output, analysing it in order to find out something about the system itself. In this way we have already proposed [2] a calculation method for a well-known chaotic measurement, Lmax, over sEEG and talked about its suitability for seizure prediction, and we have proposed a novel framework based on integration of Lmax with an Evolving Spiking Neural Network (ESNN). Others [3] already analysed Spiking Neural Networks (SNN) models and proposed a new one improved on EEG data. Thus in this paper, our aim is to compare the use of an ESNN on EEG profiles and on their Lmax profiles.

The paper is organized in this way: in section 2 a state of the art on Chaotic approach and SNN approach on EEG recordings is presented, in section 3 methodology and data used for analysis, with theoretical explanation of chaotic and NN techniques used are exposed, in section 4 our new integrated methodology and experiments with results are reported, and finally in section 6 conclusions are inferred with future work scheduled.

2 State of the Art Presented in Literature for the Two Single Methods

2.1 Artificial Spiking Neural Networks for of Epileptic Seuizure Detection

Several, but not many authors, proposed SNN architecture for analysing pattern in EEG recordings, in particular for capturing epileptic activity. The last work was proposed in [3] where a multi-spiking neural network (MuSpiNN) and a new training algorithm, called by authors Multi-SpikeProp, for training the network have been presented. In their works authors discussed about different SNN learning paradigms, but they tested the network and the training algorithm investigating complex different classification problems. Their conclusion was that SNNs demonstrate great potential for solving complicated time-dependent pattern recognition problems defined by time series thanks to their intrinsic dynamic representation. In fact previously the same authors presented an improved and efficient single-spiking SNN model and applied it for epilepsy and epileptic seizure detection, a complicated pattern recognition problem [4], here a SNN model for EEG classification and epilepsy and seizure detection using RProp as training algorithm was proposed providing a very high classification accuracy of 92.5%. Others authors [5] focuses, specifically, on models of spike-based information coding, synaptic plasticity and learning to yield survey real-life applications of spiking models. This work was meant to be an introduction to spiking neural networks for scientists from various disciplines interested in spike-based neural processing, and Epilepsy was presented as an application, but not unique. On the other hand, despite the promise of improved performances, SNN research is still in its early stages, and a lot of research paper has been presented in literature about [6][7], also as new paradigms [8], but the most relevant paper on its suitability on the epilepsy problem remain [3]. In this sense, can be interesting analysing SNNs approach on EEG recordings or on their processing methodology.

2.2 Largest Lyapunov Exponenent - Lmax

In this section we will provide a short state of the art about Lmax to seizure prediction. For an overview of the literature on seizure prediction see [1][9].With the advent of the physical–mathematical theory of non-linear systems in the 1980s, novel approaches were introduced that were aimed at a better characterization of dynamical systems exhibiting complex behaviour than hitherto possible with conventional linear approaches. Soon time series analysts became aware of seizure prediction as a potential field of application. In the early 1990s, Iasemidis et al. [10] estimated Lmax as an indicator for chaotic behaviour from the intracranial EEG (IEEG) of epileptic patients by means of a moving window analysis and reported a decrease in chaoticity in the minutes before an epileptic seizure. During the 1990s and around the turn of the millennium, a number of studies were highly optimistic about seizure prediction becoming feasible for clinical application in the near future. However, starting from 2003, a number of studies were published (most of them carried out on extensive databases), questioning both the validity and reliability of these findings, showing that earlier optimistic results could not be reproduced. All studies on this topic have been reproduced with not good results and with many criticisms, between them, also the suitability of Lmax [10][11] for seizure prediction has been doubted by Lai et al. [12][13] that raised doubts about. In 2008, Iasemidis' group member published a paper [14] were problems pointed out are in part acknowledged and approached, theoretical problems discussed by Lai remains, as previously showed, but also incredible results published with use of Lmax in following years [15].

3 Methodology

3.1 ANN Paradigm - ESNN

SNN represent information as trains of spikes, rather than as single scalars, thus allowing the use of such features as frequency, phase, incremental accumulation of input signals, etc. Neuronal dynamics of a spiking neuron are based on the increase in the inner potential of a neuron (post synaptic potential, PSP), after every input spike arrival. When a PSP reaches a certain threshold, the neuron emits a spike at its output. In this application we will use the Spike Response Model (SRM) [16].

ESNN evolve/develop their structure and functionality in an incremental way from incoming data based on the following principles [17]: (i) New spiking neurons are created to accommodate new data, e.g. new patterns belonging to a class or new output classes, (ii) Spiking neurons are merged if they represent the same concept (class) and have similar connection weights (defined by a threshold of similarity). In [16] an ESNN architecture is proposed where the change in a synaptic weight is achieved through a simple spike time dependent plasticity (STDP) learning rule:

$$\Delta w_{j,i} = \mathrm{mod}^{\,order(j)} \tag{1}$$

where: $w_{j,i}$ is the weight between neuron j and neuron i, mod $\in (0,1)$ is the modulation factor, *order(j)* is the order of arrival of a spike produced by neuron j to neuron i.

For each training sample, it is the *winner-takes-all* approach used, where only the neuron that has the highest PSP value has its weights updated. The postsynaptic threshold (*PSPTh*) of a neuron is calculated as a proportion $c \in [0, 1]$ of the maximum postsynaptic potential, max(*PSP*), generated with the propagation of the training sample into the updated weights, such that:

$$PSP_{Th} = c \max(PSP) \tag{2}$$

Creating and merging neurons based on localised incoming information and on system's performance are main operations of the ESNN architecture that make it continuously *evolvable*.

3.2 Calculation of Lmax

The exponential divergence or convergence of nearby trajectories in state space is conceptually the most basic indicator of deterministic chaos and can be sufficiently estimated using Lmax. The first proposed algorithm (used by Iasemidis' groups) to compute Lmax from a time series suffers from severe drawbacks that occur particularly with short and noisy time series, strongly depends on parameters used for the state space reconstruction, and is computationally highly expensive [18]. In order to avoid these shortcomings we here use a combination of improved algorithms [2], [19] according to which the Lmax can be estimated from:

$$d_j(i) \approx C_j e^{L_{max} \cdot i \cdot t} \tag{3}$$

where $d_j(i)$ denotes the average divergence between two trajectory segments at time t_i, C_j with $j = 1, \ldots, M$ is a constant that is given by the initial separation of a reference vector z_j in state space and its nearest neighbour. In order to improve statistics we follow Kantz [20] and search for all neighbours starting within a hypersphere of radius 3 around z_j using a box-assisted algorithm[20]. Based on the relation

$$\ln d_j(i) \approx C_j + L_{max} \cdot i \cdot \Delta t \tag{4}$$

Lmax is then calculated using a least-squares fit to an average line defined by $y(i) = (1/\Delta t)\langle \ln d_j(i) \rangle$, where $\langle \ldots \rangle$ denotes the average over all values of j. In order to reduce the unwanted influence of temporal correlations Rosenstein et al. [19] suggested to choose a Theiler window of a length given by the reciprocal of the mean frequency of the power spectrum.

Criticism: Inability of Lmax Epileptic Seizure Prediction

Lai et al. sustained in [12][13] that two major obstacles can fundamentally hinder the predictive power of Lmax computed from time series, in particular for seizure prediction: 1) statistical fluctuations of the Lyapunov exponents due to finite time computation; 2) noise from the time series. They showed that increasing the amount of data in a moving window will not improve the exponents' detective power for characteristic system changes, and that the presence of small noise can ruin

completely the predictive power of the exponents. In section 4 we will use a type of data that remove 2nd problem. However use of technique presented in section 3.2 should make Lmax more robust to noise and to statistical fluctuations (1st problem). But, there is another limitation in the adaptive algorithm for selection of critical electrodes starting from Lmax profiles for each electrode developed by Iasemidis et al. Indeed this procedure implies that the spatiotemporal dynamics preceding a seizure do not change from seizure to seizure so that it would have been optimal for the seizure that has just occurred. Such a procedure is based on the implicit assumption that pre-ictal dynamics change to a certain degree from seizure to seizure, but the pre-ictal dynamics of a seizure still depend on the dynamics of the previous one. This is a very strong constraint made on initial hypothesis of pre-ictal dynamics. This assumption could be a problem for individuating correct pattern in pre-ictal state, in particular for different patients and for different types of epilepsy. To eliminate it, making system of "evolving" type, could be the key for a right modelling, but, in this case, T-index would not be more a good indicator.

3.3 An Evolving Dynamical Modelling Proposed

Our idea is based on the hypothesis that the brain is an "complex evolving-dynamical- non linear- system", and each dynamic that seems different from the previous one is a new pattern useful as a training step, generalizing the previous hypothesis, building a learning method continuously adaptable over time. For this aim we have used a suitable ESNN described above. Thus, first, we calculated, an Lmax profile for each EEG channel, obtaining a multichannel profile considering this one as input of the ESNN for detecting a seizure (pre-ictal and ictal) pattern in the channel where there is an "anomalous" pattern. That channel is also considered a candidate for the epileptic focus individuation, but this is not the aim of this paper. In this way we have obtained a graph with Lmax (bit/s) as a compressed function portrayed in the state space, the new problem space! Now it is possible integrate this analysis with a NN approach for a good epileptic brain modelling, applying it not to EEG recordings time series (in time or frequency domain as used so far), but, for the first time in literature, to their portrait in the state space [2].

4 Experimental Setup and Results

4.1 Intracerebral Stereo-EEG Data - sEEG

The main works about seizure prediction, present results obtained from IEEG, and only a few works presents results about scalp or sEEG. In this paper we have measured and quantified the spatio-temporal dynamics of the brains of two patients affected by drug resistant types of epilepsy, each monitored through intracerebral sEEG. These recording are different from classical IEEG for the position of the electrodes in the brain, indeed they are positioned inside the brain in 3 dimensions and not in the surface of the brain like classical IEEG. Doctors and Neurologists have implanted these electrodes in the brain after a preliminary analysis of long term scalp

EEG and clinical observations under functional Magnetic Resonance Imaging (fMRI) and in-depth study of the patient history, thus a surgical implantation of the electrodes and a magnetic resonance for analyzing a correct implantation of the electrodes are necessary, with this procedure it is possible to individuate the critical sides for recordings that can give us important information about the focus and the functioning of the brain analyzed. The surgeons after to have identified the cerebral area that are the cause of the epiletogenesis with a certain accuracy, remove these zone (the necessary minimum part). We will illustrate results about two patients (with pharmacoresistant focal epilepsy) that have solved their problems in this centre with this method, and we have analyzed their long term sEEG recordings for giving confirmation of the focus removed and to analyze these brain activities. Patient A, has been recorded with sEEG for 32 hours, Patients 2 for 44 hours of continuous recordings. A Nihon Kohden® Software has been used only for analyzing and for converting the *.EEG files (a format property of Nihon Kohden®) in ASCII files. After we elaborated these data with a toolbox we had implemented in MATLAB®. Fig. 1.A and 1.B are respectively the 3D visual situation described above for electrode implantation in each patient.

4.2 Framework Application

We already presented our framework where Lmax profiles as compressed graphs of each channel are the input or a suitable ESNN for capturing patterns that represents abnormal condition in the brain. But the principal difficulty represented from the brain is that it is an "evolving" system that changes over time and for each different person, and in a same person there are different pattern in a pre-ictal phase (in contrast with hypothesis discussed in 3.2). Thus, for solving these complex issue, we have integrated Chaotic measurements with an evolving- adaptive- learning system robust also to variations of the information in the EEG pattern for different evaluations. Framework is presented in fig. 2. It has given very good results in our preliminary study tested on two very good long term sEEG recordings, moreover it can be seen as a solution for limitations identified by Lai et al.[12][13]. In this paper we want to compare our framework with a suitable ESNN like the one described in section 3.1. Our simulation results are interesting and give us several useful information and encourage us to follow this path.

4.3 Results

Results are presented in table 1 for Patient A and B and compared with application of ESNN. *Patient A*: with our framework described in 4.2, we have obtained a Sensitivity of 82% and a false prediction rate of 0.14/h. Instead with the ESNN architecture we obtained a lower sensitivity and a higher false positive rate. *Patient B*: results for patient A are confirmed and there is a higher improvement in the application of the ESNN on lmax profiles instead that its application on EEG profiles, this probably because paroxysmal events are more frequent and there is a faster convergence. In this way the patterns that has been originated by the electrodes selected and related to focuses removed from neuro-surgeons, with a consequent complete disease solution of patient.

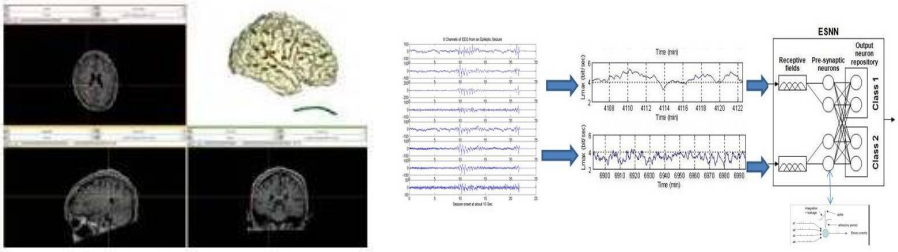

(1) (2)

Fig. 1. Modelling of the brain of the two patients (a) patient A; (b) patient B, both with magnetic resonance and with a computerized simulation, and sEEG electrodes position.
Fig. 2. Framework Architecture

Table 1. Results for patients A and B compared with our framework and ESNN on EEG recordings

	Our Framework		ESNN	
Samples	Sensitivity	False positive rate	Sensitivity	False positive rate
Patient A	82%	0.14h	75%	0.2
Patient B	95%	0.09h	67%	0.3

5 Conclusions and Future Developments

In this paper, the complex problem of epileptic seizures analysis was approached, and a comparison between our novel integrated method and a simple ESNN approach has been carried out. We proposed a different method from [18] for calculating Lmax [19][2] for overcoming any theoretical critical state present in literature about his suitability as indicator of epileptic seizure. Always with this aim and for improving performances about its prediction capability in the epileptic brain, we thought to integrate this chaotic measurement with a suitable ESSN, improving identification of pre-ictal patterns on EEG in an adaptive and evolving way. This is one of the first application of a NN approach for pattern recognition on Lmax profiles, instead of temporal or in frequency domain profiles as reported in literature and compared here. Thus, we presented these new framework testing it on two samples of long SEEG recordings. These preliminary results are exciting and promising, our framework improves predictability of seizures. In the future more experiments on other long EEG recordings will be needed. Moreover a more suitable ESNN architecture, already in a test phase, will be considered.

References

1. Lehnertz, K., Elger, C.E.: Can epileptic seizures be predicted? Evidence from nonlinear time series analysis of brain electrical activity. Phys. Rev. Lett. 80, 5019–5023 (1998)
2. Fiasché, M., Schliebs, S., Nobili, L.: Integrating neural networks and chaotic measurements for modelling epileptic brain. In: Villa, A.E.P., Duch, W., Érdi, P., Masulli, F., Palm, G. (eds.) ICANN 2012, Part I. LNCS (LNAI), vol. 7552, pp. 653–660. Springer, Heidelberg (2012)
3. Ghosh-Dastidar, S., Adeli, H.: A new supervised learning algorithm for multiple spiking neural networks with application in epilepsy and seizure detection. Neural Networks 22(10), 1419–1431 (2009)
4. Ghosh-Dastidar, S., Adeli, H.: Improved spiking neural networks for EEG classification and epilepsy and seizure detection. Integrated Computer-Aided Engineering 14(3), 187–212 (2007)
5. Ponulak, F., Kasiński, A.: Introduction to spiking neural networks: Information processing, learning and applications. Acta Neurobiologiae Experimentalis 71(4), 409–433 (2011)
6. Kasabov, N.: Evolving spiking neural networks for spatio-and spectro-temporal pattern recognition. In: Proceedings of the 2012 6th IEEE International Conference Intelligent Systems, IS 2012, pp. 27–32 (2012)
7. Schliebs, S., Fiasché, M., Kasabov, N.: Constructing robust liquid state machines to process highly variable data streams. In: Villa, A.E.P., Duch, W., Érdi, P., Masulli, F., Palm, G. (eds.) ICANN 2012, Part I. LNCS (LNAI), vol. 7552, pp. 604–611. Springer, Heidelberg (2012)
8. Kasabov, N.: NeuCube EvoSpike architecture for spatio-temporal modelling and pattern recognition of brain signals. In: Mana, N., Schwenker, F., Trentin, E. (eds.) ANNPR 2012. LNCS (LNAI), vol. 7477, pp. 225–243. Springer, Heidelberg (2012)
9. Mormann, F., Andrzejak, R.G., Elger, C.E., Lehnertz, K.: Seizure prediction: the long and winding road. Brain 130(2), 314–333 (2007)
10. Iasemidis, L.D., et al.: Phase space topography and the Lyapunov exponent of electrocorticograms in partial seizures. Brain Topogr. 2, 187–201 (1990)
11. Iasemidis, L.D., et al.: Adaptive epileptic seizure prediction system. IEEE Trans. Biomed. Eng. 50, 616–627 (2003)
12. Lai, Y.C., Harrison, M.A., Frei, M.G., Osorio, I.: Inability of Lyapunov exponents to predict epileptic seizures. Phys. Rev. Lett. 91, 068102 (2003)
13. Lai, Y.C., Harrison, M.A., Frei, M.G., Osorio, I.: Controlled test for predictive power of Lyapunov exponents: their inability to predict epileptic seizures. Chaos. 14, 630–642 (2004)
14. Sackellares, J.: Seizure Prediction. Epilepsy Curr. 8(3), 55–59 (2008)
15. Nair, S.P., et al.: An investigation of EEG dynamics in an animal model of temporal lobe epilepsy using the maximum Lyapunov exponent. Exp. Neurol. 216(1), 115–121 (2009)
16. Brette, R., et al.: Simulation of networks of spiking neurons: A review of tools and strategies. Journal of Computational Neuroscience 23(3), 349–398 (2007)
17. Kasabov, N.: Evolving Connectionist Systems: The Knowledge Engineering Approach. Springer, London (2007)
18. Wolf, A., Swift, J.B., Swinney, L., Vastano, A.: Determining Lyapunov exponents from a time series. Physica D 16, 285–317 (1985)
19. Rosenstein, M.T., Collins, J.C., De Luca, C.: A practical method for calculating the largest Lyapunov exponents from small data sets. Physica D 65, 117–134 (1993)
20. Kantz, H.: A robust method to estimate the maximal Lyapunov exponent of a time series. Phys. Lett. A 185, 77–87 (1994b)

Spike Sorting Using Hidden Markov Models

Hailing Zhou, Shady Mohamed, Asim Bhatti, Chee Peng Lim, Nong Gu, Sherif Haggag, and Saeid Nahavandi

Centre for Intelligent Systems Research
Deakin University, Australia
{hailing.zhou,shady.mohamed,asim.bhatti,chee.lim,nong.gu,
sherif.haggag,saeid.nahavandi}@deakin.edu.au

Abstract. In this paper, hidden Markov models (HMM) is studied for spike sorting. We notice that HMM state sequences have capability to represent spikes precisely and concisely. We build a HMM for spikes, where HMM states respect spike significant shape variations. Four shape variations are introduced: silence, going up, going down and peak. They constitute every spike with an underlying probabilistic dependence that is modelled by HMM. Based on this representation, spikes sorting becomes a classification problem of compact HMM state sequences. In addition, we enhance the method by defining HMM on extracted Cepstrum features, which improves the accuracy of spike sorting. Simulation results demonstrate the effectiveness of the proposed method as well as the efficiency.

Keywords: Spike sorting, HMM, Cepstrum, confusion matrix.

1 Introduction

It is observed that complex brain processes are reflected by activities of millions of neurons. To study brains, research on understanding neuron actions is crucial. Electrodes are implanted in brains to record actions of surrounding neurons through firing potentials. The action potentials are also referred as "spikes" in neuroscience, as they appear sharp spikes in the signal waveforms. Each neuron produces spikes with a particular shape. Spike sorting is to cluster these recorded spikes into groups. In each group, spikes have similar shapes. The ultimate goal of spike sorting is to find the correspondence between spikes and neurons. Based on this research, the possibilities of new investigations on brains will be increased dramatically.

The assumptions for spike sorting are that the shapes of spikes from a specific neuron are similar and they are unique for each neuron [5]. Many spike-sorting techniques have been developed [1,2]. The challenges of spike sorting lie in that (i) the number of neurons is unknown; (ii) the spike recording is associated with physical and biological noise [4]; (iii) spikes in the local area are not easy to be distinguished [2]. Traditional spike sorting methods [10,11] usually rely on shape measurement such as comparing height, width, and peak-to-peak amplitude of

M. Lee et al. (Eds.): ICONIP 2013, Part I, LNCS 8226, pp. 553–560, 2013.
© Springer-Verlag Berlin Heidelberg 2013

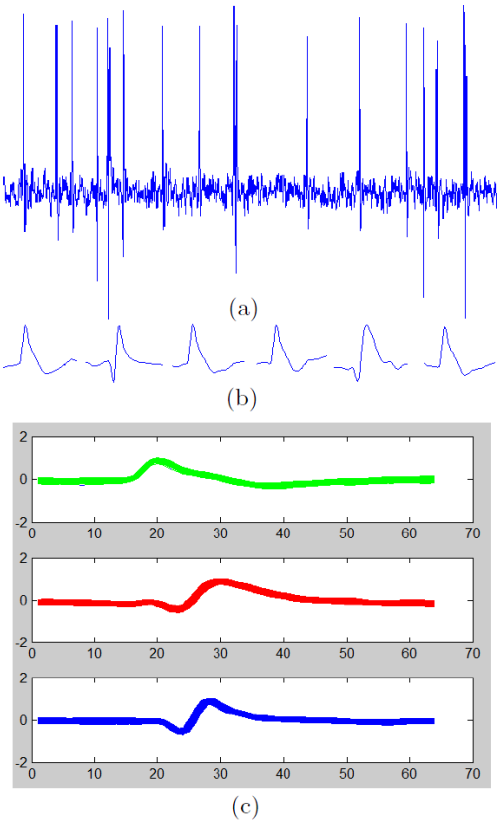

Fig. 1. The illustration of our method. (a)Raw data recorded from electrodes; (b)spike detection using a threshold-based method; (c) clustering the detected spikes into three groups automatically using HMM.

spikes. However, these approaches often produce inaccurate clustering because of the sensitivities to noise.

Statistics tools are widely used for spike sorting. In [6], Principal Component Analysis (PCA) is introduced to group spikes through analyzing spikes to get several principal components and projecting spikes into each component. Takahashi et al. apply Independent Component Analysis (ICA) [7,8] to separate spikes. As both PCA- and ICA-based methods require strong spike correlation and variances, they will not work well in case of low signal to noise ratio (SNR). In [12], Pouzat et al introduce a Markovian approach with a Monte Carlo simulation to solve spike sorting. However, high accuracy is achieved at the expense of a great computational complexity.

In this paper, we propose an effective and efficient method for spike sorting shown in Fig.1. The methods consists of two major procedures: spike detection and representation [3] and HMM based spike clustering. The main contribution

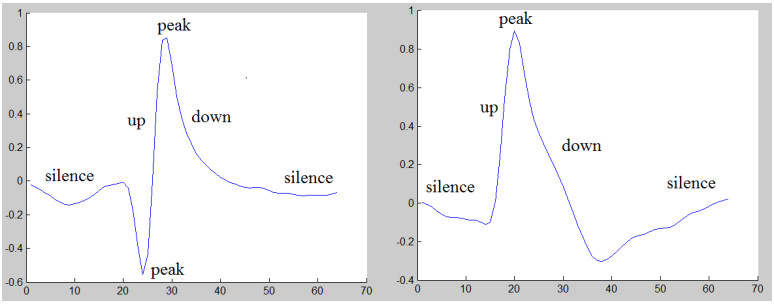

Fig. 2. Significant shape variations in spikes, which are assigned to HMM states

is the use of HMM to cluster the shapes of different spikes. For each spike, we observe that it contains four significant shape variations: silence, going up, peak and going down. We partition each spike into several segments and define observations of HMM as these spike segments. The states of HMM are corresponding to the four shape variations. The expectation maximization(EM) algorithm is used to compute the HMM parameters. The Viterbi algorithm is then used to find the most likely state sequence that correspond to each spike shape. After that, the sorting of spikes becomes to classify the obtained state sequences. Experiments demonstrate the effectiveness and efficiency of the proposed method.

The rest of the paper is organised as follows: Section 2 discusses the use of HMM for spike sorting. Section 3 shows the experimental results.

2 HMM-Based Spike Sorting Method

HMM is a statistical tool to model sequences and describe the probability distribution over a set of observations, which has been successfully used for speech recognition. There are five basic elements in a HMM: 1) the number of states N; 2) the number of observations M ; 3) the state transition probability matrix A; 4) the observation probability matrix B and 5) the initial state distribution Π. The triplet $\lambda = (A, B, \Pi)$ is often used to denote a HMM.

2.1 Spike HMM

In this paper, we utilize a HMM to model spikes in order to understand its underlying states over a sequence of observations. For a spike, the significant shape states are silence (flat), going up, peak and going down, shown in Fig. 2. Each of them is assigned to a state (from s1 to s4) of the HMM (i.e. $N = 4$). The state structure of the spike HMM and the state transitions with non-zero probability are shown in Fig. 3. It is noticed that for a general spike, the transitions between s2 (up) and s3 (down) or between s1 (silence) and s4 (peak) have zero possibilities. Moreover, most spikes start from the silence state and

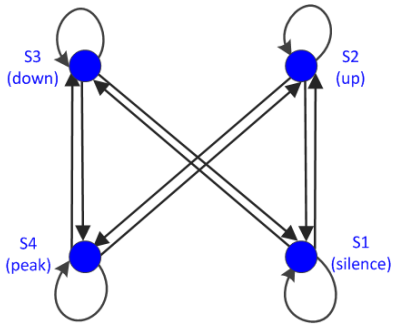

Fig. 3. HMM with 4 states (labeled s1 to s4) and 12 state transitions. The transition probabilities between s2 and s3 or between s1 and s4 are zero.

end in the silence state. Based on the basic knowledge about spike, the following transition probability matrix and the initial state distribution are given for the initialization of the HMM.

$$A = \begin{pmatrix} 0.4 & 0.3 & 0.3 & 0.0 \\ 0.3 & 0.4 & 0.0 & 0.3 \\ 0.3 & 0.0 & 0.4 & 0.3 \\ 0.0 & 0.4 & 0.4 & 0.2 \end{pmatrix}$$

$$\Pi = \begin{pmatrix} 0.6 & 0.2 & 0.2 & 0.0 \end{pmatrix}$$

2.2 Spike Detection and Feature Extraction

Given a sequence of neuron signals for spike sorting, the first step is the detection of the spikes. We adopt the amplitude thresholding method [3], which can quickly locate spikes. A bandpass filtering (bf) is firstly applied to the input signals S and then the standard deviation σ of the background noise is estimated using

$$median\{|S_{bf}|/0.6745\}. \tag{1}$$

The threshold is set to be 4σ.

After spike detection, L samples are saved for each spike. A typical value of L is set to 64. We divide a spike into overlapping segments of length of l. The amount of overlap between consecutive segments is o. The number of segments is actually the number M of HMM observations, which can be calculated by using $M = (L - o)/(l - o)$. The choice of parameters l and o significantly affects the spike clustering accuracy. With an amount of overlap between consecutive spike segments, more spike features can be captured to improve the performance. It is very delicate to choose the parameter l. If l is too small, there is no sufficient discriminant information in the observation. If l is too large, the probability of cutting across the distinct spike features are increased. Based on the knowledge

of spikes, the number of samples that cover a whole peak (i.e. s2-s4-s3 or s3-s4-s2) of a spike is about 20. l set to the half value (i.e. 10) is a reasonable choice, which has been proved in our experiments. Refer to Fig. 4 for illustration.

Based on the partition of a spike, we obtain M observations for the HMM. For each observation vector, it has l samples of the raw waveform data. The use of raw data as HMM observation vectors has a disadvantage of being sensitive to noise. To reduce the effect of noise, Cepstrum coefficients are extracted from each spike segment. We employ Cepstrum features because they have a property to capture both the amplitude property of spikes and the phase of the initial spectrum. This property makes Cepstrum features be able to separate the meaningful features from noisy signals. Cepstrum coefficients are calculated as the Inverse Fourier Transform (IFT) of the logarithm of the Fourier Transform of a spike segment, as

$$c = F^{-1} log|F(s)|, \tag{2}$$

where s is the spike segment and c is the Cepstrum feature vector.

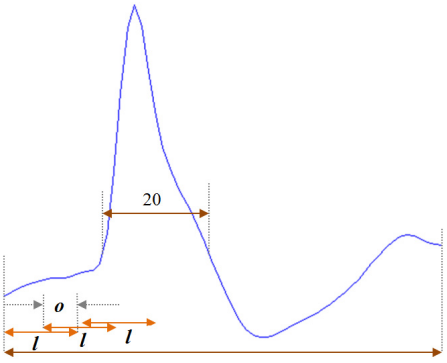

Fig. 4. Spike parameterization and partition. There are L samples for a spike. The spike is partitioned into M segments with each length of l and overlap of o between neighboring segments.

2.3 HMM Training and Clustering

A set of 300 detected spikes are used to train a HMM $\lambda = (A, B, \Pi)$, where there are $300 \times M$ observation vectors with l Cepstrum coefficients for each. In the HMM, the number of states N is 4, the number M of observation vectors is defined in Section 2.2, the transition probability matrix A and the initial state distribution Π are given in Section 2.1. The only unknown parameter is the observation probability matrix B. We adopt the mixture of Gaussians with the number of 3 to initialize B. In order to optimize the HMM to maximize the probability of the model generating the observations, we adjust the parameters A, B, and Π using the EM procedure [14].

In the clustering stage, the optimized HMM is used to group spikes. Every spike is represented by M observation vectors, same as the description above.

Table 1. Statistics of the number of spikes in each generated clusters using the proposed method and the method of [3]

Methods	The proposed method			The method [3]		
Spike sets	0.05	0.10	0.15	0.05	0.10	0.15
Cluster 1	807	837	878	810	952	962
Cluster 2	756	761	724	753	562	466
Cluster 3	756	711	629	741	477	456
Cluster 4	-	85	97	15	370	398
Cluster 5	-	-	20	-	19	40
Cluster 6	-	-	-	-	14	23
Total cluster Num.	3	4	5	4	6	6
Dominant cluster Num.	3	3	3	3	1 or 4	1 or 4

The Viterbi algorithm [15] is employed to find the most likely state sequence in the model that produces the observations. The output state sequence consists of M elements received values from 1 to 4 that are corresponding to s1 to s4 respectively. As the order of states respects primary spike geometry that is dominant to distinguish different spikes, state repetitions are removed from output state sequences by using the $diff$ and $find$ operations in MATLAB. Take the spike in Fig. 4 for an instance. The output state sequence $(1, 1, 2, 2, 4, 3, 3, 3, 1, 1)$ is reduced to be $(1, 2, 4, 3, 1)$. After that, spike sorting becomes the clustering of the unique state sequences, which can be easily implemented by using the *unique* operation in MATLAB.

3 Experimental Results

In this part, we show our experimental results on simulation data given in [3]. In the simulation data, it is known that there are 3 spike types. In addition, the spikes with different noise levels are provided as well as the true classes for each spike. In the experiment, there are 3 sets of spikes with 3 noise levels: 0.05, 0.1 and 0.15 respectively. We implement our method using MATLAB on Intel Core i7-2600K. To sort 2319 spikes from 3 classes, the proposed classification method siginificantly improves the computational complexity. The classification process takes about 10 seconds to complete. We set the parameters as $l = 10$, $o = 4$ and $M = 10$. Other parameters are described in the Section 2. To evaluate the performance of our proposed method, we compare our results with the method in [3] regarding the number of generated clusters and the spikes in each cluster. The clustering accuracies are also compared via the confusion matrix that is introduced in [13] specifically for evaluating clustering techniques.

Table 1 summarizes the results, where the number of spikes in each cluster is listed. It should be noted that the number of total clusters and the number of dominant clusters, referring to Fig. 5(a) for illustration. Based on the results, it

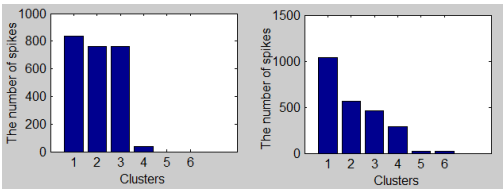

(a)

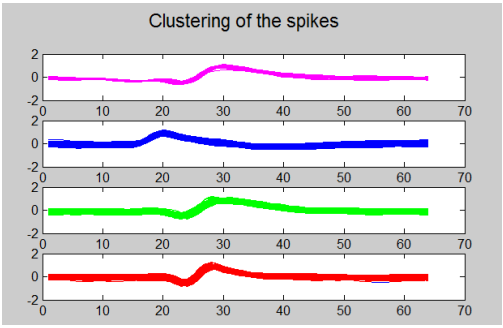

(b)

Fig. 5. Experimental results. (a) The illustration of the number of spikes in each generated clusters using the proposed method (left) and the method [3] (right). (b) The spikes are grouped into 3 major clusters (blue, green and red) using the proposed method.

Table 2. Performance comparison using confusion matrices

Methods	The proposed method			The method [3]		
	Class 1	Class 2	Class 3	Class 1	Class 2	Class 3
Class 1	235	11	17	239	29	21
Class 2	5	292	15	7	272	12
Class 3	11	18	280	5	20	279
Accuracy	91.2%			88.9%		

is obvious that the number of dominant clusters using our proposed method is more distinct than the one using [3] and our proposed method can produce 3 (the actual number of spike classes) dominant clusters for all the data with different SNRs. The spikes in each group are shown in Fig. 5(b), where we can see that the shape variations of spikes in each dominant cluster are small. Moreover, the clustering accuracy is measured using a confusion matrix given in Table 2, where we divide the spikes into two parts - one for building prototypes of clusters and the other for testing the accuracy using the Euclidean distance. The comparison indicates that our method produces more accurate spike sorting.

4 Conclusion

We presented an effective and efficient spike sorting method. A threshold-based method is applied to quickly locate spikes. Cepstrum coefficients are calculated to robustly represent spike segments. The main contribution is the introduction of HMM for spike sorting, where four HMM state are defined and searched to respect the spike geometry. Experimental results demonstrate the superiorities of our proposed method.

References

1. Brown, E.N., Kass, R.E., Mitra, P.P.: Multiple Neural Spike Train Data Analysis: State-of-the-art and Future Challenges. Nature Neuroscience 7, 456–461 (2004)
2. Lewicki, M.S.: A Review of Methods for Spike Sorting: The Detection and Classification of Neural Action Potentials. Network: Computation in Neural Systems 9(4), R53–R78 (1998)
3. Quiroga, R.Q., Nadasdy, Z., Ben-Shaul, Y.: Unsupervised Spike Detection and Sorting with Wavelets and Superparamagnetic Clustering. Neural Computation 16, 1661–1687 (2004)
4. FMitra, P., Bokil, H.: Observed Brain Dynamics. Oxford university Press (2007)
5. Samiee, S., Shamsollahi, M.B., Vigneron, V.: A New Markovian Approach Towards Neural Spike Sorting. In: 8th International Conference on Information, Communications and Signal Processing, pp. 1–5 (2011)
6. Lagerlund, T.D., Sharbrough, F.W., Busacker, N.E.: Spatial Filtering of Multichannel Electroencephalographic Recordings through Principal Component Analysis by Singular Value Decomposition. Journal of Clinical Neurophysiology 14(1), 73–82 (1997)
7. Takahashi, S., Sakurai, Y., Tsukada, M.: Classification of Neuronal Activities from Tetrode Recordings using Independent Component Analysis. Neurocomputing 19(1-4), 289–298 (2002)
8. Takahashi, S., Anzai, Y., Sakurai, Y.: Automatic Sorting for Multineuronal Activity Recorded with Tetrodes in the Presence of Overlapping Spikes. Journal of Neurophysiology 89(4), 2245–2258 (2002)
9. Takahashi, S., Anzai, Y., Sakurai, Y.: Automatic Sorting for Multineuronal Activity Recorded with Tetrodes in the Presence of Overlapping Spikes. Journal of Neurophysiology 89(4), 2245–2258 (2002)
10. Dinning, G.J.: Real-time Classification of Multiunit Neural Signals using Reduced Feature Sets. IEEE Transactions on Biomededical Engineering 28, 804–812 (1981)
11. Schmidt, E.M.: Computer Separation of Multi-unit Neuroelectric Data: A Review. Jouranl of Neuroscience Methods 12, 95–111 (1984)
12. Pouzat, C., Delescluse, M., Viot, P.: Improved Spike-Sorting By Modeling Firing Statistics and Burst-Dependent Spike Amplitude Attenuation: A Markov Chain Monte Carlo Approach. Journal of Neurophysiology 91, 2910–2928 (2004)
13. Stehman, S.V.: Selecting and Interpreting Measures of Thematic Classification Accuracy. Remote Sensing of Environment 62(1), 77–89 (1997)
14. Baum, L.E., Petrie, T., Soules, G., Weiss, N.: A Maximization Technique Occurring in the Statistical Analysis of Probabilistic Functions of Markov Chains. The Annals of Mathematical Statistics 41(1), 164–171 (1970)
15. Rabiner, L.R.: A Tutorial on Hidden Markov Models and Selected Applications in Speech Recognition. Proceedings of the IEEE 77(2), 257–286 (1989)

Analysis of Cognitive Load for Language Processing Based on Brain Activities

Hyangsook Park[1], Jun-Su Kang[2], Sungmook Choi[1], and Minho Lee[2,*]

[1] Department of English Education
[2] School of Electrical Engineering, Kyungpook National University, 1370 Sankyuk-Dong, Puk-Gu, Taegu 702-701, South Korea
susy_kim2001@yahoo.com, {wkjuns,mholee}@gmail.com, sungmookchoi@knu.ac.kr

Abstract. The present study attempted to investigate the role of memory or cognitive load in language processing using an EEG. Twelve healthy right-handed male adults were asked to read a story twice and their brain activities were recorded using an EEG: (i) focusing on meaning of the content only (M) and (ii) focusing on both meaning and form or grammar (M+F). The results demonstrated significant differences in upper alpha and upper beta bands according to reading instructions, which indicates different degrees of cognitive load. The findings make a significant contribution to language acquisition in that they offer valuable information regarding memory and cognitive load in language processing. Thus, they help language researchers and educators in the field of second language acquisition (SLA) develop more effective ways of instructional design and in turn lead their students to better learning outcomes.

Keywords: reading comprehension, grammar acquisition, cognitive load, memory load, EEG, attention, second language acquisition.

1 Introduction

The present study investigated the role of cognitive load in second language acquisition (SLA) in terms of brain activities. Cognitive Load Theory (CLT) have been concerned with concocting teaching tools to help learners maintain an optimal level of load in various learning context [1]. SLA researchers have utilized CLT to account for differences in learner performance with regard to different learning tasks and reported that various factors, including learner's different cognitive abilities, level of English proficiency, and types of tasks, can cause cognitive overload which can diminish instructional outcomes [2, 3].

The majority of studies on the effects of cognitive load in language acquisition, including vocabulary acquisition and reading comprehension, have used performance scores and subjective worlkload self-evaluation [4-6]. As Gevins et al. [7, 8] address, performance scores and subjective measurements have provided overall cognitive load but appeared to lack objective and temporal information regarding mental efficiency. Conversely, using an EEG can measure concurrent brain activities and thus contribute to

M. Lee et al. (Eds.): ICONIP 2013, Part I, LNCS 8226, pp. 561–568, 2013.
© Springer-Verlag Berlin Heidelberg 2013

guiding better learning situation. Therefore, the present study attempted to compare relative mental efficiency in terms of cognitive load in language processing. Moreover, unlike previous studies that evaluated brain activities using sentence level texts [9], this study used a discourse level text (a story) and aimed to obtain more extended evidence regarding the shift of frequency bands in two reading conditions. Thus, this study can provide the evidence how brain reacts to different amount of attention or memory load in terms of reading comprehension and grammar learning.

This paper is organized as follows: Section 2 briefly introduces CLT for reading comprehension, and the proposed method based on an EEG signal analysis will be followed in Section 3. Section 4 includes the experimental results, and conclusion and future works will be described in Section 5.

2 Cognitive Load Theory and Reading Comprehension

CLT is mental effort for successful completion of a task [10]. CLT has three types of cognitive load: intrinsic (the level of inherent difficulty), extraneous (i.e., instructional materials), and germane (construction and automation of schema) cognitive load. CLT suggests that learning happens best under conditions that are aligned with human cognitive architecture, consisting of working memory that is limited in capacity when dealing with novel information. Some researchers argue that students learn better when provided with an optimum learning condition where cognitive load is minimized as much as possible [7, 8, 11].

Researchers have studied the relationship between cognitive load and language acquisition, For instance, Al-Shehri and Gitsaki's study [2] findings revealed that learners' reading comprehension (RC) performance can be enhanced by reducing the learners' extraneous cognitive load induced by format of instructional materials. For example, the students who read a text physically integrated with RC questions outperformed those presented the text split with the questions on the RC tests. In a similar vein, Akbulut [3] argues that too much input, such as glossaries, illustration, underlined, colored, or bolded words, can interfere with RC due to the increase in cognitive load. Moreover, Gevins el al's study findings [7, 8] also reported that task difficulty resulted in decreases in alpha signals but increases in amplitude of a frontal theta rhythm due to the increased memory load. These findings suggest that it is necessary for educators to eliminate redundant and distractive elements in order to maximize the effects of instruction or input and thus facilitate their students' learning.

3 Methods

3.1 Participants and Design

Twenty right-handed male undergraduate students whose L1 was Korean (eight participants were excluded from data analysis due to noise) participated in the study, and each of them were given a $10 certificate as a token of appreciation. Most of the participants included in the data analysis majored in English Education, except for three

students who majored in Electrical Engineering (ages 19-21). Handedness, and gender were screened in order to control confounding variables. Also, all participants were with no history of neurological or psychiatric disorders, and their eyesight was normal or corrected to normal vision.

For this within-subject design experiment, the participants were instructed to read an African folktale, modified by Park, et al. [12], under two instructional conditions at their own pace. Specifically, the degree of attention and cognitive load were manipulated by giving different reading instructions. In the first reading, the participants were asked to simply read the text to understand the meaning of the content (M), whereas in the second reading task, they were asked to pay attention to grammatical features as well as meaning (M+F). The text was divided into eight slides, and four slides contained visually enhanced grammatical features (i.e., gerund and to infinitive), **boldfaced**, colored, and underlined in order to intentionally draw their attention to linguistic features. For instance, for the first reading, the first half of the text was visually enhanced (VIE+), and the second reading, vice versa, as in Figure 1.

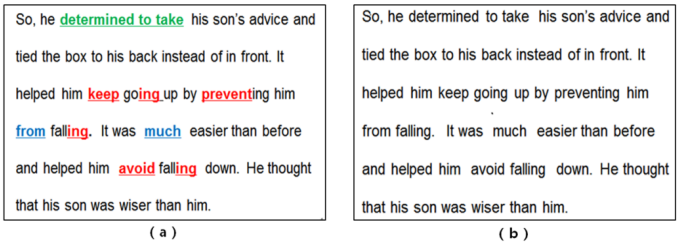

Fig. 1. Text samples presented on the computer screen (a) enhanced text (b) unenhanced text

3.2 EEG Recording and Stimuli

During the recording, the participants comfortably seated in front of a computer monitor in a laboratory and were requested to control blinking, swallowing, and other muscle movements to ensure the quality of the EEG data. Each session lasted about one hour including subject preparation. Based on the 10/20 international system, EEG activities were continuously recorded from 13 scalp locations (F3, F4, Fz, FCz, C3, C4, Cz, CPz, P3, P4, Pz, O1, and O2) by means of Ag/AgCl electrode caps. The electrode impedance was kept below 10 kΩ using a glass ohmmeter. The electrode Fz on the cap served as grounding, while a reference electrode was placed on the right and left ear lobes. The text appeared on a computer monitor, and the participants' brain activities were recorded using an EEG while reading the text by focusing on meaning only and then both meaning and grammar.

The hypothesis is that reading a text to understand the meaning of the content and to focus on grammatical features at the same time can lead to an increase in cognitive load and thus results in selective decreases in upper alpha and upper beta [11, 13]. On the other hand, an escalated cognitive load leads to a selective increase in theta and gamma power [14].

3.3 Data Analysis

All of the data were individually checked and excluded all contaminated with ocular, muscle, or other non-EEG activity. To differentiate the various frequency ranges, the EEG signal as a function of time is transformed into a function of frequency (spectrum) by Fast Fourier Transform (FFT). Broadband EEG was divided into the six frequency ranges: theta (4-7Hz), low alpha (8-10), upper alpha (10-13 Hz), low beta (13-18 Hz), upper beta (18-30.Hz), and gamma (30-70 Hz). Band powers within-subject factors were evaluated using separate paired *t*-tests on the differences in time varying amplitude between the degrees of cognitive load depending on reading conditions. Reading instructions (M/M+F) and two versions of text presentation (VIE- vs. VIE+) served as independent variables while band powers served as dependent variables.

4 Results

The paired *t*-test revealed that there were significant power differences between reading instructions at upper alpha and upper beta bands. In general, the participants spent longer reading time when reading the enhanced text (M = 102.41 s) than the unenhanced text (M = 89.59 s). However, there were no statistically significant power differences induced by visually enhanced input which is supposed to require greater memory and cognitive load. The reading conditions resulted in selective mean differences in upper alpha, upper beta, and theta.

4.1 Analysis of Upper Alpha Band

Reading instructions led significant mean differences at occipital (t = 2.166, P = .041). Also, a marginally significant mean difference was observed at frontal (t = 1.910, P = .068), as in Fig. 2. Specifically, alpha power at the frontal and occipital in the M+F condition was smaller than that of the M condition. The amplitude of both hemispheres was smaller in the M+F condition than that of the M condition, but the differences were marginally significant (t = 1.847, P = .078; t = 1.970, P = .061, respectively).

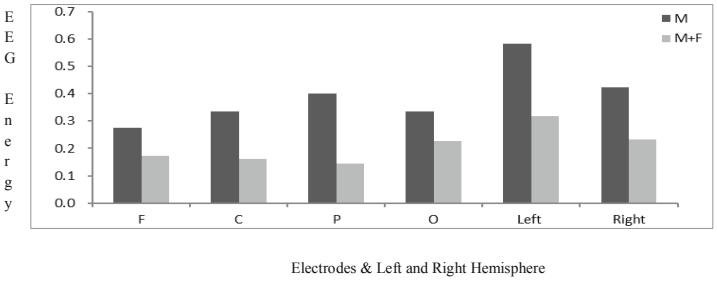

Fig. 2. Mean differences of reading instructions in upper alpha:

*F (Frontal), C (Central), P (Parietal), O (Occipital)

4.2 Analysis of Upper Beta Band

A significant mean difference was observed between the two reading conditions. That is, as shown in Fig. 3, reading the text in the M+F condition resulted in a significant decrease in the amplitude at the frontal, central, and occipital regions than the M condition: F (t = 8.228, P < .001), C (t = 4.082, P < .001), O (t = 3.566, P = .002). Also, hemispheric power declines in the M+F condition were significant compared to the M condition. Specifically, the two conditions yielded significant mean power differences in the right and left hemispheres: t = 7.119, P < .001; t = 3.975, P = .010, respectively.

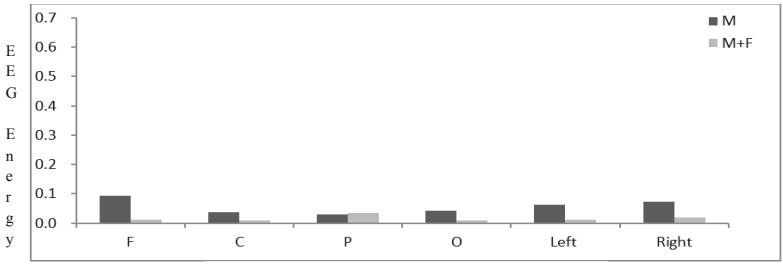

Fig. 3. Mean differences of reading instructions in upper beta:

*F (Frontal), C (Central), P (Parietal), O (Occipital)

4.3 Analysis of Theta Band

Theta power in the parietal region was greater in the M+F condition than that of the M condition, as in Fig. 4. No statistical significances, however, were observed. Also there were no hemispheric mean differences between the two reading conditions.

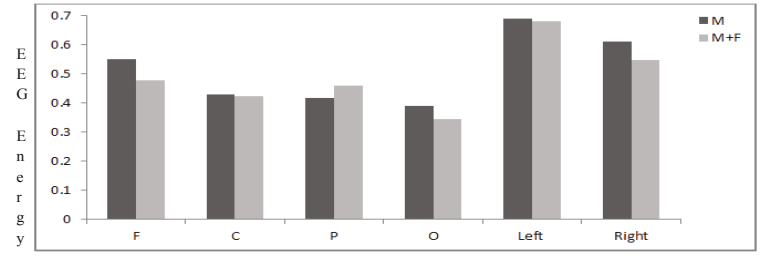

Fig. 4. Mean differences of reading instructions in theta:

*F (Frontal), C (Central), P (Parietal), O (Occipital)

4.4 Analysis of Gamma Band

Surprisingly, no significant mean differences were found between the two reading instructions, as shown in Fig. 5. However, when the participants were reading the text to comprehend the content only, the right hemispheric power of selective regions was greater than that of the left. Particularly, in the M condition, the hemispheric differences were significant at frontal and central regions: $t = 3.796$, $P = .001$; $t = 2.281$, $P = .032$, respectively. Conversely, reading a text with focusing on both form and meaning resulted in significant differences in frontal and parietal areas: $t = 4.808$, $P < .001$; $t = 2.529$, $P = .019$, respectively.

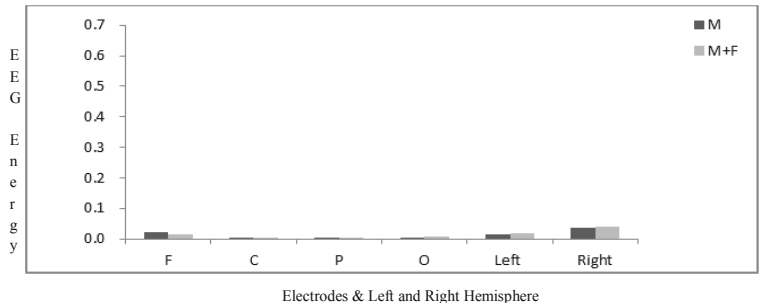

Fig. 5. Mean differences of reading instructions in gamma

*F (Frontal), C (Central), P (Parietal), O (Occipital)

5 Discussion and Conclusion

The present study differentiated cognitive load or mental effort by manipulating reading instructions. First of all, the findings show that the increased task load, reading the text with paying attention to both form and meaning, led to selective decreases in amplitude of upper alpha power at the frontal and occipital regions. The findings partially support Gevins et al's study findings [7, 8] in that reading a text by focusing on both form and meaning simultaneously escalated the level of attentional demands as well as cognitive load. In line with Bastiaansen et al's study [15], upper beta tends to behave like upper alpha. Specifically, upper beta power at frontal, central, and occipital regions attenuated in the M+F condition. As Bastiaansen et al. suggest, the beta response might be related to the sensory processing of the visual input.

In contrast to previous studies [13, 15], theta band power changes between two reading conditions displayed no significant differences in frontal area, although a decrease of theta amplitude in the M+F condition was greater than that of the M condition. Both the right and left hemispheres showed differences between the two reading conditions, which suggests that both hemispheres are related to comprehending meaning and learning grammar through reading.

Unlike Landau et al's study [16] that reported an increased gamma activity in states of attention, no significant mean differences in gamma band were found

between the two reading conditions. The unexpected findings suggest that knowing the content of the text through the first reading might alleviate task load which could be induced by comprehending and focusing on grammatical elements concurrently.

Despite the contribution to the EEG literature in language processing, the present study has some limitations. First, this study analysis was based on rather small number of participants, so larger scale future studies are necessary for generalization. Second, this study collected mental effort data during reading a text only; therefore, future study needs to include mental effort or mental efficiency during both reading and testing in order to obtain broader understanding regarding the role of cognitive load in grammar learning as well as reading comprehension.

To conclude, the study revealed that cognitive load seemed to be varied according to the degree of memory or cognitive load manipulated by reading instructions. Specifically, EEG features in upper alpha and upper beta bands were sensitive to load manipulation. No significant correlation, however, between reading instructions and brain activities in theta and gamma bands. The results suggest that deliberate attention to both meaning and form might hinder meaning construction [12]. Nonetheless, cognitive load will have positive effects as long as the load is imposed by relevant activities such as practice which enhances or leads to the construction or automation of schemas [6]. Therefore, language educators should keep in mind not to present excessive load when designing instructional materials: instead, they should guide their students to develop both the construction and automation of schemas and thus learning to occur.

Acknowledgement. This work was supported by the R&D program of the Korea Ministry of Knowledge and Economy (MKE) and the Korea Evaluation Institute of Industrial Technology (KEIT) [10041826, Development of emotional features sensing, diagnostics and distribution s/w platform for measurement of multiple intelligence from young children]

References

1. Sweller, J.: Cognitive load during problem solving: Effects on learning. Cognitive Science 12(2), 257–285 (1988)
2. Al-Shehri, S., Gitsaki, C.: Online reading: A preliminary study of the impact of integrated and split-attention formats on L2 students' cognitive load. ReCALL 22(3), 356–375 (2010)
3. Akbulut, Y.: Effects of multimedia annotations on incidental vocabulary learning and reading comprehension of advanced learners of English as a foreign language. Instructional Science 35(6), 499–517 (2007)
4. Paas, F., Renkl, A., Sweller, J.: Cognitive load theory and instructional design: Recent developments. Educational Psychologist 38, 1–4 (2003)
5. Paas, F., Tuovinen, J.E., Tabbers, H., Van Gerven, P.W.M.: Cognitive load measurement as a means to advance cognitive load theory. Educational Psychologist 38, 63–71 (2003)
6. Paas, F., Renkl, A., Sweller, J.: Cognitive load theory: Instructional implications of the interaction between information structures and cognitive architecture. Instructional Science 32, 1–8 (2004)

7. Gevins, A., Smith, M.E., McEvoy, L., Yu, D.: High-resolution EEG mapping of cortical activation related to working memory: Effects of task difficulty, type of processing, and practice. Cerebral Cortex., 374–385 (1997)
8. Gevins, A., Smith, M.E., Leong, H., McEvoy, L., Whitfield, S.: Monitoring working memory load during computer-based tasks with EEG pattern recognition methods. Human Factors 40(1), 79–91 (1998)
9. Röhm, D., Kilmesch, W., Haider, H., Doppelmayr, M.: The role of theta and alpha oscillations for language comprehension in the human electroencephalogram. Neuroscience Letters 310, 137–140 (2001)
10. Sweller, J.: Instructional Design in Technical Areas. ACER Press, Melbourne (1999)
11. Klimesch, W., Schimke, H., Ladurner, G., Pfurtscheller, G.: Alpha frequency and memory performance. Journal of Psychophysiology 4, 381–390 (1990)
12. Park, H., Choi, S., Lee, M.: Visual input enhancement, attention, grammar, & reading comprehension: An eye movement study. English Teaching 67(4), 241–265 (2012)
13. Klimesch, W.: EEG alpha and theta oscillations reflect cognitive and memory performance: a review and analysis. Brain Research Reviews 29, 169–195 (1999)
14. Müller, M., Gruber, T., Keil, A.: Modulation of induced gamma band activity in the human EEG by attention and visual information processing. International Journal of Psychophysiology 38, 283–299 (2000)
15. Bastiaansen, M.C.M., van der Linden, M., ter Keurs, M., Dijkstra, T., Hagoort, P.: Theta responses are involved in lexical–semantic retrieval during language processing. Journal of Cognitive Neuroscience 17(3), 530–541 (2005)
16. Landau, A., Esterman, M., Robertson, L., Bentin, S., Prinzmetal, W.: Different effects of voluntary and involuntary attention on EEG activity in the gamma band. The Journal of Neuroscience 27(44), 11986–11990 (2007)

Robust Meter Placement against False Data Injection Attacks on Power System State Estimation

Isamu Watanabe[1], Kazuyuki Masutomi[2], and Isao Ono[2]

[1] System Engineering System Laboratory,
Central Research Institute of Electric Power Industry
isamu@criepi.denken.or.jp
[2] Department of Computational Intelligence and Systems Science,
Interdisciplinary Graduate School of Science and Engineering,
Tokyo Institute of Technology
masutomi@ic.dis.titech.ac.jp, isao@dis.titech.ac.jp

Abstract. This paper presents a new algebraic approach for robust meter placement against false data injection (FDI) attacks on power system state estimation with DC power flow models. One of the most promising strategies against FDI attacks on DC state estimation is to protect measurements. It is important to select a subset of measurements to be protected so that, even if any k measurements are compromised by attackers or are lost due to malfunction, we can detect FDI attacks with the rest of them. Protecting a set of essential measurements to ensure observability of the system is reportedly a necessary and sufficient condition for detecting the FDI attacks on DC state estimation. Castillo et al. have proposed an algebraic approach to determine the minimum required measurement set to ensure observability even if any k meters fail. However, their problem formulation is nonlinear and they showed the results only with $k \leq 2$. In this paper, we propose a new linear formulation and show the results with not only $k = 2$ but also $k = 3$.

Keywords: Meter Placement, Power System, State Estimation, Observability.

1 Introduction

The power system is a complex system consisting of power generators and power consumers connected by transmission and distribution lines. System monitoring plays an important role to ensure the reliable operation of the power system. The measurements may include line power flows, bus injections and voltage magnitudes. These measurements are usually stored in a telemetry system known as Supervisory Control And Data Acquisition (SCADA) system.

State estimation is used in system monitoring to estimate the state of the power system based on the measurements. Many power system applications such as contingency analysis rely on the output of the state estimator. Various techniques have been developed to detect and identify bad measurements and it seems that these techniques can also defeat malicious measurements injected by attackers. However, Liu et al. demonstrated that an attacker, armed with the knowledge of the network configurations, can

M. Lee et al. (Eds.): ICONIP 2013, Part I, LNCS 8226, pp. 569–576, 2013.
© Springer-Verlag Berlin Heidelberg 2013

inject false data into DC state estimation, which uses DC power flow models, without being detected [1].

One of the most promising strategies against false data injection (FDI) attacks is to protect measurements. However, it may not be feasible to protect all measurements due to some reasons such as budgetary constraints. We believe that it is important to select a subset of measurements to be protected so that, even if any k meters are compromised by attackers or are lost due to malfunction, we can detect FDI attacks with the rest of measurements.

Bobba et al. have showed that protecting a set of essential measurements is a necessary and sufficient condition for detecting the FDI attacks on DC state estimation [2]. A set of essential measurements is composed of the minimum number of measurements needed to ensure observability of the power system. On the other hand, Castillo et al. have proposed an algebraic approach to determine the minimum measurement set required to ensure observability in state estimation even if any k meters fail [3]. However, their problem formulation is nonlinear and they showed the results only with $k \leq 2$.

In this paper, we propose a new linear formulation for robust meter placement against FDI attacks on DC state estimation. We also show the results with not only $k = 2$ but also $k = 3$ to demonstrate the effectiveness of the proposed formulation.

2 Problem Definition

In this section, we briefly define the robust meter placement problem handled in this paper. As commonly done in observability analysis, conventional measurements that include line power flows, bus injections and voltage magnitudes are assumed to exist. Furthermore, the analysis is carried out on the decoupled real power versus voltage phase angle model:

$$\boldsymbol{z} = \boldsymbol{H}\boldsymbol{\theta} + \boldsymbol{e} \tag{1}$$

where $\boldsymbol{\theta} = (\theta_1, \theta_2, \ldots, \theta_n)^T$ is the true state of the system to be estimated and $\boldsymbol{z} = (z_1, z_2, \ldots, z_m)^T$ and $\boldsymbol{e} = (e_1, e_2, \ldots, e_m)^T$ represent the measurements and the random errors in measurement, respectively. $\boldsymbol{H}$ is the $m \times n$ Jacobian matrix.

A state estimation problem can not be solved unless the system is fully observable. One indicator of observability is the rank of the Jacobian $\boldsymbol{H}$. Since the rank of $\boldsymbol{H}$ essentially depends on the meter placement, it is sufficient to evaluate $\boldsymbol{H}$ in order to study the effects of loss of measurements (and branch outages) on its rank [4]. In the context of the robust meter placement, the rank of $\boldsymbol{H}$ should remain full if any k of measurements are lost. If this condition is not met, then several pseudo-measurements should be added to meet the condition. The selection of these additional measurements must be optimal so that the overall cost of adding these measurements (e.g., the number of additional measurements) should be a minimum. Therefore, the robust meter placement problem, known as the general $m - k$ robust observability problem [3], can be defined as the problem of selecting a minimum number of measurements such that if any k of them are lost, the system remains observable.

For an observable system, available measurements can be classified into two groups, *essential* and *redundant*. The set of essential measurements includes n_{e} available measurements that allow expressing the remaining (redundant) n_{r} measurements as a function of the n_{e} essential measurements. In other words, the essential measurements are

enough to make the system observable and the loss of redundant measurements does not influence the observability of the system. Thus, only the loss of essential measurements is considered in the robust meter placement problem.

3 Conventional Formulation and Its Problems

For the robust meter placement problem defined above, Castillo et al. proposed a technique to determine the minimum required measurement set to ensure observability even if any k meters fail [3]. The technique relies on solving a nonlinear integer programming problem. In this section, we review their mathematical formulation.

Suppose a partition of the Jacobian matrix $\boldsymbol{H}$ such as

$$\boldsymbol{H} = \begin{bmatrix} \boldsymbol{H}_{\mathrm{e}} \\ \boldsymbol{H}_{\mathrm{r}} \end{bmatrix}, \tag{2}$$

where the $n_{\mathrm{e}} \times n_{\mathrm{e}}$ submatrix $\boldsymbol{H}_{\mathrm{e}}$ corresponds to essential measurements and the $n_{\mathrm{r}} \times n_{\mathrm{e}}$ submatrix $\boldsymbol{H}_{\mathrm{r}}$ corresponds to redundant measurements. Here, $n_{\mathrm{e}} = n$ and $n_{\mathrm{r}} = m - n$. Sensitivity matrix $\boldsymbol{S}$ is obtained as

$$\boldsymbol{S} = \boldsymbol{H}_{\mathrm{r}} \boldsymbol{H}_{\mathrm{e}}^{-1}. \tag{3}$$

If k essential measurements are lost simultaneously, they can be replaced by any k redundant measurements such that the $k \times k$ submatrix of matrix $\boldsymbol{S}$ corresponding to the considered columns and rows is non-singular. Thus, the general $m-k$ observability problem is formulated as

$$\underset{x_\ell}{\text{minimize}} \quad \sum_{\ell=1}^{n_{\mathrm{r}}} c_\ell x_\ell, \tag{4}$$

$$\text{subject to} \quad \sum_{\{i(1),\ldots,i(k)\} \in I_k} B_{i(1),\ldots,i(k);j(1),\ldots,j(k)} \times \prod_{s=1}^{k} x_{i(s)} \geq 1, \quad \forall \{j(1),\ldots,j(k)\} \in J_k, \tag{5}$$

where c_ℓ is the installation and operation cost of meter ℓ and x_ℓ is a binary variable to identify redundant measurements that preserve robust observability, I_k (J_k) is the set of all subsets of k different rows (columns) of maxtrix $\boldsymbol{S}$, and

$$B_{i(1),\ldots,i(k);j(1),\ldots,j(k)} = \begin{cases} 1 & |S_{i(1),\ldots,i(k);j(1),\ldots,j(k)}| \neq 0, \\ 0 & \text{otherwise}, \end{cases} \tag{6}$$

where $|S_{i(1),\ldots,i(k);j(1),\ldots,j(k)}|$ is the determinant of the submatrix of $\boldsymbol{S}$ including rows $i(1),\ldots,i(k)$ and columns $j(1),\ldots,j(k)$.

For a set of redundant measurements to replace a given set of essential measurements, the corresponding submatrix in $\boldsymbol{S}$ must be non-singular. This condition must be valid for any combination of k redundant measurements. Therefore, the constraint (5) ensures observability even in any k measurements are lost.

The resulting optimization problem (4) and (5) is a nonlinear programming (NLP) problem, which should be solved with an efficient large-scale solver for NLP problems such as CONOPT [5]. However, even if such a solver is used, it is difficult to solve the NLP problem containing high order polynomials in general. In fact, any numerical results for the case of $k \geq 3$ are not presented in [3].

4 Proposed Formulation

In order to overcome the weakness of the conventional (nonlinear) formulation mentioned in the previous section, we propose a new linear formulation for the general $m - k$ observability problem is presented as follows:

$$\underset{x_\ell}{\text{minimize}} \quad \sum_{\ell=1}^{n_\mathrm{r}} c_\ell x_\ell, \tag{7}$$

$$\text{subject to} \quad \sum_{\{i(1),\ldots,i(k)\}\in I_k} B_{i(1),\ldots,i(k);j(1),\ldots,j(k)} \cdot y_{i(1)\cdots i(k)} \geq 1, \quad \forall\{j(1),\ldots,j(k)\} \in J_k, \tag{8}$$

$$x_{i(1)},\ldots,x_{i(k)} \geq y_{i(1)\cdots i(k)} \quad \forall\{i(1),\ldots,i(k)\} \in I_k, \tag{9}$$

where $y_{i(1),\ldots,i(k)}$ is an auxiliary (binary or continous) variable representing $\prod_{s=1}^{k} x_{i(s)}$. By introducing the auxiliary variables, the nonlinear constraints (5) are converted to the linear ones (8) and (9). Note that the number of the auxiliary variables and the constraints that are newly introduced are $|I_k| = \binom{n_\mathrm{r}}{k}$ and $k \cdot |I_k|$, respectively.

For example, for the case of $n_\mathrm{e} = 4$, $n_\mathrm{r} = 3$ and $k = 2$, the matrix representation of the constraints (8) and (9) is illustrated below:

$$\begin{bmatrix}
B_{12;12} & B_{13;12} & B_{23;12} & 0 & 0 & 0 \\
B_{12;13} & B_{13;13} & B_{23;13} & 0 & 0 & 0 \\
B_{12;14} & B_{13;14} & B_{23;14} & 0 & 0 & 0 \\
B_{12;23} & B_{13;23} & B_{23;23} & 0 & 0 & 0 \\
B_{12;24} & B_{13;24} & B_{23;24} & 0 & 0 & 0 \\
B_{12;34} & B_{13;34} & B_{23;34} & 0 & 0 & 0 \\
-1 & 0 & 0 & 1 & 0 & 0 \\
-1 & 0 & 0 & 0 & 1 & 0 \\
0 & -1 & 0 & 1 & 0 & 0 \\
0 & -1 & 0 & 0 & 0 & 1 \\
0 & 0 & -1 & 0 & 1 & 0 \\
0 & 0 & -1 & 0 & 0 & 1
\end{bmatrix}
\begin{bmatrix} y_{12} \\ y_{13} \\ y_{23} \\ x_1 \\ x_2 \\ x_3 \end{bmatrix}
\geq
\begin{bmatrix} 1 \\ 1 \\ 1 \\ 1 \\ 1 \\ 1 \\ 0 \\ 0 \\ 0 \\ 0 \\ 0 \\ 0 \end{bmatrix}. \tag{10}$$

Alternatively, the number of constraints newly introduced can be reduced to $|I_k|$ by a different linear formulation

$$x_{i(1)} + \cdots + x_{i(k)} \geq k \cdot y_{i(1)\cdots i(k)}. \tag{11}$$

Note that the auxiliary variables $y_{i(1)\cdots i(k)}$ must be binary. Although we use the constraint (9) in the following experiments, we should compare the performance with (9) and that with (11) in future work.

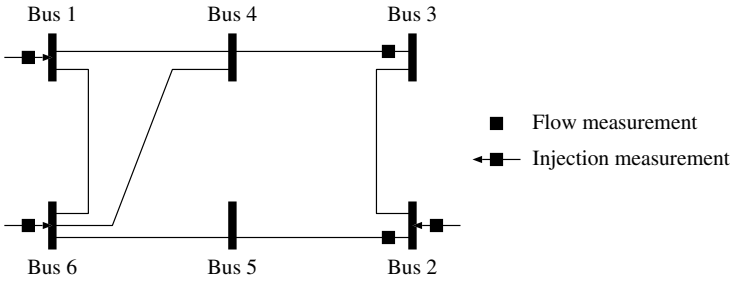

Fig. 1. A simple 6-bus example

5 Numerical Experiments

In order to verify the performance of the proposed formulation, the results of numerical experiments are presented here. All the following experiments were performed on a 3.6 GHz Intel Core i7-3820 processor and 16 GB of memory. Matrix $\boldsymbol{B}$ described above was computed using MATLAB 8.0.0 [6] and all optimization problems were solved with Gurobi Optimizer 5.5 [7].

5.1 A Simple Six-Bus Example

Firstly, the simple 6-bus example used in [3] is considered. Figure 1 depicts the considered power system and the measurement configuration. The essential measurements are active power injections P_1, P_2 and P_6 and active power flows $P_{2,5}$ and $P_{3,4}$.

For the measurement configuration in Fig.1, the sensitivity matrix $\boldsymbol{S}$ giving redundant measurements is obtained using the same Jacobian matrix $\boldsymbol{H}$ provided in [3]. Matrix $\boldsymbol{S}$ and the cost vector $\boldsymbol{c}$ are as follows:

$$\boldsymbol{S} = \begin{array}{c} \\ P_3 \\ P_4 \\ P_5 \\ P_{1,4} \\ P_{1,6} \\ P_{2,3} \\ P_{4,6} \\ P_{5,6} \end{array} \begin{array}{c} \begin{array}{ccccc} P_2 & P_{2,5} & P_1 & P_{3,4} & P_6 \end{array} \\ \begin{bmatrix} -1 & 1 & 0 & 1 & 0 \\ -0.6 & 1.2 & -0.8 & -1.6 & -0.6 \\ 0.6 & -2.2 & -0.2 & 0.6 & -0.4 \\ 0.2 & -0.4 & 0.6 & 0.2 & 0.2 \\ -0.2 & 0.4 & 0.4 & -0.2 & -0.2 \\ 1 & -1 & 0 & 0 & 0 \\ -0.4 & 0.8 & -0.2 & -0.4 & -0.4 \\ 0.6 & -1.2 & -0.2 & 0.6 & -0.4 \end{bmatrix} \end{array}, \quad \boldsymbol{c} = \begin{bmatrix} 1 \\ 0.2 \\ 0.4 \\ 0.4 \\ 0.5 \\ 1 \\ 1 \\ 1 \end{bmatrix}.$$

To select a subset of additional measurements that ensures observability, we solve the optimization problem (7)–(9). For the cases of $k = 1, 2$, the same solutions shown in [3] are obtained. The sets of additional measurements necessary to preserve observability are $\{P_4\}$ for the case of $k = 1$ and $\{P_4, P_5\}$ for the case of $k = 2$, respectively.

For the case of $k = 3$, we firstly calculate the coefficients $B_{i(1)i(2)i(3);j(1)j(2)j(3)}$ according to the expression (6). The number of these coefficients is ${}_5C_3 \times {}_8C_3 = 560$, as

Table 1. Computation time (s) for the case of $k = 2$

	9-bus	14-bus	39-bus	57-bus	118-bus	300-bus
μ	0.005	0.039	0.179	3.692	26.634	402.094
σ	0.002	0.027	0.115	6.949	15.982	595.789
min.	0.003	0.011	0.071	0.670	6.387	80.348
max.	0.023	0.163	0.783	63.359	90.087	4405.732

Table 2. Number of additional measurements for the case of $k = 2$

	9-bus	14-bus	39-bus	57-bus	118-bus	300-bus
μ	3.92	4.65	15.41	16.71	36.21	117.85
min.	3	3	12	13	31	109
max.	5	6	18	21	43	128

many as the number of 3×3 submatrics in matrix $\boldsymbol{S}$. The number of nonzero elements in matrix $\boldsymbol{B}$ is 203, thus the sparsity degree of $\boldsymbol{B}$ is 36.25%. The obtained solution is the set of three power injections $\{P_3, P_4, P_5\}$ and the objective value is 1.6. Although there are some combinations of redundant measurements with lower cost, they cannot ensure observability of the system. For instance, the set of redudant measurements $\{P_4, P_5, P_{1,4}\}$ is the combination with the lowest cost, but the set of measurements $\{P_1, P_2, P_4, P_5, P_6, P_{1,4}, P_{2,5}, P_{3,4}\}$ does not ensure the observability if three essential measurements $\{P_2, P_6, P_{2,5}\}$ are simultaneously lost. In fact, the determinant of the submatrix corresponding to these measurements is

$$|S_{P_4P_5P_{1,4};P_2P_6P_{2,5}}| = \begin{vmatrix} -0.6 & 1.2 & -0.6 \\ 0.6 & -2.2 & -0.4 \\ 0.2 & -0.4 & 0.2 \end{vmatrix} = 0. \tag{12}$$

5.2 Case Study

For the case of $k = 2$, the IEEE 9-bus, 14-bus, 39-bus, 57-bus, 118-bus and 300-bus test systems are considered. The network topologies are from MATPOWER [8]. To evaluate the average performance of the proposed formulation, for each test system, 100 different sets of essential measurements are used. Here, the objective is to minimize the number of additional measurements.

The computational results are summarized in Table 1 and 2. In the tables, μ and σ denote the average value and the standard deviation, respectively. Table 1 shows the computation time required to generate matrix $\boldsymbol{B}$ and to solve the linear problem. As shown in Table 1, for the 300-bus test system, with the proposed formulation, the average time to select the subset of additional measurements from 412 candidate measurements is only 402 seconds. In contrast, with the nonlinear formulation in [3], the total computation time is about 15.3 minutes, regardless of limiting the number of candidate measurements to 90. Table 2 shows the number of additional measurements necessary to preserve the observability of the system. As shown in Table 2, in spite of losing only two measurements, the number of additional measurements rapidly increases as the scale of the system becomes large.

Table 3. Computation time (s) for the case of $k = 3$

	9-bus	14-bus	39-bus	57-bus*
μ	0.037	1.206	68.932	6030.638
σ	0.020	0.683	74.618	3470.933
min.	0.012	0.218	14.064	3131.097
max.	0.147	3.646	621.668	14097.328

$*$ only eight different sets of essential measurements used.

Table 4. Number of additional measurements for the case of $k = 3$

	9-bus	14-bus	39-bus	57-bus*
μ	5.17	6.36	20.90	24.63
min.	4	5	18	23
max.	6	8	24	27

$*$ only eight different sets of essential measurements used.

For the case of $k = 3$, the IEEE 9-bus, 14-bus, 39-bus and 57-bus test systems are considered. In the same way as the case of $k = 2$, 100 different sets of essential measurements are used for three test systems (9-bus, 14-bus and 39-bus). For the 57-bus test system, eight different sets of essential measurements are employed.

Table 3 shows the computation time for the case of $k = 3$. It is obvious that the case of $k = 3$ requires significantly more computation time than the case of $k = 2$. As the average time required to generate matrix $\boldsymbol{B}$ is abount 233 seconds for the 57-bus system, the large percentage of total computation time is spent in solving the integer linear programming problem (7)–(9). Table 4 shows the number of additional measurements for the case of $k = 3$.

5.3 Discussion

The above computational results indicate that the size of the problem (7)–(9) increases rapidly as the value of k became large. In fact, for the 57-bus system, the number of constraints of the case of $k = 3$ is about 2.83×10^5. One approach to solve this problem is a compact representation of matrix $\boldsymbol{B}$. Since matrix $\boldsymbol{B}$ contains many unnecessary or redundant constraints, it is possible to make $\boldsymbol{B}$ compact by removing them.

The influence of rounding errors is also a critical problem. In particular, the rounding error when generating matrix $\boldsymbol{B}$ is very serious. Giving the wrong binary values to matrix $\boldsymbol{B}$ leads to the results in which feasible solutions cannot be found or incorrect sets of additional measurements are chosen. Since it is difficult to choose an appropriate tolerance, it is necessary to consider a robust approach to rounding error.

6 Conclusions

In this paper, we proposed a linear formulation for the general $m - k$ observability problem. By using the proposed linear fomulation, we are able to achieve robust meter

placement against false data injection attacks on power system. In particular, for the case of $k = 2$, our method found the minimal subsets of additional measurements more efficiently than the conventional one [3]. Moreover, for the case of $k = 3$ which was not presented in [3], we succeeded in determing appropriate subsets of additional measurements.

In future work, we should investigate the performance with the constraint (11) and devise a compact representation of matrix $\boldsymbol{B}$.

References

1. Liu, Y., Ning, P., Reiter, M.K.: False data injection attacks against state estimation in electric power grids. In: Proc. 16th ACM Conf. on Computer and Communications Security, pp. 21–32 (November 2009)
2. Bobba, R.B., Rogers, K.M., Wang, Q., Khurana, H., Nahrstedt, K., Overbye, T.J.: Detecting false data injection attacks on dc state estimation. In: Proc. First Workshop on Secure Control Systems (April 2010)
3. Castillo, E., Conejo, A.J., Pruneda, R.E., Solares, C., Menéderz, J.M.: $m - k$ robust observability in state estimation. IEEE Trans. on Power Systems 23(2), 296–305 (2008)
4. Magnago, F.H., Abur, A.: A unified approach to robust meter placement against loss of measurements and branch outages. IEEE Trans. on Power Systems 15(3), 945–949 (2000)
5. CONOPT, `http://www.conopt.com/`
6. MATLAB, `http://www.mathworks.com/`
7. Gurobi Optimizer, `http://www.gurobi.com/`
8. Zimmerman, R.D., Murillo-Sánchez, C.E., Thomas, R.J.: Matpower: Steady-state operations, planning, and analysis tools for power systems research and education. IEEE Trans. on Power Systems 26(1), 12–19 (2011)

Emotion Recognition Model Using Source-Temporal Features and Fuzzy

Wafaa khazaal Shams[1], Abdul Wahab[1], Uvais Qadwi[2], and Imad Fakhri Al-shaikhli[1]

[1] Computer Science Department, International Islamic University, Malaysia
wafaa_dth@ yahoo.com, abdulwahab@iium.edu.my, imadf@iium.edu.my
[2] Computer Science and Engineering Department, Qatar University, Qatar
uqidwai@qu.edu.qa

Abstract. This paper aims to evaluate the performance of Electroencephalographic (EEG) emotion recognition system (EEG-ER) using source-temporal domain with Takagi- Sugeno-Kang (TSK) fuzzy model. Ten healthy subjects aged 5-6 years were participated in this study. Emotion elicitation procedure has done using the Radbound faces database (RafD). The selected emotions were happy, sad, and neutral and fear. The results were compared with wavelet coefficients (WC) as feature extraction method and Regularized Least Square (RLS) and Multi-Layer Perception (MLP) neural network classifiers from our previous work. Another comparison was done between affective model of Russell and RafD. The results show the efficiency of using source-temporal features in emotion recognition system hence there was a slight difference in accuracy among different classifier; MLP, RLS and TSK however MLP and TSK results were with high accurate and stable. Moreover Russell model which is based on positive-negative dimensions shows high accuracy than RafD model that has positive dimensions. The accuracy was around 97% using Russell model.

Keywords: Emotion, EEG, Relative source temporal features, Takagi-Sugeno-Kang fuzzy approach.

1 Introduction

Emotion is one of the mysterious that has no specific psychology and physiology definition. However, it is involved in human cognition, perception and experience. Consequently it is affected on human learning process and human physical and mental health. Emotion can be expressed using verbal function like words “happy, sad …etc” or non-verbal function based on facial expression and behavior. However it is difficult to people with disability to express their feeling to others. Therefore identify others emotion is important task. Many studies have been done using bio-signals to recognize emotion state such as speech, skin temperatures, heart rate [1-3]. Recent studies concern on using EEG signal in emotion recognition system (ER) [4-8] hence EEG measures the signal from the central nervous system (CNS) making it a suitable tool for studying human emotions.

M. Lee et al. (Eds.): ICONIP 2013, Part I, LNCS 8226, pp. 577–584, 2013.
© Springer-Verlag Berlin Heidelberg 2013

Our previous study [9] shows the efficiency of using spatial source domain to present the dynamic brain activity which is consistent with the distribution theory where emotion is produced through interactions among brain regions rather than simply a function of a specific brain location [10]. The proposed model is based on applying Time Difference of Arrival (TDOA) approach [11] with EEG signals to extract the relative spatial source domain in terms of (*x, y, z*) coordinates which named Relative Source Temporal (RST) features. The previous work shows significant results using MLP [12] and RLS [13] classifiers. Fuzzy system [14] has been used widely in many applications such as control system and pattern recognition problems. In this study we apply TSK fuzzy model which is knowing of its generalization and simplicity to model complex system as well as its generated rules from given input-output data set based on subtractive clustering [15, 16]. Emotion has been modeled based on many theories. The majority of them which is based on psychology perspective consider emotion as discrete values or basic emotions while other theories are characterized emotion as continues domain which can be presented by many dimensions. One of the most widely model is 2 dimension affective model of Russell [17] that categorizes every kind of emotions in a two-dimensional model; valence (V) that reflect the cognitive perception and arousal (A) that reflect the physiological component. Russell model divided the valence and arousal to positive and negative. In this study we use Russell model and we use also RafD model [18] which is also 2dimension affective model but with positive values hence the values of valence and arousal were taken based on self –assessment test with score from (1-5). The first goal of this study is to investigate the performance of RST features with TSK fuzzy classifier and compared it with our previous results. The second goal is to examine the affection of Russell and RafD model to predicate the values of valence and arousal for each emotion.

2 Method and Materials

2.1 EEG Data Descriptions

EEG data was collected from ten healthy subjects aged (5-6) from the preschool (Malaysia International Islamic preschool) using BMCI model device. Data was recording from eight channels; F3, F4, C3, C4, P3, P4, T7, T8 placed according to international 10-20 system with Cz as references. Emotion of participant has evoked using eight pictures of children faces for each emotion states with different valence and arousal that selected from RafD [18]. Each subject asked to sit and watch sequence of these pictures on screen away 75 cm. The time for each session was 1 min. sampling rate was 250 and recorder frequency from 0.5-50 Hz. The collected data are filter using IIR filter to alpha band (7-13) Hz for RST model and filtered to the range (0.5-30) Hz for wavelet model.

2.2 Feature Extraction Methods

Relative Source –Temporal Features (RST): This technique is based on using TDOA approach with EEG signals to extract the spatial sources and temporal information. Theoretical of this technique was explained in our previous studies [9]. Brief illustration will show here.

- Initial four site electrode location and their *x, y* and *z* coordinates is taken from [19].
- Compute the time delay among the channels using Cross-Correlation (CC) [20]. One second movement window are used with 125 sample movement. Thus the time delays are computed for each one second sample within 50 sec. However the time delay among EEG signals are expected to be in less than mille-second and because of our sampling rate was 250 Hz, time delay in some epoch cannot be capture within 1 second interval. To solve this, we use regression model (polynomial function with order 3) to fit our CC data.
- Apply TDOA principle as explained in [9], three linear equations are produced which can be solved using Gaussian elimination methods to get *x,y* and *z* variables [21]. The linear equation for three receivers have (x_1 , y_1, z_1) , (x_2 , y_2, z_2) and (x_3 , y_3, z_3) coordinates with speed *v* and time delay t_{12} and t_{13} is given by :

$$R = Ax + By + Cz \tag{1}$$

Hence

$$R = vt_{13} - vt_{12} + \left(\frac{x_1^2 + y_1^2 + z_1^2}{t_{13}} - \frac{x_3^2 + y_3^2 + z_3^2}{t_{13}}\right) - \left(\frac{x_1^2 + y_1^2 + z_1^2}{t_{12}} - \frac{x_2^2 + y_2^2 + z_2^2}{t_{12}}\right) \tag{2}$$

$$A = 2\left[\frac{(x_2 - x_1)}{vt_{12}} - \frac{(x_3 - x_1)}{vt_{13}}\right] \tag{3}$$

$$B = 2\left[\frac{(y_2 - y_1)}{vt_{12}} - \frac{(y_3 - y_1)}{vt_{13}}\right] \tag{4}$$

$$C = 2\left[\frac{(z_2 - z_1)}{vt_{12}} - \frac{(z_3 - z_1)}{vt_{13}}\right] \tag{5}$$

- Choose another 4 different electrodes site locations and repeat the previous procedures.

This procedure is repeated 20 times with different electrodes sites each. At the end, 20 features with time samples are computed for three variables *x, y* and *z* that called in this work the virtual sources for the alpha wave activities.

Wavelet Coefficients based features (WC): For comparison reason, emotion recognition based wavelet transform are applied [7] .Wavelet transform decompose the signal to its component with different scale giving multi resolution analysis for EEG signal. Discreet wavelet transform with the Daubechies fourth order was applied to decompose the EEG signal to four frequencies band and the extracted coefficient (C) corresponding to alpha band (7-13) was used to compute energy (EN)and the entropy (ET) .

$$EN(j) = \sum_{i=n-1}^{N} C_j(i)^2 \tag{6}$$

$$ET(j) = -\sum_{i=n-1}^{N} C_j(i) \log C_j(i) \tag{7}$$

2.3 Fuzzy Logic Model

Takagi, Sugeno and Kang [15, 16] , introduced fuzzy model which is known (TSK)fuzzy system. TSK fuzzy model based on using simple rules generates from the input –output data. These rules consequences with a simple linear regression model to predicate the output. In TSK approach , subtractive cluster methods [16] are used to cluster the input data by finding the center of each cluster which is represent the point with highest number of neighborhood , consequently , the second cluster will be the second point of highest neighborhood. After using the subtractive cluster to identify number of cluster and its location the rules for TSK fuzzy are extracted from training data. For example, the rules of j cluster can express as:

IF x_1 is in A^j_1 and x_2 is in A^j_2 and x_3 is in A^j_3 …… x_n is in A^j_n

Then: $$y^j = p^j_0 + p^j_1 x_1 + p^j_2 x_2 + p^j_3 x_3 + \cdots + p^j_n x_n \tag{8}$$

where x is the input variables from 1 to n, y is the output variable, A^j_n is the membership function for the cluster j and p^j_n is the regression parameters for *jth* rules. For this study the input variables are the extracted features that explained in the previous section which contain 60 features and the output is labeled to two values indicate valence and arousal for each emotion states that will explain in next section. TSK fuzzy-subtractive approach was applied to the input-output variables to cluster the data and model the memberships which is that associated with each variable and clusters. There are all of these statistical techniques and we have tested some of these for the comparison and others are being implemented as part of the PhD work... however, the purpose here is to present a soft-computing based techniques more academically speaking, the data is quite noisy as well as extremely unpredictable in other words, Fuzzy. Therefore the fuzzy classification was utilized

2.4 Classification Set up

The classification process was done to separate among four emotion or classes. In this study two affective models were used to extract the label of each class. Fig.1 show the label of each class based on Russell model while Fig.2 shows the labels extracted from RafD model, hence the label present the mean value of valence and arousal for the selected images of each emotion.

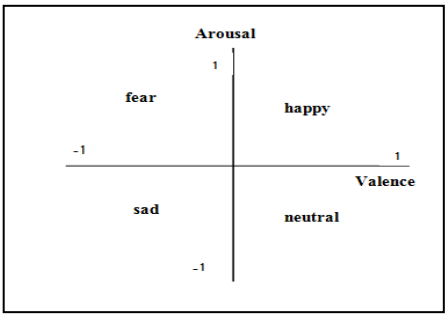

Fig. 1. 2DE affective model of Russell

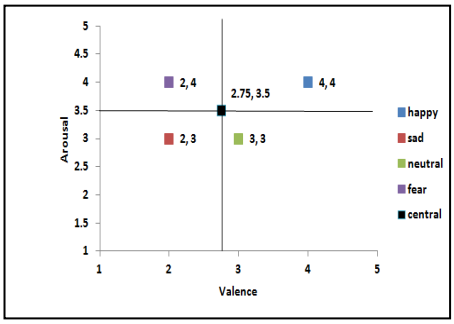

Fig. 2. D affective model of RafD

3 Results and Discussion

In this study we consider user-independent case. Features are extracted from each subject and normalized using z-score then feed to classifier. The labeled for each emotion states are identified based on Russell model. For simplicity we used 56 epochs from each emotion state per subject. We use 10 fold cross –validation with 70% of data as training and 30% of data as test. Table 1 shows the results of the classification using TSK compared with wavelet coefficients. Clearly RST –EC has high accuracy than WC-ER. Emotion recognition using TSK fuzzy model was compared with our previous work using MLP and RLS classifiers for both RST features and WC as shown in Fig.3 and Fig.4. The three classifiers combined with RST features have high accuracy to detect different emotion states compare with WC features which indicates the efficiency of spatial source domain to recognize high cognitive task like emotion. Adding data-driven classifier such as MLP and TSK are more efficiency with RST features than RLS classifier which is depends on modeling the features using Gaussian kernel. However RLS and TSK show high accuracy than MLP for WC-ER system. So far all the results were discussed before is based on predication two dimensions; valence and arousal for each emotion states using Russell model. Another scenario has been done to predicate the same dimension by using RafD model that was shown in Fig.3 hence each class or emotion states is labeled by the center of each state. Table 2 shows the classification rate for each emotion using RST features combined with different classifiers. There is slight different between the models. RafD model shows good accuracy even though all emotions labeled are

positive and their values near from each others. However, RafD model show low ability to discriminate different emotion using WC as illustrated in Table 3.

Table 1. Classification rate values in parentage of each emotion of the proposed RST features compare with wavelet coefficient features using TSK Fuzzy as RST-EC up and WC-EC down

	Happy	**sad**	**neutral**	**fear**
	98.67	0	1.33	0
happy	**60.34**	7.32	23.25	9.09
	0	**97.75**	2.25	0
Sad	27.24	**60.65**	5.77	6.34
	1.5	1.67	**96.83**	0
neutral	10.4	15.25	**64.01**	10.34
	0	2.16	0.6	**97.24**
Fear	15.62	5.33	18.3	**60.75**

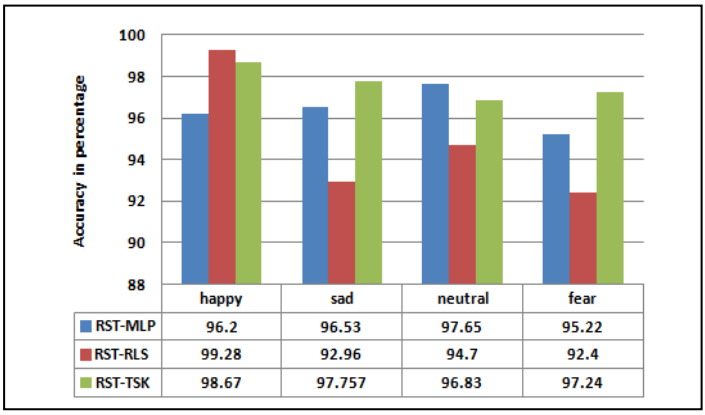

Fig. 3. Classification rate of each emotion using RST with different classifier

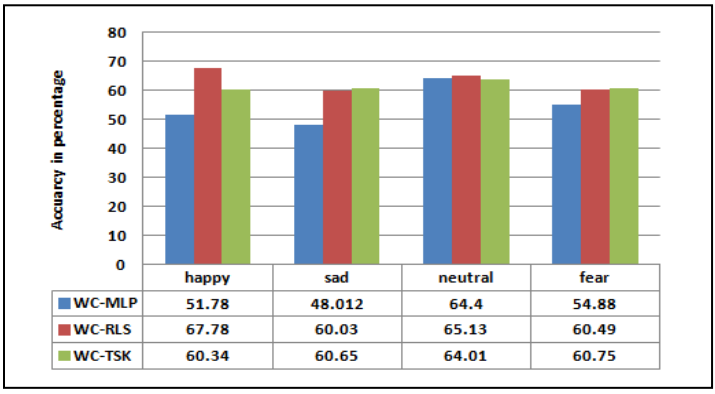

Fig. 4. Classification rate of each emotion using WC with different classifier

Table 2. Classification rate of each emotion uisng RafD and Russell model with RST

	RafD model					**Russell model**				
classifier	happy	sad	neutral	fear	A.C	happy	sad	neutral	fear	A.C
RST-TSK	97.24	98.1	94.4	94.9	96.21	98.67	97.7	96.8	97.2	97.6
RST-RLS	90.30	100	92.9	93.2	94.12	99.28	92.9	94.7	92.4	94.3
RST-MLP	97.09	98.31	96.2	97.3	97.24	96.53	96.5	97.6	95.2	96.4

Table 3. Classification rate of each emotion uisng RafD and Russell model with WC

	RafD model					Russell model				
classifier	Happy	sad	neutral	Fear	A.C	happy	sad	neutral	fear	A.C
WC-TSK	57.18	58.10	50.6	60.09	56.50	60.34	60.65	64.0	60.7	61.4
WC-RLS	28.59	73.39	57.7	26.66	46.6	67.78	60.03	65.1	60.4	63.3
WC-MLP	52.90	51.83	39.2	50.91	48.7	51.78	48.01	64.4	54.8	54.7

4 Conclusion and Future Work

This study evaluates the performance of RST features with TSK fuzzy inference system to detect brain activity under different emotion states using EEG signals. The results were so promising and show the robust and the efficiency of RST features to discriminate different classes. Also, it is noticed that RST give good results using data-driven classifier. Moreover, this study show that 2 D affective model of Russell to present the valence and arousal in positive and negative dimension help to distinguishes among emotion states more than RafD model. Future work will consider on user-dependent case and more kind of emotions states.

References

1. Cohen, I., Garg, A., Huang, T.S.: Emotion recognition from facial expressions using multilevel HMM. In: Neural Information Processing Systems. Citeseer (2000)
2. Yeasin, M., Bullot, B., Sharma, R.: Recognition of facial expressions and measurement of levels of interest from video. IEEE Transactions on Multimedia 8, 500–508 (2006)
3. El Ayadi, M., Kamel, M.S., Karray, F.: Survey on speech emotion recognition: Features, classification schemes, and databases. Pattern Recognition 44, 572–587 (2011)
4. Picard, R.W., Vyzas, E., Healey, J.: Toward machine emotional intelligence: Analysis of affective physiological state. IEEE Transactions on Pattern Analysis and Machine Intelligence 23, 1175–1191 (2001)

5. Picard, R.W.: Affective computing: challenges. International Journal of Human-Computer Studies 59, 55–64 (2003)
6. Balconi, M., Lucchiari, C.: EEG correlates (event-related desynchronization) of emotional face elaboration: a temporal analysis. Neuroscience Letters 392, 118 (2006)
7. Murugappan, M., Rizon, M., Nagarajan, R., Yaacob, S., Zunaidi, I., Hazry, D.: EEG feature extraction for classifying emotions using FCM and FKM. International Journal of Computers and Communications 1, 21–25 (2007)
8. Guntekin, B., Basar, E.: Emotional face expressions are differentiated with brain oscillations. International Journal of Psychophysiology 64, 91–100 (2007)
9. Wafaa, K.S., Wahab, A., Imad, F.: Affective compuring model using source-temporal domain. Accepted in 9th International Conference in Cognitive Science, Sarwak, Malaysia (2013)
10. Rabinovich, M.I., Friston, K.J., Varona, P.: Principles of brain dynamics: global state interactions. MIT Press (2012)
11. Schmidt, R.O.: A new approach to geometry of range difference location. IEEE Transactions on Aerospace and Electronic Systems, 821–835 (1972)
12. Rumelhart, D., Hinton, G., Williams, R.: Learning Internal Representations by Error Propagation. In: Parallel Distributed Processing, Explorations in the Microstructure of Cognition. MIT Press, Cambridge (1986)
13. Tacchetti, A., Mallapragada, P.S., Santoro, M., Rosasco, L.: GURLS: A Toolbox for Regularized Least Squares Learning. Computer Science and Artifical Intelligence Laboratory. Technical Report CBCL-306. MIT (2012)
14. Zadeh, L.A.: Outline of a newapproach to the analysis of complex systems and decision processes. IEEE Transaction on Systems, Man, and Cybernetics 3, 28–44 (1973)
15. Tagaki, T., Sugeno, M.: Fuzzy identification of systems and its application to modeling and control. IEEE Transactions on Systems, Men and Cybernetics 15, 116–132 (1985)
16. Chiu, S.: Fuzzy model identification based on cluster estimation. J. Intell. (1993)
17. Russell, J.: A circumplex model of affect. Journal of Personality and Social Psychology 39, 1161–1178 (1980)
18. Langner, O., Dotsch, R., Bijlstra, G., Wigboldus, D.H.J., Hawk, S.T., Knippenberg, A.V.: Presentation and validation of the Radboud Faces Database. Cognition and Emotion 24, 1377–1388 (2010)
19. Kayser, J., Tenke, C.: Principal components analysis of Laplacian waveforms as a generic method for identifying ERP generator patterns: I. Evaluation with auditory oddball tasks. Clinical Neurophysiology 117, 348–368 (2006)
20. Knapp, C., Carter, G.: The generalized correlation method for estimation of time delay. IEEE Transactions on Acoustics. Speech and Signal Processing 24, 320–327 (1976)
21. Atkinson, K.E.: An introduction to numerical analysis. John Wiley & Sons (1989)

An Intelligent Agent Based Land Encroachment Detection Approach

Simon Dacey, Lei Song, and Shaoning Pang

Department of Computing, Unitec Institute of Technology, Private Bag 92035, Auckland, New Zealand

Abstract. Land management and planning is essential to assist the economic growth, sustainable resource use and environmental protection of a city. This paper describes a novel approach to automatic encroachment detection to assist in land management decision making. The approach begins with training the agent to identify and understand the land cover/use features (such as buildings, parks, trees and roads) that are predominant in the region of interest, and carries out segmentation on the park data using the intelligent agent developed from the training samples. Experiments on park images from Auckland New Zealand show the effectiveness of the proposed approach.

1 Introduction

Land encroachment is defined as the change in the perceived or actual use of land from either (a) human caused encroachment: the use of public land for private purposes, or (b) environmental caused encroachment: the change in the ability of land for its original purpose from an environmental change. The use of public land for private purposes has been considered as an encroachment problem in the Auckland region in New Zealand [1]. This paper examines the use of digital image analysis in automatically detecting encroachment on public parks in two specific areas in Auckland.

When dealing with encroachment it is necessary to differentiate between land cover change and land use change. For example if an area of grassland belonging to a public park has been fenced off by the resident of a property that is adjacent to the park, the land cover of the majority of the grassland has not changed but its land use has changed from public to private. Detection of this type of change requires the use of high resolution data as features such as fences are hard to detect and/or difficult to distinguish from features, such as paths, that are not indicative of encroachment.

In practice, there are 4 general types of encroachment studied:

1. Permanent land cover/use change. For example a building has been built either wholly on the park or partially on it.
2. Permanent land use change only. For example Public Park area has been fenced off so is no longer accessible to public but land cover has not changed (i.e. land cover is still grass).

M. Lee et al. (Eds.): ICONIP 2013, Part I, LNCS 8226, pp. 585–592, 2013.
© Springer-Verlag Berlin Heidelberg 2013

3. Temporary land cover/use change. For example the park (or part of the park) has been used as a garbage dumping site in a way such that it can no longer be used by the public as a park.
4. Physical boundary concealed by land cover. For example a boundary fence has been moved, or removed completely, in an area that is obscured by dense vegetation.

A new approach is in demand because the existing methods are unsuitable for our specific needs, and the applications examined are not reproducible in the New Zealand context. The strengths of the proposed method is that it can detect the types of land encroachment identified above. Additionally, it is suited to the type of land cover (urban and rural mixed) found in Auckland, as we design, build and test a solution for our specific purpose. Trees need to be differentiated because they can blur the boundary of a park and can obscure encroachment.

2 Methodology

As seen in the literature, agent-based image analysis has been used in a variety of applications such as range-image segmentation [2], and off-road vehicle guidance, [3]. The advantage offered by such a solution includes: (1) image processing parallelization; and (2) the flexibility to concentrate on either spatial or temporal changes. A review of agent-based image segmentation can be found in [4].

The flowchart in Fig. 1 shows an outline of the proposed agent-based image solution to land-encroachment detection. The aim of the approach is to detect any changes between a pair of multi-temporal images, which we identify as source image I_0 and target image I_1 in this paper. The principle of the approach is that the more that an agent learns about I_0, the more accurate any change detection (against I_0) will be.

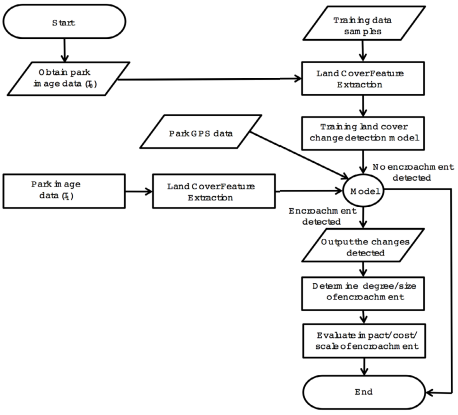

Fig. 1. Flowchart of proposed approach

To learn as much prior knowledge as possible, about I_0, in terms of the type of land cover, additional image data is collected for training the agent with the knowledge of 5 land cover patterns such as Grass, Buildings, Trees, Fences and Roads, which represent the land cover/use characteristics that are most likely to be found in or around public parks.

The agent with the prior knowledge of basic land cover is expected to learn the source image I_0 incrementally (i.e. incremental learning). When performing land encroachment detection, the target image I_1 is processed by the agent to detect the change against I_0. If encroachment has been detected then the size of the encroachment can be calculated. Then the risk factor of the encroachment is examined using the size of the encroachment and the rateable value of the land that has been encroached upon.

2.1 Land Cover Feature Extraction

The land cover of a public park is usually grassland. However, in some cases, the types of land cover in a public park can include buildings, play grounds, paths and roads. The automatic detection of encroachment has to be able to take spatial co-ordinates into consideration.

For better understanding of the image characteristics, we apply first an image processing method - Gabor filter - to enhance images characteristics, such as texture and contour information. A general Gabor filter function is expressed as

$$G(x, y; \lambda, \theta, \psi, \sigma) = \exp\left(-\frac{x' + y'^2}{2\sigma^2}\right) \exp\left(x\left(2\pi\frac{x'}{\lambda} + \psi\right)\right), \tag{1}$$

where

$$\begin{bmatrix} x' \\ y' \end{bmatrix} = \begin{bmatrix} \cos(\theta) & \sin(\theta) \\ -\sin(\theta) & \cos(\theta) \end{bmatrix} \begin{bmatrix} x \\ y \end{bmatrix}, \tag{2}$$

and λ represents the sinusoid's wavelength, θ represents the orientation, ψ is the phase offset, and σ denotes the spread of the Gaussian window [5].

Given a set of orientations θ^t,where $t = 1, 2, ..., T$, and according to (1) and (2), using an image I as input, we obtain T different images $G^I_{\theta^t}$, which are the data representatives of these Gabor filtered images in T orientations. For example, let the 2-D image I with a size of $M \times N$ be processed by Gabor filter, and the magnitude of complex-valued subbands is denoted as

$$G^I_{\theta^t} = \left\{m^I_{\theta^t}(m, n) | 1 \leq m \leq M, 1 \leq n \leq N, \text{and } t = [1, 2, ..., T]\right\}, \tag{3}$$

where $G^I_{\theta^t}$ is a set of real-valued 2-D subbands signals, representing the magnitude of complex-valued wavelet coefficients obtained at the direction θ^t. The magnitudes of each directional subband's coefficients are computed and collectively denoted by $G^{I_0}_{\theta^t}$ and $G^{I_1}_{\theta^t}$ for the multiple temporal images I_0 and I_1.

2.2 Encroachment Detection by Land Cover Change Detection

In order to learn content composition of the collected data D_0 for I_0, we employ a clustering algorithm to discriminate different image contents from each other

and group similar contents together. To maximize the flexibility of our method, the general mathematic definition of clustering is shown below.

Given $D_0 = \{D_0(r)|1 \leq r \leq R\}$, $\boldsymbol{C} = \{\boldsymbol{c_k}|1 \leq k \leq K\}$ denote the set of K clusters' core vectors, and $\Re_k$ represents the number of vectors assigned to k-th cluster, initially, $k = 1$ and $\boldsymbol{c_k} = D_0(1)$. Normally, clustering is to assign data that are more "alike" into one cluster [6]. To determine the word "alike", a function for measuring similarity among data can be formulated as (2.2),

$$\text{Similarity}(\boldsymbol{a}, \boldsymbol{b}) = \begin{cases} 0 \text{ if two vectors } \boldsymbol{a} \text{ and } \boldsymbol{b} \text{ are similar} \\ 1 \text{ otherwise} \end{cases} \tag{4}$$

According to (2.2), we compare the similarity between D_0 and C, for each $D_0(r)$ and $\boldsymbol{c_k}$, where $r = 1, 2, \ldots, R$ and $k = 1, 2, \ldots, K$.

if $Similarity(D_0(r), \boldsymbol{c_k})$=0, assign $D_0(r)$ to kth cluster, and let $c_k = \frac{\Re_k \boldsymbol{c_k} + D_0(r)}{R_k + 1}$, otherwise $Similarity(D_0(r), \boldsymbol{c_k}) = 1$, then assign $D_0(r)$ to $(k+1)$th cluster, and let $\boldsymbol{c_{k+1}} = D_0(r)$. Hereafter, let $r = 1$ we can repeat this process until the last input vector $D_0(R)$ has been assigned into one cluster. At the end of clustering, the cluster labels $Y_0 = \{1, 2, ..., K\}$ and $\acute{D_0} = [D_0, Y_0]$ can be obtained. In this paper, we apply K-means clustering to this stage as the first choice.

For the purpose of storing I_0 as small size knowledge instead of keeping the same size of I_0, weighted incremental linear proximal support vector machine (wIncLPSVM) is employed. It is suitable for our study because of its following properties: 1) it is an incremental learning algorithm capable of learning a huge size input image piece by piece; 2) in contrast to the traditional incremental LPSVM, the samples from positive and negative are processed separately in wIncLPSVM which makes it easy to observe the effect of one step incremental learning.

The core model used in this work is a matrix component in wIncLPSVM model namely $\boldsymbol{M}$ which condenses the knowledge of positive class. In practice, we train a $\boldsymbol{M_0}^{O_k}$ for each object obtained from the objects decomposition on image I_0 ($\acute{D_0}$). For the kth object in I_0, the model is calculated as

$$\boldsymbol{M}_0^{O_k} = \left[\boldsymbol{D}_0^{O_k} - \boldsymbol{e}\right]^T \left[\boldsymbol{D}_0^{O_k} - \boldsymbol{e}\right], \tag{5}$$

where $\boldsymbol{e} = [1, \ldots, 1]^T$. After the training phase, we conduct one step incremental learning to update $\boldsymbol{M}_0^{O_k}$

$$\boldsymbol{M}'^{O_k}_0(r) = \boldsymbol{M}_0^{O_k} + \left[\boldsymbol{D_0^{O_k}}(r) - \boldsymbol{e}\right]^T \left[\boldsymbol{D_0^{O_k}}(r) - \boldsymbol{e}\right], \tag{6}$$

using the each sample from data D_0 and use the eigenvalue of updated $\boldsymbol{M}'^{O_k}_0$ to measure the influence of incoming sample. By going through all samples in each object on corresponding model, a range of influences can be obtained for each object. A range $Range_0^{O_k}$ is a closed interval defined by the maximal and minimal eigenvalues as

$$Range_0^{O_k} = \left[\min(\text{eig}(\boldsymbol{M}'^{O_k}_0)), \max(\text{eig}(\boldsymbol{M}'^{O_k}_0))\right]. \tag{7}$$

The incremental learning is conducted on learning the model $\boldsymbol{M}_0^{O_k}$, so the image I_0 can be learned piece by piece. For example, $\acute{D_0}$ is separated into N

pieces with 5 objects. There are five $\boldsymbol{M}_0^{O_k}$ models, and each of them can be stored in a 20×20 matrix. In contrast, $\acute{D}_0$ is a 154814×20 matrix, the stored model $\left\{\boldsymbol{M}_0^{O_k} | k \in [1,5]\right\}$ includes five 20×20 matrices. Thus the size of stored knowledge is 154 times smaller than original image dataset $\acute{D}_0$.

2.3 Change Detection on the Target Image I_1

One-step-more incremental learning detect changes against I_0 by measuring the effect of incremental learning on new incoming data I_1. Usually, based on the model of batch learning, incremental learning is conducted continuously step by step from the appearance of the first sample to the completion of that all samples being learned. However, in our method, while a new sample appears, the incremental learning is merely conducted once (i.e., **one step**) on the basic model obtained from I_0. Hereafter, when the next sample comes, the incremental learning agent starts over from the original I_0 base model and repeat the incremental learning detection step. In other words, while conducting image change detection the incremental learning agent collects no new knowledge in memory.

In the proposed approach, as a result of knowledge discovery on I_0, I_0 now is represented as an incremental learning model $\boldsymbol{M_0}$.

$$\boldsymbol{M_0} = \{< \boldsymbol{M}_0^{O_k}, Range_0^{O_k} >\}, k = 1, \ldots, K \tag{8}$$

The basic detection model $\boldsymbol{M}_0^{O_k}$ is formulated by (5). The range $Range_0^{O_k}$ is given by one-step learning (6) and (7). Lets assume that each data sample from D_1 (the collected data from I_1) has the same object label as its corresponding sample from D_0. The one-step more incremental learning on I_1 can be conducted on each object of I_0 by (9) as,

$$\boldsymbol{M}'^{O_k}_1(r) = \boldsymbol{M}_0^{O_k} + \left[\boldsymbol{D_1^{O_k}}(r) - \boldsymbol{e}\right]^T \left[\boldsymbol{D_1^{O_k}}(r) - \boldsymbol{e}\right]. \tag{9}$$

The effect of new sample $\boldsymbol{D_1^{O_k}}(r)$ to $\boldsymbol{M}_0^{O_k}$ can be calculated via (10).

$$effects(r) = \text{eig}(\boldsymbol{M}'^{O_k}_1(r)). \tag{10}$$

Then, the change status of the r-th sample is determined by effects(r) following the rule as,

$$Change(r) = \begin{cases} 0, effects(r) \in Range_0^{O_k} \\ 1, effects(r) \notin Range_0^{O_k}. \end{cases} \tag{11}$$

Consequently, a binary image (or mask) B_{O_k}=$\{b_{o_k}(m,n) | 1 \le m \le M, 1 \le n \le N\}$ are formed for each object defined in I_0.

3 Experiments and Discussions

The data used in the experiments is digital image data of New Zealand specifically the Auckland area. The data sets used for the detection of encroachment are digital images of areas that include public parks.

1. Aerial Photographs. The aerial photographs are captured on-line. The scale is set manually to 7.5cm/234m at time of capture and the ratio is one pixel to 0.5 meters. The images are in JPEG format and are collected from Google Earth.
2. Land Boundary Data. The boundary data is used to verify that encroachment has been detected and to estimate the size of encroachment. The regional councils Manukau and North Shore supplied boundary data in GIS shape file format.

To demonstrate the automatic encroachment detection technique, for this paper, four parks: Wyllie Park, Teviot Reserve, Auburn Reserve, and Diana Reserve are selected as representative examples of the four categories of encroachment discussed above.

The experiments were carried in three phases. The first phase involves teaching the agent prior knowledge about the land cover patterns such as grass, buildings, trees, fences and roads, as they are most commonly found in and around public parks in Auckland. Note that, for this purpose, we collect data only from non-park areas for the training of the agent. After the first phase learning, the agent now has the prior knowledge (i.e., the number of clusters k and initial mean vector of each cluster). In the second phase, we set the equipped agent to perform spatial incremental learning on I_0 in order to obtain knowledge from the source image.The third phase is change detection on I_1. We set the I_0 learned agent to repeat the incremental learning process on I_1 to detect change of I_1 against I_0.

Four specific experiments are carried out:

1. To detect permanent encroachment such as buildings.
2. To detect encroachment in the form of areas of a park fenced off.
3. To detect temporary encroachment such as vegetable-growing.
4. To detect possible areas of encroachment that may obscured by natural objects such as trees.

Type 1: Permanent land cover encroachment is where a building is constructed illegally on a public park. In land management terms this is the most serious form of encroachment. Although it is relatively simple to detect the presence of a building on a park, one difficulty in detecting permanent encroachment is the misclassification of legitimate constructions. Fig. 2(a) shows Wyllie Park with the council boundary, Wyllie Park with a house encroaching near the top-left corner and the results of the image segmentation algorithm: white pixels indicate encroachment. In the next section we detail the performance of our method of classification.

Type 2: We provide a permanent land use encroachment example where a fence is built illegally on a park, see Fig.2. Fig. 2(b) shows Teviot Reserve with the council boundary, the ground truth image with an introduced fence element and the results of the image segmentation approach, white pixels classify encroachment.

Type 3: Temporary Use Encroachment, for example vegetable-growing, is not as serious as permanent encroachment as it is normally easier to resolve by the authorities. This type of encroachment can be difficult to detect especially when

(a) Wyllie park

(b) Teviot reserve

(c) Auburn reserve

(d) Diana reserve

Fig. 2. Experiment results

the colour of the vegetation is similar to the naturally occurring colours in the park. Fig. 2(c) shows Auburn Reserve with the council boundary shown on an overlay, the ground truth image with an introduced vegetation element and the results of the image segmentation approach, white pixels indicate the vegetation encroachment detection.

Type 4: Physical boundary encroachment is a difficult problem to solve, especially when the boundary encroachment is concealed under a canopy of vegetation. However, not all vegetation canopies will hide illegal encroachment. Fig. 2(d) shows the Diana Reserve park area, the ground truth image with an introduced plant elements and the results of the image segmentation approach, white pixels show the areas of newly introduced plant life. The elements detected on park boundaries could indicate a possible encroachment.

Table 1. Details of the encroachment detected on the chosen parks

Park Name	Encroachment Type	Park Size (pixels)	Encroachment Size (pixels)	Encroachment Scale	Park Rateable Value(NZD)	Encroachment Commercial Value(NZD)
Wyllie	Building	230, 214	7, 442	0.03	485, 000.00	14, 550.00
Teviot	Area of park fenced off	2007, 890	158, 297	0.07	510, 000.00	35, 700.00
Auburn	Introduced vegetation	735, 456	20, 284	0.027	2150, 000.00	59, 288.00
Diana	Newly introduced plant life	1260, 279	154, 431	0.12	690, 000.00	84, 550.00

Table 1 above shows the experiment results in the terms of the size and scale of the encroachment for each of the parks. The rateable value of each park is obtained from the Auckland City Council [7]. The size of encroachment in pixels is divided by the total area of the park in pixels to give the scale of encroachment. The rateable value of the park is multiplied by the scale of encroachment to give the commercial value of the encroachment. The impact of the encroachment depends on the type of encroachment and the scale of encroachment.

4 Conclusions and Future Work

The results of the experiments show that the approach is successful in highlighting possible occurrences of encroachment. The the main disadvantage of the approach is that cannot work as a stand-alone solution - ground survey data collection needs to take place to confirm the occurrence of encroachment. The advantages of the approach are that permanent encroachment (such as buildings and fences) can be detected and temporary encroachment (such as vegetable-growing and garbage dumping) can also be detected. Another disadvantage of the approach is that it is not as reliable in detecting encroachment and/or changes in areas where there is a high concentration of tree as these area have a high variation in colors and concentration.

References

1. Dacey, S., Barbour, R.H., Fernando, A.: Participatory Land Use Management of Public Spaces in New Zealand. In: Proceedings of the JURSE Conference on Urban Remote Sensing and Planning, Munich, Germany, pp. 449–452 (2011)
2. Mazouzi, S., Guessoum, Z., Michel, F., Batouche, M.: An Agent-Based Approach for Range Image Segmentation. In: Jamali, N., Scerri, P., Sugawara, T. (eds.) MMAS 2006, LSMAS 2006, and CCMMS 2007. LNCS (LNAI), vol. 5043, pp. 146–161. Springer, Heidelberg (2008)
3. Broggi, A., Cattani, S.: An agent based evolutionary approach to path detection for off-road vehicle guidance. Pattern Recogn. Lett. 27(11), 1164–1173 (2006)
4. Mishra, P., Srivastava, N., Shukla, K.K., Singhal, A.: Agent based Image Segmentation Methods: A Review. Interational Journal Comp. Tech. Appl. 2(3), 704–708 (2011)
5. Daugman, J.G.: Uncertainty relation for resolution in space, spatial frequency, and orientation optimized by two-dimensional visual cortical filters. Journal of the Optical Society of America A Optics and Image Science 2(7), 1160–1169 (1985)
6. Huang, Z.: Extensions to the k-Means Algorithm for Clustering Large Data Sets with Categorical Values. Data Mining and Knowledge Discovery 2(3), 283–304 (1998)
7. Auckland City Council: Auckland GIS Viewer, `http://maps.aucklandcouncil.govt.nz/aucklandcouncilviewer/`

Generic Unpacking Method Based on Detecting Original Entry Point

Ryoichi Isawa[1], Masaki Kamizono[1,2], and Daisuke Inoue[1]

[1] National Institute of Information and Communications Technology, Tokyo, Japan
[2] SecureBrain Corporation, Tokyo, Japan
{isawa,masaki_kamizono,dai}@nict.go.jp

Abstract. In this paper, we focus on the problem of the unpacking of packed executables in a generic way. That is, we do not assume specific knowledge about the algorithms used to produce the packed executable to do the unpacking (i.e. we do not extract/create a reverse algorithm). In general, when launched, a packed executable will first reconstruct the code of the original program, write it down someplace in memory and then transfer the execution to that original code by assigning the Extended Instruction Pointer (EIP) to the so-called Original Entry Point (OEP) of the program. Accordingly, if we had a way to accurately identify that transfer event in the execution flow and thus the OEP, we could more easily extract the original code for analysis (cf. by inspecting the remaining code after the OEP was reached). We then propose an effective generic unpacking method based on the combination of two novel OEP detection techniques, one relying on the incremental measurement of the entropy of the information stored in the memory space assigned to the unpacking process, and the other on the incremental searching and counting of potential Windows API calls in that same memory space.

Keywords: Packer, Kernel mode, NX bit, Malware analysis.

1 Introduction

Malware authors often make use of packers to protect their malware programs from code analysis. They can easily *pack* (compress and/or encrypt) the original code of a malware program with the packers (e.g., UPX, ASPack, and PECompact), therefore we have to extract the hidden original code from the packed malware before code analysis. Because many types of packer exist and their packing algorithms vary widely, manual unpacking operations which require us to detect the packer type used and to infer the packing algorithm can induce huge additional analyzing costs.

Many anti-malware analysts rely on automated generic unpacking techniques to skip the manual unpacking operations. The existing methods [1–6] can be classified into three groups according to their purposes: to obtain the original code of a packed malware program [1], to detect the OEP in addition to obtaining the original code [2–4], and to detect malware with an anti-virus software

M. Lee et al. (Eds.): ICONIP 2013, Part I, LNCS 8226, pp. 593–600, 2013.
© Springer-Verlag Berlin Heidelberg 2013

program even though the malware program is packed [5, 6], where OEP means the address which indicates the beginning point on the original code loaded into the memory. In this paper, our purpose is the second one, which is to detect the OEP in addition to obtaining the original code.

Finding the OEP of a packed program should provide us with several benefits in terms of code analysis. If we disassemble the original (binary) code starting from a wrong address, we are to get a wrong assembly code because some architectures like x86 architecture apply an instruction set with a variable bit length for the representation of instructions. In contrast, starting from the OEP, we can transfer the original code correctly and obtain useful information from the program, (e.g., the names of stolen files and servers used by attackers). For instance, such information can be used in computer forensics to track malware authors or attackers.

We focus on the elementary behavior of packed executables to perform generic unpacking. A typical packer such as UPX and ASProtect compresses or encrypts a program code and adds its unpacker code to the packed one. When the packed program is run, it executes the unpacker code first, then the unpacker code decrypts and writes the original code into the memory. After the unpacker code completes the decryption, the extended instruction pointer (EIP) moves from the unpacker code to an address in the original code. Note that OEP is the address to which the EIP moves from the unpacker code. To summarize, the elementary behavior is that the original code will be decrypted and written first and then executed, whichever packer is used.

In this paper, we propose a novel generic unpacking method featuring two OEP detection approaches: one is based on an entropy analysis and the other is based on the number of API-call instructions present in the memory. The first approach focuses on the entropy score of the decrypted original code. Generally, the entropy score of non-random data is low, and the entropy score of a set of instructions will be also low because it consists of often-used instructions (e.g., `mov`, `push`, `call`, `cmp`, and `add`). When caching a page fault, if the entropy score is lower than a given threshold value, that approach decides that the address to which the EIP points is the OEP. At the end of the decryption, the number of instructions should become the highest in the decrypting process. The second approach focuses on API-call instructions such as '`call APIaddress`'. The intuition is that we cannot find API-call instructions contained in the packed original code, but we can find them after the decryption is completed. If the number of API-call instructions is higher than another given threshold value, that second approach decides that the address of the EIP is the OEP. Our method outputs an address as the OEP when both the first approach and the second one reach the same conclusion at which point it outputs a memory dump of all memory areas that the packed program loaded into the memory.

Our main contribution is to propose two OEP detection approaches which are greatly different from existing methods. In particular, our method focuses on the changing information of the original code, whereas almost all existing methods focuses on the unpacker code. Distinct OEP detection techniques are strongly needed because we can combine unpacking methods to implement a simple but

practical solution. That is, each method independently detects the OEP from OEP candidates and we finally determine the best candidate as the OEP which wins most votes. The experiment shows that our method can unpack 14 of 20 files packed with distinct packers.

The rest of the paper is organized as follows: Section 2 introduces related works. Section 3 presents our method. Section 4 shows an experimental evaluation of our method. Finally, Section 5 concludes the paper.

2 Related Works

2.1 Commonly Used Techniques

The original code of a packed file, independently of the packer that was used, will be decrypted and written, then the original code will be executed. Therefore the original code will be contained inside the instructions and data that are dynamically generated.

There exist two techniques that can detect dynamically generated instructions and data: one relies on disassembly and the other relies on page protection settings named W $\oplus$ X page protection [7], where the 'W' and the 'X' stand for write and execute, respectively. The former technique disassembles each instruction and catches write operations (e.g., '`mov %eax, [%edi]`' and '`push %eax`' [2]). The technique can learn the address of the current execution from the EIP. If a dynamically generated code such as the code written by '`mov`' or '`push`' are executed, the technique memorizes the address of the written code and the code itself as an OEP candidate and part of the original code, respectively. The latter technique modifies the page protection settings to be executable/read-only and read/write-only in sequence. The technique gives the settings of executable/read-only to the whole memory or a certain memory area just after loading a packed file on the memory. When the unpacker code writes instructions to one of the unwritable areas, the technique can catch a page fault and modifies the area to be read/write-only. Similarly, when the unpacker code executes instructions of the non-executable area, the technique can catch a page fault and recognize dynamically generated instructions.

As we mentioned above, we can recognize dynamically generated instructions, but many page faults occur in practice. For example, Guo et al. show that 11 exceptions occur when they execute a file packed with UPX under only W $\oplus$ X page protection [6].

2.2 Existing Methods

Renovo [2] monitors jump instructions such as '`jmp`' to detect the OEP of a packed file. If the EIP moves to a dynamically generated instruction through a jump instruction, Renovo decides that the address of the generated instruction is the OEP. Because Renovo monitors and disassembles each instruction, it incurs a significant overhead. Note that we must apply single stepping and disassembly if we have to recognize instructions such as jump instructions.

Kawakoya et al. [4] focus on a packed file's memory access behavior to detect the OEP, where memory access means operations of read, write, and execute. They define an equation that represents the memory access behavior and they input a type of memory access, which is read, write, or execute, to the equation in order to obtain a representing value of memory access. If values that the equation outputs are changing rapidly, Kawakoya et al.'s method decides that the changing point is the OEP.

OmniUnpack [5] applies W $\oplus$ X page protection. Every time a dynamically generated instruction is executed and the instruction is for executing dangerous system calls (e.g., registry/network/file-write operations and process creation), OmniUnpack invokes anti-virus software to scan newly generated code. Indeed, if OmniUnpack was to invoke an anti-virus software program for all exceptions, it would incur a significant overhead. OmniUnpack aims to detect a malware program with anti-virus software even if the malware program is packed, and it does not aim to detect the OEP. OllyBonE [8] is a tool that is used for implementing OmniUnpack. OllyBonE supplies W $\oplus$ X page protection.

Justin [6] applies W $\oplus$ X page protection and aims to detect packed malware programs with anti-virus software as well as OmniUnpack. One of the differences between Justin and OmniUnpack is that Justin finds out OEP candidates and an anti-virus software program scans the whole memory starting from each OEP candidate. Guo et al. propose three approaches to guess if the address on which a page fault occurs is the OEP. The first is to check if dynamically generated code area contains unpacker code when a page fault occurs. The second is that several stack pointers are the same as their initial state. The third is to check if a packed file accesses the command-line argument. Justin independently combines each approach with W $\oplus$ X page protection. If the address appears to be the OEP, an anti-virus software program scans the whole memory starting from the address. Justin can supply OEP candidates but does not specify the OEP.

3 Proposed Method

3.1 Workflow

Our system consists of a manager program and an unpacking driver. For generic unpacking, just after the manager runs a packed PE file, it stops the process. At which time, a signal is sent to the driver saying that the process just ran. Having received it, the unpacking driver memorizes the initial state of the memory that the process uses. After the driver turns on NX bit flags on the memory, the manager restarts the process. When the process executes an instruction whose NX bit flag is on, a page fault occurs. After catching it, the driver stops the process. If a memory page that process is accessing at the time is different from the initial state, the driver registers/saves the address on which the page fault occurs as an OEP candidate. The driver then checks if the candidate is correct with the entropy-based approach and the approach focusing the number of API-call instructions. If both approaches decide that the candidate is correct, the driver outputs the OEP and obtains a memory dump; otherwise, the manager

restarts the process. Our system repeats the unpacking work until the OEP is determined or at most 50 times.

3.2 OEP Detection Technique Based on Entropy Analysis

We apply Lyda et al.'s file type identification method [9] as an entropy-based OEP detection technique. Their method can recognize which file type, text, executable, encrypted, or packed file as follows. It divides a whole file into successive blocks of size q bytes and calculates an entropy score for each block using the following equation:

$$H(x) = -\sum_{i=1}^{n} p(i) \log_2 p(i) \tag{1}$$

where q is a given value and $q \in \{1, 2, \cdots\}$, x means one of the blocks, n denotes the number of unique one-byte values in x, and i and $p(i)$ denote the i-th smallest one-byte value in x and a frequency of the i-th smallest one-byte value in x, respectively. We express, for example, x as hexadecimal numbers "12 34 AB 34 56". In this case, $q = 5$, $n = 4$, the first smallest one-byte value – the fourth one are 12, 34, 56, and AB, and pairs of $(i, p(i))$ are $(1, 0.2)$, $(2, 0.4)$, $(3, 0.2)$, and $(4, 0.2)$, respectively. Lyda's method then calculates the average and the maximum of the entropy scores of all blocks. If both the average and the maximum are smaller than given threshold values, Lyda's method infers that the file is neither encrypted nor packed.

As Lyda's method is not suitable for generic unpacking, we examine entropy of packed programs and customize the method. That is, we consider encrypted data as packed data and do not use the maximum value of entropy. The reason why we do not use the maximum is that a packed file definitely contains packed data, and the maximum is always high due to the packed data, no matter how much progress the unpacker code makes. If the average entropy score of the file is smaller than given threshold m, our entropy-based approach decides that the OEP candidate is correct.

3.3 OEP Detection Technique Focusing on API-call Instructions

This approach searches for API-call instructions as follows. It takes as a list API addresses of DLLs exported in the memory and searches for the API addresses based on two ways. The first one simply searches for each API address, which, for example, corresponds to the right of '`call APIaddress`', on the memory areas whose NX bit flags are on. The other searches for each API address added by given values to counter stolen bytes techniques. Figure 1 shows an example of an anti-debugging technique called the stolen bytes technique. When we call ShellExecuteW API, we just directly jump to address '`0x73813C59`' like the left disassembly code. If one intends to thwart code analysis with a stolen bytes technique, it copies several instructions in an API to the main module and write a jump instruction that points to the address just below the last copied instruction like the right code. When a code is modified with the stolen bytes technique,

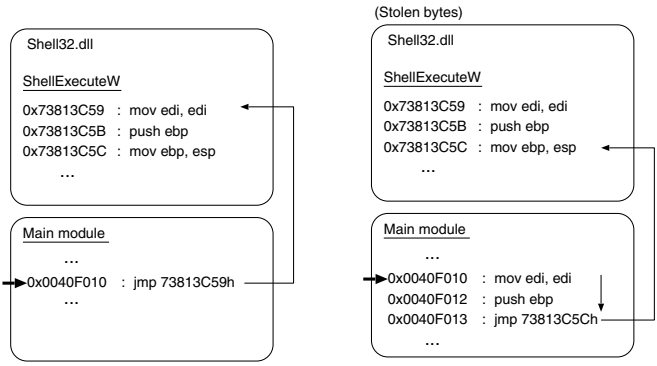

Fig. 1. An example: the left is usual and the right is used with a stolen byte technique

API addresses of the main module do not appear. For example, '`jmp 73813C59`' in the left, which is ShellExecuteW address, is modified as '`jmp 73813C5C`' in the right. To fill a gap between an original address and a modified address for search, our method searches for from an API address added by 1 through the API address added by y for each API on the memory areas, where y is a given value and $y \in \{1, 2, \cdots\}$.

When a page fault occurs, if our API-call-instruction based approach can find more than z API addresses using both the first way and the second one, the approach infers that an OEP candidate is correct, where z is a given threshold value and $z \in \{1, 2, \cdots\}$.

4 Experiments

4.1 Setup

We use 20 packers described in Table 1. As sometimes a packer cannot pack an executable file correctly, we pack three executables, calc.exe, comp.exe, and vim.exe, in turn with each packer. The calc.exe and comp.exe are obtained from the system folder of Windows XP and vim.exe is a variant of an editor tool vi for Windows XP. We take the first packed file that can run for each packer. We unpack the 20 packed files described in Table 1 with our method.

The environment for unpacking is as follows. We used a PC whose CPU and host OS are Intel Xenon 3.10 GHz and Ubuntu 12, respectively. We installed KVM to the host OS, and installed Windows XP Professional SP3 to KVM as a guest OS. We implemented our method on the guest OS.

We set block size q and threshold value m of average entropy, which are described in Section 3.2, to 256 and 5.5, respectively. We picked these values from our experiments. We set y for API address search and threshold value z of the number of API addresses, which are described in Section 3.3, to 15 and 5. The reason why we set z to 5, which is small, is that there exist executables which call just a few APIs.

Table 1. The unpacking results

No.	Packer name	exe	(1)	(2)	No.	Packer name	exe	(1)	(2)
1	ACProtect 1.32	calc	√	√	11	PE-Pack 1.0	vim	√	√
2	ASPack 2.12	calc	√	√	12	Upack 0.39	calc	√	√
3	Exe32Pack 1.4.2	comp	√	√	13	UPX 3.08	calc	√	√
4	ExePack 1.4	vim	√	√	14	WWPack32 1.20	vim	√	√
5	eXPressor 1.5.0.1	calc	√	√	15	ASProtect 2.1	calc	√	×
6	FSG 2.0	calc	√	√	16	Mew11 1.2	calc	√	×
7	Molebox pro 2.6.4	calc	√	√	17	Armadillo 4.20	calc	×	×
8	Npack 1.1.300	calc	√	√	18	Obsidium 1.4.5	calc	×	×
9	Nspack 3.7	calc	√	√	19	Morphine 1.7	vim	×	×
10	PECompact 2.79	calc	√	√	20	Themida 1.8.5.5	calc	×	×

(1) : To obtain all the original code
(2) : To detect the OEP

4.2 Unpacking Results

Table 1 shows the unpacking results for our method. '(1)' in the table shows whether or not our method is able to obtain a memory dump that contains all the original code, where '√' and '×' denote success and failure, respectively. If a result do not satisfy '(1)', our method failed to obtain any of the original code. '(2)' shows whether or not our method is able to detect the OEP. We consider results that satisfy both '(1)' and '(2)' as unpacking success.

Our method is able to unpack the packed files of cases no. 1 – 14 successfully. In cases no. 15 (ASProtect 2.1) and 16 (Mew11 1.2), our method cannot detect the OEPs of the two packed files. To find the reasons, we manually monitored each instruction of the packed file of case no. 15. When our method decides an OEP candidate is correct, the EIP has not indicated the OEP. After we skip several page faults, the EIP indicates the OEP. Threshold value m of average entropy and z of the number of API addresses are not suitable for case no. 15. The reason for case no. 16 is the same as that of case no. 15. The results of cases no. 17 – 20 do not satisfy both '(1)' and '(2)'. The failure reason for case no. 19 (Morphine 1.7) is a consequence of the implementation of our method. The packed file of case no. 19 dynamically allocates memory for writing its original code. Our implementation does not turn on NX bit flags of such dynamically allocated memory areas. When our method tries to unpack the packed files of cases no. 17 (Armadillo 4.20), no. 18 (Obsidium 1.4.5), and no. 20 (Themida 1.8.5.5), no page faults occur. We tried to uncover the reason for that, but could not find an acceptable explanation. Armadillo, Obsidium, and Themida apply strong anti-debugging techniques. We guess that they detect KVM and stop their process in the experiment to thwart analysis.

We can tell from 14 success results that our method is efficient for generic unpacking. The results of cases no. 15 and 16 are failures, but our method should be able to unpack the two if we tuned the parameter values of our method. To unpack files packed with Morphine, we will implement our method such that it

can turn on NX bit flags of dynamically allocated areas. For cases no. 17, 18, and 20, we will consider how to bypass anti-analysis techniques.

5 Conclusion

In this paper, we propose a generic unpacking method featuring two OEP detection approaches: one is an entropy-based approach and another focuses on the number of API-call instructions. Our key ideas are greatly different from those of the existing methods. For implementing a practical unpacking solution, we can independently use several methods to detect the OEP and we can decide the OEP from candidates as an election. Thus several types of OEP detection approaches are required. The experiment shows that our method can defeat 14 of 20 packers. In our future work, we plan to apply machine learning approaches instead of just using threshold values in order to overcome the issues we had with trials of cases no. 15 and 16 in the experimental phase.

References

1. Royal, P., Halpin, M., Dagon, D., Edmonds, R., Lee, W.: Polyunpack: Automating the hidden-code extraction of unpack-executing malware. In: 22nd Annual Computer Security Applications Conference, ACSAC 2006, pp. 289–300 (2006)
2. Kang, M.G., Poosankam, P., Yin, H.: Renovo: a hidden code extractor for packed executables. In: Proceedings of the 2007 ACM Workshop on Recurring Malcode, WORM 2007, pp. 46–53. ACM, New York (2007)
3. Kim, H.C., Orii, T., Yoshioka, K., Inoue, D., Song, J., Eto, M., Shikata, J., Matsumoto, T., Nakao, K.: An empirical evaluation of an unpacking method implemented with dynamic binary instrumentation. IEICE Transactions 94-D(9), 1778–1791 (2011)
4. Kawakoya, Y., Iwamura, M., Itoh, M.: Memory behavior-based automatic malware unpacking in stealth debugging environment. In: 2010 5th International Conference on Malicious and Unwanted Software (MALWARE), pp. 39–46 (2010)
5. Martignoni, L., Christodorescu, M., Jha, S.: Omniunpack: Fast, generic, and safe unpacking of malware. In: Twenty-Third Annual Computer Security Applications Conference, ACSAC 2007, pp. 431–441 (2007)
6. Guo, F., Ferrie, P., Chiueh, T.-C.: A study of the packer problem and its solutions. In: Lippmann, R., Kirda, E., Trachtenberg, A. (eds.) RAID 2008. LNCS, vol. 5230, pp. 98–115. Springer, Heidelberg (2008)
7. Egele, M., Scholte, T., Kirda, E., Kruegel, C.: A survey on automated dynamic malware-analysis techniques and tools. ACM Comput. Surv. 44(2), 6:1–6:42 (2008)
8. Stewart, J.: Ollybone v0.1, break-on-execute for ollydbg, html document (2006), `http://www.joestewart.org/ollybone/tutorial.html`
9. Lyda, R., Hamrock, J.: Using entropy analysis to find encrypted and packed malware. IEEE Security and Privacy 5(2), 40–45 (2007)

Referential kNN Regression for Financial Time Series Forecasting

Tao Ban, Ruibin Zhang, Shaoning Pang, Abdolhossein Sarrafzadeh, and Daisuke Inoue

National Institute of Information and Communications Technology
4-2-1 Nukui-Kitamachi, Tokyo, 184-8795, Japan
bantao@nict.go.jp
http://www.nict.go.jp

Abstract. In this paper we propose a new multivariate regression approach for financial time series forecasting based on knowledge shared from referential nearest neighbors. Our approach defines a two-tier architecture. In the top tier, the nearest neighbors that bear referential information for a target time series are identified by exploiting the financial correlation from the historical data. Next, the future status of the target financial time series is inferred from heritage of the time series by using a multivariate k-Nearest-Neighbour (kNN) regression model exploiting the aggregated knowledge from all relevant referential nearest neighbors. The performance of the proposed multivariate kNN approach is assessed by empirical evaluation on the 9-year S&P 500 stock data. The experimental results show that the proposed approach provides enhanced forecasting accuracy than the referred univariate kNN regression.

Keywords: Time series forecasting, correlation analysis, kNN regression, referential kNN regression, S&P 500 Indices.

1 Introduction

Time series forecasting now become a common problem in numerous areas of research (e.g., hydrology, finance, climatology and etc.), In particular financial time series prediction has been drawn substantial attention in both the computer science and financial communities recently and remains a very specialized task. Various studies have shown that financial time series is predictable by using both linear and non-linear models [1]. Actually, recent scholars have revealed that the nonparametric non-linear models tend to outperform linear models in financial time series forecasting [2]. In practice, k-Nearest-Neighbour(kNN) is one of the most commonly employed algorithm in time series forecasting due to its simplicity and intuitiveness in alike instances recovering from large dimensional feature spaces [3], and also the tolerance in high-dimensional and incomplete data [4]. The kNN algorithm assumes that sequences of time series have emerged in the past are likely to have a resemblance to the future sequences and for generating kNN based forecasts, similar patterns of behaviour are masked in

M. Lee et al. (Eds.): ICONIP 2013, Part I, LNCS 8226, pp. 601–608, 2013.
© Springer-Verlag Berlin Heidelberg 2013

terms of nearest-neighbours, and their development over time is exploited to yield the forecast [5].

Despite of the good general performance of kNN regression in financial time series forecasting, most of the existing researches in kNN regression derived financial time series forecasting are mainly focusing on individual historical data, without referencing any extra associated knowledge. The motivation of this research is, since the fluctuation of financial time series is changing dynamically due to the evolutions of many relevant economic and financial activities [6], the accuracy of the univariate forecasting model will not be optimal when insufficient knowledge has been consulted. The historical knowledges were extracted from stock own are obviously inadequate compare with the knowledges were collected from group of stocks that share similar behaviours. In this study, we attempt to develop a model to forecast the financial time series product, by conducting referencing involved multivariate kNN regression over large scaled historical time series data. The application of referential knowledges facilitate the enhancement of forecasting accuracy since the information used for forecasting will be less biased due to sparse referential consultation.

The beginning of this research is to use numerical distance measurement to extract the interrelationship between all the financial time series based on historical data, and provides a clear picture of the network which allows user to easily identify the neighbors of each time series. Once the cognates of references have been recognized, we will apply the kNN regression algorithm over such findings for each financial time series.

The outline of the paper is organized as follows: In Section 2, we briefly introduces the background of financial correlation analysis and kNN regression algorithm, plus the review of related works in the financial time series forecasting. Then, we present the proposed referential financial time series forecasting method in Section 3. Next, the experimental design regarding to proposed method, and discussion of comparison in results have been presented in Section 4. Finally, we have drawn the conclusion in Section 5.

2 Related Work

2.1 Correlation Analysis in Financial Time Series

In fundamental stock correlation analysis, the focus is on the investigation of stocks' fundamental attributes [7], regardless of any numerical financial calculation. In [8], Clarke stated that economic intuition supports the idea that firms in the same industry share high return correlations compared to firms in different industries.

Also, as suggested in [7], stocks can be categorised into homogeneous groups using criteria other than industry affiliation and in the literature, academic researchers and investment practitioners have figured a variety of approaches to construct homogeneous stock groups. Notable works include the heuristics approaches proposed by Farrell[9], Elton and Gruber[10], the clustering method proposed by Brown and Goetzmann [11].

In addition, stocks are commonly grouped on the basis of primary economic attributes such as market capitalization or operating performance.

2.2 k-Nearest-Neighbor Regression

Because of its simplicity and intuitiveness, k-nearest-neighbour (kNN) algorithm is widely adopted for classification and regression [12,13].

The application of kNN to time series forecasting under nonparametric locally weighted regression condition was presented independently by Yakowitz [14] and Cleveland [15] within the community of statistics. In financial time series forecasting field, kNN has also drawn pretty much of attention because of the work by Meade [16], Fernando et al. [3], and its performance have been validated through numerical studies.

The underlying intuition to apply kNN to univariate time series is that consistent data-generating processes often produces observations of repeated patterns of behavior. Therefore, if a previous pattern can be identified as similar to the current behavior of the time series, the subsequent behavior of previous pattern can provide valuable information to predict the behavior in the immediate future. In the kNN regression algorithm introduced by Meade [16], the target variable of a time series forecasting problem is presented as a sequence of interval scaled values. Given a pattern whose future value is to be predicted, the algorithm identifies the k most similar past patterns and combines their future values to make the prediction on future value.

3 The Proposed Model

As aforementioned, stock prices in the market fluctuates with the evolution of related economical and financial factors. Intuitively, stocks share the common characteristics more or less, as proved by related economical studies. Our correlation analysis among related stocks indicated that, stocks from the same industry are more close to each other in terms of correlation coefficients due to their consensus to the same external factors. Therefore, we propose to improve the accuracy of previous studies on kNN regression by incorporating associated knowledge from closely related stock indices.

The proposed method is implemented in two steps. In the first step, we try to identify a set of referential nearest neighbors (RNN) which are likely to provide relevant information for the prediction. In the second step, pattern searching and prediction is done by respecting all the historical information in RNN. The details of the two steps are addressed in the following two subsections.

3.1 Search for Referential Nearest Neighbors

Let $\mathbb{X} = \{\boldsymbol{x}_i | i = 1, ..., N\}$ be a collection of stock indices, where $\boldsymbol{x}_i$ is a set of observations x_{it}, each being recorded at the closing of n consecutive working

days. To retrieve the referential nearest neighbors (RNN) of a target time series $\boldsymbol{x}_i$, we make use of the Pearson's correlation coefficient,

$$\rho(\boldsymbol{x}_i, \boldsymbol{x}_j) = \frac{\sum_{t=1}^{n}(x_{it} - \bar{\boldsymbol{x}}_i)(x_{jt} - \bar{\boldsymbol{x}}_j)}{\sqrt{\sum_{t=1}^{n}(x_{it} - \bar{\boldsymbol{x}}_i)^2}\sqrt{\sum_{t=1}^{n}(x_{jt} - \bar{\boldsymbol{x}}_j)^2}}, \tag{1}$$

where $\bar{\boldsymbol{x}}_{\cdot}$ is the mean of the vector. Then the following dissimilarity metric [17] is adopted to compute the proximity between $\boldsymbol{x}_i$ and $\boldsymbol{x}_j$:

$$D(\boldsymbol{x}_i, \boldsymbol{x}_j) = 1 - \rho^2(\boldsymbol{x}_i, \boldsymbol{x}_j). \tag{2}$$

Based on this distance metric, we can identify a set $\mathbb{K}_i$ of k nearest neighbors, namely, the RNNs, which is comprised of stock indices with strong resemblance to characteristics of $\boldsymbol{x}_i$ and therefore can provide reference for predicting future values of $\boldsymbol{x}_i$. Note that $\boldsymbol{x}_i$ is included in $\mathbb{K}_i$ by default because the distance between $\boldsymbol{x}_i$ and itself is always 0.

3.2 Referential Nearest Neighbor Regression

Now we move on to forecast future values of $\boldsymbol{x}_i$ based on the historical knowledge stored in $\mathbb{K}_i$. The current state of $\boldsymbol{x}_i$ is represented by the latest z consecutive observation of $\boldsymbol{x}_i$ at time n, i.e., $\boldsymbol{p}_i = [x_{n-z+1}, x_{n-z+2}, \cdots, x_n]$, where z is the *pattern length* parameter determined later. Let $\mathbb{T}_i$ be the set of all consecutive patterns of length z that could be extracted from time series in $\mathbb{K}_i$. Based on the distance metric in (2), we select M most resembling patterns to form a referential pattern set $\mathbb{R}_i$. Then prediction of $x_{i(n+h)}$, where h denotes the *forecasting horizon*, is obtained by

$$\hat{x}_{i(n+h)} = \frac{1}{M}\sum_{j=1}^{M} p_{j(n'_j+h)}, \tag{3}$$

where n'_j is the last time index of referential pattern $\boldsymbol{p}_j \in \mathbb{R}_i$.

3.3 Evaluation Metrics

There are many criteria that can be used to evaluate the performances of forecasting models in the numerical study [4]. In this paper, the prediction performance of the proposed forecasting model is evaluated through two typical statistical metrics: Mean Absolute Percentage Error (MAPE) and Normalised Mean Squared Error (NMSE). The usage of MAPE and NMSE is to measure the derivation between the predicted and actual values, the smaller values of MAPE and NMSE means the closer between predicted value and actual value.

These metrics are determined by $x_{i(n+1)}$ and $\hat{x}_{i(n+1)}$: the current observation of time series $\boldsymbol{x}_i$ at time $n+1$, and the prediction for that observation. Then the two evaluation metrics are defined as,

$$MAPE = \frac{1}{n}\sum_{j=n+1}^{n+N}\left|\frac{\hat{x}_{ij} - x_{ij}}{x_{ij}}\right|, \tag{4}$$

$$NMSE = \frac{N-1}{N} \sum_{j=n+1}^{n+N} \frac{(\hat{x}_{ij} - x_{ij})^2}{(x_{ij} - \bar{\boldsymbol{x}}_i)^2}, \tag{5}$$

where forecast errors are evaluated over a period of N consecutive days.

4 Experiment and Discussions

The performance of proposed algorithm in forecasting stocks daily closing price has been assessed in this experiment, with the comparison between conventional k-NN regression, Empirical Mode Decomposition, and benchmark algorithms. In order to avoid biases from the training samples, we use the 'unprocessed' time series data, daily closing price, and 'processed' time series data, daily return on both traditional and modified kNN regressions.

Like most typical time series forecasting studies represented, using real financial data will draw our attention into actual problem analysis, and would be useful to an economist studying the effect of various indicators on the market. In this case, we form the data pool by entire S&P 500 stocks. The S&P 500 has been widely regarded as the best single gauge of the large cap U.S. equities market since the index was first published in 1957.

4.1 Data Selection

We examine our model over 2500 observations of 121 stocks from S&P 500, by using daily closing price between January 3, 2001 and February 29, 2011. The entire stock data was downloaded from Yahoo Finance. Those 121 stocks have been selected from the following 4 sectors: Energy, Consumer Discretionary, Health Care, and Information Technology.

4.2 Parameters Modulation

On the purpose of demonstrating robust empirical results, the determination of the most crucial parameters: length of the reference pattern z and number of referential neighbors k has been recovered prior to the evaluation stage since parameter settings are dominating the performance of proposed algorithm. During our research, one of the statistical evaluating methods, the hold-out cross-validation has been implemented for parameters' tuning, and the benefits of this cross-validation technique has been sourced by Refaeilzadeh [18].

During the parameter modulation, we record score for all parameter combinations, and at the end, we adopt the parameter configuration in accordance with the best cross-validation scores. Since it impossible to go through all the possible

Table 1. Notation of parameters and grid values

Meta-Parameters	Definitions	Grid Values
k	Number of referential neighbors for each TS	$\{1, 3, \ldots, 27, 31\}$
M	Number of neighbors for reference pattern among each TS	$\{1, 3, 5, 7, 9, 11\}$
z	Length of the referential pattern	$\{5, 10, \ldots, 25, 30\}$

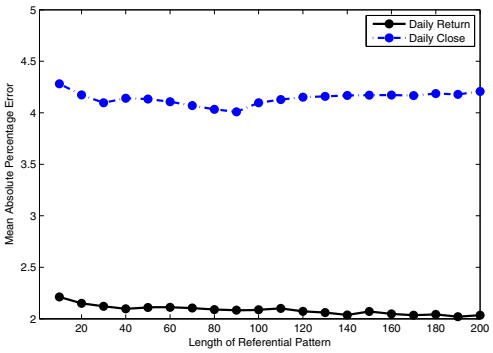

Fig. 1. Tuning parameter z using hold-out cross-validation

parameter combinations, we carefully selected sparse grid values for parameter settings, in order to provides reasonable coverage of parameter settings with optimal performance.

We have listed all the meta-parameters have been involved during the experiments, and range of grid values have been examined in Table 1, and as an instance of the parameter tuning process, Figure 1 shows how the length of referential pattern z is determined for the latter forecasting stage.

4.3 Experiment Results and Discussions

Due to the limitation of the paragraph, we only present the results of 10 randomly selected stocks across all the test data in Table 2, and the lowest error has been highlighted in bold. Despite the occasional better performance from the conventional kNN regression method on the table, the average result at the bottom of the table is concluding that, the proposed referential kNN regression provides the highest forecast accuracy that outperforms conventional kNN regression along with the benchmark algorithms by 34.69% (1.62% percentage points) and 33.7% (1.55% percentage points) respectively in MAPE, 51.90% (1.5% percentage points) and 55.31%(1.72% percentage points) respectively in NMSE.

Table 2. Random selected evaluation results among various forecasting techniques

Stock ID		NN		kNN		EMD	AR
		Price(%)	Return(%)	Price(%)	Return(%)	Price(%)	Return(%)
Stock 1	MAPE:	**3.76**	5.56	**3.76**	3.89	6.62	5.56
	NMSE:	**1.12**	2.09	**1.12**	1.16	7.22	2.41
Stock 2	MAPE:	**3.01**	4.60	**3.01**	3.07	4.72	4.33
	NMSE:	**0.69**	1.54	**0.69**	0.71	1.43	1.38
Stock 3	MAPE:	**2.84**	4.30	**2.84**	2.91	3.54	4.05
	NMSE:	**1.98**	4.23	**1.98**	2.05	3.06	4.06
Stock 4	MAPE:	2.71	4.14	2.71	**2.70**	3.67	3.91
	NMSE:	2.11	4.39	2.11	**2.01**	3.65	4.62
Stock 5	MAPE:	**4.23**	5.91	**4.23**	4.27	6.04	5.88
	NMSE:	**1.30**	2.34	**1.30**	1.31	2.29	2.52
Stock 6	MAPE:	**3.86**	5.45	**3.86**	3.93	5.43	5.40
	NMSE:	**1.22**	2.36	**1.22**	1.28	2.31	2.44
Stock 7	MAPE:	2.71	3.94	2.71	**2.70**	3.66	3.97
	NMSE:	1.60	2.75	1.60	**1.51**	2.75	3.45
Stock 8	MAPE:	2.82	4.07	2.82	**2.78**	3.74	4.08
	NMSE:	1.96	3.84	1.96	**1.93**	3.33	4.38
Stock 9	MAPE:	2.71	3.86	2.71	**2.67**	3.58	3.92
	NMSE:	1.68	3.20	1.68	**1.66**	2.58	3.63
Stock 10	MAPE	3.37	4.83	3.37	**1.60**	4.31	4.89
	NMSE:	1.09	2.20	1.09	**0.29**	1.78	2.22
Average	MAPE:	3.20	4.67	3.20	**3.05**	4.53	4.60
	NMSE:	1.48	2.89	1.48	**1.39**	3.04	3.11

5 Conclusions

In this paper, we develop a new multivariate kNN regression approach for financial time series forecasting in regards of referential nearest neighbors. We determine the referential knowledge of the target time series by conducting the financial correlation analysis among historical time series data. Then, we apply the aggregated knowledge that extracted from related rNNs with k-Nearest Neighbour(kNN) regression model to forecast the future status of the time series. The effectiveness of the proposed hybrid approach is assessed by a robust empirical evaluation over 9 years S&P 500 stock data. The experiment results demonstrate that the proposed multivariate kNN approach provides enhanced forecasting accuracy beyond classical univariate kNN regression.

References

1. Campbell, J.Y., Shiller, R.J.: The dividend-price ratio and expectations of future dividends and discount factors. Review of Financial Studies 1(3), 195–228 (1988)
2. Kanas, A., Yannopoulos, A.: Comparing linear and nonlinear forecasts for stock returns. International Review of Economics & Finance 10(4), 383–398 (2001)
3. Andrada-Félix, J., Fernadez-Rodriguez, F., Garcia-Artiles, M.-D., Sosvilla-Rivero, S.: An empirical evaluation of non-linear trading rules. Studies in Nonlinear Dynamics & Econometrics 7(3) (2003)
4. Lin, A., Shang, P., Feng, G., Zhong, B.: Application of empirical mode decomposition combined with k-nearest neighbors approach in financial time series forecasting. Fluctuation and Noise Letters 11(2) (2012)
5. Kanas, A.: Non-linear forecasts of stock returns. Journal of Forecasting 22(4), 299–315 (2003)
6. Ciora, C., Munteanu, S.M., Hrinca, I.G., Ciobanu, R.: Uncertainty and fluctuations on the stock markets. In: International Conference on Financial Management and Economics. (Singapore), International Proceedings of Economics Development and Research, vol. 11. IACSIT Press (2011)
7. Chan, L.K., Lakonishok, J., Swaminathan, B.: Industry classifications and return comovement. Financial Analysts Journal, 56–70 (2007)
8. Clarke, R.N.: Sics as delineators of economic markets. Journal of Business, 17–31 (1989)
9. Farrell, J.L.: Analyzing covariation of returns to determine homogeneous stock groupings. The Journal of Business 47(2), 186–207 (1974)
10. Elton, E.J., Gruber, M.J.: Homogeneous groups and the testing of economic hypotheses. Journal of Financial and Quantitative Analysis, 581–602 (1970)
11. Brown, S.J., Goetzmann, W.N.: Mutual fund styles. Journal of financial Economics 43(3), 373–399 (1997)
12. Wu, X., Kumar, V., Quinlan, J.R., Ghosh, J., Yang, Q., Motoda, H., McLachlan, G.J., Ng, A., Liu, B., Philip, S.Y., et al.: Top 10 algorithms in data mining. Knowledge and Information Systems 14(1), 1–37 (2008)
13. Brandsma, T., Buishand, T.A., et al.: Simulation of extreme precipitation in the rhine basin by nearest-neighbour resampling. Hydrology and Earth System Sciences Discussions 2(2/3), 195–209 (1998)
14. Yakowitz, S.: Nearest-neighbour methods for time series analysis. Journal of Time Series Analysis 8(2), 235–247 (1987)
15. Cleveland, W.S.: Robust locally weighted regression and smoothing scatterplots. Journal of the American Statistical Association 74(368), 829–836 (1979)
16. Meade, N.: A comparison of the accuracy of short term foreign exchange forecasting methods. International Journal of Forecasting 18(1), 67–83 (2002)
17. Mantegna, R.N.: Hierarchical structure in financial markets. The European Physical Journal B-Condensed Matter and Complex Systems 11(1), 193–197 (1999)
18. Refaeilzadeh, P., Tang, L., Liu, H.: Cross-validation. Encyclopedia of Database Systems 5 (2009)

A Methodology for Multipurpose DNS Sinkhole Analyzing Double Bounce Emails

HeeSeok Kim, Sang-Soo Choi, and Jungsuk Song

Science and Technology Security Center
Korea Institute of Science and Technology Information
245 Daehak-ro, Yuseong-gu, DaeJeon 350-806, Korea
{hs,choiss,song}@kisti.re.kr

Abstract. DNS sinkhole is one of the powerful techniques to mitigate attack activities of bots, i.e., zombie PCs, by blocking the communication between C&C server and them. If a zombie PC sends a DNS query to our DNS server for communicating with its C&C server, our DNS server that contains domain blacklist of C&C servers returns IP address of our sinkhole server. As a result, since the zombie PC tries to communicate with our sinkhole server, it is unable to communicate with its C&C server. On the other hand, there are many cyber attacks caused by malicious URLs included in spam emails. Therefore, if we extract malicious URLs from spam emails and apply them into DNS sinkhole system, many of spam based attacks can be blocked. In this paper, we propose a methodology to enhance the capability of DNS sinkhole system by analyzing spam emails. Especially, we use double bounce emails, which do not have any valid sender and recipient addresses, as spam emails and extract malicious URLs from them. Our preliminary experimental results demonstrate that the existing domain blacklist of DNS sinkhole system is not effective. Thus, we design a new method collecting the malicious URLs from double bounce emails and show how new domain blacklist can be generated. With DNS sinkhole system using new domain blacklist, we will be able to early detect and block the latest malicious behaviors on the Internet.

Keywords: Botnet, C&C server, DNS sinkhole, Spam, Double bounce emails.

1 Introduction

As a botnet [1] is a network of computers (i.e., zombie PCs or bots) infected by malware, this carries out various network-based attacks such as distributed-denial-of-service (DDoS) attacks [2], spam emails [3], and identify theft [4]. Actually, recent most network-based attacks on Internet are being carried out by the botnet. Botnet consists of zombie PCs and a command-and-control (C&C) server. C&C server commands zombie PCs to attack and a huge number of zombie PCs obey the command. Thus, zombie PCs carry out attacks intended by C&C server.

M. Lee et al. (Eds.): ICONIP 2013, Part I, LNCS 8226, pp. 609–616, 2013.
© Springer-Verlag Berlin Heidelberg 2013

DNS sinkhole is one of the powerful techniques to mitigate attack activities of bots, i.e., zombie PCs, by blocking the communication between C&C server and them[5]. If a zombie PC sends a DNS query to our DNS server for communicating with its C&C server, our DNS server that contains domain blacklist of C&C servers returns IP address of our sinkhole server. As a result, since the zombie PC tries to communicate with our sinkhole server, it is unable to communicate with its C&C server.

On the other hand, there are many cyber attacks caused by malicious URLs included in spam emails. Therefore, if we extract malicious URLs from spam emails and apply them into DNS sinkhole system, many of spam based attacks can be blocked. In this paper, we propose a methodology to enhance the capability of DNS sinkhole system by analyzing spam emails. Especially, we use double bounce emails, which do not have any valid sender and recipient addresses, as spam emails and extract malicious URLs from them [6].

In addition, we carry out the analysis on the packets flowed in DNS sinkhole server and then find that there are some problems in current domain blacklist of DNS server. Our preliminary experimental results demonstrate that the existing domain blacklist of DNS sinkhole system is not effective. Thus, we design a new method collecting the malicious URLs from double bounce emails and show how new domain blacklist can be generated. With DNS sinkhole system using new domain blacklist, we will be able to early detect and block the latest malicious behaviors on the Internet.

In this paper, we carry out the analysis on the packets flowed in DNS sinkhole server and then find that there are some problems in current domain blacklist of DNS server. This means that urgent investigation into malicious URLs in new ways is needed.

The remainder of this paper is organized as follows: in Section 2 we introduce some basic concepts such as botnet, DNS sinkhole system, and double bounce emails. In Section 3 we propose new method to improve the performance of DNS sinkhole system. We then show experimental results about DNS sinkhole system and further research plan in Section 4, after which we conclude.

2 Related Works

2.1 Botnet

Botnet is a network of computers which are compromised to conduct various network-based attacks, i.e. botnet consists of zombie PCs and C&C server. Botnet is 'Cyber Army' on the Internet. After gathering this cyber army, C&C server can control zombie PCs from remote and command malicious behaviors as follows:

- Conduct DDoS attacks
- Send spam emails
- Infect other computers
- Gain personal information for identify theft by phishing

The state-of-the-art network-based attack methods, which are conducted by zombie PCs and controlled by C&C server, are getting more malicious and more clever. Thus, we have to early detect and block zombie PCs and C&C server.

2.2 DNS Sinkhole System

The DNS sinkhole system is aiming to break the communication between C&C server and zombie PCs. In the case without DNS sinkhole server, if zombie PCs send a DNS query to DNS server, then they will succeed in receiving IP address of C&C server. This means that they are able to connect to C&C server and malicious commands will be supplied. But, when DNS sinkhole server is operated, DNS server will return IP address of sinkhole server, not that of C&C server . So, because zombie PCs connect to sinkhole server, we can avoid that malicious commands are supplied to zombie PCs.

In other words, DNS sinkhole system can early detect and block zombie PCs. In DNS sinkhole system, if zombie PCs connect to sinkhole server, this server writes a log file from packet information and store it in the database. After then, we can use this log file when handling comprehensive incidents. Also, by using this log files, we will be able to detect zombie PCs and respond emergency. Fig. 1 describes the management system of DNS sinkhole.

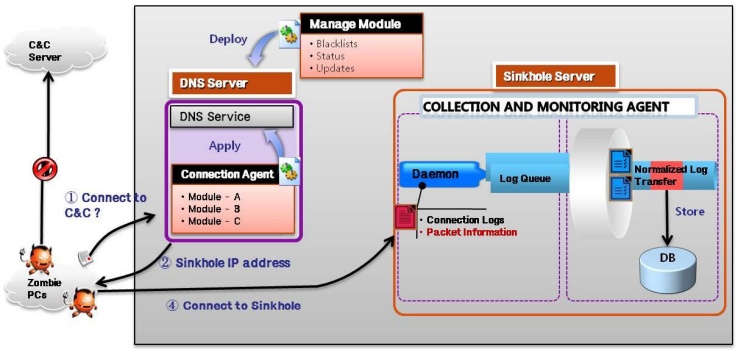

Fig. 1. DNS sinkhole system

2.3 Double Bounce Emails

During the previous years, many machine learning methods have been proposed for spam detection. However, these methods cannot accurately distinguish spams from normal emails. Further, the effective lifetime of the existing techniques is highly short, because spammers frequently change their modus operandi to compromise spam detection techniques. In other words, in order to maintain the effectiveness of spam filters, constant upgrades and new developments are essentially required.

Double bounce emails indicate that they have no valid recipient address and return-path address. In the case of a normal email, it contains one return-path address at least in its header field, even if a sender mistyped the recipient address to his/her email. In this context, double bounce emails can be regarded as pure spam. This double bounce email is quite similar to the concept of darknet which is an area of a routed, and allocated IP space where no active services or servers reside, and thus the incoming packets to it can be treated as abnormal ones. Darknet has been used for analyzing incidents in many researches [7], because many abnormal activities can be easily observed in the darknet. Similarly, we collect double bounce emails and use them as our analysis data.

3 Proposed Method

In the existing DNS sinkhole system, not considering URLs which are included in double bounce emails, general PCs can access these URLs via various routes such as spam mails, malicious replies on the Internet boards, pop-up ads, another malicious URLs, and so on. Our purpose is to find up to date malicious URLs from double bounce emails and add these URLs into domain blacklist of DNS server. This work will be able to block that the PCs are changed to zombie PCs, or infected with the computer virus. Fig. 2 describes the change of flow diagram by the proposed system.

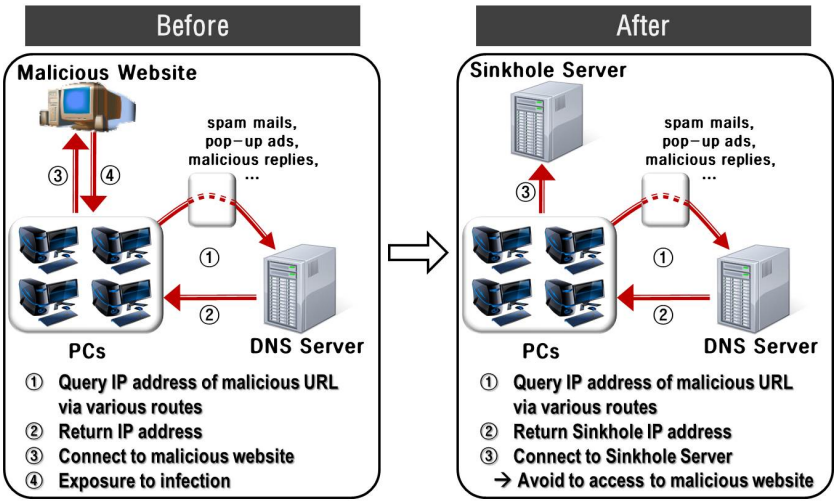

Fig. 2. The change of flow diagram by the proposed system

3.1 DNS Sinkhole System Using Double Bounce Emails

As mentioned above, the main idea of our system is to add the malicious URLs, extracted from double bounce emails, to the domain blacklist of DNS server. Proposed system is implemented by the following steps:

1. Extraction of double bounce emails from mail server
2. Automatic extraction of normalized URLs from body of double bounce emails
3. Checking if extracted URLs have malware or not
4. Generation of domain blacklist
5. Addition the malicious URLs to the domain blacklist of DNS server
6. Performance measurement for detection of malicious behavior based on new domain blacklist

The first step of our method is to gather double bounce emails from various types of spam mails. Then we extract the normalized URLs from each email by automatic tool. This second step is conducted by three sub-steps: (1) URL extraction from body of double bounce emails (2) normalization of various types of URLs (3) removal of duplicate URLs. The third step checks if the extracted URLs have malware or not. In this step, we first input the extracted URLs into the database. Then a web crawler reads the URL and downloads the available data by connecting to corresponding URL, one at a time. The third step is finished by checking if the malware is included in the downloaded data. This checking routine will be carried out by a dedicated anti-malware software in the future. Based on URLs having malware, we can generate the new domain blacklist in the fourth step. In the final two steps, we add new URLs found in the fourth step to domain blacklist of DNS servers and evaluate the impact and effectiveness of new DNS sinkhole system, while comparing with the existing system, which uses the old domain blacklist only. Fig. 3 shows the schematic diagram of new DNS sinkhole system.

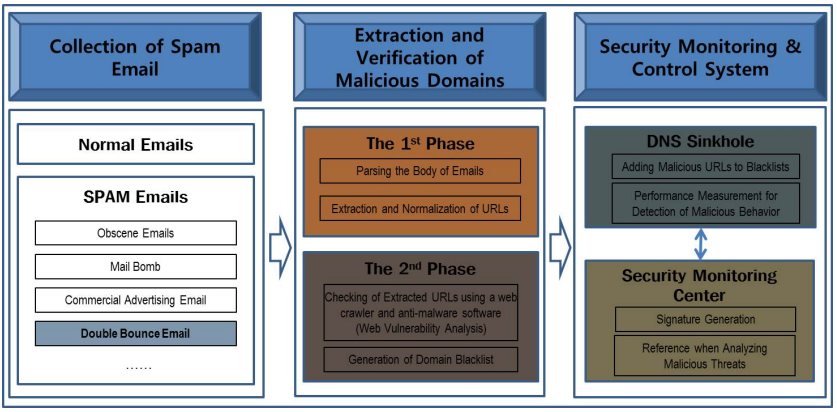

Fig. 3. The schematic diagram of our system

4 Preliminary Experiments

4.1 Experimental Results

We have built own DNS sinkhole system interworking with 28 DNS servers of the research institutes that we are providing realtime security monitoring and response service. Malicious URLs registered to the domain blacklist of 28 DNS servers have been provided by two sources. One is Science and Technology Security Center(S&T-SEC) which is operated by ourselves. The other is Korea Internet & Security Agency (KISA). The total number of malicious URLs was 1,854, among them 335 malicious URLs were from S&T-SEC and 1,589 malicious URLs were from KISA; there are 70 URLs in the intersection of two sources. We captured the packets flowed in DNS sinkhole server during one month, from 2013/06/03 to 2013/07/02. The results analyzing the packets are shown in fig 4.

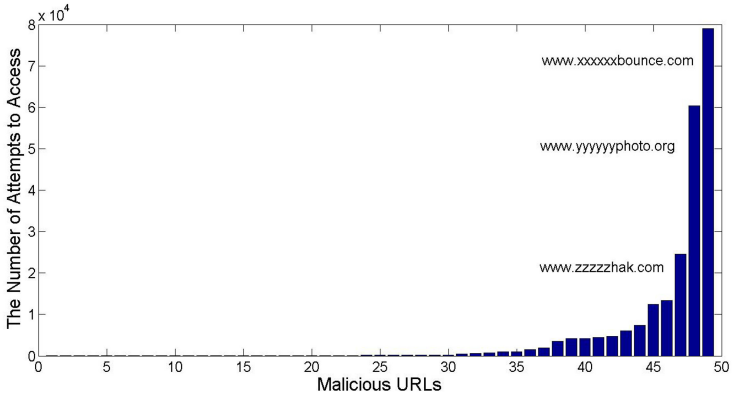

(a) The number of attempts to access according to malicious URLs

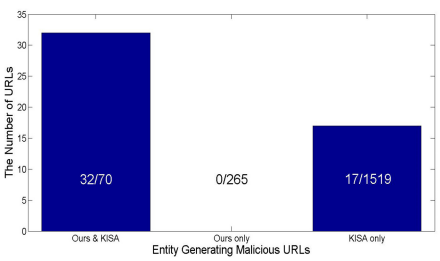

(b) The number of URLs, accessed by bots(i.e., zombie PCs), according to the vendors generating domain blacklist

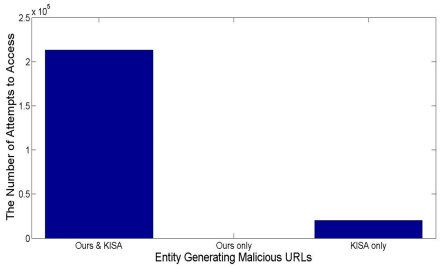

(c) The number of attempts to access according to the vendors generating domain blacklist

Fig. 4. Experimental results about DNS sinkhole system

The total number of attempts to access malicious domains was 233,598. During our analysis, we observed that the number of malicious URLs accessed by bots(i.e., zombie PCs) was only 49 of the 1854. Furthermore, as shown in fig. 4(a), most packets have been trying to access three malicious domains: www.xxxxxxbounce.com (79,026), www.yyyyyyphoto.org (60,338), and www.zzzzzhak.com (24,532). Fig. 4(b) shows the number of URLs, accessed by bots according to the sources provided malicious URLs. Among 70 URLs included in both sources (i.e., S&T-SEC and KISA blacklists), 32 URLs have been tried to be accessed by bots. And the rest 17 of 49 malicious URLs are only included in KISA blacklists. Fig. 4(c) shows the number of attempts to access according to the sources provided malicious URLs.

4.2 Discussion

From the experimental results in the subsection 4.1, some problems could be addressed as follows:

- **Dependence on few of malicious URLs:** the number of malicious URLs accessed by bots was only 49 of the entire 1854 URLs. This means that DNS sinkhole system heavily depends on a few malicious URLs.
- **Lack of effectiveness of our own domain blacklist:** while all URLs accessed by bots were included in KISA domain blacklist, no malicious URLs were registered in only S&T-SEC blacklist, but not registered in KISA blacklist. This means that our domain blacklist was useless during one month, capturing the packets at least.

Based on the above results, it could be concluded that the existing DNS sinkhole system has the unpractical problem in gathering malicious domains. Thus, we will carry out urgent investigation into malicious URLs in entirely new manner. We will use the URLs included in double bounce emails at the first attempt for it. After checking if these URLs are malicious, we will add the URLs to domain blacklist of DNS servers and then carry out the performance measurement for DNS sinkhole based on new domain blacklist. We will count the number of detection divisively in two cases of old and new domain blacklists. From these numbers of detection, we can evaluate the impact and effectiveness of new DNS sinkhole system.

5 Conclusions

Based on experimental results about DNS sinkhole system, we noticed that current system had some problems. To solve these problems, we proposed the new method to improve the performance of DNS sinkhole system by using double bounce emails; we extract the URLs from the body of double bounce emails and add these URLs to domain blacklist of DNS server after checking if those are malicious. By the new DNS sinkhole system, we will be able to collect the latest malicious domains used in various hacking techniques. In addition, it will

be possible to improve the quality for security control & emergency response. Finally, we will be able to early detect and block malicious behaviors on the Internet.

References

1. SANS Institute, Bots & Botnet: An Overview, http://www.sans.org/r-eading_room/whitepapers/malicious/bots-botnet-overview_1299
2. Ianelli, N., Hackworth, A.: Botnets as a Vehicle for Online Crime. In: Proc. First Intl. Conf. Forensic Computer Science (2006)
3. Jung, J., Paxson, V., Berger, A., Balakrishnan, H.: Fast Portscan Detection Using Sequential Hypothesis Testing. In: Proc. IEEE Symp. Security and Privacy (2004)
4. Anderson, D.S., Fleizach, C., Savage, S., Voelker, G.M.: Spamscatter: characterizing Internet scam hosting infrastructure. In: Proc. the USENIX Security Symp. (2007)
5. SANS Institute, DNS Sinkhole, http://www.sans.org/reading_room/whi-tepapers/dns/dns-sinkhole_33523
6. Song, J., Inoue, D., Eto, M., Suzuki, M., Hayashi, S., Nakao, K.: A Methodology for Analyzing Overall Flow of Spam-Based Attacks. In: Leung, C.S., Lee, M., Chan, J.H. (eds.) ICONIP 2009, Part II. LNCS, vol. 5864, pp. 556–564. Springer, Heidelberg (2009)
7. Nakao, K., Inoue, D., Eto, M., Yoshioka, K.: Practical Correlation Analysis Between Scan and Malware Proles Against Zero-day Attacks Based on Darknet Monitoring. IEICE Transactions on Information and Systems E 92D(5), 787–798 (2009)

Nonlinear Dimensionality Reduction for Visualization

Michel Verleysen[1] and John A. Lee[2]

[1] ICTEAM, Université catholique de Louvain, Belgium
michel.verleysen@uclouvain.be
http://perso.uclouvain.be/michel.verleysen/
[2] IREC, Université catholique de Louvain, Belgium
john.lee@uclouvain.be

Abstract. The visual interpretation of data is an essential step to guide any further processing or decision making. Dimensionality reduction (or manifold learning) tools may be used for visualization if the resulting dimension is constrained to be 2 or 3. The field of machine learning has developed numerous nonlinear dimensionality reduction tools in the last decades. However, the diversity of methods reflects the diversity of quality criteria used both for optimizing the algorithms, and for assessing their performances. In addition, these criteria are not always compatible with subjective visual quality. Finally, the dimensionality reduction methods themselves do not always possess computational properties that are compatible with interactive data visualization. This paper presents current and future developments to use dimensionality reduction methods for data visualization.

Keywords: visualization, dimensionality reduction, manifold learning.

1 Introduction

Data analysis has become an overwhelming discipline in many areas of our everyday life. Modern ways to acquire and to store information are responsible for a data deluge. Extracting relevant information from huge amounts of data is a challenge that is responsible for important and recent scientific developments in statistics and machine learning. Applications of such new data analysis tools range from (bio)medicine to consumer profiling, industrial and quality control, environmental monitoring, and many others.

A specific aspect of data analysis is visualization. Visual inspection of data is unavoidable in many practical situations. The main reason is that, despite the power of modern data analysis tools, few of them are really blind in the sense that they can be applied without any understanding of the data at hand: preliminary qualitative knowledge is needed, and visualization might help in this context for example in finding outliers, clusters, etc. Another reason, among many other ones, to visualize data is that non-experts are often difficult to convince about the benefits of mathematical tools, if they cannot see the results in the way they are used to see and to analyse them.

M. Lee et al. (Eds.): ICONIP 2013, Part I, LNCS 8226, pp. 617–622, 2013.
© Springer-Verlag Berlin Heidelberg 2013

Visualization has been developed rather independently by two research communities. One one side, the machine learning community has developed dimensionality reduction (DR) methods that may be used for visualization if the resulting dimensionality is restricted to be 2 or 3. One the other side, the information visualization (IV) community has developed graphic ways of representing the information under the angle that is most usable by the user. Unfortunately, only few attempts exist to combine the features and advantages of both fields.

Dimensionality reduction is a generic term including manifold learning, nonlinear projection, etc. The goal of DR is to handle data that contain a high number of attributes (and therefore cannot be visualized easily), and to reduce them (through the optimization of mathematical information content criteria) to a lower-dimensional space, while preserving as much as possible the information content in the data. If the dimension of the latter space is 2 or 3, this provides an obvious way to visualize data. On the other hand, information visualization focuses on user-centric graphic objectives, and largely relies on controllability (the user decides which is the best way he needs for representing data) and interaction (the controllability is achieved through a user interface that responds almost immediately, making different views affordable in a single session).

Controllability and interaction are two concepts that are mostly absent from dimensionality reduction. Most DR methods rely on the algorithmic optimization of a predefined information criterion; although the results can be satisfactory on the point of view of information content preservation, they are usually not in terms of effective visualization. Problems such as the sensitivity to initial conditions, possible rotations and mirroring are common. More dramatically, the criterion to be optimized has to be predefined; adjusting the criterion to another balance between conflicting goals (see below for details) needs to run the algorithm again, which implies prohibitive computational load and simulation times.

2 Dimensionality Reduction: State-of-the-Art

Dimensionality reduction [1] has its roots in methods such as principal component analysis (PCA) [3]. PCA can be used to reduce the dimensionality of high-dimensional data; new features are generated by linear combinations of the original features, by optimizing a maximum variance/minimum loss of information criterion. If the resulting dimension is limited to 2, PCA provides an easy way to represent high-dimensional data; however, PCA only aims to preserve simple second-order statistics (directions of main variance) and can miss the important characteristics of more complicated data distributions.

Except for a few older methods like Sammon's mapping [4], most nonlinear extensions to PCA were frenetically developed in the 80s and 90s. Relaxing the linearity constraint has been found to open the way to new information preservation criteria, which tend to yield better low-dimensional data representations in practice. Methods such as Sammon's mapping and curvilinear component analysis (CCA) [5] result from a nonlinear view of PCA: while PCA tries to preserve all Euclidean distances between pairs of points in a data set (while projecting it

to a lower-dimensional space), Sammon's mapping and CCA emphasize preservation of small distances, which are usually the ones that are the most important for effective visualization. At the same time, methods such as Curvilinear distance analysis (CDA) [6] and Isomap [7] were developed, where the distances to be preserved are based on the data distribution itself, such as geodesic or graph distances. The graph distances allow a better representation of the important-to-preserve similarities and distances in the data; in some sense they act against the well-known unreliability of estimating data properties in high-dimensional spaces, called the curse of dimensionality [8].

The diversity of the many DR methods has revealed how difficult it can be to analyse relationships between different methods and their suitability for a particular analyst's needs. Part of the problem is that nonlinear DR has been done by optimizing relatively abstract criteria, and the relationships of the criteria to helping analysts in a meaningful task has not been clear. Recent analysis has made it clear that (at least) two conflicting goals exist in DR: in terms of a relaxed form of distance preservation called neighbourhood preservation, 1) two data items that are neighbours in the original space should remain neighbours in the projection space, and 2) two data items should be shown as neighbours in the projection space only if they are neighbours in the original space. Recently, both two goals have been shown to correspond to performance in an information retrieval task, visual retrieval of neighbours from the output display, as measured by the information retrieval measures precision and recall respectively. The conflict between the goals yields a natural trade-off between the precision and recall measures, and between visualizations that are good for one goal versus the other [9] [10]. For example, projecting a spherical surface distribution to a two-dimensional space results in flattening the sphere surface onto a circle if only goal 2 (recall) is optimized or cutting the surface open like an orange-peel world map if only goal 1 (precision) is optimized. This example illustrates the conflicting requirements in DR and visualization; neither result is obviously better than the other, the choice, or the compromise, should be guided by the users needs.

3 Visualization

Information visualization [2] has developed ways to visualize data in a user-centric way. IV relies on the adequation between the method and the cognitive goal of understanding data. Many information visualizations are interactive, reflecting the difficulty to represent data in a unique, undebatable way. Interaction also closes the loop with the user: interaction is based on cognition, therefore helps reflecting the users' needs.

Information visualization methods are largely based on extensive software that combine user goals, modern computer visualization features, and interaction. The representation principles behind the methods are usually quite simple (parallel coordinates, dendograms, trees, heatmaps, etc.), although recent information visualization often involves dimensionality reduction methods, such as principal component analysis and Sammon's mapping.

Machine-learning based dimensionality reduction and information visualization are complementary: the DR field has developed advanced mathematical criteria and ways to optimize them, while IV takes into account users' needs, cognitive aspects and computer resources. However combining the advantages from two fields requires an in-depth study of performance criteria and computational requirements.

4 Quality Criteria and Computational Requirements

Quality criteria exist to measure the performances of nonlinear dimensionality reduction methods [10]. Most of them yield a pair of values (trustworthiness and continuity, mean relative rank errors, etc.), which also reflects these dual or conflicting requirements. These measures can assess the compromise between the requirements for a given DR result (visualization), but so far the only way to influence the compromise is to change the criterion of the DR method. Changing the criterion yields two difficulties: A) the DR algorithm must be rerun, and since most algorithms take from tens of seconds to hours on standard computers, fast interaction with the user becomes impossible; B) the link between control parameters in the mathematical optimization goal and the behaviour of the DR algorithm is far from straightforward, especially when several control parameters are involved.

These limitations exist even in the most recent DR algorithms. For example, algorithms from the stochastic neighbour embedding (SNE) family [11] [12] have been shown to outperform distance-based methods in the last years, especially when the original space is high-dimensional. They optimize a divergence between distributions of distances or neighbours in both spaces, and can partially alleviate the curse of dimensionality by adjusting priors on the distributions, but the same basic difficulties remain: the need to rerun the algorithm when the criterion is modified, and the difficulty of controlling in an intuitive way the compromise between conflicting objectives.

On the other hand quality criteria when visualization is involved are far from the information content perspective brought by such trustworthiness and continuity pairs of measures. Performances in visualization are measured in a way that takes the cognitive process into account, thus involving the user. In this context it is much more difficult to define in advance the exact mathematical criterion to be optimized. Interaction is thus needed between the method and the user: the visualization is modified by the user, who can estimate in real-time the adequacy between the visual result and his expected goal.

Interaction necessitates speed: one cannot reasonably expect the user to wait for more than a few seconds between the request and the response. In DR methods, the quality criteria (or a proxy) are directly optimized to give the resulting projection. As most modern criteria are nonlinear, non-linear optimization is involved, with a number of parameters to optimize that is proportional to the number of data in the database. In most situations, depending on the application and on the DR method, this results in unaffordable computation times.

5 New Developments

In order to lead to effective and usable visualization methods, the modern tools in the dimensionality reduction field have to be adapted from several perspectives.

First, effective visualization necessitates parameters that may be controlled by the user, in order to take cognitive aspects into account and adapt the results of the algorithm to the user's needs. Most DR methods do contain parameters. For example, often one of them implements a compromise between the trustworthiness and the continuity of the projection. Another might control the influence of outliers, ... In theory it is thus possible to influence the visualization through user-controlled parameters. However, nothing indicates that the choice of these parameters, guided by algorithmic and mathematical considerations, is appropriate with regards to the cognitive control. There is thus a need for identifying the role of existing parameters and, if necessary, to change them to parameters closer to the user's needs.

Secondly the DR methods have to be rethought in the light of visualization needs. Most modern DR methods are shown to outperform competitors in specific settings, and according to specific quality criteria. But are these criteria the most appropriate ones when visualization is concerned? Is it reasonable possible to use them as a proxy of subjective, cognitive criteria? Conversely, would it be possible to express subjective criteria in a mathematical form and optimize them directly?

Third, the question of stability has to be investigated. DR methods result in *a* representation of the data. However what concerns visual perception, several equivalent projections could be thought of (for example rotations, scalings, ...). When the parameters of the DR methods are modified, even slightly, another optimum of the criterion to optimize can be found, leading to an almost equivalent but completely different projection. Such instability is of course undesirable in the context of visualization, and must be controlled at the algorithmic level.

Finally, the computational requirements should be seriously investigated, in the light of the possibility for user interaction. Fast algorithms have a clear advantage. When necessary, incremental methods could be developed: slight changes in the parameters of a method should not result in largely different representations. This "continuity" in the process could be exploited to reduce the computation time after user interaction.

6 Conclusion

The field of Machine Learning has generated a large number of dimensionality reduction methods. These methods can be used for the visualization of data, which is a fundamental step in exploratory data analysis. In parallel, the field of Information Visualization develops user-centric graphic ways to visualize data based on cognitive results. The complementarity of the approaches is a challenge for the future developments of dimensionality-based visualization methods: how to

incorporate user control, cognitive criteria, stability and computational requirements in DR methods are key questions opening new perspectives for research on dimensionality reduction.

References

1. Lee, J.A., Verleysen, M.: Nonlinear dimensionality reduction. Springer (2007)
2. Keim, D.A., Mansmann, F., Schneidewind, J., Thomas, J., Ziegler, H.: Visual analytics: Scope and challenges. In: Simoff, S.J., Böhlen, M.H., Mazeika, A. (eds.) Visual Data Mining. LNCS, vol. 4404, pp. 76–90. Springer, Heidelberg (2008)
3. Jolliffe, I.T.: Principal Component Analysis. Springer-Verlag, New York, NY (1986)
4. Sammon, J.W.: A nonlinear mapping algorithm for data structure analysis. IEEE Transactions on Computers, CC-18(5), 401–409 (1969)
5. Demartines, P., Hérault, J.: Curvilinear component analysis: A self-organizing neural network for nonlinear mapping of data sets. IEEE Transactions on Neural Networks 8(1), 148–154 (1997)
6. Lee, J.A., Verleysen, M.: Curvilinear distance analysis versus isomap. Neurocomputing 57, 49–76 (2004)
7. Tenenbaum, J.B., de Silva, V., Langford, J.C.: A Global Geometric Framework for Nonlinear Dimensionality Reduction. Science 290(5500), 2319–2323 (2000)
8. Donoho, D.L.: High-Dimensional Data Analysis: The Curse and Blessings of Dimensionality. Lecture for the American Math. Society Math. Challenges of the 21st Century (2000)
9. Venna, J., Peltonen, J., Nybo, K., Aidos, H., Kaski, S.: Information retrieval perspective to nonlinear dimensionality reduction for data visualization. Journal of Machine Learning Research 11, 451–490 (2010)
10. Lee, J.A., Verleysen, M.: Quality assessment of dimensionality reduction: Rank-based criteria. Neurocomputing 72(7-9), 1431–1443 (2009)
11. Hinton, G., Roweis, S.T.: Stochastic neighbor embedding. In: Becker, S., Thrun, S., Obermayer, K. (eds.) Advances in Neural Information Processing Systems (NIPS 2002), vol. 15, pp. 833–840. MIT Press (2003)
12. van der Maaten, L., Hinton, G.: Visualizing data using t-SNE. Journal of Machine Learning Research 9, 2579–2605 (2008)

Autism and ADHD – Two Ends of the Same Spectrum?

Włodzisław Duch, Krzysztof Dobosz, and Dariusz Mikołajewski

Department of Informatics, Nicolaus Compernicus University,
ul. Grudziądzka 5, 87-100, Toruń, Poland
wduch@is.umk.pl

Abstract. Analysis of dynamics of biologically motivated neural networks allows for studying non-linear processes responsible for cognitive functions and thus provides adequate language to understand complex mental processes, including psychiatric syndromes and disorders. Problems with attention shifts that are at the roots of Autism Spectrum Disorders (ASD) and Attention-Deficit/Hyperactivity Disorder (ADHD), have been investigated using network model of Posner Visual Orienting Task (PVOT). Changing parameters that control biophysical properties of model neurons and cause network dysfunctions provides plausible explanations of many strange ASD and ADHD phenomena.

Keywords: Autism Spectrum Disorders, ASD, Attention-Deficit/Hyperactivity Disorder, ADHD, neural networks, neurodynamics, fuzzy symbolic dynamics.

1 Introduction

The Consortium for Neuropsychiatric Phenomics (CNP), established in 2008, aims at understanding mental disorders in a comprehensive way, comparing individual phenotypes at many levels: genetics, signaling pathways (molecular processes), structural properties of neurons, brain network responses (neuroimaging), cognitive functions, behavioral syndromes and psychiatric disorders [1]. Different disciplines contributing to neuropsychiatric phenomics, or to even more general field of neurocognitive phenomics [2], should have a common language that may be linked to behavioral, neural and molecular processes. Neurodynamics is the best candidate for such language: it may be investigated at the computational and pursued at the experimental level. Parameters of neural networks may be linked to the biophysical parameters of neurons and to the structural properties of brain networks that depend on the molecular and genetic processes. Collective states of networks investigated using neuroimaging techniques may be linked to cognitive functions and behavioral syndromes.

Understanding mental states should be based on analysis of long-time network dynamics. Multiscale brain modeling is concerned with quantitative form of electroencephalograms rather than with cognitive processes. Computational neuroscience has not yet provided general conclusions or concepts that may be of use to psychology or psychiatry. Connectionist models and cognitive architectures are constructed at too high level of abstraction to connect them with neural processes. The need for new concepts and language that will link mental states (psychology) with brain activity

M. Lee et al. (Eds.): ICONIP 2013, Part I, LNCS 8226, pp. 623–630, 2013.
© Springer-Verlag Berlin Heidelberg 2013

(neurodynamics) has been clearly stated by Spivey [3], who advocated the use of symbolic dynamics for understanding of cognitive processes. Analysis of global state of the model network activity (global neurodynamics) using variety of techniques helps to uncover deeper causes of mental phenomena, providing concepts that should be useful for both psychology and neuroscience experts. In this paper we will show how relatively simple neural model of spatial attention is analyzed to provide many insights into the nature of such disorders as ASD and ADHD.

2 Attractor Dynamics: Language of Mental States

Ample theoretical and experimental evidence has proven the importance of synchronization processes in the brain. Quasi-stable patterns formed for a range of similar initial conditions are called attractors of neurodynamics. Noise drives the network out of the attractor basins, making a series of transitions between attractor states. The time spend in a given attractor basin is called *dwell time*. Determination of dwell time depends on the noise level in the system. The strongest source of noise is "synaptic bombardment" caused by signals coming from all over the brain to the huge dendritic trees of neurons. The landscape of attractor basins is neural network is constantly changing even without any learning, because some states become inaccessible (due to neural accommodation and other effects [4]). Emotions, sounds and other percepts change this landscape by phasic arousal, activation of key brain structures in the brain stem and limbic areas, release of major neurotransmitters.

Neurodynamics of attractor networks allows for precise discussion of temporal dynamics of mental states that is of interest to psychologist [3], and of brain processes as seen using neuroimaging techniques. Brains have a large number of regions that are interconnected, and cognitive function require cooperation of many regions. Dwell time in attractor state in each region has to be sufficiently long to enable synchronization processes that lead to global attractor states. Dwell time is estimated by clustering points of trajectory and assessing size of each cluster. Fast state transitions in some neural layers (brain regions) do not leave enough time for synchronization with other regions to occur, and therefore have no influence on global neurodynamics. Only attractor states lead to conscious mental states, enabling formation of percepts, thoughts or actions. This is stressed in the Adaptive Resonance Theory (ART) [5]. Resonant top-down attentive matching leads to synchronized activity of neurons (ART describes it at a rather high level of abstraction), and only such resonant states that are point attractors are sufficiently stable to be recognized by other parts of the brain and interpreted as conscious. Therefore procedural, spatial and motor representations that do not generate point attractors do not have qualia that are experienced in a conscious way. Although ART has been very successful in explaining a lot of data about the brain it does not use biophysically plausible neural models, and thus it is rather hard to link with molecular neuroscience.

Continuous sequences of changes responsible for recall of melodies, sentences or complex gestures and movements may be described as a special kind of "sliding attractors" that have not been studied so far, probably because they will not arise in simple low-dimensional systems that are frequently studied.

Below the effects that lead to abnormal shifts of attention are analyzed using simple model of Posner Visual Orienting Task.

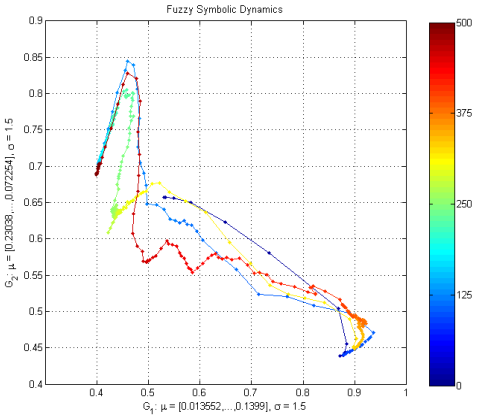

Fig. 1. Cyclic and "sliding" attractors generated by the model of motor cortex activity during repetitive movements [6], shown using Fuzzy Symbolic Dynamics technique [7,8]. In this case irregular repetitive movements have been generated, but simple movements followed by other type of actions would generate sliding attractors instead of cyclic ones. Dynamics of speech and music is full of sliding attractors.

3 Posner Visual Orienting Task (PVOT)

Many factors influence patterns of synchronized activation in neural networks: properties of neurons, their recurrent connections, competition and inhibition within the network that allow for multiple constraint satisfaction. The simplest models of neurons that may be linked to neurobiology should take into account at least 3 types of processes: excitatory synaptic inputs (ion channels that transport positive sodium ions outside and positive potassium ions into cell body), inhibitory synaptic inputs (ion channels that pump negative chloride ions), and leak channels that let the potassium ions to flow out. Many other ions may filter through membranes, and many type of pores or ion channels exist. The model of spatial attention presented here has been implemented in the Emergent environment [4] based on point neurons, trained by biologically-inspired mechanisms, using average rate coding, several types of neural noise, and neural accommodation (neural fatigue).

Analysis of the long-term neurodynamics cannot be reduced to statistical measures and asymptotic behavior. We have used recurrent plots and invented a new approach to visualization of high-dimensional trajectories that gives complementary information on trajectories. This approach, called Fuzzy Symbolic Dynamics (FSD) [7,8], is more informative than classical Symbolic Dynamics.

Using these tools we have investigated delays in attention shifts as a function of neural and network parameters. Although many brain areas are involved in attention control basic deficits in the ability for spontaneous attention shifts are at the core of ADHD and ASD. This fact is at the foundation of Grossberg's iSTART (imbalanced Spectrally Timed Adaptive Resonance Theory) model of autistic behaviors. In ART theory vigilance parameter controls learning of new exemplars vs. relying on already known categories of objects. New exemplars are learned when a mismatch between top-down expectation between currently active recognition category and current exemplar is detected and adaptation is not sufficient. This is a well-known idea that solves the stability-plasticity dilemma and has been used by many constructive neural

networks that add resources where they are needed. In case of autism the iSTART model assumes hypervigillance, and thus hyperspecificity of memory, drawing many conclusions from this assumption. Such formal models give only shallow understanding: they may be fitted to the data, but give no clue what physical mechanisms are responsible for increased vigilance, how to connect such models with neuroscience, how the brain will respond to drugs. Below we shall contrast some explanations of the iSTART with our hypothesis, linking vigilance with attractors in network dynamics.

Posner Visual Orienting Test (PVOT) is perhaps the simplest experiment probing spatial attention [4]. Reaction time to brightening (or making the box lines thicker) of a small box on a screen are measured (participants press a button), and compared to the reaction time when a target box is shown in the same place (valid cue) or in a different place (invalid cue). In the neutral case typical reaction times are about 370 ms, in the valid cue case they are about 20 ms shorter and in the invalid case 20 ms longer.

Spatial attention emerges from inhibitory competition (responsible for imposing a limitation on the total amount of activity within each region of neurons with recurrent connections), and constraint satisfaction operating throughout the network (which determines the representations that will become active in a given context). This type of attention is thus a ubiquitous property of the cortex that may be modulated by goal-oriented control processes, but for spontaneous focus of attention a simpler model is sufficient. O'Reilly and Munakata [4] have investigated the lesions of Posner model and were able to replicate slowing reaction times of hemispatial neglect patients for targets that appear in the neglected side of space, particularly when invalidly cued. The network structure is shown here. The dorsal visual streams responsible for spatial localization represented by two layers in the left upper part (Spat1 and Spat2), and the ventral object recognition stream also by two layers (Obj1 and Obj2). The spatial and object layers are connected, with stronger influence of the location on object recognition. These top layers provide increasingly spatially invariant representations, receiving inputs from the Cue/Target spatially mapped feature array that represents early visual activations (V1). The top-down influence of spatial activation after presentation of the cue weakly inhibits other locations in the input and influences object recognition. Stimuli activate one of the 7 distinct regions of the one-dimensional input array, the lower row position of the cue stimulus and the upper row the target. The cue appears at the input layer and is copied to V1, its position is recognized at the Spat2 level, and it is identified by the Obj2 layer in an invariant way. Each Spat and Obj unit represents 3 adjacent locations in the V1 layer. The Output units activate when the system settles (activity of object units exceeds 0.6) and is used to measure reaction times.

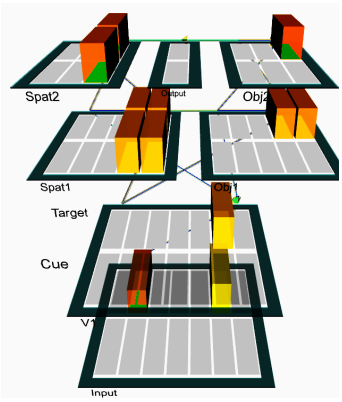

In case of autism or ADHD there are no lesions, but there may be many changes in the strength of connections and in neural properties. In the language of neurodynamics spontaneous trapping of attention is due to strong attractors, patterns that are difficult to break. This strength of a given attractor may be studied by initializing the system in the attractor basin, adding different amount of noise and observing the

dwell time before transition is made. Changes in various network and neuron control model parameters may lead to similar behaviors. To avoid too many graphs and tables only qualitative summary is given below.

- Relative strength of the influence of spatial attention on object recognition (Spat=>Obj) reduced to zero makes neutral and valid trial times identical, but leaves the 20 ms difference between valid and invalid cases (top-down modulation effect). Increase of this relative strength leads to slow increase of all reaction times but the 20 ms differences are fairly stable between 1-5, with tendency to increase the invalid/neutral difference to 30 ms and slightly decrease valid/neutral trials difference.
- Decrease of relative strength of the influence of V1 layer on parietal spatial attention areas leads to sharp increase in the invalid case, attention remains fixed for a longer time on the cue. Decrease of this parameter by half (from 2 to 1) increases the time difference between neutral and invalid trials 3 times. This may be one of the contributing factors to the problems with attention shifts in autism. While local circuits are well developed there is some evidence that distal connections are weak and functional connections in autism have been linked to a variant of MET gene that shows high expression in the occipital cortex [9].
- Relative strength of recurrent connections in Spat1 and Spat2 layers has no influence on valid trials, weak influence on neutral, but stronger local connections significantly increase reaction times of invalid trials. This mechanism may also contribute to long delays in shifts of attention. TSC gene can cause local overconnectivity in the sensory cortices (visual, auditory) reducing normal neuronal pruning.
- Self-regulatory dynamics of neurons depends on complex processes, changing conductance of the ion channels (voltage-dependent gates). Changing time constants for increases in intracellular calcium that builds up slowly as function of activation in all neurons has big influence on all reaction times, reducing the difference between all types of trials to zero and making reactions for valid trials slower than for invalid and neutral. These processes depend on many types of ion channels and thus many genes are implicated.
- Increase of maximal conductance for excitatory channels (mostly glutamatergic synaptic sodium channels) above 1 leads to sharp two-fold increase in invalid trial reaction times, and small decrease of the normal/valid trials reaction times; decrease of this parameter slows down reaction times but keeps the differences roughly constant.
- Increasing maximal conductance for inhibitory channels quickly increases the invalid trials reaction times without much change in results for other trials; decrease has relatively small effect.
- Parameter regulating maximal conductance of leak (potassium K^+) channels changed from 0.001 to 1.3 has relatively small influence on reaction times, but beyond this value all reaction times become much longer and similar to each other. Strong leak currents decrease membrane potentials and activation of neurons takes longer time. The KCNK the two-pore-domain potassium leak channels are the main suspect in this case.

- Noise may be included either as the variance of the value of membrane potential, or variance of the synaptic input. The first type of noise makes the switch from invalid cue to the target position faster, decreasing sharply the time for invalid trials and to a smaller degree also other times. Attractors become weaker and transitions may be made faster. Synaptic noise has the opposite effect, competition between competing patterns becomes stronger and achieving the threshold for decision takes longer. High density of synapses will contribute to the "synaptic bombardment" type of noise.

The network used in Posner experiments is too simple to show full range of attractor network behavior. However, these conclusions have been confirmed by more complex models of normal reading and dyslexia, and of simple repetitive movements [6,10] implemented also in the Emergent simulator. The first of these models [10] has 6 layers, representing information about orthography (6x8 units), phonology (14x14 units) and semantics (10x14 units), connected to each other via intermediate (hidden) layers of neurons. Full connectivity between each adjacent layer is assumed, with recurrent self-connections within each of these layers. The qualitative dependence of the spontaneous shifts of attention has been analyzed calculating dwell times, confirming results of the PVOT study described above. Because of the lack of space the motor cortex model is not described here [6].

Accommodation (neural fatigue) has strong influence on synchronization. Lack of accommodation with strong excitations and recurrent connections enables creation of persistent patterns, or forming deep basins of attraction with small variance, trapping neurodynamics for a long time. Attention remains focused on one concept for unusually long time, as it happens in autism spectrum disorders (ASD). Strong accommodation leads to weak synchronization, shallow basins of attractors, rapid jumps from one basin to another, with short dwell times. Such behavior is typical in case of Attention Deficit Hyperactivity Disorder (ADHD).

4 Conclusions: Towards Neuropsychiatric Phenomics

This short overview of some of the mechanisms that may contribute to deregulation of attention shows that ADHD and ASD disorders should form a continuum, with typical adults displaying some autistic or ADHD traits. Different types of neurons, connections, regions of the brain may be affected as a result of multiple etiologies, including metabolic and immune system deregulation, or prenatal and early childhood exposure to various drugs, chemicals, pollutants and stressful environmental factors.

There are over 20 theories of autism spectrum disorders [11–13], including minicolumnopathy, mirror neuron system (MNS), underconnectivity theory, empathizing–systemizing theory, executive dysfunction theory, function over/under-connectivity theories. Most of these theories mistake symptoms for real causes. Attention is at the foundation for development of all cognitive functions. Developmental perspective is needed to understand how deep basins of attraction in localized sensory cortex may lead to impoverished stimulation of the brain with complex percepts, the underconnectivity of distal connections, poor development of the theory of mind and mirror system network, lack of disengagement by the default mode network. Increased number of genomic research results in huge genomic data bases, and together with other

phenotypes gives hope for more precise diagnosis that will cluster similar ASD cases. Allen Human Brain Atlas of gene expression data contains 63 candidate genes (449 variants) that have been implicated in autism, and 292 genes that contribute to "other neurodegenerative disease" (as of August, 2013). Various perturbations of neural properties, at the synaptic, membrane and general connectivity level, may lead to very similar behavioral symptoms disturbing neural synchronization. Brain atlas helps to find links between gene mutations, regions in which expression occurs, results of computational simulations and likely disorders that results from such damage to the cell structure. Many such links have been identified in this article. Strong expression in occipital lobe (except occipital pole) of normal subjects is noted for MET, KCNS1, NRXN1, SLC6A10P, NPY1R genes. It has already been suggested that MET has influence on neural circuits relevant to the processing of complex visual stimuli, including faces. KCNS gene family coding two-pore delayed-rectifier potassium voltage-gated ion channels, that has strong expression in sensory areas, fits very well to our prediction that the leak channels may be responsible for slowing down in ASD or speeding up attention shifts in ADHD. Thus although these two disease have never been linked at least some subtypes may result from different mutations of the same genes that damage specific leak channels in a different way.

Following consequences of deep attractor basins are expected:

- deficits in attention disengagement;
- overspecific memory for images, words, numbers, facts, movements, except for impaired memory for olfaction [14], because many types of neural receptors important in olfaction are dysfunctional in ASD and ADHD;
- strong focus on single stimulus, easy absorption, possible sensory overstimulation by weak signals trapping the network in deep attractor, while stimuli of the same modality, like loud alarming sounds or visual signals, are ignored;
- in motor cortex repetitive cyclic sequential attractors or precise sliding attractors;
- problems with generalization and associations;
- integration of perception from different modalities are impaired, resulting in underconnectivity between distant brain areas;
- echolalia, repeating words without understanding (no associations);
- nouns will be acquired more readily than abstract words and verbs;
- fast changing stimuli, including faces, may be ignored because time is needed to escape from current deep attractor state, gaze will tend to focus on simple stimuli;
- play will be schematic, play with other children avoided in favor of simple toys.

Is it possible to compensate for some ASD dysfunctions by training the network, will it lead to faster attention shifts? Perhaps slow broadening of attractor basins will be a good strategy, or using transcranial magnetic stimulation to add noise that will push the network out of deep attractor. In case of ADHD psychostimulants such as Methylphenidate are used. This may be surprising but shallow basins of attractors are made deeper (neural synchronization becomes stronger) as a result of higher activation, and stimulants reduce reuptake of dopamine and norepinephrine, and thus increase activation of excitatory receptors.

There is a great need for comprehensive theories that can provide common language in the space between genetics, molecular biology and behavioral psychiatry. The development of computational models of attention, visual recognition, simple movements, and associations of concepts, models that elucidate mechanisms leading to symptoms of mental disorders, is at the very center of neuropsychiatric phenomics.

Acknowledgements. This research was supported by the Polish Ministry of Science and National Education (MNiSW/N519 5781 38).

References

1. Consortium for Neuropsychiatric Phenomics, http://www.phenomics.ucla.edu
2. Duch, W.: Brains and Education: Towards Neurocognitive Phenomics. In: Reynolds, N., Webb, M., Sysło, M.M., Dagiene, V. (eds.) Learning While We are Connected, vol. 3, pp. 12–23
3. Spivey, M.: The continuity of mind. OUP, New York (2007)
4. O'Reilly, R.C., Munakata, Y.: Computational Explorations in Cognitive Neuroscience Understanding the Mind by Simulating the Brain. MIT Press, Cambridge (2000), Emergent Neural Network Simulation System http://grey.colorado.edu/emergent/
5. Grossberg, S.: Neural Dynamics of Autistic Behaviors: Learning, Recognition, Attention, Emotion, Timing, and Social Cognition. In: Patel, V.B., Preedy, V.R., Martin, C.R. (eds.) The Comprehensive Guide to Autism, Springer, London (2012)
6. Dobosz, K., Mikołajewski, D., Wójcik, G.M., Duch, W.: Simple Cyclic Movements as a Distinct Autism Feature–Computational Approach. Computer Science (in print, 2013)
7. Dobosz, K., Duch, W.: Understanding neurodynamical systems via Fuzzy Symbolic Dynamics. Neural Networks 23, 487–496 (2010)
8. Duch, W., Dobosz, K.: Visualization for understanding of neurodynamical systems. Cognitive Neurodynamics 5(2), 145–160 (2011)
9. Judson, M.C., Eagleson, K.L., Levitt, P.: A new synaptic player leading to autism risk: Met receptor tyrosine kinase. J. of Neurodevelopmental Disorders 3(3), 282–292 (2011)
10. Duch, W., Nowak, W., Meller, J., Osiński, G., Dobosz, K., Mikołajewski, D., Wójcik, G.M.: Computational approach to understanding autism spectrum disorders. Computer Science 13(2), 47–61 (2012)
11. Just, M.A., Keller, T.A., Malave, V.L., Kana, R.K., Varma, S.: Autism as a neural systems disorder: A theory of frontal-posterior underconnectivity. Neuroscience and Biobehavioral Reviews 36, 1292–1313 (2012)
12. Rudie, J.D., et al.: Autism-Associated Promoter Variant in MET Impacts Functional and Structural Brain Networks. Neuron 75(5), 904–915 (2012)
13. Zimmerman, A.W. (ed.): Autism: Current theories and evidence. Humana Press (2008)
14. Galle, S.A., Courchesne, V., Mottron, L., Frasnelli, J.: Olfaction in the autism spectrum. Perception 42(3), 341–355 (2013)

Observer-Based Adaptive Output Feedback Control for Nonaffine Nonlinear Discrete-Time Systems Using Reinforcement Learning

Xiong Yang, Derong Liu, and Ding Wang

The State Key Laboratory of Management and Control for Complex Systems
Institute of Automation, Chinese Academy of Sciences, Beijing 100190, China
{xiong.yang,derong.liu,ding.wang}@ia.ac.cn

Abstract. This paper develops an observer-based direct adaptive output feedback control for a class of multi-input-multi-out nonaffine nonlinear discrete-time systems with unknown bounded disturbances. A neural network (NN) observer is designed to estimate unavailable system states. Then, under the framework of reinforcement learning, two other NNs are used to generate the optimal control signal and estimate the cost function, respectively. Based on Lyapunov's direct method, the stability of the closed-loop system is verified. Moreover, all signals involved are guaranteed to be uniformly ultimately bounded. Finally, an example is provided to demonstrate the effectiveness of the present approach.

Keywords: Output feedback control, Reinforcement learning, Neural network, Nonaffine system, Multi-input-multi-output.

1 Introduction

Controller designs for nonlinear systems have drawn intensive attention for several decades [1–3]. The objective of designing a controller is generally considered as finding stable controllers for nonlinear systems. Nevertheless, stability is only a bare minimum requirement in a system design. The control scheme are often required to guarantee the stability of the closed-loop system, while keeping the prescribed cost function as small as possible.

Reinforcement learning (RL) is a class of approaches employed in machine learning to methodically revise the actions of an agent based on responses from its environment [4]. It has been extensively employed to obtain optimal control for nonlinear systems [5–7]. Compared with traditional adaptive dynamic programming approaches [8], there is no prescribed behavior or training model proposed to RL schemes. Recently, RL-based feedback controllers for nonlinear systems have been presented in [9–11]. Nevertheless, none of these literatures consider adaptive control laws for unknown nonaffine nonlinear systems. The difficulty of designing adaptive controllers for nonaffine nonlinear systems lies in the output of this type of systems depends nonlinearly on the control signal. In this case, feedback linearization methods cannot be implemented. To the best of our knowledge, there are rather few literature about this field.

M. Lee et al. (Eds.): ICONIP 2013, Part I, LNCS 8226, pp. 631–638, 2013.
© Springer-Verlag Berlin Heidelberg 2013

In this paper, we develop an observer-based direct adaptive output feedback control for nonaffine nonlinear discrete-time (DT) systems with unknown bounded disturbances. An NN observer is employed to estimate unavailable system states. Then, two other NNs are utilized to derive the optimal control and the cost function, respectively. Based on Lyapunov's direct method, the stability of the closed-loop system is verified. Furthermore, all signals involved are guaranteed to be uniformly ultimately bounded (UUB).

The rest of the paper is organized as follows. Preliminaries are proposed in Section 2. An observer-actor-critic architecture is developed in Section 3. Stability analysis is presented in Section 4. Simulation results are given in Section 5. Finally, several conclusions are drawn in Section 6.

2 Preliminaries

Consider the mnth-order MIMO nonaffine nonlinear DT system described by

$$\begin{aligned} x_1(k+1) &= x_2(k) \\ x_2(k+1) &= x_3(k) \\ &\vdots \\ x_n(k+1) &= F\big(x(k), u(x(k))\big) + d(k) \\ y(k) &= x_1(k) \end{aligned} \tag{1}$$

where state $x(k) = [x_1^{\mathsf{T}}(k), x_2^{\mathsf{T}}(k), \ldots, x_n^{\mathsf{T}}(k)]^{\mathsf{T}} \in \mathbb{R}^{mn}$, and each $x_i(k) \in \mathbb{R}^m$, $i = 1, \ldots, n$. The control $u(x(k)) \in \mathbb{R}^m$ is a continuous function with respect to $x(k)$. Denote $\upsilon(k) = u(x(k))$. $d(k) \in \mathbb{R}^m$ is an unknown disturbance but bounded by $d_M > 0$, i.e., $\|d(k)\| \leq d_M$. $F\big(x(k), \upsilon(k)\big) \in \mathbb{R}^m$ is an unknown nonaffine function with $F(0, 0) = 0$.

Assumption 1. $\det\big\{\partial F(x(k), \upsilon(k))/\partial \upsilon(k)\big\} \neq 0$ *for* $\forall\big(x(k), \upsilon(k)\big) \in \Omega \times \mathbb{R}^m$ *with a compact region* $\Omega \subset \mathbb{R}^{mn}$.

Assumption 2. *Let the desired system trajectory be* $x_d(k) = [x_{1d}^{\mathsf{T}}(k), \ldots, x_{nd}^{\mathsf{T}}(k)]^{\mathsf{T}}$. $x_{id}(k)$ *is arbitrary selected and satisfies that* $x_{id}(k+1) = x_{(i+1)d}(k)$, $i = 1, 2, ..., n$. *The desired trajectory* $x_d(k)$ *is bounded by a known smooth function over* Ω.

Objective of Control: The control objective is to design an observer-based direct adaptive feedback controller such that the system output $y(k)$ follows a given bounded reference signal $y_d(k)$ to a small neighborhood of the origin, while ensuring that all the signals involved in the closed-loop system are UUB.

3 Observer-Actor-Critic Architecture

3.1 NN State Observer

Since only system output $y(k) = x_1(k)$ is measurable and the rest of system states are unavailable for feedback, we employ a single-hidden layer NN to estimate $x_i(k)$ $(i = 2, \ldots, n)$. From (1), the state observer is developed by

$$\begin{aligned} \hat{x}_1(k) &= \hat{x}_2(k-1) \\ \hat{x}_2(k) &= \hat{x}_3(k-1) \\ &\vdots \\ \hat{x}_n(k) &= \hat{F}\big(\hat{x}(k-1), \upsilon(k-1)\big) \end{aligned} \tag{2}$$

with $\hat{x}(k) = [\hat{x}_1^{\mathsf{T}}(k), \hat{x}_2^{\mathsf{T}}(k), \ldots, \hat{x}_n^{\mathsf{T}}(k)]^{\mathsf{T}}$, and $\hat{F}\big(\hat{x}(k-1), \upsilon(k-1)\big) = \hat{w}_o^{\mathsf{T}}(k-1)\sigma_o\big(\nu_o^{\mathsf{T}}\hat{z}(k-1)\big)$, where ν_o and $\hat{w}_o$ are NN weights for the input layer to the hidden layer and the hidden layer to the output layer with suitable dimensions separately, and $\hat{z}(k-1) = [\hat{x}^{\mathsf{T}}(k-1)\ u^{\mathsf{T}}(k-1)]^{\mathsf{T}}$. Since inner weights are generally initialized randomly and kept constant, for briefly, $\sigma\big(\nu_o^{\mathsf{T}}\hat{z}(k-1)\big)$ is denoted by $\sigma\big(\hat{z}(k-1)\big)$. Define $\tilde{x}_i(k) = \hat{x}_i(k) - x_i(k), \quad i = 1, \ldots, n$.

Suppose that $F\big(x(k-1), \upsilon(k-1)\big)$ can accurately be represented by NNs as

$$F\big(x(k-1), \upsilon(k-1)\big) = w_o^{\mathsf{T}}\sigma_o\big(z(k-1)\big) + \varepsilon_1(k-1) \tag{3}$$

where w_o is the ideal NN weight and $z(k-1) = [x^{\mathsf{T}}(k-1)\ u^{\mathsf{T}}(k-1)]^{\mathsf{T}}$. By using (2) and (3), we have

$$\begin{aligned} \tilde{x}_n(k) = \tilde{w}_o^{\mathsf{T}}(k-1)\sigma_o\big(\hat{z}(k-1)\big) + w_o^{\mathsf{T}}\sigma_o\big(\tilde{z}(k-1)\big) \\ - \varepsilon_1(k-1) - d(k-1) \end{aligned}$$

where $\tilde{w}_o(k-1) = \hat{w}_o(k-1) - w_o$, and $\sigma_o\big(\tilde{z}(k-1)\big) = \sigma_o\big(\hat{z}(k-1)\big) - \sigma_o\big(z(k-1)\big)$. Then, the observer NN weights update law is given by

$$\hat{w}_o(k+1) = \hat{w}_o(k) - l_o\sigma_o(\hat{z}(k))\Big(\hat{w}_o^{\mathsf{T}}(k)\sigma_o(\hat{z}(k)) + \mu\tilde{x}_1(k)\Big)^{\mathsf{T}} \tag{4}$$

where $0 < l_o < 1$ is the learning rate, and $\mu > 0$ is a design parameter. The observer error $\tilde{x}_1(k)$ is defined as $\tilde{x}_1(k) = \hat{x}_1(k) - y(k)$.

3.2 Controller Design Approach

From Assumption 2 and system (1), we can obtain $x_{(i+1)d}(k) = y_d(k+i)$, $i = 0, \cdots, n-1$. Then, the tracking error can be developed by

$$e_i(k) = y_d(k+i) - y(k+i) = x_{(i+1)d}(k) - \hat{x}_{(i+1)}(k) \tag{5}$$

where $i = 0, \ldots, n-1$. From system (1), we have

$$y(k+n) = \eta\upsilon(k) + \big[F\big(\hat{x}(k), \upsilon(k)\big) - \eta\upsilon(k)\big] + d(k) \tag{6}$$

where $\eta > 0$. Let $h(\hat{x}(k), \upsilon(k)) = F\big(\hat{x}(k), \upsilon(k)\big) - \eta\upsilon(k)$, and

$$\upsilon(k) = \big(\upsilon_s(k) - \upsilon_a(k)\big)/\eta \tag{7}$$

where $\upsilon_s(k)$ is used to stabilize linearized error dynamics, and $\upsilon_a(k)$ is designed to approximate the unknown nonlinear term $h(\hat{x}(k), \upsilon(k))$ via a single-hidden layer NN. From (6) and (7), we get

$$y(k+n) = \upsilon_s(k) + \big[h\big(\hat{x}(k), \upsilon(k)\big) - \upsilon_a(k)\big] + d(k).$$

Meanwhile, $\upsilon_a(k)$ and $\upsilon_s(k)$ are proposed as

$$\begin{cases} \upsilon_a(k) = \hat{h}\big(\hat{x}(k), \upsilon(k)\big) \\ \upsilon_s(k) = y_d(k+n) + \lambda_1 e_{n-1}(k) + \cdots + \lambda_n e_0(k) \end{cases} \tag{8}$$

where $\hat{h}(\hat{x}(k), \upsilon(k))$ approximates $h(x(k), \upsilon(k))$. $e_{n-1}(k), \ldots, e_0(k)$ are the delayed values of $e_n(k)$, and $\lambda_1, \ldots, \lambda_n$ are constant matrices selected such that $|z^n + \lambda_1 z^{n-1} + \cdots + \lambda_n|$ is stable. Define the approximation error

$$\tilde{h}\big(\hat{x}(k), \upsilon(k)\big) = \hat{h}\big(\hat{x}(k), \upsilon(k)\big) - h\big(\hat{x}(k), \upsilon(k)\big).$$

Lemma 1. *Assume that the tracking error $e_i(k)$ is defined as in (5) and $\upsilon_s(k)$ is proposed as in (8). Then, the error dynamics is developed by*

$$\boldsymbol{e}(k+1) = \tilde{A}\boldsymbol{e}(k) + \tilde{B}\big[\tilde{h}\big(\hat{x}(k), \upsilon(k)\big) - d(k)\big] \tag{9}$$

where

$$\boldsymbol{e}(k) = \big[e_0^{\mathsf{T}}(k), \ldots, e_{n-1}^{\mathsf{T}}(k)\big]^{\mathsf{T}} \quad \tilde{A} = A \otimes I_m \quad \tilde{B} = B \otimes I_m$$
$$A = \begin{bmatrix} 0 & 1 & \cdots & 0 \\ \vdots & \vdots & & \vdots \\ -\lambda_n & -\lambda_{n-1} & \cdots & -\lambda_1 \end{bmatrix} \qquad B = \begin{bmatrix} 0 \\ \vdots \\ 1 \end{bmatrix}.$$

Denote

$$G\big(\hat{x}(k), \upsilon_a(k), \upsilon_s(k)\big) = h\left(\hat{x}(k), \frac{\upsilon_s(k) - \upsilon_a(k)}{\eta}\right) - \upsilon_a(k) = 0. \tag{10}$$

Theorem 1. *Assume that the following matrix inequality holds:*

$$\eta\kappa_1 I_m \le \frac{\partial F\big(\hat{x}(k), \upsilon(k)\big)}{\partial \upsilon(k)} \le \eta\kappa_2 I_m$$

where $0 < \kappa_1 < \kappa_2 \le 2$. Then, there exist a compact set $\Omega' \subset \Omega$ and the unique $\upsilon_a(k)\big(\hat{x}(k), \upsilon_s(k)\big)$ satisfies (10) for $\forall\ \big(\hat{x}(k), \upsilon_s(k)\big) \in \Omega' \times U$, where $U \subset \mathbb{R}^m$ is a compact set.

3.3 Critic NN and Weight Update Law

Define an utility function $r(k) = [r_1(k), \ldots, r_m(k)] \in \mathbb{R}^m$ with

$$r_i(k) = \begin{cases} 0, & \text{if } \|\bar{e}_i(k)\| \le \theta \\ 1, & \text{if } \|\bar{e}_i(k)\| > \theta \end{cases} \quad i = 1, \ldots, m$$

where $\bar{e}(k) = \boldsymbol{\lambda}^{\mathsf{T}} \boldsymbol{e}(k) \in \mathbb{R}^m$, and $\bar{e}_i(k)$ is the ith element of the vector $\bar{e}(k)$. $\theta > 0$ is a predefined threshold. The cost function $J(k) \in \mathbb{R}^m$ is given by

$$J(k) = \alpha^N r(k+1) + \alpha^{N-1} r(k+2) + \cdots + \alpha^{k+1} r(N) \tag{11}$$

with $0 < \alpha \le 1$ a design parameter, and N the final instant time. The prediction error for the critic NN is described by

$$e_c(k) = \hat{J}(k) - \alpha \hat{J}(k-1) + \alpha^{N+1} r(k)$$

where $\hat{J}(k)$ is an approximation of $J(k)$. The critic NN output is given by

$$\hat{J}(k) = \hat{w}_c^{\mathsf{T}}(k) \sigma\big(v_c^{\mathsf{T}} \hat{x}(k)\big) = \hat{w}_c^{\mathsf{T}}(k) \sigma_c\big(\hat{x}(k)\big) \tag{12}$$

where $\hat{w}_c(k)$ and v_c are defined similar to observe NNs. By the gradient-based adaptation method, we can obtain the weight update rule for the critic NN as

$$\begin{aligned} \hat{w}_c(k+1) = \hat{w}_c(k) - l_c \sigma_c\big(\hat{x}(k)\big) \Big(& \hat{w}_c^{\mathsf{T}}(k) \sigma_c\big(\hat{x}(k)\big) + \alpha^{N+1} r(k) \\ & - \alpha \hat{w}_c^{\mathsf{T}}(k-1) \sigma_c\big(\hat{x}(k-1)\big) \Big)^{\mathsf{T}} \end{aligned} \tag{13}$$

where $l_c > 0$ is the learning rate for the critic NN.

3.4 Action NN and Weight Update Law

The prediction error for the action NN is defined as

$$e_a(k) = \hat{J}(k) - J_d(k) + \tilde{h}\big(\hat{x}(k), y_d(k)\big). \tag{14}$$

Since $J_d(k)$ is generally considered to be zero, (14) can be rewritten as

$$e_a(k) = \hat{J}(k) + \tilde{h}\big(\hat{x}(k), y_d(k)\big).$$

The action NN output is given by

$$\hat{h}(k) = \hat{w}_a^{\mathsf{T}}(k) \sigma_a\big(v_a^{\mathsf{T}} \bar{z}(k)\big) = \hat{w}_a^{\mathsf{T}}(k) \sigma_a\big(\bar{z}(k)\big) \tag{15}$$

where $\hat{h}(k)$ stands for $\hat{h}(\hat{x}(k), y_d(k))$, $\hat{w}_a(k)$ and v_a are defined similar to observe NNs, and $\bar{z}(k) = [\hat{x}^{\mathsf{T}}(k) \; y_d^{\mathsf{T}}(k)]^{\mathsf{T}}$. Suppose $h(k) = w_a^{\mathsf{T}} \sigma_a\big(\bar{z}(k)\big) + \varepsilon_2(k)$, where $h(k)$ denotes $h\big(\hat{x}(k), y_d(k)\big)$. Define $\tilde{w}_a(k) = \hat{w}_a(k) - w_a$. Then, the function approximation error can be developed by

$$\tilde{h}(k) = \tilde{w}_a^{\mathsf{T}}(k) \sigma_a\big(\bar{z}(k)\big) - \varepsilon_2(k).$$

By using the gradient-based adaptation approach and (9), we can derive the weight update law for the action NN as

$$\hat{w}_a(k+1) = \hat{w}_a(k) - l_a \sigma_a\big(\bar{z}(k)\big)\Big(\hat{w}_c^{\mathsf{T}}(k)\sigma_c\big(\hat{x}(k)\big) + \tilde{B}^{\mathsf{T}}\big(\boldsymbol{e}(k+1) - \tilde{A}\boldsymbol{e}(k)\big) + d(k)\Big)^{\mathsf{T}}.$$

However, $d(k)$ is typically unavailable. Hence, the ideal case of $d(k)$ is taken, i.e., $d(k) = 0$. Then, the weight update rule for the action NN beceomes

$$\hat{w}_a(k+1) = \hat{w}_a(k) - l_a \sigma_a\big(\bar{z}(k)\big)\Big(\hat{w}_c^{\mathsf{T}}(k)\sigma_c\big(\hat{x}(k)\big) + \tilde{B}^{\mathsf{T}}\big(\boldsymbol{e}(k+1) - \tilde{A}\boldsymbol{e}(k)\big)\Big)^{\mathsf{T}}. \tag{16}$$

where $l_a > 0$ is the learning rate for the action NN.

4 Stability Analysis

This section is to present our main results based on Lyapunov's direct method.

Assumption 3. *There exists a unique positive definite matrix $P \in \mathbb{R}^{mn\times mn}$ satisfying the Lyapunov equation*

$$\tilde{A}^T P \tilde{A} - P = -\beta I_{mn} \tag{17}$$

where β is a positive constant.

Theorem 2. *Consider the nonaffine nonlinear system described by (1). Let Assumptions 1–3 hold. Take the control input for system (1) as (7) with (8) and the critic NN (12), as well as the action NN (15). Moreover, let the weight update law for the critic NN and the action NN be (13) and (16), respectively. Then, the tracking error $\boldsymbol{e}(k)$, the observer error $\tilde{x}_1(k)$, the NN estimated weights $\xi_o(k)$, $\xi_a(k)$, and $\xi_c(k)$ are all UUB, provided the following conditions hold:*

$$(a)\ \ 0 < l_o\|\sigma_o(k)\|^2 < 1 \qquad (b)\ \ 0 < l_c\|\sigma_c(k)\|^2 < 1$$

$$(c)\ \ 0 < l_a\|\sigma_a(k)\|^2 < 1 \qquad (d)\ \ 0 < \alpha < \frac{1}{\sqrt{1+\delta^2}}$$

$$(e)\ \ \beta > 1,\ 0 < \mu < \frac{1}{1+\delta^2}$$

where $\delta^2 \neq 0$, μ, α, and β are parameters given by (4), (11), and (17), respectively.

5 Simulation Results

Consider the nonaffine nonlinear DT system described by

$$\begin{aligned} x_{11}(k+1) &= x_{21}(k) \quad x_{12}(k+1) = x_{22}(k) \\ x_{21}(k+1) &= 0.4x_{22}(k) - 0.3\cos(x_{21}(k)) + 0.2u_1(k) - 0.1\tanh(u_2(k)) \\ x_{22}(k+1) &= 0.1x_{11}(k) + 0.2u_2(k) - 0.3\sin^2(x_{22}(k))u_1(k) \\ y_1(k) &= x_{11}(k) \quad y_2(k) = x_{12}(k) \end{aligned} \tag{18}$$

where $x_1(k) = [x_{11}(k)\ x_{12}(k)]^{\mathsf{T}}$, $x_2(k) = [x_{21}(k)\ x_{22}(k)]^{\mathsf{T}}$, $u(k) = [u_1(k)\ u_2(k)]^{\mathsf{T}}$, and $y(k) = [y_1(k)\ y_2(k)]^{\mathsf{T}}$. The objective is to control $y(k)$ of system (18) to track the prescribed trajectory $y_d(k) = \left[2.6\sin(k\pi/200)\ 3\cos(k\pi/180)\right]^{\mathsf{T}}$. The design parameters are as follows: $\lambda_1 = 1$, $\lambda_2 = 0.25$, $\eta = 2$, $\delta = 1$, $\alpha = 0.7$, $\beta = 2$, $\theta = 8 \times 10^{-3}$, $l_a = 0.01$, and $l_c = 0.001$. The initial state $x_0 = [1\ 0.31\ 1\ 0.31]^{\mathsf{T}}$.

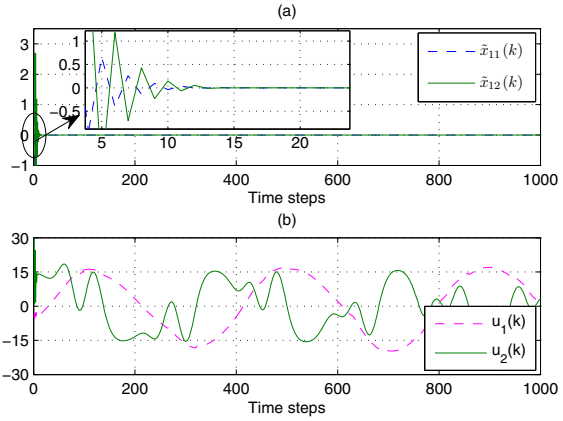

Fig. 1. (a) State estimation errors $\tilde{x}_{11}(k)$ and $\tilde{x}_{12}(k)$ (b) Control input $u(k)$

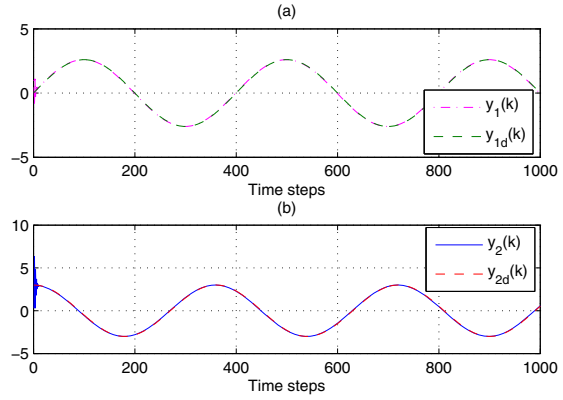

Fig. 2. (a) Trajectories of $y_1(k)$ and $y_{1d}(k)$ (b) Trajectories of $y_2(k)$ and $y_{2d}(k)$

By (18), we know that $\partial F\big(x(k), u(k)\big)/\partial u(k)$ is positive definite, and $0.01I_2 \leq \det\big[\partial F(x(k), u(k))/\partial u(k)\big] \leq 0.07I_2$. The structures of the state observer NN, the action NN, and the critic NN are 6-30-2, 6-30-2, and 4-24-2, respectively. The computer simulation results are presented in Figs. 1–2. From simulation results, we find that the state observer estimates system states very well. Meanwhile, it is also shown that the tracking errors converge to a small neighborhood of zero. Furthermore, all signals involved are bounded.

6 Conclusion

In this paper, an observer-based direct adaptive NN output feedback control scheme is developed for a class of unknown nonaffine nonlinear DT systems. Based on the proposed control scheme, all signals involved are guaranteed to be UUB, while keeping the closed-loop system stable. In addition, the computer simulation results indicate that the derived controller can successfully track a reference trajectory.

Acknowledgments. This work was supported in part by the National Natural Science Foundation of China under Grants 61034002, 61233001, and 61273140.

References

1. Chen, F.C., Khalil, H.K.: Adaptive control of a class of nonlinear discrete-time systems using neural networks. IEEE Transactions on Automatic Control 40(5), 791–801 (1995)
2. Leu, Y.G., Wang, W.Y., Lee, T.T.: Observer-based direct adaptive fuzzy-neural control for nonaffine nonlinear systems. IEEE Transactions on Neural Networks 16(4), 853–861 (2005)
3. Li, T., Li, R., Wang, D.: Adaptive neural control of nonlinear MIMO systems with unknown time delays. Neurocomputing 78(1), 83–88 (2012)
4. Sutton, R.S., Barto, A.G.: Reinforcement Learning–An Introduction. MIT Press, Cambridge (1998)
5. Lewis, F.L., Vrabie, D.: Reinforcement learning and adaptive dynamic programming for feedback control. IEEE Circuits and Systems Magazine 9(3), 32–50 (2009)
6. Liu, D., Yang, X., Li, H.: Adaptive optimal control for a class of continuous-time affine nonlinear systems with unknown internal dynamics. Neural Computing and Applications, doi: 0.1007/s00521-012-1249-y
7. Lewis, F.L., Liu, D.: Reinforcement Learning and Approximate Dynamic Programming for Feedback Control. Wiley-IEEE Press, New Jersey (2013)
8. Werbos, P.J.: Beyond Regression: New Tools for Prediction and Analysis in the Behavioral Sciences. Ph.D thesis, Harvard University (1974)
9. He, P., Jagannathan, S.: Reinforcement learning-based output feedback control of nonlinear systems with input constraints. IEEE Transactions on Systems, Man, and Cybernetics, Part B: Cybernetics 35(1), 150–154 (2005)
10. Yang, L., Si, J., Tsakalis, K.S., Rodriguez, A.A.: Direct heuristic dynamic programming for nonlinear tracking control with filtered tracking error. IEEE Transactions on Systems, Man, and Cybernetics, Part B: Cybernetics 19(6), 1617–1622 (2009)
11. Yang, Q., Jagannathan, S.: Reinforcement learning controller design for affine nonlinear discrete-time systems using approximators. IEEE Transactions on Systems, Man, and Cybernetics, Part B: Cybernetics 42(2), 377–390 (2012)

Author Index